NASA Conference Publication 3134
Part 1

LDEF — 69 Months in Space

First Post-Retrieval Symposium

Edited by
Arlene S. Levine
NASA Langley Research Center
Hampton, Virginia

Proceedings of a symposium sponsored by the National Aeronautics and Space Administration, Washington, D.C., and held in Kissimmee, Florida
June 2-8, 1991

NASA
National Aeronautics and
Space Administration
Office of Management
Scientific and Technical
Information Program
1991

Foreword

On July 20, 1989, President George Bush charted a new course for human exploration of space:

> ". . . a long-range continuing commitment. First, for the coming decade -- for the 1990's -- Space Station *Freedom*, our next critical step in all our space endeavors. And for the next century, back to the moon, back to the future, and this time, back to stay; then a journey into tomorrow, a journey to another planet -- a manned mission to Mars. Each mission should and will lay the groundwork for the next."

The Long Duration Exposure Facility (LDEF) is providing critical technology for future spacecraft, including Space Station *Freedom,* and thus plays a major role in the President's vision of human exploration of space.

LDEF was carried into orbit in April 1984 by the Space Shuttle *Challenger.* The 11-ton satellite contained 57 experiments to assess the effects of the space environment, i.e., ionizing radiation, meteoroids, cosmic dust, and high altitude atomic oxygen on materials and mechanical, electronic, optical, and living systems. In January 1990, after 69 months in low Earth orbit, LDEF was retrieved by the Space Shuttle *Columbia* and returned to Earth. The retrieval occurred 57 months after it was originally planned, due in part to the *Challenger* tragedy. The 69 months in space provided experimenters the unique opportunity to sample and measure the space environment over a longer time period than originally planned.

The 57 LDEF experiments were returned to the Principal Investigators and their science teams for analyses and interpretation. In June 1991, over 400 LDEF researchers and data users met in Kissimmee, Florida for the First LDEF Post-Retrieval Symposium. The papers presented contained important new information about space environments and their impact on materials, systems, and biology. This publication contains the material presented at the symposium, categorized by subject:

LDEF Mission and Induced Environments
Space Environments - *Ionizing Radiation*
Space Environments - *Meteoroid and Debris*
Space Environmental Effects - *Materials*
Space Environmental Effects - *Systems*
Space Environmental Effects - *Biology*
Space Environmental Effects - *Microgravity*
The Future

During the symposium Sally A. Little, NASA Headquarters, chaired the **LDEF Mission and Induced Environments** session; William L. Quaide, NASA Heaquarters,

chaired the **Space Environments** - *Meteoroid and Debris* session; Thomas W. Crooker, NASA Headquarters, and Bland A. Stein, NASA Langley Research Center, co-chaired the **Space Environmental Effects** - *Materials* session; Judith H. Ambrus, NASA Headquarters, and P. Rex Miller, W.J. Schaefer and Associates co-chaired the **Space Environmental Effects** - *Systems* session; and James L. Jones, NASA Langley Research Center chaired the session called **Others**.

Some presentations in these documents underwent a title change; others were combined with two or three presentations; two were not presented orally. However, all oral presentations are represented in written form. Where full-length papers were unavailable, the abstracts have been reprinted. All papers were reviewed for technical content as well as form.

We wish to thank the contributors, as well as the reviewers of these papers. We also wish to thank Dr. William H. Kinard, without whose vision and persistence, there would not be an LDEF project or the valuable data it has collected.

The LDEF Science Office plans to organize and conduct two additional symposia, one in San Diego in June 1992 and another in 1993. The proceedings from these two symposia will be published as NASA Conference Publications.

We believe that the LDEF data reported in this three-part document will make important contributions to charting the new course for the exploration of space.

Use of manufacturers' trade names in this publication does not constitute an official endorsement of such products or manufacturers, either expressed or implied, by the National Aeronautics and Space Administration.

Arlene S. Levine
LDEF Science Office
NASA Langley Research Center

CONTENTS

FOREWORD iii

PART 1

LDEF MISSION AND INDUCED ENVIRONMENTS

LONG DURATION EXPOSURE FACILITY--A GENERAL OVERVIEW 3
Robert L. O'Neal and E. Burton Lightner

LONG DURATION EXPOSURE FACILITY (LDEF) SPACE ENVIRONMENTS OVERVIEW 49
William H. Kinard and Glenna D. Martin

PINHOLE CAMERAS AS SENSORS FOR ATOMIC OXYGEN IN ORBIT;
APPLICATION TO ATTITUDE DETERMINATION OF THE LDEF 61
Palmer N. Peters and John C. Gregory

USE OF THE LONG DURATION EXPOSURE FACILITY'S THERMAL MEASUREMENT
SYSTEM FOR THE VERIFICATION OF THERMAL MODELS 69
William M. Berrios

MEASURED SPACE ENVIRONMENTAL EFFECTS TO LDEF DURING RETRIEVAL 85
Carl R. Maag and W. Kelly Linder

PARTICLE TYPES AND SOURCES ASSOCIATED WITH LDEF 101
E. R. Crutcher and W. W. Wascher

MIGRATION AND GENERATION OF CONTAMINANTS FROM LAUNCH THROUGH 121
RECOVERY: LDEF CASE HISTORY
E. R. Crutcher, L. S. Nishimura, K. J. Warner and W. W. Wascher

QUANTIFICATION OF CONTAMINANTS ASSOCIATED WITH LDEF 141
E. R. Crutcher, L. S. Nishimura, K. J. Warner and W. W. Wascher

MOLECULAR FILMS ASSOCIATED WITH LDEF 155
E. R. Crutcher and K. J. Warner

ORGANIC CONTAMINATION OF LDEF 179
Gale A. Harvey

SPACE ENVIRONMENTS - IONIZING RADIATION

SUMMARY OF IONIZING RADIATION ANALYSIS ON THE LONG DURATION
EXPOSURE FACILITY 199
T. A. Parnell

PREDICTION OF LDEF IONIZING RADIATION ENVIRONMENT 213
John W. Watts, T. A. Parnell, James H. Derrickson, T. W. Armstrong
and E. V. Benton,

GAMMA RADIATION SURVEY OF THE LDEF SPACECRAFT 225
G. W. Phillips, S. E. King, R. A. August, J. C. Ritter, J. H. Cutchin, P. S. Haskins,
J. E. McKisson, D. W. Ely, A. G. Weisenberger, R. B. Piercey and T. Dybler

THE INTERACTIONS OF ATMOSPHERIC COSMOGENIC RADIONUCLIDES WITH SPACECRAFT SURFACES 237
J. C. Gregory, G. J. Fishman, B. A. Harmon and T. A. Parnell

SURFACE ACTIVATION OF CONCORDE BY ^{7}BE 249
P. R. Truscott, C. S. Dyer and J. C. Flatman

CHARGED PARTICLE ACTIVATION STUDIES ON THE SURFACE OF LDEF SPACECRAFT 255
Ilhan Olmez, Forrest Burns and Paul L. Sagalyn

RADIOACTIVITIES OF LONG DURATION EXPOSURE FACILITY (LDEF) MATERIALS: BAGGAGE AND BONANZAS 257
Alan R. Smith and Donna L. Hurley

MEASUREMENTS OF INDUCED RADIOACTIVITY IN SOME LDEF SAMPLES 271
C. E. Moss and R. C. Reedy

GAMMA-RAY SPECTROMETRY OF LDEF SAMPLES AT SRL 287
Willard G. Winn

INDUCED RADIOACTIVITY IN LDEF COMPONENTS 301
B. A. Harmon, G. J. Fishman, T. A. Parnell and C. E. Laird

THERMOLUMINESCENT DOSIMETRY FOR LDEF EXPERIMENT M0006 313
J. Y. Chang, D. Giangano, T. Kantorcik, M. Stauber, and L. Snead

RADIATION EXPOSURE OF LDEF: INITIAL RESULTS 325
E. V. Benton, A. L. Frank, E. R. Benton, I. Csige, T. A. Parnell and J. W. Watts, Jr.

CHARGED PARTICLE LET-SPECTRA MEASUREMENTS ABOARD LDEF 339
I. Csige, E. V. Benton, A. L. Frank, L. A. Frigo, E. R. Benton, T. A. Parnell and J. W. Watts, Jr.

IONIZING RADIATION CALCULATIONS AND COMPARISONS WITH LDEF DATA 347
T. W. Armstrong, B. L. Colborn and J. W. Watts, Jr.

LDEF GEOMETRY/MASS MODEL FOR RADIATION ANALYSES 361
B. L. Colborn and T. W. Armstrong

THE LDEF ULTRA HEAVY COSMIC RAY EXPERIMENT 367
D. O'Sullivan, A. Thompson, J. Bosch, R. Keegan, K.-P. Wenzel, A. Smit and C. Domingo

PRELIMINARY RESULTS FROM THE HEAVY IONS IN SPACE EXPERIMENT 377
James H. Adams, Jr., Lorraine P. Beahm and Allan J. Tylka

HEAVY ION MEASUREMENT ON LDEF 393
R. Beaujean, D. Jonathal and W. Enge

SPACE ENVIRONMENTS - METEOROID AND DEBRIS

LARGE CRATERS ON THE METEOROID AND SPACE DEBRIS IMPACT EXPERIMENT 399
Donald H. Humes

STUDY OF COSMIC DUST PARTICLES ON BOARD LDEF: THE FRECOPA EXPERIMENTS AO138-1 AND AO138-2 419
J. C. Mandeville and Janet Borg

METEOROID/SPACE DEBRIS IMPACTS ON MSFC LDEF EXPERIMENTS 435
Miria Finckenor

HYPERVELOCITY IMPACT MICROFOIL PERFORATIONS IN THE LEO SPACE ENVIRONMENT (LDEF, MAP AO023 EXPERIMENT) 443
J. A. M. McDonnell and T. J. Stevenson

METEOROID AND DEBRIS SPECIAL INVESTIGATION GROUP DATA ACQUISITION PROCEDURES 459
Thomas H. See, Martha K. Allbrooks, Dale R. Atkinson, Clyde A. Sapp, Charles G. Simon, and Mike E. Zolensky

METEOROID AND DEBRIS SPECIAL INVESTIGATION GROUP PRELIMINARY RESULTS: SIZE-FREQUENCY DISTRIBUTION AND SPATIAL DENSITY OF LARGE IMPACT FEATURES ON LDEF 477
Thomas H. See, Friedrich Hörz, Michael E. Zolensky, Martha K. Allbrooks, Dale R. Atkinson and Charles G. Simon

PRELIMINARY ANALYSIS OF LDEF INSTRUMENT AO187-1 "CHEMISTRY OF MICROMETEOROIDS EXPERIMENT" 487
Friedrich Hörz, Ronald P. Bernhard, Jack Warren, Thomas H. See, Donald E. Brownlee, Mark R. Laurance, Scott Messenger and Robert B. Peterson

SIMS CHEMICAL ANALYSIS OF EXTENDED IMPACT FEATURES FROM THE TRAILING EDGE PORTION OF EXPERIMENT AO187-2 503
Sachiko Amari, John Foote, Charles Simon, Pat Swan, Robert M. Walker, Ernst Zinner, Elmar K. Jessberger, Gundolf Lange and Frank Stadermann

IDE SPATIO-TEMPORAL IMPACT FLUXES AND HIGH TIME-RESOLUTION STUDIES OF MULTI-IMPACT EVENTS AND LONG-LIVED DEBRIS CLOUDS 517
J. Derral Mulholland, S. Fred Singer, John P. Oliver, Jerry L. Weinberg, William J. Cooke, Nancy L. Montague, Jim J. Wortman, Philip C. Kassel and William H. Kinard

ION MICROPROBE ELEMENTAL ANALYSES OF IMPACT FEATURES ON INTERPLANETARY DUST EXPERIMENT SENSOR SURFACES 529
Charles G. Simon, Jerry L. Hunter, Jim J. Wortman and Dieter P. Griffis

LDEF IMPACT CRATERS FORMED BY CARBON-RICH IMPACTORS: A PRELIMINARY REPORT 549
T. E. Bunch, F. Radicati di Brozolo, Ronald H. Fleming, David W. Harris, Don Brownlee and Terrence W. Reilly

DYNAMIC (COMPUTER) MODELLING OF THE PARTICULATE ENVIRONMENT: TRANSFORMATIONS FROM THE LDEF REFERENCE FRAME TO DECODE GEOCENTRIC AND INTERPLANETARY POPULATIONS 565
J. A. M. McDonnell and K. Sullivan

LDEF DATA CORRELATION TO EXISTING NASA DEBRIS ENVIRONMENT MODELS 567
Dale R. Atkinson, Martha K. Allbrooks and Alan J. Watts

DERIVING THE VELOCITY DISTRIBUTION OF METEOROIDS FROM THE MEASURED METEOROID IMPACT DIRECTIONALITY ON THE VARIOUS LDEF SURFACES 569
Herbert A. Zook

M AND D SIG PROGRESS REPORT: LABORATORY SIMULATIONS OF LDEF IMPACT FEATURES 581
Friedrich Hörz, R. P. Bernhard, T. H. See, D. Atkinson and M. Allbrooks

PRELIMINARY MICROMETEOROID AND DEBRIS EFFECTS ON LDEF THERMAL CONTROL SURFACES 583
Martha K. Allbrooks, Dale R. Atkinson, Thomas See and Fred Hörz

THE INTERSTELLAR GAS EXPERIMENT 585
D. L. Lind, J. Geiss, F. Bühler and O. Eugster

COLOR PHOTOGRAPHS 595

AUTHOR INDEX 605

*** PART 2**

SPACE ENVIRONMENTAL EFFECTS - MATERIALS

PRELIMINARY FINDINGS OF THE LDEF MATERIALS SPECIAL INVESTIGATION GROUP 617
Bland A. Stein and H. Gary Pippin

ATOMIC OXYGEN AND ULTRAVIOLET RADIATION MISSION TOTAL EXPOSURES FOR LDEF EXPERIMENTS 643
R. J. Bourassa, J. R. Gillis and K. W. Rousslang

EFFECTS OF SPACE ENVIRONMENT ON STRUCTURAL MATERIALS 663
C. Miglionico, C. Stein, R. Roybal, R. Robertson, L.E. Murr, S. Quinones, J. Rivas, B. Marquez, A.H. Advani, W.W. Fisher and R. Arrowood

MEASUREMENT OF THE 0^{18} TO 0^{16} ISOTOPE RATIO FOR CHARACTERIZING OXIDE SURFACE LAYERS ON LDEF SAMPLES 679
Paul L. Sagalyn

CHEMICAL CHARACTERIZATION OF SELECTED LDEF POLYMERIC MATERIALS 687
Philip R. Young and Wayne S. Slemp

CHARACTERIZATION OF POLYMER FILMS RETRIEVED FROM LDEF 705
Alan Letton, Neil I. Rock, Kevin D. Williams, Thomas W. Strganac and Allan Farrow

MEASUREMENTS OF EROSION CHARACTERISTICS FOR METAL AND POLYMER SURFACES USING PROFILOMETRY 723
Ligia C. Christl, John C. Gregory and Palmer N. Peters

LONG DURATION EXPOSURE FACILITY (LDEF) PRELIMINARY FINDINGS: LEO SPACE EFFECTS ON THE SPACE PLASMA - VOLTAGE DRAINAGE EXPERIMENT 737
Brian K. Blakkolb, James Y. Yaung, Kelly A. Henderson, William W. Taylor and Lorraine E. Ryan

INTERACTIONS OF ATOMIC OXYGEN WITH MATERIAL SURFACES IN LOW EARTH ORBIT: PRELIMINARY RESULTS FROM EXPERIMENT AO114 753
J. C. Gregory, L. Christl, G. N. Raikar, J. J. Weimer, R. Wiser and P. N. Peters

EFFECTS ON LDEF EXPOSED COPPER FILM AND BULK 755
Palmer N. Peters, John C. Gregory, Ligia C. Christl and Ganesh N. Raikar

* Part 2 is presented under separate cover.

LDEF EXPERIMENT AO034: ATOMIC OXYGEN STIMULATED OUTGASSING 763
Roger C. Linton, Rachel R. Kamenetzky, John M. Reynolds and Charles L. Burris

ATOMIC OXYGEN UNDERCUTTING OF LDEF ALUMINIZED-KAPTON MULTILAYER INSULATION 781
Kim K. deGroh and Bruce A. Banks

PRELIMINARY RESULTS FOR LDEF/HEPP THERMAL CONTROL SAMPLES 797
Lonny Kauder

ATOMIC OXYGEN INTERACTIONS WITH FEP TEFLON AND SILICONES ON LDEF 801
Bruce A. Banks, Joyce A. Dever, Linda Gebauer and Carol M. Hill

VACUUM ULTRAVIOLET (VUV) RADIATION - INDUCED DEGRADATION OF FLUORINATED ETHYLENE PROPYLENE (FEP) TEFLON ABOARD THE LONG DURATION EXPOSURE FACILITY (LDEF) 817
David E. Brinza, A. E. Stiegman, Paul R. Staszak, Eric G. Laue and Ranty H. Liang

SPACE ENVIRONMENTAL EFFECTS ON SILVERED TEFLON THERMAL CONTROL SURFACES 831
C. S. Hemminger, W. K. Stuckey and J. C. Uht

RESULTS OF EXAMINATION OF SILVERED TEFLON FROM THE LONG DURATION EXPOSURE FACILITY 847
Ken Rousslang, Russ Crutcher and Gary Pippin

SILVER TEFLON BLANKET: LDEF TRAY C-08 861
E. R. Crutcher, L. S. Nishimura, K. J. Warner and W. W. Wascher

PRELIMINARY INVESTIGATIONS INTO UHCRE THERMAL CONTROL MATERIALS 875
François Levadou, Mike Froggatt, Martin Rott and Eberhard Schneider

INITIAL MATERIALS EVALUATION OF THE THERMAL CONTROL SURFACES EXPERIMENT (S0069) 899
Donald R. Wilkes, M. John Brown, Leigh L. Hummer and James M. Zwiener

UNUSUAL MATERIALS EFFECTS OBSERVED ON THE THERMAL CONTROL SURFACES EXPERIMENT (S0069) 919
James M. Zwiener, Kenneth A. Herren, Donald R. Wilkes, Leigh Hummer and Edgar R. Miller

EFFECTS OF LOW EARTH ORBIT ENVIRONMENT ON THE LONG DURATION EXPOSURE FACILITY THERMAL CONTROL COATINGS 935
Thomas R. Sampair and William M. Berrios

SPACECRAFT THERMAL CONTROL COATINGS 945
Jean-Claude Guillaumon and Alain Paillous

LONG DURATION EXPOSURE FACILITY EXPERIMENT M0003-5 THERMAL CONTROL MATERIALS 961
Charles J. Hurley

RESULTS OF EXAMINATION OF THE A276 WHITE AND Z306 BLACK THERMAL CONTROL PAINT DISKS FLOWN ON LDEF 975
Johnny L. Golden

ION BEAM TEXTURED AND COATED SURFACES EXPERIMENT (IBEX) 989
Michael J. Mirtich, Sharon K. Rutledge, Nicholas Stevens, Raymond Olle and James Merrow

ELLIPSOMETRIC STUDY OF OXIDE FILMS FORMED ON LDEF METAL SAMPLES 1005
W. Franzen, J. S. Brodkin, L. C. Sengupta and P. L. Sagalyn

SPACE ENVIRONMENTAL EFFECTS ON THE INTEGRITY OF CHROMIC ACID ANODIZED COATINGS 1023
Walter L. Plagemann

M0003-10: LDEF ADVANCED COMPOSITES EXPERIMENT 1041
Gary L. Steckel and Tuyen D. Le

LDEF - SPACE ENVIRONMENTAL EFFECTS ON MATERIALS: COMPOSITES AND SILICONE COATINGS 1055
Brian C. Petrie

PRELIMINARY RESULTS FROM THE LDEF/UTIAS COMPOSITE MATERIALS EXPERIMENT 1057
R. C. Tennyson, G. E. Mabson, W. D. Morison and J. Kleiman

LONG DURATION EXPOSURE FACILITY EXPERIMENT M0003 DEINTEGRATION/ FINDINGS AND IMPACTS 1073
M. J. Meshishnek, S. R. Gyetvay, and C. H. Jaggers

SURVEY OF RESULTS FROM THE BOEING MODULES ON THE M0003 EXPERIMENT ON LDEF 1109
H. G. Pippin, Owen Mulkey, Juris Verzemnieks, Emmett Miller, Sylvester Hill and Harry Dursch

RESULTS FROM ANALYSIS OF BOEING COMPOSITE SPECIMENS FLOWN ON LDEF EXPERIMENT M0003 1115
Pete E. George and Sylvester G. Hill

HIGH-TOUGHNESS GRAPHITE/EPOXY COMPOSITE MATERIAL EXPERIMENT 1143
David K. Felbeck

EFFECTS OF LDEF FLIGHT EXPOSURE ON SELECTED POLYMER MATRIX RESIN COMPOSITE MATERIALS 1149
Wayne S. Slemp, Philip R. Young, William G. Witte, Jr. and James Y. Shen

EFFECT OF SPACE ENVIRONMENT ON COMPOSITE MATERIALS AND THERMAL COATINGS (AO138-9) 1163
Michel Parcelier and Jean Pierre Assié

EFFECT OF SPACE EXPOSURE OF SOME EPOXY MATRIX COMPOSITES ON THEIR THERMAL EXPANSION AND MECHANICAL PROPERTIES (AO138-8) 1175
Heinrich Jabs

MECHANICAL PROPERTIES OF SILICATE GLASSES EXPOSED TO A LOW-EARTH ORBIT 1187
David E. Wiedlocher, Dennis S. Tucker, Ron Nichols and Donald L. Kinser

PATTERNS OF DISCOLORATION AND OXIDATION BY DIRECT AND SCATTERED FLUXES ON LDEF, INCLUDING OXYGEN ON SILICON 1189
A. R. Frederickson, R. C. Filz, F. J. Rich and P. Sagalyn

COLOR PHOTOGRAPHS 1201

AUTHOR INDEX 1205

* PART 3

SPACE ENVIRONMENTAL EFFECTS - SYSTEMS

SYSTEMS SPECIAL INVESTIGATION GROUP OVERVIEW 1217
James B. Mason, Harry Dursch and Joel Edelman

SPACE AGING OF SOLID ROCKET MATERIALS 1225
Dean M. Lester, Leon L. Jones, R. B. Smalley, Jr. and R. Neil Ord

EFFECTS OF THE SPACE ENVIRONMENT ON SPACE-BASED RADAR PHASED-ARRAY ANTENNA; STATUS AND PRELIMINARY OBSERVATIONS (LDEF EXPERIMENT AO133) 1227
J. B. Whiteside, D. Giangano, R. L. Heuer, E. Kamykowski, M. Kesselman, W. D. Rooney, R. Schulte and M. Stauber

AN OVERVIEW OF THE FIRST RESULTS ON THE SOLAR ARRAY MATERIALS PASSIVE LDEF EXPERIMENT (SAMPLE), AO171 1241
Ann F. Whitaker and Leighton E. Young

EXPERIMENT M0003-4 ADVANCED SOLAR CELL AND COVERGLASS ANALYSIS, AN OVERVIEW 1255
Terry M. Trumble

PRELIMINARY ANALYSES OF WL EXPERIMENT # 701, SPACE ENVIRONMENT EFFECTS ON OPERATING FIBER OPTIC SYSTEMS 1257
E. W. Taylor, J. N. Berry, A. D. Sanchez, R. J. Padden and S. P. Chapman

LDEF FIBER OPTIC EXPOSURE EXPERIMENT NO. S-0109 1283
A. R. Johnston, L. A. Bergman and R. Hartmayer

OPTICAL PERFORMANCE OF EXPOSED SOLAR CELL COVERS 1299
Thomas H. Allen, Bryant P. Hichwa, Steven R. Selee, Jerry Dodds and Greg S. Long

RULED AND HOLOGRAPHIC DIFFRACTION GRATINGS EXPERIMENT (AO138-5) 1301
Francis Bonnemason

POST-FLIGHT CHARACTERIZATION OF OPTICAL SYSTEM SAMPLES, THERMAL CONTROL SAMPLES, AND DETECTORS FROM LDEF EXPERIMENT M0003, SUB-EXPERIMENTS 6 AND 13 1315
Randall R. Hodgson, James N. Holsen and Robert A. Drerup, Jr

LDEF ACTIVE OPTICAL SYSTEM COMPONENTS EXPERIMENT 1317
M. D. Blue

EFFECTS OF LONG-DURATION EXPOSURE ON OPTICAL SYSTEM COMPONENTS 1327
Gale A. Harvey

EFFECTS OF LONG TERM EXPOSURE ON OPTICAL SUBSTRATES AND COATINGS (S0050-2) 1341
John Vallimont and Keith Havey

VACUUM DEPOSITED OPTICAL COATINGS EXPERIMENT 1343
Jean Charlier

SPACE ENVIRONMENTAL EFFECTS ON COATED OPTICS 1361
T. M. Donovan, J. M. Bennett, R. Z. Dalbey, D. K. Burge and S. Gyetvay

* Part 3 is presented under separate cover.

CONTAMINATION OF OPTICAL SURFACES IN EARTH ORBIT 1377
Donald L. Kinser, Robert A. Weller, M. H. Mendenhall, D. E. Wiedlocher, R. Nichols, D. Tucker and A. Whitaker

DURABILITY EVALUATION OF PHOTOVOLTAIC BLANKET MATERIALS EXPOSED ON LDEF TRAY (S1003) 1379
Sharon K. Rutledge and Raymond M. Olle

ADVANCED PHOTOVOLTAIC EXPERIMENT, S0014: PRELIMINARY FLIGHT RESULTS AND POST-FLIGHT FINDINGS 1395
David J. Brinker, John R. Hickey and David A. Scheiman

EVALUATION OF LDEF EXPERIMENT S1002 1405
L. Preuss

LDEF SP-HVDE (SPACE PLASMA-HIGH VOLTAGE DRAINAGE EXPERIMENT) POST-FLIGHT RESULTS: LEAKAGE CURRENT AND DISCHARGE 1419
J. Y. Yaung, W. C. Wong, B. K. Blakkolb, L. E. Ryan, J. E. Chedotte and W. W. L. Taylor

LONG DURATION EXPOSURE FACILITY (LDEF) LOW TEMPERATURE HEAT PIPE EXPERIMENT PACKAGE (HEPP) FLIGHT RESULTS 1431
Roy McIntosh, Craig McCreight and Patrick J. Brennan

LONG DURATION EXPOSURE FACILITY LOW-TEMPERATURE HEAT PIPE EXPERIMENT PACKAGE POWER SYSTEM RESULTS 1441
Smith E. Tiller and David Sullivan

RESULTS FROM THE LDEF/AO076 CASCADED VARIABLE CONDUCTANCE HEATPIPE EXPERIMENT 1455
Michael G. Grote

TRANSVERSE FLAT PLATE HEAT PIPE EXPERIMENT 1467
David Shular

EXPOSURE TO SPACE RADIATION OF HIGH-PERFORMANCE INFRARED MULTILAYER FILTERS AND MATERIALS TECHNOLOGY EXPERIMENT (AO056) 1477
Gary J. Hawkins, John S. Seeley and Roger Hunneman

PASSIVE EXPOSURE OF EARTH RADIATION BUDGET EXPERIMENT COMPONENTS LDEF EXPERIMENT AO147: POST-FLIGHT EXAMINATIONS AND TESTS 1493
John R. Hickey

TRANSMITTANCE MEASUREMENTS OF ULTRAVIOLET AND VISIBLE WAVELENGTH FILTERS FLOWN ABOARD LDEF 1511
Thomas A. Mooney and Ali Smajkiewicz

RADIATION SENSITIVITY OF QUARTZ CRYSTAL OSCILLATORS EXPERIMENT FOR THE LONG DURATION EXPOSURE FACILITY (LDEF) 1523
J. S. Ahearn and J. D. Venables

LDEF ELECTRONIC SYSTEMS: SUCCESSES, FAILURES AND LESSONS 1533
E. A. Miller, L. K. Brooks, C. J. Johnson, J. L. Levorsen, O. R. Mulkey, D. C. Porter and D. W. Smith

EFFECT OF SPACE EXPOSURE ON PYROELECTRIC INFRARED DETECTORS 1547
James B. Robertson

LDEF MECHANICAL SYSTEMS 1549
W. Steve Spear and Harry W. Dursch

ON-ORBIT COLDWELDING FACT OR FRICTION? 1565
Harry Dursch and Steve Spear

THERMAL CONTROL SURFACES EXPERIMENT - FLIGHT SYSTEMS PERFORMANCE 1577
Donald R. Wilkes, Leigh L. Hummer and James M. Zwiener

FRENCH COOPERATIVE PASSIVE PAYLOAD (FRECOPA) SYSTEM RESULTS 1593
Christian Durin

EFFECTS OF ULTRA-VACUUM AND SPACE ENVIRONMENT ON CONTACT OHMIC RESISTANCE LDEF EXPERIMENT AO138-11 1607
Jean-Pierre Assié and Alfred Perotto

MICROWELDING (OR COLD-WELDING) OF VARIOUS METALLIC MATERIALS UNDER THE ULTRA-VACUUM LDEF EXPERIMENT AO138-10 1613
Jean Pierre Assié and Eric Condé

SPACE ENVIRONMENTAL EFFECTS - BIOLOGY

SEEDS IN SPACE EXPERIMENT 1625
Jim A. Alston

SPACE EXPOSED EXPERIMENT DEVELOPED FOR STUDENTS (SEEDS) (P0004-2) 1635
Doris K. Grigsby and Nelson J. Ehrlich

SURVIVAL OF EPIPHYTIC BACTERIA FROM SEED STORED ON THE LONG DURATION EXPOSURE FACILITY (LDEF) 1637
Andrew C. Schuerger, Bret L. Norman and Joseph A. Angelo, Jr.

FIRST BIOLOGICAL AND DOSIMETRIC RESULTS OF THE FREE FLYER BIOSTACK EXPERIMENT AO015 ON LDEF 1639
G. Reitz, H. Bücker, R. Facius, G. Horneck, M. Schäfer, J. U. Schott, J. Bayonove, R. Beaujean, E. V. Benton, M. Delpoux, C. Heilmann, W. Heinrich, A. R. Kranz, H. Planel, Y. Gasset, G. Gaubin, G. Portal, E. H. Graul, W. Rüther, E. Schopper, C. A. Tobias and T. C. Yang

PRELIMINARY TOTAL DOSE MEASUREMENTS ON LDEF 1643
G. Reitz

TOTAL DOSE EFFFECTS (TDE) OF HEAVY IONIZING RADIATION IN FUNGUS SPORES AND PLANT SEEDS - PRELIMINARY INVESTIGATIONS - 1651
A. R. Kranz, M. W. Zimmermann, R. Stadler, K. E. Gartenbach and M. Pickert

PRELIMINARY RESULTS OF THE ARTEMIA SALINA EXPERIMENTS IN BIOSTACK ON LDEF 1661
E. H. Graul, W. Rüther and C. O. Hiendl

LONG-TERM EXPOSURE OF BACTERIAL SPORES TO SPACE 1667
G. Horneck, H. Bücker and G. Reitz

SPACE ENVIRONMENTAL EFFECTS - MICROGRAVITY

RESULTS OF THE TTF-TCNQ AND THE CALCIUM CARBONATE CRYSTALLIZATION ON THE LONG DURATION EXPOSURE FACILITY 1675
Kjeld Flemming Nielsen and M. David Lind

THE FUTURE

THE ROLE OF THE LONG DURATION EXPOSURE FACILITY IN THE DEVELOPMENT OF SPACE SYSTEMS 1687
Sally A. Little

RETRIEVABLE PAYLOAD CARRIER--NEXT GENERATION LONG DURATION EXPOSURE FACILITY 1691
Arthur T. Perry

COLOR PHOTOGRAPHS 1701

AUTHOR INDEX 1703

PART 1

LDEF MISSION AND INDUCED ENVIRONMENTS

LONG DURATION EXPOSURE FACILITY--A GENERAL OVERVIEW

Robert L. O'Neal
Lockheed Engineering and Sciences Company
Hampton, VA 23666
Phone: 804/864-3792, Fax: 804/864-8094

E. Burton Lightner
NASA Langley Research Center
Hampton, VA 23665-5225
Phone: 804/864-3772, Fax: 804/864-3769

INTRODUCTION

The Long Duration Exposure Facility (LDEF) is a large, low-cost, reusable, unmanned, free-flying spacecraft which accommodates technology, science, and applications experiments for long-term exposure to the space environment. The LDEF was designed and built by the NASA Langley Research Center (LaRC) for NASA's Office of Aeronautics and Space Technology. Specifically, the LDEF was designed to transport experiments into space via the Space Shuttle, to free fly in Earth orbit for an extended period, and be retrieved on a later Shuttle flight allowing experiments to be returned to Earth for postflight analysis in the laboratory. The LDEF with a full complement of experiments was placed in Earth orbit in April 1984 by the Space Shuttle Challenger and retrieved from orbit in January 1990 by the Space Shuttle Columbia.

A general overview of the LDEF, its mission, systems, experiments, and operations is covered in the following sections. Excerpts from various NASA documents (refs. 1 to 7) are extensively used.

MISSION SUMMARY

The Space Transportation System STS 41-C mission whose objective was to deploy LDEF and then retrieve, repair, and redeploy the Solar Maximum Mission satellite, was launched from Kennedy Space Center (KSC) on April 6, 1984. The LDEF was deployed in a 28.5° inclination essentially circular orbit of 257 nautical mile altitude by the Shuttle Challenger on April 7, 1984. It was planned to retrieve LDEF about 1 year later; however, Shuttle manifesting problems and later the Challenger accident together resulted in an extensive delay. The LDEF was retrieved some 69 months after launch at an altitude of 179 nautical miles. Only about 2 months of orbit lifetime remained at the time of retrieval.

On the second day of the deployment mission the remote manipulator system (RMS) was used to activate the experiment initiate system (EIS) while LDEF was still berthed in the cargo bay. After confirmation that the initiate was successful, the RMS was used to lift the LDEF from the cargo bay and place it in a preferred attitude for release and free flight. Gravity gradient torques maintained the LDEF in a position in which the axis of minimum moment of inertia was aligned with the local vertical. This resulted in one end of LDEF always pointing towards the center of the Earth and one end always pointing out in space. Coupling torques resulting from small preestablished differences in the transverse moments of inertia stabilized the facility about the longitudinal axis and resulted in one of the 12 sides always pointing forward in the direction of

travel. This established a leading side and a trailing side of LDEF. Figure 1 illustrates the LDEF orientation in orbit.

A viscous magnetic rate damper was mounted on the LDEF interior structure to accelerate the damping of any unwanted motions at the time of deployment. A photograph of the damper after deintegration is shown in figure 2. After deployment (see fig. 3) no unwanted motions were apparent. The LDEF remained in a stable attitude during the 69-month mission.

The LDEF retrieval mission was launched on January 9, 1990. Rendezvous with the LDEF was completed and LDEF retrieved on January 12. Figure 4 is a photograph of the LDEF minutes before capture by the RMS. To establish the condition of experiments prior to the reentry the flight crew used the RMS to maneuver the LDEF for an extensive photographic survey of the LDEF and each experiment tray. The LDEF was then berthed and the remainder of the mission completed with a landing at Edwards Air Force Base on January 20. The Columbia with LDEF still in the cargo bay was ferried from Edwards to KSC, landing on January 26. The LDEF was removed from the orbiter in the Orbiter Processing Facility (OPF) and moved to the Spacecraft Assembly and Encapsulation Facility II (SAEF II) for several months of deintegration operations. Operations were completed and the facility structure was placed in storage at KSC in mid-May 1990.

LDEF DESCRIPTION

Structure

The LDEF is a 12-sided, 14-foot diameter, 30-foot long aluminum open grid frame. The structure is configured with 72 equal-size rectangular openings on the sides and 14 openings on the ends (six on the Earth-facing end, and eight on the space-facing end) for mounting experiment trays. The LDEF total weight is approximately 21,400 pounds, made up of structure and systems weight of 8,900 pounds and trays and experiment weight of 12,500 pounds.

A photograph of the LDEF structure mounted on the LDEF Assembly and Transportation System (LATS) is shown in figure 5. The LATS is a combination work and transportation platform system which can rotate the LDEF for the installation and for removal of experiment trays.

The LDEF structural configuration and the identification of experiment locations is shown in figure 6. The 12 sides of the structure are numbered rows 1 through 12 in a clockwise direction when facing the end with the support beam (the Earth-facing end in orbit). The six longitudinal locations are identified alphabetically as Bay A through Bay F starting at the end with the support beam. A tray location is designated by the bay and Row A-1, B-5, F-8, etc. The Earth-facing end is designated by a G identifier and the locations have even-number clock-position identifications (G-12, G-2, G-4, G-6, G-8, and G-10). The space-facing end is designated by an H identifier, and the locations follow a similar convention (H-12, H-1, H-3, H-5, H-6, H-7, H-9, and H-11).

The LDEF is attached to the Shuttle by four trunnions and a keel pin. These are identified in figure 6. The main loads of the LDEF are transmitted through the two side support trunnions on the center ring. The keel pin on the bottom of the center ring gives lateral support. The end support beam attached to one end reacts vertical loads and has the freedom to pivot about its center pin joint.

Experiment Trays

LDEF experiments are self contained in trays that are clamped to the facility structure. The LDEF has 72 peripheral and 14 end experiment trays. To accommodate the diverse experiment requirements and characteristics, the trays are of five standard sizes: 3-inch deep, 6-inch deep, and 12-inch deep peripheral trays and 6-inch deep and 12-inch deep end trays. All of the trays are constructed of 6061-T6 anodized aluminum sheet of either 0.063 or 0.125-inch thickness, riveted to a frame made of 6061-T6 aluminum extrusions and angles. Figure 7 is a photograph of the three sizes of peripheral trays.

The structural members which form the tray bottoms provide the bolt hole pattern for attaching the experiments. These members divide the tray bottoms into six equal rectangles for the peripheral trays and four equal squares for the 14 end trays.

The rectangles establish a preferred configuration for experiments to fit either 1/6, 1/3, 2/3, or a full peripheral tray. The squares allow experiments to occupy 1/4, 1/2, 3/4, or a full end tray.

Each peripheral tray is attached to the LDEF structure by eight clamp assemblies and each end tray is attached by 12 clamp assemblies. Each clamp is held by three stainless steel bolts that fasten directly to the facility structure. A cross section of a clamp assembly and the arrangement of clamps around the trays is shown in figure 8. The clamp bolts are torqued sufficiently at tray installation to prevent motion between the tray flanges and the facility structure.

Some of the tray clamps had white dots (discs) painted on them (see fig. 9) as a visual aid in attempting to measure spacecraft motions (pitch, roll, and yaw) from video and photographs made of the LDEF immediately after deployment. The dots were made of Chemglaze A276 white paint and Chemglaze Z306 black paint.

The bottoms of all tray frames and the sides of all tray walls facing the interior of LDEF were painted with Chemglaze Z306 polyurethane black paint for thermal control.

Experiments were integrated into trays and each fully assembled tray was vibration tested to assure flight safety. Trays were shipped to KSC in sealed or protective containers and integrated with the LDEF facility under Class 100,000 clean room conditions. With the exception of an electrical connection for an on/off signal from the EIS for those trays with active electronic systems, there is only a mechanical interface between experiment trays and the LDEF facility. The experiment trays are standard NASA LaRC-qualified hardware items provided to experimenters for use in integrating their experiments.

Experiment Power and Data System

The experiment power and data system (EPDS) is designed to provide data collection and storage for experiments which have this requirement. The EPDS consists of a data processor controller assembly (DPCA), a magnetic tape module (MTM), and a primary battery source. The DPCA is hardwire programmable by the experimenter and can accommodate a variety of data collection needs. The system operates from primary batteries, and designs were selected which minimize power requirements. The system is primarily intended for the experiment which requires a number of measurements a few times per day over a 9- to 11-month period. Data from the experiment can be a mix of high- and low-level analog, and parallel and serial digital data. The MTM provides storage for about 14 megabits of data. The EPDS utilizes one 7.5-volt and one 12-volt lithium sulfide dioxide ($LiSO_2$) battery.

FL2827 TECHNICAL LIBRARY
Bldg. 7015, Room 119-A
Vandenberg AFB, CA 93437-6021

The EPDS is suitable for mounting in a 6-inch or deeper tray. A block diagram of an EPDS is shown in figure 10. Figure 11 is a photograph of an EPDS mounted in an LDEF experiment tray. Seven (7) EPDS units were flown.

Experiment Environmental Control System

The experiment environmental control canister (EECC) is an automated experiment container capable of opening and closing during the flight of LDEF. The unit provides a means of maintaining a clean, low-pressure, or inert gas environment while closed during ground operations, with the capability to open and expose the experiment to the space environment while in orbit. Five of these systems were flown on LDEF.

A photograph of the EECC assembly mounted in a tray is shown in figure 12. Each utilized 1/3 of a peripheral 6-inch deep experiment tray. An aircraft pressure fitting serves as a vacuum purge valve and allows evacuation of the closed canister by standard laboratory vacuum pumping techniques. The door of the canister uses a Viton rubber O-ring for the seal.

A timer-controller provides the logic for opening and closing the canister. The circuitry within the timer-controller contains two variable timers and a series of switches which control the electrical power for the drive motor. The LDEF EIS starts both timers which generate the signal to open the drawer and later the signal to close the drawer. An opening time of 1 hour to 4000 hours can be selected while a closing time of 2 hours to 8000 hours is available after receipt of the "on" signal from the EIS.

A 26-pin vacuum-sealed connector provides access to the experiment. The leads from the door-mounted connector mate with a flexible interconnecting cable which terminates in a 34-pin chassis connector bottled to the supporting structure of the canister. For those experiments requiring electrical access, the LDEF Project provides the mating half of the chassis connector.

Standard LDEF battery modules provide the 28-volt and 7.5-volt power required to power the EECC.

Experiment Initiate System

The EIS is that system which will send a turn on (set) or a turn off (reset) signal to each experiment when the microswitches located on the rigidize sensing grapple fixture tray are activated. Figure 13 is a schematic of the EIS system. The system consists of two 28-volt lithium sulphur dioxide batteries, four microswitches, an experiment initiate box (EIB), experiment latching relays, six status indicators, and associated wiring. A photograph of the batteries and the EIS mounted on the center ring frame of LDEF is shown in figure 14. The EIS provides for the application of primary power to electrically operate experiments by generating "set" and "reset" current pulses which operate latching relays within the experiments. The status indicators located in the C-10 tray will be white to indicate "set" (on) or black to indicate "reset" (off).

The EIS is self contained and powered by two $LiSO_2$ batteries; it has no electrical interface with the Shuttle. The EIS contains CMOS integrated circuits and discrete electronics parts. The individual "set" and "reset" current pulses to experiments are generated by separate current-limited semiconductor driver circuits. The operating sequence has a battery preconditioning pulse that preloads the battery prior to the generation of the experiment relay pulses.

The EIS is designed to be activated prior to deployment while still latched in the bay, and later after retrieval and LDEF has been latched in the bay. The initiate sequence, shown in figure 15, is started by rigidizing the end effector on the rigidize sensing grapple fixture in tray C-10. The movement of the grapple spike (center post) on rigidization operates the microswitches which energize the initiate system. This starts the $\Delta T1$ delay counter, which permits "set" pulses to be sent to the experiment initiate relays $\Delta T1$ minutes later. If the end effector is detached prior to $\Delta T1$ delay terminal count, the system deenergizes without sending any pulses. In the initiate sequence noted in figure 16, $\Delta T1 = 2.5$ minutes, and $\Delta T2 = 27$ minutes.

The system status indicators shown in figure 16 change from black to white to indicate that the EIS has been activated. The system is designed to change from white to black when the EIS is deactivated at the end of the mission. However, due to the extended mission, the EIS system was not deactivated at LDEF retrieval. This decision was based on the desire to study the EIS in the state in which it had remained for the 69-month mission.

Grapple Fixtures

The LDEF has two grapple fixtures each located in 2/3 of a 6-inch-deep experiment tray. These fixtures are standard Space Transportation System (STS) hardware items provided by the NASA Johnson Space Center (JSC) and serve as the interface between the LDEF and the Shuttle RMS. A standard grapple fixture is located in tray C-1 and a rigidize sensing grapple fixture is located in tray C-10.

The standard grapple fixture in tray C-1 is used for deployment and retrieval of the LDEF by the RMS. A photograph of this fixture is shown in figure 17. The chevron painted in the bottom of the tray is a visual aid for the STS crew to use in proximity operations for LDEF retrieval. The grapple target on either fixture is a visual aid for the RMS operator's use in positioning the end effector over the grapple spike for capture.

The rigidize sensing grapple fixture shown in figure 16 differs from the standard fixture in that the grapple spike is spring loaded and will move approximately one inch during the RMS end effector rigidization. This feature allows this fixture to be utilized as an "on"/"off" switch for the EIS. The movement of the grapple spike shaft activates microswitches in the EIS curcuit. EIS state ("on" or "off") indicators are located near the grapple target in view of the RMS wrist camera. The rigidize sensing grapple fixture is activated by the RMS while the LDEF is latched in the Shuttle cargo bay.

Batteries

The lithium/sulphur dioxide ($LiSO_2$) batteries used on LDEF were developed by LaRC to meet strict performance and safety requirements. The batteries were provided in three nominal capacities: 7.5-, 12-, and 28-volts. A 7.5-volt battery provided power to each EPDS data electronics, a 12-volt battery provided power for each tape recorder, and batteries of each capacity were used as required to power experiments. The battery cells were enclosed in hermetically sealed boxes with approximate dimensions of 6.5 in. x 11.5 in. x 2.5 in. A photograph of the components of a typical battery is shown in figure 18(a). A photograph of a typical battery installation on the back of an experiment is shown in figure 18(b).

Other types of batteries were used on two experiments. Nickel cadmium (NiCd) batteries were used on the Low Temperature Heat Pipe Experiment in tray F-12, and lithium carbon fluoride (LiCF) batteries were used on the Thermal Control Surfaces Experiment located in tray A-9.

Thermal

The LDEF thermal design is completely passive relying on surface coatings and internal heat paths for temperature control and equalization. The LDEF is a cylindrical structure which is open on the interior. The stable altitude of LDEF, one end Earth pointing and a leading and trailing side, resulted in one side facing the Sun or space for extended periods of time. All interior experiment and structure surfaces are painted with an emissivity black paint, Chemglaze Z306 (see fig. 19), to maximum radiation coupling across the facility and to minimize the thermal gradients around it.

The primary means of achieving temperature control of the average internal temperature of LDEF and of experiments is by the selection and placement of experiments and by selecting properties of thermal control coatings. Various types of experiments were placed in a checkerboard arrangement to equalize thermal properties over the surfaces of LDEF. The average internal temperature (defined as the mean average temperature of the internal surface of the experiments) is a result of the heat flow through all the experiments. The goal was to maintain this interior average temperature between 10°F and 120°F to provide temperatures compatible for batteries, electronic systems, and experiment special needs.

The experimenters thermally designed their experiments and trays within the LDEF-supplied guidelines. The experiment thermal boundary conditions are defined in terms of the external flux, the internal average radiation temperature, and the temperature of the structure where the tray is mounted. Experiments can be subjected to different thermal environments depending upon their placement on the LDEF and by the option of coupling radiatively to the interior average temperature and/or to space. The tray is considered part of the experiment and the boundary is assumed at the LDEF structure/tray interface.

The prelaunch, launch, and orbital environments in the Shuttle bay are maintained at temperatures less extreme than the free-flying on-orbit environments by means of mission constraints such as time limits and attitudes. The heat soak and resultant temperature increase after landing is maintained by preconditioning the large mass of LDEF prior to reentry and by ground purge cooling after touchdown.

Ground Support Equipment

The LDEF was mounted on its LATS for all ground operations from initial fabrication through the integration and again during deintegration at KSC. The LATS is a specially designed transportation system which allows the LDEF to be mounted on a spindle pin in each end and rotated in a "rotisserie-like" mode to provide access to the facility surface for installation, removal, and other operations involving experiments or facility systems. During transportation the LDEF is supported by its four trunnions and keel pin on the LATS in the same manner as it is supported in the Shuttle. Figure 20 shows the LDEF on the LATS after experiment deintegration. Figure 21 is a photograph of the LATS with cover installed. This was the configuration used to transport LDEF when moved from LaRC to KSC and when moved between facilities at KSC.

Various dedicated electronic equipment was used for ground operations involving batteries, EPDS, and EIS.

Special scaffolding was used in experiment integration and later deintegration in SAEF II at KSC. Tray lifting fixtures were utilized in installing/removing experiment trays from LDEF. Tray rotators were used as support systems for experiment operations and also for moving experiment trays while in SAEF II. Experiment shipping containers were designed to provide a protective environment while being shipped from experimenters' facilities to/from KSC and

LaRC. Some of these facilities are shown in photographs (figs. 22 and 23) of operations in SAEF II.

LDEF EXPERIMENTS

Table I lists the LDEF experiment complement. Figure 24 shows the location of each experiment on LDEF. These experiments addressed the fields of basic science, technology, and applications problems. They generally measured specific space environments such as meteoroids, man-made debris, and radiation levels, or, they measured the effects of the space environments on typical spacecraft hardware. A few experiments measured space environmental effects on simple forms of life (seeds, spores, and eggs) and one experiment investigated the growth of crystals in reduced gravity.

Since the LDEF and experiment hardware had remained in space for almost 6 years, it was recognized that valuable knowledge of space environmental effects could be gained from detailed examinations of each piece of retrieved hardware--not just the 10,000 test specimens that were originally planned for study by the experiment principal investigators (P.I.'s). To facilitate these expanded investigations four Special Investigation Groups (SIG's) were established: Ionizing Radiation, Materials, Meteoroid and Debris, and Systems. In addition to investigating the retrieved non-test specimen hardware, these SIG's were also chartered to generate combined data bases which will contain the data they generate and the data the experiment P.I.'s in their respective disciplines generate. These combined data bases should simplify future access to the LDEF-derived information.

There are several hundred investigators from universities, industries, and government laboratories in the United States and nine foreign countries involved with the 57 LDEF experiments. Several hundred other investigators are involved with the LDEF SIG's. Approximately 3,500,000 students around the world are also involved in the investigations of the 13,000,000 tomato seeds which flew on the LDEF.

LDEF INTEGRATION AND LAUNCH

Some LDEF experiments were integrated into trays at LaRC while others were integrated at experimenters' facilities. Each fully loaded tray was vibration tested to certify safety for flight as required by the NASA STS.

Fully loaded trays were shipped from LaRC and experimenter facilities to the KSC for integration with the LDEF. Each experiment tray was inspected, photographed, and installed on the facility and the EIS checked. The loaded LDEF was weighed and the center of gravity measured and adjusted to be within preestablished limits by adding lead ballast to the end frames of the facility structure.

The LATS was transported to the Operations and Checkout (O & C) Building, the LATS cover removed and the LDEF removed and installed in the payload transport canister. At this point all operations with LDEF were "on line" and controlled by KSC. The LDEF and other payload components were installed in the Shuttle cargo bay at the launch pad.

The STS 41-C flight was launched on April 6, 1984. Figure 25 is a photograph of the liftoff. On April 7 the RMS was used to activate the EIS and then to deploy the LDEF in a gravity gradient stabilized attitude. The LDEF was deployed in a near-circular orbit at an altitude of 257 nautical miles. Figure 26 is a photograph of the LDEF immediately after release.

RETRIEVAL AND DEINTEGRATION

Background

When LDEF was launched in April 1984 the retrieval of LDEF was scheduled for March 19, 1985, on STS 51-D. In early February shortly before the scheduled retrieval the manifest was changed to accommodate a different payload and the LDEF retrieval was delayed indefinitely. In January 1986 the Challenger accident resulted in all Shuttle flights being temporarily halted.

When it became apparent that the LDEF retrieval would be delayed, possibly by years, orbit lifetime studies were initiated at LaRC and JSC to better plan the retrieval. In August 1986 LaRC studies indicated that LDEF reentry could occur between fall 1990 and spring/summer 1991. A large uncertainty was the solar flux expected from solar cycle 22. The first post-Challenger manifest published in March 1988 showed LDEF retrieval on STS-32 in July 1989 and later that year the August 1988 manifest showed the STS-32 launch in November 1989.

In early 1988 it was becoming apparent that solar cycle 22 was more severe than normal and was resulting in decreased orbital lifetime expectancy. Lifetime predictions continued to be updated and the lifetime margin beyond expected retrieval reviewed. Concern was mounting in 1989 that any significant delay in launch of the retrieval mission would result in the loss of LDEF. In June 1989 the launch date was set for December while LDEF reentry was predicted to be late January 1990. In December problems with refurbished launch pad 39A caused the scheduled December 18 launch to be delayed. Due to the problems associated with conducting a mission over the coming holidays and some apparent relief in the orbit lifetime, the mission was rescheduled for January 8, 1990. The launch on January 8 was delayed due to weather conditions. The STS-32 LDEF retrieval mission lifted off on January 9 and LDEF was retrieved on January 12. This was some 58 months later than originally planned in 1984. At the time of retrieval it was estimated that reentry would have occurred in approximately 8 weeks. Very little margin remained.

Operational Planning

To prepare for the retrieval mission, all plans and procedures covering LDEF deintegration operations at KSC were reviewed, updated, and approved. Detailed procedures included each step involved in the deintegration of each experiment tray and the handling and operations involved with all LDEF flight hardware. Additionally, plans were made for controlling and recording environmental conditions inside the orbiter bay from the time of landing rollout at Edwards until in the OPF at KSC, and also in each KSC facility involved in subsequent LDEF operations. The length of the LDEF mission made the data from the LDEF and its experiments very sensitive and special precautions to preserve the integrity of these data became paramount in all operational planning.

In the years between deployment and retrieval all LDEF ground support equipment (GSE), with the exception of the LATS, had been returned to LaRC for storage. In the 88/89 time period, all GSE was removed from storage, inventoried, refurbished, recertified, recalibrated and shipped to KSC in preparation for deintegration operations. The LATS was removed from storage at KSC, inspected, refurbished, and made ready for use.

All GSE to be used by experimenters, SIG's, and other support groups was shipped to KSC, properly documented, cleaned, and placed in the SAEF II building where LDEF off-line deintegration operations were to occur.

Retrieval Mission

The LDEF retrieval mission (STS-32) major cargo elements consisted of a SYNCOM IV-5 deploy, the LDEF retrieval, and the IMAX camera as a mid-deck experiment. Additionally the interim operational contamination monitor (IOCM) instrument was carried in the cargo bay and served to provide quantitative data on the contamination environment experienced by the LDEF during the retrieval and reentry phases of the mission. Constraints were placed on the rendezvous operations, proximity operations, operations after capture, and return of the LDEF to KSC so the retrieved LDEF would be in the same condition it was in space at the end of the 69 months of free flight. These constraints were considered in the planning and execution of waste water dumps and propulsion/control systems burns.

The retrieval flight was launched from KSC on January 9, 1990, into a 190 x 161 nmi orbit at an inclination of 28.5^{o}. The SYNCOM was deployed on flight day 2. The orbit phasing maneuvers then began to rendezvous with the LDEF which was in a 179 nmi circular orbit. Rendezvous occurred on January 12. The proximity operations for LDEF capture are depicted in figure 27.

The capture maneuver planned was for the orbiter to pass 300 feet (was 590 feet actual) in front of LDEF's flight path, around to an inverted position approximately 300 feet (was 230 feet actual) above LDEF and to descend along the R BAR (radius vector axis) for capture. This R BAR approach minimized reaction control system (RCS) firing contamination of LDEF. The LDEF was captured, using the grapple fixture in tray C1, at 9:16 a.m. CST on orbit 50 east of Brazil. After capture and until payload bay door closing, the attitude of the Shuttle was maintained so the LDEF was always positioned in the wake of the orbiter body. This was done so as not to compromise the effects on LDEF surfaces of the atomic oxygen encountered during the 69 months of free flight.

After capture a detailed photographic survey and visual inspection of the LDEF was made. The purpose of the photo survey was to document the condition of each experiment prior to undergoing the rigors of reentry, landing, and the ferry flight back to KSC. The RMS was used to orient the LDEF so that photographs of each experiment tray and of the overall spacecraft could systematically be taken. The survey photographs were made using KODAK 5017 (Ektachrome 64) film. Original negatives of this survey are archived at JSC.

After completion of the photo survey the LDEF was berthed and the keel latched on orbit 54 at 2:40 p.m. CST over the Indian Ocean. The attitude of the Shuttle was controlled prior to the payload bay door closings at the end of the 11-day mission to thermally condition the LDEF so experiment temperatures during reentry and landing would not exceed on-orbit temperatures. After landing and roll-out at Edwards on January 20, shuttle payload bay ground purge was established to maintain the desired payload bay environment. During the 69 months in orbit the LDEF had completed 32,422 orbits of the Earth and travelled over 741,928,000 nmi.

Prior to being mated to the 747 ferry aircraft, special instrumentation was placed in the orbiter cargo bay to monitor and record environmental conditions during the ferry flight. A limited photo survey was also made of the end of LDEF facing the cargo bay hatch door.

The ferry flight which included three 747 refueling stops and an overnight stay, was completed on January 26. A photograph of the orbiter/747 aircraft just prior to touchdown at KSC is shown in figure 28. The orbiter/747 was moved to the mate/demate facility and the operation to remove the orbiter began. A photograph, figure 29, taken at the facility shows the cargo bay purge hookup. Cargo bay purge was also used at intermediate stops on the ferry flight and during the tow from the mate/demate facility to the OPF. The transfer to the OPF on January 27 started the "on-line" processing.

Shuttle-LDEF Deintegration

Inside the OPF orbiter operations were completed and the cargo bay doors opened under clean room conditions. Figure 30 is a photograph of this operation. After the doors were opened a special team made a radiation survey of the LDEF to ensure personnel safety. The removal of the LDEF from the orbiter and placement in the KSC payload transport canister is shown in figures 31 and 32. During the lift of LDEF from the orbiter a photo survey was made of all visible experiment trays. The payload canister doors were closed and made ready to leave the OPF.

The payload transport canister was moved from OPF to the O&C building. During the move, ground purge was used to control the environment inside the payload canister. Inside the O&C the LDEF was lifted from the canister and placed in the LATS. This ended "on-line" operations under control of KSC operations and began off-line operations under control of LaRC. The LATS had been cleaned to clean room conditions. A photograph of this transfer is shown in figure 33. After LDEF was placed on the LATS, the LATS cover was installed and the LATS, with a towed unit providing electrical power for the air conditioning, was moved to the SAEF II building to begin the months of LDEF deintegration.

LDEF/Experiment Deintegration

The LATS was placed in the airlock of SAEF II and its exterior cleaned. It was then moved from the airlock into SAEF II clean room. These operations are shown in figures 34 and 35. The clean room was maintained at Class 100,000 throughout the ensuing deintegration. The movement of all personnel and equipment into and out of the clean room was tightly controlled. All equipment was thoroughly cleaned before entering the clean room and all personnel wore appropriate clean room clothing. A major objective was to minimize contamination of the LDEF and experiments while in the clean room.

The LATS cover was removed and the supporting structure on the LATS was configured for the rotation mode. Figures 36 and 37 show typical operations. The LDEF was then ready for "first-look" visual inspection by the press, investigators, SIG members, and other appropriate personnel (see fig. 38).

A detailed photo survey of the LDEF and each experiment was made in parallel with the inspection. The survey was done using KODAK Vericolor III 160 film and using film identical (same lot and emulsion) as that used for the in-orbit photo survey. Strobe lighting was used. The original negatives for this survey are archived at KSC.

Radiation measurements were made by the Radiation SIG with LDEF in various rotation positions. The instrumentation was set up each evening and left overnight to collect data. The instrumentation setup is shown in figure 39.

After inspections, photo survey and radiation measurements were completed, scaffolding was rolled into place along the side and ends of LDEF to provide access for deintegration. The Meteoroid and Debris (M&D) Team made a visual survey and recorded the presence of significant meteoroid impacts on all tray clips, clip bolts, and tray flanges that would be affected by the placement of experiment covers. Protective covers were then placed on all experiment trays to protect experiment surfaces during tray removal. Tray covers were also used in other operations in SAEF II and when trays were shipped.

The deintegration of trays from the facility started on February 23 and was completed on March 27. The sequence of tray removal is shown in Table II. The correlation of tray number and experiment number is shown in Table I and figure 24.

Figure 40 shows a tray lifting fixture being bolted to a tray flange. After the tray lifting fixture was secured the clips holding the tray in place were removed. The torque required to break each clip bolt free was recorded. Figure 41 shows a typical tray after being removed and lowered to the floor being inspected for space debris impacts on tray flanges. These surfaces would later be in contact with tray rotator fixtures and any craters present could be affected.

Outside surfaces of each tray were inspected for contamination and discoloration and photographed if present while still being suspended from the overhead crane. A typical photograph is shown in figure 42. Each tray was then moved to the M&D work station where the complete surface of the experiment and tray was inspected for impact craters, and documented using special instrumentation. Figure 43 shows a tray being scanned.

Each tray was then taken to a special area for a detailed photo survey. Figure 44 shows such a typical photo setup. The front and back surface of each experiment tray was photographed in detail. Closeups of each 1/6 of the front and the back of peripheral trays and 1/4 of the front and the back of end trays were made. Additional closeups were made of any unusual details found. All photographs were processed by the KSC and all original negatives are archived there. Photographs were taken using KODAK Vericolor III 160 film using color balanced flood lights.

Experiments were checked for contamination by Systems SIG members. Measurements were made and recorded when appropriate. Figure 45 shows a typical tray setup for contamination measurements.

After M&D scan, photo survey, and contamination measurements were complete, trays were ready for deintegraton if appropriate. Experiments were removed from those trays with multiple experiments. Batteries were checked for leaks and voltages measured and then removed. MTM tape recorders were removed from each EPDS and returned to the manufacturer for checkout before data readout.

Thermal properties were measured on some tray and experiment surfaces. Figure 46 shows such measurements being made.

Each experimenter performed his unique procedures as required. This included additional photos, sample removal, measurements and examinations. Support was provided as required.

The final operation for trays and experiments was the preparation and shipping to the experimenters' laboratories. Figure 47 shows a tray being placed in a shipping container.

After the tray deintegration was complete, thermal panels and other systems were removed. The wiring harness was inspected, tested, and removed. The lead ballast used to adjust the LDEF c.g. when flown was removed. The EIS was removed and tested. Photo and video surveys were made of the LDEF structure. Each surface, both interior and exterior, was included. The M&D Team made a systematic scan of the outer surfaces of the facility structure using the same instrumentation as used in individual tray surveys. Contamination measurements, tape lifts and scrapings were made of SIG-specified areas of structure contamination.

Nondestructive tests (eddy current) were made of LDEF welds and dye penetrant tests were made on trunnion and keel pin mounting holes in the facility center ring (see fig. 48) and the trunnion mounting holes in the end support beam. Torque measurements were made on selected bolted joints of the facility structure. The flight trunnions and the keel pin were removed for testing and replaced with those used during ground transport.

After completion of LDEF deintegration and testing, the bare facility structure was then made ready for storage. The LATS cover was installed and the LATS removed from the SAEF II building (see fig. 49). The LATS was transported (see fig. 50) to a hangar for storage on May 14, 1990. At present the facility remains in storage, its future uncertain.

REFERENCES

1. LDEF 840-2: Long Duration Exposure Facility (LDEF) Experiment Users Handbook, Prepared by Staff, LDEF Project Office. January 15, 1978.

2. Greene, Robert F., Jr.: Thermal Design and Experiment Thermal Integration of the Long Duration Exposure Facility. 3rd AIAA/ASME Joint Thermophysics, Fluids Plasma and Heat Transfer Conference, St. Louis, MO., June 1982, AIAA paper No. 82-0829.

3. Berrios, William M.; and Greene, Robert F., Jr.: Long Duration Exposure Facility (LDEF) - Thermal Model Description. LDEF No. 840-008C, June 1983 revision.

4. JSC 19016. Cargo Systems Manual - LDEF Retrieval. STS 51-D. Prepared by Mariann Albjerg, NASA-JSC. Final, Revision A, January 4, 1985.

5. JSC-22959-32. National Space Transportation System Flight Data File: Rendezvous, STS-32 - Long Duration Exposure Facility (LDEF), November 22, 1989.

6. JSC-23156-32. National Space Transportation System Flight Data File: Flight Plan, STS-32 (Cycle 2R Trajectory), November 22, 1989.

7. Long Duration Exposure Facility Guide to Location of LDEF Experiments and Systems: Prepared by Glenna D. Martin, LDEF Project Office, December 15,1989.

Table 1.- LDEF experiment complement

EXP. NO.	TITLE	TRAY NOS.
A0015	Free-Flyer Biostack Experiment Institute fur Flugmedizin, DFVLR	C2, G2
A0019	Influence of Extended Exposure in Space on Mechanical Properties of High-Toughness Graphite-Epoxy Composite Material University of Michigan	D12
A0023	Multiple Foil Microabrasion Package University of Kent	C3, C9, D12, E6, H11
A0034	Atomic Oxygen Stimulated Outgassing Southern University/NASA-MSFC	C3, C9
A0038	Interstellar Gas Experiment NASA-JSC/University of Bern	E12, F6, H6, H9
A0044	Holographic Data Storage Crystals for LDEF Georgia Institute of Technology	E5
A0054	Space Plasma High Voltage Drainage TRW Space and Technology Group	B4, D10
A0056	Exposure to Space Radiation of High-Performance Infrared Multilayer Filters and Materials Technology Experiments University of Reading/British Aerospace	B8, G12
A0076	Cascade Variable Conductance Heat Pipe McDonnell Douglas Astronautics Company	F9
A0114	Interaction of Atomic Oxygen with Solid Surfaces at Orbital Altitudes University of Alabama in Huntsville/NASA-MSFC	C3, C9
A0133	Effect of Space Environment on Space Based Radar Phased Array Antenna Grumman Aerospace Corporation	H7
A0134	Space Exposure of Composite Materials for Large Space Structures NASA-LaRC	B9

Table 1.- (continued)

EXP. NO.	TITLE	TRAY NOS.
A0135	Effect of Space Exposure on Pyroelectric Infrared Detectors NASA-LaRC	E5
A0138-1	Study of Meteoroid Impact Craters on Various Materials CERT/ONERA-DERTS	B3
A0138-2	Attempt at Dust Debris Collection with Stacked Detectors CERT/ONERA-DERTS	B3
A0138-3	Thin Metal Film and Multilayers Experiment CNRS/LPSP	B3
A0138-4	Vacuum Deposited Optical Coatings Experiment Optical Division, Matra S. A.	B3
A0138-5	Ruled and Holographic Gratings Experiment Inst. SA/JOBIN-YVON Division	B3
A0138-6	Thermal Control Coatings Experiment CERT/ONERA-DERTS, CNES/CST	B3
A0138-7	Optical Fibers and Components Experiment CERT/ONERA-DERTS	B3
A0138-8	Effect of Space Exposure of Some Epoxy Matrix Composites on Their Thermal Expansion and Mechanical Properties Space Division, Matra S. A.	B3
A0138-9	The Effect of the Space Environment on Composite Materials Aerospatiale	B3
A0138-10	Microwelding of Various Metallic Materials Under Ultravacuum Aerospatiale	B3
A0139A	Growth of Crystals from Solutions in Low Gravity Rockwell International Science Center Technical University of Denmark	G6

Table I.- (continued)

EXP. NO.	TITLE	TRAY NOS.
A0147	Passive Exposure of Earth Radiation Budget Experiment Components The Eppley Laboratory, Inc.	B8, G12
A0171	Solar Array Materials Passive LDEF Experiment NASA-MSFC/NASA-LeRC/NASA-GSFC Jet Propulsion Laboratory	A8
A0172	Effects of Solar Radiation on Glasses NASA-MSFC/Vanderbilt University	D2, G12
A0175	Evaluation of Long-Duration Exposure to the Natural Space Environment on Graphite-Polyimide and Graphite-Epoxy Mechanical Properties Rockwell International Corp. (Tulsa Facility)	A1, A7
A0178	A High Resolution Study of Ultra-Heavy Cosmic Ray Nuclei Dublin Inst. for Advanced Studies, ESA-ESTEC	A2, A4, A10, B5, B7, C5, C6, C8, C11, D1, D5, D7, D11, E2, E10, F4
A0180	The Effect of Space Environment Exposure on the Properties of Polymer Matrix Composite Materials University of Toronto	D12
A0187-1	Chemistry of Micrometeoroids NASA-JSC/Univ. of Washington, Rockwell Int. Science Center	A3, A11
A0187-2	Chemical and Isotopic Measurements of Micrometeoroids by Secondary Ion Mass Spectrometry McDonnell Center for the Space Sciences Max-Planck Institute fur Nuclear Physics Munich Technical University Ernst-Mach Institute Dornier System Manufacturing Company	C2, E3, E8
A0189	Study of Factors Determining the Radiation Sensitivity of Quartz Crystal Oscillators Martin Marietta Laboratories	D2
A0201	Interplanetary Dust Experiment Institute for Space Science and Technology NASA-LaRC North Carolina State University	B12, C3, C9, D6, G10, H11

Table 1.- (continued)

EXP. NO.	TITLE	TRAY NOS.
M0001	Heavy Ions in Space Naval Research Laboratory	H3, H12
M0002-1	Trapped Proton Energy Spectrum Determination AF Geophysics Laboratory	D3, D9, G12
M0002-2	Measurement of Heavy Cosmic-Ray Nuclei on LDEF University of Kiel, Federal Republic of Germany	E6
M0003	Space Environment Effects on Spacecraft Materials The Aerospace Corporation	D3, D4, D8, D9
M0004	Space Environment Effects on Fiber Optics Systems AF Weapons Laboratory	F8
M0006	Space Environment Effects AF Technical Applications Center	C2
P0003	LDEF Thermal Measurements System NASA-LaRC	Center ring
P0004-1	Seeds in Space Experiment George W. Park Seed Company, Inc.	F2
P0004-2	Space-Exposed Experiment Developed for Students (SEEDS) NASA Headquarters	F2
P0005	Space Aging of Solid Rocket Materials Morton-Thiokol, Inc.	Center ring
P0006	Linear Energy Transfer Spectrum Measurement Experiment University of San Francisco/NASA-MSFC	F2
S0001	Space Debris Impact Experiment NASA-LaRC	A5, A6, A12, B1, B2, B6, B8, B11, C4, C7, D2, D6, E1, E4, E7, E11, F1, F3, F5, F7, F10, F11, G4, G8, H5

Table 1.- (concluded)

EXP. NO.	TITLE	TRAY NOS.
S0010	Exposure of Spacecraft Coatings NASA-LaRC	B9
S0014	Advanced Photovoltaic Experiment NASA-LeRC	E9
S0050	Investigation of the Effects of Long Duration Exposure of Active Optical System Components Engr. Exp. Station, Georgia Inst. of Technology	E5
S0050-1	Investigation of the Effects of Long Duration Exposure on Active Optical Materials and UV Detectors NASA-LaRC	E5
S0069	Thermal Control Surfaces Experiment NASA-MSFC	A9
S0109	Fiber Optic Data Transmission Experiment Jet Propulsion Laboratory	C12
S1001	Low Temperature Heat Pipe NASA-GSFC/NASA-ARC	F12, H1
S1002	Investigation of Critical Surface Degradation Effects on Coatings and Solar Cells Developed in Germany Messerschmitt-Bolkow-Blohm Space Division	E3
S1003	Ion Beam Textured and Coated Surfaces Experiment NASA-LeRC	E6
S1005	Transverse Flat Plate Heat Pipe Experiment NASA-MSFC/Grumman Aerospace Corporation	B10
S1006	Balloon Materials Degradation Texas A&M University	E6

Table 2.- Sequence of tray removal.

LANGLEY RESEARCH CENTER

APPROVAL: _____

ACCOMPLISHMENT _____

LDEF
ORDER OF TRAY REMOVAL

LEVEL

Pg 1 of 2

PLAN
3 / 28 / 90

MONTH	FEB						MARCH																			
DATE	23	26	27	28	1	2	5	6	7	8	9	12	13	14	15	16	19	20	21	22	23	26	27	28	29	
Remove F-2, C-5, C-6	▼																									
Remove D-7, D-8, D-9		▼																								
Remove F-12 MTM, E-4			▼																							
Remove D-4, D-3, A-8, A-9				▼																						
Remove B-10, C-8, C-4, B-1					▼																					
Remove C-9, C-3, H-5, F-10, F11						▼																				
Remove F-6, E-12, H-9, H-6							▼																			
Remove B-3, B-2, E-1, F-5								▼																		
Remove A-11, A-6, G-6, F-7, B-11,									▼																	
Remove B-12, A-5, A-4, A-3										▼																
Remove E-8, D-11, D-10, E-3											▼															
Remove E-9												▼														
Remove B-9, C-2, G-2, B-8													▼													
Remove F-8, H-7, E-6														▼												
Remove G-12, H-12, H-3, D-12															▼											
Remove D-2, H-11, G-10, D-6																▼										
Remove C-11, E-5, F-1, B-4																	▼									
Remove A-7, C-7, A-1																		▼								
Remove C-12, A-10, A-12, B-5, F-11																			▼							
Remove F-4, B-6, D-5, E-7, F-3																				▼						
Remove E-10, G-4, D-1, G-8																					▼					
Remove B-7, A-0139A Batteries																						▼				
Remove A-2, E-2, P-0003, H-1, F-12, P-0005, F-9																							▼			
Process Trays																										

Note: Refer to approved hardware deintegration schedule.

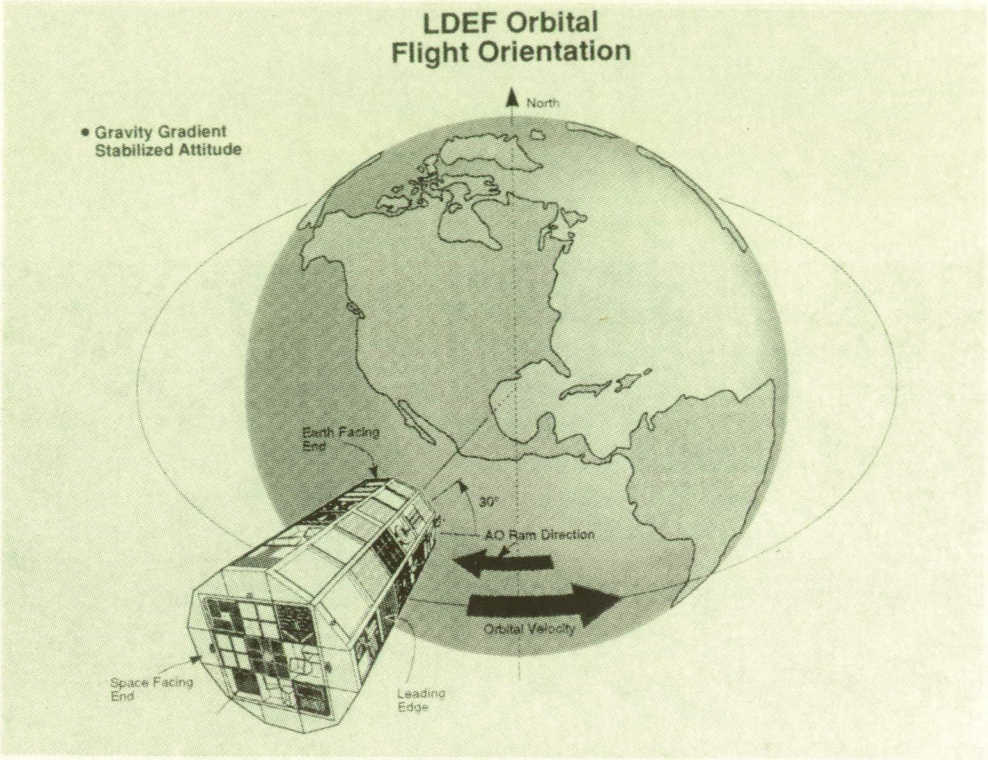

Figure 1.- LDEF orbital flight orientation. (Photo L-91-652)

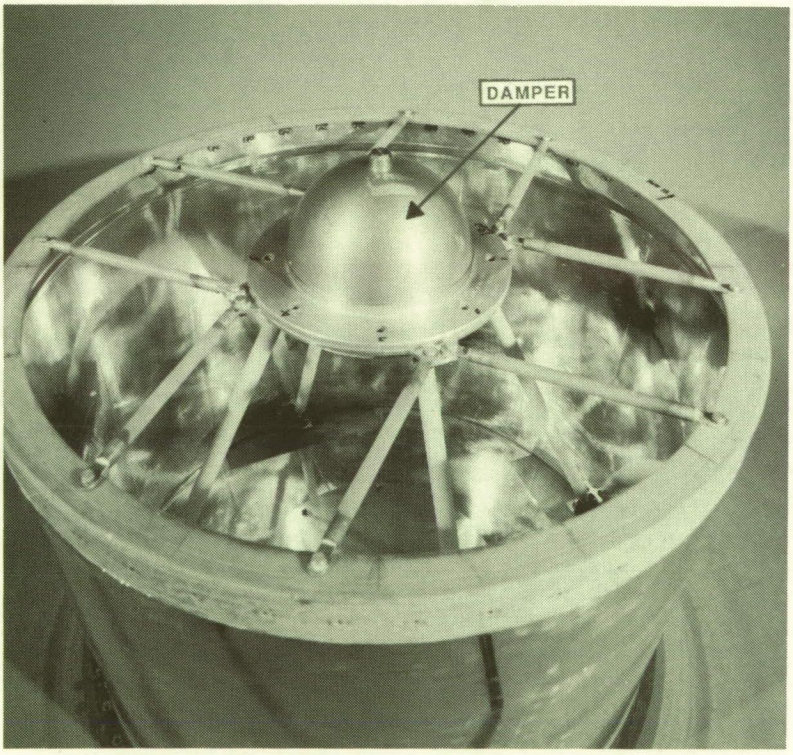

Figure 2.- Photograph of viscous magnetic rate damper and protective housing base. (Photo KSC-390C-3383.07)

Figure 3.- Photograph of LDEF several minutes after deployment. (Photo L-84-04337)

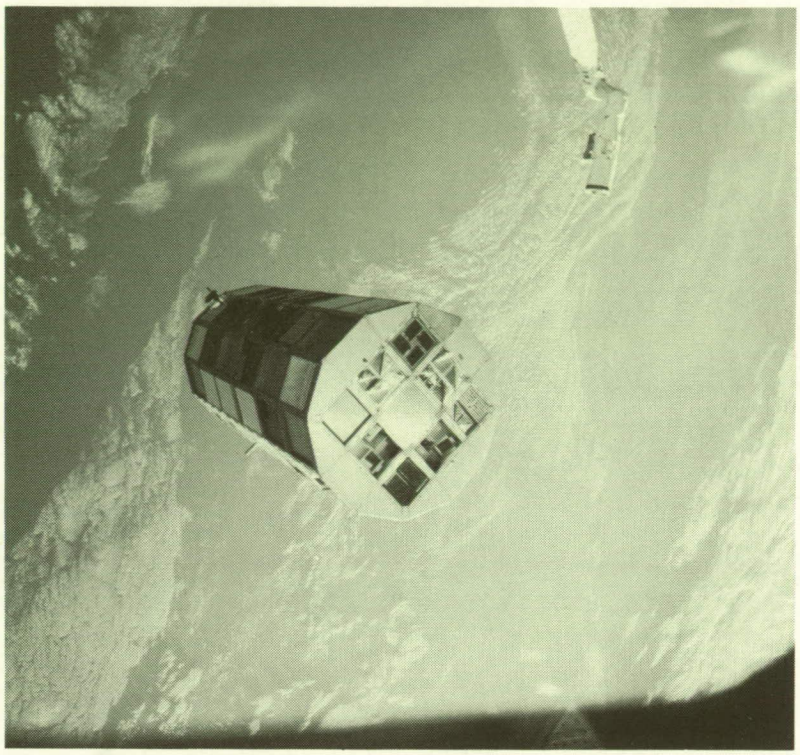

Figure 4.- Photograph of LDEF prior to retrieval. (Photo L-90-10468)

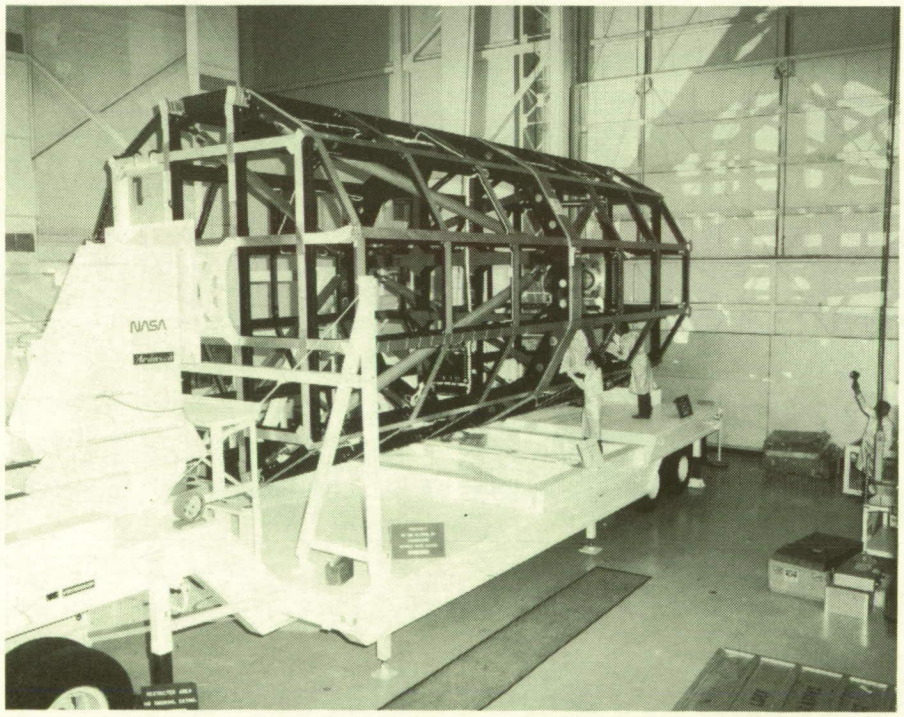

Figure 5.- LDEF structure mounted on LDEF Assembly and Transportation System (LATS). (Photo L-83-2797)

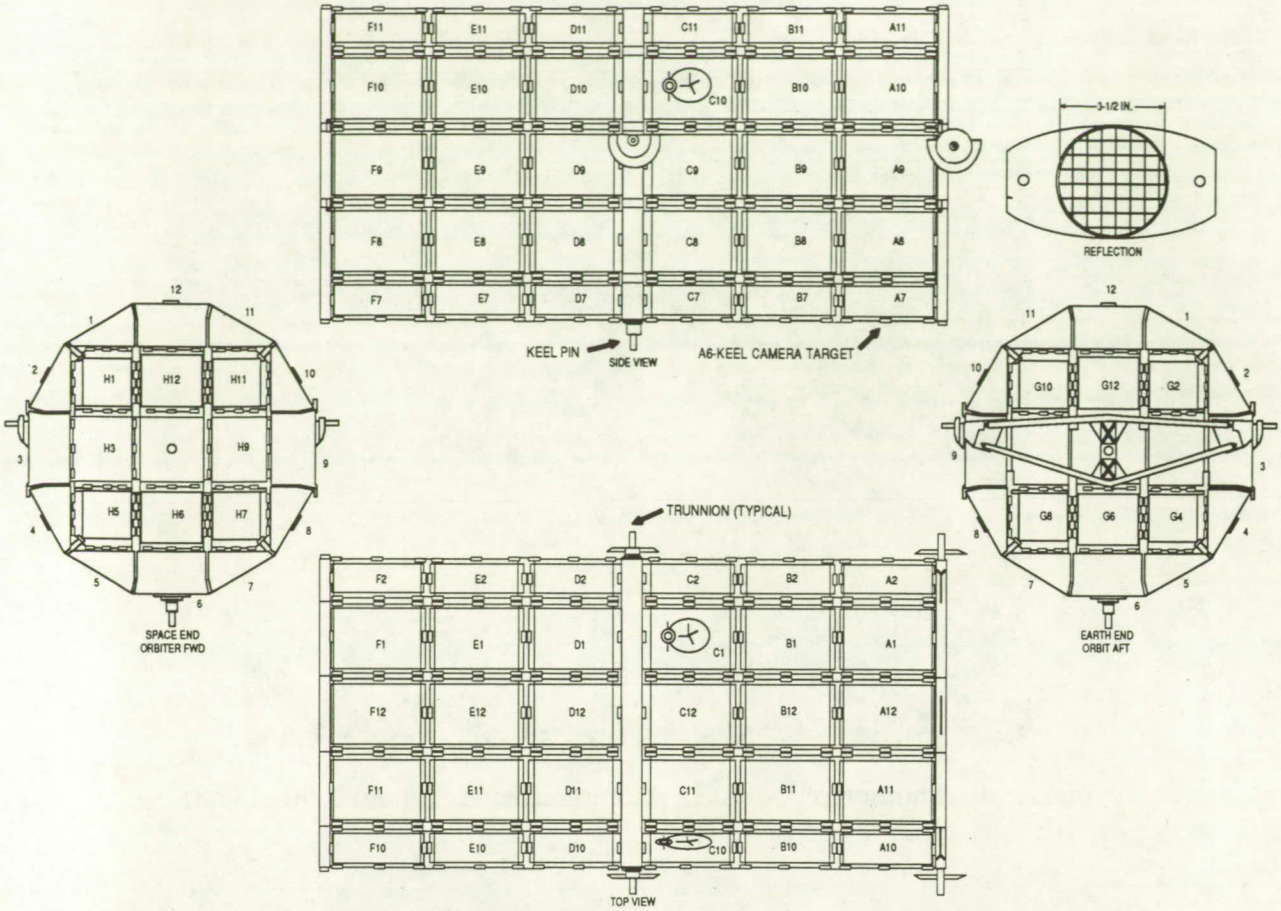

Figure 6.- LDEF structural configuration and identification of experiment locations.

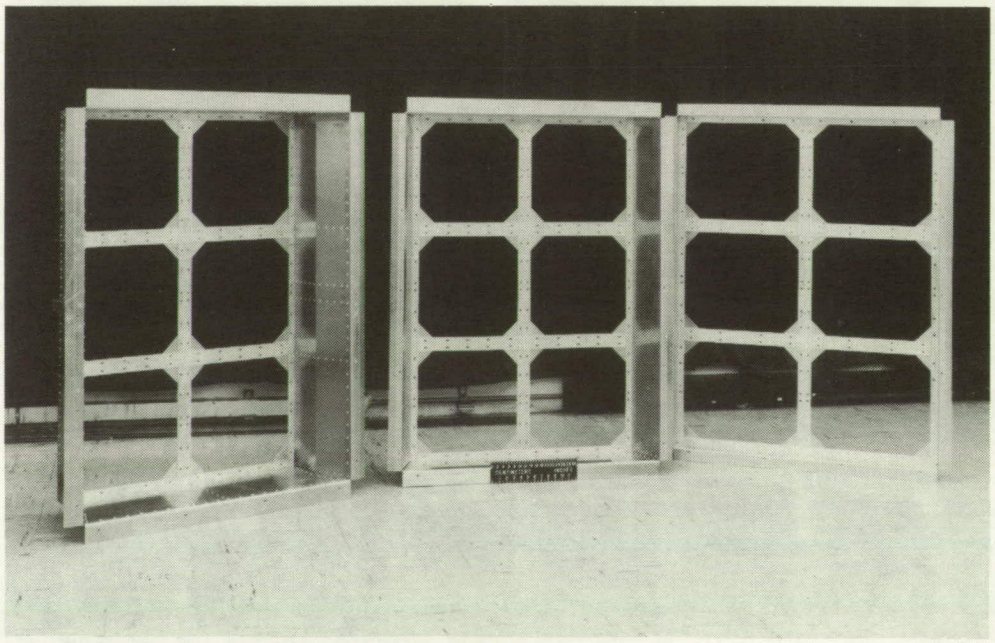

Figure 7.- Photograph of 12-inch deep, 6-inch deep, and 3-inch deep peripheral experiment trays. (Photo L-76-3431)

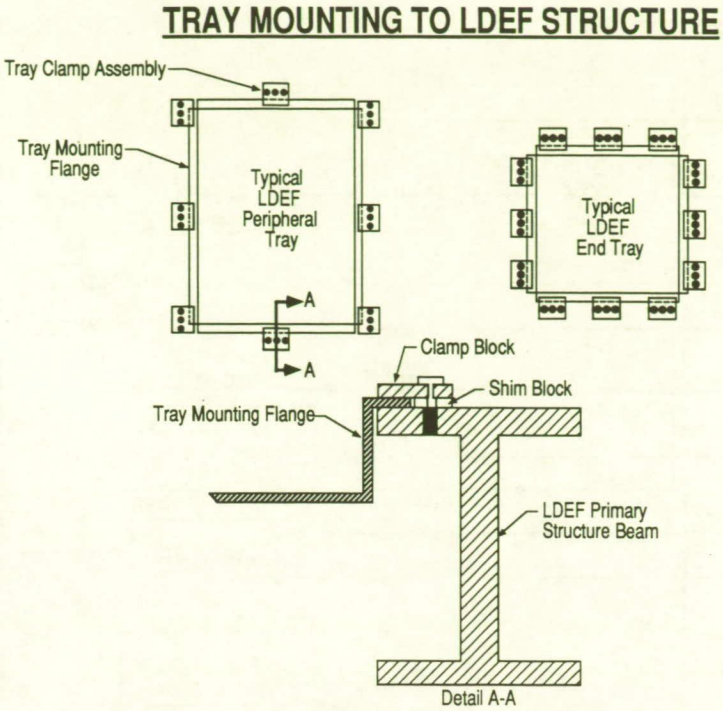

Figure 8.- Sketch of tray mounting to LDEF structure.

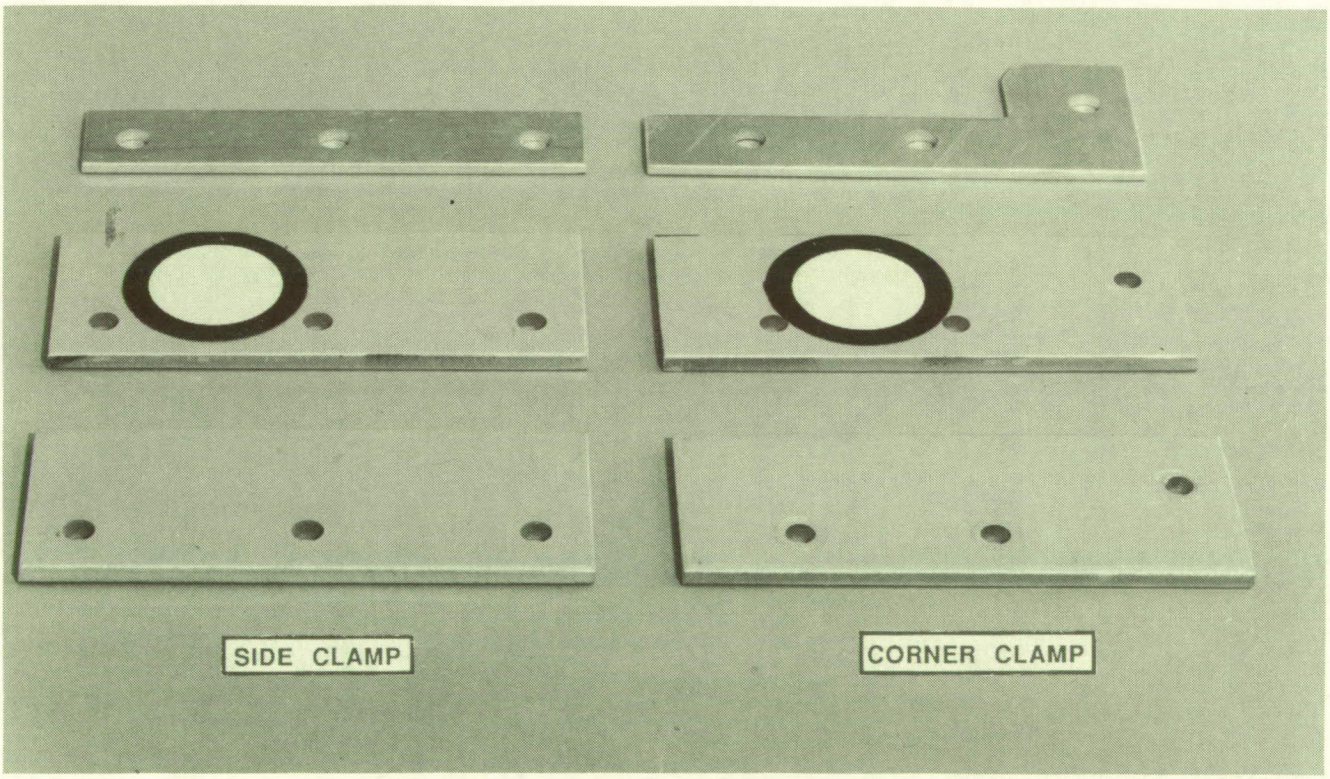

Figure 9.- Typical side and corner tray clamps. Clamps with and without white dots are shown. (Photo L-83-9460)

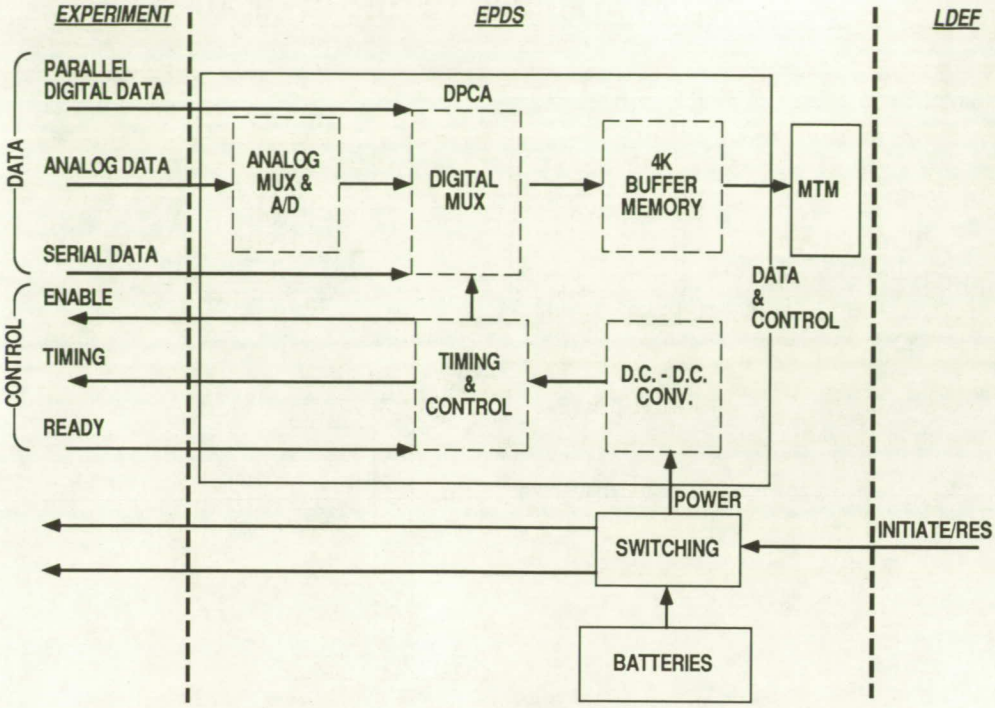

Figure 10.- Experiment power and data system (EPDS) block diagram.

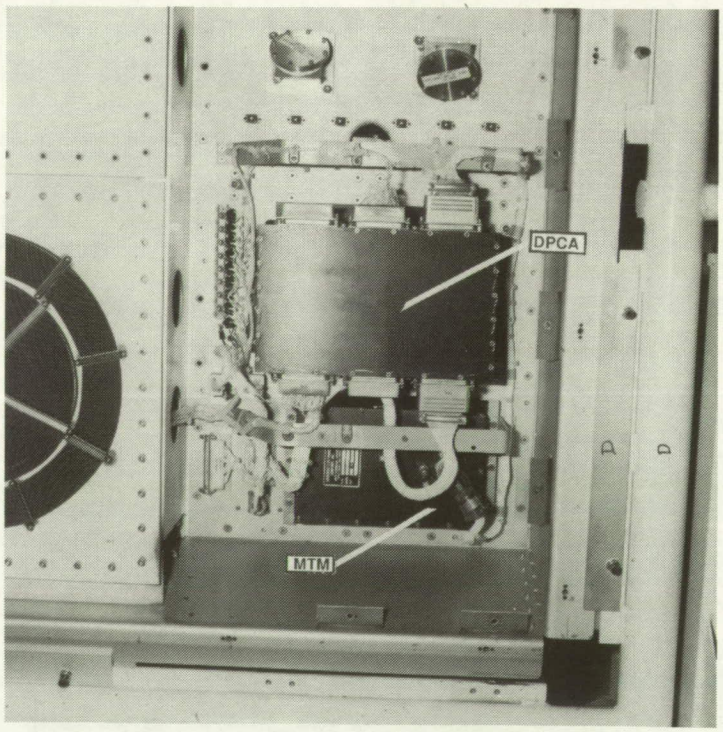

Figure 11.- Typical experiment power and data system (EPDS) installation in experiment tray. (Photo KSC-390C-2003.12)

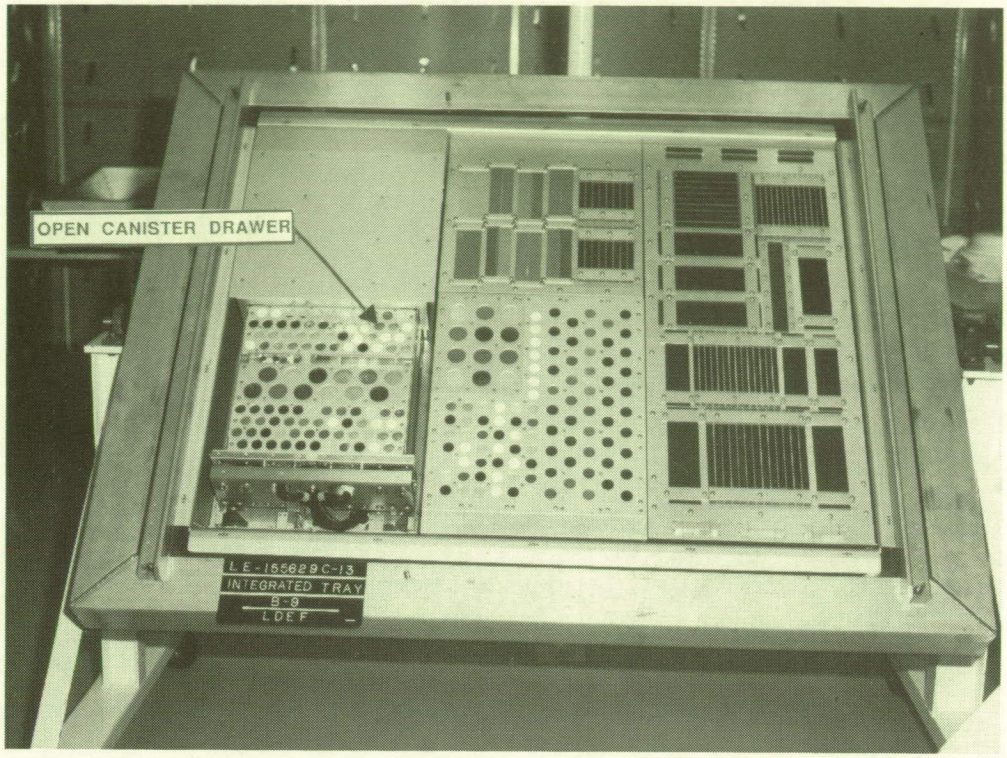

Figure 12.- Photograph of experiment environmental control canister (EECC) with test specimens installed. (Photo L-83-10,250)

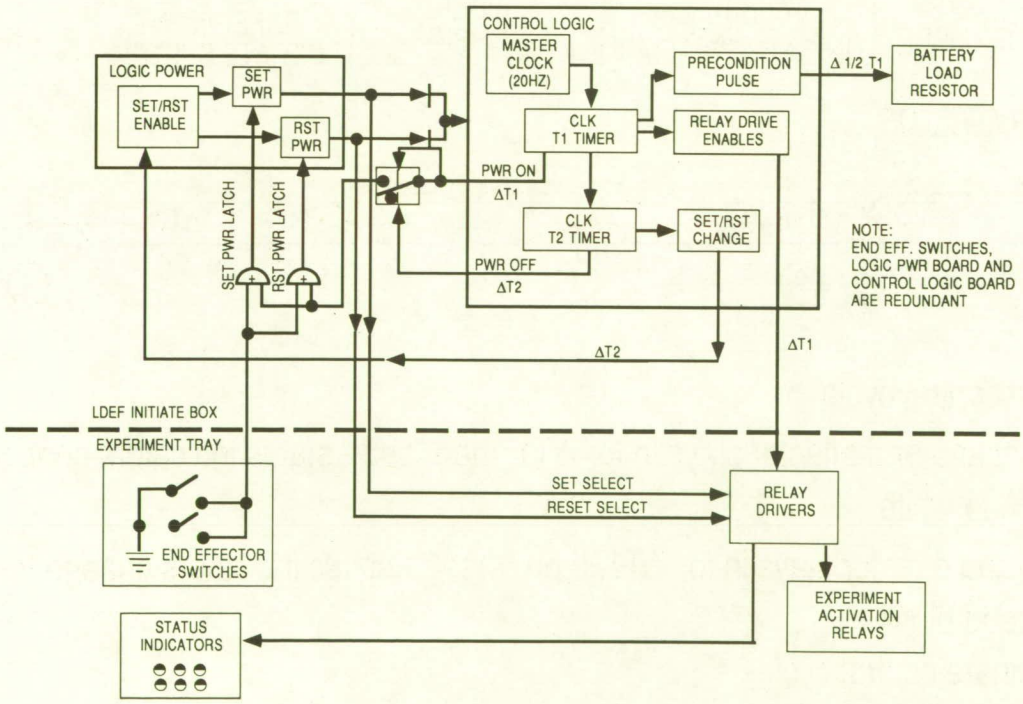

Figure 13.- Experiment initiate system (EIS) functional flow.

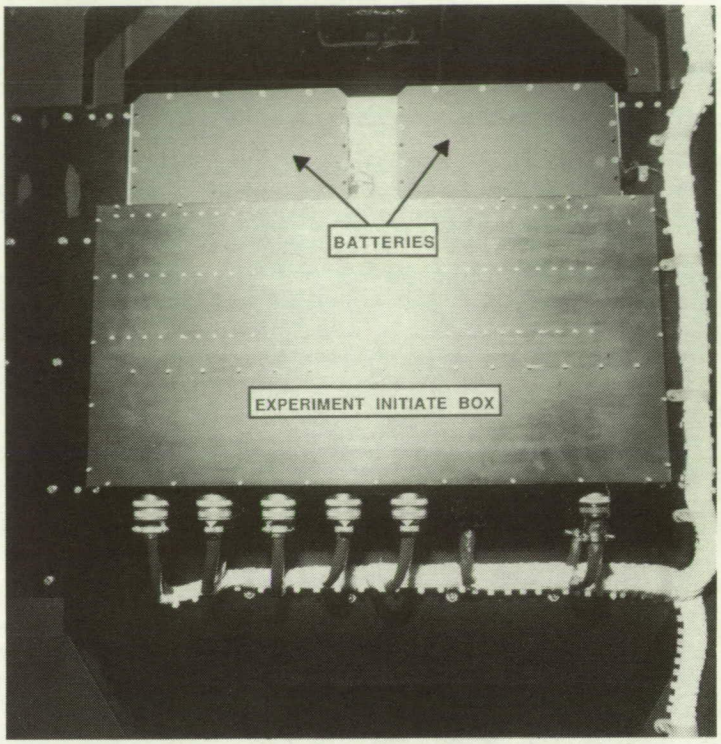

Figure 14.- Experiment initiate system (EIS) box and batteries mounted on center ring. (Photo KSC-390C-1461.02)

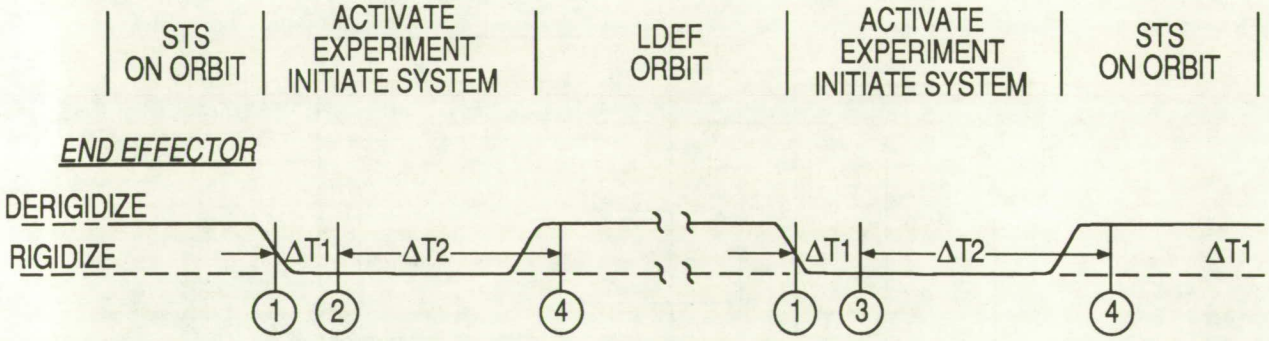

1. Begin control cycle
2. If reset and end effector stays in for ΔT1, then "set" - status indicators change from black to white
3. If set and effector stays in for ΔT1, then "reset" - status indicators change from white to black
4. Terminate control cycle

Figure 15.- Experiment initiate system (EIS) operational sequence.

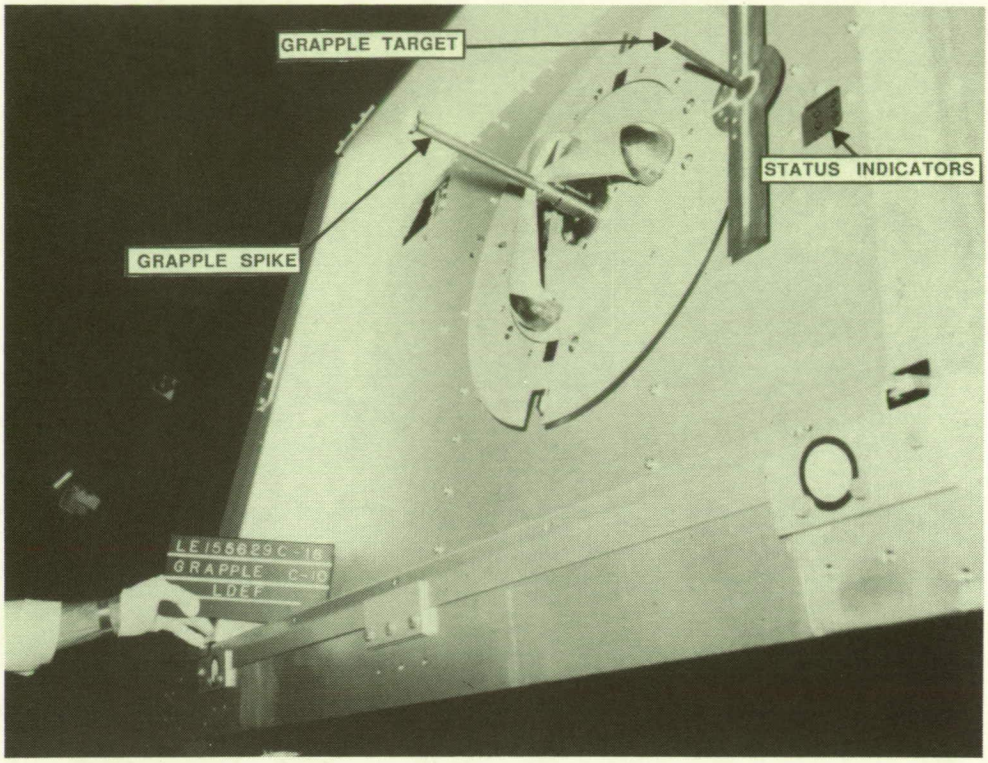

Figure 16.- Grapple fixture in tray C-10 (used to activate experiment initiate system [EIS]). (Photo L-84-7315)

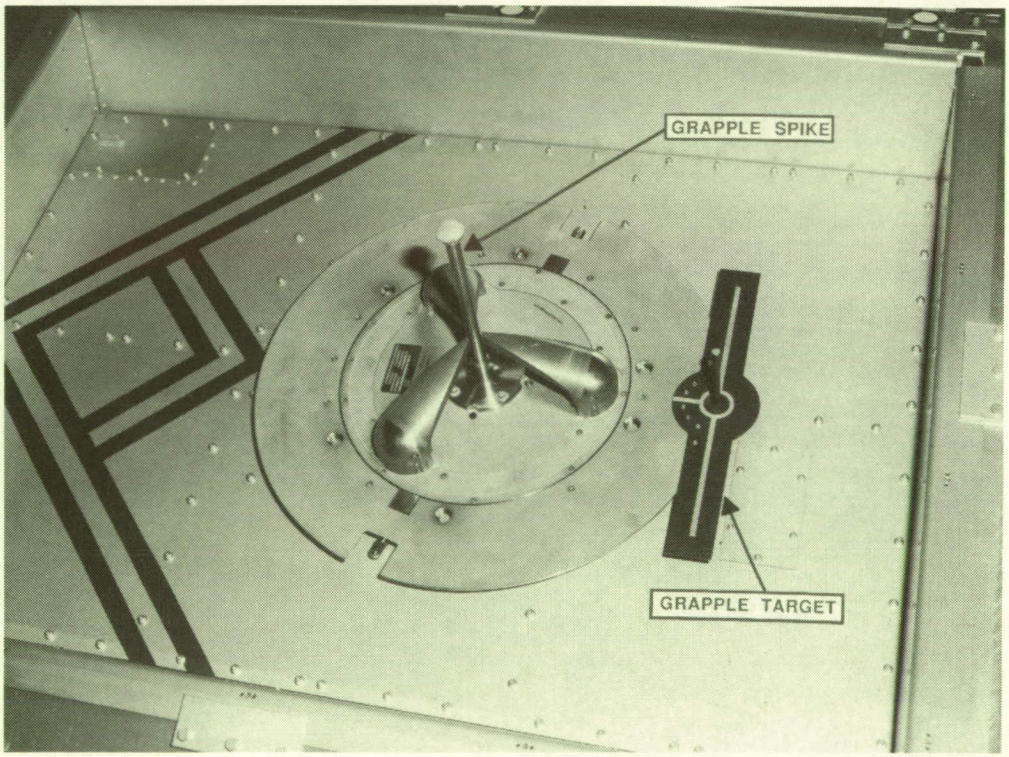

Figure 17.- Grapple fixture in tray C-1 (used for deployement and retrieval). (Photo L-90-01503)

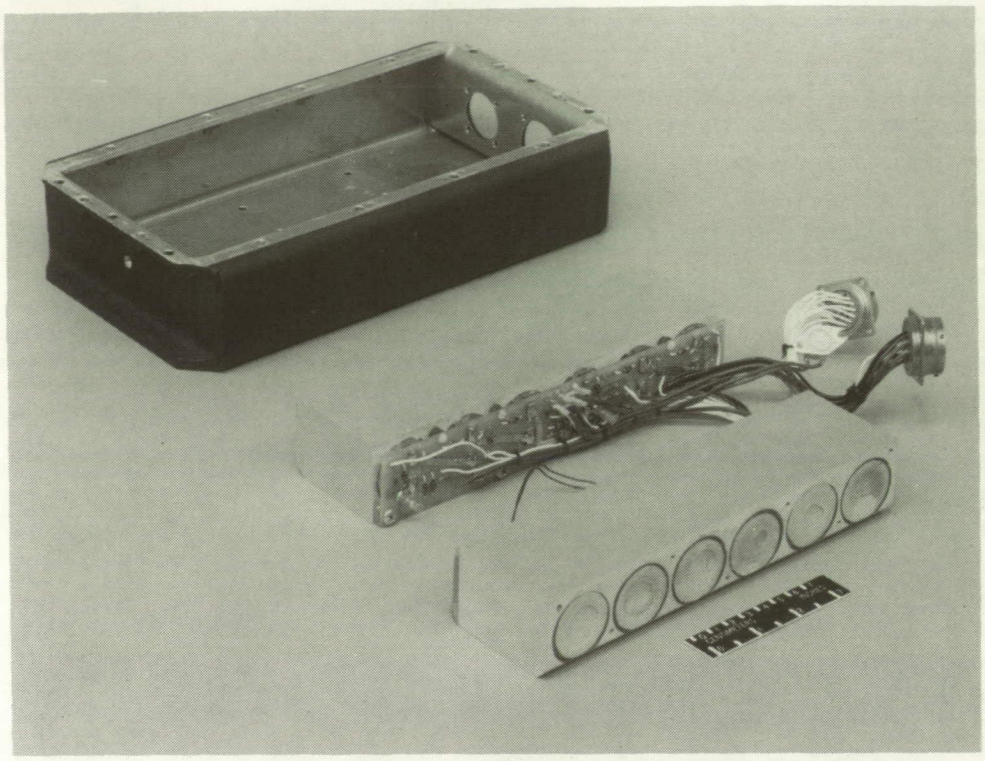

Figure 18(a).- Battery components. (Photo L-78-5152)

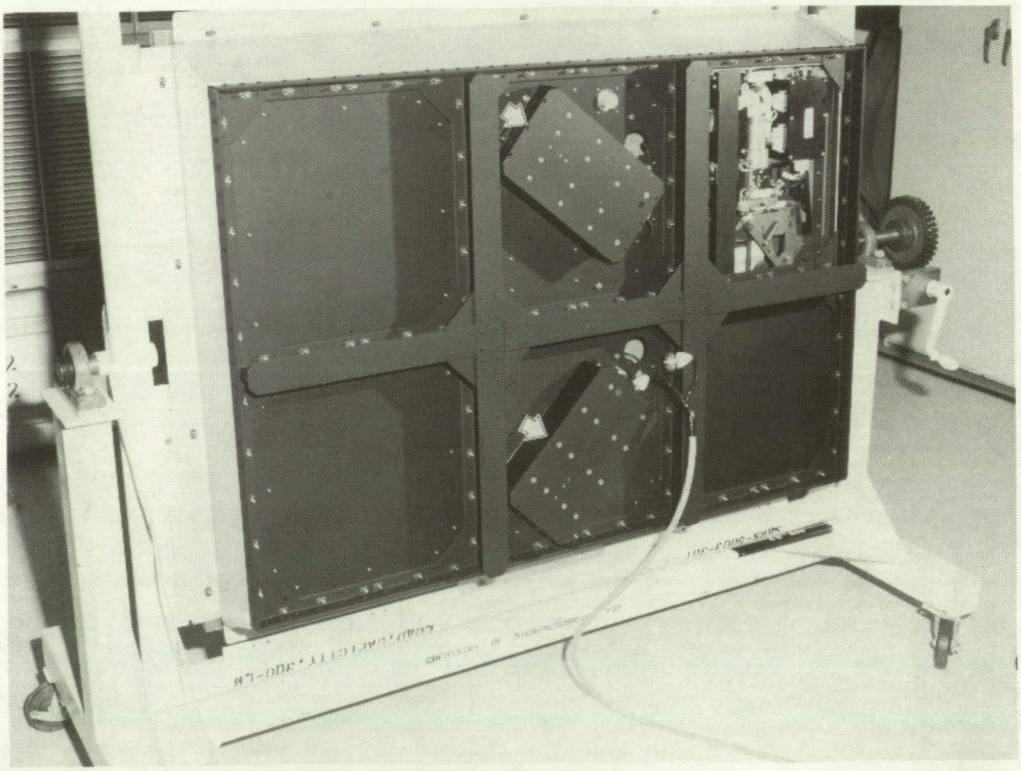

Figure 18(b).- Batteries located on back of typical experiment. (Photo L-90-03121)

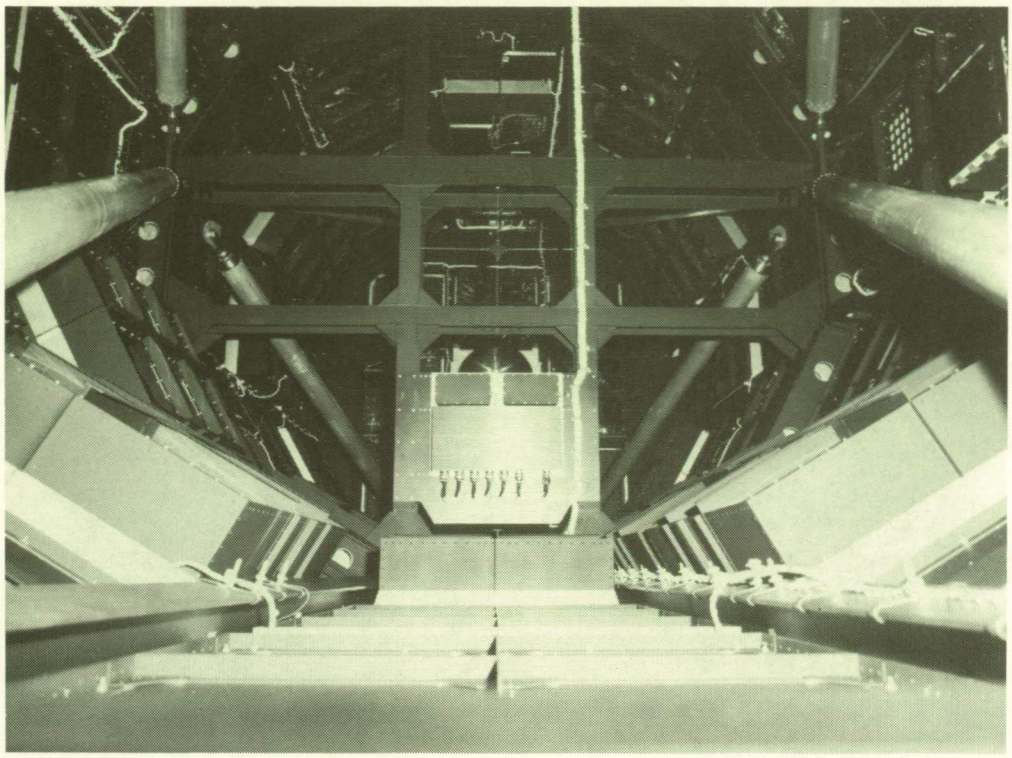

Figure 19.- Interior of LDEF. Note experiment initiate system (EIS) and batteries on center ring. (Photo L-90-01533)

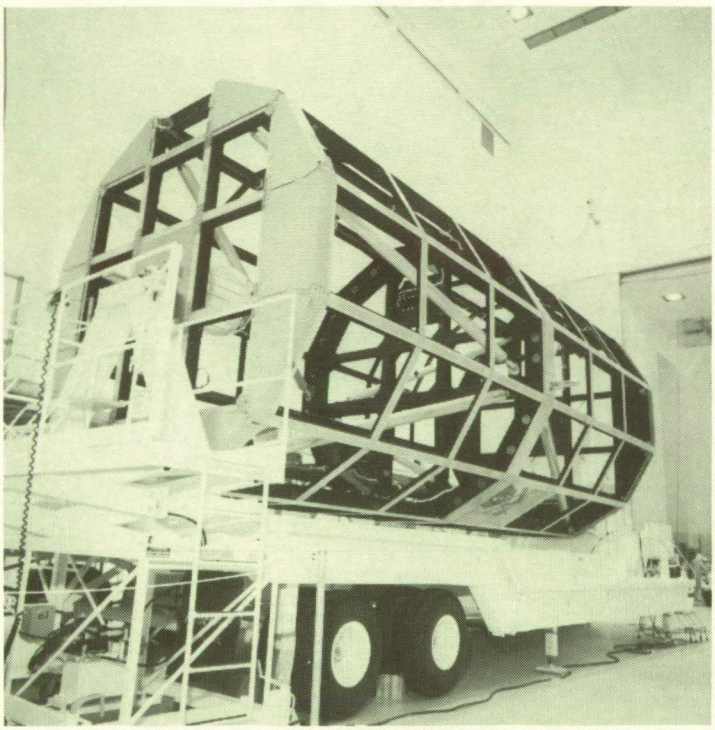

Figure 20.- LDEF on LDEF Assembly and Transportation System (LATS) after experiment tray removal. (Photo KSC-390C-2366.07)

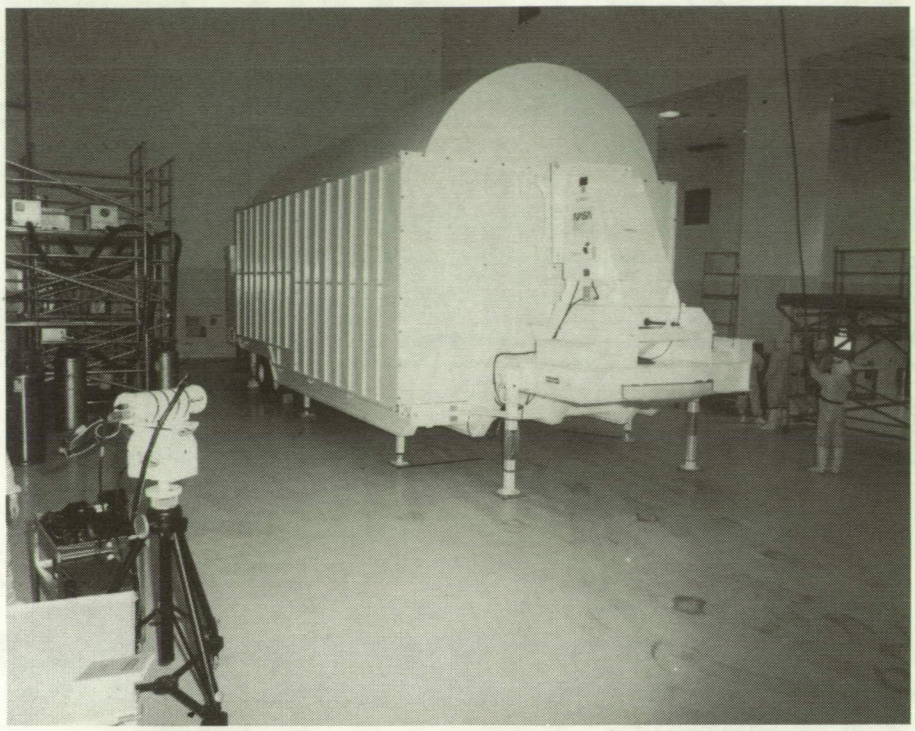

Figure 21.- LDEF Assembly and Transporation System with cover installed. (Photo KSC-390C-2774.02)

Figure 22.- Ground support equipment in use in Spacecraft Assembly and Encapsulation Facility II (SAEF II). (Photo KSC-390C-2749.08)

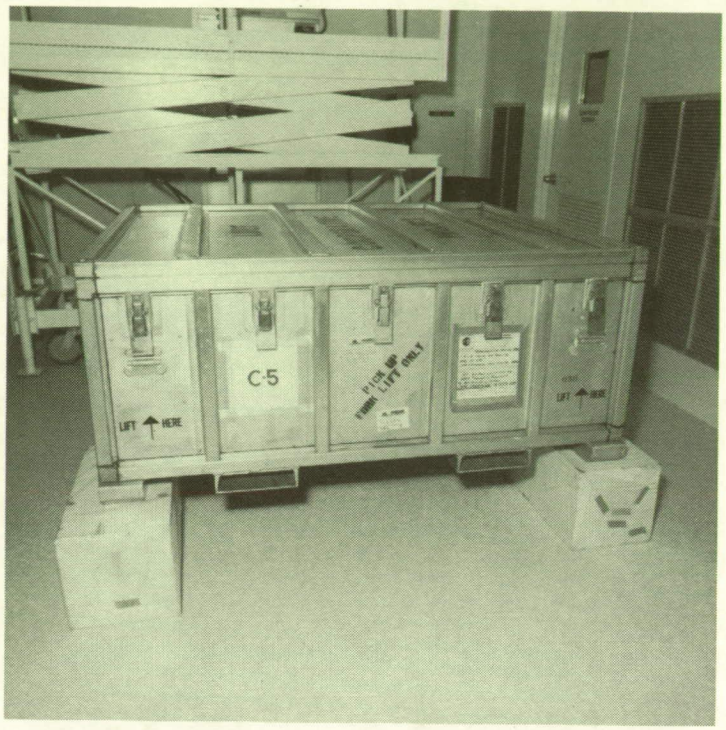

Figure 23.- Typical tray shipping container. (Photo KSC-390C-1471.12)

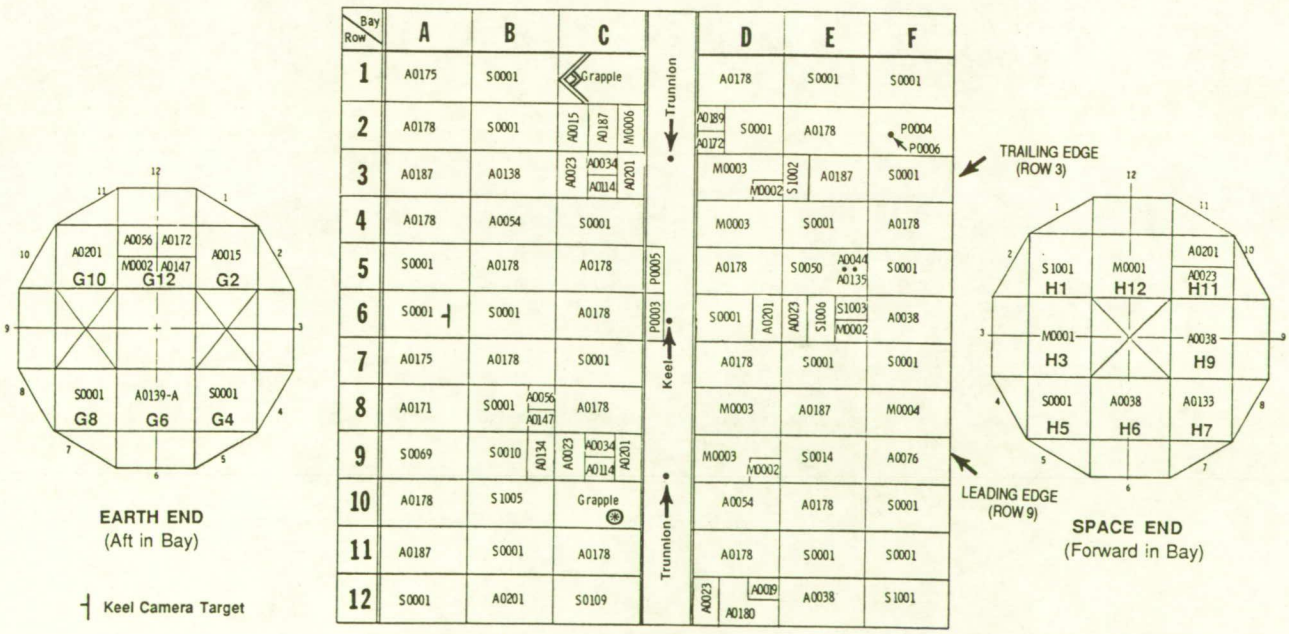

Figure 24.- Sketch showing experiment placement on LDEF.

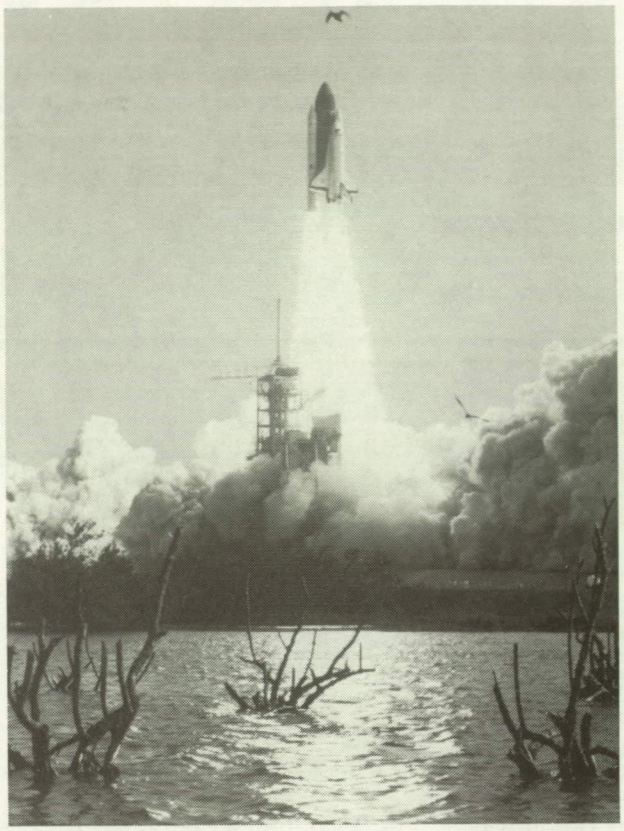

Figure 25.- Liftoff of STS-41C. (Photo L-84-5648)

Figure 26.- LDEF immediately after deployment. (Photo L-84-04318)

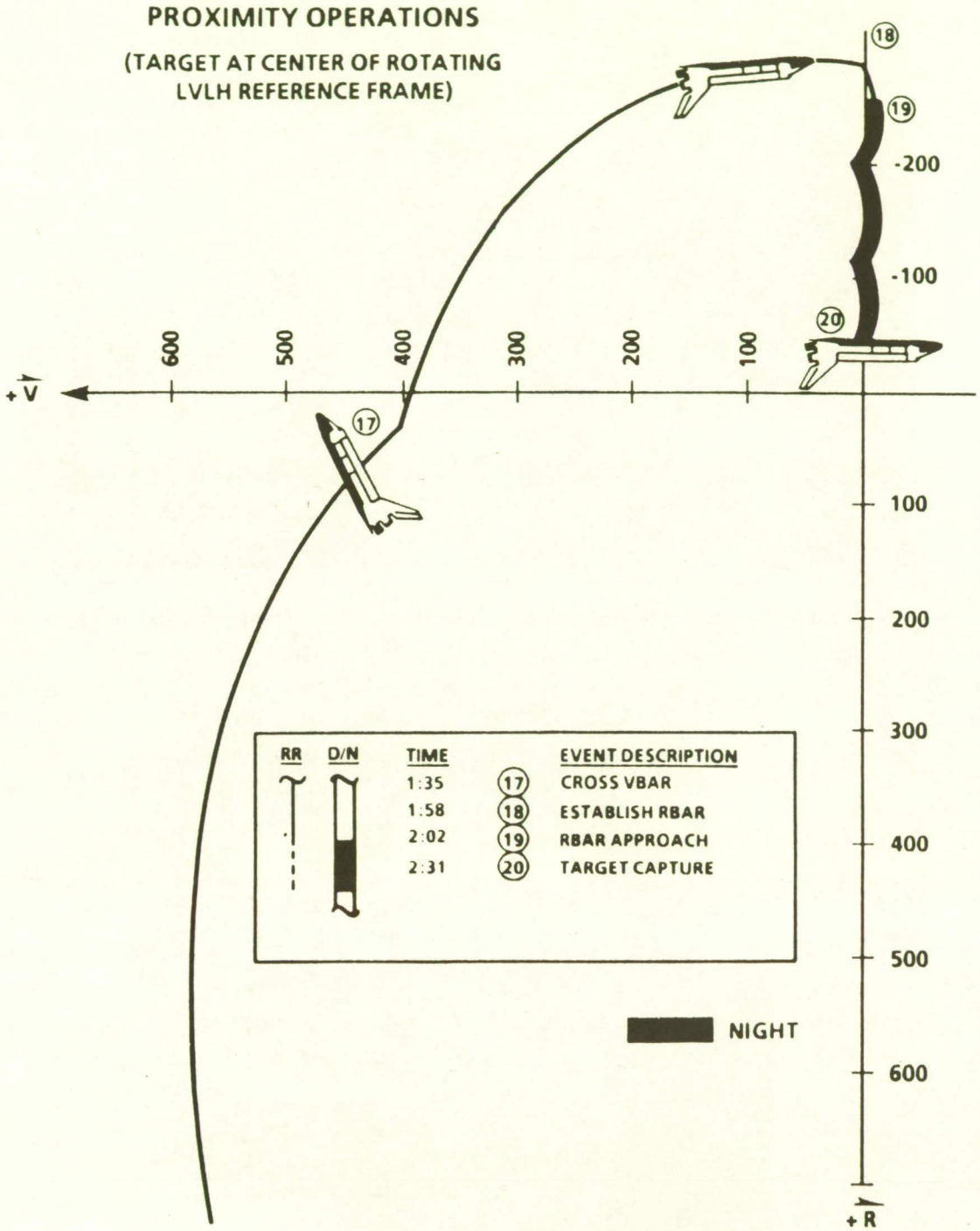

Figure 27.- Proximity operations for LDEF capture.

Figure 28.- Ferry aircraft prior to landing at KSC. (Photo L-90-10836)

Figure 29.- Orbiter in Mate/Demate Facility. Payload bay purge lines being connected. (Photo KSC-390C-583.05)

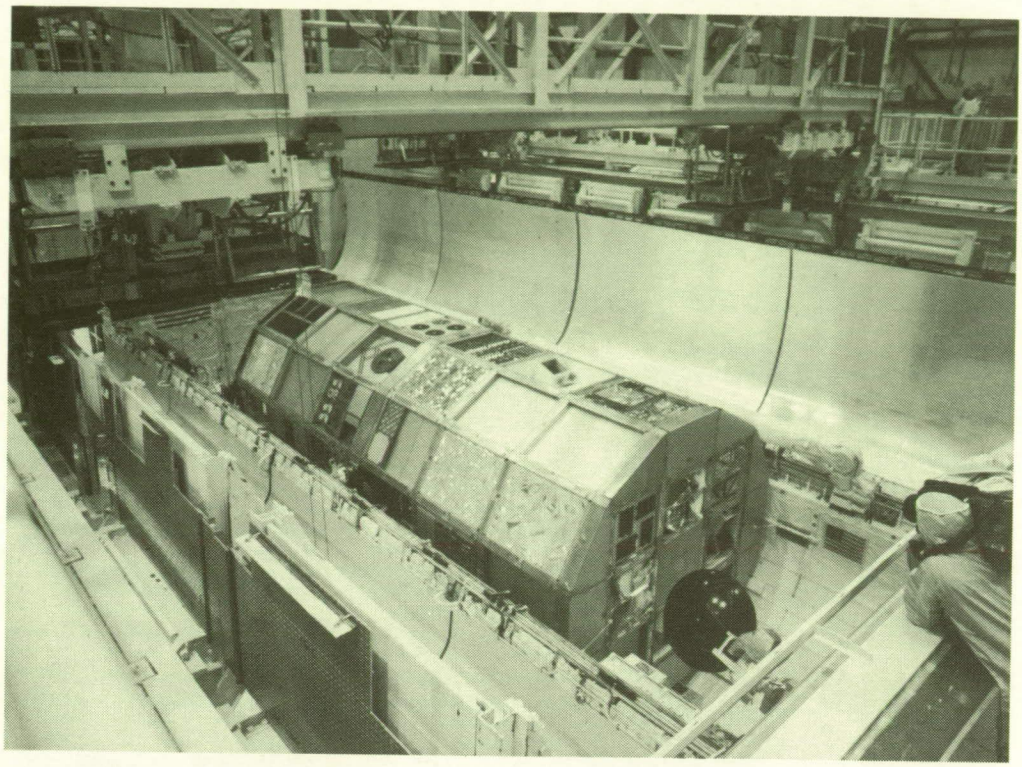

Figure 30.- Payload bay doors being opened in Orbiter Processing Facility. (Photo L- 90-01079)

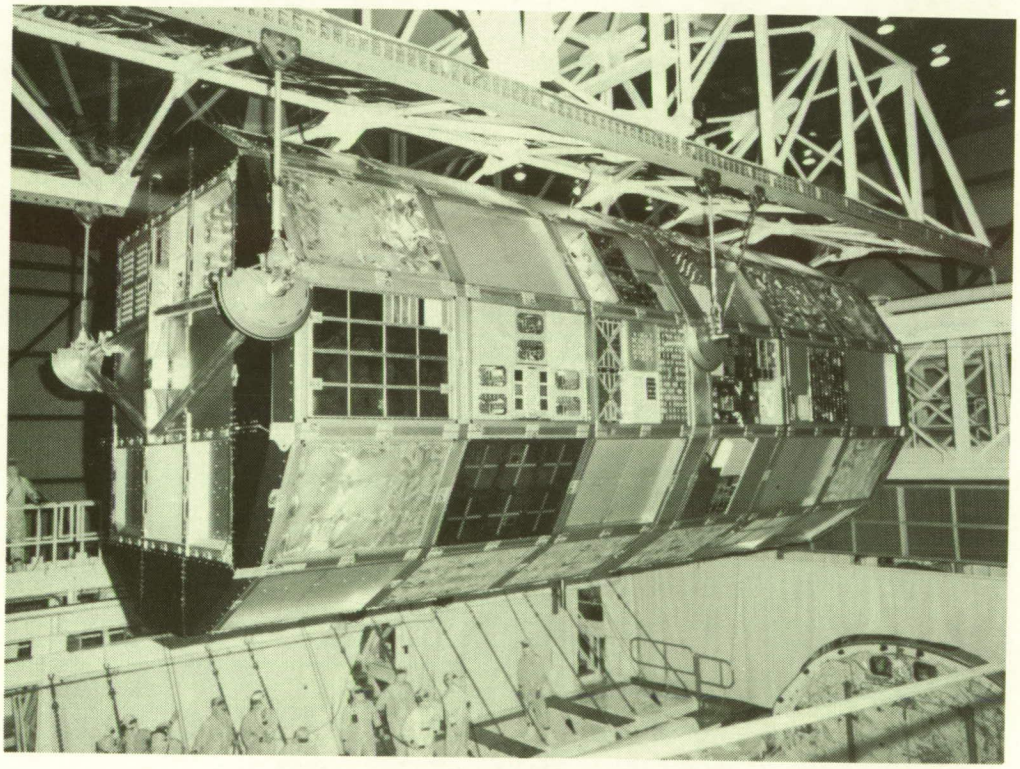

Figure 31.- LDEF being lifted from cargo bay. (Photo L-90-01087)

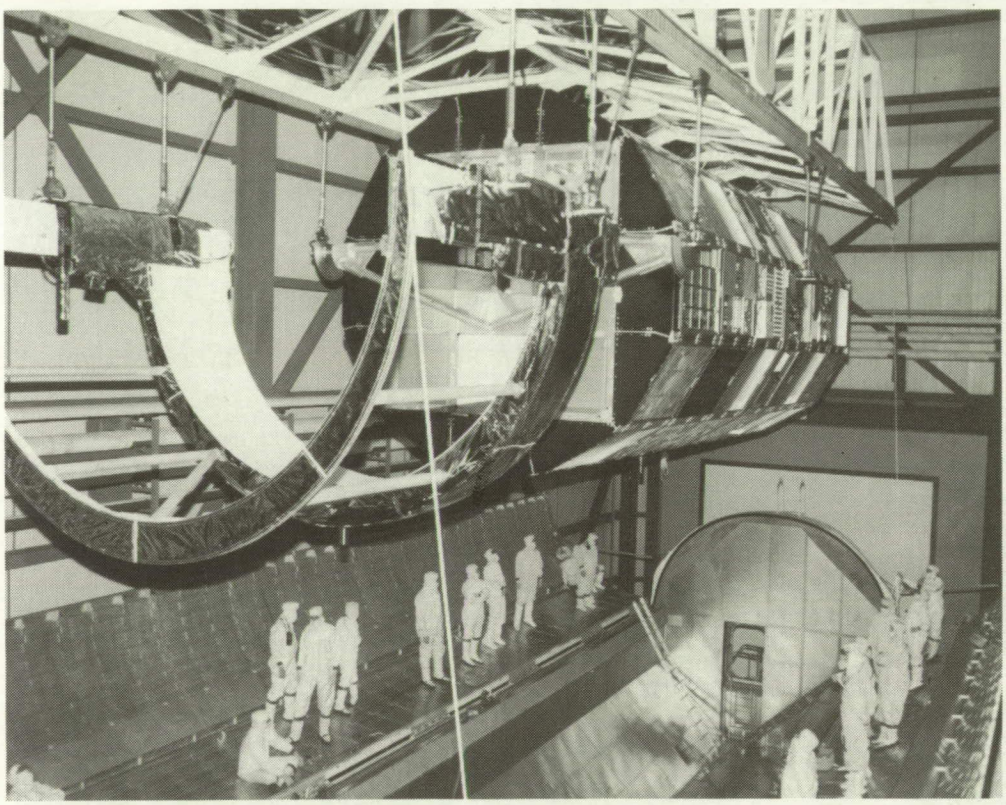

Figure 32.- LDEF being lowered into payload canister in Orbiter Processing Facility. (Photo KSC-390C-619.12

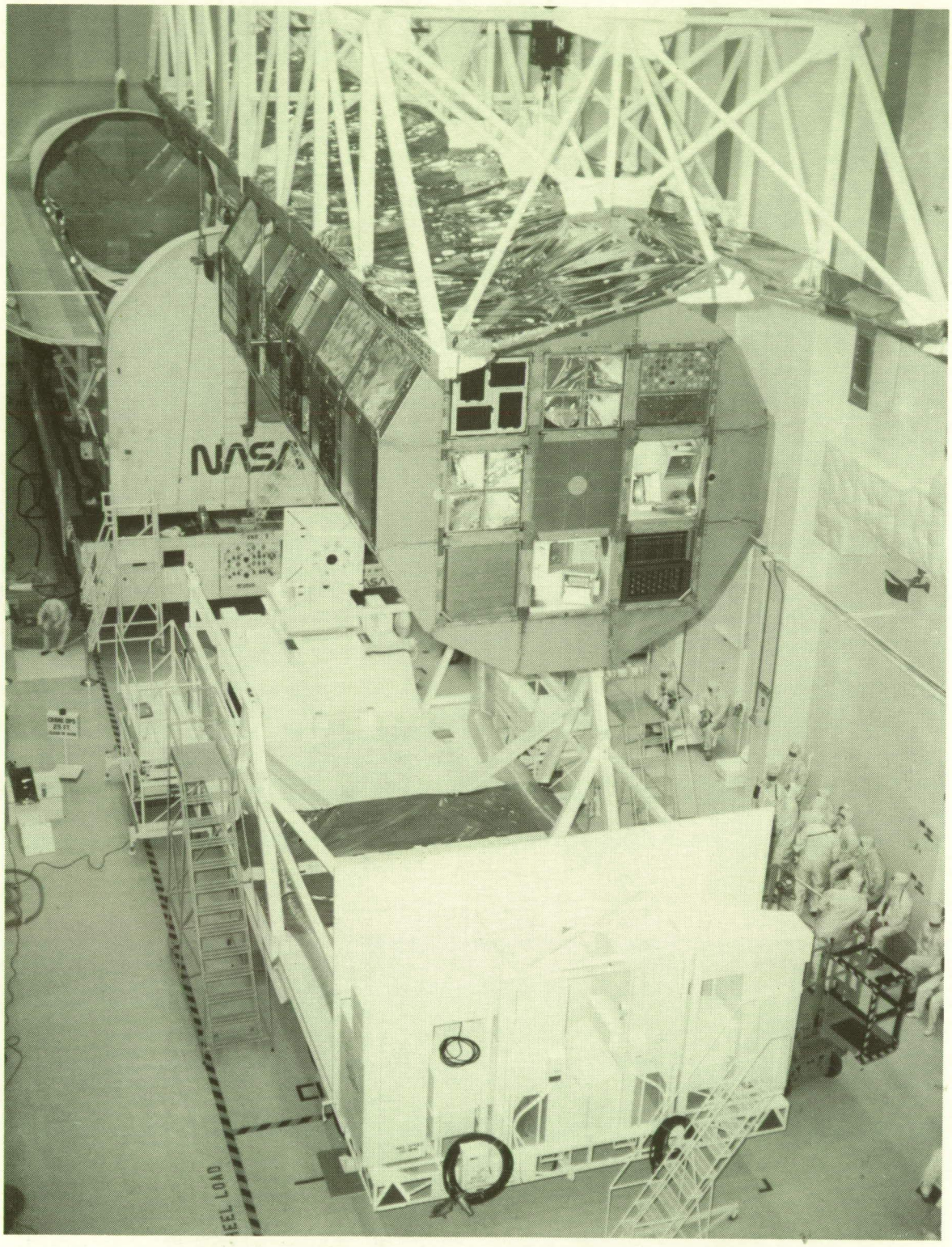

Figure 33.- LDEF being transferred from payload canister into LDEF Assembly and Transportation System in Operation and Checkout Building. (Photo L-90-1258)

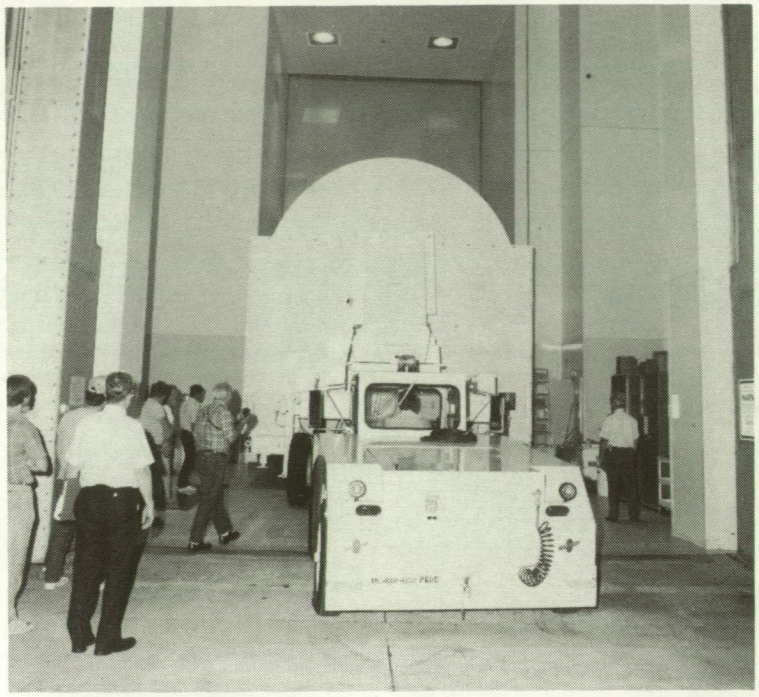

Figure 34.- Transfer of LDEF Assembly and Transportation System (LATS) into Spacecraft Assembly and Encapsulation Facility II (SAEF II) airlock. Note street clothes. (Photo L-90-01555)

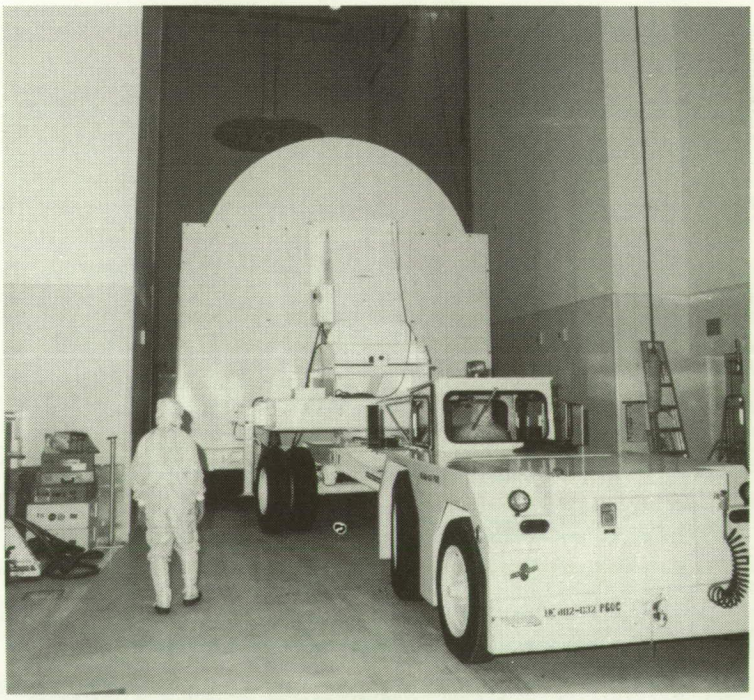

Figure 35.- Transfer of LDEF Assembly and Transportation System (LATS) from airlock into clean room of Spacecraft Assembly and Encapsulation Facility II. Note clean room clothing. (Photo L-90-01553)

Figure 36.- LDEF Assembly and Transportation System (LATS) cover being removed in Spacecraft Assembly and Encapsulation Facility II (SAEF II). (Photo KSC-390C-2774.09)

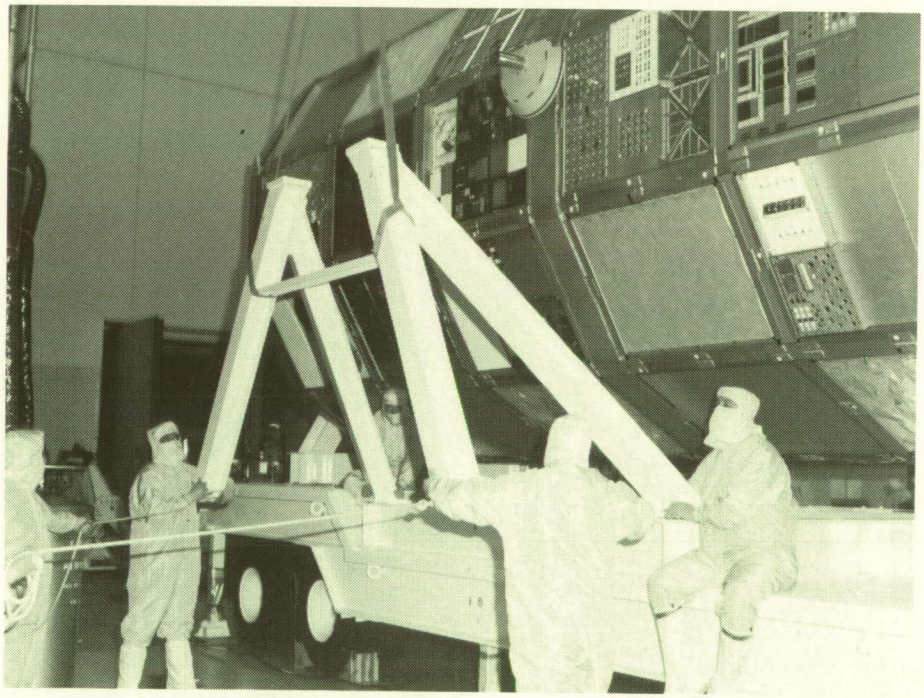

Figure 37.- LDEF Assembly and Transportation System (LATS) being configured for Spacecraft Assembly and Encapsulation Facility II (SAEF II) operations (Photo L-90-01728)

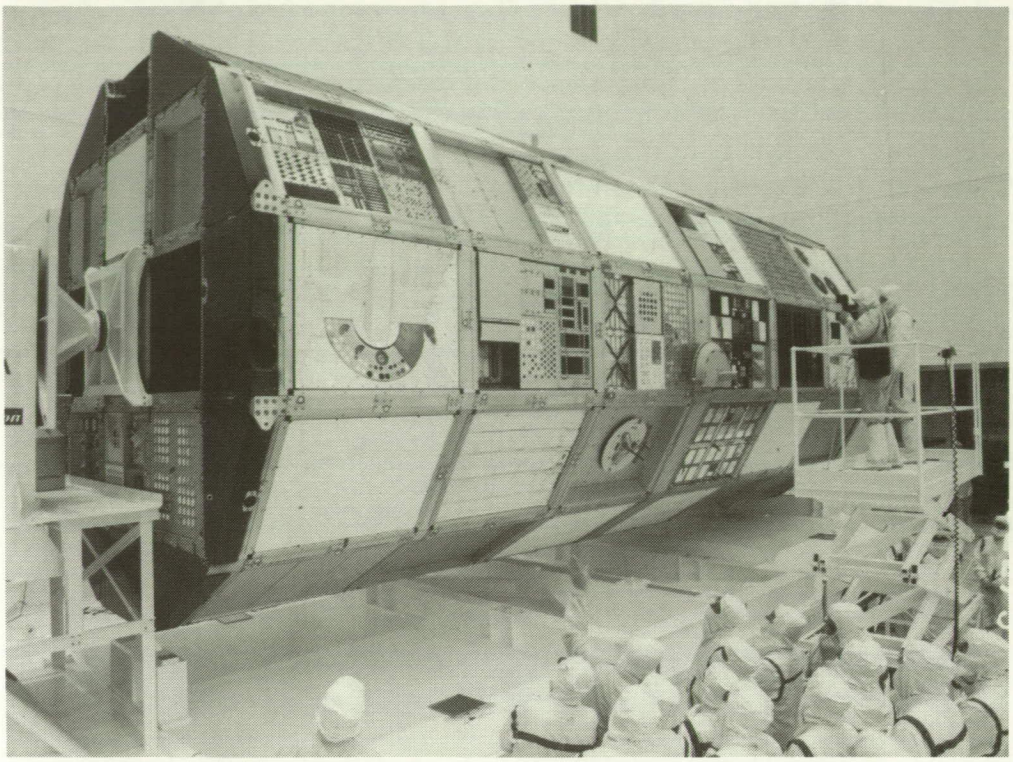

Figure 38.- Personnel inspection LDEF. (Photo L-90-02273)

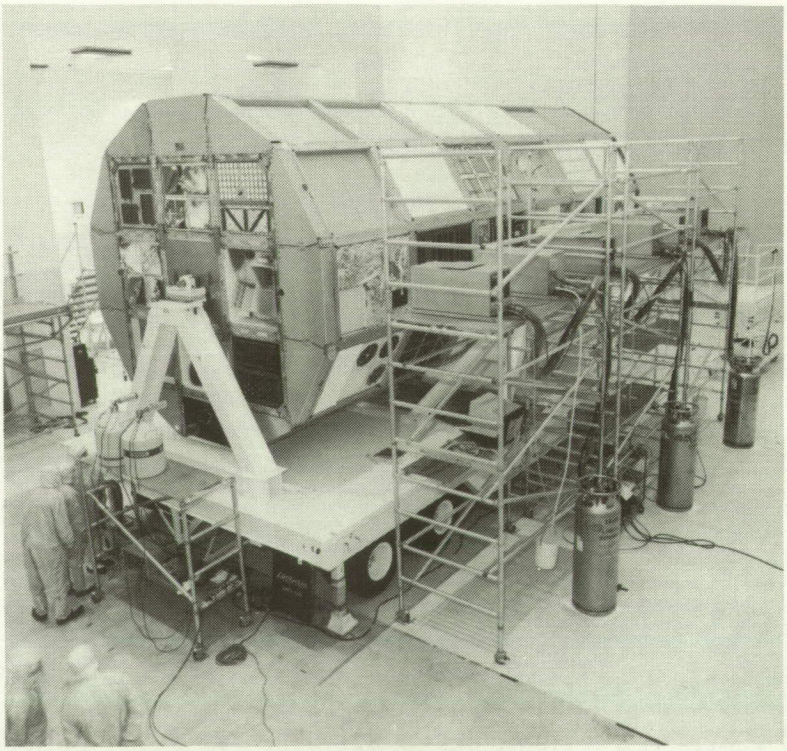

Figure 39.- Radiation measurements instrumentation setup. (Photo KSC-390C-760.07)

Figure 40.- Tray lifting fixture being attached to tray flange. (Photo L-90-03089)

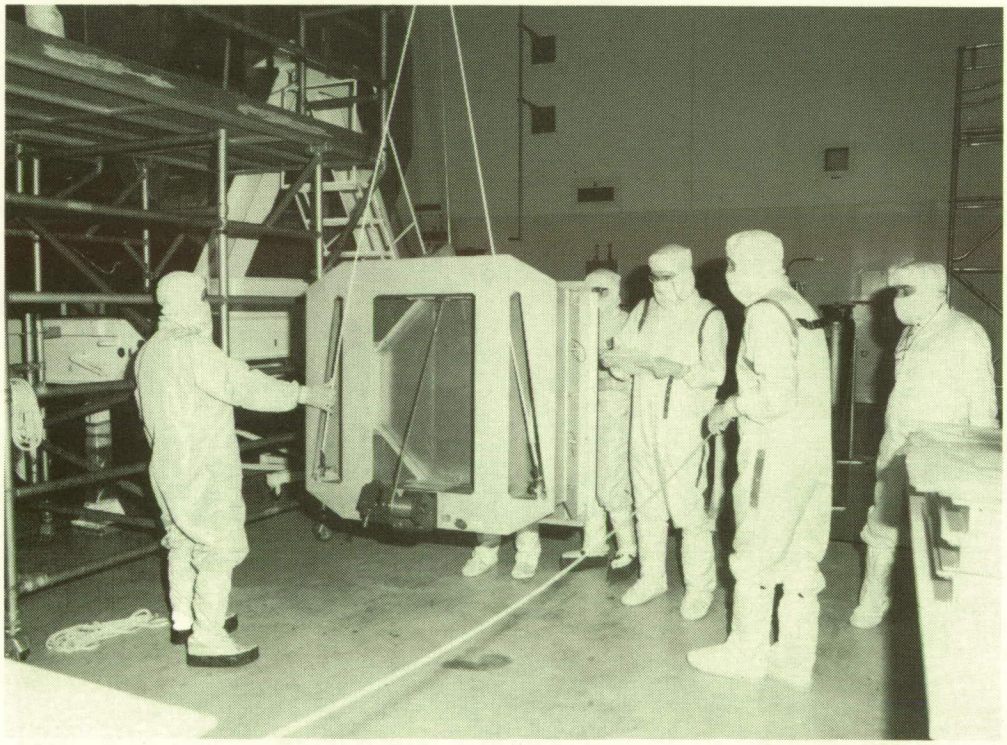

Figure 41.- Tray being inspected prior to being placed on rotator. (Photo L-90-03082)

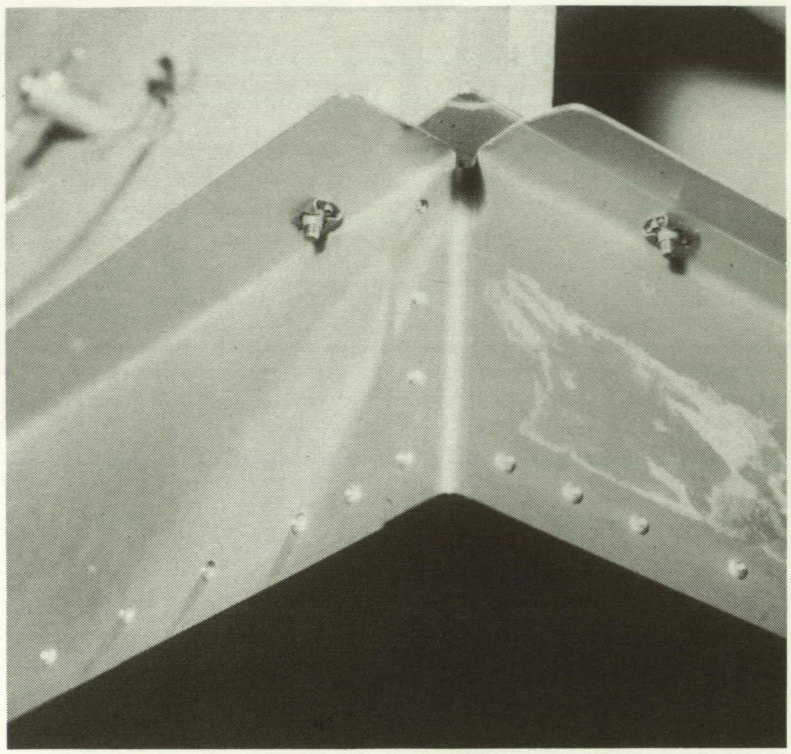

Figure 42.- Example of tray contamination. (Photo KSC-390C-1537.12)

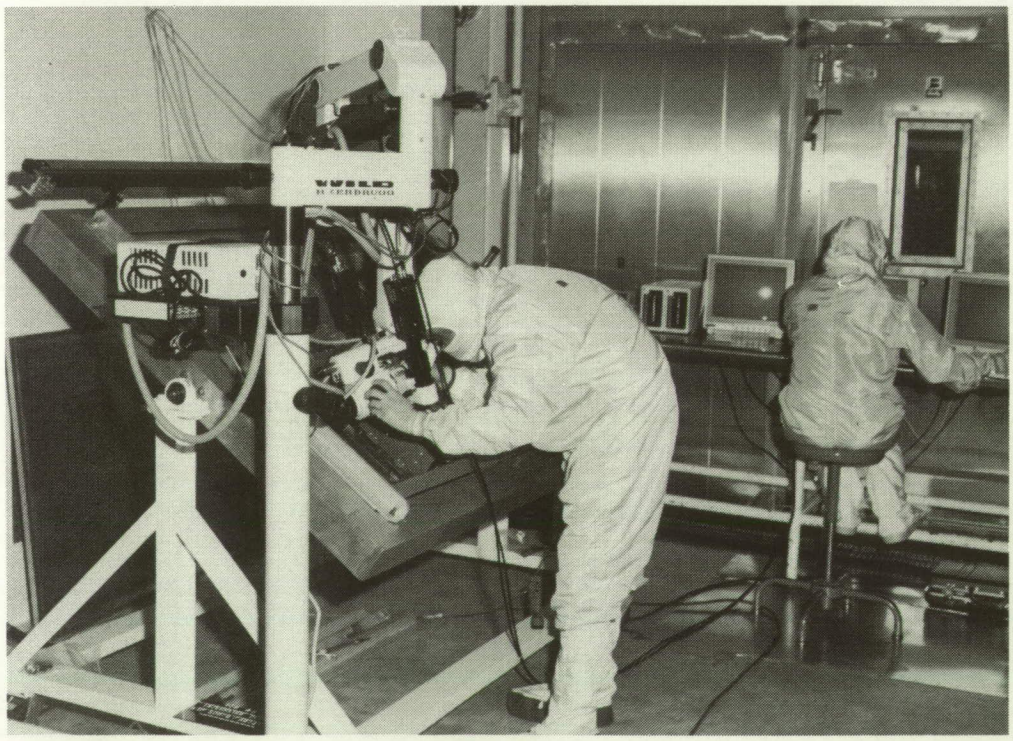

Figure 43.- Experiment being scanned for meteoroid and debris impacts. (Photo L- 90-03135)

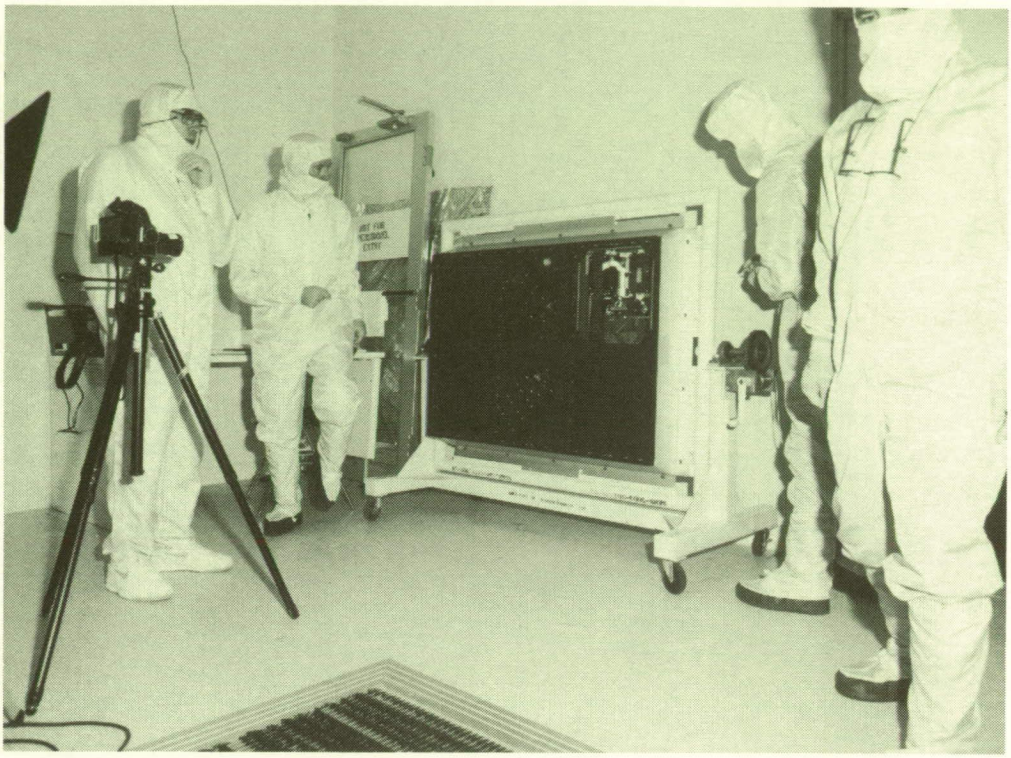

Figure 44.- Experiment tray set up for photo survey. (Photo L-90-03088)

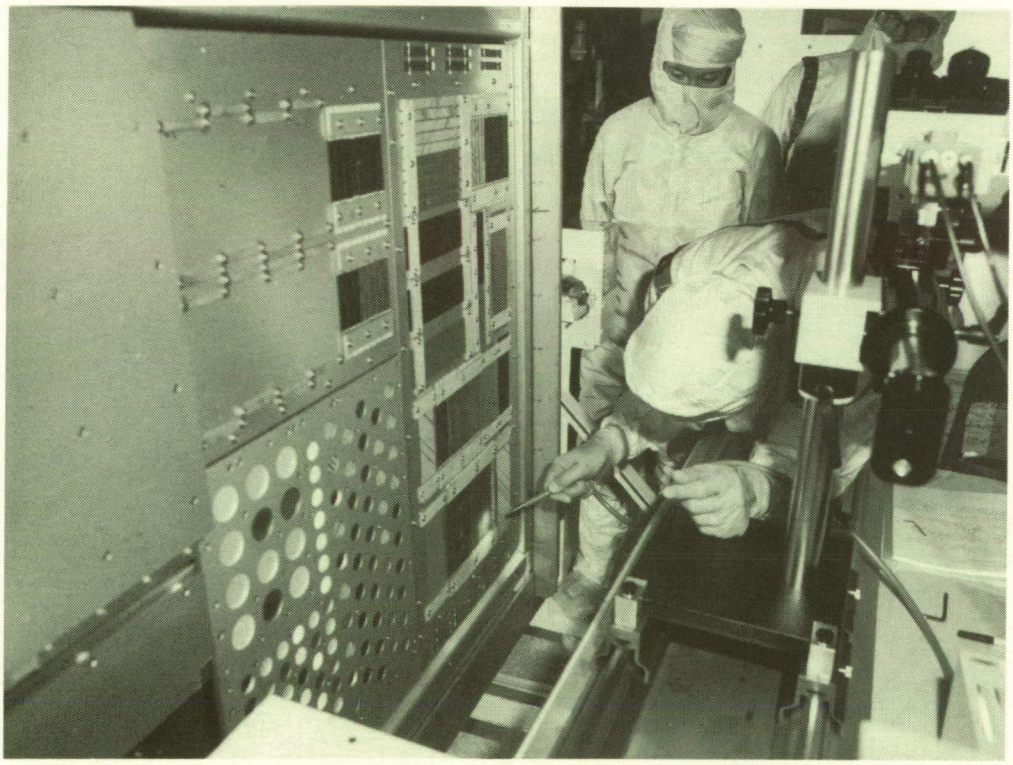

Figure 45.- Tray set up for contamination measurements. (Photo L-90-03033)

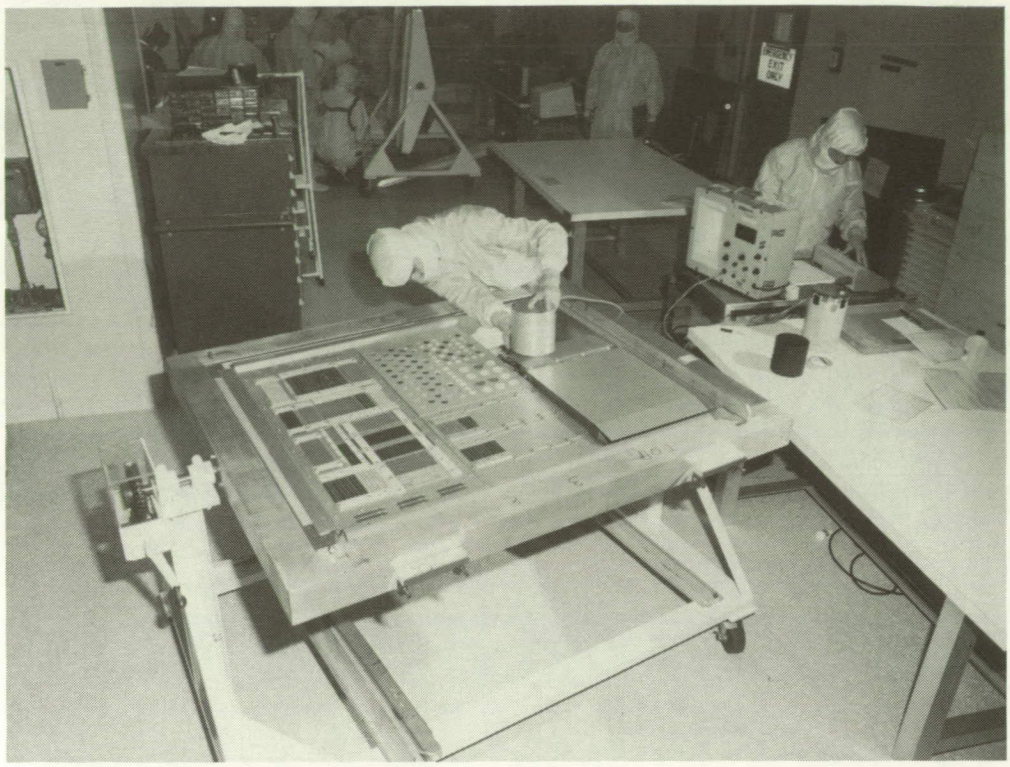

Figure 46.- Thermal properties measurements of experiment surfaces. (Photo L-90-03039)

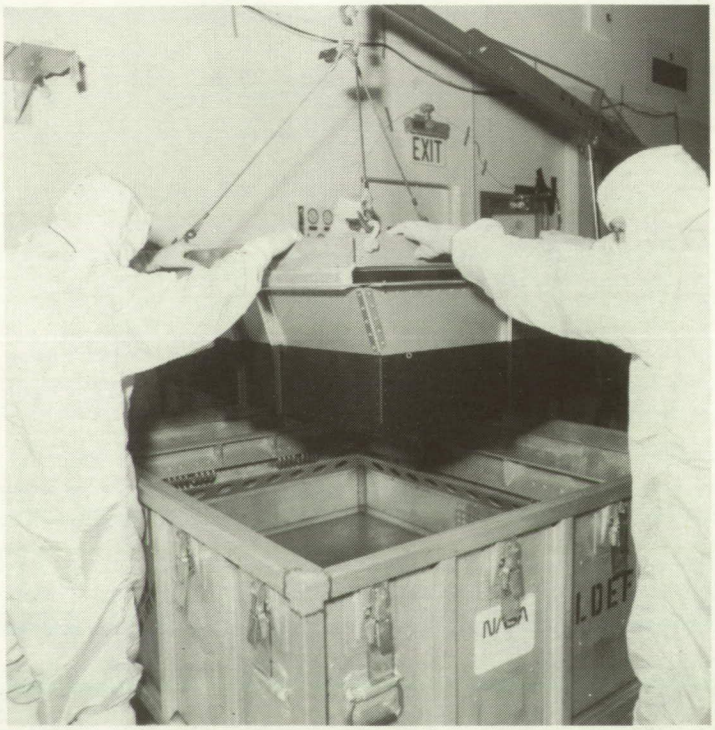

Figure 47.- Placement of experiment tray into shipping container. (Photo KSC-390C-1471.08)

Figure 48.- Dye penetrant test on trunnion mounting holes in center ring structure. (Photo KSC-390C-3768.08)

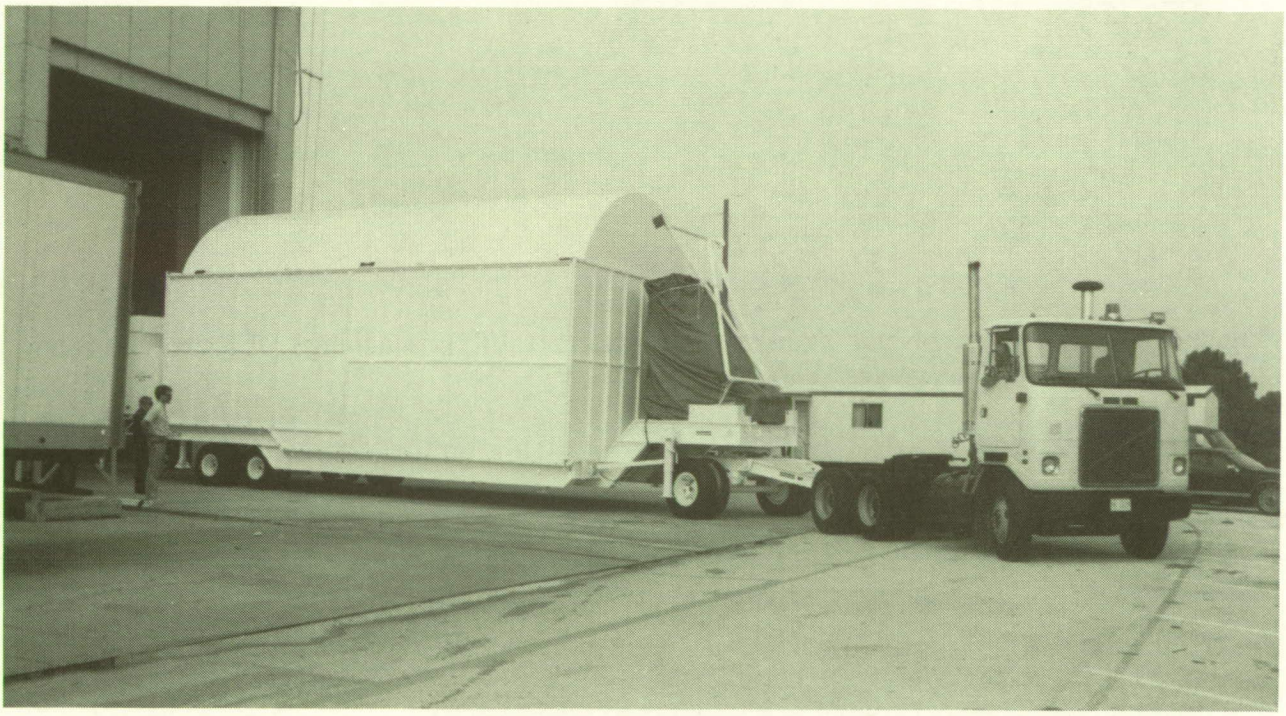

Figure 49.- LDEF Assembly and Transportation System (LATS) containing LDEF structure leaving Spacecraft Assembly and Encapsulation Facility II (SAEF II). (Photo KSC-390C-3974.05)

Figure 50.- LDEF Assembly and Transportation System (LATS) containing LDEF structure being placed in storage. (Photo KSC-390C-3976.11)

LONG DURATION EXPOSURE FACILITY (LDEF) SPACE ENVIRONMENTS OVERVIEW

William H. Kinard
NASA Langley Research Center
Hampton, VA 23665-5225
Phone: 804/864-3796, FAX: 804/864-8094

Glenna D. Martin
NASA Langley Research Center
Hampton, VA 23665-5225
Phone: 804/864-3773, FAX: 804/864-8094

SUMMARY

The LDEF was retrieved from Earth orbit in January 1990 after spending almost 6 years in space. It had flown in a near-circular orbit with an inclination of 28.5 degrees. Initially the orbit altitude was approximately 257 nautical miles; however, when the LDEF was retrieved the orbit altitude had decayed to approximately 179 nautical miles. The LDEF was passively stabilized about three axes while in free flight, making it an ideal platform for exposing experiments which were measuring the environments of near-Earth space and investigating the long-term effects of these environments on spacecraft. This paper presents a brief overview of the encountered environments that were of most interest to the LDEF investigators.

INTRODUCTION

National Aeronautics and Space Administration (NASA), Department of Defense (DOD), and other government agencies need accurate knowledge of the near-Earth space environments and the effects of these environments on spacecraft to efficiently and reliably implement their space programs. Uncertainties, for example, in our current knowledge of the man-made debris, the natural meteoroid, or the radiation environments, and the effects these environments can have on spacecraft may result in the installation of thousands of pounds of unnecessary shielding on spacecraft such as Space Station Freedom. An even more critical concern, however, is the fact that the uncertainties in our current knowledge of these same environments and their effects may also result in the development of spacecraft that will fail to accomplish their mission objectives. This would result in the loss of large national investments.

Accurate knowledge of the space environments is also highly desirable science to better understand the origin and evolution of our universe.

In-space experiments are a necessary part of research programs to define the environments of space, and in many cases are also a necessary part of research programs to define the effects of these environments on spacecraft. For example, the effects of atomic oxygen impingement and effects of hypervelocity meteoroid and debris impacts on spacecraft cannot be very well simulated in the laboratory. The effects of other environments such as reduced gravity and the synergistic effects of all of the environments found in space are impossible to study in the laboratory; they can only be studied with in-space experiments. The LDEF was developed to provide opportunities for these types of needed in-space environment and environmental effects experiments.

The environments that were of most interest to the Principal Investigators of the LDEF experiments were atomic oxygen, ionizing radiation, natural meteoroids, man-made debris, ultraviolet (UV) radiation, vacuum, and the very low gravity. This paper provides a brief overview of these environments as they are defined in pre-LDEF influenced models. The contributions from individual LDEF experiments to our knowledge of these environments, and to our knowledge of the effects of these environments on spacecraft, have been and will continue for some time to be reported by the respective LDEF experiment Principal Investigators in various publications. In a few cases, however, early reported significant contributions from LDEF experiments to the definitions of these environments are noted in this paper.

It is the intent of this paper to provide the reader with an introductory composite picture of the environments of space which the LDEF and the experiments encountered for the prolonged 69 months' stay in orbit.

BACKGROUND

The LDEF was launched into Earth orbit in April 1984 at a time of near-minimum activity in the Sun's 11-year solar cycle, and it was retrieved almost 6 years later in January 1990 at a time of near-maximum solar activity. The variation in the 10.7cm radiation levels over the mission life is shown in figure 1. The widely varying levels of solar activity, which were monitored by the 10.7 cm radiation, by counts of solar flares and Sun spots, and by measurements of the geomagnetic index, had a major effect on the near-Earth space environments encountered by the LDEF and the onboard experiments.

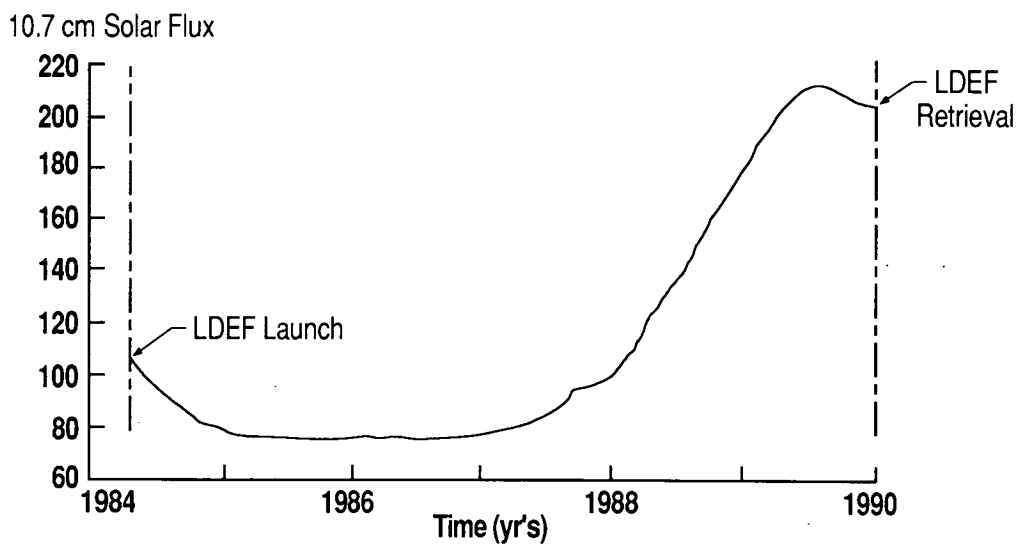

Fig. 1.- Solar activity as indicated by the 10.7 cm flux recorded during the time of the LDEF mission.

During LDEF's stay in space, it flew in a circular orbit having an inclination of 28.5 degrees. The orbit altitude was initially approximately 257 nautical miles. When the LDEF was retrieved, the orbit had decayed to an altitude of approximately 179 nautical miles. The history of the decay of the LDEF orbit altitude is illustrated in figure 2 (ref. 1).

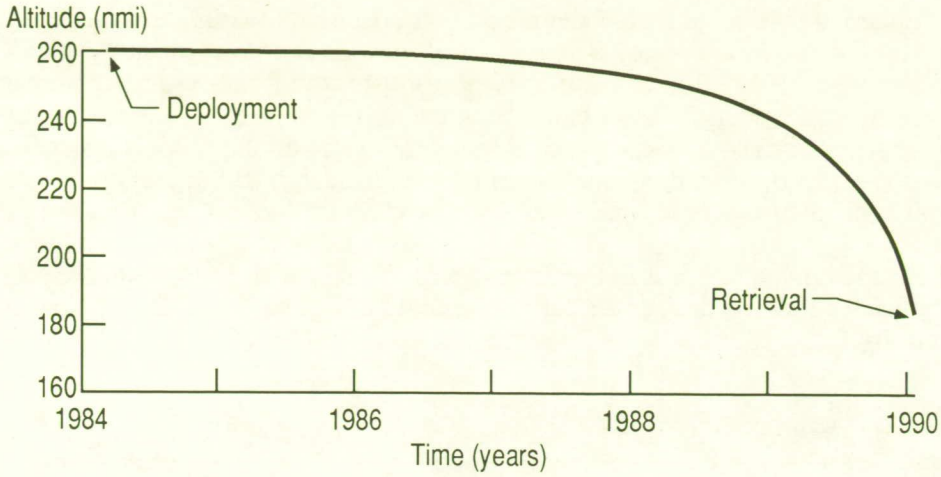

Fig. 2.- LDEF orbit altitude history.

The altitude decay, as can be seen in figure 2, was very slow during the first 4 years of the mission. The intense UV radiation from the Sun which occurred during the very high solar activity in 1989 (see fig.1) greatly expanded the effective atmospheric density at the LDEF orbital altitude, and thus the LDEF orbit was decaying very rapidly by the January 1990 recovery date. In fact, the LDEF would have reentered and been destroyed within another few months (see fig.3). The situation was so critical that some individuals in fact began to play the part of "Chicken Little" and literally cry out, "*The LDEF is falling*!"

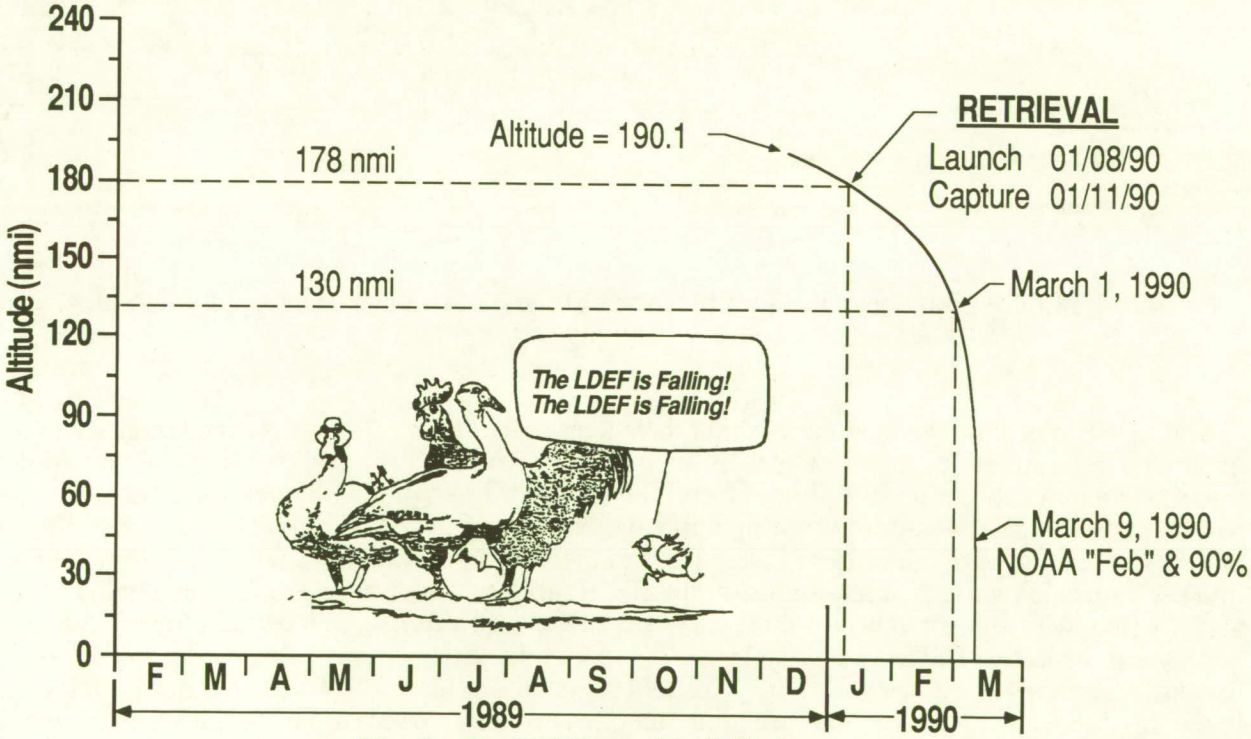

Fig. 3.- The LDEF predicted lifetime.

The orientation and stability of LDEF was such that it had a constant drag coefficient throughout the mission. Because of the constant drag coefficient, the LDEF tracking data obtained by North American Air Defense Command (NORAD) and the measurements of the solar 10.7 cm radiation and magnetic indexes obtained by the National Oceanic and Atmospheric Administration (NOAA) during the LDEF mission can be used to generate a unique set of measurements of the atmospheric density at the LDEF orbital altitude as a function of solar activity from solar minimum to solar maximum. This data set can be used by atmospheric scientists to check the current models of the Earth's upper atmosphere and its response to solar activity and to guide revisions in the models if necessary. Accurate models of the atmospheric densities are critical to the design and operation of large precision-pointing spacecraft such as the Hubble Space Telescope and Space Station Freedom.

The very rapid changes that can occur in the atmospheric density with changes in the solar activity are reflected in the LDEF altitude decay rate curve presented in figure 4 (ref. 2) for a period of rapidly changing solar activity.

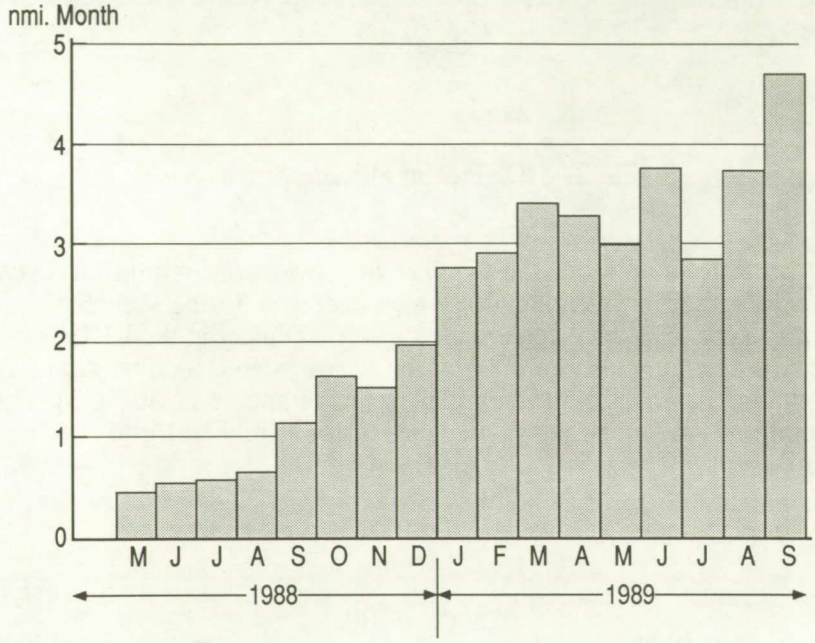

Fig. 4.- The LDEF orbit decay rate as a function of time during a period of rapidly changing solar activity.

The LDEF was passively stabilized about three axes while in free flight. Its orientation, as illustrated in figure 5, remained essentially such that one side always faced east in the direction of travel (velocity vector), one side always faced west in the trailing direction, and two sides were parallel to the velocity vector (one facing north and one facing south). One end of the LDEF always faced essentially toward the center of the Earth and the other end always pointed away from the Earth into deep space. Postflight observations of the LDEF surfaces* have revealed that the facility actually flew with a slight yaw (the most eastward LDEF face was canted 8 degrees toward the north), and the LDEF had a very slight pitch (the space end of the eastward face was also canted forward approximately 2 degrees). The postflight observations have also revealed that the facility, late in the mission, had essentially no oscillations about any of the three axes. The facility may have had some slight slow oscillations for a brief period just after it was deployed.

* Private communication from Bruce Banks, NASA Lewis Research Center, Cleveland, Ohio.

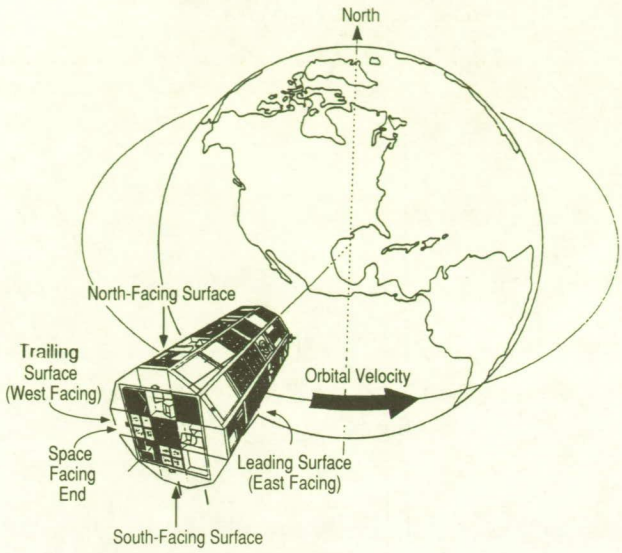

Fig. 5. - LDEF orientation.

Since many effects of the environments of space are orientation or velocity-vector dependent (meteoriod, man-made debris, trapped proton, and atomic oxygen environments for example), the very stable LDEF orientation with respect to the velocity vector was an extremely important LDEF feature.

ATOMIC OXYGEN

Atomic oxygen is the predominant species present at the LDEF orbital altitudes and thus the LDEF drag data can be viewed as an indication of the magnitude of the atomic oxygen fluence the LDEF encountered at any given time. The fluence of atomic oxygen striking a given LDEF surface was a function of the LDEF altitude, the orientation of the surface with respect to the LDEF velocity vector, the solar UV radiation, and the Earth's magnetic index. The 10.7 cm solar flux (fig.1) is used as an indicator of the UV radiation since there are no active satellites capable of monitoring the UV radiation. The UV radiation cannot be monitored from the ground because of atmospheric absorption.

The history of the atomic oxygen flux striking the leading surfaces of the LDEF during the mission is presented in figure 6. This flux history* was calculated using current upper atmospheric models, the history of the tracked LDEF altitude, and the monitored 10.7 cm solar radiation and magnetic indexes. As can be noted, the atomic oxygen flux during the latter months of the mission was almost two orders of magnitude greater than the flux encountered early in the mission.

The thermal velocity of the atomic oxygen in near-Earth space is low compared to the orbital velocity of the LDEF and, for that reason, the atomic oxygen total fluence on the leading surfaces of the LDEF was much greater than that on the trailing surfaces. Figure 7 shows the calculated distribution of the total atomic oxygen fluences on each of the 12 sides of the LDEF.* As can be seen, the fluence on the forward-facing east side is approximately 19 orders of magnitude greater that that on the trailing west. The fluence on the south side is slightly higher than that on the north because of the slight yaw in the LDEF orientation.

*See footnote on previous page.

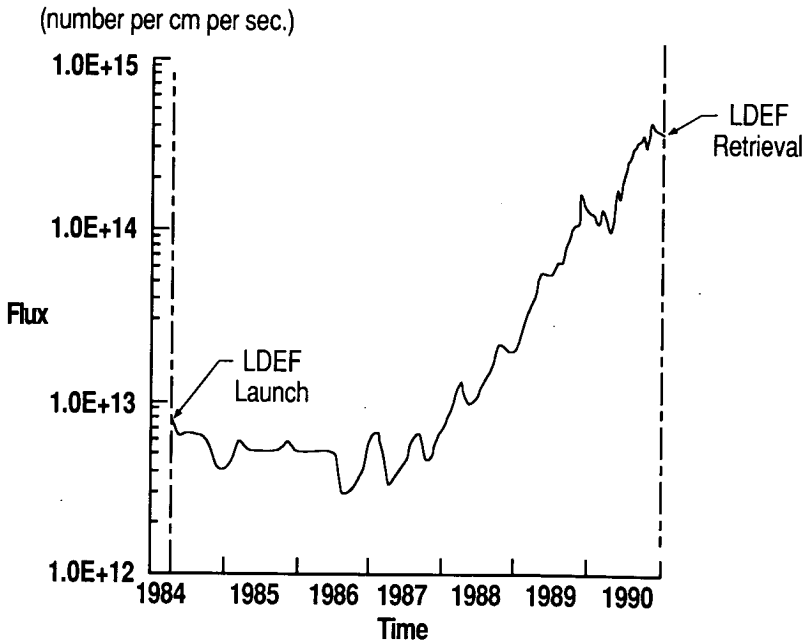

Fig. 6.- History of atomic oxygen fluence on LDEF leading surfaces.

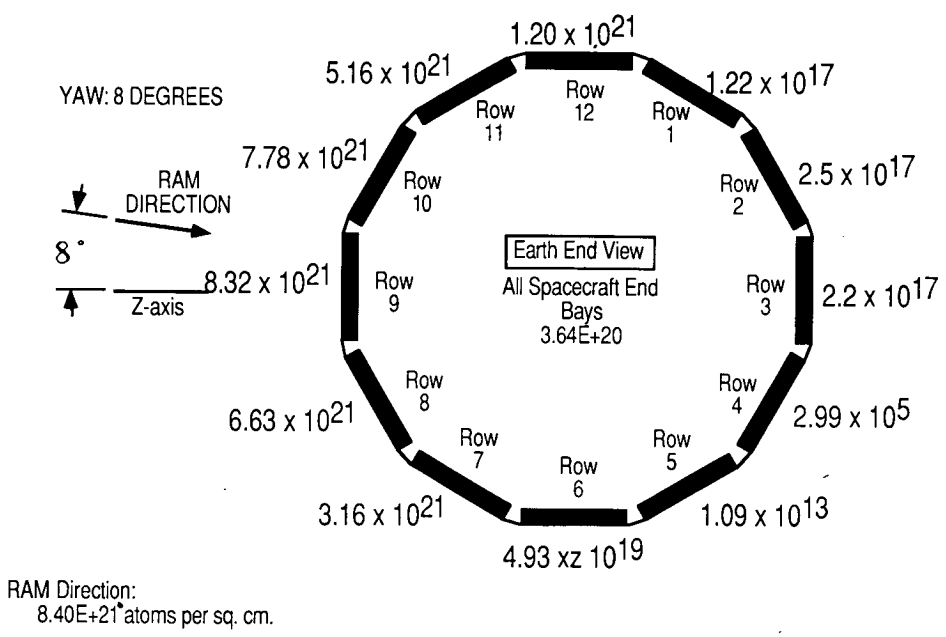

Fig. 7.- Calculated distribution of the total atomic oxygen fluence on each of the LDEF surfaces.

Because the LDEF orbit altitude was well below the Earth's Van Allen radiation belts, except at the small region of the belt that is generally referred to as the South Atlantic Anomaly, the LDEF and the onboard experiments were exposed to only modest levels of ionizing radiation. The penetrating ionizing radiation the LDEF did receive resulted primarily from protons trapped in the South Atlantic Anomaly region of the Van Allen belts and, to a much lesser degree, from galactic cosmic rays. The predicted trapped proton integral fluence for the LDEF is presented in figure 8.

The geomagnetically trapped electrons dominated the LDEF surface absorbed radiation dose. The integral fluence of the trapped electrons on the LDEF is presented in figure 9.

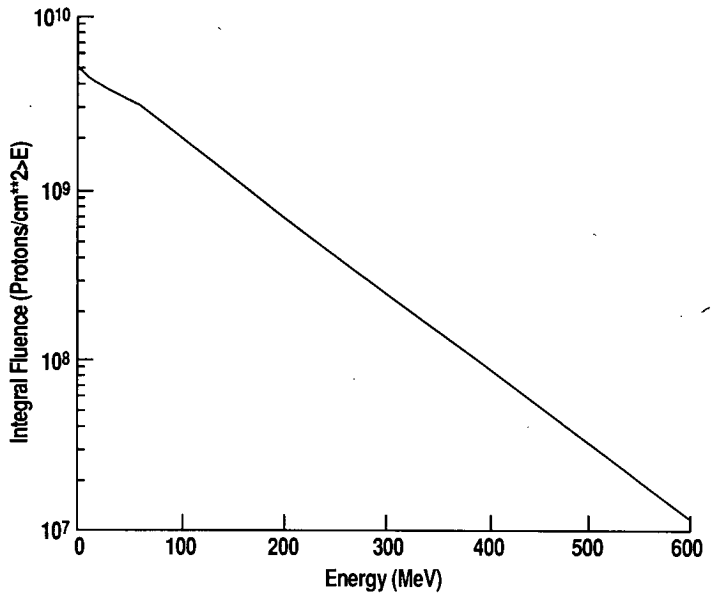

Fig. 8. - Predicted integral fluence of trapped protons striking the LDEF.

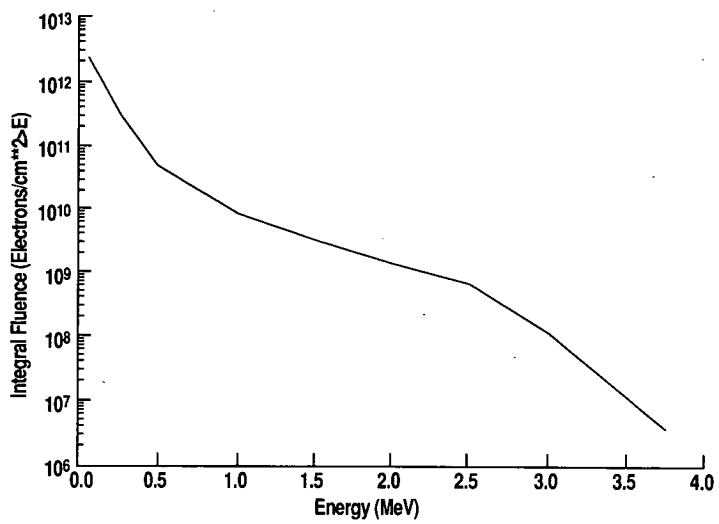

Fig. 9. - Predicted integral fluence of trapped electrons striking LDEF surfaces.

Primary ionizing passive radiation detectors were included in 15 of the LDEF experiments and these detectors along with postretrieval measurements of the induced radiation in LDEF materials have and will continue to provide valuable information for refining the current models of the radiation environment near Earth and the calculations of the ionizing radiation the LDEF actually received. Measurements of the induced radioactivity in selected aluminum experiment tray clamps from the LDEF have, for example, confirmed an anisotropy situation in the trapped protons in the South Atlantic Anomoly. The west-facing LDEF surfaces received a higher trapped proton fluence than did the east-facing surfaces.

NATURAL METEOROIDS AND MAN-MADE DEBRIS

The current models which are most frequently used to predict natural meteoroid and man-made debris impacts on spacecraft are shown in figure 10.

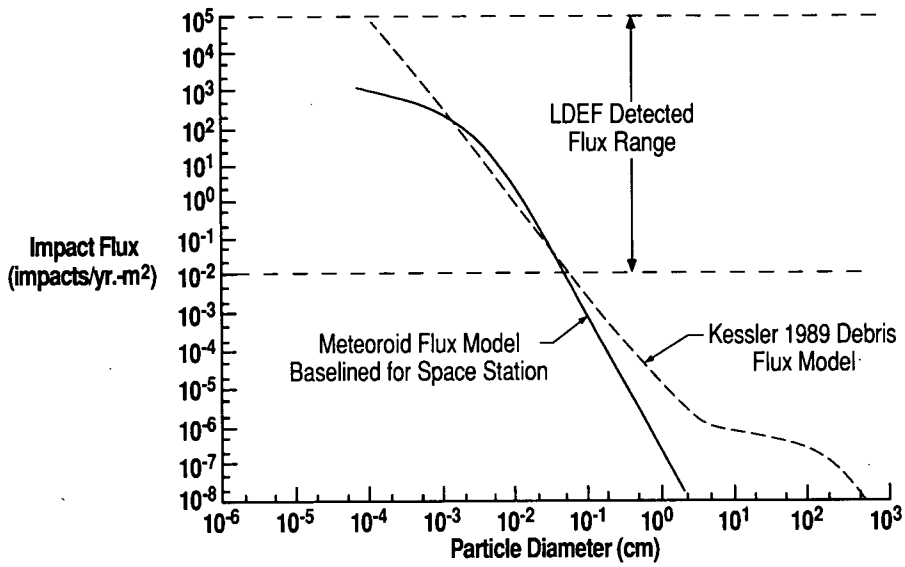

Fig. 10.-The most frequently used models for predicting meteoroid and man-made debris impact fluxes as a function of particle size.

Based on these models the largest man-made debris particles or the largest natural meteoroid particles one should expect to have impacted on the LDEF would be approximately .5 mm in diameter. An impact by a particle of this size is consistent with the size of the largest craters observed on the retrieved LDEF. These models also indicate that in the particle size range from approximately .02mm to .2mm more of the impacting particles would have been natural meteoroids rather than man-made debris. In the size range less than .02mm in diameter, the models indicate that man-made debris particles should have dominated the impacts.

The man-made debris model includes an assumption that the small debris particles are in orbits similar to the orbits observed for the large trackable Earth orbiting debris objects. This assumption means that debris particles would have impacted primarily on the leading surfaces of the LDEF and that no debris impacts should be expected on the trailing LDEF surfaces (craters with man-made debris residue in them, however, have been found on the trailing LDEF surfaces).

The model for the natural meteoroids assumes that they approach the Earth randomly from all directions with a distribution of velocities that averages about 20 km per sec. This assumption means that the leading surface of the LDEF would also have been impacted more frequently by meteoroids than the trailing LDEF surfaces. The meteoroid models (ref. 3), unlike the debris models, indicate that a substantial number of meteoroid particles will strike the trailing surfaces of the LDEF (this is generally consistent with the distribution of the craters found on the LDEF).

The Interplanetary Dust Experiment which was flown on the LDEF had very sensitive detectors mounted around the LDEF such that they faced east, west, north, south, toward the Earth, and out toward deep space. The impact counts recorded by the more sensitive of the two types of detectors flown in this experiment during the first year in orbit are presented in figure 11.†

• Detector Arrays Mounted on 6 Sides of LDEF

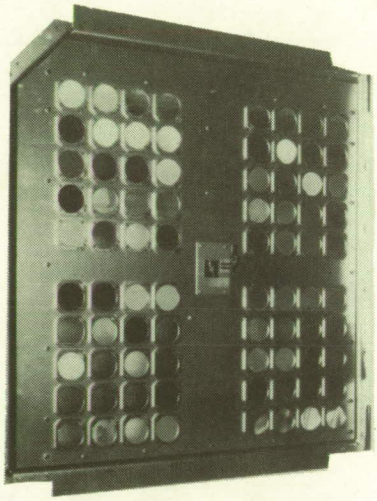

DETECTOR ARRAY MOUNTED ON EARTH SIDE OF LDEF

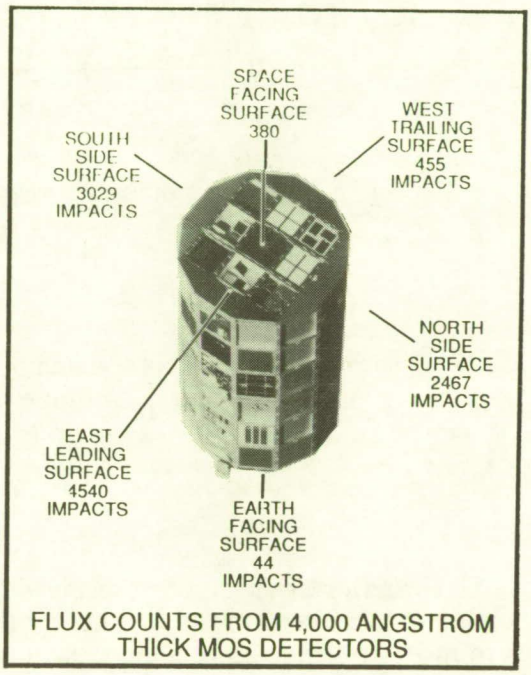

Fig.- 11. Distribution of impacts counted by LDEF Interplanetary Dust Experiment detectors mounted on the respective sides of the facility.

The Interplanetary Dust Experiment also recorded the precise time each of these impacts occurred as illustrated in figure 12. It can be noted that the events are certainly not random in time.

Measurements of the chemistry of the impactor residue that is present in most of the craters on the LDEF surfaces, which have just begun, will be extremely valuable in separating the man-made debris impacts from the natural meteoroid impacts. This separation will allow the two models (meteoroid and debris) to be evaluated independently. The preliminary indications are that errors exist in both models.

† Private communication from J. Derral Mullholland, Institute for Space Science and Technology, Gainsville, Florida.

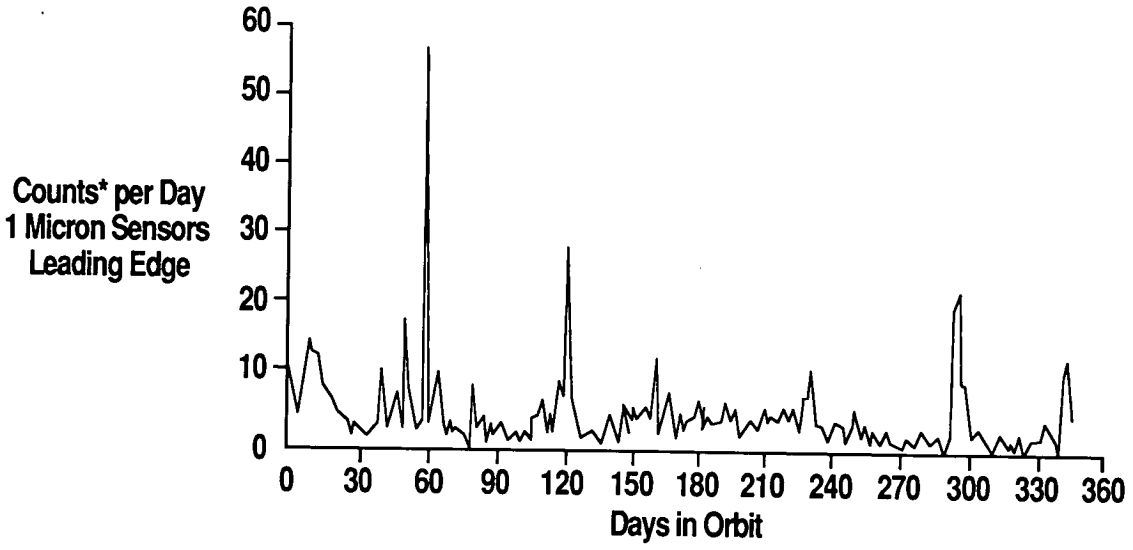

* Flight data from the LDEF Interplantary Dust Experiment

Fig.- 12. Distribution of impacts counted by LDEF Interplanetary Dust Experiment detectors as a function of time during the first year in orbit.

SOLAR FLUX

All of the exterior LDEF surfaces received direct solar illumination for periods of time during the 69-month mission. The cumulative times for the illumination of individual surfaces on the facility varied from 10 percent to 25 percent of the total mission time. The cumulative illumination time per orbit varied as the angle between the Sun's illumination vector and the plane of the LDEF orbit varied. The minimum cumulative illumination occurred when the LDEF orbit plane was in the ecliptic plane, and the maximum occurred when the LDEF orbit plane was at the maximum inclination to the ecliptic (see fig. 13).

VACUUM

Neglecting the contribution from LDEF-generated contamination, the molecular density adjacent to individual LDEF surfaces at any given time was dependent on the LDEF orbital altitude, the solar activity, and the orientation of the surface with respect to the LDEF velocity vector. The density increased as the altitude decreased and as the solar activity increased. The density also built up adjacent to leading surfaces as a result of ram effects, and it diminished adjacent to trailing surfaces as a result of wake shielding effects.

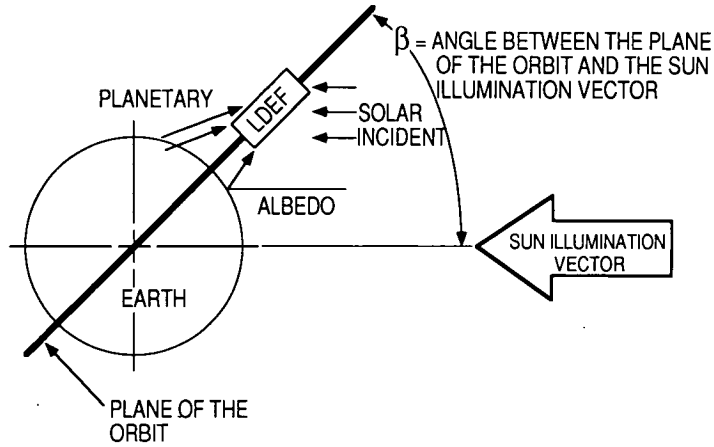

Beta Angle = (β) Angle between the plane of the orbit and the sun illumination vector.
Solar Incident = (BTU/Hr-Ft^2) Heat due to direct illumination from the sun.
Albedo = (BTU/Hr-Ft^2) Heat due to the portion of the solar incident energy reflected from the planet into the LDEF.
Planetary = (BTU/Hr-Ft^2) Heat due to energy emitted from the planet.

Fig.- 13.- Variation of the Sun's illumination vector with the plane of the LDEF orbit.

The ambient molecular density along the LDEF orbit was lowest early in the mission while the LDEF orbital altitude was above 250 nautical miles and the solar activity was near minimum (approximately 1.86 x 10^7 molecules per cubic centimeter). The predominent molecular species at that time were atomic oxygen (approximately 1.56 x 10^7 molecules per cubic centimeter), and nitrogen (second in abundance with a density several orders of magnitude lower than the atomic oxygen).

The ambient molecular density along the LDEF orbit was highest (approximately 6.58 x 10^8 molecules per cubic centimeter) late in the mission when the orbital altitude had decayed to approximately 179 nautical miles and the solar activity had increased to near-record highs. The predominant molecular species at that time was still atomic oxygen (5.42 x 10^8 molecules per cubic centimeter) and nitrogen was still second in abundance (1.06 x 10^8 molecules per cubic centimeter).

The ram effects made the molecular density adjacent to surfaces on the leading side of the LDEF approximately an order of magnitude higher than the ambient density. The wake shielding effects reduced the molecular density adjacent to surfaces on the trailing side of the LDEF more than an order of magnitude. The molecular densities presented above were calculated using the model described in Smithsonian Astrophysical Observatory Special Report 375 (ref. 4).

GRAVITY/ACCELERATIONS

The LDEF experiments were exposed to very low accelerations during the mission since the facility was passively stabilized and there were no systems on board to generate vibrations or shocks. The acceleration level at the center of the LDEF remained less than 10^{-7} g's throughout the mission.

CONCLUDING REMARKS

The LDEF flew in an orbit very similar to the orbits planned for many future near-Earth orbiting spacecraft such as the Space Station Freedom and the Earth observation satellites. Therefore the LDEF encountered the same environments as these future spacecraft will encounter, and the data obtained from the LDEF experiments and hardware will be directly applicable to the design of these spacecraft.

As stated in the introduction to this paper, the current uncertainties in a number of the near-Earth environments are a concern in the development of these future spacecraft. With the knowledge gained from analysis of the LDEF data, these current uncertainties can be appreciably reduced. When the LDEF data on the environments of space and the effects of these environments on spacecraft are completely analyzed and placed in accessible data bases, it will be obvious that the LDEF mission has provided "*Product Assurance*" for many of the future space missions.

REFERENCES

1. LDEF Orbital Decay Status Report, LDEF Project Office, Dec. 26, 1989.

2. LDEF Orbital Decay Status Report, LDEF Project Office, Sept. 12, 1989.

3. Meteoroid Environment Model [Near-Earth to Lunar Surface], NASA SP 8013, March 1969.

4. Jacchia, L. G.: Thermospheric Temperature, Density, and Composition: New Models, Smithsonian Astrophysical Observatory Report 375, March 15, 1977.

PINHOLE CAMERAS AS SENSORS FOR ATOMIC OXYGEN IN ORBIT; APPLICATION TO ATTITUDE DETERMINATION OF THE LDEF

Palmer N. Peters
Space Science Laboratory, NASA/MSFC
Huntsville, Alabama 35812
Phone: 205/544-7728, Fax: 205/544-7754

John C. Gregory
The University of Alabama in Huntsville*
Huntsville, Alabama 35899
Phone: 205/895-6028, Fax: 205/895-6349

SUMMARY

Images produced by pinhole cameras using film sensitive to atomic oxygen provide information on the ratio of spacecraft orbital velocity to the most probable thermal speed of oxygen atoms, provided the spacecraft orientation is maintained stable relative to the orbital direction. Alternatively, as described here, information on the spacecraft attitude relative to the orbital velocity can be obtained, provided that corrections are properly made for thermal spreading and a co-rotating atmosphere. The LDEF orientation, uncorrected for a co-rotating atmosphere, was determined to be yawed 8.0° ± 0.4° from its nominal attitude, with an estimated ± 0.35° oscillation in yaw. The integrated effect of inclined orbit and co-rotating atmosphere produces an apparent oscillation in the observed yaw direction, suggesting that the LDEF attitude measurement will indicate even better stability when corrected for a co-rotating atmosphere. The measured thermal spreading is consistent with major exposure occurring during high solar activity, which occurred late during the LDEF mission.

INTRODUCTION

A requirement to study the LDEF attitude was identified and a pinhole camera was developed for this purpose as part of Experiment A0114 (refs. 1-3). The atomic oxygen sensitive pinhole camera uses the fact that oxygen atoms dominate the atmosphere in low-Earth orbits, and formation of a nearly

---

*Work supported in part by a grant from UAH Research Institute and NASA grant NAGW-812 and contract NAS8-36645.

collimated beam of oxygen atoms passing through a pinhole in a satellite front surface occurs as a result of the orbital velocity being greater than the most probable Maxwell-Boltzmann speed of the oxygen atoms. Thus, the range of incidence angles of atoms to satellite surfaces is very limited, as shown by the angular distribution curves for two different temperatures in fig. 1 and described in greater detail elsewhere (ref. 4). The same maximum oxygen atom intensity was used for both temperatures to illustrate how the intensity spreads into the wings for higher temperatures. A thin film of material (silver in this case), which is sensitive to atomic oxygen, then forms an image of the impact spot.

The temperature of the thermosphere depends upon solar activity; the 700 K temperature in fig. 1 is characteristic of a solar minimum and the 1500 K is closer to a solar maximum. LDEF altitude was high during the solar minimum of September 1986 (initially deployed at 480 km in April 1984) where oxygen density was lower and had decayed by the time solar maximum was reached in June 1989 (recovery occurred at 310 km in January 1990). Most of the exposure in the pinhole camera occurred close to solar maximum. When the altitude was lower, the oxygen density was greater, and the angular distribution for atom incidence was widest. As will be described later, a well-defined spot was measured on the pinhole camera's silver sensor surface. Although overall darkening from overexposure (scattered atoms within the camera) was observed, this spot has been interpreted as being from the direct incidence beam and was used to determine the orientation of the LDEF relative to the orbital velocity.

MEASUREMENTS

The pinhole camera consisted of a 0.3 mm thick stainless steel hemisphere 3.25 cm (1.28 in.) radius, polished on the concave surface and coated with vacuum-evaporated silver. Silver was used because it discolors from formation of oxide (ref. 5). The pinhole had a conical shape with an included angle much wider than the maximum atom incidence angle and terminated as knife edges at a pinhole diameter of 0.5 mm (0.020 in.). The pinhole was positioned at the center of the silvered hemisphere. As shown in fig. 2, the exposure at any point on the hemisphere will depend upon the solid angle subtended by the pinhole from that point and the point's angular displacement from the orbital direction, i.e., the atom fluence as a function of angle from the velocity vector as shown in fig. 1. For orientations within 10° of the orbital direction, the solid angle subtended by the pinhole is constant within 2%; the predominant effects of pinhole size and thus solid angle are to reduce the overall fluence, or exposure, and increase resolution by reducing pinhole size.

Thus, the spot produced behind the pinhole should be centered with the LDEF's velocity vector and the spot's intensity should correspond to the distribution shown in fig. 1. Any variation in the attitude of the LDEF's velocity vector relative to the atmosphere would cause the spot to wander, producing a nonspherical, larger than normal, spot compared to that produced by thermal spreading of the beam.

Two techniques were used to determine the spot center and its shape: the first technique involved measurements taken directly from an enlarged photograph of the hemisphere taken on-axis with a 120 mm format camera and a 80 mm macro lens, and the second technique involved digitizing a 512 x 512 pixel CCD video camera image of the hemisphere and processing it to obtain both the spot and hemisphere centers and the spot geometry. Both techniques gave similar results.

DISCUSSION

Assuming that misalignment of the pinhole camera relative to the LDEF frame was negligible (machined surfaces and robust structures offer assurance of this), an LDEF orbiting with nominal attitude should have produced a spot centered on the hemisphere and uniformly round. The actual spot, as shown in fig. 3, was off-center, as would be produced by $8^\circ \pm 0.4^\circ$ clockwise yaw viewed from the space end. The spot was elliptical (major axis 14.8° and minor axis 14.1°, as subtended from the pinhole), with the major axis in the satellite yaw direction. It is noted that a yaw of 8° should have narrowed the spot in the yaw direction, not widened it as observed; thus, an oscillation in atom incidence along the yaw direction is the likely cause. This originally led us to conclude that the LDEF oscillated in the yaw direction (i.e., about its long axis), but it has been brought to our attention (Bourrassa, private communication, 1990) that a co-rotating Earth's atmosphere interacting with an inclined orbit produces an oscillation in the angle of incidence of oxygen atoms at the surface. We have verified that the oscillation occurs in the yaw direction, as observed, but the maximum range should be about $\pm 1.5^\circ$, not the estimated $\pm 0.35^\circ$ obtained from the ellipticity measured on the spot. While the center of the spot is rather well defined and is believed to be the average orientation for the LDEF, oscillations, thermal spreading, and other influences on exposure, such as multiple scattering must be separated. Some considerations are

1. The exposure of the silver was an integrated effect which occurred over 5 3/4 years, over a wide range in oxygen atom temperature, and with an excess background from multiply-scattered atoms. However, most of the oxygen exposure was received during the last six months of the flight.

2. We have not been able to depth profile the exposed silver film, particularly across the spot. Although a nearly circular bull'seye pattern suggests a profile similar to those in fig. 1, we have not yet devised a satisfactory technique for measuring optically opaque profiles.

3. Without a depth-composition profile it is not possible to fit the oxygen exposure to a known temperature distribution and there is some uncertainty as to the exact limits of the spot diameter (i.e., where the spot ends and the background takes over); however, it appears that rings on the spot represent equal thicknesses of oxide and provide the measured ellipticity. The minor axis of the spot could represent temperatures as high as 1500 K if assigned FWHM in fig. 1.

4. An oscillating structure and the apparent oscillation caused by an inclined orbit and rotating atmosphere do not yield the same angular flux distribution in a pinhole camera. An oscillating structure sweeps rapidly through the zero displacement and pauses at the extreme angular displacement; The opposite is true for the rotating atmosphere effect. Thus, a mechanical oscillation has a larger integral effect on spot diameter for the same number of degrees of oscillation. We are calculating these profiles with atmospheric oscillations included. Further study is needed to accurately determine the LDEF's range of oscillation.

Analysis by x-ray diffraction of the black powder flaking from much of the camera interior confirmed that it was Ag_2O. For reasons yet unknown, the primary exposed spot was more stable than the rest of the background exposed surface; this assisted our investigation.

AKNOWLEDGEMENTS

The authors are grateful for continued assistance from David Carter, William Kinard, and Jim Jones of the NASA Langley Research Center; to Howard Foulke of the General Electric Company for explanations of their satellite stabilization studies; to William Witherow for digital image measurements; and to Charles Sisk for computer assistance.

REFERENCES

1. Clark, L. G., Kinard, W. H., Carter, D. J., and Jones, J. L., Jr., Eds., "The Long Duration Exposure Facility (LDEF): Mission 1 Experiments," NASA SP-473, Scientific and Technical Information Branch, NASA, Washington, D.C. (1984).

2. Siegel, S. H. and Das, A., "Passive Stabilization of the LDEF," Final Report on contract NASI-13440, GE Document No. 74SD4264, November 1974, General Electric Company, Astrospace Division, Philadelphia, PA.

3. Siegel, S. H. and Vishwanath, N. S., "Analysis of the Passive Stabilization of the LDEF," GE Document No. 78SD4218, August 1977, General Electric Company, Astrospace Division, Philadelphia, PA.

4. Peters, P. N., Sisk, R. C., and Gregory, J. C., "Velocity Distributions of Oxygen Atoms Incident on Spacecraft Surfaces," J. Spacecraft and Rockets, 25(1), 53-58 (1988).

5. Thomas, R. J. and Baker, D. J., "Silver Film Atomic Oxygen Sensors," Can. J. Phys., 50, 1676 (1972).

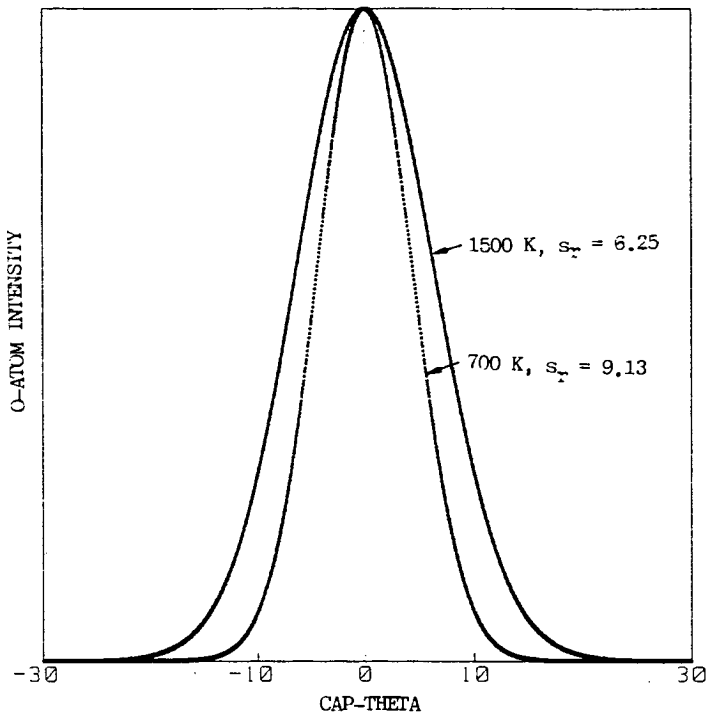

Fig. 1. Intensity of oxygen atoms versus incidence angle, cap-theta, in degrees from the orbital ram direction for two equilibrium temperatures of the atoms.

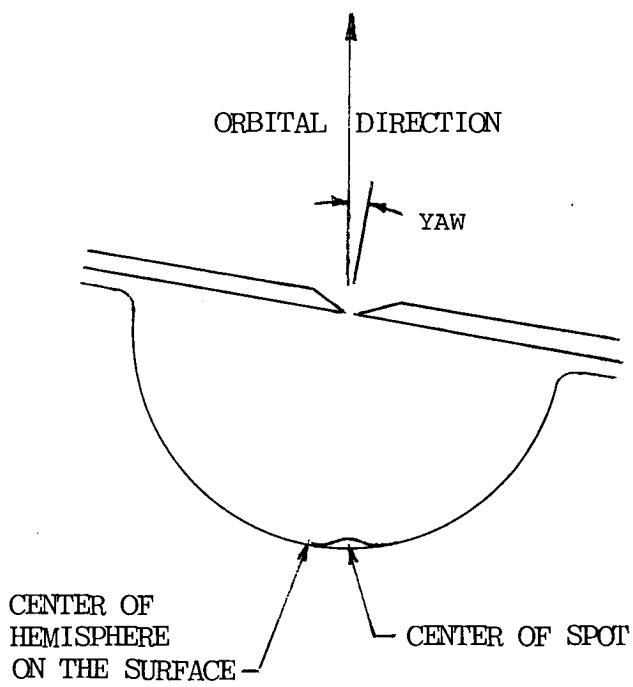

Fig. 2. Schematic of pinhole camera with off-centered spot due to yaw of the LDEF and showing thermal spreading about the spot center due to the effect shown in Fig. 1.

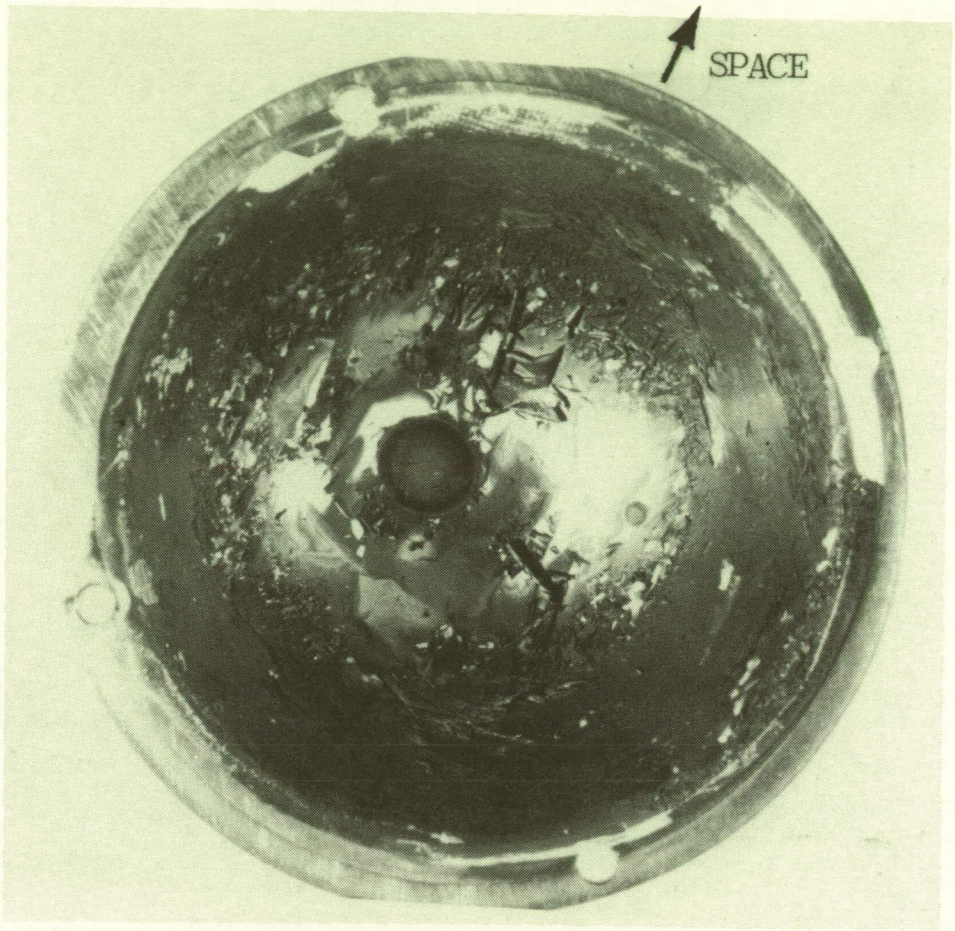

Fig. 3. Photograph of exposed silver hemisphere from pinhole camera; overall dark flaking area is interpreted as overexposure from multi-scattered atoms, and the spot, which is more stable, is believed to be from direct incidence.

USE OF THE LONG DURATION EXPOSURE FACILITY'S THERMAL MEASUREMENT SYSTEM FOR THE VERIFICATION OF THERMAL MODELS

William M. Berrios
NASA Langley Research Center
MS 434
Hampton Va. 23665-5225
804-864-8286

SUMMARY

The Long Duration Exposure Facility (LDEF) post-flight thermal model predicted temperatures have been matched to flight temperature data recorded by the Thermal Measurement System (THERM), LDEF experiment P0003. Flight temperatures, recorded at intervals of approximately 112 minutes for the first 390 days of LDEF's 2105 day mission were compared with predictions using the thermal mathematical model (TMM) . This model was unverified prior to flight. The post-flight analysis has reduced the thermal model uncertainty at the temperature sensor locations from ±40°F to ±18°F. The improved temperature predictions will be used by the LDEF's principal investigators to calculate improved flight temperatures experienced by 57 experiments located on 86 trays of the facility.

INTRODUCTION

The LDEF THERM experiment was developed to reduce the large uncertainties of ±40°F on predicted boundary temperatures calculated with the pre-flight LDEF thermal mathematical model (TMM). The high uncertainties of the model arise from the large number of complex flight hardware elements being represented by a reduced node TMM and the large number of bolted and clamped joints with uncertain thermal conductance. Due to the LDEF's large size and the logistical problems associated with experiment tray integration, it was impractical to perform a pre-flight thermal test to verify the TMM. A verified LDEF TMM with reduced calculated temperature uncertainties was needed to provide a set of boundary temperatures for the calculation of detailed temperatures of experiments located on the external surfaces of the LDEF. The THERM experiment provided an economical way for performing a post-flight verification of the TMM by recording a limited number of flight temperatures on selected locations of the LDEF structure.

The LDEF was deployed on April 7, 1984 into a gravity gradient stabilized posture at a 28½° orbit inclination with near zero rates along the pitch, roll and yaw axes. During the first 390 days of the LDEF mission, the THERM temperature data were recorded on the experiment power and data system (EPDS) recorder which was shared with the Low Temperature Heat Pipe Experiment (exp. S1001). After an LDEF mission of approximately 5¾ years (2105 days), the crew of the orbiter Columbia (STS 32) retrieved the facility from free flight on January 12, 1990 and returned the LDEF to Earth. LDEF altitude at deployment was 255 nm and it had fallen to 180 nm at the time of retrieval. Post-flight analysis indicated the LDEF was yawed 8° to 12° from row 9 towards row 8 throughout the mission, thus biasing the velocity vector towards row 10 (figure 1). Orbital beta angle (figure 2) range for the LDEF mission was ±52°. For the post-flight calculation of temperatures, a new set of orbital detailed heat fluxes were calculated for the beta angle range of ±52° for an average LDEF yaw angle of 10°. A composite daily averaged heat flux table for the first 390 days of the LDEF mission was generated with the new set of orbit detailed heat fluxes and the daily beta angle history. This new set of daily averaged thermal fluxes were used for calculation of daily averaged temperatures which allowed a direct comparison to the recorded THERM flight data.

The external surface thermal properties, absorptivity (α) and emissivity (ε), were measured during the disassembly operations of the LDEF at the Kennedy Space Center (KSC). Measurements were made on exposed and unexposed external structural surfaces, earth and space end thermal panels, tray lips, and a limited number of experiments. The measured α/ε values combined with nominal material specifications were used to formulate the LDEF surface property conditions that existed at the beginning of the mission and the end of the first year (390 days). The preflight TMM was modified by incorporating better estimates of bolted joint conductances, thermal radiation couplings omitted from the original pre-flight model, and better estimates of external surfaces α/ε degradation. The modified TMM was then used to obtain improved calculated flight temperatures for the LDEF spacecraft.

LDEF DESCRIPTION

The LDEF was developed jointly by the Office of Aeronautics And Space Technology (OAST) and Langley Research Center (LaRC) to provide a shuttle launched low cost accommodation for relatively simple experiments. These experiments would require long duration exposure to the space environment (approximately one year). Many experiments were completely passive, depending entirely on post-flight laboratory investigations for the results.

The LDEF is a reusable 12-sided bolted and welded cylindrical structure 14 ft. in diameter and 30 ft. in length (figure 3). Extrusions of 6061-T6 aluminum alloy are the main components for the LDEF structure (intercostals and longerons). The 12-sided cylinder forms a closed cavity when all 72 periphery and 14 end trays are mounted on the exterior of the spacecraft. Each tray can accommodate from one to several different self-contained experiments. The flight configuration for this mission (ref. 1) included 86 trays with a total of 57 experiments for a total weight of over 21,000 pounds.

LDEF THERMAL CHARACTERISTICS

Thermal Design

The thermal control of the LDEF is totally passive, and is accomplished by radiation coupling the inside of the facility, which consists of a hollow polygonal cylinder with closed ends. LDEF's passive thermal control design (ref. 2) maximized the internal radiation coupling between the spacecraft components by using high ε values on the internal surfaces. All interior surfaces are coated with Chemglaze Z-306 flat black paint which has an ε of 0.90. This unexposed coating did not seem to suffer any appreciable deterioration during the 6 year LDEF mission. Internal radiation blockage was decreased by minimizing the number of structural components inside the spacecraft. The cylindrical cavity was closed at all tray locations and at both ends to prevent solar flux from entering the interior. Venting holes were distributed uniformly around the facility. This venting area was approximately 0.15% of total external surface area. The thermal model accounted for the venting holes by coupling an interior dummy node to the space environment.

The bolted construction of the LDEF was a source of uncertainty in the heat conduction across the structural joints. The experiment trays were attached to the LDEF structure by eight 2"× 5" aluminum clamps along the tray perimeter. The tray mounting scheme minimized the contact area through which heat could be transferred between the facility structure and the experiment trays.

All experiments were mounted flush with the outside tray surface, simplifying the thermal modeling of the LDEF. Most tray models were reduced to two nodes (ref. 2) for input into the LDEF TMM. For better heat distribution and reduced temperature difference throughout the spacecraft, more than 50% of the experiment trays were coupled by radiation and conduction between the tray internal and external surfaces. The different panel type trays were uniformly distributed over the surface of the LDEF. Over 50% of the thermal control surface area was provided by the various chromic anodized coatings (figure 4) on the facility's aluminum structure, trays, and debris panels (Space Debris Experiment S0001, 24 trays). The external surface absorptivity to emissivity ratio (α/ε) for each of the tray lips and debris panels varied according to the LDEF thermal design requirements (ref. 3).

LDEF Thermal Model

The programs used for the calculation of the LDEF incident heat fluxes and temperatures were the Thermal Radiation Analysis System II (TRASYS II, ref. 4) and the Systems Improved Numerical Differencing Analyzer (SINDA, ref. 5). The SINDA program was used for the calculation of temperatures. SINDA is a system of computer codes used to solve lumped parameter representations of physical problems governed by diffusion type equations. Parameters include thermal mass, surface properties and thermal conductance. Hand calculated thermal conduction couplings were entered as well as thermal radiation couplings between all surfaces. Most of the internal radiation couplings were computer generated and their number

reduced to a manageable size by lumping very small values into a radiation coupling to an internal dummy node. Other detailed radiation couplings between isolated surfaces were generated by hand. LDEF orbital parameters obtained from ground tracking stations were used as input to TRASYS II to calculate the incident thermal solar and infrared heat fluxes. The calculated thermal fluxes were then integrated into the LDEF TMM in order to perform a post-flight temperature analysis.

The original thermal model (ref. 6) was created prior to the LDEF deployment and was restricted by program and computer capabilities to less than 300 nodes. The post-flight TMM size increased to 327 nodes to improve the model's accuracy and facilitate the comparison of selected nodes to the THERM experiment sensor temperatures.

Most experiment trays were described by two nodes (internal and external) with the internal node representing the tray. The external surface of the internal tray node is in the shape of a picture frame. This node was considered isothermal and the experiment was mounted inside it. The more complicated experiments were described by three and four node models. The experiment models were representations of more detailed models that could have as many as 80 nodes before reduction. The reduced node tray/experiment (T/E) models had equivalent energy balance and surface properties to the original T/E detailed models. The temperature values calculated for the T/E nodes represented an average for that tray location. For more detailed values, the T/E detailed thermal model for that location would have to be updated with the boundary temperatures from the LDEF TMM and the component temperatures recalculated using the experiment's detailed thermal model.

The original LDEF TMM was only capable of calculating day/night temperatures for one orbit. As part of the THERM effort a TMM was generated that calculated the daily averaged temperatures of the LDEF. The new model tracked the orbital beta angle (figure 5) instead of the hourly position of the LDEF within the Earth's orbit. This facilitated the direct comparison to the temperatures measured by the THERM system.

Thermal Measurements System (THERM)

The THERM system consisted of five copper-constantan thermocouples (T/C), one suspended radiometer, two thermistor reference measurements, an electronic scanning system, one 7.5-V battery, and an interface harness with the low temperature heat pipe experiment package (HEPP) experiment. The THERM data was recorded on dedicated channels of the shared EPDS tape recorder in the HEPP experiment (ref. 7).

The THERM hardware was located at selected areas of the LDEF interior in order to maximize the thermal environment characterization with a limited number of measurements (figure 6). Two thermistors measured the THERM electronic junction temperatures and were used for system calibration (thermistors #2 and #8). A measurement of the LDEF interior temperature average was made by suspending a radiometer with a T/C at the center of the LDEF interior (T/C #4). The radiometer was coupled radiatively to all of the interior surfaces providing in effect an average of all interior surfaces. T/C #1 was located on the center structure in order to provide a backup temperature value to the radiometer. The center

structure is a massive aluminum part that carries the main load of the spacecraft during the deployment and retrieval operations and is coupled radiatively to most of the internal surfaces. T/C #3 was located on top of the magnetic viscous damper thermal radiation shield. This T/C was thermally insulated from the dome and was used to measure the thermal environment around the viscous damper. The temperature measurements taken at this location showed the largest difference from the calculated values. Due to the mounting techniques and the shape of the data response to heat flux changes this measurement is suspect and is the subject of further investigation. The structural temperatures were characterized by the remaining three T/C's. T/C #5 was mounted on a structural member located on row six of the facility. This area was parallel to the orbit plane and experienced incident thermal flux environments that varied widely, depending on the orbital beta angle (β). For β's from 0° to +52° this side of the facility did not see direct solar incident thermal flux (albedo only), while for negative β's, the solar incident occurs for the full day period with orbit β= -52° being the maximum solar exposure for this row. This T/C also provided a good indication of LDEF's in-flight attitude. T/C #6 was located on the space end structure near row 12 to provide space end mounted experiments with representative boundary temperatures. The space end location had the maximum radiative coupling to space and no incident planetary or albedo thermal fluxes. The last temperature measurement, T/C #7, was located on the earth end structure near row six in order to measure the night/day (N/D) temperature cycling on that end with maximum radiative coupling to the planet. Total overall system accuracy was designed to be within ±10°F for all measurements over the range from -30°F to +170°F. The actual recorded temperature range for all seven locations was from a low of 39°F to the maximum of 134°F at the row six location.

DISCUSSION

The THERM data was designed to take a sweep of the thermal sensors with the same sampling rates as the HEPP (S1001) experiment. The fast data rate was designed to record data every five minutes when the low temperature heat pipes achieved cryogenic temperatures, thus providing a detailed orbit temperature profile for direct comparison to the TMM results. The low data rate cycle was designed to record data every 112 minutes and was not dependent on any event to be activated. The HEPP experiment did not reach a low enough temperature to activate the high data rate cycle, recording only at the low data rate and leaving no detailed orbit temperature for comparison to the LDEF thermal model. At the deployment altitude (255 nm), the LDEF orbits the Earth 15.3 times a day, or once every 94 minutes. The period of the recorded data rate for this orbit is approximately equal to six orbits (figure 7). A direct comparison between the measured data and the calculated values was achieved by using the daily averages of the measured temperatures and by modifying the TMM to calculate daily average temperatures as discussed earlier.

After comparing the pre-flight TMM temperatures to the THERM data the areas for improvement became apparent. The modeling of the Earth and space end thermal control panels was improved. The sides of the panels located on the LDEF periphery were not included in the original TMM in order to reduce the number of nodes. In addition, the conduction values across joints were reviewed in order to better account for contact resistance. The resistance to heat transfer across a bolted joint is highly variable and depends on many factors. Empirical values are most commonly used to account for joint conductances. Approximate contact resistance values were calculated by assuming 25% of the actual joint surface contact area. The net effect

from this change was to increase the heat flow across some of the joints, while reducing the heat flow across others depending upon the complexity of the joint in question.

The thermo-optical properties of the external surfaces were measured during the LDEF disassembly at KSC and used to modify the TMM (ref. 8). From the coatings assessment it was evident that the coatings on the LDEF had been affected by contamination. Unlike coating degradation, contamination does not have a typical rate of action. The THERM data provided the best estimate for the rate at which contamination affected the external surfaces optical properties. Most of the contamination effects occurred during the first year of flight. The temperature increases could not be accounted for by the orbit β seasonal changes and the materials surfaces typical α/ε rate of change alone. The effects from contamination were added to the estimated α/ε changes due to material degradation from space exposure. The degraded α/ε values used for the surface coatings were those measured during the LDEF disassembly. As the bulk of the outgassing contamination occurred during the beginning of the LDEF mission, it was assumed that the leading edge coatings had the same contamination effects as the trailing edge (Row 3). This assessment is consistent with results from the experiment S0010 (ref. 9). The experiment S0010 included an Experiment Exposure Control Canister (EECC), located on the leading edge of the LDEF. The EECC opened while in orbit at the beginning of the mission and closed prior to the first year of the LDEF flight (as programmed). The opening of the EECC by the principal investigator showed the coatings inside the canister to have contamination similar to that of the trailing edge of the facility, although the post-flight leading edge exposed surfaces' α/ε showed less effects from contamination than those on the trailing edge. The α/ε difference between the leading and trailing edge can be attributed to the cleaning effect occurring on the leading edge surfaces exposed to atomic oxygen impinging flux (AO). The amount of AO rises sharply at lower orbit altitudes and also with increased solar activity such as experienced by the LDEF during the last six months of the mission.

RESULTS

A comparison between the THERM measured temperatures and the TMM calculated values is shown on figures 8 to 14. These curves show the comparison between the calculated and the measured temperature values for all temperature measurement locations. The flight data shown in each plot are the daily average temperatures for that location. Data scans were taken 12 - 13 times a day and the data for each day were averaged into one temperature for that day thus allowing a direct comparison to be made against the thermal model temperature calculations.

A direct comparison of calculated versus measured values was done for each sensor location. The locations with the smallest model error were at the center ring, reference thermistor, and the space end which all had a standard deviation (3σ) of ±9 °F. The earth end and the row six longeron had the next lowest deviation of ±12 °F. The radiometer had the second largest 3σ T/C error of ±15 °F. A maximum uncertainty between the calculated and measured values of ±18°F was obtained at the damper dome location but as stated this T/C is suspect. The curves also show the maximum calculated temperature uncertainties occurred toward the end of the thermal analysis. The LDEF TMM assumed fully degraded α/ε values by the end of the 390 days of the THERM data period. It is likely that the fully degraded surface property values were achieved after the THERM operation, thus the diversion between the calculated and measured temperatures as seen at the end of the data period on all data figures. As the contamination effects on thermal control surfaces properties were highly variable during the course of the first

part of the LDEF mission, it was difficult to extrapolate the degradation curve for the affected coatings. A longer operation of the THERM system into the second year of the LDEF mission would have enabled an improved characterization of the contamination effects and a better agreement between the calculated and measured temperatures towards the end of the data period. The 3σ uncertainties (Table 1) are no greater than ±18°F for any of the THERM temperature sensor locations, thus achieving the desired reduction of calculated temperature uncertainties to under ±20°F. Given in Table 2 are the temperature range comparisons between the design limits, measured temperatures, and the post-flight calculated temperatures for the T/C locations.

CONCLUSION

The post-flight calculation of the LDEF flight temperatures have been achieved with an uncertainty of under ±20°F even with the use of fully degraded surface values at the end of the temperature data period. The LDEF facility design temperatures were maintained throughout the mission. The thermal control contamination made the extrapolation of the surface coatings degradation into the second year very difficult due to the lack of temperature data. The calculated temperatures would show a better agreement if the THERM data had been available for the full period of the surface degradation driven by contamination. The TMM assumed fully degraded thermal coatings thermo-optical properties towards the end of the data period.

The reduction of calculated space exposure temperature uncertainties with post-flight data proved to be feasible for spacecraft of the LDEF type. The use of this method for reducing uncertainties of calculated values was necessary due to the lack of pre-flight model verification. Second and following flights of this multi-flight spacecraft would benefit even more from this approach by using results from the previous mission for better pre-flight temperature predictions.

REFERENCES

1. Long Duration Exposure Facility (LDEF) Mission 1 Experiments, NASA SP-473, 1984.

2. Greene, R.F.: Thermal Design and Experiment Thermal Integration of the Long Duration Exposure Facility, AIAA-82-08029, June 1982.

3. Duckett, R. J.; Gilliand C. S.: Variable Anodic Thermal Control Coating on Aluminum, AIAA-83-1492, June 1983.

4. Thermal Radiation Analysis System II (TRASYS II), User's Manual, NAS9-15832, June 1983.

5. Systems Improved Numerical Differencing Analyzer (SINDA), User's Manual, NAS 9-15800, March 1983.

6. Berrios, W. M.; Greene, R. F.: LDEF Thermal Model Description, Revision C: LDEF 840-008C, NASA/LaRC, March 1983.

7. Greene, R. F.: LDEF Measurements System (THERM), NASA SP-473, The Long Duration Exposure Facility (LDEF), Mission 1 Experiments, pp 78-79, 1984.

8. Sampair, T. R.; Berrios, W. M.: Effects of Low Earth Orbit Environment on the Long Duration Exposure Facility Thermal Control Coatings, First Post-Retrieval Symposium, NASA CP- 3134, 1992.

9. Slemp,W. S.; Young, P.R.; Shen J.Y: Effects of Flight Exposure on Selected Polymeric Films and Thermal Control Coatings. First Post-Retrieval Symposium, NASA CP-3134, 1992.

TABLE 1 CALCULATED THERMAL MODEL UNCERTAINTY

MEASUREMENT LOCATION	UNCERTAINTY (± °F) 1σ	UNCERTAINTY (± °F) 3σ
THERMISTOR	3	9
RADIOMETER	5	15
CENTER RING	3	9
ROW 6 LONGERON	4	12
EARTH END STRUCTURE	4	12
SPACE END STRUCTURE	3	9
DAMPER DOME	6	18

TABLE 2 COMPARISON OF LDEF TEMPERATURE RANGES

LDEF LOCATION	TEMPERATURE DESIGN LIMITS °F	MEASURED (THERM) °F	POST FLIGHT CALCULATED °F
INTERIOR AVERAGE	10 - 120	52 - 89	58 - 89
STRUCTURE NORTH/SOUTH (ROWS 6/12)	-10 - 150	35 - 134	39 - 136
STRUCTURE EAST/WEST (ROWS 3/9)	-10 - 150	N/A	53 - 100
STRUCTURE EARTH END	10 - 135	56 - 103	57 - 104
STRUCTURE SPACE END	10 - 135	60 - 90	64 - 96

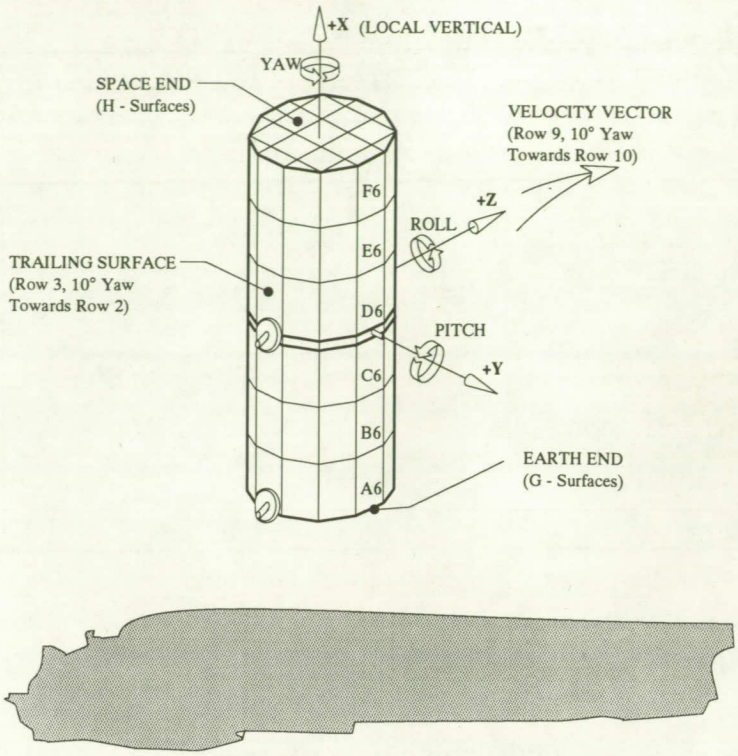

Figure 1. LDEF in Free Flight.

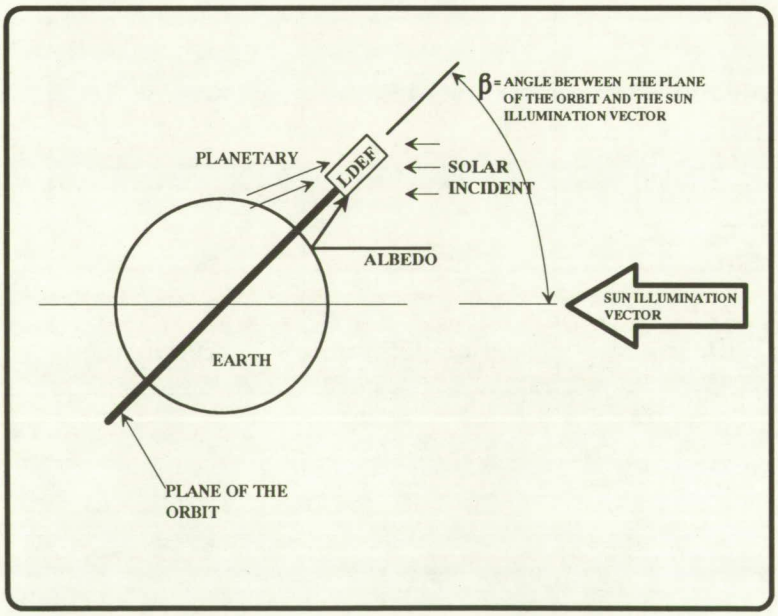

BETA ANGLE= (β) Angle between the plane of the orbit and the sun illumination vector.
SOLAR INCIDENT= (BTU/Hr-Ft^2) Heat due to direct illumination from the sun.
ALBEDO= (BTU/Hr-Ft^2) Heat due to the portion of the solar incident energy reflected from the planet into the LDEF.
PLANETARY= (BTU/Hr-Ft^2) Heat due to energy emitted from the planet.

Figure 2. LDEF Beta Angle Definition.

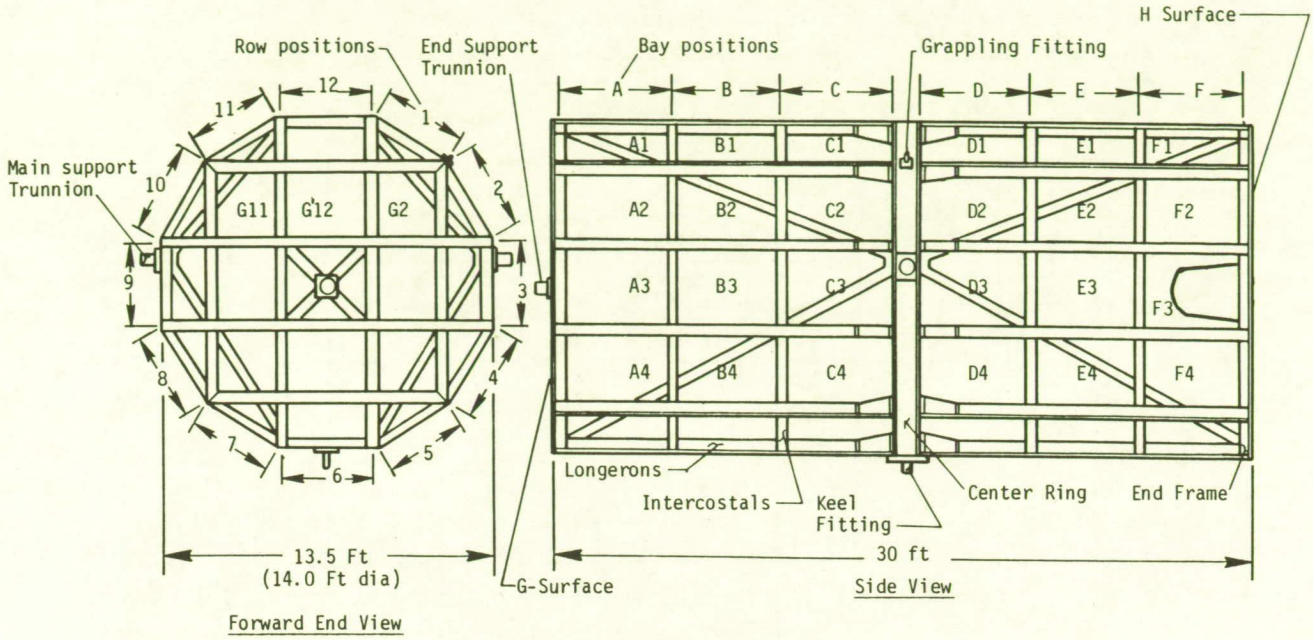

Figure 3. LDEF Structure.

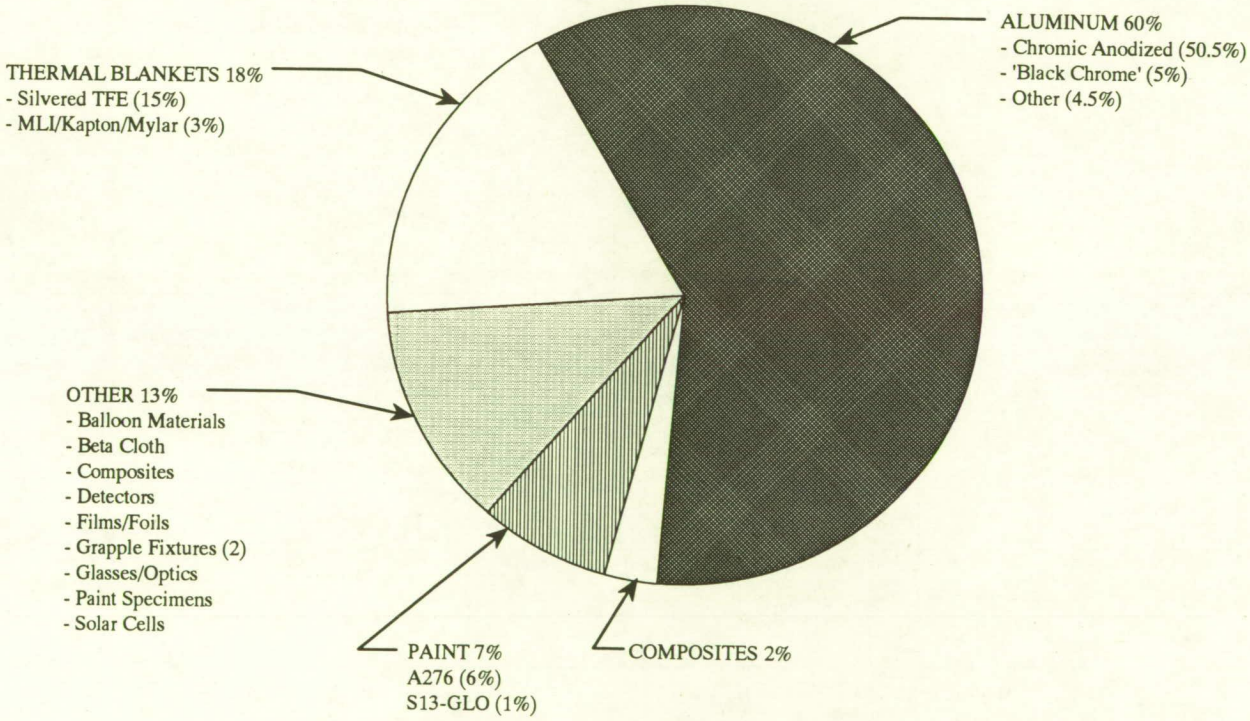

Figure 4. LDEF External Surface Coating Distribution.

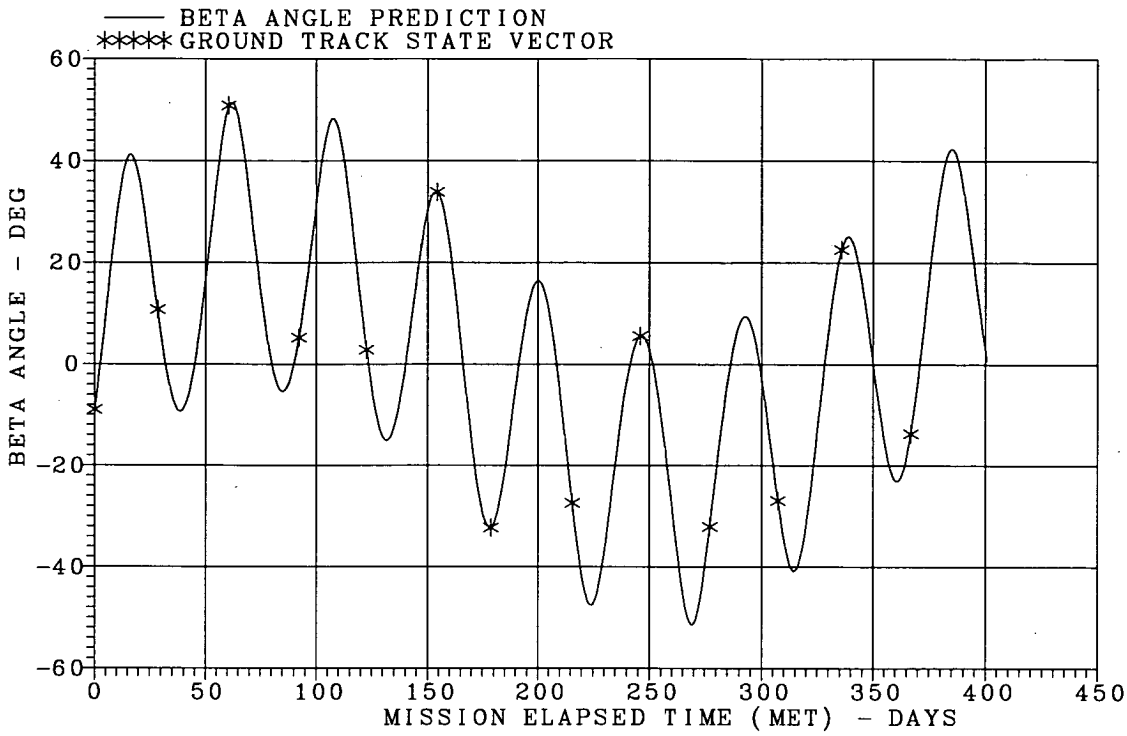

Figure 5. LDEF Beta Angle; April 7, 1984 - May 13, 1985.

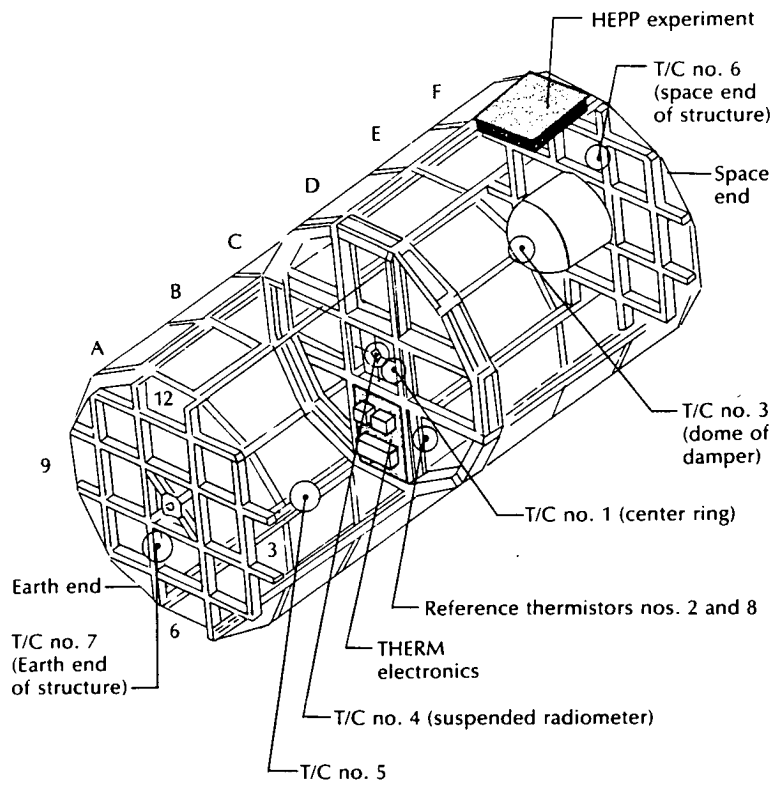

Figure 6. Location of THERM Hardware on LDEF.

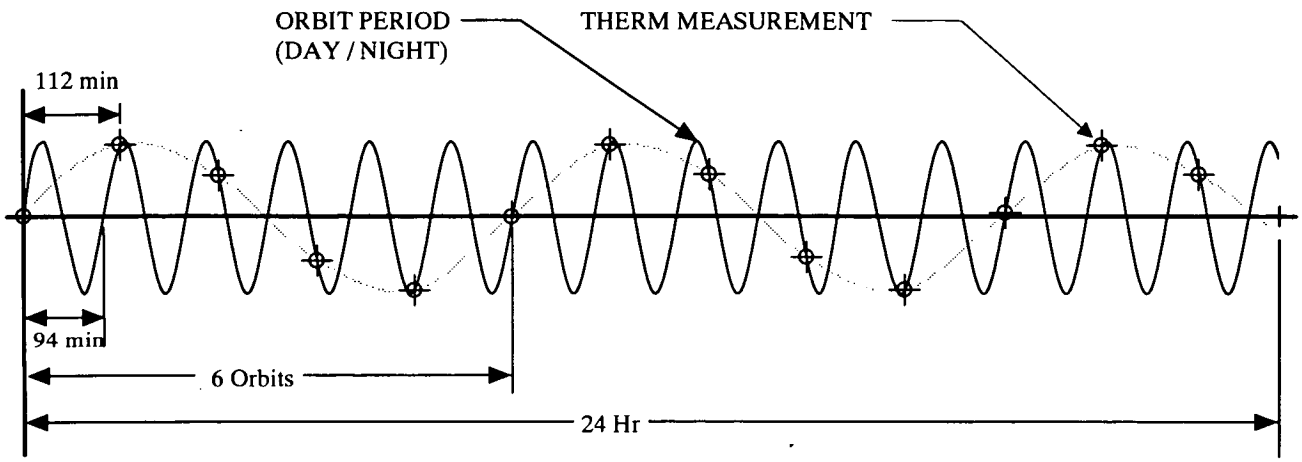

MISSION MEASUREMENTS PER LOCATION: 4983

TOTAL DAYS: 390

Figure 7. LDEF THERM Data Measurement Cycle.

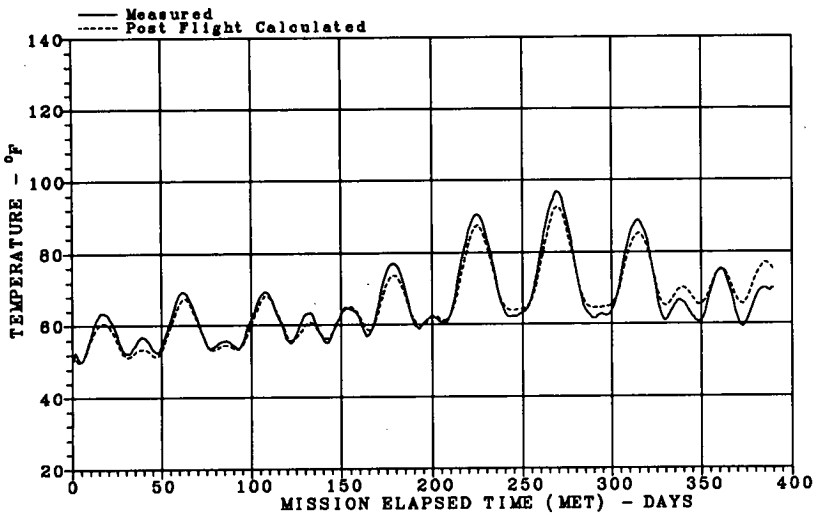

Figure 8. THERM Thermistor Data vs LDEF Post Flight Thermal Model.

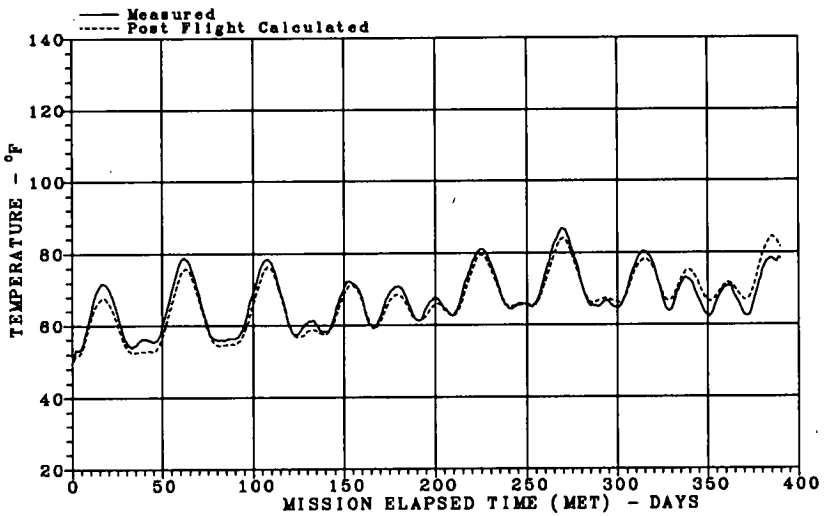

Figure 10. THERM Center Ring Data vs LDEF Post Flight Thermal Model.

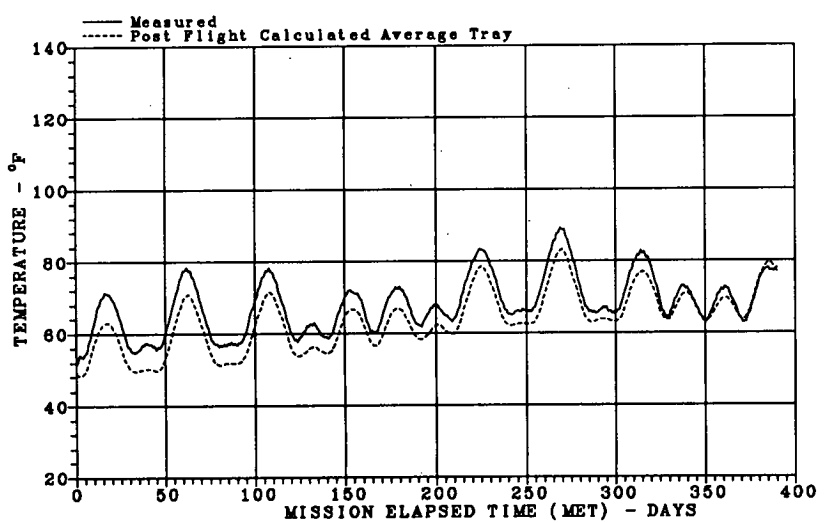

Figure 9. THERM Radiometer Data vs LDEF Post Flight Thermal Model.

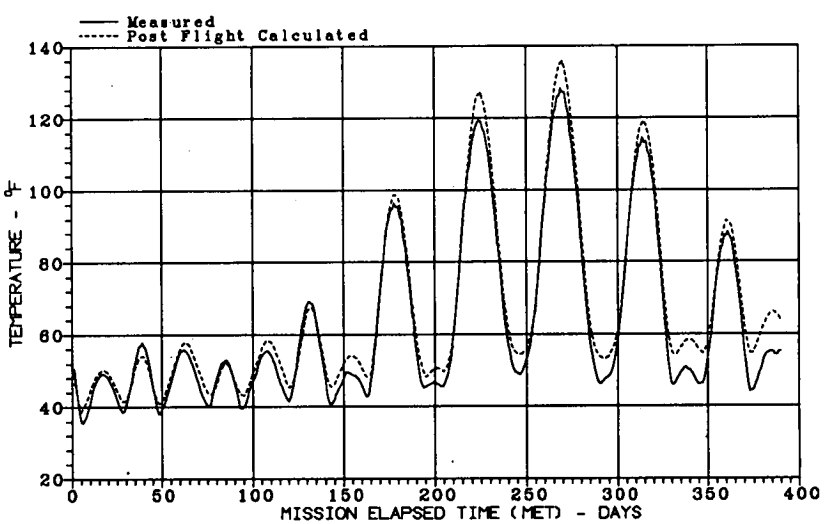

Figure 11. THERM Row 6 Longeron Data vs LDEF Post Flight Thermal Model.

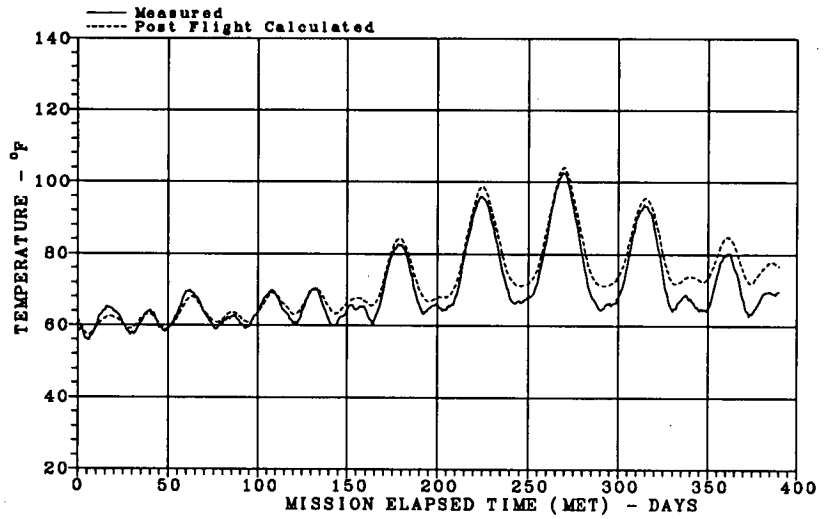

Figure 12. THERM Earth End Data vs LDEF Post Flight Thermal Model.

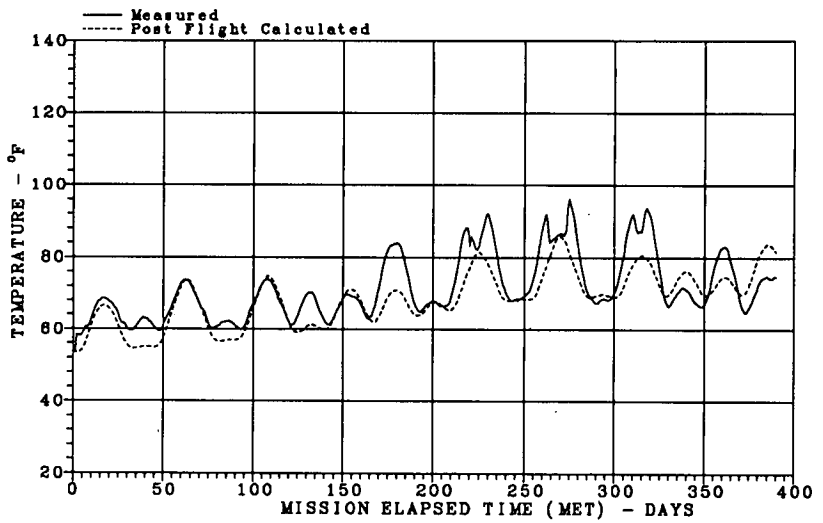

Figure 14. THERM Damper Dome Data vs LDEF Post Flight Thermal Model.

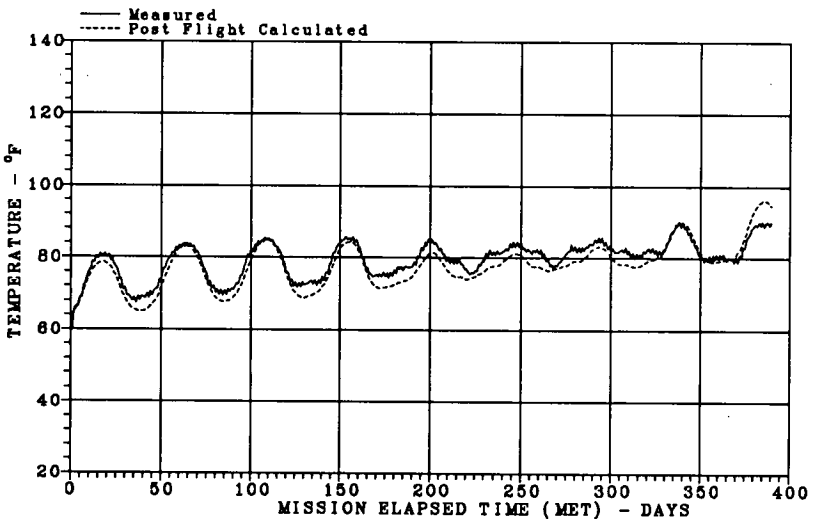

Figure 13. THERM Space End Data vs LDEF Post Flight Thermal Model.

MEASURED SPACE ENVIRONMENTAL EFFECTS TO LDEF DURING RETRIEVAL

Carl R. Maag
Science Applications International Corporation - Glendora, CA 91740 USA

W. Kelly Linder
United States Air Force, NASA Johnson Space Center - Houston, TX 77058 USA

SUMMARY

On the STS-32 shuttle mission, a space flight experiment provided an understanding of the effects of the space environment on the Long Duration Exposure Facility (LDEF) from rendezvous with the shuttle until removal from the payload bay at the Orbiter Processing Facility (OPF) at NASA/KSC. The Interim Operational Contamination Monitor (IOCM) is an attached shuttle payload that has been used on two (2) earlier flights (STS 51C and STS 28) to quantify the contamination deposited during the course of the missions.

The IOCM can characterize by direct measurement the deposition of molecular and particulate contamination during any phase of flight. In addition to these principal measurements, the IOCM actively measures the thermophysical properties of thermal control surfaces by calorimetry, the flux of the ambient atomic oxygen environment, the incident solar flux, and the absolute ambient pressure in the payload bay. The IOCM also provides a structure and sample holders for the exposure of passive material samples to the space environment, e.g., thermal cycling, atomic oxygen, and micrometeoroids and/or orbital debris, etc.

One of the more salient results from the STS-32 flight suggests that the LDEF emitted a large number of particulates after berthing into the shuttle. The mission atomic oxygen fluence was also calculated. Although the fluence was low by normal standards, the Kapton™ passive samples exhibited the onset of erosion. Orbital debris and micrometeoroid impacts also occurred during the retrieval mission. The average perforation diameter was ~12.5 μm. The largest perforation diameter was measured at 65 μm.

INTRODUCTION

In the recent years of unmanned spaceflight, contamination has become a recognized source of spacecraft anomalies and failures. This realization was due in part to experience and failure analysis, and in part to the development of more sophisticated subsystems and instruments, which were more sensitive to the effects of contaminants.

Contamination may be classified approximately as molecular or particulate. In this classification, free molecular contaminants are in the gas phase, and free particulates are solids or liquid droplets. In their free forms, contaminants in the field-of-view of subsystems and instruments cause the attenuation scattering of electromagnetic radiation. Particulates reflect sunlight and may confuse star trackers by appearing as false stars. More importantly, the contaminants may deposit on sensitive surfaces. In the deposited form, solid discrete particulates can partially obscure optical surfaces and cause flare and off-axis scattering. Liquid droplets and gases deposit in layers on surfaces, especially cold ones. Both types of contamination may then change the optical, electrical, and thermal properties of the surface material. The latter effect on thermal control surfaces may be the best known spacecraft anomaly. Historical interpretations range from operating temperature increases due to the gradual degradation of thermal control surfaces, to the loss of a spacecraft from a propellant line or valve rupture caused by the deposition of Solid Rocket Motor (SRM) plume effluents.

Scientific instruments and optical sensors are typically more sensitive to contamination than spacecraft subsystems. Thus, the space science community raised the issue of contamination early in the development of the Space Transportation System. For an unmanned spacecraft or satellite, the Shuttle presents several unique contamination issues. Leakage, venting and dumping from a manned system represent contaminant species not usually encountered. The Orbiter cargo bay provides for the launch systems unprotected by an aerodynamic shroud, which traditionally provided a contamination barrier to the launch vehicle. The Orbiter also functions as a large, complex space platform for instruments. Finally, the shared cargo bay creates a new concern, inter-payload contamination.

The space experimenters, in a NASA advisory group, considered these issues and determined that the most stringent Shuttle-specific requirements were needed in the area of instrumental background presented by the Orbiter. Their recommendations for upper limits on molecular species column densities and particle sighting rates were based on the sensitivity of their instruments. This effort led to an attempt to design a clean Orbiter cargo bay. The greatest success has been the selection of materials which produce little molecular contamination (low outgassing).

As a result of this interest, the United States Air Force/Space Systems Division (OL-AW) sponsored the development of the Interim Operational Contamination Monitor (IOCM). The IOCM's purpose was to provide verification measurements of Orbiter contamination for specific payloads. The IOCM is an automatically operating system for the measurement of particulate and molecular contamination that may be present in the shuttle cargo bay during the period from before launch until after landing. The IOCM has successfully flown on two earlier flights: STS 51-C and STS-28 . Excellent data has been obtained on gaseous and particulate contaminants and their effects on materials. The IOCM has demonstrated that Orbiters with mostly empty bays and proper ground processing can meet the NASA goals, but with significant variability. In its latest flight during the LDEF retrieval, the IOCM showed its capability to provide quality data from pre-launch to payload removal.

SYSTEM CAPABILITY

The IOCM can characterize by direct measurement the deposition of molecular and particulate contamination during any phase of flight, i.e., pre-launch, ascent, on-orbit operations, descent and ferry flight of the shuttle. Measurements can be, and usually are, made continually during these periods. The molecular contamination is further classified in terms of the temperature of the surface (a pre-programmed function) on which it is deposited and from which it is re-emitted. Two types of particulate collection sensors are employed in order to avoid efficiency of collection uncertainties. One of these sensors is also capable of studying the temperature effect on the efficiency of collection.

The IOCM is of a modular design capable of molecular and particulate contamination measurements at multiple physical locations in the shuttle cargo bay. The modules provide for measurements on the various Cartesian axes of the Orbiter by the use of multiple identical sensors. In addition to these principal measurements, the IOCM actively measures the optical property changes of thermal control surfaces by calorimetry, the flux of the ambient atomic oxygen environment, the incident solar flux, and the absolute ambient pressure in the payload bay. The IOCM also provides a structure and sample holders for the exposure of passive material samples to the space environment, e.g., thermal cycling, atomic oxygen, and micrometeoroids and/or orbital debris, etc.

SYSTEM DESCRIPTION

The IOCM is an attached shuttle payload. In its baseline configuration, it is usually mounted on three (3) Adaptive Payload Carriers (APC's) in the cargo bay. The mounting locations are determined for each specific flight on which the IOCM is manifested. For STS-32, the IOCM was mounted on a Get-Away Special (GAS) Adapter Beam and installed on the starboard side in Bay two (2). The system is self-

contained except for an Orbiter power interface. The system is designed for no crew involvement and for no command and control support.

IOCM Functional Description

The IOCM provides for the continuous measurement of collected particulate and molecular mass at preprogrammed collection surface temperatures during the time period from power-up (prelaunch) until power-down (post-landing). A Programmed Read Only Memory (PROM) provides the operational command profile for the IOCM during all mission phases.

IOCM STS-32 Elemental Description

The baseline design of the IOCM consists of six (6) equipment modules mounted on three (3) APC's. For STS-32, the sensors from the six (6) equipment modules were relocated and condensed into one carrier so as to provide the maximum amount of data to the LDEF principal investigators and to the LDEF project office. Figure 1 depicts the IOCM hardware mounted in the shuttle bay during the STS-32 flight. A description of the more salient sensors is provided in the following paragraphs.

The IOCM, as flown on STS-32, contained nine (9) actively controlled contamination sensors: six (6) Temperature-controlled Quartz Crystal Microbalances (TQCMs), two (2) particle capture (PARCAP) devices, and one thermal coatings calorimeter. Also included were two nude ionization pressure gauges for sensing and measuring ambient pressure (10^{-3} to 10^{-8} torr), three solar flux gauges (light-intensity sensors), and temperature sensors for internal housekeeping.

The TQCMs measure contamination by means of a frequency shift of a quartz crystal oscillator. This occurs when the crystal mass increases as a result of contamination accretion. The device is extremely sensitive, 1 Hz corresponding to 1.56×10^{-9} g/cm^2. This sensitivity is achieved by using a specially cut crystal which produces an extremely small temperature dependence and by using a reference quartz crystal. The signal from the reference quartz crystal, when mixed with the signal from the sensing crystal, gives a beat frequency totally independent of temperature and power supply fluctuations.

The TQCMs were manufactured by Faraday Laboratories, Inc., La Jolla, California. The sensor consists of a matched pair of quartz crystals; each resonates at approximately 15 MHz. The crystals are designated as sensor and reference crystal. The sensing crystal is displaced in frequency approximately 1 KHz below the reference crystal. The crystals are optically polished and plated with gold. The output of a mixer circuit provides a frequency which increases when the sensing crystal is contaminated. In addition, a two-stage thermoelectric device is located directly behind the crystals to allow for the cooling or heating of the sensor quartz crystals. The thermoelectric device will control the temperature of the sensor crystals between -50°C and +100°C to ±1°C when its heat sink is maintained below +40°C.

The Thermal Coating Calorimeter is a refined version of the type developed by NASA/GSFC. This device can measure discrete changes in the thermal radiative properties of the coatings applied to the calorimeter. Similar units have successfully flown on numerous missions including the IOCM, NOAA-C and NOVA contamination monitor projects. The thermal coating on the calorimeter was a second surface type mirror SiO_2/Ag). These mirrors are also known as Optical Solar Reflectors (OSRs). This surface was designed to act as the primary contamination effects monitor.

Passive Sample Array

The Passive Sample Array (PSA) is a passive structure designed to expose selected material samples to the Orbiter bay environment. Figure 2 shows an oblique view of the samples. This array

contained samples to help understand what additional environmental damage (if any) occurred to LDEF during the retrieval mission. Table 1 shows the participating organizations.

SIGNIFICANT ACTIVE SENSOR FLIGHT DATA

TQCM 1 was mounted in the IOCM facing toward the forward bulkhead (+ X direction). The intent of this sensor was to observe molecular species from the forward bulkhead area.

Figure 3 shows an end-to-end plot of TQCM 1 during the on-orbit phase of the mission. The data suggests exposure to a high flux of condensible material. It should be re-emphasized that the temperature of the sensors was at 15° C until 12 hours into the mission. At this time, the temperature was reduced to 0°C. Data suggests that an event centered near 42.5 hours caused this mass deposition.

Examination of Table 2 suggests that the COAS maneuver (a manual IMU alignment) is the source of this deposition. The maneuver rotates the Orbiter from the -ZLV attitude to the +XLV attitude over a period of 38 minutes. This places the payload bay into the velocity vector while using the vernier thrusters. This suggests that these species are returning to the shuttle payload bay. Figure 4 shows a less course portion of the data. The data is centered about the event at 42.5 hours. Examination of the temperature data shows that the programmed cleaning cycle occurs after the deposition. The deposition could not be removed by a temperature of 80° C. Figure 4 also shows an increase in mass occurring at about 29 hours. Table 2 also indicates an OMS burn occurring at this period of time. Maximum deposition was 0.70 $\mu g/cm^2$ at approximately 42.5 hours into the flight. Some re-emission occurred after the bakeout of the crystals. This strongly suggests that the deposited mass has a reasonably high molecular weight.

TQCM 5 was mounted on the IOCM facing across bay (+Y,-X direction). The intent of this sensor was to observe particulate and molecular species as incident flux during the mission. The sensor looks aft at a 45° angle. Figure 5 shows an end-to-end plot of the mass accumulation after lift-off. As can be seen, numerous events occurred during the course of the mission to affect the mass accumulation.

The onset of mass deposition can be seen at the 42.5 hour time period (COAS maneuver). Figure 5 shows the increase in mass deposition and the subsequent re-emission of material after cleaning of the sensor crystals. The total mass deposition from this event was 0.78 $\mu g/cm^2$. After sensor burn-off, an additional 0.47 $\mu g/cm^2$ remained.

Figure 5 also shows the accumulation of material on this sensor from latchup through the end of the on-orbit phase of the mission. The mass accumulation on the sensor is indicative of the mass loss from the LDEF. The data suggests that the average mass loss rate is 2.38×10^{-12} g/cm^2-sec.

TQCM 6 is also mounted on the IOCM facing across bay (+Y,-X direction). The intent of this sensor was also to observe molecular species as incident flux during the mission. The sensor is mounted next to TQCM 5 and accordingly, looks aft at a 45° angle.

Figure 6 shows an end-to-end plot of the mass accumulation after lift-off. As can be seen, numerous events occurred during the course of the mission to affect the mass accumulation on this sensor. This sensor was also cleaned with a high temperature bakeout of the crystals.

As observed on other sensors, the onset of mass deposition can be seen at the 42.5 hour time period (COAS maneuver). Figure 6 shows the increase in mass deposition and the subsequent re-emission of material after cleaning of the sensor crystals. The total mass deposition from this event was 0.60 $\mu g/cm^2$. After sensor burn-off a negligible (0.003 $\mu g/cm^2$) amount remained.

Figure 6 also shows the accumulations of material on this sensor from latchup through the end of the on-orbit phase of the mission. The mass accumulation on the sensor is, again, indicative of the mass loss from the LDEF. The data suggests that the average mass loss rate is 2.53×10^{-12} g/cm^2-sec. The data from TQCM 6 agrees quite well with that of TQCM 5.

The thermal coating calorimeter operated as designed and has provided insight in the effects of contamination from the bipropellant thrusters. Figure 7 shows the mission temperature profile. The range of the sensor is between -50° C and +50° C. The sensor initially averaged -22.2° C. The lowest temperature recorded was -50.0° C. The absolute temperature of the calorimeter was obviously lower than the recorded temperature. The lower temperatures occurred during maneuvers to rendezvous and latchup LDEF. One interesting observation is the obvious change in temperature after the 42.5 hour time period, i.e., after the COAS maneuver. The temperature increased to and leveled at an average of -18.8° C, subsequently dropping near the end of the mission to an average of -19.1° C. This data suggests that the effective solar absorptance (α_s) of the OSR increased from 0.100 to 0.107 in approximately 80 hours. It should be noted that the calorimeter equilibrium temperature was approximately 20° C colder than the TQCM set temperature, thus allowing more mass to deposit during the COAS maneuver. During the cool down of the calorimeter, in the latter portion of the mission, an estimate of the hemispherical emittance (ε_{th}) was made. The value agrees within 1% (absolute) of the measured value, i.e, 0.76.

ACTIVE SENSOR POSTFLIGHT DATA

One of the IOCM goals was to provide an understanding of the environment experienced postflight to the LDEF. In order to provide this information the IOCM required power at all facilities at which the orbiter would be located after landing. It is our understanding that the combination of positive pressure within the PLB and the opening of the airlock hatch to place additional instrumentation created a "snowstorm" of the particulates that were sloughing/shedding from LDEF. This event compromised the postflight data.

In general, the ferry flight did not contribute to the overall contamination of the LDEF. The most deleterious impact occurred within the last 24 hours at Julian day 030. This appears to be the period when the strongback was placed over the PLB.

PASSIVE ARRAY DATA

The IOCM exposed twenty-five (25) samples to the environment. As can be seen in Figure 1, the samples were mounted facing out of the payload bay. The discs are nominally one (1) inch diameter (4.1 cm^2 exposed area). The discs are held in place by compression between highly baked-out Nylon washers. Three (3) non-standard size samples were accommodated in the array. The majority of the samples were selected from a list generated by a request placed to NASA centers, USAF laboratories, Universities and European space R&D centers.

Figure 8 shows one of the many impact films flown in the passive array. The film is one (1) mil black Kapton™. Figure 9 shows an impact site observed postflight. The perforation is ~1 μm diameter. One of the more interesting observations seen on this sample is the micron and sub-micron sized particles and agglomerates on the surface. The analysis of the particles show the majority to be Aluminum. It is obvious that the material deposited on the surface after the impacts occurred. Particles are evident both on the edge and in the interior of the perforation. Figure 10 shows a perforation through a sample of two (2) mil Kapton™. Also evident is a sub-micron perforation along with micron and sub-micron sized particles and agglomerates on the surface. Table 3 provides a catalog of observed perforations during the mission.

Coatings of inorganic silicon compounds (oxide, p-SiO_2 and amorphous hydrogenated silicon, α:Si:H) over Kapton™ were exposed during the experiment by the Canadian Space Agency. As a reference standard, an uncoated specimen of Kapton™ was also included. Analysis of the exposed surface of the uncoated Kapton™ using the Scanning Electron Microscope (SEM) showed that the threshold fluence after which Kapton™ erodes had just been exceeded. The uncoated Kapton™ surface had begun to pit and erode in Figure 11, but had not yet developed the familiar rug-like pattern. From this degree of erosion it is possible to estimate that the fluence of atomic oxygen seen by the specimens was approximately 10^{19} atoms/cm^2. In contrast, surface analysis of the coated specimens of Kapton™ showed no deleterious effects of the space environment exposure on either material coating.

Results of samples flown by NASA/LeRC indicate that low, but observable, atomic oxygen interaction has occurred on the samples. Uncoated polyimide Kapton™ films have developed a very small surface texture. At the sites of defects in protective coatings over polyimide such texture can also be observed. Figure 12 shows these defects and the underlying "carpet-like" morphology typical of the onset of AO erosion of Kapton™. Table 4 provides a comparison of Kapton™ films exposed during the mission.

CONCLUSIONS

Based on the data gathered by the IOCM [1], it is felt that the instrument performed extremely well and met or exceeded its goals. The active and passive sensors, in concert with analytical chemistry techniques, have provided a wealth of information on the effect of the environment to STS-32 and the LDEF.

Two of the more salient observations made during the period of active sensor operation were the fact that the IOCM observed what appears to be prelaunch contamination and that the "return flux" phenomena first seen on the STS-3 OSS-1 Contamination Monitor Package was observed again. The data also confirms the fact that the payload bay was in an extremely clean condition when launched. Return flux from the Orbiter RCS system has been observed. The resultant deposition required a high temperature bakeout to initiate removal of the accreted mass. The deposit increased the solar absorptance of the calorimeter sample by 0.007.

In addition, the Orbiter did not appear to contribute to the gaseous environment as observed by the active sensors. On the other hand, LDEF acted as a large source of contamination (mainly micron and sub-micron sized particulates) to the shuttle. The source emission rate of LDEF averaged 2.5×10^{-12} g/cm^2-sec for a period of eighty hours following berthing, falling off to a rate of 4.1×10^{-13} g/cm^2-sec just prior to re-entry. Postflight obscuration ratios on IOCM surfaces were measured at 2.4 percent. The LDEF appears to have contaminated itself, principally after landing.

The mission atomic oxygen fluence was calculated to be 2×10^{19} atoms/cm^2. Although the fluence is low by normal standards, the Kapton™ passive samples on the IOCM exhibited the onset of erosion. Trailing edge trays of the LDEF should be examined for the onset of erosion. Orbital debris and micrometeoroid impact plates suggest a flux of 6×10^2 impacts/m^2 occurred during the mission, with an average perforation diameter of ~12.5 μm. The largest perforation diameter was measured at 65 μm.

Measurements of contamination during the postflight phases, i.e., ferry flight and de-integration processing in the OPF, show negligible to very low particle transfer, respectively. Obscuration ratios during ferry flight were calculated at 0.2 percent on horizontal surfaces. The largest mass deposition occurred during activities in the OPF.

The reduction of the sensor data confirmed what was self-evident upon opening the payload bay doors in the OPF. The LDEF was shedding significant amounts of ultrafine particulate material. This material was identified as residue of aluminized Mylar thermal blankets.

REFERENCES

1. Maag, C.R., "Results of the Interim Operational Contamination Monitor (IOCM) as Flown on the STS-32 Mission". Final Report JPL D-8170, March 1991.

TABLES

TABLE 1. PASSIVE ARRAY PARTICIPATING ORGANIZATIONS

ORBITAL DEBRIS IMPACTS

UNIVERSITY OF KENT (UK)
- Aerogel
- Aluminum Foil

INSTITUT d'ASTROPHYSIQUE SPATIALE (FR)
- Gold Foils
- Nickel Foils

BAYLOR UNIVERSITY (USA)
- Aluminum Films

SCIENCE APPLICATIONS INTERNATIONAL CORP. (USA)
- Polyimide Film

ATOMIC OXYGEN EROSION

NASA/LeRC (USA)
- Coated Polyimide Films

CANADIAN SPACE AGENCY
- Coated Polyimide Films

NASA/JPL (USA)
- Polyimide Films
- Teflon Films

UNIVERSITY OF ALABAMA @ HUNTSVILLE (USA)
- Carbon
- Fused Silica

DU PONT (USA)
- Coated Polyimide Films

SCIENCE APPLICATIONS INTERNATIONAL CORP. (USA)
- Polyimide Film

CONTAMINATION

NASA/JPL (USA)
- Germanium (IRE) Crystals

NASA/MSFC (USA)
- UV Mirrors

TABLE 2. STS-32 TIMETABLE OF MAJOR EVENTS

R1 A1 SW30 ENABLED	T minus 43 hours
PLB DOOR OPENING	T plus 1.6 hours
SYNCOM IV DEPLOY	T plus 24.7 hours
SYNCOM BURN/STAGING	T plus 25.5-27.5 hours
NORMAL CORRECTION BURN	T plus 29.0 hours
FIRST WATER DUMP	T plus 42.0 hours
OMS BURN	T plus 42.5 hours
LDEF LATCHUP	T plus 74.7 hours
LDEF BERTHING	T plus 80.0 hours

TABLE 3. CATALOG OF OBSERVED PERFORATIONS

d (μm)*	N**
.1	TBR
1	384
5	320
10	256
20	64
40	32
65	32
• Average Perforation Diameter: ~ 12.5 μm • Maximum Perforation Diameter: ~ 65.0 μm	

* Equal to or less than

** Approximate number of impacts/m^2

TABLE 4. COMPARISON OF KAPTON FILMS DURING STS-32 MISSION

INVESTIGATOR	ESTIMATED MISSION FLUENCE*	ESTIMATED TRAILING EDGE FLUENCE
B. BANKS (NASA)	NONE	~ $2 \cdot 10^{17}$ atoms/cm^2
C. MAAG (SAIC)	~ $9 \cdot 10^{18}$ - $2 \cdot 10^{19}$ atoms/cm^2	NONE
D. ZIMCIK (CSA)	~ $2 \cdot 10^{19}$ atoms/cm^2	NONE

*Best estimate from erosion

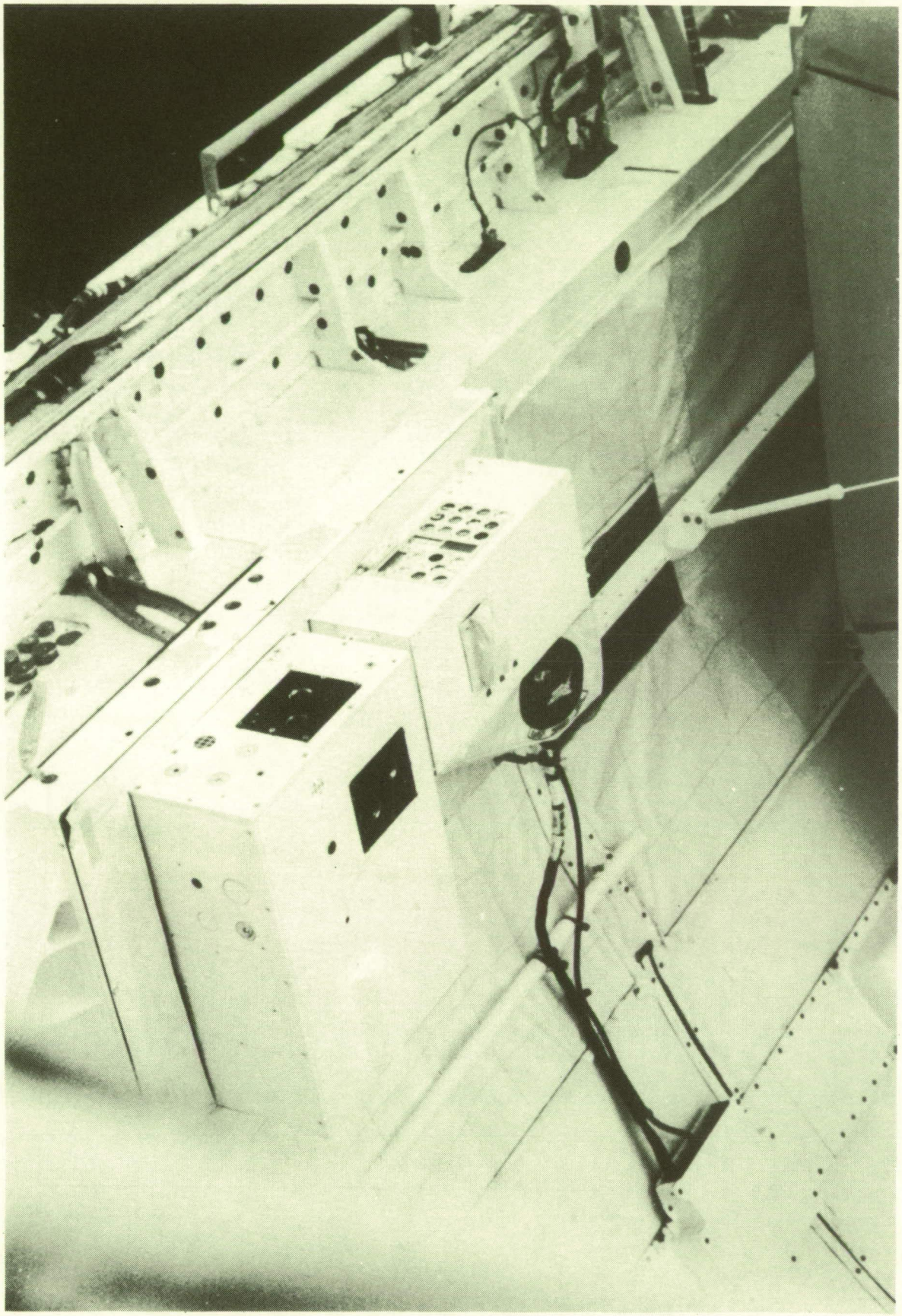

FIGURE 1. IOCM HARDWARE MOUNTED IN SHUTTLE BAY

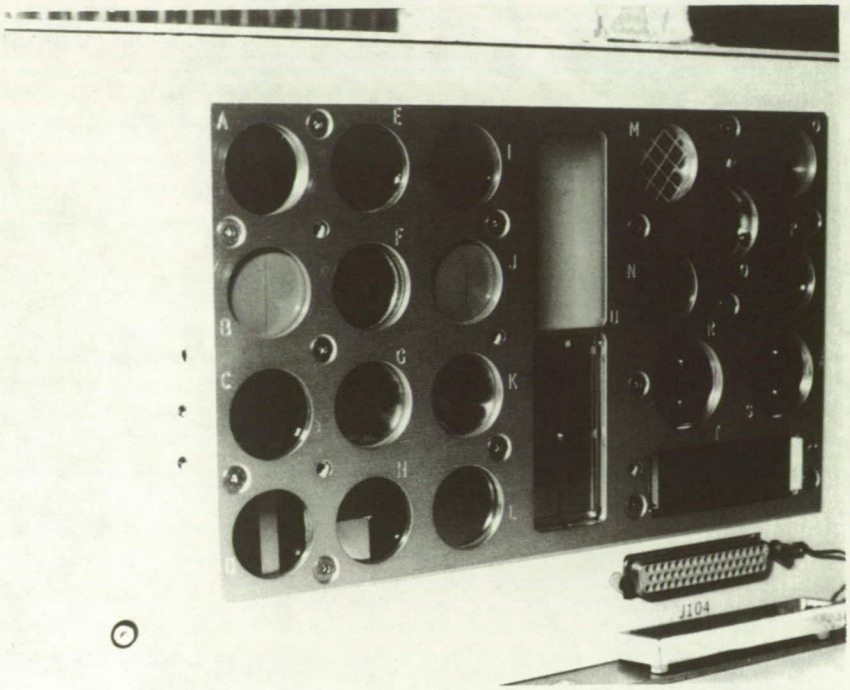

FIGURE 2. IOCM PASSIVE SAMPLE TRAY

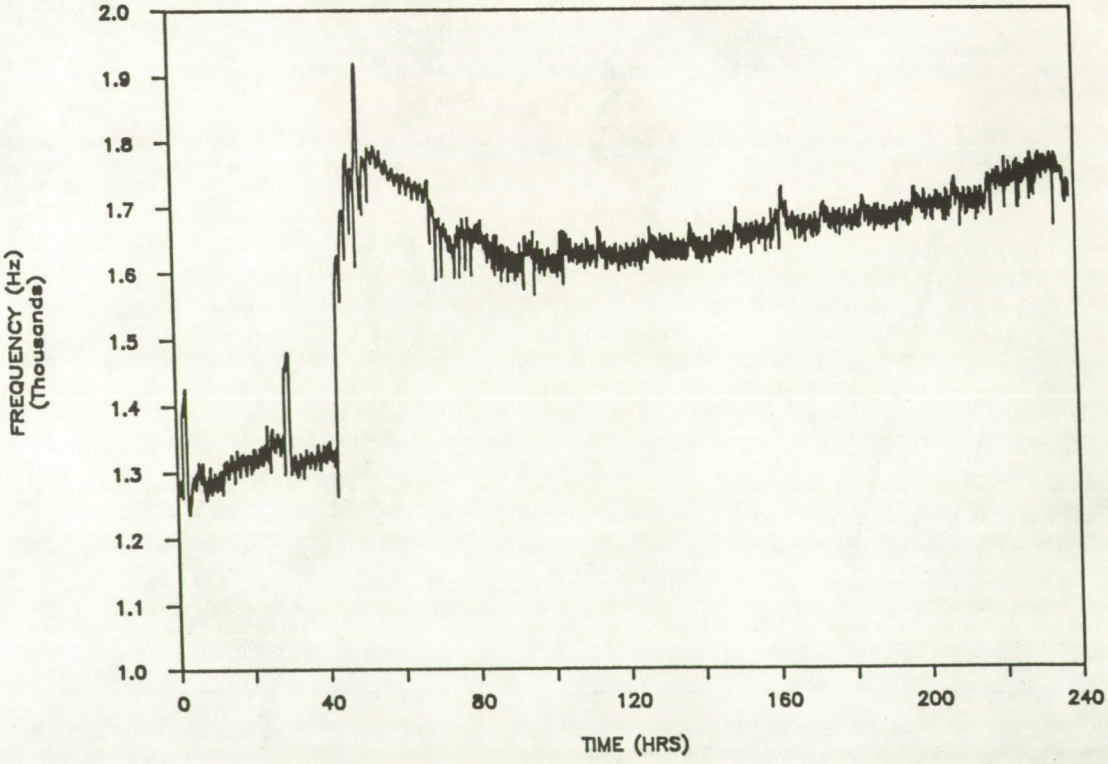

FIGURE 3. FREQUENCY CHANGE (MASS ACCUMULATION) OF TQCM 1; LAUNCH TO LANDING

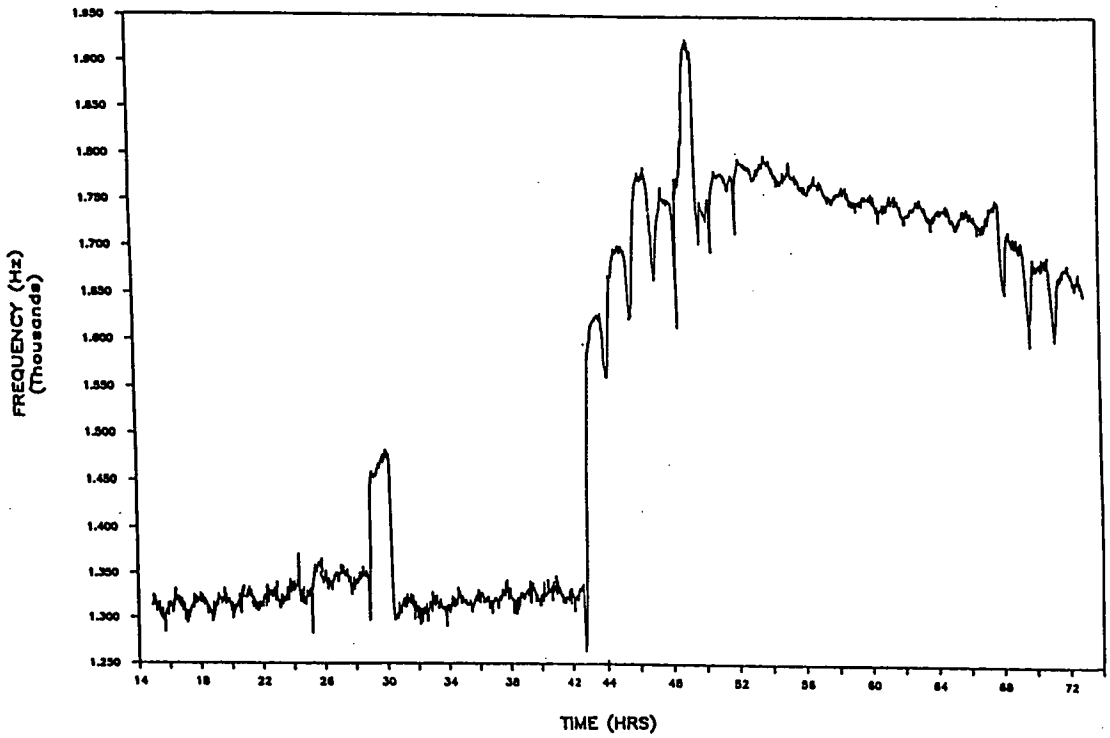

FIGURE 4. FREQUENCY CHANGE (MASS ACCUMULATION) OF TQCM 1; EARLY PHASE OF MISSION

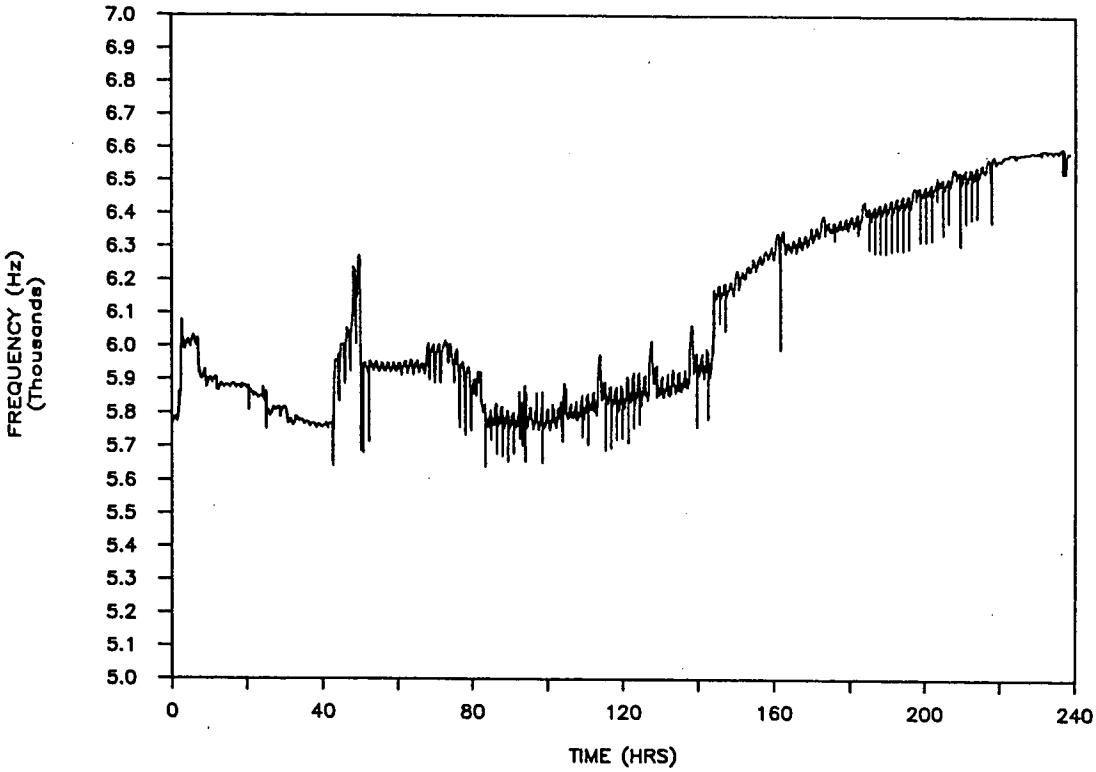

FIGURE 5. FREQUENCY CHANGE (MASS ACCUMULATION) OF TQCM 5; LAUNCH TO LANDING

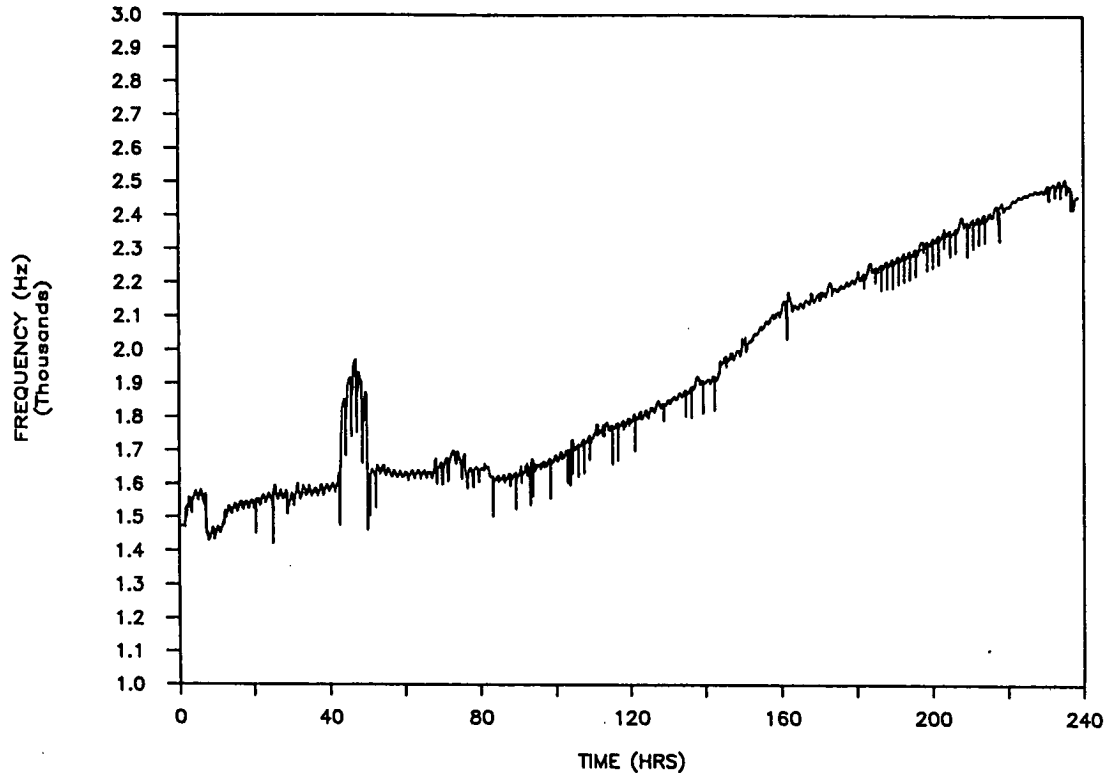

FIGURE 6. FREQUENCY CHANGE (MASS ACCUMULATION) OF TQCM 6; LAUNCH TO LANDING

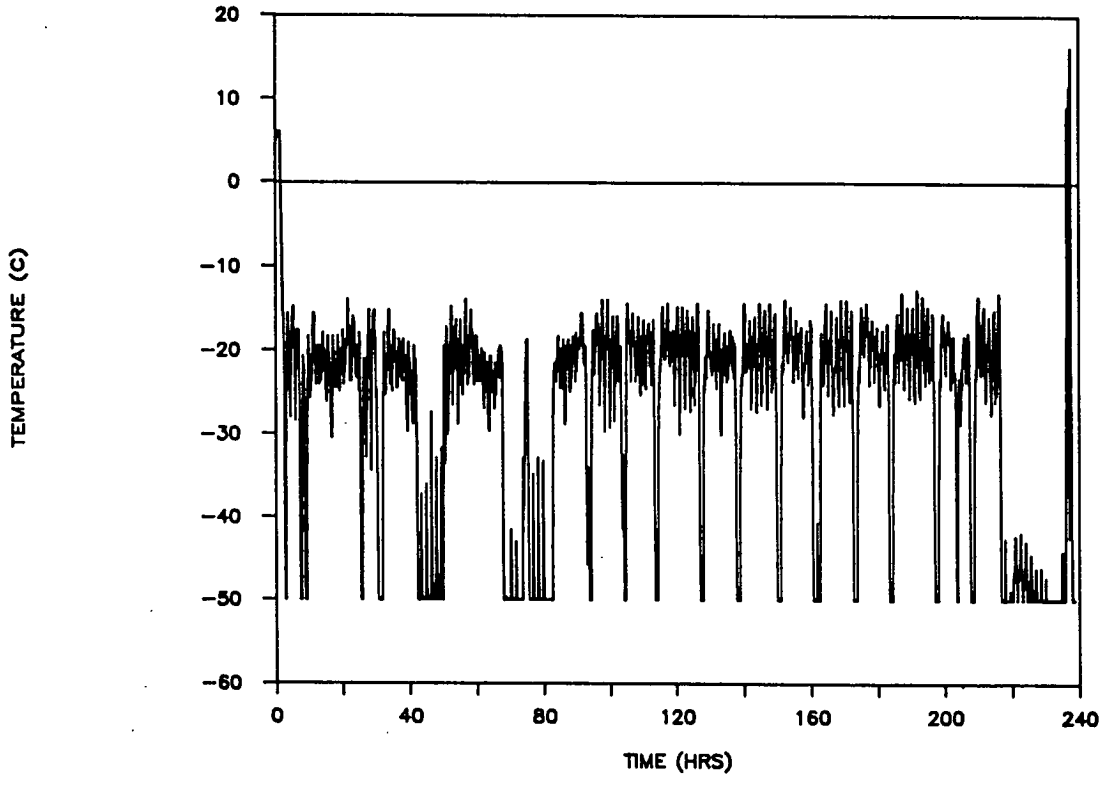

FIGURE 7. TEMPERATURE PROFILE OF THERMAL COATING CALORIMETER; LAUNCH TO LANDING

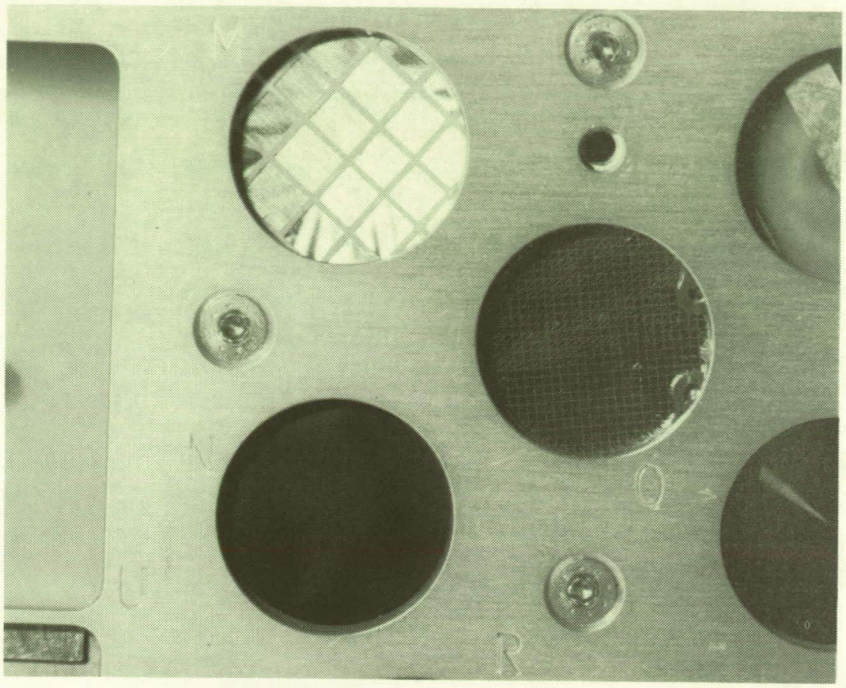

FIGURE 8. PASSIVE ARRAY IMPACT FILM

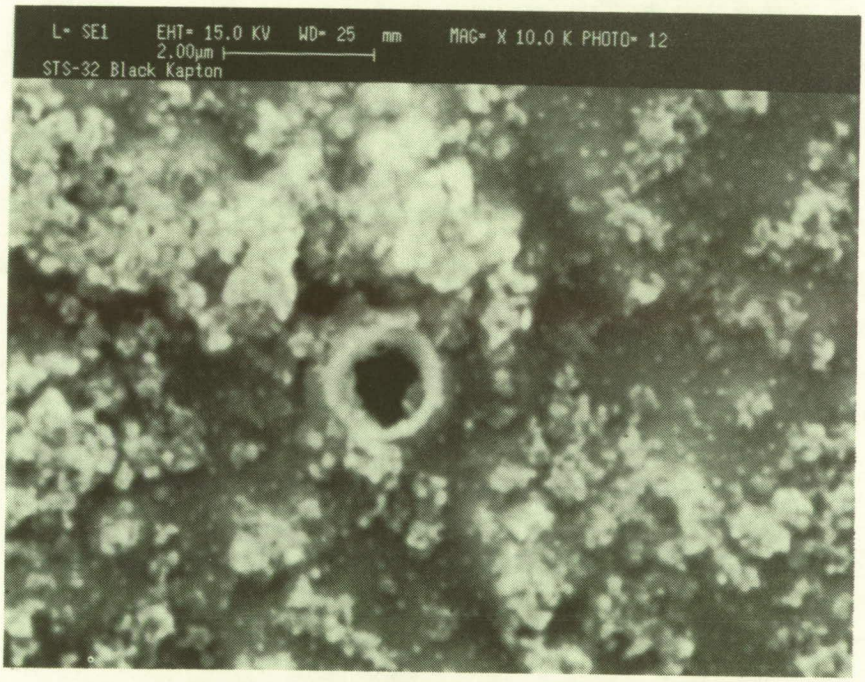

FIGURE 9. PERFORATION OF IMPACT FILM AND LDEF THERMAL BLANKET RESIDUE

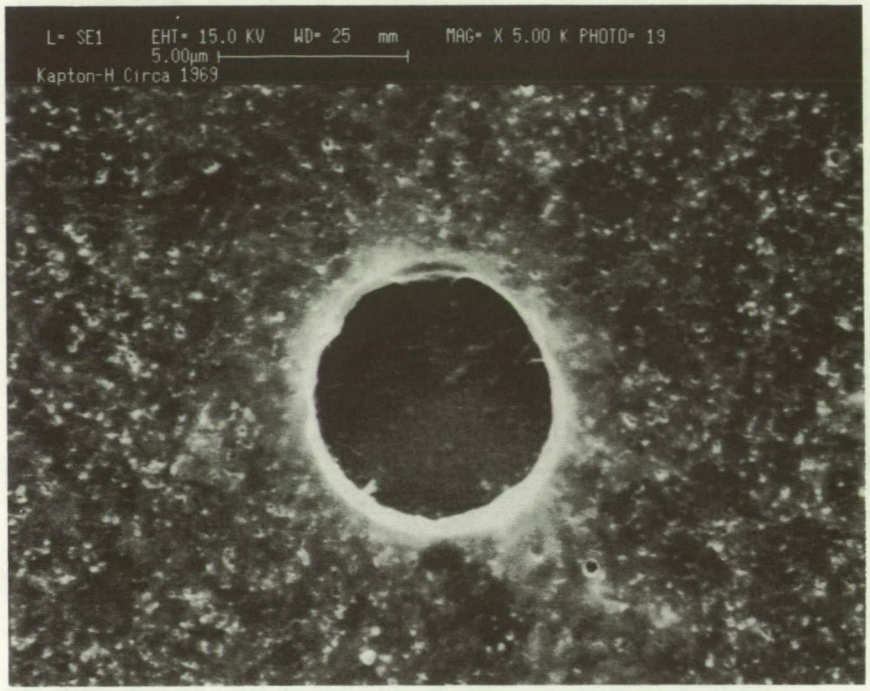

FIGURE 10. PERFORATION EVENTS IN IMPACT FILM

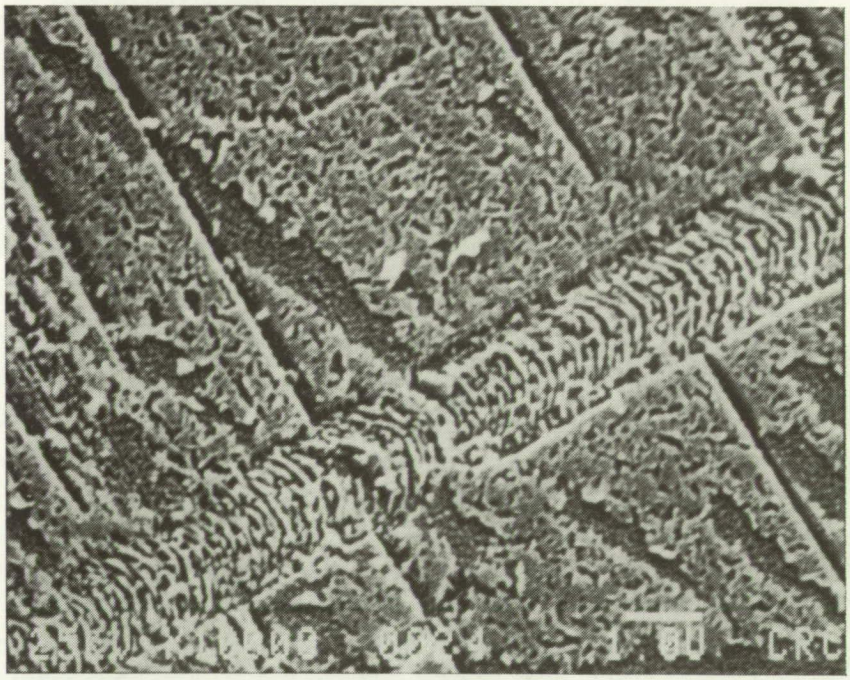

FIGURE 11. ONSET OF AO EROSION OF UNCOATED KAPTON

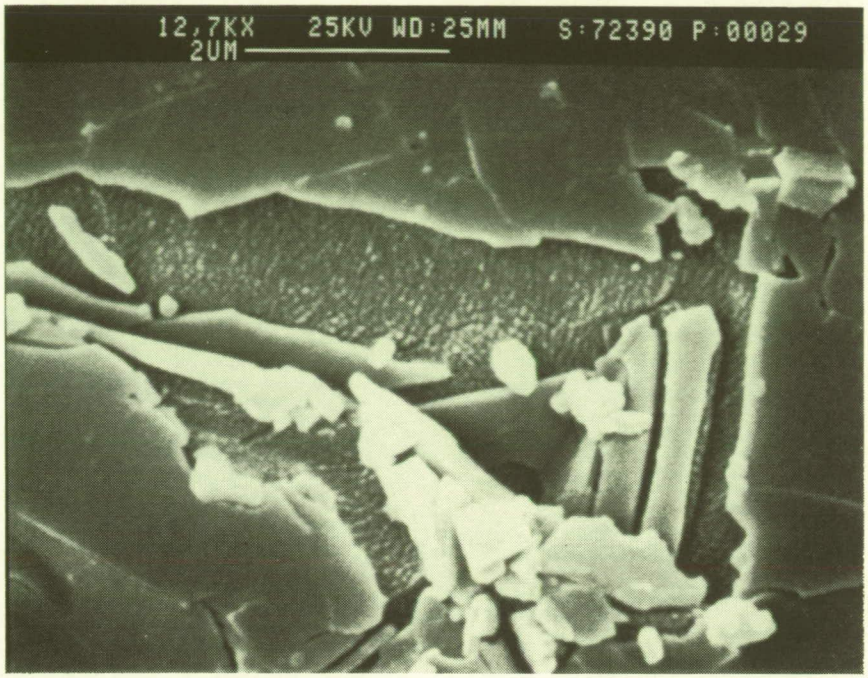

FIGURE 12. ONSET OF AO EROSION UNDER KAPTON PROTECTIVE COATING

PARTICLE TYPES AND SOURCES ASSOCIATED WITH LDEF*

E. R. Crutcher and W. W. Wascher
Boeing Defense and Space Group
Seattle, WA 98124-2499
Phone: 206/773-7002, Fax: 206/773-1473

SUMMARY

The particulate contamination history of LDEF is evident through the particles, the surfaces on which the particles are found, and the most probable sources for the types of particles found. The particles were identified as residues from fabrication, residues from assembly, cross-contamination from integration or launch, orbit generated debris, cross-contamination from reentry or ground operations up to Kennedy, and contamination at Kennedy. It was easy to distinguish between the particles present during orbit and those deposited during or following recovery by the shielding of the surface provided by particles present during orbit. On the ram facing trays particles protected the surface from atomic oxygen erosion. On the trailing trays particles shielded the surface from the deposition of outgassed materials. Once it had been determined if the particle was present prior to orbit or introduced following orbit possible sources could be sought. In this manner the raw material for a history of LDEF contamination was collected.

When LDEF entered orbit it carried a variety of contaminants from assembly operations and from the shuttle bay itself. Residues from fabrication and assembly included abrasives, abrasion generated metal, plastic, wood dust, spray paint, wear metals, and other debris. General fallout and handling debris such as skin flakes, paper and clothing fiber, natural minerals, etc. were also included with the assembly contaminants. Shuttle tile material and the bay liner Beta Cloth materials were used as indicators of cross-contamination between the payload and the Shuttle Bay. Once LDEF entered orbit the contaminants on the surface of LDEF began interacting with the environment. Most particles appear to have been associated with an outgassing phase, probably water, that created a local 'high pressure' zone. These zones were evident around the particle as an area where molecular films from other sources could not deposit. The effect was to create an optical inhomogeneity much larger than the original particle's obscuration area. Some particles were associated with a condensable outgassing material and generated a halo around themselves. This also resulted in an optical effect larger than the particle's obscuration value. A third mechanism in which a particle created an enlarged optical footprint was the actual movement of the particle creating shadows in more than one area. This movement appears to have been the result of thermal effects and of impacts near the particle.

New particulate contaminants were generated in orbit by impacts with micrometeorites or space debris. These contaminants were predominantly LDEF materials shattered, ejected as molten metal, or ejected as a gas phase that could then redeposit on LDEF. Many examples of such deposition were evident on LDEF.

The exposure to atomic oxygen in orbit eroded carbon based materials leaving 'ash' and jagged remnants of what had been solid sheets of plastic. Plastic films with vapor deposited metal backing were reduced to flakes of very thin metal foil. Paint films became a layer of free pigment particles protecting the remaining paint film beneath them. These materials were reasonably stable in orbit but with the

*Work done under NAS 1-18224, Task 12

repressurization of the Shuttle Bay during reentry they became free moving particles contaminating the interior of the Shuttle Bay and the surface of LDEF. Small fragments of the molecular films created in orbit on the surface of LDEF were also blown free and became particulate contaminants in the Shuttle Bay.

During ground operations from the OPF through SAEF-2 additional particulate contaminants accumulated on the surface of LDEF. This photoessay provides documentation of many of these particle types and of the surface effects mentioned above. LDEF provided the first opportunity to quantify contaminants over the entire surface of a satellite and to document the effects of contaminants on that surface.

INTRODUCTION

This paper is a brief photoessay of the particulate contaminants found on the various surfaces of LDEF with a description of their probable source and the methods used to establish that source. It includes photographs taken directly from LDEF surfaces in SAEF-2 as well as those taken later in the laboratory. Photographs of tapelift samples collected from the surface of LDEF, the shuttle bay, and from different Kennedy facilities or fixtures associated with LDEF are also included.

Determining the source of a particle on a surface necessarily involves some knowledge of the history of the sources to which the surface was exposed and the duration or conditions of that exposure. In the case of LDEF there were a number of well documented events that had an effect on the exposure of the satellite to surface contaminants (Ref. 1). Photographic evidence documenting those effects along with a description of the criteria used to establish both the time of the arrival for particles at the surface of LDEF and their probable source are included here.

DETERMINING PARTICLE ARRIVAL TIME

One of the early concerns regarding the interpretation of the contamination history of LDEF was the ability to distinguish new contaminants from those that were present on the surface during orbital exposure. The first microscopic examination of the Teflon blanket material revealed a remarkably well recorded chronology of events in the tracks of deposited molecular films. The surface of the Silver/Teflon blanket from the first tray removed, the seeds experiment tray F-02, was examined the day of its removal using the Nomarski microscope station adjacent to the LDEF satellite in the SAEF-2 clean room. The pattern of shadows characteristic of particles on the surface during the orbital exposure and the non-shadowed "new" particles were documented that same day (see Photograph 1). The patterns seen on the surface beneath the particles tended to indicate the time at which the particle had arrived at the surface. Particles with no "shadow" had clearly arrived after the "shadowing" event. On tray F-02 this was the deposition of molecular contaminants and the ultraviolet modification of the Teflon surface. Absence of both shadow effects indicated that these particles arrived at their current location during recovery or subsequent activities. Particles with shadows could be placed in two groups; those with shadows of their projected area and those with shadows much larger than their projected area. Cellulose particles tended to have shadows much larger than their fiber diameter. Cellulose also has the tendency to retain large amounts of water absorbed into its structure. With elevated temperature or vacuum it tends to give up the absorbed water. This relatively high partial pressure of water vapor may be responsible for the extensive "protected" area or shadow seen around cellulose particles. Any particle at rest on a surface for extended intervals of time tends to adsorb water at the interface between the particle and the surface. The extended shadow of minerals or other non-absorbing particles may be due to this effect. These particles would then be those that were present on the surface of LDEF prior to launch. Particles with only a sharp silhouette would be new arrivals at the time LDEF went into orbit. These would be the particles that relocated during the launch and orbit insertion events. Photograph 1 illustrates mineral particles with extended shadows

around the particle, those without extended shadows (discounting the "comet tail"), shadows without particles indicating where a particle had been during orbit but that moved sometime during recovery, and new particles with no shadow (including no comet tail).

Row 2 was a trailing row (as were rows 1, 3, 4, and 5), and was not exposed to any significant level of atomic oxygen. The leading rows (rows 7, 8, 9, 10, and 11) exhibited a different pattern when the surface was protected by particulate contaminants. Areas of uneroded surface material projected above the eroded surface of carbon based materials (see Photographs 2, 3, and the second photo of Figure 1). A few particles on the leading row trays moved while in orbit. The particles left an eroded pattern of their silhouette where they had been and created a new silhouette on the eroded surface that they then protected (Photograph 4 and Figure 2 tray C-08 photographs). The relative time the particle spent in each position could be deduced by the relative amount of atomic oxygen erosion that had occured at each location. As some carbon based surfaces were eroded metal oxide ash was left in proportion to the trace metals present as part of catalysts, antioxidants, inorganic fillers, or contaminants present in the material. Resin systems were often coated with a fine white ash resulting from atomic oxygen erosion as can be seen in the background of Photograph 3, a carbon fiber/resin composite. Some particulate contaminants were carbon based and did not survive the atomic oxygen exposure on the leading rows but left their outline as a slightly less eroded pattern on the surface (see Figure 1, photograph 3). Particles that had moved while in orbit as opposed to those that were carbon based and had been eroded away by the atomic oxygen left different patterns in the underlying eroded surface. When a particle moved it exposed edges that began eroding rapidly resulting in rounded rather than sharp edges. Eroded particles left an inert ash behind, often concentrated near the edges of the particle, with the result that the edges were often less eroded than the area where the main body of the particle had been. Photograph 6 is a good example of this effect.

Three types of shadows characterized the presence of particles on the exterior surface of LDEF during its orbital exposure; molecular film, atomic oxygen, and ultraviolet light. Molecular film shadows are shown in Photograph 1 and Figure 2, photograph 1. Molecular film shadows often exhibit what appears to be an outgassing positive pressure zone around the particle that prevents local deposition of films. This is most pronounced around particles with significant amounts of water to outgas as is the case with cellulose fibers (Figure 2, photograph 1). Atomic oxygen shadows were characterized by less surface erosion as seen dramatically in carbon based systems and to a lesser degree on other surfaces. The ultraviolet shadow effect is seen in Figure 1, photograph 2. The smooth surface of glass fiber and the ultraviolet transmission of some glasses created an atomic oxygen shadow but not an ultraviolet shadow. The ultraviolet modification of the Teflon surface under the fibers on tray C-08 shown in figure 2 may have contributed to their final movement. Because of the position of the tray with respect to the ram direction the ray path through the fiber would not have been normal to the surface of the Teflon. As a result the ultraviolet modification of the Teflon surface under the fiber would have been asymmetric, increasing the instability of the fiber's position.

The particles themselves often exhibited the evidence of orbital exposure. Photographs 9 and 10 show two organic fibers modified by their exposure to atomic oxygen and energetic ultraviolet light. In Photograph 9 the straight chain nylon polymer has been reorganized through disruption of the bonding along the chain and the generation of crosslinkages. This is evident by the change in the electron density distribution indicated by the change in the color effects exhibited when the fiber is viewed between crossed polarizing filters. In Photograph 10 both atomic oxygen and ultraviolet light exposure effects are evident on a cellulose fiber.

Secondary evidence based on the identification of contaminants found on the surface, the location of those contaminants, and their most likely source or sources was used to elaborate on the chronology established by the direct evidence. For example a cellulose particle found on a leading edge tray surface could not have survived the atomic oxygen exposure of orbit. It would have to have arrived at the surface during or after recovery. The position of LDEF in the Shuttle bay during nearly all of the ground operations had row 12 facing upward. This row has special significance for monitoring fallout while LDEF was on the ground and in the Shuttle Bay. Just prior to and during launch the space end of LDEF

was facing upward to collect fallout characteristic of those events. Once in orbit the Shuttle Bay doors were opened and row 12 was the first part of LDEF to receive ultraviolet radiation. Information of this type has been providing and will continue to provide evidence to evaluate various contamination scenarios.

Contaminants created by impacts with space debris or micrometeorites constituted a special class of materials. Figure 3 illustrates a few specific impacts. One of these impacts was the result of a micrometeorite impact with a bolt on a tray clamp of tray E-10. Molten metal droplets were ejected to a distance of about a centimeter onto the tray clamp. Many examples of the transport of molten metal contaminants have been seen on LDEF. On tray H-06, molten droplets were spattered over the bottom of the tray more than 10 centimeters from an impact. Figure 3 also shows impacts with Teflon surfaces, painted surfaces, and anodized aluminum surfaces.

IDENTIFICATION OF CONTAMINANTS AND THEIR SOURCES

The contaminants found on LDEF were from a variety of sources and represented a complex variety of materials. The analytical compound light microscope is the most effective analytical tool available for this type of work and was used extensively for this study. Microchemical tests, microphysical tests, micro-FTIR spectroscopy, electron microscopy, X-Ray fluorescence microscopy, and other techniques were used as appropriate. Below are a few examples of the kind of information used to differentiate particle types during the analysis.

The first example of this type of analysis is that of the variety of glass fibers present and their sources. The glass fiber from the shuttle bay liner has a refractive index of approximately 1.55, a very constant diameter of 15 micrometers, and a gentle wave set into each fiber by the weave of the fabric (Photograph 7 and Figure 1, lower set photograph 2). Shuttle tile fiber has a refractive index of approximately 1.48, is highly variable in diameter, and irregular in shape (Photograph 8 and Figure 1, lower set photograph 1). Glass fiber from fiberglass is a third type present. This material has a refractive index of approximately 1.52, a diameter of about 25 micrometers, and the individual fibers are very straight. Glass fiber from insulation blankets have a refractive index of about 1.52, are highly variable in diameter, and tend to be irregular in shape though not as variable as the Shuttle tile fiber. HEPA filter glass fiber has a refractive index of about 1.5, is variable in diameter but the diameter is less than 10 micrometers and often less than one micrometer, and the fibers tend to be short and straight. These first level discriminators can then be refined further by more accurate characterization of the refractive index or other parameter to identify different sources of the same type of glass fiber.

The Shuttle Bay liner fiber was found widely distributed over the surface of LDEF and on the samples from the Shuttle Bay not collected from the liner. The tapelifts from the liner material contained very large amounts of this fiber and the associated Teflon material. Teflon was found associated with this fiber only on a few occasions from samples collected from the surface of LDEF. These were presumably new materials deposited during recovery. There was no evidence that these particular specimens had seen extended LDEF exposure. Many of the bay liner type of fiber were found on LDEF surfaces with atomic oxygen or molecular film shadows beneath them indicating they were present during orbit. These particles were presumably deposited on LDEF during launch or payload integration. Most of these particles are under 500 micrometers in length.

Glass fiber from insulation batting and glass fiber from glass fiber/resin composites were also common on LDEF. The frequency of encountering these types of fiber varied by location and by proximity to sources on LDEF. Variations in the refractive indices of the glass fiber from composite materials indicated at least four sources. These sources include fiber freed by atomic oxygen erosion of LDEF materials (Photograph 11), a glass fiber/phenolic material, and two glass fiber/epoxy materials. The atomic oxygen freed fibers were redistributed on the surface of LDEF during reentry pressurization and during other pressurizing events in the Shuttle Bay. Glass fiber insulation also was present from multiple sources as indicated by variations in refractive indices.

HEPA filter fiber is very regular in its properties and different HEPA filter sources are more difficult to distinguish though the HEPA source is well characterized (Photograph 12). HEPA filter fiber was found in the Shuttle Bay samples as well as on LDEF. During a layover in the ferry flight the Shuttle was connected to a new HEPA filter purge air cart that had not been blown down. HEPA fiber may have been blown onto LDEF at that time but it was not the only source of such fiber. HEPA fiber concentrations never exceeded the trace level.

No glass fiber attributable to an impact with a ceramic or optic was seen in any of these samples. Glass fiber is a very common contaminant that can provide much information with respect to contaminant sources if it is properly identified as to type. If it is not so characterized the presence of glass fiber indicates little due to the wide variety of potential sources.

Organic fibers illustrate additional morphological and optical properties useful for the identification or characterization of particles. Organic fibers exhibit two different refractive indices. In synthetic polymer fibers one refractive index is characteristic of the polymer crosslinkages and the other of the bonding along the backbone of the polymer. The manufacturing process tends to align the polymer molecule so that crosslinkages are aligned at right angles to the length of the fiber and the core of the molecule is aligned with the length. These indices can be measured separately by using a single linear polarizing filter on the light microscope. With two refractive indices the orientation of the higher refractive index, parallel or perpendicular to the length, becomes a useful characteristic called the sign of elongation. Orlon has a negative sign of elongation, the high refractive index is perpendicular to the length, and nylon has a positive sign of elongation, the high refractive index is parallel to the length. The absolute difference in the two refractive indices is another property called the birefringence of the fiber. The birefringence is low for Orlon (0.002), moderate for Saran, and high for polyester (0.18). Morphological properties include the lumen (tube) down the center of plant fibers, cuticle scales characteristic of mammalian hair, linear striations of crenelate plastic fiber, black specks of rutile in plastic fibers, clay sizing on the surface of paper fiber, and other characteristic structures.

Most of the organic fibers found on LDEF were clothing or paper fibers. Polyester, nylon, and rayon fiber has been used in clean room garments but not Saran, Orlon, polyethylene, cotton, wool, or Teflon fiber. Intensely colored fibers of polyester, nylon, or rayon also generally indicate street clothing and not clean room garments. Trilobate nylon, a common rug fiber, was also found on LDEF. Some of these fibers had been exposed to the orbital environment. Photographs 9 and 10 show modifications due to that exposure. On the leading row trays these fibers were eroded by atomic oxygen leaving only tracks as in upper photograph 3 of Figure 1. These types of fibers are one of the most common Shuttle Bay contaminants. An analysis of the HEPA vacuum bag sample collected from the Shuttle Bay door prior to opening indicated these types of fibers were present at high concentrations along the door joint. The Interim Orbiter Contamination Monitor (IOCM) monitoring the Shuttle Bay at the time of the Shuttle Bay door opening in the OPF indicated the most intense contamination response of the entire mission at that time. These types of fibers were rather common on LDEF surfaces both during orbit and as sampled in SAEF-2. Paper fibers were the most common type of fiber added to LDEF during its stay in SAEF-2. Paper fiber is often associated with "sizing" material such as starch, clay, or plastic.

CONCLUSION

The particulate contamination history of LDEF can be resolved by careful analysis of particle types, the LDEF time line, evidence of the relationship between particles and the surface of LDEF, and a consideration of probable sources. This work is far from complete but has been initiated as part of the characterization of the condition of experimental trays that have been returned to principal investigators for their analysis. The work presented in this photo essay is continuing and will be updated in subsequent reports to NASA and at future technical meetings.

REFERENCES

1. Crutcher, E. R., L. S. Nishimura, K. J. Warner, and W. W. Wascher: Migration and Generation of Contaminants From Launch Through Recovery: LDEF Case History. First LDEF Post-Retrieval Symposium, NASA CP-3134, 1992.

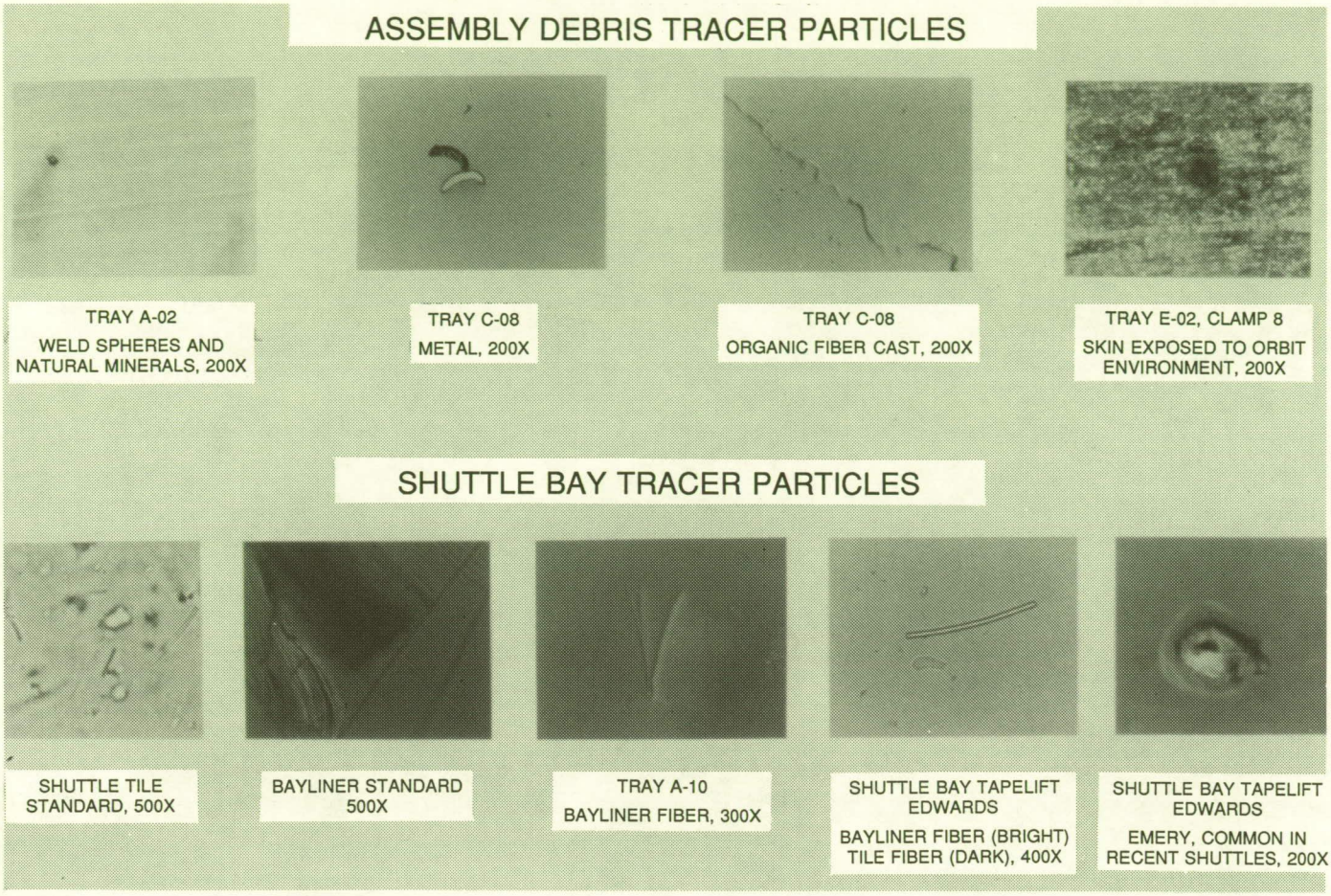

Figure 1: Particles Used To Trace Sources

Upper Set of Photographs: Assembly Debris

Photograph 1: Tray A-02, Silver/Teflon blanket showing a magnetite sphere typical of welding or cutting iron alloys and a natural mineral particle that were present on this blanket when LDEF entered orbit as indicated by the comet tail shaped molecular film shadow.

Photograph 2: Tray C-08, Silver/Teflon blanket showing a crescent shaped wear metal particle that was present on this blanket when LDEF entered orbit and the smooth topped Teflon island that indicates that fact.

Photograph 3: Tray C-08, Silver/Teflon blanket showing the cast of an organic fiber that was consumed by atomic oxygen. The parts of the fiber that were in intimate contact with the surface left concentrations of ash on the surface that further slowed the AO attack of the Teflon surface. Where the fiber was not in intimate contact the ash was more dispersed when it reached the surface or failed to reach the surface so provided less protection. Where the fiber was not in intimate contact it did not provide any protection from ultraviolet light. This also would reduce the net benefit of the shielding provided by this part of the fiber.

Photograph 4: Tray E-02, clamp 8, chromic acid anodized aluminum with UV browned skin flake.

Lower Set of Photographs: Shuttle Bay Tracers

Photograph 1: Shuttle tile fiber standard.

Photograph 2: Shuttle bay liner fiber standard.

Photograph 3: Tray A-10, Silver/Teflon blanket showing bay liner fiber with two AO Shadows.

Photograph 4: Tapelift from the Shuttle bay at Edwards. Shuttle tile fiber and bay liner fiber.

Photograph 5: Tapelift from the Shuttle bay.

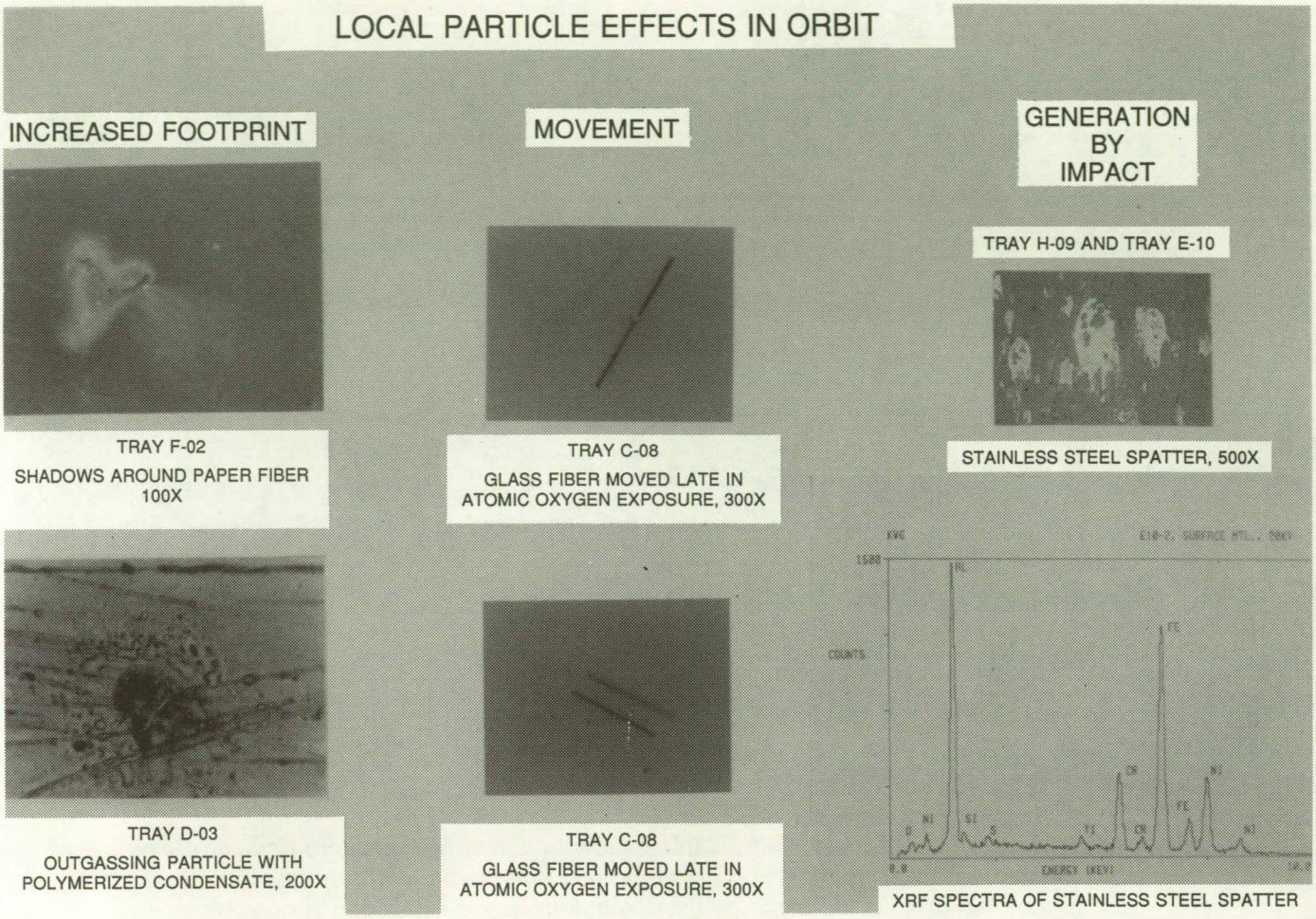

Figure 2: Local Particle Effects

Photograph 1: Tray F-02, Silver/Teflon blanket showing the 'positive pressure' effect seen as the clear area around the cellulose fiber. The roughened areas are a molecular film deposit. The comet tail type shadow is also seen in this photograph.

Photograph 2: Tray C-08, Silver/Teflon blanket showing two AO shadows made by the same glass fiber. The upper lighter shadow was the last location of the fiber.

Photograph 3: Tray E-10, stainless steel splatter on the surface of anodized aluminum from an impact with a tray clamp bolt.

Photograph 4: Tray D-03, Carbon fiber /epoxy composite showing the outgassing deposit from a particle on its surface.

Photograph 5: Tray C-08, Silver/Teflon blanket showing two AO shadows made by the same glass fiber.

Photograph 6: Tray E-10, clamp 2, X-Ray fluorescence analysis of the metal splatter from bolt A on the anodized aluminum.

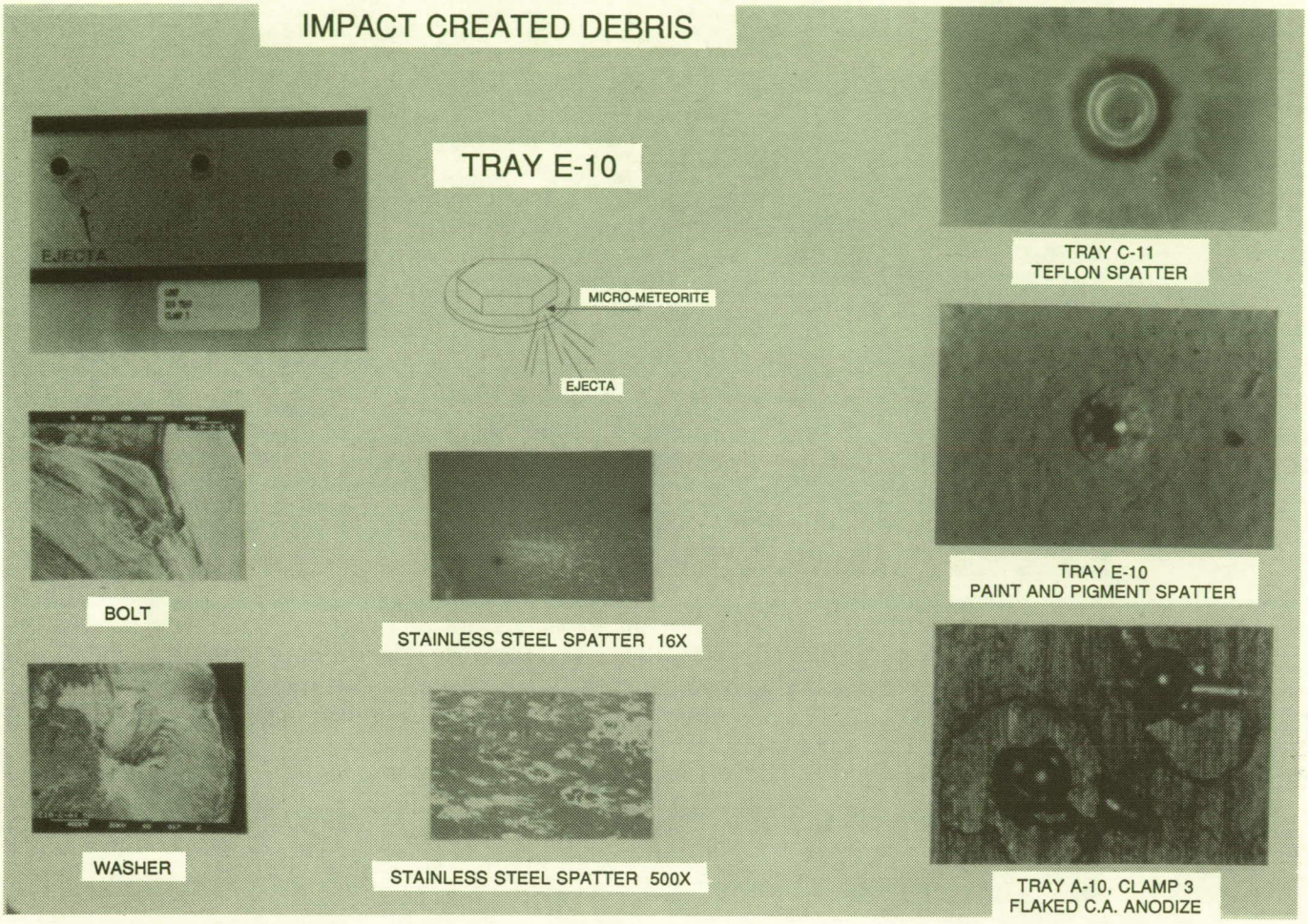

Figure 3: Impact Created Debris

Photograph 1: Tray E-10, clamp 2, showing the stainless steel ejecta field on the clamp from the impact.

Photograph 2: Illustration of the impacted bolt and washer of tray E-10, clamp 2 showing the direction of the impact and the path of the ejected material.

Photograph 3: Tray C-11, Silver/Teflon blanket showing the splattering of Teflon from an impact.

Photograph 4: Tray E-10, clamp 2, bolt A showing the impact site on the bolt using electron microscope.

Photograph 5: Tray E-10, clamp 2 showing the field of ejected material using the electron microscope.

Photograph 6: Tray E-10, clamp 6, paint button showing an impact that released an outer ring of AO freed pigment particles and an inner ring of paint flakes. Oblique toplight illumination.

Photograph 7: Tray E-10, clamp 2, washer A showing the impact site on the washer using electron microscope.

Photograph 8: Tray E-10, clamp 2, stainless steel splatter on the surface of anodized aluminum from an impact with bolt A. Scanning electron microscopy photograph at about 500x.

Photograph 9: Tray A-10, clamp 2 showing flaking of anodized coating caused by impacts in orbit.

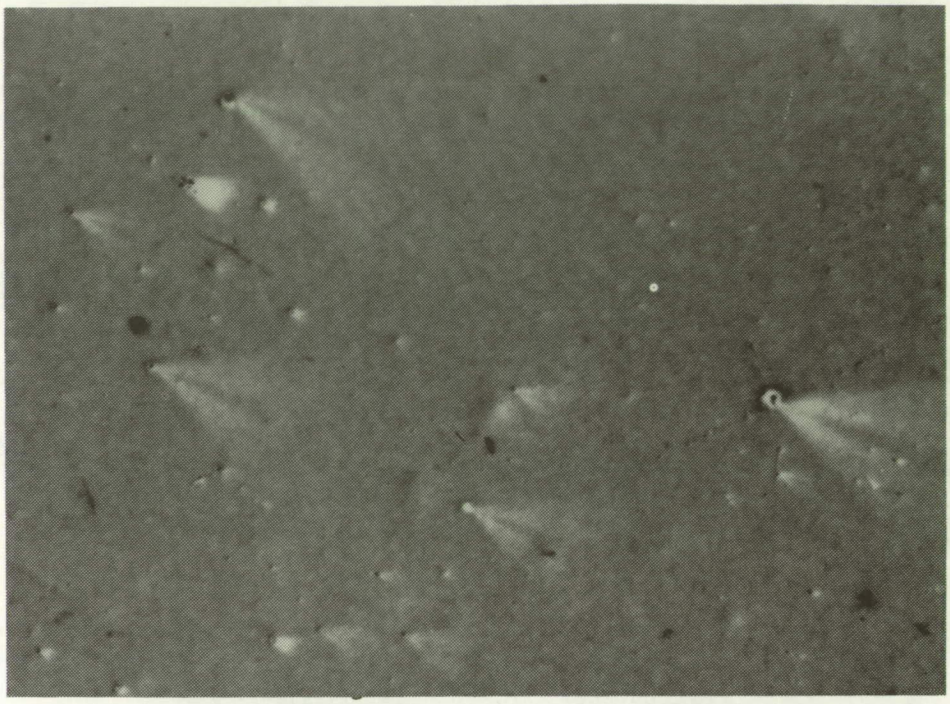

Photograph 1: Tray F-02, Silver/Teflon blanket showing particle shadows in the molecular film (comet tails), relocation or new particles with no shadows, and particles now missing that had been present during orbit (white patches with no black particles present). This photograph was taken in SAEF-2 using brightfield episcopic illumination so that all particles appear black and smooth clear surfaces appear white. 125x magnification.

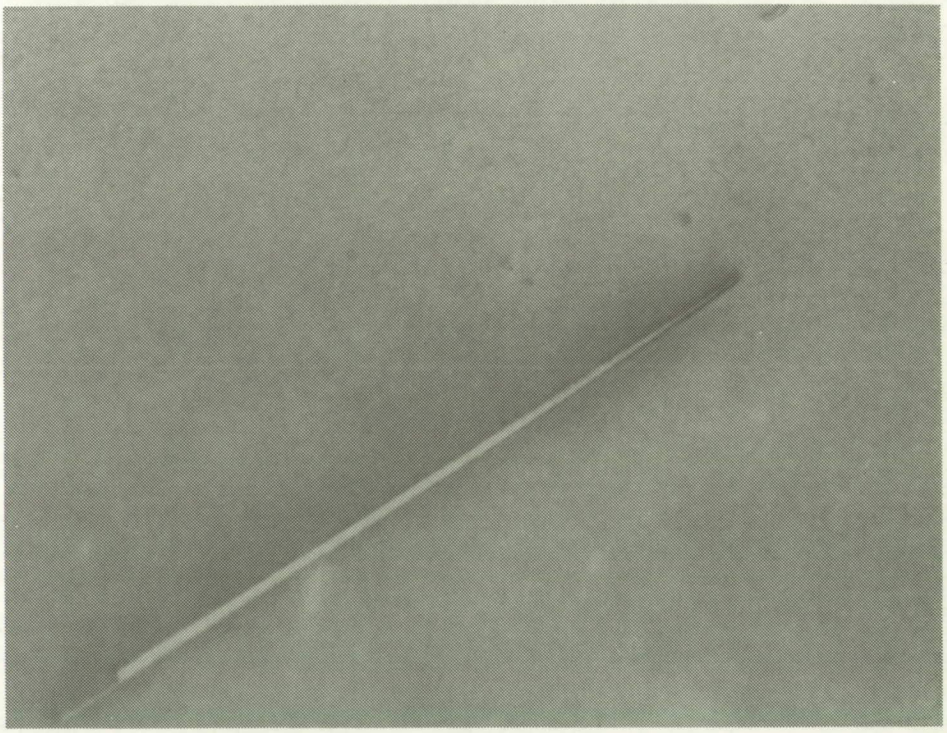

Photograph 2: Tray A-10, Silver/Teflon blanket showing a glass fiber cast. The fiber was in place during the entire orbital exposure as is indicated by the smooth surface of the cast. 125x magnification.

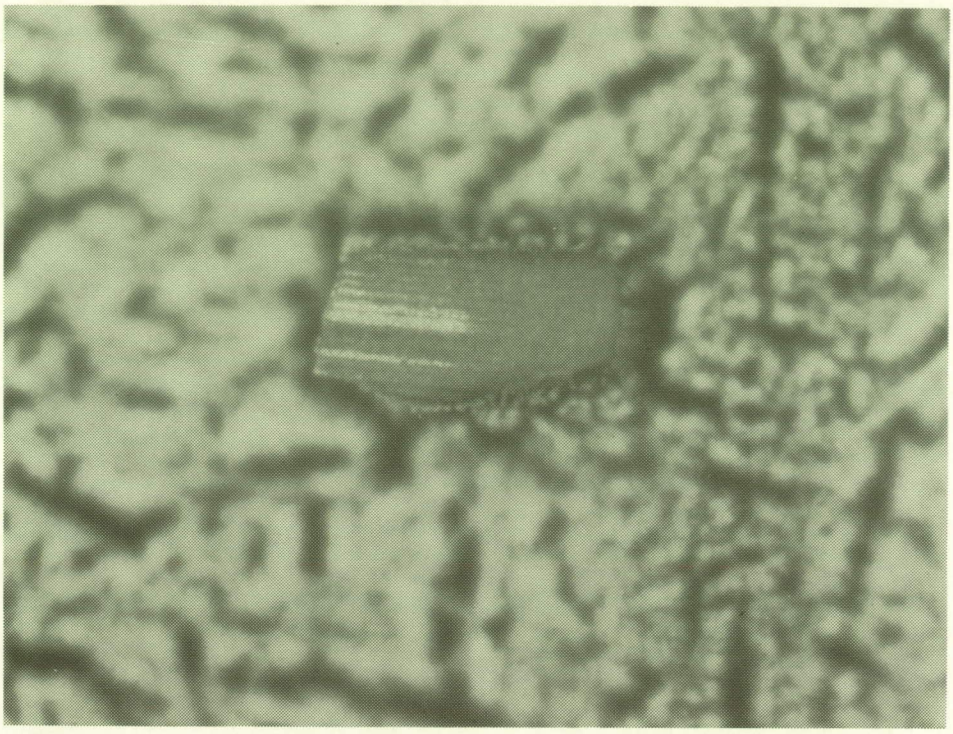

Photograph 3: Tray D-09, Carbon fiber/epoxy composite sample, L3-4-8-65-10, showing a particle protected island that projects 65 micrometers above the atomic oxygen eroded surface. 320x magnification.

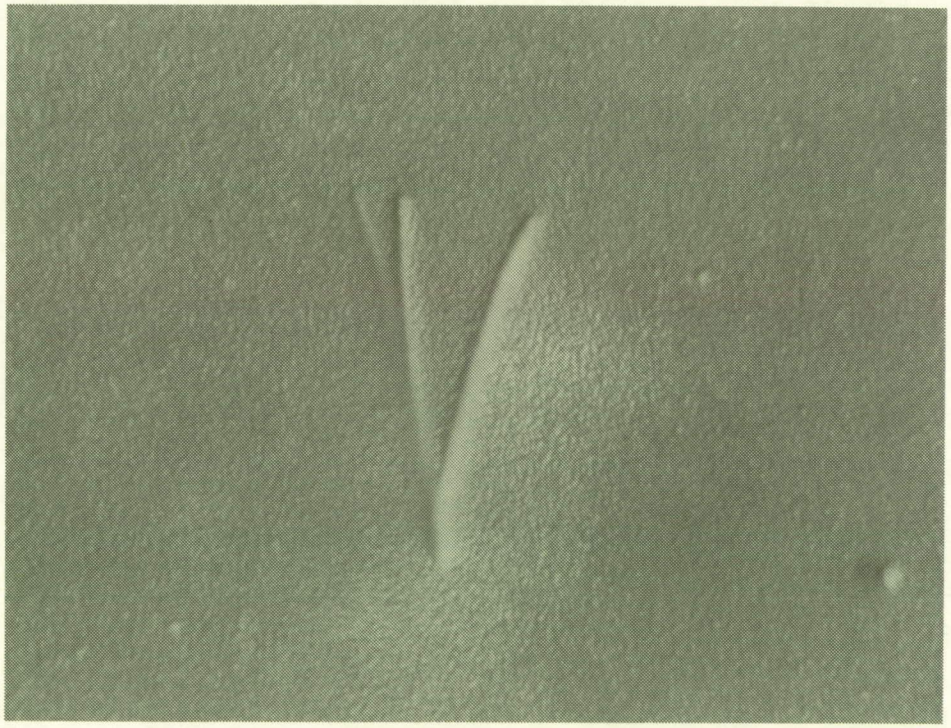

Photograph 4: Tray A-10, Silver/Teflon blanket showing a bay liner fiber (note gentle curve and diameter) with two AO shadows. The actual fiber is the center image of the three linear images and extends above the surface of the Teflon. 575x magnification.

Photograph 5: Tray E-10, Silver/Teflon blanket showing a pattern from a tangle of fibers. The fibers protruded above the surface resulting in only partial protection for part of the surface.

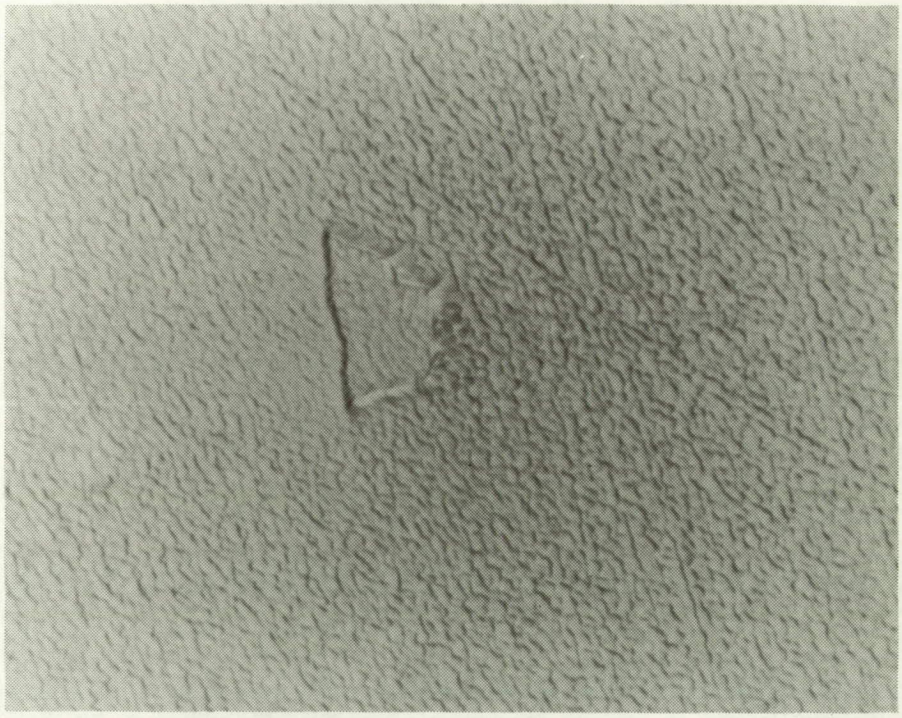

Photograph 6: Tray C-08, Silver/Teflon blanket showing the pattern left by an organic particle that was consumed by atomic oxygen. It provided some protection of the surface while it was being burned away and its ash provided additional protection, at the edge especially. 575x magnification.

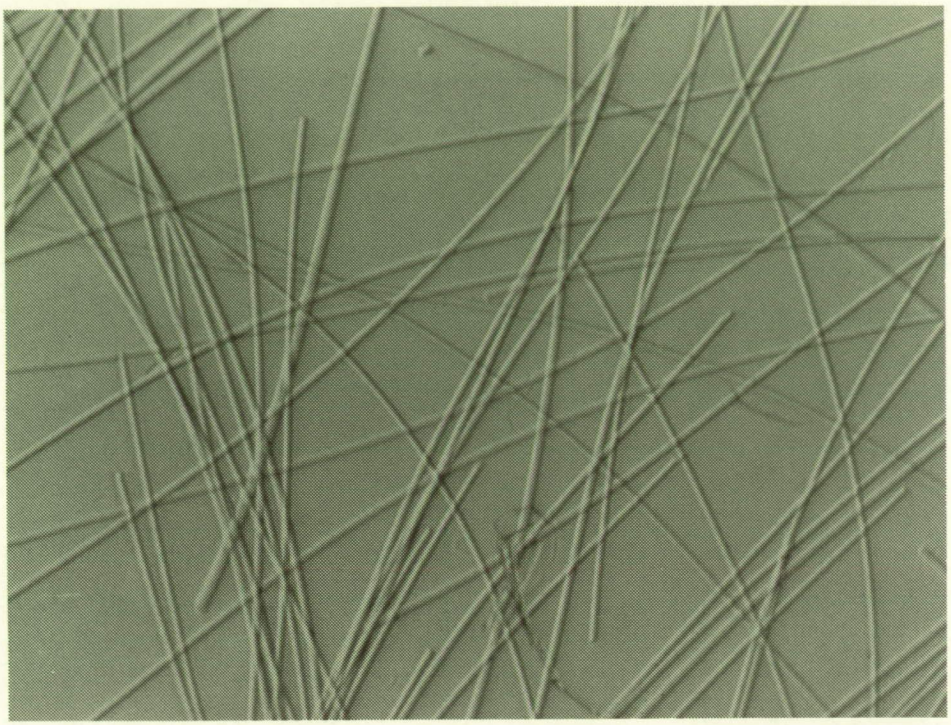

Photograph 7: Bay liner fiber standard from the Columbia showing the gentle curve of the fiber and constancy of the diameter. 320x magnification.

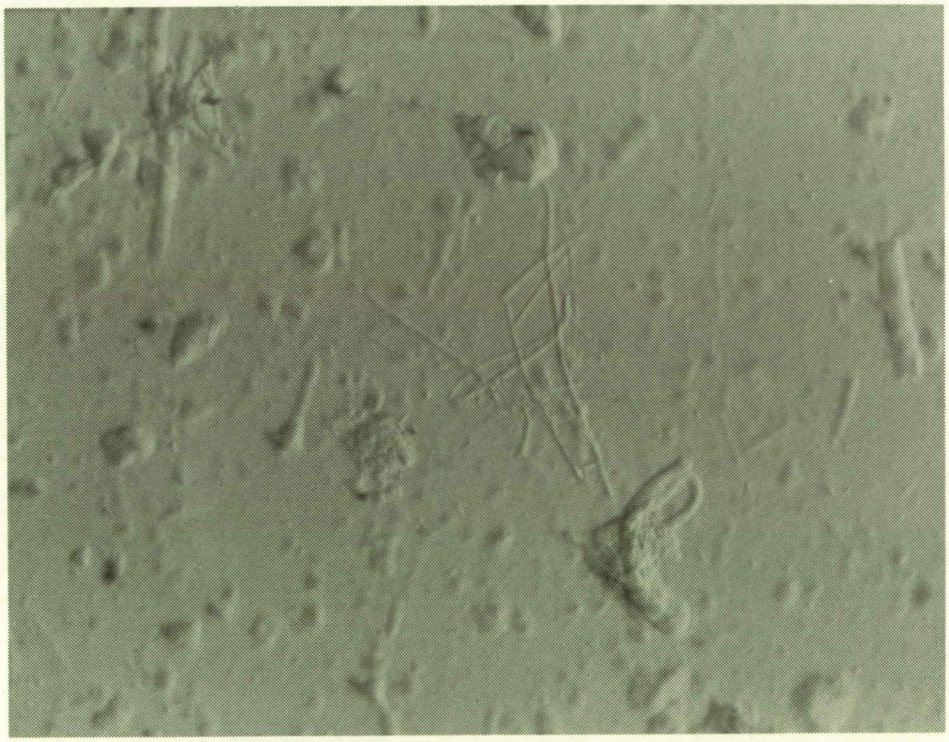

Photograph 8: Shuttle tile fiber standard from a shuttle tile removed from Columbia during preparation for flight. Note the variability in diameter, irregular shapes, and fiber tangles. 320x magnification.

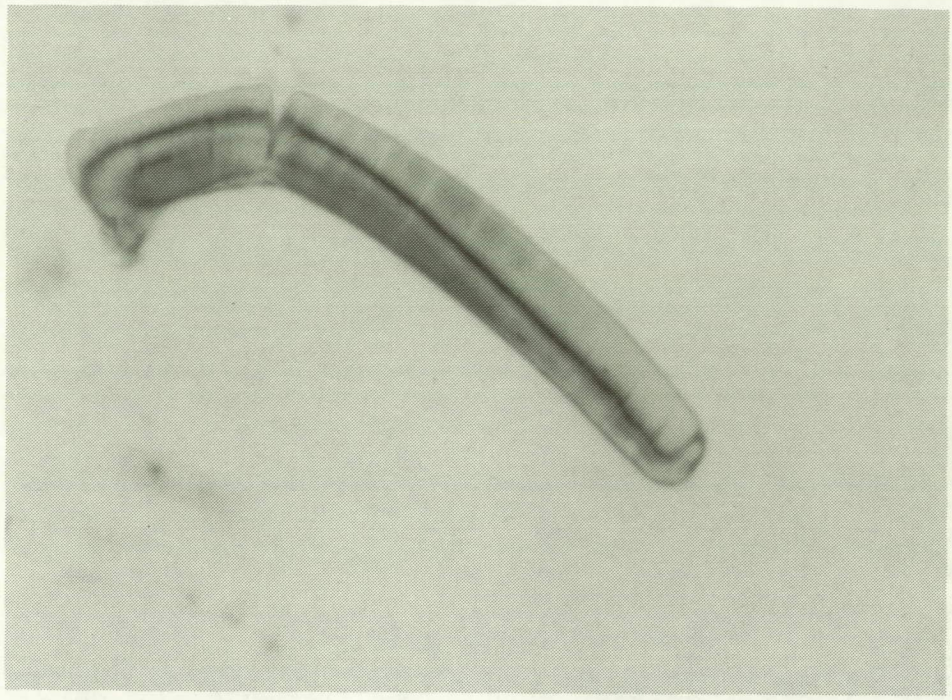

Photograph 9: Tapelift from the Shuttle Bay at Edwards showing ultraviolet modified nylon fiber. The photograph was taken using polarizing filters 15 degrees off crossed. 955x magnification.

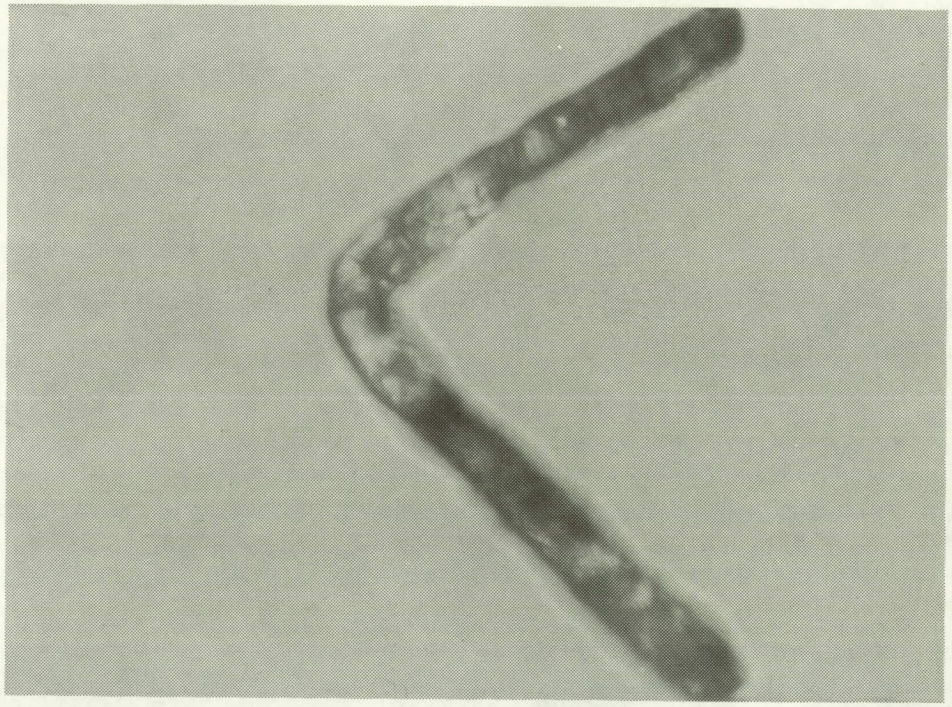

Photograph 10: Tapelift from the Canister under LDEF showing an atomic oxygen and ultraviolet modified cellulose fiber. The photograph was taken using polarizing filters 15 degrees off crossed. 255x magnification.

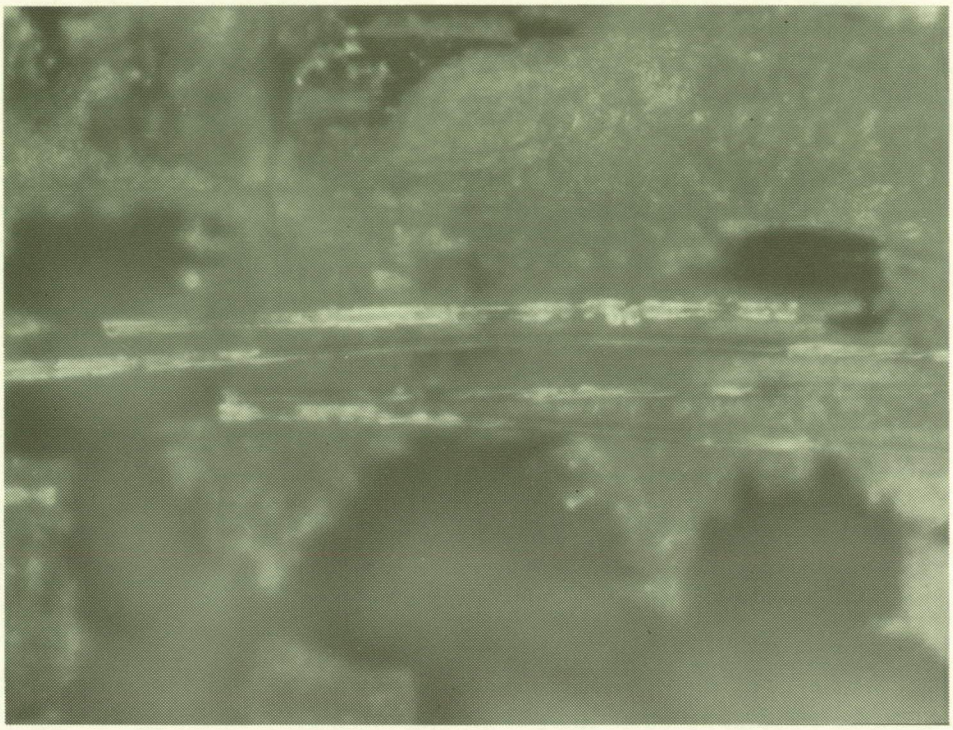

Photograph 11: Tray D-09 showing glass fiber freed by atomic oxygen erosion of a glass fiber reenforced adhesive. 320x magnification.

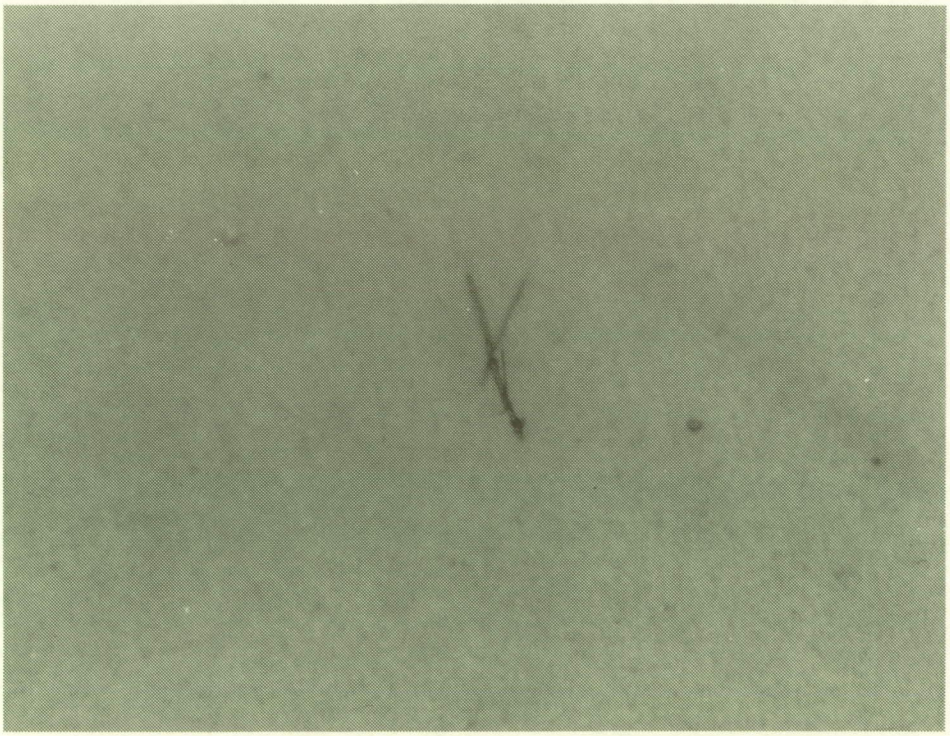

Photograph 12: Tray C-11, Silver/Teflon blanket showing HEPA filter fiber. 285x magnification.

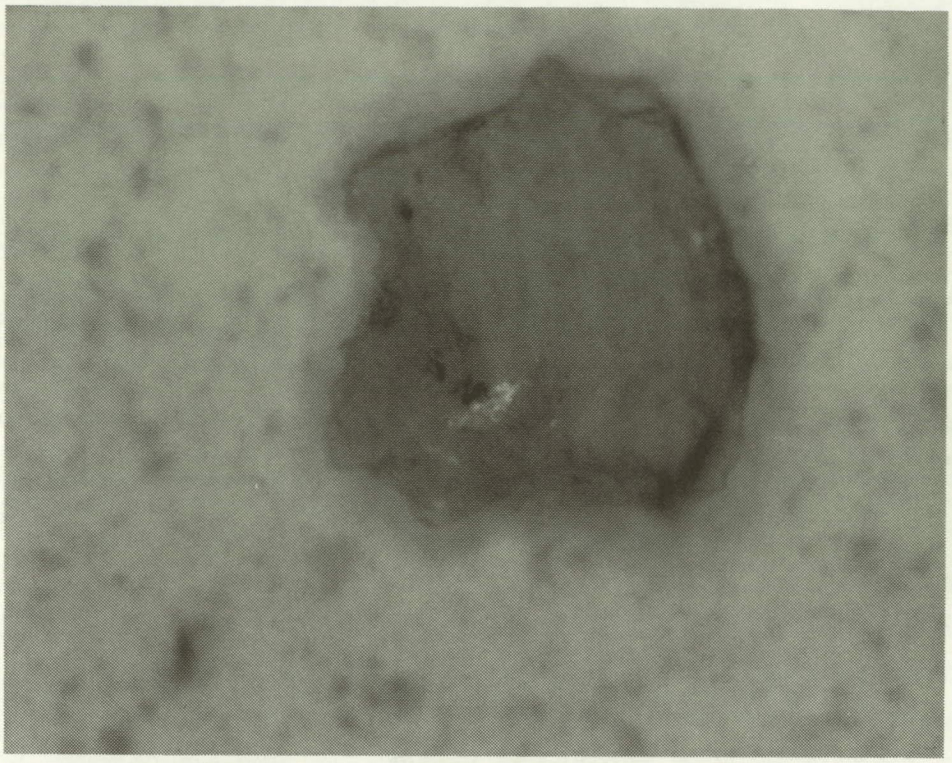

Photograph 13: Tray B-07, clamp 7 showing brown film particle that relocated to the surface of a paint button. 445x magnification.

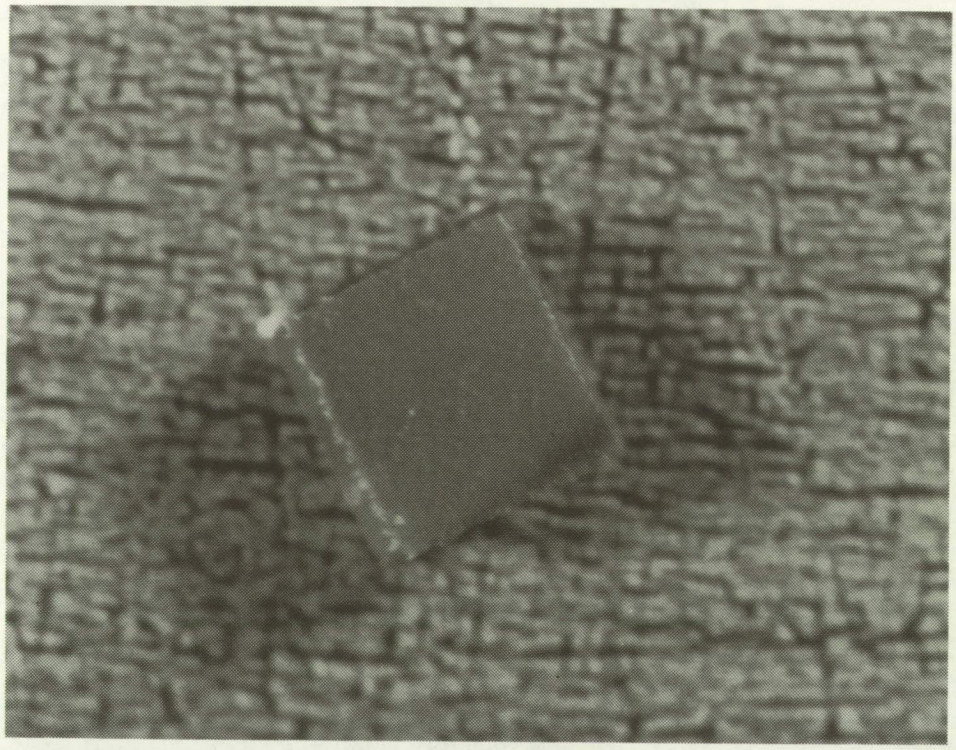

Photograph 14: Tray D-09 showing an antenna particle created by atomic oxygen erosion of the Kapton substrate upon which the vapor deposited aluminum array of half millimeter squares had been placed. These squares were found distributed all over LDEF, the shuttle bay, and the LATS. 70x magnification.

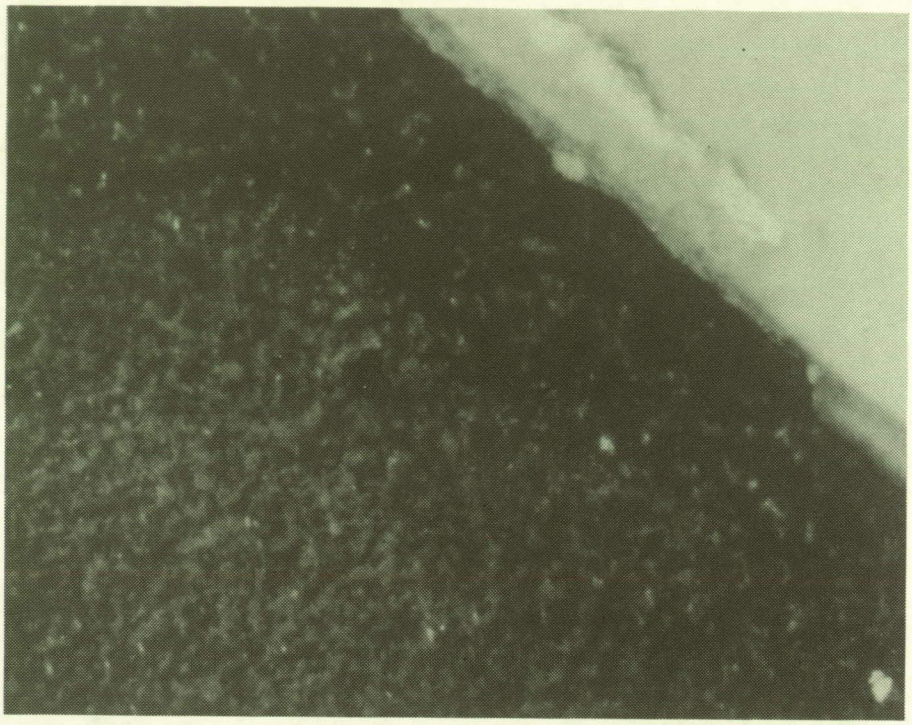

Photograph 15: Tray B-07, clamp 7, showing the fluid flow erosion of the edge of a paint button and the deposition of white pigment on the rough surface of the adjacent black paint. 110x magnification.

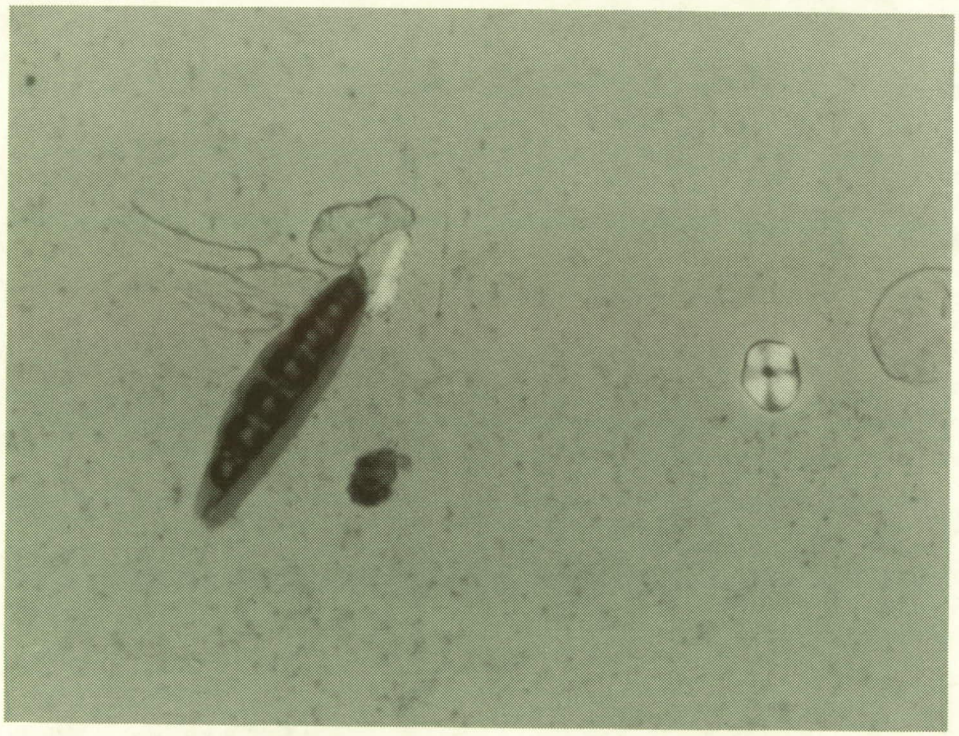

Photograph 16: Tapelift from the SYNCOM Cradle after transport of LDEF in the O&C building. A multichambered fungal spore, latex spheres, a starch grain, AO eroded Kapton fragment, skin, and a clay particle are shown. The photograph was taken using polarizing filters 15 degrees off crossed. 320x magnification.

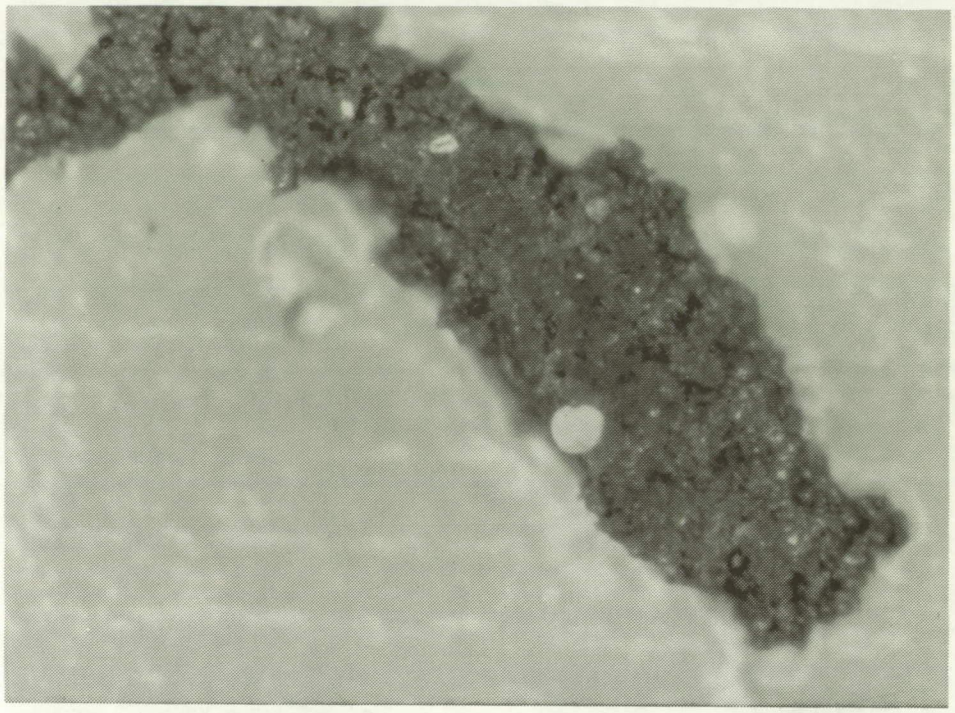

Photograph 17: Tapelift from kit 22, M0002 edge showing rubber wear with attached pine pollen and other debris. Rubber wear may be from the crane or from another tire source. 110x magnification.

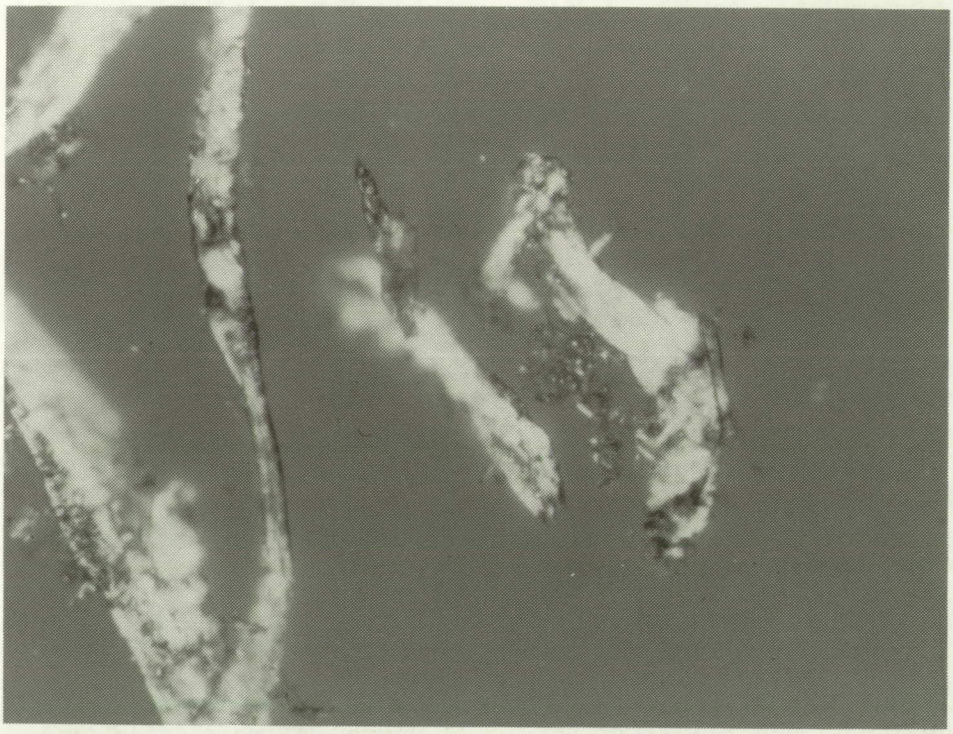

Photograph 18: Paper fiber standard showing cellulose fiber with clay sizing. The photograph was taken using polarizing filters 15 degrees off crossed. 320x magnification.

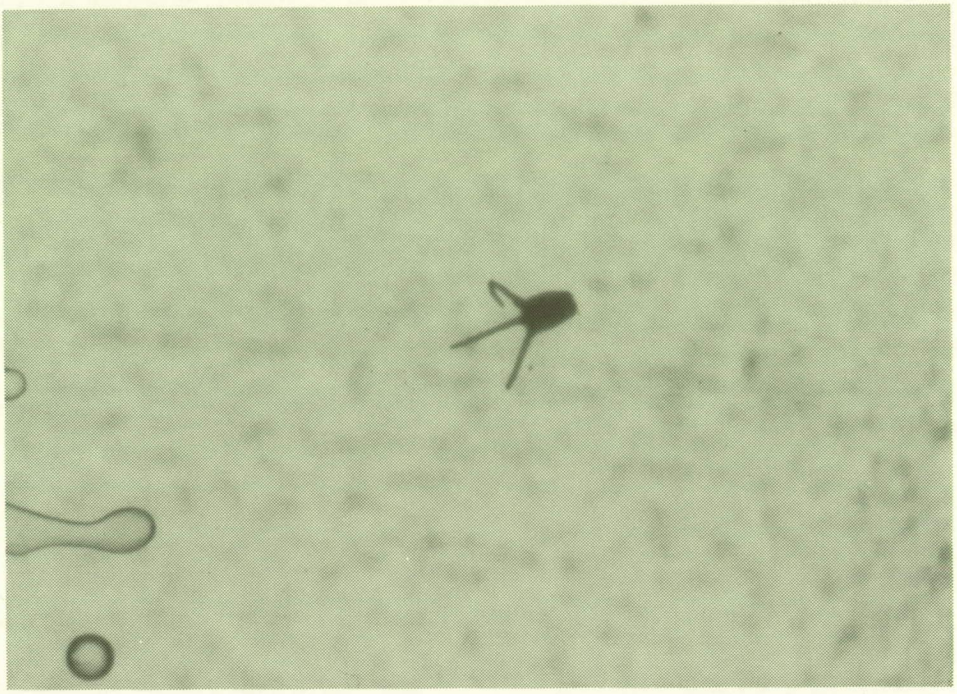

Photograph 19: Tapelift from the shuttle bay at Kennedy, OPF, showing insect foot. 255x magnification.

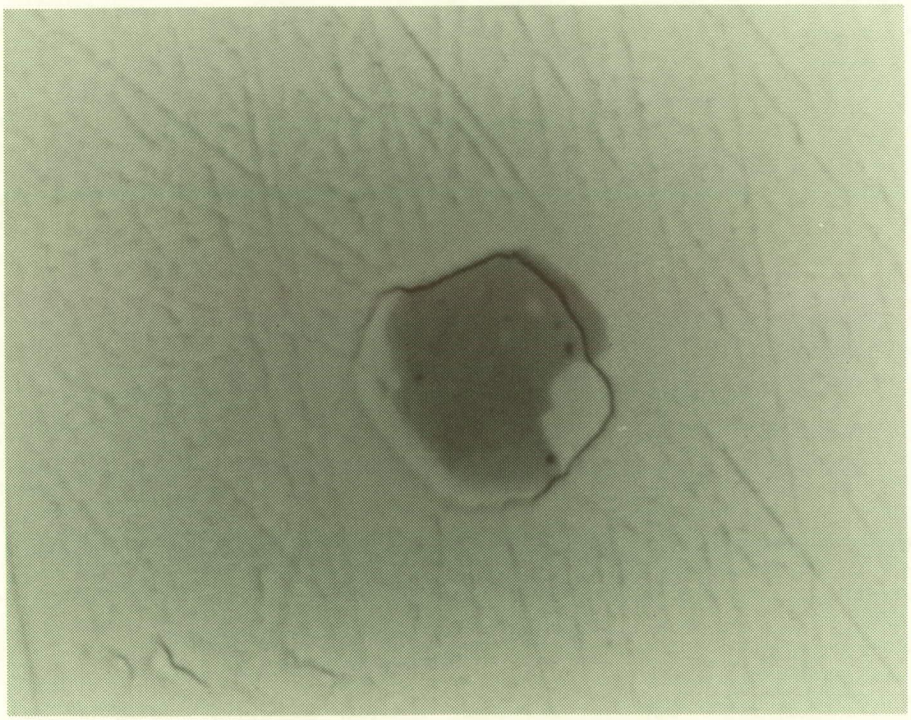

Photograph 20: Tray A-04, Silver/Teflon blanket showing mica protecting the Teflon surface from atomic oxygen and ultraviolet light degradation. 1100x magnification.

MIGRATION AND GENERATION OF CONTAMINANTS FROM LAUNCH THROUGH RECOVERY: LDEF CASE HISTORY*

E. R. Crutcher, L. S. Nishimura, K. J. Warner, and W. W. Wascher
Boeing Defense and Space Group
Seattle,WA 98124-2499
Phone: 206/773-7002, Fax: 206/773-1473

SUMMARY

When LDEF entered orbit its cleanliness was approximately a MIL-STD-1246B Level 2000C. Its burden of contaminants included particles from every part of its history including a relatively small contribution from the shuttle bay itself. Although this satellite was far from what is normally considered clean in the aerospace industry,contaminating events in orbit and from processing after recovery were easily detected. The molecular contaminants carried into orbit were dwarfed by the heavy deposition of UV polymerized films from outgassing urethane paints and silicone based materials. Impacts by relatively small objects in orbit could create particulate contaminants that easily dominated the particle counts within a centimeter of the impact site.

During the recovery activities LDEF was 'sprayed' with a liquid high in organics and water soluble salts. With reentry turbulence, vibration, and gravitational loading particulate contaminants were redistributed about LDEF and the shuttle bay. Atomic oxygen weakened materials were particularly susceptible to these forces. The ferry flight exposed LDEF to the same forces and again redistributed contaminants throughout the bay.

Once in SAEF-2 there was a steady accumulation of particulate contaminants. These included skin flakes, paper fiber, wear metals, sawdust, and pollen to name a few. Some surfaces had a tenfold increase in their particle loading during their stay in SAEF-2. A few of the cleaner surfaces experienced a hundredfold increase.

It was possible to recreate the contamination history of LDEF through an analysis of its contaminants and selective samples that were collected from surfaces with better documented exposure histories. This data was then used to compare estimates based on monitoring methods that had been selected for the purpose of tracking LDEF's exposure to contaminants. LDEF experienced much more contamination than would have been assumed based on the monitors.

Work is still in progress but much of what has been learned so far is already being used in the selection of materials and in the design of systems for space. New experiments are being prepared for flight to resolve questions created by the discoveries on LDEF. This paper is a summary of what has been learned about LDEF contaminants over the first year since recovery and deintegration. Over thirty-five specific conclusions in five contamination related categories are listed at the end of this paper. Much more information will be available with further study.

*Work done under NAS 1-18224, Task 12

INTRODUCTION

The Long Duration Exposure Facility (LDEF) satellite has had a complex history of exposure to contaminants and exotic environments as illustrated in Figure 1. Prior to launch (Fig. 1, position 1) LDEF had on its surfaces an extraordinary variety of contaminants collected during all phases of preparation, including cleaning activities. During its launch (Fig. 1, position 2) in April of 1984 aboard the space shuttle Columbia it accumulated additional contaminants from the shuttle bay. Once in low earth orbit at an altitude of approximately 280 nautical miles (Fig. 1, position 3) hydrocarbon and silicone components, paints, adhesives, and contaminant films began outgassing or offgassing into the local LDEF environment. Much of this material condensed on surfaces of the satellite exposed to ultraviolet light and became a stable surface film modifying the optical and thermal properties of that surface. LDEF also began accumulating micrometeorites and space debris as it swept through space. These energetic impacts redistributed fragments, droplets, or condensates of LDEF materials. The high energy ultraviolet light of low earth orbit also began modifying surface carbon based materials creating new outgassing species. Initially low levels of atomic oxygen slowly interacted with the ram facing surfaces of the satellite. As its orbit decayed the flux of atomic oxygen increased,burning away hydrocarbon films and converting silicones into inert silicates. In January of 1990 the crew of the space shuttle Columbia grappled LDEF in orbit (Fig. 1, position 4) and gently moved the satellite into its cradle in the bay. As gentle as it was the grappling released clouds of small particles along with a few solar cells and other large objects. Again nested in the shuttle bay the satellite was brought back into the rich gaseous environment of this planet's surface (Fig. 1, position 5 and 6). Turbulent flow over the surface of the shuttle bay and LDEF during this return redistributed and mixed contaminants from both surfaces. LDEF's contribution to this mix significantly exceeded that from the shuttle bay but the contribution of new particles to the surface of LDEF was evident. The ferry flight exposed LDEF to another variety of environments and again to turbulent flow (Fig. 1, position 7 and 8). At some time during its recovery LDEF was sprayed with an aerosol of fine droplets of a hydrocarbon containing material (Ref. 1). Finally at Kennedy Space Center the satellite was removed from the shuttle bay (Fig. 1, position 9) and transported to the SAEF-2 clean room (Fig. 1, position 10). The contamination in the shuttle bay was monitored from before the launch of the Columbia through the removal of LDEF from the shuttle bay by the IOCM experiment package.

In the SAEF-2 clean room LDEF continued to interact with its new gas rich environment. When the LATS was first used to rotate LDEF, materials fell from the surface of many of the trays and a liquid began slowly running from the vicinity of tray C-12. Tray C-12 had been oriented horizontally on the top of LDEF as it sat in the shuttle bay and throughout recovery up until the first rotation in SAEF-2. This liquid was an early indication of atmospheric and/or operationally induced changes to orbitally stable or pseudo-stable materials.

The atomic oxygen degraded materials on the surface of LDEF were a considerable source of particulate contaminants but they were not the only source of particles in SAEF-2 and an additional set of new particles began accumulating on the satellite. Contaminants in SAEF-2 were monitored by automatic particle counters and by fallout and witness plates. Tapelifts were also taken of the surface of LDEF. The trays containing the experiments were removed beginning on February 22 and ending on March 29. A final set of tapelifts were collected from LDEF on April 13 and 14. Boeing was commissioned with the task of extracting contamination information from LDEF surfaces to provide the principle investigators of each experiment on LDEF with background information that may affect their analysis. Specifically the Boeing study was to "determine which contaminants were present before the LDEF was flown, which were created during space flight, and which contaminants were acquired by post flight exposures" (MATERIALS SPECIAL INVESTIGATION GROUP HANDBOOK). Our approach was to consider LDEF as a large contamination experiment. This paper is a preliminary presentation of the data collected over the first year since recovery.

When LDEF was considered as a contamination experiment five subexperiments became apparent:

1. LDEF as a particle witness plate for the shuttle bay
2. LDEF as a molecular deposition experiment
3. An experiment to determine the orbital effects on contaminants
4. An experiment to evaluate the accumulation of contaminants in orbit
5. An evaluation of contamination monitoring systems

Each of these experiments has a legacy of data from past missions, from theoretical models, and from basic constraints imposed by physics. The LDEF data is unique in that because of the duration of its stay in orbit second order effects are clearly present that aid in the refinement of models and there is a reduction in the effects of spurious events seen on shorter missions. A summary of the results from each of these experiments is presented below along with a final comment on precautions for principle investigators evaluating parameters that may have been influenced by the presence of contaminants.

LDEF AS A SHUTTLE BAY WITNESS PLATE

The migration of contaminants from the shuttle bay to payloads has been a concern since the beginning of the concept of the shuttle (Ref. 2). The term 'visibly clean' was frightfully unquantitative and anyone familiar with particulate contamination control knew the control of contaminants for such a large and delicate craft was complex in the extreme. A series of sophisticated instruments have been used to try and quantify the amount of particulate matter in the shuttle bay that migrates as a result of launch vibration and other shuttle related events but the results have been circumstantial with respect to the payload and somewhat contradictory (Ref. 3, 4, 5). In the case of LDEF it was the payload itself that was being examined. LDEF provided an excellent opportunity to evaluate the transport of contaminants between the shuttle bay and a payload. As a payload LDEF was exceptional in that it closely paralleled thirty feet of the bay as a large witness plate. There were some problems with this approach in that the preexisting cleanliness level of LDEF had not been ascertained prior to exposure. An additional complication was that the LDEF witness plate consisted of a variety of different surface materials and surface geometries. Each material had a different propensity for retaining contaminants which in some situations was dominated by the specific geometry of the material in terms of how it was attached to LDEF or its orientation. Because of these problems some types of quantitative data would be largely circumstantial. Particle types that were tracers, highly indicative of specific sources, were needed to provide qualitative substantiation and some lower boundary quantification. Because LDEF had been exposed to the shuttle bay on two different occasions a way of differentiating between them was required for a more reliable evaluation of the impact of each exposure. The interaction between particles and surfaces in an orbital environment provided a method for that differentiation in many instances. Below is a summary of what has been accomplished to date.

Pre-Launch Cleanliness of LDEF

The particle cleanliness of LDEF varied significantly from area to area on a tray, from experiment to experiment, and from tray to tray. Cleanliness was not a priority concern for most of the experiments. Visibly Clean Level II (SN-C-0005) was the only requirement and the expense of elaborate precautions could not and would not have been justified by the original mission goals. Many if not most of the experimental trays were handled with bare hands. Fingerprints and handprints were evident widely dispersed over LDEF and inside the trays (Ref. 1, photograph 6 and Ref. 6, photograph 3).

Contaminants, particulate and molecular, from a variety of sources have been identified as being present on LDEF prior to the exposure to the shuttle. The best estimate for the cleanliness of LDEF prior to shuttle exposure is a modified MIL-STD-1246B Level 2000C, or, using a slope of 0.38 rather than the slope of 0.93 used in the military standard, a level 5000 as presented in Reference 6, "Quantification of Contaminants Associated with LDEF".

LDEF Configuration in the Shuttle Bay and Particle Location

LDEF was located between bay 2 and the SYNCOM cradle in the shuttle bay with its exterior surface approximately a foot from the bay liner. Row 12 was in the 'z' normal position facing out of the shuttle and row 6, on the opposite side of LDEF, was immediately above the floor. Row 3 and row 9 were oriented in the 'x' normal position just below the level of the door hinges. The space end of LDEF was directed toward the shuttle cabin. This geometry is important because it is a configuration unique to the shuttle exposure of LDEF (see Figure 2). In orbit a bifold symmetry about the plane through rows 9 and 3 existed. In LATS a rotational environment with alternating rows directed downward in a unit gravity field defined the exposure. Only in the shuttle was row 12 open and facing upward for extended intervals of time. When the shuttle was rotated to a vertical position the space end acted as a collection plate for fallout from the cabin bulkhead. There have not been enough of the specific surfaces of interest studied to adequately document the results of this geometry for particles but it has been very useful in documenting the arrival of a spray of hydrocarbon containing material at the surface of LDEF (Ref. 1). Work by John Scialdone (Ref. 7) provides a model for selecting surfaces of interest related to the launch environment as well as for the evaluation of some of the micro-environmental effects seen on some trays and reported in Reference 8, "Silver/Teflon Blanket: LDEF Tray C-08".

Tracer Particles and Their Time of Arrival

The best tracer particles for the shuttle bay are the glass fibers used as part of the bay liner and those from the shuttle tiles (Ref. 9, photographs 7 and 8). These are characteristic of the shuttle bay environment and though reported by NASA investigators to be a minor part of the total contaminant burden in the shuttle bay,their durability in orbit makes these fibers an excellent tracer for the bay contributed contaminants. These particles were found widely distributed over the surface of LDEF. The actual number of shuttle glass fiber particles positively identified is less than one hundred but that represents a significant number of the total glass fibers analyzed and is too high a number to suggest that such cross contamination is rare. These small colorless glass fibers could be present at fairly high levels in the shuttle bay and still not be readily visible. The distinguishing characteristics of these fibers are discussed in Reference 9 along with documentation of their post-launch distribution. The shuttle fibers contributed at launch and those that were added during the recovery and transport activities were essentially the same, which complicated the assignment of fibers to those separate events. No attempts have been made at this time to differentiate between them. Many of the fibers deposited originally on the surface of LDEF during launch and present during orbit had moved by the time LDEF was in SAEF-2. Shuttle fibers found on the surface of LDEF in SAEF-2 that were not associated with surface shadows may have been new fibers or relocated older fibers. The relocation of shuttle fibers during recovery operations and their redeposition are documented in Reference 9.

MOLECULAR DEPOSITION EXPERIMENT

Most of the molecular film deposited on the surface of LDEF was the product of LDEF's design and not the result of contaminant residues on its surface at launch. Though before launch LDEF was not

particularly clean in the sense of non-volatile residues these residues amounted to less than ten percent of the final film found on LDEF (Ref 1). Over ninety percent of the final film came from materials intentionally used on LDEF, RTV silicone materials and urethane thermal control paints; Z306 black and A276 white. The silicones and the large amount of Z306 paint used on the back side of the trays and on the interior structure of LDEF contributed an estimated two to three kilograms (4 to 6 pounds) of outgassed materials to the environment of LDEF (Ref. 6).

Another major factor in the deposition of these films was the geometry of the vents from the interior of LDEF. The vents consisted primarily of the corners of each tray, the edges of the trays, and the edges of the earth and space end panels. All of these vents tended to direct outgassing molecules at low angles over the surface of LDEF. The end panels and the tray edges consisted of openings between two closely paralleling sheets of metal. The most favored escape path was one that nearly paralleled the surface of LDEF. This trajectory kept the molecules in close proximity to the satellite over a greater pathlength, increasing the molecular density near the surface and the probability for an interaction directing a molecule to the surface of the satellite. Where molecules had condensed on a surface that was then exposed to ultraviolet light the molecule was fixed in place or quickly emitted leaving a stable polymerized solid film behind. During the next cycle (cyclic deposition discussed below) the molecules flowing over this surface would not encounter a high density of molecules escaping this surface and so encounters with other molecules would increase the probability of the molecule being directed toward the surface of LDEF. This effect is not dependent upon the RAM effect but rather on vent streams from adjacent trays creating a higher molecular density very near the surface. Considering the amount of vented material available this could account for the deposits seen on the trailing structural elements of LDEF between the trays (Ref. 1, photograph 9). The corner vents consisted of a complex hollow with condensation surfaces parallel to, and normal to, the surface of the tray. The parallel surfaces faced back into the interior of LDEF but were elevated slightly above the face of the tray. The edges of the neighboring trays and the stanchions and longerons constituted collection surfaces at right angles to the face of the tray. These surfaces of the stanchions and longerons faced out onto the trays and would emit molecules paralleling the face of the trays. The double shadows seen around some particles (Ref. 1, photograph 9) could be explained by emissions from these surfaces, both at right angles to the tray surface and to each other.

The vents in LDEF constituted a relatively small opportunity of escape due to their size and the complexity of the escape path for multiple bounce paths. The vent area of LDEF's surface for a single straight path escape was only about 0.2 percent of the total surface. Multiple bounce trajectories or repeated thermal cycling events of vaporization and condensation blended the interior sources into a reasonably uniform composition of molecular species prior to escape. This is indicated by the characteristic uniformity of the infrared spectra of the films found on widely separated surfaces of LDEF (Ref. 1, figures 1, 2, and 6). Another characteristic of the film from the vents was their layering. As many as 34 discreet layers were found in some of these films (Ref. 1, photograph 7). The layers were from tens of nanometers to micrometers in thickness. The most obvious cycle that would result in this layering is that of the orbit. If the cycle was orbital then the majority of the film would have been deposited very early in the mission with relatively high molecular densities and rapid 'fix' times for the polymerization of the films once exposed to ultraviolet light. The film with the 34 or more layers was collected from a vent of tray C-12. C-12 faced out of the shuttle bay and had the earliest exposure to fixing ultraviolet light prior to release into free orbit. Some of these layers may have been fixed in place before LDEF had left the shuttle bay. If this is true deposits on the vents of rows 1, 2, 10, 11, and 12 should be the most developed. Those on the earth and space end should also have a deposition pattern that corresponds to that orientation rather than an orientation dominated by the ram deposition characteristic of LDEF's free orbit. Such a deposit pattern has not been documented for these trays but the search is continuing. Row 12 does seem to have rather well developed deposits compared to row 6 and the apparent thickness of many of the layers seen in these films does seem to support an early, and therefore, orbital cycle deposition sequence.

There is much evidence supporting an orbital deposition sequence but there is also evidence of much longer deposition intervals. The canisters that did not open until a month after entering orbit exhibited depositions of these films. It is possible that some longer cycle was involved in forming some of these

layers. Longer cycles have been documented such as thermal variations and ultraviolet light exposure times for different parts of the satellite. The release of some of the film forming materials may have been markedly non-linear with respect to the heating of some collection surfaces. There is no reason to reject multiple deposition scenarios, all occuring at the same time,though one mechanism may dominate in one area for a given interval of time. The rate at which the Z306 and the silicone materials released their outgassing products is not known. There are a number of combinations of release rates, vapor pressures, chemical affinities or stabilities, and rates of interior venting that would account for the composition of the films over the time required for their deposition but it is possible the final film is simply the most stable of a variety of chemical possibilities. Modeling LDEF as a large diffusion tube would help to establish a scale of time over which the amount of material released from surfaces inside could escape to the outside. This has yet to be done. Another long duration source of molecular material is the decomposition and release of fragments of polymers due to the effects of ultraviolet light. Evidence for the loss of material from polymer surfaces through this mechanism is seen on trailing tray Teflon surfaces (Ref 8., photograph 6) and other polymer surfaces.

There were a variety of smaller sources of molecular material on LDEF that had only local effects. These ranged from the microscopic fragments of skin that affected areas on the order of tens of square micrometers, to large packages such as the fiberoptic bundles on tray C-12 that affected areas on the order of a square meter. Each of these small 'diffusion cells' had specific emission rates and and outgassing species that dominated the cell's local environment for some distance dependent upon other local sources and their relative strength. A cellulose fiber outgassing water vapor seems to have created a local zone of protection around the fiber as seen in Reference 9, figure 2, frame 1. The interaction of these cells of various types may help establish the timing of the deposition sequence on LDEF. Determining the timing is critical to understanding how to minimize the effects of these films on satellites or to preventing their deposition on critical surfaces of future payloads.

Though the original molecular film contaminant layer present on LDEF at launch was minor compared to later depositions there were some areas where this pre-launch contaminant was at high enough levels to be of interest. Those deposits were associated with tray clamps and shims or fasteners. In these areas sufficient material had been concentrated by solvent cleaning or other activities to have an effect above the background levels. These objects acted as simple diffusion tubes releasing materials at a rate determined by the volatility of the material, its location with respect to the point of final release into the outer environment, and the temperature at its location on LDEF. The result was a gradient of functional groups that seems to suggest the variability of vapor pressure, release rates, and interaction with the molecular species venting from the interior of LDEF (Ref. 1, figures 17, 18, and 19). These areas should also be useful in developing a better understanding of the formation mechanics of the LDEF molecular films.

CHANGES IN CONTAMINANTS WITH TIME IN ORBIT

Contaminants are not dormant in orbit. Molecular films are an obvious example but particulate contaminants also change and migrate over surfaces in orbital environments. The effect is to increase the apparent footprint of the particle on the surface. In Reference 9, figure 2 a number of examples are provided and are referenced by frame number below in this paragraph. The fractional obscuration of surfaces by particles or the absorption, emission, or scattering of UV, visible, or infrared wavelengths of light are principal areas of concern regarding particles on surfaces. From the standpoint of imaging optics the footprint of a particle is the area of optical inhomogeneity created by the particle. The shadowing effects of particles tends to increase the size of the particles effect by as much as an order of magnitude (Ref. 9, fig.2, frames 1 and 4). Some of this change is due to molecular contaminants that are generally associated with the interface between the particle and the surface on which it sits. If these materials are volatile condensable materials they may spread from the particle along the surface and become fixed molecular films.

The movement of particles from one area of a satellite's surface to another was documented on the ram facing Teflon covered trays (Ref. 9, fig.2, frames 2 and 5). The documented movement was limited to very short distances, less than 100 micrometers, but longer transport distances may also occur though their documentation would be difficult due to the areas that would have to be searched and the number of measurements that would have to be made.

The darkening of molecular films on surfaces with ultraviolet light exposure is a well known phenomena, but with LDEF, knowledge of the nature of the UV modified film and of its optical properties will improve. These molecular films have been implicated in failures due to thermal effects as well as power loss through decreased efficiency of solar cells.

When LDEF was retrieved there was an inhomogeneous distribution of contaminants. That by itself was not surprizing but it raises the question of preferred sites or 'contamination sinks' where contaminants persist or collect preferentially. Reference 8 provides an example of one such location for particles at the edge of tray C-08. The distribution of molecular films on the surface of LDEF is another example. The nature of the specific contamination sink will vary with the type of contaminant and the collection mechanism. Some are active before launch and some are only active in orbit. The concept of contamination sinks may be useful in satellite design.

ACCUMULATION OF CONTAMINANTS IN ORBIT

As a satellite sweeps through its orbit it accumulates man made space debris by impaction. Rapidly moving meteorites from all directions impact with the satellite adding to the accumulated contaminants. The total mass of these two sources is dwarfed by the amount of contaminants they create as a result of the impact. These impacts often generate thousands of times their mass in the form of new particulate contaminants deposited on local surfaces. In Reference 9, figure 3 an example is given of one impact with a bolt and washer on a tray clamp of tray E-10. Droplets of molten metal from the bolt and from the washer were spread over the surface of the clamp at a distance of nearly a centimeter. Many such examples have been found on LDEF, some involving transport on the order of a number of centimeters. Vapor phases generated by these impacts often condense on the surface locally and may redeposit on the satellite's surface at greater distances as part of the return flux in the ram direction. The types of contaminants generated by these impacts is dependent upon the surface impacted. Examples of Teflon, atomic oxygen eroded paint, stainless steel, and anodized aluminum are provide in Reference 9, figure 3. The fluorine detected on many metal surfaces of LDEF may be from the redeposition of materials, gaseous or particulate, created by impacts with Teflon surfaces.

Polymeric materials are another source of new contaminants in orbit as mentioned earlier. Energetic ultraviolet light degrades the bonds holding polymers together, often creating free radicals that may form other bonds or diffuse as an outgassing product into the volume around the satellite. These new outgassing materials are then free to contribute to the molecular films depositing on the surface. This is another possible mechanism for the release of fluorine into the environment of LDEF coming from Teflon and from fluorine catalyzed 934 resin used in many LDEF samples. This deposition should be most prevalent on the ram surfaces (Ref. 10) but due to the atomic oxygen fluence on the ram surface of LDEF carbon based residues would be destroyed though the presence of fluorine and silicon on these surfaces may in part be due to this source. Depositions in the canisters that were closed after ten months may also contain traces of these materials.

Atomic oxygen erosion of paint surfaces liberates inorganic pigment particles that are then free to migrate. Inorganic ash particles or atomic oxygen weakened surfaces are also sources of particles that can become free of the surface as a result of a nearby impact and migrate. Thermal effects may be sufficient to free some of these particles from the surface. There was a very significant relocation of these particles

during recovery which would have destroyed any such evidence following recovery. Photographs taken in orbit may provide some information.

EVALUATION OF CONTAMINATION MONITORING SYSTEMS

The presumption of product cleanliness based on the cleanliness of nearby collection surfaces or witness plates, or based on low levels of half micrometer particles in the air as determined by an automatic airborne particle counter is common in high-tech industries. The product itself is often too fragile, inaccessible, or prone to degradation to sample directly. LDEF provided an opportunity to directly examine a surface whose cleanliness, in terms of new contaminants or cross-contamination, had been monitored by environmental sensors placed in proximity to the satellite. The first set of proximal sensors used to monitor the environment to which LDEF would be exposed were all part of the IOCM experiment. This experiment consisted of an impressive array of substrata for later analysis as well as active TQCMs that measured real time variations in the harmonic oscillation frequency of a quartz collection surface (see Ref. 5). These sensors began monitoring the shuttle bay over forty hours before launch and continued through the removal of LDEF from the bay after recovery. The second battery of proximal sensors consisted of witness plates, automated airborne particle counters, and tapelifts from surfaces near LDEF. Tapelifts from nearby surfaces were first collected from the shuttle bay at Edwards, then at Kennedy after the ferry flight, from the canister before and after LDEF's transport from the OPF to the O&C building, and from the LATS until the removal of the last tray in SAEF-2. All of these results were compared to tapelifts taken directly from the surface of LDEF and to direct analysis of selected LDEF surfaces.

In comparing the IOCM results to the tapelift data from the SYNCOM cradle surfaces as well as the shuttle and LDEF surfaces a few apparent inconsistencies are evident. The first has to do with the cross contamination of payload surfaces in the shuttle bay. The analysis of the IOCM data was interpreted as indicating no cross contamination. Tapelift data from the SYNCOM cradle indicated significant amounts of bay liner fiber and tile fiber. It is possible that this material collected on the surface of the cradle prior to activation of the IOCM but some migration of the particles during launch certainly seems likely. The SYNCOM cradle samples were collected in the canister after removal from the shuttle bay with LDEF. A significant amount of LDEF material was present on these tapelifts indicating high levels of cross contamination during recovery activities (Photograph 1). The QCM data failed to indicate particulate deposition of the magnitude that occured. The witness plates, as part of the IOCM, indicated a post flight surface obscuration of 2.4% which closely matches tapelift evidence. The QCM data collected, as currently interpreted, does not correlate well with other analytical method used to monitor the bay, including other parts of the IOCM monitoring system. The QCM's are providing real time data that is potentially of great value but at this time the QCM data from the STS-32 mission is best described as requiring careful and cautious interpretation that must be supported by evidence collected using other techniques.

At some time during the recovery LDEF was 'sprayed' with fine droplets of an organic containing aqueous material that also contained potassium and sodium chlorides. This material has been found on ram facing trays and shows no signs of atomic oxygen degeneration. Its distribution is from row 3 through row 1 and row 12 through row 7. These are the rows that were exposed above the edge of the bay when the doors of the shuttle bay were open and along the port side. None of the IOCM systems detected this event as far as is known at this time. The source of this material is still unknown (Ref. 1).

During the ferry flight the IOCM QCM's behaved erratically, possibly in response to pressure and temperature differences on the exposed crystal created by turbulent flow. Direct examination of the surface of LDEF and paired tapelifts from the same surface before and after the ferry flight indicate significant migration of particles and air erosion of unstable surfaces such as those weakened by atomic oxygen attack while in orbit (Ref. 9, photograph 15). The IOCM witness plates and other surfaces of the IOCM also indicated a very significant redistribution of particles during different parts of the LDEF recovery

operation. Small, half millimeter on a side, squares of aluminum coated Kapton from tray D-09 were found widely distributed on LDEF. The shuttle bay floor was littered with them when the shuttle reached the OPF. They were also found on trays B-04, C-12, all over D-09, and in other areas of the interior structure. Reference 9, photograph 14 shows the back side of one of these squares. The other side is vapor deposited aluminum.

The transport of LDEF from the OPF to its final position in SAEF-2 was monitored by witness plates and by tapelifts. The witness plates used to monitor particle fallout at Kennedy were small, 47 millimeter, membrane filter pads. Part of the data is presented in reference 6, figures 1, 2, and 4. The witness plate technique used seemed to lack sensitivity with values at least an order of magnitude lower than tapelift results even when the tapelift results were based only on counts of LDEF materials. Larger particles tended to be even more significantly underestimated on the witness plates resulting in an inversion of the shape of the distribution curve compared to standard models and to the tapelift curves.

Once in SAEF-2 the environment was monitored by automatic airborne particle counter and witness plates. The results of both are illustrated in Reference 6, figures 4 and 7. The SAEF-2 facility was a large room with two exterior walls. The exterior walls had door and window openings. These walls were as much as thirty feet or more high. The air in the facility was provided through diffusers in the high bay ceiling after being filtered through HEPA filters. The air exchange rate was reportedly better than six room volumes per hour. The return air diffusers were in four columns that stood between the high bay and the main work and storage area. The automatic particle counter was on the wall opposite the work area. LDEF was between the work area and the particle counter. Witness plate samples for the room were located near the edges of the room to be out of the way. Witness plate samples were also placed on the LATS to monitor fallout next to LDEF.

The automatic particle counter in the high bay was mounted about ten feet high on one wall of the room. The particle count in the room at that location exceeded 100,000 particles greater than half a micrometer in scattering diameter only for a short time when a twenty foot high scaffolding was being moved in its vicinity. Generally the particle count was less than 10,000 per cubic foot. That included an interval when wood was being sawed in the clean room and an episode during which hundreds of feet of regular chart paper were fed through a high speed chart recorder. Both events left their evidence on LDEF surfaces but neither affected fallout monitor counts or the automatic airborne particle counter (Photographs 1 and 2).

Tapelifts from surfaces in SAEF-2 were collected only to determine the cleanliness of specific surfaces and the types of particulate contaminants present and not to generate fallout rate data. Most of the surfaces that were tested were cleaned once a day but the tape was a more efficient surface cleaner than the method used to clean the surfaces so there was a consistent elevated background. Quantitative rate data can not validly be derived from these results. Tapelift samples were often collected later in the day as a worst case example of cleanliness. Some of these results are shown in Reference 6, figure 2.

Direct examination of LDEF surfaces indicated a steady accumulation of paper fibers, skin flakes, clothing fiber, flooring particles, sawdust, and other materials generated within SAEF-2. Pollen grains, natural minerals, and insect debriswerealso seen,indicating exterior sources for particulate contaminants. The mechanism for the entry of these exterior contaminants is not clear but there are two good candidates. Mechanical transport with the particles being carried in by the large number of personnel in and out of the facility each day is certainly part of the answer. Another is the penetration of contaminants through leaks in doors or windows of exterior walls as a result of wind conditions. The design of the facility makes the establishment of constant positive pressure impractical and certainly not obtainable under the operating conditions when LDEF was in the facility. The pollen types in the samples collected at various times during LDEF's stay in SAEF-2 changed as different plants came into season. A few of the pollen types are shown in Photographs 3 through 6. SAEF-2 has since been remodeled.

CONDITION OF LDEF AS DELIVERED FOR ANALYSIS

All exterior surfaces of LDEF accumulated some contamination from integration with the shuttle bay until release into orbit. The particulate contaminants included skin cells, clothing fibers, paper fibers, clay paper sizing, glass fibers, natural minerals, wear metals of aluminum and iron alloys, and other materials. These particles are identifiable by the shadow effect they had on the surface of LDEF or by orbital environmentally induced modifications of the particle itself. Some surfaces had relatively few surface particles in orbit. Others were quite contaminated. Particle populations varied by a few orders of magnitude over the surface, sometimes even on the same tray. Once in orbit a molecular film was deposited on nearly all exterior surfaces and any interior surface where light could penetrate. The film consisted of hydrocarbon, carbonyl, amine and amide, and silicone functionalities. This film is inert to most solvents but can be scrubbed off the surface. Flushing with organic solvents will not remove this film.

Impacts with space debris or with micrometeorites created additional particulate contaminants including molten metal droplets. Atomic oxygen degraded carbon based materials and silicones generating inorganic ash or silica. Much of the molecular film deposited on the ram facing trays was converted to a film of silica.

Particles from LDEF surfaces began moving to other LDEF surfaces beginning with the grappling of LDEF by the shuttle, if not before. This cross contamination increased and included the shuttle bay surfaces with the turbulent flow of reentry. The ferry flight again exposed the surface to turbulence induced cross contamination. These particles tended to be aluminum film materials, ash, paint pigment, and glass fibers. Some time after grappling LDEF and placing it in the shuttle bay it was showered with a mist of fine aqueous organic liquid droplets with a high water soluble salt content that hit the surface as a slush. These droplet deposits have been found on rows 3, 2, 1, 12, 11, 9, and 7. They seem to be most common on row 12. Row 10 has not been examined for this material. Examination of row 6 materials for the presence of these droplets has been negative to date.

At Kennedy new skin, fibers, pollens, and natural minerals began accumulating on the surface of the trays. On some surfaces the particle count increased by an order of magnitude over the value from orbit. One structural surface increased by two orders of magnitude from the time it arrived in SAEF-2 until the last tray was removed. References 6, 8, and 9 of this proceeding provide additional information.

CONCLUSION

After presenting these five "experiments" it is evident that LDEF has added a great deal to our understanding of contaminants and spacecraft cleanliness. In a broader sense this paper is about materials and systems. When we design a spacecraft and the processes that will be used to construct and deliver it to its final functional environment we are programing reliability into the product. The greatest value of studying the contaminants on LDEF is in deriving information that may aid in the design of more reliable spacecraft. The conclusions below are listed by category with design considerations in mind.

Molecular Films

1. Nearly a pound of contaminating molecular film was deposited on the surface of LDEF while it was in orbit.

2. Although LDEF carried into orbit a surface molecular contaminant film of about 2.5 milligrams per square foot this contributed significantly less than ten percent of the final film burden.

3. The deposited molecular film covering LDEF was the result of outgassing from the urethane paints and the RTV-silicones used on LDEF. These materials were considered space qualified though no bakeout had been performed.

4. The deposited film was layered indicating a cyclic deposition. The cycle may have been an orbit in which case the majority of the film would have been deposited very early in the mission.

5. Fixation of the condensed molecular film required ultraviolet light exposure and possibly some atomic oxygen exposure.

6. Numerous small outgassing sources were present that created local variation in the deposited film.

7. Some outgassing materials seemed to 'protect' small areas of the surface from deposition of films. Some of these materials typically outgas water or other material that is a non-condensable in orbit.

8. A high percentage of the outgassed materials available for the formation of a film contributed to that film. The design of the vents created a high molecular density at the surface by directing much of the venting material parallel to the surface of the satellite. Thermal divergence, the ram effect, and direct impingement explains most of the deposition given the surface concentration.

9. Thermal cycling of surfaces as a result of their exposure to the sun played a significant role in the development of the fixed films. Surfaces that were exposed to the rising sun had thicker films than surfaces that saw the setting sun for any given location. This is believed to be the result of the condensation/evaporation cycle of the molecular film precursor materials prior to fixing by ultraviolet light. The surface that is exposed to the rising sun is always cooler than an adjoining, thermally coupled, surface that is not exposed to the sun until a later time.

10. Organic material associated with potassium and sodium chlorides was deposited as an aerosol over LDEF after it was placed in the shuttle bay for return from orbit.

11. Much of the molecular film deposited on the ram facing tray surfaces was converted to films of oxides of silicon.

Particles

1. The particle cleanliness level for LDEF when it entered orbit was approximately a MIL-STD-1246B Level 2000C.

2. The MIL-STD-1246B particle distribution curve has too steep a slope, 0.93, to represent the distributions seen on LDEF and for most associated surfaces sampled. A slope of 0.4 fits much better.

3. Cross contamination during launch and during recovery between surfaces in the shuttle bay is evident.

4. Particles move along the surface under some conditions in an orbital environment. Thermal effects and local impacts with debris or micrometeorites may provide the force to move the particle and ram effects may be responsible for redeposition. All redepositions of trackable particles occurred on the ram facing trays.

5. Micrometeorite and debris impacts create particulate and molecular debris,a fraction of which collects on the surface of the spacecraft.

6. The majority of the particles on the surface of LDEF while it was in orbit were residues from the assembly of the trays and exposures prior to launch, not transfer from the shuttle bay.

7. The obscuration area of a particle may grow in orbit as a result of outgassing or as a result of shadowing effects involving atomic oxygen, ultraviolet light, or deposition of molecular films.

Shuttle Bay/Payload Cross Contamination

1. Particles move from the shuttle bay surfaces to that of the payload and from one part of the payload to other parts of the payload and to the shuttle bay surfaces.

2. The shuttle bay surfaces have significant populations of free tile and bayliner fiber at the conclusion of the mission. Based on the LDEF study detectable populations of these fibers have transferred to payload surfaces prior to release of the payload in orbit.

3. Shuttle dumps may create debris that lands in part on the contents of the shuttle bay.

4. Reentry and the ferry flight exposed LDEF to turbulent air flow resulting in some erosion of atomic oxygen eroded surfaces and a redistribution of particulate contaminants about LDEF and the shuttle bay.

Contaminant Monitoring Systems

1. In general contaminant monitoring systems did not correlate well with the accumulation of contaminants on the surface of LDEF.

2. The IOCM QCM's detected a number of events of interest but the interpretation of the data is still not clear.

3. The IOCM QCM's behaved in an unexpected manner during the STS-32 mission and ferry flight.

4. The IOCM witness plates provided useful data on contaminants as did the entire exterior surface of the unit.

5. Tapelift samples from the same locations following specific activities provided good qualitative data and appears to provide good quantitative data.

6. Airborne particle counts in SAEF-2 didn't correlate well with activities in the clean room or the particle exposure of LDEF as determined by direct examination of the surface or by examination of tapelifts from the surface.

7. Particle witness plate monitors as used at Kennedy didn't correlate any better than the airborne particle counts. This may have been due to the small size of the plates used, about one square inch. The particle size distribution curves generated by counts from these plates showed an inverted shape deficient in large particles.

Effects of Orbital Exposure on Satellite Cleanliness

1. Contaminants are mobile in orbit.

2. Impacts with space debris or micrometeorites generate quantities of both particulate and molecular contaminants, some of which will contaminate the surface of the spacecraft.

3. Atomic oxygen erosion of carbon based or silicone materials may release inorganic debris on the surface of the satellite.

4. Ultraviolet light breaks bonds in carbon based materials resulting in the erosion of surfaces and the release of new molecular species that may redeposit on the satellite.

5. Particles are often associated with outgassing materials which may increase the effective footprint of the particle once in orbit.

6. Specific types of surfaces may act as local contamination sinks.

These conclusions are based on work still in progress. Much more information can and should be gathered to refine and to add to these conclusions. As important as LDEF is it is still only one data point. As with any good experiment it provided many needed answers but it also generated a whole new set of questions that can best be resolved by future flight experiments. Many of these experiments are already well into the design phase and some are currently being fabricated. LDEF's importance can not be over estimated. It will provide the benchmark against which future progress in the knowledge of contaminants, materials, and systems in space will be compared.

REFERENCES

1. Crutcher, E. R. and K. J. Warner: Molecular Films Associated with LDEF. First LDEF Post-Retrieval Symposium, NASA CP-3134, 1992.

2. Leger, L., S. Jacobs, and H. K. F. Ehlers, "Space Shuttle Contamination Overview", JOURNAL OF ENVIRONMENTAL SCIENCES, Vol. 21, Sept/Oct. 1978.

3. Miller, E. R.: STS-2, -3, -4 Induced Environmental Contamination Monitor (IECM). NASA TM-82524, MSFC, Huntsville, Al, February, 1983.

4. Green, B. David, G. Kenneth Yates, Mark Ahmadjian, and Henry Miranda, "The Particulate Environment Around the Shuttle as Determined by the PACS Experiment", OPTICAL SYSTEMS CONTAMINATION: EFFECTS, MEASUREMENT, CONTROL, SPIE Vol. 777, 1987.

5. Maag, Carl R. and W. Kelly Linder: Measured Space Environmental Effects to LDEF During Retrieval. First LDEF Post-Retrieval Symposium, NASA CP-3134, 1992.

6. Crutcher, E. R., L. S. Nishimura, K. J. Warner, and W. W. Wascher: Quantification of Contaminants Associated with LDEF. First LDEF Post-Retrieval Symposium, NASA CP- 3134, 1992.

7. Scialdone, John J., "Particulate Contaminant Relocation During Shuttle Ascent", OPTICAL SYSTEMS CONTAMINATION: EFFECTS, MEASUREMENT, CONTROL, SPIE Vol. 777, 1987.

8. Crutcher, E. R., L. S. Nishimura, K. J. Warner, and W. W. Wascher: Silver/Teflon Blanket: LDEF Tray C-08. First LDEF Post-Retrieval Symposium, NASA CP-3134, 1992.

9. Crutcher, E. R. and W. W. Wascher: Particle Types and Sources Associated with LDEF. First LDEF Post-Retrieval Symposium, NASA CP-3134, 1992.

10. Rantanen, R. O. and T. D. Gordon: Contaminant Buildup on Ram Facing Spacecraft Surfaces. OPTICAL SYSTEMS CONTAMINATION: EFFECTS, MEASUREMENT, CONTROL, SPIE Vol. 777, 1987.

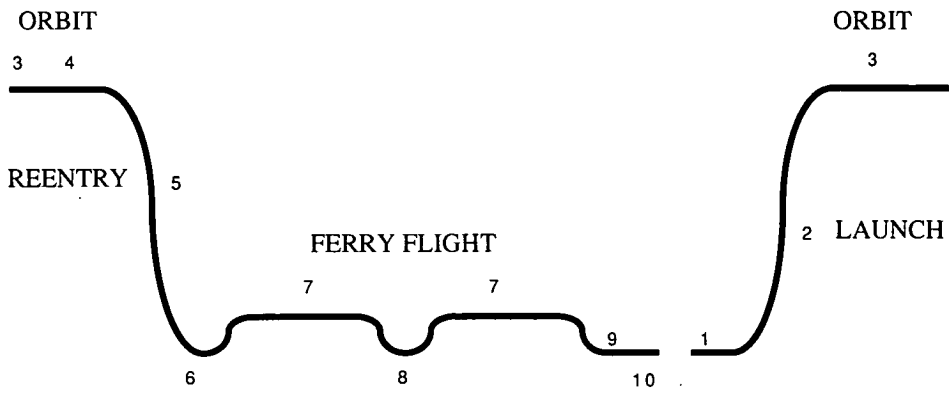

1. Condition of LDEF prior to launch: >MIL STD 1246B level 1000C for many trays.
2. During launch particulate contaminants are redistributed and Shuttle Bay debris is added
3. Contaminants are modified and new contaminants are generated in the orbital environment.
4. Grappling jars particles and films free, some may have relocated of LDEF.
5. During reentry particles and brittle molecular contaminant films relocate.
6. The shuttle is exposed to the Edwards environment, accumulation of natural dusts.
7. High humidity, high gas flow velocities, thermal and pressure stresses occur.
8. HEPA filter fibers appear on tape lifts after exposure to new filters.
9. Ground operations prior to SAEF-2 include many manipulations to LDEF in complex environments.
10. SAEF-2 exposure.

Figure 1. The Contamination Exposure History of LDEF.

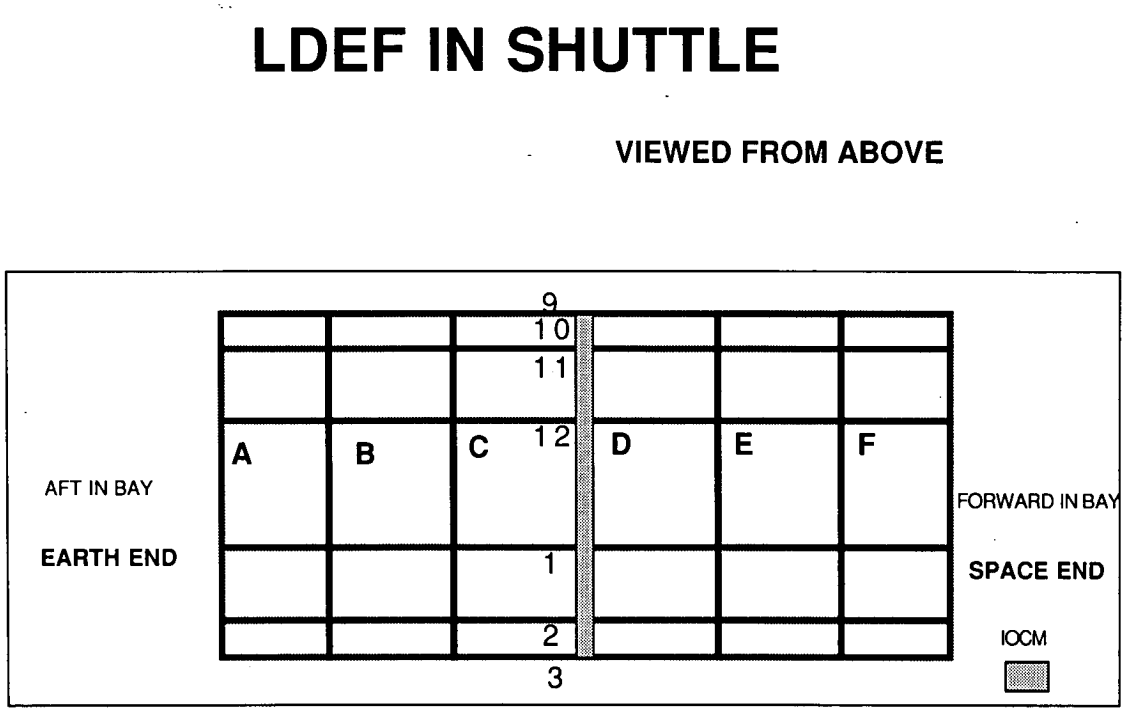

Figure 2. Position of LDEF in the Shuttle Bay.

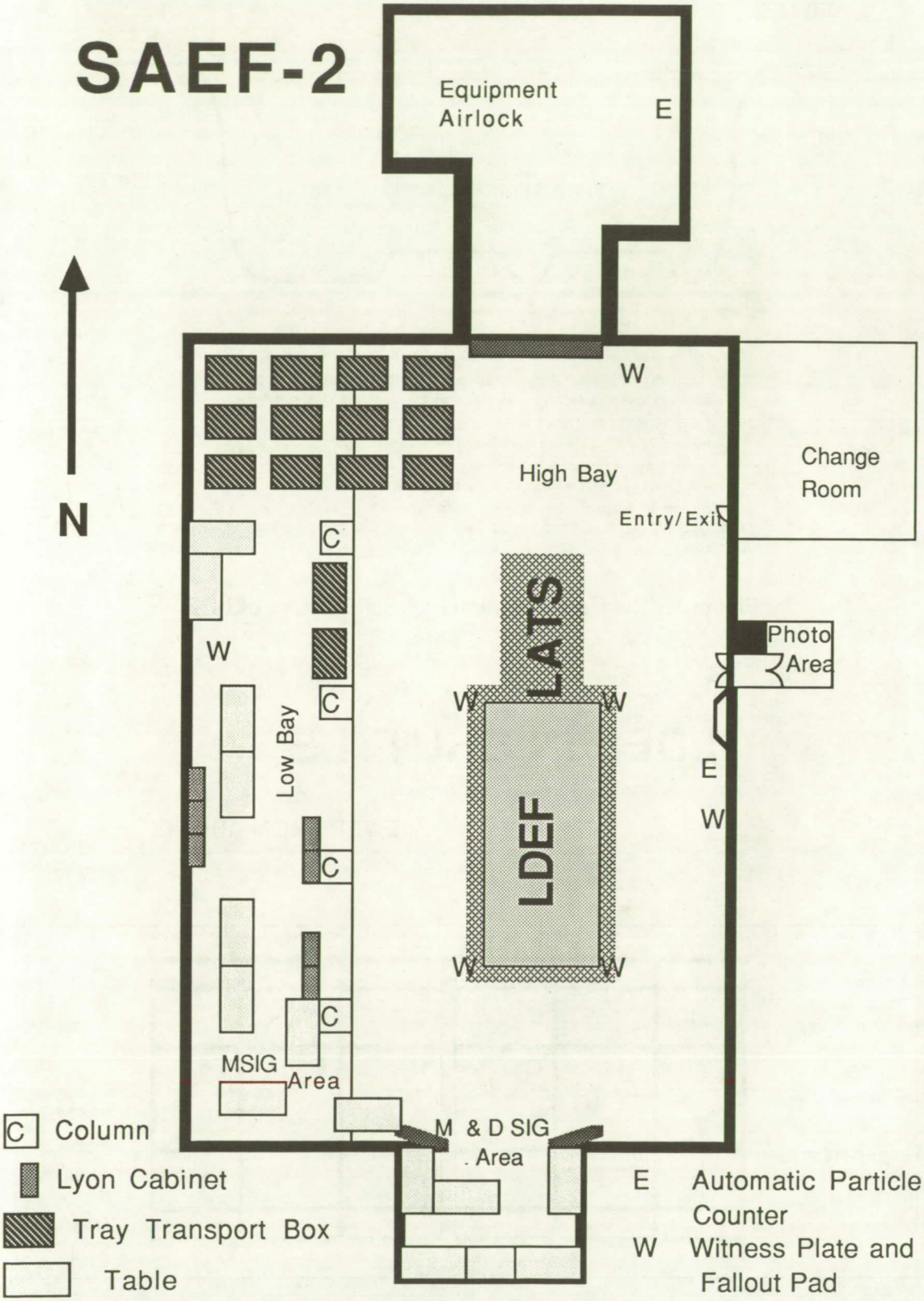

Figure 3. SAEF-2 with LDEF Showing Key Areas.

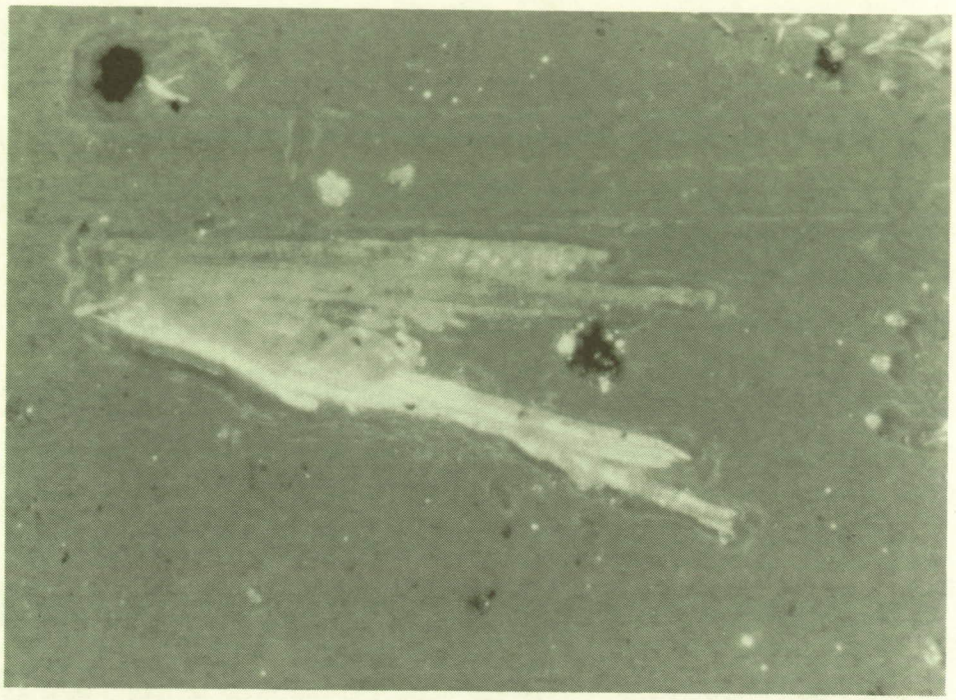

Photograph 1. Sawdust particle from the LDEF longeron surface under the edge of tray D-03. Transmitted illumination of tapelift using slightly off crossed polarized light at a magnification of 100X.

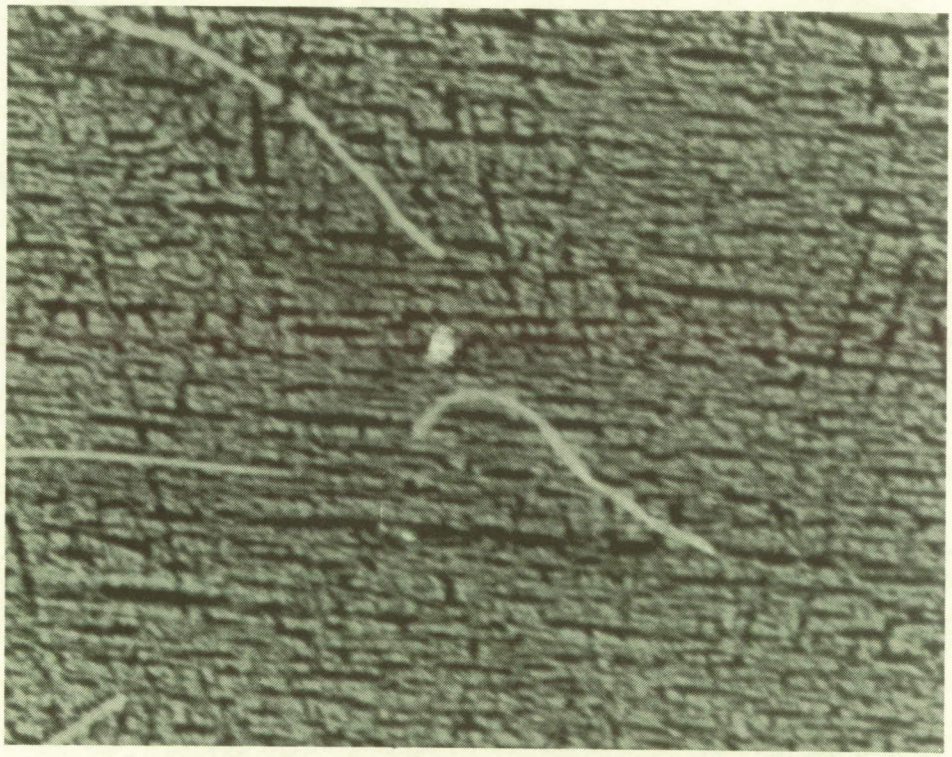

Photograph 2. New and old cellulose fibers of atomic oxygen exposed resin/carbon fiber composit, M0003, tray D-09. Old fiber has been converted to ash. Incident illumination at a magnification of 150X.

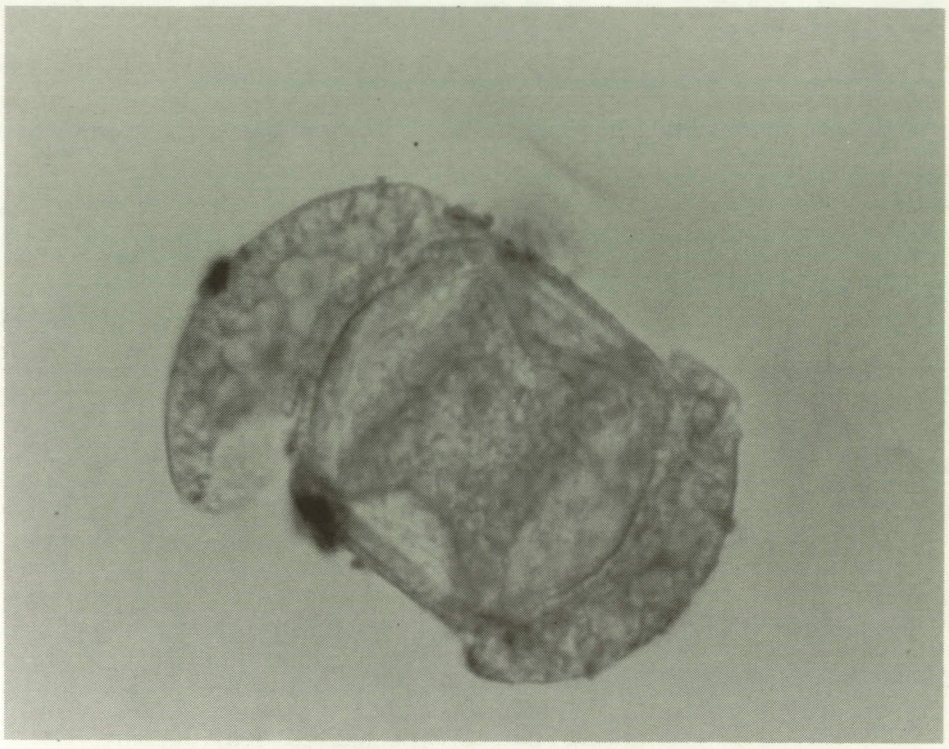

Photograph 3. Pine pollen after brief orbital exposure on shuttle bay surface. Tapelift collected at Edwards. Transmitted light at a magnification of 1,500X.

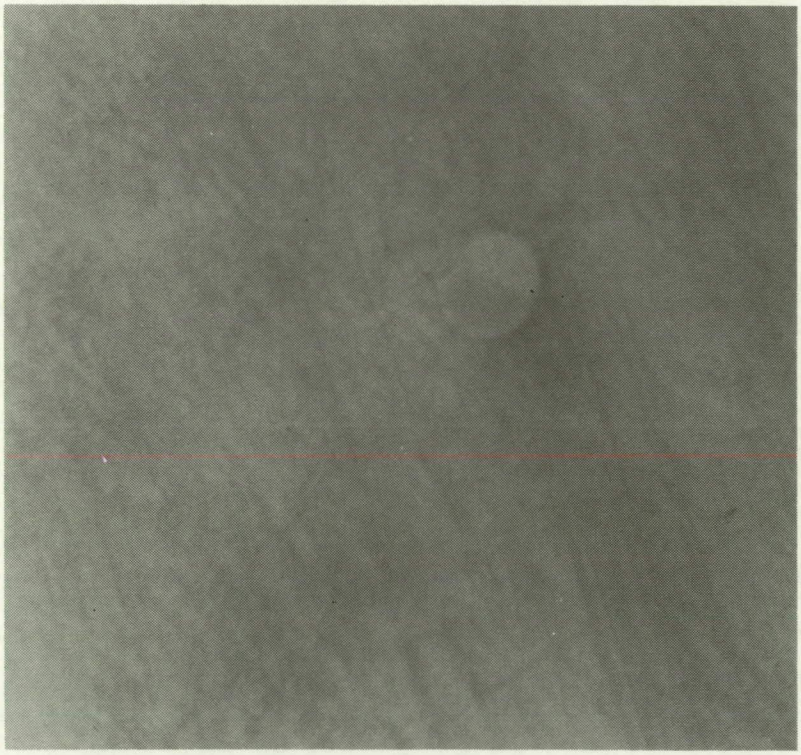

Photograph 4. New pine pollen (yellow) on the surface of tray A-02. Taken in SAEF-2 using Nomarski illumination at a magnification of 320X.

Photograph 5. Willow pollen from the LDEF longeron surface near tray B-09, clamp 6. Tapelift sample collected April 13, 1990. Transmitted illumination at a magnification of 1,100X.

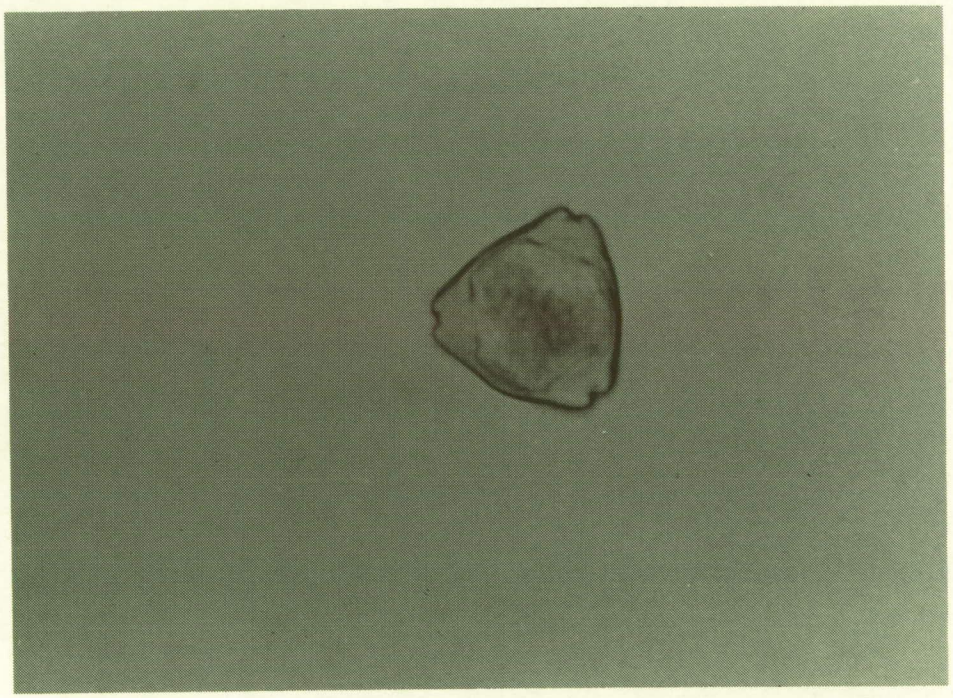

Photograph 6. Pollen from the surface of the LATS under the space end of LDEF. Tapelift sample collected March 16, 1990. Transmitted illumination at a magnification of 1,100X.

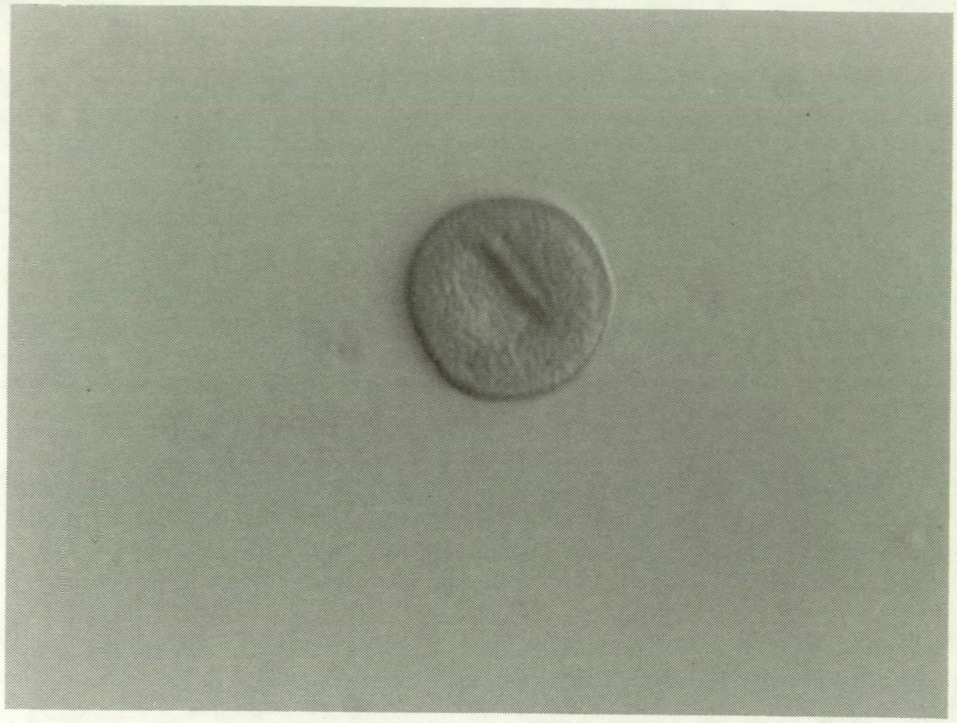

Photograph 7. Pollen from the LDEF longeron surface under tray B-08, clamp 4. Tapelift sample collected April 13, 1990. Transmitted illumination at a magnification of 1,100X.

QUANTIFICATION OF CONTAMINANTS ASSOCIATED WITH LDEF*

E. R. Crutcher, L. S. Nishimura, K. J. Warner, and W. W. Wascher
Boeing Defense and Space Group
Seattle, WA 98124-2499
Phone: 206/773-7002, Fax: 206/773-1473

SUMMARY

The standard particle size distribution curves of MIL STD 1246B are not representative of particle distributions found on LDEF. The distribution follows a log/log squared plot but there are far fewer small particles than would be predicted by the standard curve based on the population of larger particles. By changing the slope of the distribution curve to about 0.40 rather than the standard curve slope of 0.93 the LDEF particle distribution is better represented. Using a slope of 0.40 and labeling the curve by its intercept with the abcissa value of 1 the cleanliness of LDEF is approximately a level 5000. This new curve intercepts the standard Level 1000 curve at about 250 micrometers and a Level 500 curve at about 50 micrometers. The results of forty-four separate surface particle counts are presented in this paper. They represent counts made directly from LDEF surfaces as well as the results from tapelifts taken from LDEF or associated surfaces. Consecutive tapelift samples collected from the exact same locations in the Shuttle Bay before and after various operations were used to monitor the redistribution of particles during those events. Based on these studies a significant redistribution of particulate matter occurred during the reentry and during the ferry flights. Airborne particle counts and particle fallout monitoring in the SAEF-2 clean room appear to underestimate the particulate contaminant impact on surfaces in SAEF-2. Tapelift samples of surfaces in SAEF-2 suggest particle fallout rates of non-LDEF materials near LDEF much higher than those predicted by the particle fallout monitoring samples. The airborne particle counts in SAEF-2 indicated a well controlled environment though pollen grains and other natural airborne particles from exterior environments were found distributed over the surface of LDEF.

When LDEF was first seen close-up in orbit a brown molecular film was evident over much of its surface. The amount of molecular film deposited or fixed in place on the surface of LDEF while it was in orbit is estimated at approximately one pound. This represents approximately 10 to 15% of the material outgassed from paints, silicones, and other materials present on or in the experiment trays. The amount of non-volatile residue (NVR) on LDEF when it entered orbit was approximately 2.5 milligrams per square foot (MIL STD Level C) based on analyses of the remaining residues found under tray clamps. If all of this film had been converted to a fixed film in orbit it would have represented less than 10% of the estimated amount of molecular film found on LDEF after recovery.

INTRODUCTION

This paper addresses the quantification of contaminants on the LDEF satellite and associated hardware or tools. The purpose of this study was to provide a background database for the evaluation of the surface of LDEF and the effects of orbital exposure on that surface. This study necessarily discusses the change in the distribution of contaminants on LDEF with time and environmental exposure. Much of this information may be of value for the improvement of contamination control procedures during ground base

*Work done under NAS 1-18224, Task 12

operations. The particulate data represents the results of NASA contractor monitoring as well as the results of samples collected and analyzed by the authors. The data from the tapelifts collected in the Shuttle Bay at Edwards and at Kennedy are also presented. The amount of molecular film distributed over the surface of LDEF is estimated based on measurements made at specific locations and extrapolated over the surface area of LDEF. Some consideration of the total amount of volatile-condensible materials available to form the resultant deposit is also presented. All assumptions underlying these estimates are presented along with the rational for the conclusions. Each section of this paper will be presented in a subsection for particles and another for molecular films.

Method for the Quantification of Particulate Contaminants

Tapelifts of particles were collected from some LDEF surfaces directly as well as from associated hardware; the Shuttle Bay, the Transportation Canister, LDEF Active Transport System (LATS), etc. Numbered kits, each containing specially prepared and numbered microscope slides and a roll of lifting tape, were provided to NASA investigators, principal investigators, and other interested parties. The tapelifts collected by the authors and those returned to us by others for analysis were then processed to facilitate both qualitative and quantitative analysis. The tape used to collect the particles was 3M "Magic ™ Tape" with the acrylic adhesive. This tape was used because the plastic film can be dissolved with acetone leaving the particles behind in a thin layer of adhesive. The adhesive has a refractive index of approximately 1.49. This particle containing film was then mounted in a synthetic resin with a refractive index of 1.515. The quantitative analysis was performed using an Olympus Corporation "Cue" system automated image analyzer and transmitted darkfield illumination. One square inch of tape surface was analyzed which corresponded to one to four square inches of surface area depending on the number of times the tape had been applied to the surface; multiple lifts with a single piece of tape were often made to improve the statistical basis of the analysis. The size of each particle was taken as its greatest dimension in accordance with MIL STD 1246B. The Cue image analysis system was configured with a pixel dimension of 5.5 micrometers (video resolution limit) using an objective with a resolution limit of about 4 micrometers (NA = 0.1). Transmitted darkfield illumination tends to cause particles to look larger than they are by creating a halo of light around the particle. The halo effect is significant for particle images on the same order of magnitude as the pixel dimension but becomes a small positive bias for larger particles. This bias was reduced by electronically removing the outermost edge of detected particles (the one pixel wide halo around the particles) prior to analysis. Darkfield illumination was used because it produces a bright ring of light around the edge of all particles, transparent or opaque, with the interior being bright for transparent particles and dark for opaque particles (see Photograph 1). By electronically filling in the ring and then removing the halo the particles were more accurately imaged for analysis.

The quantification of particles directly from LDEF surface materials was performed in a Class 100 clean room using an Olympus BH-2 microscope on a boom stand, or a Nikon Optiphot for smaller objects, both with episcopic darkfield and oblique toplight illumination. These counts were performed manually. A few of these counts were further subdivided into those particles present at the time LDEF entered orbit, those that remained fixed in position during reentry and the ferry flight, and those that were present on the surface at the time of analysis that were new or that were not in a position they had occupied while in orbit. These detailed counts were made on the assumption that spot shadows indicated the presence of particles during orbit, particles with shadows beneath them of a similar shape had remained in position since orbit insertion, and particles not associated with such a shadow had moved or been added to the surface during recovery or later (see Ref. 1). These manual counts often involved relatively small areas of the surface and frequently areas very near a tray edge. No single analysis of contaminants on the surface of LDEF can be considered characteristic of the total surface of LDEF but rather of a specific type of micro-environment (Ref. 2). The tray edge constituted one such environment, the center of flat ridged panels another, the longeron surfaces another, etc. The significance of each microenvironment in terms of the dynamics of contaminants is still being evaluated but the combined data provides a good indication of the range of variation in surface cleanliness of LDEF and of the relative cleanliness by specific location. Many areas of

specific interest have not been available for analysis but similar surfaces or a study of the range of values from different surfaces should be useful for extrapolation to specific cases.

The results of the quantitative analyses were plotted on a log/log graph along with a chart of MIL STD 1246B (see Figures 1 through 3, 5, and 6). The counts made manually begin at particles fifty micrometers or greater in length. Those made using image analysis begin at twenty-five micrometers though the value of total detected particles, including those below twenty-five micrometers, is plotted beginning at the one micrometer position on the graph. Figure 4 illustrates the particle fallout rate reported for the SAEF-2 facility and the LATS during the time between LDEF arrival in SAEF-2 and the end of LDEF related activities in SAEF-2. These counts are based on the particles that were collected on a forty-seven millimeter membrane filter over a specific time interval. In SAEF-2 this interval was generally fourteen days. The values for the Transportation Canister (Jan 30 - Feb 1) are based on a two day interval and those for the transport of LDEF to SAEF-2 on the LATS (Feb 1 to Feb 6) are for a five day interval. Figure 7 illustrates the hourly airborne particle count as determined by an automated particle counter for the SAEF-2 Airlock and the SAEF-2 Highbay from the arrival of LDEF in SAEF-2 until the removal of the last tray. The data for Figures 4 and 7 was provided by NASA.

Methods for the Quantification of Molecular Films

Brown molecular films were widely dispersed over the surface of LDEF. Some of these films were quantified by direct measurement of their cross-section. These thicker films occured at vent surfaces facing the ram direction primarily on the earth and space ends of LDEF but also along the edges of longerons and tray edges with that orientation. In many areas these films were peeling or curling away from the surface. The curling was always convex to the surface of LDEF as a result of stresses accumulated over the thickness of the film. Attempts to flatten the film caused it to break. Samples of these films were collected and cross-sectioned or optically sectioned to determine their thickness. Optical sectioning is done by carefully focusing on the top of the film and then focusing through the film to its lower surface. The distance moved between the two focal planes times the refractive index of the film is the thickness of the film.

Another technique used is based on the thin film interference colors such as those seen in oil films on water. The sequence of colors seen is a direct measure of optical thickness which can be converted to actual thickness by multiplying the optical thickness by the refractive index of the film. The color effects are due to destructive and constructive interference between the light reflected from the top of the film and that reflected by the back surface. Film thicknesses of one quarter of a wavelength result in destructive interference for that wavelength or color with the result that its complimentary color is seen. Differences of half a wavelength create constructive interference and enhance the brightness of that color. These effects produce characteristic colors over a range of from about 50 nanometers to about 2000 nanometers for the films on LDEF. The interference technique is illustrated on the left side of Figure 8. Figure 8 also provides the film thickness that corresponds to specific colors or sequences of colors based on the measured refractive index of the film, 1.58. Photograph 2 illustrates the interference colors seen on white paint (A276) on a corner bracket of tray H-06.

These two techniques were adequate for very thick films, those over about 20 micrometers, that could be peeled, or those between 0.1 to 2.0 micrometers that generated quantifiable interference colors or sequences of colors. Thinner films could be detected by very slight discoloration but could not be quantified reliably. Films on anodized aluminum didn't produce reliable interference colors due to the effects of the anodized film thickness and irregular surface and the optical complexity of the interface between the aluminum oxide film of the anodize coating and the molecular film. Films between 2.0 and 20 micrometers were semiquantified by their color saturation (brown intensity). Black or browns that were unusually dark could not be semi-quantified in this manner because these films had a stronger absorption coefficient and a broader absorption spectrum than was typical in most of the films. Additional films or

surface alterations of materials were detected by ultraviolet light (see Ref. 3, photograph 4). Some films could only be detected by ultraviolet light or by infrared analysis, having no visible light image. These films are noted but no attempt has been made to quantify them at this time. Some of these fluorescing films are known to be the result of surface chemical modifications and not depositions of molecular contaminants.

Evidence used to estimate the amount of pre-launch non-volatile residue (NVR) was of three main types. The first was the analysis of residues found under clamps, on shims, and on other 'protected' surfaces of LDEF to determine the amount and nature of the deposits after nearly six years in orbit. The second involved estimates based on evaporitic rings around bolts or fixtures (Ref. 3, photograph 3), distribution of fingerprints (Photograph 3), and 'drip' marks on the surface of panels in trays on LDEF. The third was based on the tendency for unpainted anodized aluminum surfaces to collect hydrocarbons. No direct tests for surface cleanliness, particulate or NVR, had been performed prior to the launch of LDEF. Material inventories, the direct measurement of paint film thicknesses, and the weights of silicone materials collected from some trays were used to estimate the amount of volatiles and volatile/condensable materials available on LDEF.

Results for the Quantification of Particles

The particle distribution curves representative of LDEF surfaces do not relate well to the cleanliness standard curves of MIL STD 1246B (Ref. 4). The MIL STD 1246B graph of the log of particle population (abcissa) by the log squared of the particle diameter (ordinate) with a slope of 0.93 is reasonable for a freshly cleaned surface (Ref. 6) but, as has been reported elsewhere (Ref. 5), the slope of 0.93 used on the standard curves is much too steep for the accumulated debris seen on surfaces exposed to particle fallout. The actual particle distribution on LDEF follows a log/log squared distribution and can be well described by its slope on the graph and by the value on the ordinate of its intercept with the abcissa value of 1. This is the most convenient method of identifying a particle distribution curve and is the method used to identify the curves used in MIL STD 1246B. The last chart in Figure 3 presents the standard curves for MIL STD 1246B Level 500 and Level 1000 and the curves with a slope of 0.38 for level 500, 1000, and 5000, the numerical designation in each case indicating the ordinate value when the abcissa value is 1. Trying to describe a particle size distribution with a slope other than 0.93 in terms of the 0.93 curves becomes a listing of the intercepts of the actual distribution curve with standard curves of various "cleanliness" designations. For example, a surface with a particle distribution having a slope of 0.38 and an ordinate value of 5000 when the abcissa is 1 can be said to meet a MIL STD 1246B Level 1000 for particles less than 250 micrometers in diameter and a Level 500 for particles less than 50 micrometers in diameter. Its actual "cleanliness" becomes rather arbitrary, dependent upon the particle size considered "relevant". The set of curves on the last graph of Figure 3 will be referenced when discussing the cleanliness level of LDEF surfaces. Notice that when the log/log squared curves of MIL STD 1246B are plotted on log/log charts, as in Figure 3, the curves are concave downward. This pattern was typical of nearly all of the tapelift and surface count data.

The earliest particle samples of an LDEF associated surface were those collected from the Shuttle Bay at Edwards. Nine tapelifts were collected in the bay at Edwards. The first three were collected shortly after landing but only the first two were recovered with good spatial relationships and are reported here as "Rt preOp" and "Lt preOp" (the third sample, collected from the purge duct ,was damaged during sampling). These samples were collected from the right and left blanket above the purge duct before any payload bay operations had been initiated. The next set of three lifts at Edwards were collected after the payload bay operations had been performed and were collected in exactly the same locations as the original lifts. The last three were collected from different locations as pre-ferry flight references. The sample labeled "Rt PreFerry1" was collected from the right blanket near the adapter plate. The other sample from the right side, "Rt PreFerry2", was collected from the lower center of the square one over from the PSA. The final lift from Edwards is plotted on the OPF chart and is labeled "Lt PreFerry". It was collected from the left

side blanket near the optical target. These samples all fell between log/log squared curves with a slope of 0.38 for level 5000 and level 10,000. Using a slope of 0.93 from MIL STD 1246B they met the Level 1000 requirements for particles 100 micrometers in greatest dimension or smaller, and those of a Level 2000 at 500 micrometers or smaller.

The samples with the highest counts for this set were those collected just before the ferry flight. These samples are consistent with the eyewitness account regarding the visible airborne particulate matter in the Shuttle Bay during sampling. The first two lifts collected tended to have fewer large particles than the lifts from the same location taken later. This testifies to the constant redistribution of particles within the Shuttle Bay while the purge system was in operation and the Shuttle was being moved. Thin aluminum flakes, the residue of vapor deposited aluminum on Kapton after the Kapton had been removed by atomic oxygen, was the most obvious "snow" in the Shuttle Bay but the tapelift samples indicated they were not the only particles being redistributed. The three samples collected in the OPF are essentially identical in location to the preferry flight samples and again indicate the continued redistribution of contaminants. The redistribution of particles in the Shuttle Bay seems to be associated with turbulence in the bay. Low velocity flow created sufficient turbulence to circulate the vapor deposited aluminum flakes. Higher velocities were required to redistribute smaller particles and particles with lower effective Reynold's numbers. The effects of higher velocity airflow erosion of surfaces has been seen in a number of areas on LDEF and one such case is documented in Reference 1, photograph 15. All samples from the Shuttle Bay indicate the same basic types of particles and similar particle populations. The particles in the original tapelifts contained considerable amounts of small vapor deposited aluminum flakes and angular fragments of etched Kapton. Small yellow spherical ash particles of Kapton were also seen associated with the vapor deposited aluminum particles and as separate particles. Minerals were common and were identified as calcite (calcium carbonate), chalcedony (silicon dioxide), emery (aluminum oxide), and a variety of silicates. Some of these may have been industrial abrasive residues. A variety of glass fibers were found. Glass fiber from the Shuttle tile and from the bay liner were identified but filter fiber, insulative fiber, and glass from composite materials was also seen though specific sources have not been identified. Sequential lifts from the same locations indicated the redistribution of particles with a tendency for a gradual increase in population with time as the surfaces of LDEF continued to degrade. More fragments of aluminum flake and of the brown molecular film from LDEF were seen in the later lifts as well as more minerals and industrial residues not associated with LDEF as a source. These trends continued from the second set of lifts at Edwards through the set at Kennedy in the OPF.

The next set of samples were collected from the Transportation Canister used to transport LDEF from the OPF to the O&C building. The control sample count was a bit high but was still an order of magnitude less than the sample counts. This high particle count on the control is generally indicative of a non-laminar flow controlled environment and is the result of the static charge on the tape when it is first pulled from the roll collecting particles before the tape is sealed on the microscope slide. The surface cleanliness of the canister met a Level 1000 for particles less than 250 micrometers. The curves were consistent with a level 5000 when a slope of 0.38 was used. Most of these particles were from LDEF materials though pine pollen was first evident in these samples. After moving to the O&C the surfaces were over an order of magnitude higher in particle count. Most of these additional particles were from LDEF. These samples were all collected from the floor of the canister, to the side and below LDEF.

LDEF was placed on the LATS in the O&C building. Tapelifts were taken from the LATS after LDEF was in place and then again after the transport to SAEF-2. Large numbers of pollen grains, cellulose fibers, and other non-LDEF particles were seen in the first samples though degraded LDEF materials still were the majority of the population. Once in SAEF-2 the LATS was periodically cleaned. The LATS tapelift particle population in SAEF-2 reflects 'recent' depositions plus the background to which the LATS was cleaned. Initially most of the particulate was from LDEF though many other sources were well represented. By March particulate contaminants from SAEF-2 sources began exceeding those from LDEF sources on the LATS. This included paper fiber, worn flooring material, natural minerals, pollen and plant parts, skin, clothing fiber, hair, sawdust, and other materials. The tapelift samples from other areas in SAEF-2 always tended to be from sources other than LDEF.

By April 14, 1990 all trays had been removed and a detailed survey had been made of the surface of the LDEF structure by the Meteorite and Debris Special Investigation Group. At that time the Materials Special Investigation Group was given access to LDEF to collect tapelift samples directly from the LDEF structure. All of these samples were collected from the anodized aluminum exterior surface. Samples were collected from surfaces that were covered by tray clamps and adjacent areas that had always been exposed. A detailed analysis of these samples has not been completed though some of them have been analyzed for the particle size distribution. The distribution curves were a bit steeper than 0.38 but were around a level 5000 of that slope. All but one sample fell below a MIL STD Level 1000 for particles smaller than 250 micrometers.

The average fallout counts reported in Figure 4 would seem to indicate a relatively clean environment in SAEF-2 as would the airborne particle counts of Figure 7. The results for particles per square foot per twenty-four hours from the fallout monitoring technique appear to be about an order of magnitude lower than would be expected based on those seen on actual surfaces. The particle population by size distribution curve indicated by the fallout monitoring technique suggested a semilog plot (log population by linear diameter). This indicates a disproportionately low number of larger particles compared to a log/log or log/log squared distribution. Tapelift results and the direct inspection of LDEF surfaces did not support the suggestion of a scarcity of large particles in the SAEF-2 environment. The relative absence of large particles from the fallout monitoring technique used may be a statistical effect of the small area sampled.

Results of the Quantification of Molecular Films

The presence of molecular films on the surface of LDEF was easily detected by the characteristic brown discoloration of many surfaces. Reference 3 at the end of this paper is an article on LDEF molecular contaminants and discusses the detection and qualitative analysis of these films. The discoloration of surfaces is evident at thicknesses less than those required to produce the first interference color fringe. The brown layer on the FEP Teflon of tray C-08 is clearly visible before the first red/brown interference fringe. That first fringe corresponds to a film thickness of approximately 0.1 micrometers (see Figure 8). The distribution of films on the surface was very complex with vent area deposits often tens of micrometers to hundreds of micrometers thick, large area deposits on the backs or sides of trays on the order of micrometers thick, and exterior surfaces with deposits of tens to hundreds of nanometers. There were also surfaces with no detectable deposited films. These were typically surfaces that were outgassing non-condensing materials, such as water, or that were chemically attacked and eroded by atomic oxygen. Numerous individual measurements of film thickness and area of coverage were made for specific trays. A first approximation of the total volume of the molecular films on LDEF was made by extrapolating data from selected trays to the entire surface of LDEF. The molecular film volume data for these trays projected onto the face area of the trays (34 by 50 inches) averaged a little under one micrometer in thickness, but this did not include the thick deposits found on the earth and space ends of LDEF. The projected surface of LDEF had a combined surface area (inside plus outside surface) of approximately 304 square meters. A thickness of one micrometer was assumed for the film spread out over the entire surface of LDEF with a density of 1.68 as measured on fragments of the thicker films. Multiplying the surface area by the film thickness and density results in a value of 511 grams of material. Considering the nature of this estimate this value can be represented as approximately one pound.

The interior of LDEF was coated with over 260 square meters of black urethane paint (Z306) at a thickness of approximately sixty micrometers and a primer coating of approximately twenty micrometers for a total volume of 0.026 cubic meters or 26,000 cubic centimeters. With a density of about 1.5 grams per cubic centimeter this amounts to 39,000 grams of paint. Test coupons with this same configuration of primer and Z306 were tested using the standard Volatile/Condensable Materials (VCM) test procedure. The painted surface was heated to 125 degrees Celsius and the collector surface was at 25 degree Celsius.

These conditions were maintained for nearly forty-eight hours. The painted surface lost 2.4 percent of its weight and the collector surface collected 0.4% of the weight of the original paint film. This would amount to 975 grams of volatile material from the Z306 covered surfaces alone, of which 156 grams would condense on surfaces at 25 degrees Celsius. Temperatures on LDEF were often significantly lower than 25 degrees Celsius. Tests to determine the amount of silicones present on LDEF indicate about 6,000 grams on experiment A0178 and at least that much more on other experiments for a total of over 12,000 grams. None of these materials had been baked out so the weight loss in orbit may have been near 5%. This corresponds to 600 grams of volatile material. If these two materials are assumed to contribute half of all of the outgassing products from LDEF then the molecular film on the interior and exterior surfaces of LDEF constitute approximately 10 to 15% of the outgassed materials available.

During the preliminary examination of LDEF shortly after it arrived at SAEF-2 a number of areas were found that indicated the presence of non-volatile hydrocarbons or silicones prior to orbital exposure as mentioned earlier in this paper. Subsequent analyses in the laboratory of the back surfaces of clamps and shims indicated that some of them contained residual hydrocarbons, silicones, or combinations of the two that were thick enough to generate suitable infrared spectra directly from their surface even after nearly six years in orbit. Such spectra required a pathlength on the order of a micrometer thick (see Figure 8). Considering the area of coverage for some of the thicker deposits and that the areas providing no suitable spectra also contained some background level of non-volatile residue an average film thickness of about 0.025 micrometers would seem to be a reasonable estimate. This value, assuming a density for the film of one gram per cubic centimeter, would equate to a MIL STD 1246B NVR Level C. This amount of NVR would account for a total weight of about 25 grams if it had all been converted to brown film and been fixed in place. This is an order of magnitude less than the estimated weight of the film deposited on the surface of LDEF while in orbit.

CONCLUSION

Based on the results of the analyses completed to date and first approximation values for outgassing materials and films the following conclusions can be presented:

In discussing the cleanliness levels of LDEF surfaces slopes other than the standard MIL STD 1246B slope of 0.93 are more useful. Slopes between 0.4 and 0.6 seem to be most useful.

Using a modified slope of approximately 0.4 the surface of LDEF corresponds to approximately a level 5000. This corresponds to a MIL STD 1246B Level 1000 or less for particles smaller than 250 micrometers and a Level 500 for particles smaller than 50 micrometers.

The number of particles on some LDEF surfaces increased by nearly an order of magnitude from orbital values to those measured after removal from SAEF-2.

For many surfaces of LDEF the particle count remained reasonably constant though the types of particles and their sources changed.

Redistribution of particles during purging operations and the ferry flight was indicated by repeated tapelift analysis of the same locations before and after these operations.

The deposited molecular films amounted to approximately one pound of material.

Materials intentionally used on LDEF accounted for nearly all of the contaminating film found after recovery of the satellite. Based on outgassing estimates the molecular films on LDEF represent 10 to 15% of the ougassed materials available.

Non-volatile residues (NVR) present as contaminants on the surface of LDEF at launch are estimated at about 2.5 milligrams per square foot of surface, MIL STD 1246B Level C. This would account for less than 10% of the total deposited contaminating film found on LDEF after recovery from orbit.

REFERENCES

1. Crutcher, E. R. and W. W. Wascher: Particle Types and Sources Associated with LDEF. First LDEF Post-Retrieval Symposium, NASA CP-3134, 1992.

2. Crutcher, E. R., L. S. Nishimura, K. J. Warner, and W. W. Wascher: Silver/Teflon Blanket: LDEF Tray C-08. First LDEF Post-Retrieval Symposium, NASA CP-3134, 1992.

3. Crutcher, E. R. and K. J. Warner: Molecular Films Associated with LDEF. First LDEF Post-Retrieval Symposium, NASA CP-3134, 1992.

4. Military Standard 1246B, United States Department of Defense.

5. Hamberg, O and E. M. Shon, "Particle Size Distribution on Surfaces in Clean Rooms", Proceedings of the 1983 Annual Technical Meeting, Institute of Environmental Sciences.

6. Heridan, G., Small Particle Statistics, 2nd Edition, Academic Press, New York, NY, 1960.

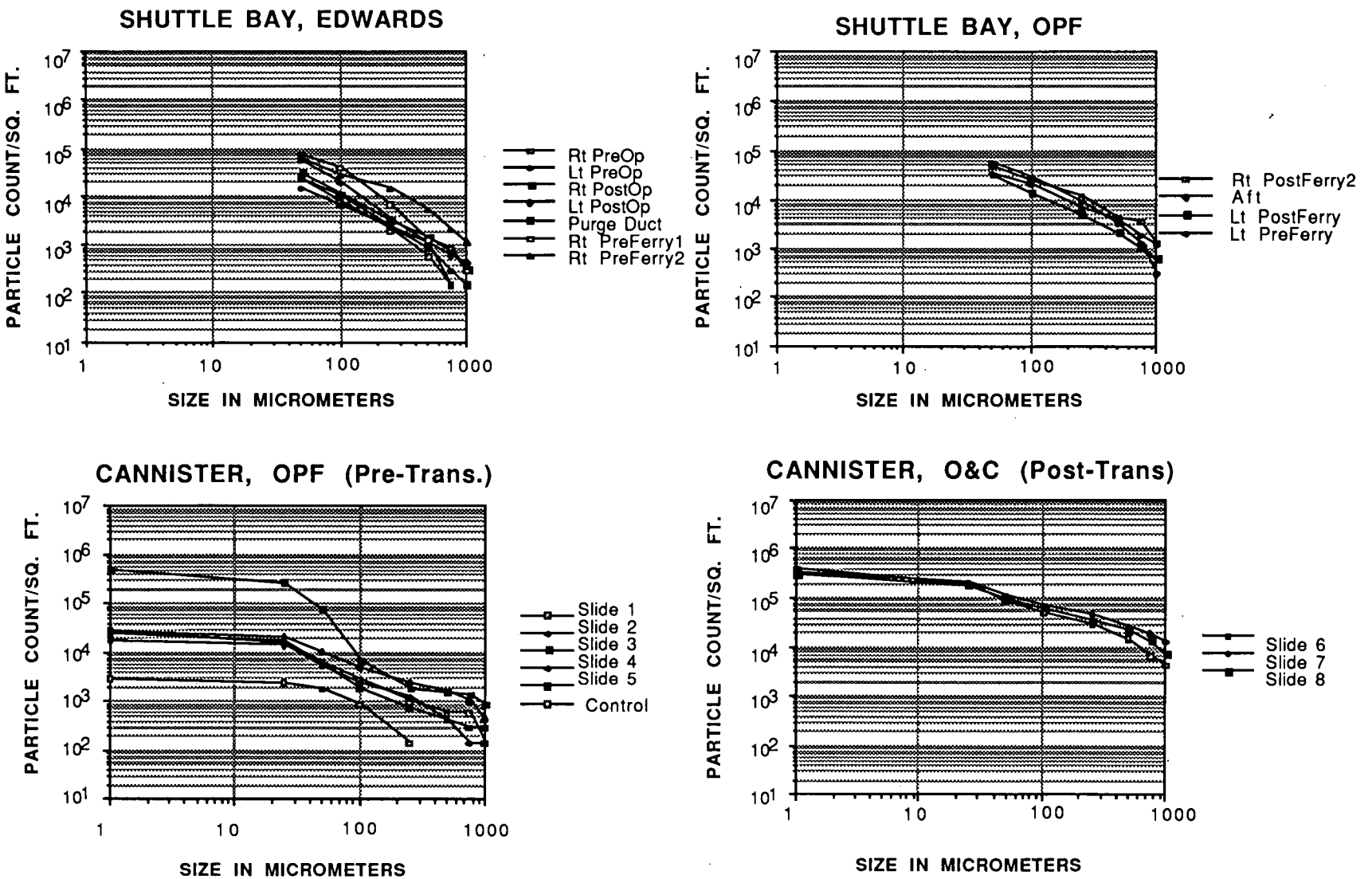

Figure 1: Tapelift data from the shuttle bay at Edwards and the OPF and from the canister at OPF and the O&C.

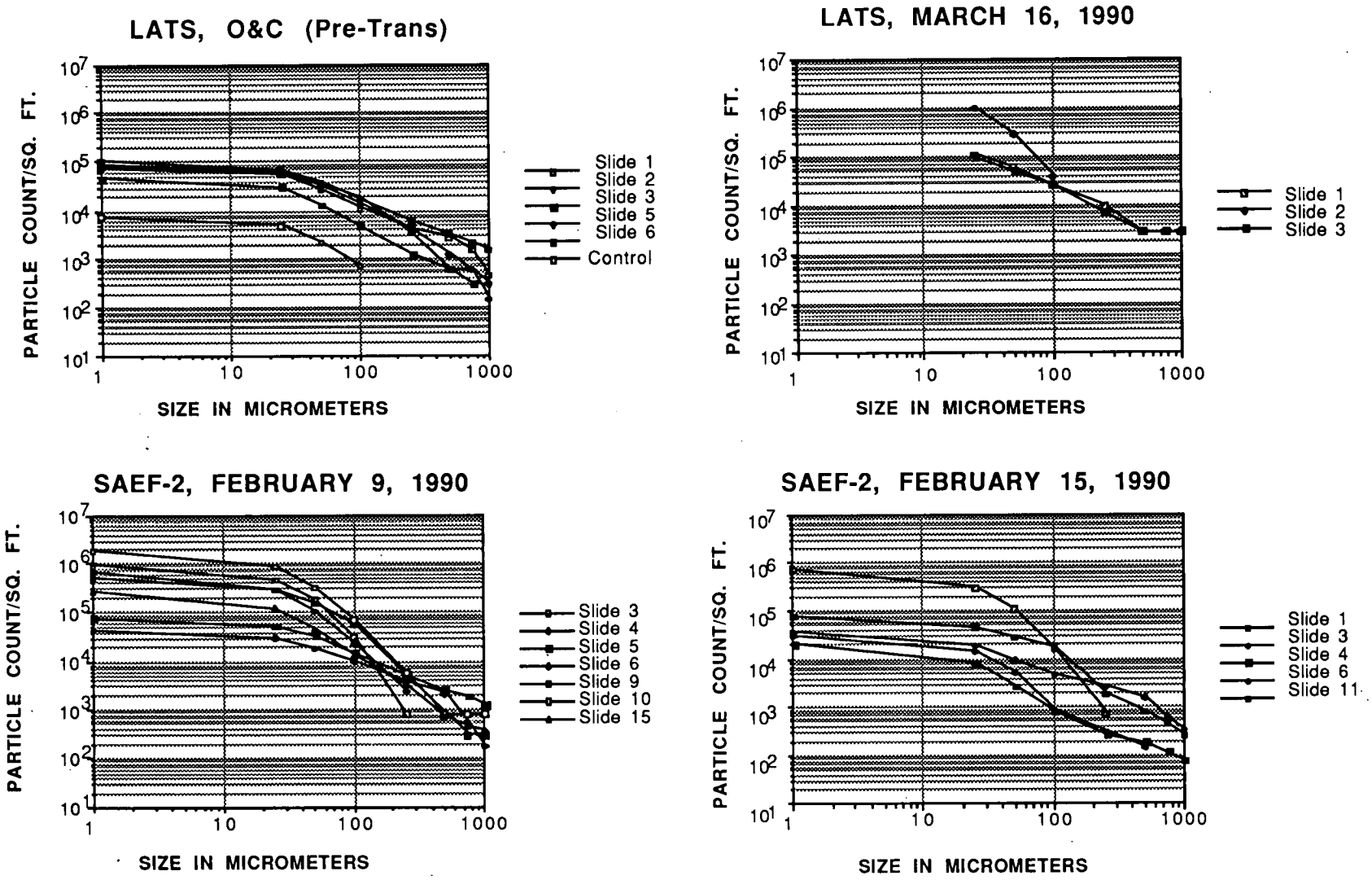

Figure 2: Tapelift data from the LATS at O&C and SAEF-2 on March 16, 1990 and SAEF-2 from February 9th and 15th, 1990.

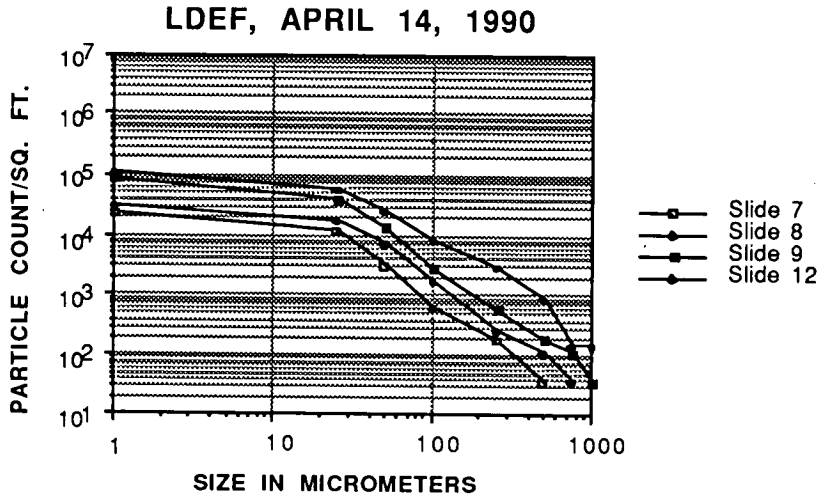

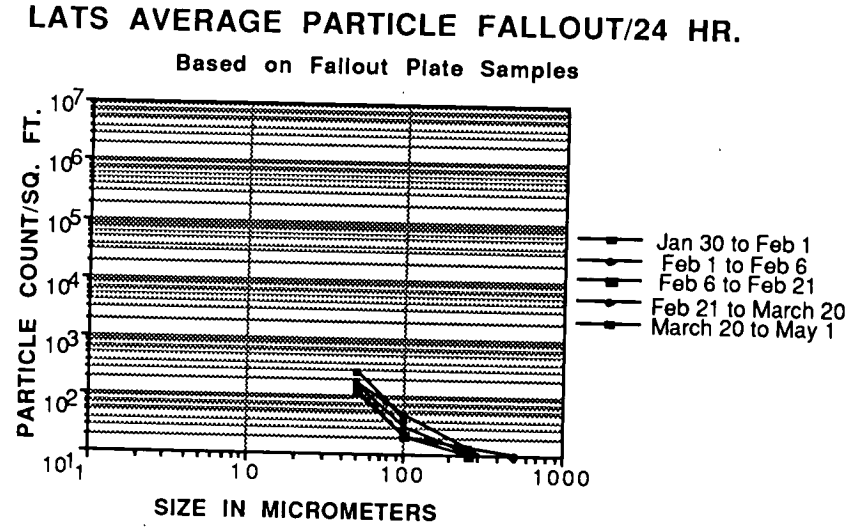

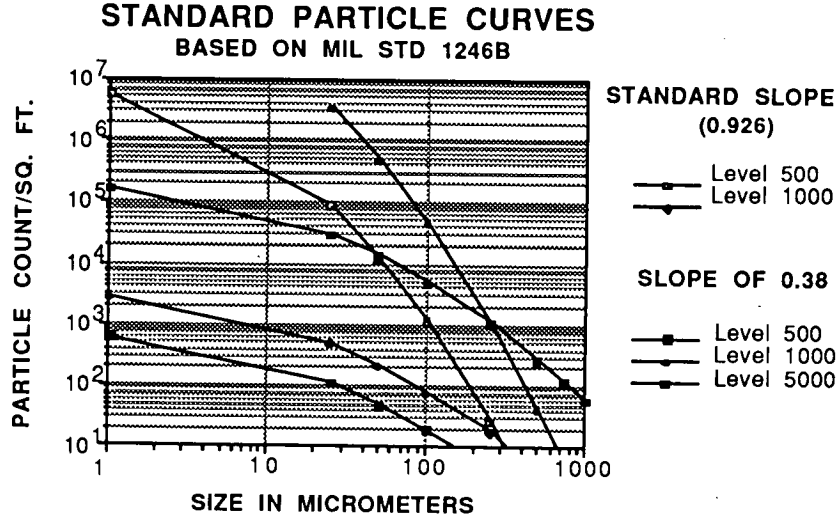

Figure 3: Tapelift data from the surface of LDEF collected on April 14th, 1990 and standard particle distribution curves.

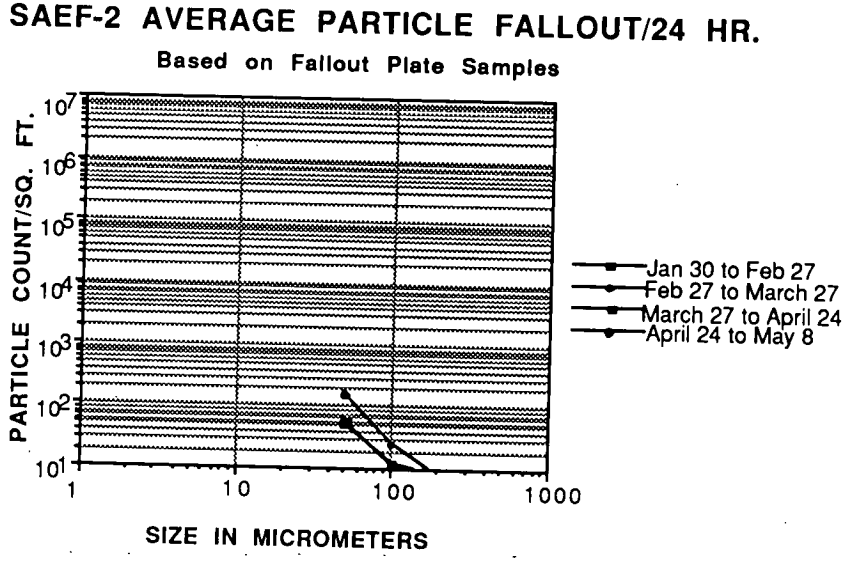

Figure 4: Data provided by NASA based on particle fallout test plates used to monitor SAEF-2 and the LATS.

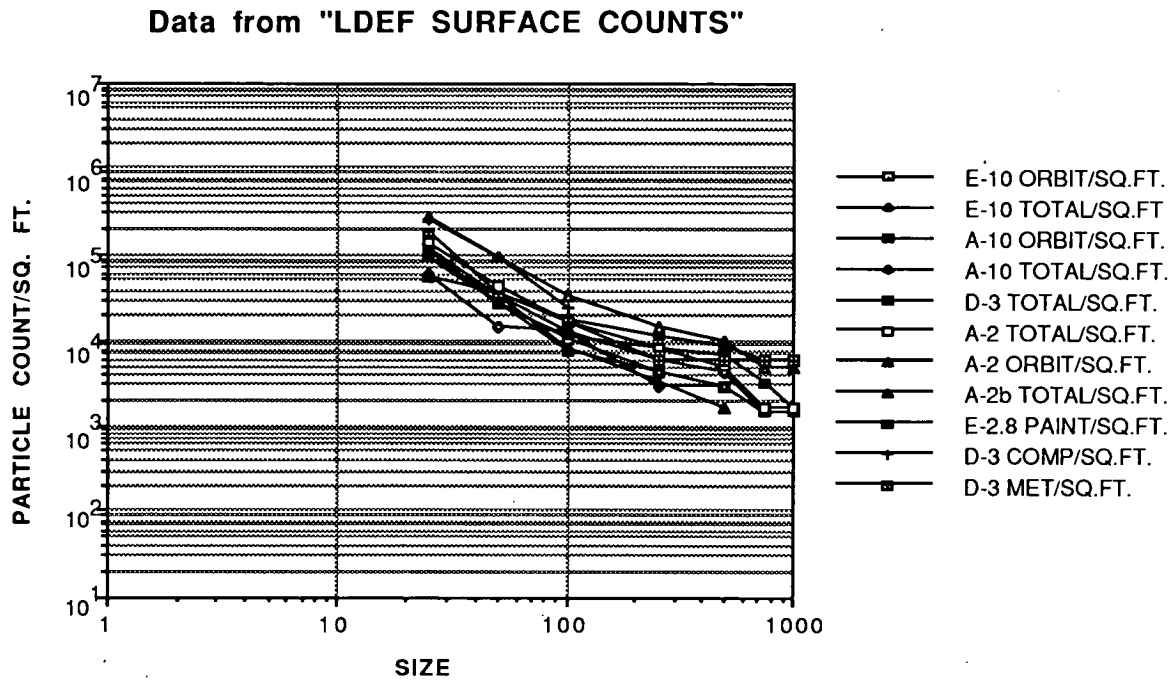

Figure 5: Particle counts directly from LDEF surfaces; total counts and counts for particles present in orbit.

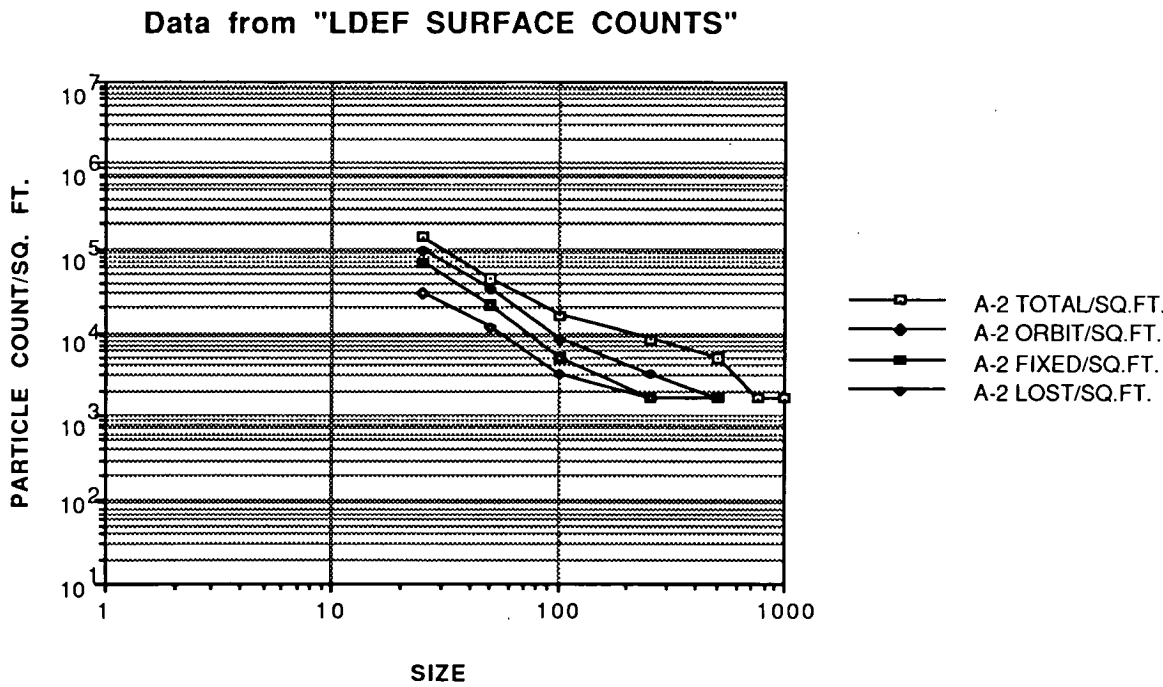

Figure 6: Detailed count of particles near the edge of tray A-02 by particle history; the total number of particles present at the time of analysis, the number of particles present while in orbit, the number of particles present in orbit that moved during recovery, and the number present in orbit that were still present following recovery and SAEF-2 exposure.

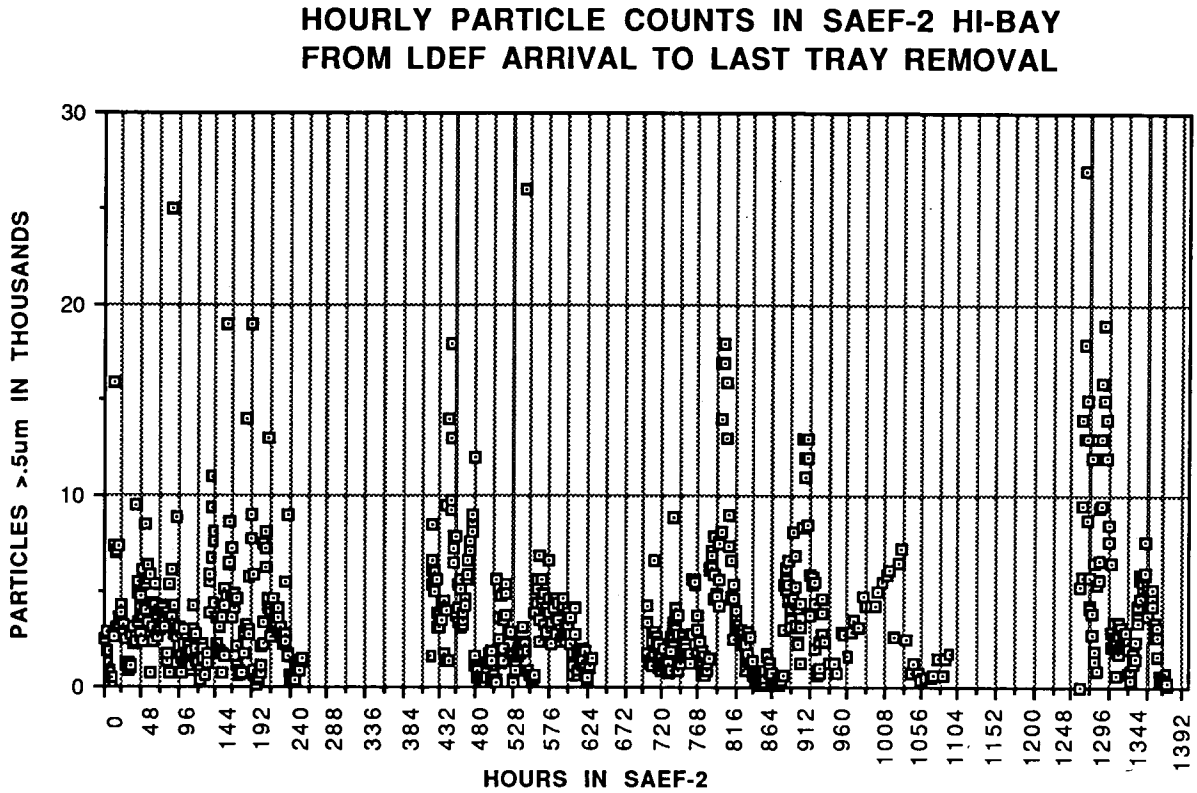

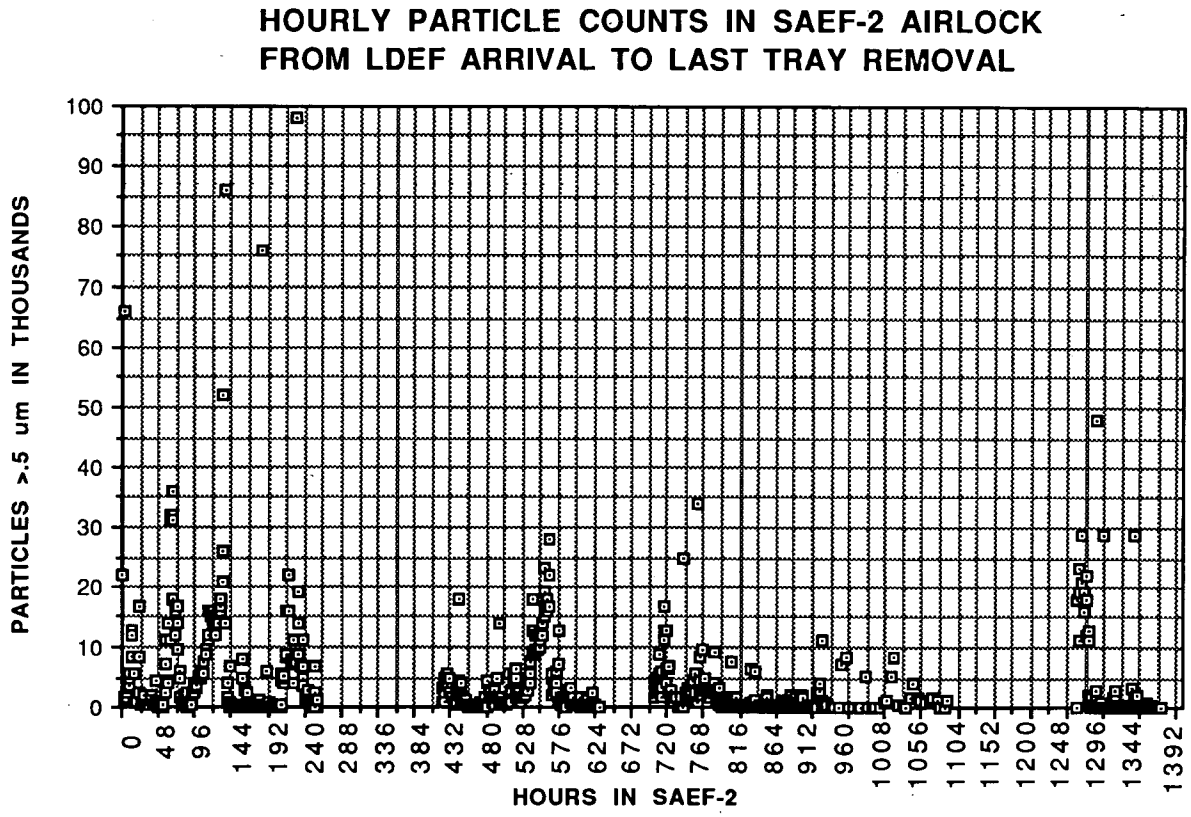

Figure 7: Hourly automatic airborne particle counts for the SAEF-2 airlock and highbay from LDEF arrival to the removal of the last experiment tray.

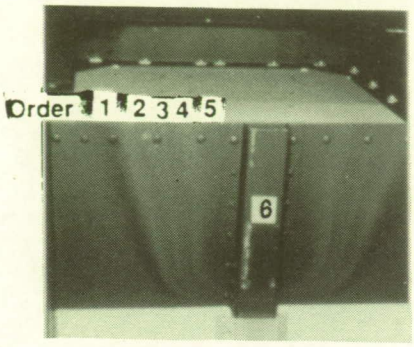

Interference Film
Colors on Tray F-06

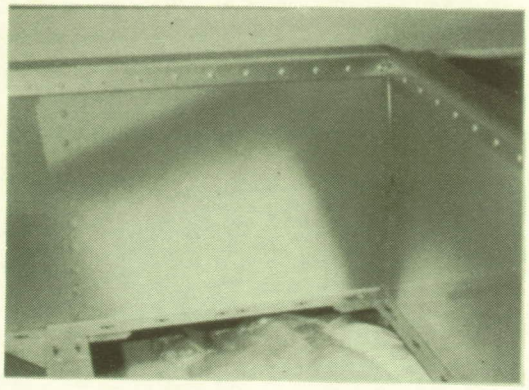

Diffuse Reflectance IR
Spectral Response
by Thickness

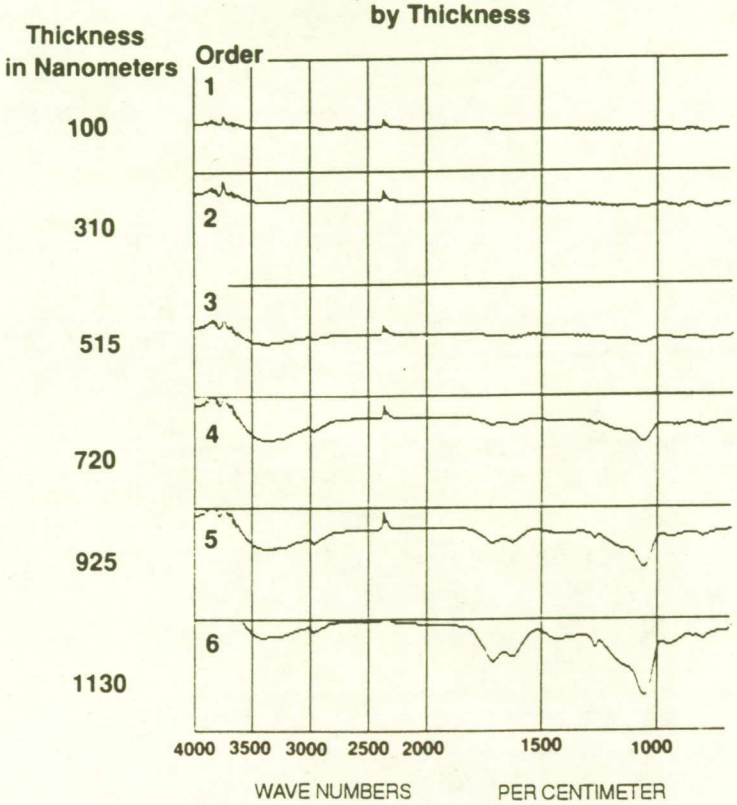

Thickness as a Function
of Interference Color

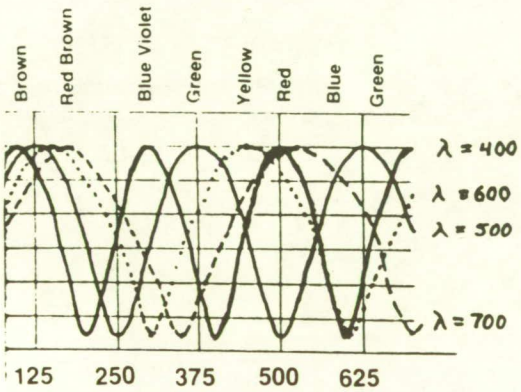

Figure 8: Quantification of molecular films by interference color and the calculation of the total film weight.

(See color photograph, p. 597.)

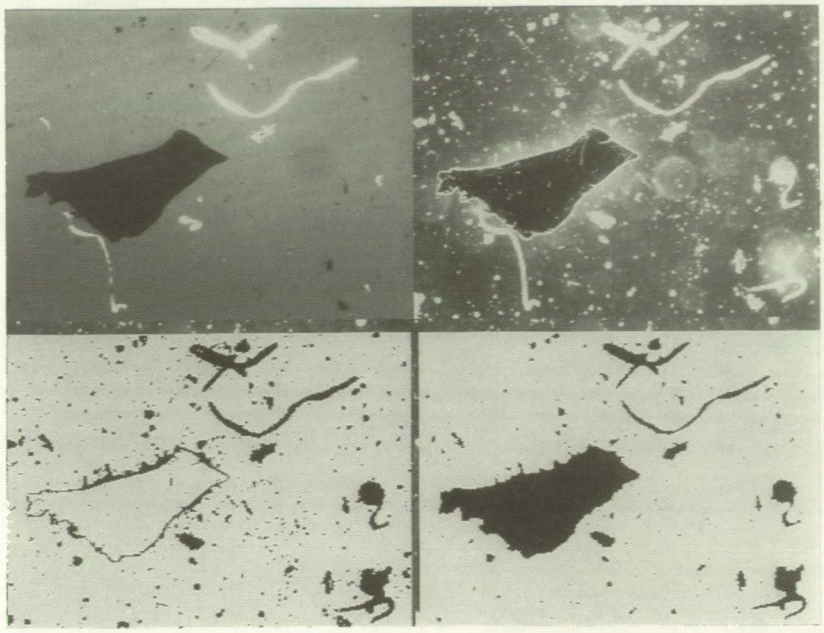

Photograph 1: Processing of the image for automated image analysis particle counts
Frame 1: Transmitted brightfield, off crossed polarizing filter illumination.
Frame 2: Darkfield illumination image.
Frame 3: Computer detected darkfield image.
Frame 4: Final field with particles imaged as analyzed.

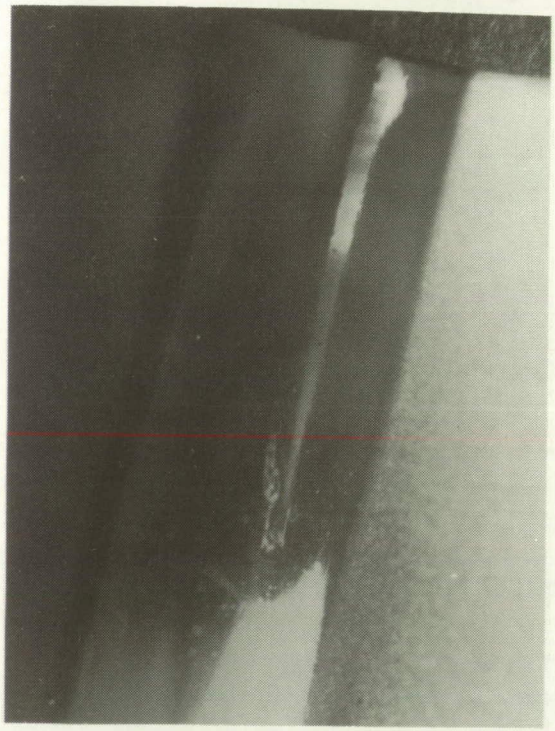

Photograph 2: Interference colors indicating the thickness of the brown film on tray H-06.

(See color photograph, p. 598.)

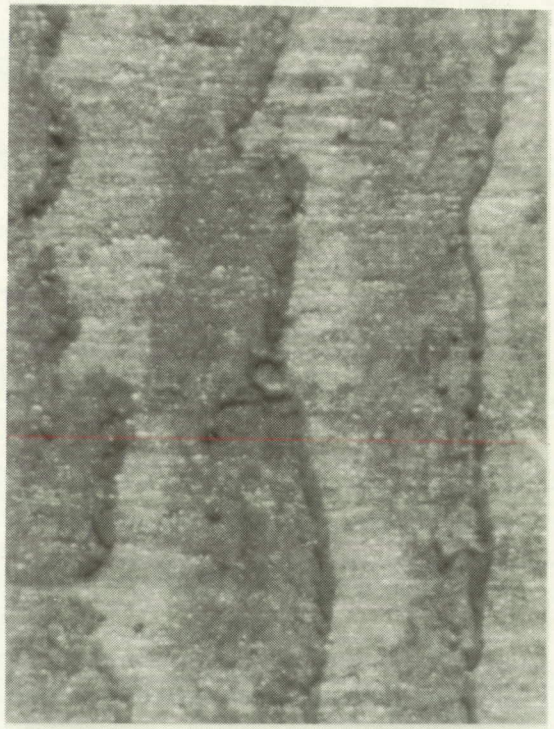

Photograph 3: Fingerprint residue, tray B-04, clamp 2.

MOLECULAR FILMS ASSOCIATED WITH LDEF*

E. R. Crutcher and K. J. Warner
Boeing Defense and Space Group
Seattle, WA 98124-2499
Phone: 206/773-7002, Fax: 206/773-1473

SUMMARY

The molecular films deposited on the surface of LDEF originated from the paints and RTV silicone materials intentionally used on the satellite and not from residual contaminants. The high silicone content of most of the films and the uniformity of the films indicates an homogenization process in the molecular deposition and suggests a chemically most favored composition for the final film. The deposition on interior surfaces and vents indicated multiple bounce trajectories or repeated deposition-reemission cycles. Exterior surface deposits indicated a significant return flux. Ultraviolet light exposure was required to fix the deposited film as is indicated by the distribution of the films on interior surfaces and the thickness of films at the vent locations. Thermal conditions at the time of exposure to ultraviolet light seems to be an important factor in the thickness of the deposit. Sunrise facing (ram direction) surfaces always had the thicker film. These were the coldest surfaces at the time of their exposure to ultraviolet light. The films have a layered structure suggesting cyclic deposition. As many as 34 distinct layers have been seen in the films. The cyclic nature of the deposition and the chemical uniformity of the film one layer to the next suggest an early deposition of the films though there is evidence for the deposition of molecular films throughout the nearly six year exposure of the satellite. A final 'spray' of an organic material associated with water soluble salts occurred very late in the mission. This may have been the result of one of the shuttle dump activities.

INTRODUCTION

This paper provides a spectrographic and photographic summary of the molecular films created in orbit along with the spectra of suspected source materials. Over four hundred infrared spectra have been collected from different areas of LDEF and compared to specific source materials. Twenty spectra are presented here. The molecular films on LDEF resisted solvents very well. Alcohol wipes of the films and even those using more aggressive solvents generally failed to remove the film for analysis. All of the data presented here is the result of direct analysis of the deposit in place on the LDEF substrate material or was mechanically removed by scraping the surface. Extraction performed under the microscope using a variety of solvents confirmed the film's resistance to solvent collection.

The distribution of the film is shown in this paper as it appeared after recovery and evidence is presented for a greater distribution of the brown film earlier in the orbital exposure of LDEF. Evidence is also provided suggesting the contribution of different source materials to the total deposit. The instruments used and associated analytical procedures have been presented previously (Ref. 1).

*Work done under NAS 1-18224, Task 12

COMPOSITION OF LDEF MOLECULAR FILMS

The discoloration of the LDEF surface was one of the earliest observations made. The discoloration was expected but the extent of the coverage was a bit surprizing. Some of the films were so thick that they were peeling from surfaces as large flakes. In other areas the films were very thin but as a result of their dark color were still quite evident. Typical brown film spectra is shown in Figures 1 and 2. These are spectra from the earth end and space end of LDEF respectively. Both are from openings in the satellite surface that vent the interior of the satellite and from sides of the vent that faced in the ram direction, the direction of travel. The principle absorption bands are essentially the same. The broad band between 3200 and 3600 wave numbers corresponds to O-H and N-H groups. Nitrogen containing groups in the film have been confirmed by micro-chemical tests and by electron beam elemental analysis. Most of the peak is due to the presence of the O-H group. Some of the O-H present may be the effect of hydration following recovery. The C-H stretch at about 2960 is evident in both spectra as is a distinct carbonyl at 1710 and 1630. The region below this is a bit more complex due to the similarity of the absorption region of urethanes from the paints used (Figures 3 and 4), those of the silicones used on LDEF (Figure 5), and the organo-phosphates used in materials on some trays (Figure 6). For the space end film about 45% of the weight of the film was recovered after ashing as a transparent, colorless, film of silicon dioxide. This would correspond to a weight percent of 21% silicon in the film tested.

Tray C-12 was a special case. When LDEF was first rotated in SAEF-2 a liquid began running from this tray. The spectrum of the liquid (Figure 7) essentially matched that of the triocyl phosphate used as a fire retardant material in the plastic insulation around the fiber optic bundles on that tray (Figure 6). The brown film around tray C-12 contained very little silicones as is indicated by the absence of the peak near 800 wave numbers in this spectrum (Figure 8).

Tray H-06, being on the space end, had a complex exposure with the trailing side of the tray being exposed to atomic oxygen (AO) and the leading side of the tray being shielded. The fluence of AO has not been estimated for the microenvironments of tray H-06 but in the AO exposed area the patches of brown film persisted (Photograph 1). The film was analyzed in three layers. The top layer spectra is shown in Figure 9 and is dominated by the silica absorption band at 1060. The broad band around 3200 to 3600 wave numbers is probably due to moisture absorbed since recovery. Some carbonyl is also present. Beneath that layer the silicone pattern becomes more evident, the carbonyl peaks become more defined and larger and the O-H/N-H band becomes more pronounced, again probably due to hydration (Figure 10). The C-H absorption peak is absent or so small that it is lost in the broad water absorption band. Still lower the silicones disappear and the characteristic white urethane paint pattern is seen (Figure 11). Figure 12 shows the spectra of brown film in tray H-06 facing the trailing direction. The brown film here appears to be a UV exposed modification of the A276 white paint with very little deposited silicones, based on the intensity of the peak at 800 wave numbers. The strong absorption around 700 and below is due to the pigment of the paint. A more typical brown film pattern was collected from the head of bolt A on clamp 12 of tray H-06 (Figure 13). Photograph 2 illustrates the deposition of the brown film in the opposite corner of tray H-06 and shows the small circular deposits associated with each wire tie wrap. Figure 14 shows the infrared spectrum of these deposits. They had essentially no silicones and were dominated by the C-H absorption band. Photograph 3 shows the appearance of this area of tray H-06 under visible light illumination and ultraviolet light illumination. Ultraviolet light illumination was found to often make visible patterns not visible with normal illumination. Ultraviolet light was never used until all initial spectra had been collected to minimize induced changes in the films.

The thickest brown films always formed on vents from the interior on the side facing into the ram direction. Figure 15 is an example from tray F-06. Notice that this spectrum is very similar to that in Figures 1 and 2. A yellow deposit on the front of tray E-02, clamp 6 had a pattern that was quite diferent than the typical brown film (Figure 16). No precursor of this deposit has been found at this time.

The backs of the tray clamps and shims were examined to evaluate the types of molecular film contaminants that were launched with LDEF. The material on the back surface of tray E-06, clamp 1 had a large silicone component (Figure 17). Closer to the edge of the clamp the hydrocarbon component increased (Figure 18) until at the edge of the clamp the pattern had become very similar to the typical brown film pattern (Figure 19).

Another interesting spectrum was shown by brown spots found on a number of surfaces (Figure 20). These brown spots were often associated with a variety of particulate matter, paint spheres, wear metals, fibers, and other debris (Photograph 5) and a significant concentration of sodium chloride, potassium chloride, and other water soluble salts. These materials were also found on leading edge trays indicating they were not present during the nearly six years LDEF was in orbit. These may be the residue of waste dumps made after the retrieval of LDEF by the shuttle.

Photograph 6 shows a handprint in the bottom of tray F-06. The handprint is lighter than the surrounding area indicating the print acted as an ultraviolet light filter or as a sacrificial surface layer reducing the effect on the paint vehicle underneath or it represented an area of positive pressure preventing the deposition of brown molecular film. Fingerprints in other areas were seen to become dark brown or black but this was always on metal surfaces rather than paint. Similar "lightening" effects were seen on other trays such as the pre-flight scuff patterns seen in the brown deposits in Photographs 1 and 2.

The brown film was deposited in layers. As many as 34 distinct layers have been counted in a single deposited film. Photograph 7 shows such a piece of film from a corner vent of tray C-12. These layers suggest a cyclic deposition. The most obvious cyclic event is an orbit but this would indicate that these solvent insoluble, polymerized films form and become stable with one orbit. Many other cycles exist of much longer duration but it is difficult to conceive of a slow steady release rate maintaining the same proportion of functional groups from multiple sources that would persist over years in orbit to deposit these layered films. These films do not change significantly from layer to layer which would also suggest an early release and deposition. There is some evidence on the canister trays that suggest later deposition of materials. This evidence is still being evaluated.

On the leading edge trays there was often little evidence of deposition by discoloration. Elemental analysis of the surface in many areas did indicate silicate films, presumably the remnant of the hydrocarbon/silicone film after reacting with atomic oxygen. Figure 21 is the infrared spectrum of one of these films on clamp 4 of tray F-09. Figure 22 shows the elemental mapping of this "shadow" seen next to bolt A of clamp 4 on tray F-09. The aluminum map shows the bare aluminum exposed under the washer and the aluminum in the anodized surface of the clamp. The oxygen map illustrates the distribution of oxides. In the area of the weaker aluminum signal the silicon map illustrates a concentration of silicon. This is a silicon dioxide film over the anodized aluminum. Photograph 8 shows the LDEF structure with the trays removed and a slight discoloration in the exposed area of the structure associated with the presence of the silica film compared to the areas covered by the tray edges and tray clamps. This is in contrast to the obvious dark film seen on the trailing structure clearly delineating the position of the tray edges and clamps (Photograph 9).

DISTRIBUTION OF THE MOLECULAR FILMS

The distribution of molecular films on LDEF was one of the most obvious features of its orbital exposure. All exterior trailing surfaces and surfaces shielded from atomic oxygen on LDEF exhibited a brown discoloration. Those surfaces that faced into the atomic oxygen were bleached white or were mottled in shades of pastel green and red as a result of thin film interference effects on the surface of aluminum panels. The whites of the painted surfaces were not bright but tended toward the gray as a result of the formation of color centers in the rutile pigment that absorbed the visible wavelengths of light. When LDEF was finally back at Kennedy the distribution of the color effects could be studied in more and

closer detail. The gray of the white paint pigment disappeared quickly back on earth but the brown discoloration and the discoloration caused by thin film effects persisted. In areas associated with the venting of the interior of the satellite thick brown films had developed, some of which were a few hundred micrometers thick and were peeling from the surface on which they had been deposited. When the inside of LDEF was opened for viewing by the removal of experiment trays molecular films deposition patterns were seen on interior surfaces. Circular patterns, sharp silhouettes of interior structures, and broad linear areas of discoloration were evident.

The one common thread in all of these deposits was the exposure to ultraviolet light. The exterior surface was bathed in ultraviolet light every orbit. The interior was a region of sharp shadows and rastering beams cut short by the geometry of LDEF's structure. Two conditions for the creation of these durable brown films were the presence of a condensed material suitable for polymerization and ultraviolet light to polymerize the film.

The ram direction always exhibited the thickest films. There are two attributes characteristic of the ram direction. The first is that the ram direction always received ultraviolet light exposure before any adjacent surface that faced in the trailing direction. The earth end ram surfaces were exposed as the satellite came from the shadow of the earth. The second attribute is that the surfaces facing the ram direction always received more exposure to the effects of atomic oxygen than the surfaces facing the trailing direction. The temperature of the satellite is at its lowest when it leaves the shadow of the earth. The cool surfaces are relatively good collectors (high sticking coefficient) for condensible molecular materials. As a result the ram facing surfaces are still cool when they are first exposed to the ultraviolet light from the sun. As the ultraviolet light polymerizes the exposed film the sun's light warms the satellite and the condensed molecular materials not polymerized become more mobile. By the time the trailing surfaces receive ultraviolet light they have warmed considerably and lost much of the condensed film.

The source materials for this film were everywhere on the interior and vented outward through every available vent as can be seen by the wide distribution of the films. The urethane paint was literally on every interior surface and the silicone materials were widely distributed about the interior on experiment A0178 (see Ref. 2, figure 2). Vent paths from the interior were often tortuous due to the depth of some of the trays and the dimensions of the longeron and brace I-beams. Most exiting molecules encountered a number of surfaces before exiting the satellite and being available for redeposition as part of the return flux. The heaviest return flux should have been on the surfaces facing the ram direction (Ref. 3). That may have been but the ram directed surfaces have been scoured of thin hydrocarbon films by the atomic oxygen exposure. Silica films would be expected to be present if a film had first been deposited and then burned away but the presence of silica is not as uniform in distribution as the brown film seen deposited on the trailing edge surfaces (compare Figure 22 and Photograph 9). The tray surfaces facing in the trailing direction and exposed to return flux only have films of less than 100 nanometers in thickness. These films also exhibit a directionality that may be related to the nearest corner vent of the tray. This directional dependency is independent of the ram direction and may help explain the distribution of silica films found on the ram facing trays. In Figure 22 the silica is on the side of the bolt toward the space end cover panel. The space end cover panel directed venting materials toward this clamp (tray F-09, clamp 4) and its bolts. The heaviest deposits of silica extend from the edge of the washer toward the edge of the clamp toward the space end panel. In the areas of the clamp where there was no bolt the silica concentration is on the order of the background for the aluminum clamp. The presence of the bolt enhanced the concentration of the film between the source and the bolt. These examples indicate that much of the return flux was not redirected by 180 degrees but rather by less than 90 degrees as a result of configurational geometries that tended to direct escaping molecules at relatively low angles over the surface of the satellite.

CONCLUSION

1. The films consisted primarily of modified outgassing products of the RTV silicone materials used and the urethane paints.

2. Fixation of the deposit was dependent on ultraviolet exposure and possibly a low level of atomic oxygen exposure.

3. The films were deposited cyclically with up to 34 layers being counted in a single fragment of film.

4. Local sources of outgassing material contributed to local films.

5. On the leading rows the films were converted to silicon dioxide type films or were removed by the attack of atomic oxygen on carbon based substrates.

6. Organic materials were deposited on LDEF after retrieval that had a high hydrocarbon content and were associated with potassium and sodium chlorides.

REFERENCES

1. Preliminary Report on LDEF Contaminants, 1991 NASA Publication.

2. Crutcher, E. R., L. S. Nishimura, K. J. Warner, and W. W. Wascher: Silver/Teflon Blanket: LDEF Tray C-08. First LDEF Post-Retrieval Symposium, NASA CP-3134, 1992.

3. Rantanen, R. O. and T. D. Gordon: Contaminant Buildup on Ram Facing Spacecraft Surfaces. OPTICAL SYSTEMS CONTAMINATION: EFFECTS, MEASUREMENT, CONTROL, SPIE Vol. 777, 1987.

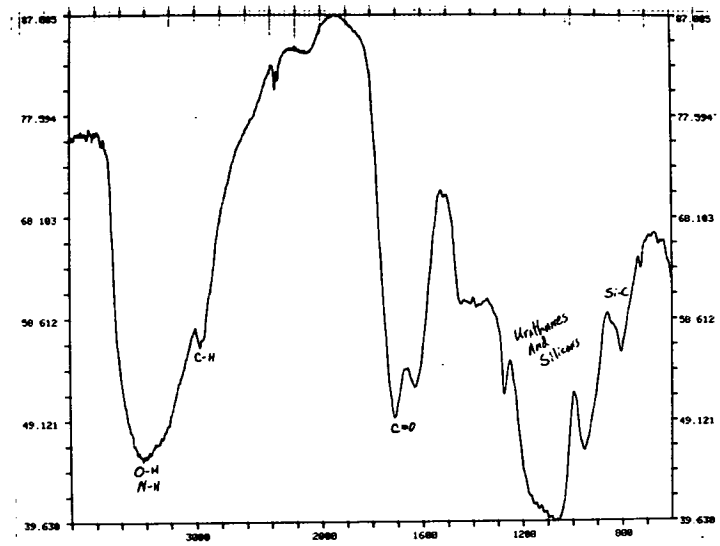

SPACE END FRAME BROWN FILM

Figure 1: Brown film from longeron exposure at tray G-12 facing ram direction.

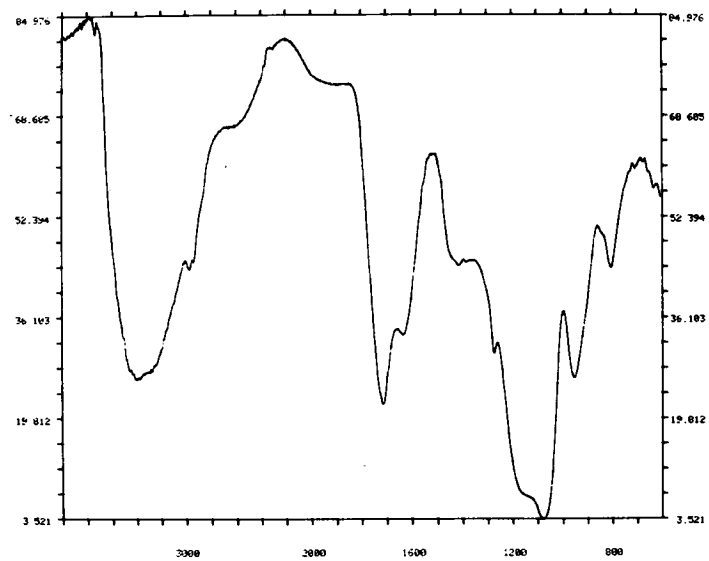

EARTH END FRAME BROWN FILM

Figure 2: Brown film from longeron 13, space end, exposure facing ram direction.

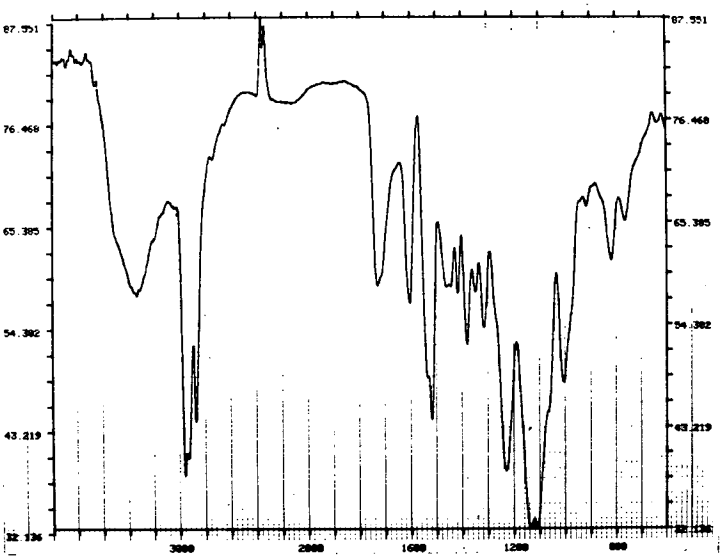

Figure 3: Black paint from back surface of tray F-06.

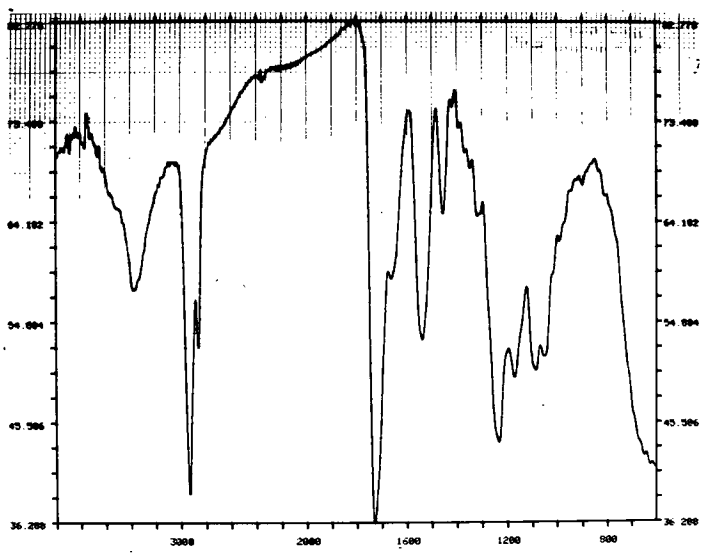

Figure 4: White paint from beneath bolt, interior of tray H-06.

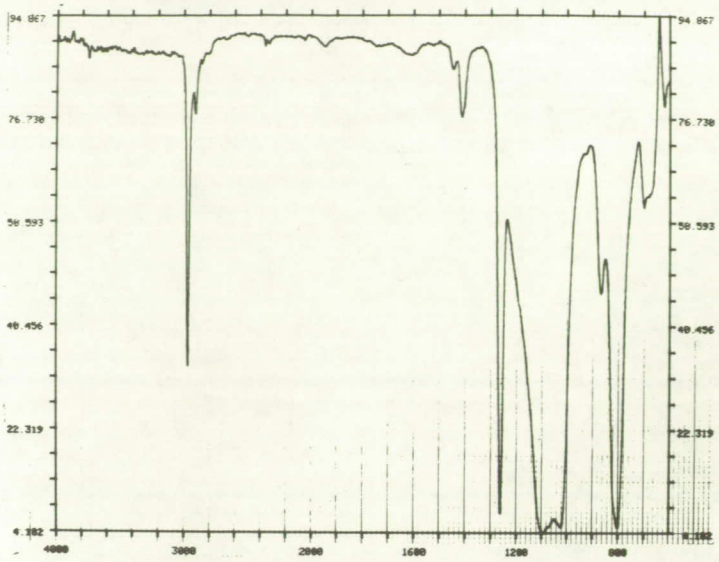

RTV SILICONE FROM THERMAL BLANKET

Figure 5: Silicone adhesive used to attach velcro tape to back of Silver/Teflon Blankets, tray F-02.

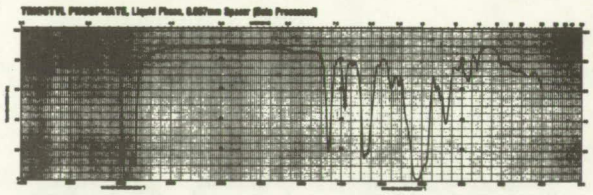

MATERIAL BELEIVED TO BE THE LIQUID ON TRAY C 12

Figure 6: Trioctyl phosphate standard spectrum.

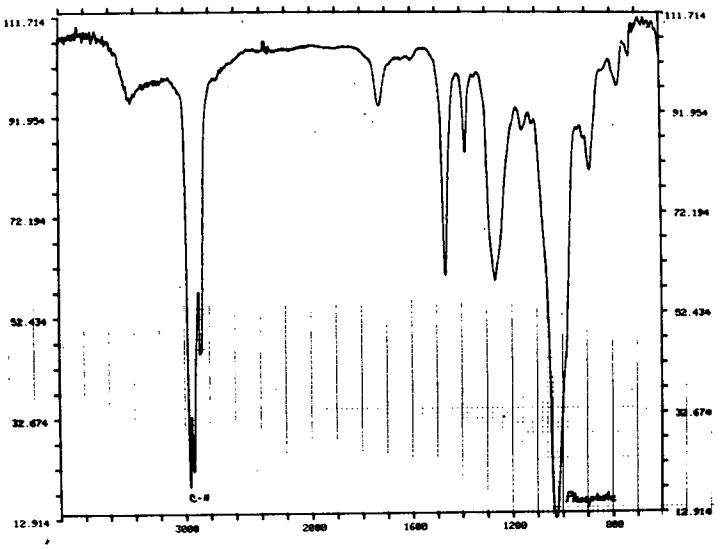

Figure 7: Tray C-12, liquid collected on glass fiber paper during deintegration.

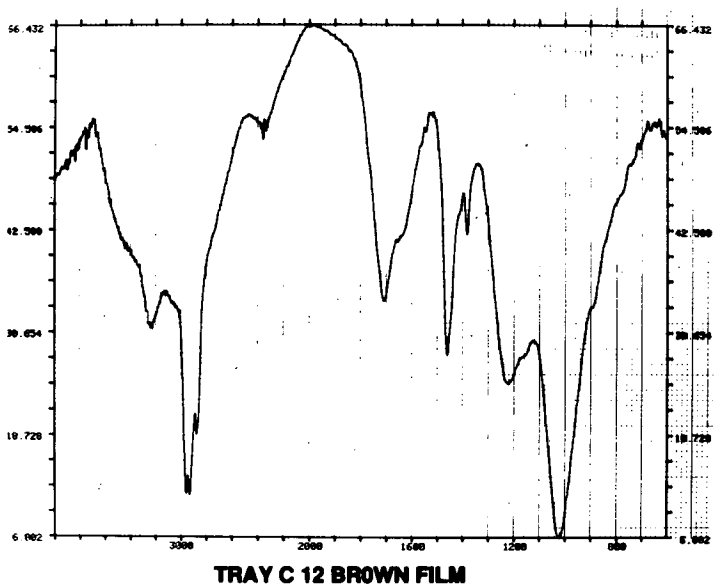

Figure 8: Tray C-12, brown film from corner vent.

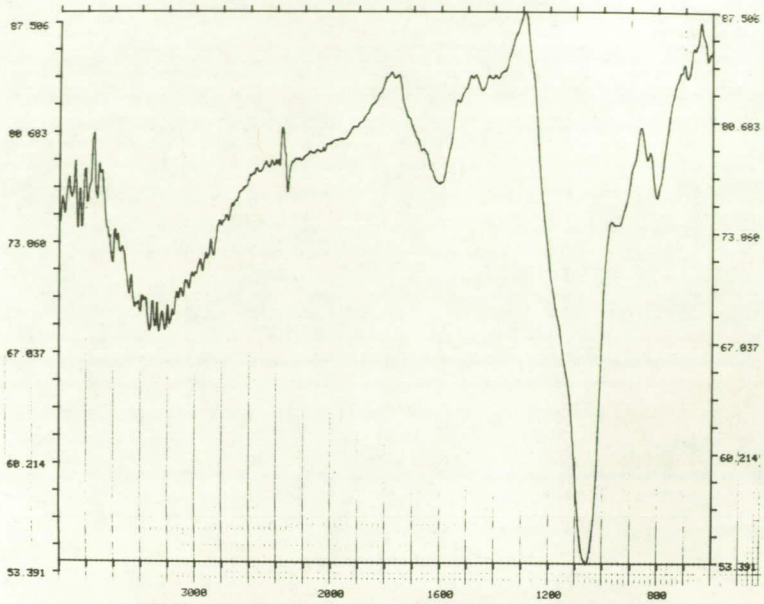

TRAY H 06 TOP LAYER OF BROWN FILM ON AN EXPOSED SURFACE

Figure 9: Tray H-06, top layer of AO exposed brown film.

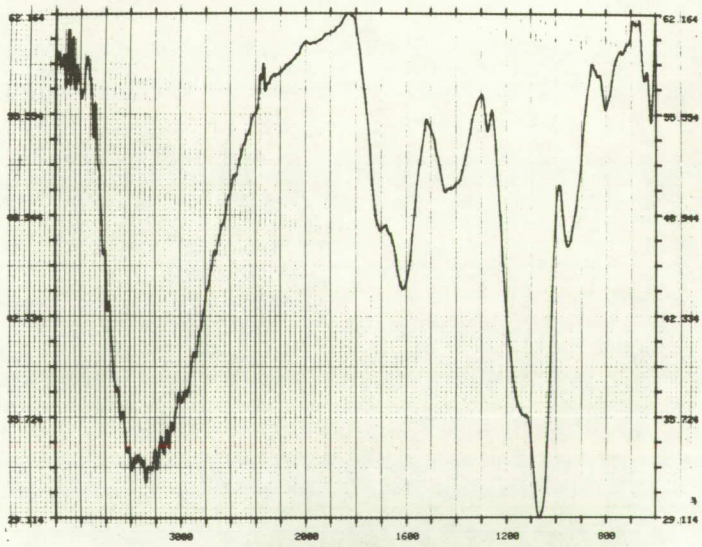

TRAY H 06 MIDDLE LAYER OF BROWN FILM ON AN EXPOSED SURFACE

Figure 10: Tray H-06, middle layer of AO exposed brown film.

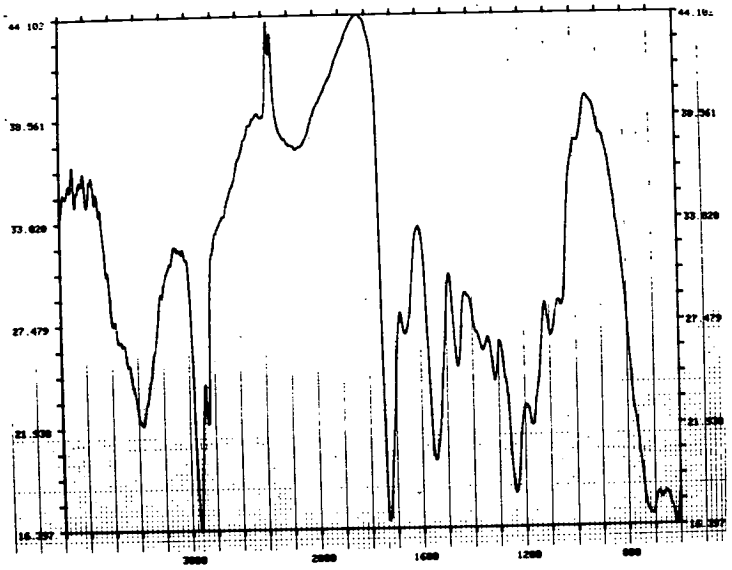

TRAY H 06 WHITE PAINT UNDER BROWN FILM

Figure 11: Tray H-06, bottom deposit (paint surface) of AO exposed brown film.

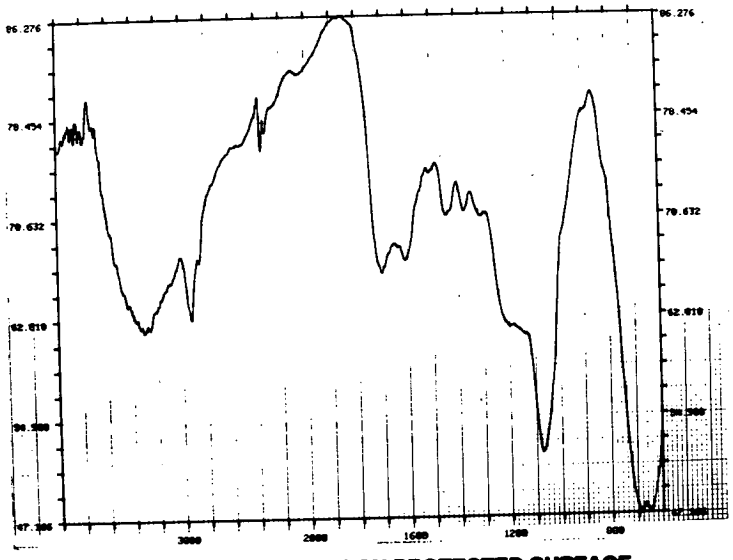

TRAY H 06 BROWN FILM ON PROTECTED SURFACE

Figure 12: Tray H-06, brown deposit on trailing exposure.

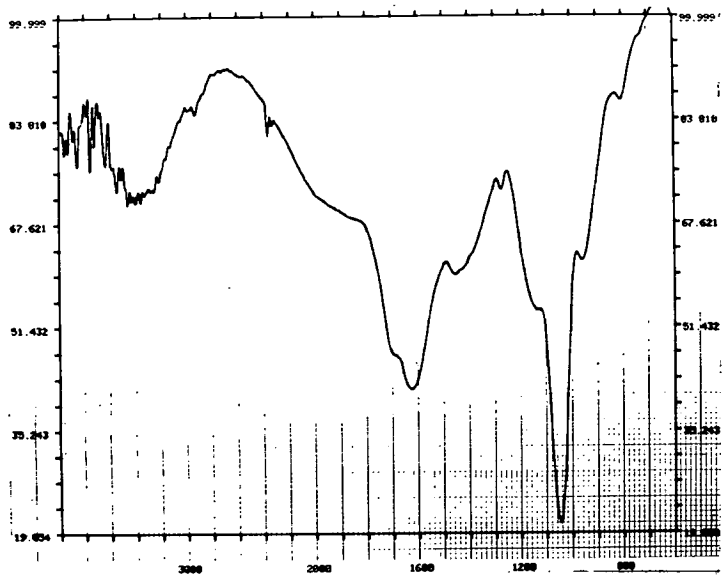

Figure 13: Tray H-06, clamp12, bolt A.

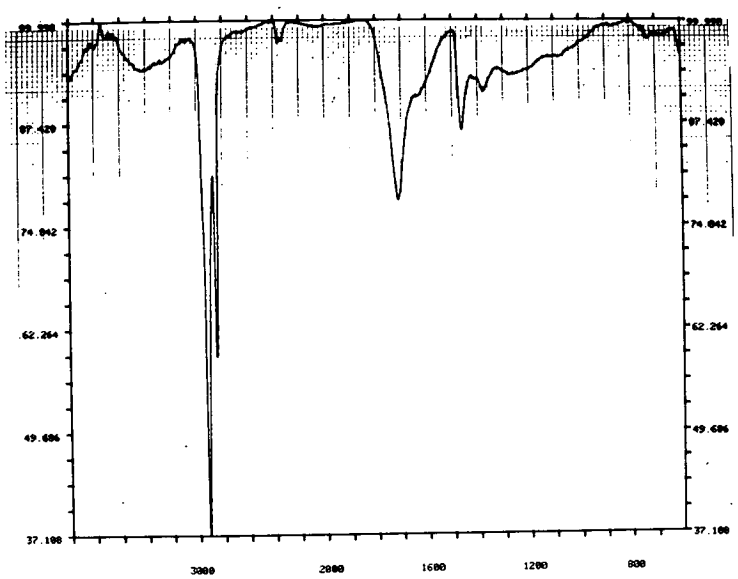

Figure 14: Tray H-06, deposit beneath wire tie wrap.

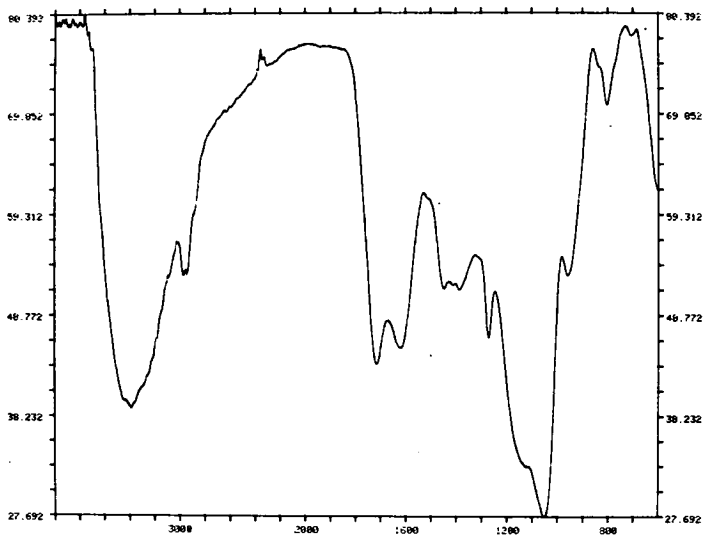

TRAY E 06 CORNER VENT FACING RAM DIRECTION

Figure 15: Tray F-06, corner vent deposit facing ram exposure.

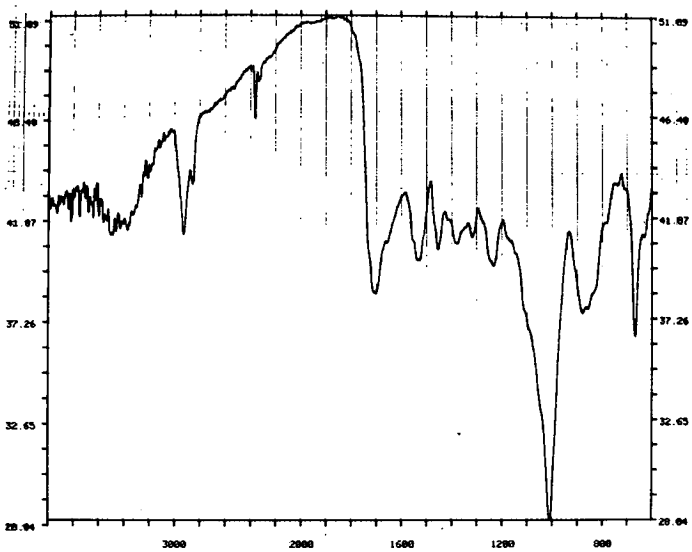

TRAY CLAMP E 02 6 YELLOW DEPOSIT ON FRONT SURFACE

Figure 16: Tray E-02, clamp 3, yellow deposit.

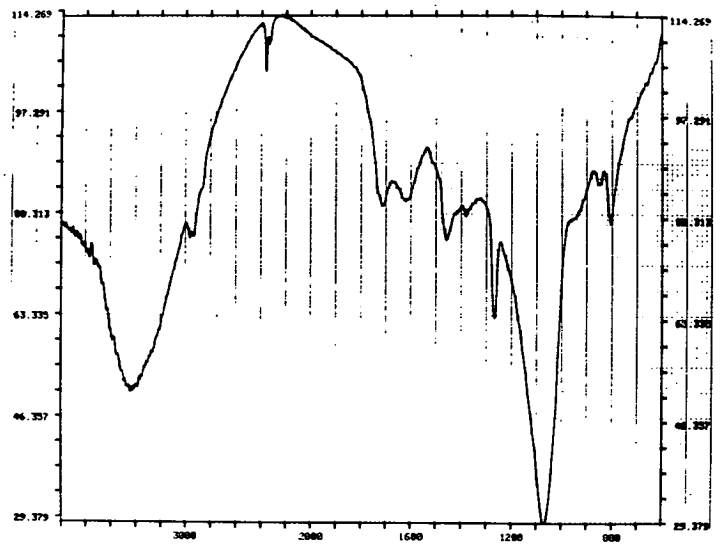

Figure 17: Tray E-06, clamp 1, deposit between clamp and shim at center.

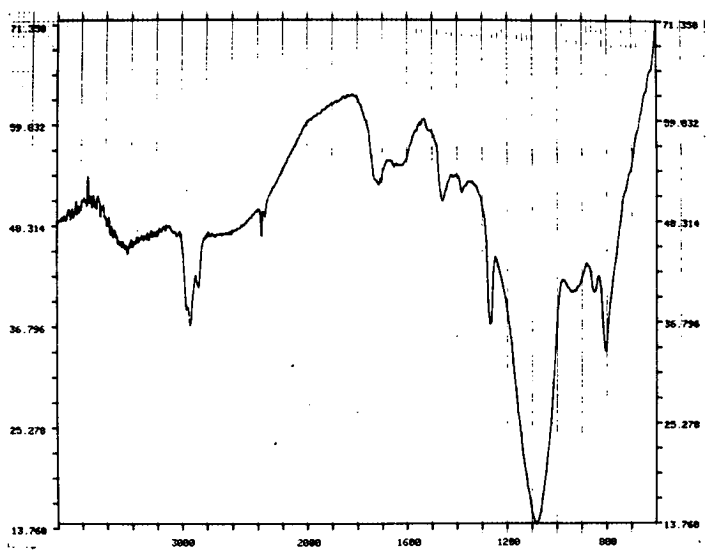

Figure 18: Tray E-06, clamp 1, deposit between clamp and shim near edge of clamp.

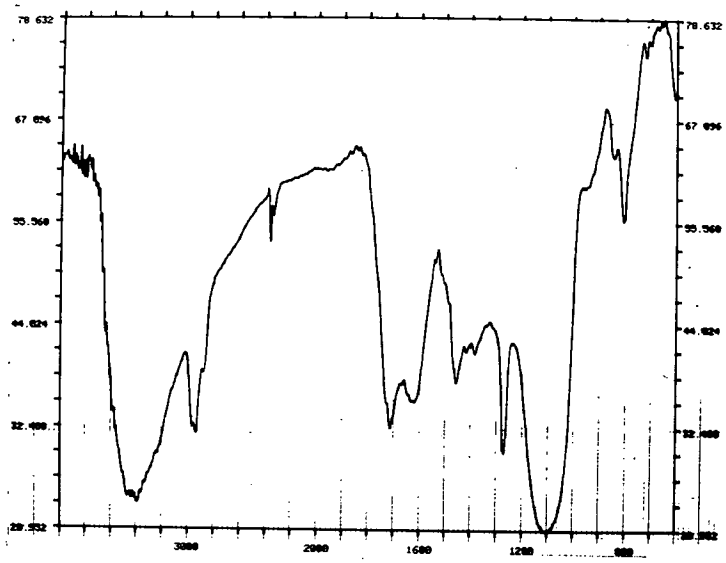

TRAY CLAMP E 06 1 BACK SURFACE BESIDE SHIM
BEVELED EDGE

Figure 19: Tray E-06, clamp 1, deposit on beveled edge of clamp.

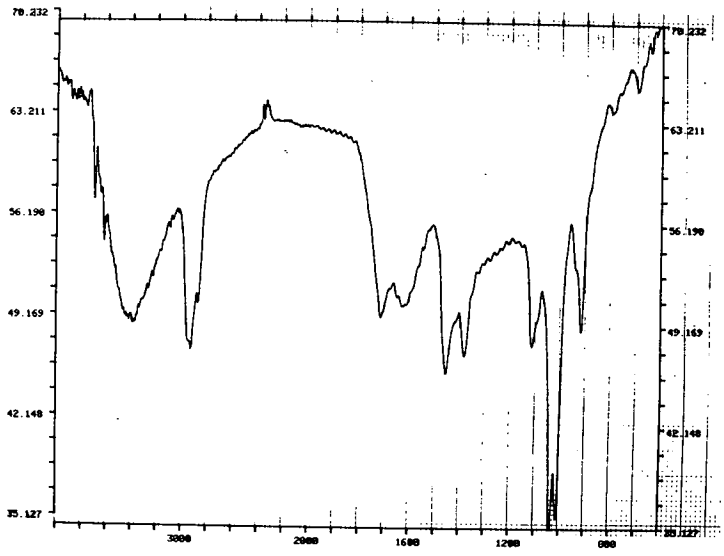

Figure 20: Tray F-09, clamp 8, brown spot.

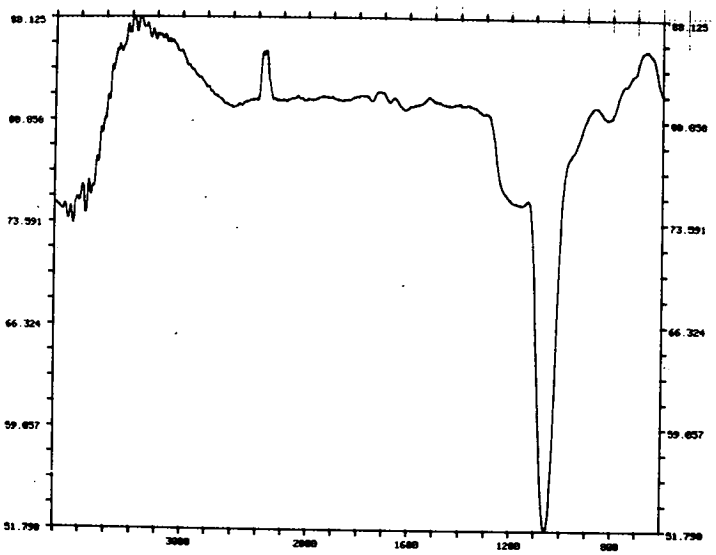

Figure 21: Tray F-09, clamp 4, surface with change in interference color.

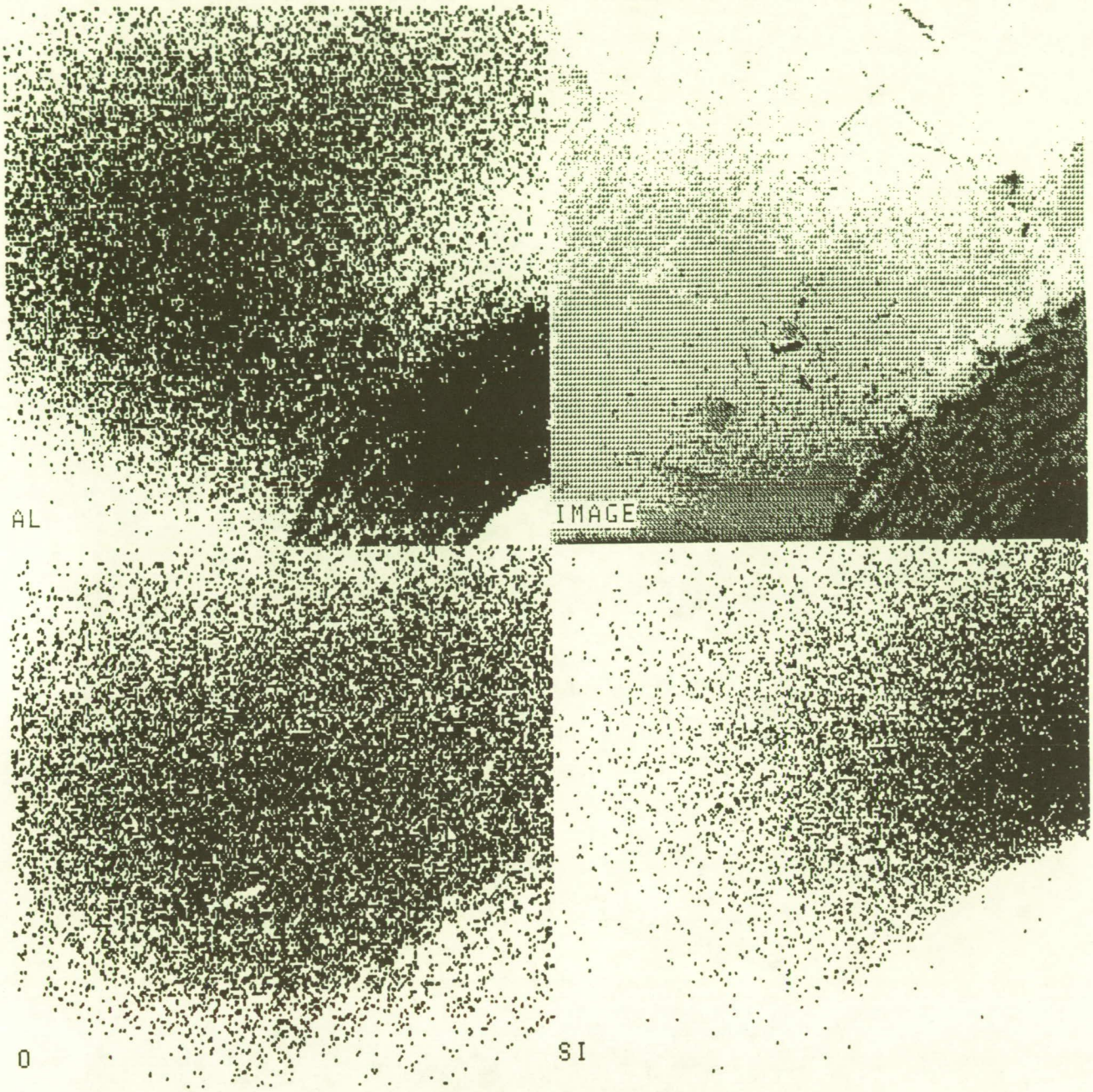

Figure 22: Tray F-09, clamp 4, elemental map of area with different interference color.

(Original figure not available at time of publication.)

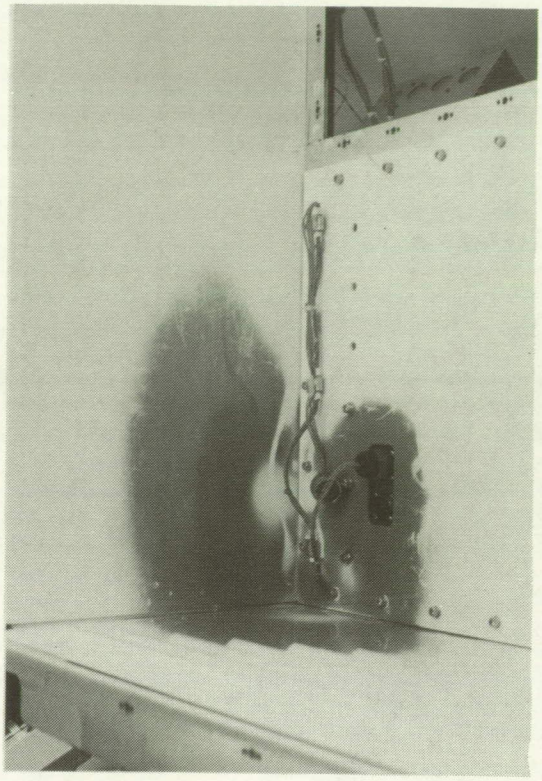

Photograph 1: Tray H-06, brown deposit in AO exposed corner.

(See color photograph, p. 599.)

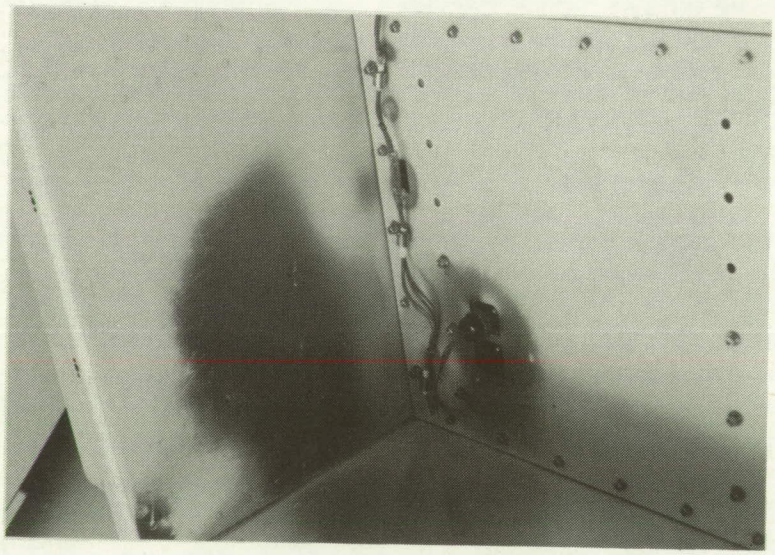

Photograph 2: Tray H-06, brown deposit and tie wrap deposit in other corner.

(See color photograph, p. 599.)

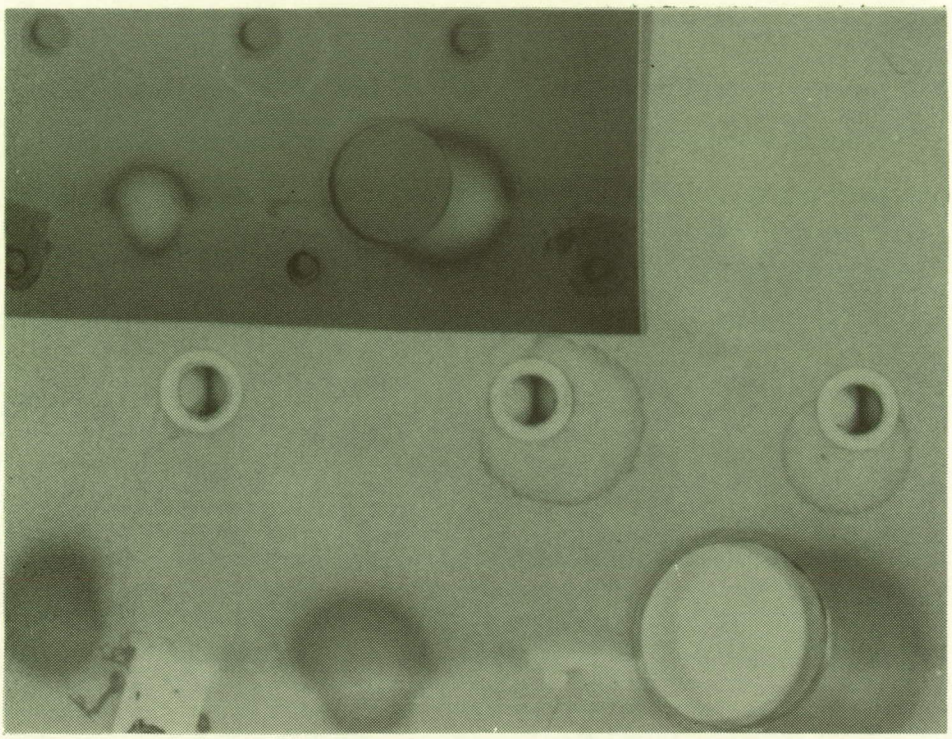

Photograph 3: Tray H-06, visible and UV illumination view of the tie wrap deposit.

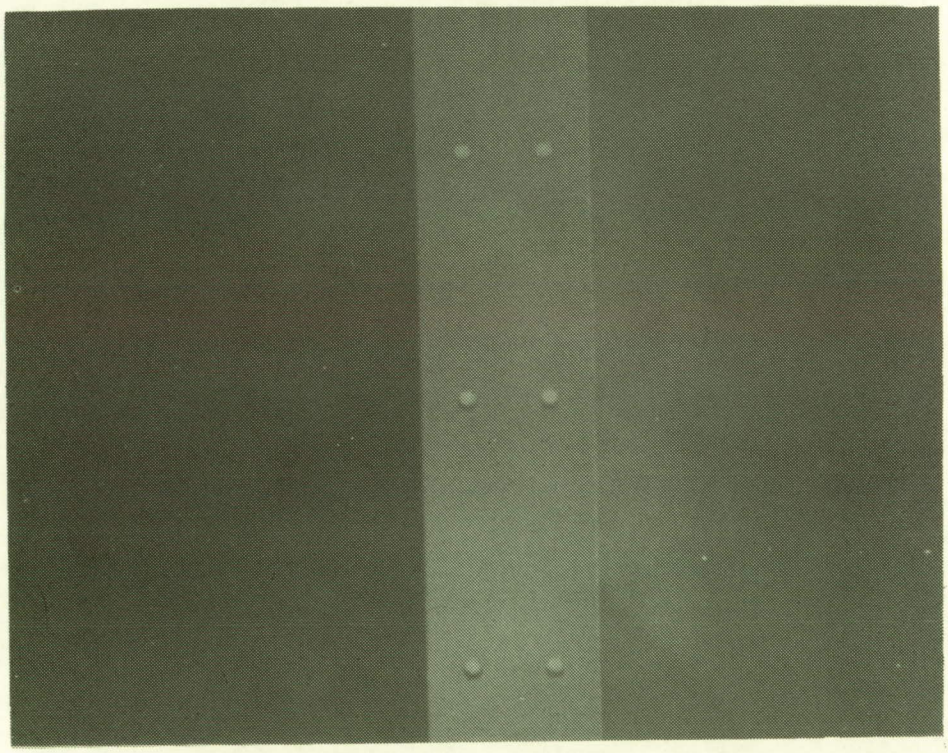

Photograph 4: Tray F-06, back of bottom panel showing shadow only visible with UV illumination.

Photograph 5: Tray F-02, clamp 6, brown droplet deposit.

(See color photograph, p. 600.)

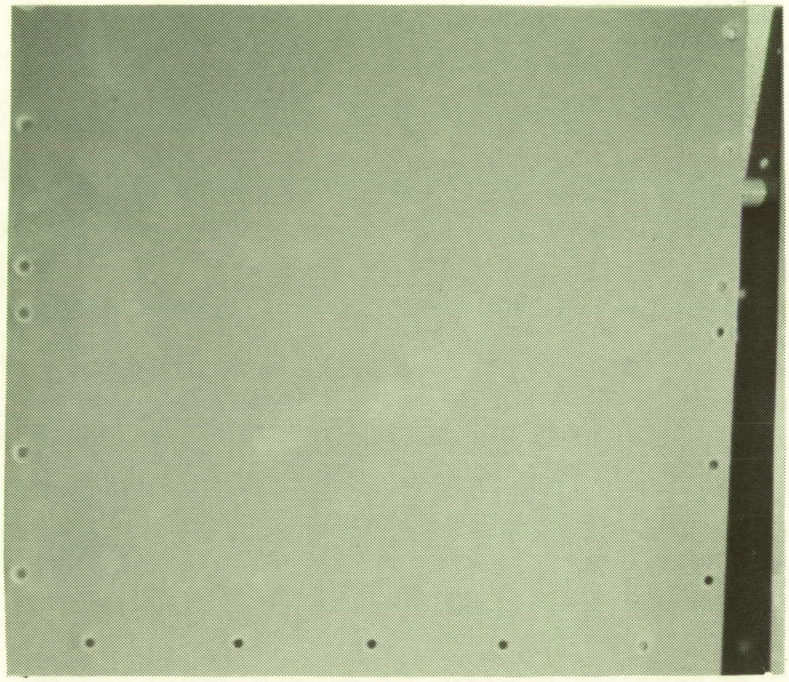

Photograph 6: Tray F-06, handprint on bottom panel.

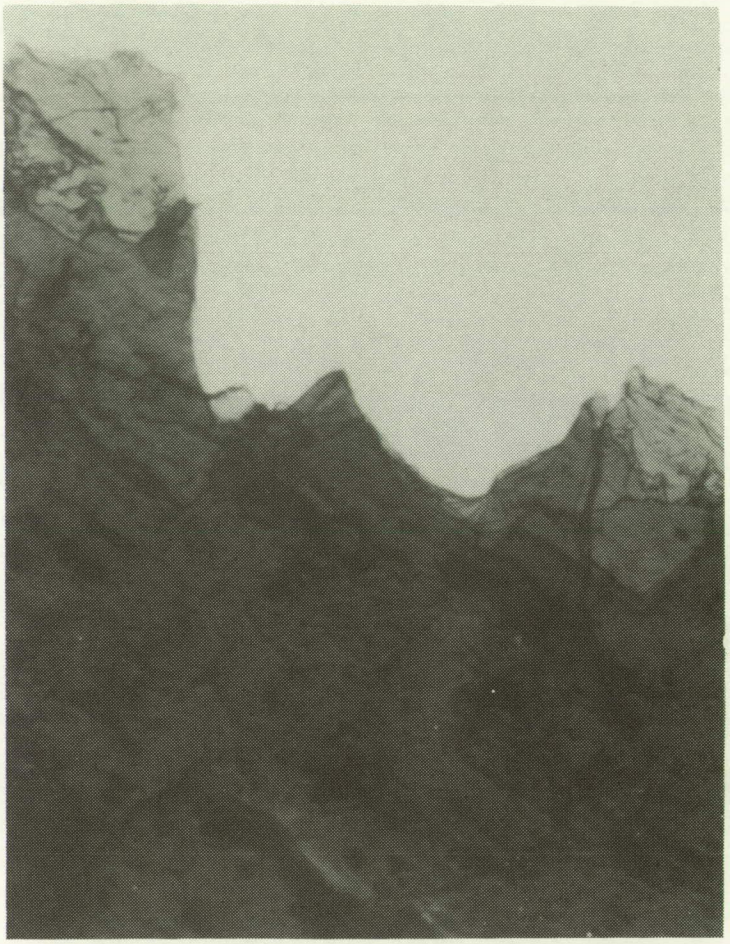

Photograph 7: Tray C-12, layered brown film.

(See color photograph, p. 600.)

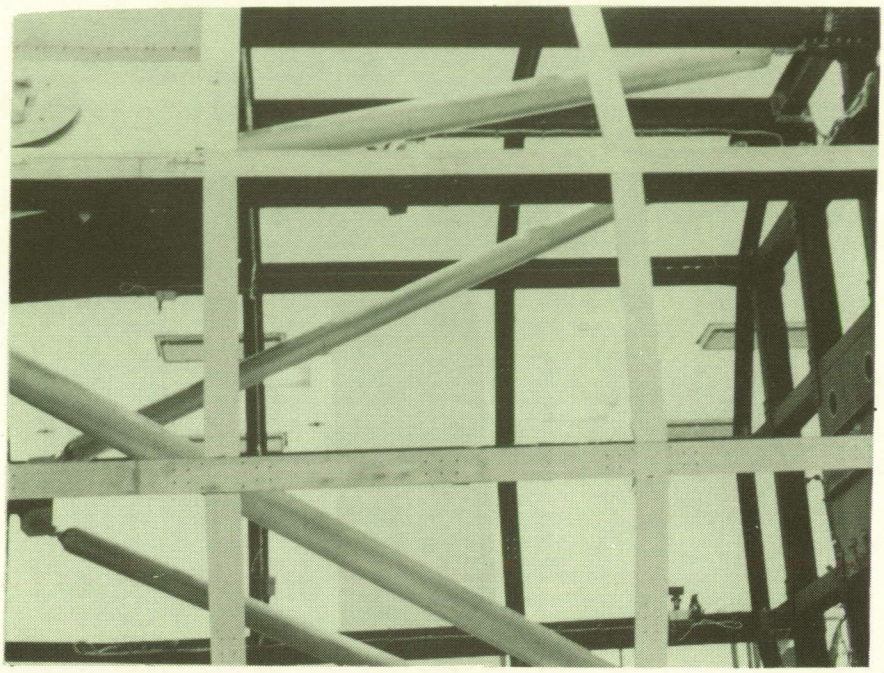

LDEF Leading edge (ram direction)

Photograph 8: Leading edge view of LDEF structure.

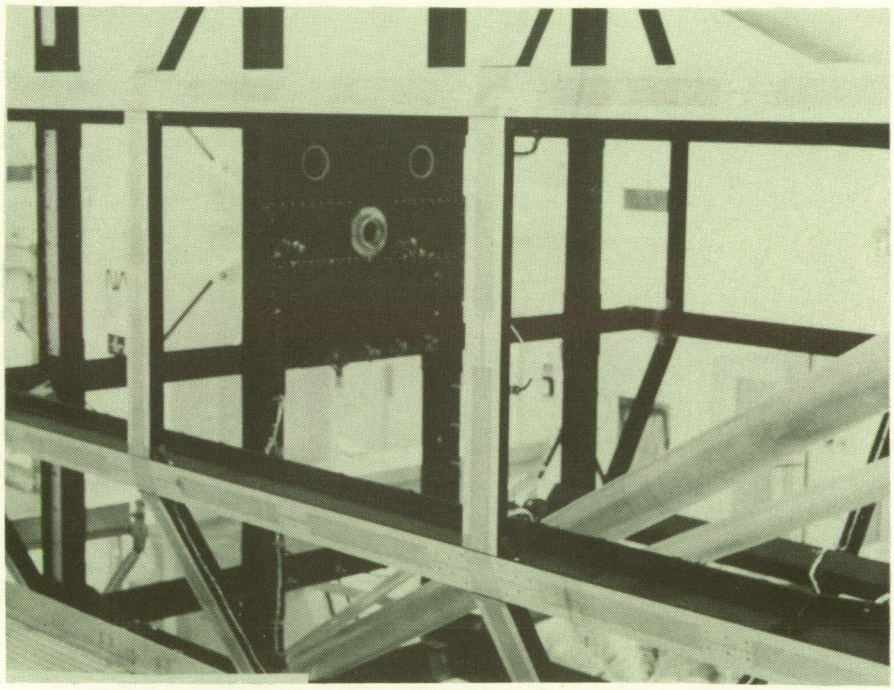

NVR stain LDEF trailing edge Earth end

Photograph 9: Trailing edge view of LDEF structure.

ORGANIC CONTAMINATION OF LDEF

Gale A. Harvey
NASA Langley Research Center
Hampton, VA 23665-5225
Phone: 804-864-6742, Fax: 804-864-7790

SUMMARY

A brown stain of varying thickness was present on most of the exterior surface of the retrieved LDEF. Tape lifts of Earth-end LDEF surfaces taken in February 1990 showed that the surface particle cleanliness immediately after retrieval was very good, but faint footprints of the tape strips on the tested surfaces indicated a very faint film was removed by the tape. Solvent wipes of these surfaces showed that the stain was not amenable to standard organic solvent removal. Infrared spectra of optical windows from tray E5 and scrapings indicate that the film is primarily of organic composition, but is not similar to the oil that seeped from tray C12. Very dark and heavy deposits of the stain are present at openings and vents to the interior of LDEF. Heavy brown and blue-green deposits are present in the interior of LDEF where sunlight penetrated through cracks and vent openings. Photographs of the deintegrated LDEF graphically show the stain distribution.

The exterior of LDEF had significant areas painted with a white polyurethane paint for thermal control, and almost all of the interior was painted with a black polyurethane paint for thermal control. The brown staining of LDEF is consistent with long-term outgassing of hydrocarbons from these paints followed by rapid solar-ultraviolet-induced polymerization of the outgassed hydrocarbons when the outgassed molecules stuck to surfaces exposed to sunlight.

INTRODUCTION

The Langley Research Center developed and manages the Halogen Occultation Experiment (HALOE, ref. 1) to measure stratospheric ozone chemistry on a global basis. The HALOE instrument is a mid-infrared optical instrument which is sensitive to organic film on optical surfaces because the two spectral bandpasses for measurement of HCL and CH4 include the 3.4μ hydrocarbon absorption band (ref. 2). The HALOE contamination control program makes extensive use of high-resolution-in-transmission Fourier Transform Infrared (FTIR) spectroscopy of the 3.4μ band to monitor HALOE organic cleanliness (ref. 3). The HALOE measurement-of-organic-film techniques have been applied to the retrieved LDEF.

TAPE LIFT DATA

Taking of tape lifts is an established procedure for measuring surface particle cleanliness. Particle cleanliness is related to MIL-STD-1246B (ref. 4) which gives the particle cleanliness level, CL, which is a standard method of specifying particle cleanliness. Specific descriptions of particles and their size distributions are used to evaluate sources of particle contamination and to evaluate cleaning procedures.

The procedure consists of preparing tape-lift kits, taking tape lifts of a test surface, and reading the tape lift strips in a clean environment.

Sixteen tape lifts of removed LDEF Flight hardware and surfaces in the SAEF 2 clean room were taken on February 14, 1990. The cleanliness levels are plotted in Figure 1. The particle cleanliness level of the retrieved LDEF end panels as seen in Figure 1 was better than 300, which is quite clean. However, observers of the tape lift operation noticed faint "footprints" of the contact area of the tape strips were visible on the tested LDEF surfaces indicating a faint film was removed by the tape. Subsequent tape lifts indicated the surface cleanliness rapidly deteriorated with deintegration activities.

SOLVENT WIPE DATA

Extracted clean room wipes (ref. 5) were used extensively in the cleanliness certification of thermal-vacuum chambers used for testing the HALOE instrument. The procedure is to wet the test surface with a cleaning solvent (ie spectroscopic grade isopropyl alcohol) which will allow transfer of some of the organic film (typically about 75 percent) to an extracted cleanroom wipe. The wipe is air dried at the field site, bagged, and transported to an analytical lab. The cleanroom wipe is soaked in a high purity transfer solvent at the lab, and the organic contamination is then extracted and transferred to an IR window for weighing and FTIR spectroscopy. The surface concentration factor from wipe to IR window is 1,000. The 3.4μ spectrum of an isopropyl alcohol wipe of 1 square foot of an LDEF Earthend thermal control panel is present in Figure 2 along with the spectrum of a control wipe. The LDEF Earthend thermal control panel wipe had about twice the NVR as the control wipe. That is, the thermal control panel had about 0.06 mg/ft^2 of organic film that would dissolve in isopropyl alcohol.

ABSORPTION SPECTRA OF E5 OPTICAL WINDOWS

Experiment S0050-1 contained several infrared transmitting windows. These optical windows were in a 1/6 compartment of tray E5 which was covered with a 50 percent transmitting/50 percent blocking sunscreen. The inside surface of the sunscreen was painted with Chemglaz Z306 black paint for thermal control.

A 3.4μ spectrum of the CaF_2 window flown on LDEF is presented as Figure 3. Similar CaF_2 windows are used extensively in the HALOE contamination control program (ref. 6) and a large data base of organic films on CaF_2 windows exists at LaRC. The 3.4μ absorption on the LDEF window is about 7 percent.

An estimate of the organic film mass per square foot can be obtained by ratioing the NVR mass with 7 percent absorption on an IR window/weighing pan of small area (0.08 in^2) to 1 square foot of area. Numerous measurements of organic film show 0.1 mg of organic residue on a 0.08 in^2 of CaF_2 corresponds to 7 percent absorption at 3.4μ. Thus, a calculated mass/ft^2 of organic film on the LDEF window is:

$$\frac{144\ in^2}{1\ ft^2} \times \frac{0.1\ mg}{0.8\ in^2} = 180\ mg/ft^2$$

This is a lot of organic film. One mg/ft^2 or less of organic film is the standard cleanliness level "A" typically required of contamination sensitive flight hardware.

The visual discoloration of this film can be seen in a photograph of a film-bracket-covered area and uncovered area in tray E5, shown in Figure 4.

ABSORPTION SPECTRA OF SEEPAGE FROM TRAY C12

Tray C12 of LDEF was observed to be leaking fluid several days after LDEF was moved to SAEF 2 for deintegration. This tray had heavy deposits at the edges of the tray cover, ranging from yellow-brown stains to a black layer of deposited material. The interior contained runs of fluid along the walls and a wet band about 6 cm wide by 60 cm long on the bottom of the tray against one end. Fluid from one of the runs was contact transferred to a clean CaF_2 window. The 3.4μ spectra of this fluid is presented as Figure 5. The great strength of the methel stretch at 2860 cm^{-1} and 2960 cm^{-1} shows that the hydrocarbon composition of this fluid is much different than the hydrocarbon composition of the contamination of Tray E5.

EXTERIOR PHOTOGRAPHS

Visual inspection of the deintegrated LDEF in April of 1990 clearly revealed several characteristics of the organic stain on LDEF. Figures 6 and 7 show the stain on the trailing edge (row 3) of LDEF. Figures 8 and 9 show a much fainter stain on the leading edge (ram direction=row 9) of LDEF. But Figures 10, 11, 12, and 13 show the heaviest deposits on end plates surface near vents from the interior. At these locations the deposits were so heavy they were curling off the rough milled surfaces of the end plates. It is concluded that the stain at one time was greatest on all leading edges, but that the direct ram surfaces were effectively cleaned by atomic oxygen during the later months in orbit. Figure 14 shows light NVR on the trailing edge of an end plate.

INTERIOR PHOTOGRAPHS

Brown stains were present on unpainted diagonal braces behind cracks between two sections of micrometeoroid panels (Figure 15). Brown stains were also present on unpainted end braces. Dark blue and blue-green deposits were present on interior surfaces facing the ram direction where sunlight was incident through cracks or vent holes. Figure 16 and 16a show the undeposited shadow of a fastener surrounded by a blue-green deposit. A blue deposit is shown in Figure 17 with a rail clip and its shadow. The deposit behind a 3/4" x 3/4" tray corner vent hole is shown in Figure 18. These deposits could be scraped off to uncover the black thermal-control paint underneath.

These photographs demonstrate that the organic stain was polymerized by sunlight and that the heaviest deposits were on the ram side.

OUTGASSING MEASUREMENTS OF THE THERMAL CONTROL PAINTS

Three independent measurements of outgassing of the black thermal control paint (Z306) used on LDEF were made at LaRC following the retrieval of LDEF. Exposures in a vacuum oven gave

0.1 percent mass loss after 1 week at 24° C;
1.4 percent mass loss after 1 week at 60° C;
and 23.0 percent mass loss after 16 hours at 177° C.

The 16 hours at 177° C would correspond to 6 years at ambient (25° C) temperature if the 10° C rise in temperature produces a doubling of outgassing rule applied.

High resolution FTIR spectra (Figures 19 and 20) of Z306 heated in an evacuated gas cell show considerable CO_2 and CO, and some CH_4 and H_2O outgassing during the first few hours at approximately 120° C. Heavier hydrocarbon absorption is also present at 2960 cm^{-1} (CH_3 stretch) in Figure 21. The mass loss during heating was 2.8 percent. A brown film coated the gas cell walls after heating of the 16 mg paint sample. Also shown in Figure 20 is a spectrum of scraped film from an LDEF end plate. The 3.4μ spectrum of the end plate scraping is almost identical to the gas cell film, but very unlike the spectrum from Tray E5 (Figure 3) and Tray C12 (Figure 5). The LDEF end plate scraping has 2 gm/ft^2 of mass per unit area.

Time-sequence FTIR spectra were obtained of outgassing of the white Chemglaz paint (A276) in an evacuated gas cell heated to 115°C. Spectra were obtained after 5, 10, 25, 40, 65, and 155 minutes of heating. Spectra of the unheated cell were also obtained 1 and 2 days later. These spectra are presented in figures 21-24. The 3.4 m absorption is the same as that of Chemglaz Z306. This absorption is the strongest feature in the 5 minute spectrum, but is surpassed in strength by CO_2 after 25 minutes of heating at 115°C. The mass loss after 155 minutes at 115°C was 2.7 percent.

Atomic mass spectra (figure 25) of outgassing at room temperature from a 5 month cured sample of Chemglaz Z306 was obtained with a residual gas analyser. A mass fragment of 113 amu is the most abundant paint outgassing heavy-mass-fragment. Additional mass-spectral data are reported in references 6 and 7.

CONCLUSIONS

The major conclusions drawn from studies of LDEF relating to organic film contamination are:

1. The primary source of the ubiquitous brown stain was outgassing of the black thermal control paint (Chemglaz Z306). The stain is a different hydrocarbon composition at the vent openings than on tray surfaces.

2. The paint outgassing and redeposition was temperature driven and retention on surfaces was strongly affected by solar ultraviolet induced polymerization of outgassed molecules.

3. Atomic oxygen severely eroded the stain on the leading edge (row 9) late in the mission.

REFERENCES

1. UARS Project Data Book, General Electric Astrospace Division, April 1987.

2. Harvey, G. A., J. L. Raper, and R. N. Messier, "Microcontamination of IR Spacecraft Optics," in Proceedings of Microcontamination Conference and Exposition, Anaheim, CA, pp. 237-259, October 1989.

3. Harvey, G. A. and J. L. Raper, "Halogen Occultation Experiment (HALOE) Optical Witness-Plate Program," NASA TM 4081, February 1989.

4. Military Standard Product Cleanliness Levels and Contamination Control Program, MIL-STD-1246A, August 18, 1967, Department of Defense, Washington, DC 20301.

5. Harvey, G. A., J. L. Raper, and D. C. Zellers, "Measuring Low-Level Nonvolatile Residue Contamination on Wipes, Swabs, and Gloves," Microcontamination, 8(11): 43-46, 69, 1990.

6. Colony, J. A., "Mass Spectrometry of Aerospace Materials," NASA TN D-8261, June 1976.

7. Glassford, A. P. M. and J. W. Garrett, "Characterization of Contamination Generation Characteristics of Satellite Materials, WRDC-TR-4114," WRDC/MLBT, WPAFB, Ohio, November 1989.

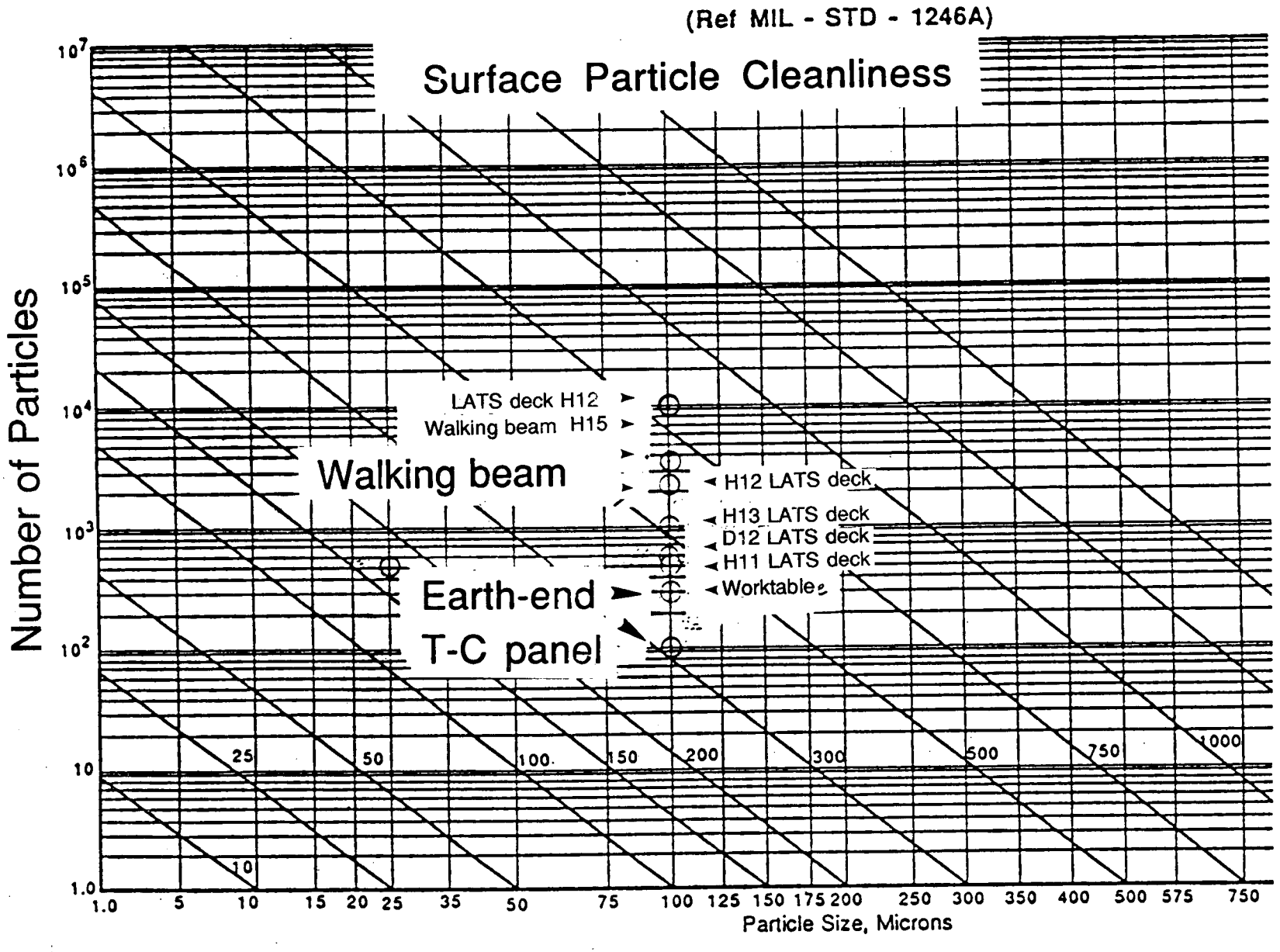

Figure 1. Surface particle cleanliness of LDEF Earth-end panel and walking beam.

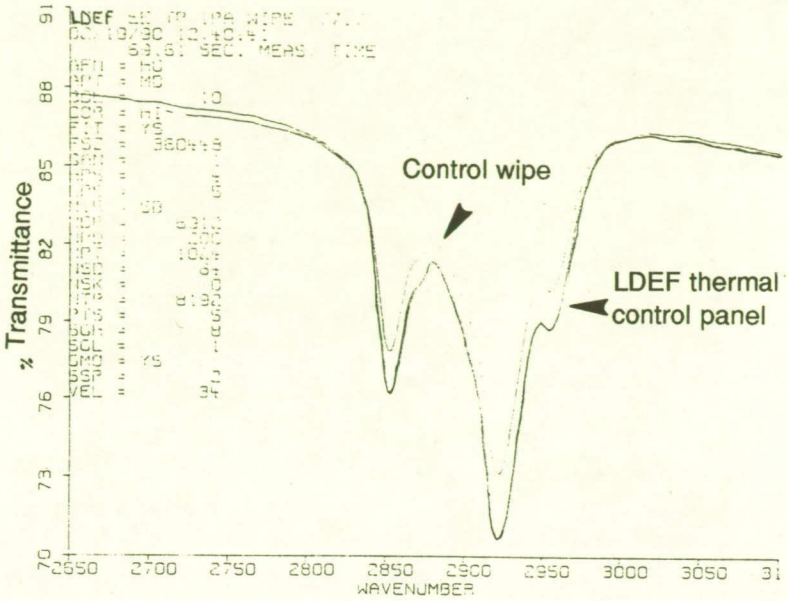

Figure 2. 3.4 μ spectra of Earth-end-panel NVR.

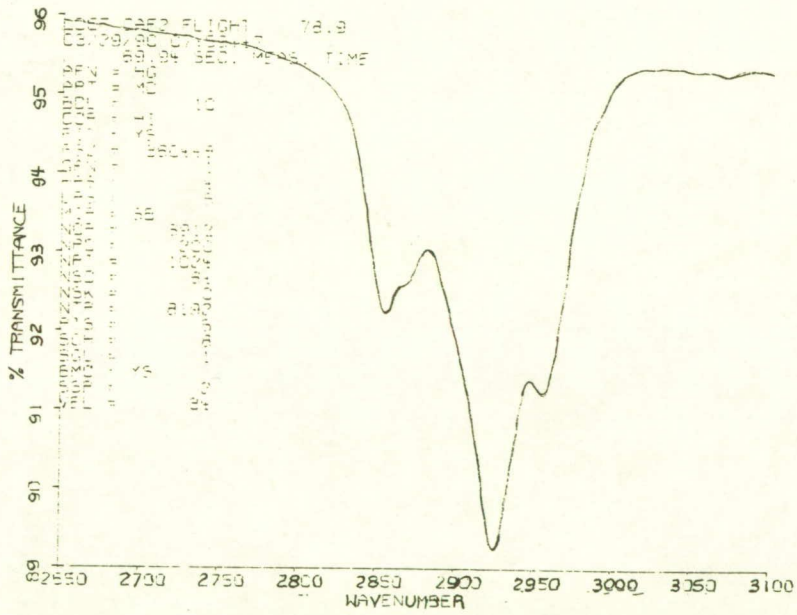

Figure 3. 3.4 μ spectrum of CaF_2 window from Tray E5.

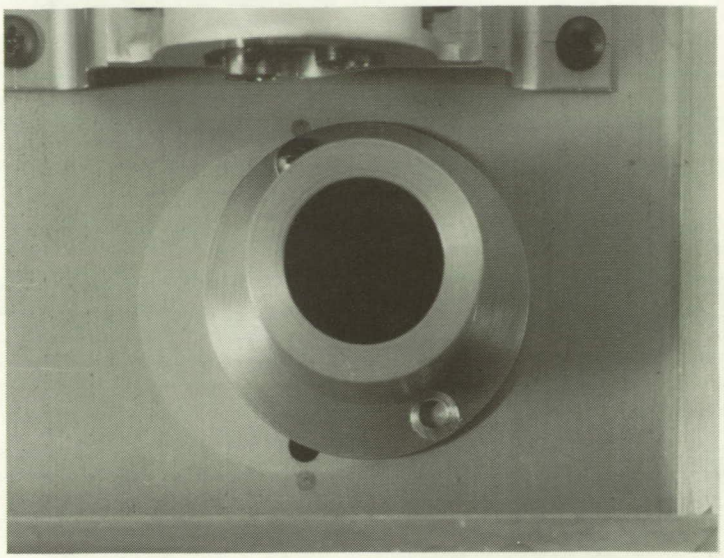

Figure 4. NVR stain in Tray E5.

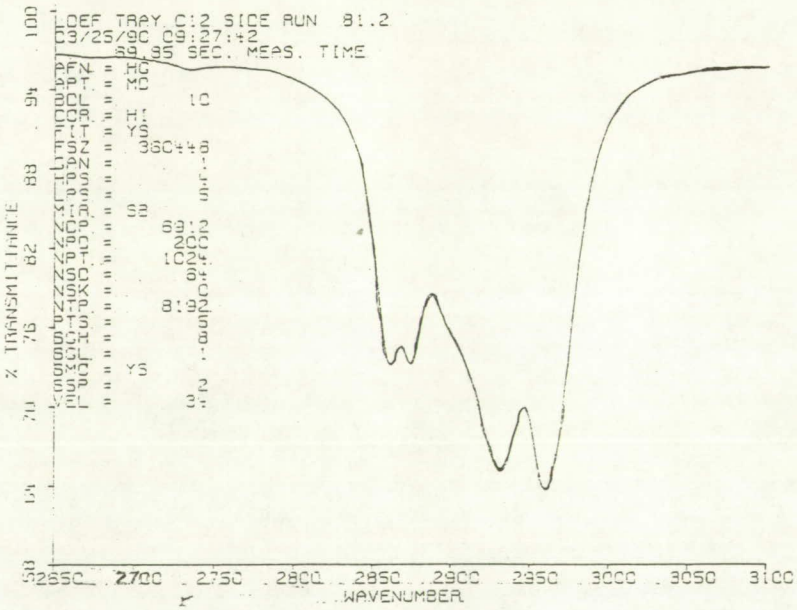

Figure 5. 3.4 μ spectrum of NVR from Tray C12.

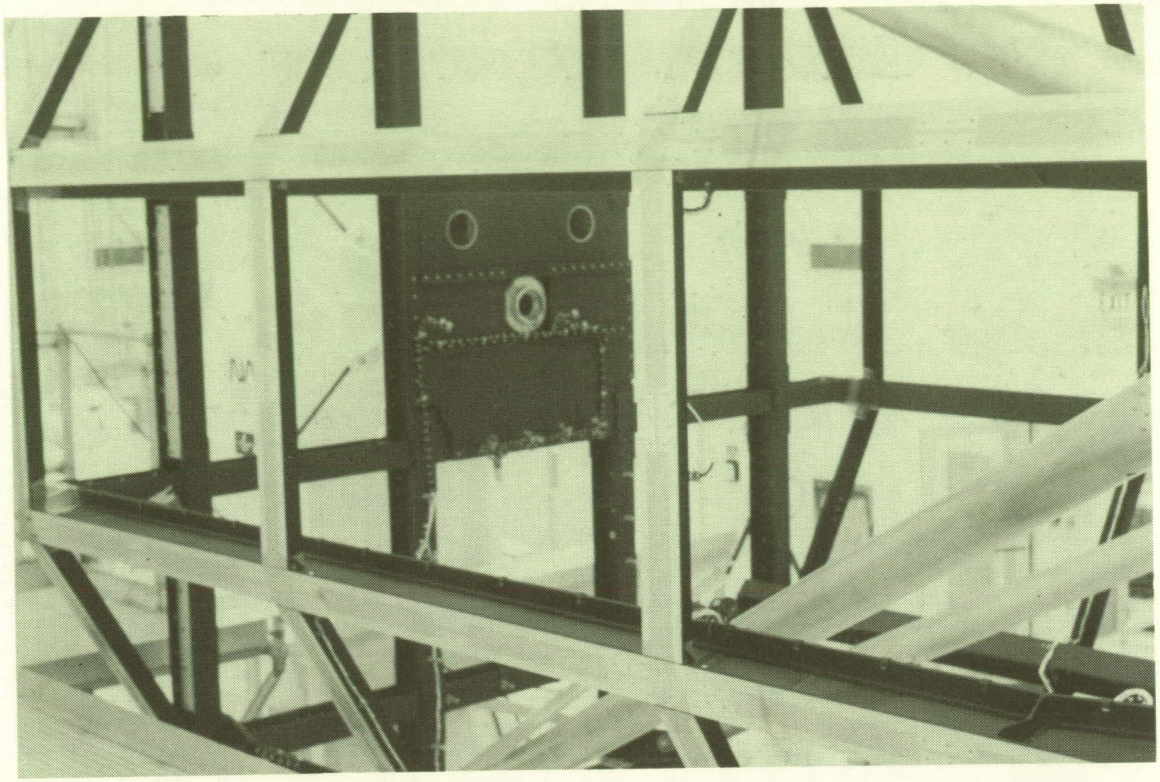

Figure 6. NVR on Earth-end Row 3.

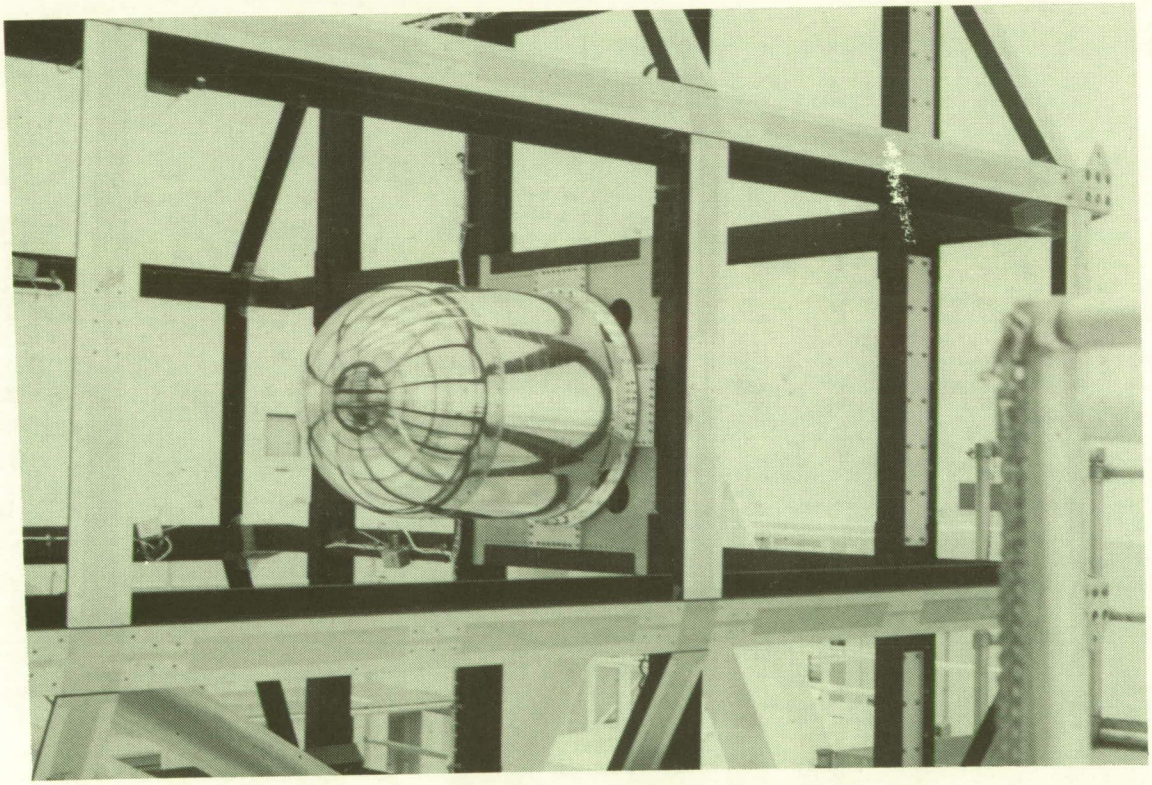

Figure 7. NVR on Space-end Row 3.

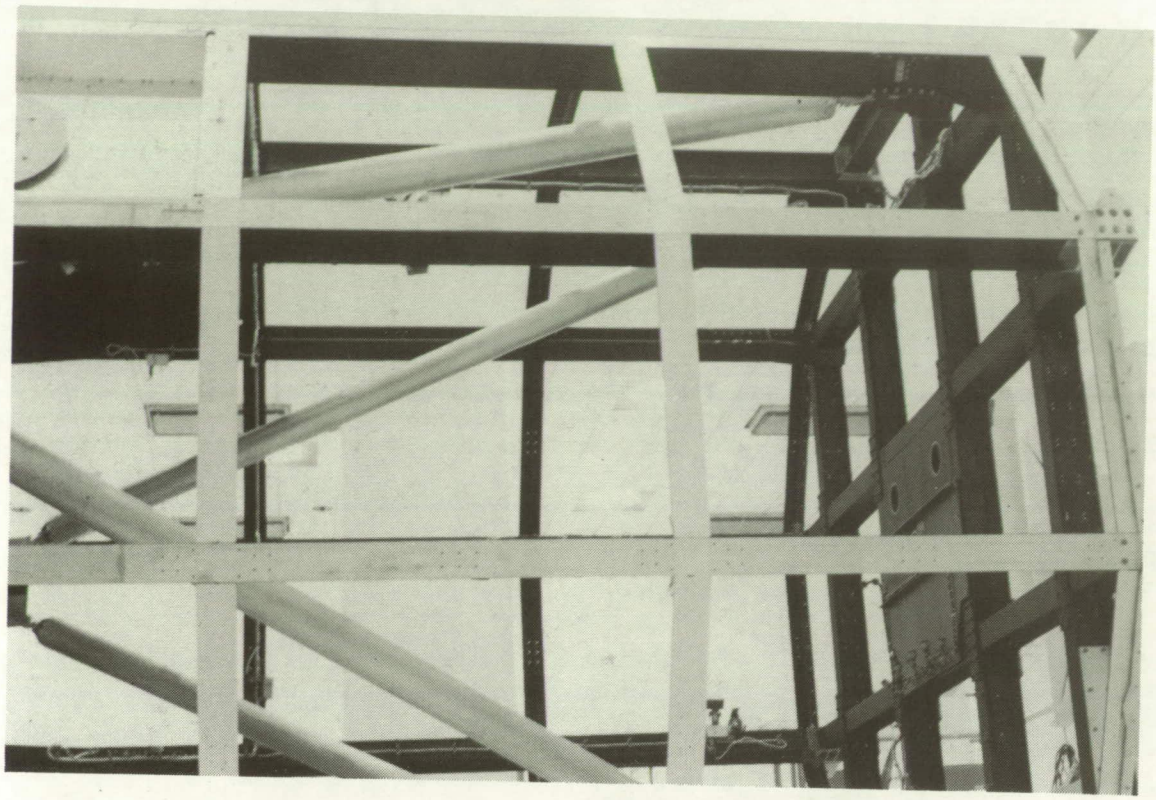

Figure 8. NVR on Earth-end Row 9.

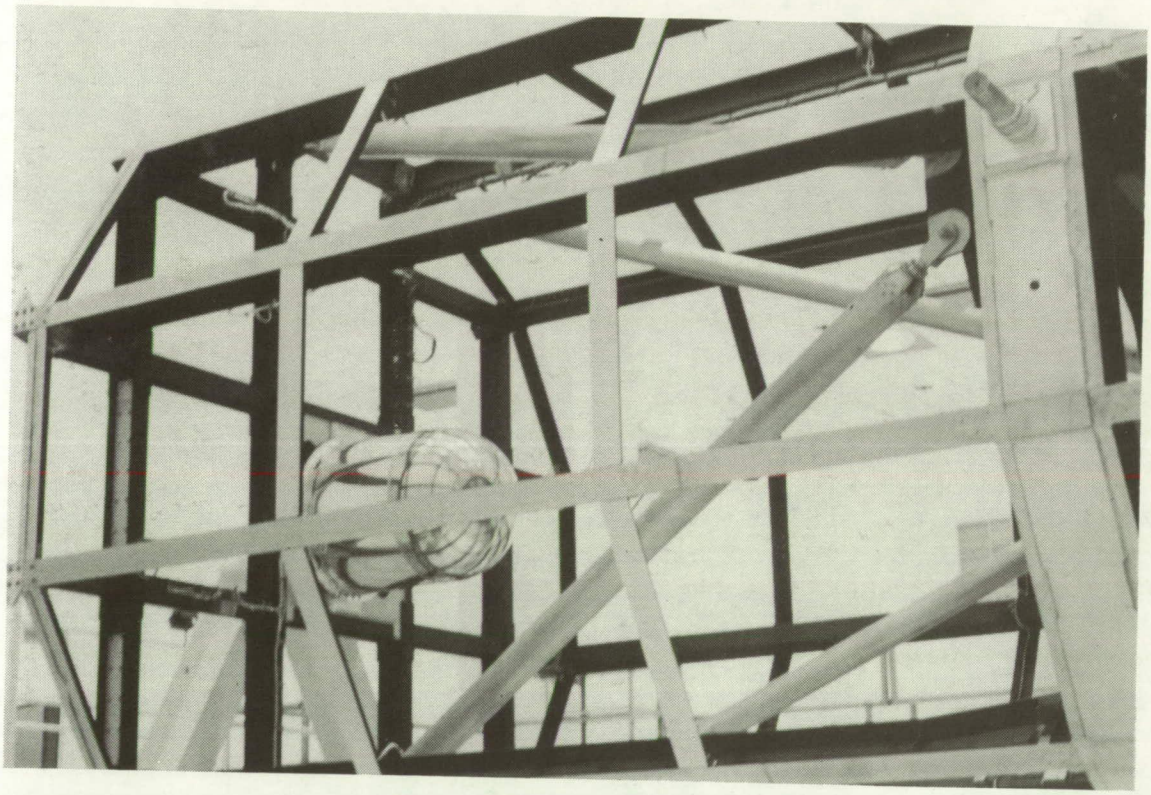

Figure 9. NVR on Space-end Row 9.

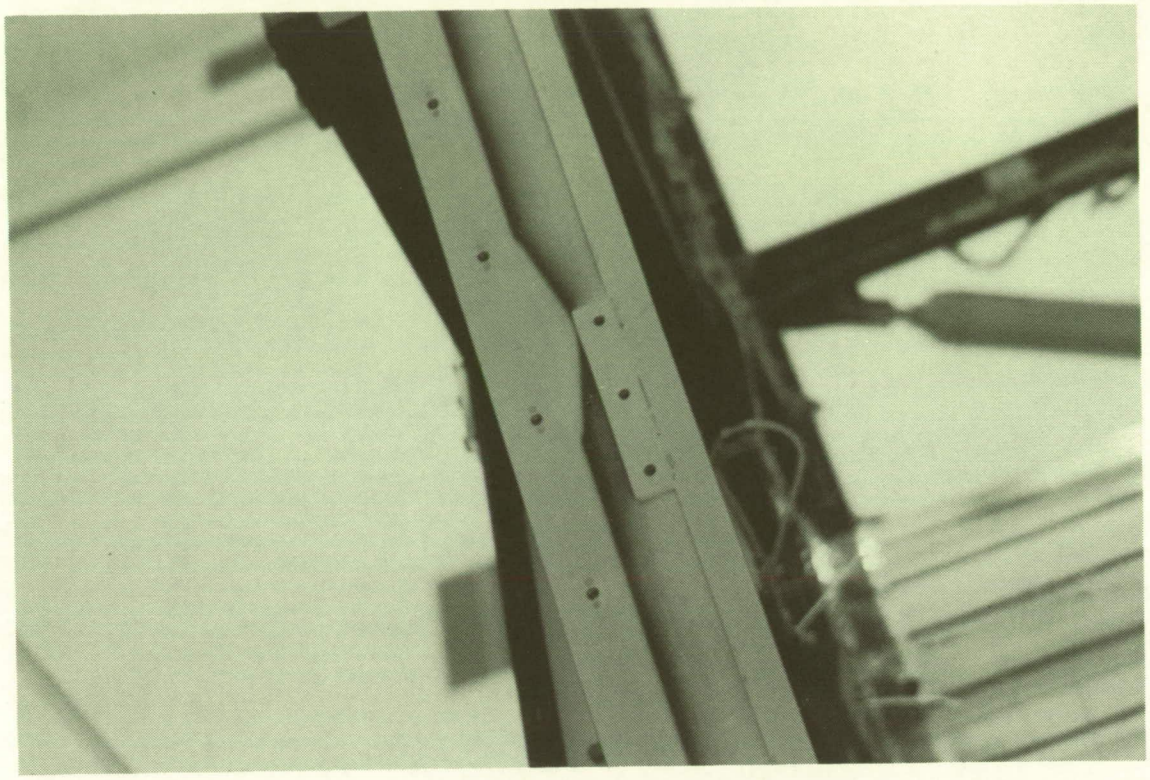

Figure 10. NVR on Space-end intercostal.

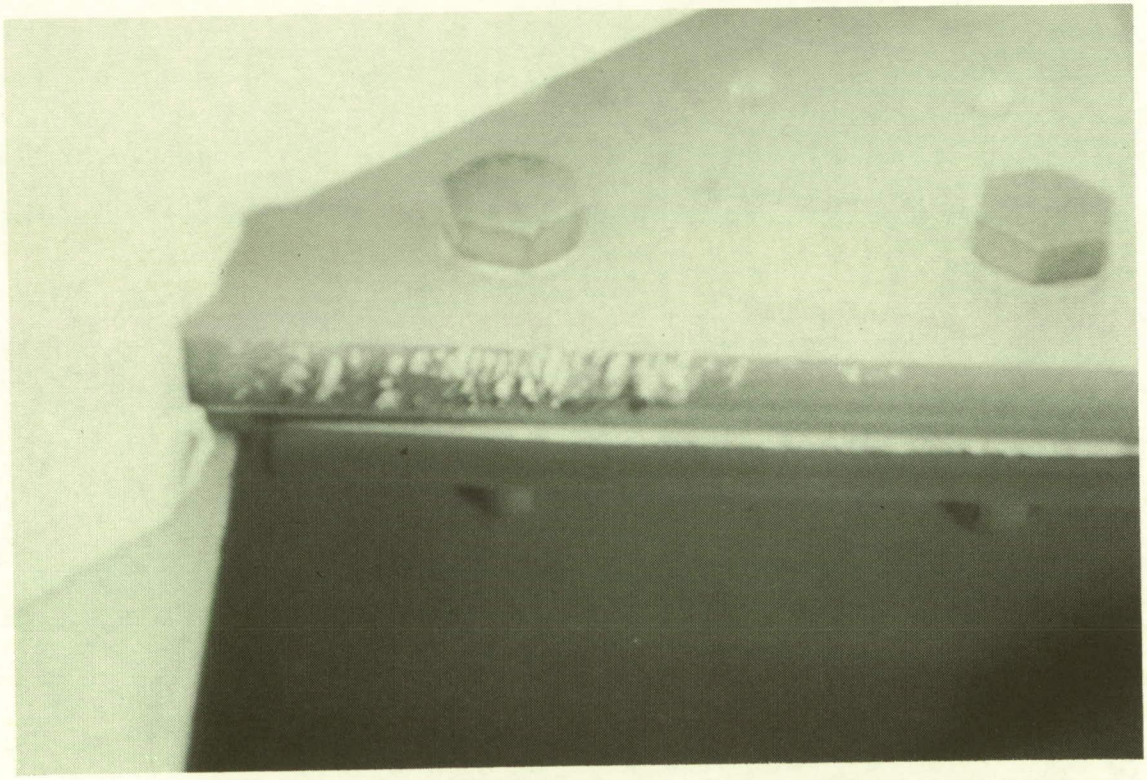

Figure 11. Peeling NVR on Earth-end plate.

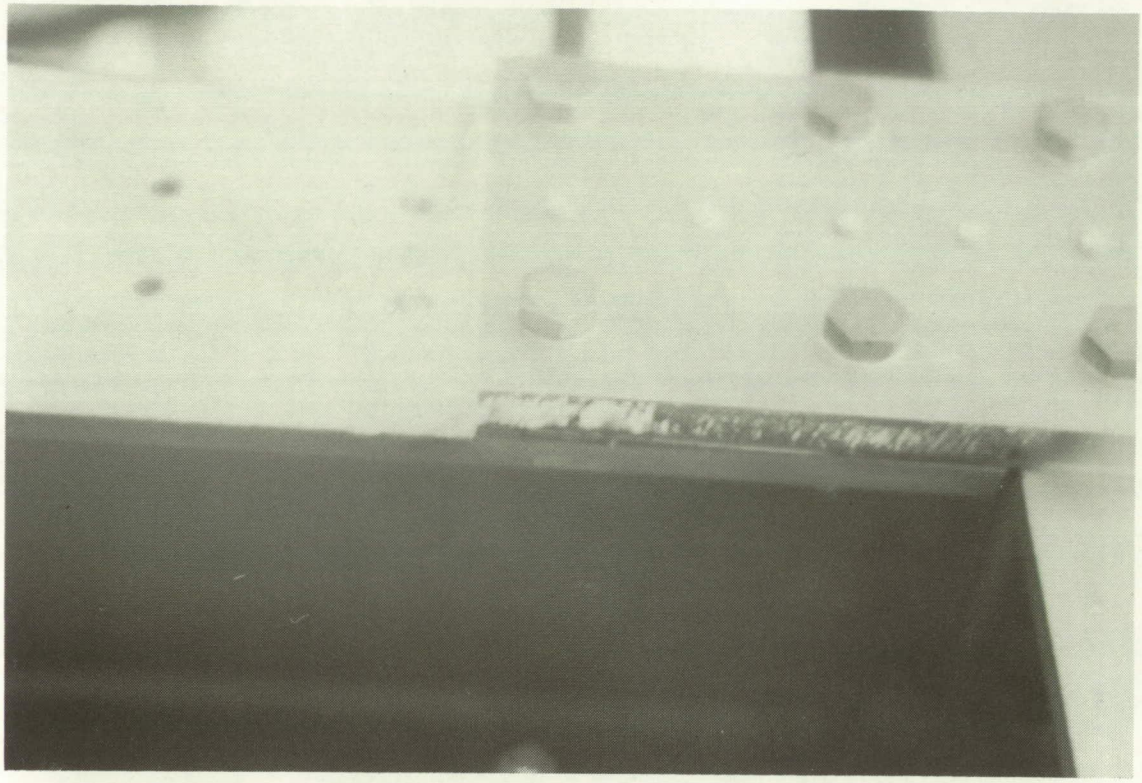

Figure 12. Peeling NVR on Space-end plate.

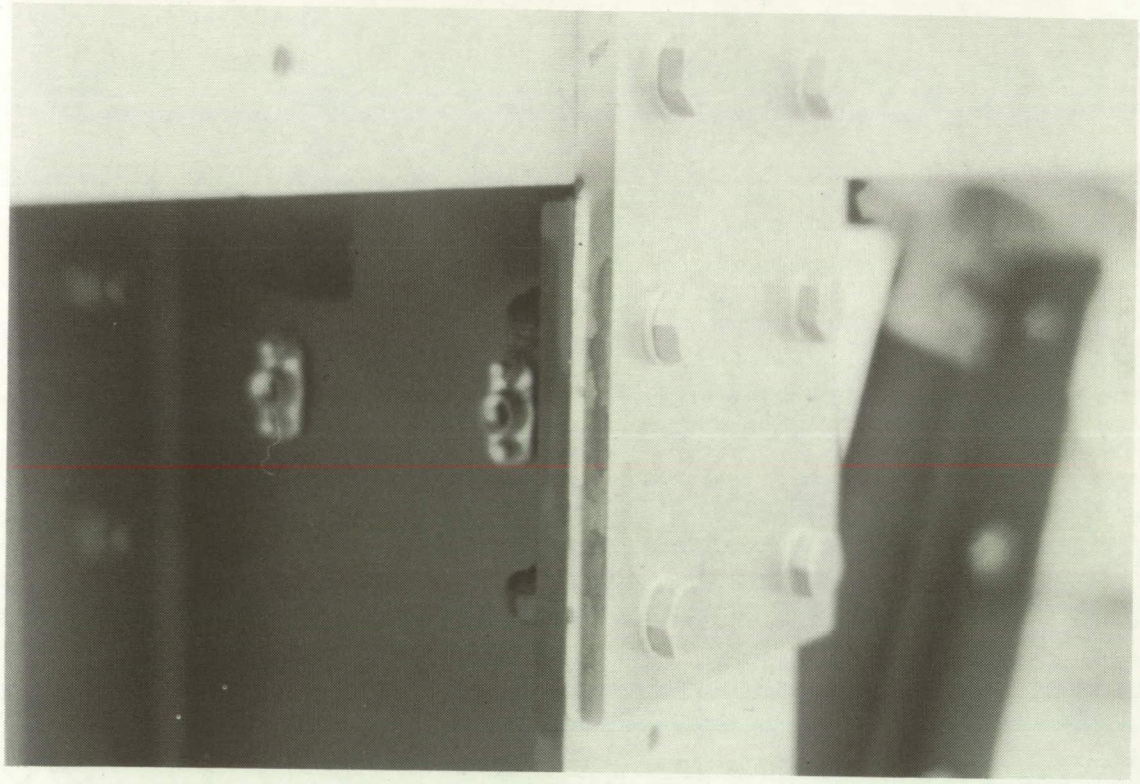

Figure 13. NVR on Space-end plate (ram direction).

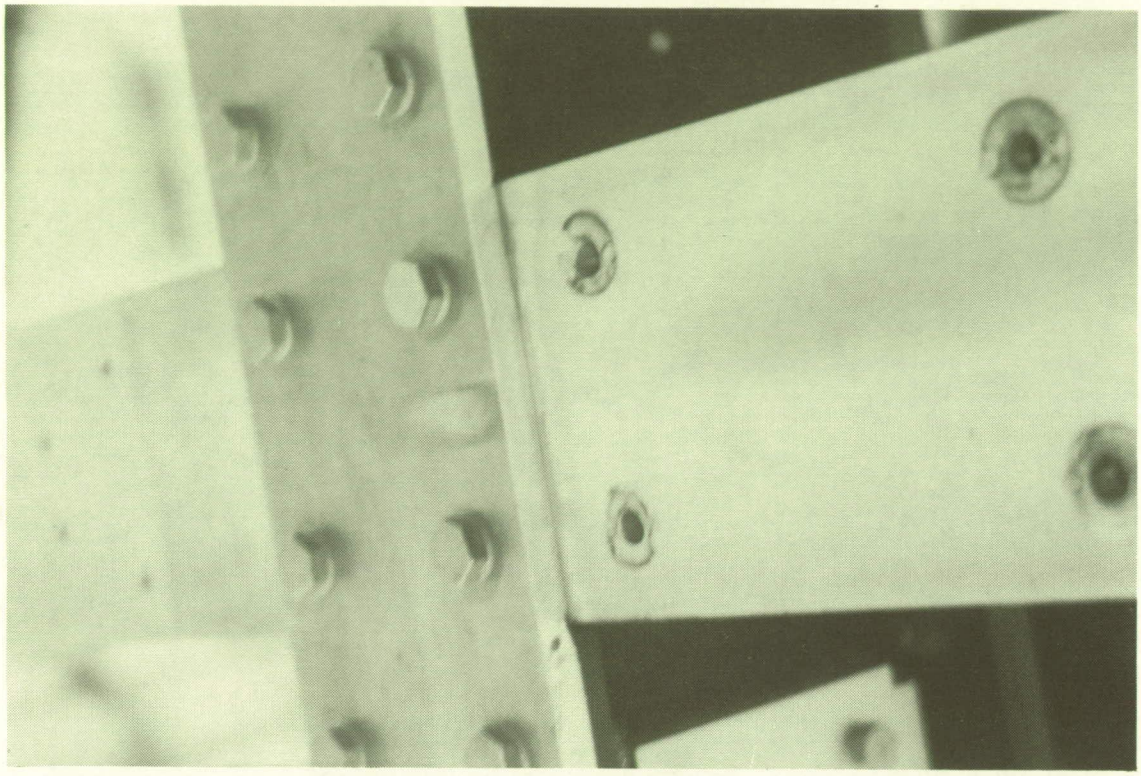

Figure 14. NVR on Space-end plate (trailing edge).

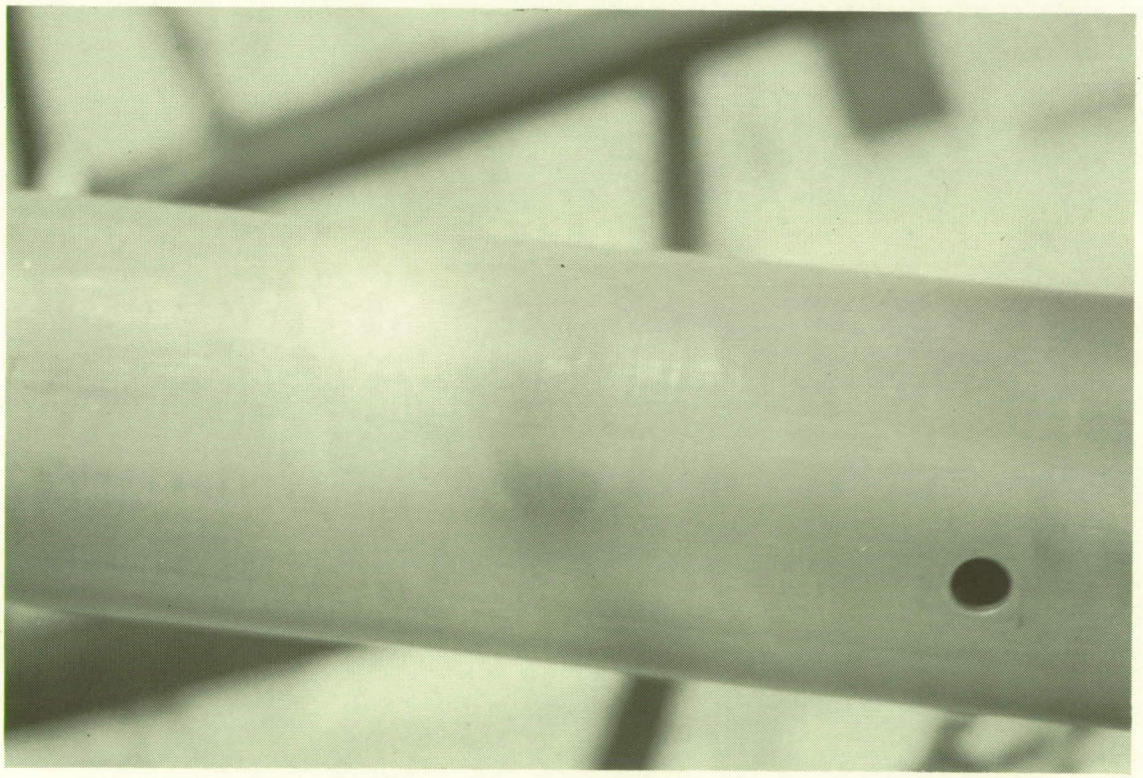

Figure 15. Diagonal brace with NVR stain.

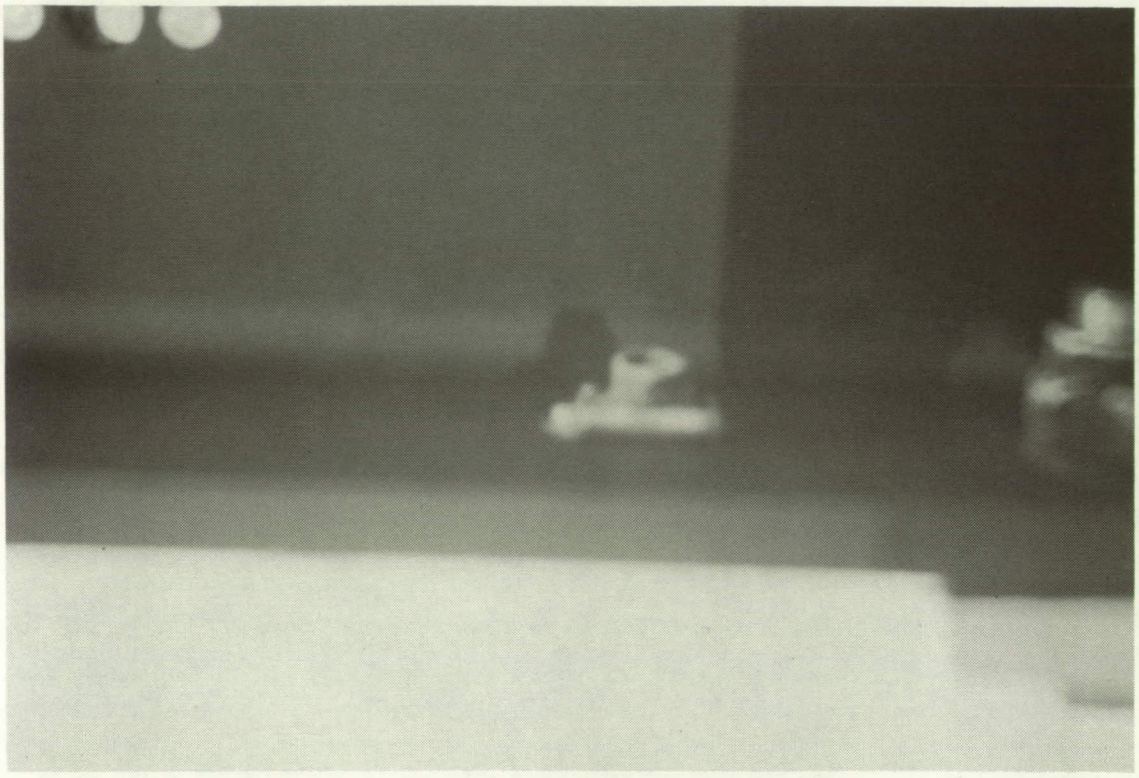

Figure 16. Earth-end interior fastener.

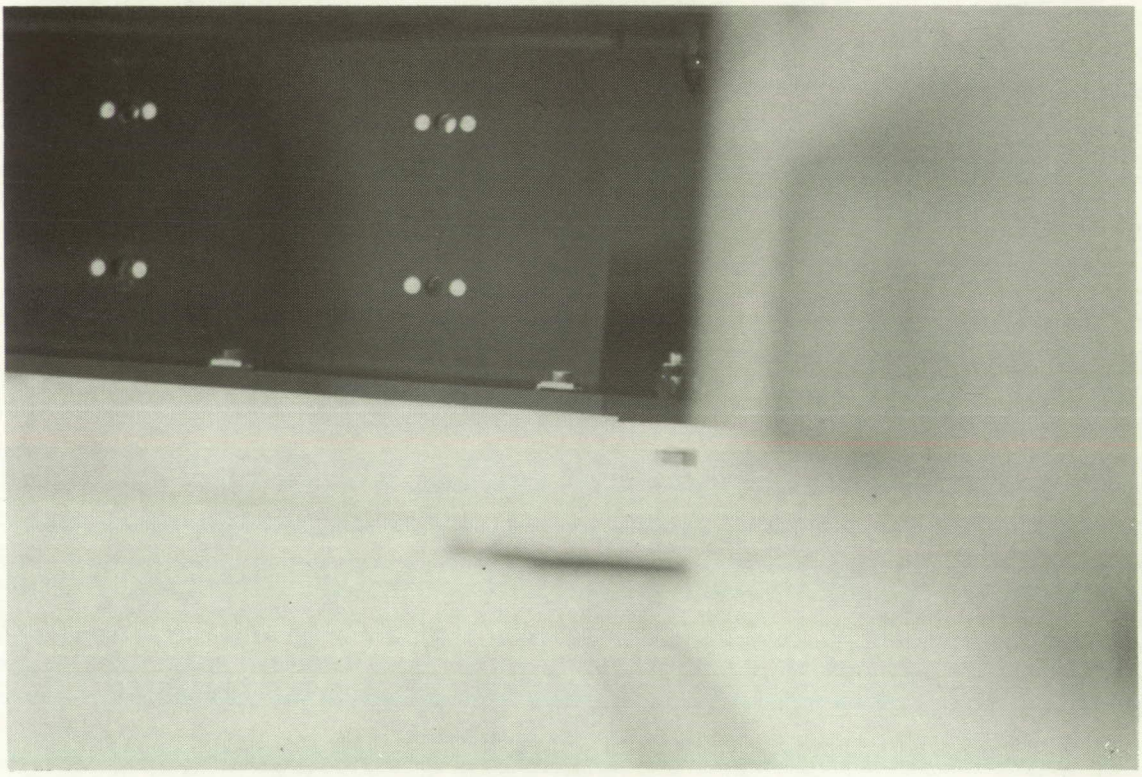

Figure 16a. NVR around interior fastener.

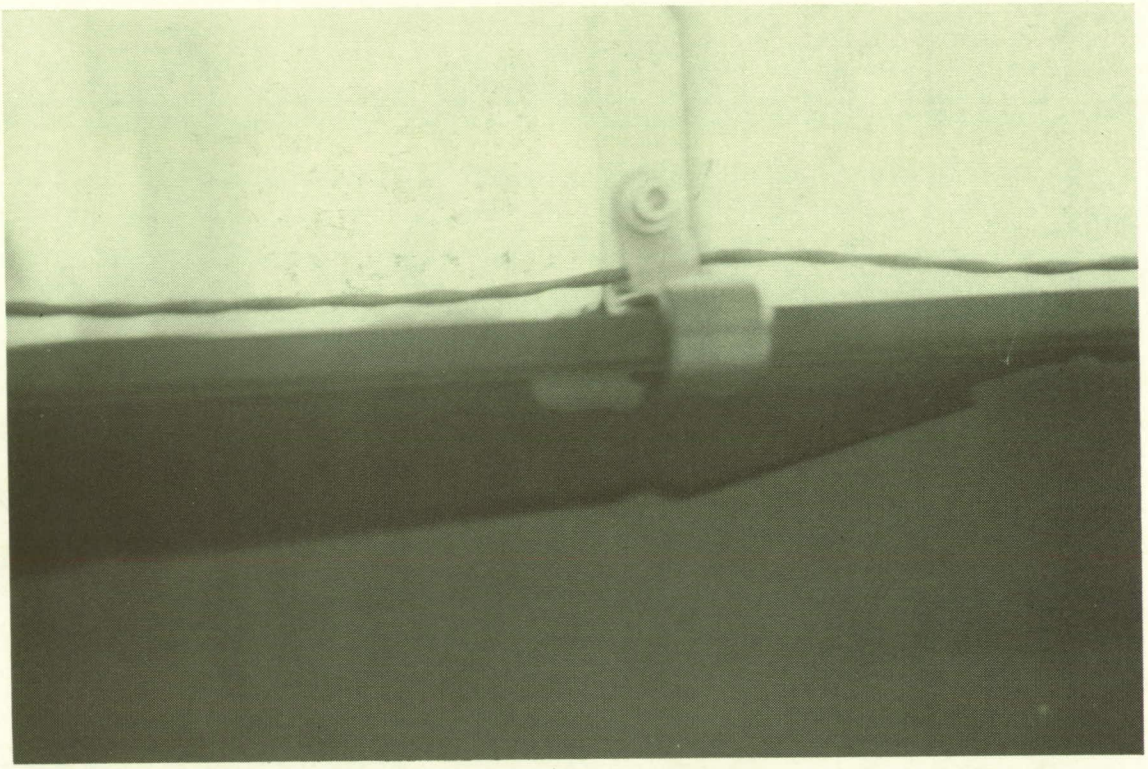

Figure 17. Blue NVR at cable clamp.

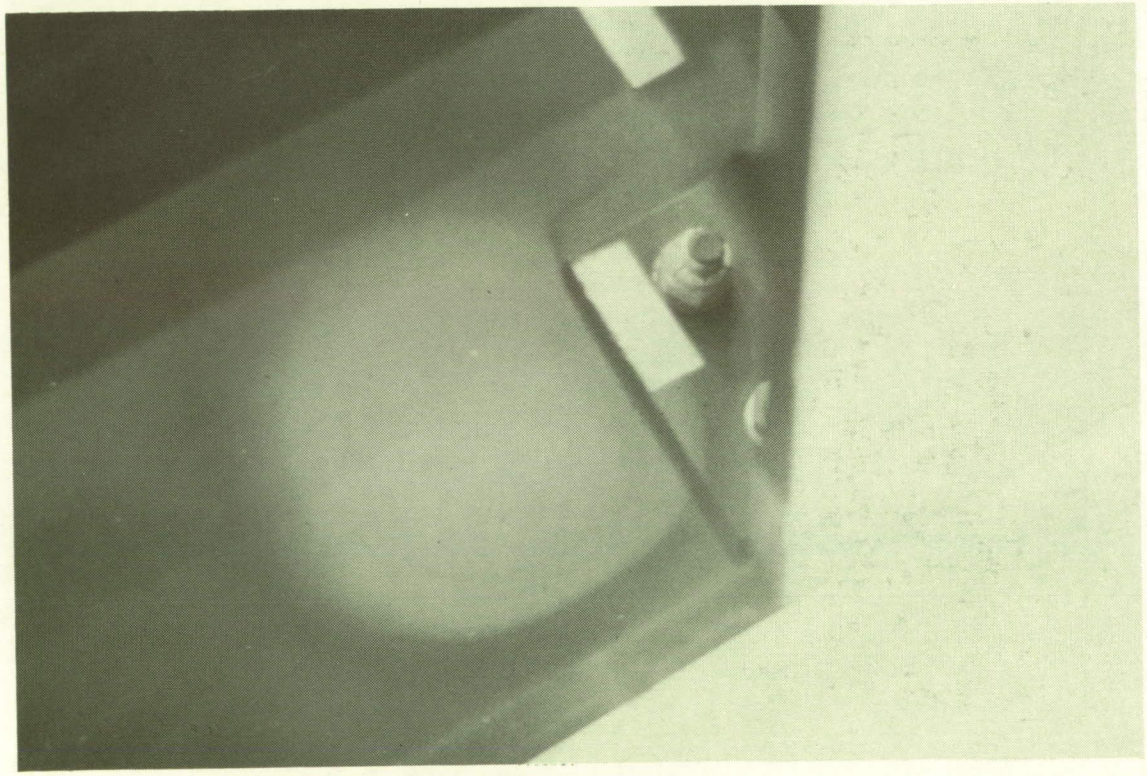

Figure 18. NVR behind tray-corner hole.

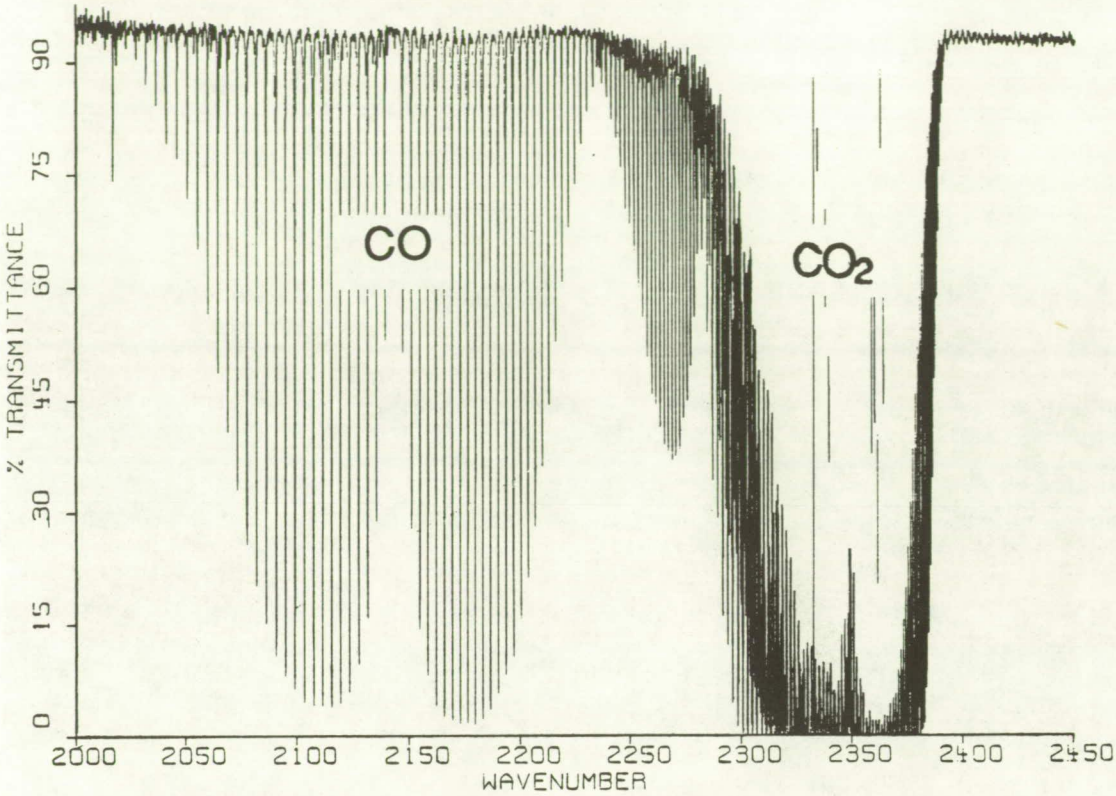

Figure 19. Outgassing of Chemglaz Z306 at 120°C.

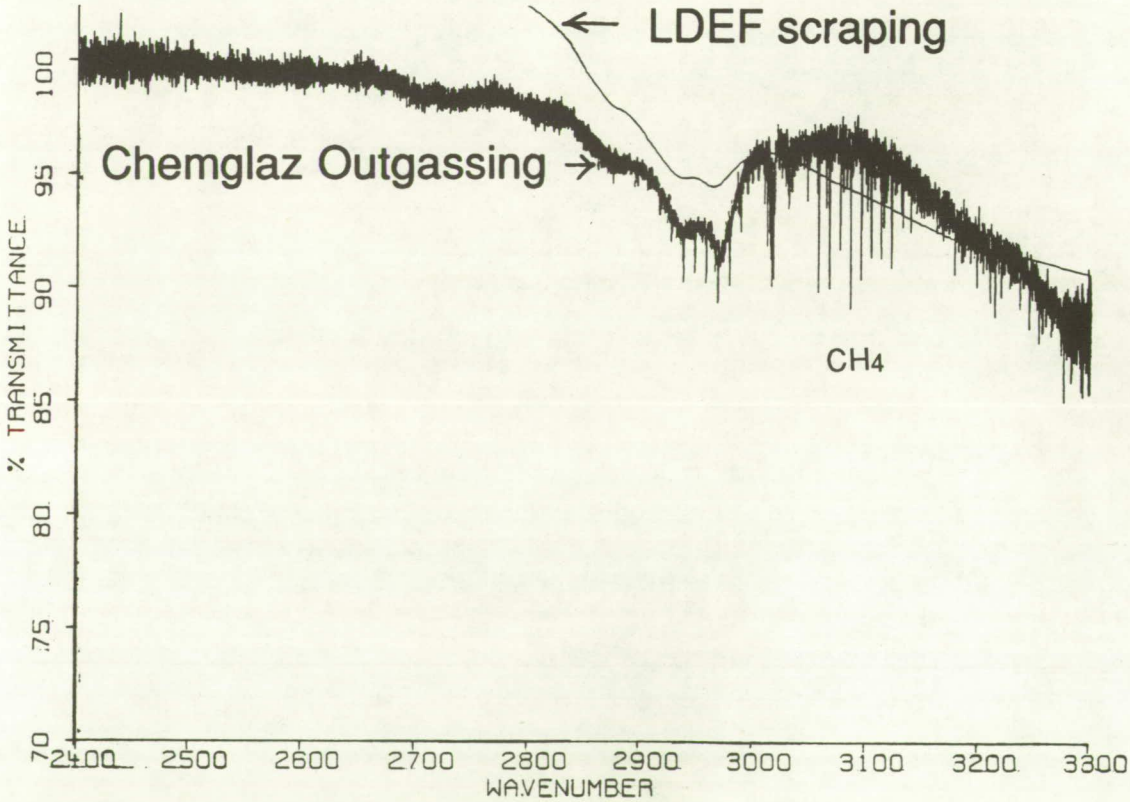

Figure 20. 3.4 μ outgassing of Chemglaz Z306 and LDEF scraping.

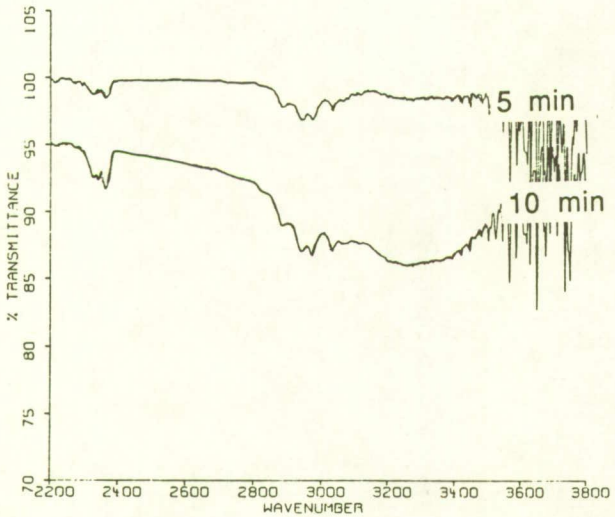

Figure 21. Outgassing of Chemglaz A276 during heating.

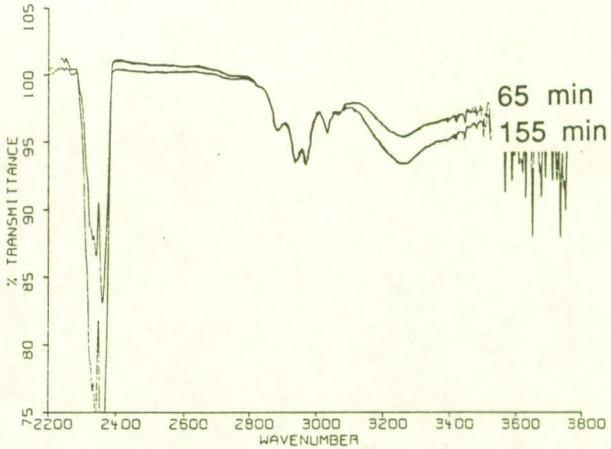

Figure 23. Outgassing of Chemglaz A276 during heating.

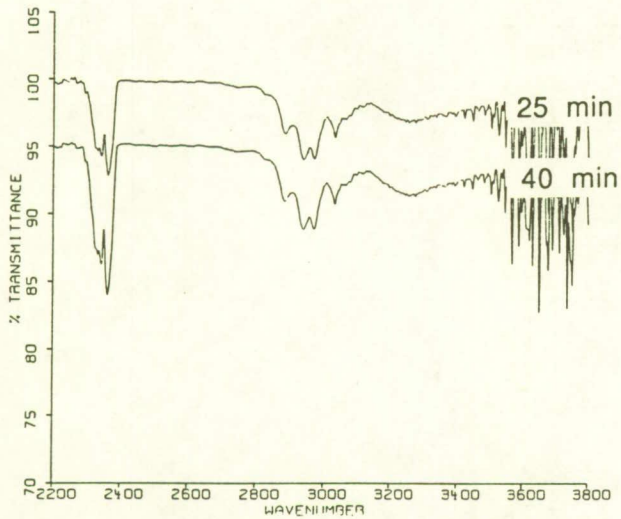

Figure 22. Outgassing of Chemglaz A276 during heating.

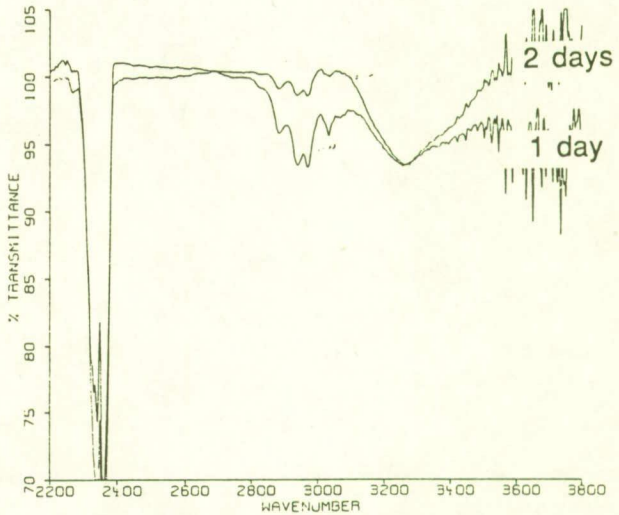

Figure 24. Chemglaz A276 residue.

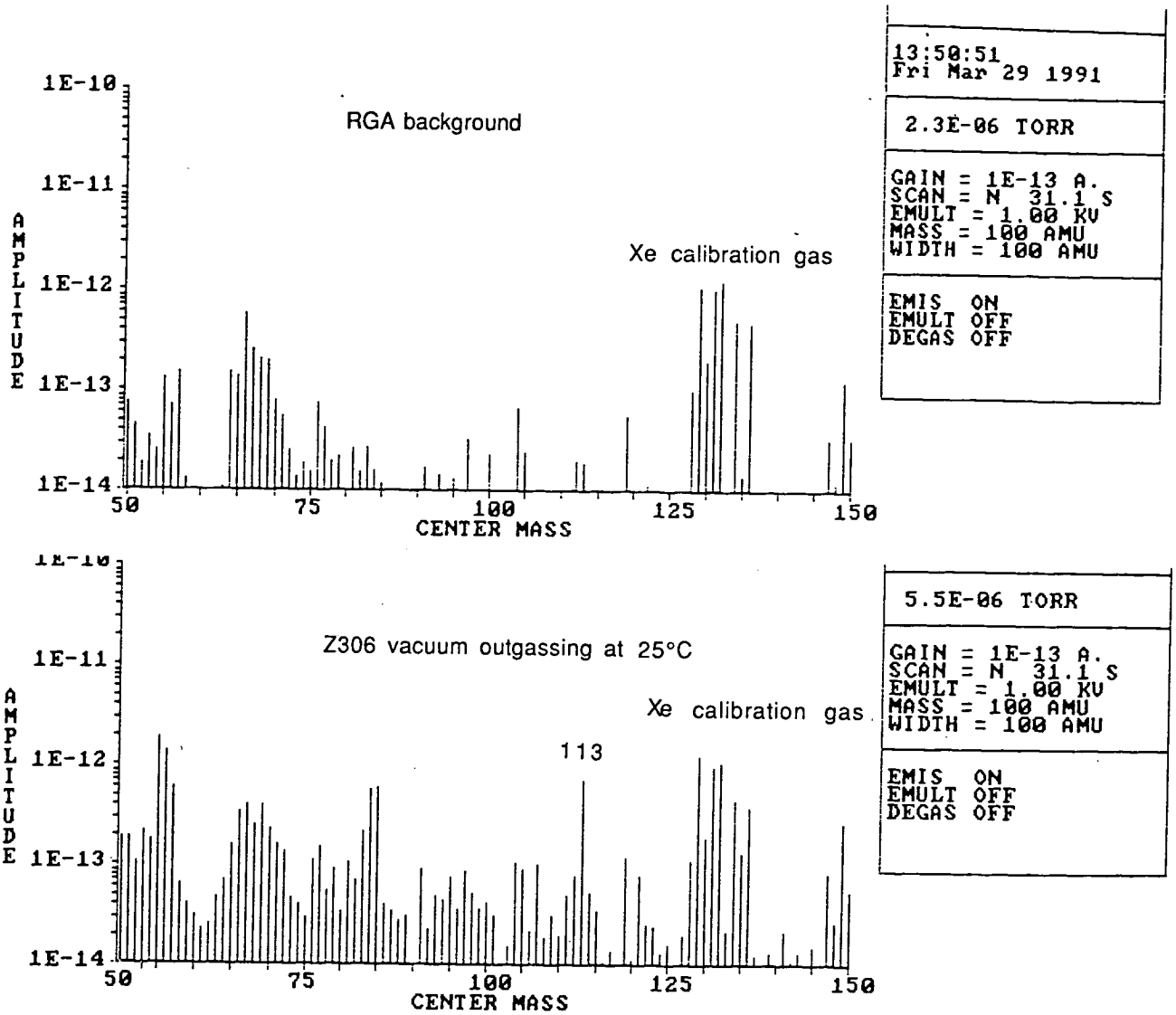

Figure 25. Atomic mass spectrum of Chemglaz Z306 outgassing.

SPACE ENVIRONMENTS
IONIZING RADIATION

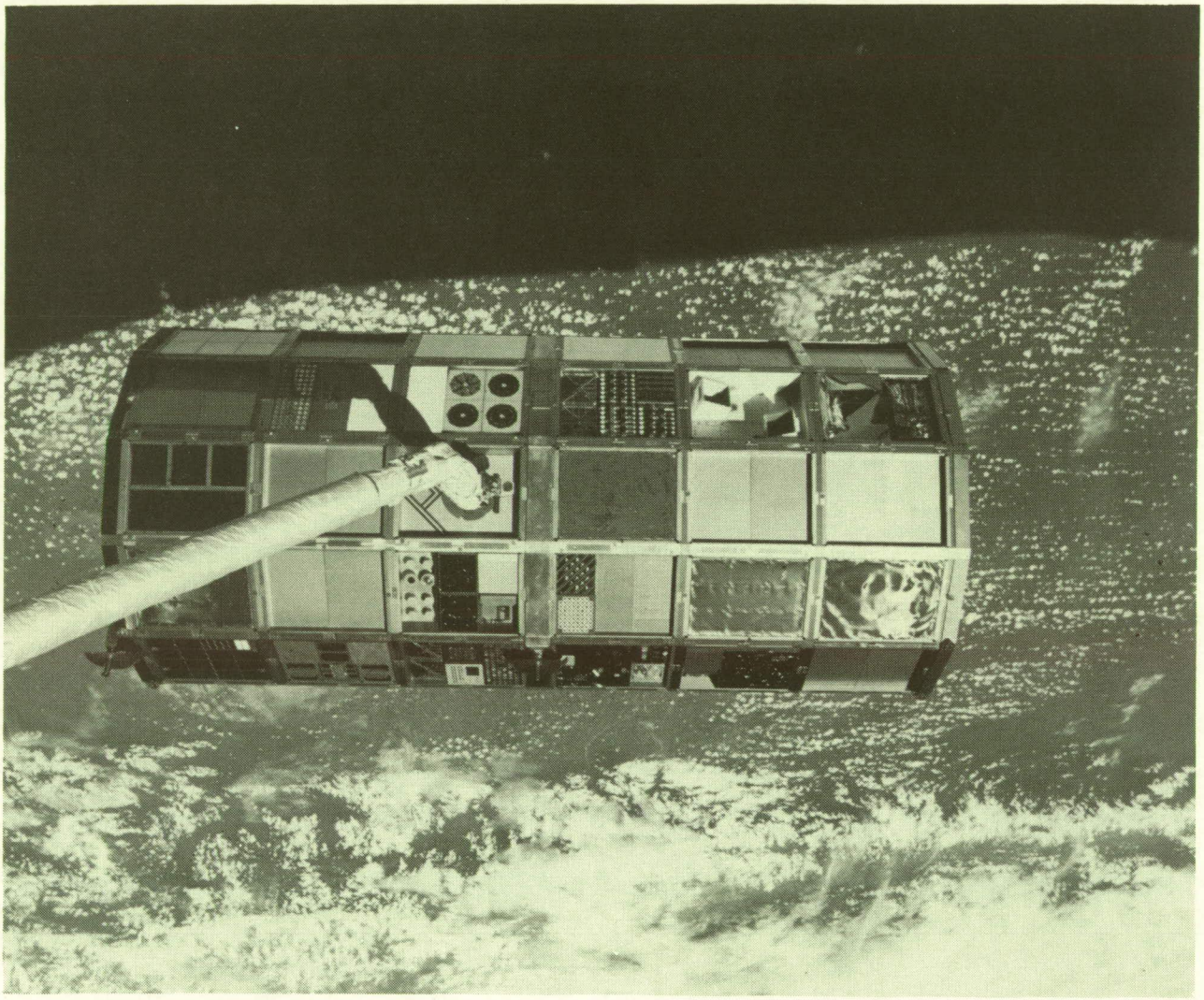

SUMMARY OF IONIZING RADIATION ANALYSIS ON THE LONG DURATION EXPOSURE FACILITY

T. A. Parnell
NASA Marshall Space Flight Center, AL 35812
Phone: 205/544-7690, FAX: 205/544-7754

ABSTRACT

The ionizing radiation measurements flown on the LDEF were contained in 15 experiments which utilized passive detectors to pursue objectives in astrophysics and to measure the radiation environment and dosimetric quantities. The spacecraft structure became sufficiently radioactive to permit additional important studies. The induced activity allows extensive radiation mapping in the structure, an independent comparison with experiment dosimetric techniques, and significant studies of secondary effects. The long exposure time, attitude stability, and number and types of measurements produced a unique and critical set of data for low Earth orbit that will not be duplicated for more than a decade. The data allows an unprecedented test, and improvement if required, of models of the radiation environment and the radiation transport methods that are used to calculate the internal radiation and its effects in spacecraft. Results of measurements in the experiments, as well as from radioactivity in the structure, have clearly shown effects from the directional properties of the radiation environment, and progress has been made in the dosimetric mapping of LDEF. These measurements have already influenced some Space Station Freedom design requirements. Preliminary results from experiments, reported at this symposium and in earlier papers, show that the 5.8 years exposure considerably enhanced the scientific return of the radiation measurements. The early results give confidence that the experiments will make significant advances in the knowledge of ultraheavy cosmic rays, anomalous cosmic rays, and heavy ions trapped in the radiation belts. Unexpected phenomena have been observed, which require explanation. These include stopping iron group ions between the energy ranges anticipated for anomalous and galactic cosmic rays in the LDEF orbit. A surprising concentration of the ^{7}Be nuclide was discovered on the "front" surface of LDEF, apparently transported up from the stratosphere with exceptional efficiency. LDEF will clearly be a landmark mission in astrophysics and in the study of the radiation environment in LEO.

INTRODUCTION

The Long Duration Exposure Facility (LDEF) carried 9 experiments designed to study particular aspects of the ionizing radiation encountered during the mission. Six more experiments included detectors for radiation monitoring. In addition, the spacecraft structure and experiment materials acquired a low (~1 to ~100 pico Curies per kg) level of radioactivity. The distribution of the induced radionuclides in samples of the LDEF structure, measured in sensitive gamma ray spectroscopy facilities, allows significant additional studies of the radiation environment and its interaction with the spacecraft.

The radiation measurements on LDEF are listed in Table 1. Three experiments (A0178, M0001, M0002-2) (refs. 1,2,3,4) were designed to measure the composition and spectra of galactic or "anomalous" cosmic rays. M0002-2 also studied heavy ions trapped in the Earth's magnetic field. Experiment M0002-1 (ref. 1) had multiple detectors at different locations to measure the trapped proton

fluence, energy spectra and directional characteristics. Experiments P0006, P0004, M0004, and A0015 (refs. 1,5,6,7,8,9,10) contained a variety of passive detectors to measure the radiation dose, heavy particle fluence, linear energy transfer (LET) spectra, and several aspects of the secondary radiations including neutrons and the concentration of heavily ionizing recoil nuclei. These experiments contained detectors at various shielding depths typically encountered in manned spacecraft. The experiments are described further in NASA SP 473 (ref. 1), papers of this symposium, and the referenced experiment reports. Table 1 summarizes the radiation measurements and lists the detector types and principal measurement categories in each.

The cosmic ray experiments address fundamental questions about the nucleosynthesis of heavy elements in the galaxy, and acceleration of the nuclei to high energies. A0178 measured the elemental abundances of galactic cosmic rays above atomic number 65. It will make the most significant study yet of the actinides (eg. thorium, uranium) in the cosmic rays, and will define their abundance relative to lighter elements (eg., platinum, lead). This data will reveal the importance of rapid (explosive) nucleosynthesis for heavy element production in the galaxy. M0001 was designed to study both galactic and anomalous cosmic rays. The low energy "anomalous" nuclei are now thought to be from the interstellar gas which enters the solar system, becomes partially ionized, and is then accelerated (by shock waves) up to a few tens of MeV. These particles carry information about the interstellar medium and particle acceleration in the solar system. In addition to anomalous cosmic rays, experiment M0002-2 also studied low energy heavy ions that are trapped in the inner radiation belt. The trapping mechanism for these particles is not understood.

Experiments P0006, P0004, A0015, and M0004 contained a variety of passive detectors to measure absorbed dose, particle fluences, linear energy transfer spectra, and neutrons. The P0004 detectors were distributed at various depths in the seeds experiments (P0004-1,2)(ref. 1). A0015 carried many detectors to characterize the radiation exposure of biological samples. Some of these detectors were used to locate heavy nucleus tracks which passed through the biological samples. P0006 comprised a comprehensive set of dosimetric detectors at precisely defined shielding depths in the seeds experiments tray. Experiments M0003, M0006, and A0138-7 (ref. 1) also carried detectors for local radiation dose monitoring.

A set of 5 metal samples (Co, Ni, Ta, V, In) (ref. 11) of approximately 100 gm each were placed in 5 separate locations around LDEF. The metals were selected for specific activation products and cross-sections to study the activation process and to measure the flux of the activating particles (trapped protons, cosmic rays, and neutrons). The flux and spectra of neutrons, which have not been frequently nor definitively measured in spacecraft, can be studied through activation reactions which are exclusively, or partially, caused by neutrons.

In addition to the activation detectors intentionally placed on LDEF, the 5.8 years of exposure caused the radioactivity induced by trapped protons and cosmic rays in aluminum, stainless steel, titanium, lead, and other metals of the spacecraft structure to reach significant levels (11,12,13,14,15). Although the activity was small (~1 to ~100 pico Curies/kg), it was readily measured with high resolution gamma ray spectrometers. The initial activation measurements were made of the full spacecraft (between 2 weeks and 2 months of LDEF recovery) with a cooled germanium detector array (ref. 16) at Kennedy Space Center. Subsequently, about 400 samples of the metal structure of LDEF (and some experiment samples) have been measured in shielded low background spectrometers at nine laboratories (refs. 17,18,19,20). The activation data set is an important complement to dosimetry measurements performed in experiments. It forms a complete dosimetric map of LDEF, filling in gaps where other experiment data do not exist, and gives a measurement independent from other dosimetric techniques (e.g., thermoluminescent dosimeter (TLD) dose), which could be subject to different errors. This data set will be a

definitive benchmark for methods that are used to calculate activation in space.

The set of passive radiation measurements on LDEF is the most comprehensive yet flown on low Earth orbit missions. The value of these measurements is enhanced by the spacecraft's Earth-fixed flight attitude (which is the same for SSF). This allows the directional characteristics of the ambient radiation (refs. 21,22,23,14), and its effects at various shielding depths, to be studied. The large number and variety of measurements at various locations and shielding depths, the orbit, the attitude stability, and the long duration make this a valuable and unique data set for studies of the LEO radiation environment.

RADIATION ENVIRONMENT PREDICTIONS

Predictions of characteristics of the radiation environment and its effects, such as absorbed dose, in LEO have been generally accepted as accurate to a factor of ~2, but predictions with different codes and assumptions have often differed by a larger factor. Single event upset predictions can differ among methods by a factor of 10. Secondary radiations such as neutrons and recoil nuclei have been difficult to measure on spacecraft. Measurements of the secondaries are scarce and corresponding predictions are more rare. Furthermore, the directional characteristics of the trapped proton flux have been previously ignored in predictions of effects, and for spacecraft stabilized like LDEF in 28.5° orbits, this causes a variation in magnitude of 2-3, which is strongly dependent on location in the spacecraft. The present uncertainties in radiation prediction would lead to significant impacts in a number of future programs. For long duration missions such as the Space Station and AXAF, uncertainties in predictions can lead to increased costs in electronic parts, or unfavorable trade-offs between manned mission duration and orbital decay rates, or uncertainty in degradation and replacement cycle of observatory instruments. The LDEF radiation data will considerably improve prediction methods for resolution of these kinds of issues.

IONIZING RADIATION SPECIAL INVESTIGATION GROUP

The LDEF Special Investigation Groups (SIG's) (Materials, Meteroid and Debris, Systems, Ionizing Radiation) were chartered to perform measurements and analyses that were not a part of the LDEF experiments objectives but are important for application to future missions. The SIG's must ensure that relevant and applicable information for design and development of future missions is reported and archived, and that the results will be in a form useful to those programs. Each SIG defined specific objectives toward these general goals, in accord with programmatic constraints. The main elements of the Ionizing Radiation Special Investigation Group (IRSIG) operating plan are shown in Figure 1.

The IRSIG has concentrated its efforts in the following areas:

1. Pre-recovery predictions of radiation dose, particle fluences, LET spectra and radioactivity (refs. 11,12,13,22,24).

2. A post-recovery radiation safety inspection. This inspection was performed soon after Columbia's payload bay doors were opened in the Orbiter Processing Facility (OPF) with hand-held survey detectors, and dry wipes of small areas. No radioactivity enhancements above background were detected with the survey instruments. KSC personnel performed these surveys.

3. A full spacecraft activation measurement. This measurement was performed for two months in the SAEF II building, while experiment trays were removed, with a very sensitive germanium spectrometer array (ref. 11,16).

4. A program was organized to measure the induced activity in about 400 samples of the spacecraft structure and experiments materials selected at many locations and shielding depths (refs. 11,14,15). The activation measurement data set provides an excellent test of calculational methods such as the directional trapped proton environment model, the High Energy Transport Code (HETC), and other methods to predict activation in spacecraft. Furthermore, the activation measurements and prediction methods are of great interest to the gamma ray astronomy community (e.g., GRO, Mars Orbiter, etc.).

5. Accumulate the radiation data and analysis results from experiments as available, and supply the experimenters with environment calculations and analyses as they become available.

6. Using LDEF data, validate or improve models of the radiation environment and the calculation methods for radiation transport and effects. The environment modeling and calculation program is described in refs. 12,13,14,23,25. The main models and calculations to be applied are the AP8 trapped proton model, AE 8 trapped electron model, a new model for trapped protons which combines AP8 with the directional properties of the protons, methods for calculating induced radioactivity (e.g., the HETC), the cosmic ray environment and methods for calculating linear energy transfer (LET) spectra [e.g., the Cosmic Ray Effects on Microelectronics (CREME) code, and the HETC code]. The definitive application of these methods requires a detailed mass model of the LDEF structure and selected experiment trays, which is currently under development (ref. 25). The principal environments and calculational codes to be employed by the IRSIG are shown in Figure 2 from (ref. 23).

7. The LDEF IRSIG is supporting a number of post-recovery radiation analysis efforts which require accelerator exposures for the calibration of detectors or for the assessment of possible radiation effects. Due to the low altitude and inclination orbit, and the relatively low radiation dose (refs. 22,24), significant radiation effects were not anticipated. Only a few experiments have reported either confirmed or suspected radiation effects.

8. The documentation and archival of data, models, and methods is a major task of the IRSIG. In addition to written reports and summaries of results, the environment models and calculation methods will be documented and placed in accessible networks. The induced activity data and prediction methods will be a major subset of the archive. Activation results (including the occurrence of unusual amounts of nuclides in the original material that have been discovered) will be archived in the Materials and Processes Technical Information System (MAPTIS).

MOST SIGNIFICANT EARLY RESULTS

The early results of the LDEF radiation measurement are covered in subsequent papers of this symposium and in referenced published results. Only a few highlights are listed here.

1. The effects of directional properties of trapped protons have been clearly observed in the following measurements:

a. Absorbed dose from thermoluminescent dosimeters (TLD's) in P0006, P0004, M0004. The West/East ratio is about 2.5 near the LDEF surface (refs. 14,23,26*).Figure 3 illustrates the dose

* unpublished

data along with predictions using the AP8 proton omnidirectional model. These calculations, using two simple shield configurations, show that the omnidirectional proton model cannot match the LDEF data.

b. Induced radioactivity in aluminum tray clamps (^{22}Na gamma ray line) from locations around LDEF (refs. 14,15). Figure 4 displays the ^{22}Na activation data from the tray clamps with a simplified calculation using the proton directional model.

c. The Na^{22} line variation around LDEF observed by the full spacecraft activation measurements (ref. 16).

d. Radioactivity in two stainless steel trunion layers (^{54}Mn gamma ray line) from the leading and trailing sides (refs. 14,15,23).

The analysis of these data (and additional measurements in progress) will provide a high precision test of the new directional model of trapped protons, and the AP8 fluxes.

2. A large body of data has been gathered on induced radioactivity in spacecraft and experiment samples (refs. 14,15) (aluminum, stainless steel, titanium, lead, copper, nickel, etc.). This data set provides a benchmark for calculation methods and environment models. It also is of considerable interest to gamma ray astronomers, whose experiments are sensitive to the background radiation.

A surprising finding was considerable uranium in titanium clamps (in the original material) from the LDEF structure.

Figure 5 is a sample of activation data from small pieces of two stainless steel trunions.

3. Radioactive ^{7}Be (half life 56 days) was found on the front surface of LDEF on all materials examined (refs. 14,16,27,28), but was absent from the trailing surfaces. Figure 6 shows ^{7}Be data from the aluminum experiment tray clamps. It is known to be produced by cosmic ray bombardment of the atmosphere with maximum production near ~20 km. Its concentration on LDEF is small (~10^6 atoms/cm^2), but is about 1000 times the quantity that might be expected from simple atmospheric diffusion. At the symposium several processes that could explain the observation, such as production in the atmosphere by solar flare particles and exceptional transport mechanisms, were speculated. Accelerator mass spectrometry is being employed to search for other atmospheric spallation products (^{10}Be, ^{14}C). ^{7}Be accommodated to a variety of LDEF surfaces (e.g., aluminum, stainless steel, Teflon).

A recent measurement of ^{7}Be in the removable surface "oil" film on the Concorde aircraft was reported (ref. 29). Repeated measurements on Concorde will allow the speculated solar flare enhancements of atmospheric ^{7}Be to be tested.

4. Secondary neutrons and short range recoil nuclei have been measured in P0006 (refs. 5,6). Past measurements of neutrons in spacecraft have been infrequent and subject to large primary particle backgrounds. The LDEF data contain the first statistically significant measurements in space of spectra from high LET recoil nuclei (6). These secondary particles are of importance in determining equivalent dose (biological effects) and the rates of "single-hit" phenomena (e.g., single event upsets (SEUs), sensor noise). The secondary particle measurements are also very important in assessing calculational methods which predict equivalent dose (REM) and high LET particle effects.

5. Radiation Effects: No damaging radiation effects have been reported in LDEF surface materials. This is consistent with the pre-recovery surface dose calculation of ~500,000 rads from electrons. However, possible radiation effects were reported in uncovered solar cells in experiment A0171 * , the electronics in M0004 (ref. 30), and in quartz crystal resonators (A0189) (ref. 31). Analysis and post-flight testing is continuing.

*Willowby, D. J.; and Whitaker, A. F.: Private Communications.

Genetic damage effects have been observed in experiments containing seeds (P0004-1, P0004-2, A0015) and other biological samples (A0015) (refs. 10,32).

6. Anomalous Cosmic Rays and Ultra-Heavy Cosmic Rays: Three experiments on LDEF were designed to measure rare particles in the cosmic ray flux. These are the low energy "anomalous cosmic rays", and the "ultra heavy cosmic rays" (atomic number above 65). These experiments (M0001, M0002-2, A0178) (refs. 2,3,4) showed results indicating good detector sensitivity and resolution. Only a few percent of the detector material had been processed prior to the symposium. The LDEF measurements are a factor of ≥ six more sensitive than any previous measurements, and will be the most sensitive for a decade or more. In addition to astrophysics the anomalous cosmic rays are of interest in single event upset predictions at thin shielding depths (e.g., electronics on the space station truss).

The investigators of M0001 reported stopping iron group ions with incident energies near 600 MeV/nucleon. This is above the energy of anomalous cosmic rays, but below the geomagnetic cut-off for galactic cosmic rays in the LDEF orbit. Their energy range and flux levels suggest they are partially ionized solar energetic particles, but further investigation is required.

7. Heavy ions trapped in Earth's magnetic field: Experiment M0002-2 has measured a small but significant flux of heavy nuclei stopping in the detector and with an angular distribution consistent with trapped belt particles (ref. 4). The trapping mechanism for these particles is yet to be explained.

8. It should be noted that LDEF carried no radiation detectors at sufficiently shallow shielding depths (< .1 cm Al) to measure trapped electrons (refs. 22,24). Attempts to measure the electron dose in some surface samples with electron paramagnetic resonance (EPR) techniques are planned.

9. The radiation environment models and transport calculations: Progress has been made in using radiation environment models (refs. 12,13,23) (trapped protons, cosmic rays, earth albedo protons and neutrons), and radiation transport models with simple shield geometries, to estimate various features (such as directional properties) of the radiation, and to guide the emphasis on various measurements (e.g., activation sample priority). A detailed mass model (ref. 25) is under development for use in three-dimensional calculations, which are required for definitive testing of the environments models with LDEF data. Experiments A0178 and M0001 will also make significant use of the mass model in data analyses. The quality of the data reported in these early results indicates that the major objectives of the calculation and analysis program will be met.

The early results presented at this symposium have clearly shown that LDEF will make significant advances in the knowledge of the radiation environment in low Earth orbit (LEO), radiation transport modeling, the biological effects of the space radiation environment, radiation dosimetry, and astrophysics.

REFERENCES

1. Clark, L. G.; Kinard, W. H.; Carter, D. J.; and Jones, J. L.: The Long Duration Exposure Facility (LDEF) Mission 1 Experiments. NASA SP-473, 1984.

2. Sullivan, D. O., et al.: The LDEF Ultra Heavy Cosmic Ray Experiment. First LDEF Post-Retrieval Symposium, NASA CP-3134, 1992.

3. Adams, J. H., Jr.; Beahm, L. P.; and Tylka, A. J.: Preliminary Results from the Heavy Ions in Space Experiment. First LDEF Post-Retrieval Symposium, NASA CP-3134, 1992.

4. Beaujean, R.; Jonathal, D.; and Enge, W.: Heavy Ion Measurement on LDEF. First LDEF Post-Retrieval Symposium, NASA CP-3134, 1992.
compilation.)

5. Benton, E. V.; Frank, A. L.; Benton, E. R.; Csige, I.; Parnell, T.A.; and Watts, J. W.: Radiation Exposure of LDEF: Initial Results. First LDEF Post-Retrieval Symposium, NASA CP-3134, 1992.

6. Csige, I., et al.: Charged Particle LET-Spectra Measurements Aboard LDEF. First LDEF Post-Retrieval Symposium, NASA CP-3134, 1992.

7. LDEF Experiment P-0006-Linear Energy Transfer Spectrum Measurement (LETSME) Quick Look Report, NASA/MSFC Contract NAS8-38188 Final Report, Eril Research, Inc., Corte Madera, CA, December 1990.

8. P0004 Quick Look, Task 1: Measurement of Total Absorbed Dose from TLD's, NASA/MSFC Contract NAS8-38676 Progress Report #1, Eril Research, Inc., Corte Madera, CA, December 1990.

9. LDEF Experiment M0004 - TLD Measurements Technical Report - Eril Research, Inc., Corte Madera, CA Air Force Technology Center Contract Report, Contract F29601-90-L-005., June 1990.

10. Reitz, G., et al.: First Biological and Dosimetric Results of the Free Flyer Biostack Experiment A0015 on LDEF. First LDEF Post-Retrieval Symposium, NASA CP-3134, 1992.

11. Fishman, G. J.; Parnell, T. A.; and Harmon, B. A.: Long Duration Exposure Facility - Induced Radioactivity Analysis Plan. NASA/MSFC, December 1989.

12. Armstrong, T. W.; and Colborn, B. L.: Scoping Estimates of the LDEF Satellite Induced Radioactivity, NASA/MSFC Contract NAS-38427 Final Report, Science Applications International Corporation Report: SAIC-90/1462, September 1990.

13. Armstrong, T. W.; and Colborn, B. L.: Predictions of Induced Radioactivity for Spacecraft in Low Earth Orbit, Nuclear Tracks and Radiation Measurements, Elsevier Press, in press 1991.

14. Harmon, B. A.; Benton, E. V.; and Frank, A. L.: LDEF Radiation Measurements; Preliminary Results, Nuclear Tracks and Radiation Measurements, Elsevier Press, in press 1991.

15. Harmon, B. A.; Fishman, G. J.; Parnell, T. A.; and Laird, C. E.: Induced Radioactivity in LDEF Components. First LDEF Post-Retrieval Symposium, NASA CP-3134, 1992.

16. Phillips, G. W., et al.: Gamma Radiation Survey of the LDEF Spacecraft. First LDEF Post-Retrieval Symposium, NASA CP-3134, 1992.

17. The ~400 structural samples are being counted for periods of 12-168 hours each in low background high resolution gamma ray spectrometers by R. L. Brodzinski and J. Reeves (Batelle North West Laboratories), D. C. Camp (Lawrence Livermore Laboratories), C. Frederick (Tennessee Valley Authority), A. B. Harmon (Marshall Space Flight Center), D. C. Lindstrom (Johnson Space Center), C. E. Moss and R. C. Reedy (Los Alamos National Laboratory), A. R. Smith and D. Hurley (Lawrence Berkeley Laboratory), and W. C. Winn (Savannah River Laboratory).

18. Winn, W. G.: Gamma-Ray Spectrometry of LDEF Samples at SRL. First LDEF Post-Retrieval Symposium, NASA CP-3134, 1992.

19. Smith, A. R.; and Hurley, D. L.: Radioactivities of Long Duration Exposure Facility (LDEF) Materials: Baggage and Bonanzas. First LDEF Post-Retrieval Symposium, NASA CP- 3134, 1992.

20. Moss, C. E.; and Reedy, and R. C.: Measurements of Induced Radioactivity in Some LDEF Samples. First LDEF Post-Retrieval Symposium, NASA CP-3134, 1992.

21. Watts, Jr., J. W.; Parnell, T. A.; and Heckman, H. H.: Approximate Angular Distribution and Spectra for Geomagnetically Trapped Protons in Low-Earth Orbit. A. C. Rester, Jr., and J. I. Trombka (Eds.), AIP Conf. Proc., New York, 1989.

22. Ionizing Radiation Exposure of LDEF, edited by E. V. Benton and W. Heinrich, NASA/MSFC Grant NAG8-138 Report, USF Report USF-TR-77, August 1990.

23. Armstrong, T. W.; Colborn, B. L.; and Watts, Jr., J. W.: Ionizing Radiation Calculations and Comparisons with LDEF Data. First LDEF Post-Retrieval Symposium, NASA CP-3134, 1992.

24. Watts, J. W.; Parnell, T. A.; Derrickson, J. H.; Armstrong, T. W.; and Benton, E. V.: Prediction of LDEF Ionizing Radiation Environment. First LDEF Post-Retrieval Symposium, NASA CP-3134, 1992.

25. Colborn, B. L.; and Armstrong, T. W.: LDEF Geometry/Mass Model for Radiation Analyses. First LDEF Post-Retrieval Symposium, NASA CP-3134, 1992.

26. Parnell, T. A.: Long Duration Exposure Facility - Ionizing Radiation Special Investigation Group - Briefing to Space Station Freedom Project Office, NASA/MSFC, September 1990

27. Fishman, G. J.; Harmon, B. A.; Gregory, J. C.; Parnell, T. A.; Peters, P.; Phillips, G. W.; King, S. E.; August, R. A.; Ritter, J. C.; Cutchin, J. H.; Haskins, P. S.; McKisson, J. E.; Ely, D. W.; Weisenberger, A. G.; Piercey, R. B.; and Dybler, T.: Observations of ^{7}Be on the Surface of LDEF Spacecraft, Nature, Vol. 349, pp. 678-680, February 1991.

28. Gregory, J. C.; Fishman, G. J.; Harmom, A.; and Parnell, T. A.: The Interactions of Atmospheric Cosmogenic Radionuclides with Spacecraft Surfaces. First LDEF Post-Retrieval Symposium, NASA CP-3134, 1992.

29. Truscott, P. R., et al.: Be^{7} Deposited on the Surface of the Concorde. First LDEF Post-Retrieval Symposium, NASA CP-3134, 1992.

30. Taylor, E. W., et al.: Preliminary Analysis of WL Experiment #701, Space Environment Effects on Operating Fiber Optic Systems. First LDEF Post-Retrieval Symposium, NASA CP-3134, 1992.

31. Ahearn, J. S.; and Venables, J. D.: Study of Factors Determining the Radiation Sensitivity of Quartz Crystal Oscillators (A0189). First LDEF Post-Retrieval Symposium, NASA CP-3134, 1992.

32. Alston, J. A.: Seeds in Space Experiment Results. First LDEF Post-Retrieval Symposium, NASA CP-3134, 1992. Grigsby, D. K., Space Exposed Experiment Developed for Students, Ibid.

Table 1. The radiation measurements on LDEF.

Radiation Detectors on LDEF

Experiment No.	*TLD's*[a]	*PNTD's*[b]	*Activated Materials*	*Fission Foils*	*Other Detectors*	*Main Objective of Radiation Measurement*
	Absorbed Dose (rads - Tissue)	Heavy Ion Fluence & LET Spectra	Proton & Neutron Fluence	Neutrons & Spectra	Heavy Ions	
P0004-1 (c)	X	X				Dosimetry
P0004-2 (c)	X	X				Dosimetry
P0006 (c)	X	X	X	X		Environment
M0001 (c)		X	X			Astrophysics
M0002-1 (c)	X	X	X		Microsphere	Environment
M0002-2		X	X			Astrophysics
M0003-12	X					Dosimetry
M0003-17	X					Dosimetry
M0004 (c)	X	X				Dosimetry
M0006	X					Dosimetry
A0015 (c)	X	X		X	AgCl	Environment
A0138-7	X		X			Dosimetry
A0114-1 (c)			X			Effects
A0114-2			X			Effects
A0178		X				Astrophysics
LDEF Structure (c)			X			Effects
No. Detectors	190	> 500	> 400	22	4	

(a) TLD's = Thermoluminescent Dosimeters (b) PNTD's = Plastic Nuclear Track Detectors

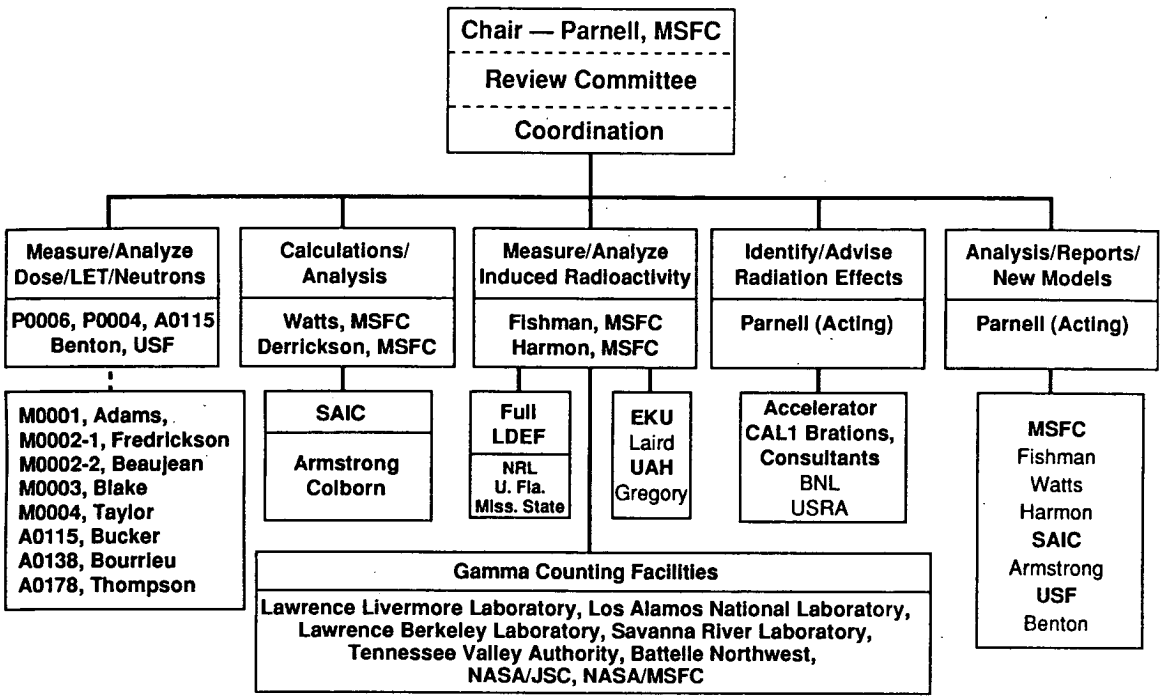

Figure 1. The LDEF Ionizing Radiation Special Investigation Group Functional Organization.

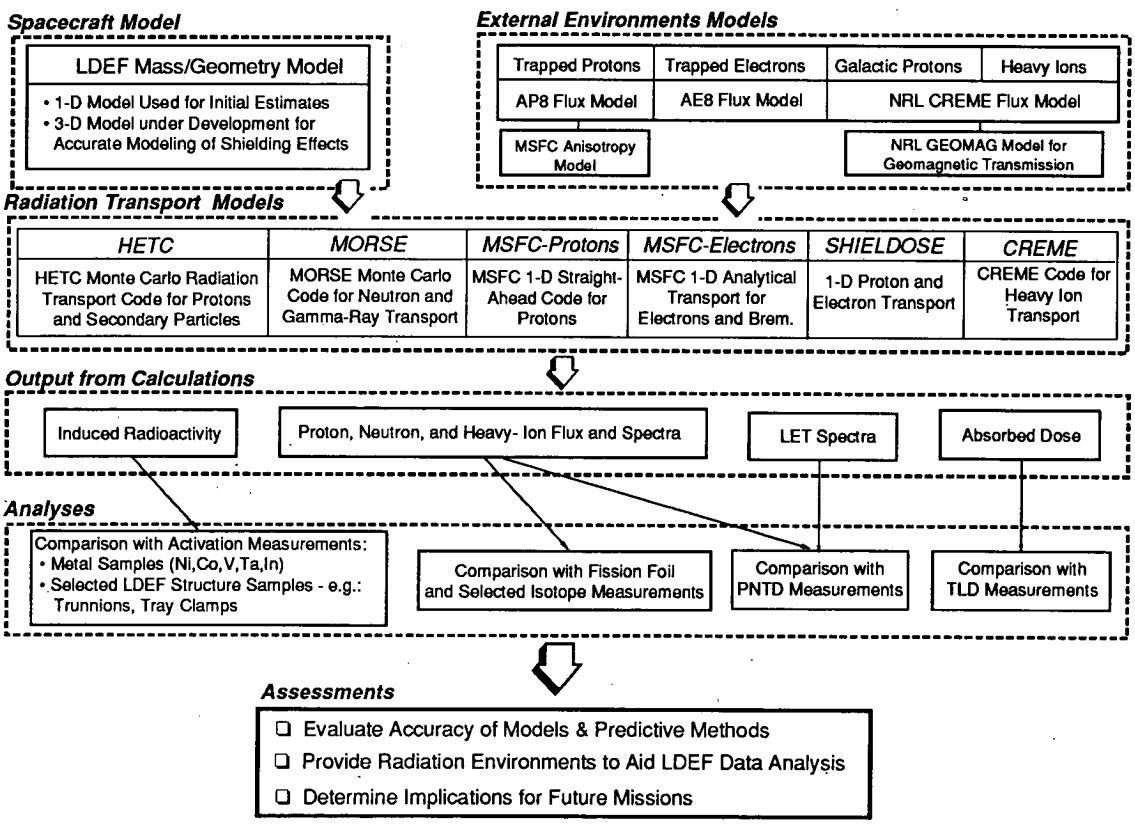

Figure 2. The approach and principal models for the LDEF ionizing radiation calculations (from ref. 23).

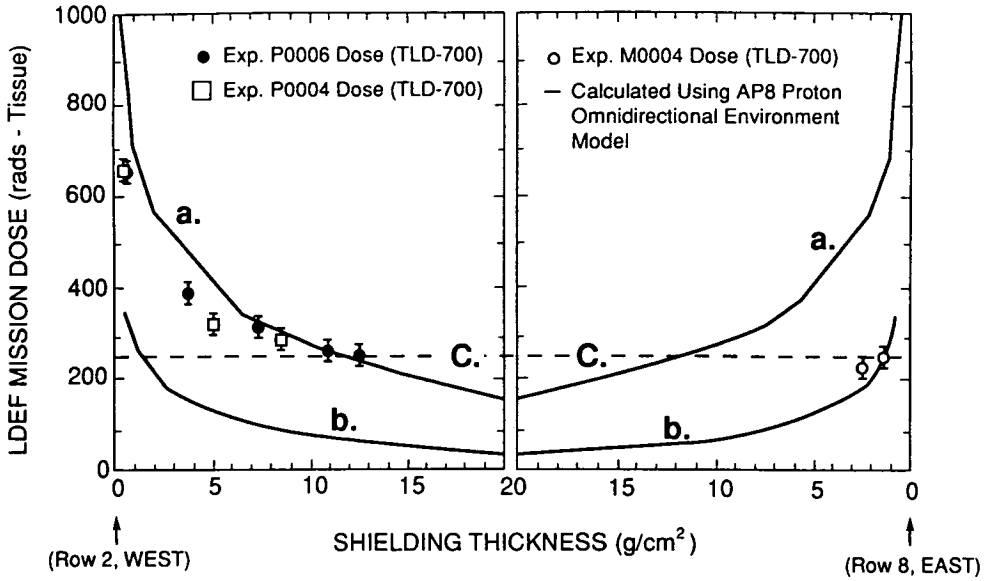

Figure 3. Absorbed dose measurements with thermoluminescent dosimeters (TLD) from three LDEF experiments, with calculations of dose from the AP8 trapped proton omnidirectional model (ref. 22,24,26). Curve A assumes simple spherical shields. Curve B assumes planar (slab) shields. The dotted line indicates the 50 rem annual crew dose limit.

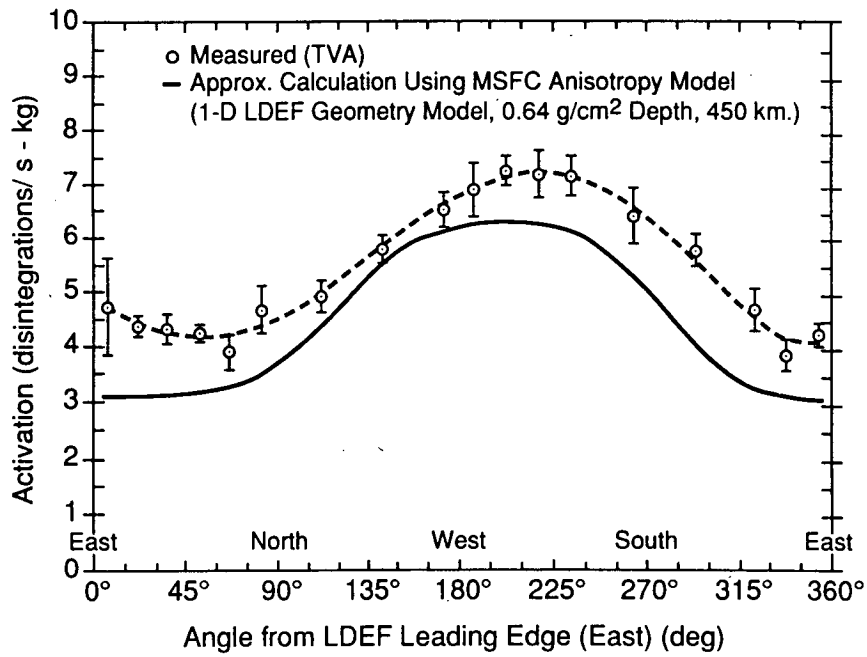

Figure 4. Measurements of the concentration of ^{22}Na in aluminum tray clamps around LDEF. The statistical error bars are due to the short counting time for each sample. The calculation is from a simplified (one-dimensional) planar shield calculation for each data point using a vector proton flux (from ref. 14,15).

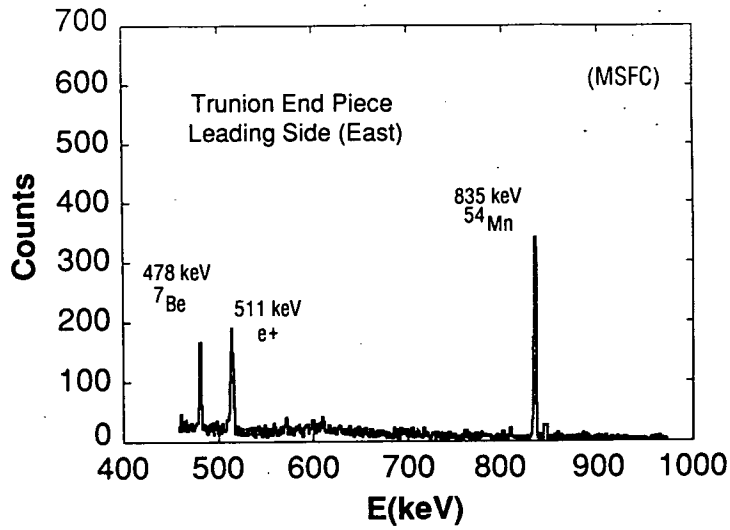

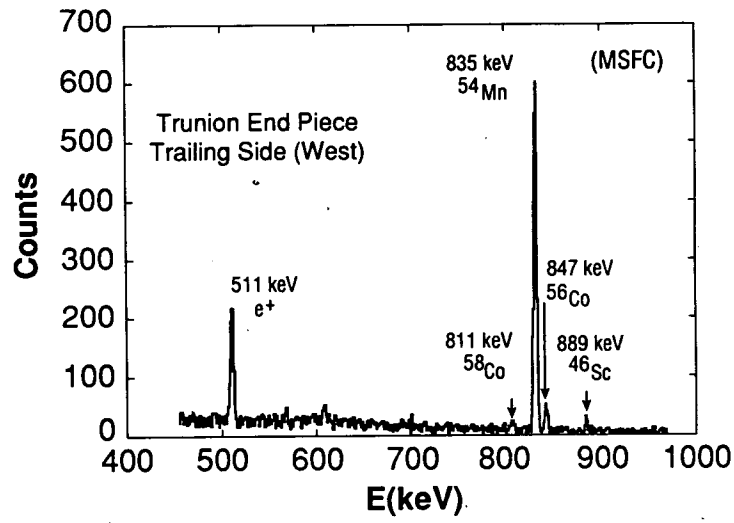

Figure 5. An example of the high resolution gamma ray spectra obtained. These spectra are from twelve hour counts of the end slices (1 cm thick) of two stainless steel trunions, from the leading and trailing sides of LDEF. The east-west effect is clearly seen in the Mn, Co, and Sc lines. The ^{7}Be line is strong on the east (leading) side and is absent on the trailing side. The 511 keV line (positron annihillation) is an artifact of the laboratory spectrum from cosmic rays (from ref. 14,15).

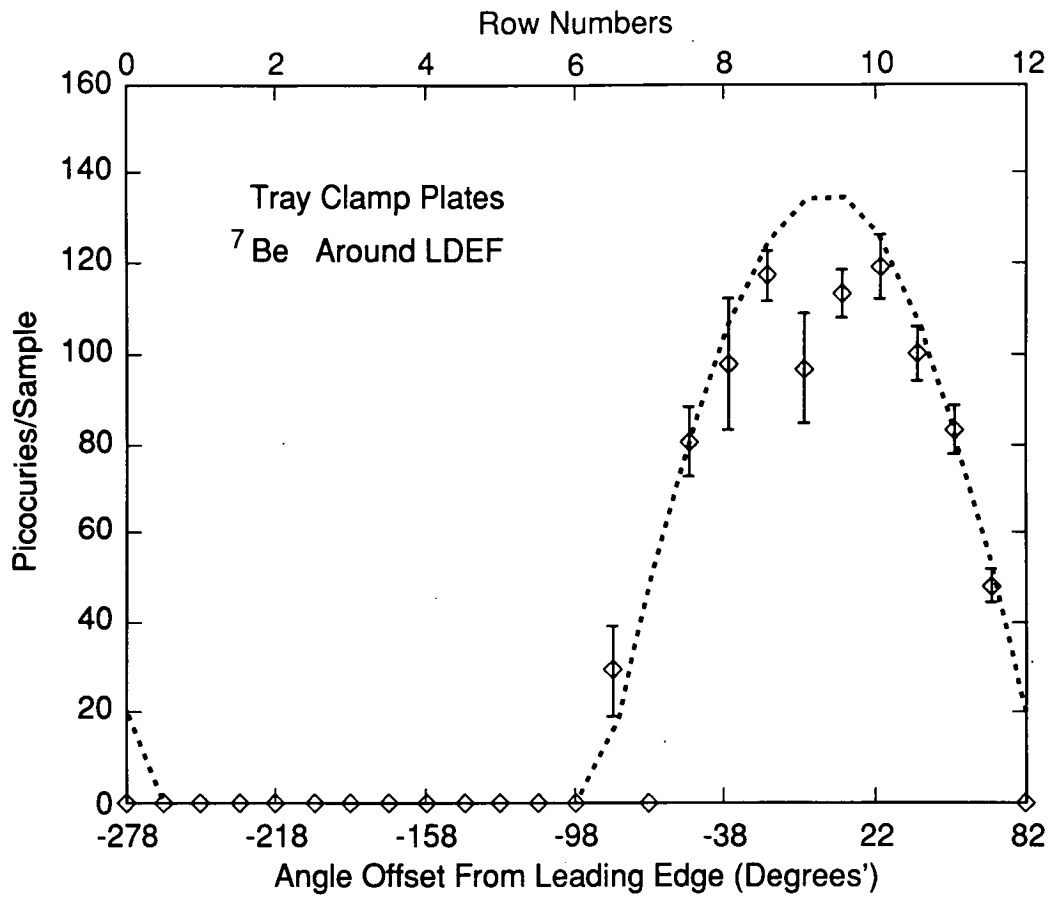

Figure 6. The ^{7}Be gamma ray line from aluminum experiment tray clamps, taken from each row around LDEF, and counted for 24 hours (each clamp) (from ref. 28).

PREDICTION OF LDEF IONIZING RADIATION ENVIRONMENT

John W. Watts
ES62, NASA/Marshall Space Flight Center
AL 35812
Phone: 205/544-7696, Fax: 205/544-7754

T. A. Parnell
ES62, NASA/Marshall Space Flight Center
AL 35812
Phone: 205/544-7690, Fax: 205/544-7754

James H. Derrickson
ES62, NASA/Marshall Space Flight Center
AL 35812
Phone: 205/544-7698, Fax: 205/544-7754

T. W. Armstrong
Science Applications International Corporation
Route 2, Prospect, TN 38477
Phone:615/468-2603, Fax:615/268-2676

E. V. Benton
Physics Department, University of San Francisco
2130 Fulton St., San Francisco, CA 94117-1080
Phone:415/666-6281, Fax:415/386-1074

SUMMARY

The LDEF spacecraft flew in a 28.5° inclination circular orbit with an altitude in the range from 172 to 258.5 nautical miles. For this orbital altitude and inclination two components contribute most of the penetrating charge particle radiation encountered—the galactic cosmic rays and the geomagnetically trapped Van Allen protons. Where shielding is less than 1.0 g/cm^2 geomagnetically trapped electrons make a significant contribution. The "Vette" models (ref. 1-3) together with the associated magnetic field models (ref. 4) were used to obtained the trapped electron and proton fluences. The mission proton doses were obtained from the fluence using the Burrell proton dose program (ref. 5). For the electron and bremsstrahlung dose we used the MSFC electron dose program (ref. 6,7) The predicted doses (ref. 8) were in general agreement with those measured with on-board thermoluminescent detector (TLD) dosimeters (ref. 9). The NRL package of programs, CREME, (ref. 10) was used to calculate the linear energy transfer (LET) spectrum due to galactic cosmic rays (GCR) and trapped protons (ref. 8) for comparison with LDEF measurements (ref. 11).

INTRODUCTION

The LDEF spacecraft flew in a 28.5° inclination circular orbit with an altitude in the range from 172 to 258.5 nautical miles. It was gravity-gradient stabilized and oriented so that one side always pointed along the velocity vector. For this orbital altitude and inclination two components contribute most of the penetrating charge particle radiation encountered—the galactic cosmic rays and the geomagnetically trapped Van Allen protons. Where shielding is less than 1.0 g/cm^2 geomagnetically trapped electrons make a significant contribution. All three sources are strongly modulated by the Earth's magnetic field. The trapped particles follow a helical path about a magnetic field line as shown in figure 1. As the field intensity increases, both the diameter and the pitch of the helix decrease until the pitch becomes zero. The point with zero pitch angle is called the mirror point and the center of the helical path is called the guiding center. From here the helix reverses direction and particles travel up the field line toward decreasing field intensity and away from the Earth. Almost all the trapped flux at LDEF altitudes will be encountered in the region called the South Atlantic Anomaly (SAA) shown in figure 2, which is produced because the Earth's magnetic field, though approximately dipolar, is not centered on the Earth. In the South Atlantic Anomaly almost all the particles observed are near their mirror points. Any trapped particle there which is not nearly mirroring will travel deep into the atmosphere and be scattered or stopped by atmospheric interactions. Thus the flux is anisotropic with most of the flux arriving from a narrow band perpendicular to the local geomagnetic field direction. Atmospheric interactions also affect the trapped proton angular distribution in another fashion as shown in figure 3. Trapped protons that are observed traveling eastward are following guiding centers above the observation point and protons traveling westward are following guiding centers below the observation point. The gyroradius (the radius of the helical path) for energetic protons in the SAA is on the same order as the atmospheric density scale height. Thus westward traveling protons encounter a significantly more dense atmosphere and are more likely to suffer atmospheric interactions and be lost. The resulting energy-dependent anisotropy is called the east-west effect. Galactic cosmic rays experience a similar effect. A model for predicting the trapped proton angular distribution has been developed (ref. 12) recently. A large part of the calculational effort (ref. 13) of the LDEF Ionizing Radiation Special Interest Group has been directed toward testing the prediction of this model against LDEF measurements (ref. 9, 14).

GEOMAGNETICALLY TRAPPED PROTON AND ELECTRON FLUXES

To predict the trapped fluxes the current environment model in use is the "Vette" model (ref. 1-3) together with the associated magnetic field models (ref. 4). To obtain the LDEF mission fluences we calculated long-term average fluxes for five circular orbits at 258.5, 255.0, 249.9, 230.0, and 172.0 nautical mile altitudes which occurred on mission days 0, 550, 1450, 1950, and 2105, respectively, and did a numerical integration over time assuming a straight line between time points. The solar F10.7 cm radio flux which characterizes solar activity exceeded 150 about mission day 1540 (June 27, 1988). Thus the last 565 days or 27 % of the mission was spent under solar maximum conditions. The environment models used for solar minimum (the first three times) were AP8MIN (ref. 2) for protons and AE8MIN (ref. 2,3) for electrons and the magnetic field model was the IGRF 1965.0 80-term model (ref. 4) projected to 1964, the epoch of the environmental model. The environment models used for solar maximum (the last two times) were

AP8MAX (ref. 2) for protons and AE8MAX (ref. 2,3) for electrons and the magnetic field model was the Hurwitz USCS 1970 168-term model (ref. 4) for 1970, the epoch of the environmental model. (The references provided for the electron environment document the previous models to AE8MIN and AE8MAX which remain undocumented.) Since LDEF was at a lower altitude during the last part of the mission about 15% of the proton fluence and 24% of the electron fluence was received under solar maximum conditions. In figure 4 the trapped proton fluence is compared to the galactic proton fluence and the atmospheric albedo fluences due to protons and neutrons produced by GCR interactions in the atmosphere. The galactic proton fluence was produced by the CREME code (ref. 10) which modified the free space spectrum external to the geomagnetosphere based on the vertical rigidity cutoff at points along the LDEF orbit. The albedo fluence was calculated from atmospheric transport of GCR (ref. 15). Figure 5 shows the predicted electron fluence.

TOTAL MISSION DOSE

The mission proton doses were obtained from the fluence using the Burrell proton dose program (ref. 5) which is based on the "straight-ahead" and "continuous-slowing-down" approximations for transporting the protons. Two simple geometries were used–a point tissue receiver material at the center of a spherical aluminum shell and a point tissue receiver material behind a plane aluminum slab with infinite shielding behind the receiver. For the electron and bremsstrahlung dose we used the MSFC electron dose program (ref. 6). The electron dose is based on fits to data from the ETRAN electron Monte Carlo program (ref. 7). Bremsstrahlung dose is based on exponential attenuation with buildup factors from an approximated source. It yields fair agreement with more complicated transports. It only performs the slab geometry calculation. As an estimate for the spherical shell geometry we doubled the slab results which underestimates the actual result. The dose due to trapped protons plus secondary particle, the dose due to electrons plus bremsstrahlung and the total of the two are shown in figures 6 and 7 for the two geometries. A comparison between the predicted total doses and doses measured with onboard TLD dosimeters (ref. 9) is shown in figure 8. Although there is general agreement between the measurement and the simple geometry calculation the planned three-dimensional geometry calculation (ref. 16) will better clarify the spatial variations about LDEF due to shielding configurations and proton angular distributions.

MISSION LINEAR ENERGY TRANSFER (LET) SPECTRUM

The LET of a charged particle specifies how much energy is deposited per unit length along its path in passing through material. Particles with higher LETs are more likely to produce single event upsets (SEUs) in electronic devices and their biological effects are larger compared to low LET particles. The NRL package of programs, CREME, (ref. 10) was used to calculate the LET spectrum due to GCR, the singly-charged anomalous cosmic ray component, and trapped protons for comparison with LDEF measurements. The CREME package calculates the LET spectra at LEO by attenuating the GCR and anomalous flux to the orbital position based on a magnetic rigidity cutoff model and material shielding transport, and then combining this result with the contribution due to trapped protons, also modified by material shielding transport.

Secondaries are not handled. The CREME results (ref. 8) for LDEF are shown in figure 9. Because of the long mission time, experimentally measured LET spectra from the LDEF data (ref. 11) will have greatly improved statistical accuracy at high LET compared to previous measurements.

CONCLUSIONS

Predictions of the LDEF mission's ionizing radiation exposure have been made using the currently accepted models. The LDEF experimental measurements are providing an opportunity to validate the model predictions. Preliminary results for the measured dose are in general agreement with predictions, suggesting that the Vette AP8 model, although more than 20 years old, is still valid, at least for predictions of long-term average dose. The observed variation in dose and activation about the spacecraft shows that the angular distribution of the trapped protons must be considered where more accurate predictions are needed. Because no dose measurements were at thinly shielded locations where the electron contribution to the dose is dominant, the LDEF results will provide little information about the trapped electron environment. The measured LET spectra from LDEF will provide a test of the CREME model with the best measurements at high LET to date.

REFERENCES

1. Sawyer, Donald M. and Vette, James I.: AP-8 Trapped Proton Environment for Solar Maximum and Solar Minimum. National Science Data Center, Goddard Space Flight Center, NSSDC/WDC-A-R& S 76-06, 1976.

2. Teague, Michael J. and Vette, James I.: A Model of the Trapped Electron Population for Solar Minimum. National Science Data Center, Goddard Space Flight Center, NSSDC 74-03, 1974.

3. Teague, Michael J.; Chan, King W. and Vette, James I.: AE6: A Model Environment of the Trapped Electrons for Solar Maximum. National Science Data Center, Goddard Space Flight Center, NSSDC/WDC-A-R&S 76-04, 1976.

4. Stassinopoulos, E. G. and Mead, Gilbert D.: ALLMAG, GDALMG, LINTRA: Computer Programs for Geomagnetic Field and Field-Line Calculations. National Space Science Data Center, Goddard Space Flight Center, NSSDC 72-12, 1972.

5. Burrell, Martin O.: The Calculation of Proton Penetration and Dose Rates. Marshall Space Flight Center, NASA TM X-53063, 1964.

6. Watts, John W. and Burrell, M. O.: Electron and Bremsstrahlung penetration and Dose Calculation. National Aeronautics and Space Administration, NASA TN D-6385, 1971.

7. Berger, Martin and Seltzer, Steve: Penetration of Electrons and Associated Bremsstrahlung through Aluminum Targets. Protection Against Space Radiation, National Aeronautics and Space Administration, NASA SP-169, 1968.

8. Benton, E. V. and Heinich, W. (editors): Ionizing Radiation Exposure of LDEF (LDEF Pre-Recovery Estimates). USF-TR-77, August 1990.

9. Benton, E. V.; Frank, A. L.; Benton, E. R.; Csige, I.; Parnell, T. A. and Watts, J. W.: Radiation Exposure of LDEF: Initial Results. First LDEF Post-Retrieval Symposium, NASA CP-3134, 1992.

10. Adams, James: Cosmic Ray Effects on MicroElectronic, Part IV. NRL Memorandum Report 5901, December 31, 1986.

11. Benton, E. V.; Csige, I.; Frank, A. L.; Frigo, L. A.; Benton, E. R.; Parnell, T. A. and Watts, J. W.: Charged Particle LET-Spectra Measurements Aboard LDEF. First LDEF Post-Retrieval Symposium, NASA CP-3134, 1992.
tion.)

12. Watts, J. W.; Parnell, T. A.; and Heckman, H. H.: Approximate Angular Distribution and Spectra for Geomagnetically Trapped Protons in Low-earth Orbit. High Energy Radiation Background in Space, Proceedings of AIP Conference, Sanibel Island, Florida, vol. 186, 1989, pp. 75-85.

13. Armstrong, T. W.,; Colborn, B. L. and Watts, J. W.: Radiation Calculations and Comparisons with LDEF Data. First LDEF Post-Retrieval Symposium, NASA CP-3134, 1992.

14. Harmon, B. A.; Fishman, G. J.; Parnell, T. A.; and Lair, C. E.: Induced Radioactivity in LDEF Components. First LDEF Post-Retrieval Symposium, NASA CP-3134, 1992.

15. Armstrong, T. W.; Chandler, K. C. and Barish, J.: Calculation of Neutron Flux Spectra Induced in the Earth's Atmosphere by Galactic Cosmic Rays. J. Geophysical Research, vol. 78, 1973, p. 2715.

16. Colborn, B. L.and Armstrong, T. W.: LDEF Geometry/Mass Model for Radiation Analyses. First LDEF Post-Retrieval Symposium, NASA CP-3134, 1992.

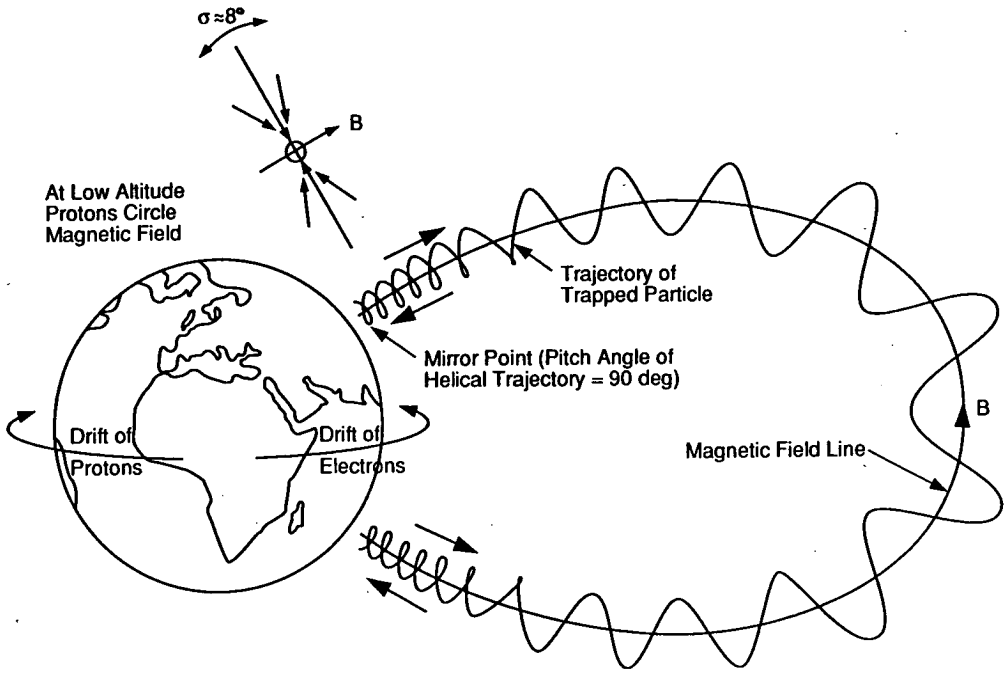

Figure 1. Path of trapped charged particles in the geomagnetic field.

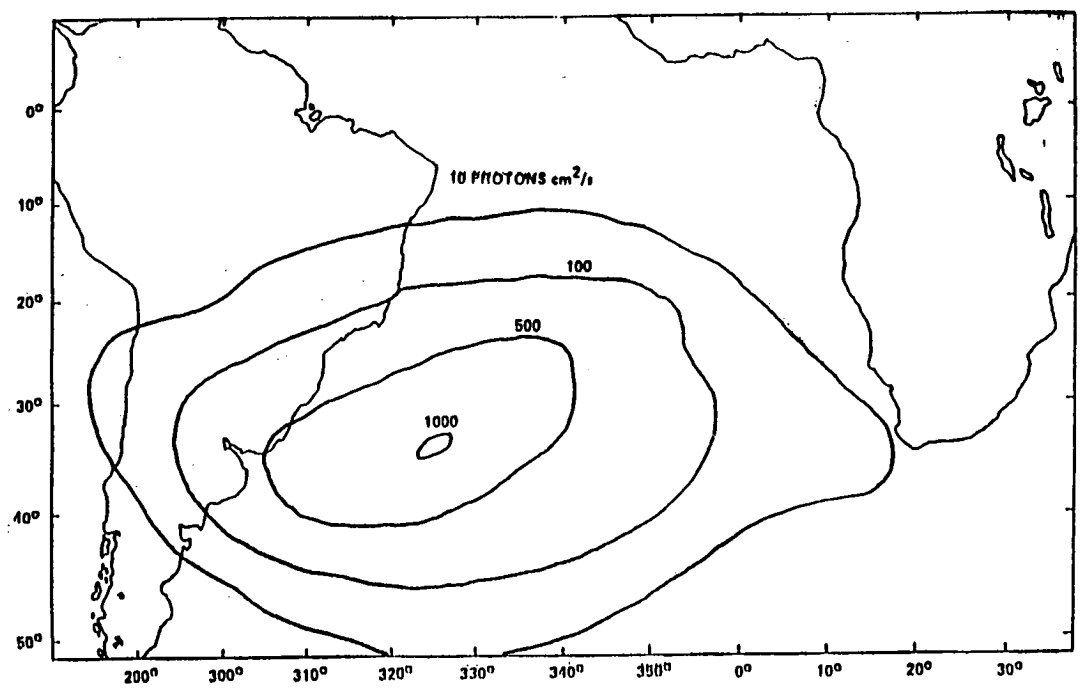

Figure 2. Proton isoflux contours for energies above 34 MeV in the South Atlantic Anomaly at 440 km (240 nautical mi.) altitude.

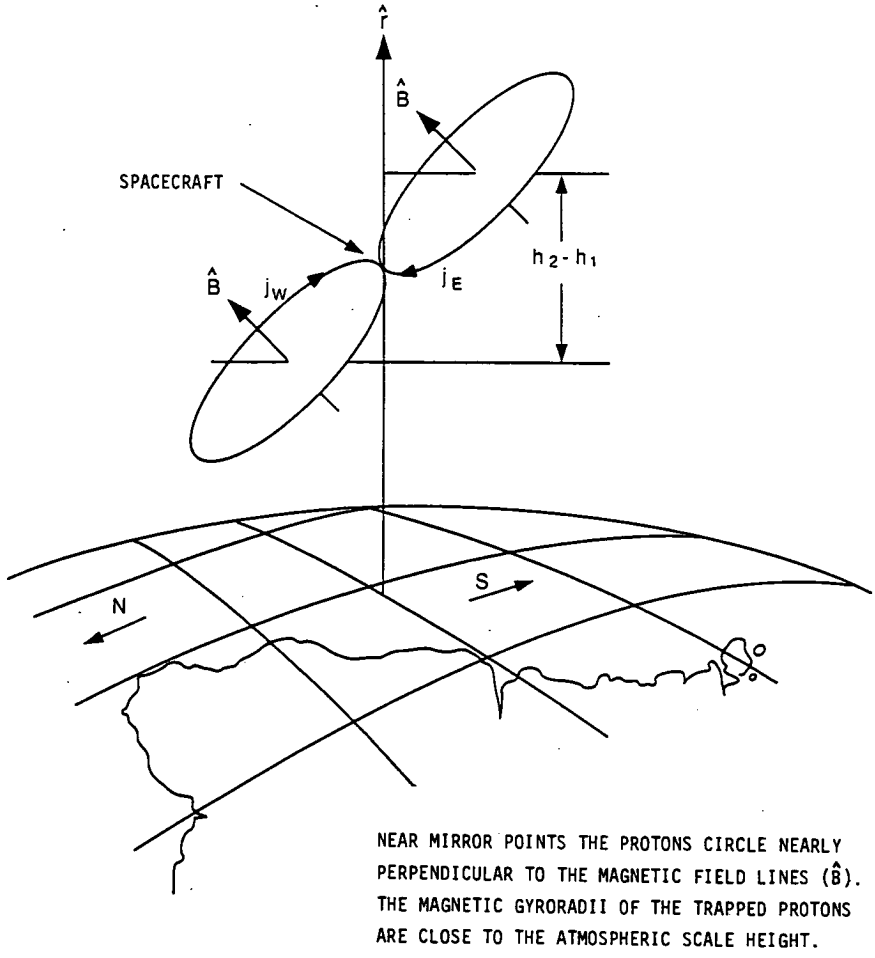

Figure 3. Charged particle path near the mirror point.

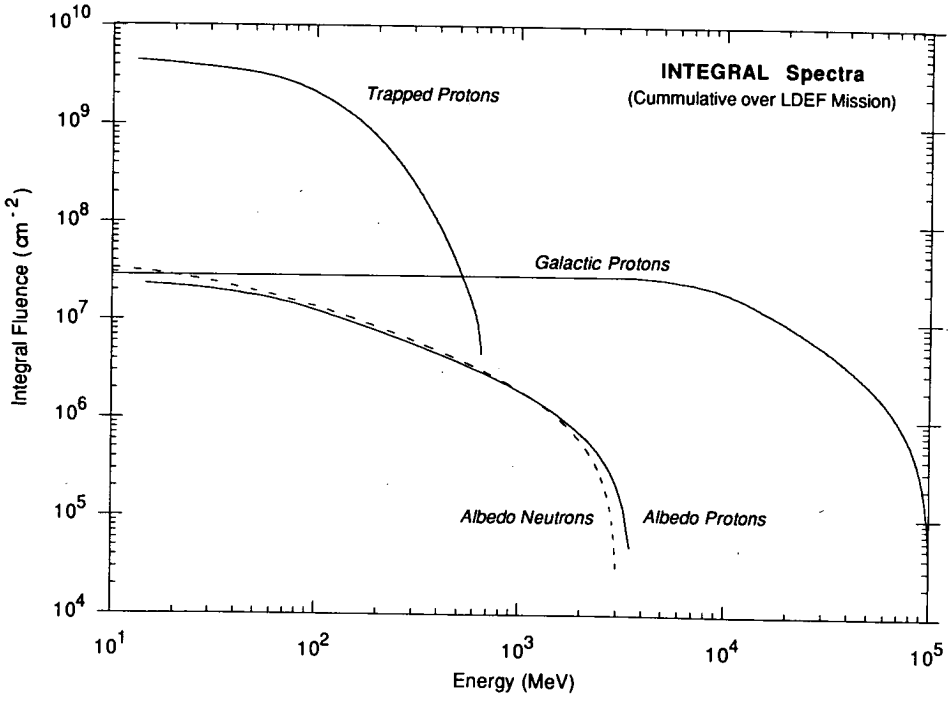

Figure 4. LDEF integral fluences from various sources (ref. 8).

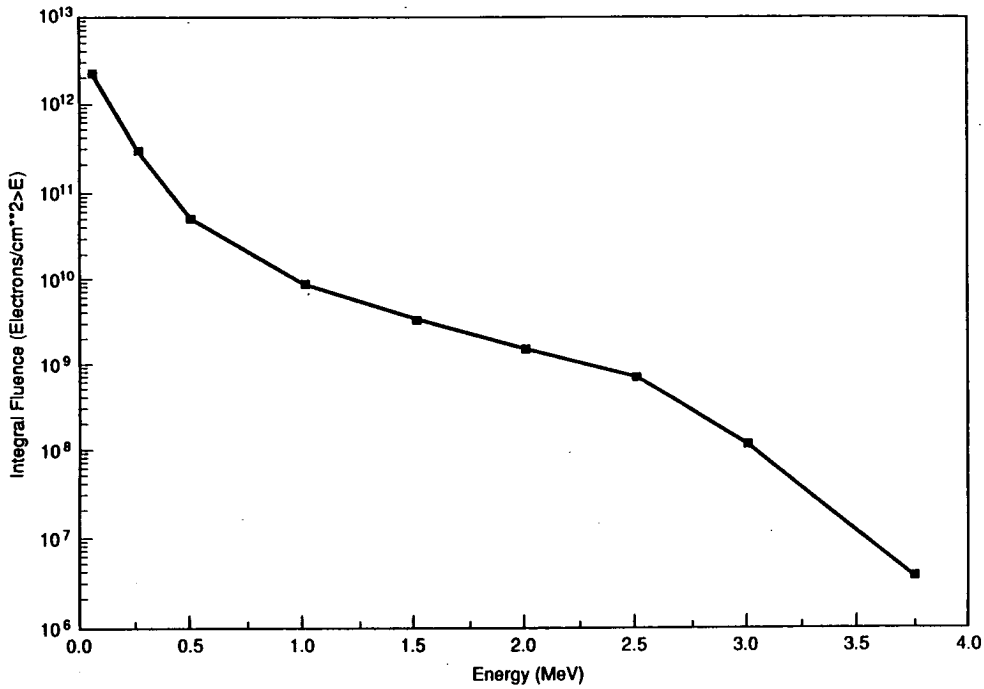

Figure 5. LDEF integral electron fluences (ref. 8).

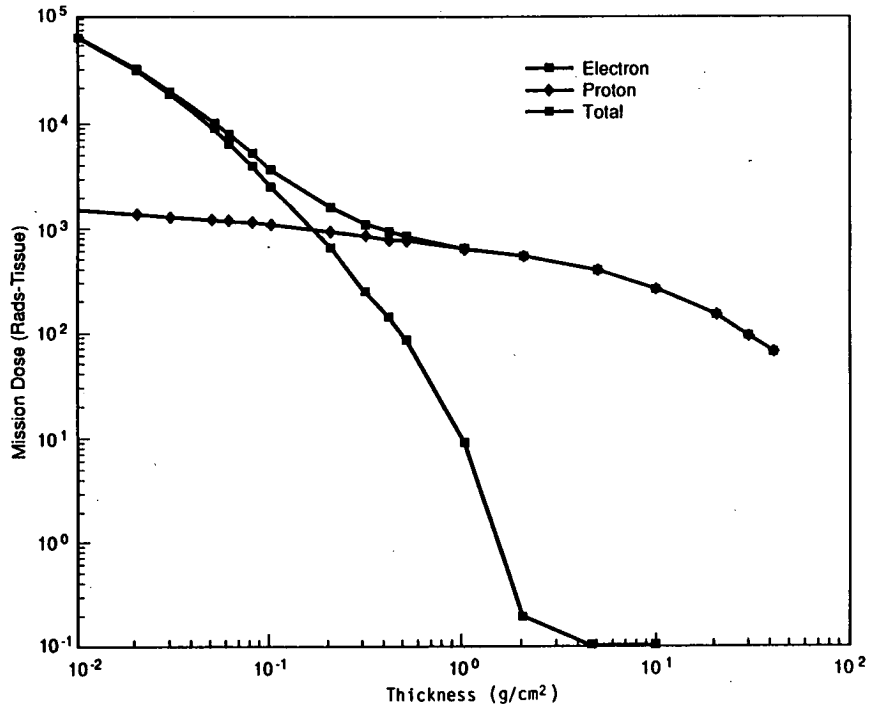

Figure 6. The calculated LDEF mission absorbed dose from trapped protons and electrons (ref. 8). The geometry consists of a point tissue receiver at the center of a spherical aluminum shell of the given thickness.

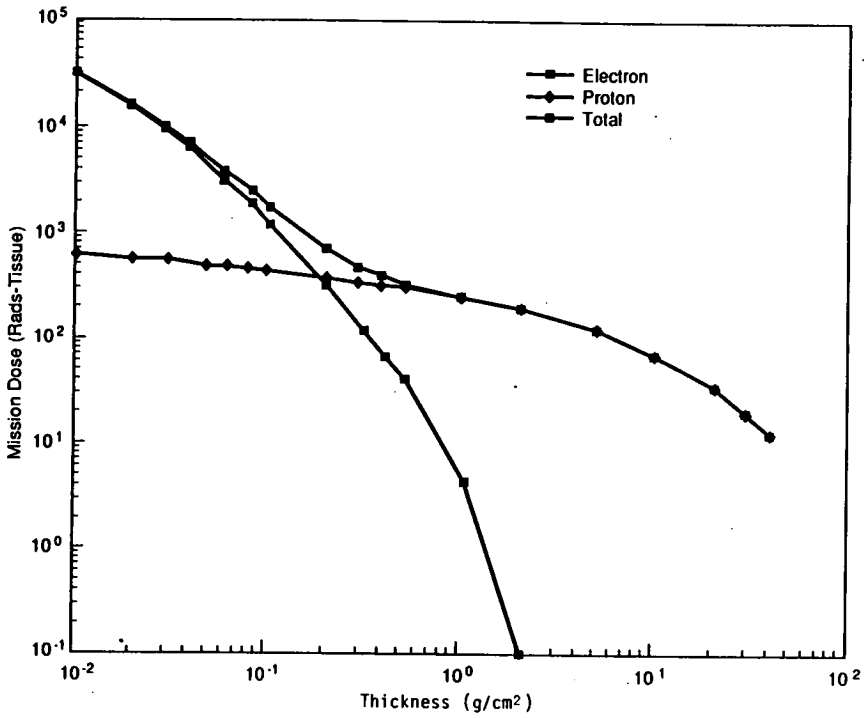

Figure 7. The calculated LDEF mission absorbed dose from trapped protons and electrons (ref. 8). The geometry consists of a tissue receiver behind a plane aluminum slab of given thickness with the receiver completely shielded from behind.

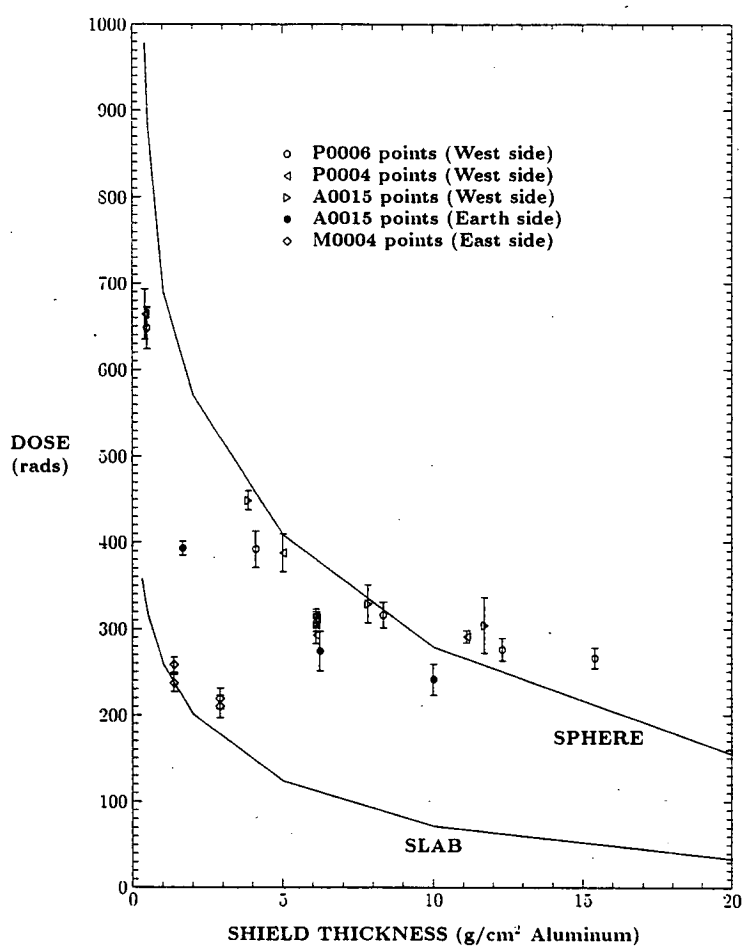

Figure 8. Comparison of the predicted LDEF total mission dose (ref. 8) with on-board TLD dosimeter measurements (ref. 9).

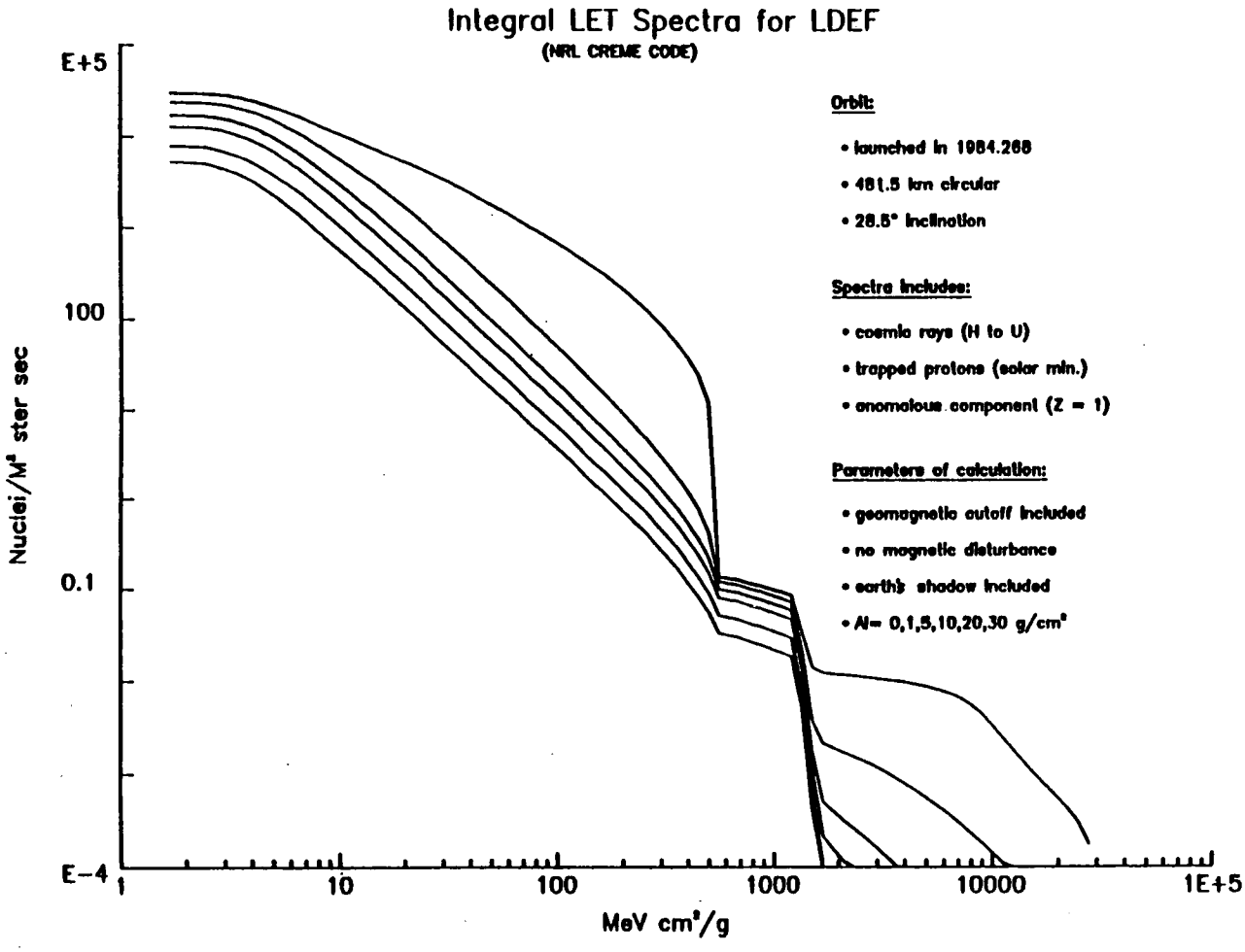

Figure 9. Predicted LET spectrum at the LDEF orbit (ref. 8) from the CREME code (ref. 10).

GAMMA RADIATION SURVEY OF THE LDEF SPACECRAFT

G.W. Phillips, S.E. King, R.A. August, and J.C. Ritter
U.S. Naval Research Laboratory
Washington, DC 20375
Phone: 202/767/5692, Fax: 202/767-3709

J.H. Cutchin
Sachs/Freeman Associates
Landover, MD 20785
Phone: 202/767/5692, Fax: 202/767-3709

P.S. Haskins
University of Florida
Gainesville, FL 32609
Phone: 904/371-4778, Fax: 904/372-5042

J.E. McKisson, D.W. Ely, and A.G. Weisenberger
Institute for Space Science and Technology
Gainesville, FL 32609
Phone 904/371/4778, Fax: 904/372-5042

R.B. Piercey, and T. Dybler
Mississippi State University
Mississippi State, MS 39762
Phone: 601/325-2806, Fax: 601/325-8898

SUMMARY

The retrieval of the Long Duration Exposure Facility (LDEF) spacecraft in January 1990 after nearly six years in orbit offered a unique opportunity to study the long term buildup of induced radioactivity in the variety of materials on board. We conducted the first complete gamma-ray survey of a large spacecraft on LDEF shortly after its return to earth. A surprising observation was the large ^{7}Be activity which was seen primarily on the leading edge of the satellite, implying that it was picked up by LDEF in orbit. This is the first known evidence for accretion of a radioactive isotope onto an orbiting spacecraft. Other isotopes observed during the survey, the strongest being ^{22}Na, are all attributed to activation of spacecraft components. ^{7}Be is a spallation product of cosmic rays on nitrogen and oxygen in the upper atmosphere. However, the observed density is much greater than expected due to cosmic-ray production in situ. This implies transport of ^{7}Be from much lower altitudes up to the LDEF orbit.

INTRODUCTION

Spacecraft in orbit around the earth undergo continuous bombardment by high-energy cosmic rays and energetic trapped protons. This results in the build up of small but observable amounts of induced radioactivity, depending on the material and the exposure history. The return to earth of the Long Duration Exposure Facility (LDEF) after nearly six years in orbit provided a unique opportunity to study the activation of the variety of materials on board due to exposure to the space radiation environment. Shortly after landing, and prior to removal of the experimental trays, we conducted a complete survey to determine the distribution of induced gamma radiation about the spacecraft. These observations should be useful in predicting the activation of future long-duration spacecraft such as the space station, orbiting earth sensors, and astronomical observatories.

Radiation is also induced in the upper atmosphere by the interaction of cosmic rays and trapped protons with nuclei of carbon, nitrogen, and oxygen. One of the products of these interactions, ^{7}Be, was observed during the survey of LDEF on the leading edges of the spacecraft in quantities much larger than expected from the known production cross sections and the known flux of cosmic rays and trapped protons at the altitudes of the LDEF orbit. In this article, we will describe the radiation survey results and discuss possible production and transport mechanisms for the ^{7}Be.

THE LDEF SPACECRAFT

The LDEF spacecraft was launched by the Space Shuttle Challenger on 7 April 1984. It was retrieved in orbit by the Shuttle Columbia on 12 January 1990 and brought back to Earth on 20 January 1990. The spacecraft is a 12-sided cylindrical aluminum structure, 9.1 m long by 4.2 m diameter, with a total weight of about 9700 kg. Along the sides and on both ends were 86 trays containing a broad range of passive or low-powered experiments designed to study the space environment in low-earth orbit and to determine the effects of the environment on various materials, coatings, and spacecraft components. It was launched into a nearly circular orbit at an altitude of 480 km and an inclination of 28.5 degrees, where it was exposed continuously to cosmic rays, interplanetary dust and the residual atmosphere. In addition, the orbit took it through the South Atlantic Anomaly (SAA) exposing the spacecraft to energetic trapped protons and electrons. In the months prior to retrieval, the orbit was decaying rapidly and LDEF was down to an altitude of about 310 km when recovered by the shuttle.

The orientation of the spacecraft was gravity-gradient stabilized while in orbit so that its axis was aligned to the Earth's radius vector, with one end always pointed toward space and the other end toward Earth. Also, rotation about this axis was stabilized with respect to the orbital velocity so that the leading edge was always side number 9 (plus about 8 degrees). There were a number of duplicate experimental trays positioned around LDEF in order to get information about the differential flux of particles and micrometeoroids. The LDEF orbital velocity (7.8 km/s at retrieval) exceeded the average thermal velocity of the rarified atmosphere so that exposure to the atmosphere was primarily on the leading edge of the spacecraft.

GAMMA RAY SURVEY

After landing, LDEF was returned to Kennedy Space Center (KSC) for post-recovery examination. There the spacecraft was mounted on a stand so that it could be rotated about its axis for inspection. During this period, an array of high-purity germanium detectors from the Naval Research Laboratory (NRL) and single detectors from the Institute for Space Science and Technology (ISST), were used to conduct the first detailed gamma-ray survey of a large spacecraft after exposure in low-earth orbit. The residual gamma-ray emission depends both on the flux of high-energy particles to which LDEF was exposed and on the particular materials in each experimental tray. To observe the distribution of gamma-ray activity about the spacecraft, we set up the array with detectors facing each tray position along one side of LDEF. The single detectors were positioned at each end facing one of the experimental trays. The distance from the detectors to each tray was about 0.6 m. Background spectra were taken prior to the arrival of LDEF, and the detectors were calibrated in place using known gamma-ray sources.

So as not to interfere with activities during the day, gamma-ray spectra were accumulated overnight for a minimum of 12 hours along each side . Each night, LDEF was rotated so that a new side faced the array and new trays faced the detectors at each end. In this manner the entire spacecraft was surveyed over the period from 4 to 20 February 1990. During the disassembly period which followed, spectra were taken of selected experimental trays after they were removed from LDEF.

GAMMA RAY OBSERVATIONS

We expected to see gamma rays from the decay of isotopes produced by the long bombardment of energetic protons, neutrons, and heavier cosmic rays. Figure 1 shows the accumulated gamma-ray spectrum over the six trays along side 9, which was at the leading edge. The strongest peaks observed above background were from positron annihilation (511 keV), and from the decays of ^{7}Be (478 keV) and ^{22}Na (1274 keV). Weaker peaks were observed from the decays of ^{54}Mn, and ^{56,57,60}Co. The observed activities were primarily due to activation of the most common materials on the spacecraft, aluminum and stainless steel (iron, nickel, and cobalt.) The exception is the unexpectedly strong activity from ^{7}Be which is discussed below. During post-collection data analysis, spectra were analyzed for each detector and peak intensities were extracted using the computer program HYPERMET (ref. 1). Table I gives the observed isotope, its gamma-ray energy, halflife, and observed activity averaged over the LDEF spacecraft and decay-corrected to the landing date (ref. 2).

Distribution of Gamma Ray Activities

The strongest isotopic activities observed during the radiation survey were from ^{22}Na and ^{7}Be, both of which are produced by spallation from high-energy protons on aluminum, the material of the spacecraft body and experimental tray holders. At equilibrium, the activity from

^{7}Be was expected to be lower than 22Na in intensity by two orders of magnitude from the ratio of their spallation yields on aluminum. However, the 478 keV line from ^{7}Be was unexpectedly strong at some positions around the LDEF. After the survey was complete, a plot of count rate versus position around the spacecraft showed that the ^{7}Be activity at the leading edge was strongly enhanced compared to the trailing edge. Figure 2 shows the distribution of the average ^{22}Na and ^{7}Be activities for each row of LDEF corrected to date of retrieval.

In contrast to ^{7}Be, the ^{22}Na activity in figure 2 shows a small enhancement at the trailing edge, although there is some variation due to the distribution of aluminum and other activation material around the spacecraft. The trailing edge enhancement can be attributed to the asymmetry in the trapped proton flux in the SAA (ref. 3). This flux is strongly peaked from the westward direction, the trailing direction in orbit . Although many of the trapped protons are energetic enough to penetrate LDEF, they could produce the asymmetry seen in the ^{22}Na activation data. In figure 3, the distribution of the positron annihilation activity shows a similar trailing edge enhancement. Although statistics are poor, there also appears to be a trailing edge enhancement in ^{54}Mn and possibly in the Co activities.

Unlike all the other observed distributions, a strong leading edge enhancement for the ^{7}Be activity is evident in figure 2. The weak activity seen from the trailing edge can be wholly accounted for by penetration of gamma rays from the opposite side of the hollow spacecraft. This distribution of the ^{7}Be activity is not consistent with any known mechanism for activation of the spacecraft materials. It can only be explained by accretion of the isotope onto the leading surfaces of LDEF as it moved through the thin upper atmosphere in orbit.

The overlay in figure 2 gives a diagram of LDEF. Each experimental tray position around the cylinder is identified by row, numbered 1 through 12, and bay, lettered A through F. The view is toward the space end and the leading edge; the arrow vectors indicate the direction of the orbital velocity. Figure 4 shows a two dimensional mapping of the ^{7}Be and ^{22}Na activity. The mapping shows the data as it would appear after cutting the cylinder between rows 1 and 12 and unrolling it flat. The data for each tray position is plotted by row (running from 1 to 12) along the right axis and by bay (running from A to F) along the left axis. The leading and trailing edges in orbit are identified by the dashed lines in the figure. The ^{7}Be activity is shown to be distributed along the entire leading edge and not confined to a single tray.

The data in figure 4 tend to be somewhat higher in the middle compared to the edges of the spacecraft. This can be explained by gamma rays from adjacent trays penetrating the 3 mm lead collimators which surrounded the detectors. Similarly, the weak trailing edge activity for ^{7}Be can be explained by penetration of gamma rays from the opposite leading edge.

The absence of ^{7}Be activity on the trailing edge was demonstrated by measurements of gamma-ray spectra from individual experimental trays after they were removed from LDEF. Figure 5 shows a comparison of spectra from nearly identical trays from the leading and trailing edges, containing germanium plates covered with a thin foil designed to capture interplanetary dust particles. The ^{7}Be peak is indicated in the figure and appears only on the tray from the leading edge.

Further confirmation of the lack of ^{7}Be on the trailing edge of LDEF came from low-level activity measurements of aluminum plates and tray clamps by NASA/Marshall Space Flight Center (MSFC) (ref. 4), which showed ^{7}Be activity only on parts from the leading edge. In addition, they found that an acid etch of an aluminum plate from the leading edge removed most of the activity, demonstrating that most of the ^{7}Be is on the surface.

DENSITY OF ^{7}BE IN THE UPPER ATMOSPHERE

Assuming that the ^{7}Be was accreted onto the surface of LDEF in low-earth orbit, the question arises: how did it get there with such intensity? From the literature, we can estimate the ^{7}Be density at 310 km due to cosmic-ray production for comparison to our measurements. Using curves of cosmic-ray interaction rates derived from measurements during a period of high solar activity (ref. 5) and including interactions due to the trapped proton flux, we obtain an estimated ^{7}Be density of 5.4×10^{-5} atoms/m^3 in the upper atmosphere at 0° to 30° and 310 km due to production in situ (see the Appendix for details.) From our measurements we can derive a capture rate which gives a minimum ^{7}Be density in orbit of 0.10 ± 0.03 atoms/m^3. This exceeds the estimated in-situ production by a factor of 1800.

It is difficult to explain such a large enhancement in the ^{7}Be density. One possibility is the mixing of air from the poles where the production rate is higher than at lower latitudes, which are partially shielded from cosmic rays by the Earth's magnetic field. Measurements in the stratosphere (ref. 6) imply significant mixing between polar and low-latitude air, showing increases in the ^{7}Be density by a factor of 2 to 5 over the equilibrium value at 31° N. In the upper atmosphere, above 120 km, the polar production rate is about a factor of 10 higher than the average rate from 0° to 30° latitude (ref. 5). Thus, complete displacement by polar air would still leave a factor of 180 unexplained.

A second possible source of increased activity is diffusion or convection of ^{7}Be from air at lower altitudes where production rates are higher due to increased atmospheric density. The onset of diffusive equilibrium, known as the turbopause, occurs between 100 and 120 km (ref. 7). Below this the atmosphere is well mixed, while above this the various components tend to diffuse independently. Because ^{7}Be is considerably lighter than the mean atmospheric molecular weight, it will tend to diffuse upward. During periods of high solar activity (ref. 8), the estimated in-situ production rate at 120 km is a factor of 300 higher than the rate at 310 km. Below 120 km production increases rapidly; at 100 km it is a factor of 7000 higher than at 310 km. Thus, the amount of diffusion will be effected by the height of the turbopause. Temperature is also an important factor. The equilibrium distribution of atmospheric molecules due to diffusion is a decreasing exponential function of the altitude with a scale height (ref. 9) which is proportional directly to the temperature and inversely to the atomic weight. The mean global temperature (ref. 10) rises rapidly from about 380K at 120 km to 1040K above 200 km. During periods of high solar activity, temperatures as high as 1700K have been measured (ref. 11,12). For ^{7}Be, this corresponds to a scale height of 206 km and an average thermal velocity of 2.5 km/s.

Several large solar flares occurred in 1989, including the late September-early October flare which was the largest in 33 years and had a very hard spectrum (ref. 13). Such events cause heating and expansion of the upper atmosphere, where winds have been measured at several hundred meters per second (ref. 11,12), driven by solar activity, diurnal solar heating and geomagnetic storms. These act both to mix polar and lower latitude air and to transport air upward from lower altitudes (ref. 9,11). The relative importance of diffusion versus convection in contributing to the increased ^{7}Be density at 310 km needs to be determined by detailed modeling of the upper atmosphere.

CONCLUSIONS AND IMPLICATIONS FOR FUTURE SPACECRAFT

Our observations of ^{7}Be activity on the leading surfaces of the LDEF spacecraft imply a minimum density for ^{7}Be in low-earth orbit which greatly exceeds the local equilibrium due to cosmic-ray production in situ. One possible explanation would require the transport by diffusion or atmospheric mixing of ^{7}Be from much lower altitudes and higher latitudes into the LDEF orbit. Thus, the current results should be important for validating and refining models of the upper atmosphere. With more extensive measurements, ^{7}Be should prove valuable as a natural tracer for studies of upper atmospheric mixing. The next step is to combine existing atmospheric circulation models with calculations of ^{7}Be production rates at lower altitudes in order to predict the upward transport of ^{7}Be. Future observations should focus on sampling at both lower and higher altitudes and should extend to polar latitudes. These should be closely correlated with data on wind, temperature, pressure and solar activity.

In addition, the observation of the accretion of significant quantities of ^{7}Be is an indication of possibly similar behavior for other light cosmic-ray produced isotopes. Table II gives the spallation yields (ref. 5) for all light isotopes with yields greater than or of the order of ^{7}Be. Also given are their halflives and decay modes. ^{3}He is stable and non-reactive. The remaining isotopes, other than ^{7}Be, are all pure beta emitters and thus would not be seen in the present survey. They could, however, be significant sources of noise for low-level sensors on spacecraft in low-earth orbit and could slowly degrade other components by coating or by surface reactions. Lithium, the decay product of ^{7}Be, could affect exposed semiconductor sensors even in very low concentrations. As a result of our observations, other groups are currently looking for trace amounts of Li, ^{14}C and ^{10}Be on LDEF components.

A period of 23 days elapsed between the time of the LDEF capture by the shuttle and the start of the gamma ray survey. Thus much of the short-lived activity had decayed away before we were able to observe it. A gamma ray survey should be made of a shuttle immediately after landing to determine the magnitude and significance of this activity.

APPENDIX

Equilibrium ^{7}Be Density from Cosmic-Ray Production

Lal and Peters (ref. 5) provide curves of cosmic-ray production rates (interactions per gram of air per second) versus latitude and altitude, using a model derived from measurements during a period of high solar activity. From these curves and the known spallation yields (ref. 5), we obtain a ^{7}Be production rate per gram of air between 0° and 30° latitude of 9.0×10^{-5} atoms/g-s at the "top" of the atmosphere (above 120 km). The mean atmospheric density during periods of high solar activity (ref. 8) at an altitude of 310 km is about 6.1×10^{-8} g/m^3. This gives an in-situ production rate for ^{7}Be at 310 km of 5.5×10^{-12} atoms/m^3-s. Multiplying by the equivalent in seconds of the 77 day mean ^{7}Be lifetime gives an equilibrium density for ^{7}Be of 3.6×10^{-5} atoms/m^3, due to production in situ.

The trapped proton flux provides an added production source of ^{7}Be at 310 km. Using the trapped proton fluence for solar maximum given by Stassinopoulos (ref. 14), the average equilibrium density of ^{7}Be is 1.8×10^{-5} atoms/m^3. Adding this to the density due to cosmic-ray production gives a total density which is then 5.4×10^{-5} atoms/m^3. However, the "average" density calculated for the trapped protons is somewhat misleading since virtually all the production occurs in the South Atlantic Anomaly where the density would be considerably higher.

Minimum ^{7}Be Density from Our Measurements

Our measurements of the ^{7}Be activity on the LDEF leading edge give an average surface density for ^{7}Be of $(5.4 \pm 1.4) \times 10^9$ atoms/m^2, corrected to the date of retrieval of the spacecraft. With an orbital velocity of 7.8 km/s, LDEF traveled a distance of 5.2×10^{10} m during one mean lifetime of ^{7}Be. Dividing the surface density by this distance gives the mean capture rate of ^{7}Be in orbit. Assuming 100% adherence of ^{7}Be to the surface of LDEF, this implies a minimum density in orbit for ^{7}Be of 0.10 ± 0.03 atoms/m^3. (Less than 100% adherence would imply an even greater ^{7}Be density in orbit.)

REFERENCES

1. G.W. Phillips and K.W. Marlow, Nucl. Instr. and Methods, vol. 137, 1976, pp. 525-536.
2. S.E. King, et al., IEEE Transactions in Nuclear Science, vol. 38, 1991, pp. 525-530.
3. J.W. Watts, T.A. Parnell, and H.H. Heckman, AIP Conference Proceedings, no. 186, High Radiation Background in Space, ed. A.C. Rester, Jr., and J.I. Trombka, AIP, New York, 1987, pp. 75-85.
4. G.J. Fishman, et al., Nature, vol. 349, 1991, pp. 678-680.

5. D. Lal and B. Peters, Encyclopedia of Physics, vol. 46/2, ed. K. Sitte, Springer, New York, 1967, pp. 551-612.
6. N. Bhandari, J. Geophys. Res., vol. 75, 1970, pp. 2927-2930.
7. I. Harris and N.W. Spencer, Introduction to Space Science, ed. W.N. Hess and G.D. Mead, Gordon and Breach, New York, 1968, pp. 93-131.
8. Appendix C, COSPAR International Reference Atmosphere: 1986, Part 1: Thermospheric Models, ed. D. Rees, Pergamon Press, New York, 1989, pp. 315-470 (see Table 5.12.)
9. J.K. Hargreaves, The Upper Atmosphere and Solar-Terrestrial Relations, Van Nostrand Reinhold, New York, 1979.
10. A.E. Hedin, COSPAR International Reference Atmosphere: 1986, Part 1: Thermosphere Models, ed. D. Rees, Pergamon Press, New York, 1989, pp. 9-25.
11. N.W. Spencer and G.R. Carignan, ibid., pp. 107-117.
12. G. Hernandez and T.L. Killeen, ibid., pp. 149-213.
13. J.H. Allen, 1989 Solar Activity and its Consequences at Earth and in Space, presented at the DOD-DOE-NASA Seventh Symposium on Single Event Effects, May 1990.
14. E.G. Stassinopoulos and J.M. Barth, Goddard Space Flight Center Report No. X-600-87-7, Greenbelt, MD, 1987.

TABLE I. - OBSERVED GAMMA-RAY ACTIVITIES ON LDEF

Isotope	γ-ray Energy	Half-Life	Activity	
	keV		10^{-3}c/s/det	% error
β^+ annih.	511	na	112.	0.8
^{22}Na	1274	2.6 y	39.7	0.3
^{7}Be*	478	53 d	23.0	3.
^{54}Mn	835	312 d	3.1	4.
^{57}Co+	122	272 d	2.8	23.
^{56}Co	847	78 d	0.75	25.
^{60}Co	1173, 1332	5.3 y	0.34	27.
* Peak activity at row 9 is given for ^{7}Be				
+ Activity for ^{57}Co is averaged over 4 rows only				

TABLE II. - COSMIC RAY PRODUCED LIGHT ISOTOPES

Isotope	Yield/Interaction	Half-Life	Decay Modes
^{14}C	1.5*	5.7 x 10^4 y	beta
^{3}H	0.14	12.3 y	beta
^{3}He	0.12	stable	none
^{7}Be	0.045	53 d	ec+, gamma
^{10}Be	0.025	1.6 x 10^6 y	beta
* Relative yield, produced mainly by thermal neutrons			
+ Electron capture, gamma branching ratio 10.4%			

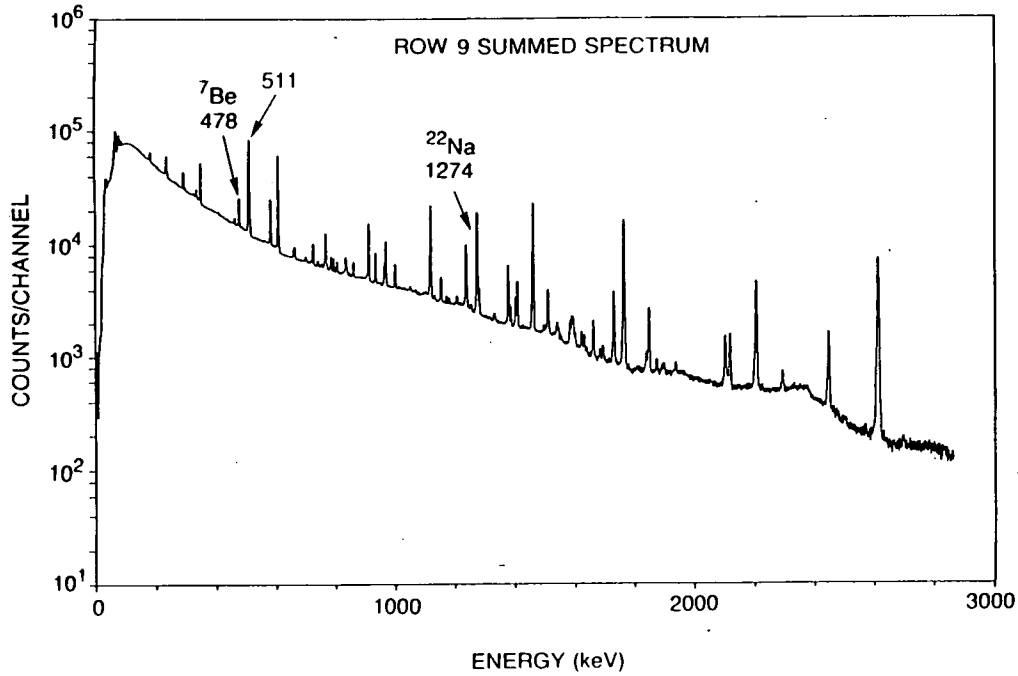

Figure 1. Summed spectrum along LDEF row 9 at the leading edge of the spacecraft. The peaks from ^{7}Be, ^{22}Na, and positron annihilation (511) are indicated. Most of the remaining prominent peaks are from the background. Accumulation time was 29 hours, and the energy calibration is 0.706 keV/channel.

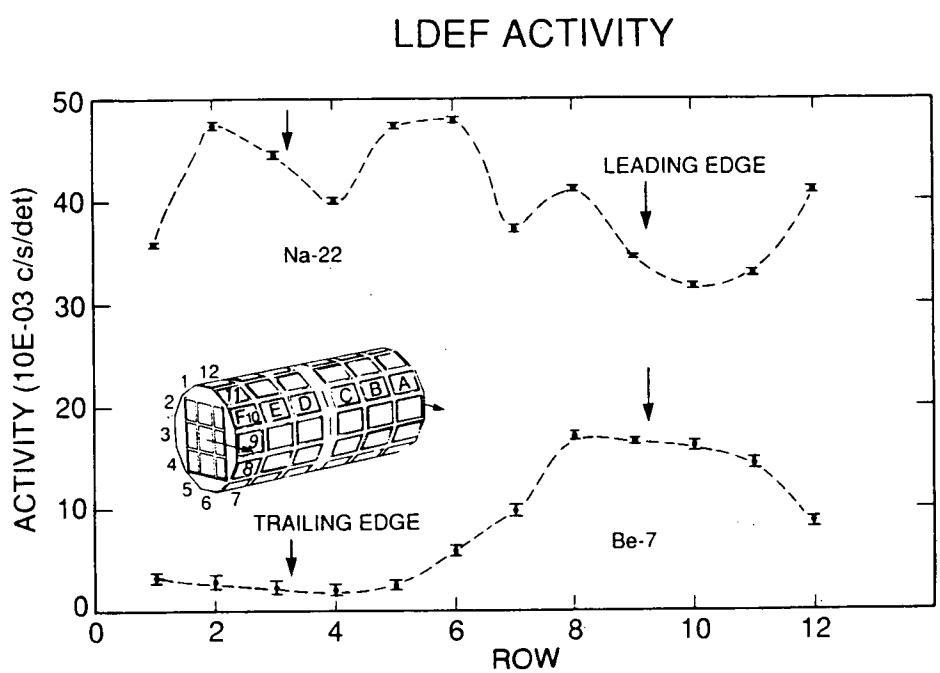

Figure 2. Comparison of activities of ^{7}Be (lower) and ^{22}Na (upper) seen during the gamma-ray survey of the LDEF spacecraft. The average counts per second per detector are shown for each row of LDEF for an average detector efficiency of 38.8% at 1332 MeV relative to a 7.6 x 7.6 cm diameter NaI(Tl) detector. The error bars include statistical and peak-fitting uncertainties. As a visual aid, dashed curves are drawn connecting the data points. The overlay is a diagram of LDEF.

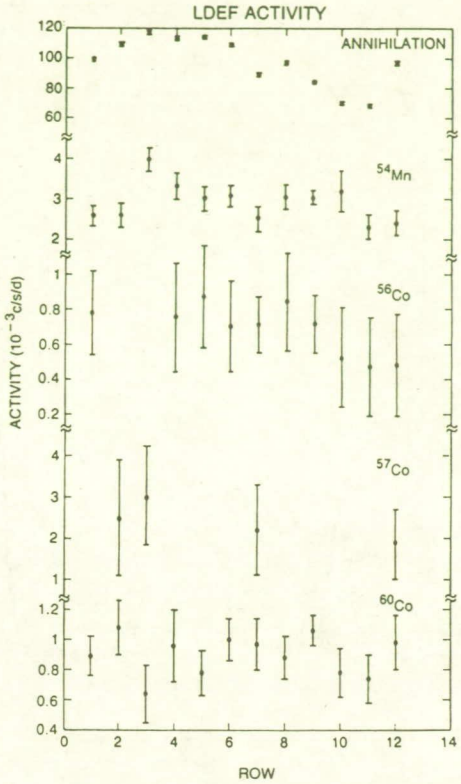

Figure 3. Distribution of activities from positron annihilation, ^{54}Mn and ^{56,57,60}Co around the LDEF spacecraft. Background activity has been subtracted. The error bars include statistical and peak-fitting uncertainties.

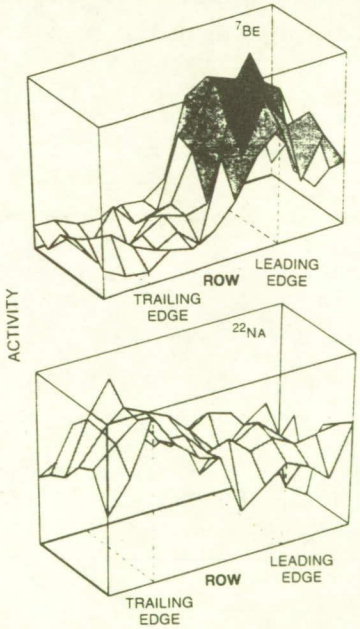

Figure 4. Map of the distribution of ^{7}Be and ^{22}Na activities around the LDEF spacecraft. There are 12 rows along the right axis and six bays along the left axis, with data from one experimental tray plotted for each bay and row. The dashed lines indicate the positions of the leading and trailing edges. The ^{7}Be activity is strongly peaked along the leading edge, while the ^{22}Na activity is higher along the trailing edge.

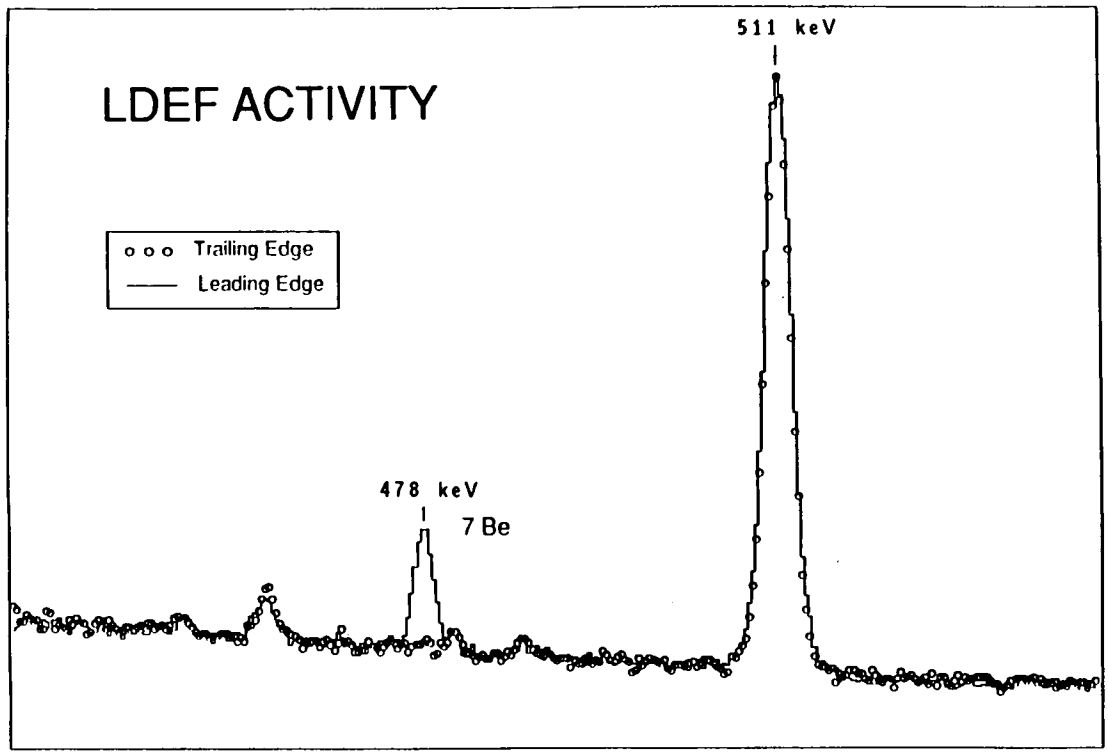

Figure 5. Comparison of gamma-ray spectra of germanium plates from trays E3 and E8 after their removal from LDEF. Shown is the region including the 478 keV gamma ray from ^{7}Be which is seen on tray E8 near the leading edge and not on tray E3 at the trailing edge. The 511 keV peak due to positron annihilation is seen both in the background and from ^{22}Na. The weaker unlabeled peaks are all in the background.

THE INTERACTIONS OF ATMOSPHERIC COSMOGENIC RADIONUCLIDES WITH SPACECRAFT SURFACES

J. C. Gregory
The University of Alabama in Huntsville
Materials Science Building Room 111
Huntsville, Alabama 35899
Phone: 205/895-6028, Fax: 205/895-6819

G.J. Fishman, B. A. Harmon, T.A. Parnell
NASA Marshall Space Flight Center
Space Science Laboratory ES-62
Huntsville, AL 35812
Phone: 205/544-7690, Fax: 205/544-7754

SUMMARY

The discovery of the cosmogenic radionuclide ^{7}Be on the front surface (and the front surface only) of the LDEF spacecraft (ref. 1) has opened opportunities to investigate new phenomena in several disciplines of space science. Our experiments have shown that the ^{7}Be found was concentrated in a thin surface layer of spacecraft material. We are able to explain our results only if the source of the isotope is the atmosphere through which the spacecraft passed. We should expect that the uptake of beryllium in such circumstances will depend on the chemical form of the Be and the chemical nature of the substrate. We have found that the observed concentration of ^{7}Be does, in fact, differ between metal surfaces and organic surfaces such as PTFE (Teflon). We note however that (a) organic surfaces, even PTFE, are etched by the atomic oxygen found under these orbital conditions, and (b) the relative velocity of the species is 8 $km^{-1}s$ relative to the surface and the interaction chemistry and physics may differ from the norm.

^{7}Be is formed by spallation of O and N nuclei under cosmic ray proton bombardment. The principal source region is at altitudes of 12-15 km. While very small quantities are produced above 300km, the amount measured on LDEF was 3 to 4 orders of magnitude higher than expected from production at orbital attitude. The most reasonable explanation is that ^{7}Be is rapidly transported from low altitudes by some unknown mechanism. The process must take place on a time scale similar to the half-life of the isotope (53 days).

Many other isotopes are produced by cosmic ray reactions, and some of these are suited to measurement by the extremely sensitive methods of accelerator mass spectrometry. We have begun a program to search for these and hope that such studies will provide new methods for studying vertical mixing in the upper atmosphere.

INTRODUCTION

The LDEF spacecraft was launched by the space shuttle Challenger on 7 April 1984 into a nearly circular orbit with an inclination of 28.5° and an altitude of 480 km. It was retrieved by the space shuttle Columbia on 12 January 1990 at an altitude of 310 km. Because of its large mass, long space exposure and the wide variety of materials onboard, the LDEF provided a unique opportunity for induced radioactivity studies. These measurements are still in progress and will be reported elsewhere.

The LDEF spacecraft has a twelve-sided cylindrical aluminium structure, 9.1 m long by 4.3 m in diameter (see Fig. 1). Its structure consisted of an open grid to which were attached various experiment trays designed to measure the effects of long space exposure on spacecraft materials and components. Throughout its orbital lifetime, the spacecraft was passively stabilized about all three axes of rotation, allowing one end of the spacecraft to point always toward the Earth, and fixed leading and trailing with respect to the orbital motion.

After its return to the Kennedy Space Center, gamma ray spectra were obtained along each of the 12 sides of the spacecraft using a germanium detector array provided by the Naval Research Laboratory. The gamma-ray line at 478 keV from the radioactive decay of ^{7}Be was observed to emanate strongly from the leading side of the spacecraft. (ref. 2) The weaker signal observed from the trailing side of the spacecraft was later traced to the gamma-ray flux from the leading surfaces after attenuation from passing through the body of the LDEF.

EXPERIMENTAL MEASUREMENTS OF RADIOACTIVITY

Individual components were brought to the Marshall Space Flight Center to quantify the residual radioactivity on the LDEF. Much of the counting work was performed at other radiation laboratories around the country. The authors are particularly indebted to Dr. Charles Frederick of the TVA Western Area Radiation Laboratory, Muscle Shoals, Alabama for many of the Al clamp plate assays. A high-purity germanium detector inside a low-level background facility was used to obtain spectra of small aluminium and steel samples taken from the leading and trailing sides. In Figs 2 and 3, gamma-ray spectra of two identical aluminium plates and two steel trunnion end pieces taken from the leading and trailing sides of the spacecraft are shown. A clear ^{7}Be gamma ray signal was seen on materials from the leading side, with little or no signal above background on the trailing side.

In Figure 4 the ^{7}Be activities for aluminum tray-clamps taken from trays all round the LDEF are shown, clearly demonstrating the leading edge effect. While ^{7}Be is also produced by spallation of Al nuclei in the spacecraft by cosmic rays, first order calculations have shown it to be barely measurable. Also the known anisotropy of the cosmic ray flux (the east-west effect) should have resulted in higher production on the rear (west-facing side) of the LDEF. Another isotope ^{22}Na, produced by spallation of spacecraft Al, clearly shows higher activity on the trailing edge of the satellite. Figure 5 shows tray clamp activities of ^{22}Na about twice as high on the trailing as on the leading edge, in agreement with the east-west anisotropy of the cosmic rays and trapped protons. This evidence clearly pointed to a source of ^{7}Be in the atmosphere being swept up by the front surface of the spacecraft.

In Table 1, the measured number of ^7Be atoms per unit area on various spacecraft surfaces is shown. The results are corrected to the retrieval date of 12 January 1990 and for the offset angle from the leading direction. The areal density for ^7Be on the aluminium and steel is the same within the experimental uncertainty, and is apparently not a strong function of the type or surface condition of the metal. However, the Teflon thermal coating which was used on many LDEF experiment trays, has a density of ^7Be an order of magnitude lower than that found on the aluminum surface. The reason for this apparent difference in uptake efficiency is unknown, but could be related to the covalent-bond structure of the material. The explanation may be complicated, also, by the observed erosion of the Teflon surface by atomic oxygen.

TABLE 1

LDEF Be-7 Surface Concentrations*

Material	Be-7 Areal Density (x 10e5 atoms/cm2)
Stainless steel trunnion face	5.3 +- 0.7
Polished aluminum plate- Exp. A0114	6.7 +- 1.0
Anodized aluminum experiment tray clamp	4.6 +- 0.5
Teflon thermal cover	0.9 +- 0.2

* Corrected for decay since recovery and for surface orientation relative to spacecraft ram direction.

^7Be PRODUCTION, DECAY AND DYNAMICS IN THE ATMOSPHERE

The short-lived isotope ^7Be was first detected in the atmosphere by Arnold and Al-Salih in 1955, (ref. 3) and later mapped by others as a function of altitude and latitude (ref. 4-8). It is produced in the atmosphere by high-energy cosmic-ray interactions with air as are other radioisotopes such as ^{14}C and ^3H. Once formed, ^7Be ions are presumed to oxidize rapidly and attach to small aerosol particles, which provide a downward transport mechanism from peak production regions of the atmosphere (ref. 9-16). The primary removal process for ^7Be, which occurs on a timescale comparable to its half-life, 53.2 days, is the washout of the aerosol-attached ^7Be in rain water (ref. 3-6).

At a given latitude above ~20 km, the production rate of ^7Be varies vertically and directly in proportion to the oxygen-nitrogen gas density. Peak production per unit volume occurs in the lower stratosphere, at 12-15 km, below which the cosmic-ray flux is substantially attenuated. At higher altitudes, the number of ^7Be atoms produced per unit volume decreases rapidly, but the number of ^7Be atoms produced per unit mass of air is essentially constant. Balloon and aircraft measurements (ref. 6, 15) are in approximate agreement with this, although few measurements extend much above the peak production altitudes.

From the measured densities of ^7Be on LDEF surfaces and in making some simplifying assumptions, we can estimate the concentration of ^7Be atoms per cm^3 of air at the LDEF orbital

altitude. Since the lifetime of LDEF is much greater than the mean lifetime of a ^7Be atom, and ignoring changes in altitude over the last 6 months in orbit, we assume a steady state relationship between pick-up of ^7Be and loss by decay:

$$\frac{dn}{dt} = 0 = -k\ n_{eq} + n^*\ v\ p_s$$

where: n is the density of ^7Be atoms on the surface at time t
k is the first-order decay constant for ^7Be
n_{eq} is the steady-state surface density of ^7Be in atoms cm^{-2}
n^* is the concentration of ^7Be atoms in orbital space (atoms cm^{-3})
v is the spacecraft velocity (cm)(s^{-1})
p_s is the sticking probability of Be on a metal surface

for first order kinetics of radioactive decay:

$$k = \frac{\ln 2}{t_{1/2}}$$

where: $t_{1/2}$ is the half life

Thus we have:

$$n_{eq} = n^*\ v\ t_{mean}\ p_s$$

where $t_{mean} = \frac{t_{1/2}}{\ln 2} = 76.8$ days for ^7Be

From the measured value of n_{eq}, assuming $p_s = 1$,

we have $n^* = 1.2 \times 10^{-7}\ cm^{-3}$ at 320km

or a relative concentration of 3.8×10^6 atoms per gram of air. In the peak production region, below 20km, previous measurements (ref. 4-8) yield a concentration of 1000 ^7Be atoms per gram of air, or ~0.1 atoms cm^{-3}, in agreement with a simple calculation using known values of the cosmic-ray flux and the production cross-section for the isotope. Thus, the measured concentration of ^7Be per unit mass of air at 320km is three to four orders of magnitude greater than it would be if it had been produced at that altitude.

The simplest explanation is that Be is quickly transported upwards from regions of the atmosphere where its numerical concentration is much higher (but not its relative concentration with respect to oxygen and nitrogen). This transport must take place on time scales similar to or shorter than the radioactive half-life (53.2 days).

Vertical transport timescales at altitudes of several tens of km to 100km are considered to be too long to provide an efficient source, but Petty (ref. 17) has shown that above a certain altitude (not well defined, but about 100km) simple diffusion of the light nucleus in the Earth's gravitational field would provide an enrichment of a factor of 500 or more at 300km. Turbulent mixing below 100km cannot be easily invoked as it proceeds at times scales longer than the isotope half-life. More detailed calculations are needed to see if closer agreement can be reached.

Thus far we have considered the chemical form of Be to be single atoms of mass 7. At low altitudes, rapid oxidation would be expected and in regions close to the tropopause, this would be followed by rapid absorption onto aerosol particles. The raining-out of these Be-bearing aerosols has proved a useful tool for measuring the efficiency of tropospheric mixing by thunderstorms.

If the Be were in the form of its normal oxide BeO (mass 23) at altitudes above 100 km, we can no longer rely on rapid diffusion to higher altitudes. While not much appears to be known of Be chemistry in the upper atmosphere, a great deal of work has been done on the chemistry of metals ablated into the upper atmosphere from meteorites. These metals include Mg, Ca, Al, Si and Fe.

^{7}Be is formed as a "hot" atom or ion, which must rapidly thermalize with the atmosphere. From studies of meteoritic ions in the atmosphere we may draw some general conclusion as to the chemical form in which the Be atom will finally take. The form of the meteoritic ions is highly variable with altitude and between day and night. Electropositive metals readily form positive ions:

$$Fe + h\nu \rightarrow Fe^+ + e$$
$$Fe + O_2^+ \rightarrow Fe^+ + O_2$$

At low altitudes neutralization may occur (X is a third molecule):

$$Fe^+ O_2 + X \rightarrow FeO_2^+ + X$$
$$FeO_2^+ + e \rightarrow Fe + O_2$$

In general at altitudes in excess of 100km the metal (M) oxides cannot survive in appreciable quantities due to reactions such as

$$MO^+ + h\nu \rightarrow M^+ + O$$
and
$$MO^+ + O \rightarrow M^+ + O_2$$

Thus at higher altitudes the singly-charged positive ion dominates for most metallic species studied. Of interest is the ratio M^+/M which varies with altitude and electropositive character of the metal. Examples of some measured ratios from the literature (ref. 18) for silicon and iron are:

Si^+/Si	=	0.006 at 96km
		0.2 at 110km
Fe^+/Fe	=	5 at 100km
		220 at 110km

Thus above 150km (and perhaps as low as 100km) most Be should exist as Be^+.

Important reactions might be:

$$Be + h\nu \rightarrow Be^+ + e$$
$$BeO + O_2^+ \rightarrow BeO^+ + O_2$$
$$BeO + h\nu \rightarrow BeO^+ + e$$
$$BeO^+ + O \rightarrow Be^+ + O_2$$

It is reasonable that a positive metal ion striking a clean metal oxide surface, especially with several eV kinetic energy, should easily enter the oxide lattice and remain trapped. While most metal (and metal oxide) surfaces in the ground-level atmosphere are usually found (by ESCA techniques) to be covered with a layer of hydrocarbon contamination, this is not the case with the leading surfaces of LDEF which are known to be continuously cleaned of combustible material by the action of atomic oxygen in the atmosphere. These atomic oxygen/satellite surface interactions have been intensively studied on the LDEF. The interaction of Be ions with metal oxides is an example of a new kind of chemical reaction between atmospheric species and satellite surfaces and has implications yet to be explored.

We investigated the form of binding of the Be to the aluminium surfaces on LDEF. Possibilities included (1) binding within an adsorbed contaminant layer, for example of hydrocarbon; (2) binding of Be-containing particulates, perhaps aerosols or meteoritic debris and (3) binding within the native oxide found on aluminum and other metals. Two kinds of Al plates from the LDEF were measured, some with several microns of oxide produced by anodization and the second type a polished Al plate from the UAH Atomic Oxygen Experiment A0114 (ref. 19). The oxide on this was only expected (ref.20) to be 50 - 100 Å thick.

The polished Al plate was coated with a solution of Collodion, which was then dried, stripped off and counted. No Be activity could be associated with the Collodion film. The method is used in industry to reliably and quantitatively remove particulates from sensitive surfaces. Next the plate was wiped first with alcohol, then with xylene. No activity was removed with the wipes. Finally an acid etch was used to remove the top 10 microns of the surface. The etch solution contained most of the Be activity formerly on the plate: that remaining being associated with either unetched surface or with re-adsorption of Be^{2+} ions onto the Al. This might be expected since a stable Be carrier solution was not used. The experimental results are consistent with the hypothesis that the Be species were penetrating the aluminium oxide layer on the surface of the plates and becoming permanently fixed in the oxide lattice. We believe the penetration to be of the order of one nanometer, since the kinetic energy of the Be species relative to the spacecraft was only 2.5eV. We do not have the capability to remove such a thin layer from large areas of metal surfaces, and thus cannot measure a depth/composition profile for the species.

^{7}Be is not the only nucleus produced by cosmic rays in the atmosphere. In fact all stable nuclei of lesser atomic weight than oxygen, nitrogen and argon must be formed. The means to detect the extremely small concentrations of most of these nuclides (in the presence of naturally occurring levels) do not exist. A few other unstable nuclides exist however with half-lives long enough to allow measurement, and short enough that there is no other natural background concentration. These are ^{14}C, ^{10}Be and possibly ^{26}Al (from argon).

The only method sensitive enough to measure these nuclides is accelerator mass spectrometry (AMS) (ref. 21). While the method has proved most useful for radioactive nuclei, emission of radiation by decaying nuclei is irrelevant to the AMS technique. Rather, all atoms of the nuclide are counted in the mass-spectrometer, giving some major advantages over radiation-counting methods.

^{10}Be is produced in a similar manner to ^{7}Be, by spallation of N and O induced by secondary neutrons from cosmic ray interactions in the atmosphere. The production efficiency is about 0.5 that of ^{7}Be, however its half-life is 1.5×10^{6} yrs (compared with 53.2d for ^{7}Be), resulting in measured ratios $^{10}Be/^{7}Be$ of about 3 in the stratosphere (ref. 22). While the atmospheric chemistry of the two isotopes should not differ appreciably, the diffusion of neutral atoms to higher altitudes should show measurable differences because of atomic mass.

^{10}Be decays to ^{10}B by internal conversion, emitting electrons over a wide energy range, while ^{7}Be decays to ^{7}Li by electron-capture, emitting gamma-rays of very narrow energy

distribution. The latter allows rates of a few decays per day to be measured in our low-level counting apparatus, while the former poses insurmountable counting problems. AMS however can detect ^{10}Be with undiminished sensitivity. We are currently working on chemical separation techniques* and plan a ^{10}Be run at the University of Pennsylvania† in fall of 1991.

We also plan a search for another cosmogenic radioisotope, ^{14}C, also using AMS. We plan to use the NSF-Arizona facility†† to investigate the take up of ^{14}C species by blanket material from LDEF. Carbon chemistry is completely different from that of the metals. Cosmogenic carbon should form CO and CO_2 rapidly in the lower atmosphere but its behavior at higher altitudes is unknown. Upwards diffusion of the oxide species would not be favored (their masses are 28 and 44) and the adsorption on spacecraft materials is unknown.

---

*Herzog, G.F. and Albrecht, A., Rutgers University, Dept. of Chemistry, Wright-Rieman Laboratory, New Brunswick, NJ, 08901, personal communications.

†Klein, J. and Middleton, R., University of Pennsylvania, Dept. of Physics, David Rittenhouse Lab, Room 1N12, 209 South 33rd St., Philadelphia, PA 19104-6396, personal communications.

††Jull, A.J.T., University of Arizona, NSF-Arizona Accelerator Facility, Tuscon, Arizona 85721, personal communications.

REFERENCES

1. Fishman, G.J., Harmon, B.A., Gregory, J.C., Parnell, T.A., Peters, P., Phillips, G.W., King, S.E., August, R.A., Ritter, J.C., Cutchin, J.H., Haskins, P.S., McKisson, J.E., Ely, D.W., Weisenberger, A.G., Piercey, R.B., and Dybler, T. *Nature*, **349**, 678-680, (1991).

2. Phillips, G.W., King, S.E., August, R.A., Ritter, J.C., Cutchin, J.H., Haskins, P.S., McKisson, J.E., Ely, D.W., Weisenberger, A.G., Piercey, R.B., and Dybler, T: Gamma Radiation Survey of the LDEF Spacecraft. NASA, Proceedings of the First LDEF Post-Retrieval Symposium, Kissimmee, FL, June, 1991.

3. Arnold, J.R. & Al-Salih, H. *Science* **121**, 451 (1955).

4. Beniof, P.A. *Phys. Rev.* **104**, 1122-1130 (1956).

5. Lal, D., Malhotra, P.K. & Peters, B. *J. Atmos. Terr. Phys.* **12**, 306-328 (1958).

6. Lal, D. & Peters, B. *Encyclopedia of Physics* (ed. Sitte, K.) 46/2, 551-612 (Springer, New York, 1967).

7. Bhandari, N.*J. Geophys. Res.* **75**, 2927-2930 (1970).

8. O'Brien, K. *J. Geophys. Res.***84**, 423-431 (1979).

9. Shapiro, M.H. & Forbes-Resha, J.L. *J. Geophys. Res.* **81**, 2647-2649 (1976).

10. Husain, L., Coffey, P.E., Meyers, R.E. & Cederwall, R.T. *Geophys. Res. Lett.* **4**, 363-365 (1977).

11. Bleichrodt, J.F. *J. Geophys. Res.* **83,** 3058-3062 (1978).

12. Viezee, W. & Singh, H.B. *Geophys. Res. Lett.* **7**, 805-88 (1980).

13. Raisbeck, G.M. *et al. Geophys. Res. Lett.* **8**, 1015-1018 (1981).

14. Sanak, J., Lambert, G. & Ardouin, B. *Tellus* **37B**, 109-115 (1985).

15. Dutkiewicz, V.A. & Husain, L. *J. Geophys. Res.* **90,** 5783-5788 (1985).

16. Dibb, J.E. *J. Geophys. Res.* **94**, 2261-2265 (1989).

17. Petty, G.W. *Geophys. Res. Lett.* **18 (9)**, p1687-1690 (Sept. 1991)

18. Solomon, S., Ferguson, E.E., Fahey, D.W. & Grutzen, P.J. *Planet. Space Sci.* **30** (11) 1117, (1982)

19. Gregory, J.C. and Peters, P.N., *The Long Duration Exposure Facility (LDEF)* NASA Publication **SP 473**, Edited by L.G. Clark, et al, pp 14-18, (1984).

20. Gregory, J.C., Peters, P.N., and Swann, J., *Applied Optics* **25**, 1290 (1986)

21. Elmore, D. and Phillips, F.M., *Science* **236**, 543, (1987)

22. McHargue, L.R. & Damon, P.E., *Reviews of Geophysics* **29** (2), p 141-158, May, 1991

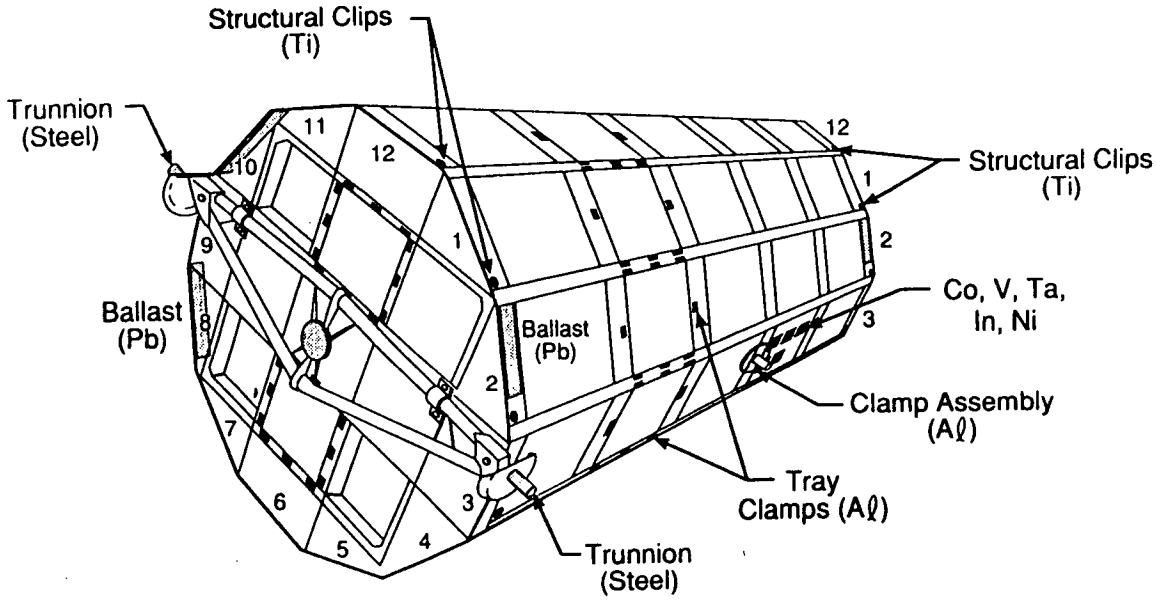

Figure 1. The LDEF spacecraft, showing the location of pieces of material studied for induced radio-activity

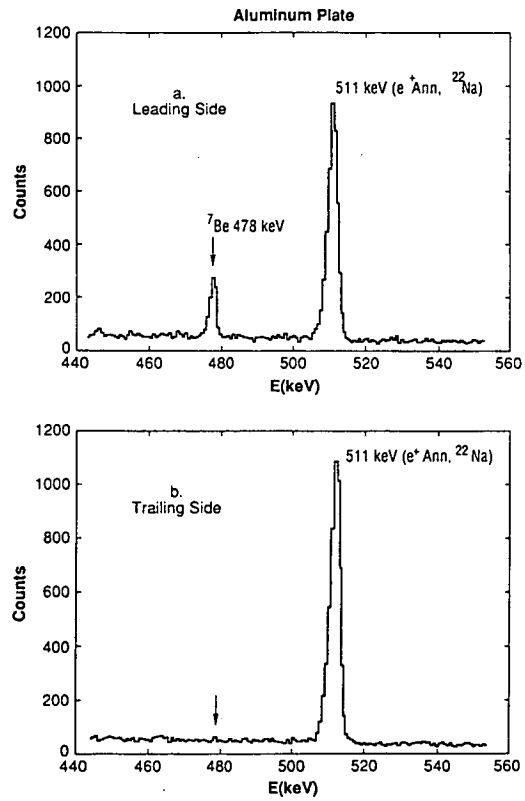

Figure 2. Portion of the gamma-ray spectrum obtained from an aluminum plate (a) on the leading side and (b) on the trailing side of the LDEF. The ^{7}Be line at 478 keV is seen only on the leading side.

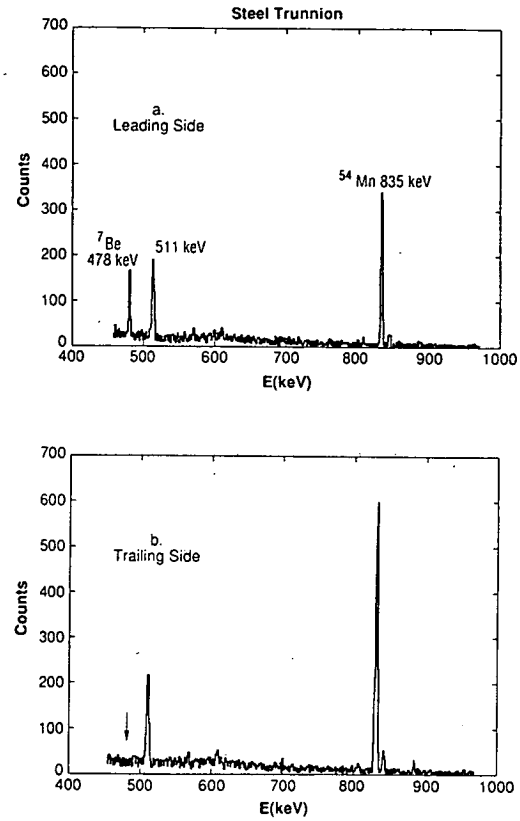

Figure 3. Portion of the gamma-ray spectrum taken from the stainless steel trunnion (a) on the leading side and (b) on the trailing side of the LDEF. The ^{7}Be line is seen only on the leading side, whereas the spallation products produced within the steel itself, ^{54}Mn and ^{22}Na are seen on both trunnions.

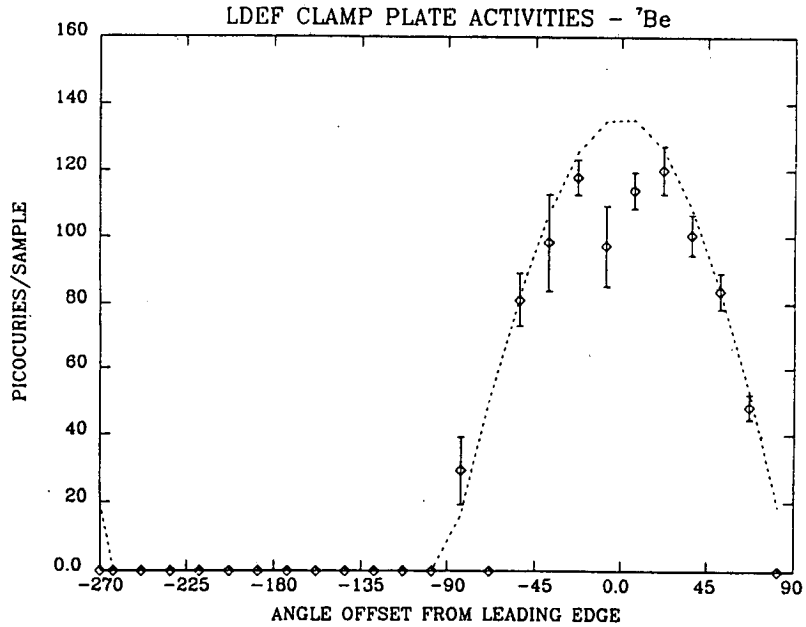

Figure 4. ^{7}Be activities for aluminum tray-clamps taken from all round the LDEF. The leading edge is nominally 0 deg and the trailing edge 180 deg. ^{7}Be activity is clearly a function of surface area projected in the forward direction of the spacecraft.

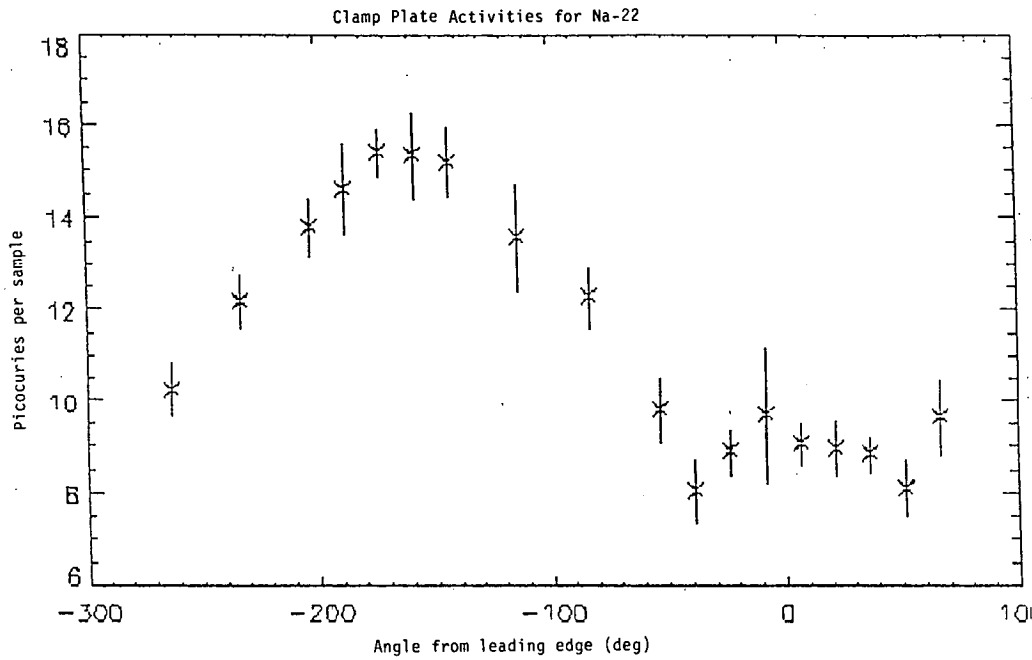

Figure 5. ^{22}Na activities for aluminum tray clamps taken from around the LDEF. The leading edge is 0 deg. and the trailing edge 180 deg. Activity is peaked at the trailing edge but found all round the spacecraft. As expected from the anisotropic cosmic ray and trapped proton fluxes, more activity is induced in materials on the westerly (trailing) side of the spacecraft.

SURFACE ACTIVATION OF CONCORDE BY ^{7}Be

P. R. Truscott, C.S. Dyer, and J.C. Flatman
Space Department
Defence Research Agency (Aerospace Division)
Farnborough, Hampshire, GU14 6TD, England
Phone: 44 252 24461 x3290, Fax: 44 252 377121

SUMMARY

Activation analysis of two airframe components from Concorde aircraft has identified the presence of ^{7}Be, a nuclide found by other investigators to have been deposited on the forward edge of the LDEF structure. The results of the Concorde analysis indicate that this phenomenon is very much a surface effect, and that the areal densities of the ^{7}Be are comparable to those found for LDEF. The collection of ^{7}Be by the aircraft must be greater than in the case of LDEF (since the duration for which Concorde is accumulating the nuclide is shorter) and is of the order of 1.2 to 41 nuclei-cm^{-2}s^{-1}, depending upon assumptions made regarding the altitude at which collection becomes appreciable, and the efficiency of the process which removes the radionuclide.

INTRODUCTION

Post-flight measurements of the Long Duration Exposure Facility (LDEF) have identified the presence of radioactive contamination by the beryllium isotope ^{7}Be (refs. 1-3). For the LDEF spacecraft the areal densities of the radionuclide were found to vary between 0.9×10^5 and 6.7×10^5 nuclei/cm^2, depending upon the material which had been contaminated. The source of this contaminant is believed to be cosmogenic, *ie* the spallation products of the interactions of primary and secondary cosmic rays with atmospheric nitrogen and oxygen. These spalled nuclei are then 'swept-up' by the spacecraft as it passes through the tenuous atmosphere at orbital altitudes. In support of this theory is the fact that the contamination is superficial, and only observed on the leading edges of the spacecraft.

RAE Farnborough initiated a similar activation analysis as a direct result of the LDEF findings, this time searching for ^{7}Be contamination in airframe components of Concorde aircraft. The normal cruising altitude for these aircraft (between 50,000 feet and 60,000 feet, or approximately 15 km and 18 km) is significantly higher than those of other commercial aircraft, and lies just below the Pfotzer maximum (at 18 km), where the cosmic-ray secondary particle flux peaks (ref. 4). At Concorde altitudes therefore the production rate for ^{7}Be is expected to be at or near its maximum (ref. 5).

© British Crown Copyright 1991/MOD
Published with the permission of the Controller of
Her Britannic Majesty's Stationery Office

The study of ^7Be deposition on high-altitude aircraft is not of isolated interest and has relevance to the LDEF analysis, since, as suggested by Parnell (ref. 6), aircraft studies may also provide a method of investigating proposed solar flare enhancements of this cosmogenic nuclide.

ACTIVATION ANALYSIS OF CONCORDE SAMPLES

Two samples of Concorde airframe were provided by British Airways for analysis, both of which had been exposed to the external airflow during flight:

(1) Strip of engine cowling, approximately 0.2cm x 1cm x 10cm.

(2) Access door from the upper port-wing of G-BOAB, approximately elliptical in shape, 61.2cm x 31.2cm. When affixed to the aircraft, the door is located above the port engine towards the centre of the wing (fig. 1).

γ-ray analysis of these samples using a high-resolution germanium detector has identified the presence of ^7Be in both cases. For the access door, the 477.5 keV γ-ray peak was found to decay with a half-life of 52±2 days, which agrees well with the half-life which is expected for ^7Be (53.29 days). The analysis also showed no other radionuclides in quantities exceeding nominal background levels.

After analyzing the decay of the radionuclide in the access door over the period of 1.5 months, the door was swabbed with a solution of mild detergent and water. This swabbing process was found to remove 47±4% of the ^7Be contaminant, transferring it to the swabs. A control sample of swabs (containing an identical detergent/water solution) did not identify any sources of 477.5 keV γ-rays. This indicates that the contaminant was from the door and, as with the LDEF analysis, is very much a surface effect. The high efficiency with which the contaminant was removed is believed to be because of an oil/grease layer on the door which collected a significant amount of the ^7Be during flight.

Based upon the γ-ray count rate observed, and estimates of γ-detection efficiency (refs. 7 and 8), it is estimated that the ^7Be activity from the door before it was removed was 219±22 decays/s, which equates to an areal density of $(9.6\pm0.9)\times10^5$ nuclei/cm^2 †. This density is of the same order as those found in the LDEF analysis (ref. 1) of the polished aluminium plate in Experiment A0114 ($(6.7\pm1.0)\times10^5$ nuclei/cm^2) and an anodized aluminium experiment tray clamp ($(4.6\pm0.5)\times10^5$ nuclei/cm^2).

---

†It should be noted that these levels of radioactivity are extremely low; this areal density equates to an activity from the access door surface of 3.9 pCi/cm^2, which is less than the background activity in ordinary window glass alone (4.2 pCi/cm^2).

^{7}Be ACCRETION RATE

Estimation of the accretion rate of the radionuclide is largely dependent upon the assumptions made regarding the altitude at which ^{7}Be collection becomes significant, and the efficiency with which the nuclide is removed when the aircraft is washed, approximately every month, using high-speed water-jets. The accretion rates (in nuclei-cm^{-2}s^{-1}) shown in Table 1 have been estimated based upon the best and worst case situations for collection and removal efficiencies. These values were calculated using specific information about the times and durations of the flights (from take-off and above 50,000 feet) before the door was removed, and the date the aircraft was last washed prior to analysis. Naturally the largest value for the ^{7}Be collection rate (41 nuclei-cm^{-2}s^{-1}) relates to when the nuclide has the least opportunity to accumulate on the surface; *i.e.* collection is only finite (and constant) above 50,000 feet, and the cleaning process is 100% efficient. Conversely, if both these factors are in favour of prolonged accumulation (deposition of ^{7}Be begins just after take-off, and washing removes none of the contaminant) the value becomes 1.2 nuclei-cm^{-2}s^{-1}. It should be noted that the assumption that the airframe begins to accumulate an appreciable amount of ^{7}Be immediately after take-off is clearly unrealistic (ref. 5), and this value is only given to indicate that changing the altitude at which collection starts is not as important to the accretion rate as the effects of surface-cleaning.

DISCUSSION

In Table 1, for two of the cases the percentage efficiency of the collection mechanism is given in parentheses. To calculate these values it was assumed that the ^{7}Be concentration above 50,000 feet was ~0.1 nuclei/cm^3 (ref. 1). It can be seen that in both instances the efficiency is significantly less than 100%. Therefore, unlike in the case of LDEF, there appears to be a sufficient concentration of the radionuclide at Concorde altitude to explain the high accretion rate, although this is dependent upon the exact mechanism by which the ^{7}Be attaches itself to the aircraft, a process which is as yet to be explained.

Any mechanisms which are hypothesized to explain ^{7}Be accretion on high-altitude aircraft must be capable of explaining the collection of the radionuclide on surfaces which are almost tangential to the velocity vector of the aircraft (and hence to the mean airflow), since the access door from Concorde was located towards the centre of the wing and not on a leading edge. Indeed any future experiments which investigate this process should be aimed at determining the collection rate as a function of the air velocity local to the sample, and the ^{7}Be depth profile in the sample, as well as the atmospheric density of the nuclide. Such experiments could involve, for example:

(1) Placing foil patches on various locations of the aircraft surface which may be frequently replaced (so that they do not build up deposits of oil or get washed), and which may then be electrochemically etched to obtain the depth profile.

(2) Flying an active γ-ray detector in the cabin area (such as the Shuttle Activation Monitor (refs. 9 and 10), or a germanium detector) to measure the ^{7}Be density in the atmosphere -

although careful consideration will obviously have to be given to the high γ-ray background expected from being near the Pfotzer maximum.

ACKNOWLEDGEMENTS

The authors would like to thank Doug Walker and Pat Colledge (of the Flight Data Recording Group, British Airways at Heathrow Airport) for the enthusiastic assistance they have given in the analysis which is presented in this paper.

REFERENCES

1. Fishman, G.J., Harmon, B.A., Gregory, J.C., Parnell, T.A., Peters, P., Phillips, G.W., King, S.E., August, R.A., Ritter, J.C., Cutchin, J.H., Haskins, P.S., McKisson, J.E., Ely, D.W., Weisenberger, A.G., Piercey, R.B., and Dybler, T.: Observation of ^{7}Be on the surface of LDEF spacecraft. Nature, 349, 1991, pp678-680.

2. Phillips, G.W., King, S.E., August, R.A., Ritter, J.C., Cutchin, J.H., Haskins, P.S., McKisson, J.E., Ely, D.W., Weisenberger, A.G., Piercey, R.B., and Dybler, T: Gamma Radiation Survey of the LDEF Spacecraft. Proceedings of the First LDEF Post-Retrieval Symposium, NASA CP- 3134, 1992.

3. Gregory, J.C., Fishman, G.J., Harmon, A., Parnell, T.A., Herzog, G., Klein, J., and Jull, A.J.T.: The interactions of atmospheric cosmogenic radionuclides with spacecraft surfaces. Proceedings of the First LDEF Post-Retrieval Symposium, NASA CP-3134, 1992.

4. Sandström, A.E.: Cosmic-ray physics. North-Holland Publishing Company, Amsterdam, 1965.

5. Benioff, P.A.: Cosmic ray production rate and mean removal time of beryllium-7 from the atmosphere. Phys. Rev., 104, 1956, pp1122-1130.

6. Parnell, T.A.: Summary of the First LDEF Post Retrieval Symposium (ionizing radiation). LDEF Spacecraft Environmental Effects Newsletter, 2 No. 3, 1991.

7. Truscott, P.R.: Application of the effective solid-angle method of calculating absolute peak efficiencies to extended cylindrical sources. Defence Research Agency (Aerospace Division) Working Paper SP-90-WP-60, 1990.

8. Truscott, P.R.: Methods for estimating absolute efficiencies of germanium detectors for cylindrical sources using geometric reduction. Defence Research Agency (Aerospace Division) Working Paper SP-91-WP-18, 1991.

9. Haskins, P.S., McKisson, J.E., Ely, D.W., Weisenberger, A.G., Piercey, R.B., Dyer, C.S., Ramayya, A.V., and Camp, D.C.: The Shuttle Activation Monitor: A system for direct comparison of gamma-ray detector materials in a space environment. IEEE Trans. Nuc. Sci., 37, No. 3, 1990, pp1256-1263.

10. Haskins, P.S., McKisson, J.E., Ely, D.W., Weisenberger, A.G., Ballard, T.A., Dyer, C.S., Truscott, P.R., Piercey, R.B., Ramayya, A.V., and Camp, D.C.: Performance of a BGO detector in low-Earth orbit. IEEE Trans. Nuc. Sci., 38, No. 3, 1991.

TABLE 1

^{7}Be accretion rate (nuclei-cm^{-2}s^{-1}) and accretion efficiency, in parentheses

Efficiency with which nuclide is removed during cleaning:	Altitude at which collection starts:	
	>50,000 feet	Immediately after take-off
All contaminant removed	41±4 (~0.7%)	26±0.3
No contaminant removed	1.9±0.2 (~0.03%)	1.2±0.1

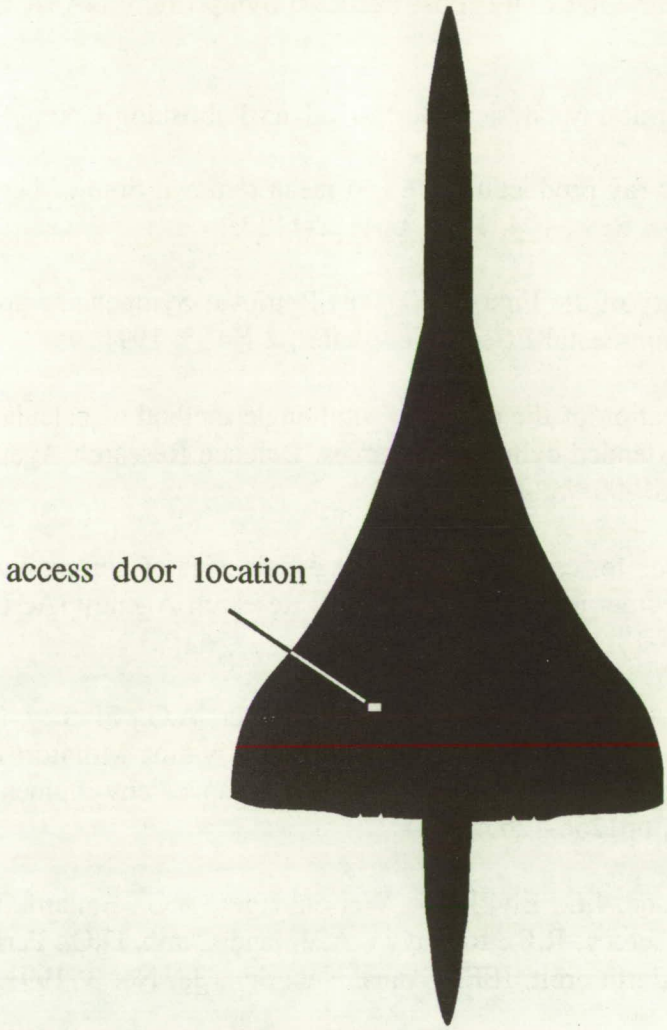

FIGURE 1
Plan view (silhouette) of Concorde indicating location of access door used in activation analysis

CHARGED PARTICLE ACTIVATION STUDIES ON THE SURFACE OF LDEF SPACECRAFT

Ilhan Olmez
Massachusetts Institute of Technology
Nuclear Reactor Laboratory
138 Albany Street
Cambridge, MA 02139

Forrest Burns and Paul Sagalyn
Army Materials Technology Laboratory
Watertown, MA 02172-0001

ABSTRACT

High energy proton induced nuclear reaction products are examined using seven elements, namely; Aluminum, Silicon, Nickel, Copper, Zirconium, Tantalum and Tungsten. We detected activities due to ^{22}Na from Al, ^{56}Co and ^{57}Co from Ni, ^{58}Co from Cu and ^{88}Y from Zr targets. No induced activity was observed in Si, Ta and W, most probably due to the long cooling times. Only the Zr sample contained a weak ^{7}Be peak, although Ta and W were also located at the leading edge of the spacecraft. Gamma-rays of individual isotopes were measured using high-resolution Ge(Li) solid state detector coupled to 4096-multichannel analyzer. Activities were calculated for ^{56}Co (846 keV) and Co-57 (122 and 136 keV's) at the time of the entry of the spacecraft and found to be 0.014 ± 0.005 c/sec. g, 0.018 ± 0.002 c/sec. g, and 0.0024 ± 0.0007 c/sec. g, respectively.

RADIOACTIVITIES OF LONG DURATION EXPOSURE FACILITY (LDEF) MATERIALS: BAGGAGE AND BONANZAS

Alan R. Smith and Donna L. Hurley
Engineering Division
Lawrence Berkeley Laboratory
University of California
Berkeley, CA 94720
Phone (415) 486-5679 FAX (415) 486-4122

ABSTRACT

Radioactivities in materials onboard the returned Long Duration Exposure Facility (LDEF) satellite have been studied by a variety of techniques. Among the most powerful is low-background Ge-semiconductor detector gamma-ray spectrometry, illustrated here by results obtained at the Lawrence Berkeley Laboratory's (LBL) Low Background Facilities, in a multi-laboratory collaboration coordinated by Dr. Thomas Parnell's team at the Marshall Spacecraft Center, Huntsville, Alabama.

The observed radioactivities are of two origins: those radionuclides produced by nuclear reactions with the radiation field in orbit; and, radionuclides present initially as "contaminants" in materials used for construction of the spacecraft and experimental assemblies. In the first category are experiment-related monitor foils and tomato seeds, and such spacecraft materials as aluminum, stainless steel, and titanium. In the second category are aluminum, beryllium, titanium, vanadium, and some special glasses.

INTRODUCTION

The voyage of the Long Duration Exposure Facility (LDEF) in low earth orbit was unexpectedly extended to nearly 6 years -- several years longer than originally planned. This circumstance greatly enhanced the opportunity for post-flight measurement of induced-activity radionuclides created in onboard samples and spacecraft materials. Our earthbound task is to measure these minute quantities of radioactivity -- as many as possible and as accurately as we are able, to insure the description of the radiation field calculated from these measurements will reflect the reality of LDEF' experience. Since the quantities of radioactivity to be measured are so small compared to normally encountered terrestial intensities, we must apply the most advanced techniques in radiation detection, in particular: detectors with very high sensitivity and energy selectivity, operated in environments that provide the lowest possible interference (background) with respect to the signals we seek to record.

In the broader context, participation in the LDEF analysis program is truly an opportunity of a lifetime. We consider it a rare privilege to be a part of this worldwide team, and an honor to contribute this report to the Symposium Proceedings.

DETECTOR SYSTEMS AND EXPERIMENTAL PROCEDURES

At LBL, "low-background" radiometric analysis is done at two facilities, one at Berkeley and one at Oroville, using three high-resolution γ-ray spectrometer systems based on high-purity intrinsic germanium semiconductor detectors. All three detectors are of the closed-end coaxial type, with "rated" efficiencies of about 30% -- relative to the efficiency of a 3-in. diameter by 3-in length NaI (Tl) scintillation crystal detector for the 661 KeV γ-rays from Cs-137.

The GEM and NGEM systems are at the Berkeley Low Background Facility (a large room-size facility shielded by 5 feet of low-activity concrete), and use p-type germanium detectors. The GEM detector has a passive Pb shield, while the NGEM detector has a passive Pb shield that is surrounded by an active cosmic-ray veto "shield". Data are collected in the format of 8192-channel multi-channel analyser (MCA) spectra, usually spanning the energy range 35 - 3600 KeV. The MERLIN system has a passive Pb shield, and is located under 600 feet of bedrock at the LBL Oroville Facility. Data are collected in the format of 4096-channel spectra, usually spanning the energy range 15 - 3300 KeV.

The background (BKG) spectra of our Ge-detector γ-ray spectrometers exhibit two distinctly different characteristics: relatively featureless and slowly varying continuous distributions that extend across the entire energy range, and well-isolated peaks superimposed on this continuum. The sharp peaks contain all the information used here for identification and quantification of radionuclides. It is a fortunate circumstance that induced-activity peaks we need to measure rarely overlap peaks in the BKG distributions; hence, our sought-after peaks are usually measured only against the continuum component of the BKG.

Representative values of BKG continuum counting rates are listed below for the three LBL systems. Count rates are given for several energies, in units of counts per minute in a 5-KeV wide interval of suitable width for measurement of a small peak:

	5-KeV Wide Interval		
Energy KeV	GEM c/min	NGEM c/min	MERLIN c/min
500	0.15	0.04	0.015
1000	0.045	0.012	0.004
1500	0.022	0.008	0.002
2000	0.016	0.0035	0.0006
3000	0.0077	0.0014	0.00023

The MERLIN system at Oroville has by far the lowest background of any system available for these measurements, and so is the "star" in our LDEF sample analysis program. It always provides the most accurate results on measurement of the smallest peaks; hence, samples that required measurements for both the lowest intensity peaks and the most comprehensive radionuclide inventories were analysed with the MERLIN system.

Sample analysis times ranged from as short as a few 10's of minutes for some of the system efficiency calibration runs to as long as 10000 minutes for runs on the lowest-activity LDEF samples. Samples were almost always counted at a position as close as possible to the detector -- directly on the flat end face of the detector vacuum vessel, a distance of 6 to 10 mm (detector-dependent).

The tabulation of results appearing in the following sections includes the counting rates observed from the diagnostic peaks used for assay of each radionuclide, and estimates for the decay-corrected absolute activity of each radionuclide, in units of pico-curies per kilogram (pCi/Kg) of metal. The count rates represent net peak areas obtained directly from spectral data in units of counts per minute (c/min), with associated uncertainties of one standard deviation (S.D.) that are based only on the statistics of counting data. Each net peak area was determined through an operator-controlled MCA-resident algorithm: the area equals the difference between the summed counts in the peak-containing interval and a linearly interpolated continuum whose magnitude is determined from the interval endpoints. No use was made of algorithms that employ channel-by-channel peak-shape fitting.

Calculations for absolute radionuclide activities are based on nuclear parameters given in the most recent edition of Table of Isotopes (Ref 1). Conversion of peak count rates to absolute activity values also incorporate empirically determined parameters for detection efficiency and combined geometric/absorption corrections for the three spectrometer systems used in these measurements. Any summing effects that may occur in detectors from cascade (coincident) γ-rays are NOT taken into account in these preliminary analyses. The calculated activity values have NOT been adjusted to conform with any assumptions relating the degree of secular equilibrium between in-orbit activating particle flux and the activity level existing at satellite recovery time. The only time-domain correction applied was to account for the decay of each radionuclide between recovery time and the time of γ-ray spectrometric analysis.

The evaluation of uranium-series disequilibrium observed in some materials was greatly facilitated through use of the comprehensive lists of γ-rays from this decay chain assembled in the early 1970's by Smith and Wollenberg (ref 2). These lists detail the three decay chains (U-238), U-235, and Th-232), giving energies and intensities appropriate to equilibrium conditions for all known γ-rays in each chain.

RESULTS OF GAMMA-RAY SPECTROMETRIC MEASUREMENTS

Metal Radioactivation Monitors

Among the "Intentional Samples" onboard the LDEF satellite were four sets of five different metal "foils", specially selected for their nuclear reaction properties. Radioactivities (with appropriately long halflives) induced in these materials during spaceflight would be measured after satellite recovery, to provide valuable insight on characteristics of the integrated radiation exposure received in orbit. The selected metals were cobalt, indium, nickel, tantalum, and vanadium (Co, In, Ni, Ta, V), in the form of 2-inch squares of 1/8" thickness. All sets of metals were recovered and later distributed to several of the participating laboratories for radiometric analysis.

We initially received the 4-member set from Experiment P0006 (on the same tray as the tomato seeds); there was no cobalt square in this set. Later in 1990 we received the three other indium squares, to permit analysis of all 4 members of this element at the same laboratory. We also received the three cobalt members in July 1991, and are presently measuring their radioactive content.

Reported here are quantitative results for the major γ-emitting radionuclides found in all four members of the Experiment P0006 set, all four indium members, and two of the three cobalt members. Tabulations include the counting rates observed from the diagnostic peaks used for assay of each radionuclide, and estimates for the decay-corrected absolute activity of each radionuclide in units of pico-curies per kilogram (pCi/Kg) of metal. The count rates listed represent net peak areas obtained directly from spectral data in units of counts per minute (c/min), with associated uncertainties of one standard deviation (S.D.) that are based only on the statistics of counting data.

Cobalt Metal Monitors

The three cobalt members were received in July 1991 and are presently being analysed. Preliminary results from two cobalt squares are included here. (Note, there was no cobalt in the Experiment P0006 set.) No evidence was found for the presence of radioactivity brought in this material from earth. Note however, the same suite of Uranium-series radionuclides observed in Vanadium Square #4 and the titanium alloy clips (see elsewhere, this report) were observed in "reactor grade" cobalt samples obtained at LBL in the early 1960's. The following tabulation summarizes results obtained from 10000-minute runs on the GEM and NGEM system at our Berkeley facility.

				Observed		Activity	
Sample	Nuclide	Obs. Peaks	Diagnostic Peaks (KeV)	Net c/min	S.D.	pCi/Kg	S.D.
Co #C9	Mn-54	1	835	0.143	0.004	40.8	1.1
	Co-57	2	122	0.772	0.010	124.9	1.6
	Co-60	2	1173+1332	0.141	0.004	18.6	0.5
Co #G12	Mn-54	1	835	0.076	0.004	28.0	1.4
	Co-57	2	122	0.404	0.008	83.6	1.7
	Co-60	2	1173+1332	0.118	0.004	20.0	0.7

All three radionuclides observed in both cobalt squares were measured with good statistical precision. The activities of Co-60, a product of slow-neutron capture, were seen to be nearly the same in both samples. However, the activities of Mn-54 and Co-57, products of energetic-particle reactions, were about 1.5 times greater in Co #C9 than in Co #G12. This ratio is similar to the north/south ratio for activities measured in near-surface trunnion slices (see the section on Trunnion Slice Activities).

Indium Metal Monitors

The γ-ray spectral data from Indium Square #4 were acquired in late March 1990, about 2 months after LDEF recovery, and contained peaks from seven different space-produced radionuclides (Co-60, Y-88, Rh-101, Rh-102, Ag-110m, Sn-113, and In-114m). Data were also acquired from the indium members belonging to the other three monitor sets, received at a later time and analysed during the period June-July 1990. Space-produced radionuclides observed in these three samples included Rh-102, Ag-110m, Sn-113, and In-114m. No evidence was found for the presence of radioactivity brought in this material from earth.

Each sample was counted for approximately a one-week period. The MERLIN system was used to analyse samples #4 (Experiment P0006), C9 (IC9-IN), and Bars. Indium G12 (G-12-B-3-F) was analysed with the NGEM system at Berkeley. Results are tabulated below for the four radionuclides Rh-102, Ag-110m, Sn-113, and In-114m.

				Observed		Activity	
Sample	Nuclide	Obs. Peaks	Diagnostic Peaks (KeV)	Net c/min	S.D.	pCi/Kg	S.D.
In #4	Rh-102	5	475	0.010	0.004	2.2	0.9
	Ag-110m	5	657+884	0.026	0.005	5.1	1.0
	Sn-113	1	392	0.121	0.008	54.0	3.6
	In-114m	1	191	0.042	0.008	105.	20.
In #C9	Rh-102		475	0.013	0.002	3.2	0.4
	Ag-110m		657+884	0.016	0.002	3.9	0.5
	Sn-113		392	0.059	0.004	40.9	2.7
	In-114m		191	0.008	0.005	55.	35.
In #G12	Rh-102		475	0.014	0.002	2.3	0.3
	Ag-110m		657+884	0.014	0.002	2.3	0.3
	Sn-113		392	0.047	0.003	21.0	1.2
	In-113m		191	0.008	0.003	35.	15.
In Bars	Rh-102		475	0.006	0.002	2.2	0.6
	Ag-110m		657+884	0.008	0.002	3.2	0.8
	Sn-113		392	0.025	0.003	35.1	4.2
	In-114m		191	0.008	0.005	190.	115.

While the statistical precision is adequate for comparing Sn-113 values, activity values for the other three radionuclides have large uncertainties and are marginally suitable for comparison purposes. Quantitative use of values for relatively short-lived In-114m is not recommended, except possibly from Indium #4, which was received and counted much earlier than were the other three samples.

Nickel Metal Monitor #4 (Experiment P0006)

The γ-ray spectral data from this sample were acquired about 2-1//2 months after LDEF recovery. Many peaks from space-produced radionuclides were present; in addition, there was no evidence for the presence of radioactivity brought in this material from earth. The results tabulated below were obtained from a MERLIN system run of 10476 minutes duration at the end of March 1990.

				Observed		Activity	
Sample	Nuclide	Obs. Peaks	Diagnostic Peaks (KeV)	Net c/min	S.D.	pCi/Kg	S.D.
Ni #4	Sc-46	2	889+1121	0.0065	0.0017	1.6	0.4
	Mn-54	1	835	0.0973	0.0033	27.3	0.9
	Co-56	9	847	0.0714	0.0029	33.2	1.3
	Co-57	2	122	2.098	0.0029	322.	2.
	Co-58	1	811	0.0851	0.0033	41.7	1.6
	Co-60	2	1173+1332	0.0288	0.0021	4.7	0.3

Of the six radionuclides reported here, all have activity values with good statistical precision except for Sc-46. All six radionuclides are products of energetic-particle reactions. In addition, a tiny peak appeared in the spectral data at about 1274 KeV energy, indicating the possible presence of Na-22 at a very low level (about 0.5 pCi/Kg); this nuclide was most likely produced by interactions with the galactic cosmic rays.

Tantalum Metal Monitor #4 (Experiment P0006)

The γ-ray spectral data from Tantalum Square #4 were acquired from a MERLIN run of 8562 minutes duration in late March 1990. The data are rich in observable peaks, although a relatively small number of radionuclides is responsible: the five nuclides Lu-172, Hf-172, Lu-173, Hf-175, and Ta-182 generated at least 40 observable peaks. Results are tabulated below for the four radionuclides Lu-172, Lu-173, Hf-175, and Ta-182.

				Observed		Activity	
Sample	Nuclide	Obs. Peaks	Diagnostic Peaks (KeV)	Net c/min	S.D.	pCi/Kg	S.D.
Ta #4	Lu-172	20	1093	0.128	0.004	35.9	1.1
	Lu-173	1	272	0.107	0.006	161.4	8.3
	Hf-175	1	343	0.121	0.006	36.6	1.9
	Ta-182	18	(5 peaks)	0.307	0.008	90.3	2.3

All four radionuclides listed above were measured with good precision. One of the dominant activities, 115-day halflife Ta-182, was produced by slow neutron capture in Ta-181. Its production mechanism is similar to that for production of Co-60 from Co-59; its activity can be compared to the Co-60 activity in Cobalt Square C9 and G12, given in an earlier section of this report. A simple calculation implies the observed Ta-182 activity is significantly greater (perhaps 2-fold greater) than would be expected from a tantalum monitor located with either of the two cobalt monitors. The proximity of Ta #4 to a substantial quantity of hydrogenous moderator (the tomato seeds, for example) could serve to explain such a circumstance.

All other listed radionuclides were produced by energetic-particle reactions, predominantly energetic protons. The other dominant radionuclide, 6.7-day halflife Lu-172, reflects the presence of its parent, 1.37-year halflife Hf-172; thus its activity actually provides a measure of Hf-172 activity.

We found no evidence for the presence of primordial terrestrial radionuclides in this sample of tantalum. This negative finding is consistent with results obtained at LBL on the "natural" radioactivity of this material, in connection with use of similar-size pieces of tantalum in fast neutron flux integrators over the past 25 years.

Vanadium Metal Monitor #4 (Experiment P0006)

The γ-ray spectral data were acquired 3 months after LDEF recovery, and contained few peaks that originated from space-produced radionuclides. The results tabulated below were obtained from a MERLIN run of 9748 minutes duration in mid-April 1990.

				Observed		Activity	
Sample	Nuclide	Obs. Peaks	Diagnostic Peaks (KeV)	Net c/min	S.D.	pCi/Kg	S.D.
V #4	Sc-46	2	889+1121	0.042	0.003	17.4	1.1

Uranium Concentration:	U-235 (via U-235)	1.5	0.1 ppm
	U-238 (via Pa-234m)	1.1	0.2 ppm

The only space-produced radionuclide measurable at counting time was 84-day halflife Sc-46, produced by energetic-particle reactions, predominantly energetic protons. Many other peaks were present at above-BKG intensities, revealing the presence of "baggage" brought from earth as a consequence of the origin and processing of this metal.

The γ-ray evidence is interpreted to show the presence of uranium at a mass concentration of 1.5 ppm (parts per million), or about 500 pCi/Kg. The U-235/U-238 ratio appears to be normal within statistical accuracy of the data. Late members of the U-238 series (Ra-226 and daughters) are virtually absent. The comparable late members of the U-235 series were not observed; however, their expected intensities based on equilibrium with the observed U-235 concentration, would be obscured by the spectrometer system BKG. (See comments elsewhere in this report concerning the titanium alloy radioactivities.) Several peaks useful in Th-series assay (238, 583,

911, 2614 Kev) are slightly above BKG intensities, indicating a mass concentration of about 0.1 ppm (20 pCi/Kg), with a 30% uncertainty (standard deviation). Th-series disequilibrium cannot be accurately determined from data of such poor precision.

This suite of radionuclides in vanadium has been observed previously at LBL, dating from a sample obtained in 1960. We have observed the same radionuclides in titanium alloy Type 6-4, (discussed elsewhere in this report) and in several other samples of this alloy obtained in the last 5 years as candidate material for low-level counting systems.

Tomato Seeds

Representative samples of tomato seeds (from the SEEDS Experiment, described elsewhere in this Proceedings) retrieved from the LDEF satellite were analysed for long-lived gamma-emitters with LBL's lowest-background γ-spectrometer, the MERLIN system, located underground in the power plant of the Oroville Dam (a facility of the California Department of Water Resources). Four 50-gram sealed-in-plastic packets were received, one from each of Layers A, B, C, D of Canister 3 -- wherein Layer A was least shielded and Layer D most heavily shielded from Space Radiation. Short runs (about 1000 minutes) on the A and D packets failed to disclose any differences in their respective content of radionuclides. All four packets were then counted together to achieve maximum sensitivity, in a run of 6767 minutes duration.

The dominant radionuclide observed in all three runs was K-40, the naturally occurring radioisotope of potassium, present as a consequence of the potassium content of the seeds. Both Be-7 and Na-22 were detected at very low concentrations in this 4-packet run, produced from energetic-particle reactions on carbon, nitrogen, oxygen, and sodium--major chemical elements in the seeds. These findings are summarized as follows:

Potassium (1461 Kev):	2.39 ± 0.01 c/min	$\rightarrow$	5400 pCi/Kg
Be-7 (477 KeV):	0.014 ± 0.002 c/min	$\rightarrow$	16 pCi/Kg
Na-22 (1274 KeV):	0.0095 ± 0.0014 c/min	$\rightarrow$	2 pCi/Kg

The induced activity intensities are totally inconsequential, even in comparison to the (benign) activity of essential potassium. The appropriate LDEF researchers were notified immediately of our radiometric analysis results, to facilitate quick distribution of tomato seeds to the millions of eager young grower-participants.

SPACECRAFT STRUCTURAL MATERIALS

Titanium Alloy Clips

Four sets of titanium alloy Type 6-4 (90% Ti, 6% Al, 4% V) two-piece "clips" (#916AE2, #916A12, #920FE1, #920FI1) were sent to LBL for special study, arriving in late June 1990 and analysed immediately thereafter. The only space-produced radionuclides measurable at analysis time were Na-22, Sc-46, and possibly Ti-44. The observed Sc-46 counting rates (889 and 1121 KeV peaks summed) were in the range 0.1 - 0.2 c/min, which translated into an estimated activity

level of 30 - 40 pCi/Kg at satellite recovery time. (These estimates will be refined for inclusion of more precise values in the later comprehensive report.) The Na-22 activity is estimated at about 4 pCi/Kg, and could have been produced mainly by reactions on the 6% abundant aluminum component, rather than by higher-energy reactions on the 90% abundant titanium component. (See the section on Aluminum Keel Plates, this report.)

Detailed analysis of the γ-ray spectral data reveals the presence of a significant concentration of uranium in this material--in the range 12-14 ppm uranium by weight; in fact, uranium series γ-ray peaks are dominant in these spectra. The γ-ray evidence confirms existence of a "normal" U-235/U-238 ratio. Later members of the U-238 chain, Ra-226 and its γ-emitting daughters are virtually absent; however, the later γ-emitting members of the U-235 chain, Th-227 through Pb-211, are present in concentrations appropriate to the observed U-235 abundance. The thorium series is not present in measurable concentration.

We have analysed a number of pure titanium samples at LBL in the past 10 years; none contained measurable uranium (at a detection limit of about 0.003 ppm), and thorium only in the range 0.01 - 0.05 ppm. Several other samples of titanium alloy 6-4 have also shown the presence of the same radionuclides seen in the LDEF parts,but at lower concentrations. The 6% aluminum component could reasonably contribute only 0.05 - 0.1 ppm thorium and 0.02 - 0.05 ppm uranium to the alloy.

This unusual suite of radionuclides is believed to enter the alloy through the 4% vanadium component. (We have previously observed these radionuclides in samples of metallic vanadium.) Implicitly, there must have been a uranium concentration of about 300 ppm in the vanadium fraction of the alloy. Note that carnotite is a major ore of vanadium, and is also a major ore of uranium. The chemistry of the vanadium recovery process could allow uranium and Ac-227, the 21.6-year halflife parent of the observed U-235 daughters, to come through into the finished product, while at the same time rejecting Ra-226 and thorium.

Whatever the route, the presence of these radionuclides at concentrations of the magnitude observed in the LDEF parts is of serious concern to designers of any spacecraft instrument packages that contain nuclear radiation detection systems whose BKG responses are to be minimized.

Trunnion Section Slices

One of our major efforts was to establish depth profiles for induced activities in sections cut from the 3.25-inch diameter stainless steel trunnions. (See elsewhere, this Proceedings, for description of these spacecraft parts.) Our sample suites included four sets of radially-cut slices from both north-facing and south-facing quadrants of trunnion sections LHG and RHG. The outer faces of slices (N1, S1) are the actual trunnion surface, while the inner faces of slices (N7, S7) represent material at a depth of about 1.0 inches (~20 g/cm^2) below this surface. Slices ranged in thickness from 0.034" to 0.251", and weighed between 19.3 and 75.1 grams. Spatial positions of the slices are as follows:

Slice Number	Depth Interval Inches
1	0.000 - 0.034
2	0.049 - 0.114
3	0.128 - 0.232
4	0.247 - 0.383
5	0.398 - 0.564
6	0.578 - 0.774
7	0.789 - 1.040

All three spectrometer systems were used for this series of measurements, spanning the interval from April 1990 through June 1991, employing sample counting times that ranged from 2400 to 10100 minutes. Results are tabulated here for the two radionuclides (Mn-54 and Co-57) that dominated after the unavoidable decay period of 2 months between the time of satellite recovery and sample availability. Much smaller quantities of the radionuclides Na-22, Sc-46, Co-56, Co-58, and Co-60 were also observed in some of the slices. These results will be included in a later report summarizing all the measurements made at LBL on samples from the LDEF satellite mission.

Observed count rates for the Mn-54 834KeV peak ranged from 0.074 c/min to 0.470 c/min; rates for the Co-57 122 KeV peak ranged from 0.021 c/min to 0.177 c/min. The resulting Mn-54 values are of higher precision than are the Co-57 values, mainly because of the greater peak count rates, but also as a consequence of the lower BKG rate at the higher γ-ray energy.

Tabulated below are calculated active values for both Mn-54 and Co-57, in units of pCi/Kg of sample. The "S.D." values are in terms of a single standard deviation on counting data, as propagated through the calculations, and do not include any estimates of uncertainty in detection efficiency or non-uniformity in sample activity.

Trunnion Slice		Mn-54 pCi/Kg	Mn-54 S.D.	Co-57 pCi/Kg	Co-57 S.D.	Trunnion Slice		Mn54 pCi/Kg	Mn54 S.D.	Co-57 pCi/Kg	Co-57 S.D.
LHG	N1	171.3	6.0	38.0	3.6	RHG	N1		(not available)		
	N2	137.3	5.2	33.2	1.6		N2	85.1	2.6	21.7	1.5
	N3	117.5	3.7	25.0	1.6		N3	84.4	3.2	19.7	2.3
	N4	105.1	2.0	21.8	0.9		N4	75.3	1.7	18.9	1.0
	N5	95.0	2.5	22.9	1.6		N5		(not counted)		
	N6	93.1	3.8	21.6	2.5		N6	73.2	1.7	17.2	1.3
	N7	97.0	3.2	18.5	2.2		N7	65.5	3.1	17.0	3.4
	S7	82.6	2.6	17.1	2.2		S7	62.7	2.8	16.4	2.5
	S6	73.4	2.8	17.1	1.6		S6	61.5	2.3	12.4	1.7
	S5	69.3	2.1	13.4	1.3		S5	65.1	2.1	13.6	1.4
	S4	68.4	2.8	14.0	1.7		S4	59.6	2.0	11.6	1.3
	S3	75.8	2.4	15.3	1.1		S3	70.7	2.4	14.2	1.0
	S2	88.2	2.7	15.9	1.0		S2	84.6	2.4	18.0	1.1
	S1	107.3	4.7	20.9	3.0		S1		(not available)		

The Mn-54 activity values in the north-side profile of trunnion section LHG are higher than values in the south-side profile, where the average for the N/S ratio is about 1.56 for the first four outer layers. Activity values for the N7 and S7 slices suggest there may be a broad low peak of Mn-54 activity located near the center of the trunnion section. We can explain the major features of these profiles in a qualitative sense. The inwardly descending profiles are the result of interactions with trapped protons, while the broad centrally located "peak" is associated with additional interactions caused by the buildup of secondaries produced by the very energetic galactic cosmic rays. The north-side and south-side Mn-54 activity profiles for the RHG section are much more similar in magnitude than were observed from the LHG section set. The Co-57 activity profiles from both trunnion sections are similar in shape to their Mn-54 counterparts. However, the lower precision of Co-57 data makes it less appropriate to ascribe the same kind of detailed description as is possible for the Mn-54 profiles.

Co-60 was detected in some of the slices, at count rates in the range 0.003 - 0.006 c/min for each of the two peaks. The data are of relatively low precision, making for large uncertainty in the shapes of activity-vs-depth profiles, and hence difficulty in determining whether this activity is space-produced. The implied Co-60 activity values are on the order of 1 pCi/Kg, and fall within the range of Co-60 content of earth-bound stainless steels analysed at LBL, dating from material obtained in the mid 1960's to the present. Analysis of stainless steel "blanks" traceable to the LDEF trunnions could clarify this situation.

Aluminum Keel Plate Radioactivity

Two aluminum (alloy 6061) Keel Plates (KP-4 and KP-9) were analyzed in early 1991, at which time the only measurable space-produced radionuclide was Na-22. (Analysis of two aluminum alloy Scuff Plate Spacers in late March 1990 also revealed the presence of Be-7, as well as the much longer-lived Na-22.) We also obtained values for the "natural" radioactivity content of the keel plate alloy. Tabulated below are results for both space-produced and "natural" radionuclides:

Sample	Nuclide	Diagnostic Peak (KeV)	Observed c/min	S.D.	Activity pCi/Kg	S.D.
KP-4	Na-22	1274	0.238	0.012	140	7
Kp-9	Na-22	1274	0.194	0.007	86	3

Uranium (U-235)	2 ppm
Ra-226 (Bi-214)	0.02 ppm (U-equivalent)
Thorium (TI-208)	0.355 ppm

The measured uranium-series and thorium-series radioactivities lie within the ranges observed for other pure aluminum and aluminum alloy samples analysed at LBL since the early 1960's. (See next section this report.)

Natural Radioactivity in Spacecraft Materials

We have investigated the "natural" radioactivity of a wide variety of materials at the LBL Low Background Facilities in an ongoing effort since 1960, through application of high-sensitivity γ-ray spectrometric techniques. These studies have almost always been conducted in support of specific requirements of various research programs. The resultant body of information relating to "radioactivity in stuff" is neither comprehensive nor complete, and has usually been passed bit by bit to those who requested specific analyses, and without explicit formal publication. Even so, generalities can be gleaned from the 30-year accumulation in this radioactivity "lore" bank that are relevant to the LDEF mission and to the design and construction of future spacecraft.

While the trace radioactivities in engineering materials are usually inconsequential to their intended uses--and hence are not deliberately controlled during production, there are two special cases of concern here in which these radioactivities become very important.

In the first case, their presence in a material interferes with post-flight measurement of radioactivites induced in the material while it was "exposed" to an in-orbit nuclear particle flux, for example: measurement at a terrestrial laboratory of space-produced activities induced in LDEF samples and materials during the satellite's nearly 6-year voyage in low earth orbit. We have already discussed (earlier sections, this report) the presence of uranium-series nuclides in the titanium alloy and pure vanadium, as well as the presence of both uranium-series and thorium-series nuclides in the aluminum alloy. The possibility of earth-borne Co-60 in trunnion stainless steel has been noted.

In the second case, their presence in an instrument and/or its surroundings interferes with measurements the instrument is designed to accomplish in real time during a mission. For γ-ray detection, the radioactivities carried aloft in spacecraft and detector assembly materials (baggage) may contribute significantly to the detector system BKG response, particularly in the matter of identifiable peaks -- the most useful features in γ-ray spectra. It may be necessary to select materials of low intrinsic radioactivity, to reduce BKG interference with radiation detection mission objectives. The brief discussions of materials that follow are supplementary to comments include earlier, and bear directly on this point.

ALUMINUM: Aluminum and its alloys have been measured to contain uranium at concentrations ranging from 0.3 to 2 ppm; however, Ra-226 and its late-member γ-emitting daughters are virtually absent. Thorium-series γ-emitters are present in the range of 0.05 - 2 ppm equivalent thorium. Note that the γ-ray data does not give direct evidence for the content of Th-232, the parent of the thorium series.

BERYLLIUM: Beryllium has been assayed to contain uranium as the only important radioactive contaminant. Ra-226 and its γ-emitting daughters are virtually absent. Early domestic production (before about 1970) was from beryl ore and yielded metal containing less than 10 ppm uranium. Later domestic production (continuing to the present) from bertrandite ore yielded metal containing 20 - 50 ppm uranium, and recently up to 150 ppm. One sample of metal obtained recently (1989) from China contained about 4 ppm. Also assayed in 1989 was metal from a small domestic "stockpile" of high purity metal, which contained only 1 ppm uranium. Another possible

source of low-uranium metal might be the U.S. National Stockpile, which is at least partly stocked with beryllium recovered from beryl ore.

RARE EARTH OXIDE GLASSES: These glasses are used in high-quality short-focus wide-aperture lens systems, for example: 35-mm single-lens reflex (SLR) cameras of mid-to upper price range. The suite of radionuclides described here has been seen in several SLR lens systems, as well as in samples of "raw" glass. The radionuclides belong to the U-235 series, although U-235 itself is not present. (U-238 is also not present.) The γ-ray evidence confirms presence of 21.6-year halflife Ac-227, the long-lived parent of the observed γ-emitters (Th-227 through Pb-211). Longer-lived Pa-231 may also be present. Uranium concentrations appropriate to the intensities of daughter γ-rays are in the ppm range.

SUMMARY

We have made measurements of in-orbit induced radioactivities and "natural" radioactivities in a number of samples and materials from the LDEF satellite. Success in this effort required the use of state-of-the-art low-background germanium semiconductor detector γ-ray spectrometric technology. Results of our measurements, in combination with results obtained at several other laboratories, will lead to a clearer understanding of the radiation field in which LDEF travelled for nearly 6 years. This information will be useful in design of future spacecraft, such as Space StationFreedom. Our LDEF analysis experience can also serve to guide improvements in future efforts of this kind: arranging more suitable earth-bound analysis facilities, as well as selecting the types and quantities of materials sent on spacecraft voyages.

ACKNOWLEDGMENTS

We express our deepest appreciation to all NASA personnel associated with the LDEF mission: in particular, the 1984 Challenger crew who launched the satellite and the 1990 Columbia crew who brought it back to earth; the LDEF mission primary team at Langley, headed by Dr. William Kinard; the Langley team headed by Dr. Arlene Levine, who organized this Symposium on very short notice; and the Special Investigation Group for radioactivity measurements at Huntsville, headed by Dr. Thomas Parnell and including Dr. Gerald Fishman and B. Alan Harmon. Special thanks are due Alan Harmon for his masterful effort at overseeing distribution of samples among participating laboratories on a timely schedule.

We are also appreciative for the superb support afforded by Fred Goulding's group at LBL in detector and electronics technology, particularly in regard to the creation of our MERLIN spectrometer system. And -- thanks to Kevin Hurley of the U.C. Space Science Laboratory, whose phone call alerted us to this opportunity of a lifetime: participation in the LDEF analysis program.

We respectfully dedicate all our efforts in this program to the last crew of the Challenger, lost at launch in early 1986, but long remembered in the annals of man's journey into space.

BIBLIOGRAPHY

1. Lederer, C.M., et al: Table of Isotopes, Seventh Edition, John Wiley and Sons, New York, NY, 1978.

2. Smith, A.R., and Wollenberg, H.A.: High-Resolution Gamma Ray Spectrometry for Laboratory Analysis of the Uranium and Thorium Decay Series, in The Natural Radiation Environment II, CONF-720805-P1, 1972, pp. 181-231.

This work was supported by NASA under Marshall Flight Center Order No. H-06815D through U.S. Department of Energy under Contract No.DE-AC03-76SF00098.

MEASUREMENTS OF INDUCED RADIOACTIVITY IN SOME LDEF SAMPLES

C. E. Moss and R. C. Reedy
Space Science and Technology Division
Los Alamos National Laboratory
Los Alamos, NM 87545-0010
Phone: 505/667-5066, Fax: 505/665-4414

SUMMARY

Twenty-six stainless steel trunnion samples, five aluminum end support retainer plate samples, two aluminum keel plate samples, and two titanium clips were analyzed. The shielded high-purity germanium detectors used had relative efficiencies of 33%, 54%, and 80%. Detector efficiencies as a function of energy and corrections for self-absorption in the samples were determined with calibrated sources and unactivated control samples. Several measurements were made on most samples. In the trunnion samples, ^{54}Mn and ^{57}Co were seen and limits were obtained for other isotopes. The results agree well with 1-dimensional activation calculations for an anisotropic trapped proton model. In the aluminum and titanium samples, ^{22}Na was seen. Other results are presented.

INTRODUCTION

Los Alamos National Laboratory is one of several laboratories involved in the analysis of induced radioactivity in samples from the Long Duration Exposure Facility (LDEF). We analyzed samples of the spacecraft rather than samples deliberately placed on board. The goal of this work was to provide data that could be used in modeling calculations to determine the integrated radiation environment at LDEF. From these results the radiation environment of Space Station Freedom and other spacecraft in similar low-Earth orbits can be predicted.

The 20 samples from section D of the trunnions were received about 65 days after the shuttle Columbia landed with LDEF at 12:30 am PST on 20 January 1990. We corrected all induced radioactivities to this time. The end support retainer plate, trunnion sections C, H, and N, titanium clip, and keel plate samples were received about 155, 178, 200, and 430 days, respectively, after this time.

EXPERIMENTAL DETAILS

Detectors

We used three high-purity germanium detectors to measure gamma rays from the samples. The smallest two had efficiencies of 33% and 54% at 1332 keV relative to a 3" x 3" NaI(Tl) scintillator. Each was part of an automated counting system (figure 1) used for programmatic work at Los Alamos. The germanium crystal was shielded from background by several inches of lead. The samples were mounted on thin aluminum plates and placed on the carousel. As each station came into position under the detector, a hydraulic ram pushed the sample and sample holder up into position such that the aluminum plate was about 1.46 cm from the detector. Data were acquired into a multichannel analyzer and transferred to a computer for storage and analysis. The spectra, which had 4096 channels from ~50 keV to 2 MeV, were analyzed with two codes based on the GAMANAL spectral analysis code of Gunnink at Lawrence Livermore National Laboratory. (ref. 1).

The largest detector (figure 2) had an efficiency of 80%. It was mounted on a portable liquid nitrogen dewar for field nuclear safeguards work. The sample was placed in contact with the detector can, which was shielded by 2 to 4 inches of lead. The data were acquired in a PC-based multichannel analyzer operated manually. Peak areas in the spectra were determined with the code MAESTRO from EG&G ORTEC.

Efficiencies

The detector efficiencies were determined in geometries similar to those used to measure the samples. Each sample had to be placed close to the detector, which meant that the efficiencies were very sensitive to the distance from the detector. Table I lists the radioactive nuclides, half-lives, and gamma-ray energies in the mixed calibration source provided by A. Harmon of the Marshall Space Flight Center. The activity was contained in many small spots placed in a matrix on a 2" x 2" sheet of mylar 0.002 inches thick and supported by an aluminum backing ~0.020 inches thick. The activity was sealed in place with another sheet of mylar 0.002 inches thick.

Plots of the efficiencies at several distances are shown in figure 3. With the source close to a large detector, summing reduces the efficiencies for the ^{88}Y and ^{60}Co gamma rays in the mixed source. That is, if a radionuclide emits two gamma rays in coincidence, there is a significant probability that both will interact with the detector thus producing the wrong pulse height and not being included in the correct peak area. The dashed lines indicate the expected efficiencies without summing. At larger distances and for smaller detectors, summing was smaller. Note that the shapes of the efficiency curves for the 33% detector are different at low energy because the 33% detector had a beryllium window and the other two had aluminum windows, which attenuated the low energy x-rays, gamma rays, and beta particles. The distances we used were 0 cm with the

80% detector and 1.46 cm with the 33% and 54% detectors. The counting rates at 5.95 cm were too low for our LDEF samples.

Self Absorption

Self absorption was larger in the LDEF samples than it is in most radiochemistry samples because the LDEF samples were thicker. To determine the self absorption for the 80% detector we placed several different thicknesses (x in figure 4) of absorber between the source and the detector. The absorber had the same composition as the LDEF samples except, of course, it had not been activated. This procedure varied not only the absorption but also the distance from the source to the detector. Each measurement determined the combined efficiency and self absorption at the distance x in the LDEF sample. Integrating over x gives the average combined efficiency and self absorption as a function of the LDEF sample areal density (figure 5).

For the 33% and 54% detectors a different procedure was used because the sample shelf height could only be varied in relatively large steps. We chose to use a shelf height of 1.46 cm. The source mounted on an aluminum planchet was placed on the shelf, and several different thicknesses of absorber were placed on top (figure 6). Representative data and fits are shown in figure 7. The attenuation coefficients are ~1.2 to 1.25 larger than those in the literature because of the special geometries.

Other Factors

Other factors are also involved in quantifying the activation of the samples. Counting statistics were limited by the time the detectors were available. Background determinations were important because radon levels vary and other measurements were in progress in the facilities. Only three sample holders were used with each of the 33% and 54% detectors because we found that backgrounds varied with the sample holders. One holder was found to have appreciable ^{152}Eu and was not used again. The spatial distributions of activities in the samples can affect the effective efficiencies; we assumed they were uniform. Well known factors include the gamma-ray energies, half-lives, branching ratios, sample masses, and dimensions.

RESULTS AND DISCUSSIONS

Trunnion Samples

Figure 8 shows the labeling convention for the trunnion samples. For section D (figure 8b), we analyzed layers two through six on the space side and two through six on the earth side, thus ten layers per trunnion. Since there were two trunnions, right hand (east) and left hand (west), we analyzed a total of 20 layers. The top layers, labeled one, which contained ^{7}Be, (ref. 2) were analyzed elsewhere. The layers had been flattened when we received them. Note that the thicknesses varied, which complicated the absorption corrections. The material was 17-4 PH stainless steel, which contains about 75% Fe, 15% Cr, 4% Ni, and 3% Cu.

The ^{54}Mn and ^{57}Co activities are listed in Table II and plotted in figure 9. Because the procedures and results for the 33% detector and the 54% detector were very similar, the results from these detectors have been combined in column two of Table II. Not all of the samples were counted with the 80% detector because this detector was operated manually and was less available than the others. The uncertainties shown are one standard deviation (1 σ). The values plotted in figure 9 are averages of columns two and three weighted by $1/\sigma^2$. Note that the activities near the surface are higher because fewer protons penetrate to the the center. The dashed line shows the region for which we did not have samples. Also note that the activities on the west are higher because protons trapped by the earth's magnetic field and striking LDEF on the west side are not limited in energy by the earth's atmosphere. These results are in good agreement with a trapped proton model calculation, (refs. 3 and 4) except near the center where the results are higher, probably reflecting production by galactic cosmic-ray particles. There is an indication that the Earth side had more ^{54}Mn than the space side. We also analyzed thick 3.25-inch diameter disk samples from sections C, H, and N. Data were taken only with the 80% detector because the samples were too big to fit into the automated systems on the other detectors. Again ^{54}Mn and ^{57}Co were detected. Additional studies of the self absorption in these thick samples are required before we can quote reliable values.

Limits on ^{51}Cr, ^{7}Be, ^{22}Na, ^{58}Co, ^{56}Co, ^{46}Sc, and ^{60}Co were also determined for all of the trunnion samples.

Aluminum Samples

We analyzed five end support retainer plate samples and two keel plate samples. The material was 6061 aluminum, which contains 1% Mg, 0.6% Si, 0.4% Fe, 0.24% Cu, and 0.2% Cr. Figure 10 shows that ^{22}Na is clearly present; limits were obtained for ^{7}Be. Table III gives the value for ^{22}Na determined with the 33% and 54% detectors. With the 80% detector ^{22}Na was seen, but no values are quoted pending more self absorption studies.

Titanium Samples

Of the nuclides listed above, only ^{22}Na was detected in the two titanium clips we analyzed (Table IV). The clips used an alloy of titanium with about 6.5% aluminum and 4% vanadium. We only could set limits (3 σ) on the ^{46}Sc, which should be compared with values for the ^{54}Mn in the trunnion pieces that is made by a similar nuclear reaction. We detected many gamma-ray lines from uranium and its daughters, which were not expected. We saw lines from ^{235}U and all of its daughters in equilibrium; we saw lines from the ^{238}U chain down to ^{234m}Pa. Because the same lines have been seen from vanadium, the uranium might have been introduced by the 4% vanadium in this titanium alloy. (ref. 5) These lines will contribute to the background of gamma-ray detectors on spacecraft if this titanium alloy is used nearby.

CONCLUDING REMARKS

The sensitivity of this experiment was limited not only by the sensitivities of the counting facilities used but also by how soon the samples were available and by the physics. Only a few possible product nuclides emit gamma rays and have sufficiently long half-lives to be counted post flight. Most activation was due to trapped protons, although the galactic cosmic rays contributed significantly to shielded locations. This simple LDEF experiment provided fluence data integrated over a long period of time, which will be useful in designing future spacecraft.

ACKNOWLEDGMENTS

G. W. Butler provided the 33% and 54% detector systems. L. E. Ussery provided the 80% system. S. G. Bobias assisted in the analysis of the counting results. This work was supported by a contract from NASA/MSFC and done under the auspices of the U.S. Department of Energy.

REFERENCES

1. Gunnink, R.; Computer Techniques for Analysis of Gamma-Ray Spectra. Proceedings of the American Nuclear Society Topical Conference at Mayaguez, Puerto Rico, April 30- May 4, 1978 on Computers in Activation Analysis and Gamma-Ray Spectroscopy, CONF 780421, 1979, pp. 109-138.

2. Fishman, G.J.; *et al.*: Observation of ^{7}Be on the Surface of the LDEF Spacecraft. Nature, vol. 349, Feb. 1991, pp. 678-680.

3. Watts, J. W.; Parnell, T. A.; and Heckman, H. H.: Approximate Angular Distribution and Spectra for Geomagnetically Trapped Protons in Low-Earth Orbit. Proceedings of the American Institute of Physics Conference at Sanibel Island, Florida, in 1987 on High-Energy Radiation Background in Space, AIP Conference Proceedings 186, 1989.

4. Armstrong, T. W.; and Colborn, B. L.: Ionizing Radiation Calculations and Comparisons with LDEF Data, First Post-Retrieval Symposium, NASA CP-3134, 1992.

5. Smith, A. R.; and Hurley, D. L.: Radioactivities of Long Duration Exposure Facility (LDEF) Materials: Baggage and Bonanzas, First Post-Retrieval Symposium, NASA CP-3134, 1992.

TABLE I. MIXED RADIOACTIVE SOURCE

Nuclide	Half-life	Gamma-ray Energies keV
^{109}Cd	463d	88
^{57}Co	272d	122
^{139}Ce	137d	166
^{203}Hg	47d	279
^{113}Sn	115d	392
^{85}Sr	65d	514
^{137}Cs	30y	662
^{88}Y	107d	898,1836
^{60}Co	5.27y	1173,1332

TABLE II. ACTIVITIES IN THE TRUNNION LAYERS

Sample	Activity (picoCuries/kg)			
	^{54}Mn		^{57}Co	
	33% & 54% Detectors	80% Detector	33% & 54% Detectors	80% Detector
LH, D, Space, 2	95 ± 35	126 ± 18	27 ± 17	41 ± 11
LH, D, Space, 3	116 ± 18		30 ± 11	
LH, D, Space, 4	86 ± 17	111 ± 13	12 ± 12	8 ± 9
LH, D, Space, 5	89 ± 16		20 ± 6	
LH, D, Space, 6	79 ± 16	98 ± 10	21 ± 23	17 ± 7
LH, D, Earth, 2	145 ± 40	140 ± 15	36 ± 19	22 ± 9
LH, D, Earth, 3	126 ± 26		31 ± 12	
LH, D, Earth, 4	109 ± 13	121 ± 14	19 ± 10	15 ± 10
LH, D, Earth, 5	98 ± 12		12 ± 8	
LH, D, Earth, 6	93 ± 14	97 ± 12	22 ± 9	19 ± 9
RH, D, Space, 2	99 ± 28	104 ± 21	45 ± 37	10 ± 13
RH, D, Space, 3	94 ± 21		-4 ± 11	
RH, D, Space, 4	83 ± 19	81 ± 11	12 ± 11	9 ± 8
RH, D, Space, 5	73 ± 22		35 ± 22	
RH, D, Space, 6	70 ± 17	85 ± 9	-9 ± 29	20 ± 7
RH, D, Earth, 2	116 ± 31	151 ± 18	30 ± 21	13 ± 11
RH, D, Earth, 3	113 ± 21		22 ± 15	
RH, D, Earth, 4	87 ± 18	94 ± 9	12 ± 11	18 ± 7
RH, D, Earth, 5	79 ± 16		10 ± 15	
RH, D, Earth, 6	87 ± 17	70 ± 10	10 ± 10	18 ± 8

TABLE III. ACTIVITIES IN THE ALUMINUM SAMPLES

Sample	^{22}Na Activity (picoCuries/kg)
ESR 3	103 ± 17
ESR 6	113 ± 19
ESR 7	114 ± 25
ESR 8	122 ± 29
ESR 9	117 ± 18
KP 1	135 ± 18
KP 12	140 ± 17

TABLE IV. ACTIVITIES IN THE TITANIUM ALLOY SAMPLES

	Activity (picoCuries/kg)	
Sample	^{22}Na	^{46}Sc
916AC1	16 ± 8	< 90 (3 σ)
920FC2	20 ± 9	<110 (3 σ)

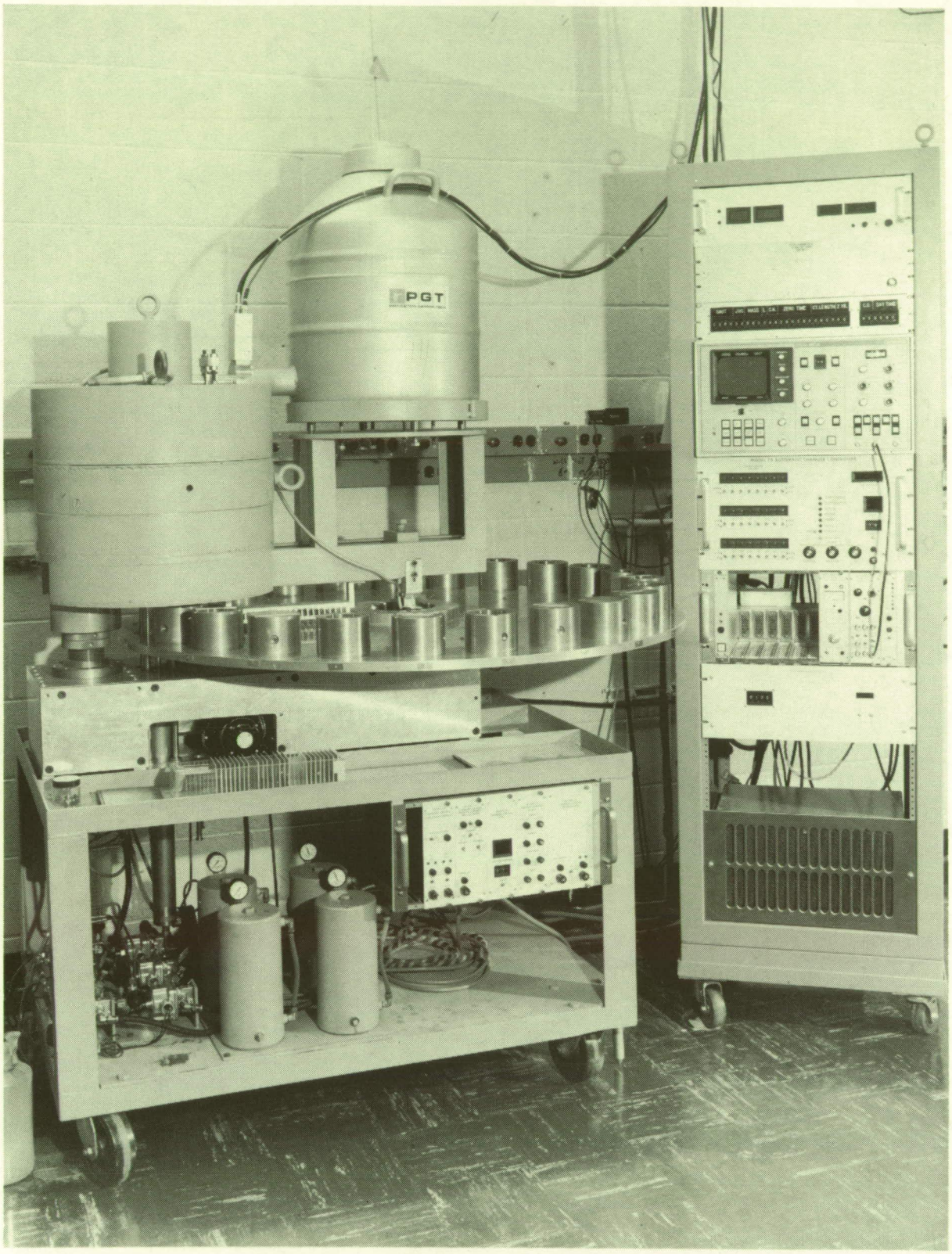

Figure 1. Automatic counting system used with the 33% detector.

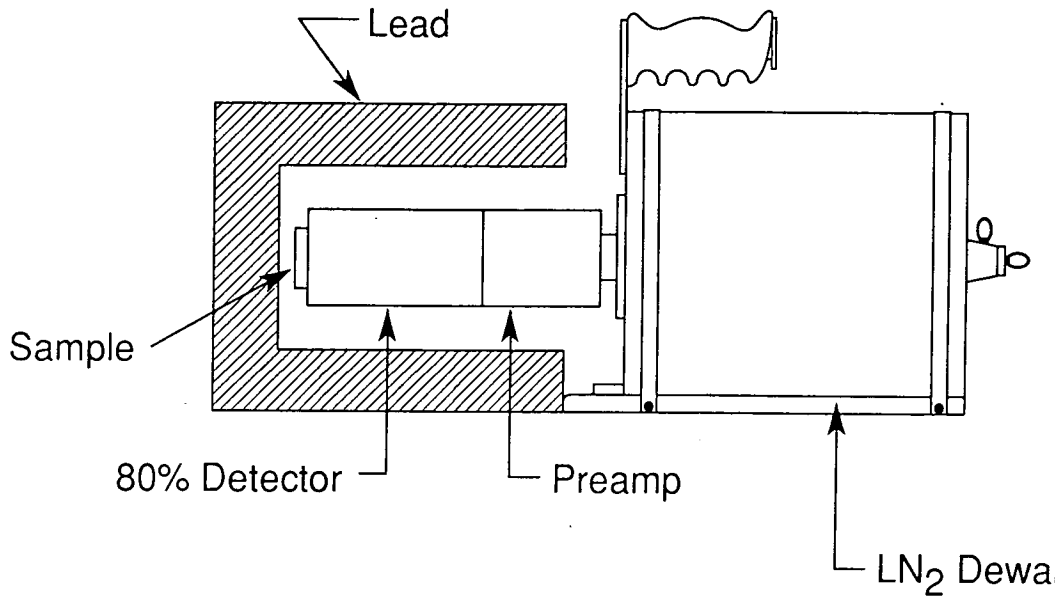

Figure 2. 80% detector setup.

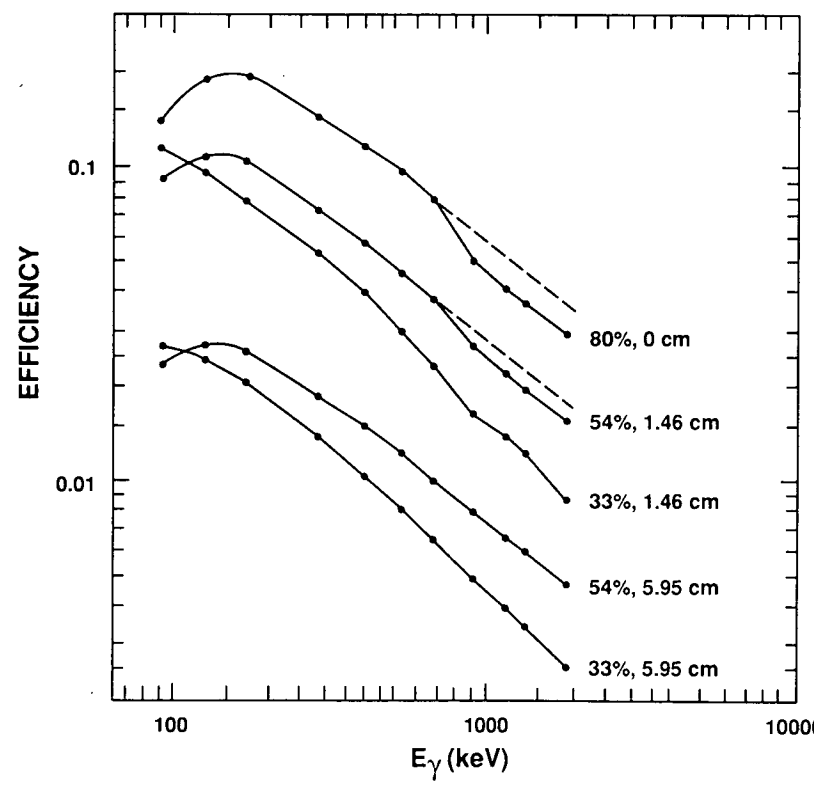

Figure 3. Efficiencies measured with the 2" x 2" matrix of sources for the three detectors at various distances.

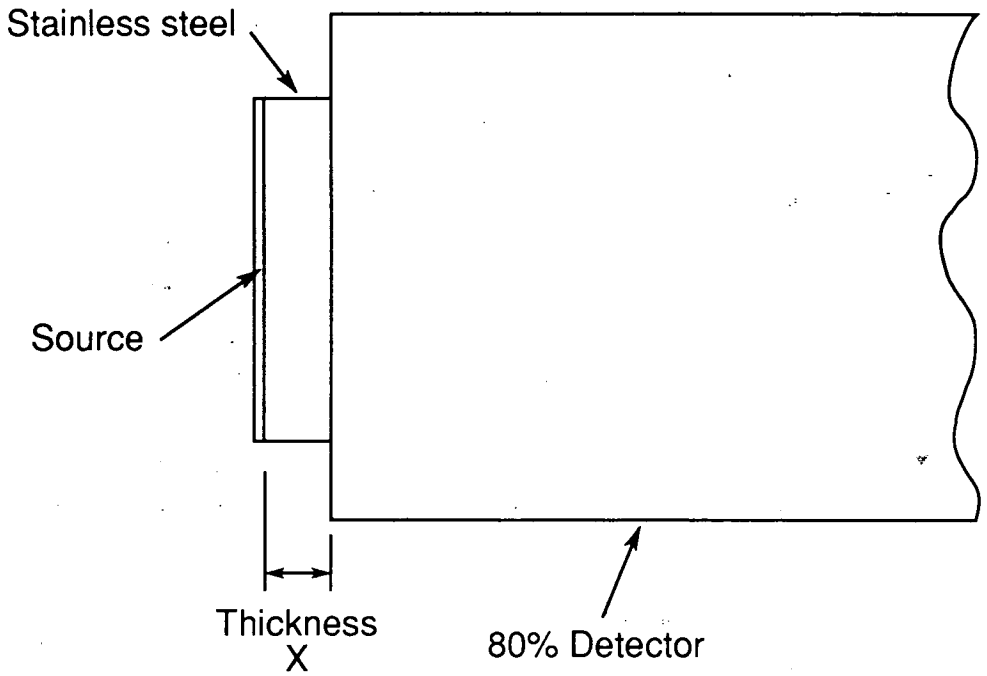

Figure 4. 80% detector absorption setup.

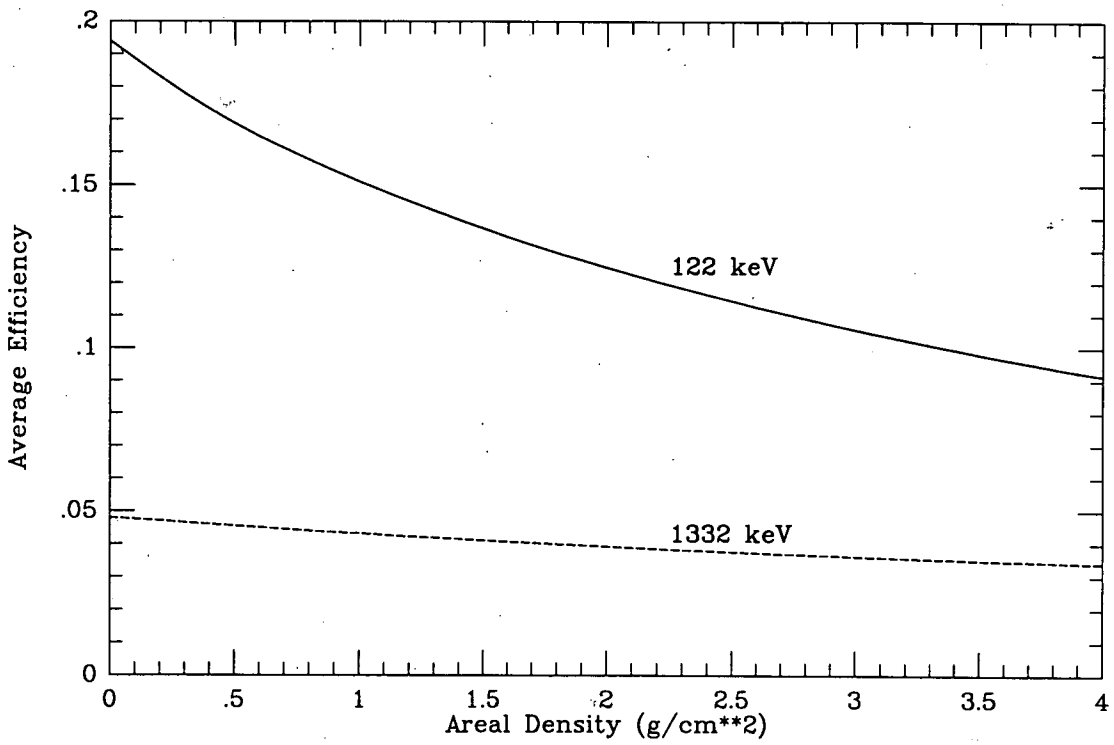

Figure 5. Average efficiency for the 80% detector including the effects of absorption in steel and distance.

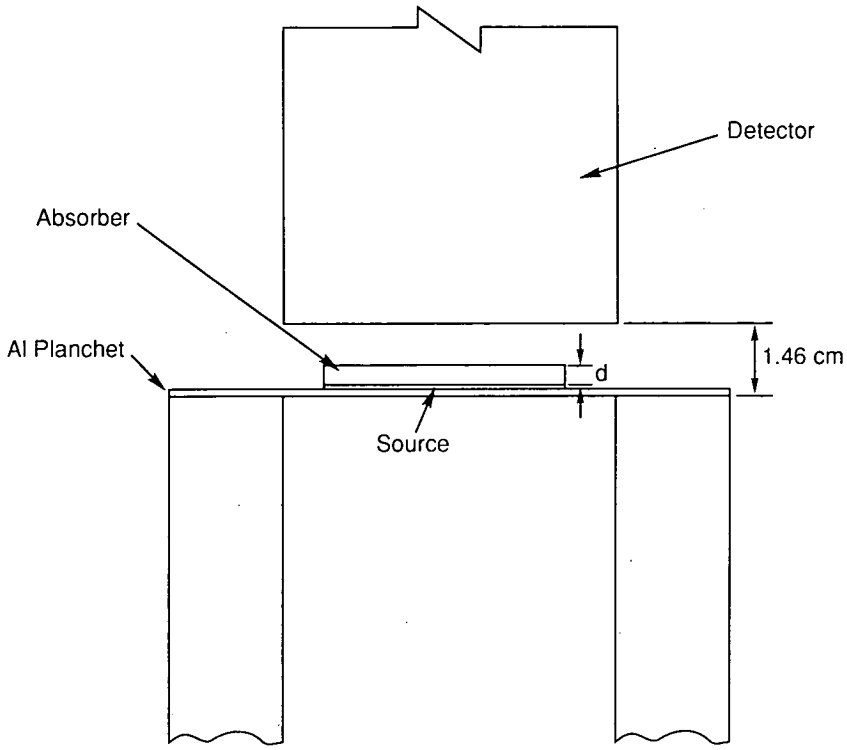

Figure 6. 33% and 54% detector absorption setup.

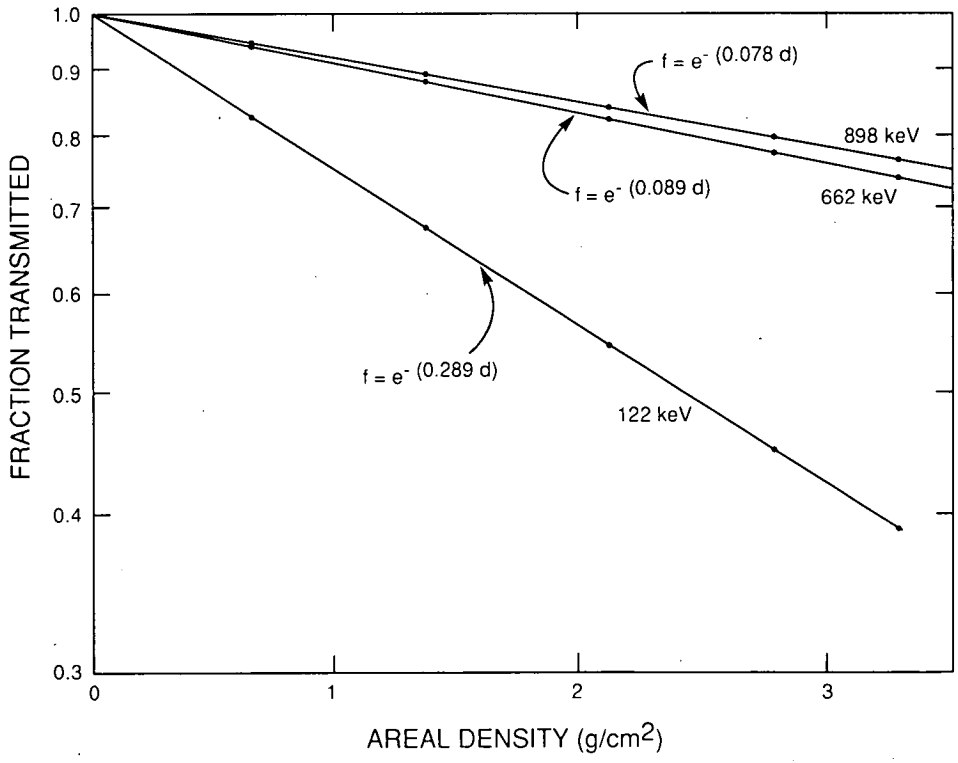

Figure 7. Fraction transmitted through the trunnion layers with the 33% or 54% in the setup shown in figure 6.

a)

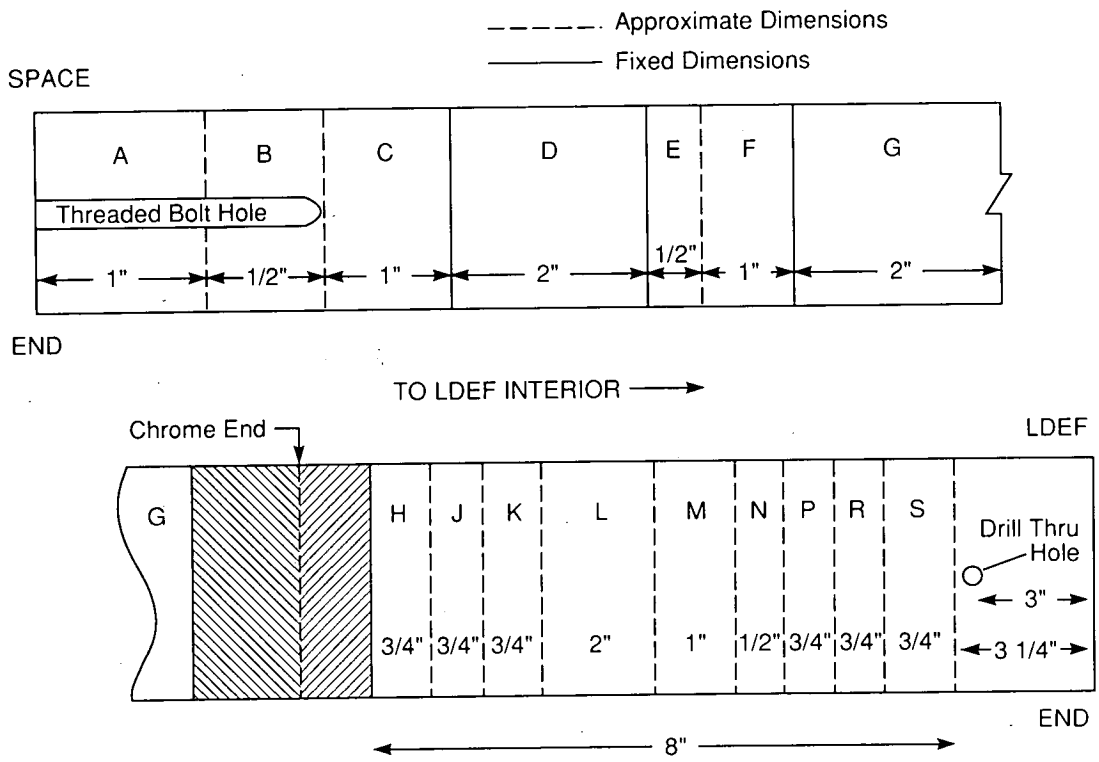

b)

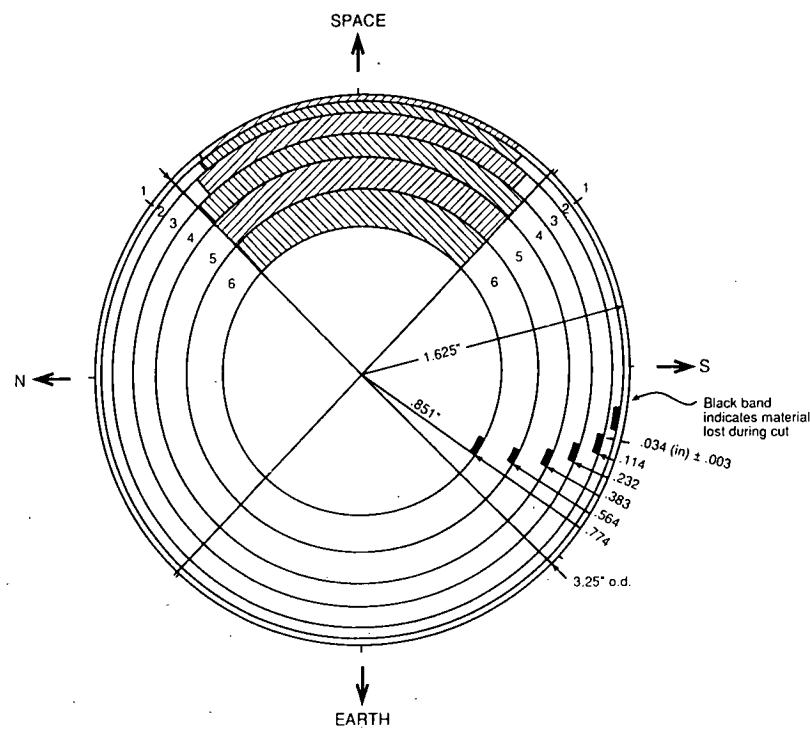

Figure 8. LDEF trunnion labeling convention: a) sections and b) layers in section D.

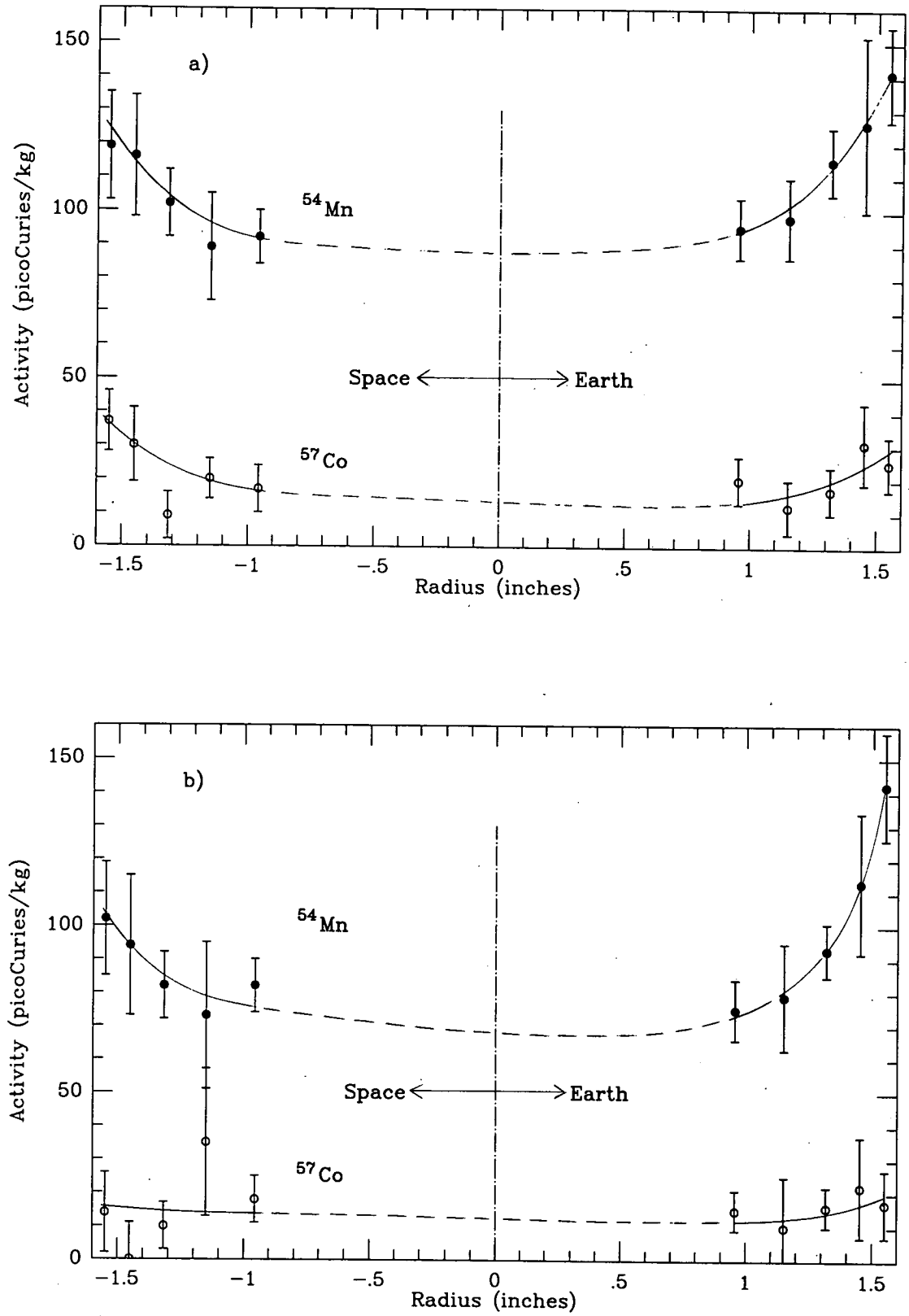

Figure 9. Induced activity in trunnion section D, a) left hand (west) and b) right hand (east). Curves are to guide the eye.

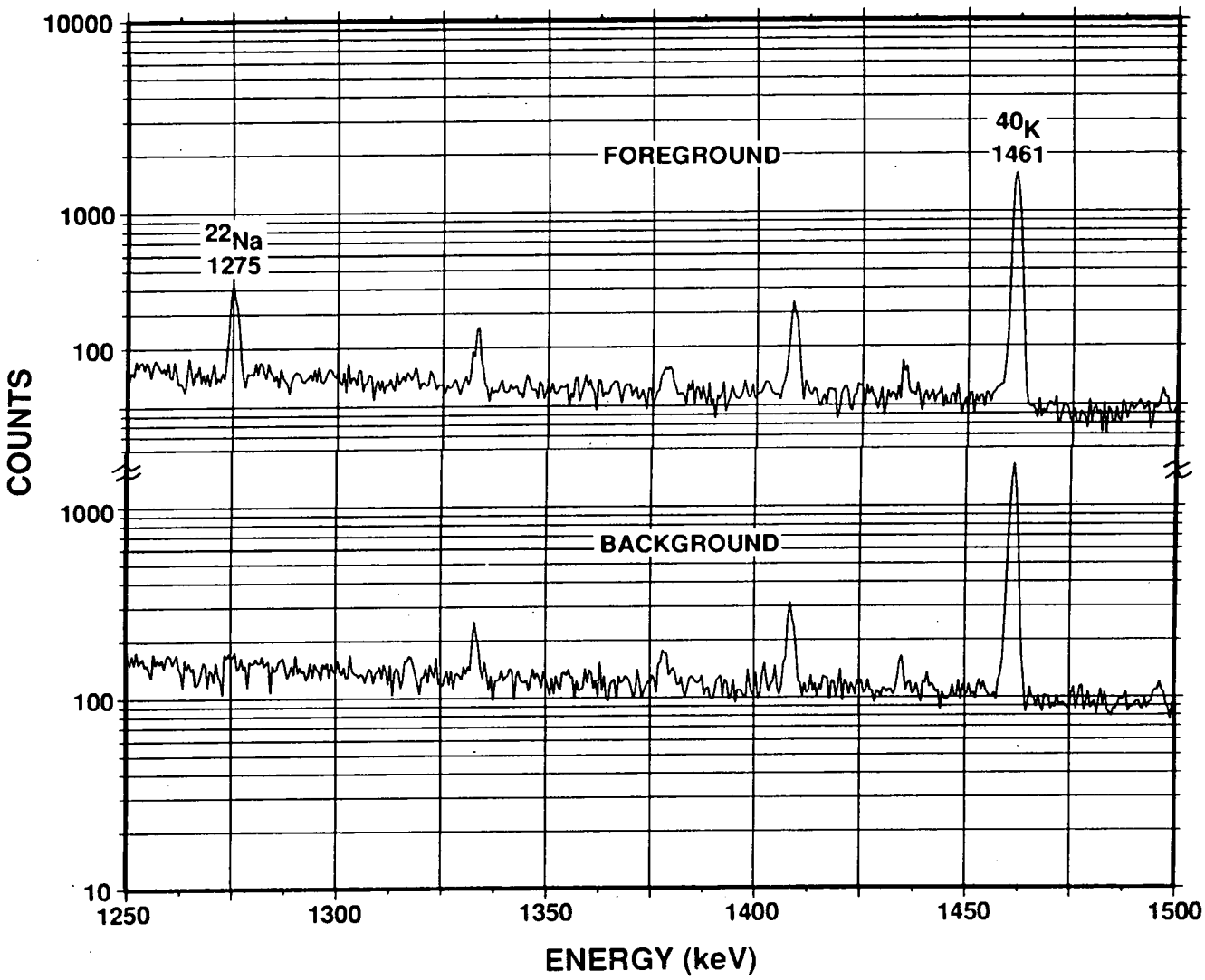

Figure 10. Spectrum for a 4000-minute count of the keel-plate sample KP-12 (top) and a background count of the same length for the same position (bottom) on the 54% detector.

GAMMA-RAY SPECTROMETRY OF LDEF SAMPLES AT SRL

Willard G. Winn
Westinghouse Savannah River Company
Savannah River Site
Aiken, SC 29808
Phone: 803/725-2057 Fax: 803/725-3272

SUMMARY

A total of 31 samples from LDEF, including materials of aluminum, vanadium, and steel trunnions were analyzed by ultra-low-level gamma spectrometry. The study quantified particle induced activations of ^{22}Na, ^{46}Sc, ^{51}Cr, ^{54}Mn, ^{56}Co, ^{57}Co, ^{58}Co, and ^{60}Co. The samples of trunnion sections exhibited increasing activity toward the outer end of the trunnion and decreasing activity toward its radial center. The trunnion sections did not include end pieces, which have been reported to collect noticeable ^{7}Be on their leading surfaces. No significant ^{7}Be was detected in the samples analyzed.

The Underground Counting Facility at Savannah River Laboratory (SRL) was used in this work. The facility is 50 ft underground, constructed with low-background shielding materials, and operated as a clean room. The most sensitive analyses were performed with a 90%-efficient HPGe gamma-ray detector, which is enclosed in a purged active/passive shield. Each sample was counted for one to six days in two orientations to yield more representative average activities for the sample. The non-standard geometries of the LDEF samples prompted the development of a novel calibration method, whereby the efficiency about the sample surfaces (measured with point sources) predicted the efficiency for the bulk sample.

INTRODUCTION

Prior to retrieval of LDEF in January 1990, NASA Marshall Space Center initiated a program for radiometric analysis of the LDEF samples.[1] Due to extensive experience in ultra-low-level counting of environmental samples at the SRL Underground Counting Facility, NASA selected it as one of the laboratories for LDEF analyses. SRL received its first LDEF samples on March 7, 1990, and a total of 68 gamma spectrometry analyses were conducted on 31 samples submitted during 1990-1991. Round robin gamma analyses of these or similar samples were conducted at PNL, LNL, LBL, LLL, ORNL, TVA, and at NASA facilities in Houston, Texas and Huntsville, Alabama.

This report emphasizes the measurements of the induced radioactivity in the LDEF samples submitted to SRL, whereby it identifies particle reactions for producing the observed radionuclides, and examines trends within the data. These results will be used to appraise and improve models for characterizing trapped particles and cosmic rays.[2-4] A special emphasis is also given to the development of efficiencies for these somewhat unorthodox samples.

SYMBOLS

Symbols and units are given below. Efficiencies are unitless.

r,z	Cylindrical coordinates of sample (cm, cm)
$\epsilon(r,z)$	Gamma detection efficiency at sample point r,z
$\epsilon(r)$	Gamma detection efficiency of sample annulus r
ϵ	Gamma detection efficiency of sample
g(r)	Efficiency coefficient equal to $\epsilon(r,0)$
A,B,p	Constant in $\epsilon(r)$ fit of Equation 5 (–, cm^{-p}, –)
μ	Linear gamma attenuation coefficient (cm^{-1})
f	Average path length correction factor for μ (–)
c	Effective gamma geometric attenuation coefficient (cm^{-1})
U	$c + \mu f$ or total attenuation coefficient (cm^{-1})
U(r)	U expressed as function of r (cm^{-1})

MEASUREMENTS

The SRL Underground Counting Facility[5] was used to conduct gamma spectrometry on the LDEF samples. This facility is 50 ft below ground, and constructed with low-background materials. The 4 in. walls of the counting chamber are constructed of pre-World War II steel. The chamber is shielded by four to 7 ft of specular hematite. The total overburden is equivalent to 104 ft of water shielding, which reduces the cosmic background by an order of magnitude. Airborne particles are removed by filtering, classifying the facility as a Class 10,000 clean room. The very stable spectrometry electronics uses an uninterruptable power supply to protect against data losses during extended counting times.

HPGe detectors with standard efficiencies of 20%, 25%, and 90% were used in this study. A low-level lead shield encloses each detector and its sample cavity, which is purged of radon with the nitrogen that evaporates from its LN_2 dewar. The 90% HPGe has an inner shield of cadmium and copper to reduce X-ray backgrounds induced in the shielding by gammas from the sample. Figure 1 gives a typical background spectrum for this detector. Near the end of the study, the detector background was further reduced with an active plastic scintillator shield, which detects cosmic background events in anti-coincidence with the gamma counting to veto this background. In the present study, which used 1- to 6-day counting intervals, detection limits[6] for a ^{60}Co point source atop these detectors ranged from 0.04 to 0.4 pCi.

A total of 31 LDEF samples were examined by HPGe gamma spectrometry. The samples were trunnion disks and rectangular slabs of steel, vanadium, and aluminum. The disks had a diameter of 3.25 in. and 0.4 to 0.9 in. thickness; the slabs had maximum dimensions of 2 by 2 in^2 area and 0.35 in. thickness. Some of the slab samples were from radial layers of the trunnion disks. Each sample was counted with one side facing the detector, and then recounted with its other side facing the detector, so that activity distributions within the sample could be detected and averaged.

Detector efficiency calibration for the above samples used a method of mapping the point source efficiency over the sample surfaces. Point sources of ^{54}Mn, ^{57}Co, ^{60}Co, ^{133}Ba, and ^{137}Cs were used. Such a non-destructive calibration technique was important in this work because NASA required the samples be returned intact for round robin analyses at other laboratories.

ANALYSES

General

The HPGe data were collected as 4000 channel gamma spectra, as illustrated in Figure 1. The GRABGAM code,[5] which was developed at SRL for low-level counting, analyzed the spectra. This code uses three peak-area trapping windows, the largest of which is very sensitive for picking out peaks with low counting statistics. The peaks are examined as integral probability functions $F(x)$ per channel x to provide better statistics than afforded by fitting the peaks to differential probabilities $f(x)dx$. Such enhanced statistics are useful in characterizing the centroids and widths of low-level peaks. Following the analysis any peak contributions from the background spectrum are subtracted. The HPGe efficiency analyses procedures are overviewed in Figure 2 where methods for the trunnion disks and slab samples are outlined. Cylindrical coordinates r and z, relative to the sample, are used in the development of the HPGe efficiencies.

Trunnion Disks

Figure 2 depicts the counting geometry for a trunnion disk giving the point source locations used for calibration. Counting the point source at each location yielded an efficiency $\epsilon(r,z)$. The efficiency ϵ of a disk of uniform activity is the average of $\epsilon(r,z)$ over the disk volume V,

$$\epsilon = \frac{\int_V \epsilon(r,z)\, 2\pi r dr dz}{\int_V 2\pi r dr dz} \tag{1}$$

The only measured $\epsilon(r,z)$ are the $\epsilon(r,h)$ and $\epsilon(r,o)$ on the top and bottom surfaces of the disk; thus, a model is needed to infer the $\epsilon(r,z)$ within the disk. The model assumed in the present work was

$$\epsilon(r,z) = g(r)\, e^{-U(r)z} \tag{2}$$

where the z-dependence is exponential and the r-dependence is dictated by functions $g(r)$ and $U(r)$. An exponential is supported experimentally,[7] and it is shown to model both geometry and material absorption dependencies of the efficiency.[8]

Substituting Equation 2 into Equation 1 yields a ratio of radial area integrals.

$$\epsilon = \frac{\int_A \epsilon(r)\ 2\pi r dr}{\int_A 2\pi r dr} \quad , \tag{3}$$

where $\epsilon(r)$, resulting from integrals over z, is given by

$$\epsilon(r) = \frac{g(r)e^{-U(r)z}\ |_o^h}{-U(r)\ z\ |_o^h} = \frac{\epsilon(r,h) - \epsilon(r,o)}{\ln[\epsilon(r,h)/\epsilon(r,o)]} \quad . \tag{4}$$

Note that $\epsilon(r)$ is an exponential average along z *within* the sample volume, but it depends only on values $\epsilon(r,h)$ and $\epsilon(r,o)$ measured on the surface *outside* the volume.

Individual $\epsilon(r)$ were determined using Equation 4 with experimental measurements, and these values were fitted to a function

$$\epsilon(r) = A - B\ r^p \quad , \tag{5}$$

where A, B, and p are positive constants, and p is approximately equal to 2. Integrating this $\epsilon(r)$ in Equation 3 yields

$$\epsilon = A - [2/(2+p)]\ B\ a^p \quad , \tag{6}$$

where $r = a$ is the radius of the trunnion disk. Values of ϵ were determined as a function of energy, using the different point source standards. The resulting ϵ have better than 5% accuracy,[8] and refer to calibrations with standards from the National Institute of Standards and Technology.[9] The method directly calibrated the 20% HPGe and 25% HPGe detectors, which in turn cross-calibrated the 90% HPGe.

Metal Slabs

The 90% HPGe detector was used to appraise the low activities of the metal slabs. Efficiencies for these rectangular slabs were determined using techniques similar to those for the trunnion disks. However, because the slabs were smaller in area and thickness, an effectively constant $U(r) = U$ was assumed, consistent with experimental results,[7] so that Equation 2 could be expressed with separable variables in r and z, yielding

$$\epsilon(r,z) = g(r)\ e^{-U(r)z} = \epsilon(r,o)\ e^{-Uz} \quad . \tag{7}$$

When inserted in Equation 1, this $\epsilon(r,z)$ yields

$$\epsilon = \frac{\int_A \epsilon(r,o)\, 2\pi r dr}{\int_A 2\pi r dr} \quad \frac{\int_o^h e^{-Uz}\, dz}{\int_o^h dz} = \langle\epsilon(r,o)\rangle_A \frac{1-e^{-Uh}}{Uh} \tag{8}$$

where the first term is the numerical integrated average over the rectangular bottom surface, and the second term is integrated average over z. The point source mappings on the detector surface are used to determine the first term. The second term requires a knowledge of U, which may be expressed as

$$U = c + \mu f \quad , \tag{9}$$

where c models the geometry dependence, and μf models the material absorption.[8] Here, the material attenuation coefficient μ is increased by a factor of f to correct for the average attenuation path, which is somewhat greater than z. The entire energy-dependence of U is primarily contained in μ, as c and f are essentially geometric parameters. Experimental measurements with sources of ^{54}Mn, ^{57}Co, ^{60}Co, and ^{137}Cs yielded U as a function of μ, to allow interpolation for predicting U for the other radionuclides. The μ for the gamma energies of these radionuclides were obtained from tabulations.[10] The resulting U were then used in Equation 8 to yield the slab efficiency ϵ.

A correction to ϵ needed to be developed for the ^{22}Na that was produced in the aluminum slabs, as its detected 1274 keV gamma peak is depleted by summing with its 511 keV annihilation gammas. Experimental measurements and calculations deduced that the observed 1274 keV count rate should be multiplied by a summing correction of 1.41 for the 90% HPGe detector.[8]

RESULTS

Trunnion disk sample results are summarized in Table 1. Specific activities are given for ^{7}Be, ^{46}Sc, ^{51}Cr, ^{54}Mn, ^{56}Mn, ^{57}Co, ^{58}Co, and ^{60}Co, where ^{54}Mn is dominant and ^{7}Be is only marginally detected at best. Here the results from counting both sides of the disk have been averaged to yield the values presented. Figure 3a plots the disk results for ^{54}Mn and ^{57}Co as a function of axial position along the trunnion, showing that these activities decrease as the position nears the LDEF end of the trunnion from the space end. Both trunnions were from the earth end of LDEF, where the LH-trunnion faced west, and the RH-trunnion faced east.

Trunnion radial layer activities are given in Table 2. The only significant radionuclides detected in these relatively small samples were ^{54}Mn and ^{57}Co. The results are the average from counting both sides of the sample. Figure 3b plots the layer results, showing that the activities increase with increasing radial position of the trunnion. The data also suggest that the radial profiles on the space side of the trunnion differ from

those on the earth side. The axial position of this RH–trunnion piece is 18 cm from its space end.

Vanadium and aluminum sample activities are presented in Table 2. Only ^{46}Sc was detected in the vanadium and only ^{22}Na was detected in the aluminum. Again, the activities are the average from counting both sides. The vanadium samples were from extreme LDEF locations, as the DISCUSSION will describe. The aluminum samples were from the keel plate and the end support retainer plate.

DISCUSSION

The LDEF samples examined in the present work implied cosmic activations induced by protons and neutrons. The trunnions imply activations as $^{14}N(p,2\alpha)^{7}Be$; $^{46}Ti(n,p)^{46}Sc$; $^{54}Fe(n,\alpha)^{51}Cr$; $^{56}Fe(p,2pn)^{54}Mn$; $^{58}Ni(p,2pn)^{56}Co$; $^{58}Ni(p,2p)^{57}Co$; $^{58}Ni(n,p)^{58}Co$; and $^{59}Co(n,\gamma)^{60}Co$. Actually, little if any ^{7}Be was observed. Noticeable ^{7}Be had been reported on samples with leading surfaces that can collect particles in the LDEF path,[11] but none of the samples analyzed at SRL had such surfaces. The only respective activations in the vanadium and aluminum samples were $^{51}V(p,*)\ ^{46}Sc$ and $^{27}Al(p,*)^{22}Na$, where spallation (*) reactions occurred.

Trunnions

The activities of ^{54}Mn and ^{57}Co decrease for axial positions closer to the LDEF body. The activities also decrease for decreasing radial position. Both decreasing trends are consistent with increased cosmic ray shielding. In addition, the LH or west–facing trunnion was activated somewhat more than the RH or east–facing trunnion; this is a signature of the trapped proton anisotropy in the South Atlantic Anomaly region.[3] The results are further supported by independent measurements on trunnions,[7] which are consistent for predictions for trapped and galactic protons.[4]

The data of Figure 3 also provide a self–consistency test between the modeled gamma efficiencies for the layer and disk samples. For the RHG section, its two radial activity profiles (earth side and space side) for ^{54}Mn were combined to yield their average radial profile, which was integrated to yield an activity of 79.8 pCi/kg for the RHG disk. This is consistent with the RH–trunnion trend of Figure 3 as the adjacent RHF disk activity was 78.98 ± 1.34 pCi/kg. Although the ^{57}Co radial profile is consistent with that of the ^{54}Mn, the imprecise data allow rather different profiles as well. However, no reasonable ^{57}Co profile yielded an integrated activity that was consistent with the trunnion trend in Figure 3. Specifically, the reasonable ^{57}Co profiles predicted a range of 10.5 to 13.7 pCi/kg for the RHG disk[8] while the adjacent RHF disk activity was 7.00 ± 0.59 pCi/kg.

The above comparison neglects the impact of the radial activity profile on the detection efficiency of the disk. Addressing this profile $p(r)$, the corresponding efficiency ϵ_p is given as

$$\epsilon_p = \frac{\int_A p(r)\, \epsilon(r)\, 2\pi r dr}{\int_A p(r)\, 2\pi r dr} \quad . \tag{12}$$

The tabulated disk values should be corrected by a factor of ϵ/ϵ_p. Using the activity profile of the RHG layers and the $\epsilon(r)$ measured for the adjacent RHF disk, an $\epsilon/\epsilon_p = 1.022$ was calculated[8] for ^{54}Mn. Applying this correction to the ^{54}Mn of the RHF disk yields 80.73 ± 1.37 pCi/kg compared with the 79.8 pCi/kg determined from the layers of the adjacent RHG disk. A similar treatment using the same $p(r)$ with the ^{57}Co $\epsilon(r)$ also yields a small correction, but this does not resolve the difference between the ^{57}Co layer and disk results. Apparently, a different $p(r)$ applies for ^{57}Co. Using a $p(r) = kr^2$ profile, which corresponds to the lowest reasonable profile-based activity of 10.5 pCi/kg for RHG, the resulting $\epsilon/\epsilon_p = 1.269$ for RHF yields 8.88 ± 0.75 pCi/kg. This illustrates that the ^{57}Co layer and disk results may become more consistent depending on the detailed nature of $p(r)$.

The trunnion disk results of Table 1 are all based on the assumption of uniform sample activities. Because appropriate ϵ/ϵ_p corrections are not generally available for these samples, such corrections were not applied. At the same time, a single available example for correcting ^{54}Mn illustrated a small correction in this case implying that ^{54}Mn values in Table 1 are reasonably accurate. Values for other radioisotopes of Table 1 can also be considered accurate if their corresponding $p(r)$ is in reasonable agreement with that for ^{54}Mn. However, caution should be exercised here, as the ϵ/ϵ_p examination for ^{57}Co implied a quite different $p(r)$, suggesting that the ^{57}Co of Table 1 might need to be increased by a factor of 1.6 ± 0.3. Finally, these observations suggest scrutiny in comparing round robin results from the different participating laboratories, because the ϵ determined for the various detectors will need to be corrected by their *different* ϵ/ϵ_p before precise agreement can be expected. Unfortunately, current experimental data appears insufficient for determining these ϵ/ϵ_p ; however, model predictions based on particle fluxes may be possible.[3,4]

Vanadium

The ^{46}Sc activated in vanadium indicated some trends; however, the photographs suggest that some of the samples may have been shielded so that only signatures of these trends are evident. The corresponding data of Table 2 is discussed below for signatures of anisotropic radiation received by the space/earth ends and east/west sides of LDEF.

The ^{46}Sc density of two samples (I–H12–VA and I–H12–VB) on the space end of LDEF was about 30% larger than that of a single sample (G12–A2–FNV) on the earth end; however, the error for the comparison is also about 30%. Because the photographs

imply that the space end samples were probably more shielded, the observation implies that the radiation received from the space side is greater. This is consistent with the earth acting as a cosmic shield for irradiation aimed at the earth end of LDEF.

The ^{46}Sc density of a sample (I–F2–V) on the west side of LDEF is only about 5% larger than that of a sample (I–C9–V) on the east side, and the error for the comparison exceeds 5%. However, the photographs imply that the sample on the west side is more shielded suggesting that the radiation from the west is higher. This is a signature of the South Atlantic Anomaly.[4]

Aluminum

The ^{22}Na activated in aluminum supports the anisotropic trends more dramatically than the vanadium results. The evidence for east/west and space/earth anisotropies are discussed below in logical order of development.

Two aluminum samples of the keel plate are on opposite sides of the keel, and tend to be shielded from each other by the keel. Consequently, one sample (KP–3) received radiation preferentially from the west, and the other (KP–10) from the east.[8] The ^{22}Na density of the west side sample was 48 ± 6% higher than that of the east side sample showing an unmistakable signature for the east/west anisotropy.

The keel itself is midway between the space and earth ends, so that the aluminum samples (KP–3 and KP–10) of the keel plate are closer to the space end than are the two samples (ESR–1 and ESR–2) of the retainer ring on the earth end.[8] The ^{22}Na densities of the two samples from the retainer ring agree having a difference of 1.2 ± 4.2%, as these samples were both unshielded and exposed to the same radiation. Both keel plate samples were partly shielded so that a hypothetical unshielded sample at this location would have ^{22}Na density in excess of either of the measured samples, but not more than their sum. Thus, the ^{22}Na density of the hypothetical unshielded keel plate sample would be 23 to 105% larger than that of the retainer ring samples indicating strong evidence for the space/earth anisotropy.

ACKNOWLEDGEMENTS

C. D. Ouzts is thanked for counting the LDEF samples and assisting with the development of the detector efficiency calibrations. Initial confirmation measurements supporting the efficiency model were provided by D. J. Lindstrom, NASA Johnson Space Center, Houston, Texas. Guidance and partial funding for this project were provided through the efforts of G. J. Fishman and B. A. Harmon, NASA Marshall Space Center, Huntsville, Alabama. Also, information contained in this work was developed during the course of work under Contract No. DE–AC09–89SR18035 with the U.S. Department of Energy.

REFERENCES

1. G. J. Fishman, T. A. Parnell, and B. A. Harmon, "Long Duration Exposure Facility (LDEF) Induced Radioactivity Plan", NASA Marshall Space Center, Huntsville, AL, Astrophysics Division, Space Science Laboratory Report, Dec. 1989.

2. E. V. Benton and W. Heinrich, "Ionizing Radiation Exposure on LDEF", University of San Francisco, San Francisco, CA, USF-TR-77, Aug. 1990.

3. T. W. Armstrong and B. L. Colborn, "Scoping Estimates of the LDEF Satellite Induced Radioactivity", Science Applications International Corp., Prospect, TN, SAIC-90/1462, Sep. 1990.

4. T. W. Armstrong and B. L. Colborn, "Radiation Calculations and Comparisons with Data", First LDEF Post-Retrieval Symposium, Kissimmee, Florida (June 2-8, 1991), NASA CP-3134, 1992.

5. W. G. Winn, W. W. Bowman, and A. L. Boni, "Ultra-Clean Underground Counting Facility for Low-Level Environmental Samples", *The Science of the Total Environment* Vol. 69, February 1988, pp. 107-144.

6. W. G. Winn, "Ultrasensitive Examination of Environmental Samples by SRL Underground Counting Facility", *Trans. Am. Nuc. Soc.* Vol. 54, June 1987, pp. 34-35.

7. C. E. Moss and R. C. Reedy, "Measurements of Induced Radioactivity in Some LDEF Samples", First LDEF Post-Retrieval Symposium, Kissimmee, Florida (June 2-8, 1991), NASA CP-3134, 1992.

8. W. G. Winn, "Gamma-Ray Spectrometry of LDEF Samples", Westinghouse Savannah River Company, Aiken, SC, WSRC-RD-91-16, Aug. 1991.

9. W. G. Winn and R. A. Sigg, "Pre-Operational Radio-Environmental Studies of Plant Vogtle", Westinghouse Savannah River Company, Aiken, SC, WSRC-RD-89-161 May 1, 1989.

10. K. Debertin and R. G. Helmer, *Gamma and X-ray Spectrometry with Semiconductor Detectors*, North-Holland, Elsevier Science Publishing Co., New York, 1988.

11. G. J. Fishman, B. A. Harmon, et al, "Observation of ^{7}Be on the Surface of LDEF Spacecraft", Nature, Vol 439, Feb. 1991, pp. 678-680.

Table 1. Trunnion Disk Results

Decay Correction Date – January 20, 1990

Sample	Isotopic Activities in pCi/kg Sample							
	Be-7	Sc-46	Cr-51	Mn-54	Co-56	Co-57	Co-58	Co-60
LHB	–	4.31 ±.59	–	120.21 ±1.53	4.58 ±.75	15.17 ±.73	3.31 ±1.15	1.96 ±.18
LHE	–	4.57 ±.71	–	95.21 ±1.75	2.92 ±.77	9.60 ±.66	1.33 ±1.35	1.59 ±.30
LHF	–	3.37 ±.51	–	100.50 ±1.41	4.84 ±.75	10.47 ±.63	4.06 ±1.16	1.40 ±.19
LHP	0.95 ±3.29	3.53 ±.20	16.38 ±7.38	79.43 ±.68	2.65 ±.21	7.48 ±.28	4.90 ±.33	1.58 ±.11
LHR	-7.48 ±3.65	3.78 ±.21	34.35 ±8.43	76.71 ±.68	2.66 ±.23	7.23 ±.36	4.68 ±.35	1.52 ±.11
LHS	2.56 ±3.28	4.34 ±.19	23.14 ±8.15	75.25 ±.59	2.53 ±.20	6.22 ±.25	4.92 ±.30	1.55 ±.09
RHB	–	5.04 ±1.00	–	82.52 ±1.36	3.21 ±.79	7.34 ±.59	4.67 ±1.27	1.39 ±.25
RHE	–	1.96 ±.75	–	79.77 ±1.57	2.15 ±.95	6.63 ±.57	2.35 ±1.27	1.16 ±.22
RHF	–	2.99 ±.64	–	78.98 ±1.34	3.75 ±.89	7.00 ±.59	2.45 ±1.26	1.32 ±.20
RHP	5.36 ±3.53	3.46 ±.21	35.22 ±8.84	72.56 ±.66	2.67 ±.22	7.28 ±.30	4.39 ±.33	1.45 ±.11
RHR	8.75 ±3.07	3.48 ±.19	26.16 ±8.13	72.75 ±.60	2.41 ±.19	6.20 ±.24	4.29 ±.30	1.55 ±.09
RHS	2.67 ±3.74	3.94 ±.23	31.89 ±10.08	74.66 ±.71	2.73 ±.25	6.01 ±.32	4.32 ±.41	1.44 ±.12

All errors are 1-σ counting errors

Table 2. Metal Slab Sample Results

Decay Correction Date: January 20, 1990

Space Side Trunnion Layers		
RHG-SP-	pCi/kg	
	Mn-54	Co-57
2	95.10 ±3.44	19.57 ±3.17
3	83.24 ±2.77	14.78 ±1.88
4	77.62 ±2.25	11.98 ±1.72
5	70.89 ±1.44	12.18 ±1.27
6	70.26 ±1.63	12.74 ±1.43

Earth Side Trunnion Layers		
RHG-ER-	pCi/kg	
	Mn-54	Co-57
2	98.46 ±3.60	17.50 ±2.51
3	93.62 ±2.04	15.02 ±1.69
4	87.82 ±2.36	17.48 ±2.22
5	80.00 ±1.47	10.92 ±1.19
6	76.64 ±1.63	12.07 ±1.22

Vanadium	
Sample	pCi/kg Sc-46
G12-A2-FNV	16.00 ±1.32
I-C9-V	20.24 ±1.51
I-F2-V	21.12 ±2.70
I-H12-VA	19.82 ±12.84
I-H12-VB	21.59 ±6.77

Aluminum	
Sample	pCi/kg Na-22
ESR-1	90.60 ±3.31
ESR-5	91.70 ±1.94
KP-3	111.47 ±1.95
KP-10	75.33 ±2.60

All errors are 1-σ counting errors

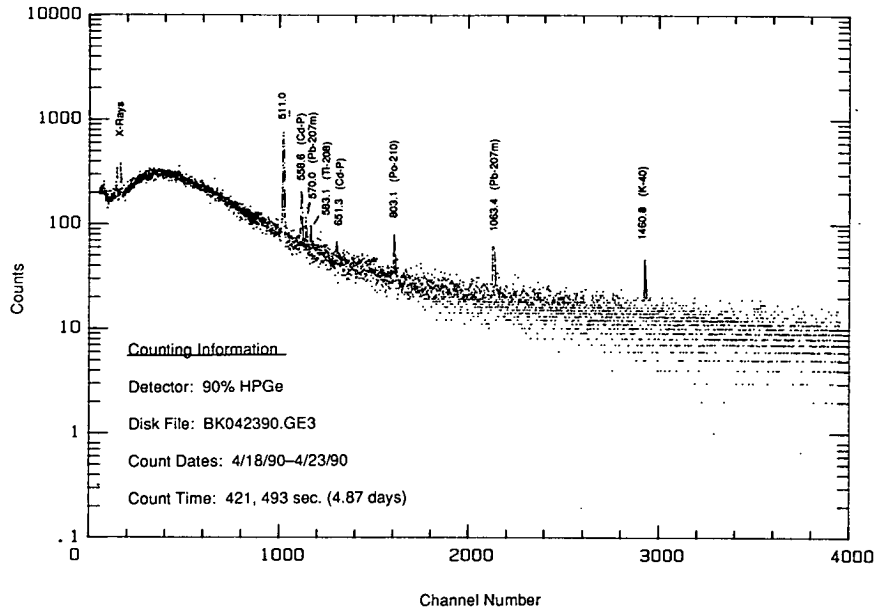

(a) Background

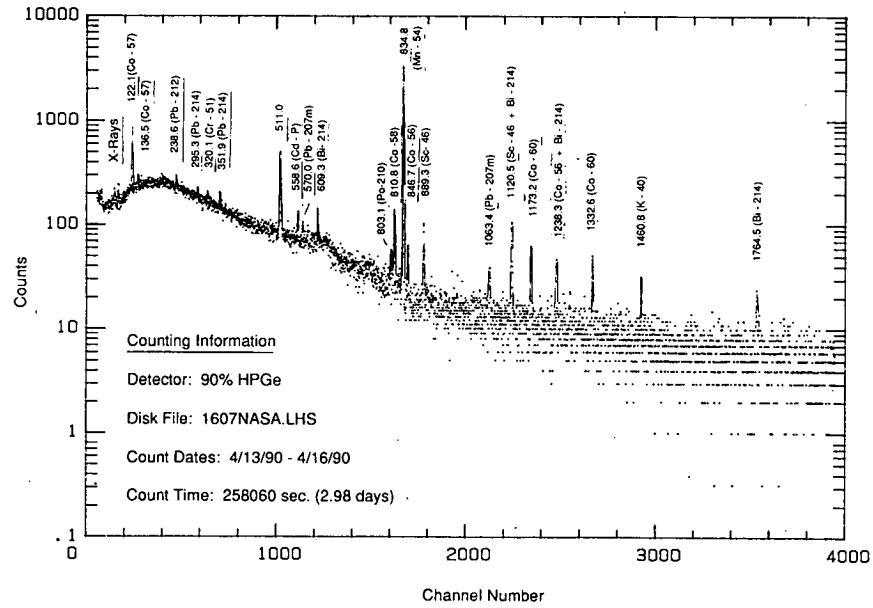

(b) Sample LHS

Figure 1. Typical Gamma-Ray Spectra

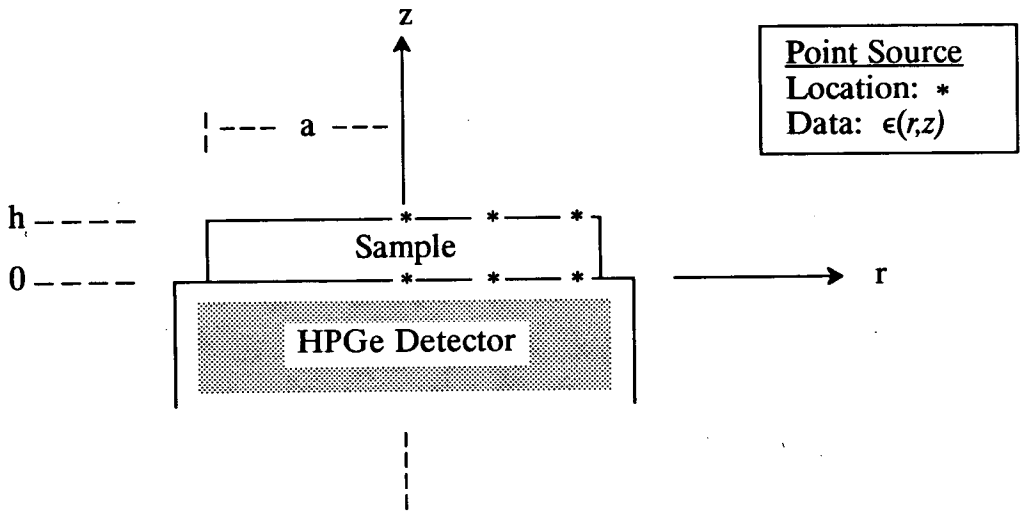

DISK ANALYSIS	SLAB ANALYSIS
(1) Exponential Average $\epsilon(r) = \dfrac{\epsilon(r,h) - \epsilon(r,0)}{\ln[\epsilon(r,h) / \epsilon(r,0)]}$	(1) Separable *r,z* Model $\epsilon(r,z) = \epsilon(r,0)\, e^{-Uz}$
(2) Radial Fitting $\epsilon(r) = A - Br^P$	(2) Sample Average $\epsilon(r,0)$ $\langle \epsilon(r,0) \rangle_A$
(3) Sample Average $\epsilon = A - [2/(2+p)]Ba^P$	(3) Measure U/ Average e^{-Uz} $(1-e^{-Uh})/Uh$
	(4) Sample Average $\epsilon = \langle \epsilon(r,0) \rangle_A (1-e^{-Uh})/Uh$

Figure 2. HPGe Efficiency Calibration

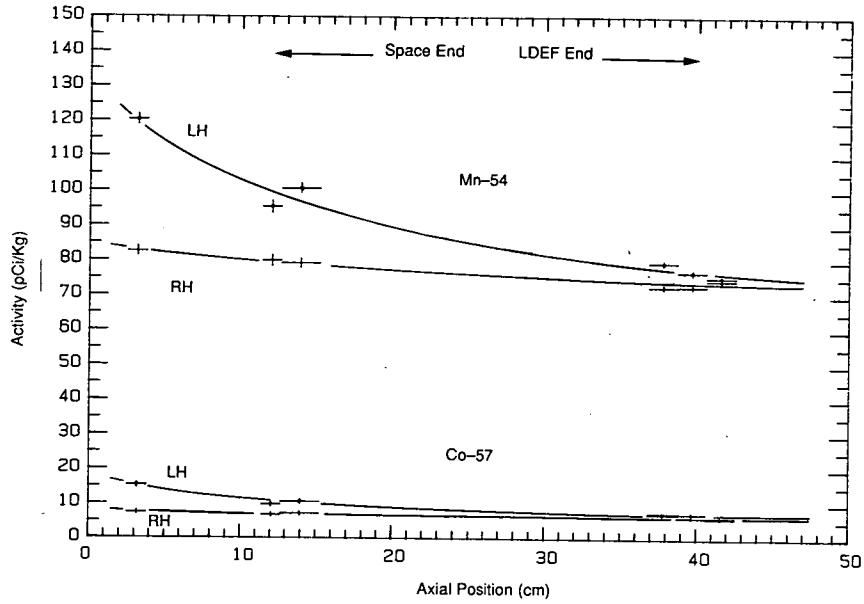

(a) LH and RH Samples B,E,F,P,R,S (plotted left–to–right)

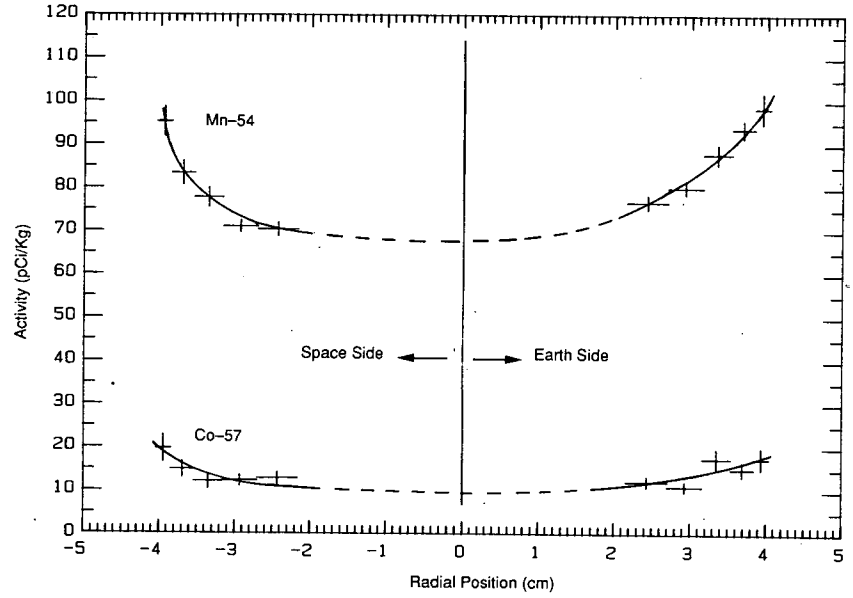

(b) RHG Samples

Figure 3. Results for Trunnion Samples

INDUCED RADIOACTIVITY IN LDEF COMPONENTS

B. A. Harmon
NASA Marshall Space Flight Center
Huntsville, AL 35812
Phone: 205/544-4924, Fax:205/544-7754

G. J. Fishman and T. A. Parnell
NASA Marshall Space Flight Center
Huntsville, AL 35812
Phone:205/544-7693, Fax:205/544-7754

C. E. Laird
Department of Physics
Eastern Kentucky University
Richmond, KY 40475
Phone:606/622-1526, Fax:606/622-1020

SUMMARY

A systematic study of the induced radioactivity of the Long Duration Exposure Facility (LDEF) is being carried out in order to gather information about the low earth orbit radiation environment and its effects on materials. The large mass of the LDEF spacecraft, its stabilized configuration, and long mission duration have presented an opportunity to determine space radiation-induced radioactivities with a precision not possible before. Data presented include preliminary activities for steel and aluminum structural samples, and activation subexperiment foils. Effects seen in the data show a clear indication of the trapped proton anisotropy in the South Atlantic Anomaly and suggest contributions from different sources of external radiation fluxes.

INTRODUCTION

A systematic study of induced radioactivity in materials carried aboard the Long Duration Exposure Facility has provided a significant and very useful database for space radiation-related applications. This study was broad-based to include as many different materials as could be obtained from the LDEF structure and experiments. In essence, the entire spacecraft was used as a passive detector to sample the radiation environment in low earth orbit.

The uniqueness of the LDEF spacecraft for radiation studies not only stems from its extended flight time (mission duration 5.8 years), but also its large mass and passively stabilized geometry. The stabilized configuration was designed to control exposure of various experiments to the space environment, and in particular, allowed directional aspects of the induced radioactivity to be studied on the leading (eastern), trailing, north and south sides of the spacecraft, as well as the earth and spaceward directions.

The induced radioactivity is produced by several sources of particle fluxes: galactic protons, trapped Van Allen protons (encountered in the South Atlantic Anomaly and accounting for the bulk of the activity), atmospheric and secondary neutrons, and to a small extent heavier ions. All of these particles induce radioactivity by colliding with a stable nuclide in the spacecraft material, and occasionally forming a radioactive nuclide. If its half-life is long enough, it can be detected in the laboratory following retrieval. The sources of external radiation flux, the nuclear reactions with the spacecraft material, and the spacecraft geometry can be combined, in principle, into a model to predict the experimentally measured activities. Such a comparison of calculation and experiment can be very useful for future long duration missions in low earth orbit (LEO), such as Space Station Freedom and the Earth Observing System, where accurate radiation dose predictions are required.

SAMPLE PROCESSING AND DISTRIBUTION

Following retrieval of the LDEF in January of 1990, samples for measurement of induced radioactivity were obtained from the Kennedy Space Center over a period of a

few months. Some samples were obtained from the structural components of the spacecraft; others were taken from experiment trays under agreements with the experiment investigators. Approximately 400-500 samples were processed at the Marshall Space Flight Center and distributed to eight nationally recognized laboratories for analysis: Lawrence Berkeley Laboratory, Los Alamos National Laboratory, Johnson Space Center, Lawrence Livermore National Laboratory, Savannah River-Westinghouse, the Tennessee Valley Authority-Western Area Radiological Laboratory, Battelle-Northwest Laboratory, and the Marshall Space Flight Center.

High-purity germanium detectors are used to detect gamma rays from decaying radionuclides, and must be well-shielded from gamma rays produced by secondary emission from cosmic rays and naturally radioactive materials in the laboratory. Typical measured results are in the range of 0.1-100 picoCuries per kilogram of material in the LDEF spacecraft. Some radionuclide activities, as in the steel and aluminum structural components, were strong enough to allow mapping of their directional and depth-dependent characteristics.

Figure 1 shows the positions of various materials on the LDEF spacecraft that were analyzed for induced radioactivity. The steel trunnions (alloy 17-4PH) from the end support frame (Earth end) of the LDEF were the first components acquired for analysis. Other structural materials obtained later included aluminum experiment tray clamp plates and trunnion clamp assemblies, titanium structural clips, and lead ballast plates. An activation subexperiment consisting of metal foils (ref. 1) was also included in several experiment trays. These included sets of five different metals (cobalt, vanadium, tantalum, indium and nickel). These were chosen because of their simple isotopic makeup and significant long-lived radionuclide production. In addition some samples were obtained by agreement from other experimenters, such as magnesium, copper, germanium, niobium, silver, and teflon. Many of these samples, however, were not of sufficient mass to yield good signal-to-background ratios for accurate measurement.

PRELIMINARY RESULTS

In this section, preliminary results obtained in the analysis of LDEF induced radioactivity are presented. Absolute activities have been corrected for decay since retrieval and for detection geometry, and are estimated to be good to 20%.

A detailed representation of the west trunnion (adjacent to experiment tray row 3 in figure 1) with respect to the external environment and the pattern in which samples were prepared from it is shown in figure 2. Samples were cut in 1.3, 1.9 and 2.5 cm- (0.5, .75 and 1 in) thick cylindrical sections 8.3 cm (3.25 in) in diameter for bulk activity measurements, and thinner 5 cm (2 in) square layers of varying thickness to study depth and directional dependences.

Examples of spectra showing peaks from gamma-decaying radionuclides produced in the end section (section A in figure 2) in each of the two steel trunnions are shown in figure 3. These two samples were activated primarily by the trapped proton flux from (a) the east (onto the leading side of the spacecraft) and (b) the west (onto the trailing side of the spacecraft), respectively. These spectra indicate production of ^{56}Co, ^{58}Co, ^{54}Mn and ^{46}Sc with half-lives ranging from 71 to 312 days. An enhancement of the intensity of 835 keV ^{54}Mn peak by a factor of ~2 in the west-facing sample relative to the east-facing sample can clearly be seen. This effect is caused by the interaction of the trapped protons in the South Atlantic Anomaly with upper atmospheric gases. In the SAA the flux encountered by the leading (east) side of the spacecraft is attenuated relative to the trailing (west) side flux because the east side flux is traveling about a magnetic field line below the spacecraft, and thus penetrates deeper into the atmosphere. This effect has been quantified recently by Watts, et al. (ref. 2) and is being incorporated into the radiation models being developed currently. The 478 keV line observed on the leading side of the spacecraft (top figure) was determined to be caused by a deposition of atmospheric ^{7}Be on the surface of the spacecraft, and was not produced by spallation within the spacecraft material (ref. 3) (See also J. C. Gregory, et al., these conference proceedings).

Figure 4 illustrates the effect of the anisotropic SAA flux, where the west/east ratio of the ^{54}Mn activities as a function of distance is plotted along the axis of the trunnion. The difference in activity from one side to the other decreases with depth due to attenuation of the proton flux, even though the anisotropy of the external flux is known to increase with energy. The majority of the SAA protons which activate the steel are in the range of 20-120 MeV, and are stopped in the first 2 cm (0.8 or 15 g/cm^2) of material. The bulk activity for ^{54}Mn in the trunnion interior does not drop to zero, however, but reaches approximately 80 picoCuries/kg (see C. E. Moss and R. C. Reedy;

W. G. Winn, these conference proceedings), which may be caused by secondary activation by neutrons as well as high energy background fluxes of cosmic ray protons in the energy range of several GeV. These contributions are currently being included in a simplified three-dimensional spacecraft mass model (See B. L. Colborn and T. W. Armstrong, these conference proceedings).

A large number of aluminum experiment tray clamps (alloy 6061-T6) were obtained from the LDEF following de-integration of the spacecraft. The clamps were approximately 5 cm (2 in) by 12.7 cm (5 in) and 0.47 cm thick (.185 in or 1.3 g/cm^2). A total of 50 clamps have been counted at the TVA Western Area Radiological Laboratory to investigate the variation of activating flux with direction. Clamps were obtained from the spacecraft on each row to allow measurement of the change in flux every 15 degrees. In figure 5, the ^{22}Na activity based on the 1275 keV line is shown as a function of angle from the leading direction of the spacecraft (east). A comparative one-dimensional calculation is also shown (see T. W. Armstrong and B. L. Colborn, these conference proceedings.) based on the proton anisotropy model (ref. 2) normalized to AP8 omni-directional flux, and measured cross sections for protons on aluminum, which is within 30% agreement with the measured activation. The peak of the ^{22}Na activity in the trailing side plates is clearly apparent.

The activation subexperiment foils of vanadium, cobalt, indium, tantalum and nickel were analyzed as they were obtained from LDEF experiments M0001, M0002, P0006, and A0114. The results for each of the four nickel samples counted at Marshall Space Flight Center are shown in figure 6 along with predictions of a one-dimensional calculation with the AP8 flux for proton activation of the 5 cm (2 in) square by 0.32 cm (.125 in) thick nickel foils. The upper and lower limits of the calculation represent the range of proton-induced activation caused by (a) normally incident flux on the nickel surface, (b) a uniform exposure in all directions, and (c), same as (a) and (b) but shielded by 1 cm (0.4 in) of aluminum. These calculations represent the range of shielding/flux conditions to which the nickel samples were exposed around the spacecraft. By modeling the local geometry of these samples, it may be possible to separate shielding effects from contributions due to different activation sources. For example, the small amount of ^{60}Co observed in these samples can be produced alternately by an (n,p) reaction on ^{60}Ni (abundance 26.1%) above 5 MeV, or proton reactions on the other stable isotopes of nickel (^{61}Ni, ^{62}Ni and ^{64}Ni, total abundance 5.6%). More refined calculations may be able to distinquish these two contributions. Further analyses of

the nickel samples and the indium cobalt, tantalum, and vanadium samples are in progress.

ANALYSIS PLAN/CONCLUSION

Most of the low level counting has now been completed and the effort has shifted to collection and analysis of data from the counting laboratories. Much of the analysis and archiving of these data will be performed at Eastern Kentucky University to produce a large database of the measured induced radioactivities. The current scope of this effort is to be able to provide specific activities for different materials whenever the detection geometry is reasonably convenient for normalization of the gamma ray counting measurements. In other cases, where only relative measurements were possible, information about depth and directional dependences can still be extracted.

Measurements and analyses of the induced radioactivity in the Long Duration Exposure Facility will continue through 1991. Detailed plans can be found in the Long Duration Exposure Induced Radioactivity Analysis Plan (ref. 4). A program of calculations in order to extract as much information as possible about various sources of radioactivity is now underway (See T. W. Armstrong and B. L. Colborn, these conference proceedings.). It is hoped that these studies will yield a complete and accurate picture of the low earth orbit radiation environment.

REFERENCES

1. Clark L. G.; Kinard, W. H.; Carter, D. J.; and Jones, J. L.: The Long Duration Exposure Facility Mission 1 Experiments. NASA SP-473, 1984, pp. 1-189.

2. Watts, J. W.; Parnell, T. A.; and Heckman, H. H.: Approximate Angular Distribution and Spectral for Geomagnetically Trapped Protons in Low-Earth Orbit. AIP Conference Proceedings 186, 1989, pp. 75-85.

3. Fishman, G. J.; Harmon, B. A.; Parnell, T. A.; Gregory, J. C.; Peters, P.; Haskins, P. S.; McKisson, J. E.; Ely, D. W.; Weisenberger, A. G.; Piercy, R. B.; Phillips, G. W.; King, S. W.; August, R. A.; Ritter, J. C.; and Cutchin, J. H.: Observation of ^{7}Be on the Surface of the LDEF SPacecraft, Nature 349, 1991, pp. 678-680.

4. Fishman, G. J.; Parnell, T. A.; and Harmon, B. A.: Long Duration Exposure Facility (LDEF) Induced Radioactivity Analysis Plan, NASA TM-103545, 1991, pp. 1-32.

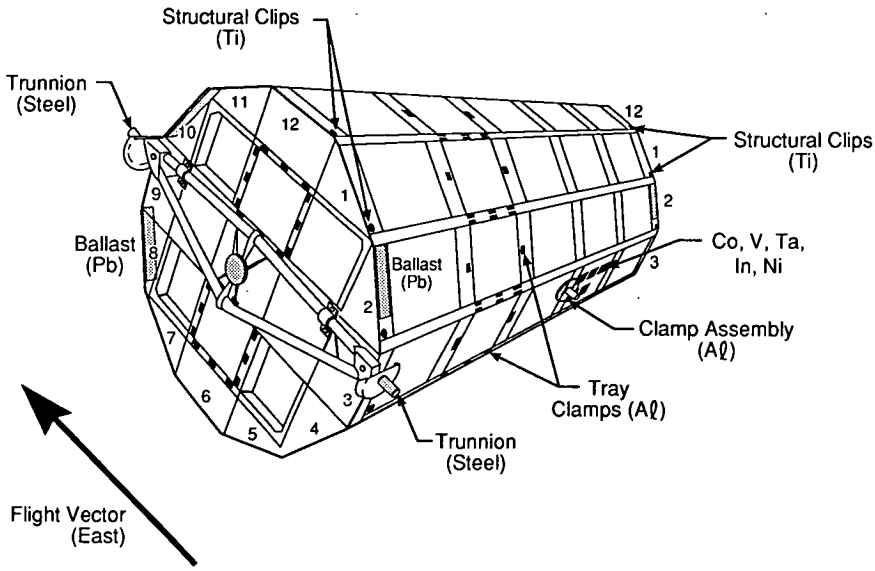

Figure 1

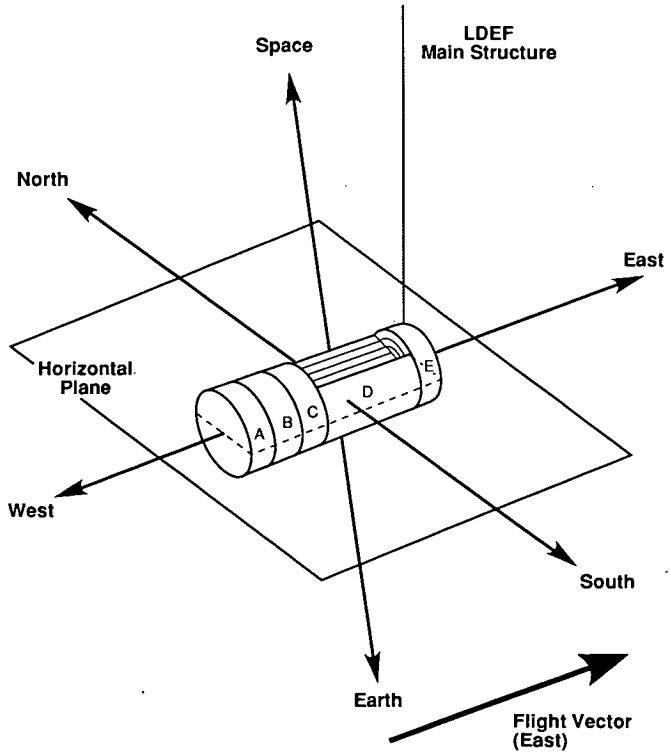

West (Trailing) Trunnion Orientation

Figure 2

LDEF Acquired Activity

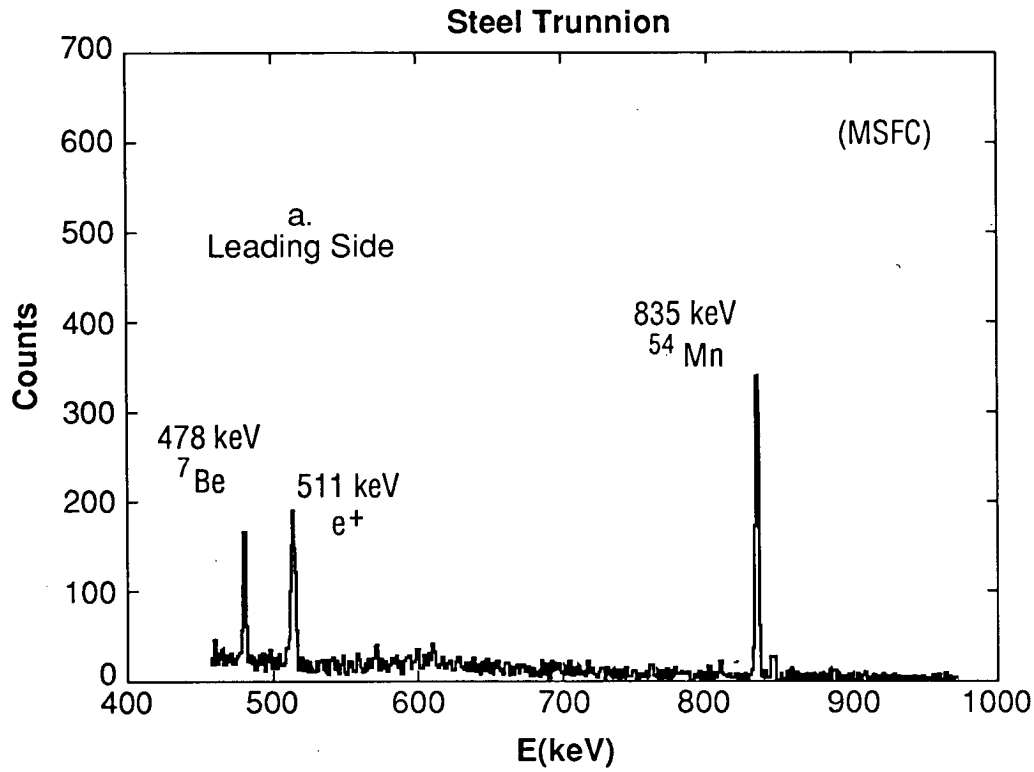

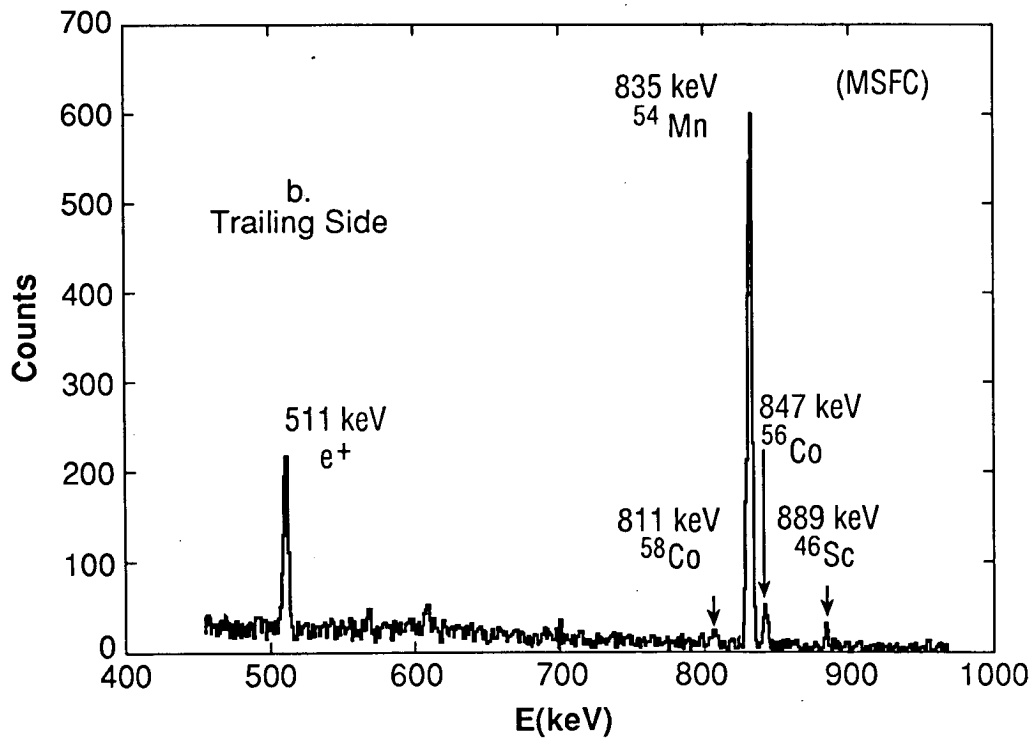

Figure 3

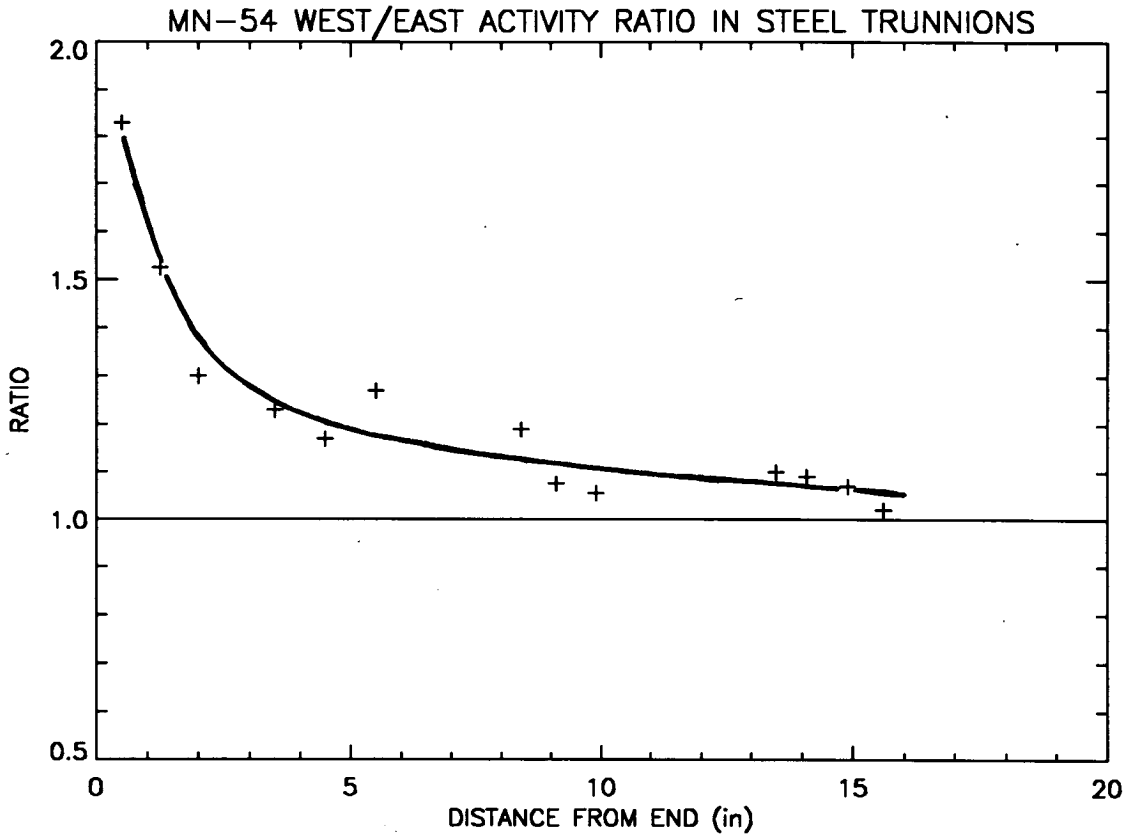

Figure 4

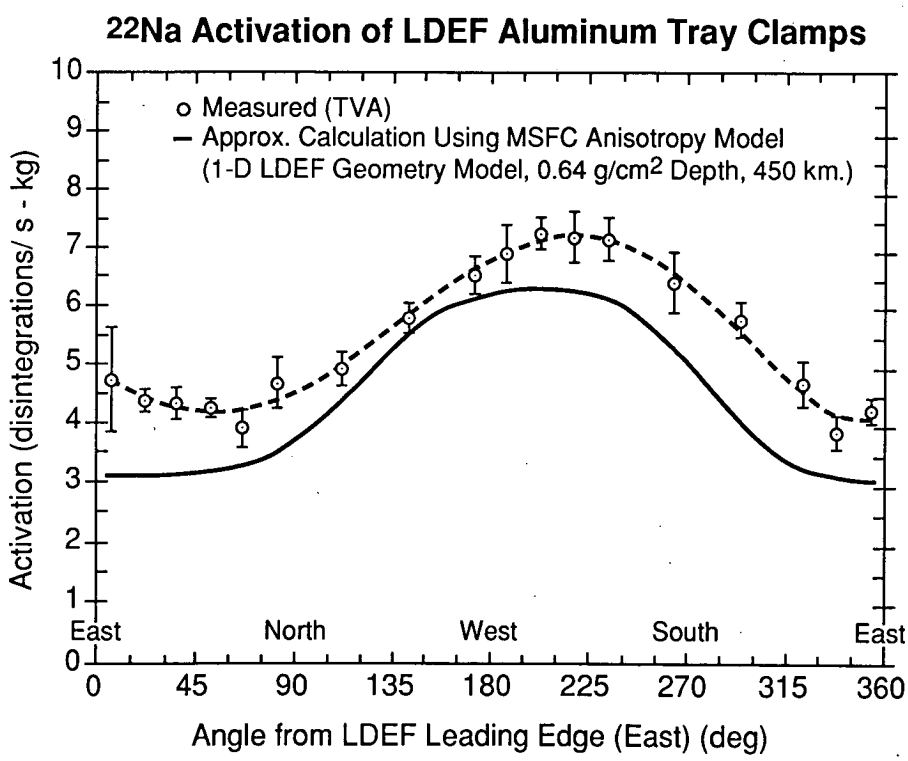

Figure 5

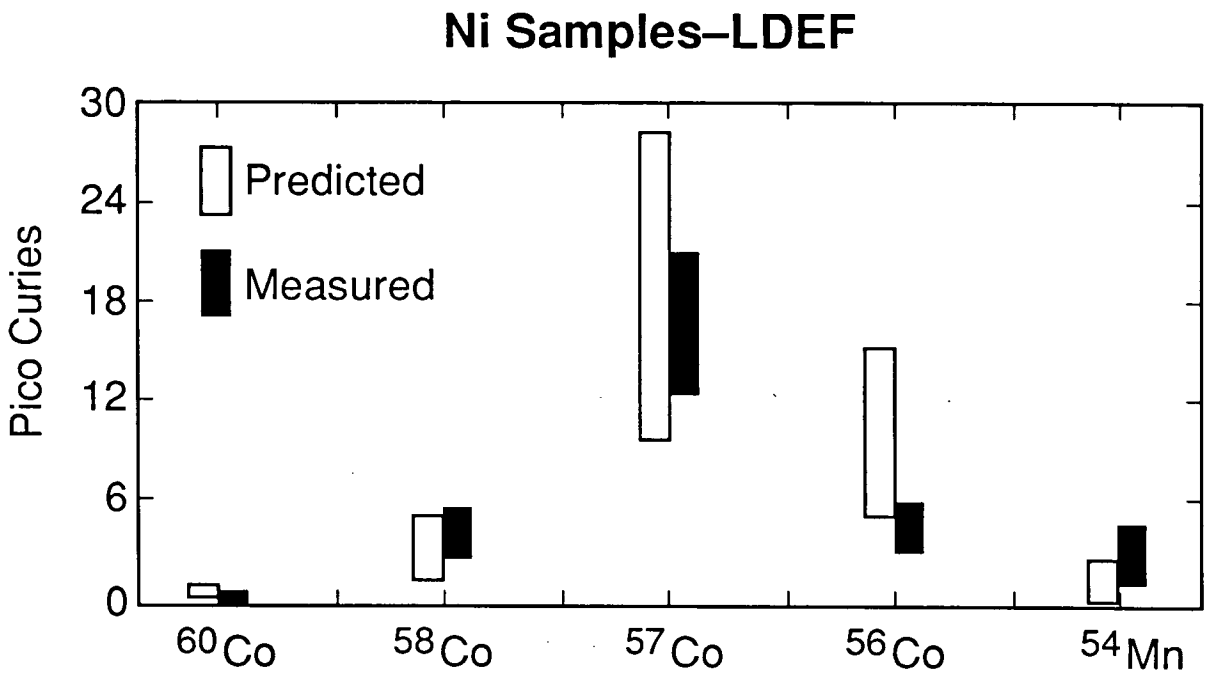
Ni Samples–LDEF
Pico Curies
30
24
18
12
6
0
Predicted
Measured
60Co
58Co
57Co
56Co
54Mn

Figure 6

Thermoluminescent Dosimetry for LDEF Experiment M0006

J.Y. Chang, D. Giangano, T. Kantorcik, and M. Stauber
Grumman Corporate Research Center, Bethpage , New York 11714

L. Snead
Department of Nuclear Energy, Brookhaven National Laboratory
Upton, New York 11973

INTRODUCTION

Experiment M0006 on the Long Duration Exposure Facility had as its objective the investigation of space radiation effects on various electronic and optical components, as well as on seed germination. It was a team effort involving the Perkin Elmer Corporation, the City University of New York, Patrick Air Force Base, the Walt Disney Epcot Center, and the Grumman Corporate Research Center (CRC). The Grumman CRC provided the radiation dosimetric measurements for M0006, comprising the preparation of TLD dosimeters and the subsequent measurement and analysis of flight exposed and control samples. In addition, various laboratory exposures of TLD's with gamma rays and protons were performed to obtain a better understanding of the flight exposures.

DOSIMETER PHYSICAL DATA AND EXPOSURE CONDITIONS

Experiment M0006 was located in Row 2 (near the trailing edge), Bay C, i.e., facing west and approximately midway between the earth end and space end. The payload was contained in a drawer located in an aluminum canister. The canister had a honeycomb milled out of the top surface to promote heat transfer, and was between 1.5 and 3 cm thick. The honeycomb surface had a sheet of aluminum attached, with thickness between .2 and .4 cm. The drawer was programmed to open 10 days after launch and remain open for 10 months before retracting into the aluminum canister. Several small craters observed on the mirror samples in the test array indicated that the drawer did open during flight. To provide for the radiation dosimetry of the payload, we prepared a set of 50 Harshaw TLD-100 dosimeters, each of dimensions 0.32 cm x .32 cm x .038 cm and nominal weight 0.01g. These dosimeters were preselected for weight uniformity, annealed to 450°C while recording their preflight luminescence response (nominally zero), and sent to Patrick AFB for LDEF deployment. However, only five dosimeters were incorporated into

M0006 and five more were retained as ground controls. The five flight samples were imbedded in 15-25g of seed in a sealed aluminum tube (7 in. long ,and 1 in. ID) with a wall thickness of 1/16 in. (.43 g/cm^2).

Predictions of the AP8/AE6 trapped particle model are that LDEF during its 2105 day mission encountered an omnidirectional proton integral fluence (E>10 MeV) of 4.5 of 10^9 cm^{-2} and an omnidirectional electron integral fluence of 5.3 x 10^{10} cm^{-2} (E>0.5 MeV), as reported in Ref. 1, taking into account the decay of the orbit (from 258.5 to 172 NMi). Also, the last 27% of the mission (565 days) were spent under solar maximum conditions, during which time 15% of the proton fluence and 24% of the electron fluence were accumulated, according to the AP8/AE6 Solar Max./Solar Min. model predictions (Ref. 1). The dose at the center of a variable-radius aluminum sphere, as calculated with the SHIELDOSE code (Ref. 2) is shown in Fig. 1, displaying separately the dose contribution from protons and electrons. It is seen that while the total dose is dominated by electrons up to aluminum thicknesses of ~.1 g/cm^2, the dose for aluminum thicknesses greater than ~.5 g/cm^2 essentially is all due to protons.

The proton environment for low-earth orbits has become known not to be omnidirectional, however, but to exhibit a west (LDEF trailing edge) - east (LDEF leading edge) asymmetry. This is evidenced in dosimetry results for LDEF experiments P0006 and P0004 (trailing edge deployment) versus M0004 (leading edge), where the trailing edge (west) results, at least up to ~2 g/cm^2 of effective shielding, are about 2.5 times larger than for leading edge deployment and are reasonably well fitted by the omnidirectional trapped particle model with a spherical shield approximation (while the leading edge data appear to agree with a planar shield approximation). Since experiment M0006 was located at the trailing edge, these considerations are relevant to our dosimetry results. We also note that since the effective shielding for the M0006 dosimeters was substantially larger than .5 g/cm^2, the dose results are due to only protons, according to the model.

DOSIMETER EVALUATION RESULTS AND DISCUSSION

LDEF Flight and Control Specimens

The LDEF dosimeters were received in our laboratory in April 1990. We labeled the flight specimens with the prefix F and the ground control samples with G; the other part of the flight specimen designation refers to the seed variety whose exposure was monitored. The F samples were expected to have a variation of ~10%; multiple dosimeters at each location in the seed capsule would have reduced the variation considerably. The G (control) samples experienced a cumulative

background exposure on the ground during about 6 years, plus a dose incurred in one New York-Florida round-trip flight. We cite our measurement of a New York-Los Angeles round trip flight exposure of 20-30 mr as an upper limit to the commercial flight exposure. These control samples, because of their low-level exposure, were expected to show a much larger relative variation in reading than their flight sample counter parts.

For the dose measurements we typically heated the dosimeter samples to temperatures high enough to obtain a complete thermoluminescence release (about 400°C), recording both the total counts and the glow-curve. The glow curves in all cases were recorded as the output of a logarithmic amplifier, the ordinate thus being proportional to the logarithm of the luminescence counts per unit temperature interval. This form of data recording accentuates differences in the glow peak shapes as an aid to studying differences in exposure conditions. The calibration was based on Frick dosimetry for Co-60 exposures up to a kilorad. The results of our dose readings for both F and G sets of TLD specimens are shown in Table 1. For the flight specimens the dose measurements, accurate to within 10%, range from 180 to 244 rads (LiF), with an average of 210 rads. The control samples (G set) show a minimal exposure, averaging 0.9 rad. The large scatter in the flight sample results is remarkable, since the TLD's were deployed in close proximity (seed tube interior) under virtually identical conditions. A predominantly electron/bremsstrahlung environment would have produced a much greater exposure uniformity. The flight sample dose readings generally are comparable to the results reported for Experiment P0006: ~260 rads (tissue) or ~205 rads (LiF) at an estimated effective shield thickness of ~12.5 g/cm^2 (Ref. 3). However, our determination of effective shielding for Experiment M0006 is still pending, since the LDEF mass distribution analysis (Ref. 4) has not yet been completed; we also have the complication of an open experiment drawer for the first 10 months of the mission.

LDEF Samples ±10%		Controls	
FPINTO-1	244 rads	GPINTO-1	1.4 rads
FPINTO-2	205 rads	GPINTO-2	0.4 rads
FM-1	230 rads	GM-1	0.9 rads
FM-2	180 rads	GM-2	1.4 rads
FCORN	192 rads	GCORN	0.4 rads

Table 1. TLD Measurement Results

As part of our analysis of the flight sample glow curves, the 5 F-set TLDs upon readout and anneal were re-irradiated with Co-60 gammas to a level of ~240 rads and their glow curves remeasured. Figure 2 illustrates the measurements for sample FCORN: The upper glow curve refers to the LDEF signal (a net of 5090 counts), while the lower glow curve obtains for the subsequent gamma exposure of the same TLD (a net of 6193 counts). We note that the gamma-exposed sample has two low-temperature peaks (at 100° and 135°C for this measurement, although the exact temperature location of the glow peaks depends somewhat on the readout heating rate), which are absent for all flight-exposed samples. A third peak (at 170°C) is considerably weaker in the flight exposure. Higher-temperature peaks (at 220°C and 290°C, labeled as peaks A and B, respectively) are common to both glow curves, although the intensity ratio of the 220°C peak to 290°C peak is smaller for the LDEF exposure (~3.7) than for the re-exposure with gammas (~5.1). This difference in intensity ratios for the two peaks was observed consistently for the entire F set, as shown in Table 2. It is tempting to attribute the glow curve differences to a long-term annealing process in the flight-exposed samples. Preliminary estimates indicate that the M0006 average tray temperature remained within a range of 10-30°C (*), so that the anneal would have proceeded at room temperature. Regarding the glow curve comparison in Fig. 2, the 100° peak and 135° peaks in the re-irradiation glow curve are known to have a half-life of 10 hours and 0.5 years, respectively, so that their absence in the LDEF dose signal plausible might be due to annealing (although they also have been found absent in fresh laboratory proton exposures). Another peak at ~170° which appears as a shoulder to the 220° peak in the gamma-exposed sample and has a half-life of 7 years is also noticeable in the LDEF signal. The main peak, at 220°C, however, has an 80-year half-life and, therefore, should not have been subject to signal loss in the LDEF sample. Hence, the differences in the ratios of the A and B glow peaks between the LDEF signal and gamma reirradiation results are hard to explain by annealing considerations.

---

*T. Sampair, Lockheed, Private Communication

Sample	LDEF Exposure	Fresh Gamma
FPINTO-1	3.82	5.43
FPINTO-2	3.74	4.82
FM-1	3.38	5.10
FM-2	3.58	4.63
FCORN	3.92	5.39
AVERAGE	3.69	5.07

Table 2. Ratio Peak Intensities at 220°C and at 280°C

Laboratory Proton Exposures

Prompted by the observation that the shapes of the glow curves obtained for the M0006 dosimeter flight exposures, especially the A to B peak ratios, were not reproduced in gamma ray exposures to comparable dose levels, we undertook a series of dosimeter exposures with protons, ranging in energy from 200 MeV down to 3.7 MeV. The specific purpose of this work was to determine whether proton exposures could produce a better match to the LDEF-exposed sample glow curves than the gamma exposures in emulating some of their main features. The dosimeters used in these laboratory simulations were again TLD-100 of dimensions .32 cm x .32 cm x .09 cm with a luminescence response about 2.1 times stronger than for the specimens flown on LDEF. The monoenergetic proton exposures were performed at the proton LINAC (200 and 141 MeV) and at the tandem Van de Graaff accelerator (27 and 10 MeV), both at Brookhaven National Laboratory, as well as at the Grumman Van de Graaff accelerator (3.7 MeV). Exposure levels ranged from ~200 to ~4600 Rads (LiF); for two of the bombarding energies (200 and 29 MeV) samples were exposed to two dose levels. The various irradiation conditions and the results obtained for glow peaks A and B are summarized in Table 3. As indicated earlier, peak A appears between 220 and 230°C, and peak B between 280 and 290°C. The peak data listed are proportional to the logarithm of the peak luminescence counts per unit temperature interval, with all data for the same exposure condition (energy and dose) having the same proportionality factor. The listed irradiation conditions, in addition to the bombarding energy include the average and peak values of

the ionization depth dose, as well as the energy deposition per ion, the exposure depth range, and the LET average over the exposure depth. For proton ranges less than the dosimeter thickness, the energy deposition contains the Bragg peak and the depth dose profile becomes significantly nonuniform. For example, for the 10-MeV exposure the entrance dose is 300 Rads, while the end-of-range dose is ~1.7 KRad. The dose data listed are analytical estimates, obtained with the Monte Carlo code TRIM (Ref. 5) on the basis of the measured bombarding proton fluence; for the 200- and 141-MeV exposures they are confirmed independently by carbon nuclear reaction dosimetry. The measured glow peak ratios A/B in Table 3 generally are much lower than those listed in Table 2 for laboratory gamma exposures and except for one exposure also lower than the LDEF flight sample values. There is no clear cut dependence on the proton energy, nor on the average LET value. However, where two exposure levels were produced at the same bombarding energy (200 and 29 MeV), the larger dose shows a smaller A/B peak ratio. For the 29-MeV exposure, where the 200-Rad entrance dose most closely resembles the LDEF flight exposures, the ratios of the peaks also approximate the corresponding LDEF data and also are significantly smaller than the ratio values for laboratory exposures with gammas at the same dose level. Again for the 29-MeV proton exposure an increase in the entrance dose to ~1000 Rad produces a nearly factor-of-two decline in the peak ratio. A comparable trend, although weaker, is seen for the 200-MeV exposure, where a 3.25-fold increase in the dose results in 25% decrease in the ratio. We note that for the proton measurements, reductions in the A/B peak ratio stem predominantly from a relative growth of peak B. This and other significant features of the proton glow curve structures are apparent in Fig. 3 and 4 (see footnote*), which should be compared with the glow curves given in Fig. 2. A main point in the comparison is that, just as for the LDEF flight samples, none of the proton laboratory exposures have the low-temperature glow curve structure observed for the laboratory gamma exposure (Fig.2). (Annealing considerations for the proton exposures do not apply, because of prompt readout.). This feature and the relative increase in peak B suggest a qualitative difference between the response of TLD-100 to protons (locally strongly ionizing) and to weakly ionizing radiation (gammas). The tentative conclusion, based on a limited set of laboratory simulations, is that the dose read from TLD flight samples was predominanly due to protons, in agreement with the radiation transport prediction.

---

*T. Sampair, Lockheed, Private Communication

PROTON ENERGY (MEV)	ESTIM. ABSORBED DOSE (RAD(LiF))			EXPOSED DEPTH (μm)	GLOW CURVE DATA FOR A & B PEAKS			Avg. LET
	AVG.	MAX.	ENERGY DEPOS. (MeV/Ion)		kxA	kxB	A/B	$\frac{MeV\ cm^2}{g}$
200	1.45x10 3	$1.45x10^3$	0.86	889	26.0	14.7	2.26	3.68
					27.0	15.2	2.21	
	$4.56x10^3$	$4.56x10^3$			74.8	44.2	1.69	
					73.0	44.2	1.69	
141 (200 MeV Atten. by 15.42 g/cm^{2}Al)	$3.59x10^3$	$3.59x10^3$	1.1	889	45.0	26.1	1.72	4.64
					45.8	27.0	1.67	
29	216	228	4.0	889	29.9	9.2	3.25	16.9
					28.9	7.8	3.71	
	$1.08x10^3$	$1.14x10^3$			48.6	26.5	1.83	
					44.5	22.3	2.00	
10	560	$1.69x10^3$	10.0	569	49.0	34.9	1.40	66.7
					27.4	19.1	1.69	
3.7	$2.95x10^3$	$5.31x10^3$	3.7	101	47.8	49.7	.96	139
					49.5	50.2	.98	

Table 3. Proton TLD Glow Curve Analysis

SUMMARY

Measurements on TLD-100 specimens flown in a seed capsule in LDEF experiment M0006 have registered exposures ranging from 180 to 244 Rads (LiF). Glow curves for the flight specimens were found to differ significantly from those obtained for gamma exposures in the laboratory at comparable dose levels. The flight samples showed a virtual absence of the low-temperature peak structure seen in the gamma exposures, and a relatively larger glow peak at 280°C as compared to the main peak at 220°C. A series of laboratory exposures of TLD-100 with protons from 3.7 to 200 MeV resulted in glow curves agreeing with the characteristic features of the flight samples. A tentative conclusion from this work is that the M0006 exposure was primarily due to protons, in agreement with the AP8/AE8 environment model and radiation transport analysis. The measured dose levels are consistent with an omni-directional effective shield mass of 12 g/cm^2 Al.

REFERENCES

1. J. Watts, NASA-MFSC, Geomagnetically Trapped Proton and Electron Fluences Encountered on the LDEF Mission, Presented at IRSIG Meeting, Jan. 24, 1991
2. S. M. Selzer, SHIELDOSE, IEEE Transactions on Nuclear Science, Vol. NS-26, No. 6, Dec. 1979
3. E.V. Benton et al., First LDEF Post Retrieval Symposium, June 1991
4. B.L. Colborn and T.W. Armstrong, First LDEF Post Retrieval Symposium, June 1991
5. J. F. Ziegler, J. P. Biersack, and U. Littmark, "The Stopping and Range of Ions in Solids," Pergamon Press, New York, 1985

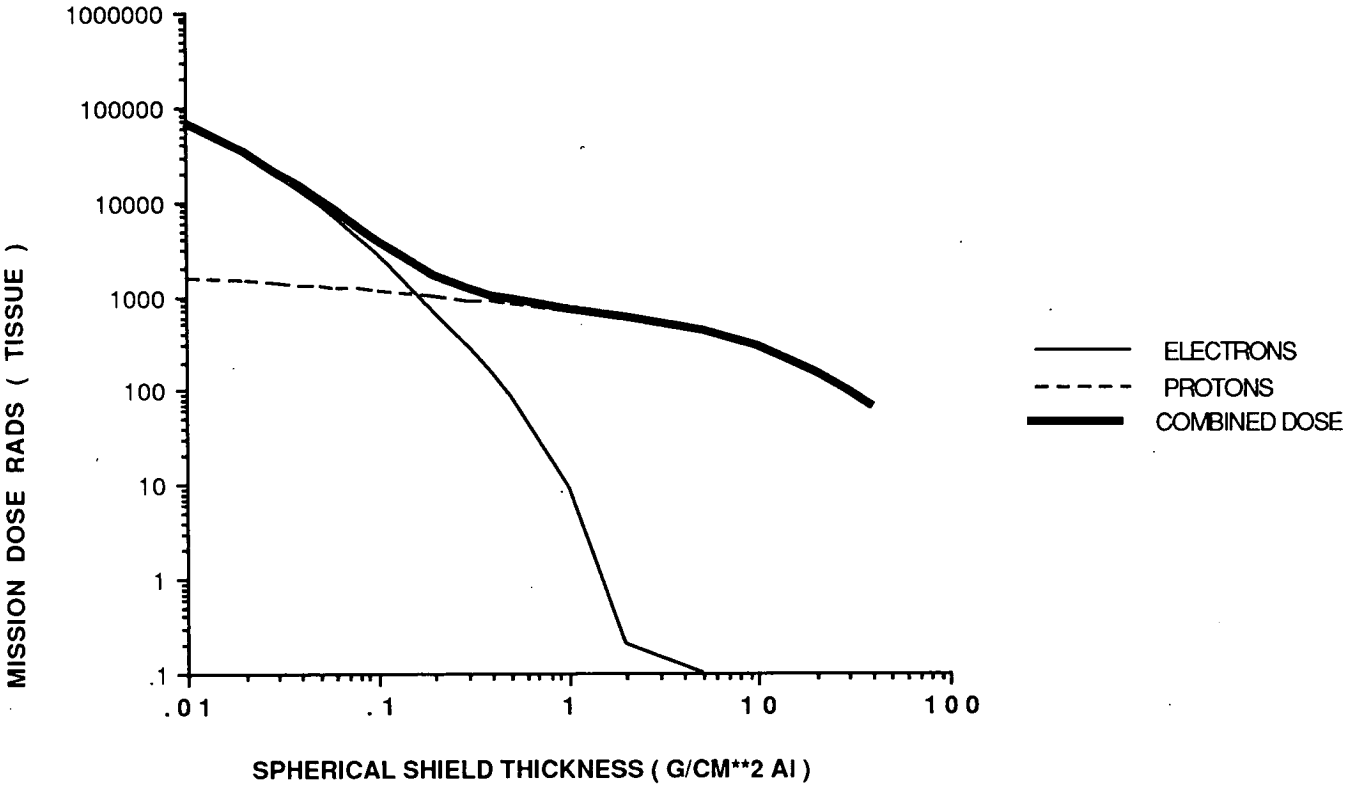

Fig. 1 LDEF Mission Dose from Trapped Radiation (Spherical Aluminum Shield)

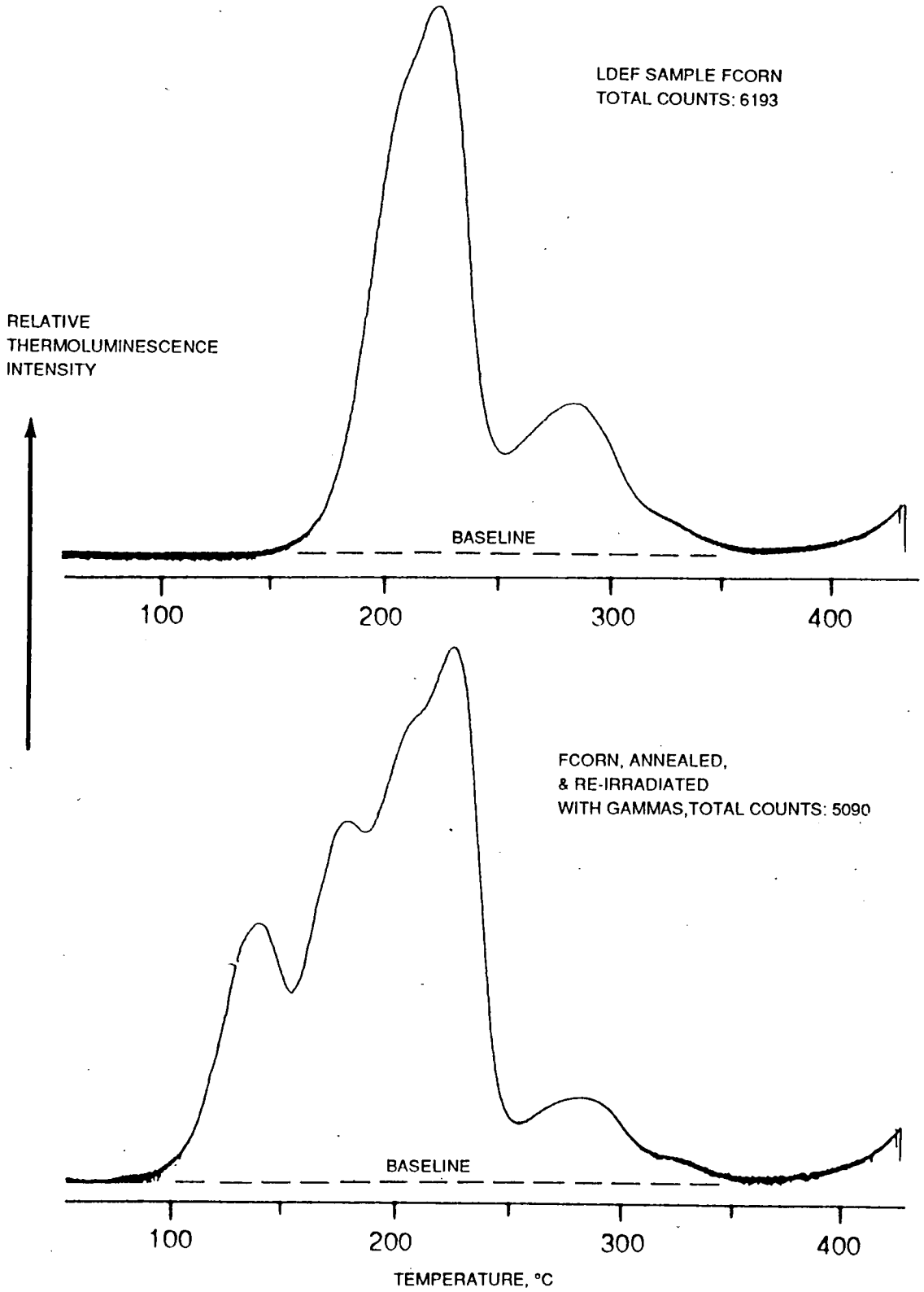

Fig. 2 Glow Curves for LDEF Sample FCORN, and for Same Sample Freshly Irradiated with Co-60 Gammas

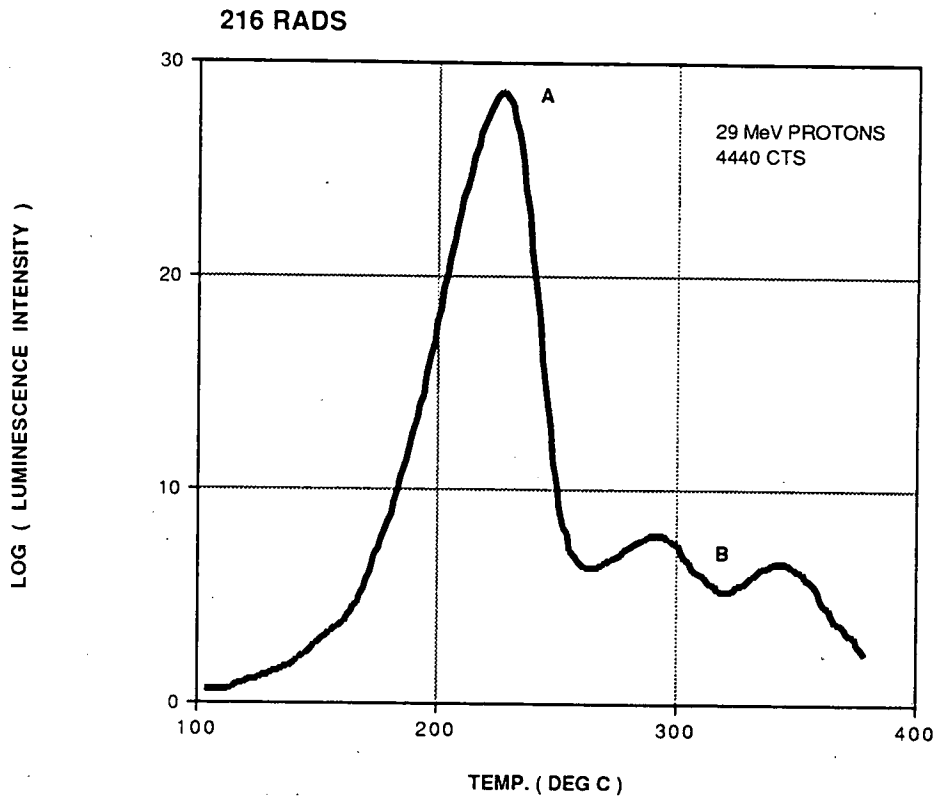

Fig. 3 Glow Curve for TLD-100 Irradiated with 29-Mev Protons to 216 Rads (LiF)

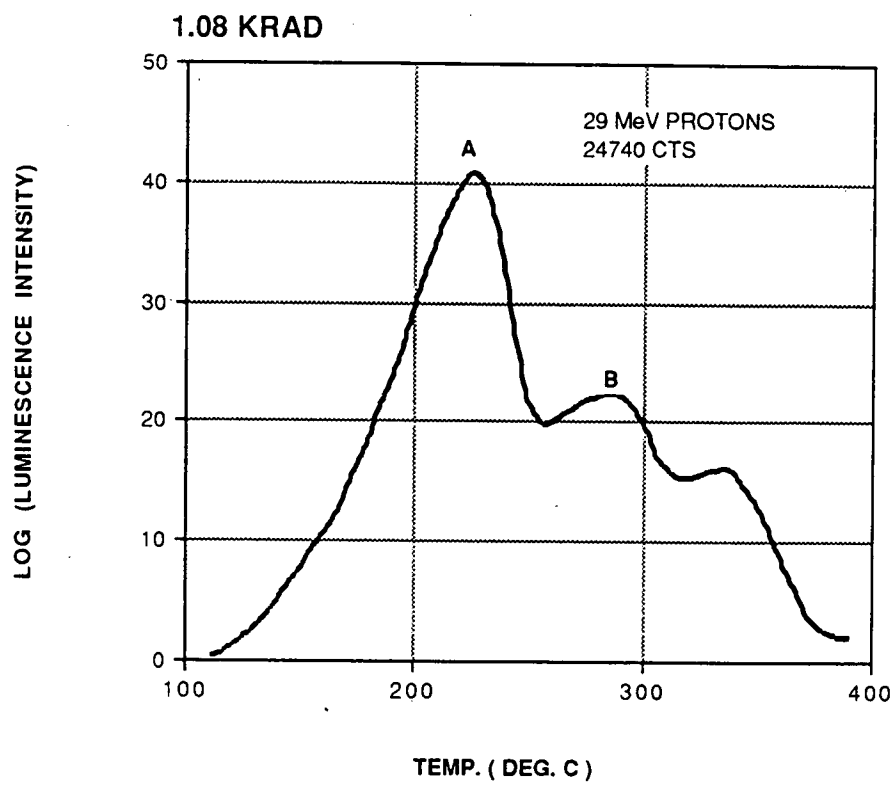

Fig. 4 Glow Curve for TLD-100 Irradiated with 29-MeV Protons to 1.08 KRad (LiF)

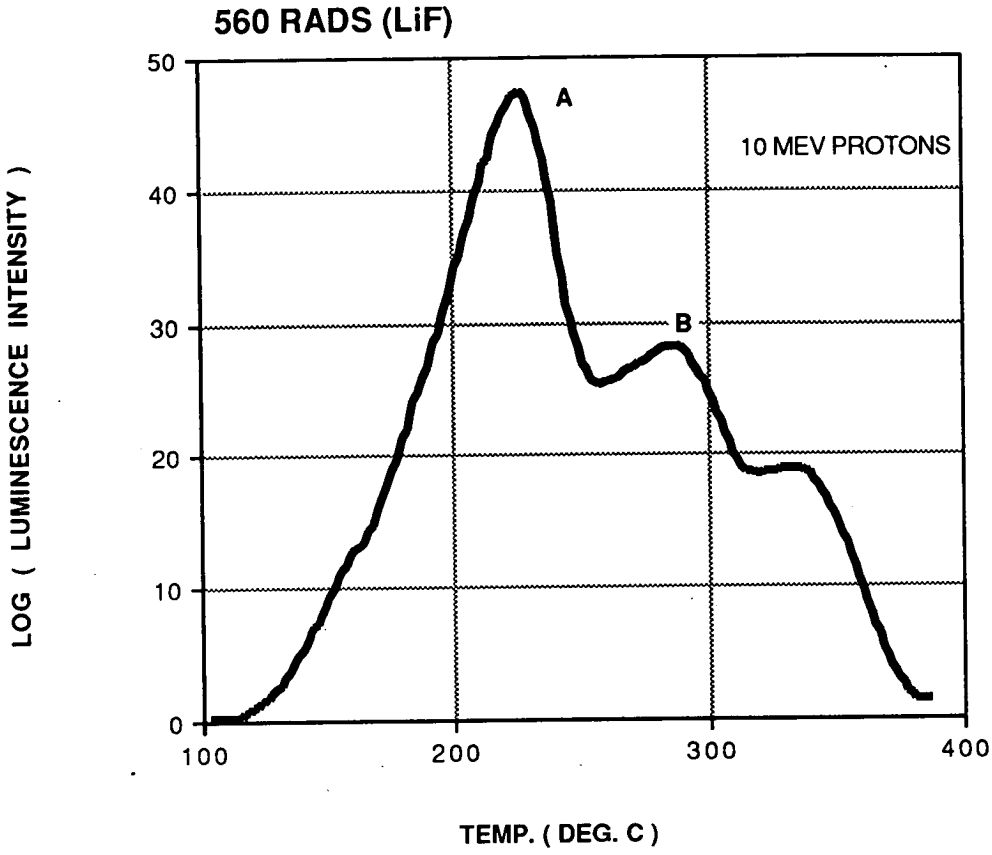

Fig. 5 Glow Curve for TLD-100 Irradiated with 10-Mev Protons to 560 Rads (LiF)

RADIATION EXPOSURE OF LDEF: INITIAL RESULTS

E. V. Benton, A. L. Frank, E. R. Benton and I. Csige
Physics Department, University of San Francisco
2130 Fulton St. San Francisco, CA 94117-1080

T. A. Parnell and J. W. Watts, Jr.
ES-62, NASA-Marshall Space Flight Center
George C. Marshall Space Flight Center, AL 35812

ABSTRACT

Initial results from LDEF include radiation detector measurements from four experiments, P0006, P0004, M0004 and A0015. The detectors were located on both the leading and trailing edges of the orbiter and also at the Earthside end. This allowed the directional dependence of the incoming radiation to be measured. Total absorbed doses from thermoluminescent detectors (TLDs) verified the predicted spatial east-west dose ratio dependence of a factor $\sim$2.5, due to trapped proton anisotropy in the South Atlantic Anomaly (SAA). On the trailing edge of the orbiter a range of doses from 6.64 to 2.91 Gy were measured under Al equivalent shielding of 0.42 to 1.11 g/cm^2. A second set of detectors near this location yielded doses of 6.48 to 2.66 Gy under Al equivalent shielding of 0.48 to 15.4 g/cm^2. On the leading edge doses of 2.58 to 2.10 Gy were found under Al equivalent shielding of 1.37 to 2.90 g/cm^2. Initial charged particle LET (linear energy transfer) spectra, fluxes, doses and dose equivalents, for LET in $H_2O \geqslant 8$ keV/μm, have been measured with plastic nuclear track detectors (PNTDs) located in two experiments. Also preliminary data on low energy neutrons were obtained from detectors containing ^{6}LiF foils.

INTRODUCTION

The LDEF orbiter carried four experiments which contained passive integrating detectors from the University of San Francisco. The P0006 LET Spectra Measurements experiment consisted of a single canister in Tray F-2 in which TLDs, PNTDs and neutron detectors were included. The P0004 Seeds in Space experiment consisted of seven canisters in Tray F-2 in which packets containing TLDs, PNTDs and neutron detectors were distributed within the seed component. The M0004 Radiation Effects in Electronics experiment included two detector canisters in Tray F-8 containing TLDs and PNTDs. The A0015 Biostack experiment consisted of two USF (Tray C-2 and G-1-2) and one partial USF (Tray F-2) canisters containing TLDs, PNTDs and neutron detectors.

The purpose of the detectors was to define the radiation environment as a function of shielding depth at the experimental sites on the orbiter. As seen from the Tray locations P0006, P0004 and two A0015 canisters were near the trailing edge. The third A0015 canister was at the earth end while M0004 was at the leading edge.

Work partially supported by NASA Grant No. NAG8-168 (NASA-Marshall Space Flight Center, Huntsville)

EXPERIMENTAL PROCEDURES

The passive radiation detectors were arrayed in stacks within the LDEF flight canisters. All the canisters (except the one partial A0015 unit) were sealed with O-rings to prevent venting to space. The placement of the different detector types was made to enable measurements to be made as a function of shielding depth.

TLD Procedures

Single batches of TLD - 700 were divided into flight, calibration and background portions. The calibration TLDs were irradiated with a standard ^{137}Cs source at two-month intervals over the 5.7 year orbital period in order to approximate both the LDEF absorbed doses and any signal fading which might occur. A high-dose TLD response supralinearity study was also conducted with ^{137}Cs standard doses up to 100 Gy.

After the mission TLDs were read out with a model 4000 Harshaw reader. Calibration and backgrounds were read out along with the flight detectors. The measured signals, averaged over a series of mission TLDs, were then converted to absorbed doses (^{137}Cs gamma ray equivalent). The minimum vertical shielding between each series of TLDs and space was measured and the shielding materials converted into the equivalent mass thickness of Al.

PNTD Procedures

The five types of PNTDs included on the LDEF experiments were pure CR-39, CR-39 with DOP plasticizer, Tuffak and Sheffield polycarbonates and Melinex polyester. Some of the CR-39 has been processed and read out to yield particle flux, dose rate and dose equivalent rate for $LET_{\infty} \cdot H_2O \geqslant 8$ keV/μm.

The CR-39 was processed in 6.25N NaOH solution at 50°C for 36 or 48 hr. After processing pairs of CR-39 layers from the flight stacks were reassembled in their original configurations. The pairs were scanned at the inner, adjacent surfaces under an optical microscope. Coincident track pairs were located in the adjacent surfaces (#2 and #3), then surfaces #1 and #4 were examined to determine whether the particle was of long range (it penetrated both CR-39 layers and resulted in four aligned tracks) or short range (it penetrated only the adjacent surfaces or the adjacent surfaces and one outer surface, resulting in two or three aligned tracks). The long range particles were classified as galactic cosmic rays (GCRs) and also included projectile fragments. The short range (SR) tracks are mainly stopping primary protons and secondary particles deriving from target nuclei within the PNTDs. Because of their short registration ranges protons are classified as SR particles.

The detected track parameters were measured at the #2 surface to determine particle LET. The semimajor and semiminor axes of the elliptical track surface openings were measured with an electronic micrometer. With the PNTD bulk etch and the LET calibration curve for the detectors, the track measurements were converted to LET spectra.

Low Energy Neutron Detectors (LENDs)

The LENDs were composed of ^{6}LiF radiation foils and CR-39 PNTDs. Alpha particles from the ^{6}Li(n, α)T reaction were emitted from the foils and detected in the CR-39. The LENDs were exposed in pairs with one detector covered by Gd foils. This allowed the separation of the neutrons into thermal ($<$ 0.2 eV) and resonance (0.2eV - 1MeV) energy regions.

The CR-39 PNTDs were processed in 6.25N NaOH solution at 70° C for 1.25 hours. The alpha particle track densities on the PNTDs were counted manually at 430 x under an optical microscope. The backs of the detectors were also counted to provide the backgrounds due to other charged particle sources present in space. The track densities were converted to neutron fluences and dose equivalents by previously established calibrations. The dose equivalent conversion factors (ref. 1) incorporated QF values of 2 for thermal neutrons and 6.4 for resonance neutrons.

MEASUREMENTS

TLD Results

The TLD measurements from experiments P0006, P0004, M0004 and A0015 are given in Tables I, II, III and IV respectively. The trailing edge TLDs (P0006, P0004) are seen to measure higher dose rates than the leading edge (M0004) and earthside (A0015) TLDs, although the shieldings are somewhat different for the maximum dose rate.

PNTD Results

Measurements of LET spectra from the leading and trailing edges of the orbiter are shown in Figures 1 and 2, respectively. Integral particle flux is plotted against LET_{∞} H_2O for the Total, GCR and SR particles. Integral flux, dose rate and dose equivalent rate from these measurements are given in Tables V and VI, respectively. In comparing the spectra it is seen that the M0004 (leading edge) curve is much steeper than that of P0006. M0004 has a higher total integrated flux but a smaller flux in the LET region above $\sim$ 12 keV/μ m. The greater importance of high LET particles in contributing dose and dose equivalent can be seen by comparing Tables V and VI, where the P0006 spectrum leads to higher dose rates and considerably higher dose equivalent rates. The differences in the spectra in the two experiments are due both to the position of the experiment on the orbiter and to the considerably different shielding depths. Note that the GCR spectra are truncated, and also perhaps under-measured, due to the difficulty in discriminating between GCR and SR particle tracks in the very high track densities found on the LDEF PNTDs.

LEND Results

Measurements of the low energy neutrons from the trailing edge of the orbiter are given in Tables VII and VIII. The P0004 (Table VIII) fluences and dose equivalents are larger than those in P0006 (Table VII). The P0004 detectors

were surrounded by a greater mass of hydrogenous material (seeds) which contributed to the moderation of high energy neutrons. The two P0004 measurements also have significant variations. The LENDs were located in two different canisters with that in #3 having higher neutron levels than that in #6. From Table II it is seen that the TLDs in mid #6 yielded higher doses than those in mid #3. There was probably a shielding difference from the side for the two canisters.

CONCLUSIONS

Radiation measurements have been made at different positions and shielding depths on the LDEF orbiter. Total absorbed doses measured with TLDs ranged from 6.64 to 2.66 Gy, for shielding of 0.42 and 15.4 g/cm^2, at the trailing edge to 2.58 to 2.10 Gy, for shielding of 1.37 and 2.90 g/cm^2, at the leading edge. This difference reflects the East-West anisotropy of trapped protons at the South Atlantic Anomaly. For heavy particle measurements with PNTDs (LET_{∞} $H_2O \geqslant 8$ keV/μm) absorbed doses of 19 and 31 mGy were found at the leading and trailing edges. The shielding at the two positions was 2.74 and 8.88 g/cm^2, respectively. The corresponding dose equivalents were 124 and 328 mSv. Neutron detectors at the trailing edge measured from 0.12 to 0.82 mSv for thermal neutrons and from 7.0 to 14.2 mSv for resonance neutrons. The shielding varied from 16.8 to 6.1 g/cm^2 for the extremes. Further information on charged particle measurements being performed with the LDEF detectors is given by Csige et al (ref. 2).

The preliminary measurements have revealed some of the differences in radiation levels over the surface of the LDEF orbiter and with shielding depth. Future measurements will allow the development of a more comprehensive picture of the quantities and of directional radiation variations.

REFERENCES

1. NCRP Report No. 38, NCRP, Washington D.C., 1971.

2. Csige, I; Benton, E. V.; Frank, A. L.; Frigo, L. A.; Benton, E. R.; Parnell, T. A. and Watts, J. W. Jr.: Charged Particle LET-Spectra Measurements Aboard LDEF, First LDEF Post-Retrieval Symposium, NASA CP-3134, 1992.

TABLE I

P0006: LDEF ABSORBED DOSE MEASUREMENTS WITH TLD-700

TLD Plate No.	Tissue Absorbed Dose (Gy)	Dose Rate (mGy/d)	Al Equivalent Shielding (g/cm^2)
1	6.48 ± 0.24	3.07 ± 0.11	0.48
2	3.92 ± 0.21	1.85 ± 0.10	4.10
3	3.16 ± 0.15	1.49 ± 0.07	8.34
4	2.76 ± 0.13	1.31 ± 0.06	12.2
5	2.66 ± 0.12	1.26 ± 0.06	15.4

The doses were approximately uniform over Plates 1 and 2 and were non-uniform over Plates 3, 4 and 5 (due to lesser shielding through the sides than through the top of the detector assembly for the deeper TLD plates). The minimum shielding to the side (for only the detector assembly) of the individual TLDs was 1.96 to 6.66 g/cm^2 Al equivalent. All shielding was converted to Al equivalent on the basis of the relative ranges of 100 MeV protons in the materials.

TABLE II

P0004: LDEF ABSORBED DOSE MEASUREMENTS WITH TLD-700

Detector No.	Canister No.	Tissue Absorbed Dose (Gy)	Dose Rate (mGy/d)	Al Equivalent Shielding (g/cm^2)
1	6	6.64 ± 0.29	3.14 ± 0.14	0.42
2	6	2.91 ± 0.07	1.38 ± 0.03	11.1
3	6	3.88 ± 0.22	1.83 ± 0.10	∿5
4	4	3.12 ± 0.08	1.48 ± 0.04	6.11
5	2	3.05 ± 0.08	1.44 ± 0.04	6.10
6	5	3.09 ± 0.08	1.46 ± 0.04	6.10
7	7	2.93 ± 0.10	1.39 ± 0.05	6.10
8	3	3.15 ± 0.08	1.49 ± 0.05	6.10
GC1		$3.2 \pm 0.2 \times 10^{-3}$	1.3×10^{-3}*	
GC2		$3.2 \pm 0.2 \times 10^{-3}$	1.3×10^{-3}*	

* For a total detector assembly time of 2418 days. The flight detectors are averaged over the LDEF orbital duration of 2115 days.

The minimum shielding to the side (for only the detector assembly) of the individual TLDs was ∿12.4 g/cm^2 Al equivalent. All shielding was converted to Al equivalent on the basis of the relative ranges of 100 MeV protons in the materials. The proton range in the seed was assumed to be equal (in units of g/cm^2) to that of polycarbonate plastic.

TABLE III

M0004: LDEF ABSORBED DOSE MEASUREMENTS WITH TLD-700

Detector No.	TLD Plate No.	Tissue Absorbed Dose (Gy)	Dose Rate (mGy/d)	Al Equivalent Shielding (g/cm^2)
1	1	2.10 ± 0.13	0.99 ± 0.06	2.90
	2	2.37 ± 0.10	1.12 ± 0.05	1.37
2	1	2.19 ± 0.12	1.04 ± 0.06	2.90
	2	2.58 ± 0.09	1.22 ± 0.04	1.37
3(GC)	1	$2.9 \pm 0.2 \times 10^{-3}$	$1.3 \pm 0.1 \times 10^{-3}$*	
	2	$3.2 \pm 0.2 \times 10^{-3}$	$1.4 \pm 0.1 \times 10^{-3}$*	
4(GC)	1	$2.9 \pm 0.2 \times 10^{-3}$	$1.3 \pm 0.1 \times 10^{-3}$*	
	2	$2.9 \pm 0.2 \times 10^{-3}$	$1.3 \pm 0.1 \times 10^{-3}$*	

* For a total detector assembly time of 2271 days. The flight detectors are averaged over the LDEF orbital duration of 2115 days.

All shielding materials were converted to Al equivalent on the basis of the relative ranges of 100 MeV protons in the materials.

TABLE IV

A0015: LDEF ABSORBED DOSE MEASUREMENTS WITH TLD-700

Canister No.	TLD Plate No.	Tissue Absorbed Dose (Gy)	Dose Rate (mGy/d)	Al Equivalent Shielding (g/cm^2)
1	1	3.93 ± 0.08	1.86 ± 0.04	1.66
	2	2.74 ± 0.23	1.30 ± 0.11	6.23
	3	2.41 ± 0.18	1.14 ± 0.09	10.0
2	1	4.49 ± 0.11	2.12 ± 0.05	3.85
	2	3.29 ± 0.22	1.56 ± 0.10	7.83
	3	3.04 ± 0.32	1.44 ± 0.15	11.7
3	1	3.47 ± 0.22	1.64 ± 0.10	---

Canister #1 was to Earthside.
Canister #2 was at the trailing edge.
Canister #3 was vented to space and at the trailing edge.

Minimum shielding to the side (for only the detector assembly) of the individual TLDs was 2.52 to 5.31 g/cm^2 Al equivalent.

All shielding materials were converted to Al equivalent on the basis of the relative ranges of 100 MeV protons in the materials.

TABLE V. PNTD MEASUREMENTS FROM M0004 (7-1C-1, 2)

	Flux ($cm^{-2} \cdot s^{-1} \cdot sr^{-1}$)	Dose rate ($\mu Gy\ d^{-1}$)	Dose equiv. rate ($\mu Sv\ d^{-1}$)
TOTAL	2.847×10^{-4}	9.09	58.8
GCR	6.322×10^{-6}	0.47	5.0
SR	2.784×10^{-4}	8.62	53.8

$LET_{\infty} \cdot H_2O \geq 8$ keV/μm
Minimum shielding was 2.74 g/cm^2 Al equivalent

TABLE VI. PNTD MEASUREMENTS ON P0006 (7-119, 120)

	Flux ($cm^{-2} \cdot s^{-1} \cdot sr^{-1}$)	Dose rate ($\mu Gy\ d^{-1}$)	Dose equiv. rate ($\mu Sv\ d^{-1}$)
TOTAL	2.526×10^{-4}	14.8	155
GCR	7.980×10^{-6}	1.15	17.0
SR	2.446×10^{-4}	13.6	138

$LET_{\infty} \cdot H_2O \geq 8$ keV/μm
Minimum shielding was 8.88 g/cm^2 Al equivalent

Table VII. Thermal and Resonance Neutron Measurements for P0006

Neutron Energy Range	Fluence (cm^{-2})	Dose Equivalent (mSv)	Dose Equivalent rate (μSvd^{-1})
$\leqslant$ 0.2 eV	$1.22 \pm 0.24 \times 10^{7}$	0.124 ± 0.024	0.059 ± 0.011
0.2 eV - 1 MeV	$1.43 \pm 0.72 \times 10^{8}$	7.0 ± 3.5	3.3 ± 1.6

Minimum shielding above the detector was 16.8 g/cm^2 Al equivalent. To the side it was 3.3 g/cm^2 plus shielding external to the canister.

Table VIII. Thermal and Resonance Neutron Measurements for P0004

Canister #	Neutron Energy Range	Fluence (cm^{-2})	Dose Equivalent (mSv)	Dose Equivalent Rate (μSvd^{-1})
3	$\leqslant$ 0.2 eV	$8.1 \pm 1.6 \times 10^{7}$	0.82 ± 0.16	0.38 ± 0.07
	0.2 eV - 1 MeV	$2.9 \pm 1.4 \times 10^{8}$	14.2 ± 7.1	6.7 ± 3.4
6	$\leqslant$ 0.2 eV	$4.0 \pm 0.8 \times 10^{7}$	0.41 ± 0.08	0.19 ± 0.04
	0.2 eV - 1 MeV	$1.9 \pm 0.9 \times 10^{8}$	9.2 ± 4.6	4.3 ± 2.2

Minimum shielding above the detector was 6.1 g/cm^2 Al equivalent. To the side it was approximately 12.4 g/cm^2 plus shielding external to the canister.

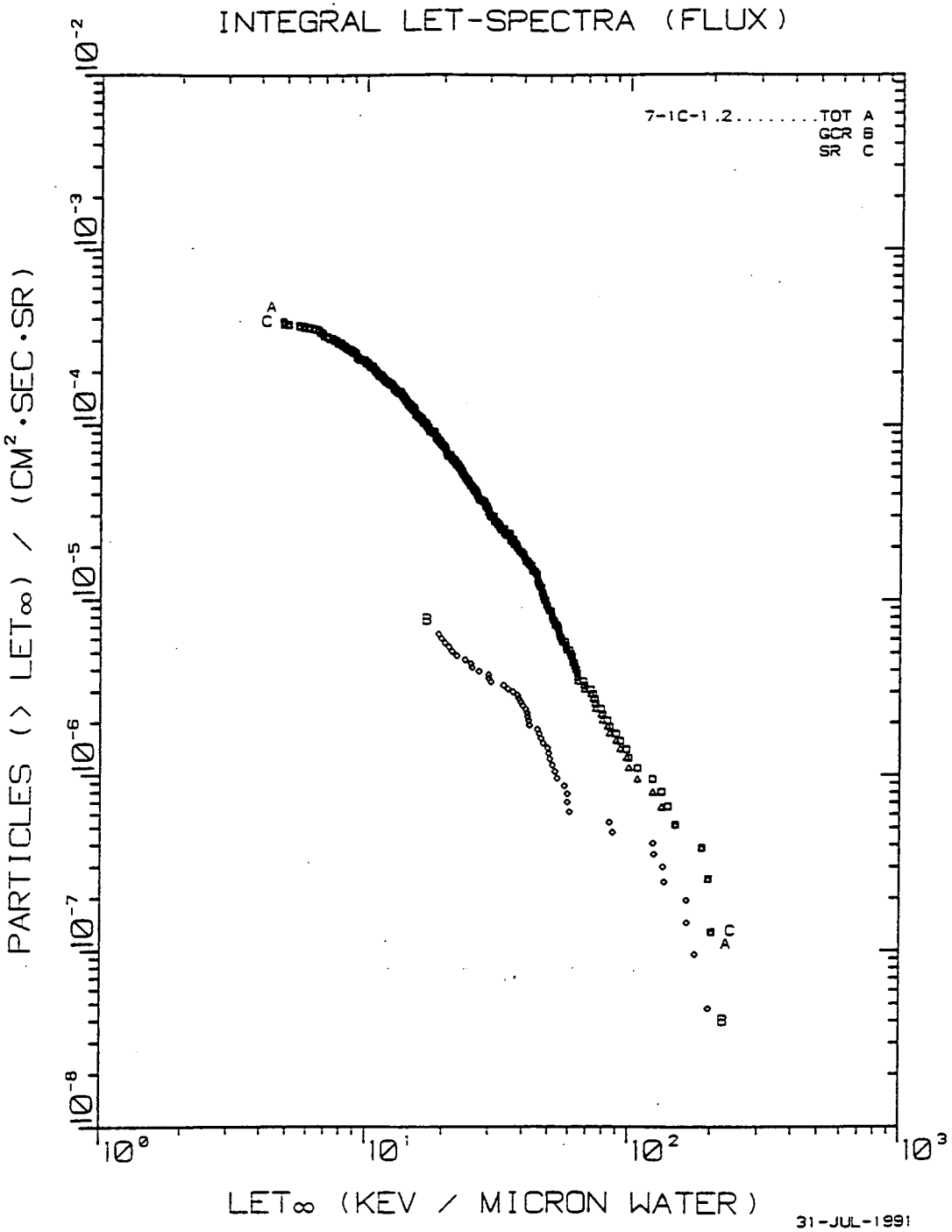

Fig. 1 Integral LET flux spectra from the M0004 experiment on the leading edge of the orbiter. The minimum shielding was 2.74 g/cm² Al equivalent.

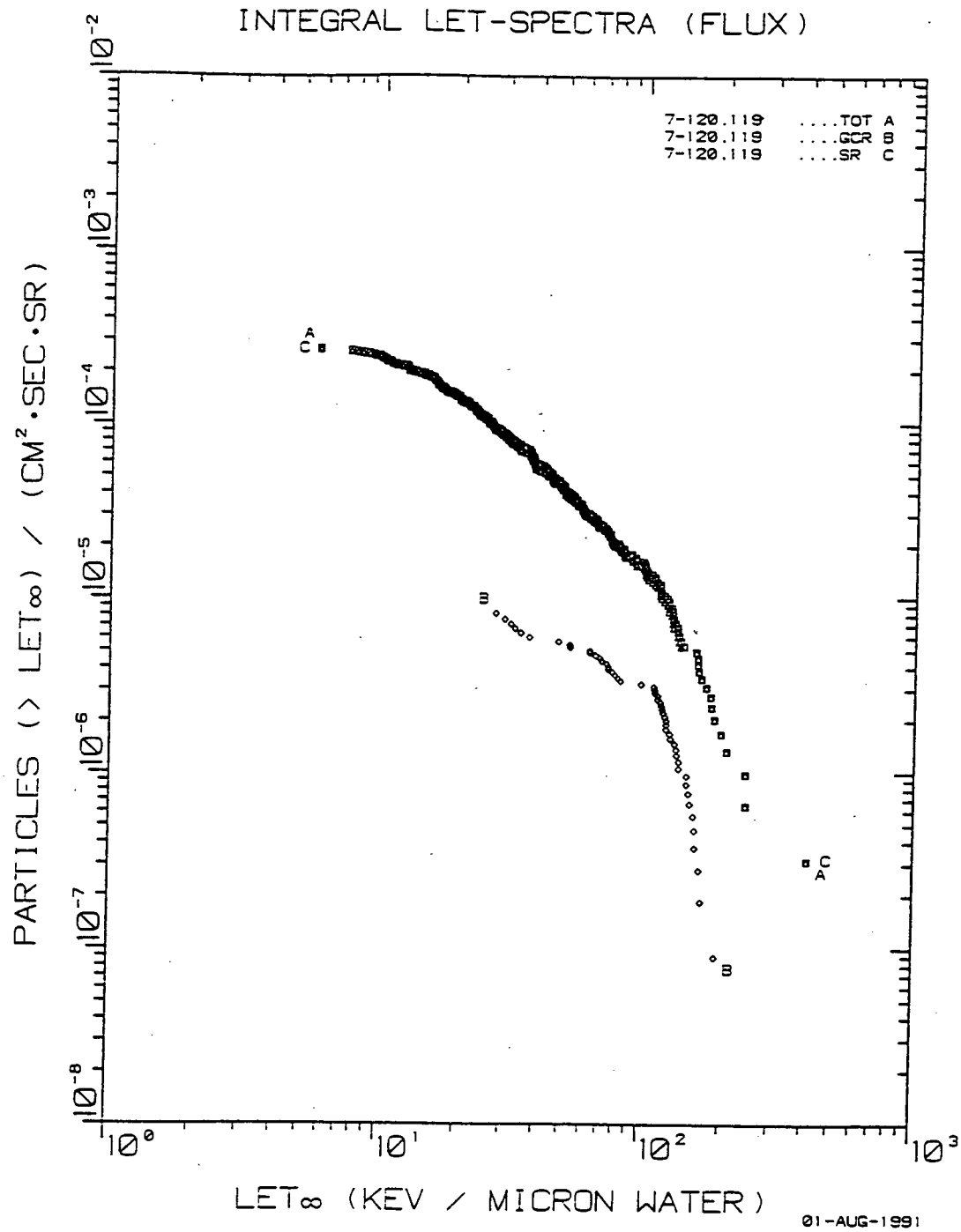

Fig. 2 Integral LET flux spectra from the P0006 experiment on the trailing edge of the orbiter. The minimum shielding was 8.88 g/cm² Al equivalent.

CHARGED PARTICLE LET-SPECTRA MEASUREMENTS ABOARD LDEF

I. Csige, E. V. Benton, A. L. Frank, L. A. Frigo and E. R. Benton
Physics Department, University of San Francisco, 2130 Fulton St., San Francisco, CA 94117-1080, USA

T. A. Parnell and J. W. Watts, Jr.
ES-62, NASA-Marshall Space Flight Center, George C. Marshall Space Flight Center, Al 35812, USA

SUMMARY

The linear energy transfer (LET) spectra of charged particles has been measured in the 5-250 keV/μm (water) interval with CR-39 and in the 500-1500 keV/μm (water) interval with polycarbonate plastic nuclear track detectors (PNTDs) under different shielding depths in the P0006 experiment. The optimal processing conditions were determined for both PNTDs in relation to the relatively high track densities due to the long-term exposure in space. The total track density was measured over the selected samples, and tracks in coincidence on the facing surfaces of two detector sheets were selected for measuring at the same position on each sheet. The short range (SR) and Galactic Cosmic Ray (GCR) components were measured separately with CR-39 PNTDs and the integral dose and dose rate spectra of charged particles were also determined. The high LET portion of the LET spectra was measured with polycarbonate PNTDs with high statistical accuracy. This is a unique result of this exposure due to the low flux of these type of particles for typical spaceflight durations. The directional dependence of the charged particles at the position of the P0006 experiment was also studied by four small side stacks which surrounded the main stack and by analyzing the dip angle and polar angle distributions of the measured SR and GCR particle tracks in the main stack.

INTRODUCTION

In the past a series of cosmic ray radiation dosimetry measurements — including charged particle measurements — has been carried out both by Americans and Soviets (ref. 1). These measurements were usually performed on short term flights and with changing orientations of the spacecraft and detectors during the flights. The unique features of the LDEF mission, such as the very long duration time (2115 days) in space and the fixed gravity orientation, provide

Work partially supported by NASA grant No. NAG8-168 (NASA-Marshall Space Flight Center, Huntsville)

excellent opportunities for dosimetric experiments on LDEF. For example plastic nuclear track detectors (PNTDs) can measure the high LET-tail of the LET (linear energy transfer)-spectra with superior statistical accuracy and can determine the directional dependence of cosmic ray particles as well as of their secondaries.

The Physics Department of the University of San Francisco in collaboration with the NASA-Marshall Space Flight Center has carried out several space radiation dosimetry measurements aboard LDEF. Data from experiments at different positions on the orbiter can be correlated. The unification of the results should provide accurate cumulative exposures of the LDEF orbiter from different directions. Early results of these experiments are discussed by Benton et al. (ref. 2). In this paper we present preliminary results obtained by evaluating PNTD sheets from one of the major dosimetric experiments (P0006) on LDEF. The heavy cosmic ray charged particles detected with PNTDs have a high quality factor and the ability to produce special effects in biological samples and single event upsets in microelectronic circuits which underlines their importance especially in long duration flights.

EXPERIMENTS

Experiment P0006 on LDEF contained a stack of passive integrating detectors to measure different components of the accumulated radiation exposure on the LDEF. It includes stacks of different kinds of PNTDs and thermoluminescent detectors (TLDs) designed to measure the variation of LET spectra of cosmic ray charged particles and the total absorbed dose as a function of shielding depth. Activation foils for neutron and proton fluences, fission foil detectors also for neutrons and muscovite mica for heavy HZE particles are also included.

The structure of the detector stack, showing the major components, is given in Figure 1. Of the 9 central stack modules, the upper 8 contain PNTDs in separate arrays. The PNTDs used were pure CR-39, CR-39 with DOP, Tuffak and Sheffield polycarbonate and Melinex polyester. Initial studies have been conducted with CR-39 and Sheffield polycarbonate.

The high sensitivity CR-39 (USF-4, University of San Francisco) track detectors were used to measure the LET-spectra in the 5-250 keV/μm (water) interval.The standard technique normally used with space flight materials had to be modified because of the very high track densities obtained in these samples due to the long-term exposure in space. Hence shorter etching time (36 hrs at 50°C in 6.25 N NaOH, which corresponds to about 10 μm removed layer) and higher magnification ($\times$600) for scanning and measuring of these samples has been applied. Detector saturation, due to track overlapping, would occur for the normal processing time of 168 hrs (40 μm). For the measurement of the high LET-tail of the LET-spectra the Sheffield polycarbonate was used. Although the track density in this detector was found to be much lower than in CR-39 (due to the lower sensitivity of this detector) the optimal etching time was found to be even shorter than in the case of CR-39. This is because the majority of the tracks in this detector are formed by short range secondary particles which are over-etched after a few micron-thick layer is

removed. Even after a 4 μm removed layer — applied in our study — about half of these tracks were found to be overetched. This means that information about charge, energy and LET of the particles which can be obtained from the measured etched pit diameters is limited.

In both CR-39 and polycarbonate measurements the coincidence method of track detection has been used. Processed sheets were reassembled as pairs in their original flight orientations. The doublets mounted on the microscope stage were scanned at the inner adjacent surfaces and tracks in coincidence were selected for measuring. Tracks at one surface are neglected because they do not contribute to the flux of charged particles present at the pre-etched surfaces of the track detector sheets. In the case of CR-39 PNTDs detected events were then separated into long range (the particle left tracks on all four surfaces of the doublet) or short range (the particle left tracks on the two inner surfaces or the two inner and one outer surface). The short range (SR) particles are usually due to stopping primary protons (mainly trapped) or to secondaries from target nuclei in the CR-39.

The track parameters were measured at the upper of the two adjacent surfaces and particle LET was calculated using the measured detector response curves. Integral and differential LET-spectra for flux, dose rate and dose equivalent rate were then generated.

RESULTS AND DISCUSSION

LET-spectra Measurements

The integral LET-spectra — measured with CR-39 track detectors — in the main stack and in the side stacks A and B are presented in Figure 2. The shielding depth in the main stack was 6.5 g/cm^2 and 0.5 g/cm^2 in the case of the side stacks. Side stacks A and B, however, were facing to different directions (see Figure 1), hence the difference in the LET-spectra measured by these detectors can be explained by the directional dependence of the charged particle radiation field at the position of the P0006 experiment.

Figure 3. shows the high LET-tail of the LET-spectra measured by Sheffield polycarbonate PNTDs in the main stack of P0006 at two different shielding depths. Most of the tracks measured in polycarbonate were found to be rounded on both the second and third surfaces of the detector doublet. These tracks are formed by short range secondary particles, when the total trajectory is fully etched out for both directions. Primary particles usually produce double pointed or a pointed and a rounded track at the adjacent surfaces. About half of the tracks look like small bubbles, which means that the trajectory of the particle was completely within the bulk layer removed during the etching process. The etch rate ratio and LET value which are obtained for these tracks (from the measured diameters of the tracks) usually underestimate the real value. Also the size of these tracks is very small and the scanning efficiency is less than optimum. For these reasons the reliability of LET-spectra obtained with polycarbonate detectors is better for values of LET$\geq$600 keV/μm. The relatively low sensitivity of this material also suggests

that these tracks are probably formed by ions heavier than alpha particles. An interesting and important observation is that the flux of the particles in the 800-1200 keV/μm region does not depend on the shielding depth of the evaluated samples. Measurements with higher shielding depths are in progress.

Some of the problems mentioned above can be compensated for by using two or multiple step etching. The advantage of this technique is higher accuracy of LET measurement at the adjacent surfaces and a possible charge and energy determination of short range recoils. The application of the approximately tissue equivalent PNTDs to perform this kind of measurement is also unique because the LET, charge and energy distribution of heavy recoils depends on the chemical composition of the target material, which in the case of PNTDs is the detector material itself. If a material other than PNTD is used, the recoils will differ. The ideal detector for this study would be a tissue equivalent detector, with dimensions equal to at least the average range of heavy recoils. To measure the LET value or to identify the particle, however, we need local information along the particle trajectory.

Directional Dependence

The contour of the surface openings of etched particle tracks can usually be considered to be elliptical. From the measured diameters of the ellipse it is possible to calculate the dip angle (the angle between the trajectory and the surface of the detector) and from the orientation of the ellipse the azimuthal angle of the particles. The dip angle distribution of measured particles is strongly modified by the detection efficiency of the detector, that is,particles with low LET can be detected only at high dip angles (close to normal incidence). The azimuthal angle measurement is also limited. Tracks of particles close to normal incidence and those over-etched into the spherical phase are circular, hence the azimuthal angle cannot be determined. Another problem is that the direction of movement of the particle along the trajectory is not always known. This means that the azimuthal angle can be determined to the extent of a rotation by π. In our azimuthal angle measurements we assumed that all the particles were moving into the stack and none out of it. Figures 4 and 5 show the azimuthal angle distribution of GCR particles (measured with CR-39) and short range secondary particles (Sheffield polycarbonate) in the main stack of P0006 experiment. (The orientation of P0006 experiment on the LDEF is not yet confirmed.)

Although there are some limitations in studying the azimuthal angle distribution of cosmic ray charged particles, the results presented here clearly indicate that there is a strong directional dependence both of GCR and secondary heavy ions. These effects are probably related to the effect of the Earth's magnetic field and the anisotropy of trapped protons.

CONCLUSIONS

Initial results of the P0006 experiment show that:

- The LET-spectra of cosmic ray charged particles depend on the orientation of the PNTD stack.
- The high LET-tail of the LET-spectra does not change significantly with the shielding depth.
- There is a significant directional dependence of both GCR and short range secondary heavy ions.

The preliminary results of P0006 experiment show that the LDEF mission provided a unique and unprecedented opportunity to gather data on the space radiation environment in low earth-orbit. The collection of more comprehensive experimental data and its detailed analyses will be invaluable in addressing the numerous issues concerning the ionizing radiation environment in space and its impact on manned and unmanned space missions.

REFERENCES

1. Benton, E. V. and Parnell, T. A.: Space radiation dosimetry on U.S. and Soviet manned missions. In *Terrestrial Space Radiation and its Biological Effects*, P. McCormack, C. E. Swenberg and H. Buecker, eds., NATO-ASI Series A, Life Sciences 154, New York: Plenum Press, 1988, pp. 729-794.

2. Benton, E. V., Frank, A. L., Benton, E. R., Csige, I., Parnell, T. A. and Watts, J. W., Jr.: Radiation Exposure of LDEF: Initial Results. First LDEF Post-Retrieval Symposium, NASA CP-3134, 1992.

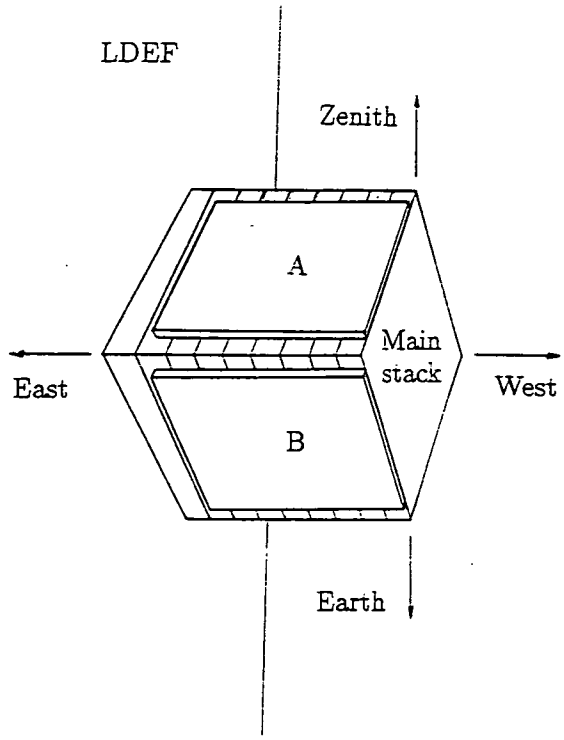

Fig. 1. The major structure of P0006 and its position on the LDEF.

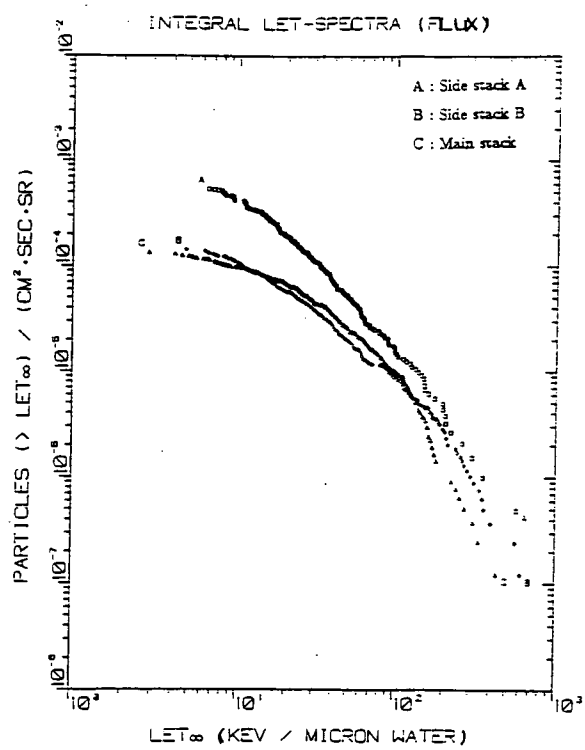

Fig. 2. Integral LET-spectra measured in the main stack and in the side stacks A and B of P0006 experiment with CR-39 PNTDs. The main stack was facing to the west and side stacks A and B were facing approximately to the space and Earth, respectively, in the F2 tray of the satellite.

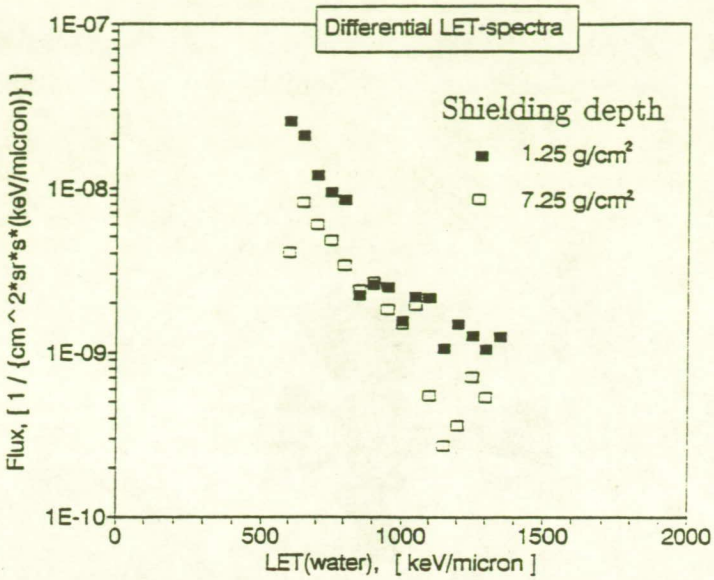

Fig. 3. The differential LET-spectra measured with polycarbonate PNTDs at different shielding depths.

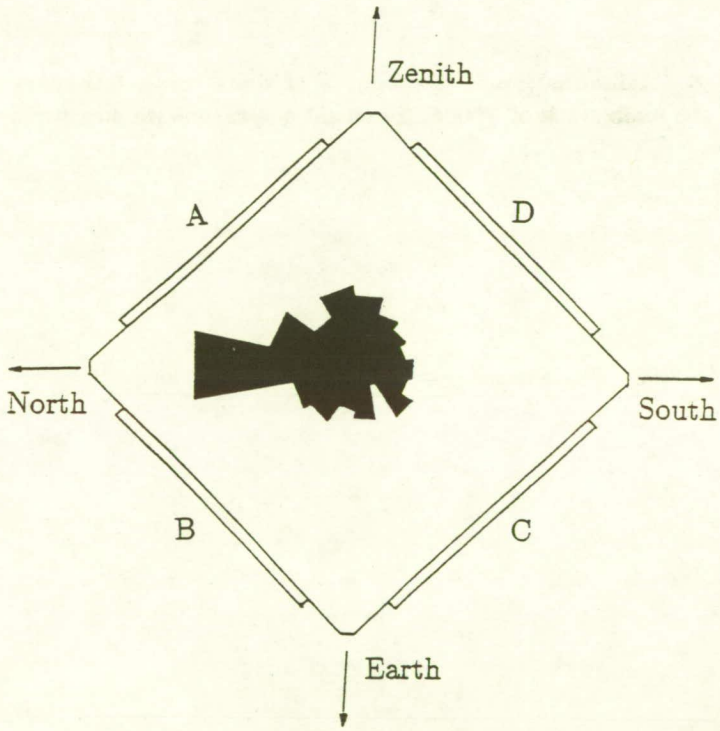

Fig. 4. Azimuthal angle distribution of GCR particles in the main stack of P0006 experiment on LDEF. All particles were assumed to arrive from the direction of space.

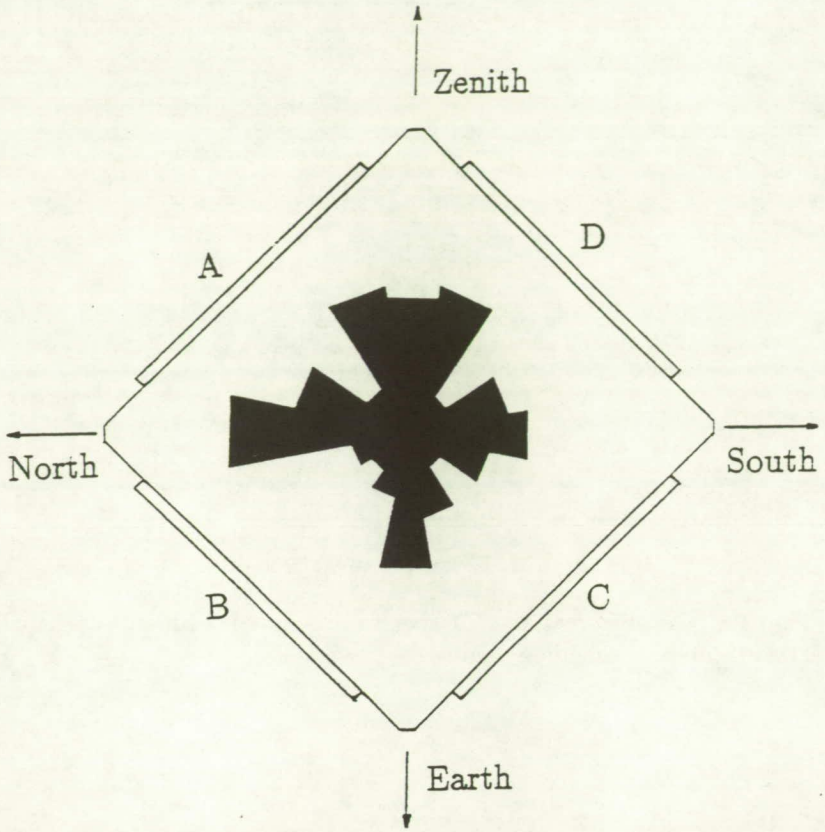

Fig. 5. Azimuthal angle distribution of short range secondary heavy ions in the main stack of P0006. (Sheffield polycarbonate measurement.)

IONIZING RADIATION CALCULATIONS AND COMPARISONS WITH LDEF DATA*

T. W. Armstrong and B. L. Colborn
Science Applications International Corporation
Route 2, Prospect, TN 38477
Phone: 615/468-2603, Fax: 615/468-2676

J. W. Watts, Jr.
ES62, NASA/Marshall Space Flight Center, AL 35812
Phone: 205/544-7693, Fax: 205/544-7754

SUMMARY

In conjunction with the analysis of LDEF ionizing radiation dosimetry data, a calculational program is in progress to aid in data interpretation and to assess the accuracy of current radiation models for future mission applications. To estimate the ionizing radiation environment at the LDEF dosimeter locations, scoping calculations for a simplified (one-dimensional) LDEF mass model have been made of the primary and secondary radiations produced as a function of shielding thickness due to trapped proton, galactic proton, and atmospheric (neutron and proton cosmic-ray albedo) exposures. Preliminary comparisons of predictions with LDEF induced radioactivity and dose measurements have been made to test a recently developed model of trapped proton anisotropy.

INTRODUCTION

Purpose

A calculational program is in progress as part of the LDEF ionizing radiation investigations, with the following objectives:

Data Analysis Support - Calculations are being used to help interpret the LDEF ionizing radiation measurements. In most cases the LDEF dosimetry data represent an integration of several effects, such as contributions from different environment sources (galactic and trapped radiation), influence of shielding variations (from both experimental apparatus and spacecraft structure), and secondary particle contributions from nuclear interactions. The calculations can be used to "unfold" the dosimetry data to estimate the influence of these individual effects, which is needed if the LDEF data are to be fully applicable for future missions having different orbit parameters and spacecraft configurations.

Model Validation - LDEF data are being utilized to evaluate the accuracy of present ionizing radiation models. This includes models for predicting both the "external" environments (ionizing radiation fields external to the spacecraft) and the "internal" environments (ionizing radiation environments at locations internal to the spacecraft, which include the effects of radiation interactions and transport).

*Work partially supported by NASA Marshall Space Flight Center, Huntsville, AL, Contract NAS8-38566.

Future Mission Applications - The overall objective of the calculational program is to fully utilize the LDEF data to test and revise current ionizing radiation models for future mission applications. This should result in more accurate models for predicting crew dose for planned long duration missions (Space Station Freedom, Space Exploration Initiative) and for assessing radiation backgrounds to sensors and determining achievable measurement sensitivities for planned space-based observatories (e.g., Earth Observing Observatory). Furthermore, benchmarking models with LDEF data will reduce present model uncertainties involved in assigning hardware design margins for meeting mission radiation requirements. This will help prevent both "under-design" (which can lead to reduced mission performance) and "over-design" (resulting in excessive costs).

LDEF Data for Radiation Model Validation

The LDEF mission had several unique features that are important to the validation of ionizing radiation models:

Well Instrumented - A variety of different types of radiation dosimetry, with multiple dosimeters of each type,were onboard, providing a high-confidence data set for benchmarking the models. Also, dosimeters were placed at various locations on the spacecraft and behind various thicknesses of shielding, allowing tests of both external environment models and the transport models for predicting the radiation environment internal to the spacecraft.

Long Exposure - Dosimetry results have high statistical accuracy due to the long mission duration. This is particularly important for checking model predictions of the high-LET component of cosmic rays and nuclear interaction products, which is of key importance in assessing radiation-induced biological and electronics damage.

Fixed Orientation - The very stable orientation of LDEF during the entire mission (< 0.2°, ref. 1), together with dosimetry placements at various positions around the spacecraft, allow the directionality of the incident radiation to be measured. This provides a unique opportunity for testing a recently-developed model (ref. 2) for predicting the directionality of the trapped proton flux. Since the radiation dose (at most shielding depths) for spacecraft in low-earth orbit is dominated by the trapped proton exposure, this anisotropy may have practical importance for planned fixed-orientation spacecraft in low-earth orbit, such as for Space Station Freedom.

Thus, the LDEF data provide a significant opportunity for model improvement in addressing ionizing radiation issues for future missions, as summarized in figure 1.

APPROACH

Figure 2 gives an overview of the calculational approach and indicates some of the specific models being used. External environment models include the AP8 and AE8 models for trapped protons and electrons (refs. 3,4), the MSFC model for predicting trapped proton anisotropy (ref. 2), and the galactic proton and heavy ion environments given by the NRL CREME model (ref. 5). Transport models include both simplified, one-dimensional models commonly used in quick assessments of space radiation effects -- the MSFC analytical models for proton and electron-bremsstrahlung transport (refs. 6,7), SHIELDOSE (ref. 8), and CREME (ref. 5) -- as well as three-dimensional Monte Carlo codes, HETC (ref. 9) and MORSE (ref. 10). The Monte Carlo codes take into account in detail the secondary particle production and transport and can treat three-dimensional, multimedia spacecraft models, capabilities which are needed in some cases for definitive comparisons with the LDEF measurements.

This calculational approach can provide predictions for all of the different types of LDEF radiation measurements - namely: (a) induced radioactivity, including both the activation of metal samples (Ni, Co, V, Ta, and In) placed in LDEF experiment packages and the activation of various spacecraft structural components (e.g., trunnions, experiment tray clamps); (b) measurements of tissue-equivalent absorbed dose using thermoluminescence detectors (TLDs); (c) measurements of linear-energy-transfer (LET) spectra by plastic nuclear track detectors (PNTDs); and (d) particle fluence and energy spectra, including secondary neutrons, as measured by fission foils, specific activation reactions, low-energy neutron detectors (^{6}LiF foils), and PNTDs.

The shaded areas in figure 2 indicate the emphasis of the modeling to date. An important approximation for the initial calculations is that a very simplified (in most cases one-dimensional) spacecraft model has been used. To obtain definitive comparisons with most of the measurements, detailed shielding variations about the detector need to be taken into account, so development of a 3-D LDEF mass model for radiation calculations is underway (ref. 11).

RESULTS

Emphasis of the initial calculations has been in two areas: (a) scoping calculations of the importance of different exposure sources and secondary particles to the induced radiation environment, and (b) calculations and comparisons with measurements to check the accuracy of a recent model for predicting the anisotropy of trapped protons.

Scoping Calculations

The penetrating radiation environment for the LDEF orbit consisted of protons (with a relatively small contribution of heavier ions) trapped in the earth's magnetic field, protons and heavier ions of galactic origin, and albedo neutrons and protons due to galactic cosmic-ray bombardment of the earth's atmosphere (ref. 12). Since the angular variation of these sources is quite different (figure 3), and since material attenuation within LDEF is different for each source, an important question for data interpretation concerns the magnitude of the contribution from each component at the LDEF measurement locations. Thus, a set of scoping calculations was made to obtain a general indication of (a) the importance of different space radiation sources, (b) the importance of secondary particles generated within LDEF, and (c) the spatial variation of the induced radiation environment.

The calculations were carried out using Monte Carlo transport methods, with the SAIC version of the HETC code (ref. 13) for high-energy transport and the MORSE code for low-energy (< 20 MeV) neutron transport. These were only scoping estimates because several important approximations have been made in this initial work -- e.g., a one-dimensional (aluminum slab) model of LDEF was used, and the angular variation of the incident radiation (particularly the trapped proton anisotropy) was not accurately simulated. Subsequent calculations using a 3-D LDEF mass model are planned to remove these approximations.

Example results are shown in figure 4 for the depth-dependent particle fluence, and figure 5 shows fluence spectra at a particular depth (10 g/cm^2). (To roughly relate these depths in terms of areal density to LDEF, if the LDEF spacecraft is represented as a cylinder the average areal density is 32 g/cm^2 across the diameter and and 68 g/cm^2 end to end.) These results indicate that the contribution from albedo neutrons and protons is negligible, and that the relative importance of

trapped vs. galactic sources depends on the shielding depth and radiation effect of interest. In terms of fluence over all energies, figure 5 shows that secondary neutrons dominate for depths $\gtrsim 10$ g/cm^2.

A report on additional results from these calculations, including the induced radioactivity in aluminum and stainless steel produced by different sources and particle types, is available (ref. 14), and a summary has been accepted for journal publication (ref. 15).

Trapped Proton Anisotropy

The ionizing radiation dose at most shielding depths for spacecraft in low-earth orbit (LEO) is produced mainly by trapped protons in the South Atlantic Anomaly (SAA) region. The standard NASA models (AP8MIN and AP8MAX) for describing the trapped proton environment do not provide an angular dependence, although the proton flux is actually highly anisotropic in the SAA. This anisotropy has not been an important practical consideration for most previous LEO missions because the varying spacecraft attitude during passage through the radiation belt "averages out" anisotropic effects over many orbits. However, for the fixed orientation of LDEF, and for several planned missions (e.g., Space Station Freedom, Earth Observing Satellite) where the spacecraft will be gravity-gradient stabilized, the cumulative proton exposure will remain anisotropic, and will result in a highly nonuniform dose distribution around the spacecraft.

Watts, et al. (ref. 2) have recently developed a model to predict orbit-average, angular dependent trapped proton flux spectra from the standard omnidirectional AP8MIN and AP8MAX data bases. Since trapped proton anisotropy effects may be an important consideration for Space Station design and operation, a priority for the calculational work has been to utilize LDEF data to evaluate the accuracy of this anisotropy model, as summarized below. These initial results must be considered as preliminary because of several simplifications in the calculations to date, and because the LDEF data are not yet fully analyzed.

Anisotropy of Tray Clamp Activation

The measured induced radioactivity of the aluminum clamps (ref. 16) used to secure the LDEF experiment trays provides very appropriate data for checking the anisotropy model since these clamps are located on all sides of the spacecraft and at various directions relative to the flight vector. Also, since the clamps are located on the outer surface and are thin (1.3 g/cm^2), we expect (based on the scoping Monte Carlo calculations; e.g., figure 4) the activation from galactic protons and secondary particles to be small, so the measured activation is predominantly from the primary trapped protons.

The ^{22}Na production in aluminum has been predicted as a function of direction (in the horizontal plane perpendicular to the LDEF longitudinal axis) and for various shielding depths (figure 6). These calculations were made for a point behind an aluminum slab shield (assuming that the direction normal to the plane is pointed in the plotted direction, and assuming that no particles enter from the "back side" of the plane). The proton transport code of Burrell (ref. 6) was used. The angular distribution of the trapped protons were taken from a pre-computed data base for discrete altitudes (ref. 17), with results for 450 km and solar minimum used here; thus, the properly averaged angular spectra for solar cycle variation and the varying altitudes during the LDEF mission have not yet been applied.

The results (figure 6) show minimum activation near the East (leading edge) of the spacecraft and maximum activation near the West (trailing) direction. The predicted anisotropy in terms of the ratio of West-side activation to East-side activation varies from a factor of about 1.8 near the surface to a factor of 3.5 at 10 g/cm^2 depth. This increase in anisotropy with depth is due to the increasing anisotropy of the incident protons at higher energies (refs. 2, 18).

A comparison of the predicted ^{22}Na activation at a depth corresponding to the mid-depth of the tray clamp (0.64 g/cm^2) with the measured activation (ref. 16) is shown in fig. 7, indicating very good agreement for these preliminary comparisons. The angular variations are similar in shape, with the maximum/minimum ratio with respect to direction being 1.8 for the measurements vs. 2.0 for the calculations.

The calculated results in figure 7 are lower than the measurements by about 15% for directions in the vicinity of West, and lower by about 50% for directions near East. These preliminary absolute magnitude comparisons suggest a better accuracy for the AP8 trapped proton model than the factor of two uncertainty commonly quoted.

Dose Anisotropy

Predictions of the absorbed dose anisotropy have also been made and compared with the initial TLD measurements reported by Benton, et al. (ref. 19) for Experiments P0006 (bay-row location F-2, near the trailing edge) and M0004 (tray position F-8, near leading edge). These initial calculations were also made assuming one-dimensional, plane-geometry shielding, so the results are preliminary.

The predicted ratios are compared with the measured P0006-to-M0004 TLD dose ratios (using data from ref. 18 with interpolation applied to obtain common shielding depths) in figure 8. These preliminary comparisons also indicate that the anisotropy model predictions are consistent with LDEF data.

Directionality of Trunnion Activation

The measured spatial dependence of radioisotopes produced in the stainless steel LDEF trunnions (refs. 20, 21) also provide an opportunity for checking the anisotropy model. To date, calculations have been made to compare with only a small subset of the measured data, with some initial comparisons for the ^{54}Mn activity given here.

The calculations were made for a "simplified" 3-D geometry with the body of the LDEF spacecraft and experiment trays modeled as a homogeneous aluminum cylinder (with an average density to preserve the total mass), and with the earth-end trunnion represented as a stainless steel rod. The activation at a point in the trunnion was computed by (a) determining the areal density along a 3-D grid of rays emanating from the point (720 rays were used, corresponding to the polar-azimuthal angular grid used in generating the directional proton environment), (b) computing the attenuation for each ray using the Burrell 1-D proton transport code, with solid-angle weighting for each ray to get the cumulative proton spectrum at the point, and (c) folding this spectrum with cross sections for ^{54}Mn production from the constituents of stainless steel.

Shown in figure 9 is a comparison of the calculational results with the measurements of Moss and Reedy (ref. 20) for the radial distribution of ^{54}Mn produced in a section of the trunnion centered 3.5 in. from the end ("Section D" in fig. 8a of ref. 20) of the East (leading edge)

trunnion. These results are for two angular segments of the trunnion having surface normals pointed in the zenith direction (labeled "space") and toward the center of the earth (labeled "earth"). The trapped proton anisotropy model predicts that the external fluxes directed toward the "space" and "earth" directions should be essentially the same, whereas the measurements and transport calculation results indicate a lower activation in the space direction. A separate calculation made with only the trunnion present shows that the lower activation observed in the space direction is due to the shielding effect of the LDEF spacecraft.

The agreement between the predicted and measured activations in figure 9 is quite good near the surface of the trunnion, but the agreement becomes somewhat worse near the center. Results from the 1-D Monte Carlo calculations (ref. 14) show that galactic protons contribute substantially at penetration depths comparable to the center of the trunnion. Thus, the underprediction of the activation deep into the trunnion indicated in figure 9 may be due to the neglect of incident galactic protons in these initial calculations.

CONCLUSIONS

LDEF has provided unique data which, based on preliminary comparisons of initial measurements and predictions, confirms a recently developed model for the anisotropy of trapped protons. This anisotropy is important in predicting the radiation exposure of other fixed-orientation spacecraft in LEO, such as the planned Space Station and Earth Observing Satellite missions.

Preliminary comparisons also indicate that the LDEF radiation dosimetry data are in good agreement with predictions using AP8 trapped proton flux model. Such results can help quantify the limits on safety margins commonly applied to account for radiation environment modeling uncertainties in spacecraft design and parts selection and in crew dose assessments.

The emphasis of near-term future calculations is expected to be on model comparisons with LDEF LET measurements (e.g., ref. 22). LET spectra generally provide a more stringent test of the environment and transport models than considered to date for induced radioactivity and dose comparisons, and LET is fundamental in assessing electronics upsets and biological damage. For future calculations a three-dimensional LDEF geometry/mass model will be implemented to properly account for dosimetry shielding effects and provide more definitive assessments of the radiation models.

REFERENCES

1. Gregory, J. C. and Peters, P. N.: LDEF Attitude Measurements Using a Pinhole Camera with a Silver/Oxygen Atom Detector. Initial Results. First LDEF Post-Retrieval Symposium. NASA CP- 3134, 1992.

2. Watts, J. W., Jr.; Parnell, T. A. and Heckman, H. H.: Approximate Angular Distribution and Spectra for Geomagnetically Trapped Protons in Low-Earth Orbit. A. C. Rester, Jr., and J. I. Trombka (Eds.), AIP Conf. Proc., New York, 1989.

3. Sawyer, Donald M. and Vette, James I.: AP8 Trapped Proton Environment for Solar Maximum and Solar Minimum. National Science Data Center, Goddard Space Flight Center, NSSDC/WDC-A-R&S 76-06, 1976.

4. Teague, Michael, J.; Chan, King, W. and Vette, James I.: AE6: A Model Environment of the Trapped Electrons for Solar Maximum. National Science Data Center, Goddard Space Flight Center, NSSDC/WDC-A-R&S 76-04, 1976.

5. Adams, James: Cosmic Ray Effects on MicroElectronics, Part IV. NRL Memorandum Report 5901, December 31, 1986.

6. Burrell, Martin O.: The Calculation of Proton Penetration and Dose Rates. Marshall Space Flight Center, NASA TM X-53063, 1964.

7. Watts, John W., Jr. and Burrell, M. O.: Electron and Bremsstrahlung Penetration and Dose Calculation. National Aeronautics and Space Administration, NASA TN D-6385, 1971.

8. Seltzer, Stephen: SHIELDOSE: A Computer Code for Space-Shielding Radiation Dose Calculations. National Bureau of Standards Technical Note 1116, May 1980.

9. Armstrong, T. W. and Chandler, K. C.: The High-Energy Transport Code HETC. Nucl. Sci. Engr. 49, 110 (1972).

10. Straker, E. A.; Stevens, P. N.; Irving, D. C. and Cain, V. R.: The MORSE Code - A Multigroup Neutron and Gamma-Ray Monte Carlo Transport Code. ORNL-4585, September 1970.

12. Watts, J. W.,Jr.; Parnell, T. A.; Derrickson, James H.; Armstrong, T. W. and Benton, E. V.: Prediction of LDEF Ionizing Radiation Environment. First LDEF Post-Retrieval Symposium. NASA CP-3134, 1992.

11. Colborn, B. L. and Armstrong, T. W.: LDEF Geometry/Mass Model for Radiation Analyses. Radiation Exposure of LDEF: Initial Results. First LDEF Post-Retrieval Symposium. NASA CP-3134, 1992.

13. Armstrong, T. W. and Colborn, B. L.: A Thick-Target Radiation Transport Code for Low Mass Heavy Ion Beams, HETC/LHI. Nucl. Instr. Meth. 169, 161 (1980).

14. Armstrong, T. W. and Colborn, B. L.: Scoping Estimates of the LDEF Satellite Induced Radioactivity. Science Applications International Corporation Report SAIC-90/1462, September 1990.

15. Armstrong, T. W. and Colborn, B. L.: Predictions of Induced Radioactivity for Spacecraft in Low-Earth Orbit, accepted for publication in Radiation Measurements.

16. Harmon, B. A.; Fishman, G. J.; Parnell, T. A. and Laird, C. E.: LDEF Induced Radioactivity Analysis. First LDEF Post-Retrieval Symposium. NASA CP-3134, 1992.

17. Colborn, B. L.; Armstrong, T. W. and Watts, J. W. Jr.: Data Base Description and Retrieval Program for the Trapped Proton Vector Flux Data Bases VF1MIN and VF1MAX. Science Applications International Corporation Report SAIC-90/1475, October 1990.

18. Armstrong, T. W.; Colborn, B. L. and Watts, J. W. Jr.: Characteristics of Trapped Proton Anisotropy at Space Station Freedom Altitudes. Science Applications International Corporation SAIC-90/1474, October 1990.

19. Benton, E. V.; Frank, A. L.; Benton, E. R.; Csige, I.; Parnell, T. A. and Watts, J. W., Jr.: Radiation Exposure of LDEF: Initial Results. First LDEF Post-Retrieval Symposium. NASA CP-3134, 1992.

20. Moss, Calvin E. and Reedy, Robert C.: Measurements of Induced Radioactivity in Some LDEF Samples. First LDEF Post-Retrieval Symposium. NASA CP-3134, 1992.

21. Winn, Willard G.: Gamma-Ray Spectrometry of LDEF Samples at SRL (U). First LDEF Post-Retrieval Symposium. NASA CP-3134, 1992.

22. Csige, I.; Benton, E. V.; Frank, A. L.; Frigo, L. A.; Benton, E. R.; Parnell, T. A., and Watts, J. W., Jr.: Charged Particle LET-Spectra Measurements Aboard LDEF. First LDEF Post-Retrieval Symposium. NASA CP-3134, 1992.

Unique Features of LDEF Mission	Importance to Ionizing Radiation Data Collection	Importance to Model/Code Validation	Importance to Future LEO Missions
• Well-instrumented for ionizing radiation measurements	• Extensive radiation dosimetry: *- 6 different types of dosimetry* *- multiple dosimeters of each type (≈ 200 TLD's, > 500 PNDT's, > 400 activation samples)* *- multiple dosimetry locations (in 16 different experimental trays)*	• Data sufficiently extensive and detailed to allow variety of modeling checks - e.g.: *- absorbed dose* *- proton and heavy ion fluence* *- energy spectra* *- LET spectra* *- secondary neutron fluence and spectra*	• Allows benchmarking and improvements of predictive methods for addressing ionizing radiation issues: *- dose to astronauts* *- electronics upset/burnout* *- materials damage* *- radiations backgrounds to sensitive instrumentation*
• Long mission duration	• High statistical accuracy of dosimetry results	• Unprecedented data accuracy for checking model predictions of high-LET radiation from high-Z cosmic rays and nuclear recoils	• High-LET radiation component is of key importance in assessing "single-hit" phenomena: *- biological effects* *- Single-Event-Upsets of electronics*
• Fixed orientation (< 0.2° wobble during mission)	• Allows measurement of trapped proton anisotropy	• Unprecedented data for testing models of trapped proton anisotropy	• Trapped proton anisotropy important for LEO, fixed-orientation spacecraft (such as Space Station Freedom, EOS)

Figure 1. Significance of LDEF data for validation of ionizing radiation models.

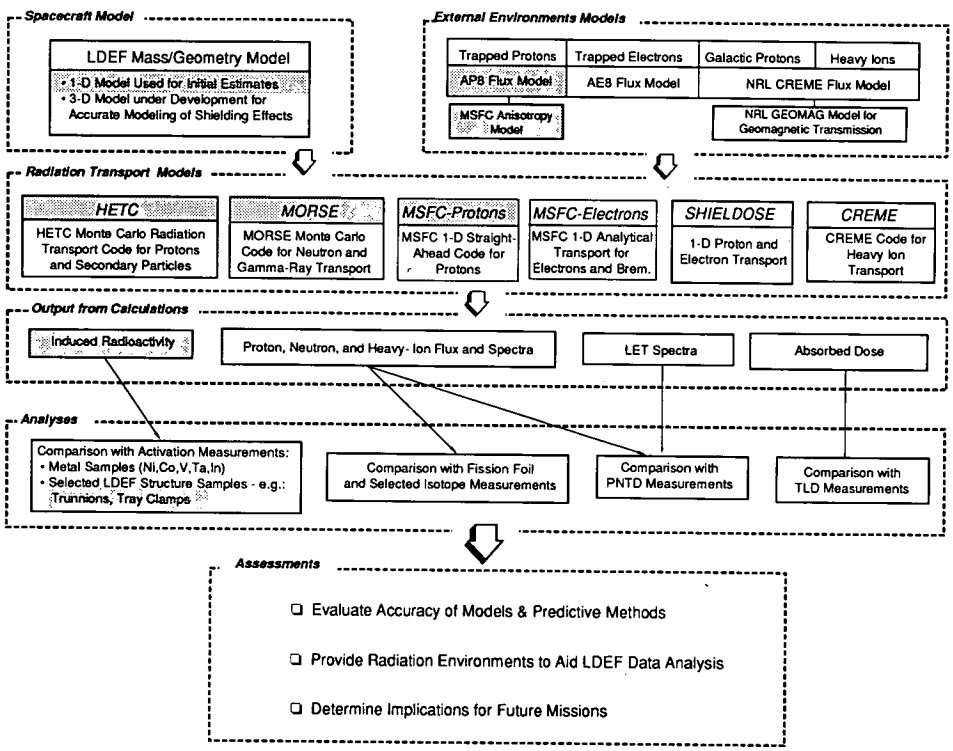

Figure 2. Overview of approach and models for LDEF ionizing radiation calculations.

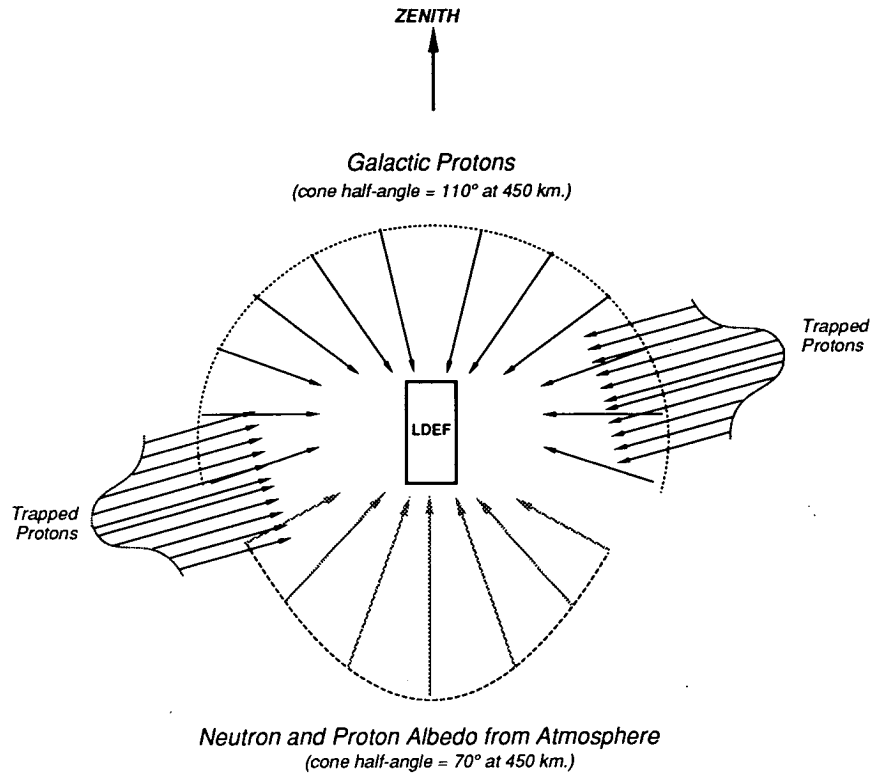

Figure 3. Illustration of the nonuniform angular variation of LDEF exposure to ionizing radiation.

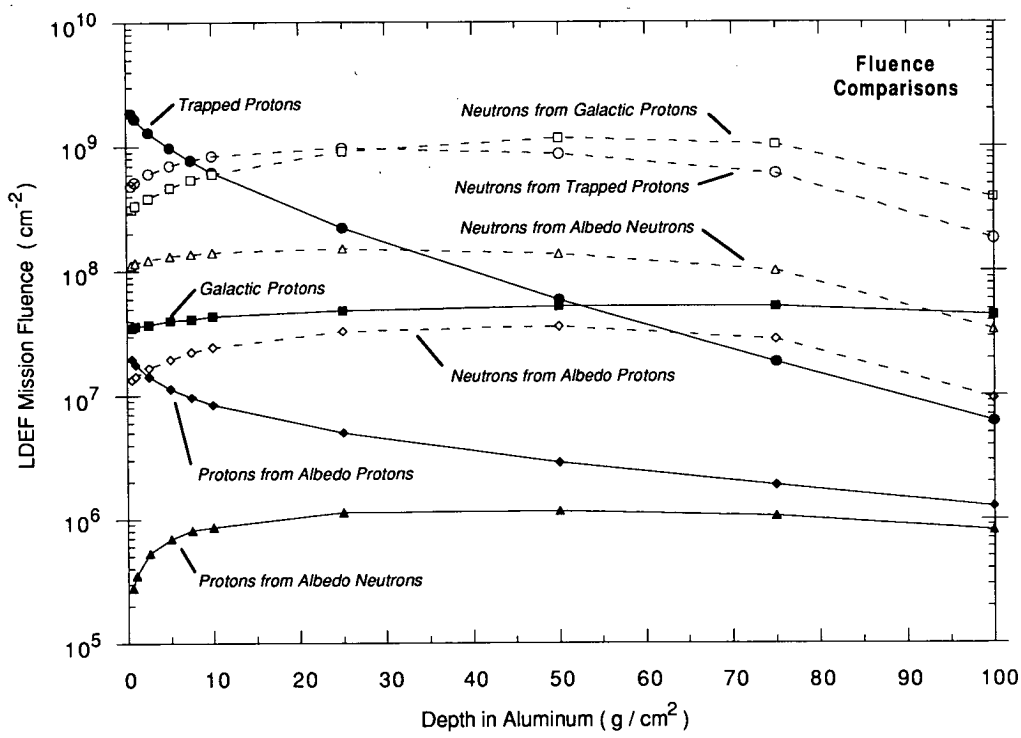

Figure 4. Predicted depth dependence of proton (primary and secondary) and neutron fluences over all energies produced by trapped proton, galactic proton, albedo proton, and albedo neutron environments over the duration of the LDEF mission. The different environments are all assumed incident isotropically on one side (0 depth) of an aluminum slab 100 g/cm2 in thickness.

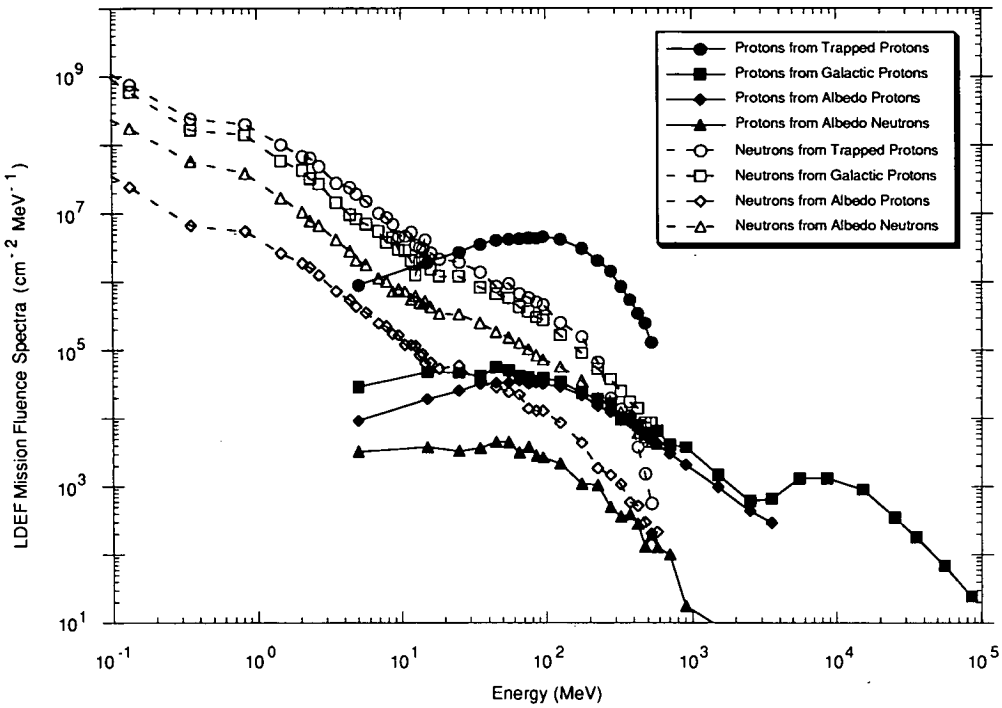

Figure 5. Comparison of predicted proton (primary and secondary) and neutron fluence at a depth of 10 g/cm^2 in aluminum from LDEF exposure to ionizing radiation sources.

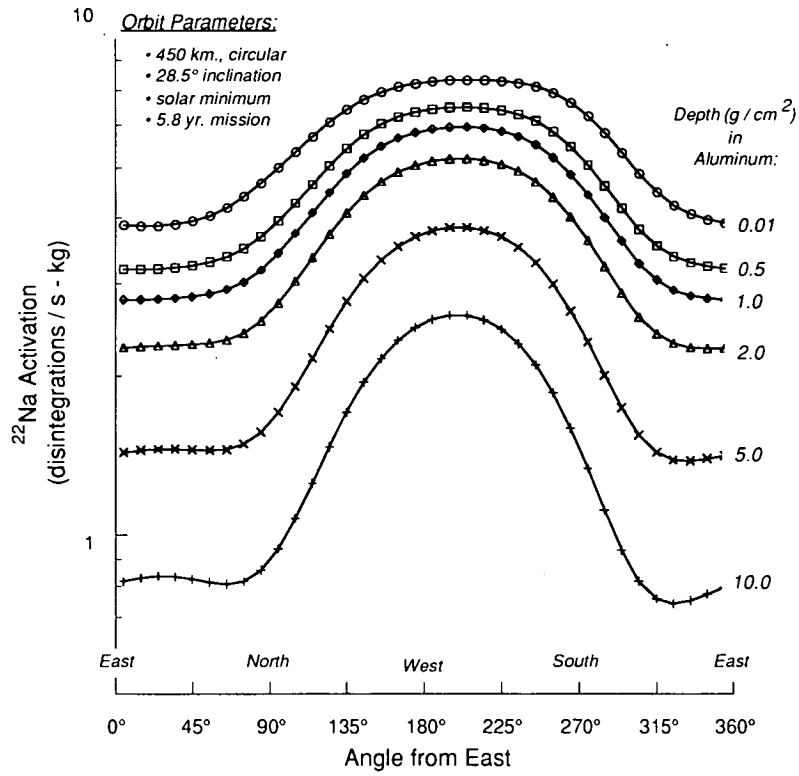

Figure 6. Predicted directionality of ^{22}Na production in aluminum due to trapped proton anisotropy.

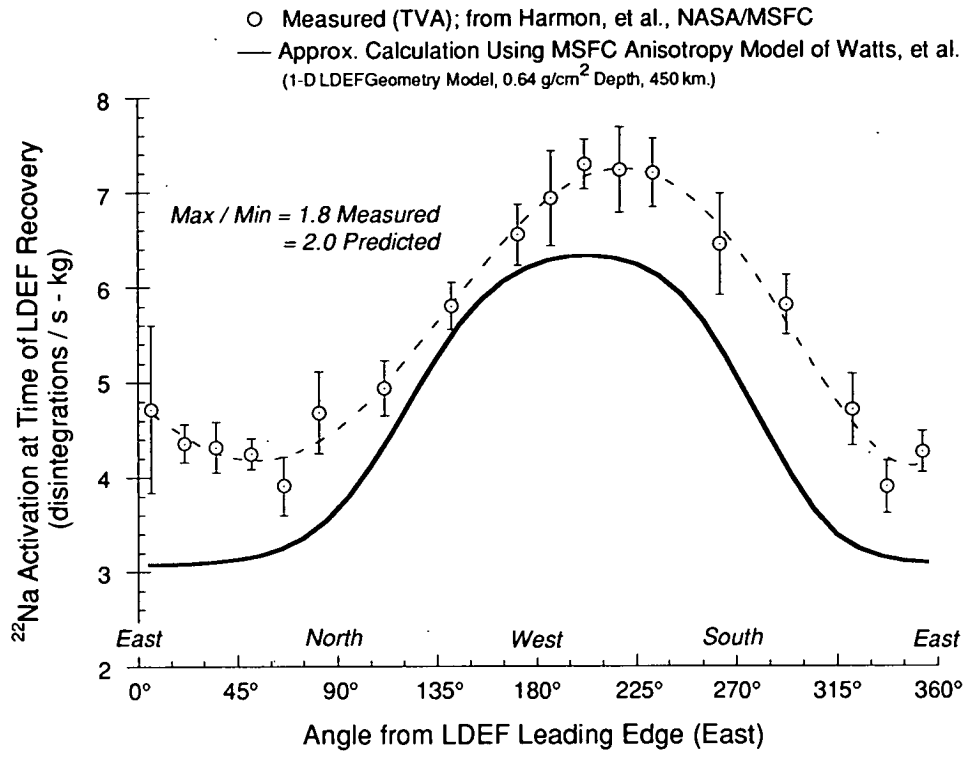

Figure 7. Preliminary comparison of predicted vs. measured (ref. 16) effects of trapped proton anisotropy in terms of ^{22}Na radioactivity induced in aluminum clamps of LDEF experiment trays.

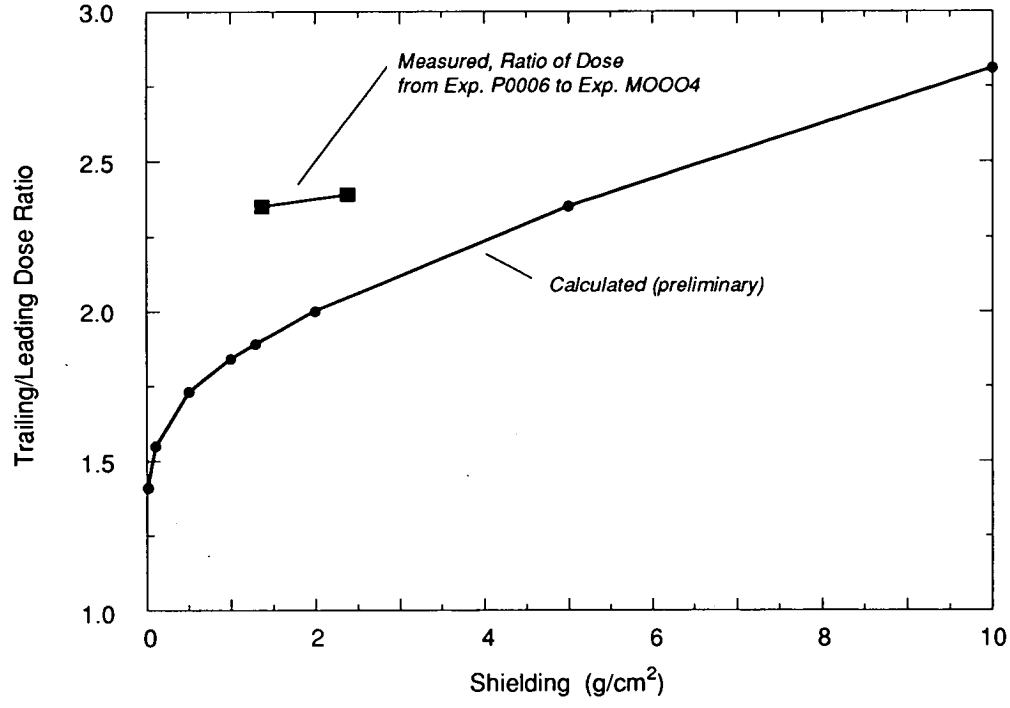

Figure 8. Calculated ratio of absorbed dose in tissue as function of shielding depth (aluminum equivalent) on trailing (West) vs. leading (East) side of LDEF compared with ratio from the TLD (thermoluminescent dosimetry) measurements of Experiments P0006 and M0004 (ref. 19)

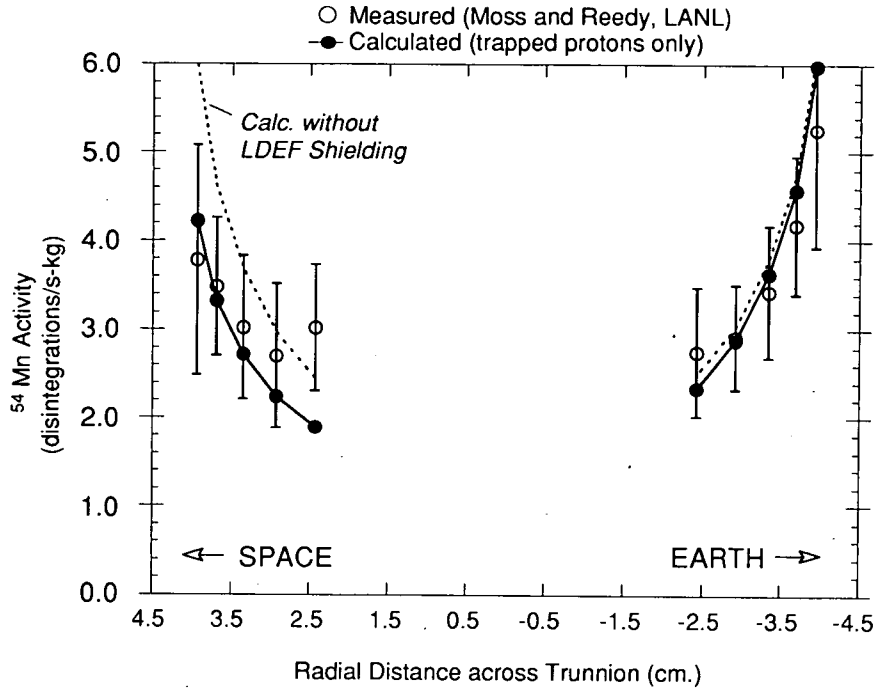

Figure 9. Comparison of calculated and measured (ref. 20) induced radioactivity in leading (East) LDEF trunnion. The solid curves were calculated with a geometry that included a mass representation of the LDEF spacecraft and the trunnion. For the dotted curves the spacecraft was removed.

LDEF GEOMETRY/MASS MODEL FOR RADIATION ANALYSES*

B. L. Colborn and T. W. Armstrong
Science Applications International Corporation
4161 Campus Point Court, San Diego, CA 92121-1513
Phone: 619/458-5282, Fax: 619/458-5067

SUMMARY

A three-dimensional geometry/mass model of LDEF is under development for ionizing radiation analyses. This model, together with ray-tracing algorithms, is being programmed for use both as a stand-alone code in determining 3-D shielding distributions at dosimetry locations and as a geometry module that can be interfaced with radiation transport codes.

INTRODUCTION

To aid in the interpretation of ionizing radiation dosimetry data, and to obtain more accurate comparisons of dosimetry measurements with model predictions, a three-dimensional geometry/mass model of the Long Duration Exposure Facility (LDEF) satellite is under development. The modeling approach and level of detail being incorporated is described below.

APPROACH

Three general categories of LDEF components are defined for modeling purposes (fig. 1). The major structural components of the spacecraft are being modeled individually, as illustrated in fig. 2. The mass of other components of the spacecraft ("miscellaneous" category of fig. 1, which amounts to about 5% of the total mass) is combined with the mass of the larger components, except that the thermal covers are modeled individually. The third category is the experiment trays, containing the tray itself and the contents of the experiment. Since the weight of individual experiments varies substantially (fig. 3), each of the 84 experiment trays is modeled separately.

For experiment trays containing radiation dosimetry, "detailed" modeling of major components within the tray is being performed so that local shielding variations in the vicinity of the dosimeters can be accounted for (fig. 4). For trays not containing ionizing radiation dosimeters, only the volume and mass of the trays are preserved. The contents of these "generic" trays are modeled as homogeneous aluminum of reduced density.

*Work supported by NASA Marshall Space Flight Center, Huntsville, AL, Contract NAS8-35866.

Input data for the model is based on information provided by the LDEF Project Office (J. Jones) and others at LaRC (R. Shearer), including engineering drawings of the spacecraft and pre-flight weight estimates and layouts of individual experiments, and information on component layouts and materials descriptions obtained from individual experimenters.

The combinatorial geometry methodology is being used. In this method Boolean logic is applied to combine descriptions of simple body shapes to simulate complex geometries.

The model is being programmed to allow operation in either of two modes: as a geometry module which can be interfaced with radiation transport codes, and as a stand-alone program with ray tracing (fig. 5). In this latter mode, the areal density and material composition along rays emanating from specified points can be computed to form a 3-D grid of shielding variations about the point. For dosimeters where individual particle tracks are measured, this ray-tracing mode will allow rays to be started that have directions corresponding to the track direction, so the material traversed in reaching the dosimeter can be estimated for individual tracks.

STATUS

At present the LDEF spacecraft structure with generic experiment trays has been modeled. Detailed modeling for several of the trays containing ionizing radiation dosimeters (Experiments P0004, P0006, and M0004) is in progress.

Category	Component	No. Places	Weight (lbs.)	Weight %	Modeling Approach
STRUCTURE	Center Ring	1	2,073	9.7%	Modeled as individual component.
	Longerons	24	2,280	10.7%	Modeled as individual components.
	End Frames	2	1,374	6.4%	Modeled as individual components.
	Diagonal Tubes	8	926	4.3%	Modeled as individual components.
	Intercostal Rings	72	758	3.5%	Modeled as individual components.
	Trunions,Pins, & Scuff Plates	10	501	2.3%	Modeled as individual components.
	End Support Beams	5	285	1.3%	Modeled as individual components.
	TOTAL STRUCTURE:		8,197	38.3%	
MISCELLANEOUS	Batteries	2	100	0.5%	Included as part of earth-end support beam weight.
	Initiate Electronics	1	105	0.5%	Included as part of center ring weight.
	Wiring	-	100	0.5%	Included as part of center ring weight.
	Nuts and Bolts	-	200	0.9%	Included as part of center ring weight.
	Damper Assembly	1	62	0.3%	Included as part of space-end support beam weight.
	Thermal Covers (Ends)	12	154	0.7%	Modeled as individual components.
	Ballast Plates	11	365	1.7%	Included as part of end frames.
	TOTAL MISCELLANEOUS:		1,086	5.1%	
EXPERIMENTS	Experiment Components + Trays	84	12,110	56.6%	Modeled each experiment tray separately, with individual experiment weights preserved. Modeling detail for components varies with experiment type.
	TOTAL LDEF WEIGHT:		21,393	100.0%	

Fig. 1. Level of detail incorporated in LDEF geometry/mass model.

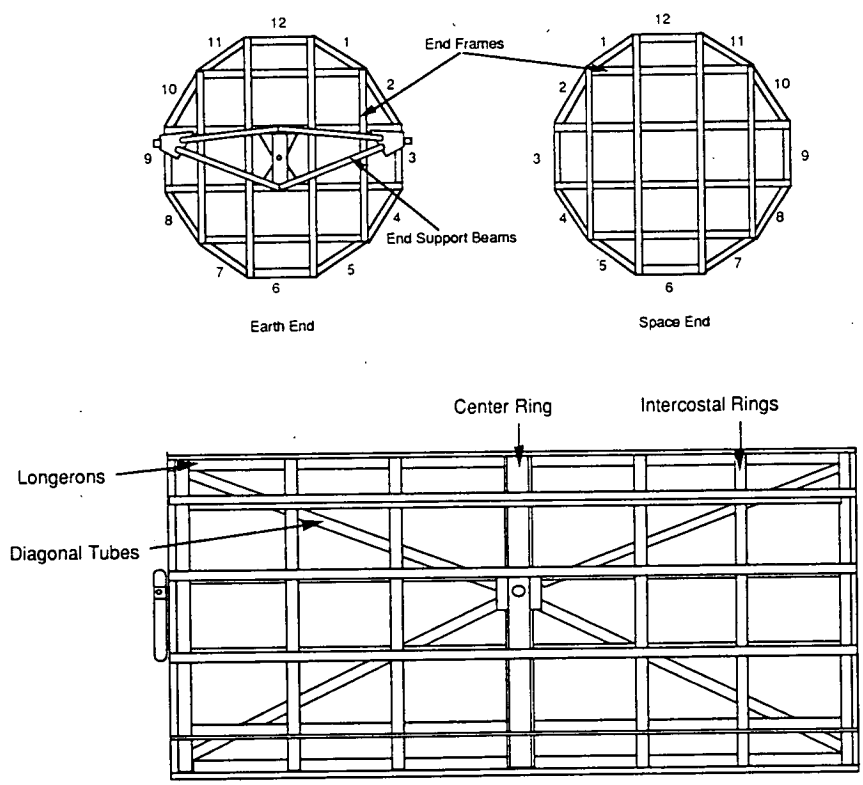

Fig. 2. Model of LDEF spacecraft structure.

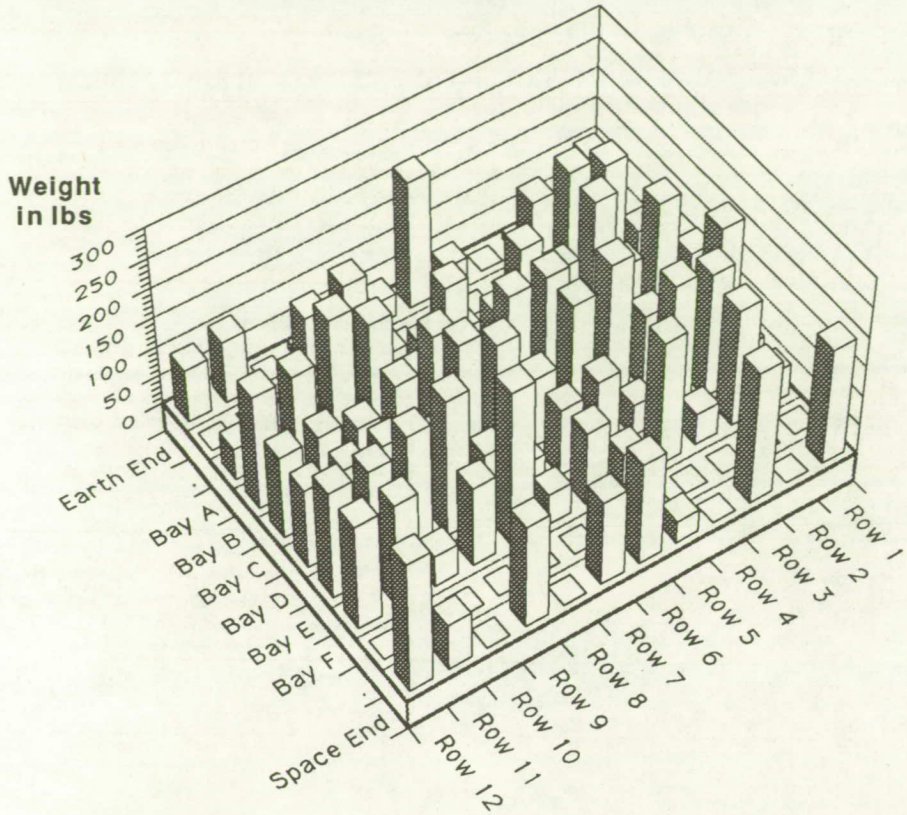

Fig. 3. Weights of individual experiments on LDEF.

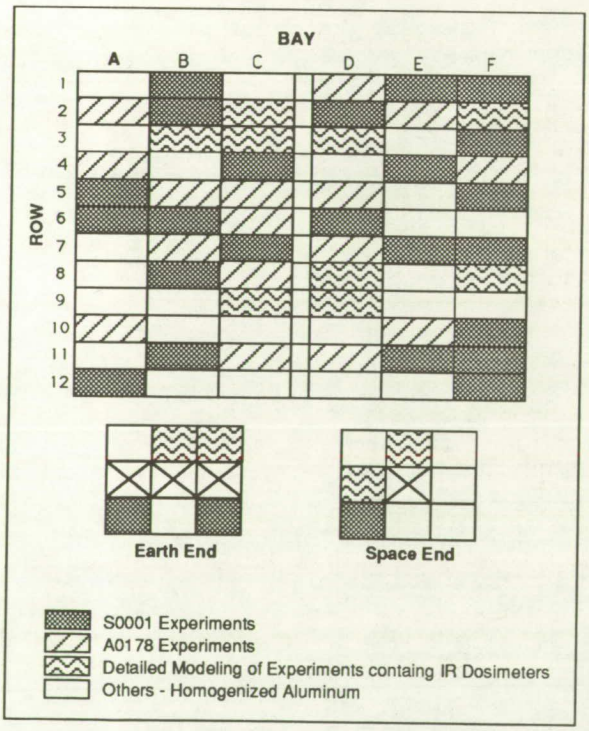

Level of Detail for Modeling Experiments:

No. Trays	Model	Experiments
26	Al plate	S0001: Space Debris (LaRC)
16	Al+plastic plates	A0178: Ultra-heavy Cosmic-Ray Expt. (Dublin Inst., ESTEC)
13	"detailed"	Experiments containing IR dosimetry - see NOTE
29	homogenized Al	(all others)

NOTE: Trays Containing IR Dosimetery for Detailed Modeling are:

Tray Bay-Row	Experiment No.	Experiment	Dosimetry
C-2, G-2	A-0015	Biostack (DFVLR)	TLD's, PNTD's
C-3, C-9	A-0114	Atomic Oxygen (UAH, MSFC)	Activation Samples
B-3	A-0138	Optical Fibers (CERT/ONERA - DERTS)	TLD'S
H-3, H-12	M0001	Heavy Ions (NRL)	PNTD's
D-3,D-9,G-12	M0002-1	Trapped Proton Spect. (AFGPL,MSFC, et al.)	PNTD's,TLD's,Act.
E-6	M0002-2	Heavy Cosmic-Ray Nuclei (U. Keil)	PNTD's
D-3,D-8,D-9	M0003	Space Envr. Effects on Matls. (Aerospace)	TLD's
F-8	M0004	Space Envr. Effects on Optics (AFWL)	TLD's, PNTD's
C-2 - F-2	M0006	Space Envr. Effects (AFTAC, Grumman)	TLD's
	P0004	SEEDS	TLD's, PNTD's
F-2	P0006	LET Spectrum Meas. (Univ. SF, MSFC)	TLD's, PNTD's, Fiss. & Act. Samples

Fig. 4. Modeling approach for LDEF experiments.

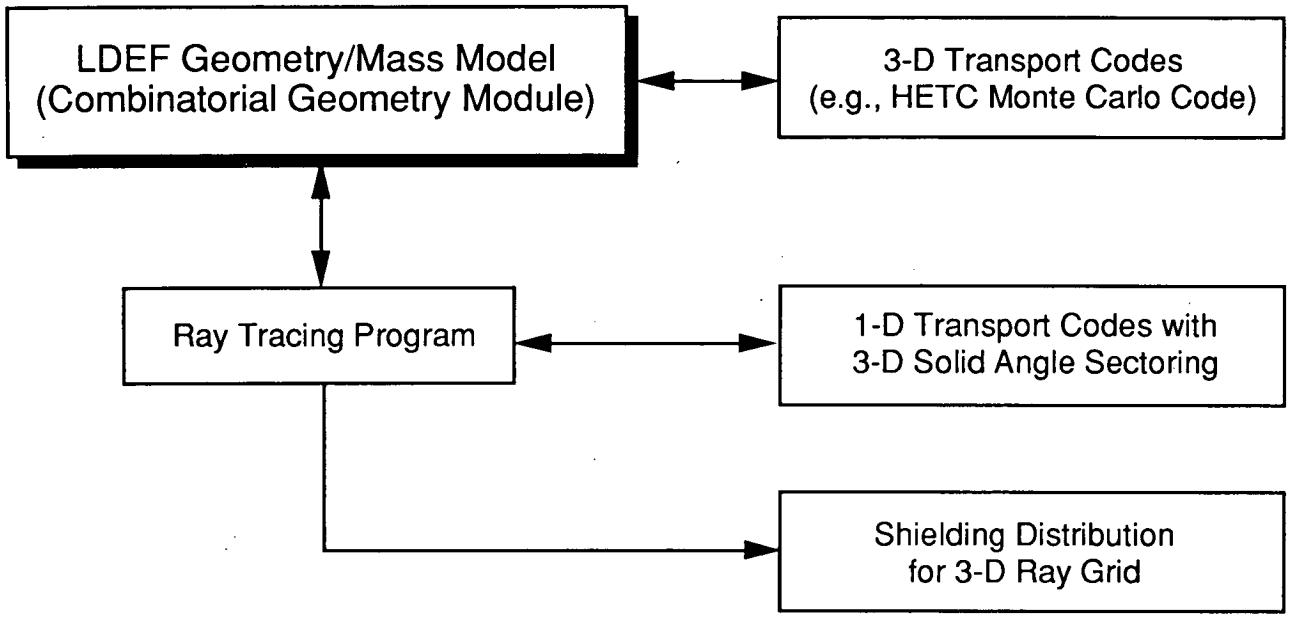

Fig. 5. Utility of LDEF geometry/mass model.

THE LDEF ULTRA HEAVY COSMIC RAY EXPERIMENT

D.O'Sullivan, A. Thompson, J. Bosch and R. Keegan
Dublin Institute for Advanced Studies (DIAS), Ireland

K.-P. Wenzel and A. Smit
Space Science Dept. of ESA, ESTEC, Noordwijk, The Netherlands

C. Domingo
Universitat Autònoma de Barcelona, Spain

SUMMARY

The LDEF Ultra Heavy Cosmic Ray Experiment (UHCRE) employed sixteen side viewing LDEF trays giving a total geometry factor for high energy cosmic rays of 30 m^2sr. The total exposure factor was 170 m^2sr y. The experiment is based on a modular array of 192 solid state nuclear track detector stacks, mounted in sets of four in 48 pressure vessels. The extended duration of the LDEF mission has resulted in a greatly enhanced potential scientific yield from the UHCRE. Initial scanning results indicate that at least 1800 cosmic ray nuclei with Z >65 have been collected, including the world's first statistically significant sample of actinides. Post-flight work to date and the current status of the experiment are reviewed.

INTRODUCTION

The Long Duration Exposure Facility (LDEF) was deployed into a near circular orbit of 257 nautical miles altitude and 28.5° inclination by the Space Shuttle Chal-

lenger in April 1984. Almost six years later on January 12 1990 it was retrieved from a decaying orbit of approximately 180 nautical miles by the Space Shuttle Columbia and returned safely to Earth. The Ultra Heavy Cosmic Ray Experiment (UHCRE), which was mounted on the LDEF, was the largest array of cosmic ray particle detectors ever flown in space. It comprised a total of 192 solid state nuclear track detectors stacks housed in 48 pressure vessels (at 1 atm of dry air) which were mounted in 16 of the LDEF experiment trays. Each stack was 20cm $\times$ 26cm in area and contained mainly lexan polycarbonate interleaved with lead velocity degraders. The average Lexan equivalent thickness of the detectors was ~ 4.7 g/cm^2. (ref.1,2)

Initial inspection and analysis of the UHCRE hardware took place in the Spacecraft Assembly and Encapsulation Facility II at Kennedy Space Center (KSC) after which the experiment trays were removed and shipped to the European Space Research and Technology Centre (ESTEC) at Noordwijk.

ACTIVITIES AT KENNEDY SPACE CENTER AND ESTEC

The extended LDEF mission resulted in (i), a greatly increased sample of ultra heavy cosmic ray nuclei ($Z \geq 65$) and (ii), a wealth of information on meteoroid and space debris impacts on the UHCRE hardware. Activities at KSC were related to the latter investigation.

Impacts of size greater than 0.5 mm on the tray flanges were located by eye inspection. This was followed by photo documentation of all front and back tray surfaces. All sixteen Scheldahl G411500 thermal blankets of the UHCRE were inspected and the positions of impacts of size greater than 0.3 mm were recorded (ref.3). The blankets were then trisected and one third of each was archived at KSC while the remainder were shipped to ESTEC. A detailed report of the preliminary investigation of meteoroid and orbital debris impacts can be found in these proceedings (ref.4). Following an eye inspection of the upper surfaces of the cylinders and support frames all UHCRE hardware was shipped to ESTEC in the original containers.

At ESTEC a preliminary survey of the thermal covers was carried out by F. Levadou (ref.5) and further studies were reported at this conference (ref.6). The aluminium cylinders were removed from their trays in clean room conditions to avoid any surface contamination. Subsequently, the gas pressure within each cylinder was measured and it was found that no leakage had occurred. Six of the cylinders containing the detector stacks scheduled for post flight calibration were shipped to the Bevalac. The detector stacks were removed from the remainder of the cylinders and were shipped to Dublin for processing and analysis.

CALIBRATION OF DETECTORS

Pre-flight and post-flight calibration of the UHCRE detectors was carried out at the Berkeley Bevalac. In the preflight calibration which was undertaken in 1983, a number of stacks were exposed to 960 MeV/N uranium and 300 MeV/N iron and earlier (1979) to 122 MeV/N iron ions. Post flight calibration in May 1990 consisted of exposures to high energy uranium (920 MeV/N), gold (1150 MeV and 663 MeV/N), krypton (1496 MeV/N), iron (1690 MeV/N and 400 MeV/N). The aim of these calibrations was twofold; namely, (i) to determine the value of the constants in the expression used to determine the charge of the individual ultra heavy cosmic ray nuclei, (the etch rate is of the form $V_t = aJ^n$ where $J = f(\frac{Z_{eff}}{\beta})$, Z_{eff} is the effective charge and a and n are constants determined from calibration) and (ii) to determine whether there was any 'ageing' of the latent tracks of the particles during the LDEF Mission.

To date, measurements on the calibration data are at a very preliminary stage. Several uranium nuclei from the post flight calibration have been followed to their stopping points and their energy determined to a high degree of accuracy. The preliminary calibration data shown in fig.1f should be taken as a rough guide until further data is processed. It is shown here to indicate that the nuclei displayed are indeed ultra heavy and are in the charge region $70<Z<92$. The bar marked uranium in fig.1f shows the range of values expected for uranium nuclei of $\beta=0.97$ (scaled up from measurements made at $\beta=0.77$), using the standard model and assuming a value of n between 2.0 and 2.5, which corresponds to the limits found in previous experiments. The gold data was calculated using the same data and assumptions. Comparison of pre flight and post flight calibration data will be available later this year.

TEMPERATURE HISTORY OF UHCRE DETECTORS

The charge resolution achievable on the ultra heavy cosmic ray experiment is dependent on the temperature history of the UHCRE modules throughout the LDEF Mission (ref.7). The thermal design of the experiment was aimed at maintaining the temperature of the detectors below 30°C(86°F) and ensuring as narrow a band as possible between maximum and minimum values. Temperatures were measured at selected locations on the LDEF structure during the first 490 days of flight. These data were used in post flight analysis to update LDEF thermal models (ref.8). The in–flight parameter data has allowed an accurate assessment of the thermal model

used and the resulting temperature uncertainties have been reduced from a preflight value of ±40°F to less than ±18°F. Table 1 shows the maximum and minimum temperatures calculated for the locations of all UHCRE trays along with the associated temperature band (Δ) for each case.

Table 1 - Maximum and Minimum Temperatures Experienced by UHCRE Trays

Tray Position on LDEF	Min Temp(°F)	Max Temp(°F)	Δ
A2	48.7	86.9	38.2
A4	52.2	85.5	33.3
A10	50.6	82.5	31.9
B5	40.7	85.7	45.0
B7	37.9	90.1	52.2
C5	39.5	83.3	43.8
C6	34.8	91.6	56.8
C8	48.7	86.9	38.2
C11	38.9	80.9	42.0
D1	33.2	81.3	48.1
D5	37.5	82.4	44.9
D7	34.3	87.2	52.9
D11	36.7	77.4	40.7
E2	38.6	74.2	35.6
E10	41.4	71.6	30.2
F4	48.2	77.9	29.7

Further refinement of the LDEF thermal model is continuing but it is unlikely that the values in Table 1 will alter significantly (private communication, T. Sampair). Overall the temperature results are very encouraging. The mean temperature of the individual trays was well below the upper limit chosen as the basis for the thermal design. Furthermore the mean width of the temperature band was 41.5°F (23°C), smaller than expected on the basis of preflight analysis.

PRELIMINARY PROCESSING AND ANALYSIS

Three Lexan Polycarbonate detector sheets were removed from a number of the stacks and were etched for periods varying from 5 to 15 days at the standard

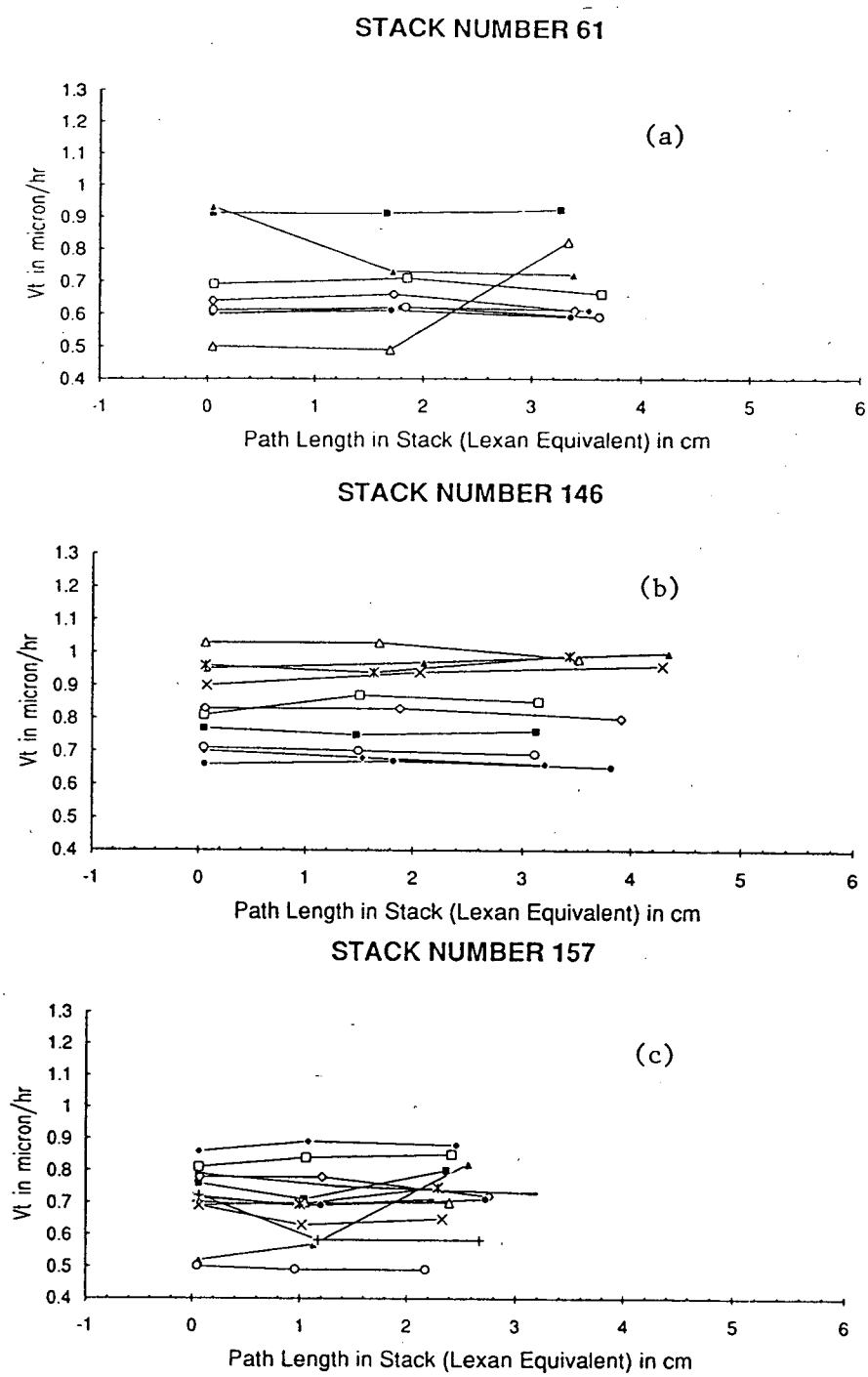

Figs. 1(a),(b),(c) : Etch rate as a function of depth in stack for ultra heavy nuclei observed in stacks 61, 146, 157 respectively.

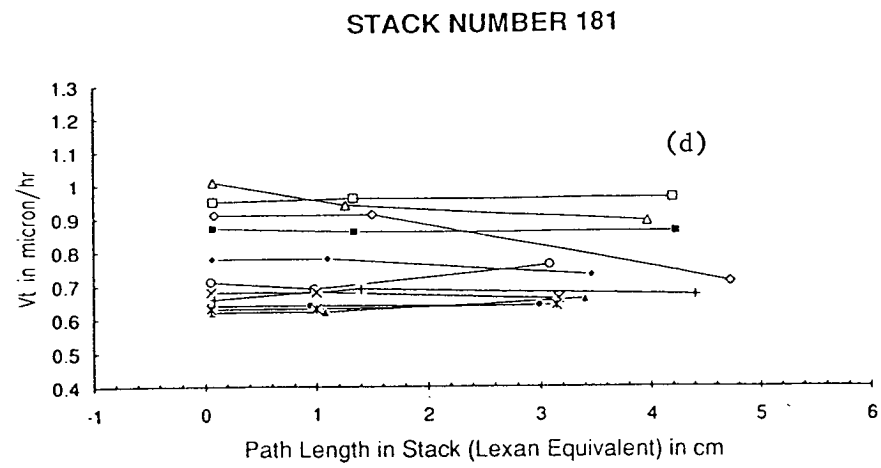

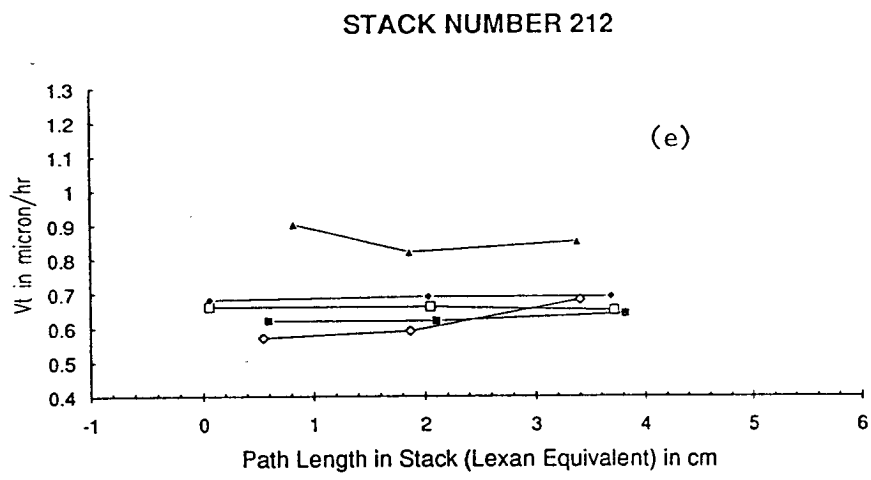

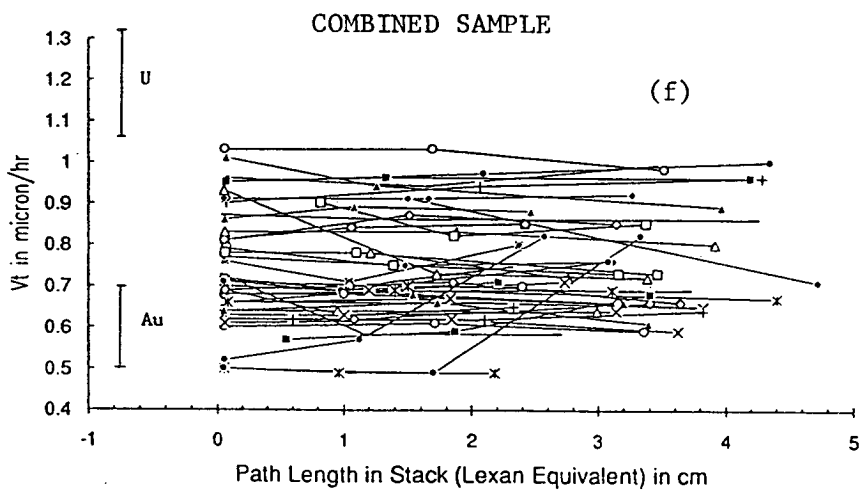

Figs.1(d),(e),(f) : Etch rate as a function of depth in stack for ultra heavy nuclei observed in stacks 181,212,and for the combined samples (a),(b),(c),(d) and (e). See text for explanation of Fig.1(f).

conditions of 40°C temperature and 6.25 N NaOH etchant. The sheets chosen were from the top, centre and bottom portions of these stacks providing a spread of path lengths varying from $\sim$ 0.01 cm to $\sim$ 4 cm in each case. Initial inspection showed that the surfaces of the sheets were of high quality and that the optical conditions for locating and measuring the tracks of ultra heavy nuclei were excellent.

Having located and measured the track parameters of a given nucleus in the top plate, its trajectory through the stack was estimated and the corresponding tracks were located and measured in the two lower parts of the stack. The number of ultra heavy nuclei observed ranged from 5 to 13 per stack indicating a total sample of >1800 collected during the LDEF mission.

Figure 1 displays the preliminary data obtained for ultra heavy nuclei in five of the UHCRE stacks. Plots of etch rate versus path length traversed in each stack is displayed for stacks 61, 146, 157, 181 and 212 (Figs. 1a, b, c, d, e resp.) These stacks were mounted in trays which were placed on rows six and eight of the twelve sided LDEF polygon (the leading edge was number nine).

It can be seen that for each stack the measured etch rates lie between 1.1 μm/hr and 0.5 μm/hr indicating a general consistency among the various sets of data. The different path lengths in the stacks for the centre and lower sections is due to different angles of incidence of the ultra heavy nuclei.

DISCUSSION

The initial post flight assessment of the UHCRE and preliminary data analysis indicate that the 69 month exposure in Earth orbit has achieved the major objectives of the experiment. The data shown in Fig. 1 display the characteristics of high energy ultra heavy nuclei as they traverse several grams of matter (ref.9). In the majority of cases there is no appreciable change in etch rate. Where a significant change does take place, the data is consistent with the occurrence of fragmentation in the stack. (In this regard it should be noted that, due to the inflight orientation of the LDEF, particles could enter the detector stacks from both top and bottom). The charge regime covered by the preliminary data as indicated by the quick look calibration measurements is consistent with that expected for relativistic cosmic ray nuclei in Lexan Polycarbonate (charge threshold Z$\sim$ 70).

The temperature history of the detectors gives rise to optimism with regard to the registration temperature effect and the long term ageing of latent tracks. On the basis of the temperature regime experienced by the UHCRE trays, (91.6 °F (33.1°C) to 33.2 °F (0.7°C) respectively), the uncertainty in charge determination is expected to be less than two charge units according to estimates made from exposures to UH

nuclei at the Bevalac (ref.10). The impact of short term differential latent track evolution is currently under study.

The total number of ultra heavy nuclei collected during the mission is estimated to be $\sim$ 1800. Thus, the UHCRE has provided a sample which is approximately six times greater than the previous world sample and includes the first significant sample of cosmic ray actinides.

Initial assessment of the charge resolution achieved indicates that it would be possible to (i) resolve some of the important charge groups such as platinum and lead and (ii) determine the abundance of the actinides in the cosmic radiation. The actinide abundance is determined by the nature of r-process contributions to cosmic ray source material and early observations suggested the presence of freshly synthesised r-process material to account for a high value of the ratio of actinides to platinum-lead nuclides. However, the upper limit of 3% for this ratio found by Binns et al (ref.11) is consistent with solar system source abundances. (A somewhat larger value was reported at the same time by Fowler et al (ref.12)). The large UHCRE sample, combined with a charge resolution which is superior to that achieved in the early experiments with solid state nuclear track detectors, should clarify the situation.

ACKNOWLEDGEMENTS

The authors wish to acknowledge the assistance of the Bevalac staff at Berkeley during calibration runs. We thank also, J. Daly, A. Grace-Casey, S. Ledwidge, G. Broderick, and H. Sullivan who undertook processing and measurements and Wai Ming Tai whose assistance with data processing was greatly appreciated. Finally, we wish to express our gratitude to R. Aarts, A.J. Daleman, V. Domingo, M. Froggatt, J. v.d. Hoek, M.J. Kikkert, F. Levadou, H. Mengs, J.P. van Meygaarden, B.C. Poot, J. Postema, G. Saenger and M.V. Slogteren who supported the de-integration activities at ESTEC.

REFERENCES

1. Thompson, A., D. O'Sullivan, K.–P. Wenzel, V. Domingo, C. Domingo, J. Daly, A. Smit. Proc. 21st ICRC (1990) 4, 441, Adelaide.

2. O'Sullivan, D., A. Thompson, K.–P. Wenzel, V. Domingo. Proc. Workshop on Cosmic Ray and High Energy Gamma Ray Experiments for the Space Station Era, 1984. (Louisiana State University), 302.

3. See, T., M. Allbrooks, D. Atkinson, C. Simon, M. Zolensky. Meteoroid and Debris Impact Features Documented on the Long Duration Exposure Facility. JSC # 24608, August 1990.

4. McDonnell J.A.M., M.T. Paley, T.J. Stevenson, A. Thompson, D. O' Sullivan, K.-P. Wenzel, G.H. Schwehm. Particulate Impacts on the UHCRE Cosmic Ray Experiment Teflon Covers: The ESA Programme. First LDEF Post-Retrieval Symposium. NASA CP-3134, 1992.

5. McDonnell J.A.M., K. Sullivan, T.J. Stevenson, D.H. Niblett. Particulate Detection in the Near Earth Space Environment Aboard the Long Duration Exposure Facility, LDEF: Cosmic or Terrestrial? Proc. IAU Coll., No. 126, Kyoto, 1991.

6. Levadou F., M. Froggatt, M. Rott, Eberhard Schneider. Preliminary Investigations into UHCRE Thermal Control Materials, First LDEF Post-Retrieval Symposium, NASA CP-3134, 1992.

7. O'Sullivan D., A. Thompson, Nucl. Tracks 4 (1980). 271.

8. Berrios, W.M., Use of the Long Duration Exposure Facility's Thermal Measurement System for the Verification of Thermal Models, First LDEF Post-Retrieval Symposium, NASA CP-3134, 1992.

9. Fowler P.H., C. Alexander, V.M. Clapham, D.C. Henshaw, C. O'Ceallaigh, D. O'Sullivan, A. Thompson. High Resolution Study of Nucleonic Cosmic Rays with $Z \geq 34$. Proc. 9th Int. Conf. on SSNTD, Munich, 1976, 1007.

10. Domingo C., A. Thompson, D. O'Sullivan, C. Baixeras, F. Fernandez, A. Vidal-Quadras. Long Term Ageing Effect for Energetic Ultra Heavy Ion Tracks in Polycarbonate Solid State Nuclear Track Detectors. Nuc. Inst. Meth. B51 (1990), 253.

11. Binns W.R., R.K. Fickle, T.L. Garrard, M.H. Israel, J. Klarman, E.C. Stone, C.J. Waddington. The Abundance of the Actinides in the Cosmic Radiation as Measured in HEAO-3. Astrophysical Journal 1982 **261**; L117.

12. Fowler P.H., R.N. Masheder, T.R. Moses, A. Morley, 1981, Nature **291**, 45.

PRELIMINARY RESULTS FROM THE HEAVY IONS IN SPACE EXPERIMENT

James H. Adams, Jr. and Lorraine P. Beahm
E. O. Hulburt Center for Space Research
Code 4154, Naval Research Laboratory
Washington, DC 20375-5000
Phone: 202/767-2747, Fax: 202/767-6473

Allan J. Tylka
Universities Space Research Association
Code 4154, Naval Research Laboratory
Washington, DC 20375-5000
Phone: 202/767-2200, Fax: 202/767-6473

SUMMARY

The Heavy Ions In Space (HIIS) experiment has two primary objectives: (1) to measure the elemental composition of ultraheavy Galactic cosmic rays, beginning in the tin-barium region of the periodic table; and (2) to investigate heavy ions which arrive at LDEF below the geomagnetic cutoff, either because they are not fully stripped of electrons or because their source is within the magnetosphere. Both of these objectives have practical as well as astrophysical consequences. In particular, the high atomic number of the ultraheavy Galactic cosmic rays puts them among the most intensely ionizing particles in Nature. They are therefore capable of upsetting electronic components normally considered immune to such effects. The below-cutoff heavy ions are intensely ionizing because of their low velocity. They can be a significant source of microelectronic anomalies in low inclination orbits, where Earth's magnetic field protects satellites from most particles from interplanetary space. The HIIS results will lead to significantly improved estimates of the intensely ionizing radiation environment.

INTRODUCTION

The space radiation environment affects spacecraft in several ways. Cosmic rays and trapped particles are the major cause of spacecraft anomalies in digital microelectronic systems. These particles can even cause components to fail suddenly. Space radiation dose slowly degrades the performance of most electronic devices and is the factor which ultimately limits the operational life of a spacecraft. The radiation dose received by astronauts ultimately limits the duration of all manned missions and may constrain the extent of human exploration of space.

LDEF carried several cosmic ray experiments. Two of these experiments are HIIS and the Ultra Heavy Cosmic Ray Experiment (UHCRE)[1]. Figure 1 compares HIIS and UHCRE with previous and planned experiments to measure cosmic ray elemental abundances above nickel. UHCRE is the largest cosmic ray experiment of all; HIIS is exceeded only by UHCRE and the proposed Heavy Nuclei Collector (HNC), which may be launched by the year 2000. HIIS and UHCRE provide complementary measurements of the cosmic ray elemental abundances. Whereas UHCRE's larger area enables it to measure the very rarest cosmic rays (at atomic numbers $Z > 65$), HIIS will extend the measurements to lower atomic numbers in the range of $Z = 45$-65, where the primary UHCRE detectors are not sensitive.

HIIS and UHCRE are also complementary in another way. UHCRE was designed to detect only relativistic cosmic rays, whose energy is so high that they pass through the detector. HIIS, on the other hand, was designed also to measure lower energy ions which come to rest in the detector. Potential sources of such stopping ions are solar energetic particles, the anomalous component of cosmic rays, and trapped heavy ions. Figure 2 compares HIIS with other existing and planned instruments to detect stopping ions. HIIS is orders of magnitude larger than any of these and can therefore make an unequalled

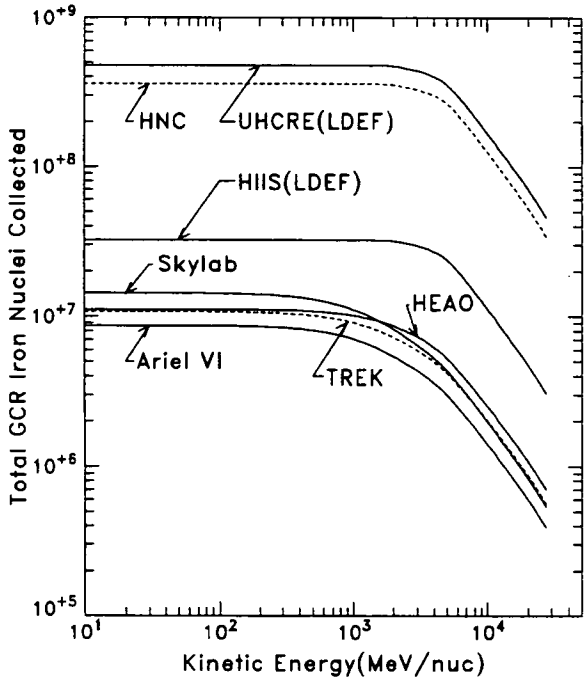

Figure 1: The collecting power of ultraheavy cosmic ray experiments, as measured by the total number of collected Galactic cosmic ray iron nuclei vs. minimum kinetic energy. In these comparisons, the effects of the different orbits are considered. Skylab[2], HEAO[3], ARIEL VI[4], HIIS, and UHCRE[1] (solid curves) have been flown. The TREK and HNC experiments (dashed curves) are planned for flight on the Soviet MIR and US Freedom space stations, respectively. The only flown experiment larger than HIIS is UHCRE. HIIS and UHCRE are complementary experiments, with HIIS ultraheavy measurements beginning at Z=45 and UHCRE's larger collecting power sensitive only to the rarest cosmic rays at Z>65.

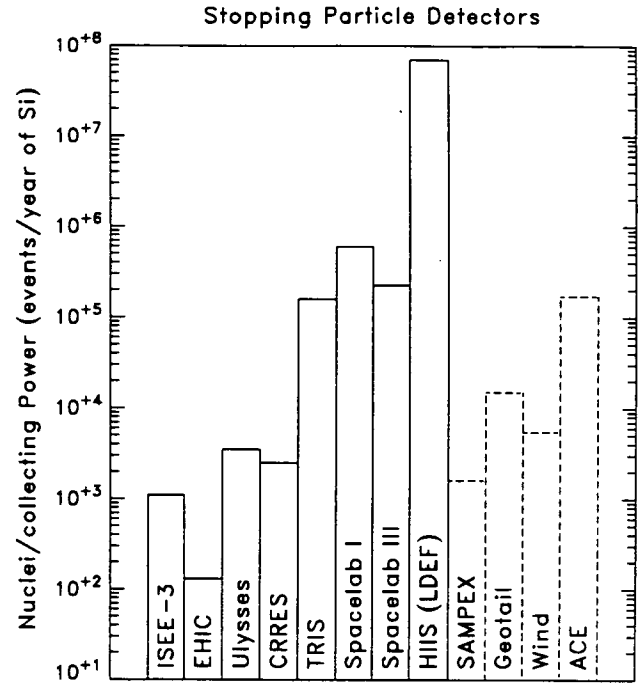

Figure 2: The collecting power of instruments which detect cosmic rays by bringing them to rest. The ISEE-3[5], CRIE/EHIC, Ulysses, CRRES[6], TRIS[7], Spacelab I[8], Spacelab III[9], and HIIS instruments (solid lines) have been flown. SAMPEX[10], Geotail[5], Wind[11], and ACE[5] (dashed lines) are planned for flight. The two spacelab missions and TRIS were flown less than a year, so for these missions the total number of Si events is plotted. Note that UHCRE[1] (Fig. 1) is not intended to detect stopping cosmic rays.

and extraordinarily deep survey of the stopping heavy ion contribution to the radiation environment. HIIS thus has the potential to make discoveries which may influence the direction of research and engineering for years to come.

EXPERIMENTAL OBJECTIVES

Ultraheavy Galactic Cosmic Rays. Galactic cosmic rays provide us with a sample of matter which originates from all over the Galaxy. We can use this sample to test our theory for the origin of the chemical elements. By comparing the composition of cosmic rays with that of the solar system and other samples of matter, we may discover differences that result from Galactic evolution over the past 5.5 billion years. These comparisons could also tell us about the special circumstances surrounding the formation of the sun and the solar system. The composition of the heaviest and rarest cosmic rays will be determined primarily by UHCRE. HIIS will contribute to the statistics of all ultraheavy cosmic ray measurements and it will extend observations down in atomic number to include the important tin-barium region of the periodic table, where we can observe the relative contributions of various nucleosynthetic processes[12].

Ions Below the Geomagnetic Cutoff. Satellites inside the magnetosphere are protected from many of the charged particles in the interplanetary medium because these particles are turned back by Earth's magnetic field. This was the case for LDEF, in its low altitude 28.5° orbit. The relevant quantity in measuring a particle's ability to penetrate into Earth's magnetic field is its magnetic rigidity, R, which is

simply the particle's momentum per unit charge. R is measured in units of GV/c, which is short for GeV/ec, where GeV/c is momentum in relativistic units and e is the charge in units of the electron charge. The minimum rigidity (ie, the so-called "geomagnetic cutoff rigidity") needed to reach the LDEF orbit is about 4 GV/c.

Because R is the momentum per unit charge, it depends upon both the particle's kinetic energy (K) and its charge (Q). Specifically,

$$R = (A/Q)[K^2 + 2KM_0]^{1/2} \quad (1)$$

where A is the ion's atomic mass number, $M_0 = 0.931$ GeV is the atomic mass unit, K is measured in GeV per nucleon (GeV/n), and Q is measured in units of the electron charge. Galactic cosmic rays are known to be fully stripped of electrons, so that Q = Z, where Z is the atomic number of the nucleus. In this case, the cutoff rigidity of 4 GV/c corresponds to a minimum kinetic energy of about 1 GeV/n. Particles which are detected at energies lower than this are said to be "below the cutoff". By definition, such particles must come from a source other than fully stripped Galactic cosmic rays.

Heavy ions trapped in Earth's magnetic field[13-15] are one source of below-cutoff ions. Another way for an ion to appear below the cutoff is if it has not been completely stripped of its electrons. In this case, Q < Z, thus giving the particle higher rigidity than a Galactic cosmic ray of the same energy. Compared to Galactic cosmic rays, such particles have enhanced access to low earth orbit. As discussed below, there are several known and possible sources of such particles. Because their relatively low velocities make these particles more intensely ionizing, they can be an important cause of satellite anomalies.

APPLICATIONS OF THE HIIS RESULTS

HIIS experiment will make a more thorough survey of the highly-ionizing particle radiation environment than has ever been possible before. We expect that the results of the HIIS experiment will lead to significant improvements in the Cosmic Ray Effects on Microelectronics (CREME) model[16-19]. CREME is widely used at present to estimate single event effect (SEE) rates on spacecraft. We anticipate that CREME will also be useful in designing the Space Station and in estimating radiation exposure to humans and hardware on future missions to the moon and to Mars. The results offered by HIIS and UHCRE cannot be duplicated by any existing or planned experiment within the next decade. These two LDEF experiments thus offer a unique and timely opportunity to increase our knowledge of the space radiation environment.

At present we can identify four areas in which the HIIS data will make CREME more accurate and improve its predictive capability:

1. *Ultraheavy Galactic Cosmic Rays*: Because these ions have such large nuclear charges, they are the most intensely ionizing particles in Nature. Although rare, these particles will affect microelectronic devices that are immune to the effects of more common cosmic rays. An accurate estimate of the flux of these particles is important in designing mission critical devices in which the mean-time-between-failures (MTBF) must be very large. HIIS and UHCRE will greatly reduce uncertainties in these flux estimates, particularly for the most intensely ionizing particles.

2. *Anomalous Component of Cosmic Rays*: These particles are known to be singly-ionized[7,20], which greatly increases their transmission through Earth's magnetic field to satellites in low-altitude, low-inclination orbits. In fact, anomalous component particles begin to dominate the linear energy transfer (LET) spectrum at LET values where many widely used electronic components become vulnerable. Current measurements of the anomalous component at Earth extend to only about 30 MeV/n for oxygen. These ions can be stopped by approximately 50 mils of aluminum shielding. At present we have only estimates of how the anomalous component spectrum extends to higher energies, where these ions can affect components behind typical amounts of shielding. HIIS will make the first high energy measurements of the anomalous component at Earth. HIIS

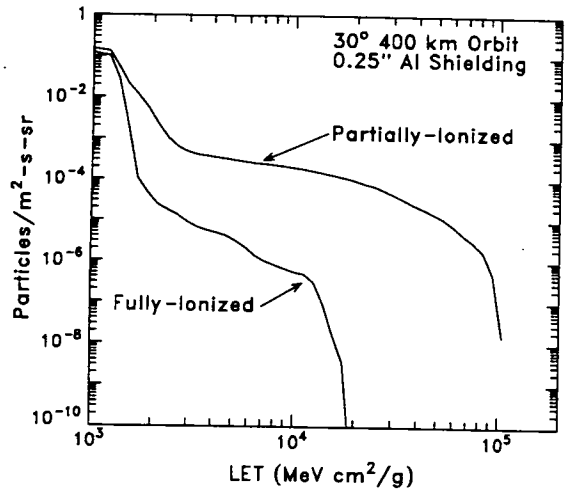

Figure 3: Linear energy transfer (LET) spectrum behind 0.25 in (0.64 cm) of aluminum for the peak particle flux of the August 1972 solar flares and as averaged around the Space Station orbit. Two possibilities are considered, that the solar energetic particles are fully ionized and that they are partially ionized as observed at low energies[21].

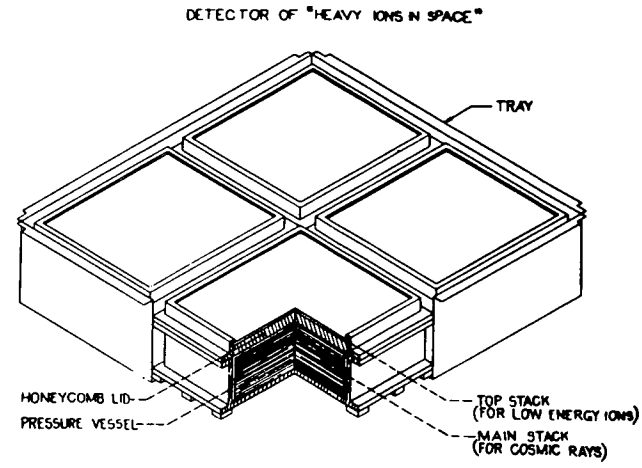

Figure 4: One of the two LDEF trays containing the HIIS experiment. Each tray contained four modules, one of which is shown in cutaway here.

will also measure heavier, more-intensely ionizing species in the anomalous component, whose contributions to the LET spectrum are presently unknown.

3. *Solar Energetic Particles (SEP)*: As discussed above, these ions can appear below the geomagnetic cutoff if they are less than fully stripped of electrons. Direct measurements[21] at low energies (~1 MeV/n) show that this is indeed the case, and indirect arguments[22] suggest that this behavior continues to energies of ~10 MeV/n. Particles of these energies can be stopped by modest amounts of shielding. At present there is no information on the ionization state of SEP's at very high energies of ~100 MeV/n. As shown in Figure 3, this lack of knowledge can lead to huge uncertainties in the radiation hazard posed by SEP events. Five large SEP events, which were also well measured on satellites outside the magnetosphere, occurred during the LDEF flight. By comparing the satellite measurements with the HIIS data, the ionization state of very high energy SEP particles can be deduced, thereby removing the uncertainties illustrated in Figure 3.

4. *Trapped Heavy Ions*: There is now good evidence for trapped oxygen ions with energies of 5-30 MeV/n in the inner magnetosphere[14]. Because LDEF was a 3-axis stabilized spacecraft, trapped heavy ions accumulate in HIIS at characteristic angles, thereby making them easily distinguishable from other particles. HIIS can extend the trapped particle measurements to higher energies and heavier species, making possible a first estimate of these particles' contribution to the satellite radiation environment.

Finally, we also note HIIS's potential to make new discoveries. For example, there have been recent published reports of below-cutoff ions which do not appear to be from any known source[23-25]. The collecting power of HIIS is orders of magnitude larger than that of the instruments which reported these results. HIIS should therefore be able to confirm (or refute) these observations and perhaps to identify the source of these particles. These particles, and others identified by HIIS, may be new and unanticipated components of the highly ionizing radiation environment.

THE HIIS DETECTOR SYSTEM

The HIIS detectors were contained in two trays (H3 and H12) on the space-facing end of LDEF. Each tray contained four modules. Figure 4 shows one of the HIIS trays and a cut-away of one of the modules. Each module comprised two separate stacks of plastic track detectors, a main stack which was sealed in

one atmosphere of dry air and a top stack which was in vacuum. Most of the sheets in the main stacks were CR-39[26], which was cast for us by Pershore Mouldings Ltd. (Pershore, UK) according to a special process for producing highly uniform, detector-quality material which we developed[27]. The top stacks and some sheets in the main stacks were Lexan[28]. The Lexan we used was manufactured especially for us without UV stabilizer, so as to make it possible to increase Lexan's sensitivity to lightly ionizing particles through UV enhancement of the latent tracks[29]. The total vertical thickness of the detector module was ~12 g/cm^2. The total number of detector sheets is 2782, each of which has an area of 1064 cm^2. The total collecting power of the eight detector modules is $A\Omega = 2.0$ m^2-sr.

Seven of our eight modules were constructed as described above. The eighth module had a special design to extend the detector's range to lower energies: both stacks were sealed in an atmosphere of dry air and the honeycomb lid shown in Fig. 4 was replaced with four thin Kapton[30] windows.

METHOD OF DETECTION

Plastic track detectors record charged particles by the trails of radiation damage they leave as they pass through the detector sheets. These tracks, which are revealed by chemically etching the detectors, are a permanent record of the particle's path and its rate of ionization in the plastic. The response of a plastic track detector is characterized by V_T/V_B, where V_T is the rate at which plastic is etched away along the damage trail and V_B is the rate at which bulk undamaged plastic is dissolved by the etchant. Because of radiation damage to the polymer $V_T/V_B > 1$, and the competition between V_T and V_B leads to the formation of a conically shaped etch pit whenever

$$(V_T/V_B)\cos(\theta) > 1 \qquad (2)$$

where θ is the angle between the trajectory of the charged particle and the normal to the detector sheet[31]. V_T/V_B is empirically found to be an increasing function of the restricted energy loss[32] (REL), which provides a numerical measure of the radiation damage generally dependent upon Z, A, and the particle velocity, β. Etch pits are measured under a high precision microscope. From the displacement of etch pits on the bottom and top surfaces of a detector sheet, the incidence angle θ can be measured. V_T/V_B can be determined by measuring the dimensions of the etch pit[33,34].

Stopping ions are identified by following them to where they came to rest in the detector and by measuring V_T/V_B in each detector surface along the particle's trajectory. When these V_T/V_B values are plotted versus the distance to the end of the track (the so-called "residual range"), they fall upon characteristic curves determined by Z and A. Once the particle's identity is known, its total range in the detector specifies its incident energy.

For relativistic particles, REL (and hence V_T/V_B) is nearly constant as the particle traverses the detector. V_T/V_B can be precisely determined by averaging measurements from many detector surfaces. V_T/V_B depends primarily upon the atomic number Z and only very weakly upon the particle velocity β, so the average V_T/V_B value identifies Z even without a measurment of β.

POST-FLIGHT ASSESSMENT OF THE DETECTOR PERFORMANCE

CR-39 and Lexan track detectors have routinely demonstrated excellent charge resolution (on the order of ~0.15 charge units or less) in short-duration accelerator exposures of small detector stacks. In extended space-based exposures of large detectors, various environmental effects can degrade the detector performance. The HIIS apparatus was designed to minimize these effects, and most of our analysis since retrieval has been directed to assessing the actual impact of these factors on the performance of HIIS.

Thermal Analysis and Temperature Effects

The single most important factor affecting the charge resolution of track detectors is temperature. In fact, several early track detector experiments, which were flown before these temperature effects were fully understood, gave misleading results[35]. More recent experiments, which have recognized the importance of temperature control, have proven reliable (cf. Ref. 7). There are two ways in which temperature affects track detectors:

Registration Temperature Effect. The response of a plastic track detector to an ionizing particle depends upon the detector's temperature at the time of the particle's passage[36]. This registration temperature effect (RTE) has been measured extensively[36-39] in both CR-39 and Lexan. To approach the track detector's high intrinsic resolution, the detector's temperature must be kept within a limited range throughout its exposure.

To limit temperature variations within the HIIS detector stacks, the HIIS design included a passive thermal control system, in which surface materials, their thermal and optical properties, thermal connections to the LDEF spacecraft, etc., were all carefully chosen. These items were combined in a detailed thermal model of the apparatus, which used input temperatures at nodes on the LDEF spacecraft to predict the temperature variation in the detector stacks. The original HIIS design, combined with LDEF's pre-flight temperature specifications, yielded a target temperature range of -11 ± 3.5 °C. At this relatively cold temperature the RTE is less severe[38] and thermal annealing (see below) can be avoided.

Since the retrieval, we have repeated this thermal analysis. The LDEF program office has used temperature data recorded during the LDEF mission and detailed thermal modelling of the spacecraft to reconstruct the temperature history at various temperature sensors on the spacecraft[40]. One of these sensors was on the boundary of our trays, so we have an accurate record of temperatures of the LDEF structure to which our experiment was attached.

Using this record, variation in the solar illumination incidence angle, measurements of the absorptivity and emissivity (α/ε) of the various surfaces on and around HIIS, and a detailed thermal model of our experiment, we have simulated the temperature history of the main detector stacks. The results of the simulation, which are shown on the left in Figure 5, indicate that the temperature in the main stack was in the range of -7.5 ± 2.0 °C. This better-than-expected temperature stability is due to two factors. First, the LDEF spacecraft underwent a smaller range of temperature variations than predicted in the pre-flight analysis. Second, LDEF was warmest in those parts of the mission when HIIS received the least sunlight, thus making it possible for the HIIS passive thermal design to compensate for variation in the spacecraft temperature.

Part of the HIIS thermal control system failed at some point: the thermal blankets protecting the HIIS modules partially detached and rolled up, exposing parts of the top detector stacks to solar UV. The pattern of UV and atomic oxygen damage on the surfaces of the blankets suggests that the failures occurred late in the mission, perhaps when LDEF was at lower altitudes and vulnerable to atomic oxygen damage. The degree of blanket failure varied from module to module. Post-flight examination of the blankets revealed that the failures were due to shrinkage of the top face sheets, causing them to tear loose from the modules.

The blanket failure appears to have had relatively little impact on the temperatures of the main stacks: we repeated our thermal analysis, using degraded blankets and the measured α/ε of the exposed top-stack surfaces. The simulated temperature history of the main stacks after the blanket failure is also shown in Figure 5. Without the blanket, the main stacks were colder (average temperature -13.0 °C) and underwent a relatively larger range of temperatures (rms width 2.3 °C). The top detector stacks, which are used only in studying very low energy particles, were more severely affected. In retrospect, the temperature shift caused by the blanket failure is also understandable. First, the measured α/ε of the exposed Lexan surfaces nearly balanced solar heating and radiative cooling. The remaining imbalance was in the direction of cooling. Second, the top detector stacks, which consist of 25 layers of 5 mil Lexan, also acted as surrogate thermal blankets. On orbit photography shows that these exposed stacks billowed up,

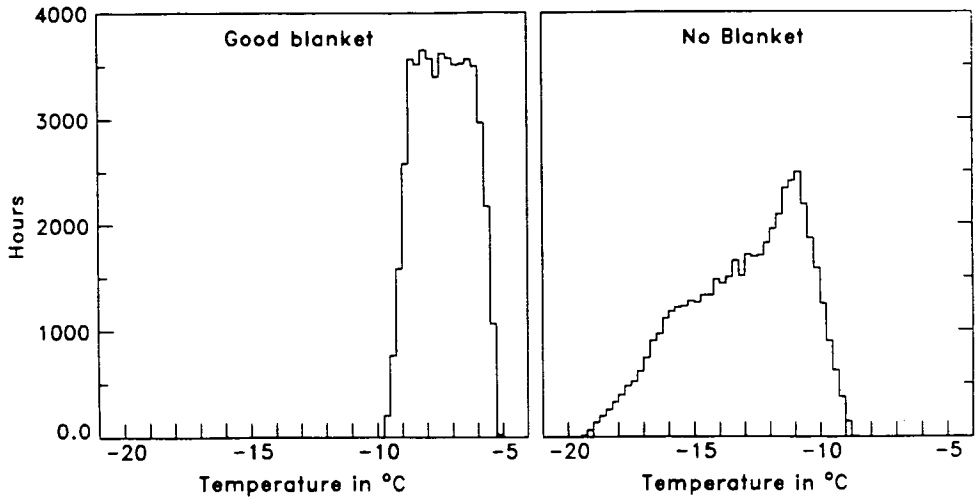

Figure 5: Post-flight reconstruction of the temperature distributions in the main detector stacks before and after the thermal blanket failures, which probably occurred near the end of the mission. Because we do not know exactly when the blankets failed, our simulations of thermal effects use the "worst-case" scenario, in which the blankets failed half-way through the mission, thereby producing the widest possible range of temperature variation.

probably due to electrostatic charging of the Lexan sheets by trapped electrons. With the sheets separated, heat transport through them was less effective.

The registration temperature effect will contribute to the widths of the elemental abundance peaks in the HIIS data. Although the post-flight examination of the blankets suggests that they failed near the end of the mission, we do not know this for certain. We therefore take a conservative approach in simulating the RTE on the detectors: we assume the "worst case" scenario, in which the blankets failed half-way through the mission, thereby averaging the histories in Figure 5 to produce the widest possible range of temperature variation. We folded this thermal history with results from accelerator studies of the RTE for particles with comparable V_T/V_B values. Even in this worst case, we find that the RTE is small: it increases the width of the Z=60 charge peak, for example, by less than 0.1 charge unit. For more heavily ionizing particles, the RTE is more severe: at Z=82, the RTE increases the width of the charge peak ~0.2 charge units.

Thermal Annealing. Thermal annealing[41] is the process in which radiation damage trails fade when the detector is held at elevated temperatures for extended periods of time after exposure. The HIIS modules were filled with dry air because measurements have shown that less thermal annealing occurs in dry air. Based on our post-flight thermal analysis and laboratory studies of thermal annealing, we conclude that the HIIS detectors remained too cool during the mission to be affected by annealing. From temperature sensors within our detector modules, which recorded the highest temperature to which they were ever exposed, we have independent verification that the temperatures in the main detector stacks never exceeded 37°C at any time since leaving our laboratory in 1984. Since retrieval, the HIIS detectors have been stored in refrigerators at ~5°C, except for ~2 months at ~20°C between retrieval and the return of the detectors to our laboratory.

Track Aging Effect

Another possible influence on the experimental charge resolution is track aging[42], in which the radiation damage continues to grow for a period of time after irradiation. Track aging has been a major concern for extended exposures of track detectors since the range of ages could degrade the charge resolution[43]. Recent experimental work[44], however, has shown that track growth occurs only in the first few weeks following exposure. Since the HIIS detectors are not etched until at least one year after the flight ended, this effect should not be present in our data.

Post-Flight Condition of the Detectors

The HIIS main detector stacks were originally sealed in 1 atm of dry air. The special module with the Kapton windows leaked because the windows were punctured by micrometeoroids after the thermal blanket rolled up. We analyzed the air in the remaining modules and compared it with air from the bottle used to fill the modules before flight. This air contained 10% helium as a tracer. The same helium concentration was found in the post-flight modules, proving that they did not leak. The analysis of the gas in the modules did, however, reveal a change in composition. The concentration of O_2 varied from module to module, with values in the range of 12-20% of the pre-flight concentration. Most of the O_2 had been replaced by carbon dioxide, but some was no longer in gaseous form. Oxygen is consumed during the polymerization process. The HIIS CR-39 was manufactured over a six month period, and some sheets were freshly polymerized when the modules were sealed. Since the detector sheets almost completely filled the module volume, residual polymerization of the CR-39 after the modules were sealed could easily account for the missing O_2 and the variation in the modules' O_2 concentrations. If residual polymerization is the explanation of the missing O_2, the oxygen concentrations probably leveled out to near their final value prior to launch.

After analyzing the gas in the detector modules, the main detector stacks were disassembled. We have etched sample sheets from the main stacks in two detector modules, C and E, in which the residual O_2 concentration was lowest and highest, respectively. Because chemical etching is an irreversible process and because we did not wish to lose valuable cosmic ray data, we first etched 10 sheets from near the bottoms of these modules. We also etched portions of a few sheets from near the top of the main stack in module C.

In all of the etched sheets, we easily found both relativistic and stopping cosmic ray tracks. The density of etch pits was not too high, and unrelated etch features did not interfere with measurements of the cosmic ray tracks. On the basis of our measurements of these tracks, we conclude that the main detector stacks, at least in the seven modules which did not leak, contain valuable cosmic ray data. Portions of the top stacks may also be useable for measuring fluxes of low energy particles, since they show no signs of UV exposure after the blanket failures.

CALIBRATION OF THE HIIS DETECTORS

We conducted extensive pre-flight accelerator calibrations of the HIIS detectors. Our present plan, however, is to internally calibrate the HIIS detectors, using the cosmic rays themselves. The detector sheets we have etched so far contained tracks, but not in the numbers we expected. Relativistic Fe, for example, appears not to have been recorded. Such apparent reduction in CR-39's sensitivity has been observed before[45]; it is consistent with the reduced oxygen concentration in the modules[46]. Because the observed detector response is so different from that in accelerator exposures, we believe that "boot-strapping" from the observed cosmic ray tracks is the most reliable calibration method. This method also ensures that the environmental effects on the HIIS detectors, whatever they may have been, will be reflected in the detector calibration.

To illustrate this internal calibration method, Figure 6 shows the raw data from stopping heavy ion tracks in CR-39 near the bottom of Module C. The data organize themselves into a densely populated band, labeled Fe, with a spread of tracks below the Fe band. There are only two ion tracks that are more intensely ionizing. This indicates a sudden drop in the elemental abundance of the ions. According to the general abundance of elements, there are only two places in the periodic table where such a drop occurs, above Fe and above Pb. Pb ions are far too rare to explain the observed fluxes, so the band must be Fe. Based on the number of ions in the Fe band, we would expect one or two Ni ions, just as observed. We therefore assumed that the heaviest ion track in the dataset was Ni. We then tried various hypotheses for the identity of the lightest track. When the lightest track was assumed to be Ar, the calculated Fe calibration curve ran through the Fe band. Using only the Ni and Ar measurements as input, we then derived the calibration curves for the other elements, also shown in Figure 6. In most cases we show

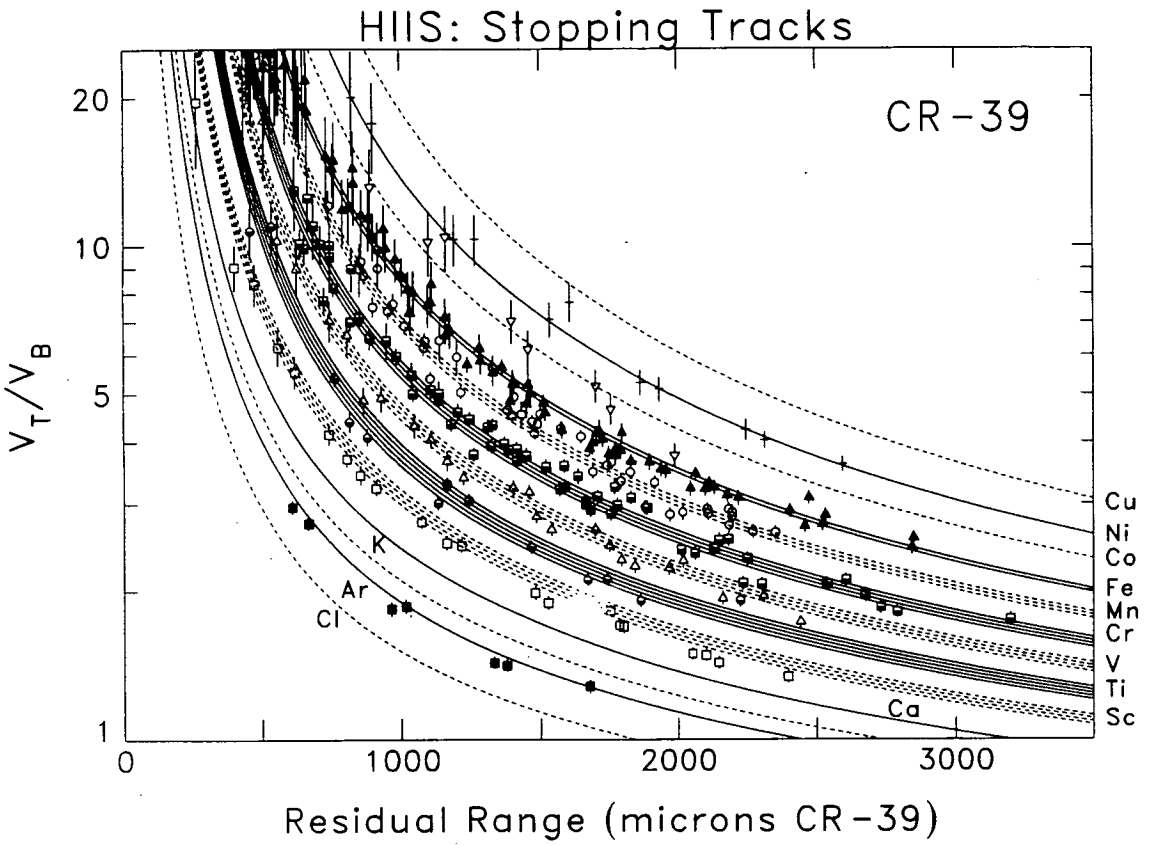

Figure 6: Raw data on 40 stopping heavy ion tracks found in detector sheets near the bottom of the main stack in Module C, each of which is measured in 9 detector surfaces on average. A different symbol is used for each element. The ordinates are the track detector response V_T/V_B and the abscissae are the distance from the stopping end of the track. The calibration curves are derived from the highest and lowest tracks shown in the figure.

curves for more than one isotope of each element. Because these ions were detected so deep in the stack, fragmentation guarantees that many isotopes are present. We have considered in our analysis only the most abundant isotopes, as indicated by a detailed calculation of transport through the detector material.

To apply the calibration, the measurements for each ion were fitted while leaving the atomic number as a free parameter. For atomic numbers with multiple isotopes, the Z/A ratio of the best-fit abundant isotope was assumed. The histogram of fitted Z values is shown in Figure 7. Most of the ions are unambiguously identified. This is illustrated in Figure 8, which shows how the "goodness of fit" (as measured by the integrated probability of the χ^2 distribution[47]) changes as the atomic number is moved up and down by one unit from the most probable integer value. The large sub-Fe to Fe ratio in Figure 7 may appear unusual. However, these tracks were found under ~15 g/cm^2 of material. Our transport calculation, combined with the Z-dependent geometry factor implicit in equation (2), shows that the observed sub-Fe/Fe ratio is consistent with an incident Fe beam.

To estimate the detector's charge resolution, we shifted all the elemental peaks in Figure 7 to overlay them at Z=26. Figure 9 shows the resulting distribution, which gives a good fit to a gaussian with standard deviation σ = 0.19 charge units.

The above internal calibration can be improved by collecting more tracks. Because the detector response varies from module to module, we will have to repeat the above process and do a separate

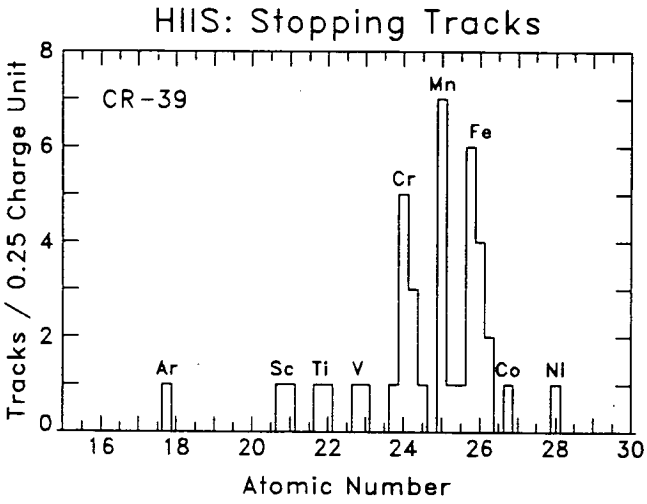

Figure 7: Histogram of the fitted atomic numbers of the stopping ions.

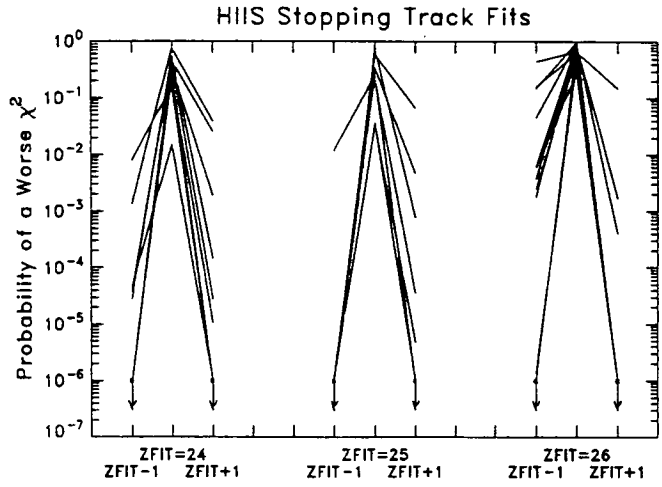

Figure 8: Goodness of fit measures for the identified Z = 24, 25, and 26 tracks in Figure 6. The goodness of fit is measured by the probability of observing a worse χ^2 when fitting the track to the specified hypothesis (Zfit, Zfit-1, or Zfit+1, where Zfit is the most probable integer value of Z). The probability is calculated by integrating over the χ^2 distribution[47]. The plot shows that the fit probability generally drops sharply when moving up or down by one unit from the most probable Zfit value. This implies that the tracks are unambiguously identified.

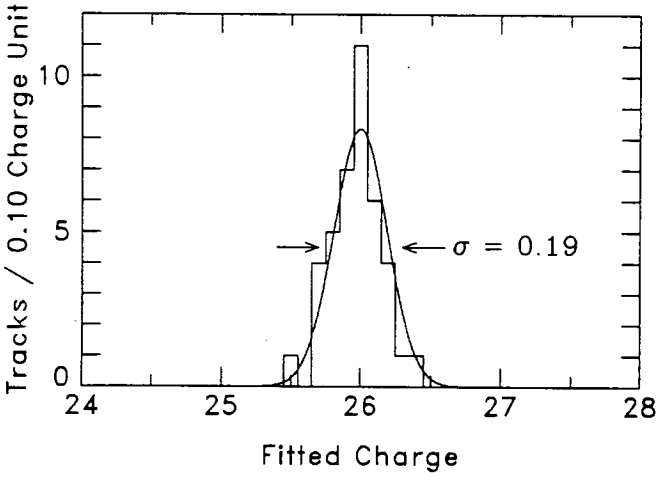

Figure 9: The atomic number measurements from all the stopping tracks, scaled to overlay at 26. A gaussian fit to the distribution yields σ = 0.19 charge units.

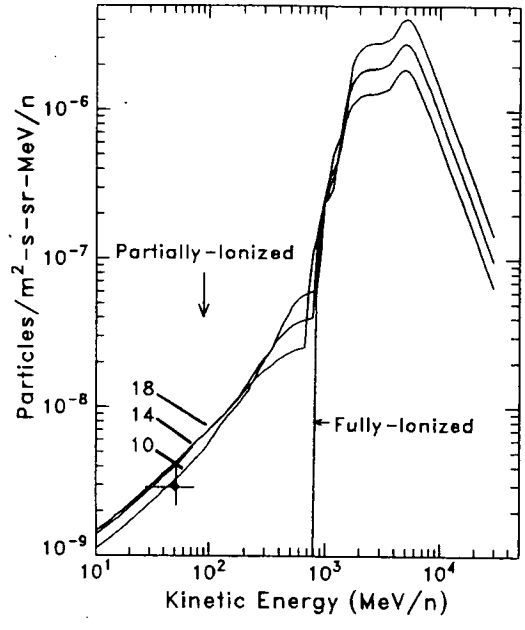

Figure 10: A comparison of the observed stopping Fe flux with estimates from solar energetic Fe ions with the same charge state distribution as observed at ~1 MeV/n. The spectra are the arriving Fe flux at depths of 10, 14, and 18 g/cm^2 in the HIIS detector stack. For comparison, we also show the spectrum for fully-stripped SEP Fe ions (which is not sensitive at low energies to the amount of material) under 14 g/cm^2. Galactic cosmic rays, which do not contribute to the low-energy flux, are also included in the calculations.

calibration for each module.* This should be no problem, since the necessary cosmic ray tracks appear to be present at the bottoms of the detector modules. Our thermal modelling indicates that the temperature in the main detector stack was uniform to within less than 0.3°C, so the calibration should be the same at both the top and bottom of a stack. The anomalous component Ne and Ar tracks, which we have already observed in the etched sheets near the top of the main stack in Module C, will provide another internal check on the calibration.

PRELIMINARY RESULTS ON STOPPING HEAVY IONS

The stopping heavy ions found near the bottoms of the stacks were a surprise: neither the anomalous component (because of its steeply falling spectrum) nor Galactic cosmic rays (which are geomagnetically excluded below ~1 GeV/n) are expected to stop at this depth in the stack. Based on the data collected so far, the average Fe flux under ~14 g/cm^2 is $(3\pm1)\times10^{-9}$/m^2-s-sr-MeV/n in the energy range $33 < E < 75$ MeV/n. These Fe ions arrived at LDEF with energies of ~600 MeV/n, much higher than previous observations of stopping ions. One possible source for these particles is re-entrant albedo of Galactic cosmic rays. We have performed numerical simulations which show that 18±6% of the incident Galactic cosmic ray iron ions must scrape through the atmosphere to explain the observed flux. This appears to be far too much, so we have rejected this explanation.

Another possibility is that these particles come from the very large SEP events which occurred during the LDEF mission. At ~1 MeV/n, SEP Fe ions are known to be only partially-ionized[21], with a distribution of charge states with mean value of about 14. If this charge state distribution is independent of the energy, the SEP's might explain our stopping heavy ions.

Figure 10 on the previous page shows a first, crude attempt to test this explanation. To estimate the SEP Fe fluence during the LDEF mission, we multiplied proton fluxes measured on NOAA's GOES satellite in 1989 and 1990 by the average SEP Fe/proton ratio[48,49]. The combined Galactic and SEP Fe spectrum was then transmitted through the geomagnetic field to the LDEF orbit, assuming the SEP Fe nuclei to be either fully-ionized or partially ionized according to the charge state distribution observed at low energies. The flux was then propagated through the detector to various depths, corresponding to a range of incidence angles and consequent shielding thicknesses at the observation point. The crudeness of the SEP Fe flux estimate makes the calculated spectra in Figure 10 quite uncertain, but the results clearly suggest that partially ionized SEP's could explain the observed flux.

We plan to continue our investigation of stopping ions in the bottoms of the HIIS stacks. So far we have examined only ~1% of the sheets that would contain partially-ionized SEP ions. Based on the data so far, we expect ~1000 stopping Fe ions with incident energies between 350 and 900 MeV/n.

PLANNED ANALYSIS OF RELATIVISTIC ULTRAHEAVY GALACTIC COSMIC RAYS

Figure 11 illustrates our method for measuring ultraheavy Galactic cosmic rays. The figure shows the raw data for 13 relativistic tracks found in scanning part of a sheet near the bottom of Module C. The tracks were followed through 10 sheets, and V_T/V_B was independently measured in ~20 detector surfaces. The error bar on each V_T/V_B measurement is determined by propagating the measurement errors on the etch pit dimensions. The average value of V_T/V_B is determined to within ~1% precision. We have checked that the scatter of measurements around these mean values follows a normal gaussian distribution.

To identify the tracks, we used the CR-39 calibration derived from the stopping tracks, which cover the

*Analysis of stopping tracks at the bottom of the second module (Module E) is still in progress. Fluxes of stopping and relativistic ions in Module E are similar to those observed in the first module (Module C). The track detector in Module E seems to be somewhat more sensitive than that in Module C, consistent with E's higher residual O_2 concentration. This increased sensitivity may allow us to extend observations to lighter ions.

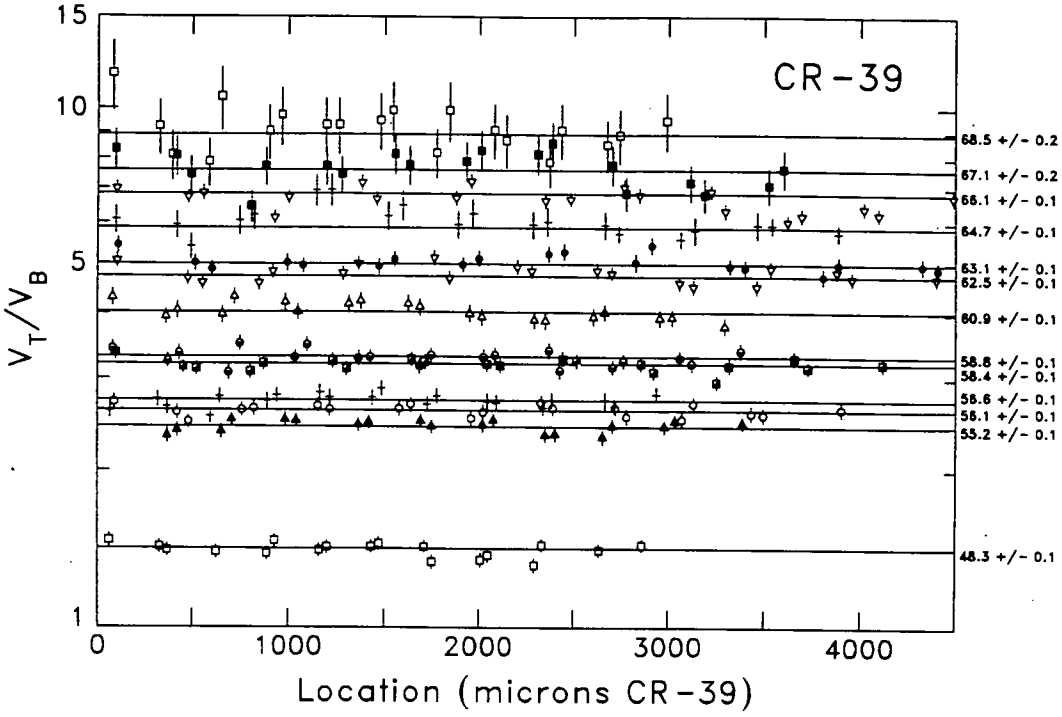

Figure 11: Raw data on relativistic tracks observed near the bottom of one HIIS detector stack. A different symbol is used for each track. The fitted atomic number and the formal error on the result are given at the right.

same range of V_T/V_B values. Figure 11 also shows the fitted atomic numbers, along with the formal error derived by propagating the uncertainty in the average value of V_T/V_B. Since these measurements were made under ~15 g/cm^2 of material, no strong elemental accumulations are expected. Also, although the formal errors are 0.1-0.2 charge units, the fitted atomic numbers do not tightly cluster around integer values. Temperature effects and uncertainties in the present calibration are too small to account for this spread in the fitted atomic numbers. Monte Carlo simulations of the HIIS resolution (discussed below) suggest that the primary reason for the spread is "kinetic smearing": the atomic numbers were fitted by assuming a particle energy of 11 GeV/n, but the actual particle energy can be anything above ~1 GeV/n. The detector response's residual weak dependence on the particle velocity combines with the Galactic cosmic ray spectrum to produce characteristic non-gaussian charge peaks. (These charge peaks are illustrated in Figure 12, discussed below.)

To measure elemental abundances of ultraheavy cosmic rays, we will apply the method shown in Figure 11 to tracks found in CR-39 and Lexan sheets near the tops of the main detector stacks. The tracks will be followed deeper into the stack and measured several more times to eliminate slowing down particles, which are a potential background for the heaviest and rarest cosmic rays.

Using previously reported relative abundances[3] and taking into account detection efficiency, geomagnetic transmission, and solar modulation of the Galactic cosmic ray flux throughout the LDEF flight, we expect to find a total of ~1500 relativistic cosmic rays at atomic numbers $Z \geq 45$ in the seven HIIS modules which did not leak. (For comparison, the HEAO dataset[3], which is currently the world's best data on the abundances of ultraheavy cosmic rays, contained ~370 such tracks.) After accounting for fragmentation losses, the number of tracks shown in Figure 11 is consistent with this flux estimate to within statistical errors.

To get an idea of the kind of composition measurements offered by HIIS, we have simulated the expected charge histogram. In this simulation we took into account: (1) the geomagnetic modulation of the cosmic ray flux and spectrum to LDEF's orbit; (2) the ultraheavy relative abundances[3,19]; (3) fragmentation in the ~2 g/cm^2 of material above the measured sheets; (4) the collecting area and exposure time of the seven HIIS modules that did not leak; (5) the detector calibration; (6) the Z-dependent

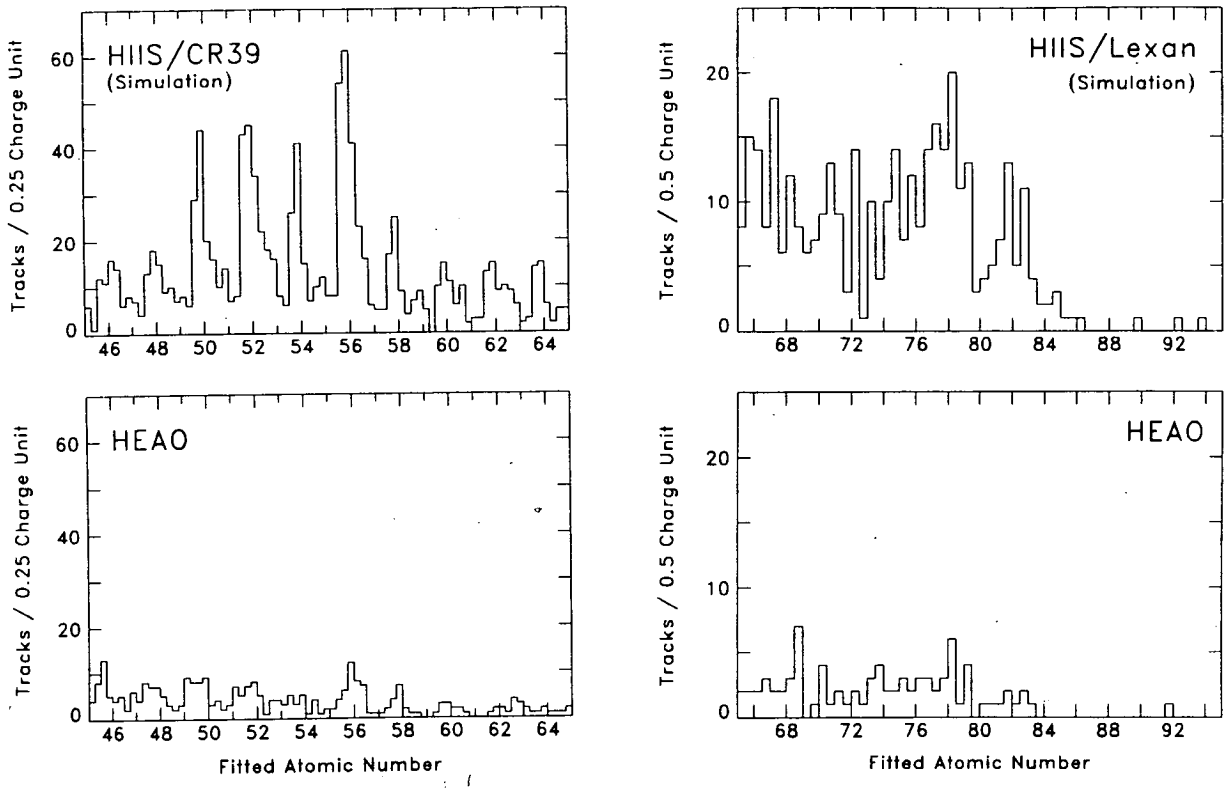

Figure 12: This figure compares the observed charge histogram from the HEAO experiment[3] with a simulation of the expected HIIS charge histogram. (See text for details of the simulation.) HIIS will primarily use CR-39 and Lexan detectors below and above Z = 65, respectively. The non-gaussian charge peaks caused by kinetic smearing are clearly seen in the Z < 65 simulation.

geometry factor implied by the detector response and equation (2); (7) kinetic smearing; (8) the registration temperature effect, based on our reconstruction of the thermal history of the detectors; and (9) measurement errors. Figure 12 compares the simulated HIIS measurements with the the HEAO data[3]. The simulation shows that HIIS offers a substantial improvement over the HEAO results. At Z < 65, HIIS will make more accurate measurements of the even-Z elements and, in some cases, the first abundance measurements of odd-Z elements. Above Z = 65 HIIS cannot resolve elements, but the Pt (Z=78) and Pb (Z=82) peaks are clearly separated. This is important because the Pt/Pb ratio is a key indicator of the nucleosynthetic processes which produce the cosmic rays.

CONCLUSIONS

The HIIS experiment has returned from its extended sojourn in space with valuable cosmic ray data covering a broad range of energies and atomic numbers. Our detailed review of environmental factors which affect plastic track detectors indicates that HIIS is able to achieve its experimental objectives. An internal calibration of the detectors has demonstrated charge resolution of ~0.2 charge units for stopping Fe ions. In determining the elemental abundances of ultraheavy Galactic cosmic rays, HIIS offers better resolution and a four-fold increase in statistics over the largest earlier experiment.

HIIS also offers a deep survey of space radiation which will thoroughly define the environment for the Space Station and other satellites using a 28° low altitude orbit. This survey is likely to lead to new discoveries about the radiation environment in space.

In fact, although we have so far examined less than 1% of the HIIS detector area, we have already made an unanticipated discovery: we observed Fe ions at ~600 MeV/n, well below the geomagnetic cutoff. Although the analysis is still too crude to permit any conclusions, the observed flux suggests that these ions may be partially-ionized solar energetic particles. Such particles could have significant effects on satellite electronics; they are not included in current models of the radiation environment.

ACKNOWLEDGEMENTS

We thank Dr. Herb Sauer of NOAA for providing us with unpublished data on the proton fluxes during SEP events in 1989-90. We thank Dr. John R. Letaw for his calculations on the transport of nuclei through the detector. We also thank Dr. R.B. Barrett of Big Three Industries, Inc. for post-flight examination and verification of the TEMPIL temperature sensors we used in the HIIS modules.

REFERENCES

1. O'Sullivan, D. et al.: The Ultra Heavy Cosmic Ray Experiment. First LDEF Post-Retrieval Symposium, NASA CP-3134, 1992.
2. Shirk, E.K. and Price, P.B.: Charge and Energy Spectra of Cosmic Rays with Z≥60. Astrophys. J., vol. 220, 1978, pp. 719-33.
3. Binns, W.R. et al.: Abundances of Ultraheavy Elements in the Cosmic Radiation: Results from HEAO 3. Astrophys. J. vol. 346, 1989, pp. 997-1009.
4. Fowler, P.H. et al.: Ariel 6 Measurements of the Ultraheavy Cosmic Rays. Astrophys. J., vol. 314, 1987, pp. 739-46.
5. Stone, E.C. et al.: The Cosmic Ray and Solar Flare Isotope Experiments in the CRRES, NOAA-I and Ulysses Satellites. in *Particle Astrophysics: The NASA Cosmic Ray Program for the 1990's and Beyond*, eds. W.V. Jones et al., AIP Conf. Proc. 203, 1989, pp. 48-57.
6. Garcia-Munoz, M.: The Cosmic Ray and Solar Flare Isotope Experiments in the CRRES, NOAA-I and Ulysses Satellites. *ibid.*, pp. 37-43.
7. Adams, J.H.Jr., Beahm, L.P.; and Tylka, A.J.: The Charge State of the Anomalous Component: Results from the Trapped Ions in Space Experiment (and references therein). Astrophys. J. vol. 377, 1991, pp. 292-305.
8. Beaujean, R.; Enge, W.; and Siegmon, S.: The Resolving Cosmic Ray Experiment with Plastic Track Detectors on Spacelab 1. Proc. 16th ICRC (Kyoto), vol. 12, 1979, pp. 350-4.
9. Singh, R.K. et al.: Ionization State of the Anomalous Cosmic Rays. Astrophys. J., vol. 374, 1991, pp. 753-63.
10. Mason, G.M.: SAMPEX Mission Overview. AIP Conf. Proc. 203, 1989, pp. 44-7.
11. Reames, D.V. et al.: The Energetic Particles: Acceleration, Composition, and Transport Experiment on the ISTP/Wind Spacecraft. *ibid.*, pp 32-6.
12. Brewster, N.R.; Frier, P.S.; and Waddington, C.J.: The Propagation of Ultraheavy Cosmic Ray Nuclei. Astrophys. J., vol. 264, 1983, pp. 324-336.
13. Chan, J.H. and Price P.B.: Composition and Energy Spectra of Heavy Nuclei of Unknown Origin Detected on Skylab. Phys. Rev. Lett., vol. 35, 1975, pp. 539-42.
14. Grigorov, N.L. et al.: The Charge State of Anomalous Oxygen of Cosmic Rays. Geomagnetism and Aeronomy, vol. 29, 1989, pp. 889-91.
15. Beaujean, R.; Jonathal, D.; and Enge, W.: Heavy Ion Measurements on LDEF. First LDEF Post-Retrieval Symposium, NASA CP-3134, 1992.
16. Adams, J.H.Jr.; Silberberg, R.; and Tsao, C.H.: Cosmic Ray Effects on Microelectronics (CREME), Part I: The Near-Earth Particle Environment. NRL Memorandum Report 4506, 1981.
17. Adams, J.H.Jr.; Letaw, J.R.; and Smart, D.F.: CREME Part II: The Geomagnetic Cutoff Effects. NRL Memorandum Report 5099, 1983.
18. Tsao, C.H. et al.: CREME Part III: Propagation of Cosmic Rays in the Atmosphere. NRL Memorandum Report 5402, 1984.
19. Adams, J.H.Jr.: CREME Part IV. NRL Memorandum Report 5901, 1986.
20. Adams, J.H.Jr. et al.: The Charge State fo the Anomalous Component. Astrophys. J. Letters, vol. 375, 1991, pp. L45-L48.
21. Luhn, A. et al.: Ionic Charge States of N, Ne, Mg, Si, and S in Solar Energetic Particle Events. Adv. in Space Res., vol. 4, 1984, pp. 161-164.
22. Breneman, H. and Stone, E.C.: Solar Coronal and Photospheric Abundances from Solar Energetic Particle Measurements. Astrophys. J., vol. 299, 1985, pp. L57-L61.
23. Oschlies, K.; Beaujean, R.; and Enge, W.: On the Charge State of Anomalous Oxygen. Astrophys. J., vol 345, 1989, pp. 776-81.

24. Biswas, S. et al.: Observation of Low-Energy (30-100 MeV nucleon^{-1}) Partially Ionized Heavy Ions in Galactic Cosmic Rays. Astrophys. J. Letters, vol. 359, 1990, pp. L5-L9.
25. Grigorov, N.L. et al.: Heavy Ions in Cosmic Rays. Nuclear Physics (Yadernaya Fizica), vol. 53, 1991, pp. 1340-5.
26. CR-39 is poly diethylene glycol bis-alyl carbonate and was invented at Pittsburgh Plate Glass's Columbia Resin Laboratory in Barberton, OH.
27. Adams, J.H.Jr.: A Curing Cycle for Detector-Quality CR-39. Nucl. Tracks: Meth., Inst. and Appl., Suppl. 3, 1982, pp. 145-148.
28. Lexan is the trade name for bis-phenol A polycarbonate, as sold by General Electric, Pittsfield MA. It is also sold under the tradenames of Tuffak and Rodyne-P.
29. Stiller, B.; Adams, J.H.Jr.; and Beahm, L.P.: Ultraviolet Enhancement of Tracks in Lexan with Black Fluorescent Lamps. Nucl. Tracks, vol. 12, 1986, pp. 137-40.
30. Kapton is a polyamide plastic manufactured by Du Pont Inc., Wilmington, DE.
31. Fleischer, R.L.; Price, P.B.; and Walker, R.M.: *Nuclear Tracks in Solids: Principles and Applications*. (Berkeley: University of California Press), 1975, pp. 57-63.
32. Benton, E.V. and Nix, W.D.: The Restricted Energy Loss Criterion for Registration of Charged Particles in Plastics. Nucl. Inst. Meth., vol. 67, 1969, pp. 343-7.
33. Henke, R.P. and Benton, E.V.: On Geometry of Tracks in Dielectric Nuclear Track Detectors. Nucl. Inst. Meth., vol. 97, 1971, pp. 483-9; Somogyi, G. and Szalay, S.A.:Track-Diameter Kinetics in Dielectric Track Detectors. Nucl. Inst. Meth., vol. 109, 1973, pp. 211-32.
34. Adams, J.H.Jr.: Automated Track Measurements in CR-39. Nucl. Tracks, vol. 4, 1980, pp. 67-76.
35. O'Sullivan, D.; Thompson, A.; and Fowler, P.H.: The Abundance of Actinide Elements in the Galactic Cosmic Radiation. Nucl. Tracks Radiat. Meas., vol. 11, 1986, pp. 95-85.
36. O'Sullivan, D. and Thompson, A.: The Observation of a Sensitivity Dependence on Temperature during Registration in Solid State Nuclear Track Detectors. Nucl. Tracks, vol. 4, 1980, pp. 271-76.
37. Thompson, A. et al.: The Dependence of Track Response on Registration Temperature in Lexan and CR-39. Nucl. Tracks: Meth., Inst. and Appl., Suppl. 3, 1982, pp. 171-4.
38. O'Sullivan, D. et al.: New Results on the Investigation of the Variation of Nuclear Track Detector Response with Temperature. Nucl. Tracks and Radiat. Meas., vol. 8, 1984, pp. 143-6.
39. Adams, J.H.Jr. and Beahm, L.P.: The Registration Temperature Effect for Lightly Ionizing Particles in CR-39. Nucl. Tracks, vol. 12, 1986, pp. 387-90.
40. Berrios, W.M.: LDEF Post-Flight Thermal Analysis: Orbital Thermal Environment Data Package. NASA/LaRC, Hampton, VA; and Use of LDEF Thermal Measurement System for Verification of Thermal Models. First LDEF Post-Retrieval Symposium, NASA CP- 3134, 1992.
41. Adams, J.H.Jr. and Beahm, L.P.: A Study of Long Term Thermal Annealing on Lexan Plastic Track Detector. Nucl. Tracks: Meth. Inst. and Appl., Suppl. 3, 1982, pp. 145-148.
42. Henke, R.P.; Benton, E.V.; and Heckman, H.H.: Sensitivity Enhancement of Plastic Nuclear Track Detectors Through Photo-oxidation. Rad. Eff., vol. 3, 1970, pp. 43-49.
43. Price, P.B. and Drach, J.: Dependence of Response of Plastic Track Detectors on Post-Irradiation Aging Time, Temperature, and Atmosphere. Nucl. Inst. Meth., vol. B28, 1987, pp. 275-9.
44. Domingo, C. et al.: Latent Track Intensification Due to Ageing in Solid State Nuclear Track Detectors. Nucl. Tracks and Radiat. Meas., vol. 15, 1988, pp. 47-50.; The Influence of Latent Track Variations on Ultra Heavy Nuclei Identification with Solid State Nuclear Track Detectors. Proc. 21st ICRC (Adelaide), vol. 4, 1990, pp. 437-40.
45. Yadav, J.S. and Singh, R.K.: Change of CR-39(DOP) Track Detector Response as a Result of Space Exposure. Nucl. Tracks Radiat. Meas., vol. 17, 1990, pp. 579-82.
46. Drach, J. et al.: Effect of Oxygen on Response of Plastic and Glass Track Detectors. Nucl. Inst. Meth., vol. B28, 1987, pp. 364-8.
47. Bevington, P.R.: *Data Reduction and Error Analysis for the Physical Sciences*. (New York: McGraw-Hill), 1969, pp. 313-6.
48. McGuire, R.E.; Von Rosenvinge, T.T.; and McDonald, F.B.: The Composition of Solar Energetic Particles. Astrophys. J. vol. 301, 1986, pp. 938-61.
49. Mason, G.M.: The Composition of Galactic Cosmic Rays and Solar Energetic Particles. Rev. Geophys., vol. 25, 1987, pp. 685-96.

HEAVY ION MEASUREMENT ON LDEF

R. Beaujean, D. Jonathal and W. Enge
Institut für Reine und Angewandte Kernphysik
Christian-Albrechts-Universität zu Kiel, D-2300 Kiel, FRG
Phone: (0)431/880-2544, Fax: (0)431/85660

SUMMARY

Stacks of CR-39 and Kodak CN track detectors were exposed on different locations on the NASA satellite LDEF. The preliminary analysis yielded heavy ion tracks on a background of low energy secondaries from proton interactions. The detected heavy ions with energies < 50 MeV/Nuc show a steep energy spectrum and a spatial confinement close to the mirror plane in the South Atlantic Anomaly. We interpret this as evidence for a radiation belt origin.

INTRODUCTION

The Kiel LDEF experiment M0002, mounted on experiment tray E6, was designed to measure the heavy ion environment by means of CR-39 plastic solid state track detectors. The detector stack with a size of $40*34*4.5$ cm^3 was exposed in vacuum covered by thermal protection foils with a total thickness of approximately 14 mg/cm^2.

Two additional stacks, each with a size of 40 mm depth and 95 mm diameter, were integrated in subunits of the Biostack Experiment A0015 on trays C2 and G2. They consist of CR-39 and Kodak cellulose nitrate foils sealed in aluminium containers under 10 mg/cm^2 Kapton shielding and support the analysis of the spatial particle distribution.

All stacks were recovered in excellent physical condition with no damage on the thermal protection foils. After etching, tracks of heavy ions can be easily detected in both detector types on a background of small etch pits, which were probably produced by secondaries from proton interactions (Fig. 1).

PRELIMINARY RESULTS

In the first step of our analysis the appropriate etching condition had to be established, as the total number of tracks and the detector response were undefined. At the time being we are not able to present a calibration for our detector material and we must be aware of a potential temporal change of the detector response during the mission. Any particle flux measurement strongly depends on this detector response.

Table 1 gives numbers of stopping tracks in CR-39 foils at position E6. From the estimated sensitivity of our CR-39 we conclude that particles with $Z > 8$ are included. Similar decrease of stopping particle numbers with increasing depth was detected in Kodak CN on trays C2 and G2 but at a 3-5 times higher fluence level. If our Kodak CN is more sensitive then CR-39, particles with $Z \geq 6$ may be registered in Kodak CN. The work on the calibration of the detector response is in progress.

As the LDEF orientation with respect to the magnetic field lines within the South Atlantic Anomaly (SAA) is expected to be constant during the mission, we measured the azimuth angle distribution on the detector foils (Figs. 2 and 3) for particles entering the topmost CR-39 foils at trays E6 and C2.

DISCUSSION

The azimuth angle distribution of Fig. 2 shows characteristics of a cylindrical symmetry. This is supported by the distribution of Fig. 3: On tray C2 the detected particles entered from the earth direction. Including the dip angle measurements we can deduce that all detected arrival directions are close to a plane perpendicular to the magnetic field line of -20^0 declination and -40^0 inclination (location 34^0 W and 27^0 S within the SAA).

From Table 1 we deduce a steep energy spectrum similar to the trapped proton spectrum. Together with the spatial distribution we take this as an evidence for the detection of heavy ions from a radiation belt population. Similar results were reported from Skylab by Chan and Price (ref. 1) and from Spacelab 1 by Beaujean et al. (ref. 2). At the present stage of our analysis neither flux values nor charge spectra can be given.

In addition to particles with energies < 50 MeV/Nuc we detected particles which penetrate several sheets with almost constant energy loss. The arrival directions and the energies (> 100 MeV/Nuc) are not yet determined. This particle flux is in agreement with predicted LET spectra for LDEF including cosmic rays from H to U. They are mainly produced by Fe-particles and their fragments after traversing LDEF material.

This work was financially supported by the "Bundesministerium für Forschung und Technologie" under grant 01 QV 297 and 50 OS 9001. We like to thank the DLR-Flugmedizin (Köln-Porz) for the integration of our detector foils in experiment A0015.

REFERENCES

1. J.H. Chan and P.B. Price: Composition and Energy Spectra of Heavy Nuclei of Unknown Origin Detected on Skylab; Phys. Rev. Lett. Vol. 35, #8, 539, 1975.

2. R. Beaujean, K. Oschlies and W. Enge: Components of the Low Energy Cosmic Ray Oxygen Flux Measured on Spacelab 1, SH-21, 12th ECRS, Nottingham, 1990.

Fig. 1: Track images in CR-39 of M0002 (E6)

Table 1:
Number of stopping particles in the topmost foils of M0002 (E6).
The range intervalls, the mean range R and the corresponding energy intervalls and the mean energy E are calculated for a 45^0 incident angle.

	stopping tracks / cm^2	$\overline{R}$ [μm]	$\overline{E}$ [MeV/Nuc] O^{16}	$\overline{E}$ [MeV/Nuc] Fe^{56}
Foil 1	3.0±0.35 [1)]	295 $\binom{154-}{546}$	10.8 $\binom{7.3-}{15.5}$	17.7 $\binom{11.2-}{26.3}$
Foil 2	0.3±0.05 [2)]	710 $\binom{546-}{1050}$	18.0 $\binom{15.5-}{22.5}$	31.0 $\binom{26.3-}{39.5}$
Foil 3	0.1±0.03 [3)]	1210 $\binom{1050-}{1554}$	24.5 $\binom{22.5-}{28.0}$	43.0 $\binom{39.5-}{49.0}$

1) 75 stopping tracks / 25 cm^2 ;
2) 30 stopping tracks / 100 cm^2 ;
3) 10 stopping tracks / 100 cm^2 ;
} Poissonian error; scanning efficiency not included

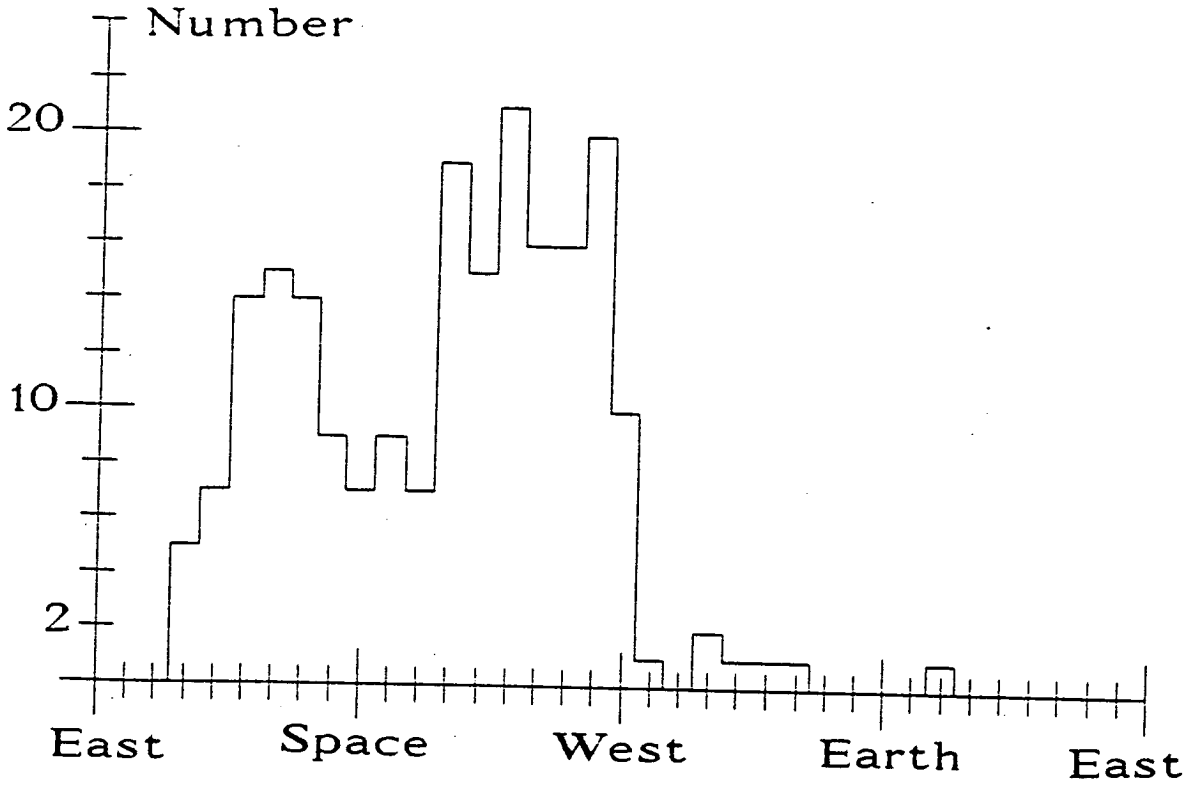

Fig. 2: The azimuth angle distribution of 212 particles entering foil 1 of M0002 (E6)

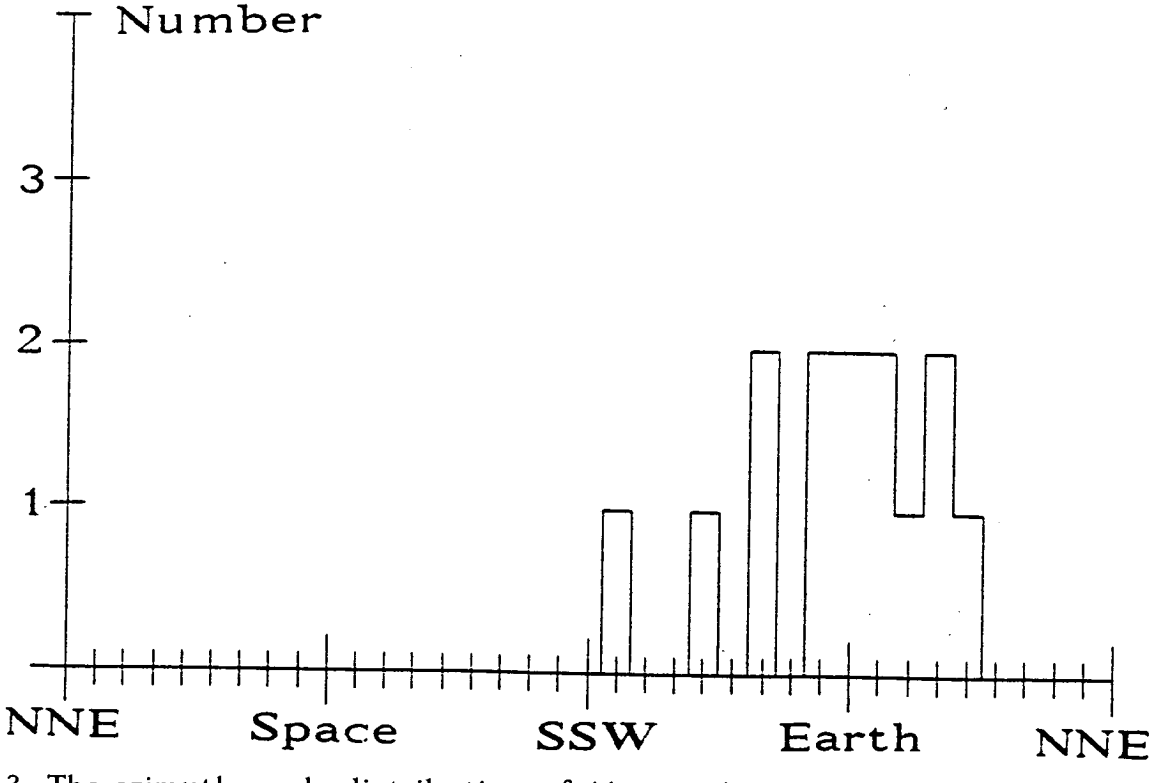

Fig. 3: The azimuth angle distribution of 14 particles entering A0015 (C2)

SPACE ENVIRONMENTS

METEOROID AND DEBRIS

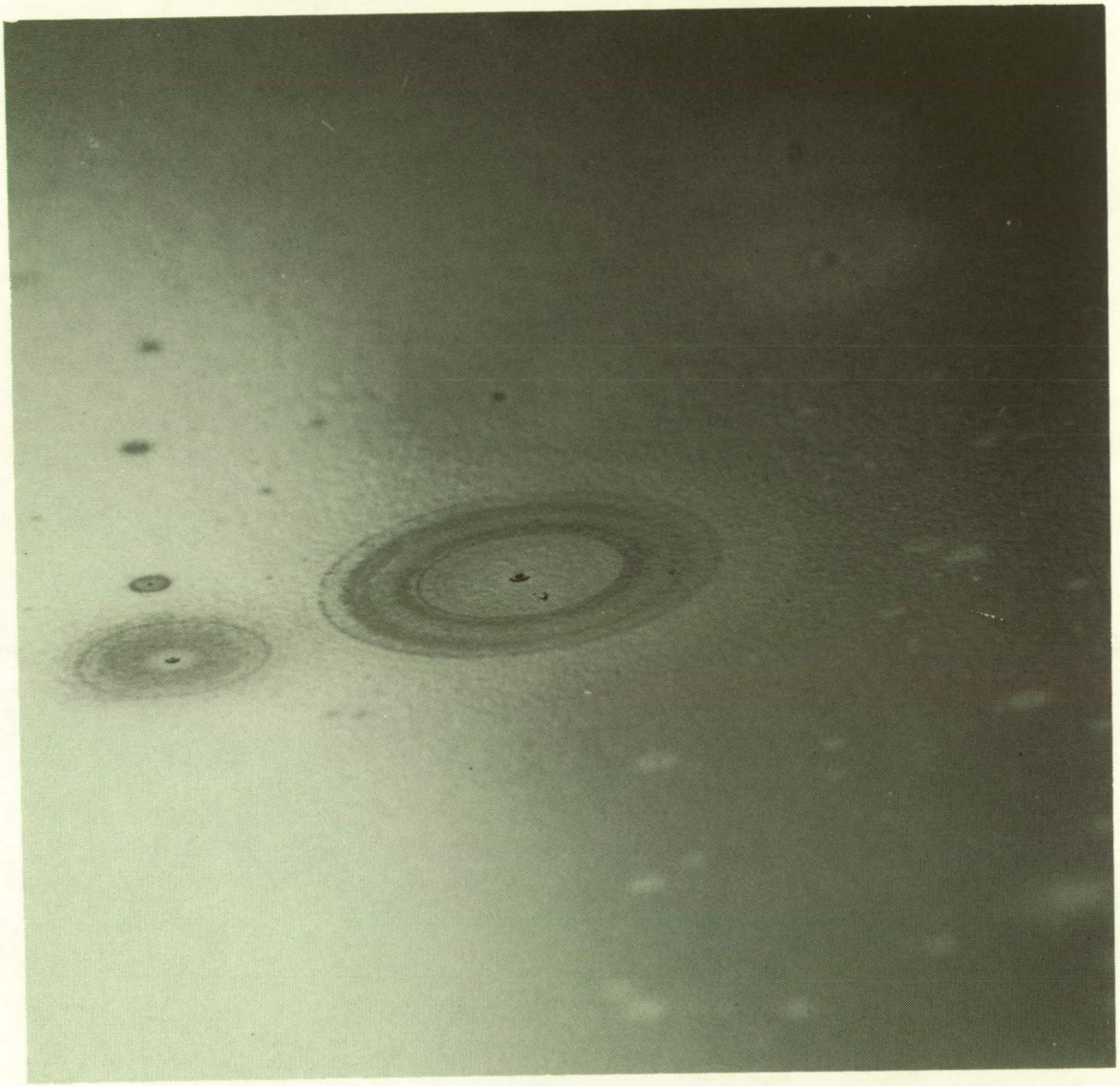

LARGE CRATERS ON THE METEOROID AND SPACE DEBRIS IMPACT EXPERIMENT

Donald H. Humes
NASA Langley Research Center
Hampton, VA 23665-5225
Phone: 804/864-1484, Fax: 804/864-7730

SUMMARY

Examination of 29.37 m^2 of thick aluminum plates from the Long Duration Exposure Facility, which were exposed to the meteoroid and man-made orbital debris environments for 5.8 years, revealed 606 craters that were 0.5 mm in diameter or larger. Most were nearly hemispherical. There was a large variation in the number density of craters around the three-axis gravity-gradient stabilized spacecraft. A new model of the near-Earth meteoroid environment, which uses a speed distribution proposed by Erickson and a direction distribution relative to the Earth, gives good agreement with the crater fluxes measured on the fourteen faces of the LDEF. The man-made orbital debris model of Kessler, which predicts that 16 percent of the craters would be caused by man-made debris, is plausible. No chemical analyses of impactor residue that will distinguish between meteoroids and man-made debris is yet available.

INTRODUCTION

For nearly six years, the Long Duration Exposure Facility (LDEF) orbited the Earth with 57 scientific experiments on board that were to be evaluated when the spacecraft was returned to the ground. There was no communication with the LDEF while it was in orbit. The Meteoroid and Space Debris Impact Experiment, designated S0001 by the LDEF Project Office, consisted of many thick aluminum plates distributed around the spacecraft to study the population, directionality, and chemical composition of meteoroids and man-made debris. All the data will be obtained from examination of the craters left in the aluminum plates.

In some places in the literature this experiment is referred to by a shortened title as the Space Debris Impact Experiment.

Meteoroids are small interplanetary particles that travel through our solar system undetected and whose encounter can only be treated statistically. They are natural particles that are in orbit about the sun. Meteoroids that pass near the Earth are drawn toward the Earth by its gravitational field and some strike spacecraft as they speed toward the atmosphere. Meteoroids have been considered a hazard to spacecraft since the beginning of space exploration. NASA has published models of the meteoroid environment near the Earth (ref.1) and in interplanetary space (ref.2), and a design criteria document for protection against meteoroids (ref.3). But the interest in meteoroids is broader than the concern about the hazard they present to spacecraft. Meteoroids may be unaltered primal material whose composition and orbital paths are important clues to the origin and evolution of the solar system.

Space debris is the man-made material left in space as a result of our space activity. It ranges in size from microscopic fragments created during explosions in space to large spent rocket motors. Some man-made debris escaped the Earth's gravity but most was left in orbit about the Earth. That space debris that is still in orbit about the Earth is of concern as a potential hazard to spacecraft. Large pieces of debris are tracked and cataloged and possible collisions with the Space Transportation System (STS) orbiter are checked for each mission so that evasive measures can be taken if necessary. Small pieces cannot be tracked and their encounter, like that of meteoroids, must be treated statistically. NASA now has a model of the man-made orbital debris environment (ref.4) to be used in hazard analysis.

The Meteoroid and Space Debris Impact Experiment is directed at both the hazard of impact damage and the nature of our solar system but this preliminary paper will deal primarily with the data most applicable to the hazard, i.e. the number and location of the large craters. All craters with diameters of 0.5 mm and greater (measured across the top of the raised lips) have been examined and their number density and distribution around the spacecraft is the primary topic of this report. The study of smaller craters is incomplete and they are referred to only briefly. No chemical analyses of the impacting particles is presented.

The LDEF maintained a three-axis gravity-gradient stable orientation, which provided a new level of sophistication in flight data on meteoroids and man-made debris. In previously obtained flight data in near-Earth space, see ref.1, the number of meteoroid impacts was obtained but the orientation of the impact site at the time of the impact was unknown. The number density of craters for the different fixed surface orientations provides a direct measurement of the degree to which the hazard to spacecraft is directional. The variation in the number density of craters with surface orientation depends on the orbital distribution of the particles. While the orbits of individual particles cannot be determined with this experiment, theoretical orbital distributions can be checked by seeing if they are in agreement with the crater distribution found on the LDEF.

Some aluminum plates donated to the LDEF Meteoroid and Debris Special Investigation Group (M&D SIG) by principal investigators of other LDEF experiments were examined and the results are included in this paper. Wayne Slemp donated the base plates, sample holders and cover plates from his experiment on the only side of the LDEF from which the Meteoroid and Space Debris Impact Experiment plates were missing. His contribution is especially significant because that side of the LDEF received the greatest concentration of impact craters. William Berrios donated a thermal panel from the space-facing end of the LDEF.

The dummy plates that covered two unused experiment compartments on the Earth-facing end of the LDEF were also examined and the results are included in this paper.

EXPERIMENTAL HARDWARE

The Meteoroid and Space Debris Impact Experiment exposed 26.32 m^2 of aluminum plate to the space environment. The plates were 4.8 mm thick and were made of aluminum alloy 6061-T6. They had a thin oxide layer on both sides produced by chromic anodization and a coat of black paint on the back for spacecraft thermal control.

The location of the Meteoroid and Space Debris Impact Experiment plates on the LDEF is shown in Fig.1 along with the location of the other hardware examined in this study. The plates were mounted on the bottom of the 7.6 cm deep trays, except for the plates in Tray D6, which were mounted even with the top of the tray.

The nineteen peripheral trays that were totally dedicated to this experiment had two plates measuring 0.62 m by 0.95 m in each tray. The three peripheral trays that were shared with other experiments had two plates measuring 0.41 m by 0.95 m in each tray. These individual plates are identified by the tray location number and the relative position of the two plates in the tray. For example, the two plates in the tray in location F10 are identified as plates F10G and F10H, with F10G being the plate nearest the G-end or Earth-facing end of the LDEF. The three end trays each contained a single plate that was 0.72 m by 0.72 m.

The plates donated by Wayne Slemp were from his B9 tray. They are anodized aluminum, 6061-T6, of various thicknesses from 1.6 mm to 6.4 mm and have an area of 0.62 m^2. The experiment was divided neatly into thirds in the tray (see Fig.2) and for the purposes of this report all the plates in the third nearest the Earth-facing end will be referred to as the B9G plates, those in the third nearest the space-facing end as the B9H plates, and those in the middle third as the B9M plates.

The thermal panel donated by William Berrios was anodized aluminum (6061-T6), 1.6 mm thick. It was attached to the space-facing end of the LDEF and had an edge that was bent to wrap around the corner of the spacecraft along the Row-6 side. Only the 0.63 m^2 of the thermal panel that was on the space-facing end is included as a part of this report. This thermal panel is identified as 920-6F by the LDEF Project Office and as H19 by the LDEF M&D SIG.

The two dummy plates on the Earth-facing end were anodized aluminum (6061-T6), 2.3 mm thick. Each plate had an area of 0.90 m^2. One was identified as G19-9 by the LDEF Project Office and as G9 by the LDEF M&D SIG, and the other as G21-3 by the LDEF Project Office and as G3 by the M&D SIG.

LDEF MISSION

The LDEF was deployed by the STS-41C crew on April 7, 1984. It was initially placed in a near-circular orbit with an apogee of 480 km, a perigee of 474 km, and an inclination of 28.5 degrees. By the time it was recovered by the STS-32 crew on January 12, 1990, it had fallen to an altitude of 331 km.

It was intended for the longitudinal axis of the spacecraft to be aligned with its Earth-centered position vector and for the normal to the Row 9 trays to be aligned with the velocity vector. Post-flight analysis showed that the actual orientation had a misalignment of about eight degrees in yaw and one degree in pitch, see ref.5. As a result, the leading edge of the LDEF was between Row 9 and Row 10. The one degree pitch angle gave the space-facing end a slight view of the forward direction of flight.

DESCRIPTION OF CRATERS

The craters in aluminum on the LDEF look very much like craters produced with hypervelocity accelerators in the laboratory at impact speeds greater than about 6 km/s. The craters are generally round with lips that rise above the surface of the plate. The photograph in Fig.3 shows the top view of a crater on the F10H plate. This 4 mm diameter crater is the largest on any of the Meteoroid and Space Debris Impact Experiment plates and is the largest crater examined in this study. A side view of another crater on the F10H plate is shown in Fig.4. The lips of this 2 mm diameter crater are touching, or nearly touching, the surface of the plate, which reflects their image at the extreme angle at which the photograph was taken.

Most of the craters are round and symmetric, which is surprising considering that the impacting particles were undoubtedly irregular in shape and must have struck at oblique angles. The dimensions of 27 large craters are given in Table I. Three measurements, the diameter at the top of the raised lips, the depth, and the diameter at the plate surface, were made. The diameter at the plate surface is considered to be a more fundamental dimension than the diameter at the top of the raised lips, but it is more difficult to measure and sometimes in the literature authors give only the lip diameter. Henceforth in this report "diameter" will refer to the diameter at the surface of the plate, which some refer to as the true diameter, and "lip diameter" will refer to the diameter at the top of the raised lips.

Nine of the craters in Table I were on the plates in the F3 tray. In general, the lowest impact speeds should occur on these plates because they are closest to the trailing edge of the spacecraft and the particles must catch up to the spacecraft to strike them. Nine of the craters were on the F10 plates. In general, very high speed impacts should occur on these plates because they are close to the leading edge of the spacecraft where head-on collisions occur. Despite the fact that the extreme differences in impact speed occur on the F3 and F10 plates, there is no noticeable difference in the shape of the craters. The other nine craters in Table I were on the H5 plate, which was on the space-facing end of the LDEF where impact speeds are intermediate. At all three locations, the diameter of the craters at the plate surface is about 0.75 times the diameter at the top of the raised lips. The depth of the craters is about 0.5 times the diameter at the plate surface, i.e. the craters are nearly hemispherical.

While the study of smaller craters, <0.5 mm lip diameter, on this LDEF experiment is not complete, many small craters on the F10H and H5 plates have been measured. Differences in the craters seem to be appearing at smaller sizes. Firstly, the small craters are not all round, i.e. they do not have a circular cross-section at the surface of the plate. About one percent of the craters measured to date on the F10H plate are oblong with the shortest axis being less than 0.7 times the longest axis. On the H5 plate, six to eight percent of the craters measured to date are that oblong. Secondly, the average depth-to-diameter ratio of the small round craters on the F10H plate is greater than that of the large craters, being about 0.55 for those craters measured to date that have lip diameters between 0.1 mm and 0.5 mm, and about 0.63 for those that have lip diameters less than 0.1 mm. The small round craters on the H5 plate have the same average depth-to-diameter ratio as the large craters on that plate.

There were no craters on any of the plates examined that penetrated through the entire thickness of the plate. The impact that created the largest crater on the Meteoroid and Space Debris Impact Experiment, the 4 mm crater on the F10H plate, produced a very short raised dome on the back of the 4.8 mm thick plate. The dome was less than 25 microns high. It is not known if it is just the black paint that delaminated and raised up or whether the aluminum plate is actually bulged. The two thinnest donated plates from Row 9 had a total of four craters in the 1.6 mm thick aluminum that caused the back of the plates to bulge. The 1.6 mm thick thermal panel from the space-facing end did not have any craters that produced a noticeable bulge on the back of the plate; however, the black paint on the back would make it more difficult to spot a bulge than on the unpainted plates from Row 9.

NUMBER AND LOCATION OF CRATERS

There were 532 craters on the Meteoroid and Space Debris Impact Experiment plates that had a lip diameter of 0.5 mm or greater. There were another 74 craters of that size on the other LDEF plates included in this study. The distribution of these 606 craters around the spacecraft is given in Table II. The orientation of the plates on the sides of the LDEF is given by the angle between the spacecraft velocity vector and the normal to the plate surface. The trays on each row are grouped together because the flux should be constant along a row for both meteoroids and man-made debris. The area of the plates is the actual area. No correction has been made for the shielding that occurs for the plates that were mounted on the bottom of the 7.6 cm deep trays.

The variation in crater flux with plate location is shown in Fig.5. The crater flux is the number density of craters divided by the duration of the mission. The flux is greatest near the front of the spacecraft and it decreases smoothly toward the back, except on the plates nearest the trailing edge where the flux increases again. The variation in the measured crater flux on the sides of the LDEF exceeds a factor of 20.

The error bars, which are the 90 percent confidence limits calculated using the chi-squared distribution function in the manner suggested in ref.6, are appreciable because of the small number of craters, especially near the back of the LDEF. It may be that the increase measured near the trailing edge is just a statistical variation. When the examination of these plates is complete, there probably will be more than 30,000 craters to consider and then, perhaps, it will be clear whether the increase in the flux near the trailing edge is real.

The data points in Fig.5 are alternately from the south-facing and the north-facing side of the spacecraft. The smoothness of the data shows that there is a north/south symmetry in the particulate environment in the size range considered in this report.

The flux on the space-facing end is about the same as it would be for a plate on the side of the LDEF that faces 60 degrees from the velocity vector and is about twice that for a plate on the side facing 90 degrees from the velocity vector.

The data points in Fig.5 are the average flux for each face. In most cases, all of the trays or plates on the same face give the same flux within the 90 percent confidence limits. The exception is the B9G and B9M groups of plates which were side-by-side but which differed by more than a factor of 3.3 in crater flux.

COMPARISON WITH CURRENT NASA MODELS

Meteoroids

The NASA model of the near-Earth meteoroid environment in ref.1 is a simple model that assumes that all meteoroids strike a spacecraft normal to the surface and at a speed of 20 km/s. A speed distribution for the meteoroids is given in ref.1, but the direction from which the meteoroids approach the spacecraft is not defined so that the model is used to calculate the average flux on a randomly tumbling spacecraft. It is not suitable for calculating the variation in flux around the LDEF. It could, of course, be used to calculate the number of craters that would be expected on a randomly tumbling LDEF.

The model gives the flux of meteoroids on a spacecraft as a function of mass although meteoroid mass was not measured directly in any of the experiments on which the model is based. Data from the Explorer 16, Explorer 23, and the Pegasus satellites, where the penetration rate for various detector thicknesses was obtained, provided much of the basis for the model. This data was converted to meteoroid mass using eq.1, an empirical equation that gives the thickness t, in cm, of a sheet of material that can be completely penetrated by a particle of mass m, in g, having a density ρ, in g/cm^3, when the impact speed is V_r, in km/s.

$$t = K_1 \, m^{.352} \, \rho^{1/6} \, V_r^{.875} \qquad (1)$$

The coefficient K_1 is a material constant equal to 0.54 for aluminum sheets. The model should provide excellent predictions of the penetration fluxes for thin sheets on randomly tumbling surfaces if the same

penetration equation originally used to convert the penetration data to meteoroid mass is used to convert meteoroid mass back to penetration capability. If a more accurate penetration equation is found and is used with the model, it will give the wrong meteoroid penetration flux.

However, the LDEF data presented in this report is not the number of penetrations through some thin sheet of material, but is instead, the number of craters above a given size in a thick plate. Therefore an equation is needed that gives the size of a crater produced by a meteoroid. The accuracy with which the model in ref.1 can predict the flux of craters above a given size depends on the relationship between this crater size equation and the penetration equation originally used to convert the flight data to meteoroid mass. The important thing is not whether the crater size equation is accurate but whether the ratio of crater size predicted to penetration thickness predicted by the original equation is correct. Of course, the goal is to obtain accuracy in both equations and in the meteoroid model. It must be remembered, however, that when a better equation for penetration thickness is obtained, the model will have to be revised correspondingly.

With only modest expectations then, the average flux of craters with a lip diameter of 0.5 mm or greater was calculated for a hypothetical randomly tumbling LDEF, using the near-Earth meteoroid environment model in ref.1 and the crater depth equation from ref.3, which for an aluminum plate is

$$P = 0.42\ m^{.352}\ \rho^{1/6}\ V_r^{2/3} \qquad (2)$$

where m is the particle mass, in g, ρ is the mass density of the particle, in g/cm^3, V_r is the speed, in km/s, and P is the crater depth from the surface of the plate, in cm. The depth of a crater having a lip diameter of 0.5 mm would be about 0.1875 mm (0.5 mm x 0.75 x 0.5), assuming the average crater shape seen in Table II. Using an average impact speed of 20 km/s and an average mass density for meteoroids of 0.5 g/cm^3, as suggested in ref.1, eq.2 gives a meteoroid mass of 7.0×10^{-7} g. The average flux of meteoroids of that mass and greater on a randomly tumbling spacecraft orbiting at an altitude of 477 km is, according to ref.1, 7.0×10^{-8} m^{-2}s^{-1}. For the 29.37 m^2 of aluminum plate considered in this study and the 1.82×10^8 s duration of the LDEF mission, that flux results in a predicted 374 meteoroid craters.

Man-made Orbital Debris

The man-made orbital debris model in ref.4 is more detailed than the meteoroid model in ref.1. It gives the velocity distribution of debris relative to a spacecraft, both speed distribution and direction distribution, and therefore predicts a crater flux that varies with location on the spacecraft.

This model gives the flux of man-made debris on a spacecraft as a function of particle diameter. The model is based on radar and optical measurements of orbiting objects where radar cross-section and optical intensity is measured and converted to particle size, and on penetration and crater size data from samples returned from the Solar Max spacecraft where penetration thickness and crater dimensions, for those impacts caused by man-made debris, were converted to particle diameter using empirical penetration equations and an assumed particle density. Man-made debris craters were identified by chemical analyses of impactor residue found in the craters.

This man-made orbital debris model assumes that the debris is in circular orbits and predicts that the LDEF, had it flown in its planned orientation, would not have been struck by man-made debris on the space-facing end, the Earth-facing end, or on the trailing edge. Because of the one degree forward pitch

angle, the space-facing end would be predicted to receive a small number of impacts. The flux of the man-made debris craters around the LDEF having diameters of 0.5 mm or greater, as predicted by the model in ref.4, is shown in Fig.6. Equation 3 was used to determine the mass of the debris required to make a 0.01875 cm deep crater. It is identical to eq.2 except that the effect of the impact angle is included.

$$P = 0.42\ m^{.352}\ \rho^{1/6}\ V_r^{2/3}\ (\cos\theta)^{2/3} \qquad (3)$$

The angle θ is the impact angle measured from the normal to the surface. It is stated in ref.3 that the crater depth depends on the impact angle, correlating with the normal component of velocity for impact angles within 60 degrees of the normal. While mentioned in the text in ref.3, this impact angle effect was not included in the equations presented. The use of the normal component of velocity to predict crater depth is common and may have been used to convert the Solar Max data to debris mass in the man-made orbital debris model.

If the man-made orbital debris model is accurate, man-made debris must have created about one-fourth of the large craters on the Row 6 plates, about 11 percent of those on the Row 9 plates, and much less than one percent of the craters on the Row 3 and Row 4 plates. The variation in the crater flux with the location on the spacecraft predicted by the man-made debris model is quite different from that found on the LDEF. This further suggests that meteoroids do indeed dominate the particulate environment in this size range. The model predicts 94 man-made debris craters with a lip diameter of 0.5 mm or greater on the LDEF surfaces being considered in this study, which is 16 percent of the number actually found on the LDEF.

Combined Models

The total number of meteoroid and man-made orbital debris craters predicted by the models is 468. The calculated number is lower than the actual number on the LDEF, perhaps because the oriented surfaces considered in this study do not approximate well a randomly tumbling plate of equal area, thus producing an error in the calculation of the meteoroid flux, or perhaps because the crater depth equation and the penetration thickness equation do not provide the proper relationship between the crater size a particle can produce and the thickness of material it can completely penetrate. It is clear, however, that a different type of meteoroid model is needed, one that gives the variation in flux with surface location or orientation.

NEW MODEL OF THE NEAR-EARTH METEOROID ENVIRONMENT

Approach

The deficiency in the current model of the near-Earth meteoroid environment (ref.1) is that the directionality of the meteoroids is not defined. The first approach taken in establishing a new model was to assume that meteoroids would approach a stationary spacecraft from all directions not shielded by the Earth with equal probability; i.e. the directionality of the meteoroids is random. There is some theoretical basis for such an assumption. Kessler showed in ref.7 that, averaged over the entire Earth, the distribution of the angles at which meteoroids enter the atmosphere is random, and Zook argues in ref.8 that for a long mission, the LDEF mission in particular, a spacecraft is in so many positions relative to the Earth, and the Earth is in so many positions relative to the sun that a large portion of space is viewed and that meteoroids appear to approach the position of the spacecraft with random directionality when all impacts over the duration of the mission are taken together.

In the very first model tested here, it was assumed that meteoroids would approach a stationary spacecraft randomly from all directions in the half-space above the spacecraft horizontal plane, i.e. the plane through the spacecraft position that is perpendicular to the zenith/nadir line. When spacecraft motion was taken into account, the model predicted well the flux on all fourteen faces of the LDEF.

However, when the model was expanded to include the regions of space below the horizontal plane that are not shielded by the Earth and its atmosphere, as it should be, agreement with the LDEF data was not quite as good. The flux predicted for the twelve sides of the LDEF was good but the flux predicted for the space-facing end was too low by more than 30 percent, which exceeds the 90 percent confidence limits for the data. It appears that the assumption of random directionality may not be completely accurate.

No attempt was made to understand theoretically the cause of the discrepancy. But, in order to provide a model of the near-Earth meteoroid environment that does not underestimate the meteoroid flux on a space-facing surface, directionality distributions that are skewed toward the zenith were tested, even though they have no basis in theory. The zenith distance, z, is the angle measured from the zenith to the direction from which a meteoroid would approach a stationary spacecraft. Values of the distribution constant C for a zenith distance distribution function f(z) of the form

$$f(z) = \sin(Cz) \tag{4}$$

were tested to see if there was some value for which the model would accurately predict the fluxes on all fourteen faces of the LDEF. A value of 1.4 provided good agreement with the LDEF data. For a random distribution of meteoroid directions, C would have a value of one. When many more craters are included in the analysis, the random directionality will be re-examined, but for the time being, an artificial distribution of meteoroid directions is proposed for the new model of the near-Earth meteoroid environment.

The new model retains the essential elements of the previous model, i.e. the size distribution, mass density, and gravitational enhancement of the meteoroid flux near the Earth. The Earth shielding factor found in ref.1 and ref. 2 is not included as a separate factor because it is inherent in the directionality assumption.

The spatial density of meteoroids, i.e. the number of meteoroids per unit volume, is a concept introduced in the interplanetary meteoroid environment model in ref.2 that is also used in this model. Spatial density can be inferred in ref.1 from the flux and average velocity, but it was not developed there as a property of the meteoroid environment.

The crater depth equation from ref.3, with the effect of impact angle included (eq.3), is accepted here and thus becomes an integral part of this new near-Earth meteoroid environment model.

Different meteoroid speed distributions, direction distributions, and spatial densities were examined and the combination that gave the best agreement with the crater flux found on the various faces of the LDEF was selected.

It is assumed that the size distribution, speed distribution and the direction distributions of the meteoroids are all independent of each other.

Some details of the proposed new model of the near-Earth meteoroid environment are given in the following five sections.

Directionality

The probability density for meteoroids approaching a spacecraft position with a zenith distance, z, is taken to be

$$f(z) = \sin(1.4\,z) \Big/ \int_{0^\circ}^{128.6^\circ} \sin(1.4\,z)\,dz \qquad 0^\circ \le z < 128.6^\circ \qquad (5)$$

$$f(z) = 0 \qquad 128.6^\circ \le z \le 180^\circ \qquad (6)$$

The probability of meteoroids approaching a spacecraft from within 51.4 degrees of the spacecraft/Earth line becomes zero. Thus the Earth shielding is effectively constant for all altitudes above 2000 km. For spacecraft below an altitude of 2000 km, the shielding from meteoroids provided by the Earth and its atmosphere, assumed to be 165 km high, varies with altitude.

Two angles define the meteoroid directionality, the zenith distance is one, the azimuth is the other. The azimuth is the angle from a reference direction in the horizontal plane of the spacecraft. The probability density for meteoroids approaching a spacecraft with an azimuth, a, is independent of a and is

$$f(a) = 1/360 \qquad 0^\circ \le a \le 360^\circ \qquad (7)$$

Speed Distribution

The speed distribution of meteoroids, as given in refs.1,9,10 and 11, is the speed distribution of meteors observed in the Earth's atmosphere corrected to a constant meteoroid mass. It gives the fraction of the meteoroid flux on the atmosphere that is in various speed ranges. There is a bias in the observational data of meteors toward the faster meteoroids because they produce more easily detected radar and optical trails. As a result, smaller and more numerous meteoroids are observed at the higher velocities. The differences in the speed distributions from refs.1,9,10 and 11 are caused largely by the methods used to extract this bias from the data and get the speed distribution for constant mass meteoroids.

Because the concept of spatial density is being used in this new model, the speed distribution of meteoroids in a volume of space is required, and that is different from the speed distribution of the meteoroid flux on the atmosphere. For a unidirectional flow of particles, the relationship between the spatial density, S, and the flux, ϕ, on a surface perpendicular to the flow direction is

$$\phi = S\,V \qquad (8)$$

where V is the speed. Thus the speed distribution of meteoroids striking the atmosphere can be

transformed to the speed distribution of meteoroids in a volume of space just outside the atmosphere with the relationship

$$f(V) = (f_\phi(V)/V) / \int_V f_\phi(V)/V \, dV \qquad (9)$$

where f(V) is the probability density for meteoroids in a volume of space having speed V, and $f_\phi(V)$ is the probability density for meteoroids striking the atmosphere with speed V.

The speed distributions from refs.1,9,10,and 11 were tested in the new model. The speed distribution from ref.1 has more high speed meteoroids than the others and does not give enough variation in crater flux around the LDEF, while the speed distribution in ref.9 has an abundance of very low speed meteoroids and gives too great a variation in crater flux. The speed distributions found to provide the best agreement with the crater distribution found on the LDEF are those proposed by Erickson (ref.10) and by Kessler (ref.11). These independently derived distributions, which used different sets of meteor data, are nearly identical. A mathematical description of the Erickson speed distribution is given by Zook in ref.12 as

$$f_\phi(V) = 0.112 \qquad 11.1 \leq V < 16.3 \text{ km/s} \qquad (10)$$

$$f_\phi(V) = 3.328 \times 10^5 \, V^{-5.34} \qquad 16.3 \leq V < 55 \text{ km/s} \qquad (11)$$

$$f_\phi(V) = 1.695 \times 10^{-4} \qquad 55 \leq V \leq 72.2 \text{ km/s} \qquad (12)$$

where $f_\phi(V)$ is the probability density for meteoroids entering the atmosphere with speed V, in km/s. These equations also describe the Kessler speed distribution.

Density

The mass density of 0.5 g/cm^3 for meteoroids, given in both ref.1 and ref.2, is adopted for the new model.

Gravitational Focusing

The flux of meteoroids on a spacecraft is enhanced by gravitational focusing, so that the closer the spacecraft is to the Earth, the greater the meteoroid flux tends to be. In this new model, as in ref.2, the flux on a spacecraft is calculated, firstly, ignoring gravitational focusing, and then, that flux is multiplied by the gravitational enhancement factor, G, which from ref.2 is

$$G = 1 + 0.76 \, (r_e/r) \qquad (13)$$

where r_e is the radius of the Earth and r is the distance of the spacecraft from the center of the Earth.

Spatial Density and Size Distribution

The spatial density of meteoroids used in the new model is 2.33 times the spatial density given in ref.2 at 1 AU, thus preserving the size distribution of meteoroids inherent in the spatial density function. The spatial density, S, in no./m^3, is therefore taken to be

$$\log_{10}S = -17.775 - 1.584 \log_{10}m - 0.063 (\log_{10}m)^2 \qquad m \leq 10^{-6}\,g \qquad (14)$$

$$\log_{10}S = -17.806 - 1.213 \log_{10}m \qquad m > 10^{-6}\,g \qquad (15)$$

where m is the meteoroid mass, in g.

Using the Model to Calculate Crater Flux

Meteoroids that approach a spacecraft from some small region of space, with speeds in the small speed range around V, will produce a crater in an aluminum plate that is deeper than P, if their mass exceeds m, where

$$m = P^{2.84} / ((0.42)^{2.84} \rho^{.473} V_r^{1.894} (\cos\theta)^{1.894}) \qquad (16)$$

and where V_r is the relative speed between the spacecraft and the meteoroid and θ is the impact angle on the plate relative to the normal to the plate surface. This is eq.3 with the terms rearranged. The spatial density of meteoroids of mass m and greater is obtained from eq.14 or eq.15. The flux of meteoroids of mass m and greater on the plate, and hence the flux of craters of depth P and deeper, from this small component of the meteoroid environment is

$$\Delta\phi = G\,S\,V_r \cos\theta\, f(z)\Delta z\, f(a)\Delta a\, f(V)\Delta V \qquad (17)$$

where Δz is the size of the zenith distance range and Δa is the size of the azimuth range of the region of space being considered, and ΔV is the size of the speed range being considered. The meteoroid velocity relative to the spacecraft, and relative to the Earth, both appear in this equation.

The total flux of craters from the entire meteoroid environment is obtained by summing the contributions to the flux from all speed ranges and from all regions of space not shielded by the Earth. Care must be taken to make sure that the proper units are used in eq.17 where V has been expressed in km/s and S in m^{-3}, and one must be converted to make the length units consistent.

Comparison with the LDEF Data

The crater flux predicted by the new near-Earth meteoroid environment model of this paper for the fourteen faces of the LDEF is shown in Fig.7. The agreement with the data is excellent with the exception of the face nearest the trailing edge. The disagreement for the Earth-facing end is not significant because the measured flux is based on only one crater.

Comparison with Pegasus Data

While the LDEF provides the best data on meteoroid impacts on an orbiting spacecraft, some consideration should be given to the flight data used to form the original near-Earth meteoroid environment model in ref.1, particularly the data from the 406-micron-thick aluminum penetration detectors on the Pegasus satellite. The penetration flux for that detector was 5.6×10^{-8} penetrations/m^2s (ref.13). The value of 8.0×10^{-8} $m^{-2}s^{-1}$ that appears in ref.1 is a hypothetical flux derived from the Pegasus data for the case of an Earth with a gravitational field but no size to shield the spacecraft from meteoroids.

The accuracy with which the new near-Earth meteoroid environment model will predict the Pegasus penetration flux depends on the relationship between the penetration thickness equation selected and the crater depth equation that is an integral part of the new model. The equation used in ref.1 to relate meteoroid properties to penetration thickness (eq.1) does not provide good agreement with the Pegasus data when used with the new model, see Table III. It overestimates the penetration flux because it uses the impact velocity instead of the normal component of the impact velocity. Modifying eq.1 to include the effect of impact angle, improves the agreement somewhat but the penetration flux is still overestimated by a factor of 2.8, suggesting that the velocity dependence may be wrong.

A new penetration thickness equation is proposed where the velocity dependence for complete penetration is assumed to be the same as that for crater formation at meteoroid impact speeds. It is

$$t = K\, m^{.352}\, \rho^{1/6}\, V_r^{2/3}\, (\cos\theta)^{2/3} \qquad (18)$$

where K is a material constant that was determined to be 0.72 for aluminum by requiring that two conditions be satisfied. Firstly, eq.18 must predict about the same penetration thickness as eq.1 in the 5 km/s to 8 km/s speed range because eq.1 is an empirical equation derived from laboratory tests in that speed range. It agrees within 14 percent. Secondly, when eq.18 is used in the new near-Earth meteoroid environment model, the predicted flux for the Pegasus detector must be about the same as the measured flux. It agrees within 17 percent.

DISCUSSION

The new model of the near-Earth meteoroid environment predicts crater fluxes of 0.5 mm diameter and greater craters on the fourteen faces of the LDEF that are in good agreement with the measured fluxes, for the most part. The exception, for the face nearest the trailing edge, is taken to be the result of a statistical variation in the measured flux.

The new meteoroid model accounts for all the craters found on the LDEF plates studied. No adjustment has been made to make the combined meteoroid and man-made debris models predict precisely the total number of craters found on the LDEF because the accuracy of the models is not expected to be near 16 percent, i.e. the contribution from man-made debris to the total flux.

The directionality proposed for the meteoroids, specifically the zenith distance dependence, gives a greater flux on the space-facing end of the LDEF relative to the sides than a random distribution of meteoroid directions would give. When random directionality is used in this new model and the spatial density is adjusted so that 606 craters are predicted, the crater flux on the space-facing end is only 1.4×10^{-7} $m^{-2}s^{-1}$, compared to the measured flux of 2.0×10^{-7} $m^{-2}s^{-1}$. When the zenith distance probability density function given in this paper is used, the predicted crater flux on the space-facing end is 1.9×10^{-7} $m^{-2}s^{-1}$.

The fraction of the craters that were caused by man-made debris is not known. Hopefully, impacting particle residue will be found in the craters and chemical analyses will distinguish between meteoroids and man-made debris. Because the model of the man-made debris environment predicts that the debris would create only 16 percent of the craters found on the LDEF, it is entirely plausible.

REFERENCES

1. Meteoroid Environment Model - 1969 (Near Earth to Lunar Surface). NASA Space Vehicle Design Criteria (Environment). NASA SP-8013, 1969.

2. Meteoroid Environment Model - 1970 (Interplanetary and Planetary). NASA Space Vehicle Design Criteria (Environment). NASA SP-8038, 1970.

3. Meteoroid Damage Assessment. NASA Space Vehicle Design Criteria (Structures). NASA SP-8042, 1970.

4. Kessler, D.J.; Reynolds, R.C.; and Anz-Meador, P.D.: Orbital Debris Environment for Spacecraft Designed to Operate in Low Earth Orbit. NASA Technical Memorandum 100471, 1989.

5. Peters, P. N.; Gregory, J. C.: Pinhole Cameras as Sensors for Atomic Oxygen in Orbit; Application to Attitude Determination of the LDEF. NASA CP- 3134, 1992.

6. Alvarez, J.M.: Statistical Analysis of Meteoroid Penetration Data Including Effects of Cutoff. NASA TN D-5668, 1970.

7. Kessler, D.J.: A Guide to Using Meteoroid-Environment Models for Experiment and Spacecraft Design Applications. NASA TN D-6596, 1972.

8. Zook, H.A.: The Velocity Distribution and Angular Directionality of Meteoroids that Impact on an Earth-Orbiting Satellite. Lunar and Planetary Science Conference XVIII Abstracts, 1138-1139, 1987.

9. Southworth, R.B.; and Sekanina, Z.: Physical and Dynamical Studies of Meteors. NASA CR-2316, 1973.

10. Erickson, J.E.: Velocity Distribution of Sporadic Photographic Meteors. Journal of Geophysical Research, vol.7, no.12, 3721-3726, 1968.

11. Kessler, D.J.: Average Relative Velocity of Sporadic Meteoroids in Interplanetary Space. AIAA Journal, vol.7, no.12, 2337-2338, 1969.

12. Zook, H.A.: The State of Meteoritic Material on the Moon. Proceedings of the Sixth Lunar Science Conference, 1653-1672, 1975.

13. Naumann, R.J.: The Near-Earth Meteoroid Environment. NASA TN D-3717, 1966.

Table I. Dimensions of twenty-seven large craters on the Meteoroid and Space Debris Impact Experiment plates from LDEF.

Location	D_{lips}, mm	D, mm	P, mm	D/D_{lips}	P/D
F3	1.92	1.46	0.73	0.76	0.50
	1.50	1.16	0.58	0.77	0.50
	1.50	1.12	0.58	0.75	0.52
	0.97	0.72	0.37	0.74	0.51
	0.86	0.65	0.33	0.76	0.51
	0.75	0.56	0.33	0.75	0.59
	0.73	0.59	0.24	0.81	0.41
	0.64	0.45	0.24	0.70	0.53
	0.63	0.47	0.27	0.75	0.57
				0.75 ave	0.52 ave
F10	4.02	3.02	1.55	0.75	0.51
	2.04	1.58	0.75	0.77	0.47
	1.96	1.46	0.75	0.74	0.51
	1.44	1.09	0.59	0.76	0.54
	1.42	1.08	0.54	0.76	0.50
	1.34	1.02	0.48	0.76	0.47
	1.22	1.06	0.52	0.87	0.49
	1.20	0.88	0.48	0.73	0.55
	1.14	0.82	0.41	0.72	0.50
				0.76 ave	0.50 ave
H5	1.12	0.89	0.41	0.79	0.46
	0.90	0.68	0.35	0.76	0.51
	0.85	0.63	0.32	0.74	0.51
	0.84	0.62	0.38	0.74	0.61
	0.75	0.57	0.29	0.76	0.51
	0.68	0.51	0.30	0.75	0.59
	0.68	0.55	0.25	0.81	0.45
	0.66	0.53	0.23	0.80	0.43
	0.62	0.50	0.23	0.81	0.46
				0.77 ave	0.50 ave

Table II. Location on LDEF of all large craters considered in this report.

Tray	Number	Area, m^2	Orientation, deg
B1	16	1.18	112
E1	20	1.18	112
F1	9	1.18	112
B2	5	1.18	142
D2	2	0.78	142
F3	9	1.18	172
C4	2	1.18	158
E4	7	1.18	158
A5	6	1.18	128
F5	7	1.18	128
A6	11	1.18	98
B6	16	1.18	98
D6	13	0.78	98
C7	32	1.18	68
E7	30	1.18	68
F7	39	1.18	68
B8G	17	0.39	38
B8H	21	0.39	38
B9G	29	0.227	8
B9M	7	0.185	8
B9H	15	0.207	8
F10G	46	0.59	22
F10H	32	0.59	22
B11	48	1.18	52
E11	50	1.18	52
F11	48	1.18	52
A12	26	1.18	82
H5	19	0.52	Space End
H19	23	0.63	Space End
G4	1	0.52	Earth End
G8	0	0.52	Earth End
G19-9	0	0.90	Earth End
G21-3	0	0.90	Earth End

Note: Orientation for trays on the sides of the LDEF is the angle between the normal to the tray surface and the spacecraft velocity vector.

Table III. Calculated penetration flux for 406-micron-thick aluminum detectors on the Pegasus satellites using the new near-earth meteoroid environment model and various penetration equations.

Penetration Equation	Source	Calculated Penetration Flux, $m^{-2}s^{-1}$
$t = 0.54\ m^{0.352}\ \rho^{1/6}\ v^{0.875}$	ref. 1	3.29×10^{-7}
$t = 0.54\ m^{0.352}\ \rho^{1/6}\ v^{0.875}\ (\cos\theta)^{0.875}$	ref. 1 (modified)	1.56×10^{-7}
$t = 0.72\ m^{0.352}\ \rho^{1/6}\ v^{2/3}\ (\cos\theta)^{2/3}$	this paper	6.55×10^{-8}

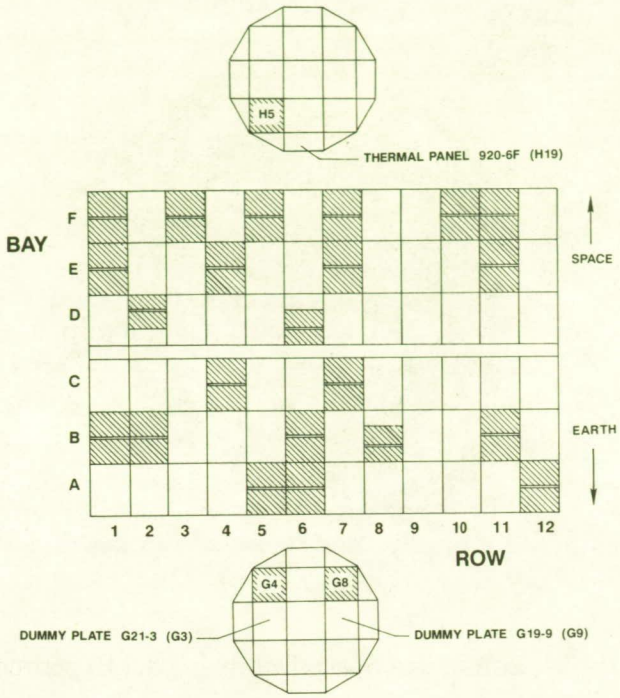

Fig. 1. Identification system used for the tray locations on the LDEF. The shaded areas show the location of the Meteoroid and Space Debris Impact Experiment plates. The location of the thermal panel and dummy plates used in this study are also shown.

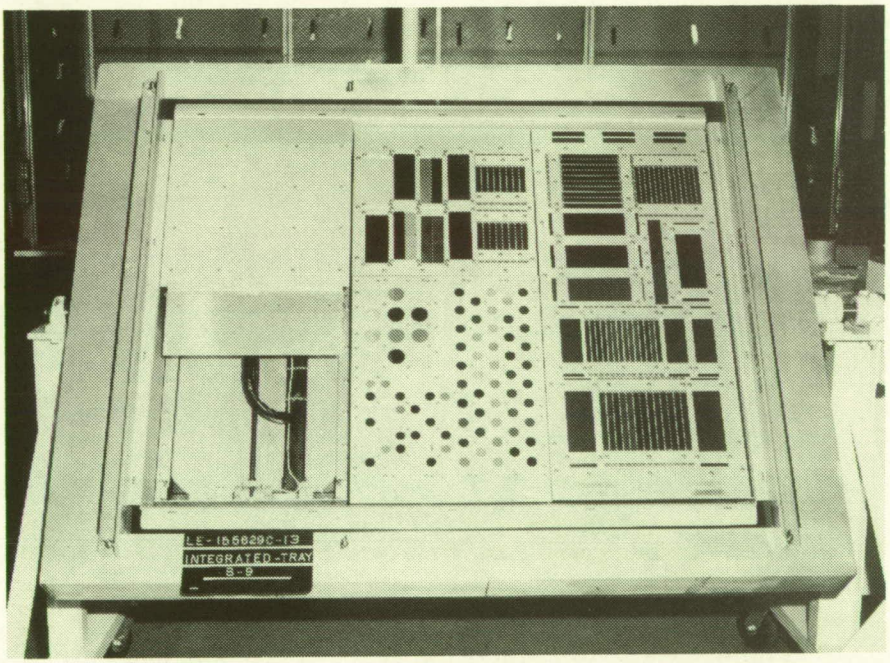

Fig. 2. Tray B9 containing aluminum plates donated by Wayne Slemp to the LDEF M&D SIG that were examined and included in this study.

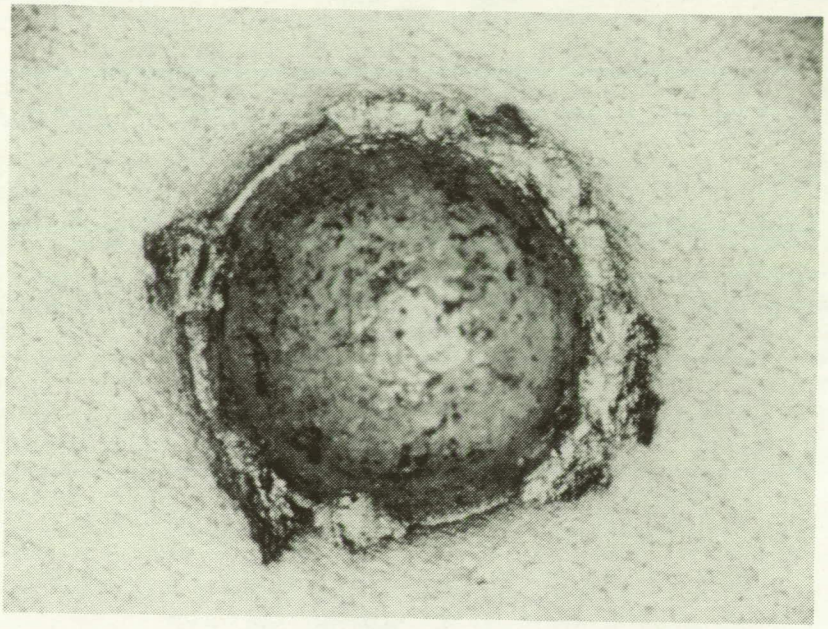

Fig. 3. Largest crater on the Meteoroid and Space Debris Impact Experiment. A 4 mm diameter crater on plate F10H.

Fig. 4. Side view of a 2 mm diameter crater on plate F10H.

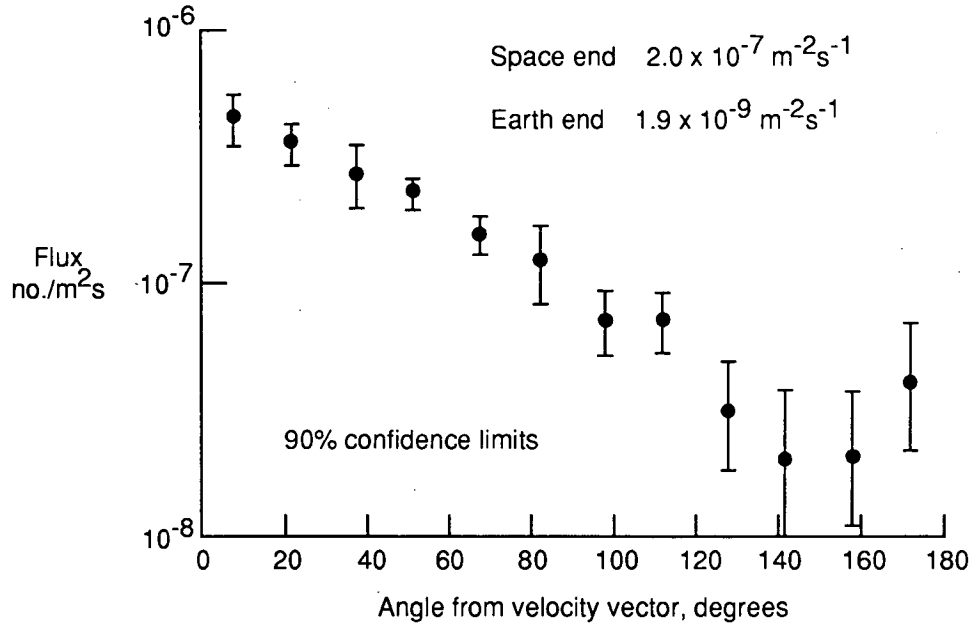

Fig. 5. Measured crater flux around the LDEF for craters with a lip diameter of 0.5 mm or greater.

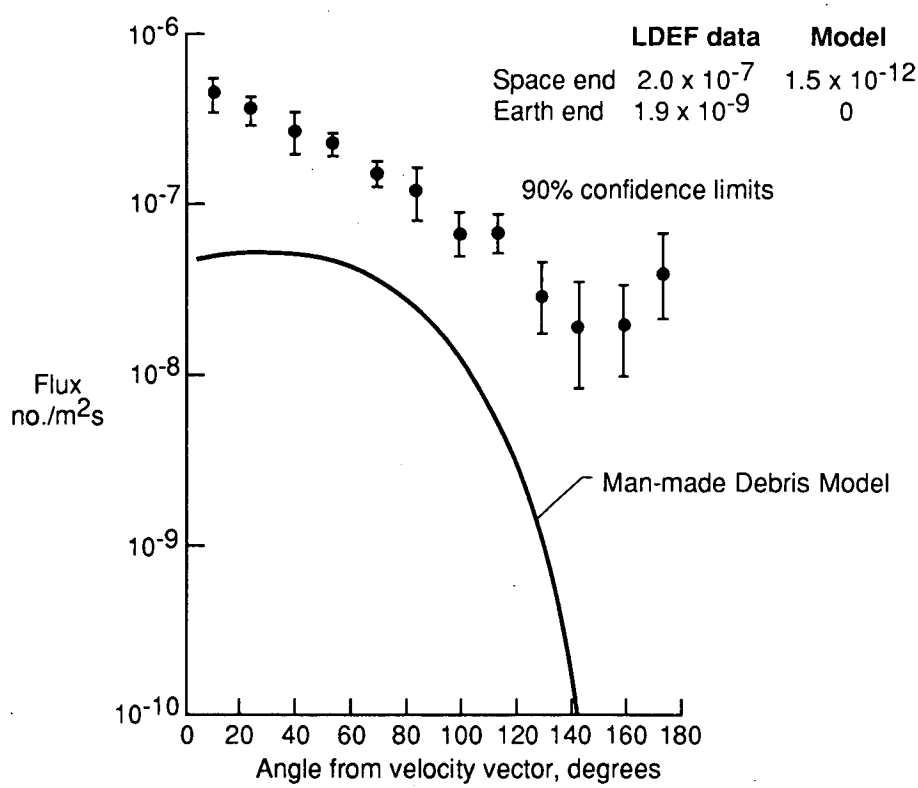

Fig. 6. Predicted crater flux from man-made orbital debris using the model in ref. 4 by Kessler, for craters with a lip diameter of 0.5 mm or greater.

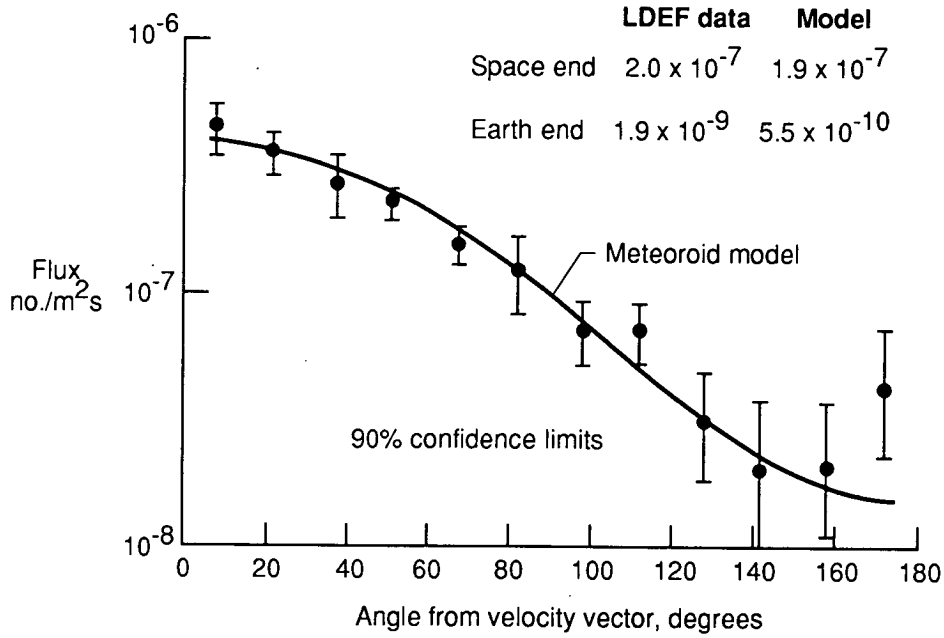

Fig. 7. Predicted crater flux from meteoroids using the new near-Earth meteoroid environment model proposed in this paper, for craters with a lip diameter of 0.5 mm or greater.

STUDY OF COSMIC DUST PARTICLES ON BOARD LDEF THE FRECOPA EXPERIMENTS AO138-1 AND AO138-2

J.C. Mandeville
ONERA/CERT Space Technology Department
BP 4025, 31055 Toulouse cedex France
Phone : 3361557117, Fax : 3361557172

Janet Borg
C.N.R.S Orsay Campus France
Phone : 3369415225, Fax : 3369415268

SUMMARY

Two experiments, within the French Cooperative Payload (FRECOPA) and devoted to the detection of cosmic dust have been flown on the Long Duration Exposure Facility (LDEF), launched in April 1984, and retrieved in January 1990. A variety of sensors and collecting devices have made possible the study of impact processes on materials of technological interest. Preliminary examination of hypervelocity impact features gives valuable information on size distribution and nature of interplanetary dust particles in low earth orbit, within the 0.5-300 micrometer size range. Most of the events detected on the trailing face of LDEF are expected to be the result of impacts of meteoritic particles only. So far, chemical investigation of craters by EDS clearly shows evidence of elements (Na,Mg,Si,S,Ca and Fe) consistent with cosmic origin. Systematic occurrence of C and O in crater residues is an important result, to be compared with the existence of CHON particles detected in P-Halley comet nucleus. Crater size distribution is in good agreement with results from other dust experiments flown on LDEF. However no crater smaller than 1.5 μm has been observed, thus suggesting a cut-off in the near earth particle distribution. Possible origin and orbital evolution of micrometeoroids is discussed. Use of thin foils detectors for the chemical study of particle remnants looks promising for future experiments.

INTRODUCTION

Interplanetary space contains solid objects whose size distribution continuously covers the interval from submicron sized particles to km sized asteroids or comets. Some meteoroids originate from comets (mainly dust ejected at perihelion), some originate from collisions within the asteroid belt. The relative contribution of these two sources is still a matter of debate. A majority of particles are likely to come from comets but recent data from the Infrared Astronomy Satellite (IRAS) indicates that asteroids could be a source larger than expected. In addition to natural particles, a significant and growing number of particles has been added by human activity in near earth space. Present knowledge of the occurrence and physical properties is based primarly on earth bound observation of meteors, comets, zodiacal light, data from infrared satellites (IRAS) as well as on board measured flux by instrumented spacecraft (Pegasus,Vega, Giotto, Space Shuttle and the MIR Soviet Space Station), study of lunar samples and dust collection in the upper atmosphere /1,2/.

The spatial density (number per unit volume) of meteoroids varies as a function of distance from the sun, distance from a planet, ecliptic latitude and longitude. The lifetime of interplanetary dust is dynamically limited, gravitational and solar radiation pressure (Poynting Roberston effect) gradually reducing the size of the orbit after typically 10^4 years; the lifetime of particles is also controlled by collision processes. Submicron particles will be blown out off the planetary system by

solar radiation pressure (β meteoroids). In the vicinity of earth, gravitational perturbations and the influence of the atmosphere greatly affect the distribution of the particles. In-situ detection and collection of dust by experiments flown on LDEF are expected to improve our current understanding of this aspect of the space environment. Originally launched for a nine month mission, the NASA Long Duration Exposure Facility (LDEF) has been retrieved after 2105 days in orbit. During its mission LDEF was stabilized with the long axis continually pointed toward the center of the earth, and surfaces perpendicular to this axis pointed at fixed angles with respect to the direction of orbital motion.

EXPERIMENTAL APPROACH

Part of the tray allocated to French experiments, known as the **FRECOPA** payload, has been devoted to the study of dust particles. The photograph (fig.1) shows the experiment in its flight configuration. The tray was located on the face of LDEF directly opposed to the velocity vector (west facing direction) in location B3 according to the LDEF description.

Two entirely passive experiments have been flown for the detection of microparticles. The first one: **Study of Meteoroid Impacts on Various Materials** (AO138-1) was composed of a set of thick glass and metallic samples; the second one: **Dust Debris Collection with Stacked Detectors** (AO138-2) was composed of multilayer thin foil detectors. The collection area was about 2000 cm^2. In addition to these dedicated experiments a large variety of materials on the same tray (8500 cm^2) have been exposed to the bombardment of microparticles and are expected to provide additional data. Detailed description of the hardware has been given elsewhere /3,4/ and will be only summarized here. Samples of interest for both experiments are listed on tables 1 and 2.

The thick target experiment (**AO138-1**) comprises selected metallic (Al, Au, Cu, W, Stainless Steel, thickness : 250 μm) and glass surfaces (1.5 mm thickness). Samples have been exposed to space for all the mission duration (5.5 years). Crater size distribution from these thick target experiments will enable, with the aid of laboratory calibration by solid particle accelerators, the evaluation of the incident microparticle flux in the near earth environment. Information on the velocity, particle density and incident direction will be generally difficult to decode; however this could be partially determined by studying the geometry of impact craters.

A more critical issue is the determination of the chemical composition of the impacting particles. In general they are physically destroyed and mixed with target material in the process of crater formation. Although little or no pristine material is likely to be left for chemical analysis, particularly in metals such as tungsten or gold, it is possible to collect quite sufficient projectile residue material for analysis /5/. Based on laboratory experiments such residues may be reduced to a probable initial composition.

The multiple foil penetration and collection experiment (**AO138-2**) was located inside one of the three canisters, for maximum protection of fragile thin metal films before and after exposure to space /3,4/. The canisters have been opened a short time after LDEF deployment and closed nine months later. The aim of the experiment is primarily to investigate the feasability of multilayer thin film detectors acting as energy sorters in order to collect micrometeoroids, if not in their original shape, at least as "break-up" fragments suitable for chemical analysis. The behaviour of hypervelocity particle impacts on thin foils has been extensively studied in the laboratory and data will provide a basis for interpretation. Upon perforation of a thin foil, a particle undergoes either a deceleration or a fragmentation, depending on impact velocity, density of the target or projectile and thickness to diameter ratio /6,7/. One or more thin metallic foils are set in front of the main target in order to produce size selective detectors. Foil thickness ranges from 0.75 μm to 5 μm of aluminium; such foils are expected to slow down particles with diameters between 1 and 10 μm diameter, without complete destruction. Separation distance between foils is 1 mm, enough to have eventual fragments dispersed over a large area.

PRELIMINARY RESULTS

The experiment has been recovered in good conditions after exposure to space. As a consequence of its position on LDEF, exposure to atomic oxygen erosion was kept to a minimum. In this paper we shall give results concerning the largest impact features found on the experiments and on the FRECOPA payload and some first data concerning the size distribution of small size craters. After preliminary observation by the M&D SIG team during LDEF deintegration at KSC, the FRECOPA tray has been carefully searched for impact features, at CNES prior to deintegration of experiments and at CERT. The survey was made with an optical microscope Nikon Profile Projector V12 at magnifications 20X and 100X. Scanning electron microscopy (SEM Jeol JSM-840A at CERT and Orsay) has been used for the samples purposely dedicated to the experiment and for any peculiar feature observed on other surfaces. Energy dispersive spectroscopy (EDS Link Analytical eXL analyser at CERT and EDAX Analysis Tracor system at Orsay) chemical investigation of projectile remnants has been carried out in some craters. Materials not specifically dedicated to dust detection have provided useful data, mostly because of the large area time exposure. As expected, the number of impact craters varies significantly with the location on the LDEF surface. Comparison with data from different locations on LDEF and comparison with other experiments will be made later.

Large Craters into Thick Targets

Three main types of materials have been exposed to micrometeoroid impacts: metals, fiber glass thermal covers backed by mylar foil, and quartz samples.

Two large impact features have been found : one full penetration (diameter 1.25 mm) and one marginal penetration (diameter 1.07 mm) of a 1mm aluminium shield. About 90 craters larger than 50 µm have been found on a total area of one square meter. Four craters are larger than 500 microns. Most of the large craters are circular in outline, though some small craters do indicate oblique incidence. Table 3 summarizes all the large craters found on different materials. The figures 2 to 5 show typical hypervelocity impact craters into different materials. Craters on aluminium, stainless steel and copper are typical of hypervelocity impact in metals /8/, with a depth to diameter ratio of about 0.55. Few large impacts have been found so far on quartz targets, two of them show a morphology typical of impacts on brittle materials (figure 3): a central pit with evidence of fusion, an inner ring of spalls and an outer more or less symmetrical spallation zone /9/; similar features have been found extensively on lunar samples. For the elongated shape of the central pit, it is possible that the projectile was irregularly-shaped or impacted at a large angle of incidence (greater than 45° in order to change the shape of the central pit). A number of impacts have been found on the thermal covers (tefloned glass fabric). Figure 4 shows a typical perforation. The hole diameter is approximately the same on the reverse side of the composite, as would be expected from a thin plate. Damage consists of broken fibres with missing binder material, confirming initial findings by NASA /8/. The picture shows evidence of both brittle fibre fracture and of fibre melting. Features of peculiar interest are damages caused to the mylar foil located beneath the fiber glass fabric. Under UV irradiation the mylar became very brittle and was badly damaged upon impact. This is an illustration of synergistic effects on the degradation process occurring in space.

Microcraters into Thick Targets

Four cm^2 of aluminium sample A54 from the AO138-1 experiment have been thoroughly analyzed in search of microcraters less than 20 µm in size. We used a JEOL 840 Scanning Electron Microscope, equipped with an EDAX Analysis Tracor system. The detector had no window protection allowing a quantitative analysis of elements down to Z=23 and a qualitative research of Carbon and Oxygen (nitrogen could not be detected with this equipment). A first scanning of the samples at a magnification of 750 X allows a selection of events showing typical crater features (circular feature, ridge). A typical flux density of a 2.10^{-4}/m2/s crater larger than 1.5 µm has been estimated; flux mass distributions found for larger craters can thus be extended with very good agreement to such small

sizes. Data are consistent with results from the IDE experiment in the same size range.* We observed no craters smaller than 1.5 μm in size, thus implying a cut off in the particle size distribution, orbiting the earth and impacting our samples, a similar trend has been observed by E. Zinner[1] on another experiment. Considering simulation experiments concerning the crater diameter to particle diameter ratio, for various collector thicknesses, we can admit a factor 5 between the crater size and the particle size : the smallest impacting particles have a mass in the 10^{-13} g. region.

Microcraters into Thin Targets

Of peculiar interest was the study of impact features on the thin foil detectors. As the exposure was limited to nine months areal density of impacts is small and study is still in progress. The figure 5 shows the perforation of a 5 microns aluminium foil (sample AD11). The perforation formed an ellipse measuring 55 by 40 microns (oblique impact or elongated projectile). It is a typical "supramarginal perforation" with a crater diameter to foil thickness ratio of D/f=10; diameter of the particle is estimated to be 40 microns. The bottom plate beneath the perforation shows a star-shaped distribution of small secondary craters (sample AD12). The top foil acted as a shield, fragmenting the projectile and spreading the fragments over the surface of the thick plate. The craters range in size from 0.6 μm to 15 μm and are mostly distributed along two axes. An angular particle, 18 mm by 15 mm is visible at the intersection of the axes. EDS analysis has provided evidence of impactor fragment. As shown later, chemical investigation of secondary craters has given information on the composition of an impacting particle. Detectors consisting of a thin shield and thick bottom plate appear to offer a significantly higher return of information concerning chemical analysis of impactor residues than single plate detectors.

Crater Size Distribution

The cumulative flux size distribution of craters (in aluminium) larger than 30 microns is shown in the lower part of the figure 6. Several trends are visible : the flattening of the distribution at small sizes is largely an observational artifact, due to the limited resolution of optical microscopy; the middle part of the curve is consistent with the general size spectrum of microparticles and data obtained elsewhere on LDEF; the change of slope at large sizes could be an artifact due to the limited time-area of sampling, or more likely real as discussed by McDonnell et al. /10/. The upper part of the figure shows the crater size distribution of craters between 1 micron and 10 microns as derived from preliminary SEM scanning of small craters on aluminium samples (A54).

Figure 7 shows the flux, or number of particles/m^2/s able to perforate a plate of aluminium of given thickness as derived from perforations observed on our experiments. On the figure 8 is shown a comparison betwween the distribution of craters observed on the Frecopa experiment (A54-4/AO138) and an average value of the distribution of impact craters on the leading edge and on the trailing edge of LDEF as obtained from other experiments (S0001, MAP, IDE).† Agreement between A0138 data and average trailing edge data is good.

Flux Mass Distribution

The impact site survey yields a crater size distribution, which should be converted to a particle mass distribution by using the relevant relationship between crater sizes and particle mass and velocity. The discussion is out of the scope of this paper; however assuming an average impact velocity of 20 km/s, the value of the ratio of crater diameter (D) to the particle diameter (d), could be chosen as : D/d = 5. Figure 9 shows the cumulative flux versus the mass of particles, as derived from AO138 dust experiments; for comparison is shown the flux derived from the Grün et al. model /11/, computed for an altitude of 500 km above the earth surface (randomly oriented plate).

The mass distribution in comparison to a review of comparable near-earth data shows a good agreement /10/; the flux on the west face of LDEF is about 10 times lower than on the east face, for

---

[1] E.Zinner, private communication

* J.D. Mulholland et al. LDEF Interplanetary Dust Experiment : A high time resolution snapshot of the near-earth particulate environment, in : *Proc. Hypervelocity Impact in Space,* Canterbury, 1-5 July 1991, (to be published 1992).

† M. Zolensky et al. Meteoroid and orbital debris record on LDEF, in : *Proc. Hypervelocity Impact in Space,* Canterbury, 1-5 July 1991, (to be published 1992).

large particles. Most of the particles impacting this west face should be interplanetary dust particles, not orbital debris. This fact is substantiated further by the chemical identification of projectile remnants inside craters.

Chemical Analysis of Particle Remnants

The first EDS X ray analysis of a few small craters has shown occurrence of elements Ca, K, Ti, Fe and S. Typical spectra are shown on figure 10. Further analysis will doubtless give an insight on the origin of the impacting objects.

A chemical analysis of all the craters found on sample A54 has been performed : X ray identification of elements down to C is possible, because the detector used in the Edax-Tracor system is window less. However nitrogen cannot be identified and of course as the collector is made of Aluminium, no information on Al is possible; semi quantitative analysis is only possible beyond Z=23 (Na).

Table 4 summarizes our results for the 15 craters identified so far : light elements C and O are present, with a ratio C/O varying from 0.1 to 3. Significant variations appear inside the distribution of individual craters. The other main elements identified in the various craters are usually refered to as "chondritic" elements, as they exist in various proportions and are signatures of extraterrestrial particles : Na,Mg,Si,S, Ca and Fe. For these elements also, important variations are found from point to point inside the crater reinforcing the idea that the particles are truly aggregates bursting apart during the impact. The systematic presence of C and O components in the various residues analyzed is an important result: the occurrence of CHON particles detected in P-Halley nucleus (PUMA and PIA experiments) would not be a particularity of this comet but could be a constant for extraterrestrial particles of cometary origin, as seems to be the case for such particles .

For the sample AD12 located beneath the thin foil perforation described earlier, the elements identified, in the central part of impact feature : Si,Fe,Na,Mg are characteristic of interplanetary dust particles from the mafic silicate family with olivine as a strong candidate. The variation in chemical composition between and within craters confirms the idea of an aggregate particle which burst apart on impact. None of the above elements were found in the outside craters (far from center of impact feature) which implies that these were caused only by aluminium fragments from the top foil.

We found no evidence of elements characteristic of orbital debris (Ti,Zn). We are thus highly confident that all the craters analysed are of extraterrestrial origin, as expected due to the fixed orientation of LDEF during its flight and to the exposition side of FRECOPA payload on board LDEF. However there is still a possibility to record impacts from orbital debris in highly eccentric orbits.† Further investigation is obviously needed.

CONCLUSION

LDEF offers a unique opportunity for the study of the many processes involved upon high velocity impact phenomena and for the comprehensive description of the LEO microparticle population. Particle collection in space will remain generally difficult, perhaps impossible for the highest meteoritic velocities. Deceleration of lower velocity particles by multiple layer foils tentatively proved sufficient to expect the retention of material suitable for identification. As shown by the preliminary investigation of experiments and materials retrieved on FRECOPA, use of opportunities to gain access to an orbiting hypervelocity impact laboratory offers considerable promise for the future. The investigation of this near-earth region of space is a necessity not just for scientific but also for technical reasons. However a great deal more research needs to be carried out to confirm the validity of the findings.

Acknowledgements : Support from CNES for completion of experiment and for data analysis and support from NASA for completion of the mission are greatly acknowledged.

† M. Zolensky et al. Meteoroid and orbital debris record on LDEF, in : *Proc. Hypervelocity Impact in Space,* Canterbury, 1-5 July 1991, (to be published 1992).

REFERENCES

1. C.Leinert and E. Grün, Interplanetary Dust, in: *Physics and Chemistry in Space*, Springer (1988) p.34.

2. J.C.Mandeville, Aragatz Mission Dust Collection Experiment., *Adv.Space Res.* 10, 3,397, (1990).

3. J.C.Mandeville, AO138-1 and AO138-2 Experiments, in: *LDEF Mission 1 Experiments*, eds L.G. Clark, W.H. Kinard, D.J. Carter, J.L. Jones, NASA SP-473, (1984) p.121.

4. J.C. Mandeville and J.A.M. McDonnell, Micrometeoroid multiple foil penetration and particle recovery experiments on LDEF, in: *Solid particles in the solar system*, ed. I. Halliday and B.A. McIntosh, D.Reidel (1980) p.395.

5. J.L. Warren, The detection and observation of meteoroid and space debris impact features on the Solar-Max satellite. *Proc XIXth Lun.Plan.Sci.Conf.* (1989) p.641.

6. J.A.M. McDonnell, Factors affecting the choice of foils for penetration experiments in space, in *Space Research X,* North Holland pub. (1970).

7. F.Hörz, Laboratory simulation of LDEF impact features, in: *First LDEF Post-retrieval symposium abstracts,* NASA CP-10072, (1991).

8. LDEF M&D SIG in: *Meteoroid and debris impact features documented on LDEF,* a preliminary report, NASA JSC, (1990).

9. J.Vedder and J.C. Mandeville, Microcraters formed in glass by projectiles of various densities, *JGR* 79,23, (1974).

10. J.A.M.McDonnell et.al. First results of particulate impacts and foil perforations on LDEF, in *Adv.Space Res.* 10, 3, XXVIII Cospar 1990, (1990).

11. E.Grün et al., Collisional balance of the meteoroid complex, *Icarus* 62,244, (1985).

Table 1 : Experiment A 0138-1 Sample List

Designation:	**Material:**	**Thickness (microns)**	**Size (mm)**
A1	Tungsten	150	100 x 100
A2	Aluminium	250	"
A3	Copper	125	"
A4	Steel	250	"
A5	Aluminium	250	"
A6	Aluminium/Kapton	50	"
B1 to B27	Glass	1.9 mm	diam: 25

Table 2 : Experiment A 0138-2 Sample List

Designation:	Material:	Thickness (microns)	Size (mm)
D1 - D5	Aluminium	125 5	40 x 40
D6	Aluminium	125	"
D7 - D8	Aluminium	125 2 2	"
D9 - D11	Aluminium	125 5 2	"
D12	Aluminium	125	"
E1 - E3	Gold Aluminium	125 2	30 x 30
E3 - E6	Aluminium	125 2 2	"
E7 - E9	Aluminium	125 0.75 0.75	"
E10 - E12	Gold Aluminium	125 0.75	"
E13 - E14	Gold	125	"
E15 - E17	Gold Aluminium	125 2 0.75	"
E18 - E19	Aluminium	125	"

Table 3

ao138crat

	Identification	Diameter, um	Depth, um	P/D	Material	Comments
1	es11	215,000			fg	
2	es110	80,000			fg	
3	es12	250,000			fg	
4	es13	350,000			fg	
5	es14	250,000			fg	
6	es15	150,000			fg	
7	es16	250,000			fg	
8	es17	200,000			fg	
9	es18	180,000			fg	
10	es19	90,000			fg	
11	es21	350,000			fg	
12	es22	250,000			fg	
13	es23	400,000			fg	
14	es24	300,000			fg	
15	es25	250,000			fg	
16	e31	350,000			fg	
17	e32	192,000			Al	
18	e33	147,000			Al	
19	e34	320,000			Al	
20	e35	198,000			Al	
21	e36	510,000			Al	
22	e37	160,000			Al	
23	e38	80,000			Al	
24	e39	135,000			Al	
25	e310	58,000			Al	
26	e311	148,000			Al	
27	e312	72,000			Al	
28	e41	315,000			Al	
29	e42	108,000			Al	
30	e43	80,000			Al	
31	e44	75,000			Al	
32	e45	130,000			Al	
33	e46	200,000			Al	
34	e51	1250,000			Al	perf. 1 mm
35	e52	1070,000	920,000	0,860	Al	
36	e53	395,000	240,000	0,608	Al	
37	e54	320,000	190,000	0,594	Al	
38	e55	125,000			Al	
39	e56	175,000			Al	
40	e57	200,000			Al	
41	e58	165,000			Al	
42	e59	140,000			Al	
43	e510	55,000			Al	
44	e511	115,000			Al	
45	e512	75,000			Al	
46	mv51	375,000			fg	
47	ca11	142,000	65,000	0,458	Al	
48	ca21	48,000			Al	
49	ca31	155,000	80,000	0,516	Al	
50	ca32	199,000	110,000	0,553	Al	
51	ca41	225,000	130,000	0,578	Al	
52	ca42	60,000	40,000	0,667	Al	
53	a21	176,000	90,000	0,511	Al	
54	a22	158,000	80,000	0,506	Al	
55	a23	165,000	90,000	0,545	Al	
56	a31	127,000	70,000	0,551	Cu	
57	a41	64,000	35,000	0,547	ss	
58	a42	49,000	22,000	0,449	ss	
59	a51	550,000			Al	perf 250 um
60	a52	55,000	30,000	0,545	Al	
61	a53	50,000			Al	
62	a54	100,000	65,000	0,650	Al	
63	a55	62,000	35,000	0,565	Al	
64	a56	36,000			Al	
65	a61	50,000			kapton/Al	
66	d11	60,000			Al	perf 5(um
67	b251	330,000	180,000	0,545	Al	
68	b261	320,000	170,000	0,531	Al	
69	a24	75,000	35,000	0,467	Al	
70	a11	50,000	15,000	0,300	W	
71	b15	180,000			quartz	pit = 30
72	b16	400,000			quartz	pit= 95
73	ds1	65,000			Al	
74	ds2	110,000			Al	

LDEF AO138-1 SAMPLE A54-2,4 : CHEMISTRY

Crater n°	Size,µm	C/O (a)	Na	Mg	Si	S	Ca	Fe	Ni (c)
1	1.5	1-1.5	ε	ε	ε				
2	1.5	0.5	ε		1				
3	1.5	0.7		0.2	1				
4	1.5	0.5-1			1			5	
5	2	(b)			ε			1	
6	2.5	1.5-3		0.17	1				
7	3	1-2	ε	ε	1				
8	3	(b)	0.3	1	(d)	1	1		
9	3.5	1			1				
10	4	0.3-04	0.4	0.2	1	ε	0.5	3	
11	4	0.5	ε	ε	1	ε	ε	ε	
12	5.5	0.5		0.1	1		0.3		
13	6	0.2		1.6	1	5	3		
14	10	0.1-1	ε		1		ε		
15	10	0.5	0.13	0.07	1	0.13	0.3	8	

Notes :
(a) : peak height
(b) : no C present
(c) : reported to (Si) =1; ε : very weak peak
(d) : no Si present ; reported to (Mg) = 1

Table 4

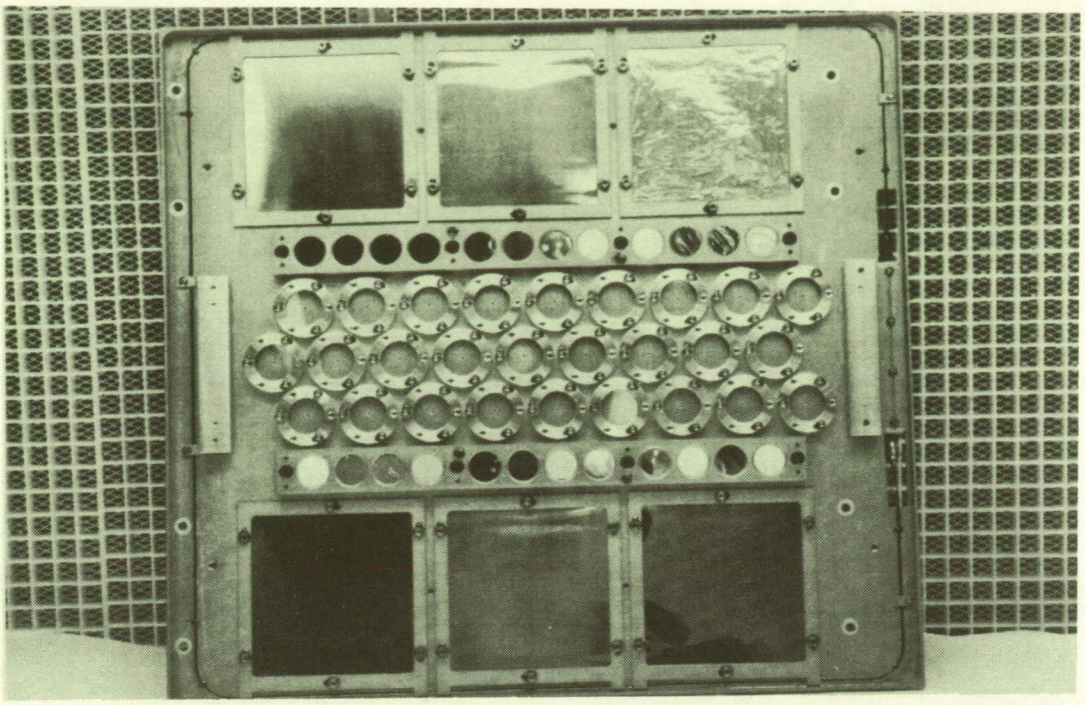

A0138-1 Experiment

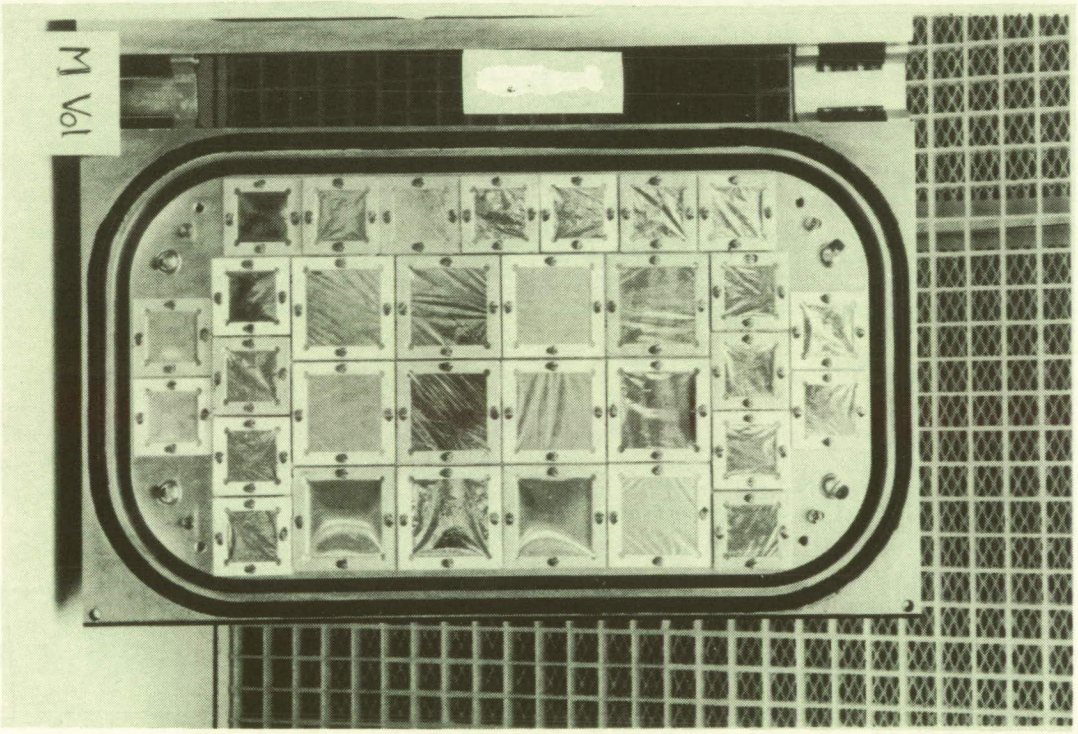

A0138-2 Experiment

Fig.1. This figure shows the FRECOPA experiment tray on LDEF, one of the dust experiment is shown on the upper middle part of the tray, the other one is located inside one of the cannisters (closed upon recovery).

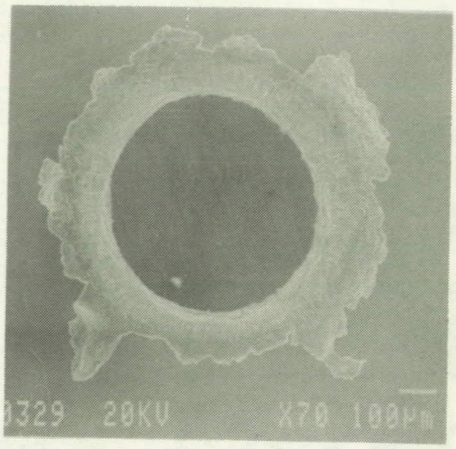

Fig.2. This figure shows a typical medium sized impact on aluminium surface.

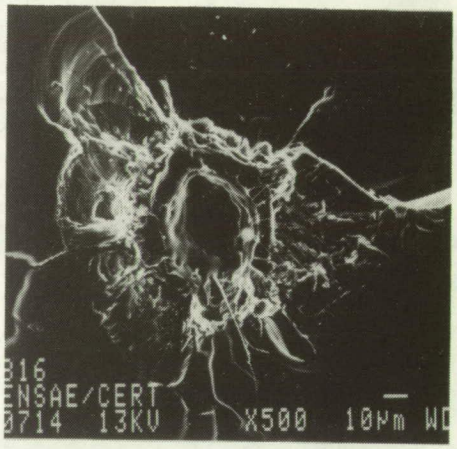

Fig.3. This figure shows an impact crater on quartz sample.

Fig.4. This figure shows a typical crater on tefloned fiber glass fabric.

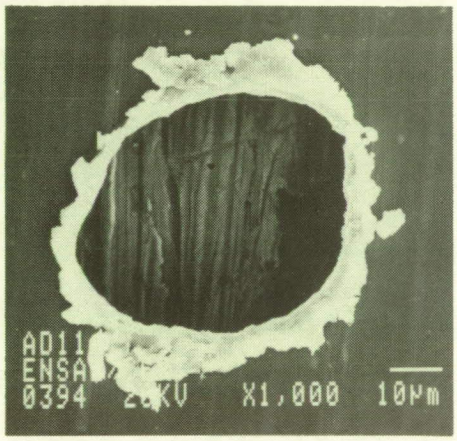

Fig.5. Perforation of a 5 microns thick aluminium foil.

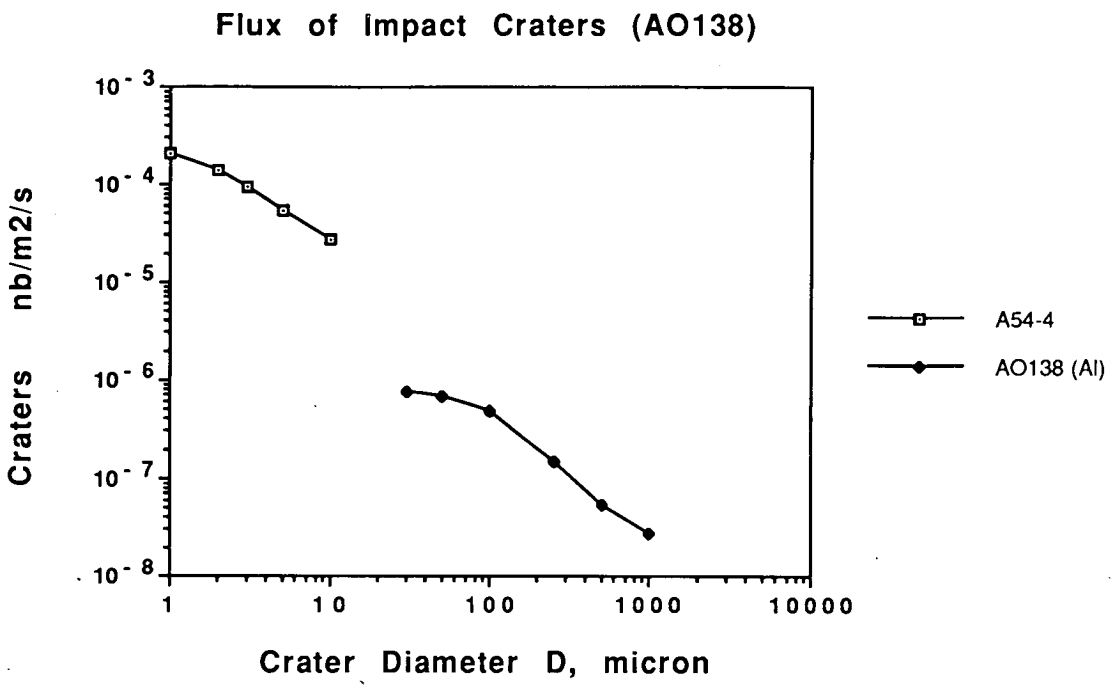

Fig.6. Cumulative flux size distribution of craters on AO138-1 and AO138-2

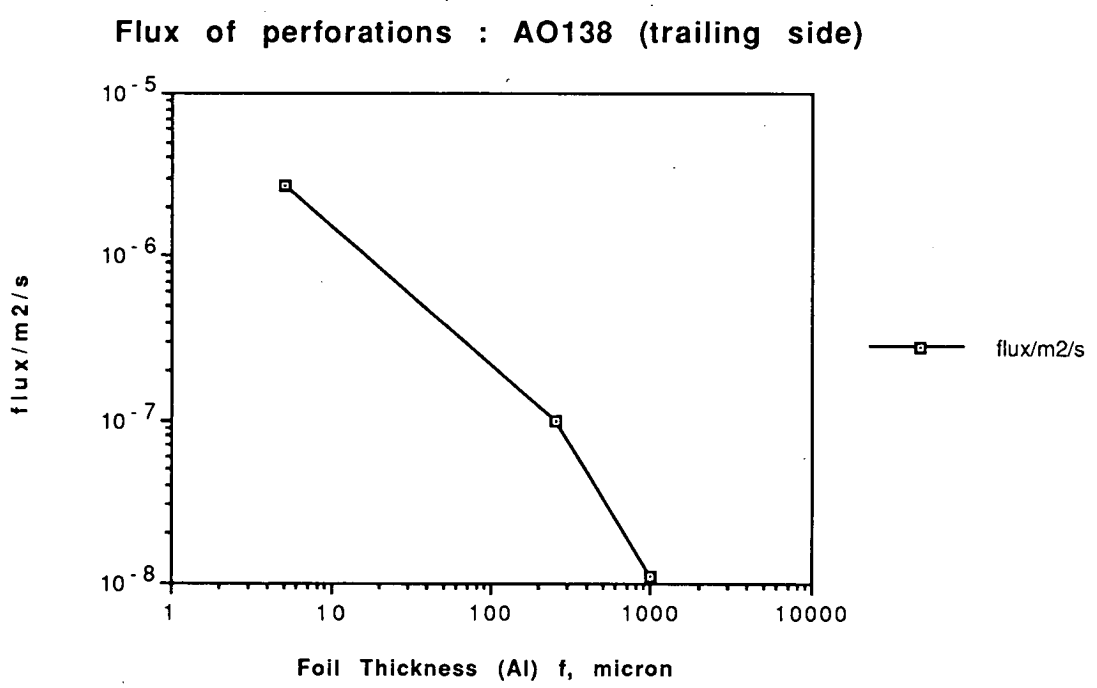

Fig.7. Flux of perforating particles.

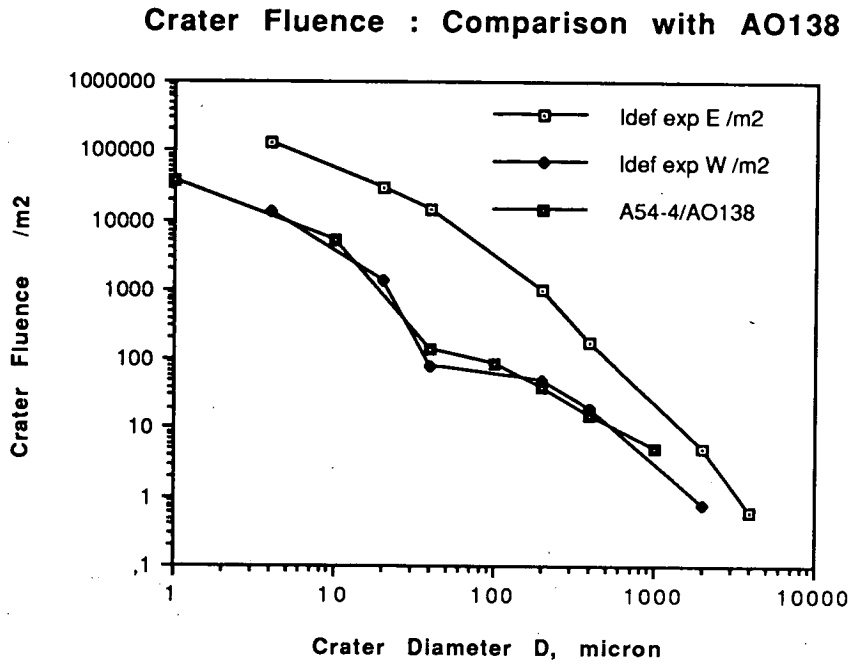

Fig.8. Comparison of crater fluences observed on FRECOPA with data from other dust experiments on LDEF.

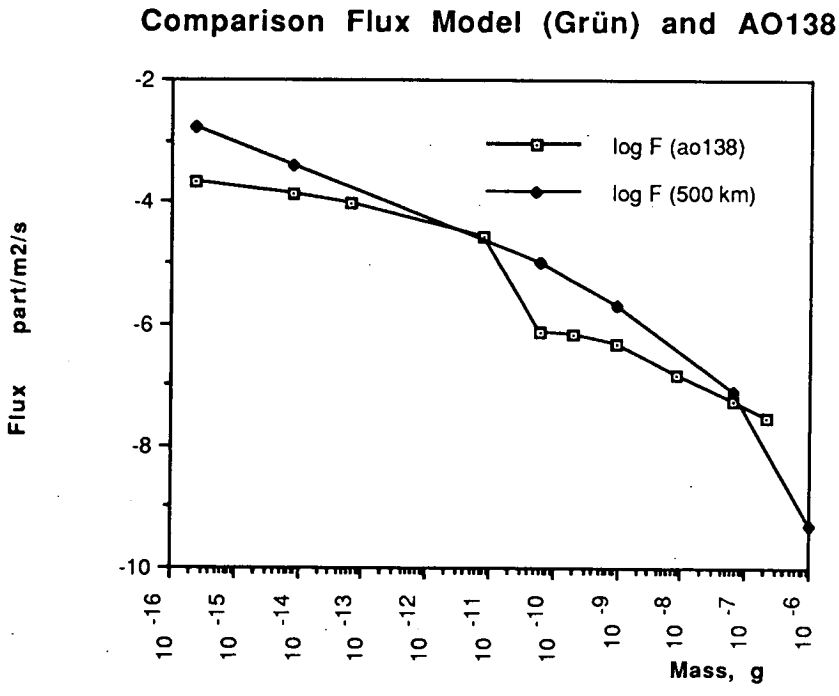

Fig.9. Cumulative flux on trailing side of LDEF as compared with flux model from Grün et al.(1985), see ref.13.

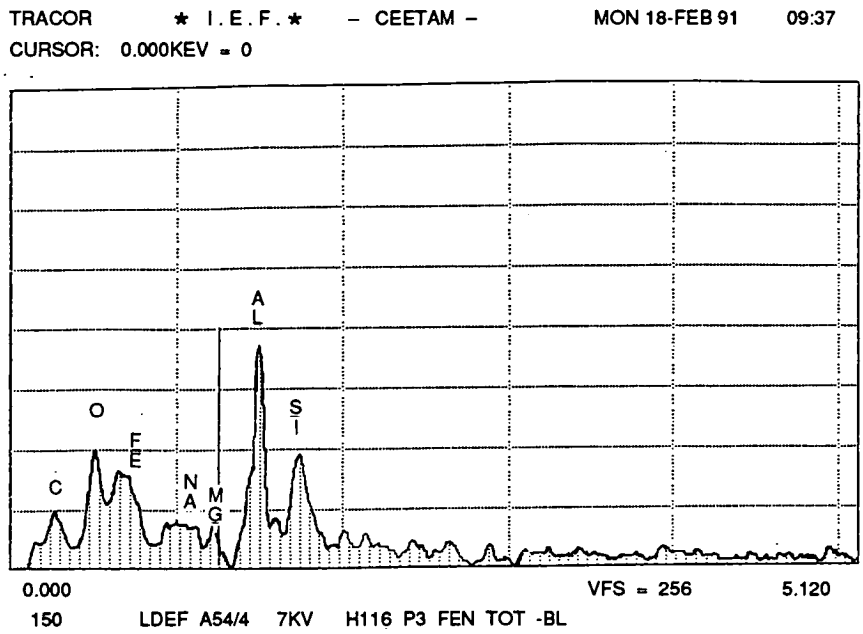

SQ: TRASH

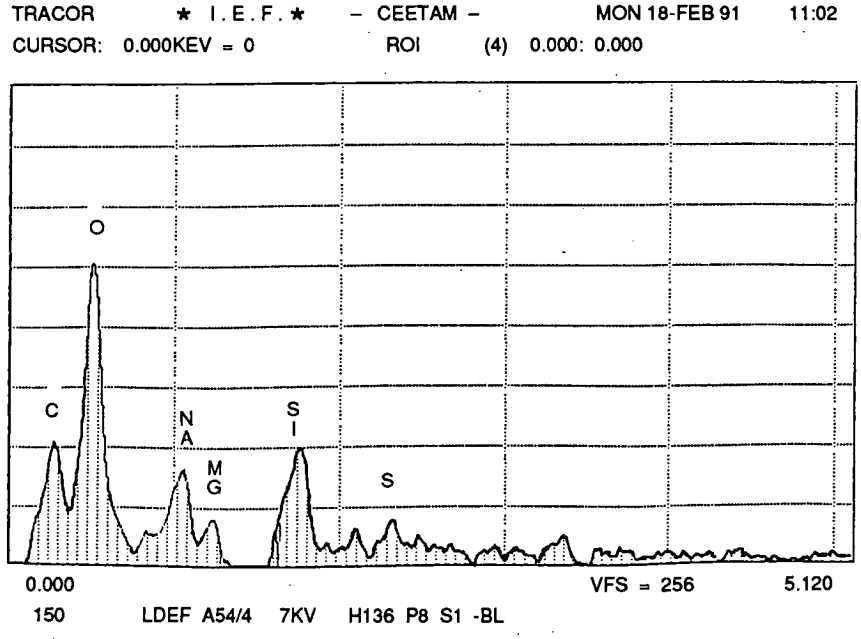

SQ: TRASH

Fig.10. These figures shows typical X-ray spectra of points located inside impact craters

METEOROID/SPACE DEBRIS IMPACTS ON MSFC LDEF EXPERIMENTS

Miria Finckenor
NASA/Marshall Space Flight Center (NSFC)
Marshall Space Flight Center, AL 35812
Phone: 205/544-9244, Fax: 205/544-0212

SUMMARY

This paper presents the many meteoroid and space debris impacts found on A0171, A0034, S1005 and other MSFC experiments. In addition to those impacts found by the meteoroid and debris special investigative group at KSC, numerous impacts less than 0.5 mm were found and photographed. The flux and size distribution of impacts will be presented as well as EDS analysis of impact residue. Emphasis will be on morphology of impacts in the various materials, including graphite/epoxy composites, polymeric materials, optical coatings, thin films, and solar cells.

INTRODUCTION

The meteoroid and debris special investigative group noted over 34,000 impacts on the LDEF surfaces. Due to time constraints, only about 6000 of these were optically recorded. The general guidelines for photography were 0.50 mm or greater crater diameter in any material, 0.25 mm or greater penetration in any material, and any impact crater or penetration in an unusual material.

For each experiment, photographs and optical disk recordings were taken before and after sample de-integration at MSFC. Spall, impact particle residue, and secondary impact debris, if any, were photographed. The photographs were then archived with a description of the impacted material and location, crater diameter, magnification, and any comments. The optical disk recordings also have this information stored in each file.

RESULTS

A graph of the number of impacts versus the size of impact craters shows an approximate logarithmic curve, as expected. While this is a good approximation, Figure 1 should not be directly compared to the meteoroid/debris environment model, which charts the impact fluence versus the impact particle size. The particle size versus the size of crater formed varies according to material properties of both the impact particle and the impacted material.

Meteoroid and Debris Impact Features Documented on the Long Duration Exposure Facility, JSC #24608, hereafter referred to as the Meteoroid and Debris Impact Catalog, has listed for each part of the LDEF the number of impacts found and the number of those impacts photographed. The following data from each MSFC experiment are the results of the photographic scans both at Kennedy Space Center and Marshall Space Flight Center.

A0171 - Solar Array Materials Passive LDEF Experiment (SAMPLE)

The Meteoroid and Debris Impact Catalog notes that 327 features were found on tray A08, including the tray clamps, shims, and bolts. Thirty-six of the impacts on the experiment tray itself were recorded on optical disk. Unfortunately, the LeRC, GSFC, and JPL sub-trays of this experiment were returned to the co-investigators before a more detailed scan could take place. Paul Stella/JPL has identified 157 impacts on one solar cell sub-plate, with seven being >0.5 mm. At MSFC, an additional fifty-four impacts have been identified and photographed on the main experiment tray, with special emphasis on the graphite/epoxy tensile samples. Meteoroid and debris impacts may have some effect on the mechanical testing of these samples. However, some small impacts from early in the mission may have been eroded away by atomic oxygen erosion.

Generally, few material properties have been determined that would be directly affected by meteoroid and debris impacts. Solar cells with debris impacts and cracked cover slips {Figure 2} provide maximum power output similar to those not impacted. Interconnect tabs were penetrated, but a negligible amount of material was removed. Impacts and penetrations did not interfere with the mechanical peel tests of thermal control tape on fiberglass/epoxy substrates. However, impacts have interfered with optical property measurements. For example, the 1" dia. Tiodize K-17 sample from Plate IV has a relatively small (0.55 mm) crater with a large (4.1 x 3.0 mm) spall zone. {Figure 3}

Some of A0171's samples have had EDS analysis. While this is not as sensitive as SIMS analysis, it does provide some data on impactor residue and contamination. Titanium, probably from white paint, and aluminum have been found in impact craters.

A0171 had one of the more interesting impacts of the MSFC trays. Shown in Figure 4, the aluminum tray has been hit by a meteoroid or debris particle, spraying debris onto the nearby polymeric sample. Analysis is underway to correlate the crater diameter and debris cone angle to the velocity, mass, and angle of impact of the particle.

S0069 - Thermal Control Surfaces Experiment (TCSE)

The Meteoroid and Debris Impact Catalog notes that 582 features were found on tray A09. Thirty-four of these impacts on the experiment tray were optically recorded. At time of publication, this tray has not been fully scanned for impacts. Analysis has been concentrated on the complete penetration of the 0.063" thick aluminum plate. This plate is made of aluminum alloy 6061-T6 and is comparable to the current bumper design for Space Station

Freedom. There was no apparent damage to the underlying structure, indicating a full break-up of the impactor. Several of the paint samples have been impacted, but the atomic oxygen erosion and UV degradation seem to have had a far greater effect on the material properties.

S1005 - Transverse Flat-Plate Heat Pipe Experiment

The Meteoroid and Debris Impact Catalog notes that tray B10 had 414 impacts. Fifty-six of these impacts on the experiment tray were recorded on optical disk. The SIG team found thirty-one impacts on the aluminum tray flanges. A photographic scan at MSFC found ten additional impact craters on the flanges and photographed another ninety-two impacts on the heat pipes and beta cloth blankets.

The heat pipes were covered with 5 mil silver/Teflon. Impacts into this material were typical, with the darkened rings around the impact area and delamination of Teflon. {Figure 5} There were also craters through the silver/Teflon into the aluminum of the heat pipes. The diameters of these secondary craters have been noted in the photographic record as well.

In between the heat pipes were thermal blankets consisting of beta cloth and multi-layer insulation. Penetrations through the beta cloth resulted in typical secondary debris penetrations and melting of the aluminized Mylar and Dacron netting of the MLI. One particle penetrated the beta cloth layer and five layers each of the Mylar/Dacron netting. Performance loss in the thermal blankets is currently being analyzed.

A0034 - Atomic Oxygen Stimulated Outgassing and
A0114 - Interaction of Atomic Oxygen with Solid Surfaces at Orbital Altitudes

The Meteoroid and Debris Impact Catalog notes that 83 and 508 impacts were found on the entire C03 tray and C09 tray, respectively. A0034 and A0114 each occupied only one-sixth of these trays. No impacts were optically recorded on the trailing edge sub-trays. At KSC, eleven and eight impacts were noted on the ram direction A0034 sub-tray and the A0114 sub-tray, respectively.

The MSFC photographic scans for A0034 have found forty-two impacts on the leading edge sub-tray and four impacts on the trailing edge sub-tray. This agrees with the approximate ratio of hits for leading edge versus trailing edge of 10:1. Only one impact, measuring 0.20 mm, was found on a UV window sample. {Figure 6} Optical property tests were performed in an unaffected area. The remaining impacts were found on the cover plates.

At the time of publication, impact scans are incomplete for A0114. However, four impacts have been found in sample materials. Two impacts were found on a carbon sample with 400 A of gold, one was found in a solid fused silica sample, and one was found in a quartz sample with 5000 A of silver. These impacts were typical of those found in glassy materials, with large spall zones and cracking.

Continuing Analysis

There are other experiment trays with MSFC co-investigators, such as A0172 (Effects of Solar Radiation on Glasses) and M0002 (Trapped-Proton Energy Spectrum Determination), but these were located on the trailing edge or the earth end, with very few impacts.

With the same stereo microscope system used at KSC during LDEF de-integration, the experiments are being more fully scanned for impacts as time permits in the laboratory. The stereo microscope has sufficient magnification for ~0.20 mm diameter and larger impact craters. Currently, smaller impacts are being photographed using a low-power stand microscope, but this survey has not been completed. Also, some of the smaller impacts have been photographed using a scanning electron microscope, but this is not practical for the thin films and polymeric samples.

CONCLUSION

For the leading edge trays, atomic oxygen erosion and ultraviolet degradation seem to have had a much greater effect on material properties than meteoroid and debris impacts. The optical property changes caused by meteoroid and debris impacts are only in small areas around the impact craters. Mass loss due to impacts is negligible. Maximum power output in solar cells is comparable in both impacted and non-impacted solar cells. However, impacts' effect on mechanical properties has yet to be determined. There are valid concerns over spacecraft protection from meteoroid/debris impacts and penetrations as the amount of space debris in orbit increases with every launch. Further analysis of the impact flux and damage should validate current debris models as well as aid applied research in debris protection systems and impact-resistant materials.

METEOROID/DEBRIS IMPACTS ON MSFC EXPERIMENTS
LEADING EDGE TRAYS

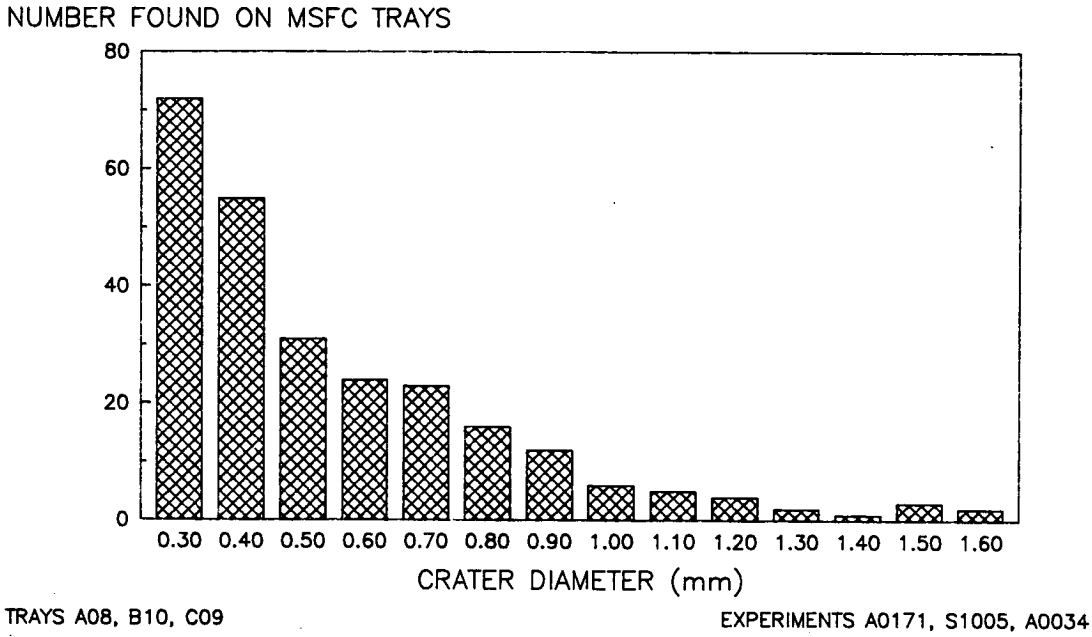

TRAYS A08, B10, C09

EXPERIMENTS A0171, S1005, A0034

FIGURE 1

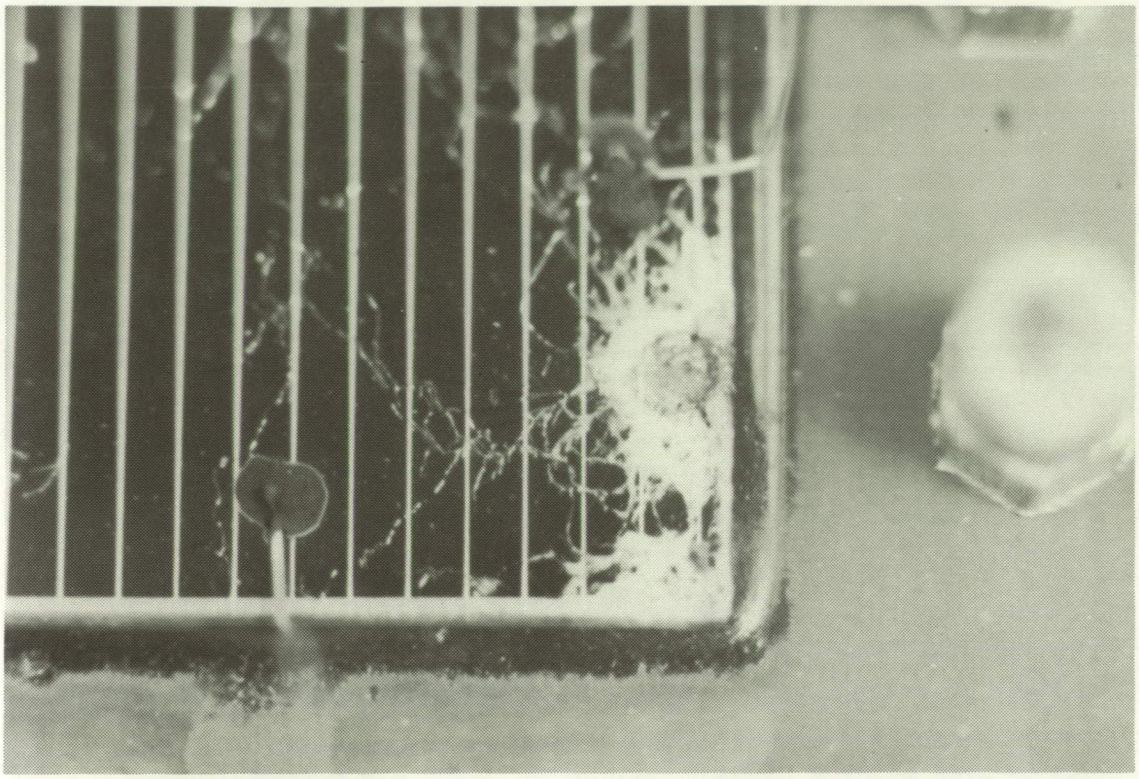

Figure 2. Solar cell, ~2 mm dia. impact crater, ~5 mm dia. fracture zone

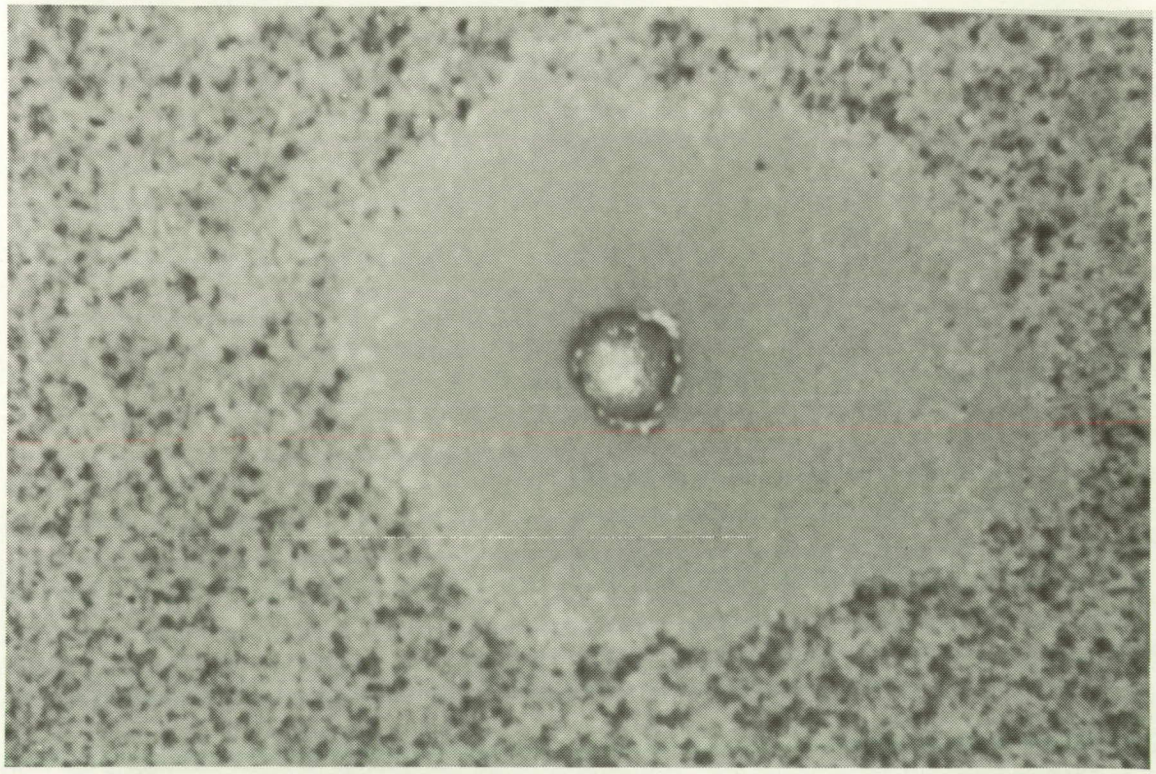

Figure 3. Tiodize K-17 on titanium, 0.55 mm dia. impact crater, 4.1 x 3.0 mm spall zone

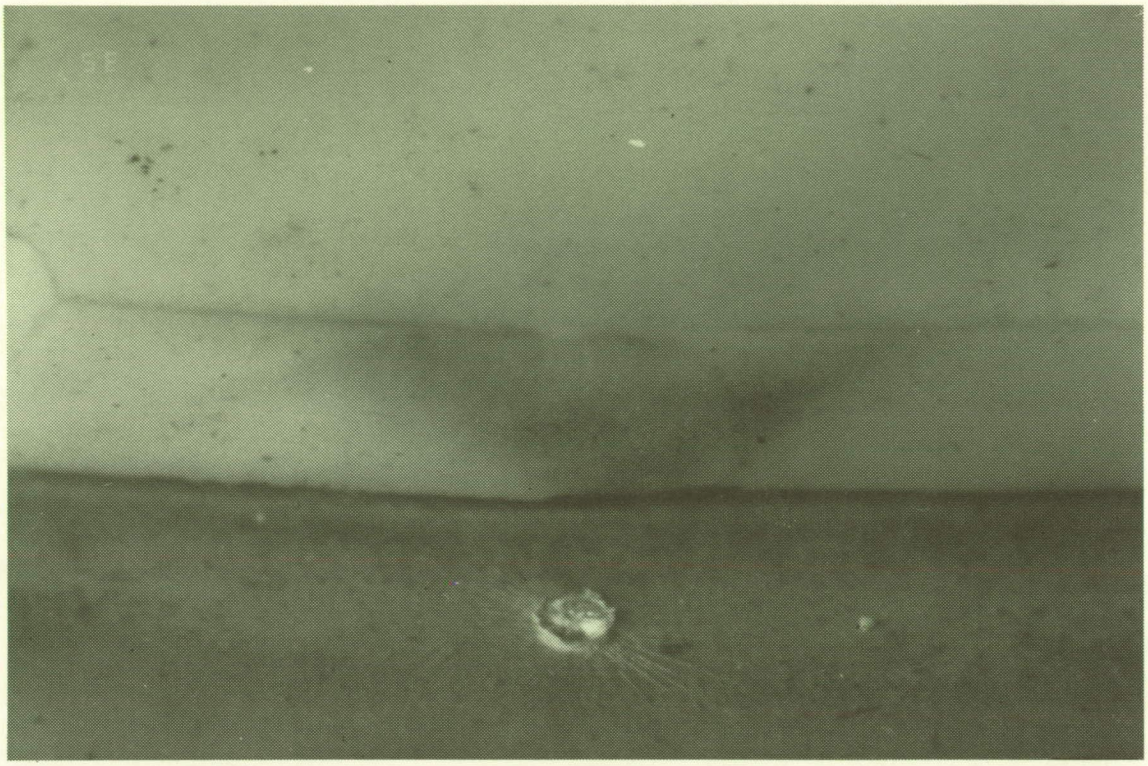

Figure 4. Aluminum tray, 0.78 mm dia. impact crater, debris spray onto RTV 511 sample

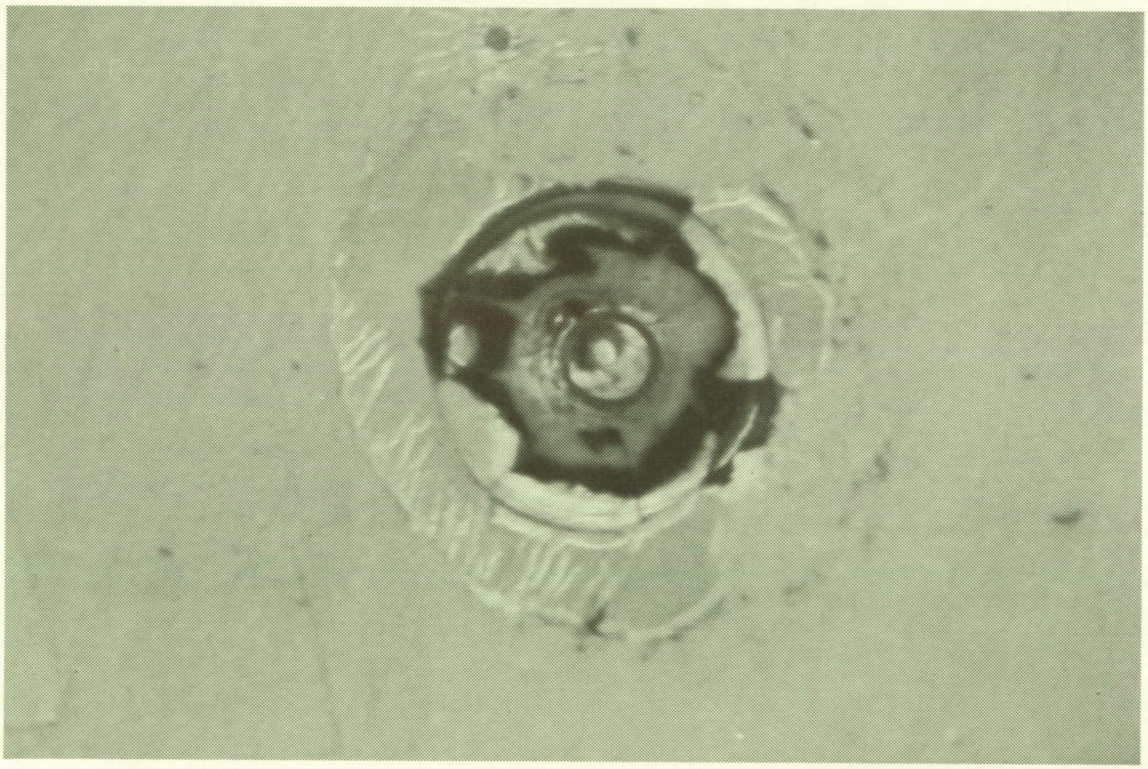

Figure 5. 5 mil Silver/Teflon on aluminum, 1.2 mm dia. crater, ~4 mm dia. dark spall ring

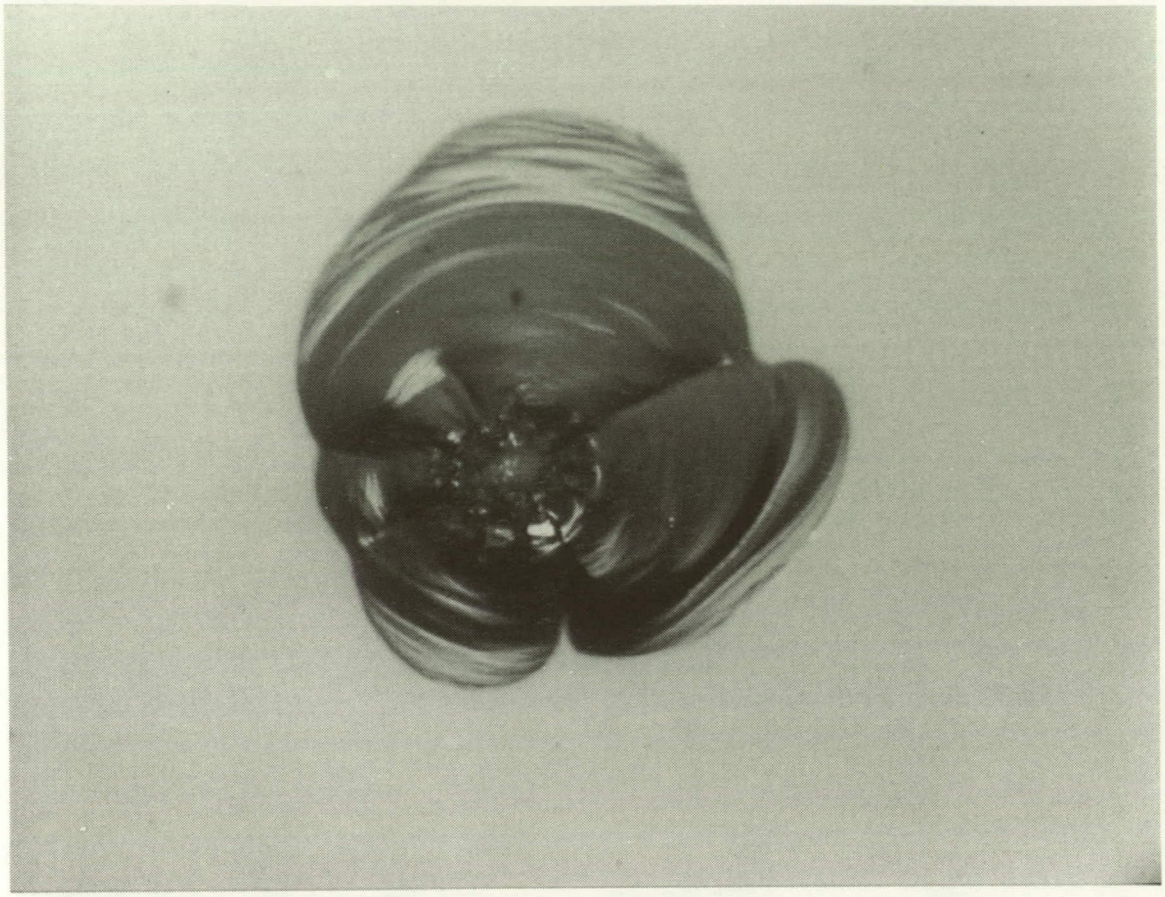

Figure 6. UV window, 0.20 mm dia. crater, 0.71 x 0.76 mm spall

HYPERVELOCITY IMPACT MICROFOIL PERFORATIONS IN THE LEO SPACE ENVIRONMENT (LDEF, MAP AO 023 EXPERIMENT)

J.A.M. McDonnell
and
T.J. Stevenson
Unit for Space Sciences
Physics Laboratory
University of Kent
Canterbury, Kent UK CT2 7NR
Phone: [44] (227) 459616, Fax: [44] (227) 762616

SUMMARY

The Microabrasion Foil Experiment, comprises arrays of frames, each supporting two layers of closely spaced metallic foils and a back-stop plate. The arrays, deploying aluminium and brass foil ranging from 1.5 microns to some 30 microns were exposed for 5.78 years on NASA's Long Duration Exposure Facility (LDEF) at a mean altitude of 458 km. They were deployed on the North, South, East, West and Space pointing faces; results presented here comprise the perforation rates for each location as a function of foil thickness. Initial results refer primarily to aluminium of 5 microns thickness or greater. This penetration distribution, comprising 2,342 perforations in total, shows significantly differing characteristics for each detector face. The anisotropy confirms, incorporating the dynamics of particulate orbital mechanics, the dominance of incorporating extraterrestrial particulates penetrating thicknesses greater than 20 microns in aluminium foil, yielding fluxes compatible with hyperbolic geocentric velocities. For thinner foils, a disproportionate increase in the flux of particulates on the East, North and South faces demonstrates the presence of orbital particulates which exceed the extraterrestrial component perforation rate at 5μm foil thickness by a factor of approximately four. Although in terrestrially bound orbits, their origin has not yet been established exclusively as space debris. Sources and sinks of particulates in the LEO environment are discussed and improved relationships for conversion to impacting particle mass invoked to derive LEO and interplanetary mass distributions.

1. MICROABRASION PACKAGE (MAP) - AO 023

1.1. Introduction

Microfoil penetration techniques have been successfully employed as space particulate detectors since the beginning of space exploration. They offer high sensitivity of detection and yet are rugged and simple. Early measurements on rockets and satellites are reviewed (McDonnell, 1970) and again some 18 years later following the development of more reliable techniques and sophistication (McDonnell, 1978). The sensitivity of foil detectors is achieved by the quality of the foil and its thickness. For example at 5 microns foil thickness and for a foil defect density of 1 per 10 cm^2, optical scanning (even by the simplest of techniques such as a well adapted eye over a light table) yields an effective sensitivity of 10^{-11}g impacting particle mass (< 1 micron diameter) and a "background" flux rate of 3.10^{-5} m^{-2} sec^{-1} for 1 year of exposure. If such defects are logged or painted out before flight as in the case of LDEF MAP, reliability of detection is further improved. Combined with the identification of hypervelocity impact features by Scanning Electron Microscopy (SEM) post-flight examinations, not only can the highest confidence in a true space impact be established, but parameters of the particle such as mass or velocity can be inferred from the morphology. When, further, a second surface is placed immediately behind this foil, a *capture cell* is formed. Although *marginally* penetrating particles cannot be expected to provide ejecta which is detectable behind the foil, larger particles will penetrate and be retained even without a significant mass loss. Their matter, shocked through impact, is spread out over a cone of typically ± 30° and condenses on

the second surfaces; it is thus readily available for e.g. SEM and Energy Dispersive X-Ray (EDX) spectroscopy. With the use of a windowless detector, light elements including carbon may be studied. First results of the capture cell technique from a space deployment were reported (McDonnell et al. 1984) on NASA Shuttle flight STS-3 (Columbia). They showed, however, a flux of particles at some 10^{-11}g mass considerably lower than that inferred from the Solar Maximum Mission (SMM) surfaces (Laurance & Brownlee, 1986). More recently this SMM data has seen the benefits of the application of an improved penetration formula (McDonnell, 1991) in contrast to the initial interpretation of the craters by a formula not representative of the nature of the materials involved (e.g. Pailer & Grün, 1980).

This picture of the near Earth space environment is now being reshaped by the wide diversity and good statistics of the LDEF data over its 5.78 years exposure. Complemented by data from time-tagged events such as the IDE experiments on LDEF (Mulholland et al. , 1991) a very powerful base for the potential understanding of the properties of the flux distribution is available. Objectives of the MAP experiment can be identified.

(i) Definition of the flux distribution as a function of crater size or perforation thickness,
(ii) Determination of the 3-dimensional flux distribution,
(iii) Characterisation of the velocity distribution and angular distribution on a detector surface,
(iv) Discrimination between particle sources e.g.:
  (a) Earth-orbital or interplanetary?
  (b) if Earth-orbital, are they natural or space-debris?
  (c) if natural, are they asteroidal or cometary?
(v) Particulate chemistry.

We shall, no doubt, find that the answers reveal a mixture of sources since the mixing and comminution of matter within the solar system and the LEO environment appears to be an essential characteristic of the equilibrium distribution surrounding the Earth.

1.2. Technique and Experiment Details.

The LDEF Multiple Foil Microabrasion Package (MAP) system comprises a double layer of foils and a back-stop plate (Schematic Figure 1). The foils are bonded to meshes, in turn bonded to frames, which are bolted to a base plate occupying (for the NSEW faces) one third of an LDEF tray; the space-pointing array occupies one half tray. Figure 2 shows a sample of the spatial distribution of impacts on 5μm space-pointing aluminium foil and the effective areas of each frame.

Foils, generally comprising T6 temper rolled aluminium of 99.9% purity, range from 3.5 to 30 μm nominal thickness. Thinner foils (down to 1.5 μm of aluminium) are beaten and do contain considerable defects requiring the discrete post-flight verification of each impact site. For this reason the impacts tabulated for these foils are shown in parentheses. Rolled brass of 5μm nominal thickness was also flown to permit chemical discrimination of impactor residues from the possible presence of aluminium-rich space debris.

1.3. Exposure Configuration.

Four (double) frames were deployed on the space end, comprising top surfaces of 5μm aluminium and brass for a combination of maximum sensitivity and reliability. Eight frames of varying thickness were deployed on each of the four faces: North, South, East and West. The exposure configuration of MAP in orbit is shown in Figure 3. The offset of some 8° to 9°of the East face relative to the orbital motion vector (LDEF Newsletter May 1991) becomes significant when considering East-West flux ratios and, more especially, the North-South ratios. We shall see that it is these *ratios* that critically determine our viewpoint on whether flux particles are perhaps either orbital or interplanetary, because the access to different detector surfaces is so critically dependent upon the orientation of detectors. Figure 4 shows the MAP peripheral tray at recovery and in Figure 5 the space-pointing array (upper right).

1.4. LDEF Orbit Exposure.

The temporal mean altitude (H) of LDEF (Figure 3) over its entire exposure duration is calculated as 458 km; the total exposure time was 5.778 years (1.822×10^8 seconds). The orbital velocity at this altitude, assuming a circular orbit (LDEF's initial eccentricity e = 0.00015) is 7.64 km s^{-1} using 6371 km for the mean radius of the Earth (R_E); the escape velocity at this mean altitude is 10.81 km s^{-1}. A value of 185 km for the effective atmospheric height (h_a) is used, based on atmospheric drag calculations on a particle of 10^{-11}g, corresponding to the capture of a typical interplanetary particle within one Earth revolution. Summary exposure factors are listed in Table 1.

The effective solid angle of a flat plate parallel to the Earth's radius vector is given by $[\Delta - 0.5\sin(2\Delta)]$ steradians, where D (radians) is the angle from the nadir to the horizon (Figure 3). This corresponds to $\pi/2$ steradians effective solid angle for $\Delta = \pi/2$ radians, namely a very low orbit, and π steradians for an unshielded plate. The effective solid angle for a cone of θ radians half angle from the normal to the surface is $\pi(1 - \cos^2 \theta)$ steradians. Δ is given by $\sin^{-1}(A/R)$, where $A = R_E + h_a$ and $R = R_E + H$ (Figure 3). The mean LDEF effective peripheral tray exposure solid angle (including Earth shielding) is 2.125 steradians.

Concerning exposure, we note that the radius vector of LDEF's 28.5° geocentrically inclined orbit is swept by rapid precession through a wide range of pointing directions relative to the solar ecliptic , and can perhaps in the first instance be considered "random". LDEF's orbital plane will have an average ecliptic referenced inclination of +23.5° (the polar declination) with a swing of ± 28.5°. The space-pointing end will then be exposed to interplanetary particulates over a very wide range of ecliptic latitudes throughout its orbit, namely ± 52°. This angle is further combined with the acceptance angle of a flat plate detector. We should view therefore the extraterrestrial flux on the Space end as an "average" of all ecliptic latitudes and longitudes. We also note especially that the Space and West-pointing faces have a very low probability of interception with Earth-orbital particulates. The West face cannot be impacted by orbital particulates at all unless they are on eccentric orbits and, further, only if they are near perigee when they strike LDEF. This excess velocity is required to enable them to "catch up" LDEF and though possible, the interception probability is low. The effective *penetrating* flux for the Space and West faces is further reduced due to the lower velocity of this population.

2. PERFORMANCE AND RESULTS.

2.1. Analysis Methods.

Performance of the MAP experiment, which was entirely passive in nature, was well demonstrated by the excellent condition of the aluminium and brass foils post flight. Few defects were detected due to experiment integration, launch or retrieval; in-flight exposure damage was found to be restricted to that of the experiment objective, *impact erosion*. Foil thicknesses given in Table 2 were determined by establishing the weight per unit area from samples of foil retained from the time of assembly to the meshes. An accuracy of 10μg in mass and some 1% in area measurement leads to an error of typically some 2% in thickness; this "calibration" leads to significant changes from nominal foil thicknesses. Because of the small statistical errors in the MAP flux determinations on, e.g. the East facing foils, the data is able to establish the significance of changes in the *slope* of the measured flux distribution - an indicator of perhaps the changing physics of impact or environmental changes. Scanning, performed optically in the first instance with a computer controlled 3 colour stereo television microscopy system (Paley, 1991), is followed by SEM and microanalysis using a Philips 525M microscope and PGT windowless EDS system. Hard copy colour images and digital images are available and are also archived into a database via an Ethernet network. A Sun workstation is used for feature analysis (e.g. as per Figure 6).

Results presented in this paper are restricted to foils of 5 microns or greater where the defect rate after pre-flight "painting out" is essentially zero. Sample tests on the hypervelocity characteristics of individual perforations were performed for quality control purposes, but generally the results presented here are from optical scanning without discrete impact site examination.

In scanning operations for marginal and larger (supra-marginal) holes, the area of the hole under back-lighted CCD imaging is established by pixel counting above a threshold light level. Figure 7 shows typical features. The transmitted light area is compared to a calibration curve determined by holes measured under

SEM examination. This "photometric" hole size determination is complemented by SEM analysis of the few very large perforations in a typical distribution.

MAP data - because of the multiplicity of thicknesses involved and the generally high perforation rates - is comprised of two types of data: (i) the marginal hole count (namely the number of perforations irrespective of size); this is evaluated and plotted as a function of the foil thickness at the ballistic limit f_{max}, and (ii) the perforation size distribution (hole diameter D_H) for any one value of foil, f_{max}. Marginal fluxes thus determined are shown in Table 2.

The flux distribution Φ as a function of f_{max}, $\Phi(f_{max})$, readily transforms to a particle size distribution $\Phi(d_p)$, or mass distribution $\Phi(m_p)$ of the same form because f_{max}/d_p is not a strong function of size of particle. The distribution of D_H for any value f_{max} does not, however, so transform. For the latter, the increase of hole size as a function of increasing particle size shows a rapid "onset" just above the ballistic limit; thereafter there is a convergence of the hole size D_H towards the particle diameter d_p for $d_p >> f_{max}$. Such relationships have been published by Carey et al (1985) (see Appendix) and more recently studied by Hörz et al (1991). Figures 7(a) to (c) show various hypervelocity impact features on the MAP aluminium foils ranging from marginal (at the exit side, 6(a) and (b)) and in 7(c) one which is clearly the record of a very large particle of some 30 microns diameter which continued through to deposit a spider's web of impacting particulate matter within the capture cell behind.

2.2. Marginal Flux Distributions.

The number of perforations, irrespective of size D_H, is established first for various thicknesses of foil. This yields the *cumulative* distribution $\Phi(f_{max})$ for the peripheral faces (N,S,E,W). Because only 5 microns brass and aluminium was flown on the space-pointing faces, a single value for each of the surfaces is presented. Data is shown in Figure 8 and also that from the Solar Maximum Mission Satellite (Laurance & Brownlee, 1985). We shall later use the size distribution D_H of these foils to generate an interpreted equivalent distribution (section 2.3) as a function of f_{max} e.g. Figure 9.

The marginal distribution in Figure 8 shows high definition with, generally, the exception of the West-pointing faces where counts are low. When these marginal counts are transformed to an actual size distribution, some of the coarseness of the foil thickness "quantisation" can be removed. Currently a fit through the West data is used since each point is independent.

We see an interesting divergence in the flux between the side faces of LDEF (N,S) relative to the velocity vector. As stated these (because of precession) show average exposure relative to the ecliptic elevations North and South; they might also be expected to be exposed randomly to the satellite-derived space debris flux. For the small particulates, LDEF's offset of 8° to 9° increases the observed excess of the south flux relative to the North if true orbit pointing directions are considered. For larger particulates - shown to be predominantly interplanetary in origin (McDonnell, 1991), this offset correspondingly reduces the excess of the North relative to South for the penetrating flux at $f_{max} > 20$ microns but it remains significant. Explanations of this North-South asymmetry and its reversal within the MAP sensitivity regime call for a non-random spatial distribution of dust in Earth orbit, if the fluxes are dominated by "orbitals". Alternatively, if they are interplanetary a non-random distribution in interplanetary space is called for. Though precession generally randomizes the satellite population regarding the ascending nodes and argument of perigee, the geocentric inclination is retained except for the very smallest particles which can be influenced by the Lorentz force due to electromagnetic coupling of their electrostatic charge and the Earth's magnetic field. For one particular type of orbit - Molniya - an inclination of some 70° locks the precession into a stable geocentric relationship from which asymmetry *could* result. The IDE experiment (Mulholland et al, 1991) sheds significant light on the non-random time variations of what, on the MAP experiment, we see as a total 5.78 year accumulation.

Though LDEF offers unprecedented definition of the 1984-1990 flux, we should compare this to other data. We take, as one example, the SMM data, but not in terms of inferred impacting mass. The crater diameter D_C is referenced to an expected crater depth by the ratio observed for LDEF clamps (Newman, 1991) giving $P_c/D_C = .58$. We also use $f_{max} = 1.15\ P_c$ (McDonnell 1970), and combining these, $f_{max} = 1.15 \times .58\ D_C = .67\ D_C$. Alternatively we could choose $f_{max} = 1.7 \times .58\ D_C$ according to Humes (1990); this data from SMM is shown dotted line on Figure 8, and - if a random SMM exposure is simulated by

some averaging of the NSEW faces of LDEF MAP data - we see that the SMM data and LDEF MAP data are quite compatible.

2.3. Supra-Marginal Perforations.

Where $D_H > 0$ we have information which can sometimes lead to the clues on the particle size, mass or velocity. We cannot in general separate out these three parameters explicitly since in general the crater dimensions are a function of total particle *energy* at hypervelocities. For particle diameters $d_p > f_{max}$, however, we must see a trend towards a perforation comparable to the particle size. The velocity may also be inferred within broader limits from crater morphology. We summarise relevant penetration relationships used (Appendix) to transform the D_H distribution for one foil, the 5μm aluminium space-pointing foil, to an equivalent thickness of foil which would just be penetrated (Deshpande, 1991). Figure 9 shows this transformation; it is compared to the crater distribution on the space-pointing clamp analysed at Canterbury. Though this conversion is preliminary, and no doubt in need of refinement, we see some convergence. At large dimensions, statistical limits restrict the comparison, but the total LDEF data set will permit refinements of this transformation in due course.

2.4 Ultraheavy Cosmic-Ray Nuclei Experiment (UHCRE - AO178) Thermal Cover Penetration Data.

The $18m^2$ area of Fluorinated Ethylpropylene Teflon (FEP) thermal closeout covers show excellent promise for meteoroid and debris studies. Under agreement between the Principal Investigators (O'Sullivan et al, 1984), NASA LaRC and ESA, scanning operations were performed at NASA KSC after recovery and now continue at NASA JSC and the University of Kent at Canterbury, UK. These laminar foils comprise 120 microns of FEP Teflon, backed by a Silver/Inconel flash and some 80 microns of Chemglaze Z306 black paint. The equivalent thickness of aluminium penetrated may possibly be related using relationships in the Appendix. However this presumes we know the *dynamic* strengths involved; - the behaviour of the Teflon under impact is indeed complex and poses one of the more interesting morphological studies on LDEF. Figure 10 shows optical photographs of sample Teflon penetrations. They show (on the Silver surface beneath the Teflon) radial light and dark bands corresponding to variations in the Fluorine/Oxygen ratio. Though akin to "growth rings" it is uncertain whether they are formed completely at impact or involve a subsequent combination of delamination and the ingress of powerfully oxidizing atomic oxygen.

As a first sample of the UHCRE data we plot the hole size distribution on faces 10 and 4 from this experiment (Figure 11); corresponding approximately to an East-West configuration they yield small ratios e.g. 10 which demonstrates the need for a geocentric particle velocity much greater than LDEF's orbital velocity, namely from interplanetary hyperbolic sources. This is confirmed by the MAP data at $f_{max} = 30$ μm and the SDIE data (Humes, 1991).

2.5 Other LDEF data.

We piece together in Figure 12, albeit in tentative fashion, other data comprising that of the Interplanetary Dust Experiment (IDE - AO201, Mulholland, 1991); LDEF MAP (ibid), the Canterbury scanning of the UHCRE covers (O'Sullivan et al, 1984) and data from LDEF Meteoroid and Debris Special Interest Group (M+DSIG) data (See et al, 1990) including the preliminary scanning of the surfaces of the Humes Space Debris Impact Experiment (SDIE - S0001) performed at KSC after retrieval. We show also the data from the (West-pointing) French Co-operative Payload (Frecopa) tray (Mandeville, 1990). Data models for the West and East fluxes (representing approximately minimum (interplanetary) and maximum (interplanetary and earth-orbital)) have been developed (e.g Sullivan & McDonnell (1991)). This is used (Section 3) in the reduction of the data to a geocentric (compared to LDEF's orbital) reference frame. The first step requires comparison of the West and Space fluxes which are both predominantly interplanetary.

We shall later see this larger body of data refined in terms of resolution and accuracy but also in terms of the *calibration* i.e. the equivalence of different types of detector such as the IDE solid state SiO_2 detectors, the thicker targets of the Teflon UHCRE targets and the aluminium SDIE surfaces. Not all detectors have a common pointing direction, although we shall see that the IDE, MAP, UHCRE and SDIE experiments offer the fullest of angular coverage.

We also show data from the M+D SIG database, representing the LDEF tray clamp and frame impact crater counts on either 12 (x30°) or 24 (x15°) peripheral pointing directions (Figure 13) (See et al., 1990). The bias (for these larger particulates) towards geocentric North is seen. Accepting the discussions in Section 5 which support the interplanetary origin of these particulates, we see this argues for more of the large interplanetary particulates to be in the descending mode at 1 AU heliocentric distance. This has implications for the number of sources responsible for the sporadic micrometeoroid flux at some 50 μm particle diameter, a size which corresponds to particles responsible for the Zodiacal Light (e.g. Giese et al, 1976). These particulates were found assuming the single velocity (average) model, to have a geocentric velocity in the region of 17.4 ± 3 km sec^{-1}, transforming to a V_∞ of 12 ± 4 km sec^{-1} as the geocentric inferred average approach velocity to the Earth in our initial modelling (McDonnell, 1991) This is comparable to values derived from meteoroid studies e.g. see Zook 1975 for review. It is interesting to note that in similar modelling by Zook (1990), quantitative differences are obtained. For given Space-to-West and East-to-West ratios, Zook's modelling calls for geocentric velocities higher by some 5 km s^{-1} than ours leading to interplanetary approach velocities of some 19 kms^{-1}. *Both* modelling approaches however demonstrate the extraterrestrial (and interplanetary) nature of the large particles.

The transformation of Sullivan & McDonnell (1991) is further applied to the West flux to predict the East, using a data model developed from Figure 12. This yields a flux lower, by a factor of 4, than the measured East flux, and calls for the presence of Earth-orbitals; the transformation and discussion is described in McDonnell (1991) and results shown in Figure 14.

3. MODELLING OF LDEF'S EXPOSURE IN THE PARTICULATE ENVIRONMENT.

In all modelling of the dynamics of particle orbits and interception with a moving spacecraft, the examination and interpretation of impact/flux data from differing spacecraft attitudes or pointing directions must be conducted either at *constant mass* or alternatively at *constant crater size*. Crater size is, of course, directly related to the marginal perforation foil thickness.

Flux enhancement at constant mass is the "sweeping-up" effect of the satellite into the particulate cloud and leads to an enhancement of numbers intercepted compared to the trailing face. A consequential effect of this, but quite separate physically, is that those particles will also have a different relative velocity for the two faces, and hence, will upon impact lead to different crater dimensions; because most impact observations (and observed crater flux distributions) refer to a particular crater *dimension*, the experiment detector surfaces receiving greater numbers of particles will yield a flux value which is relevant to smaller (and invariably more numerous) particles. The latter *sensitivity enhancement* depends on the size distribution of particulates which, fortunately, can be deduced from the data.

The approach to this dynamic *modelling* is described by McDonnell et al (1990), and uses a geocentric distribution of particle directions at a particular velocity; when combined with LDEF's motion the incidence frequency (flux) on LDEF's faces and also the impact velocity is calculated. The normal velocity (which determines the effective velocity for impact penetration) is calculated. The results are applied first to the West and Space flux, which cannot intercept significant orbital particulates. The transformation is effected as a function of velocity and a particle velocity is found which leads to best agreement between the West and Space flux data.

We see in Figure 14 the resultant Earth-orbital component identified, which dominates the East, and also the North and South fluxes for $f_{max} < 20$ μm. This is in contrast to the larger particulates where the interplanetary component is dominant. We can also transform (McDonnell, 1991) to the expected interplanetary flux at 1AU beyond the gravitational influence of the Earth. This compares very favourably with deep space data and meteoroid fluxes (as reviewed by Grün et al 1985), confirming our hypothesis of the dominant sources of the LDEF impacts.

As to the astrophysical or terrestrial *origin* of the Earth orbitals, from consideration of the IDE flux and temporal variations, Mulholland et al (1991) have claimed they are space debris related. A contrary viewpoint has been proposed by McDonnell (1991) and McDonnell & Ratcliff (1991) where the possibility of captured interplanetary dust either through *aerocapture*, and *aero-fragmentation* capture is discussed. The

electrostatic disruption of fragile meteoroids near the earth has been proposed as a means of explaining the groups and swarms of particulates seen by Heos II (Hoffman et al., 1975(b)).

We probably must await chemical evidence before the *true* origin is ascertained. Although the SMM data had previously been attributed to space debris and calculated to be some 50 times higher in flux than the natural component, we see that improved penetration formula lead to the excess being much less because of the lower inferred mass of these particulates (even though they might comprise space debris). That data did show their chemistry to be debris-related, but the equivalence of LDEF MAP and SMM flux data, separated by some 5 years in epoch shows little evidence of a change of flux in a period when activity might have expected to increase. We shall have to "watch this space" for further developments!

ACKNOWLEDGEMENTS

To the Science and Engineering Research Council UK for financial support and Auburn University Space Power Institute (USA), N660921-86-OC-A226, subcontract 87-212. To the whole LDEF MAP team; Ken Sullivan, Piers Newman, Sunil Despande, Matthew Paley particularly. To the USS secretarial complement, Alison and Margaret, and to NASA Langley Project Office especially Jim Jones and Bill Kinard for every encouragement throughout the project.

APPENDIX

Penetration Relationships Used

For thin (micron dimension) aluminium foils impacted by iron particles, we refer to calibration data established to velocities of 15 km s^{-1} using a 2 MV van der Graaff accelerator (McDonnell, 1970). This yields a marginal penetration relationship:

$$f_{max} = 0.79\ V^{0.763} \qquad \text{(eq 1)}$$

where V is the impact velocity (km s^{-1}) and f_{max} (μm) is the foil thickness penetrated, not referred to the *ballistic limit*, but to a value of $D_H = f_{max}$. In practice, the minimum hole size close to the ballistic limit yields a value of $D_H/f_{max} = 0.6$ for iron particles impacting aluminium at velocities of some 5 km s^{-1} due to the formation of deeper craters. At higher velocities, the ballistic limit perforation leads to a minimum hole size which is typically $D_H \approx f_{max}$, although in principle a hole of $D_H = 0$ is (on the limit) still technically feasible.

The above formula was extended to cover the region beyond the ballistic limit (Carey et al. 1985) for iron projectiles impacting on aluminium targets namely:

$$\frac{D_H}{d_P} = 1 + 1.5\,(f/d_P)\,V^{0.3}\left[\frac{1}{1 + (f/d_P)^2\,V^{-n}}\right] \qquad \text{(eq 2)}$$

where V is in kms^{-1} and n is given by,

$$n = 1.02 - 4\exp(-0.9\,V^{0.9}) - 0.003\,(20 - V) \qquad \text{(eq 3)}$$

A formula derived from iron projectiles impacting on gold targets (and hence comparable to low density meteoroids impacting aluminium, because of the similar projectile-to-target density ratios) was also derived in the same work:

$$\frac{D_H}{d_P} = 1 + 5\,(f/d_P)\,V^{0.3}\left[\frac{1}{1 + 7\,(f/d_P)^2\,V^{-n}}\right] \qquad \text{(eq 4)}$$

The value of n is as above.

These formulae are solved to yield the diameter of impacting particle d_P from a given value of D_H and velocity V. The marginal penetration distance is then calculated from d_P and V to yield an equivalent value of f_{max}. This transformation (illustrated in Figure 9) is relatively insensitive to the velocity assumed.

Neither of these relationships include dimensional scaling, and the first relationship (eq 1) applies only to iron projectiles on aluminium. The ballistic limit formula has therefore been generalised by McDonnell & Sullivan (1991) to yield a relationship applicable to foils over a wider range of dimensions and for various projectile-target densities and strengths:

$$\frac{f}{d_P} = 1.023\, d_P^{0.056} \left(\frac{\rho_P}{\rho_T}\right)^{0.476} \left(\frac{\sigma_{Al}}{\sigma_T}\right)^{0.134} V^{0.664} \qquad \text{(eq 5)}$$

Here, f and d_P are in units of cm, the densities, ρ, are in g cm^{-3}, the velocity in km s^{-1} and the target tensile strength, σ_T, in units of MPa. It is to be noted that this contrasts with the dimensional dependence of the ballistic limit formula of Pailer and Grün (1985) where a very strong dimensional dependence of the form $d_P^{0.21}$ is demonstrated compared to a dimensional dependence of the form $d_P^{0.056}$ in ours and other work. The formula of Pailer & Grün (1985) yields

$$\frac{f}{d_P} = 0.772\, d_P^{0.2}\, \varepsilon^{-0.06}\, \rho_P^{0.73}\, \rho_T^{-0.5}\, (V \cos\alpha)^{0.88} \qquad \text{(eq 6)}$$

where ε is the target foil ductility and α is the angle of impact relative to the normal.

This formula (eq 6) however, has been shown to be unsuitable to interpret the SMM data (McDonnell, 1991) and previously led to an overestimate of the flux of space micro-debris relative to the natural environment (Lawrence & Brownlee, 1985).

Reference may also be made to other formula commonly used, namely that of Fish and Summers (1965):

$$\frac{f}{d_P} = 0.57\, d_P^{0.056}\, \varepsilon^{-0.056} \left(\frac{\rho_P}{\rho_T}\right)^{0.5} V^{0.875} \qquad \text{(eq 7)}$$

Nauman (1966) developed the relationship:

$$\frac{f}{d_P} = d_P^{0.056}\, \rho_P^{0.52}\, V^{0.875} \qquad \text{(eq 8)}$$

and Cour-Palais (1969) used a similar equation, namely:

$$\frac{f}{d_P} = 0.635\, d_P^{0.056}\, \rho_P^{0.5}\, V^{0.67} \qquad \text{(eq 9)}$$

All formulae have been converted to the same units as in equation 5. The McDonnell-Sullivan equation concurs with the more accepted of these relationships at centimetre scale but also has the benefit of fitting the microscale regime. LDEF's impact record may enable some of these parametric dependencies to be tested at the more realistic velocities occurring during its 5.75 year exposure.

REFERENCES

Carey, W.C., McDonnell, J.A.M. and Dixon, D.G., (1985) "An Empirical Penetration Equation for Thin Metallic Films used in Capture Cell Techniques", In Properties and Interactions of Interplanetary Dust, D. Reidel, R.H., Giese and Ph. Lamy (eds.), pp. 131-136.

Cour-Palais, B.G., (1969) "Meteoroid Environment Model -1919", NASA SP-8013.

Deshpande, S.P. and Paley, M.T., (1991) "Supra-Marginal Impacts Detected on the Microabrasion Package (MAP) Experiment Situated on LDEF's Space Face", Proc. Workshop on Hypervelocity Impacts in Space, University of Kent at Canterbury, Dec. 1991.

Fechtig, H., (1976) "In-situ records of interplanetary dust particles - methods and results", Proc. IAU Colloq. 31, Lecture Notes in Physics, **48**, p 143, Eds. H. Elsasser & H. Fechtig, Springer-Verlag.

Fish, J.L. & Summers, J.L. (1965) Proc. Hypervelocity Impact Symposium, 7th, **3**, 2.

Giese, R.H. and Grün E., (1976) "The Compatibility of Recent Micrometeoroid Flux Curves with Observations and Models of the Zodiacal Light", Lect. Notes Phys. **48**, pp. 135-139.

Grün E., Zook, H.A., Fechtig, H. and Giese, R.H., (1985) "Collisional Balance of the Meteoritic Complex", Icarus **62**, pp. 244-272.

Hoffmann, H.J., Fechtig, H., Grün, E. and Kissel, J., (1975(a)) " First Results of the Micrometeoroid Experiment S215 on HEOS 2 Satellite", Planet. Space Sci. **23**, pp. 215-244.

Hoffmann, H.J., Fechtig, H., Grün, E. and Kissel, J., (1975(b)) "Temporal Fluctuations on anisotropy in the Earth Moon System", Planet. Space Science, **23**, pp. 985-991.

Hörz, F., See, T.H. and Bernhard, R., (1991) "Thin Film Penetrations by 50 to 3200 μM Diameter Glass Projectiles", Proc. Workshop on Hypervelocity Impacts in Space, University of Kent at Canterbury, Dec. 1991.

Humes, D.H., (1991) "The SDIE Impact Experiment on LDEF", Proc. Workshop on Hypervelocity Impacts in Space, University of Kent at Canterbury, Dec. 1991.

Laurance, M.R. and Brownlee, D.E., (1986) "The Flux of Meteoroids and Orbital Space Debris Striking Satellites in Low Earth Orbit", Nature, **323**, pp. 136-138.

Mandeville, J.C. and Berthoud L., (1991) "Hypervelocity Impacts on Space Retrieved Surfaces (LDEF and MIR)", Proc. Workshop on Hypervelocity Impacts in Space, University of Kent at Canterbury, Dec. 1991.

McDonnell J.A.M., Carey, W.C. and Dixon, D.G., (1984) "Cosmic Dust Collection by the Capture Cell Techniques on the Space Shuttle", Nature, Vol. **309**, No. 5965, pp. 237-240.

McDonnell, J.A.M., (1970) "Factors Affecting the Choice of Foils for Penetration Experiments in Space", COSPAR Space Sci. Sym., Prague, 1969, Space Research **X**, pp. 314-325.

McDonnell, J.A.M., (1970) "Review of In-Situ Measurements of Cosmic Dust Particles in Space", XIIIth COSPAR Space Sci. Sym., Leningrad, Space Research XI-Akademie-Verlag (Berlin), pp 415-435.

McDonnell, J.A.M., (1978) "Microparticle Studies by Space Instrumentation", In Cosmic Dust , Chapter 6, pp. 337-419. Editor J.A.M. McDonnell, Publishers John Wiley and Sons.

McDonnell, J.A.M., (1991) " Impact Cratering from LDEF's 5.75 year Exposure: Decoding of the Interplanetary and Earth-Orbital Populations", Proc. 22nd Lunar & Planetary Science Conference, Houston.

McDonnell, J.A.M., Deshpande, S.P., Green, S.F., Newman, P.J., Paley, M.T., Ratcliff, P.R., Stevenson, T.J. and Sullivan, K., (1990) "First Results of Particulates Impacts and Foil Perforations on LDEF", Adv. Space Res. Vol. II, No. 12, [12]109–[12]114, 1991.

Mulholland, J.D., Oliver, J.P., Singer, S.F., Weinberg, J.L., Cooke, W.J., Montague, N.L., Kassel, P.C., Wortman, J.J., Kinard, W.H. and Simon, C.G., (1991) "LDEF Interplanetary Dust Experiment: A high Time-Resolution Snapshot of the Near-Earth Particulate Environment", Proc. Workshop on Hypervelocity Impacts in Space, University of Kent at Canterbury, Dec. 1991.

Naumann, R.J., (1966) "The Near Earth Meteoroid Environment", NASA TN D-3717.

Newman, P.J., (1991) "A Comparison of the Micrometeoroid Environment as Measured by Thick and Thin Targets from the East Face of the Long Duration Exposure Facility", Proc. Workshop on Hypervelocity Impacts in Space, University of Kent at Canterbury, Dec. 1991.

O'Sullivan, D., Thompson, A., Ceallaigh, C., Domingo, V. and Wenzel, K.P. (1984) "The Long Duration Exposure Facility (LDEF) Mission 1 Experiments, A High Resolution Study of Ultra-Heavy Cosmic-Ray Nuclei (AO178)", NASA SP-473.

Pailer, N. and Grün, E., (1980) "The Penetration Limit of Thin Films", Planetary and Space Science **28,** pp. 321-331.

Paley, M.T., (1991) "An Automated System for Obtaining Impact Penetration, Location, Size and Circularity, on a Foil with Special Reference to LDEF," Proc. Workshop on Hypervelocity Impacts in Space, University of Kent at Canterbury, Dec. 1991.

See, T., Allbrooks, M., Atkinson, D. Simon, C. and Zolensky, M., (1990) "Meteoroid and Debris Impact Features Documented on the Long Duration Exposure Facility, NASA JSC Planetary Materials Branch Publication #84, August 1990.

Sullivan, K., and McDonnell, J.A.M., (1991) "LDEF Flux Anisotropy: Dynamic Modelling and Flux Transformations to Define the Interplanetary Micrometeoroid Environment", Proc. Workshop on Hypervelocity Impacts in Space, University of Kent at Canterbury, Dec. 1991.

Zook, H.A., (1975) "The State of Meteoritic Material on the Moon" Proc. Lunar Sci. Conf. 6th, pp. 1653-1672.

Zook, H.A., (1991) "Meteoroid Directionality on LDEF and Asteroidal versus Cometary Sources", Abstract, Proc. Lunar Planet Sci Conf. 22nd, pp 1577-1578.

Year	Altitude H (km)	H+R_E (km)	Fraction of year	Horizon angle (deg)	Effective flat plate solid angle (ster)
1984	478	6849	0.745	106.82	2.141
1985	473	6844	1.000	106.68	2.137
1986	470	6841	1.000	106.60	2.136
1987	468	6839	1.000	106.54	2.134
1988	459	6830	1.000	106.28	2.124
1989	410	6781	1.000	104.80	2.077
1990	340	6711	0.033	102.34	1.995

Table 1. Exposure Factors of MAP aboard LDEF, giving yearly mean altitudes and Earth shielding history.

Face	Nominal Thickness (μm)	Measured Thickness (μm)	# holes	Area (m^2)	Flux ($m^{-2}s^{-1}$)
East MAP	5	4.83	435	1.02×10^{-2}	2.35×10^{-4}
	12	12.13	49	2.67×10^{-3}	1.01×10^{-4}
	14	14.11	73	5.21×10^{-3}	7.69×10^{-5}
	18	18.16	104	1.02×10^{-2}	5.61×10^{-5}
	25	24.13	40	7.89×10^{-3}	2.79×10^{-5}
	30	31.14	21	1.02×10^{-2}	1.13×10^{-5}
West MAP	3	3.1	(22)	5.33×10^{-3}	2.27×10^{-5}
	2.5	3.72	(6)	5.33×10^{-3}	6.19×10^{-6}
	5	4.83	26	2.03×10^{-2}	7.02×10^{-6}
	12	12.13	1	2.67×10^{-3}	2.06×10^{-6}
	14	14.11	2	5.21×10^{-3}	2.11×10^{-6}
	18	18.16	5	1.02×10^{-2}	2.70×10^{-6}
	25	24.13	11	1.81×10^{-2}	3.35×10^{-6}
	30	31.14	3	2.03×10^{-2}	8.10×10^{-7}
North MAP	1.5	2.02	(361)	5.33×10^{-3}	3.72×10^{-4}
	2.5	3.72	(298)	1.07×10^{-2}	1.54×10^{-4}
	5	4.83	467	2.03×10^{-2}	1.26×10^{-4}
	12	12.13	22	5.80×10^{-3}	2.08×10^{-5}
	14	14.11	26	5.21×10^{-3}	2.74×10^{-5}
	18	18.16	41	1.02×10^{-2}	2.21×10^{-5}
	25	24.13	38	2.04×10^{-2}	1.03×10^{-5}
	30	31.14	43	2.03×10^{-2}	1.16×10^{-5}
South MAP	1.5	2.02	(1158)	1.07×10^{-2}	5.97×10^{-4}
	3	3.1	(218)	5.33×10^{-3}	2.25×10^{-4}
	2.5	3.72	(187)	5.33×10^{-3}	1.93×10^{-4}
	5	4.83	570	2.03×10^{-2}	1.54×10^{-4}
	12	12.13	28	2.67×10^{-3}	5.75×10^{-5}
	14	14.11	45	5.21×10^{-3}	4.74×10^{-5}
	18	18.16	61	1.02×10^{-2}	3.29×10^{-5}
	25	24.13	23	1.81×10^{-2}	7.00×10^{-6}
	30	31.14	13	2.03×10^{-2}	3.51×10^{-6}
Space MAP	5	4.83	193	3.10×10^{-2}	3.42×10^{-5}

Table 2. Characteristic areas and detected numbers of perforations of the MAP deployment on LDEF. Only the surfaces scanned to date are shown; for foils of less than 5 microns, penetrations (in parentheses) are tentative. For foils of 5 microns or greater. 2,340 perforations are reported.

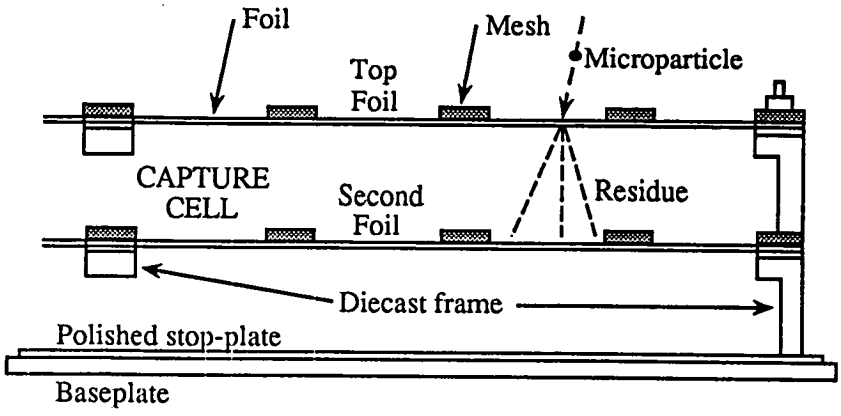

Fig. 1. Schematic cross-section of Microabrasion Package (MAP) Experiment configuration. The capture cell system is formed between the top and second foil surfaces. By inversion of the frame orientation differing foil spacings are achieved.

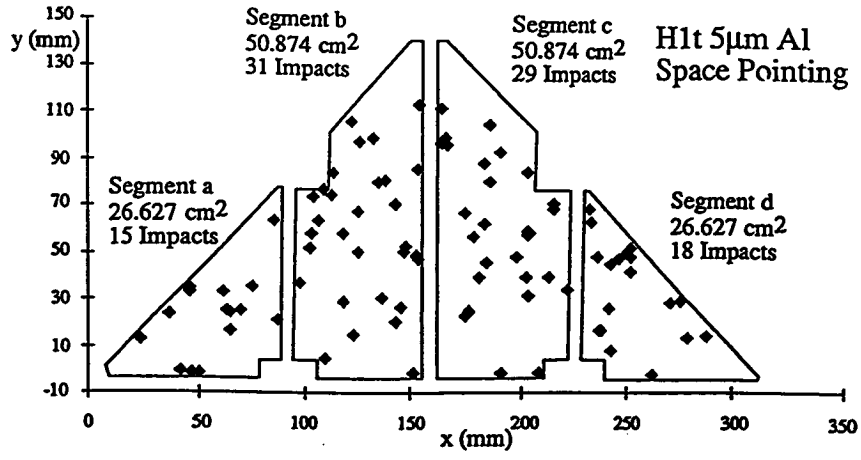

Fig. 2. Plan view of MAP package giving effective foil areas and the distribution of perforations determined by post-flight optical scanning.

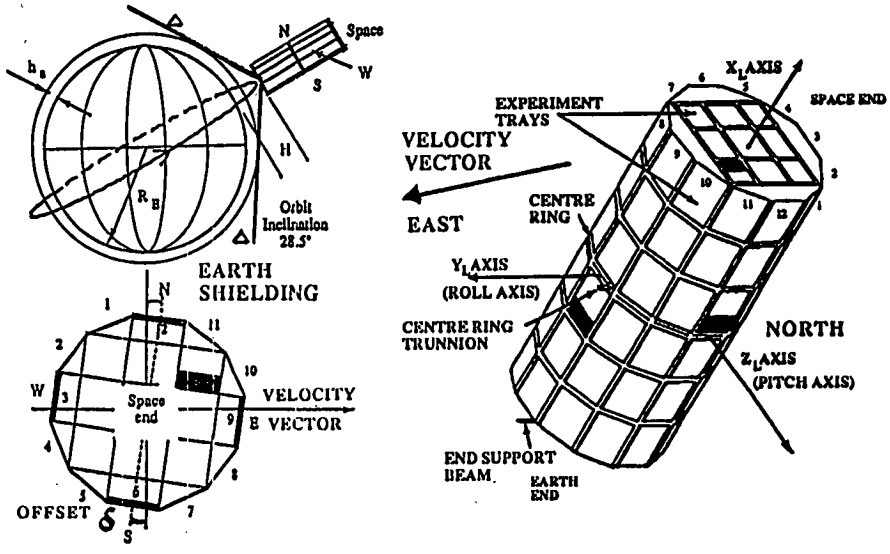

Fig. 3. MAP locations (shaded) on LDEF and the offset of deployment δ illustrated relative to the motion vector (8° to 9°). The Earth shielding angle Δ is illustrated (left).

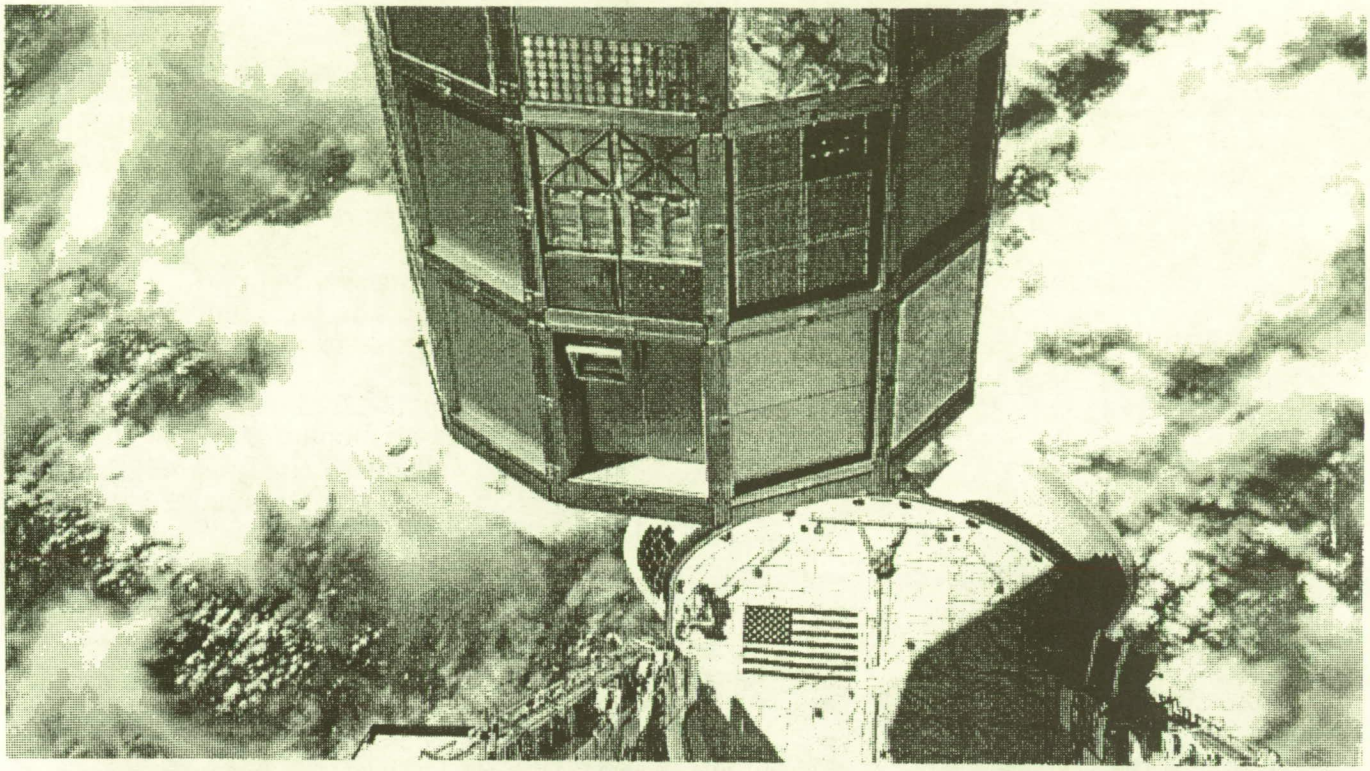

Fig. 4. Peripheral experiment locations photographed at LDEF retrieval. The MAP experiment (top of second tray up, left of centre) is one of the five such locations. NASA Photo.

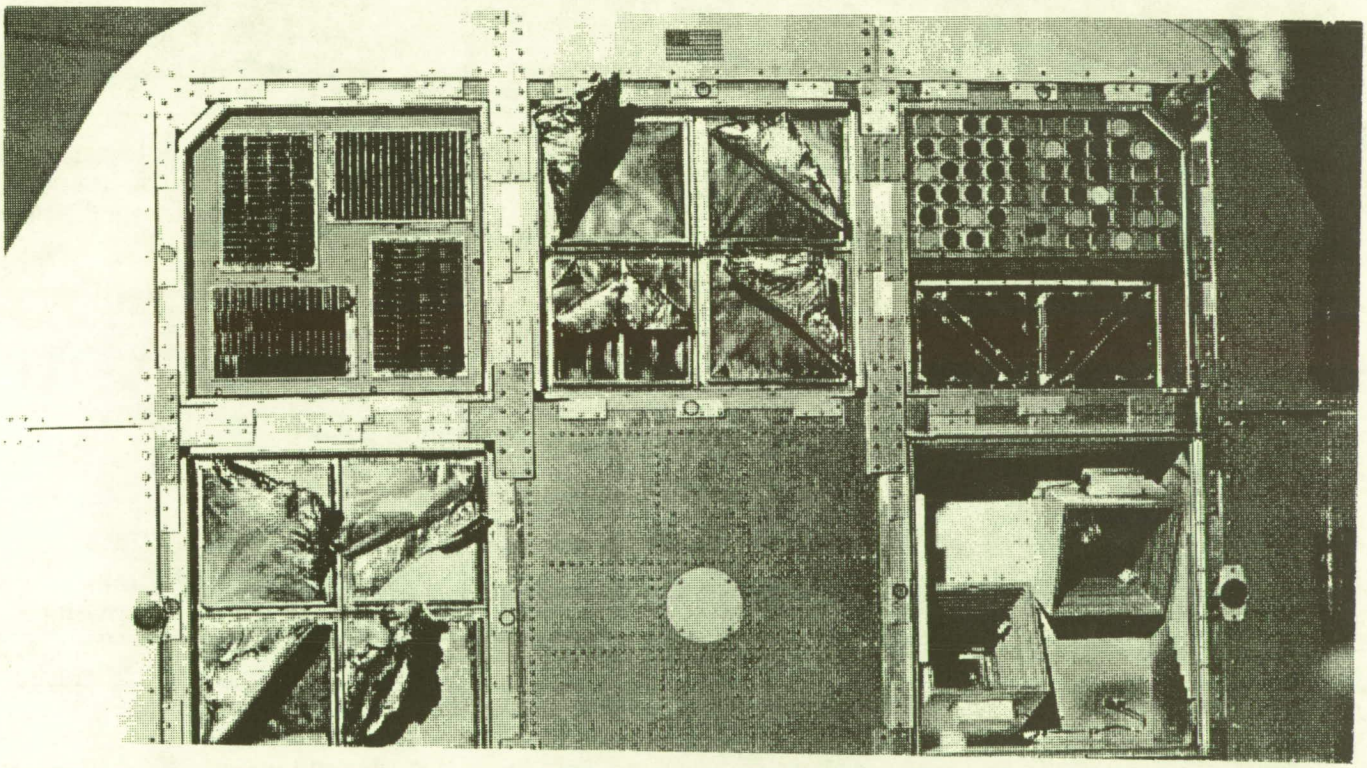

Fig. 5. Space-facing MAP location at LDEF retrieval. The micron dimensioned foils (upper right tray, lower half) show excellent integrity despite a thermal cycling, totalling some 35,000. By contrast, the coated Mylar capture cell covers of the other impact experiments and the multilayer insulation of the NRL cosmic ray experiment (shown in this photograph) suffered considerable degradation. NASA Photo .

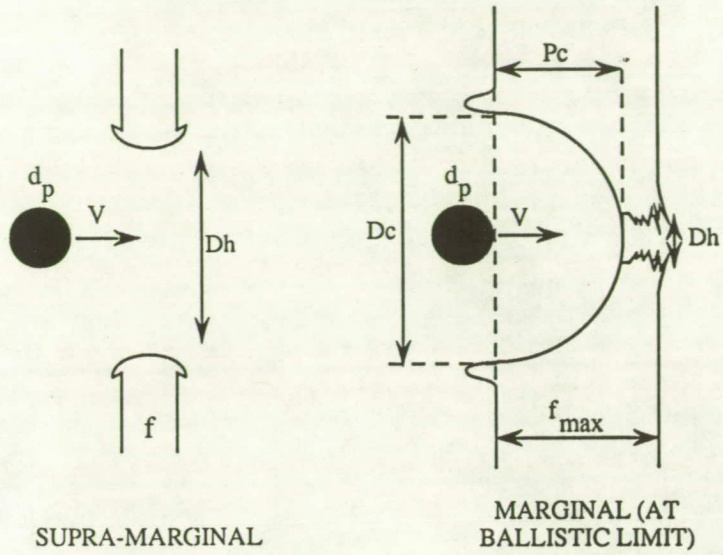

Fig. 6. Parameters of hypervelocity impact craters measured for non-penetrating impacts in (a) the penetration of foils and a semi-infinite target (b). Where $D_H > f_{max}$ the opportunity to capture material on the second surface exists. The maximum thickness a foil perforated f_{max} is related to the semi-infinite target penetration by the relationship $f_{max} = KP_c$. K = 1.15 has been reported for iron particles impacting on aluminium (McDonnell, 1970) and alternatively K = 1.5 to 1.7 (Humes, 1991) reported based on LDEF studies.

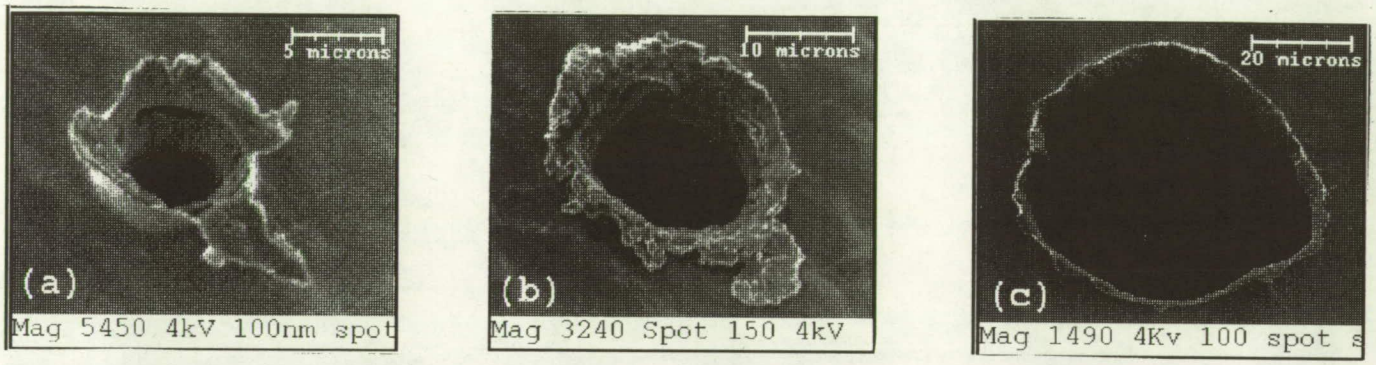

Fig. 7. Perforations in the MAP aluminium foils showing various morphologies dependent largely on the particle size and velocity relative to foil thickness. (a) shows the exit side just above the ballistic limit (b) the exit side for a large impact. In (c) a very large particle, perhaps 30 microns diameter, leads to a 60 micron diameter perforation and a clear signature for capture cell analysis.

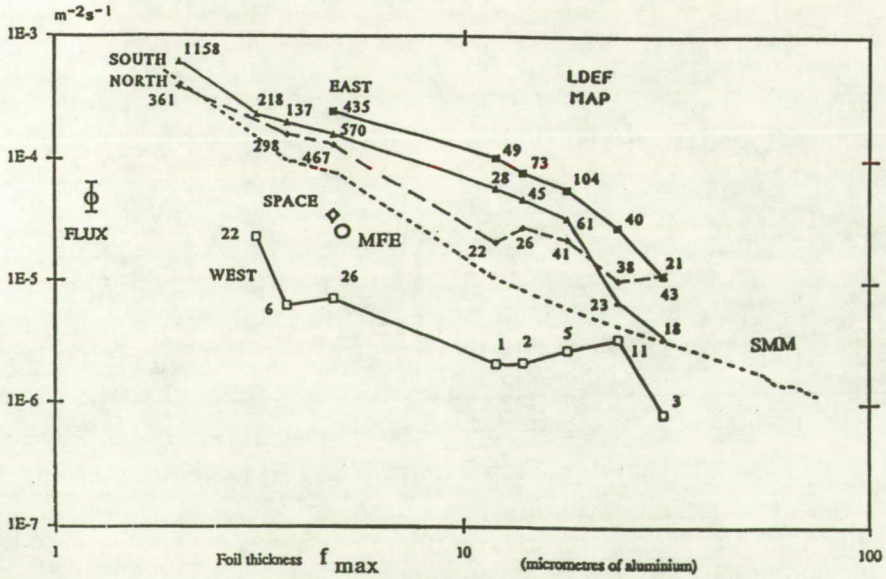

Fig. 8. MAP cumulative penetration distributions for 5 pointing directions showing the number of particles detected. Statistical errors are largely insignificant except for e.g. the low flux West directions. The North-south asymmetry is significant as indeed its reversal between large and small particulates.

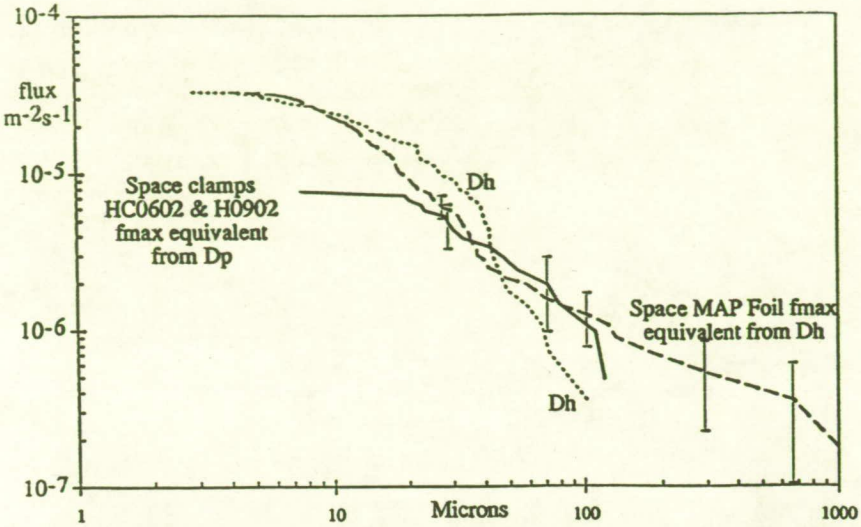

Fig. 9. MAP data from Space-pointing 5 micron foil plotted as a function of the hole diameter distribution D_H (dotted line). It is then transformed using a penetration relationship (Carey et al. 1985) to an equivalent foil penetration distribution (dashed line) and compared to LDEF clamp crater data also transformed to an equivalent foil penetration distribution (solid line).

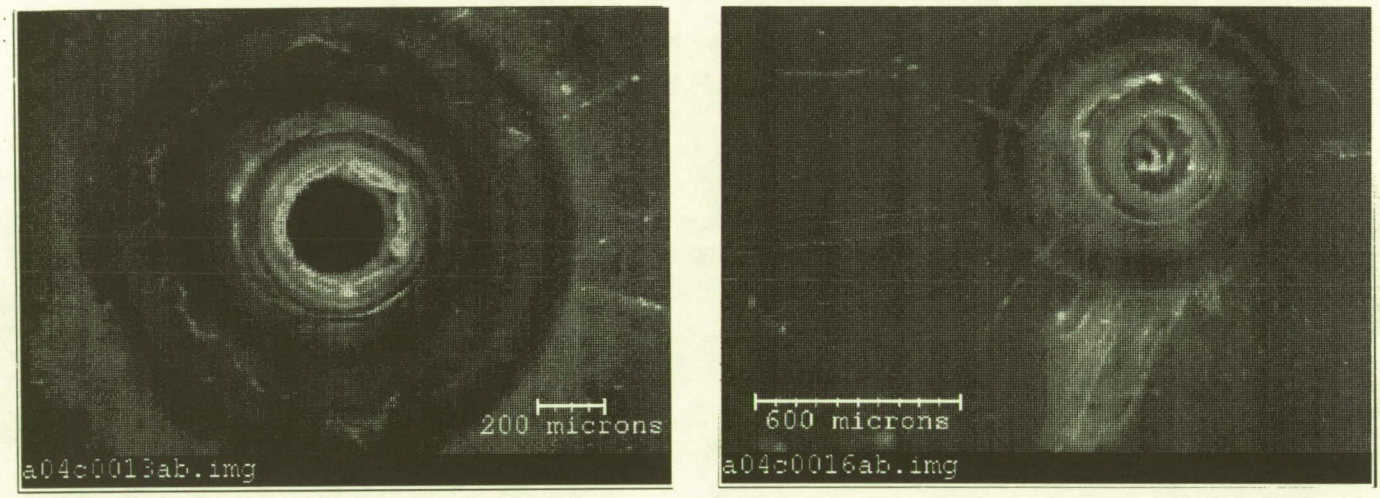

Fig. 10. Impacts of the FEP UHCRE Teflon covers showing (a) central pit . and (b) an extended spallation zone with radial cracks and circular features.

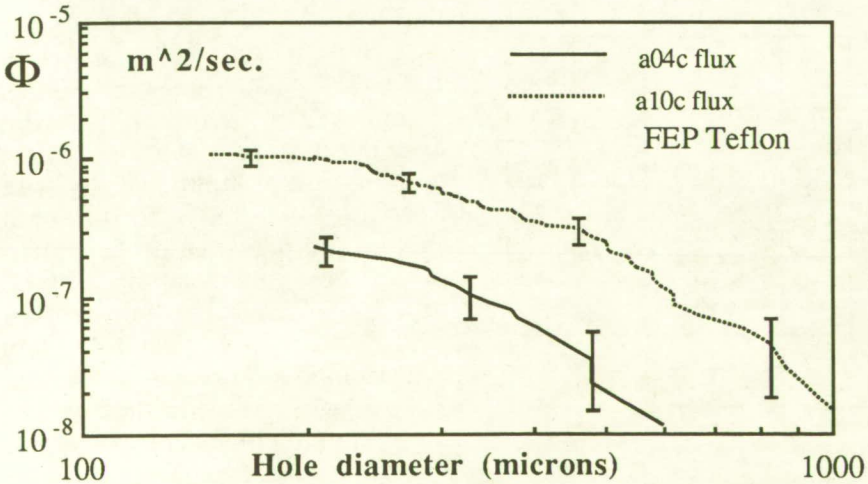

Fig. 11. Perforation hole distributions for a near East (Row 10) and near West (Row 4) FEP UHCRE Teflon surface. The flux ratio calls for particle velocities characteristic of interplanetary sources which are hyperbolic at LDEF's orbit. Particle velocities correspond to 17.4 ± 3 kms^{-1} in geocentric space and a V_∞ of some 12 kms^{-1} on approach to the Earth.

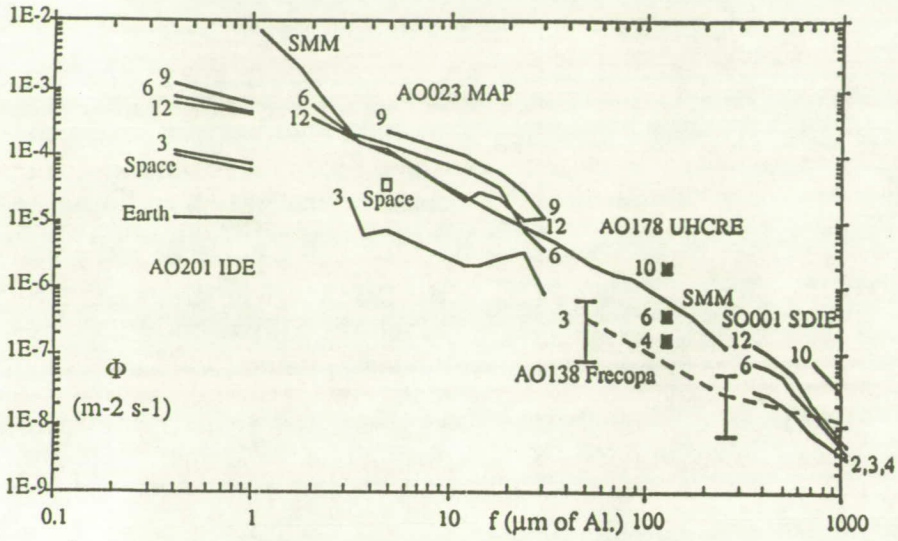

Fig. 12. Data from MAP foils set in the wider context of other LDEF data referenced to an equivalent penetration thickness of aluminium. A data model is derived for the East and West fluxes (section 3.1).

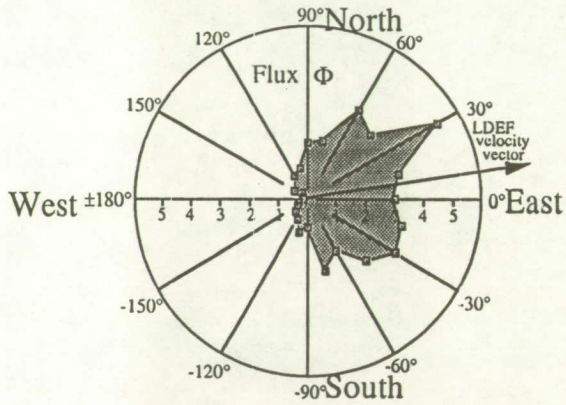

Fig.13 Angular dependence of the flux Φ (x10^7m-2s-1) for larger craters Dc>500µm for the Meteoroid and Debris Special Interest Group (M+D SIG) data base. A clear departure from symmetry is seen with a bias towards North, as distinct from the South bias at smaller dimensions seen on the MAP thin foils (<20µm).

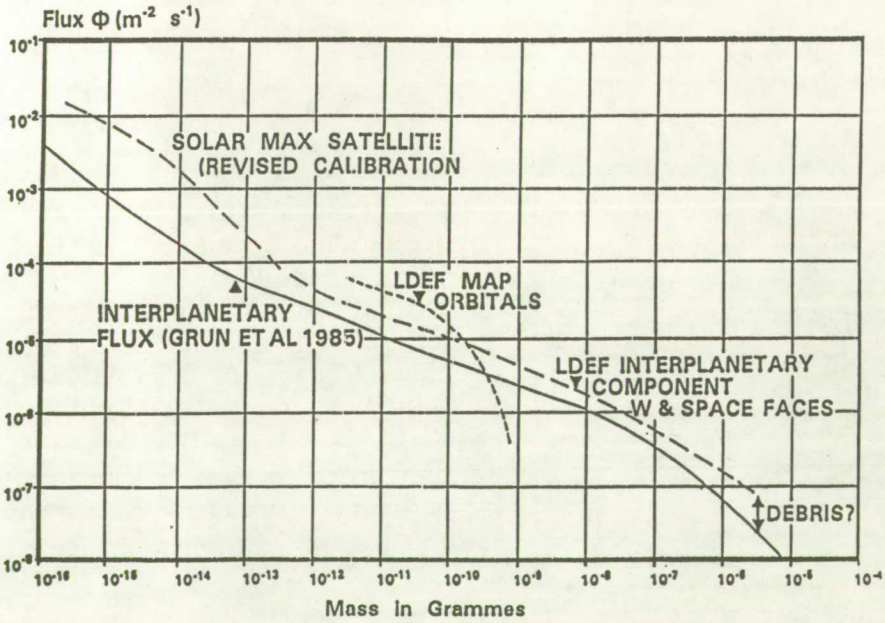

Fig. 14. Characteristics of the near Earth space particulate environment. Modelling involving a transformation between the West and Space (interplanetary dominated fluxes) yielding a geocentric particle velocity of 17.4 ± 3 kms^{-1}. The same particulates cannot fully account for the observed East fluxes and demonstrate (supported by the Space-to-North and Space-to-South fluxes) the presence of an Earth orbital component labelled MAP orbitals. Agreement between the LDEF space and West flux data transformed to interplanetary space at 1 AU (using Earth shielding and gravitational enhancement factors) is seen to be good.

METEOROID AND DEBRIS SPECIAL INVESTIGATION GROUP
DATA ACQUISITION PROCEDURES

Thomas H. See
Lockheed Engineering & Sciences Co.
Houston, Texas 77058
(713)483-5027 / FAX (713)483-5347

Martha K. Allbrooks
POD Associates, Inc.
Albuquerque, New Mexico 87106
(505)243-2287 / FAX (505)243-4677

Dale R. Atkinson
POD Associates, Inc.
Albuquerque, New Mexico 87106
(505)243-2287 / FAX (505)243-4677

Clyde A. Sapp
Lockheed Engineering & Sciences Co.
Houston, Texas 77058
(713)483-5141 / FAX (713)483-5347

Charles G. Simon
Inst. for Space Sciences & Technology
Gainesville, Florida 32609
(904)371-4778 / FAX (904)372-5043

Mike E. Zolensky
NASA Johnson Space Center
Houston, Texas 77058
(713)483-5128 / FAX (713)483-5347

SUMMARY

The entire LDEF spacecraft was examined by members of the M&D SIG for impact (*i.e.*, craters ≥0.5 mm and penetrations ≥0.3 mm in diameter) and related features (*e.g.*, debris, secondaries). During the various detailed surveys conducted at KSC, approximately 5,000 impact-related features were photodocumented, and their locations measured and recorded; an additional approximately 30,000 smaller features were counted. The equipment and techniques utilized by the M&D SIG permitted the determination and recording of the locations and diameters of the 5,000 imaged features. A variety of experimental and LDEF-structural hardware was acquired by the M&D SIG and is presently being examined and curated at JSC.

INTRODUCTION

The Long Duration Exposure Facility (LDEF) exposed several dedicated experiments designed to study the hypervelocity particle environment in low-Earth orbit (LEO). While most of these experiments were intended to investigate natural micrometeoroids, a substantial concern regarding the contributions of man-made orbital debris emerged since the conception of these experiments. These developments made it paramount that LDEF's cumulative impact history be quantified to the greatest extent possible. Because of the stochastic nature of the bombardment process, this quantification required that efforts be made to obtain the best statistical information possible from LDEF.

It was realized prior to the retrieval of LDEF that the dedicated meteoroid experiments would not suffice to accomplish these objectives, and that systematic scanning of the entire LDEF spacecraft would be necessary to obtain information complementary to, or in addition to, that expected from the dedicated instruments. Issues that would benefit from this additional information include (1) addressing theoretically predicted variations in the absolute magnitude of particle fluxes as a function of instrument orientation relative to the velocity vector of a non-spinning spacecraft in LEO, (2) obtaining statistically reliable data for large impactors, which demands analysis of the largest area-time products, and (3) target-of-opportunity investigations on the dynamic behavior of any number of materials that may be incorporated in future spacecraft. All of these issues figure prominently in the understanding of collisional hazards in LEO, and in the characterization of the dynamic properties of both natural and man-made impactors, the latter ultimately yielding a better understanding of their origins and sources.

To this end, the LDEF Micrometeoroid and Debris Special Investigation Group (M&D SIG) was organized. Previous experience with the impact record on planetary surfaces and retrieved spacecraft components (*e.g.*, Solar Max) revealed the somewhat subjective nature of simple crater counts. Thus, it was decided that a limited number of experienced individuals would be best suited to perform the global LDEF survey in a systematic and internally consistent fashion. This group (*e.g.*, the M&D SIG "A-TEAM") resided at the Kennedy Space Center (KSC) during the entire LDEF deintegration (*i.e.*, February through April, 1990). The A-Team optically scanned and photodocumented all exposed LDEF surfaces (*i.e.*, measured and photographed approximately 5,000 individual impact events) for impact-related features (*i.e.*, craters ≥0.5 mm and penetrations ≥0.3 mm in diameter, as well as other related features [debris, secondaries]), and identified and secured surfaces of special interest. The long-term curation of these materials and all

documentation was subsequently transferred to the Johnson Space Center (JSC), which is responsible for open and continued access to these materials by qualified investigators, and for maintaining an up-to-date database of LDEF impact data.

This report is a brief synopsis of the A-Team activities at KSC. It summarizes a detailed report published earlier (1), and discusses post-deintegration activities of the M&D SIG at JSC. A companion paper (2) presents some first-order observational results extracted from the extensive database generated during the KSC documentation efforts. It is hoped that this synopsis provides some background and context to ongoing LDEF studies and that it introduces the uninitiated reader to the significance and unparalleled opportunities afforded by LDEF to improve our understanding of cosmic dust and orbital debris.

IMPACT FEATURE CHARACTERISTICS

Diameter Measurements

The two primary reasons for making diameter measurements of craters/penetrations at KSC were to (1) determine if the minimum feature-size criterion had been met and (2) develop a first-order database for feature sizes and locations. Ultimately, it is the goal of the M&D SIG to report diameter information which reflects the feature's diameter at the original target surface (D_c). At KSC, diameter measurements were made directly from video monitors because no reliable and practical technique was available to measure the diameters in real time at the target surface. By using this video technique, attempting to measure the diameter at the level of the original surface would have been a very subjective process. KSC measurements, therefore, were made from rim-crest-to-rim-crest (D_r) on opposing sides of the feature because (1) such locations were easy to determine and (2) subjective error was minimized. The difference in these diameters is illustrated in Figure 1.

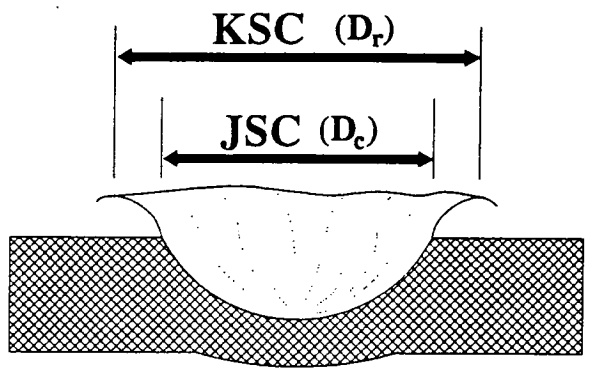

Figure 1. Diagram illustrating the relationship between the *estimated* diameter (D_r) and the actual diameter (D_c).

To ensure that all operators measured approximately the same diameters, measurements were made of a stage micrometer at the four predefined (*i.e.*, click-stop) magnifications in order to generate a set of correlation graphs which permitted diameters measured on the video screens to be converted to the *estimated* feature diameters. Feature diameters were estimated to the nearest 0.01 mm using these conversion graphs. However, because there were several possible sources of error in the measurement techniques employed, the reported diameters are given only to the nearest 0.1 mm. This represents the level of accuracy that could realistically be expected from the measurement techniques and the large number of system operators contributing to the M&D SIG database.

The majority of impact features on LDEF were located in metallic surfaces, were symmetrical and possessed raised rims. For these features the measured diameters were the rim-crest-to-rim-crest diameter mentioned above (Figures 2a-2c). For craters and penetrations not possessing a raised rim, measured diameters reflect the edge-to-edge distance between opposing sides of the feature (Figure 2d). For most penetrations in the A0178 thermal blankets, the measured diameters equal the center-of-lip-to-center-of-lip distance between opposing sides of the raised Teflon lips (Figure 2e). Lastly, for rimless craters in glass or brittle materials, the measured diameters equal the distance from opposing sides of the residual crater or central pit of the structure (Figure 2f).

Elliptical features that had major- and minor axes that varied by $\geq 10\%$ (Figure 2g), and highly-oblique (*i.e.*, extended tear-drop shaped; Figure 2h) features were measured along both axes. Accurate measurement of oblique features was often complicated by the poorly defined, diffuse boundaries of the impact-affected area. Their

dimensions were measured between the furthest points of altered surface material discernible under optical magnification.

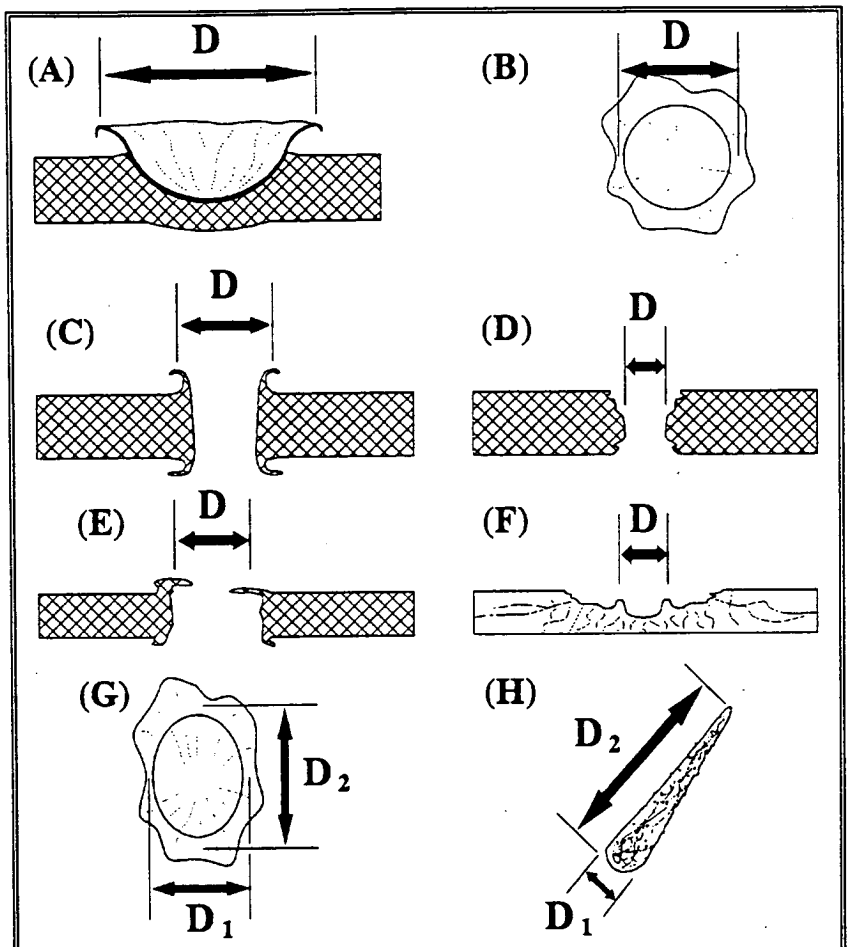

Figure 2. Typical impact feature structures and associated diameter measurements. (A) Cross-section of a typical crater with symmetrical rim and overturned lips, (B) Top view of [A], (C) Cross-section of a penetration with symmetrical rim and overturned lips, (D) Cross-section of a penetration without rims, (E) Cross-section of a penetration -- with collapsed rims -- through a single-layer thermal blanket, (F) Cross-section of residual crater (*i.e.*, central pit) in glass or brittle material, (G) Top view of elliptical crater, and (H) Top view of highly elliptical, extended tear-drop shaped feature.

Morphology

Metals

Approximately 75% of the exposed surface area on LDEF consisted of coated or uncoated aluminum alloys. All experiment-tray flanges (*i.e.*, tray lips), tray clamps (except for a few), and the structural members of the LDEF frame were constructed from chromic-anodized 6061-T6 aluminum. The same aluminum was used in the fabrication of the space-end thermal panels, space- and Earth-end dummy plates, grapple-fixture trays, experiment environment control cannisters (EECC), a variety of experiment-frame structures, and the experimental surfaces of the 25 whole or partial S0001 experiment trays. The Earth-end thermal panels were anodized by a slightly different process which resulted in their black color. Structural members which were held together with 303 stainless steel bolts. In addition, a variety of small uncoated metal samples were exposed as part of several experimental packages.

Most craters in uncoated metal surfaces were symmetrical in shape and possessed raised rims (Figure 2a and b), while only a small percentage exhibited asymmetric rim shapes or were elliptical (Figure 2g). Several dozen highly elliptical features (Figure 2h) were found on the black Earth-end thermal panels. These latter, extended tear-drop shaped features possessed semi-minor axes of <0.5 mm, while the semi-major axes were commonly >1.0 mm. A few similar features were found in various locations around the spacecraft. Several multi-cratering events were found on metal surfaces. These unusual and rare impact features consisted of tens to hundreds of smaller craters lining the bottom and walls of the host crater formed by the overall event.

Penetrations through metallic surfaces, such as the foils of the A0023 experiments, and a few large penetrations through 1.6 mm thick aluminum exhibited the general symmetrical hole and rim shapes depicted in Figure 2c. Thinner foils possessed correspondingly narrower rims that were not always evident when viewed under the microscope system. However, hole-diameter measurements were easily made for these features regardless of the rim width.

Coatings on some metal surfaces ranged from several microns to approximately 75 to 100 μm layered (*e.g.*, Teflon/silver/adhesive) coverings on several experimental surfaces (*e.g.*, S1005 and S0069). Between these extremes

were many painted aluminum surfaces which had a variety of primer and top coats totaling approximately 25 to 50 μm in thickness.

Impacts in aluminum coated with silvered-Teflon were evaluated differently than features found in other coated- and uncoated metal surfaces. Since the coating was relatively thick (75 to 100 μm) the impacts were treated as if they had occurred in Teflon foils. Impacts in these surfaces produced a penetration/melt hole and a shock delamination zone in the Teflon that commonly extended tens of hole diameters around the penetration, as well as areas of black discoloration partially around some features. In most cases there was a small crater in the underlying aluminum.

Larger craters (*e.g.*, >0.5 mm) in painted metal surfaces were often surrounded by spall zones extending outward for several crater diameters. Multilayered spall zones extending radially for tens of crater diameters were frequently encountered on aluminum coated with several layers of paint.

Glasses and Brittle Materials

Several square meters of surface area on LDEF were occupied by glass that included solar-cell covers, metal-oxide-silicon (MOS) capacitor-type detectors, and hundreds of small glass and crystalline samples. In addition, there were several experimental surfaces which utilized glass or crystalline materials as covers or windows. The morphologies of impacts into such materials depended on the physical properties of the individual material. In general, these materials behaved brittlely and exhibited several, if not all, of the following characteristics: rims, spall zones, fracture zones, and/or extended fracture zones (Figure 2f).

The extent of the spall and fracture zones, and the presence or absence of a rim around the crater or penetration were the major differences among impacts in these materials. When rims were present, or when there was a penetration hole without a rim, feature diameters were measured as discussed earlier. Rimless craters were common in these materials; for such features the residual-crater (*i.e.*, central-pit) diameter (Figure 2f) was measured and reported.

Solar-cell cover glasses exhibited more complex, local fracture zones and fewer extended fractures zones, while smaller spall zones were found around impact sites in crystalline substrates. Occasionally, the fracture zones extended tens of crater diameters to the edges of the glass or crystalline substrate. In general, spall zones were relatively large, which may account for the absence of rims. In cases were the central pit was indiscernible (due to dislodged materials), the spall-zone diameter was recorded.

Polymers

Impacts into relatively thick polymers that were not subjected to extensive atomic oxygen erosion possessed the same general morphology as impacts into uncoated ductile metal surfaces. Diameter measurements were made using the criteria described above. The few impacts in thick polymeric surfaces which were subjected to significant atomic-oxygen erosion (*e.g.*, G21 and G23 leading-edge reflectors) appeared worn and ill-defined. The diameters of these features were determined from the residual rims or craters.

Seventeen peripheral trays were covered with Scheldahl G411500 thermal blankets (STB) consisting of an outer layer of FEP Teflon (~125 μm thick) backed by a layer of silver/inconel (200 to 300 Å thick), which in turn was backed by DC1200 primer and Chemglaze Z306 black conductive paint (80 to 100 μm thick). The major difference between impacts in the STBs was the presence of a collapsed or an uncollapsed rim around the site. Most impacts produced variable delamination zones, some of which extended radially up to tens of penetration-hole diameters. Penetrations were generally surrounded by one or more (whole or partial) rings that varied in size and color. In general, rings were more pronounced around events on the leading-edge, as opposed to their trailing-edge counterparts.

Impacts into laminated polymeric films (*e.g.*, Kapton specimens on A0138) produced craters and penetration holes with the general structure described above, but also exhibited delamination zones, each of which appeared as a bubble

between layers. Fiber-reinforced layered plastics exhibited less extensive delamination zones, and frayed fibers were often noted overlapping the penetration holes.

Composite Structures

Several experiments exposed composite materials consisting of layers of carbon, glass, and/or Kevlar woven fibers laminated with resin binders. Impacts in such materials generally resulted in rimless features, while impact-induced damage commonly took the form of broken fibers and missing binder from the affected volume. Remnant fibers were often found extending over the area of excavated binder material which complicated feature location and diameter measurements. In some cases the diameter of the affected volume increased with depth. This effect appeared to be a function of the composite's density, layering style, layer spacing and fiber type. Spall zones, which generally extended only a few crater diameters, were common around impacts in layered composites and were defined by areas where the binder had been disrupted and/or ejected. Delamination-type zones were present around many large impacts that extended a few crater diameters beyond the spall zone. Images were extremely difficult to record on composite surfaces due to the overlap of broken fibers and the generally low albedo of such materials.

Multilayer Thermal Blankets and Structures

Several square meters on LDEF were covered with multilayer thermal blankets (MTB) or other multilayered surfaces. Most MTBs consisted of approximately 5 μm thick layers of aluminized Mylar separated by approximately 100 μm thick Dacron netting. One MTB in Bay B10 (S1005) consisted of 8 to 10 layers of approximately 5 μm thick aluminized Mylar separated by Dacron netting and encased with an outer covering of Teflon-coated fiberglass (beta cloth). Additional multilayer structures covered experiments in Bays B04 and D10 (A0054) and consisted of an outer layer of aluminized-Kapton followed by bonded layers of conducting epoxy, aluminum, non-conducting epoxy and Kevlar.

Large impacts in MTBs produced "normal" penetrations through the exterior layer (Figure 2c and 2d), followed by successively larger holes in subsequent layers caused by expanding debris clouds. However, the bottoms of such features were rarely visible in the assembled MTB if the overall event effected more than two or three blanket layers. In all cases the catalogued hole diameter refers to the outer foil.

Impacts in the materials similar to beta-cloth were, in many respects, like penetrations in the fibrous-composite materials. The dominant observable impact-induced damage was the rupture of the fibers that commonly overlapped the penetration. It was not possible to see beneath the beta-cloth layer of this MTB type. In addition, as a result of the strand diameter (~200 μm) and weave spacing, it was difficult to detect very small impacts into such surfaces. All impact events detected in beta-cloth surfaces were photodocumented, and their diameters measured from the apparent edges of the disrupted fibers on opposite sides of the site.

Impacts in the A0054 multilayer structures resulted in events which affected differing numbers of layers of the laminated substrate. Feature diameters were measured from the center points on opposite sides of the crater rims, as shown in Figure 2c. A variety of delamination and spall zones, and areas of rolled back foil were present around several of the large impact sites.

LDEF SURVEYS

Following *Columbia's* rendezvous with LDEF on January 12, 1990, the M&D SIG performed various inspections and surveys of the spacecraft. Cursory inspections were conducted from JSC by monitoring the recovery on closed-circuit television, and by examining photographic negatives of the LDEF on-orbit documentation. The next inspections occurred in the Orbiter Processing Facility (OPF) prior to LDEF's removal from *Columbia's* payload bay at KSC, and during the transfer of LDEF from the payload canister to the LDEF Assembly and Transportation System (LATS) in the Operations & Checkout (O&C) building. All detailed surveys occurred following LDEF's arrival at the Satellite

Assembly and Encapsulation Facility 2 (SAEF II), where LDEF was completely deintegrated. Detailed examinations included the (1) Bolts, Clamps, Shims and Experiment Tray Flanges/Lips Inspection and Bolt Orientation Survey, (2) General Experiment Tray Front- and Backside Survey, (3) Detailed Experiment Tray Survey, (4) Thermal Panel Inspection and Bolt Orientation Survey, (5) Detailed LDEF Frame Survey and (6) Detailed Thermal Panel Survey.

On-Orbit Survey

The initial spacecraft survey was conducted by the LDEF Inspection Team, which included an M&D SIG member, monitoring *Columbia's* downlink video and audio signals at JSC during the retrieval operations on January 12, 1990. Significant M&D SIG-related observations made during this survey included (1) the A0187-2 thin-foil samples which were partially detached and rolled up, (2) the A0187-1 clamshells being open, and (3) dark circular features on the A0178 thermal blankets.

The second survey involved viewing the first-generation negatives of the on-orbit LDEF photography taken by the STS-32 crew. The astronauts were present, which provided an opportunity to ask about their personal impressions and observations of the LDEF spacecraft. According to the astronauts, LDEF continued to generate debris throughout the mission following its retrieval, especially during crew exercise periods.

Orbiter Processing Facility Survey

The next opportunity to examine LDEF was after *Columbia* (containing LDEF) had been ferried to KSC and moved into the OPF. On January 31, 1990, the LDEF Inspection Team monitored payload deintegration operations for possible movement-related damage. LDEF was still located in the payload bay at that time so only Rows 1, 2, 10, 11 and 12 were completely visible; portions of Rows 3 and 9 were partially visible. This survey identified the circular features on the A0178 thermal blankets as relatively small penetration holes surrounded by substantial dark-colored rings.

Prior to removing LDEF from the payload bay, LDEF's trunnion pins were surveyed for impact features which would have been damaged during installation of the trunnion-pin caps. No such features were found at that time, nor during later detailed surveys. After LDEF was removed from the shuttle and placed in the payload canister, OPF personnel retrieved various LDEF materials from the payload bay including an approximately 10 x 10 cm solar panel.

Operations & Checkout Survey

After leaving the OPF, LDEF was moved to the O&C building were it was transferred from the payload canister to LATS on February 1, 1990. Again, the LDEF Inspection Team was present to monitor operations. Once it was in LATS, much of the spacecraft could be surveyed at a reasonable distance for the first time. This survey permitted full access to Rows 3 and 9, as well as to Rows 4, 5, 7 and 8. The primary observation made during this survey dealt with the generation of a large number of thin (~0.1 μm thick) aluminum-foil contaminants (primarily from Tray F09). These foil flakes were found floating in the air of the O&C building and, later, became a major source of contamination in SAEF II.

Bolt, Clamp, Shims and Experiment-Tray Flanges/Lips Inspections and Bolt-Orientation Survey

Preceding LDEF deintegration in SAEF II, the M&D SIG conduct an inspection of all bolts, clamps, shims and experiment-tray flanges to identify impact-related features which could be damaged by (1) experiment-tray cover installation, (2) clamp and experiment tray removal and (3) placing the experiment trays within the experiment-tray rotators. In addition, the M&D SIG had planned to record the orientation of those clamp bolts that possessed impact-related features, but, at the request of the LDEF Project Office, this effort was expanded to include every clamp- and thermal-panel bolt on the entire spacecraft.

On February 5, 1990, an M&D SIG member crawled underneath the spacecraft (Row 6) to inspect the areas where the jacks would be placed to lift the spacecraft into its rotatable configuration. This was the first opportunity to view Row 6 at close range, and no unusual features were observed.

Several pieces of hardware were removed from the spacecraft prior to the first detailed M&D SIG surveys. These pieces included the two Earth-end trunnion-pin scuff plates, the Earth-end walking beam and trunnion pins, and thermal panels G19 and H19. In addition, the layered thermal blankets of M0001 (*i.e.*, Bays H03 and H12) were removed or taped down by the PI so that LDEF could be rotated without causing further damage to these surfaces. However, all of these items were examined prior to or following their removal.

The first systematic survey was conducted one row at a time over the three-day period of February 20-23, 1990, by two teams, each consisting of a person scanning and measuring, while the other recorded the data. The bolt-orientation information and other data were recorded on specially prepared bay maps. After labeling the bay maps, the orientation of all clamp bolts was recorded. Next, the clamps, clamp bolts and tray flanges were examined for impact-related features which could be damaged during tray deintegration, and, if found, their locations were recorded. Lastly, a small section was cut out of each tray-cover gasket in those places that would have come into contact with these particular features; the actual gasket cutting took place in the outer air-lock of SAEF II. Only a small section of the gasket was removed (*i.e.*, inner, central or outer) so that the gasket could still seal against the tray flanges. Once the gasket was trimmed and cleaned, the cover was attached to the appropriate tray by Ground Operations personnel. During tray removal, Ground Operations personnel consulted these bay maps to determine if special tools or handling procedures were required. The original bay maps now reside in the Curatorial Facility at JSC.

General Experiment Tray Front- and Backside Survey

The M&D SIG performed several inspections of all experiment trays. The first was conducted while each experiment tray was suspended from an overhead crane and concentrated on impact-related features that could be damaged by placing the tray in a rotator stand. The front and back of the tray flanges were searched for impact-related features (*e.g.*, craters, bulges, spallation effects); if found, such features were photodocumented before placing the tray in the rotator. In addition, the back surface of the tray was examined for unusual features (*e.g.*, spallation, outgassing stains, discoloration). Survey results were entered in logbooks which now reside in the JSC Curatorial Facility.

Following this survey, the trays (except for the S0001s) were placed in one of the Langley Research Center (LaRC) or JSC rotators for examination, photographic documentation and ultimate instrument deintegration. Trays were held in the rotators either by two pairs of aluminum angles squeezing the side tray flanges (LaRC rotators), or by clasping the flanges between six sets of aluminum plates (JSC rotators).

Detailed Experiment Tray Inspection

The M&D SIG set-up three work stations in SAEF II to conduct their detailed examination and documentation of all LDEF hardware. Each station was equipped with a Coordinate Registration System (CRS), a Stereo-Microscope Imaging System (SMIS) and a complete computer system. Stations/Systems 1 and 2 were used primarily for documentation of entire experiment trays, while Station/System 3 was used mostly to document miscellaneous hardware (*e.g.*, bolts, clamps, reflectors, walking beam, scuff plates).

Suspected impact features that met the minimum size requirements, or smaller features that exhibited some interesting characteristic (*e.g.*, associated debris) were visually identified on the experiment tray or subcomponent surface and their coordinates determined. Impact-feature coordinates were recorded to (1) assure the ability to relocate features and (2) document location information which would permit plotting and analyses.

The Coordinate System

With the exception of a few miscellaneous pieces of hardware (*e.g.*, walking beam, scuff plates), all X-, Y- and Z-coordinates were measured (in millimeters) in a Cartesian coordinate system from a standard (0,0) reference point that was assigned by the M&D SIG. Unusually shaped hardware was assigned unique (0,0) reference points that are fully described by See *et al* (1). For such components a Cartesian grid was partially abandoned in favor of a more appropriate system (*e.g.*, a radial Y- and a linear X-coordinate).

The location of the (0,0) reference point for experiment trays was defined to be the lower-left corner at the intersection of the left and bottom tray flanges. For all but few trays, a physical reference mark was placed on the bottom of the left flange where the flange curved 90° to form the inner-flange wall. For small subcomponents (*e.g.*, clamps, bolts and shims) no physical marks were made on the hardware since their positions relative to (0,0) are readily reconstructible.

The M&D SIG standard orientation for each component is the orientation it possessed at the time of deintegration from the spacecraft. For Bays A01-F12 the "up" direction, or top flange (facing the spacecraft with the Earth-end to the left and the space-end to the right), was the long flange closest to the next lowest row number on LDEF. Similarly, the top flange of each Earth- and space-end tray was defined as the flange that was at the top of the tray as it was positioned for deintegration from LDEF.

Coordinate Registration System. Three electronic coordinate registration systems were fabricated from electronic linear spars (Mitutoyo AT11N) that had been mated to high-precision sliding tracks normally used on drafting tables (Vemco V-track 630), and fitted with adjustable-height spotter scopes. The upper and lower lenses of the scopes were etched with a crosshair and 1.0 mm circle, respectively, which helped to minimize parallax errors by allowing the crosshairs to be reliably positioned in the center of the circle. The signals from the electronic spars were displayed on a digital readout unit (DRO; Mitutoyo ALC-EC). Each CRS was paired with one of the three LaRC rotators. CRS precision was measured to be ±0.2 mm over a 100 cm distance, while the overall accuracy was determined to be within ±0.5 mm.

Manual Coordinate Registration Systems. Experiment trays that arrived in the M&D SIG area on a JSC rotator could not use the CRS due to the rotator's tubular-frame design. In addition, all S0001 trays (except B08) were documented in the horizontal position on either a workbench or rollable table, precluding the use of a CRS. In such cases, and in other instances (*e.g.*, on small subcomponents and on the frame), a metric tape measure or scale was used for determination of feature coordinates. The relative accuracy of manually determined coordinates was approximately ±2 mm for small components. On large and/or complex surfaces (like an irregular thermal blanket), the relative accuracy of manually determined coordinates varied. The overall average is believed to have been ±5 mm. This higher value is due to (1) the reproducibility of measurements using the tape measure or scale, (2) the requirement of no physical contact with LDEF surfaces, and (3) the different personnel who participated in the documentation efforts.

Surveying Procedures

As a tray entered the M&D SIG area, it was moved to the first available station (generally System 1 or 2) and the tray was cover removed by Ground Operation personnel. A CRS was attached to those trays mounted on an LaRC rotator by affixing the X- and Y-scales to the rotator.

Surveying was generally conducted by two-person teams (one surveying and one recording the information in a logbook). First, a (0,0) reference mark was placed on the tray flange (see above) and, if a CRS was used, the spotter scope was moved to the (0,0) reference mark and the X- and Y-LEDs of the DRO zeroed. Next, the coordinates of any fiducial marks on the component surface were recorded. On A0178 thermal blankets, a cross (+) was marked on the top and bottom of each blanket third and their positions recorded. In addition, on these and several other trays, the

coordinates of the left, center and right tray-cover bolt holes on the top and bottom tray flanges were determined and recorded.

Actual documentation of impact features occurred in two discrete steps: first, by naked-eye inspection and second, by detailed microscope characterization. The operational goals of the naked-eye inspection were (1) to identify all impacts visually detectable to obtain their cumulative number, (2) to identify candidate features for detailed documentation (*i.e.*, craters ≥0.5 mm and penetrations ≥0.3 mm in diameter) and record their exact locations, and (3) to identify/record any unusual features that would deserve special attention or documentation. Feature diameters were conservatively estimated during the naked-eye inspection to assure that all features meeting the established size criteria were ascertained. Features that did not unquestionably fall into either the "too small" or "to-be-documented" categories were entered in the logbook as "borderline". Further sorting of these latter features was made via the detailed microscope examination.

After surveying the entire tray, the SMIS was brought in for detailed examination and diameter determination of all indexed features. If the feature was determined to be of sufficient size, or exhibited some particularly interesting characteristics, it was documented by acquiring a digitized stereo-image pair of the object. Each image was combined with alphanumeric identifiers and other comments that were entered via a portable computer (*e.g.*, bay location, experiment number, component number, the X,Y-coordinates, magnification, rotator number, optical-disk number, and up to 130 characters of comments) and stored on two separate laser WORM (Write Once, Read Many) drives. This redundancy was undertaken to assure that no data would be lost due to the failure of a storage drive, or as a result of damage to a disk.

Following photodocumentation the tray was released by the M&D SIG and the tray cover replaced by Ground Operations personnel. All sixteen A0178 trays and the Seeds in Space tray (P0004/P0006) were returned later for trisecting, removal and packaging of the thermal blankets (see below). The original survey records and digitized image files are now located in the Curatorial Facility at JSC. The images are currently being analyzed for depth- and more accurate diameter information (see below).

Thermal Panel Inspection and Bolt Orientation Survey

The second on-spacecraft inspection was conducted on March 29, 1990, to identify impact-related features found on thermal panels, reflectors, and thermal-panel bolts that could be damaged by its removal. Similarly, the orientation of all bolts securing this hardware was documented using the procedures described earlier.

Detailed LDEF Frame Survey

The final on-spacecraft inspection was carried out between April 2-11, 1990, following the removal of all of the experiment trays and thermal panels. The purpose of this survey was to identify and photodocument impact-related features on the longerons and intercostals of the LDEF frame. During this particular survey all other activities within SAEF II had to cease, because walking on the cement floor was often sufficient to induce unacceptable vibrations into the SMIS that were located on a flat-bed trailer. Therefore, surveying and photodocumentation of the frame required dedicated operations between 5:00 pm and 3:00 am. A Balimore (*i.e.*, rollable scaffolding) and the Ground Operations deintegration platform had to used to document features on the space- and Earth-end, respectively.

As a result of the difference in length between the 9.1 m LDEF spacecraft and the approximately 6 m flat-bed trailer, the frame survey was conducted in three phases. During phase one Bays A-F were completely scanned (including the interior of frame components) and the coordinates of applicable features recorded. However, only Bays C-F and part of the Bay B longeron could be photodocumented. As a result of the approximately 61 cm vertical motion limits of the SMIS on the trailer, LDEF had to be rotated approximately 15° on LATS in order to completely photodocument an entire bay. Once photodocumentation of all accessible features was completed, the trailer was

rolled forward to permit phase two photodocumentation of the remaining features in Bays A and B. Phase three involved scanning and photodocumenting the space- and Earth-ends of LDEF.

Coordinates for documented features were determined with a metric tape measure from the corner located directly behind the experiment-tray (0,0) reference point. Craters <0.5 mm in diameter were not photodocumented unless there was some interesting characteristic associated with the feature (*e.g.*, secondaries, debris), but their cumulative numbers were counted as in the tray operations described above.

Detailed Thermal Panel Survey

The detailed survey and photodocumentation of the thermal panels were carried out on several workbenches. The (0,0) reference point was assigned to the lower leftmost corner or angle of each panel. Coordinates for features identified during the initial survey were determined with a CRS that had been attached to each workbench, while the coordinates of any features added during the detailed microscopic examination were measured with a metric tape measure. A positive Z-value was assigned to features residing on the small row-facing strip of each panel. Horizontally configured microscopes (Systems 1 and 2) were utilized to photodocument the space- and Earth-facing components of each panel, while System 3 (vertically configured) was alternated between stations to document the row-facing strips.

The detailed examination of the thermal panels revealed the apparent bimodal distribution of some highly oblique, extended tear-drop shaped features (Figure 2h); such features were common on the black Earth-end thermal panels, but were apparently absent on their space-facing counterparts. These features were found on both the Earth-facing and row-facing components of about 75% of the Earth-end panels, appearing as little more than scratches in the black panels, but were determined to be impact-related following SMIS examination. No dominant directionality was noted for these features. A re-examination of one space-end thermal panel at the Langley Research Center did not reveal the presence of similar features on that particular panel. However, a detailed microscopic scan of several space-end thermal panels is being conducted at LaRC in search of these highly-oblique features.

IMAGING PROCEDURES

Description of Equipment

Each SMIS consisted of a Wild Leitz M8 stereo-microscope body with four click-stop magnifications (6X, 12X, 25X and 50X) and could be fitted with one of four objective lenses (350 mm, 0.4X, 1.0X and 1.6X). A beam splitter was placed between the M8 body and the binocular eyepieces which directed 50% of the incoming light to the eyepieces and 50% to the CCD (or 35-mm) camera systems. Attached to both sides of the beam splitter were Cine/TV tubes, on each of which was attached a custom camera adapter housing an eyepiece (10X, 20X, or 32X). These adapters were specially designed to interface with either the Nikon F3-HP 35-mm cameras or the Sony XC-711 CCD video cameras.

Illumination was provided by a Volpi Intralux 6000 Fiber Optic, Cold-Light Illuminator and transmitted to the imaging/viewing area by fiber-optic cables. The light source was an Intralux 6000, 20-volt 150-watt tungsten light bulb. Objects were illuminated by one of three fixtures: (1) a pair of Volpi two-branch flexible "gooseneck" light pipes with focusing lenses (for directional and long-distance lighting), (2) a Volpi ringlight (for 360° uniform lighting) or (3) a Volpi "Hydra" light-pipe system (four directional and distance-adjustable lights).

The microscope/camera system was attached to a microscope carrier that was connected to a fully articulated floor-stand. The floor stand consisted of a rolling/lockable base with an approximately 1.2 m tall center post, on top of which was mounted a hydraulic counter-balanced, vertical motion and stability arm (~0.9 m long) which could be rotated 360° in the horizontal plane at both ends. Connected to the counter-balance arm was an approximately 30.5 cm long pin-stopped arm that permitted rotation to six preset positions (15°, 30°, 45°, 90°, 180° and 270°) in the vertical plane. Attached to the pin-stop arm was another 360° rotation joint, followed by another pin-stop arm. This final pin-stop arm was affixed to the microscope carrier which could be rotated about 235° horizontally around the pin-stop arm. The

integrated system provided complete mobility and permitted the microscope to be moved to virtually any position at heights ranging from approximately 0.8 to 2.1 m.

CCD output was carried by standard BNC cables to the computer system for digitization and data storage. The computer system consisted of an NEC Portable Powermate 386 SX computer containing Data Translations DT2871 and DT2869 frame grabber/digitizing and encoder/multiplexer board, respectively, and a Storage Dimensions WORM-drive controller board. Images were displayed on two Javelin CVM-13A video monitors and stored on two Storage Dimensions MAXTOR LS800AT-E External Laser WORM drives using Maxtor 5.25" (13.3 cm) OC-800 optical-disk cartridges (400 megabytes per side) that hold approximately 490 images per side. The left CCD camera was fed directly into the encoder/multiplexer that passed the signal to the digitizing board, from which the digitized image was fed back through the encoder/multiplexer to the left monitor. The right camera signal was split between two lines, with one line interfacing with the encoder/multiplexer and the other feeding directly into the right monitor (*i.e.*, the right monitor always displayed a "live" image). Digitized images (left or right) were always displayed on the left monitor.

Lockheed personnel developed the software used to control the integrated SMIS, and permitted the operator to input various information (*e.g.*, bay location, component type and number) for each feature. This software also interfaced with the digitizer/frame-grabber software (Aurora Library SP0225CN) and WORM drives to provide user-friendly operations through a single, menu-driven package. Based on the bay location and the component type, the software assign a unique feature number (in ascending order) to each image pair. The image side (left or right), component type and number, feature number and bay location were used to create the file names for each image. For example, the right image of an integrated experiment tray's (component E00) third feature (0003) from Bay D08 would be given the file name of "RE000003.D08", while the left image would be assigned "LE000003.D08". All user input, plus the file name was added as a single identification line, along with the WORM disk number and side (A or B), at the bottom of the digitized image. Additionally, two 65-character comment lines were added below the identification line.

Description of Operations

SMIS imaging began on February 4, 1990, and was conducted in one of two modes, horizontal or vertical. The vertical mode (Systems 1 and 2) was used for imaging experiment trays on the rotators and for documenting the LDEF frame, while the horizontal mode (System 3) was utilized during documentation of certain experiment trays, bolts, clamps, shims and other hardware on workbenches. During the frame survey, Systems 2 and 3 were used in the vertical configuration, while System 1 was used in the horizontal mode to image the thermal panels and associated hardware. All operations were performed in such a manner as to ensure that multiple backups were made of all collected data to minimize the possibility of data loss.

Alignment Procedures

Analysis of stereo-images is possible only after the left and right images are merged into a single 3-dimensional view. To ensure that the images could be later processed to yield depth and diameter information, the microscope/cameras were aligned daily in an effort to simplify the process of image registration. Such alignment was necessary to assure (1) the microscope lens was parallel to the imaged surface, (2) the cameras were in the same orientation, and (3) the displayed images had similar horizontal and vertical centering.

Using a sheet of metric graph paper (with a fiducial arrow) the SMIS alignment was checked for parallelism (using a metric scale) and the microscope focused on the arrow at the lowest magnification. The directional alignment was checked with the arrow. Next, the microscope was changed to the highest magnification and refocused; the magnification was then lowered through the other click-stop positions to ensure that the image stayed in focus. Finally, the images on the monitors were compared for horizontal and vertical alignment. If either was off by more than 0.5 mm, the Cine/TV tubes had to be realigned. Once alignment was achieved, the SMIS was considered operational. All three SMIS were checked daily, or every time a SMIS was changed from vertical to horizontal mode and vise versa.

Imaging Procedures

Imaging procedures varied slightly between the different scanning locations (*i.e.*, experiment-tray rotators, workbenches and the LDEF structure). The standard configuration for a SMIS utilized the 1.0X objective lens, 10X eyepieces in the camera paths, 20X eyepieces in the binocular tube and the gooseneck light-pipes. In general, imaging was conducted at the highest magnification that permitted the entire feature to remain within the camera's field of view. Imaging was normally performed by two-person teams with one individual operating the microscope, while the other operated the computer. Besides increasing efficiency, this provided verification of all information and data collected, ensuring that errors were rapidly spotted and corrected.

Experiment-Tray Rotator Operations. As was the case with surveying, imaging was performed in three zones (high, middle and low) for trays mounted in the various rotators. After the initial survey was completed, the features that had been identified were examined by the SMIS. If the feature diameter met the established criteria, or exhibited some interesting or unusual characteristics, a pair of stereo images was acquired. All features in the upper zone would be checked and imaged, if necessary, followed by those in the middle and lower zones, respectively. If a feature was judged to required 35-mm photodocumentation, the feature number was noted in the logbook. After all video imaging was completed the SMIS was reconfigured for 35-mm camera operations by removing the CCDs and installing the 35-mm cameras. Following rotational alignment of the cameras and focusing, pictures were taken by using cable releases (to minimize vibrations) to activate the shutter mechanisms.

Workbench Operations. Procedures for workbench operations were similar to experiment-tray rotator operations, but were performed with the SMIS in the horizontal configuration. When experiment trays had to be imaged on the workbench (primarily the S0001 experiment trays), the binocular eyepieces were rarely used to prevent the operator from having to lean over the tray.

LDEF Structural Frame Operations. Surveying and imaging of the frame began with Row 5. System 2 was used for imaging Bays A-C, while System 3 was utilized for Bays D-F. Generally, all features on the longeron of a particular row were imaged first. Next, the microscope was rotated (-15°) so that it was parallel to the upper portion of the intercostals and the indexed features imaged. LDEF was then rotated so the lower portion of the intercostals could be accessed and imaged. LDEF was again rotated to bring the next longeron into position, the microscopes were repositioned to be parallel, and surveying and imaging of the next row began. This process was repeated for all 12 rows of LDEF. The two ends (Bays G and H) were imaged using similar procedures with System 3 documenting the space-end (Bay H), while System 2 was used for documentation of the Earth-facing end.

Shut-down Procedures

At the end of each day's operations, the SMIS were moved into the M&D SIG area, powered-down, all BNC and power cables were unplugged, and the microscope was positioned on the floor-stand for overnight storage. The daily "all.img" and "all.com" files were downloaded to 3-1/2" floppy disks (for post-processing) and the computers were turned off. Finally, if experiment trays were to remain in the M&D SIG area overnight, Ground Operations personnel would install the tray covers to protect the experimental surfaces.

Daily File-Processing Procedures

One of the floppy disks with the downloaded files was removed from SAEF II for processing. The files were copied to a Bernoulli and an internal hard disk for processing and back-up. Each system's "all.img" file was loaded and the highest feature number from each component copied into a "master" file. When completed for all three image files, the master file was copied to a new "all.img" file for uploading during the next morning's start-up operations. This post-processing was necessary to ensure that all three systems started each day with the same feature numbers for all trays, and provided an additional back-up of all data to be kept outside of SAEF II.

KSC THERMAL BLANKET PROCESSING

Background

The 17 Scheldahl thermal blankets provided a large, uniform meteoroid-detector randomly spaced around LDEF; only Rows 3, 9 and 12 did not contain one of these blankets. The blankets provided thermal insulation to the sixteen A0178 trays and one P0004/P0006 experiment. The M&D SIG was also responsible for trisecting, removing and packaging all 17 blankets. The left 1/3 of each A0178 blanket remained in the U.S. and is now archived at JSC, while the remaining 2/3 were returned to the European Space Technology Center (ESTEC) in The Netherlands. The entire P0004/P0006 blanket (Bay F02) resides at JSC.

Thermal Blanket Boxes

Lockheed personnel at JSC designed and constructed about 60 thermal blanket boxes (TBB) to protect and transport the trisected blankets from KSC. Details of the materials used in the construction of these devices is beyond the scope of this report and can be found in See *et al.* (1). However, the main thrusts behind their design were to protect the blankets during transport and to utilize the flight velcro in securing and transporting the blankets. Following assembly, each TBB was cleaned, packaged in a vacuum-sealed polyethylene bag and placed into specially designed wooden crates for shipment to KSC.

Processing Procedures

Thermal Blanket Processing

Processing of the thermal blanket consisted of six steps: (1) TBB preparation, (2) survey and preparation, (3) trisection, (4) removal and placement into the TBB, (5) photography and (6) final sealing, packaging and shipping.

TBB Preparation. The empty TBBs were delivered to KSC inside vacuum-sealed polyethylene bags. The lexan top was removed to prepare the adjustable aluminum angle for blanket attachment. Threaded nylon rods were inserted through the holes in the outer aluminum frame, lexan standoffs and an adjustable aluminum angle inside the TBB, and secured in place with nylon nuts and washers.

Survey and Preparation. First, the 2.5 cm piece of the thermal blanket that was folded between the experiment-tray wall and the experiment canisters was unfolded to expose the entire blanket. The blanket was then inspected to determine the best places to cut the blanket, avoiding penetration features or their associated delamination zones.

Trisection. The outline of the velcro that attached the blanket to the tray-support frames was used as a cutting guide. An incision was made through the middle of the velcro such that velcro was on both sides of the trisected piece of blanket to facilitate its attachment in the TBB. The incision was slowly extended through the blanket until the bottom was reached. If and when an impact feature was found in the path of the incision, it was skirted to preserve the feature and associated delamination zone, if present. The entire blanket remained on the experiment tray while the second cut was made. Throughout trisecting operations, the A-Team observed that the leading-edge blankets tended to be thinner and easier to cut than their trailing-edge counterparts.

Grounding straps from 11 of the A0178 experiments (A02, A04, A10, B05, B07, C05, C08, C11, D05, D11 and F04) were committed to the Materials SIG. The straps were detached by cutting a semicircle approximately 10.2 cm in diameter around the point where the strap attached to the blanket.

Removal and Placement in the TBB. Following trisection, the left third was removed first by slowly separating the velcro on the blanket from the velcro on the support frame. The blanket was then placed in the TBB and held in place by matching the blanket velcro with the new pieces that had been attached to the aluminum angles in the box. After the

blanket was secured to both sides of the TBB, tension was applied by adjusting the position of aluminum angle along the nylon rods. After all blanket pieces were removed from the tray, the tray interior was surveyed for craters and/or debris. When encountered, such features were photographed with the SMIS.

From every U.S. portion an approximately 10.2-cm wide strip was removed from one end and given to the Materials SIG. Care was taken to determine which end to cut in order to sacrifice the fewest impact features. Prior to removal, all impact features in the strip were counted and the information recorded in the logbook.

After the Materials SIG specimen was removed, the lexan top was secured into position and Kapton tape was placed over the screws to prevent damage to the polyethylene bags. The bay location, experiment number, blanket orientation and blanket fraction was written on the lower right-hand corner of the lexan top.

Photography. Front- and back-surface photographs of the blankets secured in the TBB were taken (from ~2 m) with a 35-mm Nikon camera. Back-surface photographs used backlighting to illuminate the penetrations (which were counted) through the blanket.

Final Packaging and Shipping. TBBs were placed in pre-cleaned polyethylene bags and heat sealed, leaving only one small opening. A dry-nitrogen flush was performed for approximately two minutes, following which a vacuum was pulled on the bag, and the bag heat-sealed. The bagged TBB was placed into a second polyethylene bag and vacuum sealed. The doubly encapsulated TBBs were then placed vertically into a specially designed (foam-lined) wooden shipping crate (five to a crate).

JSC ACTIVITIES

Stereo Image Processing

During the three month deintegration of LDEF, the M&D SIG generated approximately 5000 pairs of digital, color stereo images of impact-related features from all space exposed surfaces. Currently these images are being processed at JSC to yield more accurate feature information (*e.g.*, the diameter of the crater at the original target surface). In addition, many features possessed structures (*e.g.*, ring diameters associated with A0178 blanket penetrations) that lend themselves to analysis by standard image-processing techniques. In order to retrieve depth, height and diameter measurements of the features, it is necessary to combine the image pairs to produce a three-dimensional representation of the imaged objects. This merging of images is accomplished by determining the pixel locations of various tiepoints (*i.e.*, points in common between the left and right images). Selection of these tiepoints is currently underway in the JSC Video Digital Analysis Systems (VDAS) Laboratory.

The Stereo Images

Parallax is exploited in determining an object's distance with stereo photograhy. Parallax is defined as the apparent change in the position of an object resulting from the change in the direction or position from which it is viewed. Objects closer to the viewer (or camera) display a greater angular displacement than more distant objects as the viewpoint changes, and it is this phenomenon which permits the determination of relative (or absolute) distance. Normal human (and most animal) eyesight is designed to make use of parallax through binocular vision. Having two eyes allows us to obtain images from two sources at once, and our brain permits us to integrate these two images and extract distance information from the inherent parallax. The LDEF imagery has been gathered in much the same way as would be by the human eyes.

Each image gathered by the M&D SIG was quantized into a digital copy of 512 samples by 512 lines, resulting in a total of 262,144 "pixels" (picture elements) per image. Each pixel contains a red, a green and a blue band of information, with each band able to contain any one of 256 intensity levels. Thus, the three bands combined enable a total of 16,777,216 discrete possible colors. Current studies underway to define the impact related geometries do not

currently make use of the color information contained in the imagery, but the presence of the data permits the future use of multi-spectral analysis techniques to pursue materials studies. The digital images can be thought of as a grid containing 512 X-positions (horizontal), and 512 Y-positions (vertical), and each pixel position within the image may then be referred to by its own unique pair of coordinates.

The Image Analysis

Figure 3 is a simplified diagram of the geometry involved in calculating the height of a point based on the parallax observed in a pair of binocular images. The parameters ***Wd***, ***Dist***, and ***f*** remain constant for a data collection system and can be determined empirically using calibrated features (*i.e.*, objects of a known height and depth). The height of each point of interest (POI) is then calculated based on the difference in X position between the two views. Note that Figure 3 has the POI projected onto the center of the field of view on the right camera for simplicity.

In practice, matching data points (tiepoints) are selected by an analyst from each of the images for several points on the original target surface so that corrections may be made for differences between the system focal plane and the target surface (*i.e.*, rotations and offsets). Next, tiepoints for impact-related features are selected, and heights for each point are calculated with respect to the original target surface. Work is currently underway for using a minimal number of data points to parametrically define impact-crater morphologies in order to minimize the man-hour intensive task of tiepoint selection. Early attempts to automate the tiepoint selection were unsuccessful, and further attempts have been postponed until a fully functional interactive system has been be completed.

Two-dimensional analysis of non-relief type features (such as the aforementioned ring diameters associated with A0178 blanket penetrations) are also under development. This analysis makes use of conventional image-analysis techniques such as Laplacian edge detectors to accurately define two dimensional impact-related features.

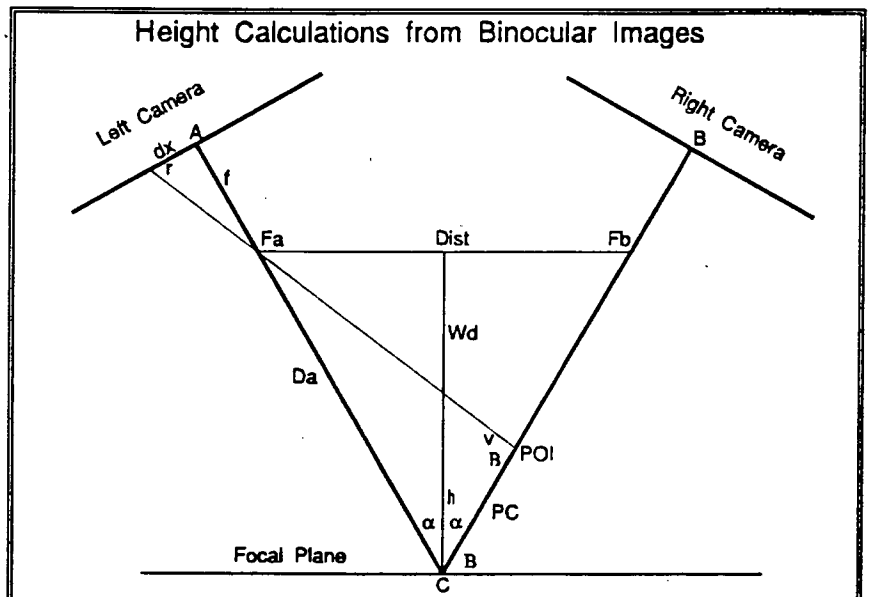

Wd = approx. working distance
Dist = Separation Distance
f = effective focal length
Da = Distance from Fa to C
dx = signed horizontal shift
POI = Point of Interest
PC = Distance from POI to C
h = distance above (or below) focal plane

$\alpha = \mathrm{atan}(Dist/2Wd)$
$B = 90 - \alpha$
$Da = Wd / \cos(\alpha)$
} System Dependent

$r = \mathrm{atan}(f / dx)$
$v = r - a$
$PC = \frac{\sin(u) * Da}{\sin(v + B)}$
$h = PC * \sin(B)$
} POI Dependent

Figure 3. Illustration depicting the geometric relationships involved in the extracting of distance (*i.e.*, depth, height and diamter) informaation from stereo photographs.

Data Acquisition and Curation

Spacecraft and experimental surfaces acquired by the M&D SIG during the KSC deintegration activities are presently being scanned for additional craters and penetrations smaller than 0.5 and 0.3 mm, respectively. These data are being incorporated into the Meteoroid & Debris database that is being managed by the JSC Curatorial Facility.

Additionally, the Curatorial Facility is handling the distribution of acquired LDEF materials to interested and qualified investigators. Persons desiring to study these surfaces should contact the JSC LDEF Materials Curator (Mike Zolensky) with a formal written request outlining the materials desired and the type of investigations planned.

FOILS Laboratory

Scanning of acquired surfaces is being carried out in the Facility for the Optical Inspection of Large Surfaces (FOILS) Laboratory at JSC, which was originally established to permit scanning of Solar Maximum and Palapa hardware returned from earlier satellite repair and recovery shuttle flights. The laboratory is in a Class 1000 clean room that contains SMIS System 3, which has been mated to a motorized X-Y comparator/scanning table. Software was written to control the scanning-table motors to permit detailed microscopic scanning of the desired surface in a systematic fashion.

A component is first placed on the scanning table and aligned such that the positive X- and Y-directions correspond to the same axes as were assigned during the KSC Detailed Experiment Inspection discussed earlier. Next, the same (0,0) reference point is employed, or the necessary offset to the original (0,0) point is input to the system such that (1) all newly documented features are assigned to locations from the same coordinate system used at KSC and (2) no features documented at KSC are counted a second time at JSC. Once the system is initialized with the necessary information, the operator scans the surface by watching video monitors or by looking down the binocular eyepieces of the microscope. Generally, the latter techniques is employed as the 3-D view aids in the identification of smaller (<100 μm) features. When a feature is found, the operator stops the scanning table and documents the feature by examining it under high magnification, looking for unusual characteristics or possible projectile residues, recording the coordinates, measuring and recording its diameter, recording other information (*e.g.*, material type, feature type), and assigning a feature number. If a feature is encountered that may have been documented previously at KSC, the operator uses the feature's coordinates and diameter to determine if it already has an assigned feature number. If it does, the operator can override the new computer-assigned number and manually input the original feature number should there be a need to redocument the feature for any reason (*e.g.*, verify diameter information, re-photograph). However, in general, stereo-image pairs are acquired only if the operator observes possible projectile residues or some unusual characteristic associated with the feature. Following documentation of a feature, the scanning table automatically returns to the spot where the operator halted scanning operations and resumes the scan from that point. After an entire view width (video or microscope) is scanned along the entire X-axis, the Y-axis is increased by approximately 0.8 of a view width, and the component is scanned in the negative X-direction; the approximately 20% overlap assures that no areas are missed in the scanning process. This process is repeated until the entire component has been microscopically examined.

Database

Once a component has been completely scanned, the file containing all acquired information is transferred to the Curatorial VAX computer and incorporated into the M&D SIG database. Presently, the database contains information on approximately 8,000 individual impact features (*i.e.*, approximately 5,000 documented at KSC and approximately 3,000 added from the JSC FOILS Lab). Investigators obtaining meteoroid and debris information that can be included in the database should send the data (in both ASCII and written formats) to the JSC Curatorial Facility, attention Claire Dardano. Access to the M&D SIG database can be accomplished by either the SPAN Network or modem. In either case, a terminal emulator must be used that is compatible with DEC computers; the preferred emulation mode is VT100.

To access the M&D SIG database

SPAN

1) Log onto your host computer.
2) Type **SET HOST 9300** at the system prompt.
3) Type **PMPUBLIC** at the *Username:* prompt.

NOTE: Your system manager may add node CURATE to the DECNET database on your host computer; the SPAN node number is 9.84. You may then access CURATE by typing **SET HOST CURATE** instead of **SET HOST 9300.**

MODEM

1) Dial (713) 483-2500 or (713) 483-2501.
2) Press **<CR>** three (3) times.
3) Type **SN_VAX** at the *Enter Number:* prompt.
4) Press **<CR>** three (3) times.
5) Type **J31** at the prompt.
6) Type **PUBLIC** at the *Enter Username>* prompt.
7) Type **C CURATE** at the *Xyplex>* prompt.
8) Type **PMPUBLIC** at the *Username:* prompt.

For problems or additional database information contact Claire Dardano at (713) 483-5329 [FTS 525-5329] during normal business hours.

ACKNOWLEDGEMENTS

We gratefully acknowledge the support provided by NASA, the LDEF Project Office and the Strategic Defense Initiative Organization. Although the authors were responsible for the M&D SIG's data collection activities during the deintegration of LDEF, numerous other individuals contributed their time to this effort. Much of the surveying work was performed by Jack Warren, Miria Finckenor, Frank Cardenas, Eric Christiansen, Samantha Lapin, Lt. Mike Black, Lt. Joe Secary, Reggie West, and Tim Stephenson. We thank the other members of the M&D SIG for their advice in the planning of these operations and for the opportunity to participate in this endeavor. In particular, we thank Fred Hörz for all his support during the months leading up to the retrieval of LDEF, and Don Humes for continued advice and support throughout the surveying operations at KSC. The outstanding support of the LDEF Ground Operations Team and LDEF Project Office personnel greatly facilitated our ability to complete this effort in the allotted time. Equipment fabrication and development were completed in record time through the efforts of Frank Cardenas, Gerald Haynes, Bill Davidson, Herman Lyle, Richard Ybanez, Anthony Biondo, and Bebe Serrato. The curatorial database was designed by Claire Dardano, and the computer algorithms used at KSC were developed by Eric Nielsen and Clyde Sapp. We thank Jack Warren for serving as the key to the JSC curatorial efforts. Other curatorial support was supplied by Bill Brown, Jimmy Holder, Rita Sosa, Anita Dodson, and Ron Bastien. Anita Dodson was instrumental in the actual production of the M&D SIG Preliminary Report. We also wish to thank Mark Cintala and Fred Hörz for their helpful comments in preparing this document.

All of this work, and LDEF itself, would not have become a reality without the continuing, career-long support of LDEF Project Scientist Bill Kinard. Finally, we thank our families whose support, during our long absences, made this work possible.

REFERENCES

1) See, T.H., Allbrooks, M.K., Atkinson, D.R., Simon, C.G., and Zolensky, M.E. (1990) *Meteoroid and Debris Impact Features Documented on the Long Duration Exposure Facility: A Preliminary Report*. NASA Publication #84, JSC #24608, pp 586.

2) See, T.H., Allbrooks, M.K., Atkinson, Hörz, F., D.R., Simon, C.G., and Zolensky, M.E. (1991) *Meteoroid & Debris Special Investigation Group: Preliminary Results using the LDEF Frame and the A0178 Thermal Blankets*. LDEF First Post Retrieval Symposium, NASA CP-3134, 1992.

METEOROID AND DEBRIS SPECIAL INVESTIGATION GROUP PRELIMINARY RESULTS: SIZE-FREQUENCY DISTRIBUTION AND SPATIAL DENSITY OF LARGE IMPACT FEATURES ON LDEF

Thomas H. See
Lockheed Engineering & Sciences Co.
Houston, Texas 77058
(713) 483-5027 / FAX(713) 483-5347

Friedrich Hörz
NASA Johnson Space Center
Houston, Texas 77058
(713) 483-5042 / FAX (713) 483-5347

Michael E. Zolensky
NASA Johnson Space Center
Houston, Texas 77058
(713) 483-5128 / (713) 483-5347

Martha K. Allbrooks
POD Associates, Inc.
Albuquerque, New Mexico 87106
(505) 243-2287 / FAX (505) 243-4677

Dale R. Atkinson
POD Associates, Inc.
Albuquerque, New Mexico 87106
(505) 243-2287 / FAX (505) 243-4677

Charles G. Simon
Inst. for Space Sciences & Technology
Gainesville, Florida 32609
(904) 371-4778 / FAX (904) 372-5043

SUMMARY

The Micrometeoroid and Debris Special Investigation group has documented all craters ≥500 μm and penetration holes ≥300 μm in diameter on the entire LDEF spacecraft. This report summarizes the observations on the LDEF frame, which exposed aluminum 6061-T6 in 26 specific directions relative to LDEF's velocity vector. In addition, the opportunity arose to characterize the penetration holes in the A0178 thermal blankets, which pointed in nine directions. For each of the 26 directions, LDEF provided time-area products that approach those afforded by all previous space-retrieved materials combined. The objective of this report is to provide a factual database pertaining to the largest collisional events on the entire LDEF spacecraft with a minimum of interpretation. This database may serve to encourage and guide more interpretative efforts and modelling attempts.

The LDEF observations are in qualitative agreement with the salient features of existing models regarding the hypervelocity environment in low-Earth orbit. The crater production rate varies between the forward- and rearward-facing surfaces by more than a factor of 10, possibly by as much as a factor of 20. Within statistical error there is no evidence for differences in the mass-frequency distribution of impactors impinging from diverse radiants.

A complete understanding of LDEF's impact record requires additional documentation of smaller impact features, combined with refined modelling of the dynamic properties of both natural and man-made particles in low-Earth orbit, as well as improvement of crater-scaling relationships and of thin-film penetrations.

INTRODUCTION

The Long Duration Exposure Facility (LDEF) exposed a total surface area of approximately 130 m^2 in low-Earth orbit (LEO) for approximately 5.7 years. This corresponds to an area-time product of approximately 750 m^2 exposed for a single year, which is almost two orders of magnitude larger than all previous opportunities combined to investigate the hypervelocity particle environment in LEO on space-exposed surfaces. The latter include diverse surfaces exposed on Apollo and Skylab (refs. 1, 2) and on Shuttle (ref. 3), all of time-area products $<<1$ m^2/y. Prior to LDEF, the most significant opportunities were in the form of thermal blankets and thin aluminum membranes that possessed a total time-area product of some 12 m^2/y (ref. 4) that were retrieved during the repair of the Solar Maximum Mission spacecraft. These Solar Max surfaces substantiated the presence of a significant man-made debris population in LEO (ref. 5) that combines with the natural particles, largely derived from comets and asteroids, to form a substantial collisional threat to spacecraft in LEO (ref. 6).

Because the number of collisional events is -- to first order -- a linear function of this time-area product, the opportunity offered by LDEF to characterize the natural and man-made particle populations is unique. In addition, there is little prospect of duplicating LDEF's impact record from any space-exposed hardware for at least a decade, much less an opportunity to surpass and improve upon it during a period when spacecraft designers must address collisional hazards to large-scale, long-duration structures in LEO (*i.e.*, Space Station *Freedom*). Analysis of LDEF's

impact record constitutes an observational baseline that will be crucial to the design of future Earth-orbiting flight-systems.

This significance was clearly recognized prior to LDEF's retrieval, and is the primary reason for the establishment of the Meteoroid and Debris Special Investigation Group (M&D SIG). Members of this group resided at the Kennedy Space Center (KSC) throughout the period of LDEF deintegration to document and preserve, for more detailed analysis, the impact record of the entire LDEF spacecraft. While all exposed surfaces were scanned and documented via a set of consistent criteria and procedures, emphasis was placed on those surfaces that were not initially intended to be investigated for impact features. These surfaces were perceived as valuable "targets of opportunity" that would be highly complementary to dedicated micrometeoroid and debris experiments provided by six Principal Investigator (PI) teams. The activities of the KSC M&D SIG team are outlined in (ref. 7), and described in detail in an extensive (600 pages) report (ref. 8).

The following extracts liberally from these reports and is intended to present an overview of the larger impact features on selected surfaces that were not part of dedicated PI-experiments, and that characterize the relative production rates of impact features on the entire spacecraft. Recent theoretical insights (see below) suggest that important dynamic properties, such as the absolute flux and mean impact-velocity of natural and man-made particles in LEO, may be extracted from impacted surfaces that point into specific directions on a non-spinning spacecraft, such as LDEF. As many future structures, including Space Station *Freedom*, will also have fixed attitudes relative to their orbital velocity vector, correct and realistic dynamic modelling becomes crucial for their protection against collisional, and possibly catastrophic damage. LDEF represents a unique and very timely opportunity to test, and hopefully improve on existing models.

The data presented here is limited to factual measurements of crater- and penetration-hole diameters and their frequency of occurrence. These data permit, yet also firmly constrain, more model-dependent, interpretative efforts. Such efforts will focus on the conversion of crater and penetration-hole sizes to projectile diameters (and masses), on absolute particle fluxes, and on the distribution of particle-encounter velocities. These are complex issues (refs. 6, 9, 10, 11, 12, 13, *) that presently cannot be pursued without making various assumptions. These assumptions relate, in part, to crater-scaling relationships, and to assumed trajectories of natural and man-made particle populations in LEO, that control the initial impact conditions.

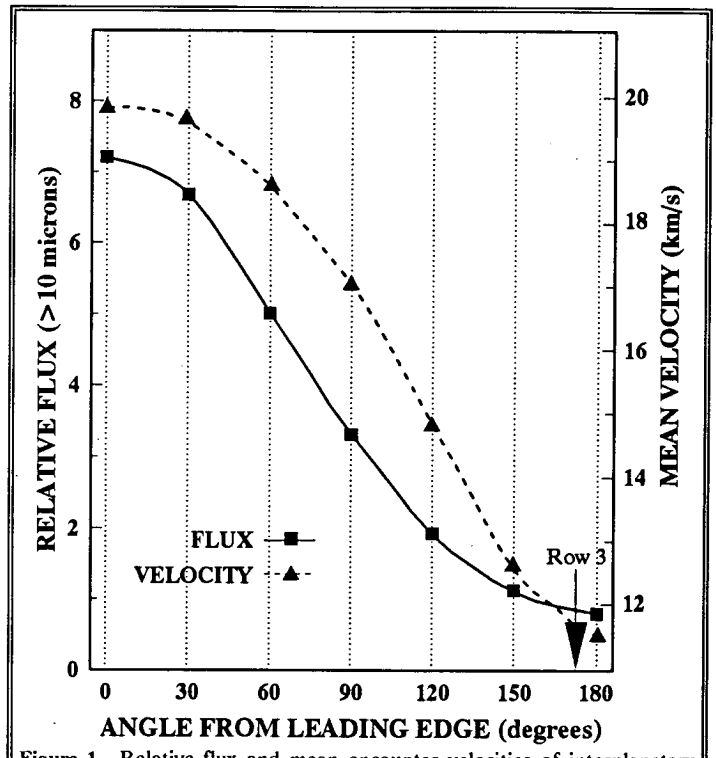

Figure 1. Relative flux and mean encounter velocities of interplanetary dust particles >10 μm colliding with surfaces of specific azimuthal orientations relative to the velocity vector of a non-spinning platform in LEO (ref. 9). Note that this plot does not account for Earth shielding.

RATIONALE FOR THE SELECTION OF ANALYZED SURFACES

The bombardment effects of a non-spinning platform encountering an (assumed) isotropic cloud of hypervelocity particles in LEO are akin to raindrops hitting the windshield of a moving vehicle. More particles are encountered in the forward-facing direction than in the rearward-facing direction, while the velocity distribution of the impactors varies from "fast" in the forward-facing (leading-edge) direction, to "slow" in the opposing (trailing-edge) direction, because particle and spacecraft velocities are added vectorially.

Figure 1 depicts the effective fluxes and mean velocities of natural particles >10 μm in size that encounter flat, vertical surfaces of specific orientations relative to LDEF's velocity vector. The detailed assumptions and algorithms used by Peterson * to derive this figure are essentially those of Zook (ref. 9, 10). These model predictions may be tested by a wide variety of LDEF surfaces. Indeed, first order comparisons were offered during the First LDEF

* Peterson, R.B. (1989) Instrument Pointing Considerations; Report to Cosmic Dust Collection Facility Open Forum, Lunar and Planetary Science Institute, March 1989; unpublished.

Symposium by some dust investigators. In addition, the active Interplanetary Dust Experiment (IDE; ref. 10) will play a substantial role in our understanding of particle dynamics in LEO. While refined calculations and observations may well lead to modifications of Figure 1, the first order findings will remain valid. From Figure 1 it can be seen that the mean encounter velocities range from approximately 20 to 11 km/s for surfaces that point into the leading- and trailing-edge directions, respectively, and that the effective fluxes, at constant projectile size, between those orientations may differ by a factor of 10. Because most impact damage is proportional to the impactor's kinetic energy, the combination of flux and mean velocities results in factors of 30 to 40 difference in the energy flux between leading- and trailing-edge directions, a substantial difference for the design and operation of flight systems. It is obvious that forward-facing systems will sustain more damage than rearward-facing surfaces per unit time, and therefore, that collisional shielding requirements may vary dramatically with specific pointing direction relative to a spacecraft's velocity vector.

The size of any crater or penetration hole depends on a number of physical properties of both the target and projectile material, and on the projectile's mass and impact velocity. A given unit impactor will generate craters of different sizes on LDEF, depending on the instrument location, because of the different effective (mean) encounter velocities as portrayed in Figure 1. The quantitative relationships among these parameters are known for a few LDEF materials, but only over a restricted range and set of initial conditions. Specifically, the prevalent impact velocities in LEO are beyond current laboratory capabilities for most impactors $>10\,\mu m$ in diameter. Therefore, it is prudent, if not mandatory, to characterize impact features on identical target materials so that the physical properties of the target can be accounted for or that they reduce to some systematic constant; this permits relative comparisons among surfaces pointing into different directions.

To fully exploit LDEF's potential in contributing to dynamic issues of the particle environment it becomes necessary to study surfaces that are manufactured from identical materials and that are widely distributed over the entire spacecraft. The highly stochastic nature of the collisional environment further mandates that such surfaces be of sufficient surface area to have accumulated a representative population of impact features. Such considerations identify LDEF's aluminum structural frame and the A0178 Teflon thermal blankets as the most outstanding opportunities to learn about the LEO particle populations (in addition to those afforded by dedicated and well calibrated micrometeoroid and debris experiments).

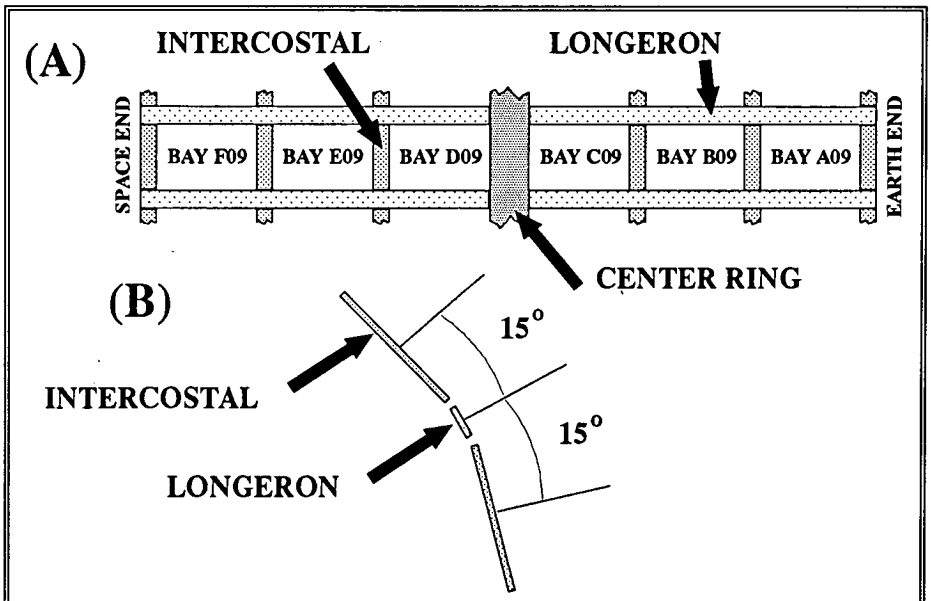

Figure 2. Geometric relationship of the LDEF frame components. (A) Arrangement of longerons and intercostals in a typical "Row" of LDEF Bays and instrument locations. (B) Angular relationship between a longeron and intercostals on adjacent LDEF's rows.

The structural frame of LDEF was manufactured from 6061-T6 aluminum beams that formed an open-grid, 12-sided frame that produced individual instrument bays (Bays A-F) and provided attachment points for the instrument trays; Figure 2 illustrates the pertinent geometric relationships. The longitudinal frame members (~4.6 m long) were termed "longerons", while cross members between longerons were called "intercostals" (~1 m in length). The angle between adjacent instrument rows, defined by the intercostals, was 30° (12-sided cylinder), while the angle between adjoining intercostals and longerons was 15° so that one longeron could accommodate instruments from two adjacent rows. Individual rows were assigned sequential numbers (1-12), with Row 9 facing in the nominal velocity vector (leading-edge direction) and Row 3 in the trailing-edge direction. For simplicity we assigned the longerons half-row numbers (*e.g.*, longeron 2.5 would reside between Rows 2 and 3). The frame components of the Earth- and space-facing ends (*i.e.*, Bays G & H) of the LDEF spacecraft were essentially flat.

LDEF's structural members represented a total exposed surface area of approximately 15.4 m^2. The exposed portions of the six intercostals and the center ring had a surface area of approximately 0.61 m^2 per row (1-12), while the longerons (1.5-12.5) exposed approximately 0.54 m^2 in each direction; the Earth- and space-facing ends exposed approximately 0.79m^2 of surface area each. Thus, LDEF's structural members represent impact "detectors" of a single material type pointing in 26 well-defined directions, each possessing $\geq$0.5 m^2 of surface area and representing an area-time product >3 m^2/y. The frame provides an unprecedented opportunity to study impact craters in infinite halfspace targets, and is of extra significance in that the impact behavior of 6061-T6 aluminum, being a common structural material in spacecraft, is fairly well understood (*e.g.*, ref. 10,*).

Although not exposed in all 26 directions, identical thermal blankets (*i.e.*, Scheldahl G411500) associated with the sixteen A0178 experiment trays and the one P0004/P0006 experiment tray provided another material type that was widely distributed around the circumference of the spacecraft (*i.e.*, all rows except 3, 9 and 12 contained at least one of these blankets). Each individual blanket exposed approximately 1.2 m^2 of surface area. The time-area product afforded by these thermal blankets was a minimum of 7 m^2/y in each of these nine LDEF orientations.

The thermal blankets consisted of an outer layer of FEP Teflon (125 μm thick) backed by a layer of silver-inconel (200 to 300 Å thick), which in turn was backed by DC1200 primer and Chemglaze Z306 black conductive paint (80 to 100 μm thick), resulting in a total blanket thickness of approximately 180 μm. Presently, the impact/penetration behavior of this composite foil is poorly understood; dedicated calibration experiments designed to address such behavior must be conducted. Furthermore, such experiments will contribute to understanding the unusual morphologies of the penetration holes observed in the LDEF blankets (*i.e.*, concentric rings of highly variable geometries, etc., ref. 8). Such features are thought to reflect some form of shock-induced delamination at the interface of the silver-inconel and Teflon layers.

FEATURE DESCRIPTIONS AND MEASUREMENTS

Figure 3 illustrates the morphology and associated diameter measurement for typical impact features encountered on the two materials discussed here. Crater diameters refer to rim-crest-to-rim-crest dimensions (D_r; Figures 3a & b) and not to the diameter measured at the intercept of the crater walls and the original target surface (D_c), which is approximately 25% smaller (refs. 12, 13) than D_r.

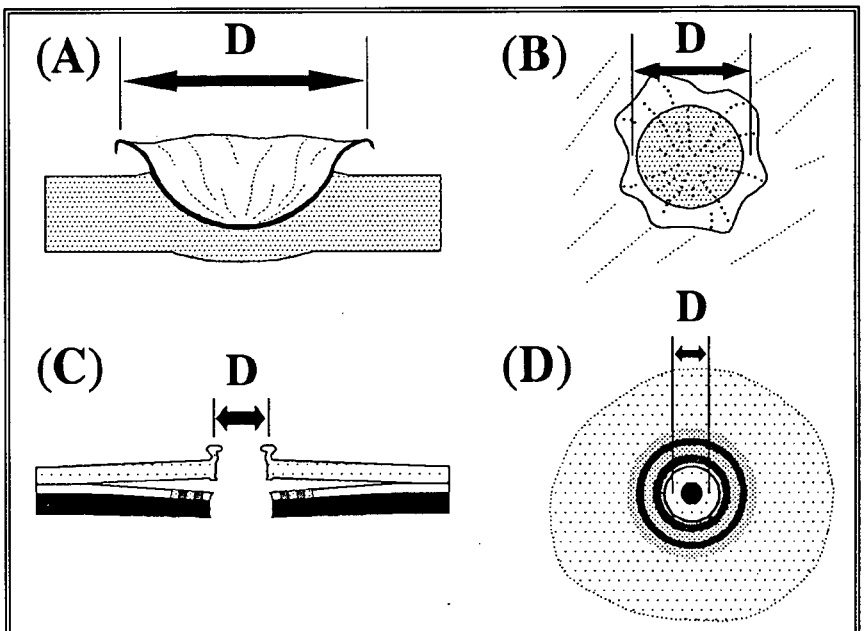

Figure 3. Drawings of typical craters (A & B) and penetration holes (C & D) morphologies encountered, and associated measured diameters for features in the aluminum LDEF frame and A0178 thermal blankets, respectively. Note the presence of the dark rings (representing delamination features) surrounding the relatively small penetration hole. The presence of distinct lips surrounding most penetration holes indicates that atomic oxygen erosion had not greatly enlarged the original hole diameters.

The measurement of the penetration-hole diameter (D_h) also refers to a rim-to-rim measurement (Figures 3c & d). Multiple diameter measurements, especially for the case of non-symmetrical holes, were performed and averaged to obtain D_h for any specific event (ref. 8). The physical penetration hole is modestly smaller than the quoted D_h; while no systematic measurements exist, the latter diameter is estimated to differ by <10% from D_h (ref 14). See *et al.* (ref. 8) described the exterior morphologies of these penetration holes which were typically characterized by various colored ring-like, delamination features of variable widths, crispness, spacings, scaled diameters and absolute ring numbers. However, not all penetration holes in these blankets were surrounded by the halo or ring features, and their presence seems to be unrelated to any macroscopic factor or characteristic, such as the diameter of the penetration hole (D_h).

*Peterson, R.B. (1989) Instrument Pointing Considerations; Report to Cosmic Dust Collection Facility Open Forum, Lunar and Planetary Science Institute, March 1989; unpublished.

During the earliest M&D SIG activities at KSC an operational decision had to be made regarding the cut-off diameter of individual craters and penetration holes to be measured and documented in detail, the latter including location information (with millimeter precision) and stereo photography. Obviously, this decision was affected by the maximum workload that could be sustained by the available resources, both observers and equipment, and the ease with which impact features could be observed on various surface materials. Cut-off diameters of 500 μm for craters in infinite halfspace targets, and 300 μm for penetration holes in thermal blankets were chosen. This dual size threshold was employed due to the differing processes associated with hypervelocity impacts into foils versus materials of much greater thickness. These cut-off diameters were applied rigorously and systematically to all LDEF surfaces, including the longerons and intercostals of LDEF's frame, leading to a complete inventory of all craters ≥500 μm in diameter for the entire spacecraft. In addition, the total number of impact structures between these cut-off diameters and approximately 50 μm in diameter, as observed with the naked eye, was counted and recorded as a single, cumulative number. However, the latter is particularly operator-sensitive, and dedicated studies are needed to characterize features smaller than the (large) cut-off diameters. As detailed in Table 1, these procedures yielded approximately 35,000 impacts ≥50 μm in diameter, which must constitute a minimum value, and approximately 4,000 larger structures that were documented individually and that represent a quantitative account of LDEF's "large" impact features.

Table 1. Distribution of impact features on LDEF. The values listed do not represent a complete count of the number of impact features on LDEF because (1) many surfaces were examined but the exact locations of the <0.3 mm and/or <0.5 mm diameter features were not recorded (*i.e.*, whether they resided on the experimental surfaces or the tray flanges) and (2) during the first several days of M&D SIG documentation activities, only those features that were photodocumented were counted. Thus, the number of features listed in the various categories represent only those features known to exist on that particular surface type, while the "Totals" column depicts the total number of known impacts counted in the various size categories, regardless of their locations.

	CLAMPS, BOLTS & SHIMS	TRAY FLANGES	EXPERIMENTAL SURFACES	LDEF FRAME	THERMAL BLANKETS	TOTALS
<0.3 mm			158		*2831	3069
≥0.3 mm			172		+625	797
<0.5 mm	1318	1923	14171	5171		27385
≥0.5 mm	161	419	2106	432		3118
TOTALS	**1479**	**2342**	**16687**	**5603**	**3456**	**34336**

* - Count is incomplete; the <0.3 mm diameter features were not counted on F02, C05, C06 and D07
\+ - Count is incomplete; the ≥0.3 mm diameter features from F02 not included.

This report summarizes these large events exclusively. The impact craters contained on LDEF's frame comprise a set of 432 individually documented craters, while the thermal-blanket data are based on 625 penetrations. These represent about 10% and 78%, respectively, of all large craters penetrations on the entire spacecraft.

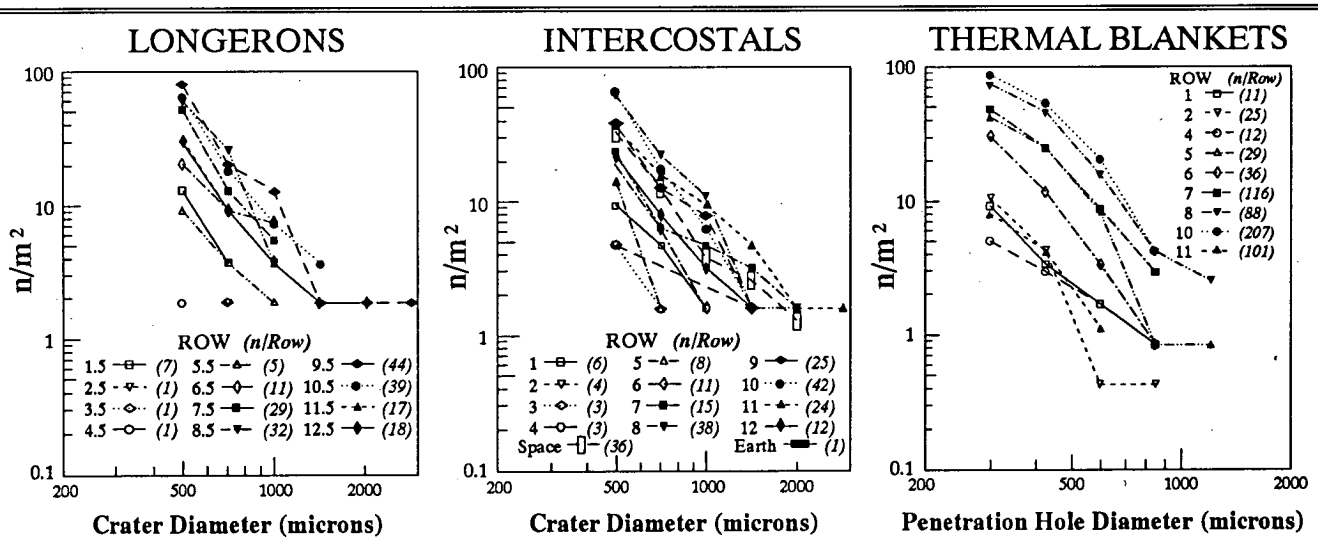

Figure 4. Absolute spatial density of "large" impact features on LDEF's longerons, intercostals and the A0178 thermal blankets. Note the order of magnitude differences in crater density among surfaces of widely different orientations as identified by row number; numbers in parentheses ( ) refers to absolute number of craters ≥500 μm and penetration holes ≥300 μm in diameter in each of the indicated LDEF pointing directions.

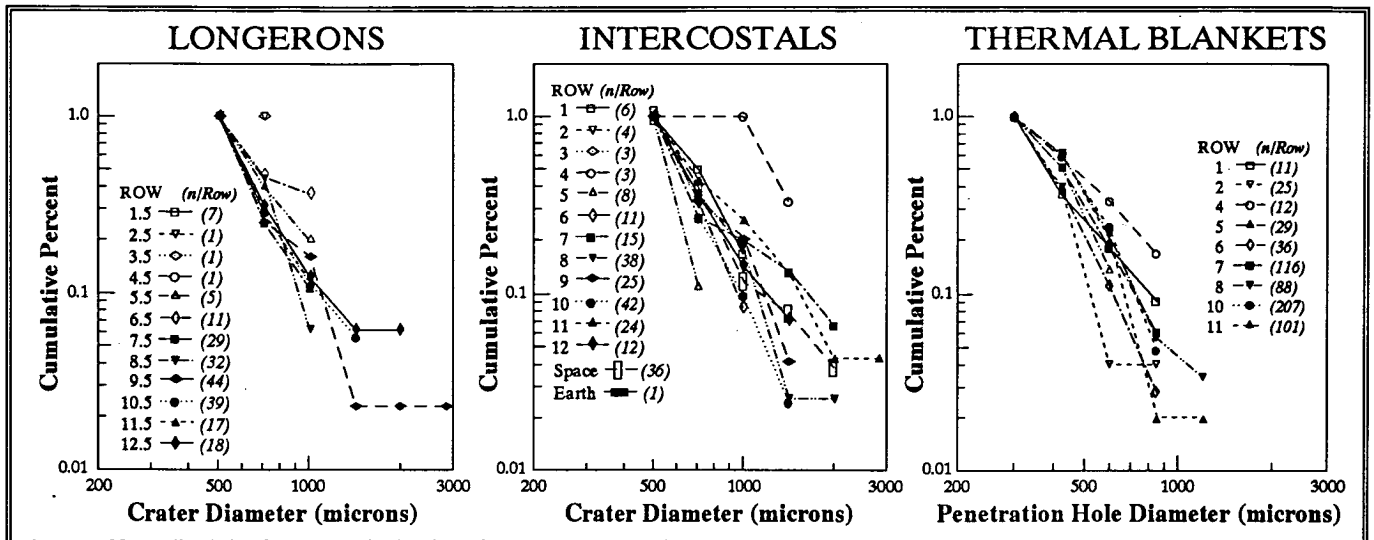

Figure 5. Normalized size-frequency distribution of crater and penetration-hole diameters for the LDEF aluminum frame and ~180 μm thick Teflon thermal blankets.

RESULTS

The cumulative size-frequency distributions and spatial densities of large craters and penetration holes are illustrated in Figure 4 where they are grouped into specific viewing directions, identified by LDEF row. Unfortunately, even for such substantial time-area products, the total number of events is still generally small, leading to poor statistics and large scatter in the data. We calculated two-sigma (95% confidence level) error bars (not illustrated for the sake of clarity in Figure 4) and conclude that effective crater-production rates depend on instrument orientation and that relative size-frequency distributions could be identical.

If taken literally, substantial variations in relative mass-frequency of the impactor populations would be obtained from the normalized crater- and penetration frequency data illustrated in Figure 5. Clearly, the latter are heavily affected by the presence or absence of a few, large, stochastic events, and is the reason why detailed measurements of (distribution) slope and associated implications are unwarranted. Nevertheless, Figure 6 illustrates the statistically most meaningful (yet tentative) ratios of small to large events that may be extracted from the data sets. "Small" refers to the (somewhat arbitrary) cut-off limits of (*i.e.*, D_r = 500 μm and D_h= 300 μm), while "large" refers to events twice that size (*i.e.*, D_r = 1000 and D_h = 600 μm). The latter size features were present on all surfaces, but total numbers are generally small. Figure 6 exhibits no systematic trends that may be related to instrument pointing direction. Note that the thermal blankets exhibit relatively high frequencies for large events on the forward-facing directions, while the longeron data seem to indicate the opposite. Obviously, both trends cannot be correct simultaneously and we conclude from Figures 4, 5 and 6 that the statistics for features larger than our threshold diameters may not suffice to state, with confidence, whether or not the size frequency of projectiles varies with viewing direction. Additional data are needed on small-scale features to provide firm answers to such questions.

Figure 7 displays the absolute frequency of observed features as a function of instrument orientation in an LDEF specific reference frame. We are aware that the actual leading edge was approximately 8° (±0.4°) off, toward Row 10, from the nominally planned Row 9 direction (ref. 14). This off-set, however, does not invalidate the premission-assignment of Row 9 as the "leading-edge", and of Row 3 as the "trailing-edge", an assignment that we maintained throughout this report. Figure 7 illustrates, in polar coordinates on logarithmic scales, the observed, absolute crater density (N/m^2) for craters ≥500 μm in diameter on the longerons and intercostals, as well as the number of penetration holes ≥300 μm in diameter for the thermal blankets. For clarity and ease of comparison, Figure 8 illustrates the data in histogram form, both in absolute and relative terms, the latter after normalization to the maximum spatial densities observed on the Row 10 intercostals (crater density) and thermal blankets (penetration-hole density).

It seems apparent that there is a strong dependence on pointing direction as implied by Figure 1, and -- in a gross sense -- the observations are consistent with modelled expectations. The effective production rate of craters or penetration holes of constant size seems to differ by more than a factor of 10 between the highest and lowest frequencies.

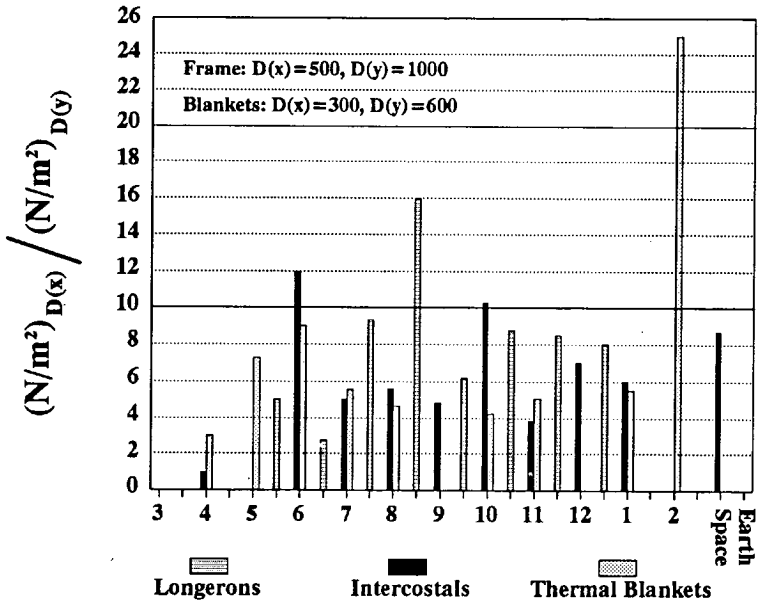

Figure 6. Ratio of "small" to "large" impact features per LDEF Row (pointing direction). Note the substantial scatter of the data and the seeming lack of systematic trends within our limited sample-statistics.

Unfortunately, leading- and trailing-edge crater densities accessible to the M&D SIG are confined to the intercostals only; no thermal blankets occupied LDEF Rows 3 and 9, and the longerons were 15° off-set from each row. Somewhat surprisingly, as detailed and emphasized earlier (ref. 15), the Row 9 longeron displays a modest crater population which is distinctly smaller than the adjacent longerons and intercostals. We consider the Row 9 intercostal data to be non-representative. Adjacent intercostals on Rows 8 and 10, and longerons at locations 8.5 and 9.5 have consistently higher crater densities. Because of the orbital precession of the Earth (~8°/day), any anisotropy in particle flux would be substantially and rapidly smeared out over neighboring LDEF locations; it seems implausible from a dynamic point of view to sustain the low impact rates implied by the Row 9 intercostals and at the same time cause the apparent higher rates on adjacent surfaces that are only 15° and 30° apart, respectively. Supporting evidence for this interpretation comes from the general trends displayed by the thermal blankets as well, that also yield maxima in the forward-facing directions (Rows 8 and 10).

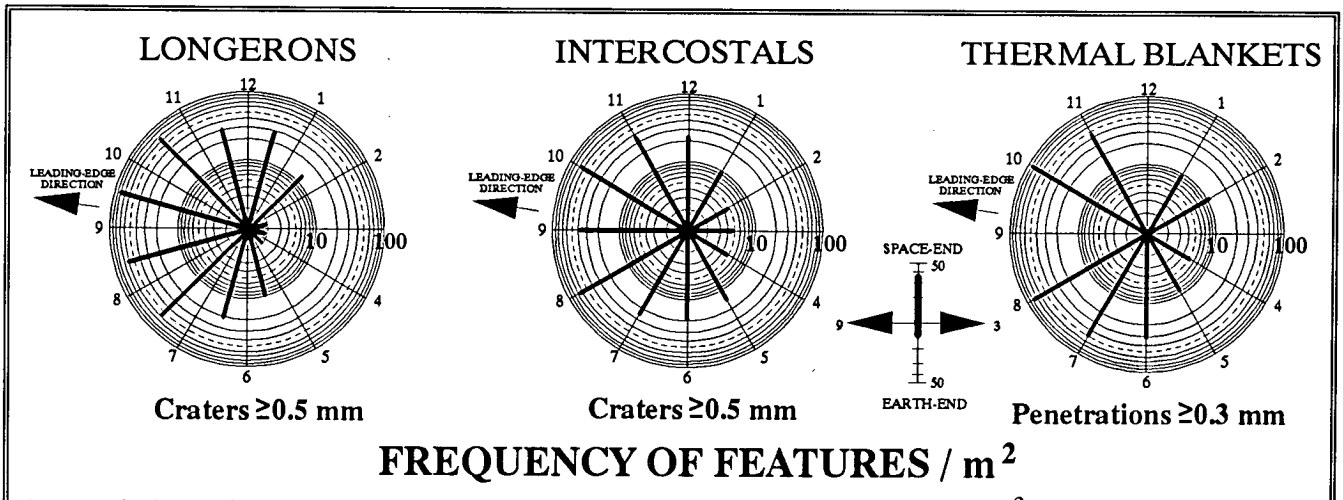

Figure 7. Absolute spatial density (plotted in polar coordinates on logarithmic scales) of impact features (N/m^2) observed on frame components and thermal blankets. Note that the differences between forward- and rearward facing surfaces are greater than an order of magnitude for craters $\geq 500\,\mu m$ in diameter and for penetration holes $\geq 300\,\mu m$ in diameter, respectively.

In detail, as previously mentioned, LDEF's orbital plane was modestly off-set by approximately 8° in the Row 10 direction. Note that the highest crater densities on LDEF were obtained on the 9.5 longeron, and that the spatial density of penetration holes is highest for Row 10. These trends differ qualitatively from those expected on the basis of Figure 1, which assumes bilateral symmetry about the plane of motion. It appears that LDEF received more impacts from the general direction of Rows 10 and 11 than on the symmetrically equivalent Rows 8 and 9.

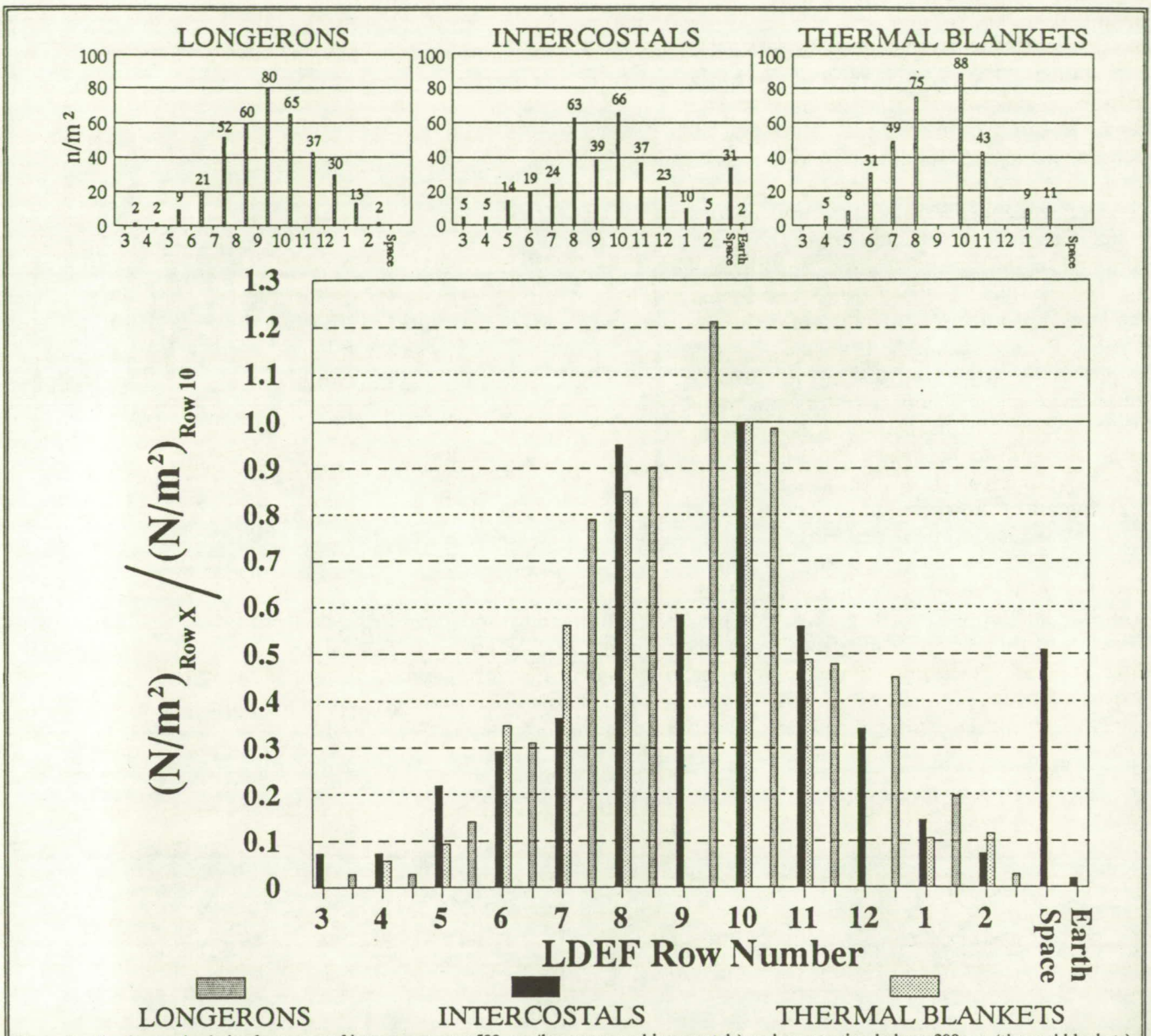

Figure 8. Absolute and relative frequency of impact craters ≥500 μm (longerons and intercostals) and penetration holes ≥300 μm (thermal blankets). Small histograms at top display absolute crater densities (n/m^2), which were normalized with the Row 10 values to yield relative production rates (large histogram) for craters and penetrations holes.

If the observed minima and maxima of crater and penetration-hole densities were taken literally, the difference in calculated production rates for impact features (at constant size) between trailing- and leading-edges would be about 1:43 (longerons), 1:14 (intercostals), and 1:17 (thermal blankets). Using a more reasonable and statistically improved approach (*i.e.*, averaging rearward-facing Rows 2, 3 and 4 and forward-facing Rows 8, 9 and 10), results in production rates for impact features between these principle orientations of 15-20 for impact features of identical sizes.

Again, we emphasize the raw observations presented throughout this report will have to be converted to projectile properties, such as mass and (mean) impact velocity, before the above production rates at constant feature diameter may be converted into absolute particle fluxes. Presently, such conversions can be accomplished only by making various assumptions.

DISCUSSION

The largest surfaces and time-area products ever retrieved from space were scanned for relatively large impact features in a very careful and rigorous manner. While these investigations were performed in parallel with other LDEF deintegration activities at KSC, the quality of the data obtained was not affected by some of the unavoidable constraints applied during these complex operations. The major constraint related to time, which dictated the cut-off diameters for craters ($\geq$500 μm) and penetration holes ($\geq$300 μm). It is recognized that more detailed and time-consuming studies are needed to characterize smaller impact features. To this end the M&D SIG acquired representative materials from LDEF that are being curated at JSC, and which are now available for detailed study by qualified investigators.

The current findings are in qualitative agreement with existing model-predictions that suggest highly differential bombardment histories for surfaces pointing into specific directions relative to the velocity vector of a non-spinning platform in LEO. The production rates for craters $\geq$500 μm in diameter in 6061-T6 aluminum and penetration holes $\geq$300 μm in diameter in thin foil materials (Teflon; 180 μm thick) differ by more than a factor of 10, and possibly by as much as a factor of 20 between leading- and trailing-edge facing surfaces. These are substantial differences and must translate into serious engineering considerations during the design of future, large-scale, long-duration platforms in LEO. The crater and penetration-hole counts do represent a valuable, empirical database to guide the design and possible collisional shielding requirements for future spacecraft, most immediately the Space Station *Freedom*. However, substantial additional work is needed in order to understand LDEF's bombardment history and the collisional hazard in LEO.

We recommend that the observable impact record be expanded to include smaller impact features. In addition, future efforts must concentrate on additional theoretical work concerning the interactions of natural and man-made impactors with non-spinning platforms, an effort which inevitably will also result in averaged conditions for spin-stabilized spacecraft. Furthermore, efforts are needed to experimentally determine the penetration behavior of the LDEF thermal blankets and to extrapolate impact conditions beyond current laboratory capabilities by means of suitable scaling-relationships to those conditions prevailing in LEO. Progress in the area of orbital dynamics, as well as crater and penetration mechanics must be combined in a highly iterative fashion to better understand and cope with the collisional environment in LEO. It was the intent of this report to demonstrate how LDEF has already contributed to these efforts, and how it can and may continue to do so.

REFERENCES

1) Cour-Palais, B.G. (1979), Results of the examination of the Skylab/Apollo windows for micrometeoroid impacts, *Proc. Lunar Planet. Sci. Conf. 10th*, p. 247-265.

2) Clanton, U.S., Zook, H.A. and Schultz, R.A. (1980) Hypervelocity impacts on Skylab IV/Apollo windows, *Proc. Lunar Planet. Sci. Conf. 11th*, p. 2261-2273.

3) McDonnell, J.A.M., Carey, W.C. and Dixon, D.G. (1984) Cosmic dust collection by the capture cell technique on the Shuttle "Pathfinder" mission, *Nature, 309, #5965*, p. 237-240.

4) Warren, J..L. and 10 Co-authors, (1989) The detection and observation of meteoroid and space debris impact features on the Solar Max satellite, *Proc. Lunar Planet. Sci. Conf., 19th*, p. 641-657.

5) Rietmeijer, F.J.M., Schramm, L., Barrett, R.A., McKay, D.S. and Zook, H.A. (1986) An inadvertent capture cell for orbital debris and micrometeoroids; the Main Electronics Box thermal blanket of the Solar Maximum Satellite, *Adv. Space. Res., 6*, p. 145-149.

6) Kessler, D.J. (1991) Orbital Debris Environment for Spacecraft in low Earth orbit, *J. Spacecraft, 28, 3*, p. 347-351.

7) See, T.H., Allbrooks, M.K., Atkinson, D.R., Sapp, C.A., Simon, C.G. and Zolensky, M.E., Meteoroid and Debris Special Investigation Group Data Acquisition Procedures. First LDEF Post-Retrieval Symposium, NASA CP-3134, 1992.

8) See, T.H., Allbrooks, M.A., Atkinson, D.R., Simon, C.G. and Zolensky, M. (1990) Meteoroid and Debris Impact Features Documented on the Long Duration Exposure Facility, A Preliminary Report, Publication #84, JSC #24608, 583 pp.

9) Zook, H.A. (1987) On cosmic dust trajectory measurements and experiment pointing considerations, in Progress towards a Cosmic Dust Collection facility on Space Station, Mackinnon, I.D. and Carey, W.C., eds., Lunar and Planetary Institute, *LPI Technical Report 88-01,* p. 76-77.

10) Zook, H.A. (1991) Meteoroid directionality on LDEF and asteroidal versus cometary sources (abstract). *Lunar Planet. Sci. XXII*, Lunar and Planetary Institute, Houston, Tx., p. 1577-1578.

11) Mullholland, J.D. and 8 Co-authors (1991) IDE Spatio-temporal fluxes and high time-resolution studies of multi-impact events and long-lived debris clouds, First LDEF Post-Retrieval Symposium, NASA CP-3134, 1992.

12) Cour-Palais, B.G. (1987) Hypervelocity Impacts in Metals, Glass, and Composites, *Int. J. Impact Eng.,.5*, p. 681-692.

13) Hörz, F., Messenger, S., Bernhard, R., See, T.H. and Haynes, G. (1991) Penetration phenomena in Teflon and aluminum films using 50-3200 μm glass projectiles (abstracts), *Lunar Planet. Sci. XXII*, Lunar and Planetary Institute, p. 591-592.

14) Gregory, J.C. and Peters, P.N. (1991) LDEF attitude measurement using a pinhole camera with a silver/oxygen atom detector, First LDEF Post-Retrieval Symposium, NASA CP- 3134, 1992.

15) Zolensky, M., Atkinson, D., See, T.H., Allbrooks, M., Simon, C., Finckenor, and Warren, J. (1991) Meteoroid and Orbital Debris Record of the Long Duration Exposure Facility's Frame, *J. Spacecraft and Rockets, 28, #2*, p. 204-209.

PRELIMINARY ANALYSIS OF LDEF INSTRUMENT A0187-1 "CHEMISTRY OF MICROMETEOROIDS EXPERIMENT"

Friedrich Hörz
NASA Johnson Space Center
Solar System Exploration Division
Houston, Texas 77058

Ronald P. Bernhard, Jack Warren, Thomas H. See
Lockheed Engineering & Sciences Company
Houston, Texas 77058

Donald E. Brownlee, Mark R. Laurance, Scott Messenger
Department of Astronomy
University of Washington
Seattle, Washington 98195

Robert B. Peterson
3738 Arnold Street
Houston, Texas 77005

SUMMARY

The "Chemistry of Micrometeoroids Experiment" (CME) exposed approximately 0.8 m^2 of gold (>99.99% pure) on LDEF's trailing edge (location A03) and approximately 1.1 m^2 aluminum (>99%) in the forward-facing A11 location. Detailed crater counts reveal a factor of 7-8 enhancement of the effective particle flux on the A11 location compared to LDEF's trailing edge. These differences are in qualitative agreement with recent theoretical models regarding dynamic properties of hypervelocity particles in low-Earth orbit.

Survey-type, compositional investigations of the impactor population(s) via electron beam methods and associated energy dispersive X-ray analysis have commenced. A large fraction (>50%) of all craters retain projectile masses below the sensitivity threshold of the SEM methods used. Projectile residues that can be analyzed may be classified into "natural" and "man-made" sources, yet our investigations have not progressed to the point where we can define their relative abundance with confidence. Most large craters seem to have been caused by natural impactors, however.

The most significant results to date relate to the discovery of unmelted pyroxene and olivine fragments associated with natural cosmic dust impacts; the latter are sufficiently large (μm) for detailed phase studies and they serve to demonstrate that recovery of unmelted dust fragments is a realistic prospect for future dust experiments that will employ more advanced collector media. We also discovered that man-made debris impacts occur on LDEF's trailing edge with substantially higher frequency than expected, suggesting that orbital debris in highly elliptical orbits may have been somewhat underestimated. Even these preliminary results illustrate the great potential of LDEF to contribute to ongoing studies of extraterrestrial materials, as well as to an improved understanding of collisional hazards in LEO.

INTRODUCTION

LDEF experiment A0187-1, the "Chemistry of Micrometeoroid Experiment" (CME) occupied two full LDEF trays, located on Rows 3 and 11. Its primary purpose was to retrieve analyzable projectile residue associated with hypervelocity craters in infinite halfspace targets. The most prolific sources of natural dust are asteroids and comets, which are primitive solar system objects that escaped the pervasive thermal processing of the inner planets. Therefore, the chemical information extracted from natural impactors will yield insight into early solar system processes. Even more so if unmelted particle fragments were found to characterize textural relationships and individual minerals. The unexpectedly long duration of the LDEF mission, some 5.7 years, enhanced these opportunities beyond expectation.

In addition, substantial developments since the inception of the LDEF experiments provide new opportunities, and a much improved interpretative context for the initial objectives. Three significant developments occurred. First, the

existence and significance of interplanetary dust was recognized in particle collections obtained from the stratosphere by high altitude aircraft (ref. 1), in deep-sea sediments and in pre-industrial polar ices (ref. 2). Also, greatly improved or innovative analytical methods enabled detailed mineralogical, chemical and isotopic investigations, rendering laboratory analysis of interplanetary dust into an integral and highly rewarding part of extraterrestrial materials research (*e.g.,* refs. 2, 3, 4, 5). Second, a number of dust instruments were onboard the GIOTTO and VEGA spacecraft as they passed close to comet Halley in 1986. Highly successful mass spectrometers provided the first *in situ* chemical analyses of cometary solids (*e.g.,* ref. 6). Many Halley particles seem to be akin to those collected in the stratosphere, but not all. Third, awareness of a substantial collisional threat in Earth orbit from man-made debris increased over the past decade, and vigorous efforts have been initiated, at international levels, to better understand and cope with this hazard (ref. 7).

Based on these developments during the past decade, an understanding of LDEF's impact record has assumed increased significance. Are terrestrial collections of interplanetary dust representative or does heating during atmospheric entry introduce bias? What are the impact rates of natural particles versus man-made debris? What are the most prolific sources of man-made particles? The detailed analysis of our CME experiment intends to contribute to these questions. The following is a progress report toward that objective.

INSTRUMENT DESCRIPTION

The CME exposed two substantially different instruments, one containing movable collector surfaces (*i.e.*, the "active" instrument), the other was totally "passive". Their salient features and underlying rationale are described below. The active tray was considered the potentially more valuable collector and was therefore located on LDEF's trailing edge which was expected to be the least contaminated LDEF location. Also, relative encounter speeds are the lowest in the rearwards-facing direction compared to any other LDEF location, as detailed below.

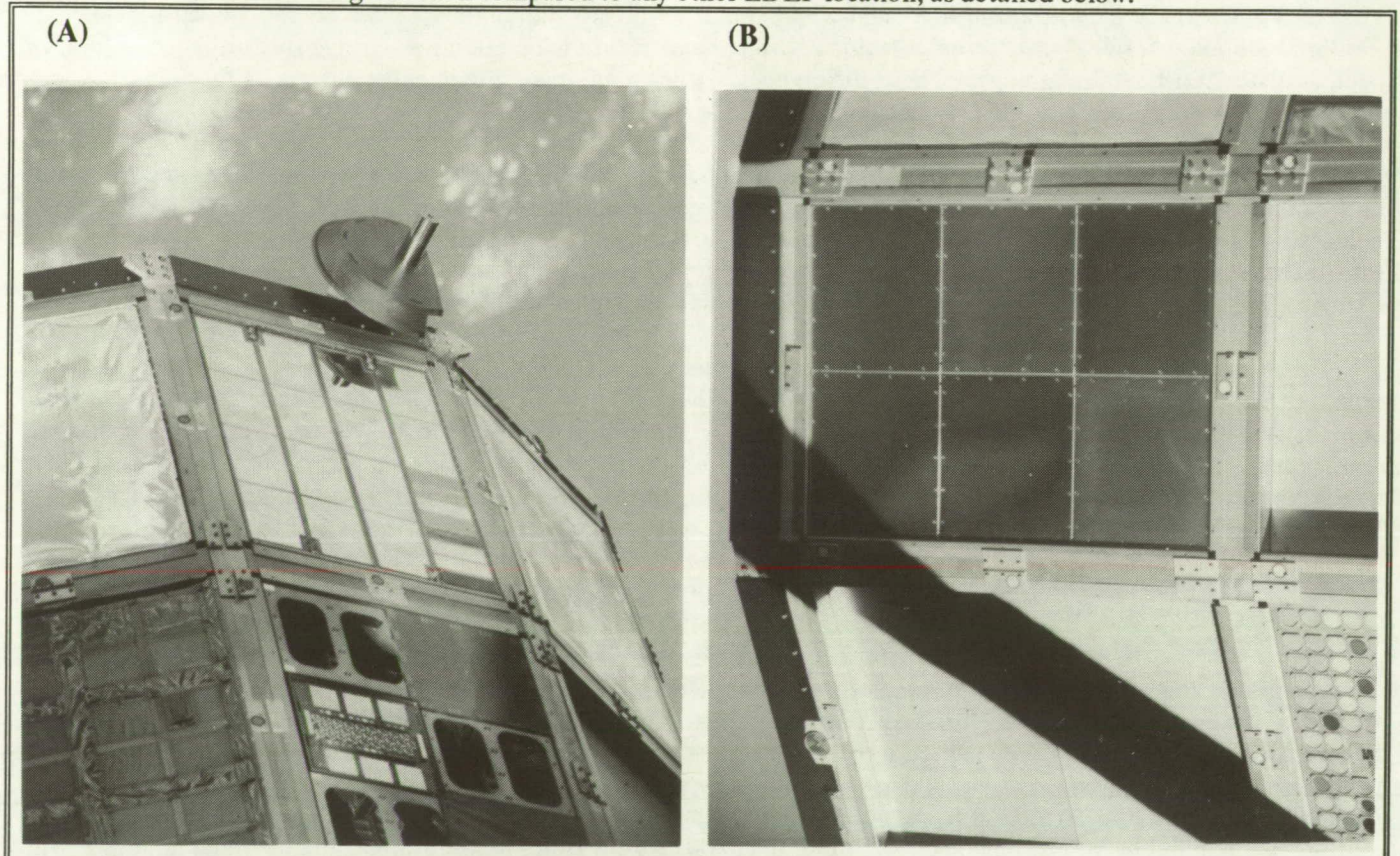

Figure 1. The CME experiment trays during retrieval operations by STS 32. (A) The active experiment on LDEF location A03 (trailing edge), exposing seven plates of gold (approximately 0.8 m^2) and some auxiliary surfaces to evaluate their suitability as micrometeoroid collectors. Note the "open" configuration of the clamshell devices. (B) "Passive" tray, located in the forward-facing A11 location and exposing 6 plates of >99% pure aluminum (1100 series), approximately 1.1 m^2 in total surface area.

Active Instrument (Tray A03)

The active instrument occupied an entire 12" deep tray located in Bay A03 and exposed seven sheets (~0.5 mm thick) of pure gold (>99.99% Au), each sheet measuring approximately 57 x 20 cm (Figure 1a). Accounting for fasteners and clamping devices, each sheet exposed approximately 1170 cm^2 for a cumulative surface area of 0.82 m^2. The rationale for selecting gold as collector substrate was as follows: Au has a characteristic X-ray spectrum that does not seriously interfere with most elements of interest during energy-dispersive analyses using electron beam methods for excitation. Also, a prerequisite for any collector medium is that it not contain elements of cosmochemical significance and Au is not a terribly diagnostic element to distinguish among diverse classes of extraterrestrial materials. The high malleability of gold leads to relatively large craters, again a favorable property. The major drawback of gold is its high density, leading to substantial shock stresses and unfavorably high temperatures during hypervelocity impacts compared to target materials of lower bulk density.

A fraction of the active CME tray, totalling approximately 1100 cm^2, was occupied by eight experimental surfaces, each about 20 x 7 cm in size but of variable thickness to empirically determine their suitability for hypervelocity particle capture (Figure 1a). They included other high-purity, mono-elemental collector plates (Al, Be, Ti, Zn, C), Kapton, and low-density, porous Teflon filters, the latter intended to impart the least shock stresses for possible recovery of unmelted particle remnants (refs. 8,9). None of these experimental surfaces have been analyzed in detail.

Figure 1a depicts the active instrument during retrieval operations in low-Earth orbit (LEO). The most noteworthy feature in Figure 1, other than the detailed geometry and arrangements, relates to the "opened" and exposed gold collectors. The gold actually occupied the insides of clamshell-type devices that opened and closed upon self-contained command. The rationale for such "active" clamshells was to protect the ultra-clean gold surfaces from contamination during all nominal ground handling and on-orbit Shuttle operations. A mechanical labyrinth seal protected the collectors from particulate contaminants in closed position, yet not from gaseous species. Under nominal operations, the clamshells should have opened about 10 days after LDEF deployment, and closed a similar period prior to the scheduled retrieval by the Shuttle 9 months later. These operations had to be preprogrammed relative to the nominal LDEF mission. In Appendix A, we detail our findings regarding the open clamshell configuration, possibly caused by a malfunctioning closing mechanism during the unexpectedly long exposure in LEO. We conclude that the instrument worked nominally throughout the entire LDEF mission and that the clamshells opened and closed repeatedly, and as designed, until actual retrieval after 5.7 years.

Passive Instrument (Tray A11)

Total instrument resources were insufficient to have two (or more) LDEF trays equipped with active clamshells and associated gold collectors. As a consequence, we utilized low-cost aluminum collectors for the second LDEF tray (Figure 1b). Commercial series 1100, tempered grade aluminum (>99% pure) was used. The total tray surface was occupied by six individual panels (each approximately 41 x 46 cm and 3.2 mm thick) for a cumulative surface area of 1.1 m^2. It was clearly recognized from the beginning that compositional analyses might be limited on these aluminum targets compared to the gold substrate, but it was also thought that lower shock stresses induced by aluminum might lead to less vaporization, yielding relatively large quantities of melt that should not be intolerably contaminated by target impurities.

Instrument Locations

Recent theoretical work (refs. 10, 11) points out that effective particle fluxes and velocity distributions strongly depend on instrument orientation relative to the velocity vector of a non-spinning spacecraft, such as LDEF or Space Station. These new insights were not part of the initial LDEF or CME rationale, yet they are paramount in understanding the cratering record on LDEF and associated implications for the dynamics of the hypervelocity environment in LEO. A number of groups (Zook; McDonnell; Humes) have therefore engaged in similar, yet complementary and in part refined calculations, as did we during the concept development of future dust collection experiments on the Space Station Freedom.

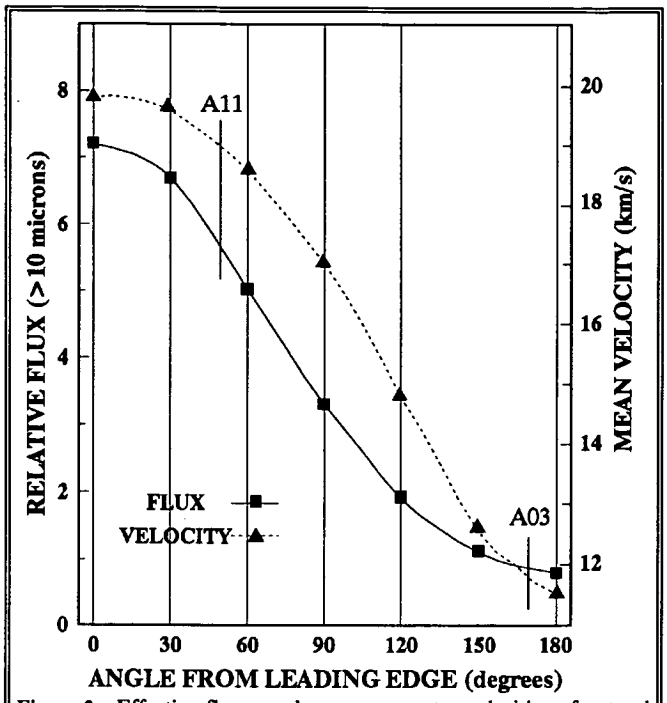

Figure 2. Effective fluxes and mean encounter velocities of natural and man-made particles >10 μm as a function of viewing direction on a non-spinning platform in LEO. The initial conditions underlying these calculations are largely those of reference 10.

Figure 2 illustrates some first order, general results and depicts the effective fluxes and mean velocities of natural particles >10 μm that encounter flat, vertical surfaces of specific, orientations relative to LDEF's velocity vector. Note that mean encounter velocities range from approximately 20 to 11 km/s for surfaces that point into the ram and anti-ram direction, respectively. Also note that the effective fluxes between those orientations may differ by a factor of 10. Because most impact damage is proportional to the impactor's kinetic energy, the combination of flux and mean velocities results in factors of 30 to 40 differences in the energy flux between ram and anti-ram directions, a substantial difference for the design and operation of flight systems. These model predictions may be tested by a wide variety of LDEF surfaces. Indeed, first order comparisons are being offered in this volume by most dust investigators.

CRATER POPULATIONS

All CME surfaces deemed useful to obtain detailed crater statistics by optical methods have been examined at resolutions that appear consistent with the quality of their surface finish, none of which is of high quality. We avoided any finishing by grinding and polishing for fear of contaminating the surfaces with embedded polishing compounds. The finishes on both surfaces were obtained by rolling processes, with the aluminum surfaces modestly improved and more homogenized after anodizing, using a sulfuric acid bath. The optical equipment and procedures used for crater counting are the same ones used during the KSC surveys by the M&D SIG (ref. 12). The actual diameters measured were rim-to-rim widths (D_r) for consistency (ref. 12), and because true crater diameters (D_c) (defined as the intercept of the crater wall with the flat target surface) are difficult to determine, especially for relatively small craters.

The crater counts are detailed in Figure 3 and summarized in Figure 4. The reasons for including all tray lips in these investigations are as follows: First, they represent substantial surface areas, each approximately 0.14 m^2, and deserve documentation in their own right. Second, they are manufactured from aluminum alloy 6061-T6, the only material common to both CME trays, and thus important for checks of internal self-consistency among our own surfaces and especially for comparison with other aluminum 6061-T6 surfaces that abound on LDEF (*e.g.*, ref. 13). This alloy is used widely on other spacecraft as well, the reason why its impact behavior is relatively well documented (*e.g.*, refs. 13, 14). The conversion of crater diameters to projectile dimensions and ultimately to mass should, therefore, be the most reliable for the Al-6061 tray lips. The actual collector materials composing CME are not as well calibrated as the tray lips, yet they should have experienced identical particle fluxes for the A03 and A11 locations. Analysis of the tray lips may thus provide internal consistency checks for the calibration and interpretation of crater diameters that accumulated on the CME collectors.

The crater statistics on the A03 tray lips also assume a pivotal role in explaining the "opened" clamshell configuration during retrieval by STS 32. These lips were continuously exposed throughout the total LDEF mission, but a nominally operating clamshell device permitted the gold collectors to be exposed only part of this time. As a consequence, the ratio of absolute crater densities on both surfaces is a direct measure of the fractional time during which the clamshells were in the open configuration.

Note in Figures 3 and 4 that the A11 tray crater densities are systematically higher than those of the A03 tray, for both the lips as well as the collector surfaces. This difference is ascribed to instrument orientation relative to LDEF's velocity vector as expected from Figure 2. The average flux in the forward-facing direction is distinctly higher than on the trailing edge.

The difference between the A03 tray lips and A03 collector data, however, cannot be due to instrument orientation. It must reflect difference in exposure time to an essentially identical impactor population. The modest crater concentrations of the gold collectors constitute first order evidence that the clamshells were not exposed continuously throughout the entire LDEF mission. The crater densities differ by approximately a factor of 2.

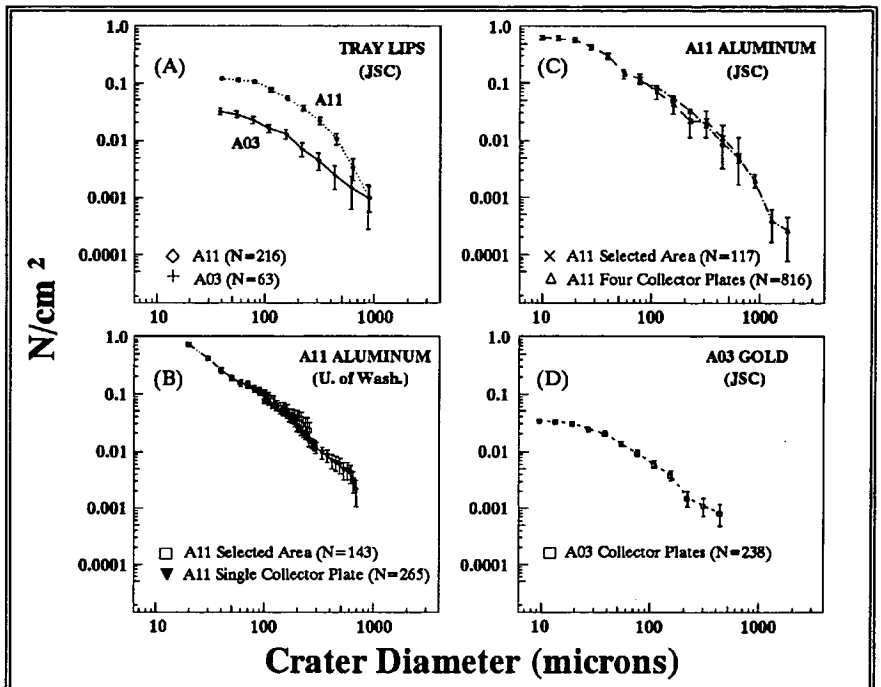

Figure 3. Detailed, optical crater counts performed on major CME surfaces. (A) Lips of instrument trays, composed of aluminum 6061-T6 measuring approximately 0.14 m^2 in surface area. These two surfaces best reflect the difference between rearward and forward-pointing directions, as the target materials were identical. (B) Crater counts on a single A11 aluminum plate (scanned at University of Washington). (C) Crater counts on a total of four A11 aluminum plates (scanned at JSC). (D) Crater counts on all gold surfaces (scanned at JSC). Error bars are statistical sampling errors (2 sigma).

PROJECTILE POPULATIONS

Conversion of the crater diameter measurements to projectile diameters is a prerequisite to derive meaningful comparisons of particle fluxes and mass frequencies for LDEF instruments. Note that the average initial impact conditions will vary with specific LDEF location as suggested by Figure 2 and that we employed targets of different physical properties, the latter strongly controlling crater growth under otherwise identical conditions.

We employed the experimentally determined crater scaling relationships derived by Cour-Palais (ref. 14) and as amended by E. Christiansen (personal communications, 1991) for all aluminum surfaces:

$$P=5.24D_p^{19/18}H^{-0.25}(d_p/d_t)^{0.5}(V/V_c)^{2/3} \qquad \text{(equation 1)}$$

where P is the crater depth, d_t and d_p the target and projectile densities (2.7 and 2.2 g/cm^3, respectively), H=Brinell hardness (90 and 40 for "6061-T6" and "1100, annealed" aluminum alloys, respectively); V_c=target sound velocity (6.1 km/s) and V=impact velocity (as extracted from Figure 2). Hemispherical crater profiles are typical for aluminum targets at light gas gun velocities, and crater diameter (D_c) thus relates to depth as D_c=2P, with both diameter and depth measured relative to the flat target surface (ref. 14). The actual measurement of rim diameter (D_r) converts to crater diameter D_c as

$$D_c=0.78\ D_r \qquad \text{(equation 2)}$$

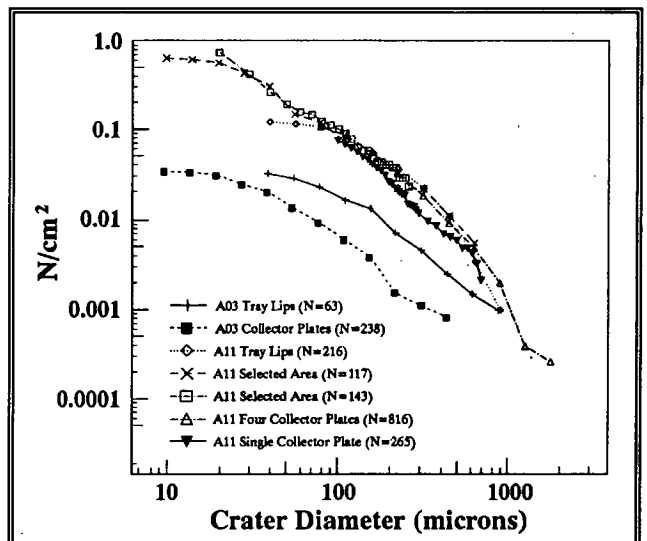

Figure 4. Summary comparisons of all CME crater counts. Note the general similarities in crater densities for all A11 surfaces that differ substantially from those of the A03 tray lips and gold surfaces. Differences among the A11 surfaces must be stochastic, yet the differences with and among the A03 surfaces relate to decreased effective flux and variable cumulative exposure time, respectively.

The latter derives from impact experiments, largely unpublished, into 1100 aluminum (ref. 15), which also found substantial agreement with the scaling relationships (ref. 14) as expressed by equation 1.

Calibration of the Au craters is based on dedicated experiments conducted with an electrostatic dust accelerator at MPI, Heidelberg, Germany, and a small caliber light gas gun at EMU, Freiburg, Germany (*e.g.*, ref. 16). Based on these data (Figure 5) a ratio of $D_c/D_p=5.7$ was extrapolated for the gold collectors at average encounter speeds of approximately 12 km/s.

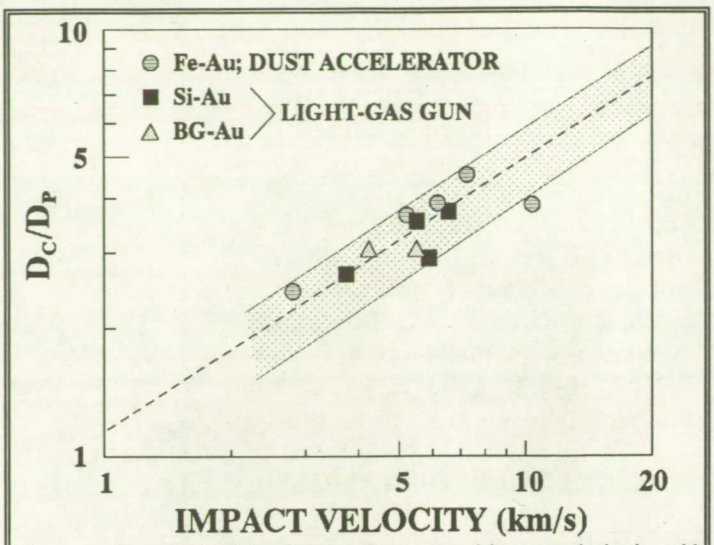

Figure 5. The relationship of crater diameter and impact velocity in gold targets based on micron-sized iron projectiles (electrostatic accelerator) and millimeter-sized glass projectiles (light gas gun).

Based on these crater scaling relationships, we converted the measured D_c or D_r into projectile diameters (D_p) and the results are presented in Figure 6. The following observations and possible interpretations are offered:

a) Note that similar absolute frequencies occur on all major A11 tray surfaces. The differences observed are within statistical error (Figure3) and we ascribe them to (expected) idiosyncrasies of the stochastic bombardment process.

b) The difference in effective flux between the A11 and A03 orientations, the major purpose of this plot, is somewhat difficult to quantify. We first note that the relative slopes of the A11 and A03 distributions seem to differ subtly, if taken at face value. However, if plotted in normalized form (not shown) and considering the statistical errors illustrated in Figure 3, the impactor size frequencies could be identical between the A11 and A03 orientations.

A statistically improved data set is needed to demonstrate whether the forward-facing surfaces do indeed experience larger numbers of "small" impactors compared to rearwards-pointing surfaces, the first order impression one derives from Figure 6. This impression, however, is not necessarily correct and could be driven by but a few random, "large" impacts on both surfaces. Note that the difference at the 100 μm projectile diameter is only a factor of 2-3 between the A11 and A03 orientations.

Based on the above, we derived our best estimates for effective fluxes or relative exposure time from 20-30 μm diameter projectiles that correspond to craters of typically 100-180 μm in diameter, a size range that should be most representative and statistically valid, as it avoids the poor statistics at the large crater end and potential errors of omission at small crater sizes. Based on these qualifications, the A11 surfaces experienced approximately a factor of 8 larger flux than the trailing edge surfaces, a value modestly larger than that expected from Figure 2.

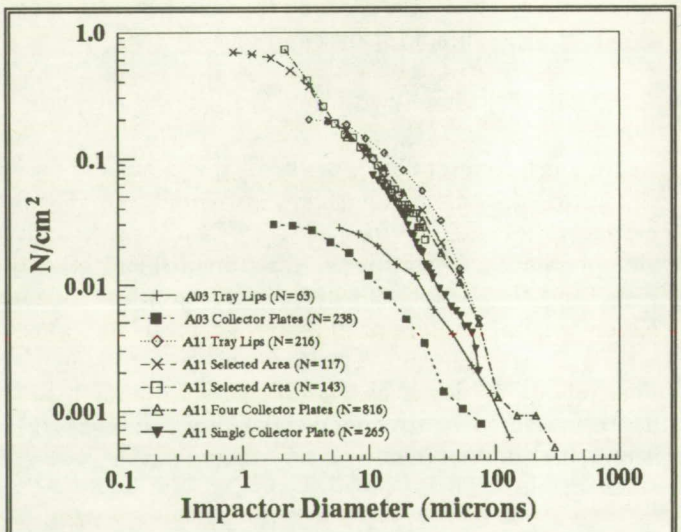

Figure 6. Projectile size frequency and relative flux for the statistically most valid CME surfaces.

The effective cumulative exposure times between the A03 tray lip and gold collectors differ by approximately a factor of 2. A continuously cycling "active" instrument (see Appendix A) would expose the gold collectors for 1279 out of 2145 days, leading to a difference of 1.68 in cumulative exposure time. This ratio is modestly smaller than the factor of 2 difference in crater counts, yet within statistical error, the gold collector data indicate nominal instrument performance. If taken literally, the observed factor of 2 would imply even less exposure time than a nominally cycling instrument and would, therefore, result in a trend that is opposite the suspicion of a failed closing operation. We are

thus confident that the CME gold collectors were not exposed for any time longer than that allowed by an instrument that cycled repeatedly, by design, throughout the entire LDEF mission.

DEPTH/DIAMETER RATIOS OF CRATERS

Absolute crater depth is a complex function of target and projectile properties that control the target's penetration behavior and it depends strongly on absolute encounter velocity and impact angle (*e.g.*, refs. 14, 17, 18). Of course, these initial conditions also control the final crater diameter, leading to the concept of proportional crater cavity growth. This concept was adopted to convert measured crater diameters into associated projectile dimensions via equation 1. We measured the depth/diameter ratios of select craters primarily to test whether constant crater cavity geometries apply, and whether their average aspect ratios are consistent with the geometries assumed in equation 1.

We selected a single, random panel from the aluminum and gold collectors for this purpose and measured the depth of all craters >40 μm in diameter (*i.e.*, 174 impacts in aluminum and 26 in gold). The observed depth/diameter ratios vary considerably as illustrated in Figure 7.

The "standard" aspect ratio of $P/D_c=0.5$, derived from normal incidence laboratory experiments, does not apply even to averaged crater geometries. The aluminum craters are biased towards deeper structures than the standard crater, while the gold craters tend to be shallower. We tentatively interpret this difference with systematically different impact velocities (Figure 2). Also, small craters tend to display much larger ranges in P/D_c than larger structures, indicating substantially more variability for initial impact conditions among small projectiles. This could be due to increased variability in velocity, and especially in projectile density, the latter ranging from compact single minerals to relatively fluffy, low-density particles. Clearly, we do not understand these differences in detail, as a number of interdependent factors and parameters combine into the final crater shape. The data shown in Figure7 merely serve to illustrate the existence of large variability in P/D_c. Projectile properties based on a single diameter or depth measurement, and on an assumed and reasonable "average" initial impact conditions may yield highly model-dependent results. While Figure 7 seemingly points towards potential pitfalls of this approach, we are not in a position to suggest improvements.

CHEMICAL ANALYSIS OF PROJECTILE RESIDUES

We have performed a survey type assessment of the compositional make-up of particles by employing a Scanning Electron Microscope with an energy-dispersive X-ray analyzer. Most analyses to date are qualitative in the sense that they relate exclusively to the major elements present (>few percent) and that they address only their approximate proportions as deduced from visual inspection of associated X-ray spectra. This qualitative assessment suffices to survey the approximate composition of a large number of particles and to explore overall chemical variability. The deliberate tradeoff between analytical precision and total number of particles analyzed qualitatively is permitted at present to determine overall chemical variability, and to explore potential compositional groupings into distinct particle types. Quantitative analysis of every single particle is simply too time consuming and must be limited to representative specimen,

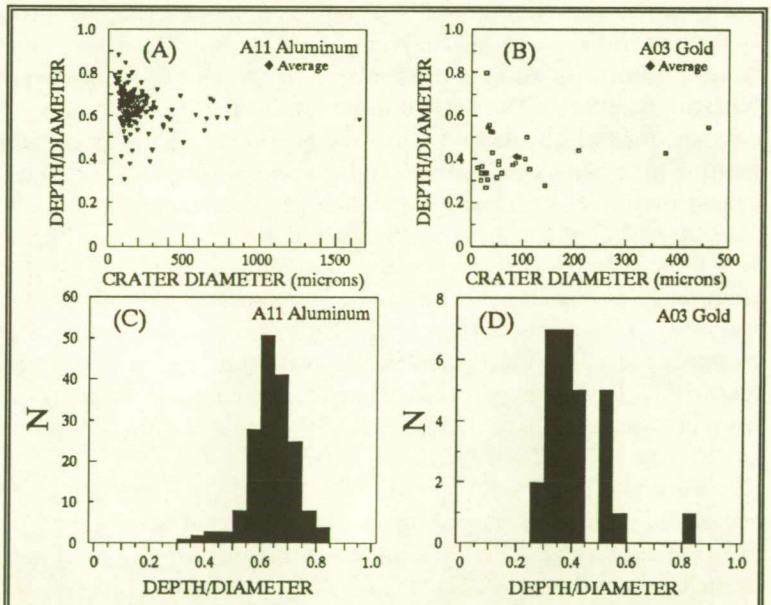

Figure 7. Measured depth/diameter ratios on representative CME surfaces. (A) and (B) display the measured ratios as a function of crater size for the A11 aluminum surfaces and the A03 gold collectors, respectively. Note the large scatter at small crater sizes. (C) and (D) are simple frequency histograms for the same surfaces. Note the bias towards relatively deep structures on the aluminum targets and towards unusually shallow structures on the gold collectors, none averaging $P/D_c=0.5$, the prevailing model assumption of a hemispherical crater cavity.

or those that are unusual by any number of criteria. Our CME approach was patterned after that developed during the analysis of Solar Max surfaces (refs. 19, 20), and after the preliminary investigation of stratospheric dust (ref. 21), all aimed at characterizing a large number of particles.

Figure 8 portrays crater morphologies and associated projectile residues. A few general comments apply. The presence of impactor residue is revealed with surprising ease during optical studies by a mostly dark coloration of the crater interiors. Craters which do not display dark crater bottoms or walls will generally not contain analyzable projectile residue. However, even dark crater liners are no guarantee that residues -- at the sensitivity levels of electron beam instruments -- are present; a fair fraction of craters that seemed promising optical candidates contained no analyzable residues.

A first order result of our compositional survey is that a significant fraction of the LDEF craters do not contain sufficient projectile remnants to be detected by the SEM methods that were employed (500 s and 30 KeV) in our initial survey. However, longer count times and higher accelerating voltages would provide better counting statistics, and thus, the resulting signal-to-noise ratio(s) might be sufficient to reveal minor traces of the impactor composition. This non-analyzable fraction of craters is >50%, even on the trailing edge gold surfaces, where mean velocities, shock stresses and temperatures are lowest. Compared to laboratory craters at 7 km/s (ref. 16), which yielded copious amounts of projectile melt, wholesale vaporization (or other loss mechanisms) seems to be common at the LDEF encounter speeds. Methods more sensitive than electron beam instruments, such as Secondary Ion Mass Spectrometry (SIMS and associated ion beams), are needed to possibly extract impactor compositions from many LDEF craters.

Projectile materials that we could detect and analyze with electron beam instruments occur commonly in the form of melts draping the crater walls or floors, mostly in the form of isolated patches, that seem to have contracted from very thin films by surface tension. Some melts have smooth surfaces, others are relatively rough and rich in vesicles. Also, genuine melt droplets occur frequently. The melt distribution inside crater cavities is generally very heterogeneous, rendering estimates about the mass fraction of the initial impactor that may be preserved in the crater interior highly impractical.

Some craters contain melts, as well as unmelted projectile fragments (Figure 8c). Such unmelted fragments are of special scientific value, as they may yield phase chemistries and mineralogic textural relationships that reflect their conditions of formation with substantially increased fidelity compared to the wholesale melts and associated average bulk compositions. The limited observations that we have on such unmelted fragments indicate mostly monomineralic compositions of olivine and pyroxene (Figure 9). It is known that olivine and pyroxene are more resistant to shock melting than many other rock-forming minerals (*e.g.,* ref. 22) and that fine-grained components melt more rapidly than coarse materials, especially if the fine-grained fraction is loosely packed and displays porosity (*e.g.,* refs. 23, 24,25). Most unmelted relicts have surprisingly uniform grain size (Figure 8c), possibly suggesting the breakup of one or more very large crystals. The presence of monomineralic relicts in a host melt of essentially chondritic average composition (Figure 9) is consistent with shock pressures in the 70-100 GPa range, mandating low impact velocities for the fragment-laden craters. Nevertheless, unmelted impactor fragments occur on both the trailing edge and forward-facing collectors, despite their substantially different mean encounter velocities. The presence of unmelted projectile materials following hypervelocity impacts into metallic targets is an important finding in view of future dust collections contemplated for Space Station that may employ somewhat improved collector media (*e.g.,* ref. 26).

We have analyzed approximately 300 LDEF craters and have found the compositional classifications and associated criteria developed during the analysis of the Solar Max surfaces (ref. 20) highly suitable for the classification of LDEF craters as well. We delineated three major groups of natural cosmic particles, in agreement with stratospheric particle populations (ref. 21).

The first group is dominated by Mg, Si and Fe, with Al, Ca and S as minor components. These are roughly "chondritic" compositions, typical for fine-grained, primitive meteorite matrices, as well as for many stratospheric particles (*e.g.,* refs. 1, 2, 27; Figures 8a, b and c). The next group is composed predominantly of Mg, Si, and Fe, with some variations in the Mg/Fe ratio. Such compositions are typical for monomineralic, mafic minerals, such as

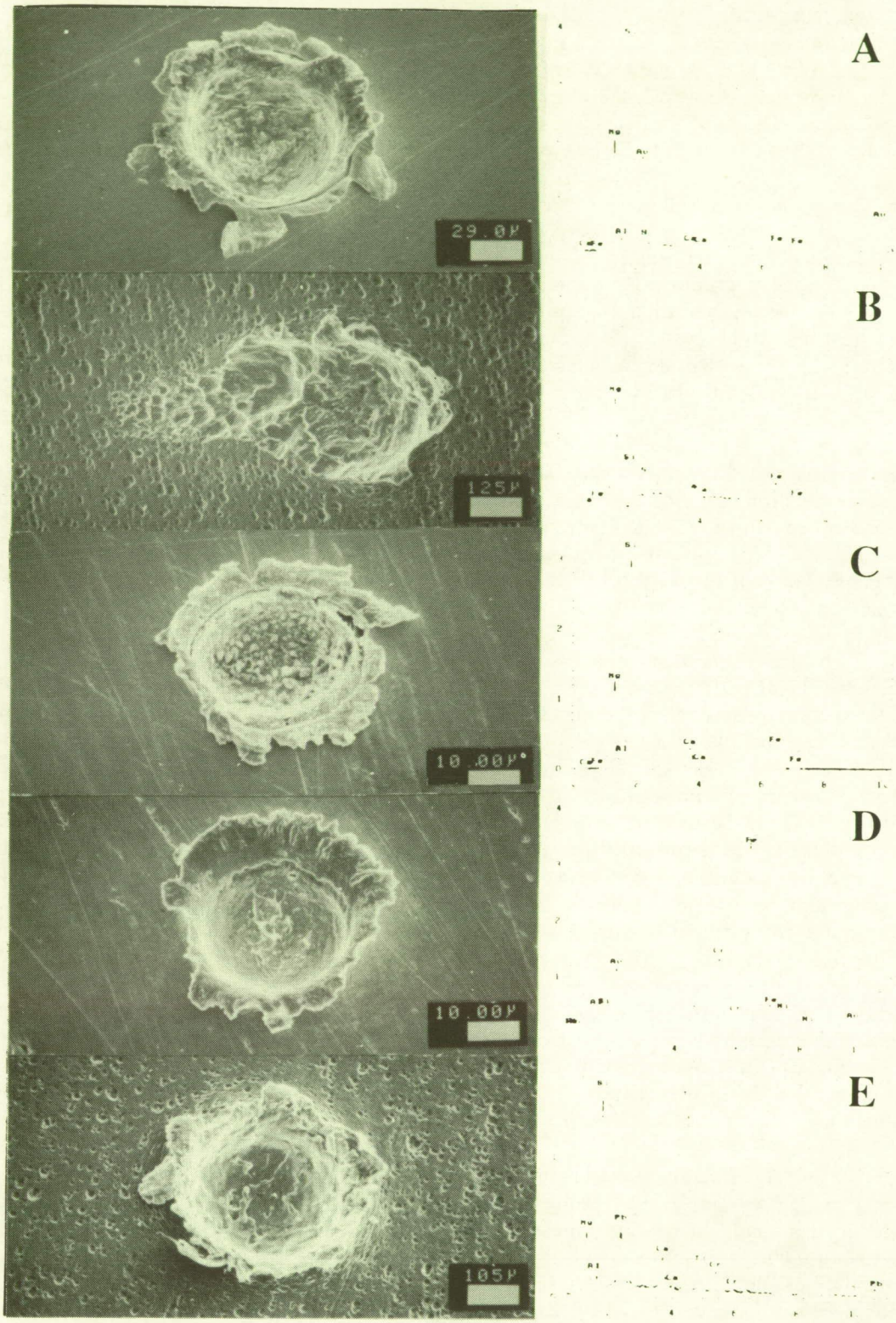

Figure 8. Representative morphologies of hypervelocity impact craters and associated X-ray spectra of projectile residues. (A) A "chondritic" impactor melt drapes the bottom and walls of a typical LDEF crater formed in gold, as evidenced by traces of the target substrate in the X-ray spectrum; (B) An unusually shallow and elongated crater indicative of a highly oblique impact angle by a natural impactor of chondritic composition; (C) Example of a rare crater displaying unmelted fragments of pyroxenes, all of relatively uniform grain size, residing in a host melt of chondritic composition (not illustrated); (D) Man-made debris (stainless steel) impact on trailing-edge gold substrate; (E) impact caused by paint flake on aluminum collector.

pyroxenes and olivines, known also from stratospheric dust or a variety of meteorites (*e.g.*, refs. 27, 28). As described above, most unmelted residue falls into this category, but most of the host melts are of chondritic composition and the entire particle would, therefore, be classified as chondritic. The third particle class is essentially monomineralic and represents Fe-Ni-rich sulfides, also known as discrete phases from carbonaceous chondrites and stratospheric particles (*e.g.*, ref. 27). Therefore, particle types 1-3 observed in LDEF craters resemble those recognized in the stratospheric dust collections or primitive meteorites. This assignment to otherwise unspecified "natural" sources rests heavily on current cosmic dust and meteorite research, as well as on general geochemical and petrological arguments applicable to natural silicate systems.

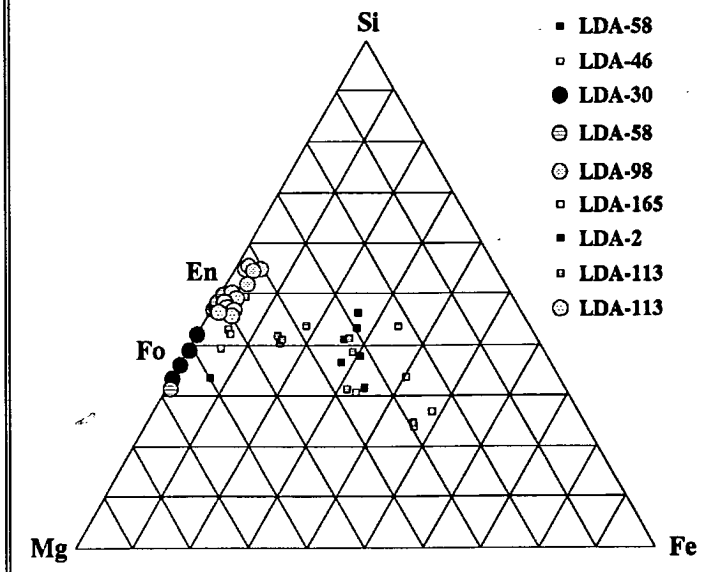

Figure 9. Quantitative analyses of select residues of natural projectiles that occurred in the form of unmelted fragments of pyroxene or olivine, typically associated with wholesale melts of different (chondritic) bulk composition that most likely reflect the particles' fine-grained matrices. Large circles reflect "monomineralic", unmelted fragments, while small squares represent the composition of melts. Note that some melts may have nearly monomineralic composition, a common occurrence in shocked, particulate targets.

Compositions that do not fall into any of the above three categories are strong candidates for man-made projectiles, as has been argued in the Solar Max case as well (refs. 19, 20). Most cannot be derived from silicate melts typical of geologic systems or from vapors that have elemental abundances similar to the overall solar system (*e.g.*, ref. 5). Any particle dominated by Fe, yet also containing substantial amounts of Ni and Cr (Figure 8d) does not seem to be a natural material on geochemical grounds, but must be interpreted as stainless steel on account of the high Cr content. Also, a particle almost exclusively made up of Ti and Pb (Figure 8e) seems incompatible with any reasonable natural substance, yet is a good match for paint pigments. Indeed, many particles of mono-elemental compositions seem excellent debris candidates, as are particles devoid of Si. In brief, substantial geochemical and petrogenetic arguments combined with knowledge of the sorts of man-made materials that exist in LEO can be used to distinguish between natural and man-made projectiles on a case by case basis. On occasion this distinction becomes difficult. For specific endmember compositions the distinction is easy, and in most cases assignment to natural and man-made sources can be made with confidence. We do not, at this time, present specific subgroups of man-made debris, because they display much more chemical variety than natural projectiles. Clearly, some groupings such as pure metals, alloys, and non-metals such as paints or composites, may be recognized with an increased data set.

Figure 10a relates to the rearward-facing gold collectors. It represents a complete survey of all craters >50 μm in diameter, combined with a representative set (approximately half of the total population) of craters between 20 and 50 μm, as well as some samples (~20% of observed population) between 10 and 20 μm. None of the <50 μm craters were selected on the basis of color or any other criterion, because we desired to analyze a "representative" suite of craters (in contrast to the Aluminum collector surfaces described below).

Note in Figure 10a the large fraction of craters that did not contain residue (134 of a total population of 196); even large structures may not possess analyzable residues. Approximately 1/3 (21 of 62) of the craters that do contain residue were caused by man-made debris; this represents approximately 10% of the total crater population on the gold collectors studied to date. This is an unexpectedly high number of man-made impactors on LDEF's trailing edge, where orbital debris contributions should be vanishingly small (*e.g.*, refs. 10, 11). It appears that contributions from highly elliptic orbits (geosynchronous sources) may have been underestimated in the past, a potentially significant result for orbital debris concerns. This conclusion, however, remains tentative until we and others confirm and quantify the possible flux of debris particles on LDEF's trailing edge. Indeed, the active Interplanetary Dust Experiment (IDE; ref. 29) advocates independently the existence of a co-orbiting dust cloud that impinged on their rearwards-pointing LDEF sensors. This cloud is interpreted as man-made debris on dynamic grounds by the original workers (ref. 29), yet others

have suggested a natural source (ref. 30). Regardless, our chemical analyses reveal debris impacts on LDEF's trailing edge supporting, at least in part, the largely dynamic arguments and conclusions derived from IDE.

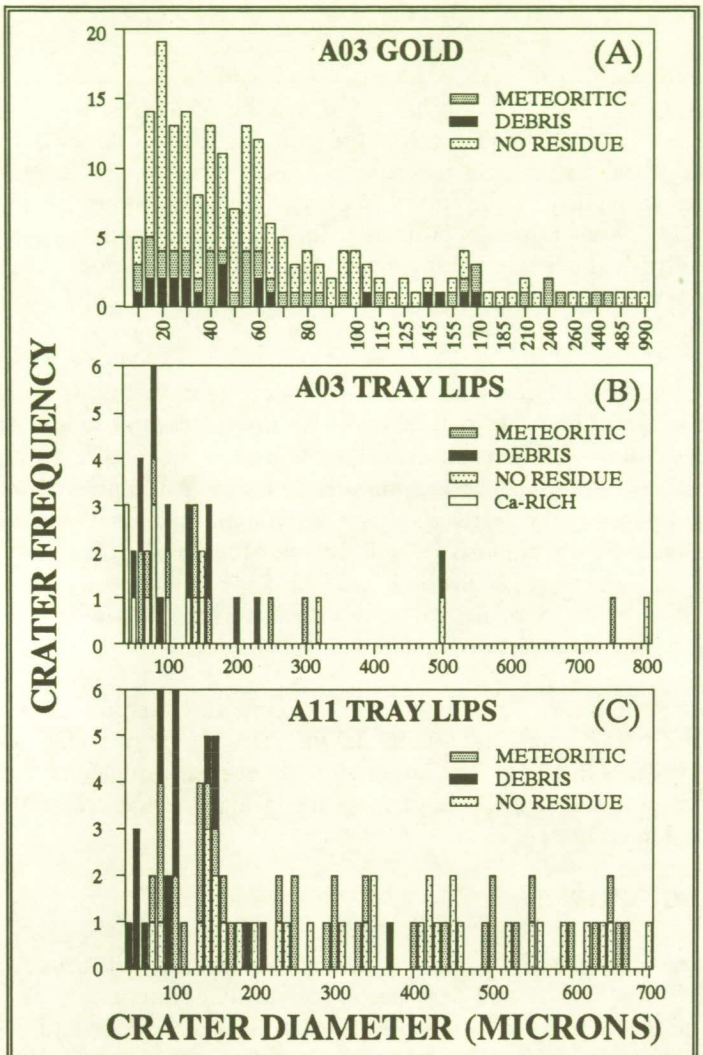

Figure 10. Overview of CME crater populations and associated projectile sources, arranged by crater size. (A) CME gold collectors; (B) A03 tray lips and (C) A11 tray lip. Note the presence of man-made debris on LDEF's trailing edge and the preponderance of debris particles producing "small" craters, especially on the A11 tray lip. For detailed classification criteria and other discussions see text.

We now turn to Figure 10b which depicts the current status of projectile analysis on the A03 tray lips, also pointing into the trailing direction. However, the statistics are not necessarily representative. These lips were our test surface used to sharpen analytical procedures, yet their intrinsic contaminants (total of 2.2%) provide omnipresent noise and background problems, and especially Fe and Ca are heterogeneously distributed throughout the alloy. In addition, these surfaces were contaminated with outgassed RTV or thermal paint forming Si and Ca-rich deposits (ref. 31), and abundant Na and Cl, including NaCl crystals derived during ground handling at KSC. We analyzed all craters >100 μm, but only optically promising candidates (dark colored liners) for structures <100 μm in diameter on the A03 tray lips.

Again, we observe man-made debris particles on a trailing edge surface, constituting approximately 1/3 of all craters >100 μm, but an ill-defined fraction of the craters <100 μm. Note that we distinguish a "Ca-rich" class of craters on the A03 tray lips. The Si-Ca-rich outgassing deposits (ref. 31) drape some craters to the degree that their signal totally overpowers any potential projectile residue. Quite frequently, this material is asymmetrically distributed in individual craters consistent with macroscopic evidence of highly laminar flow for the so called "nicotine" stains. The presence of this deposit in a fair number of craters must have implications to the temporal history of outgassing of diverse materials on LDEF.

The analyses of the A11 tray are illustrated in Figure 10c. In this case, we analyzed every crater >500 μm and a selected population of optically promising residue candidates at smaller sizes, which included basically all candidates >100 μm in diameter and a randomly selected fraction of candidates at <100 μm in diameter. Due to these selection procedures, the observations on A11 may not be readily compared with the A03 observations. Nevertheless, the ratio of natural to man-made particles seems modestly higher on the forward-facing tray, approximately 40% of all analyzable residues (yet an undefined fraction of the total). We have not analyzed, in systematic fashion ,the crater populations on the Al 1100 collector surfaces of the A11 tray.

In summarizing Figure 10 it appears that "large" craters seem to be predominantly the result of natural impactors. The largest debris craters have diameters of 220, 500 and 370 μm on the gold collectors, and the A03 and A11 tray lips, respectively (Figure 10). This size-dependent effect is particularity pronounced on the A11 tray lip, where "small" craters are distinctly biased towards man-made particles. This may be consistent with the observed projectile size frequencies (Figure 5) that may indicate increased numbers of "small" debris particles in the forward direction.

SUMMATION

This report summarizes the current status of the analysis of the Chemistry of Micrometeoroid Experiment. All optical characterizations are substantially complete, but chemical analysis of projectile residues has just begun.

The optical studies yield spatial densities of craters and resulting relative particle fluxes in substantial agreement with existing dynamic models in that effective fluxes are higher by a factor of approximately 8 in the A11 forward-facing direction. Also, the size or mass frequency of impactors seems to vary and the forward-pointing directions seem to experience numerous, additional small particles which we ascribe to man-made sources. Furthermore, the depth-diameter investigations seem to suggest substantially more variability in the initial impact conditions among "small" impactors, such as widely differing encounter velocities and a wide range in projectile densities, compared to more massive projectiles (*e.g.*, ref. 13). These findings, on an individual experiment, exposed in two different orientations relative to LDEF's velocity vector, demonstrate the significant advances that can be made from the analysis of all LDEF surfaces to improve our understanding of most aspects of the hypervelocity particle environment in LEO.

The chemical analyses concentrated on survey-type assessment of compositional variability among all impactors. Three major types of natural cosmic-dust particles could be identified: 1) particles of "chondritic" compositions; 2) monomineralic, mafic silicates such as olivines and pyroxenes; and 3) Fe-Ni sulfides. These particle types have strong affinities to those observed in the stratospheric dust collections. We also observed man-made debris particles, such as metals and paint flakes. However, at present we are unable to specify the relative abundance of man-made and natural particles in LEO. On the one hand, our analyses are not sufficiently systematic, and on the other hand, we cannot characterize the impactors for >50% of all craters, because their residues, if present, are below the detection limit for the electron beam instrument(s) and methods employed. More sensitive analytical methods, such as SIMS, are needed to obtain a more complete overview of impactor compositions and potential origins.

Nevertheless, two important results emerged from these preliminary SEM analyses. We found unmelted fragments of olivine and pyroxene, a discovery that substantiates the expectation that unmelted impactor fragments may be recovered by improved capture media on future dust experiments in LEO. The other significant result relates to the presence of man-made debris on the trailing edge, which suggests that the role of particles in highly elliptical orbits from geosynchronous sources may have been underestimated in the past.

ACKNOWLEDGEMENTS

Many individuals contributed to the design and manufacture of CME, including J. Joerns, R. Chandler, R. Scimek, and D. Demonburn, most of them retired, attesting to LDEF's longevity and endurance. Retrieval, deintegration and collector processing benefitted greatly from their advice and the skills by W. Brown, F. Cardenas, W. Davidson and G. Haynes, all of Lockheed, Houston. Lastly, without the guidance, persistence, and collaborative spirit of a dedicated LDEF staff at LaRC, foremost W. Kinard and J. Jones, this experiment and LDEF would not have been successful. Over the life span of LDEF, our scientific thinking evolved measurably thanks to numerous exchanges with M. Cintala, D. McKay, M. Zolensky, H. Zook, and many other individuals. We are grateful to all of them.

REFERENCES

1) Brownlee, D.E., Tomandl, D.A., and Olsewski, E. (1977), Interplanetary dust: a new source of extraterrestrial material for laboratory study. *Proc. Lunar Sci. Conf., 8th*, p. 149-160.

2) Brownlee, D. E. (1985) Cosmic Dust: Collection and Research, *Ann. Rev. Earth Planet. Sci. 13*, p. 134-150.

3) Bradley, J.P., Sanford, S.A., and Walker, R.M. (1988) Interplanetary Dust Particles, In *Meteorites and the Early Solar System*, J. Kerridge and M. Matthews, eds., Univ. Arizona Press, p. 861-898.

4) Zinner, E. (1988) Interstellar Cloud Material in Meteorites, in *Meteorites and the Early Solar System*, J. Kerridge and M. Matthews, eds., Univ. Arizona Press, p. 956-984.

5) Kerridge, J. and M. Matthews, eds. (1988) *Meteorites in the Early Solar System*, Univ. of Arizona Press, 1988, 1269 pp.

6) Kissel, J. and 18 coauthors (1986) Composition of comet Halley dust particles from Giotto observations, *Nature, 321*, p. 336-337.

7) Kessler, D.J. (1991) Orbital Debris Environment for Space Craft in Low Earth Orbit, *J. Spacecraft, 28, 3*, p. 347-351.

8) Tsou, P.(1990) Intact capture of hypervelocity particles, *Int. J. Impact Engng., 10*, p. 615-627.

9) Barrett, R.A., Zolensky, M.E., Lindstrom, D.J., Gibson, E.K. and Hörz, F. (1991) Suitability of Silica Aerogel as a capture medium for interplanetary dust, *Proc. Lunar Planet. Sci. Conf. 22nd*.

10) Zook, H.A. (1991) Meteoroid Directionality on LDEF and Asteroidal versus Cometary Sources (abstract), *Lunar Planet. Sci. XXII*, p. 1577-1578.

11) Kessler, D.J, Reynolds, RC. and Anz-Meador, P.D. (1988) *Orbital Debris Environment for Spacecraft Designed to operate in Low Earth Orbit, NASA TM-100-471*, April 1988.

12) See, T.H., Allbrooks, M., Atkinson, D., Simon, C. and Zolensky, M. (1990) *Meteoroid Impact and Debris Impact Features Documented on the Long Duration Exposure Facility*, Johnson Space Center (JSC) Publication # 24608, 583 pp.

13) Humes, D.H. (1991) Large craters on the Meteoroid and Space Debris Impact Experiment, *1st LDEF Symposium, NASA CP-*3134, 1992.

14) Cour-Palais, B.G. (1987) Hypervelocity Impacts in Metals, Glass, and Composites, *Int. J. Impact Engng., 5*, p. 681-692.

15) Hörz, F., Messenger, S., Bernhard, R., See, T.H. and Haynes, G. (1991) Penetration phenomena in Teflon and aluminum films using 50-3200 μm glass projectiles, *Lunar Planet. Sci. Conf. 22nd*, Abstracts, Lunar and Planetary Institute, p. 591-592.

16) Hörz, F., Fechtig, H. and Janicke, J.(1983) Morphology and chemistry of projectile residue in small experimental impact craters, *Proc. Lunar Planet. Sci. Conf. 14th, J. Geophys. Res., 88*, p. B353-B363.

17) Gault, D.E. (1973) Displaced mass, depth, diameter, and effects of oblique trajectories for impact craters formed in dense crystalline rock, *The Moon, 6*, p. 32-44.

18) Pailer, N. and Grün, E. (1980) The penetration limit of thin films, *Planet. Space. Sci., 28*, p. 321-331.

19) Warren, J.L. and 10 co-authors, (1989) The detection and observation of meteoroid and space debris impact features on the Solar Max satellite, *Proc. Lunar Planet. Sci. Conf., 19th*, p. 641-657.

20) Rietmeijer, F.J.M., Schramm, L., Barrett, R.A., McKay, D.S. and Zook, H.A. (1986) An inadvertent capture cell for orbital debris and micrometeoroids; the Main Electronics Box thermal blanket of the Solar Maximum Satellite, *Adv. Space. Res., 6*, p. 145-149.

21) Zolensky, M.E. ed. (1990), *Cosmic Dust Catalog, 11, 1*, Particles from Collection Flag L2005, JSC # 24461-SN-83, 170 pp.

22) Stöffler, D. (1972) Deformation and transformation of rock-forming minerals by natural and experimental shock processes; behavior of minerals under shock compression, *Fortschr. Mineral., 49*, p. 50-113.

23) Kieffer, S.W. (1971) Shock metamorphism of the Coconino Sandstone at Meteor Crater, Arizona, *J. Geophys. Res. 76*, p. 5449-5473.

24) Schaal, R.B., Hörz, F., Thompson, T.D. and Bauer, J.F. (1979) Shock metamorphism of granulated lunar basalt, *Proc. Lunar Planet. Sci. Conf., 10th*, p. 2547-2571.

25) Simon, S.B., Papike, J.J., Hörz, F. and See, T.H. (1985) An experimental investigation of agglutinate melting mechanisms: shocked mixtures of sodium and potassium feldspars, *Proc. Lunar Planet. Sci. Conf., 16th, J. Geophys. Res., 90*, p. D103-D115.

26) Hörz, F. ed. (1990) *Cosmic Dust Collection Facility: Scientific Objectives and Programmatic Relations, NASA TM 102160*, 1990, pp.29.

27) MacKinnon, I.D.R. and Rietmeijer, F.J.M. (1987) Mineralogy of chondritic interplanetary dust particles, *Rev. Geophys. Space Phys., 25*, p. 1527-1553.

28) Klock, W., Thomas, K.L., McKay, D.S. and Palme, H. (1989) Unusual olivine and pyroxene composition in interplanetary dust and unequilibrated ordinary chondrites, *Nature, 339, No 6220*, p. 126-128.

29) Mullholland, J.D. and 8 co-authors (1991) IDE Spatio-temporal fluxes and high time-resolution studies of multi-impact events and long-lived debris clouds, *1st LDEF Symposium, NASA CP*-3134, 1992.

30) McDonnell, J.A.M. and Sullivan, K. (1991) Dynamic (computer) modelling of the particulate environment: Transformations from the LDEF reference frame to decode geocentric and interplanetary populations, *1st LDEF Symposium, NASA CP*-3134, 1992.

31) Crutcher, E.R., Nishimura, L.S., Warner, K. and Wascher, W.W. (1991) Migration and generation of contaminants from launch through recovery: LDEF Case History, *1st LDEF Symposium, NASA CP*-3134, 1992.

APPENDIX A

The Problem

The active experiment (A03) employed two pairs of moveable clamshell-type devices that were closed at the time of LDEF deployment, but were scheduled to open approximately 10 days later. Nominal closing was scheduled to occur on mission-day 298. However, the instrument was found to be open at the time of LDEF retrieval, giving rise to the possibility that the closing operation(s) failed.

Instrument Design

The two clamshell pairs were totally independent mechanically, each pair having its own driveshaft, motor, battery-power, etc. This redundancy permitted potential mechanical failure of one pair of clamshells, while the other pair could still function nominally. However, both motors were controlled from a single electronic sequencer, with the latter being powered from a third battery. The sequencer contained a hexadecimal clock of 256 time intervals, each interval lasting two days. During design of this system, no provision was made to prevent this clock from recycling after 256 intervals, (*i.e.*, 512 days) of mission elapsed time, because the retrieval of LDEF was scheduled much earlier. Therefore, by design, the instrument could open and close indefinitely, the only constraint being battery-lifetime to power the sequencer or motors.

Post-Flight Inspection

Both sets of clamshells were fully extended (i.e., open) and it appears unlikely that any mechanical failure occurred; there was no evidence that either pair attempted to close. In addition, all three batteries were found to be sufficiently

charged to service and drive all CME systems. Unfortunately, the original ground-support system(s) were not available at KSC in 1990, particular an external frequency generator used to speed up the internal clock during assembly and pre-launch tests. Furthermore, the designer of the sequencer was unavailable for consultation so there remains doubt as to whether suitable equipment, procedures, or both were used during these post-retrieval tests; the clock simply would not respond to the external signals. A modified procedure was devised that electrically bypassed the clock and that resulted in successful closure of the clamshells. The rate of clamshell movement was nominal, as were motor torques and start up amperages, attesting to the mechanical integrity of all systems, as well as the electrical systems, except for the clock. Following clamshell closure it became evident that interior surfaces of the instrument had been exposed to the space environment (*i.e.*, craters were observed). The latter demonstrates that the instrument must have been closed for some time, and precludes the possiblity that the clamshells remained open throughout the entire LDEF mission.

Diagnosis

There was no positive design feature to shut-off the internal clock after completion of the first closing-sequence (day 298), or after completion of the clock's first full cycle (day 512). All systems were permitted to operate indefinitely in cyclic fashion with battery-power being the only limiting factor. The deployed or open clamshells found during STS 32 retrieval operations are consistent with CME's cycle period; the battery status permitted multiple cycling as well. Craters found in the instrument interior demonstrate that opening, closing, and opening operations occurred at least once. The crater populations on the gold collectors relative to those on the continuously exposed tray lips are consistent with a continuously cycling CME, but are inconsistent with failure of a closing sequence. The evidence suggest that the active CME instrument was still functioning nominally at the time of LDEF retrieval.

SIMS CHEMICAL ANALYSIS OF EXTENDED IMPACT FEATURES FROM THE TRAILING EDGE PORTION OF EXPERIMENT AO187-2

Sachiko Amari, John Foote, Charles Simon,
Pat Swan, Robert M. Walker, Ernst Zinner
McDonnell Center for the Space Sciences
Washington University
One Brookings Drive
Saint Louis MO 63130-4899 USA
Phone: 314-889-6257, Fax: 314-889-6219

Elmar K. Jessberger, Gundolf Lange, Frank Stadermann
Max-Planck-Institut für Kernphysik
Postfach 103980
6900 Heidelberg, Germany

SUMMARY

One hundred capture cells from the trailing edge, which had lost their cover foils during flight, were optically scanned for extended impact features caused by high velocity projectiles impinging on the cells while the foils were still intact. Of 53 candidates, 24 impacts were analyzed by secondary ion mass spectrometry for the chemical composition of deposits. Projectile material was found in all impacts, and at least 75% of them appear to be caused by interplanetary dust particles. Elemental ratios are fractionated, with refractory elements enriched in the impacts relative to interplanetary dust particles collected in the stratosphere. Although this could be due to systematic differences in the compositions, a more likely explanation is volatility fractionation during the impact process.

INTRODUCTION

The main scientific objective of LDEF experiment AO187-2 was the collection of interplanetary dust material in space and its elemental and isotopic analysis in the laboratory. Although interplanetary dust collected in the upper atmosphere has been available for analysis in terrestrial laboratories for more than a decade (e.g., refs. 1, 2), the stratospheric collection undoubtedly is biased since not all extraterrestrial dust particles entering the Earth's atmosphere are collected. For example, cometary dust particles have, on average, a higher velocity and are therefore expected to have a much smaller survival probability of atmospheric entry than dust grains originating from asteroids (refs. 3, 4). In order to obtain an unbiased sample of interplanetary dust it is necessary to collect this material in space. LDEF provided an unprecedented opportunity for this purpose, combining large collecting areas with long exposure times.

A fundamental problem for the collection of interplanetary dust material is the high relative velocity of dust grains (10-15 km/sec). At these high velocities a major fraction of projectile material is lost upon impact with most collection surfaces. A viable compromise is to forgo the collection of solid dust grains

or fragments thereof and to concentrate on the collection of their atoms in capture cells. LDEF carried several capture cell experiments (AO023, AO138-2); the principle of AO187-2 is shown in Figure 1. A target plate is covered by a thin foil separated by a small distance. A high velocity dust grain of sufficient size penetrates the foil and normally is disrupted in the process, spreading out into a shower of debris. This shower impacts the target plate, being further disrupted, melted and vaporized. The projectile material ejected from the impact zone is collected on the backside of the foil and then analyzed.

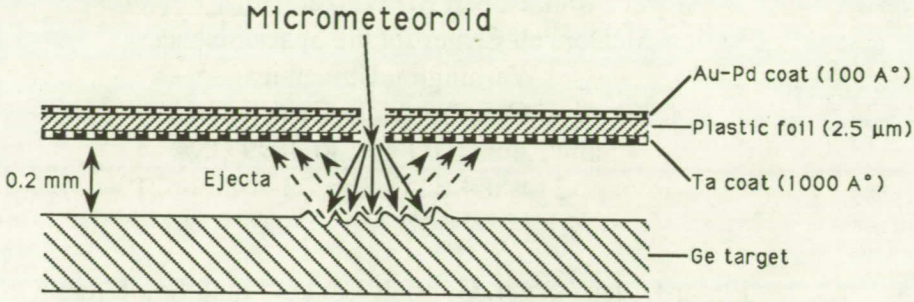

Figure 1. Principle of capture cell of experiment AO187-2.

A series of simulation experiments on laboratory dust accelerators proved this concept to be viable (refs. 5-7): projectile material could indeed be collected on the surface of the target plate and the backside of the foil and its elemental and isotopic composition measured. Since the collected material exists as a thin surface deposit, secondary ion mass spectrometry (SIMS) with its extremely high surface sensitivity proved to be the best-suited analysis technique. In fact, since one of the main objectives of the experiment was the isotopic measurement of dust material, AO187-2 was originally conceived and optimized for SIMS analysis. The choice of materials was largely determined by the requirements for extreme purity and high ion yields for SIMS analysis.

EXPERIMENT DESCRIPTION AND PRELIMINARY ASSESSMENT

LDEF experiment AO187-2 consisted of 237 capture cells, each 8.6 × 9.4 cm in size. A capture cell in turn consisted of four polished high purity germanium plates, 42 × 39 × 0.5 mm, covered with a plastic foil separated from the Ge plate by 200µm. The Ge plates were glued to an Al base plate, the 2.5 µm thick mylar cover foil was coated with 1300 Å of Ta on the backside and 100 Å of Au-Pd on the front side. Ta was chosen to optimize the SIMS analysis of deposited projectile material; Au-Pd was chosen to protect the foil from erosion by atomic oxygen in the residual atmosphere impinging on the leading edge of LDEF (refs. 8, 9).

The capture cells occupied locations on three different trays. A full tray, E8, on the leading edge contained 120 cells, 77 cells were mounted on tray E3 and 40 took up a third of tray C2, both on the trailing edge. By having capture cells on both the leading and the trailing edge, the experiment was expected to obtain information on both interplanetary dust and man-made space debris in low Earth orbit.

After the return of LDEF it was found that all capture cells on the leading edge tray E8 had lost their plastic-metal foils and only 12 cells on the trailing edge had retained them, 11 on tray E3 and one on tray C2. Four capture cells from tray E8 and 5 cells without foil from tray E3 were shipped to Messerschmitt-Bölkow-Blohm in Germany; the rest of the cells went to Washington University. At present we do not know why the foils failed or when this happened. The fact that 12 intact cells were found on the trailing

edge indicates that the failure mechanism probably was not the same for the two locations. Atomic oxygen erosion starting from impact holes or spots with damages in the protective metal coating is a likely cause for the complete failure of the cells on the leading edge of tray E8. The capture cells on the trailing edge, however, never were exposed to an atomic oxygen flux. A combination of embrittlement by solar UV and stress failure under thermal cycling is a possible cause but this hypothesis has to be substantiated by future tests. If we assume that the failure of foils on the trailing edge is an exponential function of time, 67% of the cells would have been still intact after one year, the nominal deployment duration for LDEF.

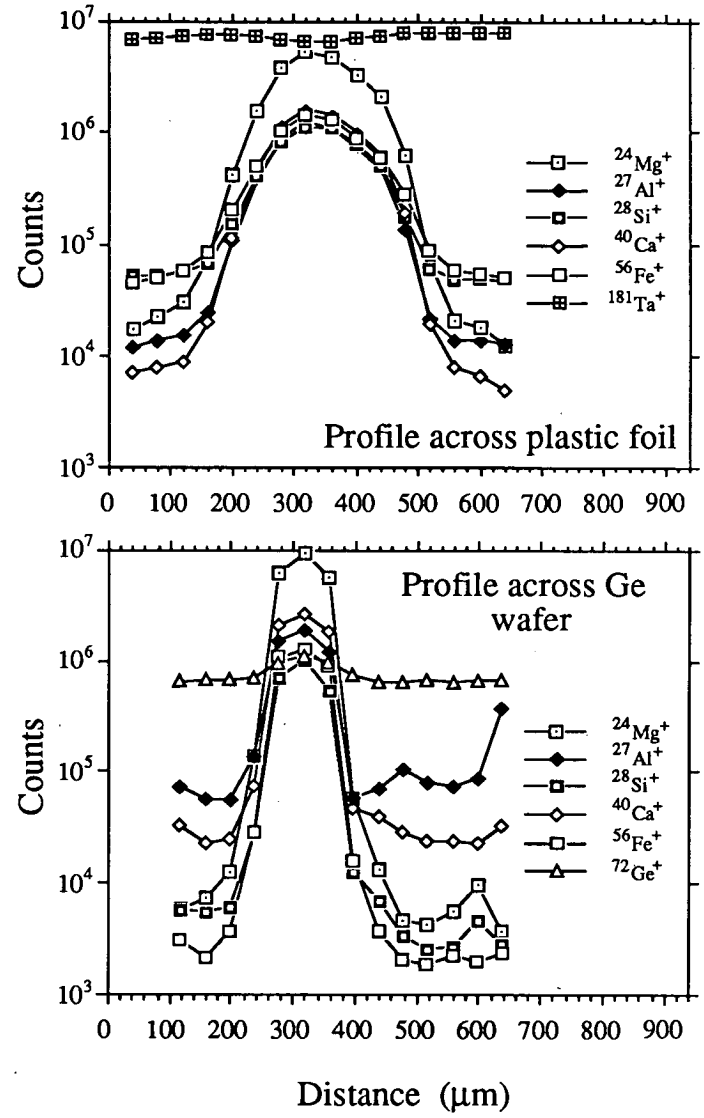

Figure 2. Lateral elemental profiles across plastic foil and Ge wafer of the same simulation impact.

Preliminary optical microscope examination of cells from the trailing edge that had lost their cover foils (bare cells) showed numerous "extended impact features" as well as typical hypervelocity impact craters produced by direct hits. The extended impact features resembled laboratory simulation impacts produced by projectile material that had penetrated plastic foils and had suffered disruption. Apparently, the extended impact features found on the bare LDEF cells were produced by high velocity impacts onto the cells while the foils were still intact. Since prior simulation studies (ref. 7) had shown that extended impacts on the Ge plates contained sufficient projectile material for chemical and isotopic analysis by SIMS (Fig. 2), we first concentrated our analysis effort on the extended impacts found in the bare LDEF capture cells from the trailing edge (trays E3 and C2). These were the best candidates to contain impacts of interplanetary dust particles with a minimum contribution from orbital debris. Furthermore, foil survival on 10% of trailing edge cells compared to none on the leading edge indicated that even foils that failed lasted, on average, longer on the trailing than the leading edge.

All 100 bare capture cells from E3 and C2 in our possession were optically scanned for impact features. During the scanning we developed criteria for the classification of these impacts and for the selection of candidates for SIMS analysis. All selected candidates were further documented in a scanning electron microscope (SEM). To date, a subset of these candidates has been analyzed by SIMS for the chemical composition of deposited material.

OPTICAL AND SEM CHARACTERIZATION

All bare cells in our possession from the trailing edge, 61 from tray E3 and 39 from tray C2, were scanned under oblique illumination in an optical stereo microscope with a 12× objective and 20× eyepiece. The Al plates with the Ge wafers were mounted on a scanning stage whose position could be read with an accuracy of 50 μm. The wafers were scanned a row (of 6.0 mm width) at a time. Recorded were the locations of impact features and their sizes and other interesting properties. Among the impacts we distinguished between "craters" and "extended impacts." Since Ge is very brittle, craters produced by direct hits (i.e. without penetration of a foil) are not likely to contain much residual material from the projectile and this expectation was confirmed by subsequent analysis. Figure 3 shows a SEM image of a crater.

The extended impacts are the most interesting since they are expected to contain projectile material. They range from 200 μm to 4000 μm in diameter and were divided into two categories, A and B. Category A comprises larger impacts that are expected to contain deposits and are high priority candidates for SIMS analysis. Category B impacts are smaller and will be studied last. Features that could not be recognized with certainty as extended impacts in the optical microscope were classified as "possible extended impacts (Category A or B)," and were examined in more detail in the SEM.

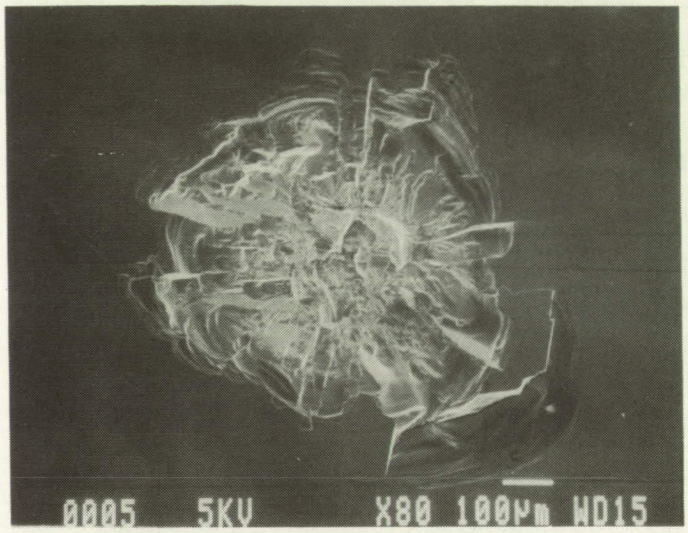

Figure 3. Crater produced by hypervelocity impact onto Ge wafer without cover foil.

Extended impacts of category A and B were further classified into four sub-categories according to their morphology.

1) Craters surrounded by deposits (CD).
2) Ring-shaped features (RI).
3) Sprays (SP).
4) Spider webs (SW).

Figure 4 shows SEM micrographs of one of each morphology. The more detailed SEM images revealed that in many cases an extended impact showed features of different categories (e.g. a crater surrounded by deposits also had spider web features).

Scanning in the SEM was performed with a twofold purpose:

a) To check all features that had been classified as "possible extended impacts" during the initial optical scanning to determine which of them are true "extended impacts."
b) To document in detail all extended impacts to be selected for SIMS analysis.

Table 1 gives a summary of the results of the optical scanning. So far, 98 of 157 possible extended impacts have been examined in the SEM and five of them have been reclassified as extended impacts (2 CD, 3 RI).

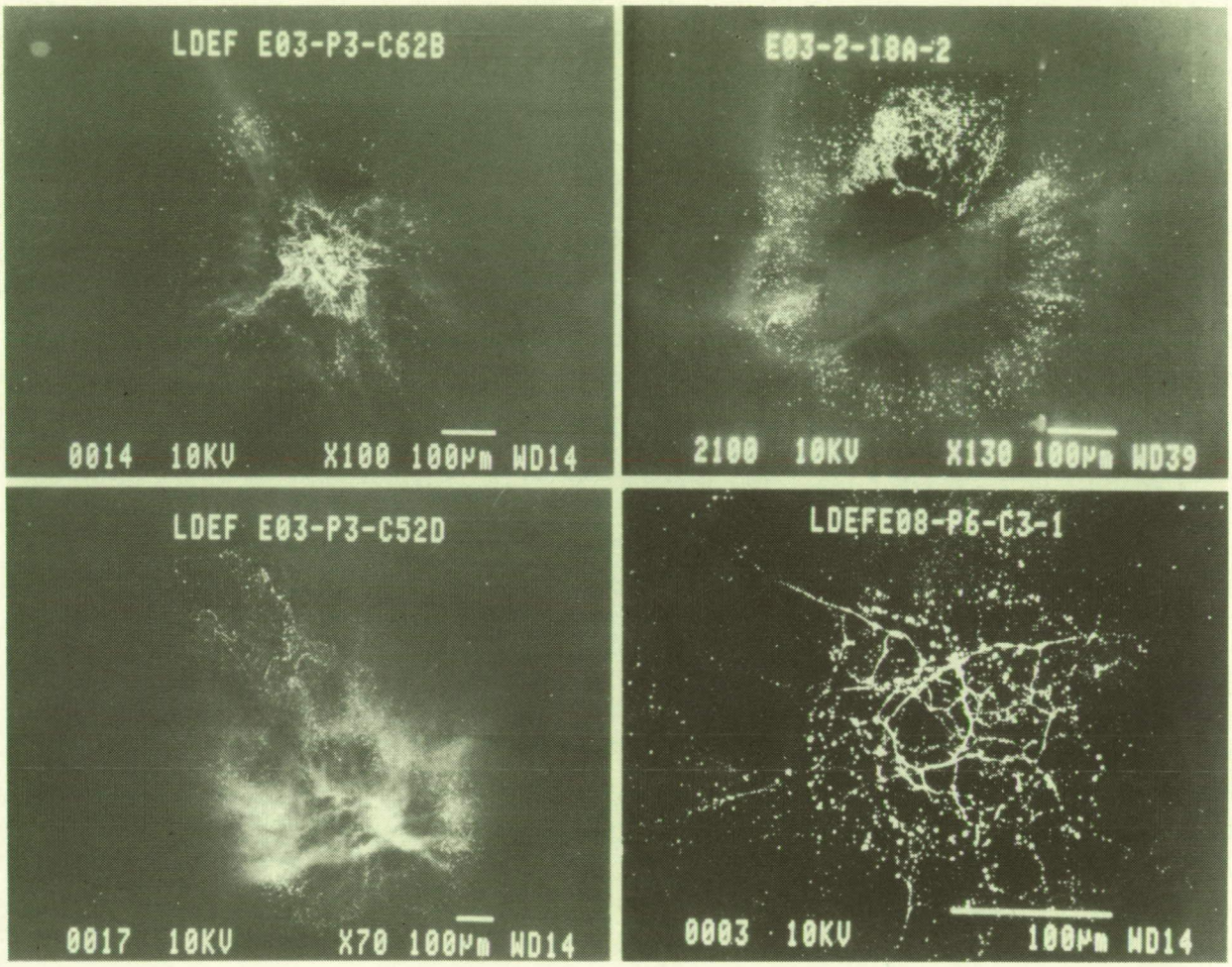

Figure 4. Morphologies of extended impacts: Craters surrounded by deposits (upper left), ring (upper right), spray (lower left), and spider web (lower right).

Table 1. Classification of impacts on bare capture cells from the trailing edge

Extended Impacts		CD	RI	SP	SW	Total
	A	14	8	8	23	53
	B	5	42	94	14	155
Possible Extended Impacts	A					157
	B					177
Craters						203

During the SEM documentation of extended impacts energy dispersive x-ray (EDX) spectra were obtained in most cases, especially if fragments were observed in the area of the impact. However, fragments usually turned out to be pieces of the Ta coating of the mylar foil or other apparent contaminants. Generally it was not possible to detect any elements besides Ge. An exception was Si which is present in quantities detectable by EDX on all Ge wafers

from the leading and trailing edge. The Si concentrations on the wafers are non-uniform, being highest on the edges and lowest in the middle of the Ge plates. The most likely cause for this ubiquitous Si background is outgassing or migration of the RTV used to bond the Ge onto the Al substrate (in spite of the space rating of this material). This unfortunate circumstance deprived us (with a few exceptions) of the opportunity to measure one of the most important cosmochemical elements in the projectile deposits.

A comparison of the extended impact features on Ge from the trailing edge and simulation impacts produced on the same foil-target assembly in the Munich plasma dust accelerator (refs. 10, 11) at velocities between 3 and 8 km/sec shows significant differences. The LDEF impacts are, on average, larger and much more irregular. The simulation impacts usually are spider webs with a high degree of rotational symmetry or ring-shaped features with typical diameters of 100-200μm. There are two possible explanations for the large irregular impact features found on the Ge plates from the trailing edge. One is that many impacts were produced by projectiles that hit the capture cells at oblique angles. The second is that the foil had already been damaged and some of it had curled up when the impact occurred, leading to a much more complex foil-target geometry than for the simulation impacts, which were produced at normal incidence.

SIMS ANALYSIS OF EXTENDED IMPACTS

For SIMS analysis the Ge wafers were cut into smaller pieces containing extended impacts of interest. This was done by a newly developed laser cutting technique, which avoids any of the contamination incurred by sawing. A CW YAG laser beam of 1.06 μm wavelength was focussed onto the rough backside of the Ge wafer (this side has a higher absorption at this wavelength than the polished front side). At a power of 50 W a short scan across the wafer at a speed of 5 cm/sec was sufficient to cause a break along the scanned line most of the time. Sometimes the wafers broke along other defects or along crystal boundaries; however, in all such cases intact pieces of appropriate size could be obtained for ion probe analysis.

To date 24 of a total 53 extended impacts of category A have been analyzed by SIMS for the chemical composition of projectile deposits. All measurements were made on the Washington University ion microprobe, a modified CAMECA IMS 3f instrument. For chemical analysis we obtained lateral scanning profiles across the impact features. For this purpose at each analysis point an O^- primary ion beam of 1-2 nA current was rastered over an area of 40μm×40μm. As the primary ion beam sputtered away the surface of the analyzed sample layer by layer, positive secondary ions selected from the central portion of the rastered area by a beam aperture were mass analyzed in a double focussing magnetic mass spectrometer and counted by an electron multiplier detection system.

Multi-element depth profiles are obtained by cycling the mass spectrometer through a set of isotopic masses of the selected elements. After analysis of a given area consisting of 40 cycles the sample is stepped (by 40 or 50 μm) to the next area. Fig. 5a shows a SEM micrograph of an extended impact after two step-scanning analyses were made on this sample. The individual depth profiles were integrated over cycles 4 to 40 to obtain lateral profiles in the form of the integrated secondary ion intensity as a function of lateral distance. The first three cycles were not included in order to reduce the effect of surface contamination and because a variety of artifacts are encountered during sputtering of the very surface.

Ion signals associated with material from the impacts could be detected in all 24 analyzed impact areas but large variations were observed between individual impacts. For example, the ratio of the maximum $^{24}Mg^+$ signal to the $^{72}Ge^+$ signal for an individual lateral intensity profile varies over almost 5 orders of magnitude.

The ideal case is shown by the profile of Fig. 5b, which corresponds to the top scan in Fig. 5a. This scan has well defined maxima for all the isotopic masses measured except for $^{72}Ge^+$. It is one of the few cases where the $^{28}Si^+$ also displays a clear maximum above background; the latter, however, is much higher for this element than for all the others (since the yield of positive secondary ions is less for Si than for Mg, Al, Ca and Fe; this discrepancy in the background is actually much larger than is indicated by the plot of Fig. 5b). The profile across impact EO3-2-19C-1 is also one of the few which gives a clear signal for Ni^+ at mass 60. The reason is that the signals associated with impact deposits are relatively high compared to the Si background. In most other cases, these signals are much lower so that the molecular interference from $^{28}SiO_2^+$ dominates at mass 60.

In order to obtain elemental abundances, the ion yields of different elements as well as the isotopic abundances have to be taken into account. Table 2 gives sensitivity factors S relative to Si so that

$$\frac{C_{El}}{C_{Si}} = \frac{I_{El}}{I_{Si}} / S_{El/Si}$$

where C are the atomic concentrations and I are the secondary ion signals (corrected for isotopic abundances) for the element of interest and the standard element Si. The sensitivity factors were determined from measurements on four different glasses (Lunar Analog Glass, Solar Glass NTR-1, Window Glass and Dunite Glass).

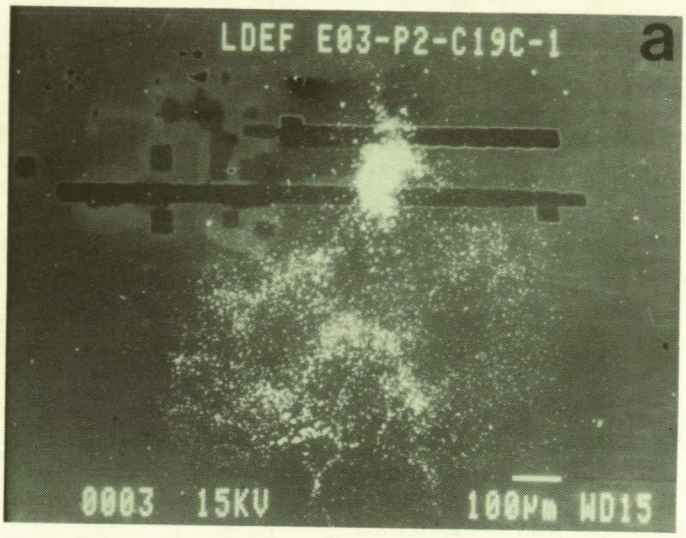

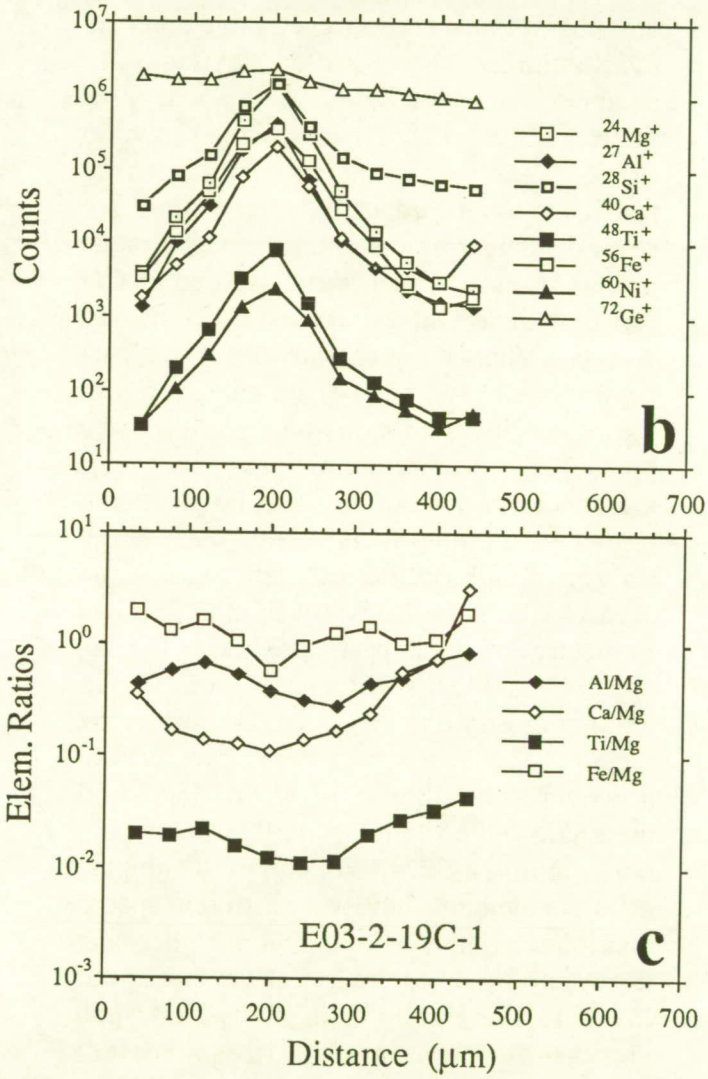

Figure 5. Ion microprobe elemental scans across impact E03-2-19C-1. Profiles in b and c correspond to the upper scan in the SEM micrograph.

Because of the problems with Si contamination of the Ge wafers we normalized the lateral intensity profiles to Mg by applying the relative sensitivity factors of Table 2. The resulting profiles of atomic elemental ratios are shown in Fig. 5c. One feature typical for almost all impacts is apparent from this figure: elemental ratios change across a lateral profile or, in other words, the deposits from the impact have different spatial distributions for different elements. For example, the Fe/Mg ratio has a minimum at lateral position 200 μm, where all the elements show a maximum, and changes by more than a factor of two 80-100 μm to the left and right of the maximum position. This can also be seen directly in Fig. 5b where the $^{56}Fe^+$ profile is slightly wider between positions 100 μm and 300 μm than the $^{24}Mg^+$ profile. This means that Fe apparently is distributed over a wider area than Mg.

Table 2. Secondary ion sensitivity factors relative to Mg.

Element	S
Na	3.28 ± .15
Al	0.77 ± .09
Si	0.13 ± .01
Ca	1.47 ± .24
Ti	0.50 ± .04
Cr	0.38 ± .15
Mn	0.51 ± .09
Fe	0.47 ± .07

Most impacts show even more complex distributions of the deposited elements. An example is impact CO2-1-20D-2 whose SEM micrograph after SIMS analysis is shown in Fig. 6a. The corresponding lateral intensity profile is displayed in Fig. 6b. There are several interesting observations to be made on this impact, which was classified as CD (crater with deposits). The first is that the ion signals of elements apparently deposited from the projectile (Mg, Ca, Fe) are much lower in the crater itself (dip in the middle of the profile) than in surrounding areas. Secondly, the concentrations of Mg and Fe are much higher to the left of the crater than to the right, although on the SEM micrograph the area to the right shows much more "structure" in the impact. The reason for this apparent paradox is that what is "seen" in the SEM is mostly damage to the Ge surface by high-velocity debris from the impact, which, however, contains only little deposited material, while the deposits themselves are not seen in the SEM. Finally, in this impact different elements have very different spatial distributions: the $^{56}Fe^+$ signal is higher than the $^{40}Ca^+$ signal to the left of the crater, but lower to the right. It is likely that such changing elemental ratios reflect heterogeneities in the chemical composition of the original projectile.

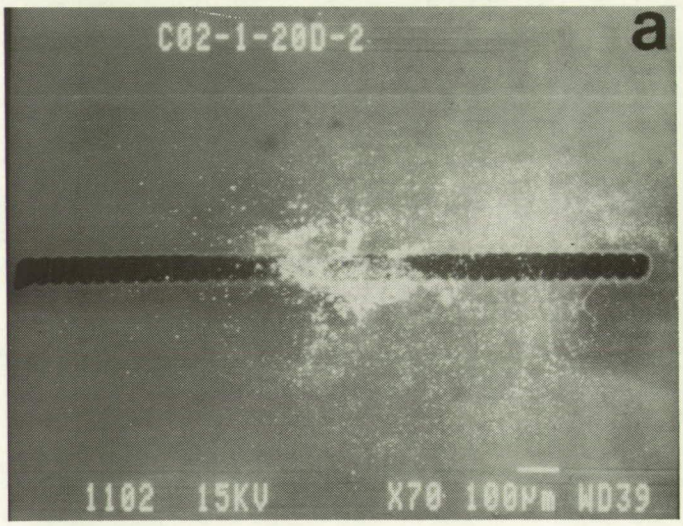

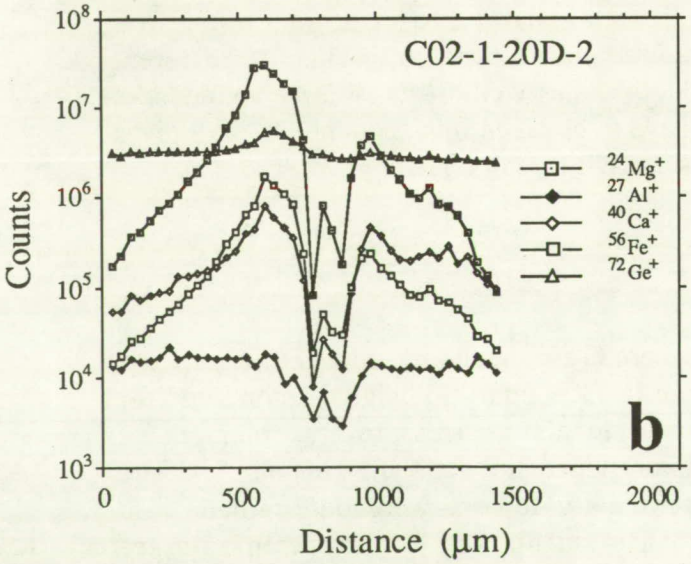

Figure 6. Ion probe scan across impact C02-1-20D-2, a crater with associated deposits.

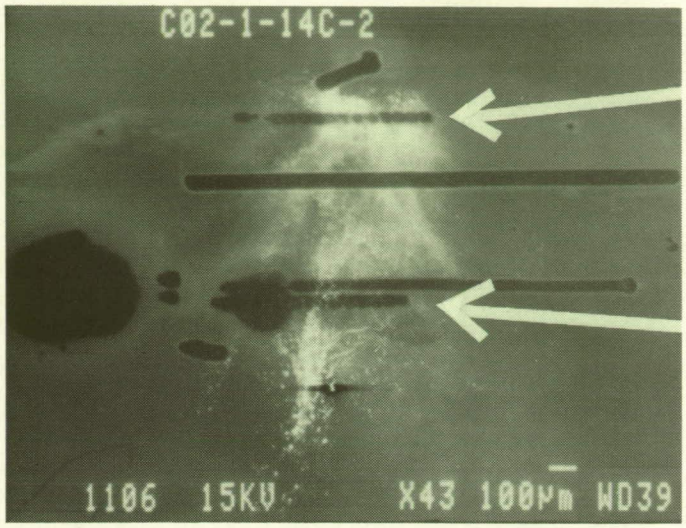

Scan 1

Scan 2

a

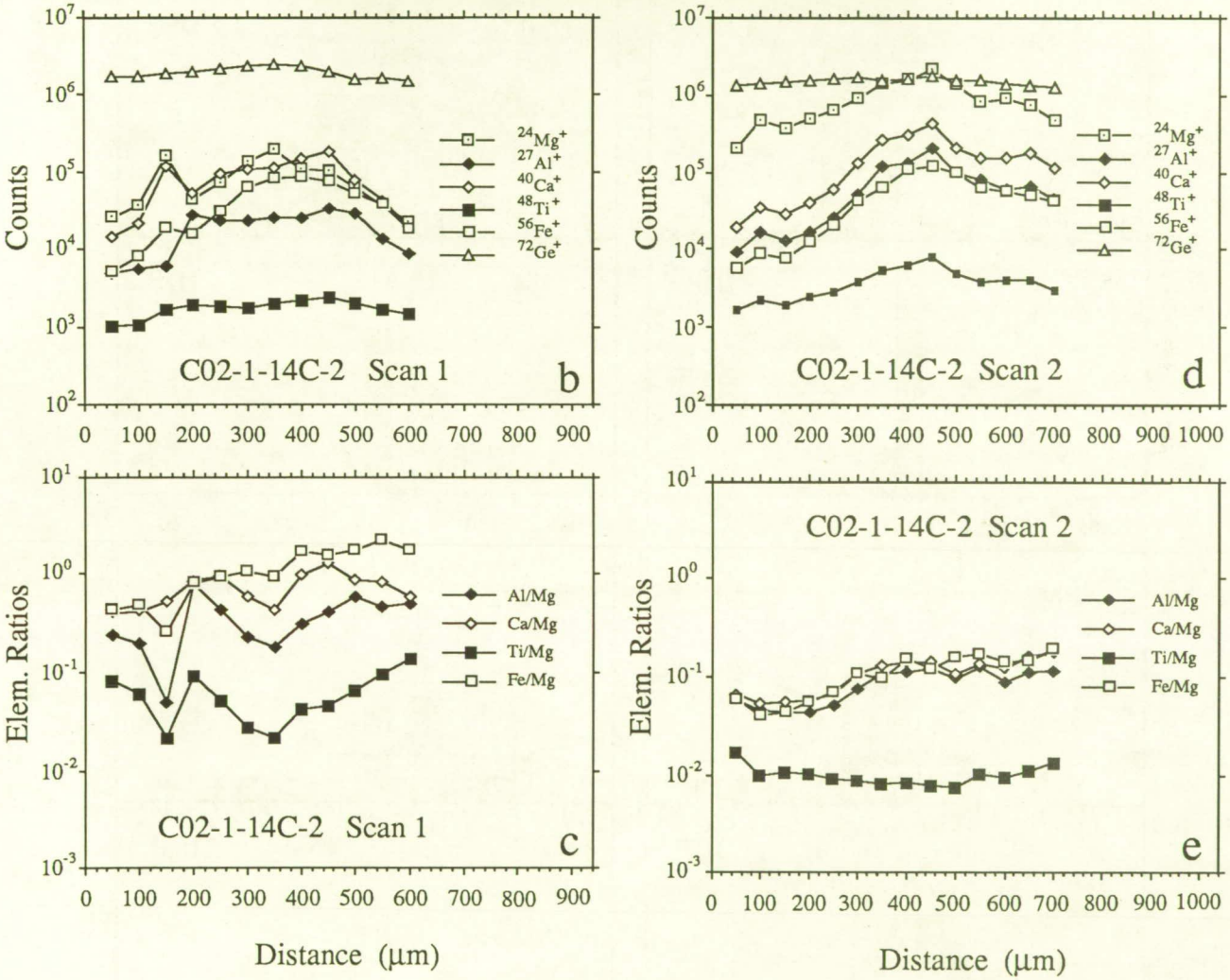

Figure 7. Two ion microprobe elemental scans across the same extended impact.

An even more extreme example of elemental heterogeneity is shown in Fig. 7, depicting a large extended impact (C02-1-14C-2) classified as SW (spider web) together with the results of two lateral scans (the short scans in the SEM micrograph). Not only do the absolute concentrations differ between the two scans (Fig. 7b,d) but there are also large differences in the elemental ratios (Fig.7c,e).

The non-uniform distribution of different elements in the deposition area of a given extended impact makes it difficult to obtain average elemental ratios. As a compromise we have taken elemental ratios determined at the maximum of the $^{24}Mg^{+}$ signal for a given scan. Histograms of these elemental ratios are plotted in Fig. 8 together with histograms of the same ratios measured by SIMS on individual stratospheric dust particles of probable extraterrestrial origin (ref. 12). Chondritic compositions are indicated for reference. The ratios measured in projectile deposits on the LDEF Ge wafers not only show much wider

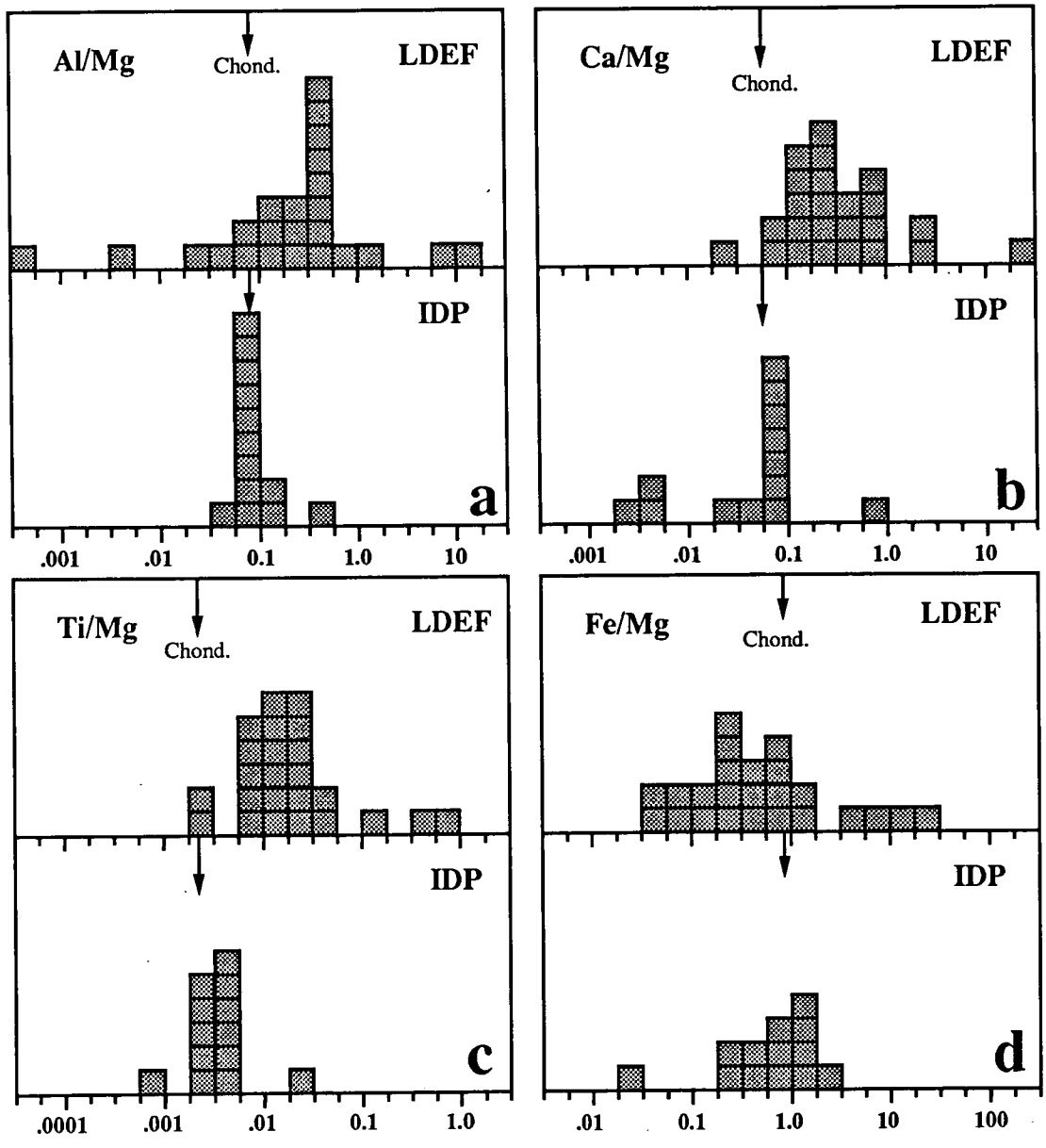

Figure 8. Histograms of elemental ratios in LDEF deposits and interplanetary dust particles.

distributions than those of IDPs but the mean of the distributions are systematically shifted relative to one another. This shift is toward lower values for Fe/Mg but toward higher values for the other three ratios, Al/Mg, Ca/Mg, and Ti/Mg.

There are at least two explanations for these differences. The first is simply that the particles whose material was collected on the Ge wafers on LDEF have chemical compositions that differ significantly from those of IDPs collected in the stratosphere. The second is that the impact process caused strong fractionation between the elements so that the compositions of the deposits do not accurately reflect those of the projectiles. One reason the particles that impacted LDEF have compositions different from IDPs could be that a major portion of them are not interplanetary dust but man-made debris. This, however, is unlikely in our case. First, collection on the trailing edge discriminates to a large extent against orbital debris. Furthermore, Mg is the dominant element in most impacts compared to Fe, Al, Ca and Ti. This is not expected for most man-made debris in orbit, which in this size range is presumably dominated by Al-oxide particles from the exhaust of solid fuel rockets. Moreover, we did not detect any impacts that contain primarily Al (Fig. 9).

Before we consider the possibility of differences in the chemical composition of interplanetary dust particles collected on LDEF and in the stratosphere, we have to discuss elemental fractionation during the impact process. There is evidence for such fractionation from simulation impacts onto the same foil/Ge wafer targets as flown on LDEF. The analysis of 12 extended impacts on the Ge produced by Lunar Analog Glass and Solar Glass showed fractionation between Mg and the other elements in the deposits with average fractionation factors relative to Mg of 0.28 for Fe, 0.58 for Si, 1.60 for Al, 1.95 for Ti and 2.41 for Ca. A fractionation factor smaller than one means that, compared to the projectile, less of the element is found in the deposition area than Mg and the

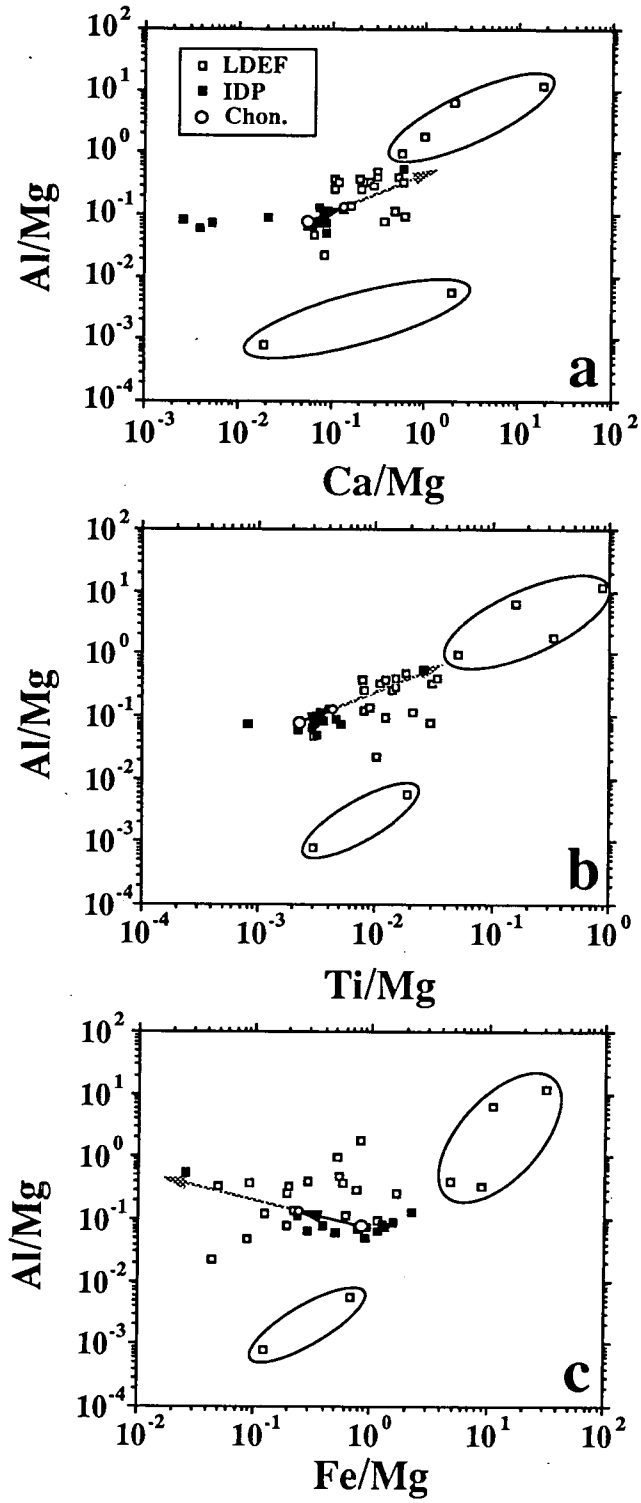

Figure 9. Scatter plots of elemental ratios in LDEF impact deposits and in interplanetary particles. Also shown are chondritic ratios, the elemental fractionations determined from simulation impacts (solid arrows) and the extension of these fractionations (light arrows).

opposite is the case for fractionation factors greater than one. We note that elemental fractionations are related to the relative volatilities of the elements during high temperature evaporation and condensation: the elements Fe and Si are more volatile than Mg and are depleted in the deposits relative to Mg while Al, Ca and Ti are more refractory and are enhanced relative to Mg.

During the impact apparently a large part of the projectile either melts or evaporates. Elements with different volatilities behave differently during this process. More volatile elements such as Fe are almost completely vaporized and expand into a larger volume before they condense onto the Ge and foil surfaces. More refractory elements, on the other hand, either remain in the melt or, if they evaporate, condense sooner and therefore onto a more limited area. Except for the (small) fraction that escapes through the penetration hole, all of the projectile material is retained inside the capture cell but some (preferentially the more volatile elements) is distributed over such a large area that it is lost in the background. For example, if the material of a 10μm projectile is spread out over an area of 1 mm diameter, its thickness is only 2.5 atomic monolayers, only 1/6 of a monolayer for the 4 mm largest observed extended impact.

Figure 9 shows scatterplots of pairs of elemental ratios for the LDEF deposits and individual IDPs. Also shown are the chondritic compositions and the shifts in these compositions if this material experienced the same elemental fractionations as those determined in the impact simulation experiments. The differences between most LDEF deposit compositions and the IDP compositions qualitatively agree with the shifts expected from fractionation during impacts, except that the differences are much larger than the shifts predicted from fractionation. However, we cannot exclude the possibility that elemental fractionations are actually much higher during impacts on LDEF than during simulation impacts. We have already pointed out that the LDEF extended impacts on the Ge are generally much larger than the simulation impacts from which the above fractionation factors were derived. It is reasonable to expect that elemental fractionation factors increase with the size of the extended impact feature. However, the uncertainty in this extension, the extremely irregular structure of most impact features and the fact that the fractionation factors undoubtedly depend on the composition of the projectile itself set a fundamental limit to the extent to which the projectile composition can be derived from the measured composition of the deposits.

Tentatively we can identify most of the LDEF impacts as being caused by cosmic dust particles. Six data points in Fig. 9 fall completely outside of the predicted trend due to elemental fractionation (they are enclosed in ellipses in the Figures). Four of them have extremely high Al/Mg, Ti/Mg and Ca/Mg <u>but also</u> very high Fe/Mg and are likely to be contaminants. The other two have low Al/Mg ratios. This leaves us with 18 (75%) impacts of likely interplanetary origin. While some of them have only little deposited material, some have plenty of it (see, e.g., Figs. 5, 6 and 7) and are candidates for future isotopic measurements. We also plan additional chemical analyses of elements that can easily be detected as negative secondary ions such as C, O, and S.

CONCLUSIONS

1. SIMS analyses of 24 extended impact features on Ge surfaces from "bare" trailing edge capture cells show evidence for projectile material in all of them, but there are large variations in the detected concentrations.

2. The deposits are very thin and cannot be detected by EDX analysis; SIMS appears to be the only method to detect them.

3. Elemental concentrations on the Ge do not correlate exactly with impact features seen in the SEM images; the latter are dominated by damaged regions which contain little projectile material.

4. There is evidence for large variations of elemental ratios within a given extended impact, indicating a heterogeneous chemical composition of the projectile.

5. Comparison with simulation impacts indicates that most LDEF impacts analyzed by SIMS were caused by small (<10μm) projectiles.

6. At least 75% of the analyzed impacts appear to be from interplanetary dust particles but elemental ratios scatter much more than those measured in IDPs collected in the stratosphere.

7. Elemental ratios are also shifted compared to IDPs, with refractory elements being relatively enriched. These shifts are likely to be due to elemental fractionation effects caused by evaporation during the impact process, but systematic differences between IDPs and LDEF impacts cannot be ruled out.

FUTURE WORK

Fractionation effects should be much less pronounced in isotopic ratios than in elemental ratios. Moreover, such effects will not obscure large anomalies of specific isotopes (if present) such as those found by us in studies of interstellar grains isolated from meteorites (ref. 13). As a consequence, future work will concentrate on isotopic measurements in those impacts that have been found in our initial survey to contain sufficient amounts of projectile material.

We have also refrained from studying the 12 intact (precious) capture cells until our handling and analysis techniques had been perfected on the more abundant, extended impacts found in the bare cells. The analysis of the intact cells should provide a critical test of the usefulness of our capture cell concept for future space flight experiments.

Detailed studies of impacts on the cells from the leading edge tray E8 should yield data relevant to the orbital debris problem. The ratios of extended impacts to single craters in these cells should allow us to determine when the plastic cover foils failed on the leading edge capture cells.

This work was supported by NASA Grant NAG-1-1174 and ESTEC AOP/WK/303284.

REFERENCES

1. Bradley, J. P.; Sandford, S. A.; and Walker, R. M.: Interplanetary dust particles. In Meteorites and the Early Solar System, eds. Kerridge, J. F.; and Matthews, M. S.; University of Arizona Press, 1988; pp. 861-895.
2. Brownlee, D. E.: Cosmic dust: collection and research. Ann. Rev. Earth Planet. Sci., 13, 1985, pp. 147-173.
3. Flynn, G. J.: Asteroids, Comets and Meteors III, 1989, pp. 59-62.
4. Flynn, G. J.: Survival of large micrometeorites on atmospheric entry: implications for their sources and the flux of cometary dust. Lunar Planet. Sci. XXII, 1991, pp. 393-394.
5. Zinner, E.; Kuczera, H.; and Pailer, N.: Simulation experiments for the chemical and isotopic measurements of interplanetary dust on LDEF. Lunar Planet. Sci. XIII, 1982, pp. 891-892.
6. Jessberger, E.; Kuczera, H.; Lange, G.; Sutton, S.; and Zinner, E.: Ion microprobe analyses of simulated LDEF impact residues. Lunar Planet. Sci. XVI, 1985, pp. 400-401.
7. Lange, G.; Eigner, S.; Igenbergs, E.; Jessberger, E. K.; Kuczera, H.; Maas, D.; Sutton, S.; Weishaupt, U.; and Zinner, E.: Ion microprobe sensitivities and their application to multielement analysis of LDEF impact residues. Lunar Planet. Sci. XVII, 1986, pp. 456-457.
8. Fraundorf, P.; Lindstrom, D.; Pailer, N.; Swan, P.; Walker, R.; and Zinner, E.: Rapid erosion of plastics in near-earth orbit and a means of prevention. Lunar Planet. Sci. XIV, 1983, pp. 205-206.
9. Fraundorf, P.; Lindstrom, D.; Pailer, N.; Sandford, S.; Swan, P.; Walker, R.; and Zinner, E.: Erosion of mylar and protection by thin metal films; AIAA Shuttle Environment and Operations Meeting; 1983; Paper 83-2636, pp. 131-137.
10. Fechtig, H.; Grün, E.; and Kissel, J.: Laboratory simulations. In Cosmic Dust, ed. McDonnell, J. A. M.; Wiley and Sons, New York, 1978; pp. 607-669.
11. Igenbergs, E.: Ein neuer Beschleuniger für die Simulation von Mikrometeoriten. Forschungsbericht, 1974, pp. BMFT-FBW 1974-03.
12. Stadermann, F.: Rare earth and trace element abundances in individual IDPs. Lunar Planet. Sci. XXII, 1991, pp. 1311-1312.
13. Zinner, E.; Tang, M.; and Anders, E.: Interstellar SiC in the Murchison and Murray meteorites: I sotopic composition of Ne, Xe, Si, C, and N. Geochim. Cosmochim. Acta, 53, 1989, pp. 3273-3290.

IDE SPATIO-TEMPORAL IMPACT FLUXES AND HIGH TIME-RESOLUTION STUDIES OF MULTI-IMPACT EVENTS AND LONG-LIVED DEBRIS CLOUDS

J. Derral Mulholland,
S. Fred Singer, John P. Oliver, Jerry L. Weinberg, William J. Cooke, Nancy L. Montague
Institute for Space Science and Technology
1810 NW 6th Street
Gainesville, FL 32609
Phone:904/371-4778, Fax: 904/372-5042

Jim J. Wortman
North Carolina State University
Raleigh, NC 27695

Phillip C. Kassel and William H. Kinard
NASA Langley Research Center
Hampton, VA 23665

IDE OVERVIEW

The purpose of the LDEF Interplanetary Dust Experiment (IDE) was to sample the cosmic dust environment and to use the spatio-temporal aspect of the experiment to distinguish between the various components of that environment: zodiacal cloud, beta meteoroids, meteor streams, interstellar dust, and orbital debris. The experiment, as well as preliminary results, has already been described in some detail elsewhere [ref. 1]. Six panels of detectors were carried on orthogonal faces: Earth, Space, East (ram, or leading edge), West (wake, or trailing edge), North and South faces. Each panel contained detectors with two different sensitivities. Approximately 60% of the detectors on each panel were the more sensitive type (0.4 μm dielectric thickness, refered to as "4"), while the remaining 40% were the less sensitive variety (1.0 μm dielectric thickness, refered to as "10"). Preflight calibrations indicated that the sensors' lower limits of detection, for hypervelocity particles, were roughly 0.2 μm and 0.5 μm diameter, respectively. The upper detection limit for both types of sensors was estimated to be particles approximately 100 μm in diameter. This represents the particle size that would physically break the detector substrate.

The use of the word "spatio-temporal" invokes the fact that, unlike most LDEF (or other) cosmic dust experiments, IDE provides both directional and precise time information on the near-Earth particulate environment. The fact that the collected data appear to contradict the conventional view that impacts occur on a spacecraft in low Earth orbit at a relatively constant rate lends a strong support to the idea that there **must** be an IDE type follow-on to LDEF. We will show that all conventional models of the orbital debris environment are grossly wrong in their predictions of the day-to-day flux.

The flight data were recorded on magnetic tape, which ran out after 49 weeks (thus exceeding the 9-month nominal mission duration). Recorded data include the time, panel, and type of detector for each impact; plus periodic detector status checks, LDEF sunrise time, and various other "housekeeping" items. The time resolution (i.e. clock tick) was 13.1s. More than 15000 impacts were recorded on the 459 detectors in 346 days [Table 1]. On the high-activity panels (East, North, South), the time history was extremely episodic [Figure 1].

The first lesson of this experiment is that the particulate environment at 500 km is extremely clumpy, and this has some profound implications with respect to orbital operations of impact -sensitive surfaces.

Sunrise data permitted a precise calibration of the spacecraft clock. IDE activation occurred at 1984 April 07d 17h 23m 43.8s ± 0.3s UTC. The difference between nominal and observed clock rate amounted to several orbits over the full mission. The estimated accuracy of any individual epoch is ~ 15-20s.

IMPACTS vs. FLUX

Impact counts and times are the real observations in IDE. Areal fluxes must be inferred from a knowledge of active detector area. With the exception of the West 4 set, all detector groups suffered permanent loss of one or more detectors during the course of the mission. The South 4 set, the second hardest hit, eventually lost 16 detectors (33%). This attrition must be accounted for in calculating fluxes. There appears to have been significant hypervelocity impact contamination by the "Shuttle Induced Atmosphere" [ref. 2] during the first few days of the mission. The first 8 days (2.4% of the mission) produced 36% of the mission hits on the Earth 4 set, 14% on West 4, 9% on Space 4, and 5% on East 4 & 10. An interesting detail is that many of the West hits were at slightly less than half an LDEF orbit period after a swarm of East impacts; we seem to have observed the effects of an eccentricity in the Shuttle contamination cloud orbit. For our analysis, we wish to distinguish between a "space environment" and a "spacecraft environment", and the evidence is that manned spacecraft produce their own extremely dirty local neighborhood. We have consequently omitted the first 8.2 days from our data set. We present here [Table 2] the first-order estimate of the areal fluxes for LDEF, based on a linear approximation to the detector failure history.

BETA METEOROIDS

Several interplanetary spacecraft have reported anomalous concentrations of very small cosmic dust grains coming from the general direction of the Sun [ref. 3]. This has been interpreted as evidence for "beta meteoroids", grains so small that, after release from a parent body, they experience a radiation pressure sufficient to modify the apparent mass of the Sun [ref. 4]. Variational analysis shows that the new orbit of the particle is Keplerian, but with increased eccentricity, semi-axes, semi-latus rectum and apsides. If the particle is sufficiently small, the new orbit is parabolic or even hyperbolic, and the particle escapes the solar system. Escape orbit or not, conservation of angular momentum requires that the speed <u>decrease</u> for some range of distances $< a_o$, increasing elsewhere, depending on release circumstances.

In the LDEF context, West panel should see beta meteoroids near sunset, East near sunrise, Space near noon. When plotted in sun-synodic coordinates, such as time since sunrise, both East and West show strong beta signatures. It appears that West is perhaps even dominated by particles from the solar direction [Figure 2]. The beta phenomenon is not episodic, but persists throughout the year as a broad, diffuse band tracking the Sun in right ascension (Figure 3.). This is apparently the first detection of beta meteoroids from low Earth orbit.

METEOR STREAMS

One of the major original goals of the experiment was the spatio-temporal exploration of meteor streams. Consequently, virtually the first task was to begin a survey of the impact record around times of known meteor showers.

The April Lyrids came only two weeks after launch, but the IDE data around that date provided a surprise: two enormous surges separated by 6 days [Figure 4]. The event of 17 April shows impacts nearly evenly divided on North and East, with essentially none on the other 4 panels. This is almost surely a debris event, but identification requires further study. The event of 23 April falls right at the time of Lyrid maximum. The hourly rate is >100 times the mission mean on both North and Space, with few on East and none elsewhere. Over several days, even North and Space were inactive at times when they could not see the Lyrid radiant. We have been tempted to call this a meteor stream event, but there are problems with this interpretation. The event is too sharp and too strong, and there was a spacecraft launch (1984-041) the preceding day. The bifurcated nature of the burst (see below) may be characteristic of debris events. On the other hand, even with this event removed from the data, there seems to be an increase in the background flux during this period. Other events have been located in the near vicinity of other meteor showers. This does not imply detection and confirmation. A definitive discussion of meteor stream activity cannot be carried out until a "sanitized" data set is produced, with identifiable debris events removed.

MEAN FLUX *vs.* EVENTS, SEQUENCES and CLOUDS

The mean fluxes given in Table 2, lacking a temporal component, do not describe the true nature of the particulate environment very well. The IDE impact record is not a random scatter diagram. It is so clumpy that long-term averages may be primarily useful for predicting mean equipment lifetimes [see Figure 1]. We are in the process of compiling a comprehensive catalogue and atlas, for which we propose the following terminology:

- Each individual detection is an *impact*, and a detection not obviously a member of a larger class is an *isolated impact*.

- Detections often occur in bursts, during which numerous impacts arrive within a short time at a rate well above the surrounding flux. We designate this as an *event*. Obviously, this is a subjective definition that depends on the time resolution with which one looks at the data. With hourly resolution, Figure 4 shows two events.

- At finer resolution, the 23 April event is bimodal and can be considered as two related events [Figure 5]. We shall call several apparently related events a *multi-event sequence*. Many of the bursts that we see in the data have similar bimodal structure to that of the 23 April encounter, and this may be a clue to understanding the spreading of orbital debris clouds.

- We find several instances of events separated by low-order multiples of one-half the LDEF orbital period. These we will call *multi-orbit event sequences* . This phenomenon has already been mentioned in the context of the Shuttle contamination event. Figure 6 shows a sequence of at least 25 events spread over about 1.6 days (4-5 June 1984), at intervals of one (or occasionally two) LDEF orbit(s).

A multi-orbit event sequence can only occur if the particulates are themselves in Earth orbit, intersecting that of LDEF. Each time that LDEF comes back to the same place in its orbit, it hits the same cloud, again and again and again. We are sampling chords through this cloud, time after time, over a day and a half. This rules out serious consideration of extraterrestrial origin. These are orbital debris clouds, and they can be seen clearly in 3-dimensional (two angles and time) representations [Figure 7]. Goldstein and Randolph (ref. 5) saw the same phenomenon, which they called rings, at larger particle sizes with groundbased radar in 1989; within the limitations of the two observation sets, a ring is only a particular type of cloud, and the data do not permit an experimental distinction.

Multi-orbit event sequences -- debris clouds (or rings) -- comprise a major fraction of the particulate environment seen by IDE. The first six clumps that we identified contain about 25% of all impacts recorded during the mission. The "May swarm" and the 4-5 June event together contain more than 80% of all impacts recorded during those two months. The first pass, alone, on 4 June contained 131 hits in about 2 minutes, 0.8% of the mission impacts in 0.0004% of the duration of the mission, 3 orders of magnitude above the average flux. The spacecraft whose instruments are subjected to such an encounter during the first weeks of its mission will experience a drastically enhanced rate of impact induced degradation over that predicted (and planned for) based on the assumption of a random distribution of impacts with time. One of the major lessons to be learned from the IDE data , and hence from the LDEF, is that orbital debris is far from isotropic, unlike the assumptions of most current models.

More sophisticated analysis of the June 4 multi-orbit event sequence may extend the sequence, and indeed Figure 6 suggests that it was longer than1.6 days. We suspect that the same cloud was re-encountered about 54 days later, after a full LDEF precessional rotation. Since the sequence begins near the equator, there are two possible ways to use precessional dynamics to infer information on the orbit of the dust cloud. The most direct way is to determine the slope of the locus of events in right ascension-declination space [N.B. to non-astronomers: right ascension is the celestial equivalent of terrestrial longitude, but measured from the equinox; declination is identical with terrestrial latitude]. It is clear from Figure 7 that the locus crosses the equator at about 30° right ascension, and that the angle of the locus is about 70°. That is only approximately the inclination of the cloud orbit, since both orbits are precessing backwards along the equator at rates determined by their inclinations [Figure 8]. A relatively simple iterative calculation will give the true orbital debris inclination since the inclination of the LDEF orbit is known.

The other approach begins with the re-encounter, which can only occur after a precessional beat period of the two orbits. In principle, this permits calculation of the cloud's precession period, from which a determination of the orbit inclination can be made. This then permits a geometric calculation of the node from mutual geometry with LDEF's orbit. When both approaches are possible, they are complementary and can provide a consistency check on the results. Analysis of this striking event is not yet complete, but the ascending node is definitely about 30°, inclination in the range 70-85° (i.e. near-polar). We are looking at candidate sources. By contrast, the "May swarm" appears to have a moderate (~30-35°) inclination, but the equator crossing is probably indeterminate from these data.

NATURAL COSMIC DUST vs. ORBITAL DEBRIS: WHICH DOMINATES THE ENVIRONMENT?

The total number of artificial Earth satellites in orbit is growing exponentially, and it is an important question to know how this affects the particulate environment. Related to this issue are the relative proportions of artificial and natural material that together compose that environment. From the LDEF Interplanetary Dust Experiment data, Singer *et al.* [ref. 1] argued that the ratio of transverse flux (mean of North and South panels) to Space panel flux, coupled with kinematic constraints, suggests a ratio of artificial to extraterrestrial particulates of about 5:1. That conclusion has not been changed by the use of mean fluxes from Table 2, replacing the raw counts of Table 1. Taking foil penetration thickness at minimum particle diameter as equivalent to IDE dielectric thickness, we obtain a ratio of about 4-6:1 from a comparison of the IDE East panel fluxes with an extrapolation of the interplanetary component predicted for that panel [e.g. ref. 6].

By contrast, it is commonplace to encounter the statement that cosmic dust predominates. Which view should prevail? An examination of the East panel predictions cited above shows that the statement is oversimplified. McDonnell shows clearly that current models predict that natural cosmic particulates should dominate strongly for sizes (d) > 100 μm, but should only slightly exceed debris for 100 μm > d > 25 μm. Man-made matter strongly dominates for d < 20 μm. This latter is the range that forms the bulk of IDE impactors.

Another element in the argument is highlighted by the discovery of multi-orbit event sequences and their characterization as orbital debris clouds. The comprehensive catalogue of IDE events and sequences is not yet available, but it is clear that clouds contain an important fraction of all the impacts detected. In addition, the direction distribution of flux makes it clear that the majority of these particulates are in Earth orbit. Even if one wishes to postulate an *ad hoc* ring of captured comet and asteroid dust [ref. 6, ref. 7], there is no convincing way to construct something like the May swarm. The clouds must be orbital debris.

The evidence supporting the idea that the debris population density has not changed over the years is based primarily on the use of 1963 data [ref. 6, Figure 3], which exerts a long lever arm over a 15 year empty gap. If only the spacecraft data since 1970 are used, the debris levels arguably track the exponential growth of the satellite population, at least within the error bars on the data.

By contrast, the IDE West fluxes, which should contain essentially no debris after removal of the initial Shuttle contamination event, are higher than an extrapolation of McDonnell's predicted trailing edge curve by a factor of 3.3. This might be explained if the prediction contained no beta meteoroid model. If that were indeed the explanation, then IDE suggests a beta meteoroid flux of about 7×10^{-5} m^{-2} s^{-1} at both sensitivity levels.

CONCLUSIONS

There are several major lessons to be drawn from these results, even though we are far from having exploited the IDE data to their fullest:

- The introduction of precise time and even rudimentary directionality as colateral observables in sampling the particulate environment in near-Earth space produces an enormous qualitative improvement in the information content of the impact data.
- The orbital debris population is extremely clumpy, being dominated by persistent clouds in which the fluxes may rise orders of magnitude above background. This aspect of the environment cannot be reflected in any model based on isotropic assumptions.
- The unexpectedly intense temporal aspect, and the fact that these data are already 7 years old, lend support to the idea that there should be a follow-on IDE type experiment to obtain updated information and to test the secular trend in the debris population.
- The IDE data suggest a strategy to minimize the damage to sensitive spacecraft components, using the observed characteristics of cloud encounters. Such a strategy based on an observing program that we designate SYNMOD (Synoptic Monitoring of Orbital Debris) and incorporating either automatic or interactive instrument control, will be detailed in a future publication.

ACKNOWLEDGEMENTS

We are grateful to our colleagues D. Kessler, J. A. M. McDonnell, C. Simon and H. Zook for helpful discussions and advice. Thanks go also to E. McDow, of Digital Equipment Corp., for personal and institutional support of improvements to the ISST computing environment essential to pursuing this research. This work was partially supported by NASA Langley Research Center, through grants NAG 1-1218 to ISST [J. L. Weinberg, Principal Investigator] and contract NAS1-16550 to the University of Virginia [S. F. Singer, Principal Investigator].

REFERENCES

1. Singer, S.F. et al.: *First Spatio-Temporal Results from the LDEF Interplanetary Dust Experiment*, Advances in Space Research, Proceedings of the 28th COSPAR Meeting, 1990, Pergamon, London..

2. Weinberg, J.L. : *Optical Observations from the Space Shuttle*, Advances in Space Research, VBol. 7, no.5, 1987, pp. 203-205.

3. Igenbergs, E. et al.: *The Present Status of the Munich Dust Counter Experiment on Board of the Hiten Spacecraft*, I.A.U.Colloq. No. 126, August 27-30, 1990, Kyoto Japan.

4. Zook, H.A. and Berg, O.E.: *A Source for Hyperbolic Cosmic Dust Particles*, Planetary and Space Science, Vol. 23, no. 1, Jan. 1975, pp. 183-203.

5. Goldstein, R. and Randolph, L.: *Rings of Earth Detected by Orbital Debris Radar*, JPL Progress Report 42-1-1, May 15, 1990, pp. 191-193.

6. McDonnell, J.A.M.: Space Debris: *Orbital Microparticulates Impacting LDEF Experiments Favour a Natural Extraterrestrial Origin*, LPSC Abstracts Volume XXII, LPSC, 1991.

7. McDonnell, J.A.M. and Sullivan, K: *Foil Perforation Particulate Impact Records on LDEF MAP A0023: Incident Mass Distributions*, First LDEF Post-Retrieval Symposium, NASA CP-3134, 1992.

Table 1. LDEF/IDE Impact Totals and Directional Ratios from April 1984 through March 1985. **Trans** denotes transverse (mean of North and South). Standard deviations are estimates based on the square-root of the number of hits. **N.B.**: The ratios are to be considered as **impact ratios** only. Ratios involving the Space panel have been normalized to reflect the smaller number of sensors on that panel.

LDEF Face	0.4 μm counts	# of sensors	1.0 μm counts	# of sensors
Earth	44	48	29	32
Space	380	35	155	24
North	2467	48	1081	32
South	3029	48	1200	32
East (Ram)	4540	48	1542	32
West (Wake)	455	48	186	32
Total Hits:	10915	275	4193	184

	Ratio	Std. Dev.	Ratio	Std. Dev.
Space/Earth	11.7	1.8	7.2	1.4
North/Space	4.8	0.2	5.2	0.4
South/North	1.2	0.03	1.1	0.05
East/West	10.0	0.5	8.3	0.06
East/Trans	1.8	0.04	1.4	0.05
Trans/West	5.4	0.3	6.1	0.5

Table 2: Preliminary mean flux values for the 338-day period beginning 1984 April 16d 0h UT, based on a first-order evaluation of the time history of active sensor area. The first 8.2 days of the mission have been omitted to eliminate the effects of Shuttle contamination, which was particularly severe on the Earth, Space, and West panels. Estimated errors are subjective.

	Sensors	# of hits	Ave. # of sensors	Ave. area (0.001 m^2)	Flux ($m^{-2}s^{-1}$)	+/- %	ratio 0.4μm to 1.0μm
Earth	0.4μm	28	45.5	89.3	.000011	20	0.7
	1.0	29	31.5	61.9	.000016	20	
Space	0.4	347	34.5	67.7	.00018	5	1.6
	1.0	150	23.5	46.1	.00011	5	
North	0.4	2408	45.0	88.4	.00093	10	1.5
	1.0	1077	30.0	58.9	.00063	10	
South	0.4	3012	40.0	78.5	.0013	20	1.9
	1.0	1198	30.5	59.9	.00069	10	
East(Ram)	0.4	4308	44.5	87.4	.0017	10	2.0
	1.0	1470	30.5	59.9	.00084	10	
West(wake)	0.4	391	48.0	94.2	.00014	5	1.4
	1.0	183	31.5	61.9	.0001	5	

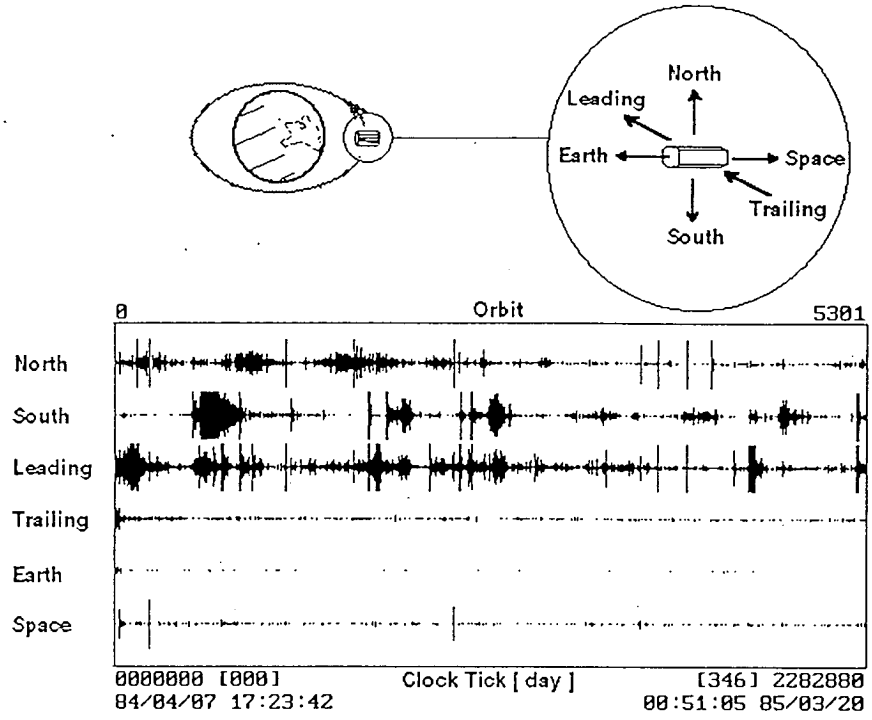

Figure 1: Time history of impacts on the 0.4μm panels over the entire 346 day period of active IDE data recording. In this "seismograph" plot, the vertical extent of each trace indicates the impact rate as a function of time. The display has been truncated in the vertical direction in the most active portions to avoid overlap between adjacent traces.

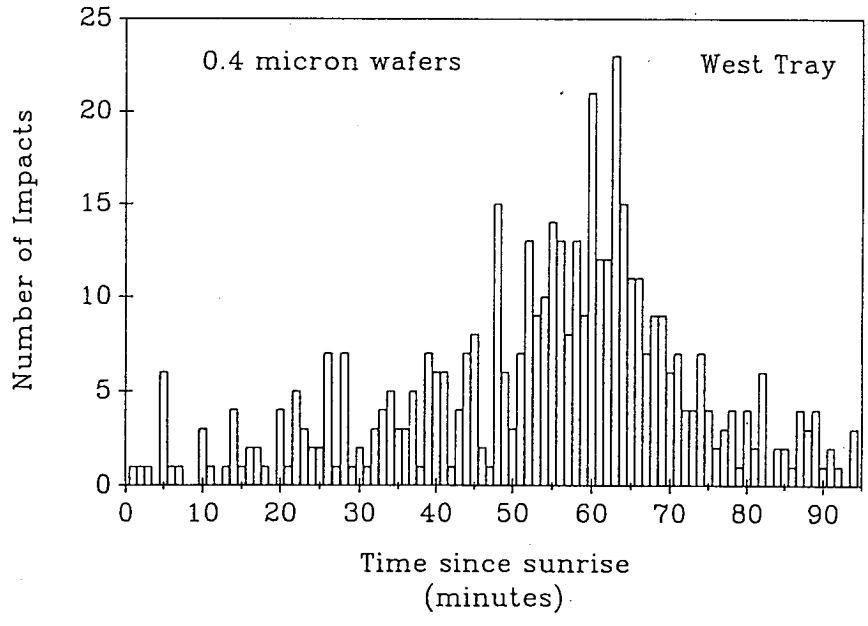

Figure 2: All 0.4μ data from West (trailing edge) panel plotted to show day-night asymmetry. West panel will most nearly face the Sun at evening quadrature, about 53 min after sunrise; sunset is about 6 min later. The 1.0μ data show the same features.

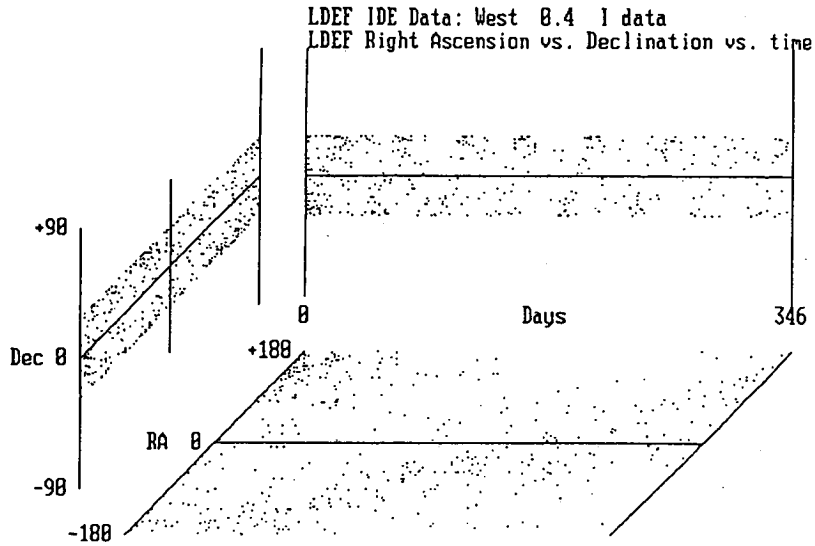

Figure 3: Three-dimensional (two angles and time) view of the sky as seen by the high-sensitivity trailing edge detectors. The RA *vs.* time plot clearly shows a large fraction of the impacts in a broad zone that tracks the Sun, with zero crossing in mid-December. Most of the West panel impacts came from near the solar direction, consistent with an important beta meteoroid population.

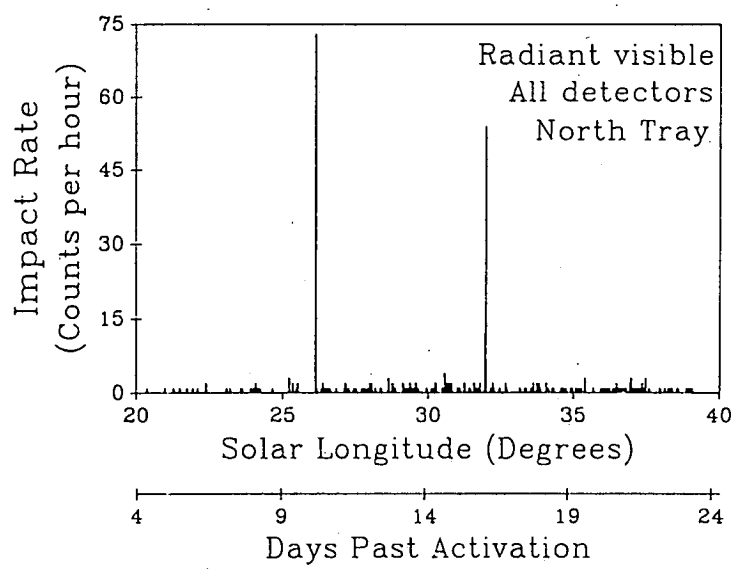

Figure 4: Apparent hit rate (counts/hr) in the vicinity of the April Lyrid meteor stream, North panel. The time of the Lyrid maximum corresponds to the later spike (23 April); that 6 days earlier is surely a debris event. Both are remarkable by their sharpness, and by the high values (10 and 14 respectively) of the detection ratio 0.4μm/1.0μm, suggesting a preponderance of submicron particles. The North flux averaged over the entire mission was roughly 0.5 impacts per hour.

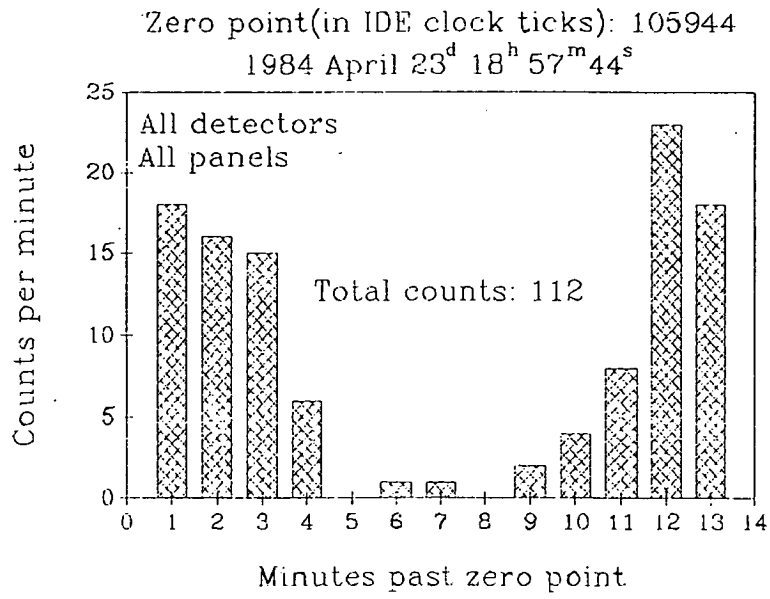

Figure 5: This is the postulated "Lyrid" event of Figure 5, but binned by minutes. It is clearly bimodal, and can be considered as two separate but related events.

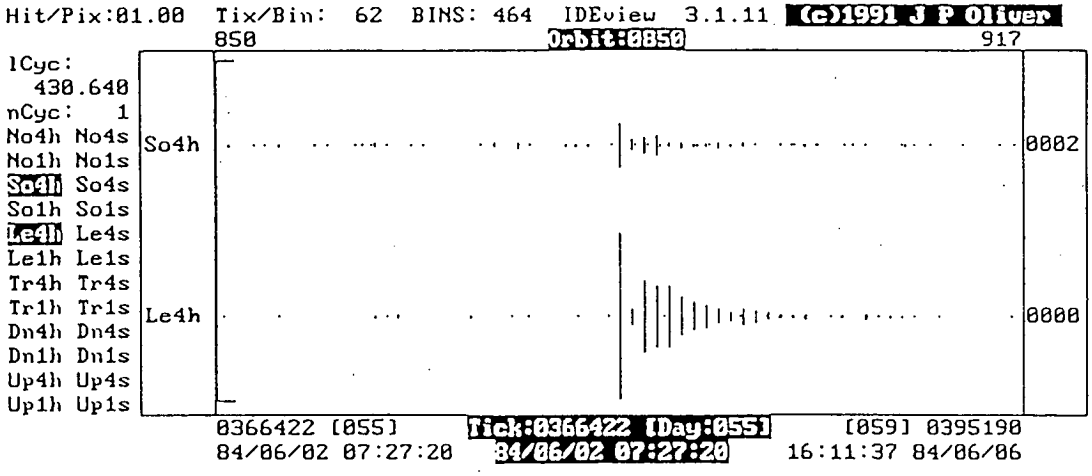

Figure 6: The "June 4" multi-orbit event sequence. Each time LDEF moved southward across the equator, it encountered a cloud of particles rising northward in a different orbit. These collisions took place on at least 25 passages through the descending node over the course of 1.6 days. Only East (and to a lesser degree South) were hit. The first event in the sequence contained 131 impacts, or 0.8% of the mission total, in less than 2 minutes.

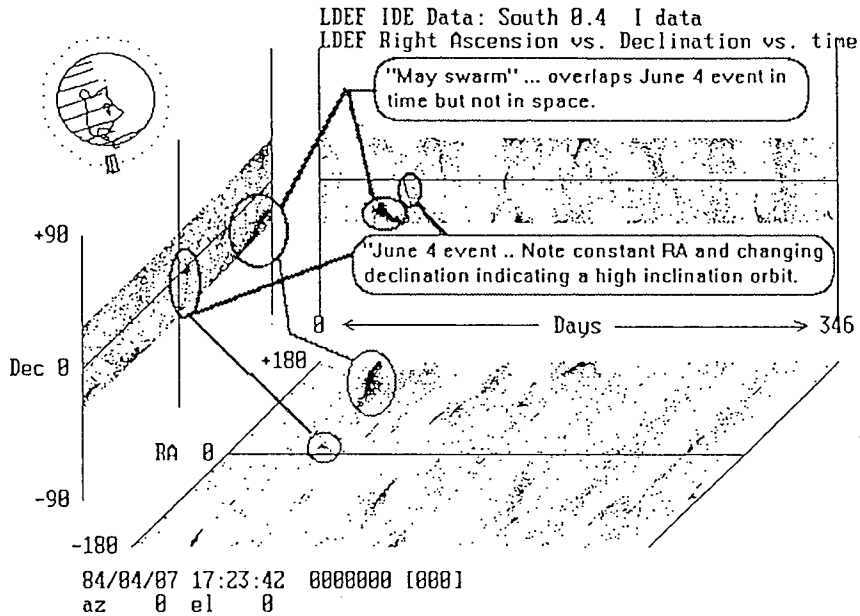

Figure 7: This 3-D plot shows all impacts recorded on the South 4 set of IDE detectors during the active phase of the mission, in right ascension-declination-time space. Clearly, a large fraction of the impacts recorded are grouped in highly episodic events and sequences, implying clouds of material in Earth orbit. Two specific examples are annotated.

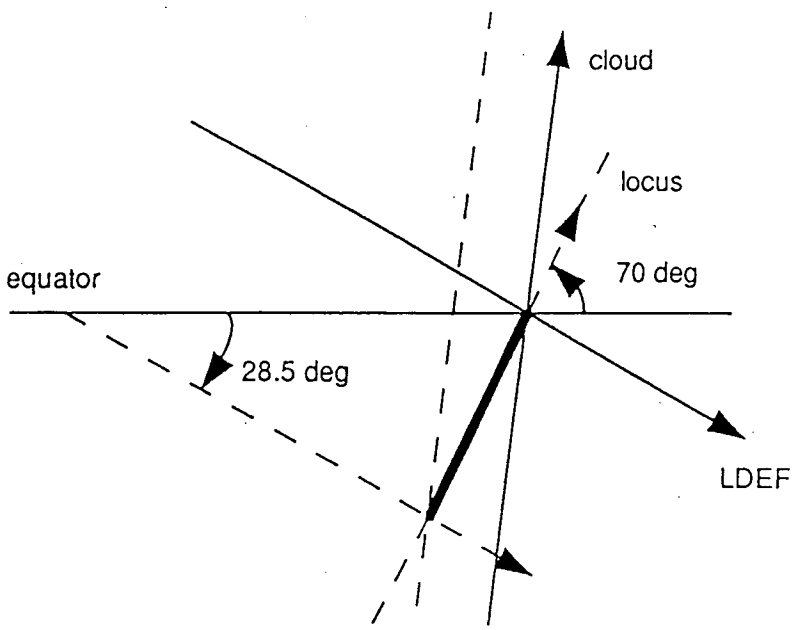

Figure 8: Both the spacecraft and the debris cloud are precessing backwards along the equator, at rates determined solely by the inclinations of their respective orbits. The locus of events in the right ascension-declination plane of events in a multiple orbit sequence is a resultant of these two precessions, and the locus characteristics thus provide a means of iteratively determining the orbital inclination of the dust cloud. The diagram shows the "ideal" case (satisfied by the 4-5 June sequence) of a locus in the equatorial zone.

ION MICROPROBE ELEMENTAL ANALYSES OF IMPACT FEATURES ON INTERPLANETARY DUST EXPERIMENT SENSOR SURFACES.

Charles G. Simon
Institute for Space Science and Technology
Gainesville, FL 32609

Jerry L. Hunter, Jim J. Wortman, Dieter P. Griffis
North Carolina State University
Raleigh, NC 27695

ABSTRACT

Hypervelocity impact features from very small particles (<3 μm diameter) on several of the electro-active dust sensors utilized in the IDE experiment (LDEF Expt. No. A0201) were subjected to elemental analyses using an ion microprobe. After etching away a layer of alkali-rich carbonaceous/silicaceous surface contamination, low mass resolution elemental survey scans are used to examine impacted areas. Normalized high mass resolution two-dimensional positive ion elemental maps of the feature and surrounding area show the distribution and relative composition of the material. The location of the high purity sensor surfaces on the six primary sides of LDEF (rows 3, 6, 9, 12, space end, and earth end) provides a unique opportunity to further define the debris environment. We have applied the same analytical techniques to impact and contaminant features on a set of ultra-pure, highly polished single-crystal germanium wafer witness plates that were mounted on tray B12. Very little unambiguously identifiable impactor debris was found in the central craters or shatter zones of small impacts in this crystalline surface. Surface contamination ubiquitous on LDEF has greatly complicated data collection and interpretation from micro-particle impacts on all surfaces.

INTRODUCTION

The Interplanetary Dust Experiment (IDE) has yielded a wealth of spatio-temporal impact data for the first year of the LDEF orbit, including the first long-term direct evidence of the episodic nature of micro-particle impacts in low Earth orbit (LEO).[1] In order to extend the usefulness of this data set we have begun a systematic analysis of impactor residues in impact features on the high-purity sensor surfaces using scanning electron microscopy with energy dispersive x-ray spectroscopy (SEM/EDS) and secondary ion mass spectrometry (SIMS). Our ultimate objective is to produce a substantial data set on major element compositions of the smallest class of impactors (<3 μm). This will allow a statistical view of the manmade/natural micro-particle population ratio. Larger craters are also being examined during the course of the study and this data will be compared to other compositional data for similar sized impactors observed by other LDEF investigators.[2-4]

Impact craters on a set of high purity germanium witness plates mounted on tray B-12 have also been examined. Pre-flight surface contamination of these witness plates has complicated analyses of impact features. EDS and SIMS analyses of several contaminant features were recorded and a proposed sample clean-up procedure is presented. Primary beam shadowing effects compromise SIMS data on large, high aspect ratio craters (discussed below), but EDS analysis has identified tentative debris in all three large craters (60, 71 and 188 μm) found on Ge surfaces scanned to date.

In this paper we describe the impacted samples and analytical methodology in detail, and report on results from SIMS and EDS analyses of 15 impacts in IDE sensors from the leading and trailing sides of

LDEF (rows 9 and 3, respectively). Results are also presented of SIMS analyses of 13 impacts in Ge witness plates from tray B12. Half of these impacts were also analyzed with EDS. All but one of the impacts analyzed with SIMS had craters <~20 μm in diameter. An additional 11 impacts in Ge, nine that were <10 μm in diameter and two that were 60 and 188 μm diameter, were analyzed with EDS only. Dimensions and analytical results for all impacts analyzed to date are presented. Examples of SIMS two-dimensional elemental maps of several impact features are also presented. They show the usefulness of the technique in observing and correlating very small amounts of impactor residue and point out the problems associated with surface contamination and beam shadowing effects on a large crater in Ge.

The bar graph in Figure 1 shows the relative amounts of surface area for each micrometeoroid experiment on LDEF, the proposed range of impactor size chemical characterization, and the experiment locations on the spacecraft. This graph illustrates the potential for micro-particle impactor chemical characterization on impacts in IDE sensor surfaces compared to the other micrometeoroid experiments. The only other group currently using SIMS routinely to analyze impact craters (Zinner, et al., Expt. A0187-2) have no plans to characterize particles <10 μm in size.[5] The foil covered germanium capture cell experiment's major objective is the chemical and isotopic characterization of natural micrometeorites >10 μm in diameter, and the group is concentrating on analysis of impact features that formed when the capture cell foils were intact. However, the ultra-pure germanium capture cells in this experiment were exposed directly to the space environment for substantial times during the mission due to catastrophic failure of their thin-film covers. Thus, the large areas of pure germanium base plates (1.51 m^2 total) on rows 2, 3 and 8 should provide a significant source for micro-particle impact sites, albeit with variable and unknown time history. The SIMS procedures reported on in this paper were developed to analyze micro-particle impact sites on pure germanium and should be directly applicable.

Other LDEF investigators that have analyzed substantial numbers of impact craters have used SEM/EDS procedures to date.[3,4] Because of the inherent lower sensitivity of EDS versus SIMS, explained briefly below, and the small amount of impactor material (femto to picograms) expected to survive a micro-particle hypervelocity impact, most investigators have concentrated on analyzing larger impact features.

A notable exception is the work reported by Mandeville, et al., (Expt A0138-2, row 3) which includes identification of chondritic residues in ~10 micro-particle impacts (<5 μm diameter thin film penetration holes) analyzed so far out of a total of ~ 40 such micro-particle impacts identified on capture cell surfaces (0.2 m^2 total area).[4] However, analyses of off-impact areas had not been performed at the time the analytical data were presented. Our experience, and that of others in the LDEF community, has shown that surface contamination by alkali-rich silicaceous species is a significant problem for all LDEF surface analysis procedures.[2,3,6,7] This factor combined with the limited number of small craters in the A0138-2 experiment, and its location only on the trailing edge of the spacecraft limit the available statistics for determination of the average manmade/natural micro-particle population ratio from this experiment.

The A0187-2 experiment (Horz, et al.) had a large (~1m^2) collection surface on both the leading and trailing edge of LDEF and a substantial set of EDS analyses of impact craters >40 μm in diameter has been reported to date.[3,8] The row 11 collector surface is anodized Al alloy (99%) and the textured surface precludes easy identification of impact craters <~20 μm in diameter. Also, the materials impurity limits the ability to analyze small amounts of impactor residue. The row 3 experiment surface is 0.999% Au and has a somewhat smoother surface. It should be possible to identify smaller craters and analyze them using SIMS. Several samples of this surface are currently undergoing analyses in our laboratory.

Experiment A0023 was composed of ~1500 cm^2 of multi-foil capture cell surface area on the four primary LDEF sides ~700 cm^2 on the space end, and provides an excellent sample set for all impactor sizes up to ~1mm. McDonnell, et al., plan on a rigorous chemical analysis program after completing their primary mission of average flux determination.[9] The inherent impurity of the commercial foils and assembly materials used in the capture cells construction will complicate and may ultimately limit the investigators' ability to analyze residues from the smallest class of impactors (<3 μm). The use of SIMS may ultimately be

required to analyze significant numbers of micro-particle impact sites, and it is hoped that our laboratory's experience will be useful in this effort.

The largest area meteoroid experiment on LDEF, S0001, consisted of ~25 m^2 of chromic-anodized 6061-T6 Al alloy plates distributed on nearly all sides of the spacecraft.[10] This experiment is not represented in Figure 1 since it was not originally designed to permit chemical analyses of micro-particle impacts. The surface texture precludes identification of impact craters <~20 μm in diameter and the substrate impurities greatly complicate chemical analyses of impactor residues. However, the principal investigator, D. Humes, is currently collaborating with our laboratory to perform chemical analyses on selected residues in and around impact features >40 μm in diameter using SEM/EDS and SIMS.

The ultra-pure materials used in the fabrication of the IDE sensors and their location on all six LDEF primary sides provides a unique sample set for the determination of the manmade/natural micro-particle population ratio via chemical analyses. The smooth sensor surfaces and the impact signature (described below) greatly facilitate the location of micro-particle impacts. In addition, the activity record over the first year of LDEF's orbit permits identification of sensors that became inactive at specific times. In future studies this could allow segregation of impacts (and average fluxes) into before and after sensor failure times, thus providing another level of temporal characterization of the micro-particle population in LEO.

EXPERIMENTAL

The general experimental approach to sample analyses was as follows:

(1.) Perform a stereo optical survey at 100X magnification (Olympus 1000X stereo microscope) and photo-document impacts at low and high magnification for later identification in other instruments.
(2.) Perform SEM/EDS analyses of impact sites and surrounding areas.
(3.) Perform SIMS analyses of impact sites and surrounding areas.
(4.) Correlate all analytical data on each impact crater and tabulate relative abundance of elements found in craters and spall zones.

SIMS analysis was left to last since it is a destructive technique. The presence of a layer of alkali-rich silicaceous surface contamination complicated these analyses as discussed below. Also, the presence of pre-flight contamination on the germanium witness plates, in addition to the orbital contamination, greatly complicated analyses of impact sites on these surfaces. As the study progressed, EDS analyses of small impacts in Ge was discontinued since no detectable debris was observed with this technique in any of the small craters that were examined. Instead, SIMS analyses were performed after optical identification of the impact craters.

Description of Hypervelocity Impacts in IDE Sensors

The IDE sensors (Fig. 2) are 2 inch (5.08 cm) diameter Metal-Oxide-Silicon (MOS) capacitor structures. The detectors were formed by growing either a 0.4 μm or 1.0 μm thick silicon dioxide layer on a 250 μm thick, B-doped polished silicon wafer (>0.99999). The top metal contact was formed by physical vapor deposition of ~1000Å of aluminum(>0.9999). Aluminum was also vapor deposited on the backside of the wafers to form the contact with the p-type Si substrate. Gold wires were then bonded to the front and back Al layers and used to connect the detectors to the circuits. The completed wafers (IDE detectors) were then mounted on Al frames by bonding the backsides with silicon RTV. A total of 459 sensors were flown on the six primary sides of LDEF; 60% had 0.4 μm thick insulator layers and 40% had 1.0 μm thick insulator layers.

The IDE capacitor detectors were placed in an electrical circuit that supplies a positive bias to the top Al electrode and a negative bias to the bottom electrode/Si-substrate. The detector operates by discharging the charge stored in the capacitor when impacted by a particle with sufficient mass and energy to cause the thin silicon dioxide layer to fail. The level of the stored charge is chosen to allow sufficient energy during discharge to vaporize a small area of the top Al electrode around the impact point. The typical diameter of this vaporized discharge zone is 50-70 μm and is directly related to the applied voltage/stored charge and the thickness of the Al layer. Once the discharge takes place the capacitor circuit recharges within a maximum of 3-4 seconds if the applied voltage is maintained. The impact event is recorded electronically by monitoring this recharge current. The recharge time is dependent on the rate at which current is allowed to flow to the detector.

The morphology of an impacted region can be seen in Fig. 3. Typically there is the impacted area at or near the center of the feature surrounded by a 25-35 μm wide area of damaged insulator (SiO_2), and a 50-70 μm wide zone where the Al has been vaporized. There is also a rim of melted Al which defines the extent of the vaporization zone. These morphological features greatly facilitate the location of micro-particle impacts on active sensor surfaces and also serve to distinguish impacts that occurred when the sensor was inactive. The smooth-bottom, low aspect central craters in the impact sites that occurred on active 1.0 sensors have a minimum diameter of ~11 μm. Since submicron particles are capable of triggering the sensors (~0.5 μm diameter particle for the 1.0 sensor and ~0.2 μm particle for the 0.4 sensor), the minimum crater diameter is interpreted as being a function of the specific electrode surface area required for electron flow to occur under the applied voltage. It is suspected that the negative potential field of the Si electrode may enhance capture of positive ions produced in the impact/sensor-discharge plasma plume. However, insufficient empirical data from ground based simulations of this phenomenon has been collected to date to unambiguously identify an enhanced ion collection effect.

It is not known at this time what maximum size impactor would inactivate a sensor, but theoretically even a broken sensor wafer should still be active on the areas attached to the electrode leads. A substantial number of large impact craters (> 0.5mm diameter) were observed on IDE sensor surfaces. An accounting of the largest impacts on those sensors that were still active when LDEF was retrieved should provide a limit for this value. Central crater and Al vaporization zone diameters are reported for all impacts subjected to residue analyses.

During the manufacture of the IDE sensors, particulate contamination and defect sites in electrode interfaces necessitated the "clearing" of sensors before mounting on the spacecraft. This was accomplished by activating the sensors at a potential higher than the flight potential and causing the contaminant and defect sites to discharge and clear themselves. Photographic records were then made of each sensor which allows an accurate accounting of all pre-flight discharge areas. Sensors varied greatly in their degree of susceptibility to pre-flight discharges. SEM and SIMS analyses of four pre-flight discharges revealed the presence of contaminants (from dust particles or tool marks) and markedly different morphology than in-flight discharges. To date we have not analyzed a true "blank" discharge, but we have plans to generate several blanks on reactivated flight sensors using a pulsed laser and subject them to SIMS analyses. The two 1.0 sensors selected for impact analyses in this study were characterized as "good" and had few pre-flight discharges.

Description of Hypervelocity Impacts in Germanium Witness Plates

Twelve 1.25 inch (3.175 cm) diameter, 250 μm thick semiconductor device quality single crystal Ge wafers were glued to Al plates with silicone RTV, mounted on tray B12, and exposed to the orbital environment during the entire mission. These wafers were intended to serve as witness plates both for hypervelocity impacts and surface contaminants. However, during optical examination it was noted that the surfaces of these wafers were covered with solid contaminants with condensate rings at a density of ~400 features (>10 μm diameter) per cm^2. Optical surveys of three other similar sized witness plates (one zirconia and two silicon) mounted adjacent to the Ge witness plates revealed only 10-27 similar contaminants per cm^2

on these surfaces. This is taken as conclusive evidence that the majority of the contaminants on the Ge wafers were deposited before they were mounted on the spacecraft with the other witness plates. Auger, EDS and SIMS analyses of dozens of these contaminant features showed a dominance of alkali-chlorides, hydrocarbons, Mg, Si, Ca, S, Ti, some Fe, and very little Al.

The contamination problems are complicated further by the morphology of the impact features in the Ge substrates. A typical impact feature has a high aspect central crater (or shatter zone if larger than ~10 μm diameter), an extremely jagged inner spall zone about twice the diameter of the crater, an outer spall zone with a maximum dimension about four times the crater diameter, and a fracture zone that spans a distance equal to 5-10 times the crater diameter (Fig. 4). About half of the craters < 10 μm in diameter did not have an outer spall zone. The jagged central shatter zones of the larger craters restricted the usefulness of SIMS analyses, as discussed below.

The high level of pre-flight particulate contamination combined with the alkali-rich silicaceous surface contamination layer deposited in orbit have greatly complicated instrumental analyses of impact sites on these surfaces. We have not cleaned the surfaces to date, beyond nitrogen blow down, prior to their introduction into the SIMS instrument. Careful examination of two-dimensional elemental concentration maps was required to identify residue located in craters and spall zones. Even with these precautions, the identification of debris must be considered tentative until more stringent sample preparation procedures are instituted. Our current plans are to use the alcohol/water surface cleaning procedures utilized by investigators that examined impact craters on Apollo spacecraft windows[11,12] to clean one Ge wafer and reanalyze several impacts that showed high concentrations of residues within impact craters. These craters should have significant material remaining despite the destructive nature of SIMS analysis.

SEM/EDS Analyses

Energy dispersive x-ray spectroscopy is based on the measurement of the characteristic X-rays from materials excited with an energetic electron beam. The EDS used in this study allowed the detection of all elements with Z > 10 (Ne), with minimum detection sensitivities for the various elements ranging from ~0.1% to >1.0% atomic concentration. All experiments were performed on an Hitachi S-530 scanning electron microscope equipped with a Tracor-Northern TN5500 EDS. SEM micrographs were recorded of the impact features and EDS spectra were recorded of various areas within the impact feature (central crater and spall zone) in both area and spot mode. All SEM micrographs were recorded with an accelerating voltage of 5 KV and EDS spectra were recorded at both 5 KV and 15 KV. Substrate background EDS spectra were also recorded at 5 KV and 15 KV away from any impact features and obvious surface particulate contamination.

SIMS Analyses

In secondary ion mass spectrometry an energetic ion beam (1 to 20 KeV) is directed toward the sample to be analyzed. The sample surface is eroded by sputtering, and the ionized, sputtered species (atoms or molecules) are extracted into a mass spectrometer where they are separated according to their mass/charge ratio and then counted or imaged. The advantages of SIMS include: [1] detection limits of ppm to ppb for most elements, [2] the ability to detect all species (including H), [3] the ability to record two-dimensional secondary ion images, and [4] excellent depth resolution (<100 Å). The major disadvantages are: [1] SIMS is an inherently destructive technique due to the sputtering process, [2] quantification is not straight-forward due to the complicated secondary ion formation processes involved, [3] large topographic features can lead to false contrast, and [4] trace contaminants complicate interpretation of data from unknown samples.

The primary ion beam impacts the sample at ~30° from normal for the primary ion energy used in this study (15 KV). Figure 5 shows the shadowing effect caused by sputtering at this angle. The sidewalls of a high aspect ratio (depth/width) feature can shadow the primary ion beam from the bottom of the deep feature, thereby preventing sputtering from this area. This is of particular importance when trying to record signals from the bottom of deep craters with jagged sidewalls. (Smooth sidewalls can actually act to focus

the ion beam into the crater, but spatial resolution within the hole is lost due to scattering.) All of the larger impacts (>20 μm) found in the Ge witness plates had central shatter zones instead of smooth walled craters (see Fig. 4b for an example). This shadowing effect and poor secondary ion extraction from these deep, jagged features resulted in a greatly reduced signal from the crater bottom.

The main advantage of SIMS, its excellent sensitivity, can be a disadvantage if sample substrates are not of sufficient purity because non-detectable amounts of elements for other techniques (i. e. EDS, Auger) can give rise to large signals in SIMS. Interferences can also arise from molecular ions having the same nominal mass as the element of interest. These interferences can be resolved in most cases by operation of the ion microscope in the high mass resolution mode, which allows the resolution of 2 species differing by only a few parts per thousand in mass. A particular interference of interest is the Si_2^+ secondary ion (mass = 55.95386 amu) interfering with Fe^+ (mass=55.93494 amu). A mass resolution of 2956 m/Δm, easily achievable in the IMS-3f, is required to separate this interference.

All experiments were performed on a CAMECA IMS-3f Ion Microscope equipped with oxygen and cesium primary beams. The IMS-3f is a double focussing magnetic sector SIMS instrument capable of achieving mass resolutions up to 10,000 m/Δm. It is also a stigmatically imaging ion microscope capable of imaging the elemental distribution with ppm sensitivity and ~1μm lateral resolution.

All data were taken with a 15 KeV O_2^+ primary ion beam. Background positive ion mass spectra were recorded of the surface away from impact features and obvious contamination at 50 nA primary ion current. After recording a mass spectra from 0-200 a.m.u., a depth profile was acquired at 500 nA primary current while monitoring C^+, Na^+, Si^+ and Ca^+ in order to assess the time required to sputter through the layer of surface contamination.

A final protocol was developed to record SIMS data of impact features on high purity LDEF surfaces. Impacts examined during the development of the protocol did not always adhere to this final form and deviations are detailed in the next section. A sample cleaning protocol based on the results of this study and intended to minimize contamination interferences is currently in the development stage. Unless otherwise noted, the following protocol was used to record SIMS data of impact features:

(1.) A Mass spectrum from 0-200 a.m.u. was taken of the central impact crater and associated discharge zone (for impacts in IDE sensors) or spall zone (for impacts in Ge witness plates) at 50nA primary current. This mass spectrum was energy filtered in order to minimize molecular interferences with elemental ion signals.[13] During this portion of the analysis <200Å of material were consumed. In practice, the reproducibility of these initial mass spectra on each substrate lead to the decision to delete this step after several features had been analyzed on each different surface.

(2.) A depth profile was recorded at 500nA primary ion current while monitoring the secondary ion signals of O^+, Si^+, Ca^+ and Na^+ in order to assure that the surface contamination layer was removed. The amount of surface material removed during this process was dependent on the thickness of the silicaceous contaminate layer and varied from hundreds to thousands of angstroms on the various substrates analyzed. Duration of the depth profile was also based on a similar profile recorded for a background area on the substrate in the vicinity of the impact sites.

(3.) A second mass spectrum was recorded of the sputtered area. Based on the results of this spectrum, and the expected compositions of manmade debris and natural micrometeoroids, positive ion images were recorded at 500 nA primary ion current for some or all of the following species: C^+, O^+, Na^+, Mg^+, Al^+, Si^+, K^+, Ca^+, Ti^+, Cr^+, Fe^+, Ni^+, Cu^+, Zn^+, Ge^+, Ag^+ and Au^+. [No images were recorded for Zn^+, Ge^+, Ag^+ and Au^+ on most IDE sensor surfaces Also, Na^+ images were not recorded for most impacts in the leading edge sensor (No. 293). Current protocol for impacts in IDE sensors includes high mass resolution analyses for all of the

positive ions listed, except Ge^+.] During this portion of the analysis <2000Å of material were consumed.

(4.) All secondary ion images were semi-quantitatively scaled based on the secondary ion yields for the elements of interest being sputtered from a pure target (i.e. Si or Ge).[16] Results were then tabulated in terms of relative abundance and location of elements found in and around the impacts.

In order to investigate the possibility of the alkali rich carbonaceous/silicaceous layer being non-uniformly sputtered from the crater bottom and spall areas in impacts in Ge due to the large topography differences, a depth profile was recorded at 500nA for ~25 minutes on one impact feature (Ge2A-15). Under these conditions the contaminate layer was removed from the smooth background area of the Ge wafer in 9 minutes, as evidenced by the precipitous drop and leveling out of the Si^+ and alkali positive ion signals. However, after 3 minutes the Si^+ and Na^+signals from the impact site leveled off at ~100X the background concentration and remained at this intensity until the depth profile was terminated (Fig. 6). This result leaves open the possibility of contaminate contribution to ion signals within the impact areas on Ge substrates due to differential sputtering effects. The significantly lower initial signals from Si and Ca over the impact site could be the result of removal of the contaminant layer by the impact event followed by redeposition of a thinner layer.

The frequent close proximity of contaminant spots that contained many or all of the elements detected in the impact feature on Ge precludes unambiguous identification of impactor residues. These complications, along with the small surface area of the Ge witness plates and their location on only one side of LDEF, have precipitated the decision to concentrate future SIMS analyses on impact features in the IDE sensors. There are similar contamination problems with these samples, but to a significantly lesser degree.

RESULTS AND DISCUSSION

This preliminary study focused on development of analytical protocols and identification of associated analytical problems. Surface contamination proved to be the most significant factor in limiting the usefulness of SIMS data collected from impact features on both the IDE sensor surfaces and the Ge witness plate surfaces. The morphology of the impacts in Ge and the high density of non-flight surface contaminants severely restricts the usefulness of the data collected from these surfaces. The experience gained in this study has resulted in development of appropriate SIMS instrumental and data handling protocols for analysis of micro-particle impact features on IDE sensor surfaces and other high purity substrates. These protocols can now be used to focus on minimization of interferences from contamination, and gaining an understanding of the impact phenomenon in active IDE sensors as it relates to the deposition and recovery of impactor residue. These issues are addressed below in the discussion of the data sets and their specific limitations.

Analytical Results for Impacts in IDE Sensors

The small number of impacts analyzed on two leading and trailing edge IDE sensors (six and nine impacts, respectively) during this development phase study provided sufficient data to allow identification of the limitations of this sample set based on our current understanding of the impact phenomenon in the active sensors and the uncertainty due to interferences from contamination. The effects of these issues will be examined in three ways. First, loose particles and/or soluble debris will be removed from sensor surfaces with three cycles of rinsing and light wiping with lint-free soft cotton using high purity water, methanol and acetone followed by vacuum bakeout at 325K. Hypervelocity impactor melt residues and ion implanted materials should not be removed by this process. Little, if any, of the UV polymerized silicaceous contaminant layer is expected to be removed by this process. Second, several "blank" discharges on an active flight sensor and on an active non-flight sensor will be produced using a pulsed laser and analyzed

with SIMS to discern the distribution of integral and flight-accumulated contaminants. Third, several Fe/C micro-particle hypervelocity impacts on an active flight sensor and on an active non-flight sensor will be produced using an accelerator and analyzed with SIMS in order to discern the distribution of the projectile material and its level of intermixing with integral and flight-acccumulated contaminants. After these studies are performed, a decision can be made on the usefulness of performing SIMS analyses on a statistically significant number (>100) of micro-particle impacts in leading and trailing edge sensors.

Six impacts randomly selected from a total of 200 in-flight discharges identified on a leading sensor (45.6 cm^2 total area), No. 293, and nine impacts randomly selected from a total of 25 identified on a trailing edge sensor, No. 300, were analyzed with EDS and SIMS. Both sensors that were active during the entire mission and the ~9/1 ratio of leading/trailing edge impacts was in the same range as the ratio for larger impactors (craters >0.5 mm diameter) observed by the LDEF Meteoroid and Debris Special Investigation Group.[10] No elements other than Si and Al were observed in EDS analyses and only Si was found in area analyses of all central craters. Spot analyses of numerous melt blebs, droplets and rims showed only Si and/or Al.

SIMS analysis showed that significant amounts of Na, Mg, K and Ca were present in the silicaceous surface contamination layer. (Ca was also present at a >10 ppm concentration throughout the Al layer on sensor 293, as evidenced by depth profile.) Due to local variations of the composition and thickness of the layer, it was impossible to be sure if the layer was etched away from the entire analysis area before ion images were taken. For example, in four of the leading edge impacts, and two of the trailing edge impacts, Ca surrounds the entire feature but is not present in any of the central craters. In fact, Ca was not found in the central craters of any of the 15 impacts examined. These observations increase the confidence that the surface layer was effectively etched away from at least the central crater portions of the features, which are considered the most critical area of the features for identifying impactor residue.

Table 1 lists the SIMS analytical results for material found in and around impact sites in order of approximate (within one order of magnitude) decreasing relative elemental abundances. Results for Al and Si (the substrate materials) are not listed, but no high concentrations of Al were noted in any of the central craters. Low concentrations of Al (<~1000 ppm) would not be visible due to dynamic range limitations of the detector. Only positive ions were analyzed since the vast majority of the elements of interest have a much greater positive ion yield compared to their negative ion yields. Notable exceptions are F, S and Cl, which were not looked for in this phase of the study because of the complexity of switching the Cameca IMS-3f Ion microscope from positive to negative ion analysis mode. In a comprehensive analytical study of large numbers of micro-particle impacts negative ion analyses of selected residues could help to identify chloride salts, fluorocarbon debris, and Fe meteorites, which usually have high S content.

Residues were found in four distinct areas (refer to Fig. 3), [1] the central crater, [2] the discharge area or, or Al vaporization zone, [3] the slightly raised Al melt rim that encircles the discharge area, and [4] the area around the outside of the feature. SIMS analysis areas were 150 μm in diameter with the impact feature positioned near the center. The diameters of the central craters and discharge areas are also listed with the results.

The leading edge sensor, No. 293, had a thicker layer of vapor deposited Al on its surface than the trailing edge sensor. Discharge zone diameters ranged from 59-79 μm in diameter with no apparent relation to the diameter of their respective central craters. Na^+ was looked for in only one feature on this sensor, No. 293-2, and was not observed. Impact No. 293-1 had significant amounts of K, Mg and Fe in roughly equal proportions in the 17 μm diameter central crater, no residue in the discharge area, a small spot of residue with Ca > Fe in the discharge rim and no significant residue around the outside of the feature. Impact No. 293-2 had a significant amount of Mg and K residue in the 24 x 31 μm central crater with Mg > K. Residue consisting of Fe > Ca was found in the discharge area, and Fe > Mg and Ca with a trace amount of K were found distributed in a ring throughout the feature's discharge rim. Ca and Fe were seen all around the outside of the feature. Impact No. 293-3 had significant amounts of K only its 18 μm central crater. Fe>>K was found in the discharge area, and Fe > Mg, Ca > K was found distributed in a ring

throughout the feature's discharge rim. Ca and Fe and a trace of K were present all around the outside of the feature.

Impact No.293- 4 was unique in that it had a very high concentration of Fe in its 12 μm central crater along with a much lesser amount of Mg. Unnormalized positive ion images of Mg, Al, Si, K, Ca and Fe are shown in Fig.7. Some Fe was also present in the discharge area close to the crater associated with a lesser concentration of K. A ring of residue composed of Fe, Mg >> K was present in the discharge rim and Ca was found all around the outside of the feature. This feature has been identified as a candidate for reanalysis after wet cleaning of the sensor surface.

Impact features Nos. 293-5 and 293-7 had no detectable residue in their respective 22 x 28 μm and 12 μm central craters or in their discharge areas. Number 293-5 did have a ring residue consisting of C > Mg, K in the discharge rim and a spot of Fe>Ni>Mg ~40 μm away from the feature. Ca was also present all around the outside of the feature. The only residue found near feature No. 293-7 was a loose particle of Fe>Mg, Cr > Ni with traces of K and Ca (a typical stainless steel composition) found just outside the discharge rim and identified in the SEM.

In summary, four of the six impacts analyzed on the leading edge sensor had residues in their central craters composed of K and/or Mg and/or Fe. Residue in one crater consisted of K only, one consisted of Mg and K, one consisted of Fe with a small amount of Mg, and one consisted of Mg, K, and Fe. Four of the six features had rings of residue in their discharge rims consisting of Mg, Ca and Fe, with lesser amounts of K in two cases, Mg and Fe with a small amount of K in one case, and C with lesser amounts of Mg and K in one case. These same four features all had substantial amounts of Ca in the analysis areas surrounding them.

The trailing edge sensor, No. 300, had a thinner layer of vapor deposited Al (positive electrode for the sensor) than sensor 293. Discharge zone diameters ranged from 44-60 μm in eight nominal impact sites. All of the impacts had moderate amounts of C spread over the area around the features and six of the nine impacts had a concentrated ring of C in the features' rims. Ca surrounded only two of the impact features, which is an indication that the Ca contamination in the bulk of the Al film is not homogeneously distributed.

Impact feature No. 300-1 on this sensor was an exception. It was the result of a large particle impact that left a 36 x 54 μm central crater with a spall zone that had a maximum dimension of 138 μm (refer to Fig. 3b). The diameter of the residual discharge rim was 91 μm. Some Mg was present in the central crater and there were two spots of residue in the spall zone composed of Fe and Ti in one case and Na, Mg, K and Ca in the other. No significant debris was found in the immediate vicinity of the large impact's borders.

Impact No. 300-2 had some Na in the 13 x 18 μm central crater, nothing in the discharge zone, and a ring of concentrated C in the discharge rim. There was also a spot of Na, Mg, K, Ca residue in the analyzed area outside of the discharge rim. Impact No. 300-3 had some Na, Mg, K residue in the 12 μm diameter central crater, nothing in the discharge zone, a ring of concentrated C in the discharge rim, and a Ca, Fe > Mg spot with traces of Na and K outside the discharge rim.

Impact Nos. 300-4 and 300-6 had no residues in their respective 13 and 10 μm diameter central craters, nor in their discharge zones. Both features had a ring of concentrated C in the discharge rim. A chloride salt crystal with significant amounts of Na, K, Ca, Mg, Fe and Ti was identified with the SEM/EDS in the discharge zone of impact 300-4. This impact has been identified as a candidate for reanalysis after wet cleaning of the sensor surface.

Impact No. 300-5 had some Na, Mg, K residue in its 11 μm diameter central crater, nothing in the discharge zone, a ring of concentrated C in the discharge rim along with a spot of high concentration C and Fe with lesser amounts of Na, Mg, and Cu. This was the only residue containing Cu identified in any of the 15 impacts examined on the IDE sensors, and a Ca, Fe > Mg spot with traces of Na and K outside the discharge rim.

Impact No. 300-7 had a residue consisting mostly of Ti with a substantial amount of Na and a trace of K. Nothing was seen in the discharge zone, but a ring of C and Na was observed in the discharge rim. This was the only example of Ti residue found in a central crater in the 15 IDE impacts , but impact No. 300-8 had a significant amount of Ti in its discharge zone along with Na, Mg, K and Ca. This feature also had a residue of Na and K in its 12 μm diameter central crater, a ring deposit of Mg, Ca and Ti in its discharge rim, and a substantial amount of Ca all around the outside of the feature. Impact No. 300-9 had a residue of only Fe in its 11 mm diameter central crater, nothing in the discharge zone or discharge rim, and one spot Na and K outside the discharge rim.

In summary, 7 out of 9 impact features analyzed on the trailing edge sensor had residues in their central craters. Two of the residues consisted of Na, Mg and K, one consisted of Ti with a lesser amount of Na and a trace of K, one consisted of Na and K, one consisted of Na only, one consisted of Mg only, and one consisted of Fe only. Five of the impacts had concentrated C rings in their discharge rims, and one of these rings also had Na distributed throughout it. A sixth discharge rim ring consisting of Mg, Ca and Ti was observed around one feature that also had these elements present in its discharge zone along with Na and K. Two of the nine impacts also had substantial amounts of Ca all around the outside of the features. (This compares with four out of six impacts on the leading edge sensor that were surrounded by Ca deposits.)

Analytical Results for Impacts in Ge Witness Plates

A total of 36 hypervelocity impact craters were identified in the 100X optical scan (and verified at up to 1000X) of two Ge witness plates (15.8 cm^2 total area). Diameters of the central crater diameters ranged from 2.5-188 μm (see Table 2). The five largest craters were 188, 71, 60, 30 and 22 μm in diameter. There were another 10 craters in the 10-20 μm size range and 18 in the 5-10 μm size range. The other three craters found in the optic scan were <5 μm in diameter.

SEM/EDS analyses were performed on 17 of the impacts, including 4 of the 5 largest ones, the three smallest ones, and about half of the mid-sized ones. The three largest craters showed the presence of impactor residue in two (both classified as "manmade" particles), and suspected contamination (silicon RTV) in a third. The lack of any impactor residue observed with EDS in any of the other craters agrees with observations by Amari, et al. for small primary impacts in Ge.[2] However, the EDS analyses performed in this study were generally limited to signal collection from the entire central crater areas at 5 KV and 15 KV, and cannot be considered exhaustive.

A 71 μm crater had high concentrations of Al and Si detected with EDS only in the central crater. SIMS analysis of this crater showed only a trace of Ca and Fe in the spall zone. No ion signals other than Ge^+ were seen from the central crater. This exemplifies the problems of beam shadowing discussed above.

A second large crater, 60 μm crater had a residue of Al and Si with lesser amounts of Cu, Zn and S identified with EDS. No SIMS analyses were performed on this impact. In both cases there was no visible evidence of contamination present in the craters and the residue was in the form of melt blebs. It is probable that the impactors responsible for these craters were of manmade origin.

Twelve additional craters, ranging in size from 6-22 μm, were analyzed with SIMS. Results are presented in Table 3 along with notes about contaminant features observed in the vicinity of impact sites. Because of the substantial contamination issues, discussed above, and the unknown extraction efficiencies of ions from the deep,jagged central craters present in most features, the discussion of the analytical results at this time would be completely ambiguous. Readers are cautioned on drawing conclusions about impactor origins based on these data. The data are presented for completeness with the previously mentioned caveats in full effect.

SUMMARY

In this preliminary study analytical protocols have been developed for sample handling and SIMS analyses of hypervelocity impact features on IDE sensors and other high purity substrates. Associated analytical problems have been identified and possible solutions proposed. Surface contamination proved to be the most complicating factor in interpretation of SIMS data. Distribution of integral and on-orbit accumulated contamination will be addressed by inducing several hypervelocity impacts with particles of known composition and several "blank" discharges on active flight and non-flight sensors using an accelerator and a pulsed laser, respectively. SIMS analyses of these features should provide significant insight into this issue and permit useful interpretation of data collected to date and in future analyses.

ACKNOWLEDGEMENTS

The authors extend their gratitude to E. Zinner of Washington University and R. F. Davis of North Carolina State University for the loan of their LDEF witness plates. This work was supported under NASA Langley Research Center grants NAG1-1214 and NAG1-1218 to North Carolina State University and ISST, respectively.

REFERENCES

1. J. D. Mullholand, S. F. Singer, J. P. Oliver, J. L. Weinberg, W. J. Cooke, P. C. Kassel, J. J. Wortman, N. L. Montague and W. H. Kinard: IDE spatio-temporal impact fluxes and high time-resolution studies of multi-impact events and long-lived debris clouds. First LDEF Post-Retrieval Symposium. NASA CP-3134, 1992.

2. S. Amari, J. Foote, E. K. Jessberger, C. G. Simon, F. J. Stadermann, P. Swan, R, Walker and E. Zinner: SIMS analysis of extended impact features on LDEF experiment A0187-2. First LDEF Post-Retrieval Symposium. NASA CP-3134, 1992.

3. F. Horz, R. P. Bernhard, T. H. See, J. Warren, D. E. Brownlee and M. Laurance: Preliminary results from the Chemistry of micrometeoroids experiment (A0187-1). First LDEF Post-Retrieval Symposium. NASA CP-3134, 1992.

4. J. C. Mandeville: Study of meteoroid impact craters on various materials (A0138-1) and Attempt at dust debris collection with stacked detectors (A0138-2). First LDEF Post-Retrieval Symposium. NASA CP-3134, 1992.

5. E. Zinner, H. Kuczera and N. Pailer: Simulation experiments for the chemical and isotopic measurements of interplanetary dust on LDEF. 13th Lunar and Planetary Science Conference Abstracts. 1982.

6. B. A. Stein (editor): *Preliminary Report on LDEF-Related Contaminants*. (Available through NASA/LaRc LDEF Office) 1990.

7. B. A. Stein and G. Pippin: Preliminary findings of the Materials Special Investigation Group. First LDEF Post-Retrieval Symposium. NASA CP-3134, 1992.

8. R. P. Bernhard, D. E. Brownlee, M. R. Laurance, W. L. Davidson and F. Horz: Survey-type analyses of projectile residues on select LDEF surfaces and craters. 22nd Lunar and Planetary Science Conference Abstracts, 1991.

9. J. A. M. McDonnell and K. Sullivan: Foil perforation particulate impact records on LDEF MAP A0023: Incident mass distributions. First LDEF Post-Retrieval Symposium. NASA CP-3134, 1992.

10. T. See, M. Allbrooks, D. Atkinson, C. Simon and M. Zolenski: *Meteoroid and Debris Impact Features Documented on the Long Duration Exposure Facility*. NASA/JSC Publication #24608, 1990.

11. B. G. Cour-Palais: Results of examination of the Skylab/Apollo windows for micrometeoroid impacts. Proc. 10th Lunar and Planet. Sci. Conf., p. 1665-1672 (1979).

12. U. S. Clanton, H. A. Zook and R. A. Schultz: Hypervelocity impacts on Skylab IV/Apollo windows. Proc. Lunar and Planet. Sci. Conf., p. 2261-2273 (1980).

13. R. G. Wilson, F. A. Stevie and C. W. Magee: *Secondary Ion Mass Spectrometry,* p App.E.11 and App.E.17 (J. Wiley and Sons) 1989.

Table 1. Summary of morphology and SIMS analytical data for impacts on IDE Al/Si sensor surfaces. SIMS analyses were for positive ions only. Results for Al and Si are excluded. No impactor debris was identified in any features using EDS. Small letters denote the presence of only a trace concentration of the species. Sequentially listed elements were present in the same area.

Impact No.	Crater dia.(μm)	Discharge Area dia.	Relative Abundance of Elements Found in Crater	Discharge Area	Rim	Notes
Sensor 293 (row 9, leading edge)						
1	17	79	Mg,K,Fe	-	Ca>Fe (spot)	
2	24 x 31	74	Mg>K	Fe>Ca	Fe>Mg,Ca>K (ring)	(Ca,Fe) all around feature
3	18	68	K	Fe>>K	Fe>Mg,Ca>K (ring)	(Ca,Fe>>K) all around feature
4	12	70	Fe>>Mg	Fe>K	Mg,Fe>>K (ring)	Ca all around feature; Fe in crater is high conc. spot
5	22 x 28	59	-	-	C>Mg,K (ring)	(Fe>Ni>Mg) spot away from feature; Ca all around
7	12	65	-	-		(Fe>Mg,Cr>Ni>K,Ca) particle just outside feature
Sensor 300 (row 3, trailing edge)						
1	36 x 54	91	Mg	Fe,Ti and Na,Mg,K,Ca spots in spall zone		large impact, 138 μm wide asymmetric spall zone
2	13 x 18	55	Na	-	C (ring)	(Na,Mg,K,Ca) spot outside of feature
3	12	44	Na,Mg,K	-	C (ring)	(Ca,Fe>Mg>>Na,K) spot outside of feature
4	13	46	-	-	C (ring)	(Na,Mg,K,Ca>Fe,Ti) particle next to crater identified as salt crystal in SEM/EDS
5	11	43	Na,Mg,K	-	C (ring);C,Fe> Na,Mg,Cu (spot)	
6	10	39	-	-	C (ring)	
7	12	46	Ti>Na>>K	-	C>Na (ring)	
8	12	50	Na,K	Na,Mg,K,Ca,Ti	Mg,Ca,Ti (ring)	Ca all around feature
9	11	60	Fe	-	-	(Na,K) spot outside Ca all around outside

Table 2. Summary of germanium witness plate impact feature dimensions and analyses. All impacts identified during a 100X optical scan are listed. Ratios of inner and outer spalls (not including attached chips or fracture zones) to crater dimensions, S_I/C and S_O/C, are for maximum spall dimensions and average crater diameters. Craters marked with an asterisk (*) and/or a triangle (Δ) were analyzed for impactor debris using SIMS and/or EDS, respectively.

Impact I.D.	Crater dia. (μm)	Inner Spall dia. (μm)	Outer Spall dia. (μm)	S_I/C	S_O/C	Tentative Impactor Debris Identified
Ge2A-						
1	30	50	75 x 88	1.67	2.93	-
2	6	8	10 x 13	1.33	2.17	-
3	8	15	22 x 25	1.88	3.13	-
Δ4	7	20	26 x 45	2.82	6.36	no
5	10	18	28 x 34	1.80	3.40	no
*6	7	14	-	2.00	-	yes
*7	8	15	28	1.88	3.50	yes
8	10	22	37 x 46	2.20	4.60	-
Δ9	7 x 10	15	-	1.83	-	no
Δ10	6	14 x 16	-	2.38	-	no
*12	6	14	-	2.33	-	yes
*13	8	20	24 x 26	2.50	3.25	yes
14	7	13	-	1.86	-	-
*15	8	16	18 x 22	2.00	2.75	yes
16	8	18	22 x 35	2.25	4.38	-
*Δ17	71	167	354 x 379	2.35	5.34	yes
*18	17	27	44 x 59	1.59	3.47	yes
19	11	27	-	2.45	-	-
Δ20	188	600	1070	3.19	5.69	yes
Δ21	2.5	5.0	-	2.00	-	no
Ge2B-						
1	12	24	27 x 42	2.00	3.50	-
*Δ2	14	32	48	2.29	3.43	yes
*Δ3	6	17	19 x 35	2.83	5.83	yes
*Δ4	17	41	80	2.41	4.71	yes
5	7	18	-	2.53	-	-
*6	15	38		2.33	5.87	yes
Δ7	60	143	293	2.39	4.89	yes
*Δ8	15	35	73 x 88	2.33	5.87	yes
Δ9	6	10	13 x 17	1.67	2.83	no
10	6	10 x 14	-	2.66	-	-
Δ11	3.2	8	-	2.41	-	no
Δ12	6	13	-	2.17	-	no
*Δ13	22	55	120	2.50	5.45	yes
Δ14	8	17 x 19	-	2.39	-	no
15	15	40	-	2.67	-	-
Δ16	4.5	11	13 x 18	2.44	4.04	no

Table 3. Summary of elemental analysis data for tentative hypervelocity impactor debris identified in impact features in germanium witness plates mounted on LDEF tray B12. Listed species were found in the craters and/or spall zones. SIMS analyses were for positive ions only. Small letters denote the presence of only a trace concentration of the species. Sequentially listed elements were present in the same area. Readers are cautioned on drawing conclusions about impactor origins based on these data due to unresolved contamination interferences.

Impact No.	Crater dia.(μm)	Analysis Method	Relative Abundance of Elements Found in Crater or Spall Zone	Notes
Ge2A-				
6	7	SIMS	Al,K>Na,Mg,Si,Ca,Fe,Zn>Ti,	
7	8	SIMS	C,Na,K,Ca>Mg,Al,Ni,Fe,Cu	
12	6	SIMS	Na,Mg,Si,K>Ca	(Na,K,Ca,Ti,Zn,Cu) spot just below impact site
13	8	SIMS	Si>Na,Mg,Al,K,Fe	(C,Na,Al,Si,K,Ca>Fe) spot near impact site
15	8	SIMS	Na,Mg,Fe	
17	71	EDS	Al,Si	In central shatter zone only. Not seen in SIMS
17	71	SIMS	Ca,Fe (only in spall zone)	(Na,Mg,Al,Si,K,Ca,Fe) spots all around impact site
18	17	SIMS	Si,Fe>Mg	(C,Na,Mg,Al,Si,K,Ca>Ti,Cr) spot in vicinity of impact site.
Ge2B-				
2	14	SIMS	Si>Na	(Na,Fe,Cu) spot near impact site. Nothing seen in EDS.
3	6	SIMS	Na,Mg,Si>K,Al	Nothing seen in EDS.
4	17	SIMS	Mg>Na (covers impact feature and ~1/2 of image field)	(Na,Mg,Fe>Si,K,Ca) present outside impact area over ~1/2 of image field. Nothing seen in EDS.
6	15	SIMS	Mg,Si>Na,K	Na in image area all around but away from impact site; (Ca,Mg) spot in image area away from impact site.
7	60	EDS	Al,Si>Cu>Zn>S	Not analyzed in SIMS
8	15	SIMS	Na ,Mg,Si,Ca,Fe>K	(Al,Si>Na,Mg,K,Ca,Fe,Zn>Ti, Cr) spot in image field away from impact site. Nothing seen in EDS.
13	22	SIMS	Na,Mg,Si>K	(Mg,Al,Si,K,Ca,Fe) spots all around impact site

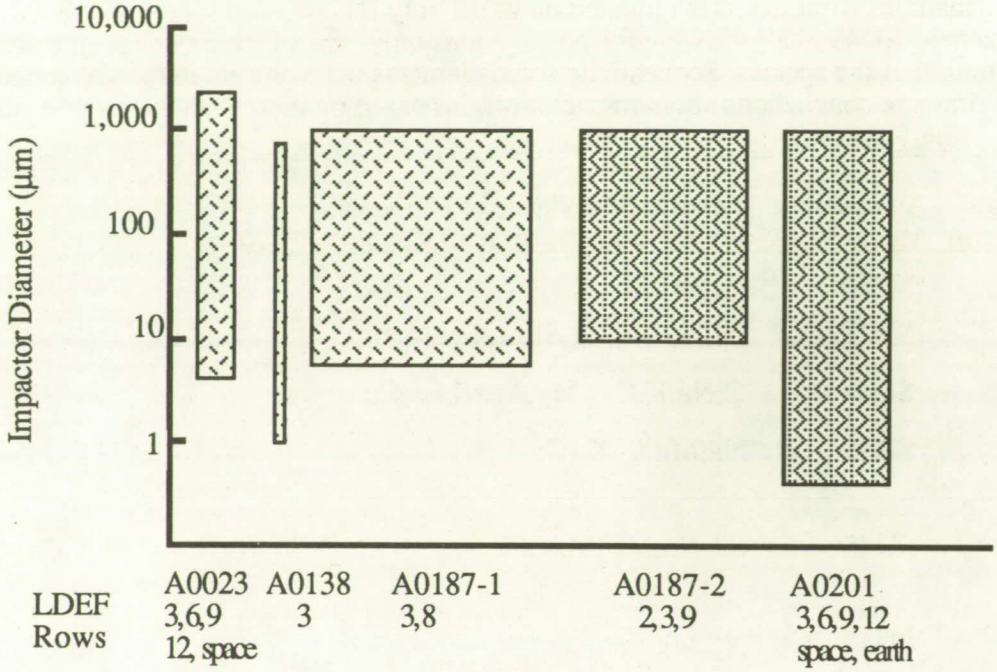

Figure 1. Range of impactor sizes characterized for LDEF micrometeoroid experiments. Width of boxes is proportional to the amount of experiment surface area exposed to space. EDS analyses = SIMS analyses =

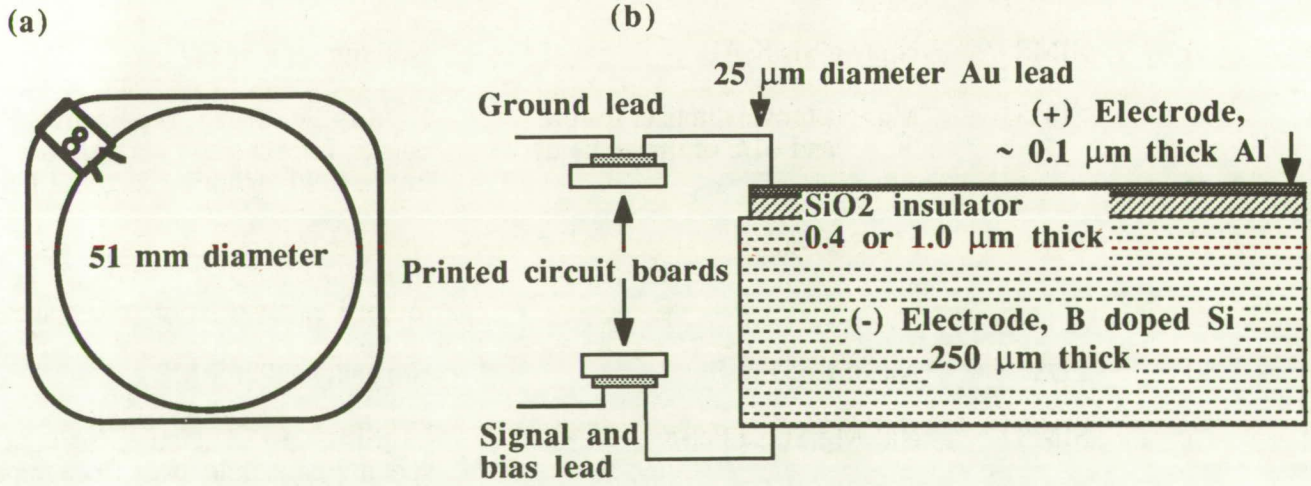

Figure 2. Interplanetary Dust Experiment electro-active sensor. (a) Overall configuration of a mounted sensor. (b) Details of the electrical connections to the sensor.

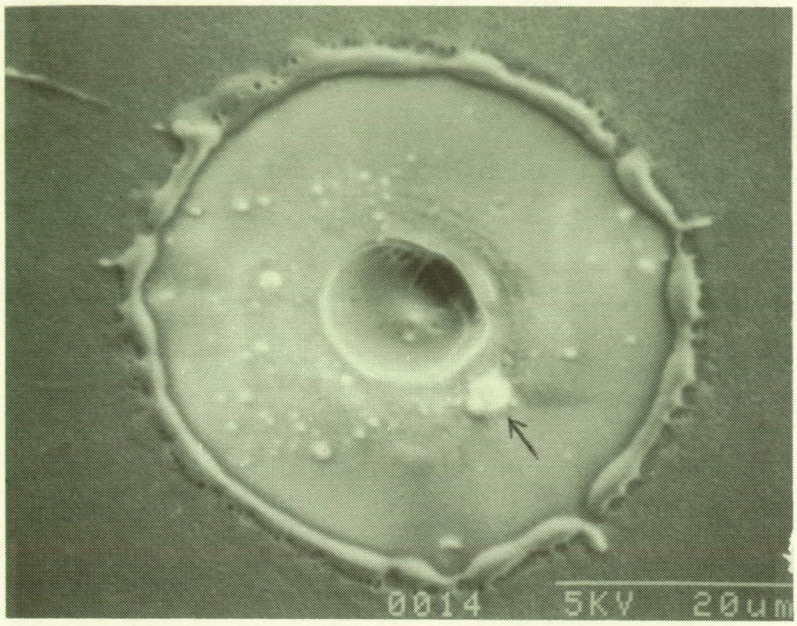

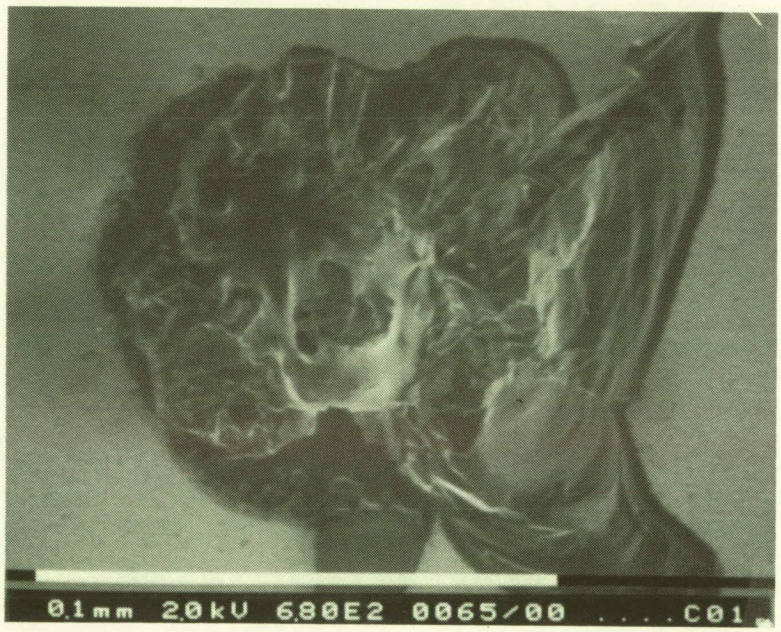

Figure 3. Small (top, No. 300-4) and large (bottom, No. 300-1) impacts on an IDE sensor . Note the four distinct morphological regions of the smaller feature: the central crater, the Al vaporization zone, the Al melt rim, and the area outside of the feature. An arrow points to a salt crystal identified in the SEM/EDS and is representative of one type of surface contamination. The larger impact feature has a spall zone that has obliterated ~1/2 of the Al vaporization zone and rim.

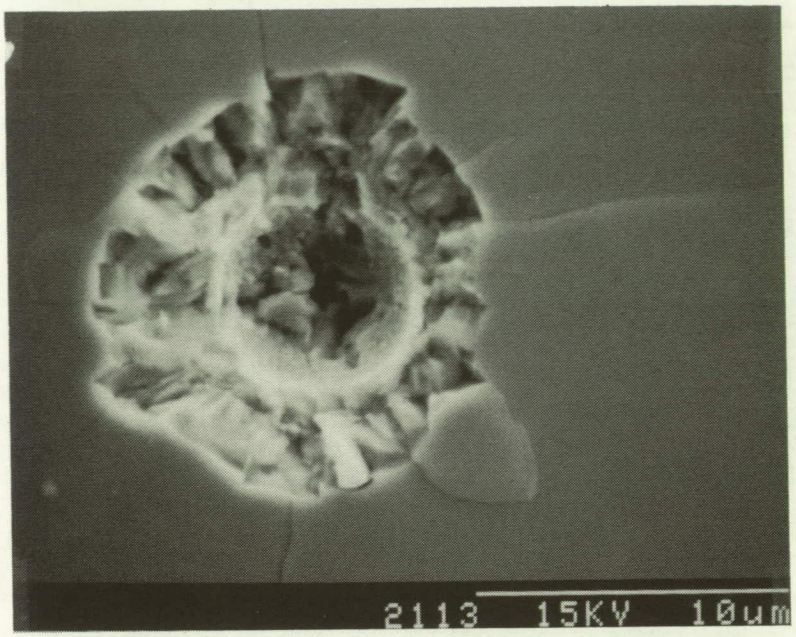

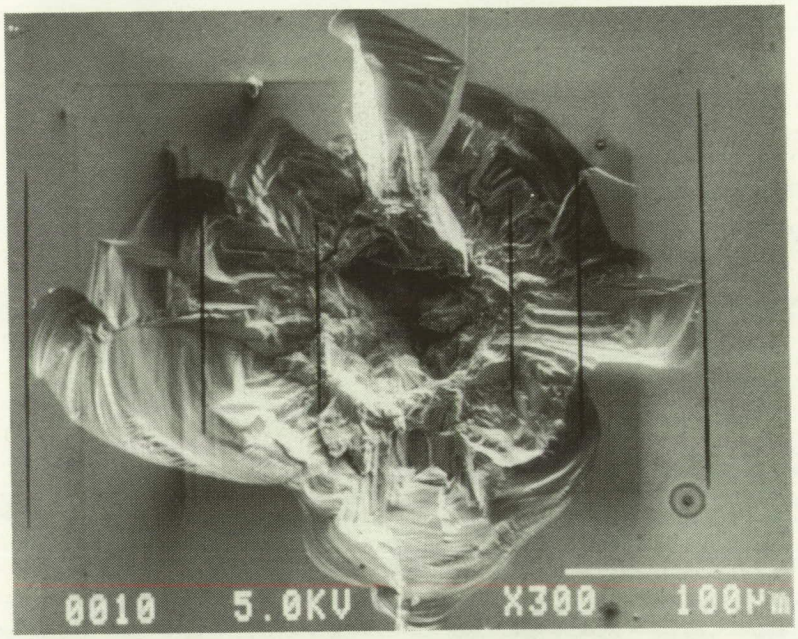

Figure 4. A small (top, Ge2B-12) and large (bottom, Ge2A-17) impact in a Ge witness plate. Note the residual hemispherical crater liner in the small impact compared to the central shatter zone in the large impact. The inner and outer spall zones are indicated on the large crater. Si and Al residue was found in the large crater with EDS, but was not indicated with SIMS presumably due to primary beam shadowing effects.

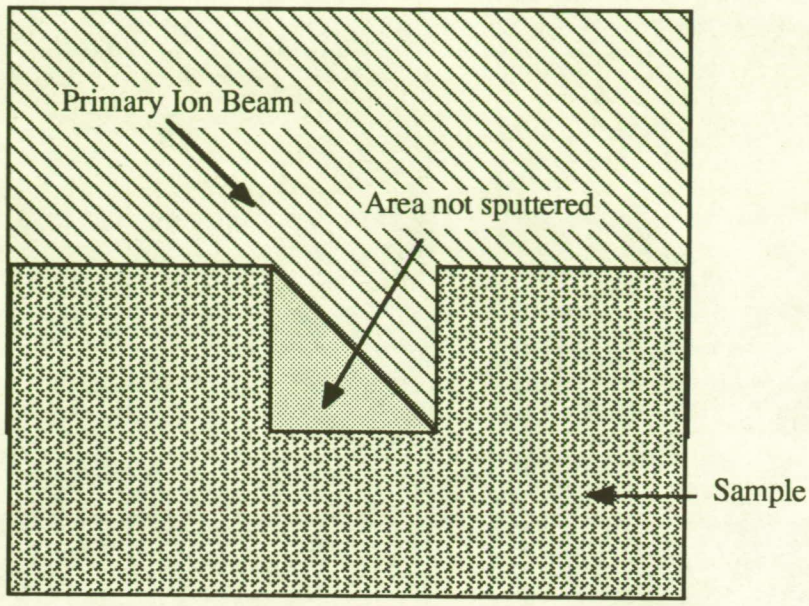

Figure 5. SIMS shadowing effect on high aspect ratio features.

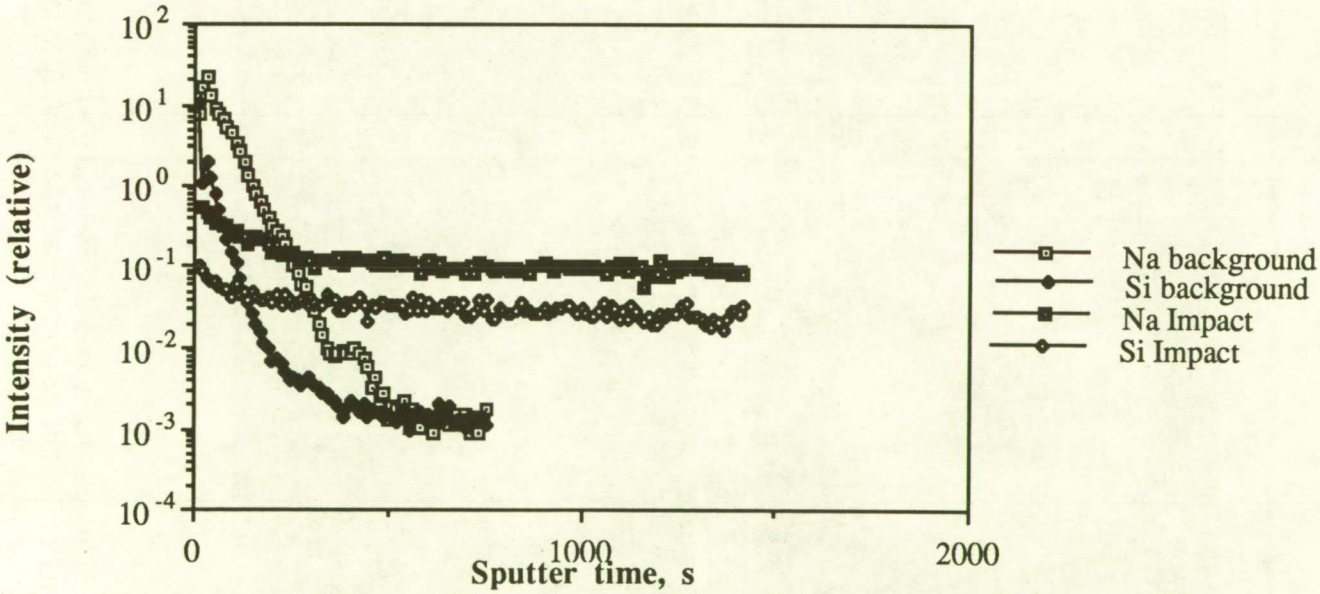

Figure 6. Comparison of depth profiles of the silicaceous contaminant layer over an impact feature and background area on Ge witness plate from LDEF row 12.

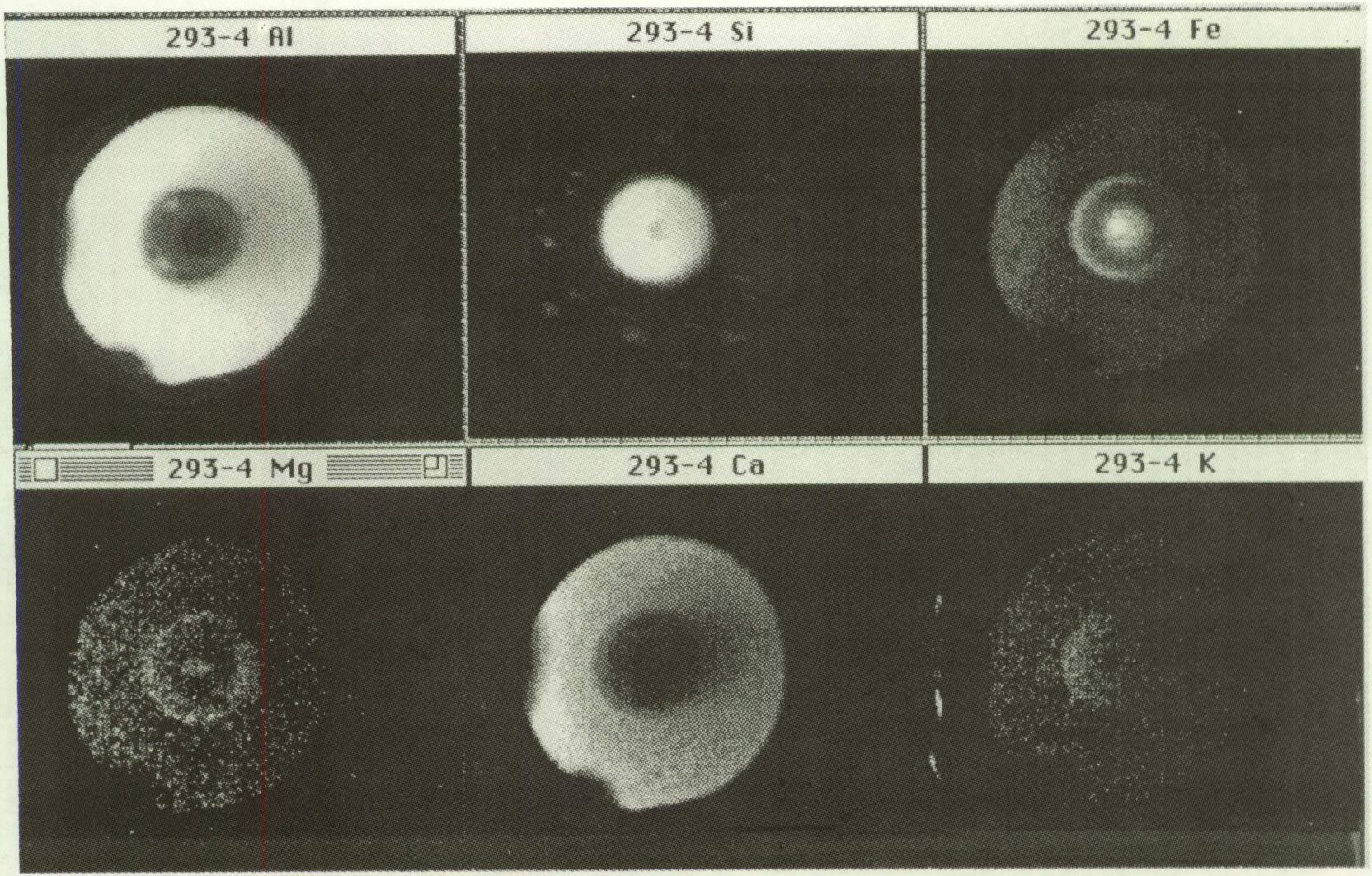

Figure 7. Unnormalized, two-dimensional positive ion images of Al^+, Si^+, Fe^+, Mg^+, Ca^+ and K^+ observed in impact No. 293-4. Note high Fe signal in the central crater and Fe/Mg in the feature's discharge rim. Dark areas on the right sides of all images are caused by a detector anomoly.

LDEF IMPACT CRATERS FORMED BY CARBON-RICH IMPACTORS: A PRELIMINARY REPORT

T. E. Bunch
NASA Ames Research Center
Moffett Field, CA 94034
Phone: 415/604-6058, Fax: 415/604-6779

F. Radicati di Brozolo, Ronald H. Fleming, and David W. Harris
Charles Evans and Associates
Redwood City CA 94063
Phone: 415/369-4567, Fax: 415/369-7921

Don Brownlee
University of Washington
Seattle, WA 98195
Phone: 209/543-8575, Fax: 209/543-0403

Terrence W. Reilly
Hitachi Scientific Instruments
Mountain View, CA 94043
Phone: 415/961-0461, Fax: 415/961-7259

SUMMARY

Two impact craters found in Al from LDEF experiment tray A11E00F have residues concentrated in the bottoms, along the walls, and on the top of overturned rims. Analyses indicate a "chondritic" compositional signature (Si, S, Ca, Fe, Mg, and Ni) for the bulk residue. In one crater (# 74) round to irregular silicate grains (crystalline in appearance) are overlain by carbon. In addition, carbon also partially covers the crater walls, the top of the raised/overturned rim and extends outwards from the crater. The second crater (# 31) also contains carbon with similiar distribution in and about the crater, although the silicate residue appears to be glassy. Silver, I, K and F (possibly some of the Ca, S, and Cl) appear to be contaminates as well as analyzed aromatic carbonaceous species associated with the raised rim and the area surrounding the crater. The origin of the impactors is assumed to be extraterrestrial. The existence of impactor residue in the two craters implies impact velocities of ≤ 6 km based on experimental hypervelocity impact studies.

INTRODUCTION

Cursory examination of LDEF by the Post Retrieval Examination Team (ref. 1) showed the existence of thousands of impact craters but a low percentage of craters with impactor debris or ejecta sprays. While the study of this debris is of interest to many science disciplines, it is of particular interest to exobiology in terms of residual carbonaceous and biogenic element contents. Moreover, a comprehensive study of impactor residue could provide information concerning IDP (interplanetary dust particle) impactor source (cometary, asteroidal, or lunar) and the characteristics of IDP carbonaceous materials. We report here the preliminary morphological and compositional study of two impact craters with carbonaceous impactor residues.

ANALYTICAL TECHNIQUES, SAMPLES, AND METHODOLOGY

Aluminium panels from LDEF experiment tray A11E00F (F. Hörz, P. I.) were scanned with a microscope for crater identification. Craters with possible partially intact impactor debris were "punched out" from the main piece to a sample size of 7 mm. These craters were further scanned with an SEM (scanning electron microscope) in order to study crater morphology and to confirm the existence of impactor residue. Of the hundreds of observed craters < 10% were found to have residues and of these only a few percent (e. g., #31 and #74) had significant intact residues. SEM/EDX (energy dispersive X-ray spectroscopy) analyses indicate that both of the residues have a "chondritic" compositional signature, i. e., presence of Si, Al, Ca, Mg, Fe, and Ni, among other elements, which strongly suggests extraterrestrial origin.

These samples were then subjected to an imagery and analytical protocol that included FESEM (field emission scanning electron microscopy), AES/SAM (Auger electron spectrometry/scanning Auger microscopy, and TOF/SIMS (time-of-flight secondary ion mass spectrometry). AES/SAM was performed using a Perkin-Elmer PHI 660 instrument operated at 10kV. Beam diameter and hence, imaging resolution is ≈ 1000 Å. Both point analysis and multielement mapping were performed. TOF/SIMS analyses were performed using the CHARLES EVANS & ASSOCIATES instrument (ref. 2). The instrument was operated in the ion microprobe mode using a microfocused Ga^+ beam as the sputtering source. After completion of these analyses, a molecular identification study of carbonaceous materials will be accomplished by LIMS (laser ionization mass spectrometry) and, finally, the residues will be excavated, microtomed into ultrathin wafers and studied for phase identification and crystal structure by TEM (transmission electron micoscopy) methods.

CRATER AND IMPACTOR MORPHOLOGY

Crater #74 Morphology

Crater #74 is 119 micrometers in diameter, measured from the points in the crater walls where the plane of the unraised surface intersects the crater (not measured from points on the raised rim walls). The depth/diameter ratio is 0.59 consistent with the average value of 0.6 for other LDEF craters (ref. 1). Figure 1 shows vertical and slighlty tilted views of the crater. Impactor residue is concentrated in the bottom with impact melt "splash" lining the crater walls. The overturned raised rim shows irregular

patches of dark to light material that consist mostly of carbon with lower amounts of Fe, Mg, Na, K, Ca, Cl, Ag, I, and F (see next section). Figure 2 shows two views from the crater edge to the bottom. Impactor debris is mostly covered by an unknown thickness of carbon. The frozen impact melt splash seen on the walls in Fig. 2b consists mostly of the Al target admixed with minor amounts of "chondritic" elements which are thinly covered by carbon. Detailed resolution of splash morphology is shown in Fig. 3. Possible intact silicate grains are shown in Fig. 4 where rounded to irregular shaped material (which may be only slightly disturbed from impact) is covered by carbon and very small (hundreds of nanometers), dark blobs.

Crater # 31 Morphology

This crater is 158 μm in diameter with a depth/diameter ratio of 0.8. Whereas crater #74 contains partially intact material, the impactor residue in #31 was completely melted (Figs. 5 and 6). The impactor appears to have melted on impact, thus, lining the crater bottom and walls with glassy impact melt. Twisted glass is present in the bottom where the morphology suggests freezing of viscous, molten material during splash rebound after impact. Small glassy beads line the upper walls of the crater (Fig. 6). Even though the impactor appears to have completely melted, a "chondritic" compositional signature remains together with a rather large amount of carbon, at least on the residue surface (see the next section).

ANALYTICAL RESULTS

Auger Electron Spectrometry/Scanning Auger Microscopy

Auger survey analyses of crater # 31 were performed in the bottom of the crater, 25μm and 1 mm away from the edge of the crater, respectively. Table 1 gives examples of some elemental concentrations, which were calculated by using nominal sensitivity factors, for three locations Carbon concentration varies from ≈ 40 at.% at the crater bottom to 6 at. % 1 mm from the crater. Similar concentrations were found for crater #74. In addition, the partially intact impactor debris in the bottom of crater 74 has surface C concentrations ranging from 72 to 54 at. %. Figure 7 is a 3-element map of crater 31 and the surrounding area in which the distribution of Al, C, and F is shown. Each image contains 128 x128 pixels. Carbon-rich areas are observed inside and outside the crater. The F-rich area outside the crater is likely to represent cross contamination from adjoining experiment trays.

Time-Of-Flight/Secondary Ion Mass Spectrometry

The resulting mass spectra and images are shown in Figures 8 through 13. Figure 8(a & b) shows negative and positive ion mass spectra of crater 31 and Figure 9(a & b) shows negative and positive ion mass spectra for crater 74. They were acquired from a rastered region 200 x 200 μm in size, which covers the craters and surrounding Al surface. The intense signals of Ag^+, I^- and AgI_2^-observed in the positive and negative ion mass spectra indicate the presence of silver iodide contamination. Organic fragment ions such as $C_8H_5O_3^+$ (m/z 149) are also likely surface contamination products.

Figures 10-13 are examples of mass separated images from crater 74. Species such as Mg^+ (Fig.10) and Na^+ , which are concentrated within the crater, appear to be intrinsic to the impactor. Iodine (Fig. 11), K^+ (Fig. 12), and some of the Ca^{2+} (Fig. 13), which are concentrated on the raised

rim, are probably contaminates. Hence, the ability to map the distribution of species is a powerful aid in the interpretation of a mass spectrum.

INTERPRETATION

From this limited crater/impactor preliminary study, no conclusions can be made regarding extraterrestrial impactor sources, impactor bulk compositions, grain crystal structures (of apparent intact grains), and the character of carbonaceous molecular species, if any. On-going laser ionization mass spectrometry, isotopic ratio imaging, and TEM studies may produce more significant and quantitative information. However, a few important aspects of this study are evident:

(1) The "chondritic" signatures of both impactors strongly indicate an unspecified extraterrestrial source.

(3) The apparent high carbon content of both impactors would seem to be, at this time, unusual with regard to an asteroidal (meteoritic) source. Known carbonaceous chondrites have nominal C contents lower than what we have tentatively assumed for the two impactors. Some cometary particles (CHONs) are higher in C content, compared with known meteorites, but little is known about their overall quantitative compositions and characteristics (e. g., ref. 3).

(3) Organic/non-organic contaminations are abundant and care should be taken in interpreting impactor compositions (see also ref. 4, these Proceedings).

(4) The characteristics and amounts of residual impactors in both craters imply impact velocities of ≤ 6 km/s based on experimental impact studies (ref. 5).

ACKNOWLEDGEMENTS

We thank M. Laurance for assistance in sample preparation and SEM-EDX analyses and the NASA OSSA Exobiology 199-52-12 and OAET 506-48 Programs for partially supporting this work.

REFERENCES

[1]. See T., M. Allbrooks, D. Atkinson, C. Simon amd M. Zolensky, Meteoroid and debris impact features documented on the Long Duration Exposure Facility a preliminary study. *Planet. Sci Branch.Publ. #73 (JSC # 24608)*, 1990.

[2]. Schueler B., P. Sander, and D. A. Reed, A time-of-flight secondary ion microscope. *Vacuum* **41**, 1990, pp. 1661-1664.

[3]. Langevin Y., J. Kissel, J-L. Bertaux and E. Chassefiere, First statistical analysis of 5000 mass spectra of cometary grains obtained by PUMA 1 (Vega 1) and PIA (Giotto). *Astron. Astrophys.* **187**, 1987, pp 761-769.

[4]. Hörz F., R. P. Bernhard, T. H. See, J. Warren. D. E. Brownlee and M. Laurance, Preliminary results from the chemistry of micrometeoroid experiment (AO 187-1). *Proceedings, First LDEF Post-Retrival Symposium NASA CP* 3134, 1992.

[5]. Bunch T., F. Radicati, R. H. Fleming, D. W. Harris, D. Brownlee and M. Allbrooks, A study of LDEF Carbon-rich impactor residues from two craters compared with hypervelocity experimental results. *Proceedings, Hypervelocity Impacts in Space*.

Table 1. Auger survey surface analyses of LDEF Crater 31 and surrounding areas (expressed as atomic %).

Element	Crater bottom	25 microns away	1 mm away
O	34.4	51.3	34.4
Si	2.0	5.7	5.4
F	1.12	1.12	1.0
S	0.24	1.02	1.0
C	39.6	12.7	6.1
Mg	1.9	1.0	n.d.
Na	n.d.	0.83	n.d.

These are surface/near surface analyses only and do not imply bulk analyses. AES depth resolution is 2-30 nm, thus if C covers silicate materials (in this case, glasses) their elemental signals are greatly surpressed or are completely missing.

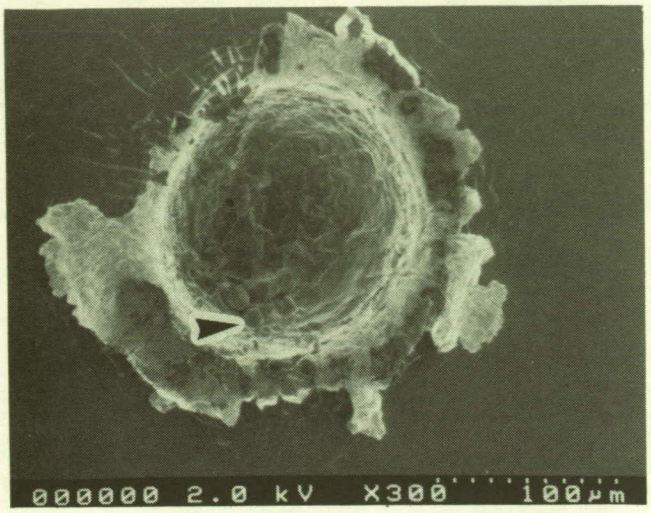

a

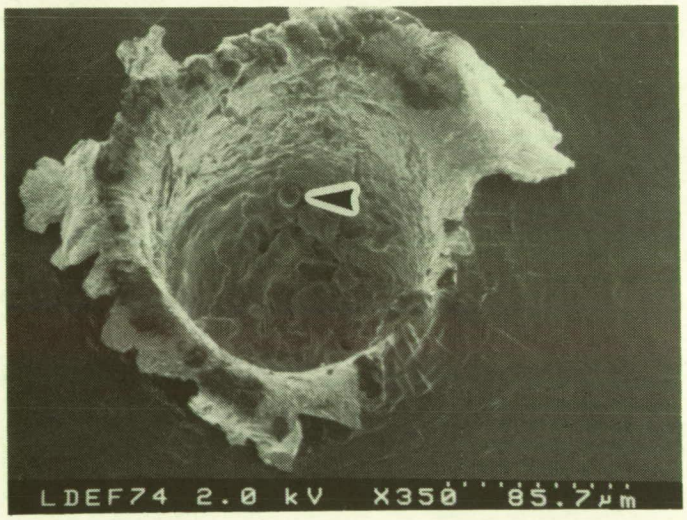

b

Figure 1. (**a**) FESEM BSE (backscattered electron) image of crater #74. Arrow points to round residual grain which is used as a reference in other figures. Fractures in Al that radiate away from the crater (NW direction), probably resulted from ductile/brittle fracturing during uplifting of the rim. Carbonaceous material (dark; curved arrow) is shown on the top of the overturned, raised rim. (**b**) Same crater as in (a) (slightly tilted and rotated 180°). FESEM BSE image. Note partially intact residual impactor in the crater bottom. 10 division scale is given in microns in the lower right corner of all FESEM images.

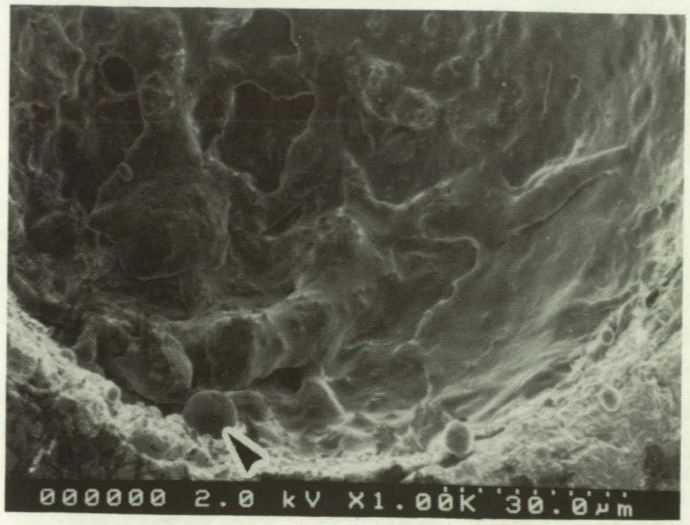

a

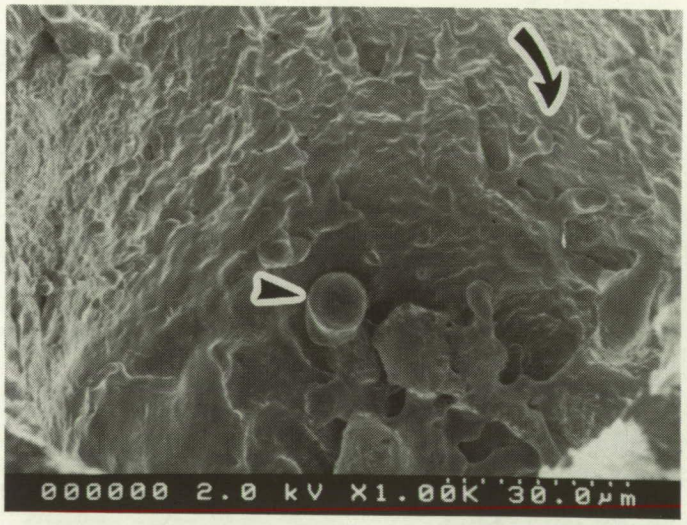

b

Figure 2. (**a**) A view (FESEM BSE image) from the top of the rim into the bottom of crater #74. Note irregular lumps (partially intact impactor) and melt/splash material. The area is mostly dark due to carbon which coats most of the debris. (**b**) Similar view but opposite the rim in (a). Curved arrow points to upward moving frozen melt .

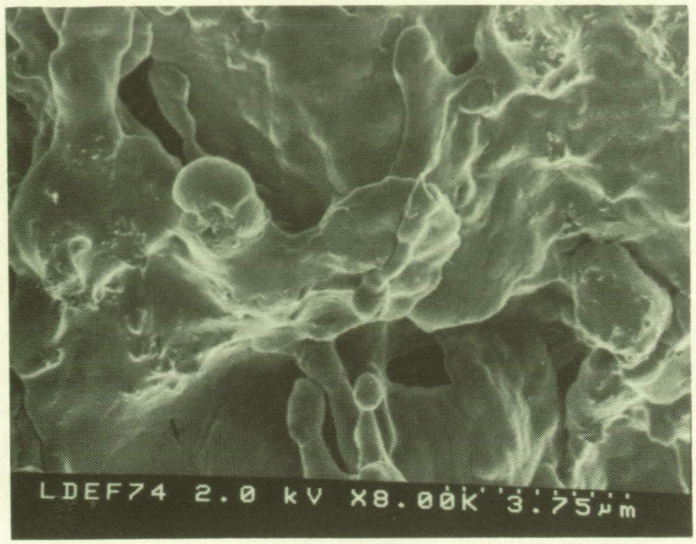

a

b

Figure 3. (**a**) Melt splash on the wall of crater #74. (**b**) Partially melted impactor grains that are coated with glass. Arrow points to twisted, pinched glass. (FESEM BSE image).

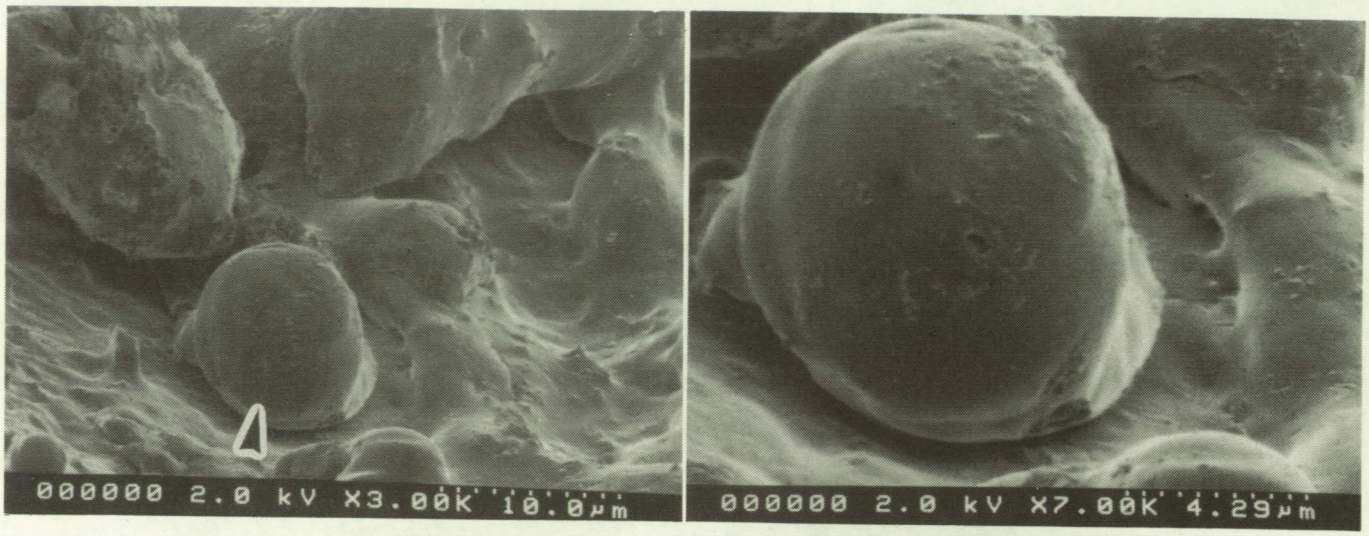

a b

Figure 4. (**a**) Round to irregular shaped impactor debris coated with carbon. Because of the morphology and qualitative composition of Mg and Si, the rounded grain may be olivine. (**b**) Enlarged view of (a). (FESEM BSE image).

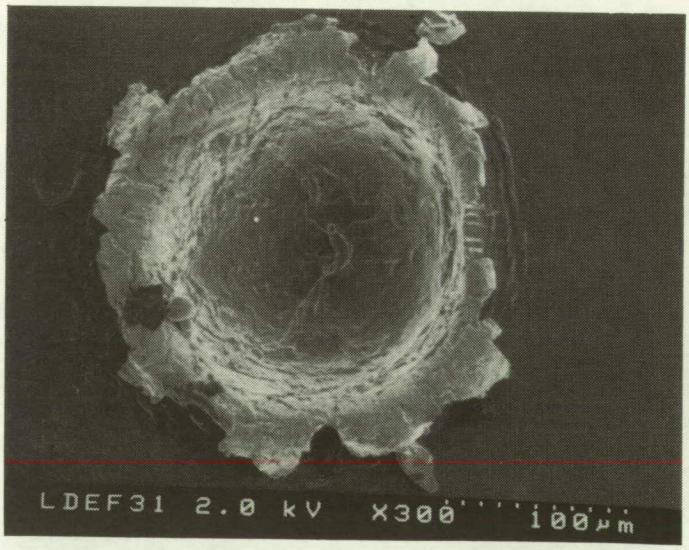

Figure 5. Crater #31. Impactor residue is probably all glass. (FESEM BSE image).

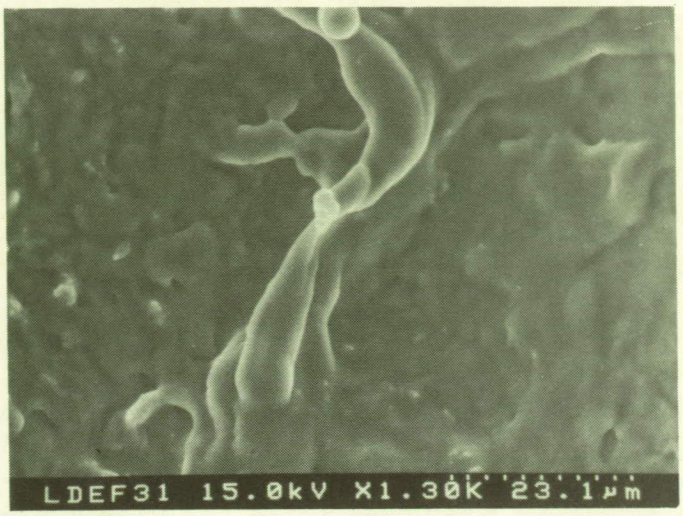

a

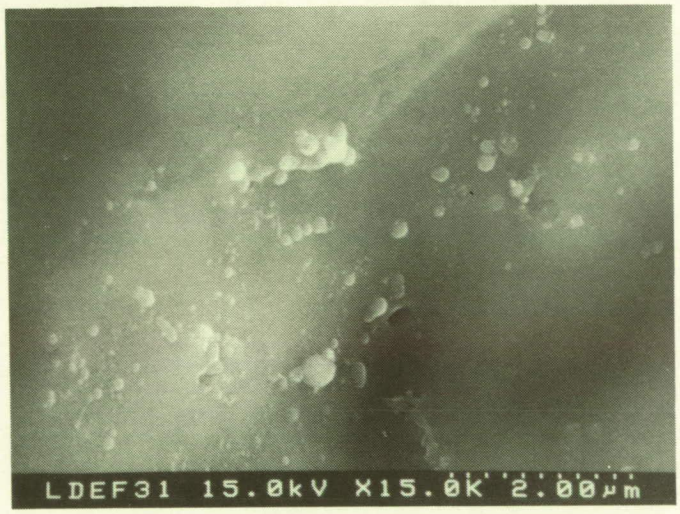

b

Figure 6. (**a**) Enlarged view of crater bottom glassy impactor debris which is mixed with melted Al. (**b**) Small glassy droplets near the top of the crater wall. The light droplets may be metal or sulfides. (FESEM BSE image).

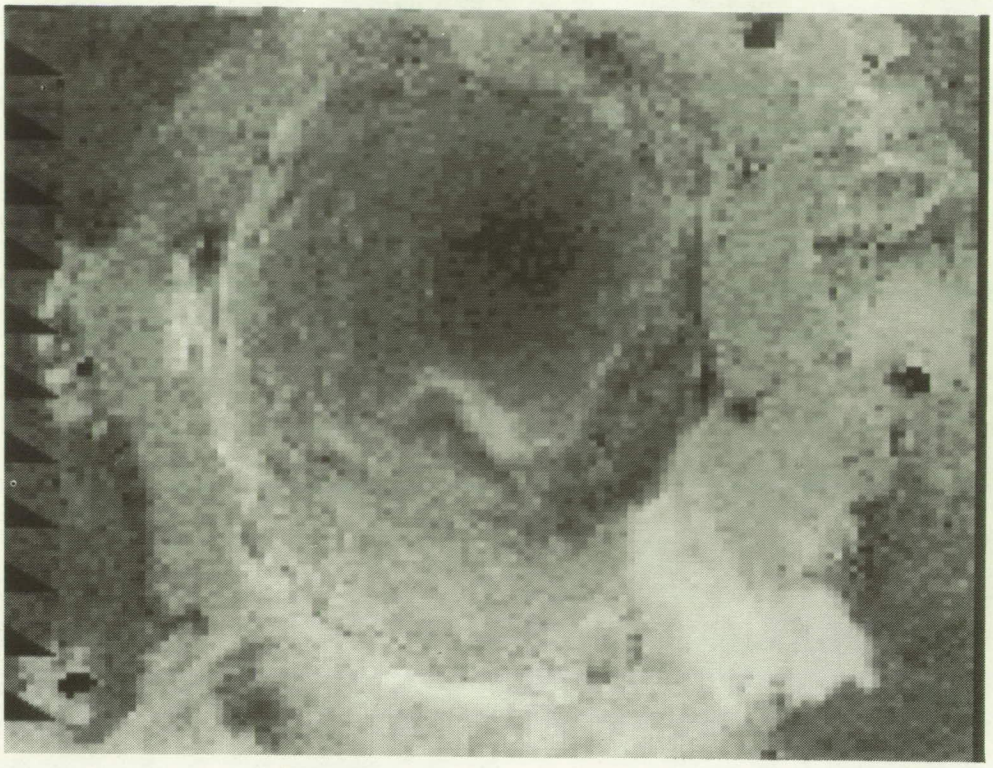

Figure 7. Three-element SAM map (Al = blue; carbon = green; F = red) of crater 31.

(See color photograph, p. 601.)

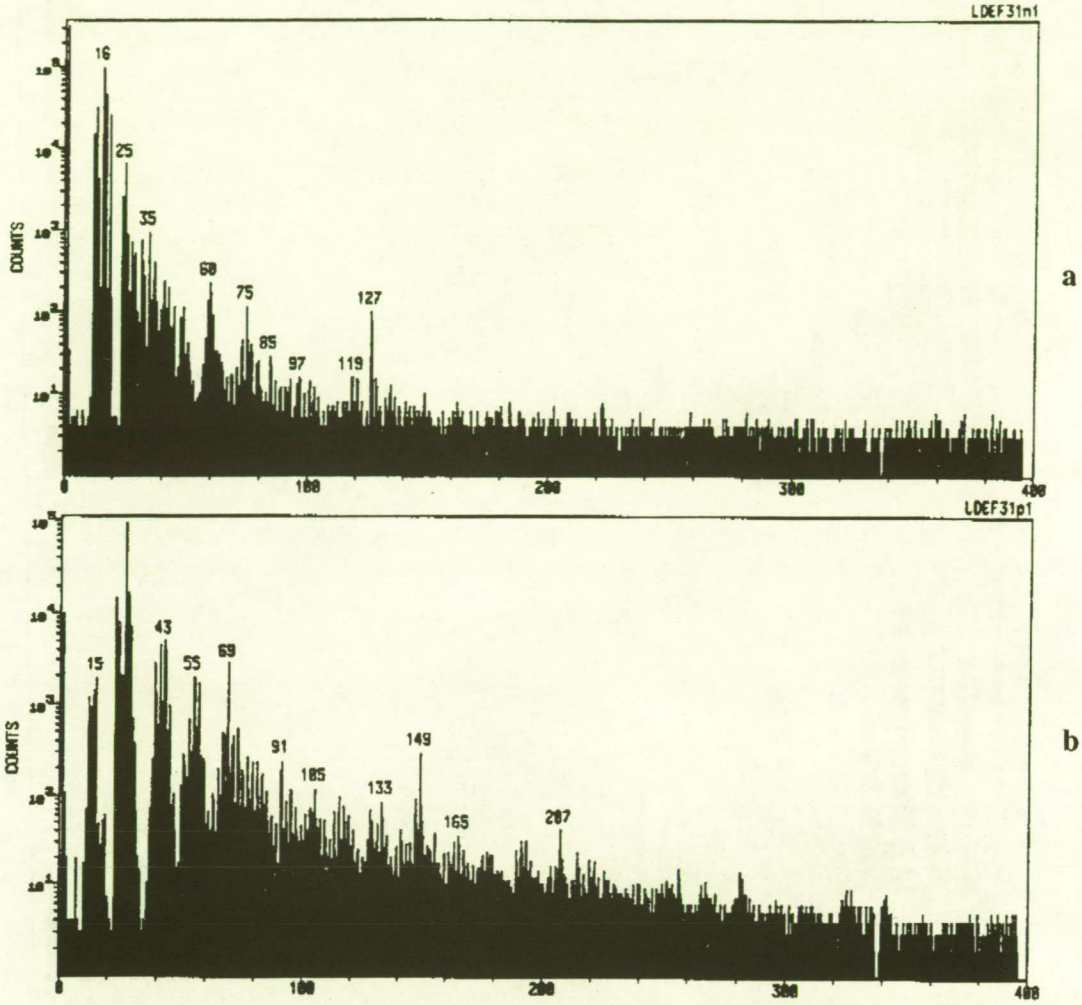

Figure 8. TOF/SIMS negative (**a**) and positive (**b**) spectra of crater 31.

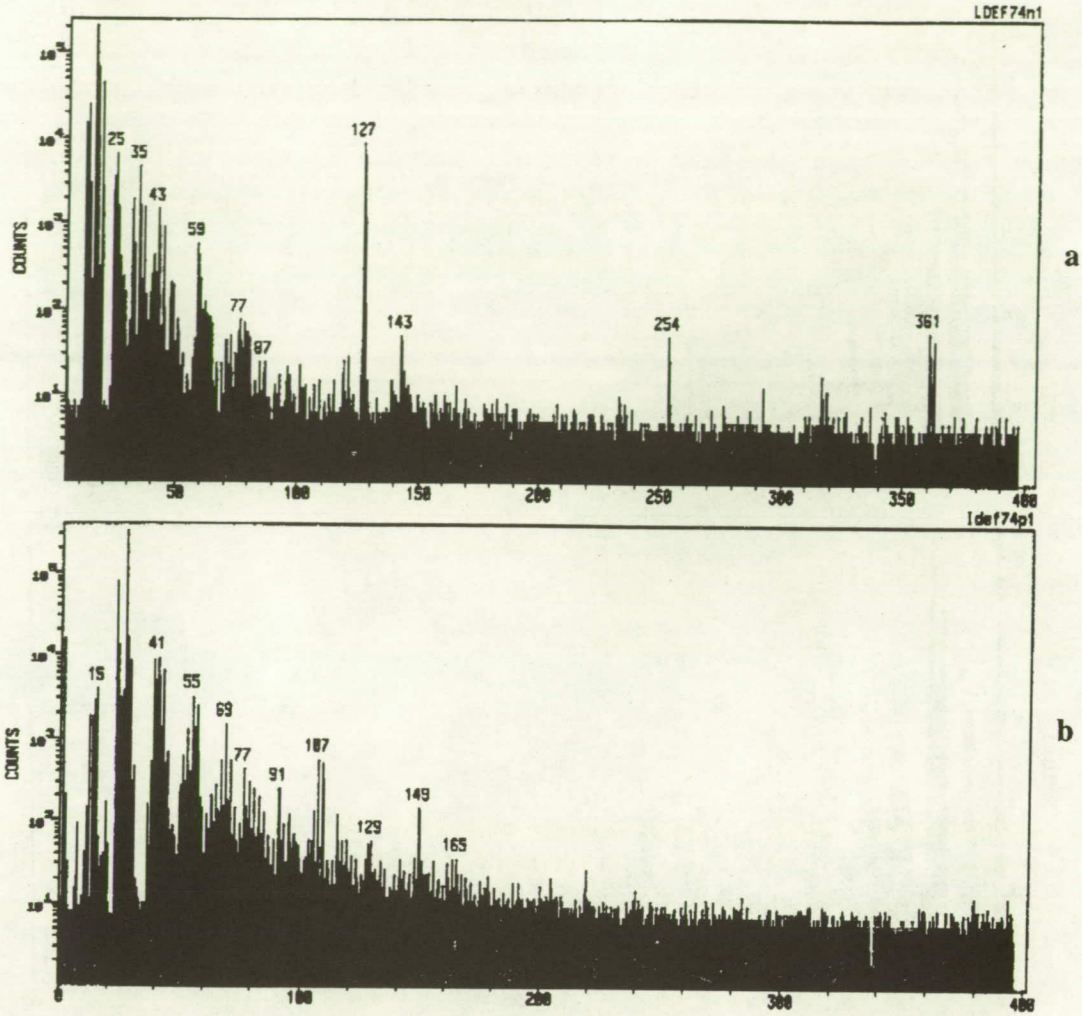

Figure 9. TOF/SIMS negative (**a**) and positive (**b**) spectra of crater 74.

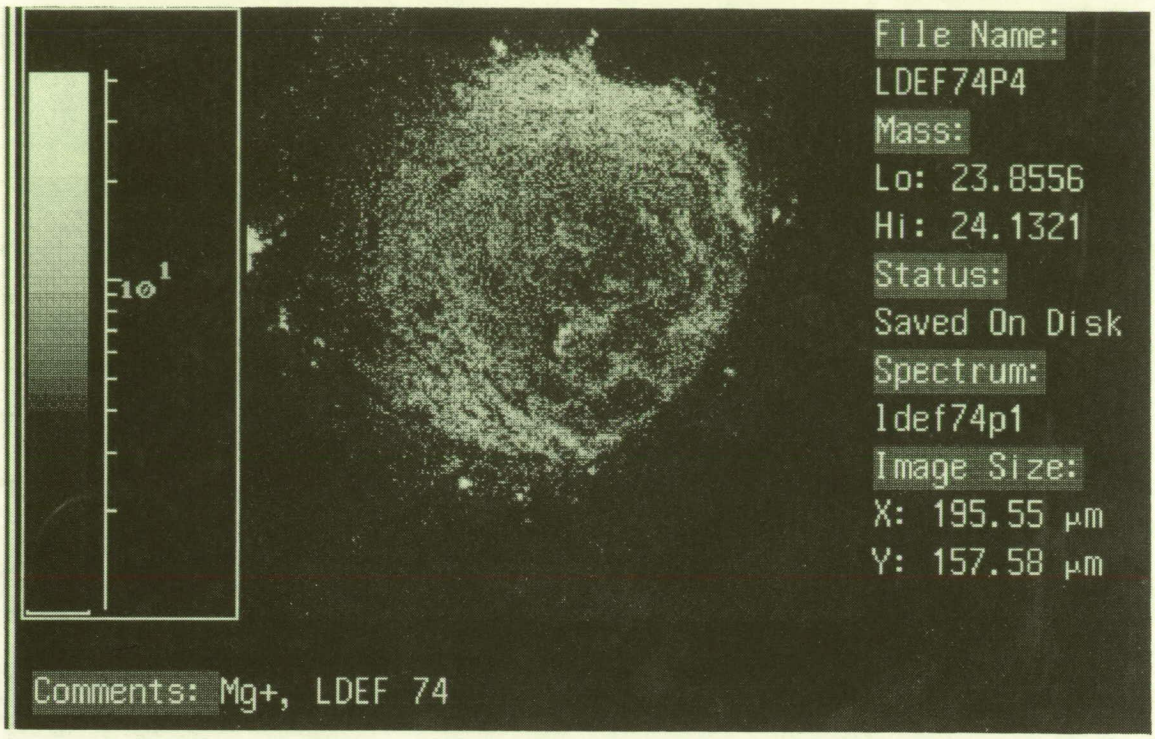

Figure 10. Mass separated image of Mg^+; crater 74.

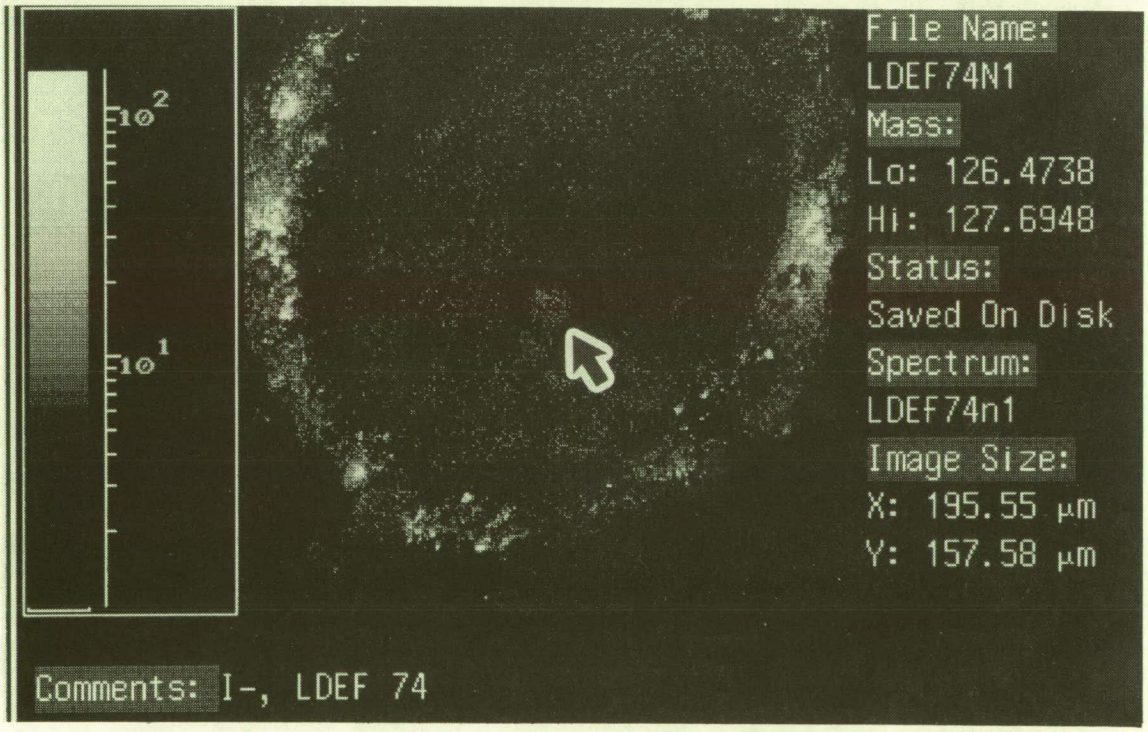

Figure 11. Mass separated image of I^-; crater 74.

(See color photographs, p. 602.)

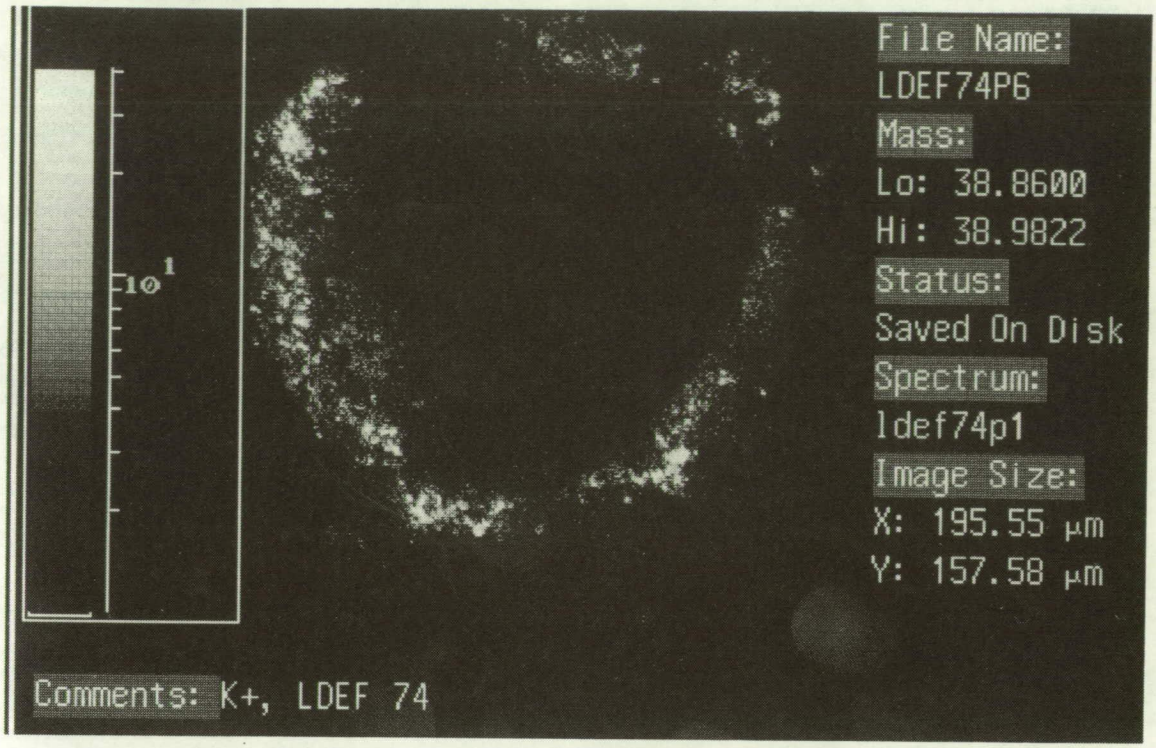

Figure 12. Mass separated image of K^+; crater 74.

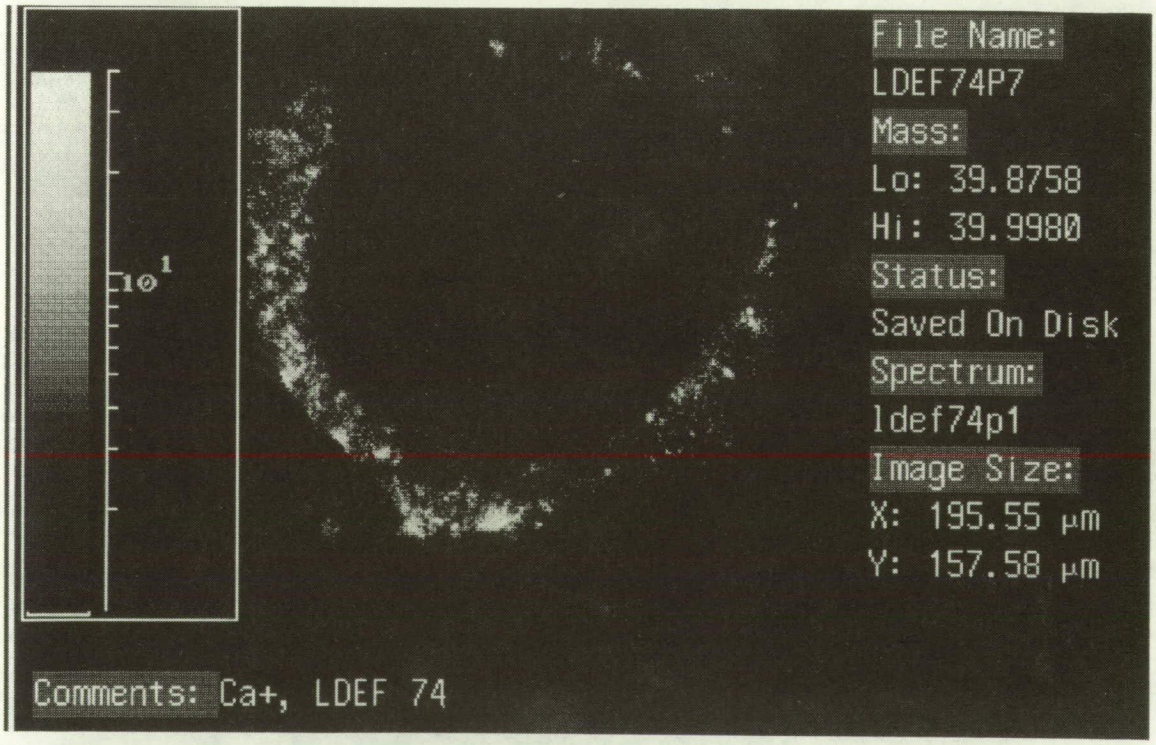

Figure 13. Mass separated image of Ca^+; crater 74.

(See color photographs, p. 603.)

DYNAMIC (COMPUTER) MODELLING OF THE PARTICULATE ENVIRONMENT: TRANSFORMATIONS FROM THE LDEF REFERENCE FRAME TO DECODE GEOCENTRIC AND INTERPLANETARY POPULATIONS

J.A.M. McDonnell and K. Sullivan
Unit for Space Sciences,University of Kent at Canterbury, Canterbury, Kent CT2 7NR, U.K.

ABSTRACT

LDEF's impact signature record and, in particular the size frequency distribution of craters and perforations (1) offers a unique record of environmental data referenced conveniently to the geocentric reference frame.

Its exposure simultaneously to both orbital and to geocentrically unbound interplanetary particulates does, however, present problems in decoding the two populations. Chemical analysis of residues can offer only limited assistance; and hence flux modelling has been developed (2,3) to transform from both geocentric orbital (e = 0) distributions and geocentrically unbound interplanetary source distributions. This is applied to the foil and crater penetration records (1,4) in the Ram (E), Trailing (W) and Space pointing directions to offer the means of decoding the records. It shows that the mix of the components is size dependent; though the interplanetary component dominates at greater than some 5 microns particulate diameter, an increasing orbital component is evident. Arguments for the space age origin of the micro particulates are not convincing dynamically and it is questionable whether the Solar Maximum Mission data (5) has been correct in the attribution of the population exclusively to space micro-debris.

Parametric forms of the modelling transformations are presented for the orbital and unbound populations.

Sources (some as yet unpublished)

1. "FIRST RESULTS OF PARTICULATE IMPACTS AND FOIL PERFORATIONS ON LDEF", J.A.M. McDonnell, S.P. Deshpande, S.F. Green, P.J. Newman, M.T. Paley, T.J. Stevenson and K. Sullivan, Presented Paper, XXVIII COSPAR Meeting, The Hague, The Netherlands, July 1990.
2. "PARTICULATE DETECTION IN THE NEAR EARTH SPACE ENVIRONMENT ABOARD THE LONG DURATION EXPOSURE FACILITY (LDEF): COSMIC OR TERRESTRIAL?", J.A.M. McDonnell, K. Sullivan, T.J. Stevenson & D..H. Niblett,,Conference Proc. IAU Colloquium No. 126, "Origin & Evolution of Interplanetary Dust", Kyoto, Japan, to be published 1991.
3. "DYNAMIC MODELLING TRANSFORMATIONS FOR THE LOW EARTH ORBIT SATELLITE PARTICULATE ENVIRONMENT', J.A.M. McDonnell, K. Sullivan, S.F. Green, T.J. Stevenson & D.H. Niblett, Poster paper, Conference Proc. IAU Colloquium No. 126, "Origin & Evolution of Interplanetary Dust", Kyoto, Japan, to be published 1991.
4. "SPACE DEBRIS: ORBITAL MICROPARTICULATES IMPACTING LDEF EXPERIMENTS FAVOUR A NATURAL EXTRATERRESTRIAL ORIGIN", J.A.M. Mcdonnell, Abstract submitted to LPSC Abstracts Volume, XXII, LPSC, 1991.
5. "THE FLUX OF METEOROIDS AND ORBITAL SPACE DEBRIS STRIKING SATELLITES IN LOW EARTH ORBIT", S. Laurance and D.E. Brownlee, Nature 323, pp 136-138, 1986.

LDEF DATA CORRELATION TO EXISTING NASA DEBRIS ENVIRONMENT MODELS

Dale R. Atkinson
POD Associates, Inc.
Albuquerque NM 87106

Martha K. Allbrooks
POD Associates, Inc.
Albuquerque NM 87106

Alan J. Watts
POD Associates, Inc.
Albuquerque NM 87106

ABSTRACT

The Long Duration Exposure Facility (LDEF) was recovered in January, 1990, following 5.75 years exposure of ~130 m^2 to low-Earth orbit. Approximately 25 m^2 of this surface area was aluminum 6061 T-6 exposed in every direction. In addition, approximately 17 m^2 of Scheldahl G411500 silver-Teflon thermal control blankets were exposed in nine of the twelve directions. These two types of surfaces provide a unique source of statistical data on impact directionality and flux into two well-characterized materials.

Since LDEF was gravity-gradient stabilized and did not rotate, the directional dependence of the flux can be easily distinguished. During the deintegration of LDEF, all impact features larger than 0.5 mm into aluminum were documented for diameters and locations. In addition, the diameters and locations of all impact features larger than 0.3 mm into Scheldahl G411500 thermal control blankets were also documented. This data, along with additional information collected from LDEF materials achieved at NASA Johnson Space Center (JSC) on smaller features, will be compared with current meteoroid and debris models. This comparison will provide a validation of the models and will identify discrepancies between the models and the data.

DERIVING THE VELOCITY DISTRIBUTION OF METEOROIDS FROM THE MEASURED METEOROID IMPACT DIRECTIONALITY ON THE VARIOUS LDEF SURFACES

Herbert A. Zook
NASA Johnson Space Center
Houston, TX 77058
Phone: 713/483-5058, Fax: 713/483-5276

SUMMARY

Because of spacecraft orbital motion about the Earth, a much higher flux of meteoroids is expected to strike spacecraft surfaces that face in the direction of spacecraft motion (apex direction) than would strike antapex-facing, or trailing edge, surfaces. Impact velocities are also higher on apex-facing surfaces compared to antapex-facing surfaces which further increases the apex/antapex ratio of spatial density of impact craters of a given size. Measurements of the areal densities of impact craters on the different LDEF surfaces should give important clues about the velocity distribution, and therefore the origins, of meteoroids. Preliminary results so far reported from LDEF investigations appear to best support the meteoroid velocity distributions derived by Erickson and by Kessler, which would lead to a mean impact velocity on the LDEF spacecraft of about 19 km/s.

INTRODUCTION

It is likely that meteoroids do not enter the Earth's atmosphere with equal probability from all directions. The true directional distribution, however, is not yet clear. Do more meteoroids, for example, approach the Earth from its direction of motion around the Sun (also called the "heliocentric apex" direction, or the "morning" side of the Earth), than from other directions? Southworth and Sekanina (ref. 1), after correcting their radar observations of meteoroids entering the terrestrial atmosphere for various experimental biases, obtain a flux—at constant meteoroid mass—with a peak in the heliocentric antapex direction (the "evening" side). There were also "peaks" in other directions, but not in the heliocentric apex direction. There remains some uncertainty, however, as to whether or not they have correctly accounted for all experimental biases. The true directional distribution of approach may also depend on meteoroid mass.

We note, however, that any given surface on the LDEF spacecraft will, over time, face in a large variety of directions relative to, say, the Earth-Sun line. This is a result of: (1) Normal vectors to the apex (leading), antapex, and space-facing surfaces of LDEF sweep through 360 degrees during each orbit about the Earth; (2) the ascending node of the LDEF orbit plane precesses with respect to the Earth-Sun line by nearly 8° per day; and (3) the spin axis of the Earth is inclined 23.5 degrees to the Earth's orbital axis about the Sun (see Fig. 1). This means that meteoroids arriving from a single

heliocentric longitude and latitude throughout the year will, before LDEF motion is taken into account, impact from a great variety of directions relative to the spacecraft geocentric apex direction.

This fact suggests the following assumption: "before satellite motion is taken into account, meteoroid radiants of every entry velocity will appear to arrive in uniform numbers from every direction not shielded by the Earth" (see also ref. 2). This will be called the "randomness" assumption for the distribution of meteoroid arrival directions. The assumption would be rigorously true, of course, if meteoroids actually enter the terrestrial atmosphere uniformly from all directions. When the actual rather broad, but poorly known, distribution of atmospherically-observed meteor radiants is considered, the assumption may be approximately true. The actual distribution of impact velocities and radiants on LDEF (or any orbiting satellite) is then obtained by permitting the LDEF spacecraft to move through this assumed random distribution of radiants with its Earth orbital velocity (similar to motion through a very rarified isotropic gas). This gives rise to a new "apparent" distribution of impact radiants and velocities relative to the spacecraft apex direction. The randomness assumption is one that makes it possible to deduce relative cratering rates on various LDEF surfaces as a function of the meteoroid velocity distribution. This, in turn, makes it possible to either test the assumption or to find out which meteoroid velocity distribution is best by comparison with the observed data. As more is learned about the true meteoroid directionality with respect to the Earth, the "randomness" assumption can be changed to fit the new facts.

ANALYSIS AND RESULTS

Consider an infinitesimal flux, dF_{va}, of meteoroids approaching the LDEF spacecraft location from a small solid angle $\sin\theta d\theta d\phi$ and in a small velocity interval dv, where θ is the angle of approach with respect to the spacecraft apex direction and ϕ is the azimuth angle around the apex direction, with $\phi = 0$ when pointed radially away from the Earth; v and θ are taken to be the velocity and apex angle before spacecraft motion is taken into account. The subscript "a" refers to the angular dependence of dF. Then, by the "randomness" assumption of the previous paragraph,

$$dF_{va} = [1/(4\pi-\Omega_E)]\sin\theta d\theta d\phi n(v)dv, \tag{1}$$

where Ω_E is the solid angle subtended by the Earth and the denser part of its atmosphere, and n(v) is the distribution of velocities with which meteoroids are observed to enter the top of the atmosphere. For an effective altitude of LDEF of 460 km, and an effective height of the atmosphere of 150 km (below which it is assumed that meteoroids cannot first pass and then strike LDEF), the top of the atmosphere appears 17.3 degrees below the local horizontal. Then $\Omega_E = 4.41$ steradians. That is, the Earth plus its atmosphere shields out 35.1% of the sky from meteoroid entry. n(v) is normalized so that

$$\int_v n(v)dv = 1. \tag{2}$$

When dF_{va} is integrated over all angles θ and ϕ (in radians) not shielded by the Earth, and over all velocities v, one obtains unity, which means F_{va} is also normalized. When θ is larger than θ_m, where $\theta_m = 17.3$ degrees, then the limits of integration of ϕ are from $-\phi_m$ to $+\phi_m$, where

$$\phi_m = \pi/2 + \arctan[\sin\theta_m/(\cos^2\theta_m - \cos^2\theta)^{0.5}], \tag{3}$$

which gives the range of ϕ angles for which the Earth is not in the field of view. When θ is less than θ_m, ϕ ranges over 2π radians.

Now consider the spacecraft in motion with its regular Earth orbital velocity, v_s ($v_s = 7.68$ km/s at 460 km altitude). The velocity, v_r, with which the meteoroid and spacecraft approach each other is given by $v_r = v - v_s$, where v_r,v, and v_s are vector velocities, and v is the meteoroid velocity. The apparent angle ψ, relative to the spacecraft apex direction, with which the meteoroids will appear to impact the moving spacecraft is obtained from

$$\cos\psi = (v\cos\theta + v_s)/v_r, \tag{4}$$

where

$$v_r = (v_s^2 + v^2 + 2v_s v\cos\theta)^{0.5}. \tag{5}$$

If dF_{va} is divided by v, we obtain the spatial density $dN(v,\theta,\phi)$ of meteoroids arriving from directions θ to $\theta + d\theta$, ϕ to $\phi + d\phi$, and in velocity interval v to v + dv. That is

$$dN(v,\theta,\phi) = dF_{va}/v = N(v, \theta, \phi)\sin\theta d\theta d\phi dv, \tag{6}$$

and, using Equation (1),

$$N(v, \theta, \phi) = [1/(4\pi - \Omega_E)]n(v)/v \tag{7}$$

for all directions not shielded by the Earth. From directions shielded by the Earth, $N(v,\theta,\phi) = 0$. Our "randomness" assumption means that N has no θ or ϕ dependence, except for Earth shielding.

When the spatial density of a differential velocity-angle subgroup of particles is multiplied by the velocity v_r relative to a spacecraft, we obtain the differential <u>flux</u> (number/(area - time)) of meteoroids impacting on the spacecraft at velocity v_r to $v_r + dv_r$ and from directions ψ to $\psi + d\psi$ and ϕ to $\phi + d\phi$. ψ and v_r are obtained from Equations (4) and (5), respectively. In equation form

$$dF_r(v_r, \psi,\phi) = F_r(v_r, \psi, \phi)\sin\psi d\psi d\phi dv_r = dF_{va}v_r/v, \tag{8}$$

where F_r is the flux per unit solid angle and per unit velocity that impacts the orbiting spacecraft.

This equation can be solved for dF_r, and hence for F_r, if the velocity distribution n(v) in Equation (7) is known. Dohnanyi (ref. 3), Erickson (ref. 4), Kessler (ref. 5), and Southworth and Sekanina (ref. 1) independently analyzed different observed distributions of atmospheric meteor entry velocities, corrected them for various selection effects, and presented meteoroid velocity distributions at constant meteoroid mass. Zook (ref. 6) assembled these different distributions together in a single paper and made approximate fits of analytical formulas to the Erickson and to the Southworth and Sekanina results (Dohnanyi had already represented his results analytically). The resulting velocity distributions are shown graphically in Fig. 2. The Kessler distribution is so similar to the Erickson distribution, that I will call the mathematical fit to the Erickson distribution the "Erickson-Kessler" distribution. References 3, 4, and 5 studied different sets of photographic meteor observations, and reference 1 studied radar meteors. It is assumed that the differences between these derived velocity distributions is due to different techniques in correcting for sensor biases, in using different data sets, and in possible true differences between photographic meteors and the smaller mass radar meteors. These different published velocity distributions give us some feel for the uncertainty in determining a "true" velocity distribution at constant meteoroid mass.

In this paper I use three separate velocity distributions for n(v) in Equation (7), to see if predicted crater statistics around LDEF depend much on the n(v) used. They are the Dohnanyi, the Erickson-Kessler, and the Southworth & Sekanina distributions (formulas given in ref. 6). Equation (8) is numerically solved by uniformly incrementing all v, θ, and ϕ values, weighting each (θ,ϕ) angle by $\sin\theta$, and each velocity by n(v) and by v_r/v; and by the differentials $d\theta, d\phi, dv$, and then storing the resulting numeric sums of the dF_r in small "bins", or intervals of (ψ, ϕ, v_r). $F_r(v_r,\psi,\phi)$ is then found by dividing the summed dF_r in a given interval by $\sin\psi d\psi d\phi$, the differential solid angle interval from which meteoroids "appear" arrive at a spacecraft orbiting with velocity v_s. The input n(v) have been very modestly modified from ref. 6, by accounting for gravity- induced increases in meteoroid velocities from LDEF altitude of 460 km to the top of the atmosphere at 100 km where meteor measurements were made. The n(v) were then renormalized. It is found that, when one integrates over all angles and velocities in Equation (8), the result does not equal 1 (i.e., F_r is not normalized). Instead, the number ranges from 1.06 for the Dohnanyi distribution to 1.10 for the Southworth and Sekanina distribution. The reason for this is that a unit flux of meteoroids (at constant mass) on a spherical spacecraft at rest with respect to the Earth is increased by several percent on a spacecraft moving with orbital velocity. The increase, as would be expected, is greater for low velocity meteoroids than for high velocity meteoroids.

If one sums only over all angles, and again normalizes, one obtains the velocity distribution with which meteoroids strike a spherical (or randomly tumbling) orbiting spacecraft. These are shown in Fig. 3 for each of the velocity distributions. It is noted that mean impact velocities have increased by about 2 km/s in each case. It is interesting to note that the percentage increase in mean relative velocity, in going from a stationary spacecraft to one with the orbital velocity, is greater than the percentage increase in impacting flux.

If, in Equation (8), one integrates ψ only over 0 to 90 degrees, and sums over all allowable v_r and ϕ, one obtains the meteoroid flux, at constant meteoroid mass, striking a flat plate with its normal facing in the forward direction. By similarly integrating ψ over 90 to 180 degrees, one obtains the

corresponding flux striking a flat plate facing in the antapex direction. The resulting ratios of fluxes on flat plates—apex to antapex—for the different velocity distributions are as follows: 5.7 for Dohnanyi, 7.2 for Erickson-Kessler, and 9.2 for Southworth and Sekanina. Not only are the fluxes different on apex and antapex-facing plates, so are the impact velocities. In Fig. 4 velocity distributions are shown separately (after normalizing) on apex and antapex-facing plates, where the Erickson-Kessler velocity distribution was the input distribution used. These distributions are valid for constant meteoroid mass and not for a constant resulting crater diameter.

Also of interest is the angular distribution with which meteoroids are expected to strike an orbiting spacecraft. To find this distribution, Equation (8) is summed over all meteoroid velocities. One then obtains the angular distributions (not normalized) shown in Fig. 5 for the Dohnanyi and Southworth and Sekanina distributions. These distributions are per unit solid angle and are valid at a given meteoroid mass and for directions not shielded by the Earth. The Erickson-Kessler distribution would lie between the other two.

Finally, however, one needs to know how the spatial density of impact craters around LDEF depends on the assumed velocity distribution of meteoroids--as crater frequency versus crater diameter and versus location on LDEF are the observed quantities. Presumably, the velocity distribution that gives rise to results that best fits the observed data is the "correct" one (and assuming the 'randomness' assumption is nearly correct). To carry out this task we use the penetration equation for 6061-T6 aluminum from ref. 7, which is as follows:

$$P = 0.42m^{0.352}\rho^{1/6}v^{2/3}, \tag{9}$$

where P is the penetration depth in cm, m is the meteoroid mass in g, ρ is the meteoroid mass density in g/cm^3, and v is the normal impact velocity in km/s. For this study, I assume $\rho = 2$ g/cm^3, and rewrite the equation to give

$$P = 0.48d^{1.056}(v\cos\theta)^{2/3}, \tag{10}$$

where d is the meteoroid diameter in cm and θ is angle with respect to the normal with which meteoroids impact a surface. For a moving spacecraft, v should be replaced by v_r. Crater diameter D is assumed to be twice the penetration depth P. For a normal impact ($\theta = 0$) at v = 20 km/s, the meteoroid masses required to generate 100 and 500 μm in diameter craters are, respectively, 8.5×10^{-9}g and 8.2×10^{-7}g. From ref. 8, the slopes of the log(flux) versus log(mass) curve at these meteoroid masses are -0.48 and -0.90, respectively.

Because meteoroids strike from the apex direction at typically higher velocities (due to spacecraft orbital motion) than from the antapex direction, smaller—and more numerous—meteoroids make more impact craters on the apex-facing surface than on the antapex-facing surface. This means that the ratio of the number of impact craters of a fixed diameter on the apex side compared to number of the same diameter on the antapex side depends not only on relative fluxes at constant mass, but on the slope of the log (meteoroid flux) versus log(meteoroid mass) curve. The analysis presented here depends on this effect and follows the technique used by Naumann (ref. 9) in accounting for the increased meteoroid flux at small meteoroid masses.

The Naumann analysis also applies to meteoroids striking surfaces at oblique angles. To make a crater of a certain fixed depth, or diameter, larger—and less numerous—meteoroids are required at oblique angles on a surface than at perpendicular, or normal, impact (at fixed velocity). The oblique angle effect should show up quite dramatically in the relative crater frequency of a given size crater on the "Top," or space-facing end of LDEF, compared to the "Bottom," or Earth-facing end of LDEF. There is a lesser effect from Top to "Side" (North or South-facing). The spacecraft orbital velocity should have no effect on these particular ratios, unless there is local shielding by the spacecraft. This is because the normal component of impact velocity has not been changed (although impacts will usually be at more oblique angles). Impacts also tend to occur at more normal incidence on the apex-facing surface than on the antapex-facing surface which, again, adds to enhance the "cratering" flux in the apex direction.

Table 1. Relative meteoroid crater production rates on LDEF as a function of crater diameter (on 6061-T6 Al), and as a function of the velocity distribution used. Meteoroid mass and the slope of the log (meteoroid flux) versus log (meteoroid mass) curve are also given at each crater diameter.

Crater dia. (μm)	Mass (g)	Slope	Vel. Dist.	Apex	Top	Side	Antapex	Bottom
500	7.8×10^{-7}	-0.90	Dohnanyi	12.2	6.4	4.7	1	0.06
100	8.1×10^{-9}	-0.48	Dohnanyi	9.9	5.9	4.2	1	0.13
500	7.8×10^{-7}	-0.90	E-K	19.2	8.7	6.4	1	0.08
100	8.1×10^{-9}	-0.48	E-K	14.4	7.6	5.4	1	0.17
500	7.8×10^{-7}	-0.90	S&S	32.8	12.8	9.4	1	0.12
100	8.1×10^{-9}	-0.48	S&S	21.2	10.1	7.2	1	0.23

Table 1 depicts the relative number/area of craters expected, depending on the crater diameter and meteoroid velocity distribution used, on each of six different surfaces facing in perpendicular directions (including north and south-facing surfaces) of LDEF. The number/area on the antapex-facing surface is taken to be 1, so all other surfaces show meteoroid fluxes relative to the antapex direction. Spacecraft motion and oblique impacts are accounted for, and the angle and velocity dependencies of (9) are integrated over all angles and velocities. The three velocity distributions used are those of Dohnanyi (3), Erickson (4)-Kessler (5) (=E-K), and Southworth and Sekanina (7) (=S&S).

As previously mentioned, it was assumed that LDEF is at a mean altitude of 460 km above the Earth, and that the effective atmospheric height is 150 km, below which meteoroids can not pass before impacting LDEF. This means that the minimum angle to the normal with which meteoroids can impact the Bottom side of LDEF is 72.5 degrees, before spacecraft velocity is considered. The reason for the strikingly high ratio (about 105) for the frequency of 500 μm wide craters on the Top surface of LDEF compared to the Bottom of LDEF is due to the steep slope of the flux-mass curve at these large meteoroid masses. It was assumed, in all cases, that there was no local spacecraft shielding.

DISCUSSION

Jackson and Zook (10) find that dust particles from the main belt of asteroids are expected to have mean velocities of 6 to 7 km/s relative to the Earth by the time they have drifted to Earth encounter (before the Earth's gravitational acceleration is accounted for). These average velocities would suggest that dust from the asteroid belt comprises from 5% (Dohnanyi vel. dist.) to 30% (S&S vel. dist.) of the meteoritic dust at 1 AU, before considering the gravitational enhancement of the flux by the Earth (11). Singer et al. (12) have sensed beta meteoroids on the antapex surface of LDEF. If the flux of beta's can also be measured on other surfaces, it should be possible to derive an "effective" velocity for these meteoroids; this would be an important experimental determination. The directionality of beta meteoroids may also be determined.

It will be of great interest to determine which one of the meteoroid crater distributions given in Table 2 above best fits the actual meteoroid impact crater data on LDEF (after orbital debris impacts have been accounted for). Or, do any of them fit? Beta meteoroids, for example, may travel at much higher velocities, on average, than other meteoroids. They also may not satisfy the "randomness" assumption very well, as they may mostly arrive at relatively small angles to the ecliptic. I note, finally, that one may make some other assumption than the randomness assumption, and again carry through the analyses that have been carried out in this paper. LDEF may help us, in this regard.

REFERENCES

1. Southworth, R.B. and Sekanina, Z. (1973) Physical and dynamical studies of meteors. NASA CR-2313, 108 pp.

2. Zook, H.A. (1987) The velocity distribution and angular directionality of meteoroids that impact on an Earth-orbiting spacecraft (abstract). In: *Lunar and Planetary Science XVIII*, p. 1138-1139. Lunar and Planetary Institute, Houston, Texas.

3. Dohnanyi, J.S. (1966) Model distribution of photographic meteors. Bellcomm TR-66-340-1, Bellcomm, Inc.

4. Erickson, J.E. (1968) Velocity distribution of sporadic photographic meteors. *J. Geophys. Res.* **73**, 3721-3726.

5. Kessler, D.J. (1969) Average relative velocity of sporadic meteoroids in interplanetary space. *AIAA J.* **7**, 2337-2338.

6. Zook, H.A. (1975) The state of meteoritic material on the Moon. Proc. Lunar Sci. Conf. 6th, pp. 1653-1672.

7. Anonymous (1970) Meteoroid damage assessment, NASA Space Vehicle Design Criteria (structures). NASA SP-8042.

8. Grün, E., Zook, H.A., Fechtig, H., and Giese, R.H. (1985) Collisional balance of the meteoritic complex. *Icarus* **62**, 244-272.

9. Naumann, R.J. (1966) The near-Earth meteoroid environment. NASA TN-3717, 43 pp.

10. Jackson, A.A. and Zook, H.A. (1991) Dust particles from comets and asteroids: Parent-daughter relationships (abstract). In: *Lunar and Planetary Science XXII*, pp. 629-630. Lunar and Planetary Institute, Houston, Texas.

11. Flynn, G.J. (1990) The near-Earth enhancement of asteroidal over cometary dust. Proc. Lunar and Planet. Sci. Conf. 20th, pp. 363-371.

12. Singer, S.F., Stanley, J.E., Kassel, P.C., Kinard, W.H., Wortman, J.J., Weinberg, J.L., Mulholland, J.D., Eichorn, C., Cooke, W.J., and Montague, N.L. (1990) First spatio-temporal results from the LDEF interplanetary dust experiment. *Advances in Space Research*, Vol. 11, No. 12, 1991, Space Dust & Debris, Pergamon Press, Oxford, England.

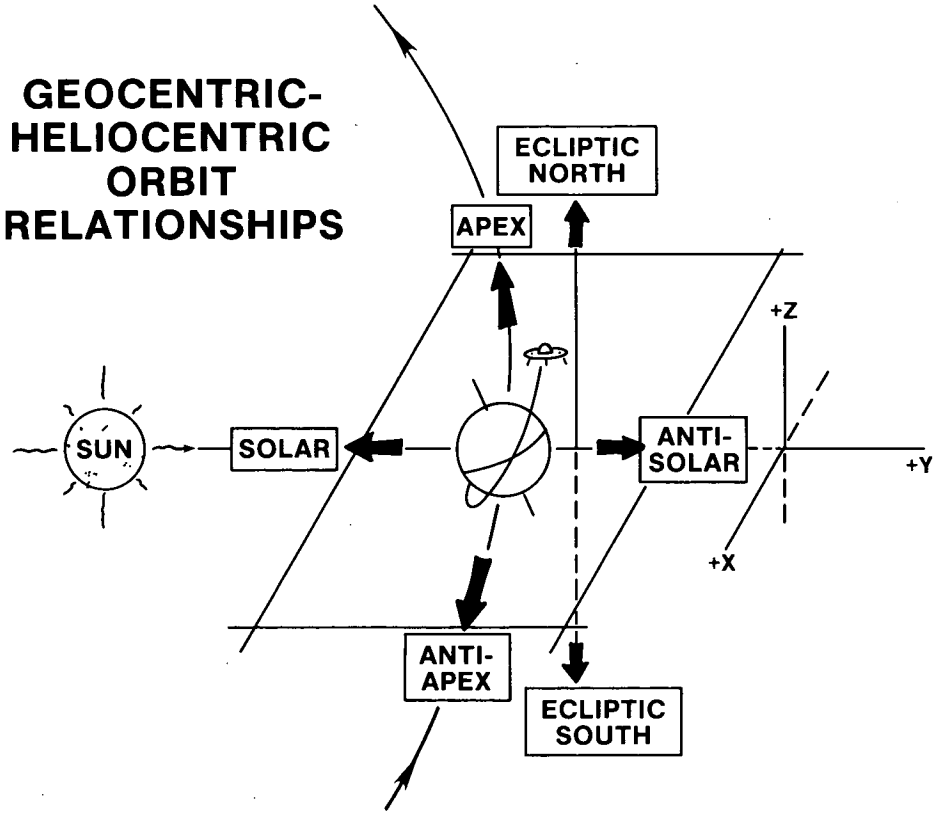

Figure 1. Spacecraft geocentric orbit and its relationship to heliocentric space.

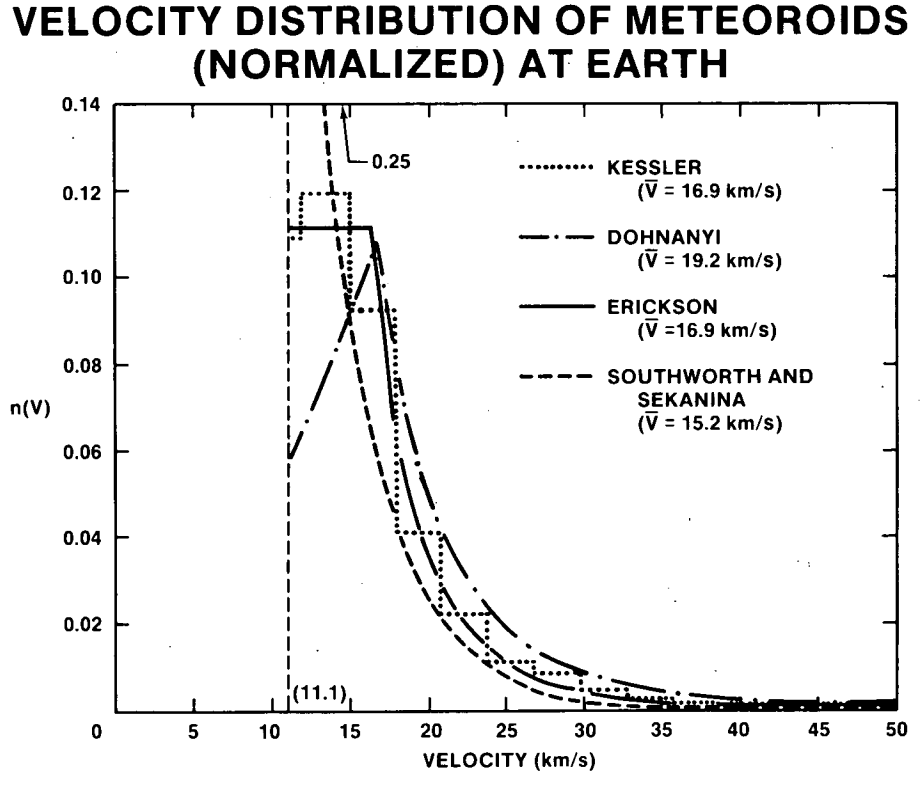

Figure 2. Velocity distributions of meteoroids entering the terrestrial atmosphere as independently corrected to constant meteoroid mass by different investigators (taken from Zook, 1975).

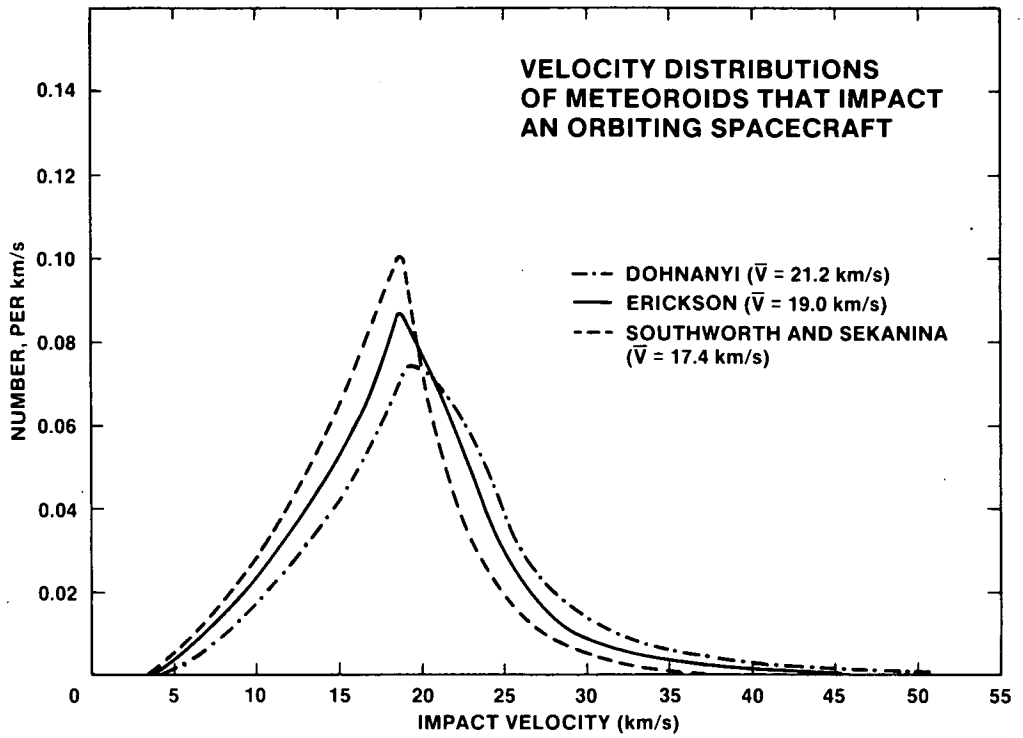

Figure 3. The velocity distributions of Figure 2 transformed to impact velocity distributions on spacecraft orbiting at 460 km above the Earth.

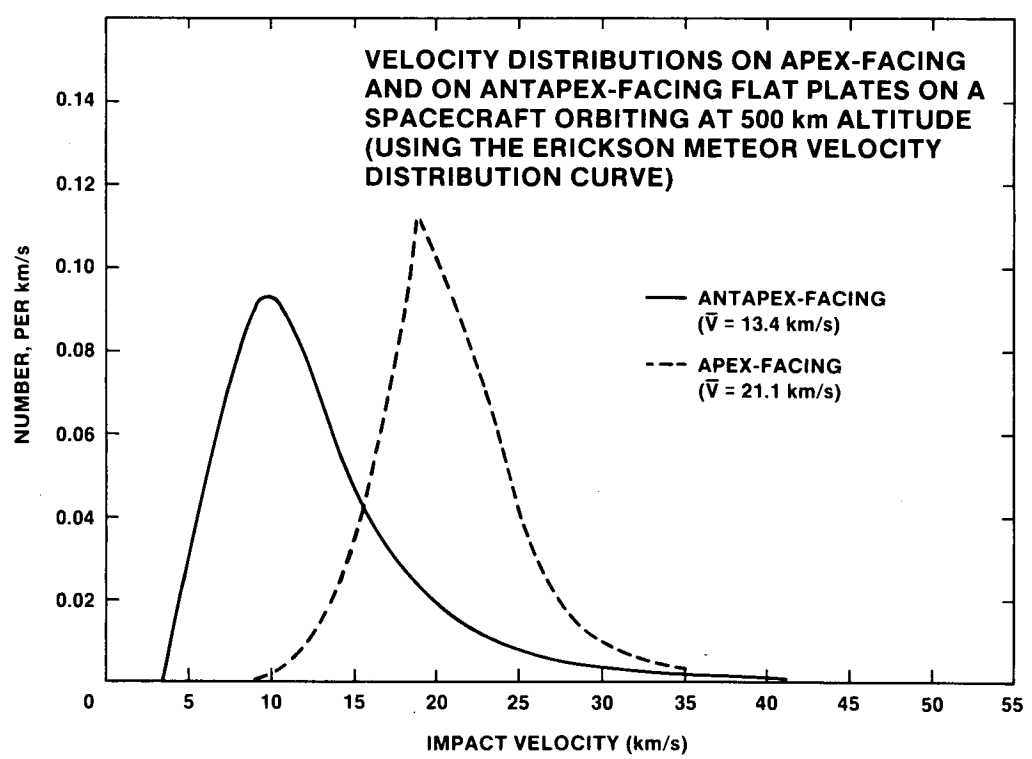

Figure 4. The Erickson-Kessler velocity distribution as transformed to velocity distributions on apex-facing and antapex-facing flat plates on a 460 km altitude orbiting spacecraft.

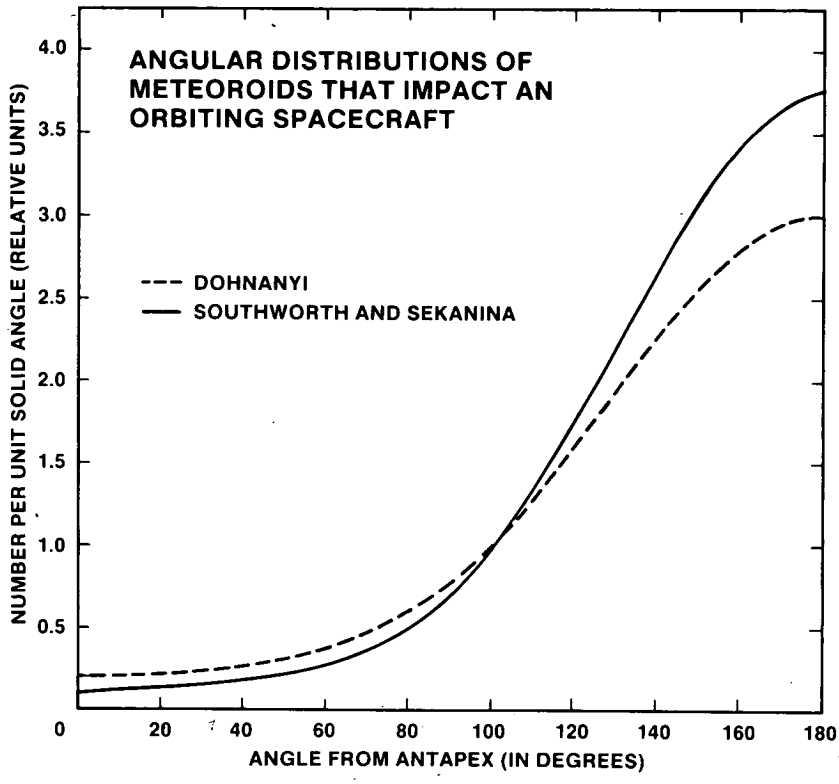

Figure 5. The flux of meteoroids per unit solid angle that approach a spacecraft orbiting at 460 km above the Earth versus angle from the apex direction. The fluxes are valid only for directions not shielded by the Earth and are those derived at constant meteoroid mass by Dohnanyi and by Southworth and Sekanina. The Erickson-Kessler distribution would lie in between the other two.

M AND D SIG PROGRESS REPORT: LABORATORY SIMULATIONS OF LDEF IMPACT FEATURES

Friedrich Horz
NASA Johnson Space Center
Houston, TX 77058

R. P. Bernhard, T. H. See
Lockheed ESC, C23
Houston, TX 77058

D. Atkinson and M. Allbrooks
POD Associates
Albuquerque, NM 87106

Laboratory impact experiments are needed to understand the relationship between a measured penetration hole diameter and associated projectile dimension in the thermal blankets of experiment A0178, which occupied some 16 m2. These blankets are composed of 125 μm thick teflon that has an Ag/enconel second mirror surface, backed by organic binder and Chemglaze paint for a total thickness of some 170 μm. While dedicated experiments are required to understand the penetration behavior of this compound target in detail, we report here on impact simulations sponsored by other projects into pure teflon and aluminum targets. These experiments will allow first order interpretations of impact features on LDEF, and they will serve as guides for dedicated experiments that employ the real LDEF-blankets, both unexposed and exposed, for a refined understanding of LDEF's collisional environment.

We employed a light gas gun to launch soda-lime glass spheres from 50 to 3200 μm in diameter (Dp) that impacted targets of variable thickness (Tf). The foil thickness is "scaled" to projectile dimensions via the ratio Dp/Tf and we systematically varied this ratio from approximately 0.2 (=infinite halfspace target giving rise to a full cratering event) to some 200 (=pure penetration without projectile fragmentation). All experiments were conducted at a nominal 6 km/s and at normal incidence. We found the crater diameter (Dc) to be some 5 times the projectile diameter in aluminum (1100 series) and some 3.8Dp in teflon. All penetrations up to Dp/Tf=1 are in essence truncated craters that are characterized by the above diameter-relationships. With successively thinner targets, the penetration holes (Dh) decrease systematically to approximate the ideal condition of Dh=Dp at some Dh/Tf > 30 in teflon and at Dp/Tf > 50 in aluminum. These systematic relationships between measured hole diameter and known blanket thickness allow unique solutions for particle diameter Dp at constant (presently 6 km/s) encounter velocity. Additional experiments are needed that explore velocity-dependent effects and how they may be scaled to applicable, cosmic velocities, which are currently beyond light gas gun launch capabilities.

The largest penetration measured in an LDEF thermal blanket is approximately 3 mm in diameter. Thus all penetrations occurred at Dp/Tf < 20. As a consequence, Dh=Dp will not apply to a single event and all holes must be larger than projectile diameter. The far majority of LDEF penetrations is < 1 mm and thus occurred at Dp/Tf < 6; the latter condition results in typical hole diameters that are factors of 2–3 larger than the projectile. Because Dp is cubed to obtain projectile mass, such factors of 2–3 become crucial in obtaining accurate particle mass-frequencies and fluxes.

PRELIMINARY MICROMETEOROID AND DEBRIS EFFECTS ON LDEF THERMAL CONTROL SURFACES

Martha K. Allbrooks
POD Associates, Inc.
Albuquerque, NM 87106

Dale R. Atkinson
POD Associates, Inc.
Albuquerque, NM
87106

Thomas See
Lockheed Missiles and Space
NASA/JSC
Houston TX 77058

Fred Horz
NASA/JSC
Houston TX 77058

ABSTRACT

Thermal control surfaces returned from space exhibited synergistic effects of simultaneous exposure to various natural environments. These environments included meteoroid and debris impacts, thermal cycling, atomic oxygen, and ultra-violet light exposure. The combined effects of these environments were most prominent in the region surrounding meteoroid and debris impact features in thermal control surfaces. Indications of these effects were noted in several phenomena, such as the silver-oxide rings and large delamination areas surrounding penetrations through silvered-Teflon thermal control blankets, and the large spallation zones and delamination rings caused by impacts into atomic oxygen eroded thermal control paints.

The thermal control surfaces on the Long Duration Exposure Facility (LDEF) were exposed to 5.75 years of low-Earth orbit environments. Since LDEF was gravity-gradient stabilized and directionally stable (i.e. no rotation), the effects of each of the environments can be distinguished via changes in material responses to hypervelocity impacts. The extent of these effects are being visually and microscopically characterized using thermal control surfaces archived at NASA Johnson Space Center (JSC) in order to determine the relationship between environment exposure and resulting ring sizes, delamination areas, and penetration diameters. The characterization of these affected areas will provide spacecraft system designers with the information they require to determine degradation of thermal control systems during satellite lifetimes.

THE INTERSTELLAR GAS EXPERIMENT

D. L. Lind
Utah State University, Logan UT

J. Geiss, F. Bühler and O. Eugster
Physikalisches Institut, Universität Bern, Switzerland

ABSTRACT

The Interstellar Gas Experiment (IGE) exposed thin metallic foils to collect neutral interstellar gas particles. These particles penetrate the solar system due to their motion relative to the sun. Thus, it was possible to entrap them in the collecting foils along with precipitating magnetospheric and perhaps some ambient atmospheric particles. For the entire duration of the Long Duration Exposure Facility (LDEF) mission, seven of these foils collected particles arriving from seven different directions as seen from the spacecraft. In the mass spectrometric analysis of the noble gas component of these particles we have detected the isotopes of ^{3}He, ^{4}He, ^{20}Ne and ^{22}Ne. In the foil analyses carried out so far, we find a distribution of particle arrival directions which shows that a significant part of the trapped particles are indeed interstellar atoms. The analysis needed to subtract the competing fluxes of magnetospheric and atmospheric particles is still in progress. The hope of this experiment is to investigate the noble gas isotopic ratios of this interstellar sample of matter which originated outside the solar system.

INTRODUCTION

When the LDEF mission was announced, an opportunity became available to collect particles in the vicinity of the earth and to later return them to earth for laboratory analysis. The Interstellar Gas Experiment was designed with precisely this goal in mind, based on a suggestion by J. Geiss in 1971. (ref. 1) Therefore, IGE was proposed for flight on LDEF and was eventually selected as part of the experiment compliment for that spacecraft. LDEF with IGE aboard was in low earth orbit from April 1984 until January 1990.

The purpose of the experiment was to detect and, if possible, to isotopically analyze the noble gas component of the local interstellar medium.

In the vicinity of the solar system, these interstellar particles are mostly individual neutral atoms. Because of their motion relative to the sun, a portion of this flux can penetrate into the solar system as far as the region of the inner planets. The presence of these particles near the earth was first confirmed by the OGO-5 spacecraft in 1969 (ref. 2) and they have provided us with considerable insight as to the nature of the nearby interstellar medium. (ref. 3)

The thin foil detection technique for these interstellar particles which we proposed for the IGE was first employed on the Apollo missions to the moon to measure the isotopic ratios of the solar wind.(ref. 4,5) Later, on the Skylab mission this same technique was used to measure the isotopes of precipitating magnetospheric particles. (ref. 6) The technique has also been utilized on a sounding rocket to analyze auroral particles. (ref. 7,8) Thus, considerable experience has been accumulated in this method of collecting extraterrestrial particle samples.

The detection technique consists of exposing very thin, high-purity metallic foils to the particle flux. For the IGE application we used 15 μm thick beryllium-copper foils with a beryllium-oxide surface layer. The impact velocities of the particles are sufficient to imbed them into the surface of the collecting foils. When the experiment is returned to earth, the entrapped particles are liberated by heating the foils. The released gases are then analyzed in a mass spectrometer. Since the collected particle sample is extremely minute, special mass spectrometer techniques are required for their measurement. The gases are passed through a chemical getter. This removes all chemical elements except the noble gases.

In the analysis of these particles, not only can the amounts of the various noble gas isotopes be measured, but additional information can be obtained by heating the collecting foils in increments. At the first relatively low temperature (450°), the least tightly bound particles are released. At higher temperature steps, the particles which had penetrated farther into the foil are released. Thus we can determine a rough approximation of the impact velocity for the various portions of the collected sample.

In IGE, the foils are located at the bottom of a collector - a rectangular box which establishes the field of view for the foil and the orientation of this field of view on the celestial sphere. IGE consisted of seven such collectors, each viewing a different direction relative to the LDEF spacecraft. Figure 1 shows the orientation of these fields of view for the various collectors. In the figure, the directions of viewing are designated by the angle

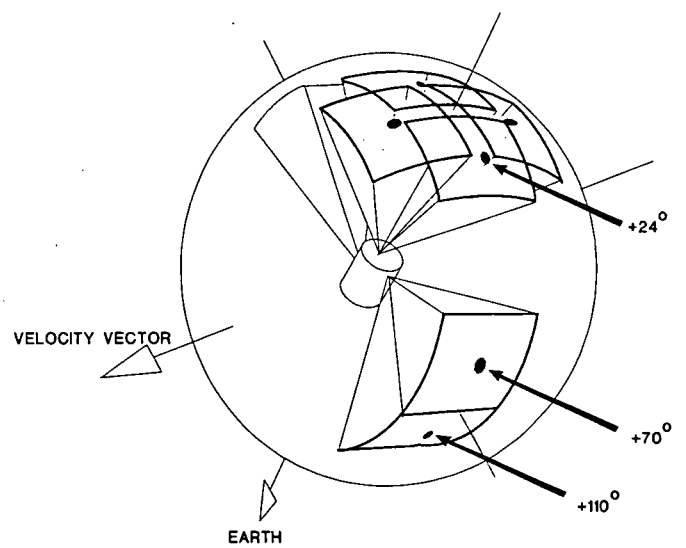

Figure 1.
The orientation of the fields of view of the seven IGE collectors relative to LDEF. See the text for the definition of the angular designation of the collectors. Besides the +24°, + 70° and +110° collectors, two collectors point in the 0° direction and one each in the -24° and -70° directions.

from the outward radius vector through LDEF to the center-line of the collector in the plane perpendicular to the velocity vector. Positive angles are to the north of the LDEF ground track. The +110° viewing direction points below the horizon where interstellar gas particles are shielded from LDEF by the earth. This collector was intended to entrap only background particles. In the event that after deployment LDEF had stabilized in the

inverted position, this collector could have performed a minimal experiment on its own. The remaining six collectors point above the horizon in five specific directions: +70°, +24°, 0°, -24° and -70°. These angles would be unaffected if LDEF had stabilized in an orientation with leading and trailing sides reversed. As LDEF moves in its orbit, these collectors sweep out five separate swaths on the celestial sphere. As shown in the figure, two collectors point in the 0° direction, but view the same part of the sky, one several minutes later than the other. The purpose of tilting these collectors slightly forward and backward in the direction of orbital motion, is to measure the background flux of ambient atmospheric particles. At the LDEF altitude, an extremely dilute portion of the earth's atmosphere remains. Although the collectors are normally pointed perpendicular to the direction of orbital motion, a small fraction of the atmospheric particles that form the high-temperature end of the velocity distribution, could have enough lateral velocity to enter the collectors as a background flux. By intentionally tipping one collector toward this flux and one collector away from it, we could measure and later subtract out these atmospheric particles.

Provisions were made to reject as many background particles as possible. Along the inner surfaces of the collectors, knife-edge baffles and serrations prevented a particle from reaching the collecting foils in a single bounce off the collector walls. This significantly reduced the number of background atmospheric particles which could be entrapped in the foils. An additional source of background particles is the flux of charged particles precipitating from the magnetosphere, particularly from the double charge-exchange reactions. IGE was designed to reject a significant fraction of these particles with a high-voltage grid (+1250 V) across the entrance of the collector.

INTERSTELLAR PARTICLE ESTIMATES

In order to estimate how the interstellar particles would be distributed among our collectors as they entrap particles approaching from different regions of the sky, and also to understand how the particle's angular distribution varies in different seasons of the year, we developed a computer model of the interstellar particle angular distribution as a function of location along the earth's orbit. The appropriate portions of these distributions were then summed as the collector's fields of view were swept across the celestial sphere by LDEF orbital motion. For the changing angular distribution calculation we followed the program developed by R.R. Meier at the Naval Research Laboratory. (ref. 9,10)

We, in effect, calculate the trajectories of individual interstellar gas particles from the time they cross the heliopause until they reach the orbit of the earth. The mean distance between collisions for these particles is so great that each individual particle follows a separate keplerian trajectory past the sun. (ref. 11,12) The gravitational attraction of the sun concentrates the particles beyond the sun (gravitational focusing) and significantly alters their original angular distribution. Figure 2 shows the trajectories of particles as they approach and pass the sun. Only neutral particles can move up-stream against the solar wind plasma as it flows outward from the sun. Therefore we must estimate the rate at which these neutral particles are ionized by solar radiation. If a particle is ionized, it is swept away from the sun by the solar wind and is dropped from the calculation. The photoionization rate at 1 A.U. determines the ionization at all locations in our calculation.

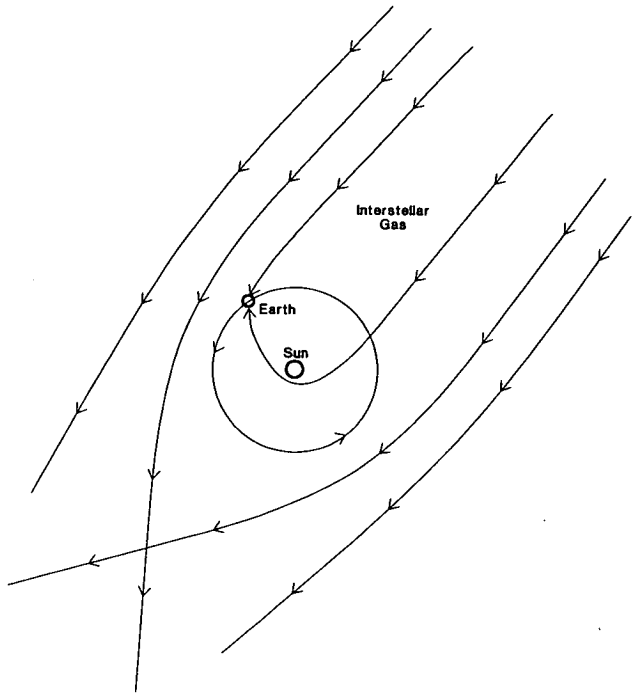

Figure 2.
Interstellar gas particle trajectories in the vicinity of the earth. Gravitational focusing by the sun significantly alters the direction from which these particles approach the earth at different points in the earth's orbit as well as their concentration and angular distribution. Only a few trajectories in the ecliptic plane are shown for simplicity.

The initial state of the interstellar gas as it penetrates the heliopause can be characterized by the following parameters: the particle velocity relative to the sun, temperature, particle density by species and the initial direction of approach toward the solar system. The apparent direction of approach of the interstellar gas is determined by the vector sum of the velocity of the sun (toward the solar apex) and the proper motion of the interstellar gas itself. This proper motion is from a galactically southern direction. We used for our model calculations the best estimates for these parameters given at the MPAE Lindau workshop, "Interstellar Gas in Interstellar Space," held in June 1980. The values of the parameters in our calculations were:

Velocity	24 km/s
Temperature	12,000 K
Helium Density	0.0124 cm^{-3}
Right Ascension	252°
Declination	-17.5°
Photoionization Rate	$0.68 \times 10^{-7}\ s^{-1}$

Since the efficiency of the trapping of the interstellar gas particles by the collecting foils varies considerably as a function of impact velocity, we calculated the velocity of each arriving particle as a function of approach direction toward the earth and multiplied the flux

from that direction by the laboratory measured trapping efficiency for that velocity. This gave us a map across the sky of the flux of particles which would be energetic enough to be entrapped in the IGE foils. Figure 3 shows four examples of these all-sky maps. In our model, a calculation of this kind was made for each day of the year, that is, entirely around the orbit of the earth. Each map is a contour plot of the particle flux over the entire celestial sphere. Only two contours are shown for clarity. In Figure 3, the Aug. 29 map shows the situation when the earth is in the up-stream portion of its orbit when particles are approaching the earth and LDEF from two widely separated directions. This situation corresponds to the two particle trajectories in Figure 2 which arrive at the earth. On this map, particles approaching from the direction on the right are only slightly deviated from the original direction from which the interstellar gas approaches the solar system. However, the particles arriving on the left have passed very close to the sun and have been significantly deviated in direction. They appear to be coming from a direction very different from the original direction of the interstellar wind. Also since they have travelled for a longer time in a region of high photoionization, their flux intensity has been reduced more than the particles arriving on the right. The relative intensity and location of these two flux populations varies considerably throughout the year.

In the winter portion of the earth's orbit, where the down-stream interstellar gas flux is located, a unique geometric singularity occurs. The initial direction of the interstellar wind, and the positions of the sun and the earth are almost in a straight line. This geometry allows particles to pass both over and under the sun and then to to be deflected toward the earth. This is not geometrically possible at other seasons of the year. This condition radically alters the angular distribution of the arriving interstellar particles. As shown in the remaining three maps in Figure 3, the flux gradually shifts into a configuration where particles are approaching LDEF from an annular region encircling the sun.

On these maps, the LDEF orbit traces out a single sinusoidal curve across the sky. As the orbit precesses, this curve moves slowly to the left, crossing the entire map once every 53 days. As a result of this motion, the five swaths which the fields of view of the IGE collectors sweep out, like-wise move in a corresponding pattern across the map of the sky. By integrating the particle flux within these moving fields of view, with proper account being taken of the shadowing effects of the collector walls, we could predict how many particles each foil would collect for any proposed exposure period. In this manner, we pre-programmed the IGE exposure sequences to optimize the recognition of the seasonally changing particle angular distribution pattern.

IGE SPACE OPERATIONS

Each of the seven IGE collectors contains six foils which were intended to be mechanically moved in sequence into the exposure position. However due to as-yet unexplained problems, this did not occur as programmed. After the flight all of the electronic and pyrotechnic components of the system separately operated properly and the analysis of why the composite system failed to initiate the deployment of most of the foils is still in progress.

As a result of this situation, in each collector a single foil collected particles for the entire LDEF mission time. This has had both a positive and a negative effect on our data. The total flux collected was almost six times more than we had planned for the original one-year LDEF mission. However, the time-history of the changing particle angular distribution was lost when the particle collection was integrated over all seasons onto one set of seven foils.

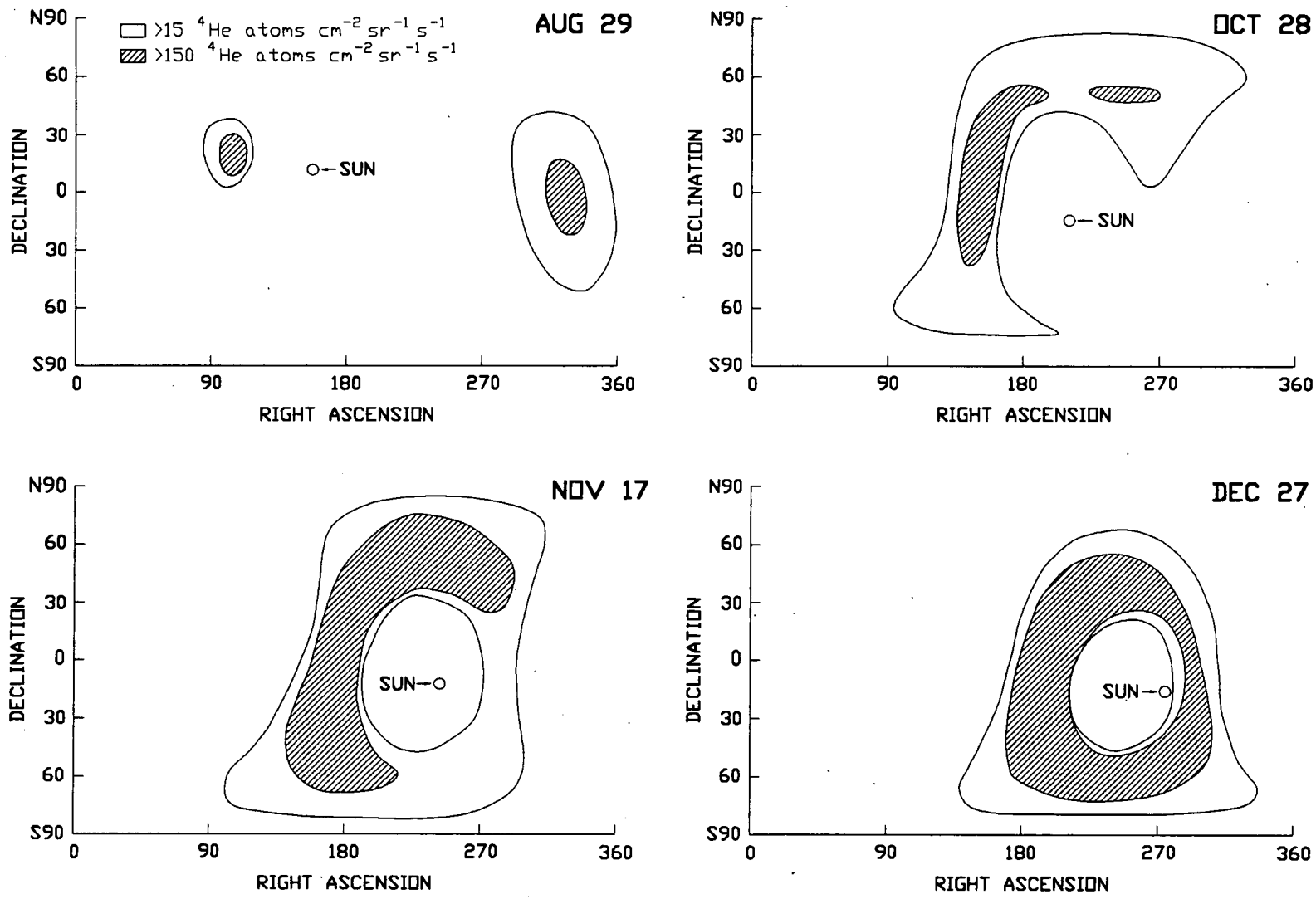

Figure 3.
Four all-sky maps of the flux of interstellar helium with sufficient energy to be entrapped in the IGE collecting foils. These contour maps (only two contours are shown) vary considerably with the season, i.e., with the position along the earth's orbit (see text).

DATA ADEQUACY

The question which had to be answered because of this malfunction was whether or not we would still be able to identify interstellar gas particles in our data. In order to address this question, we calculated with our model the integrated interstellar particle flux which each exposed IGE foil should expect to collect during the mission using the actual LDEF orbit as it had been tracked by the NORAD radar system. The results of this calculation are shown in Figure 4. The five swaths on the celestial sphere swept out by the IGE collectors still showed the clearly recognizable interstellar gas pattern, even when integrated over the entire exposure period. These five predicted valves represent all seven IGE collectors. Two collectors looked in the 0° direction and the 110° collector, which was to measure only background, had a predicted flux, of course, of zero. The predicted range of interstellar particle densities is more than an order of magnitude between the various foils. It appeared that the collected data would still be adequate to identify interstellar gas particles among the background particles which would also be in the foils.

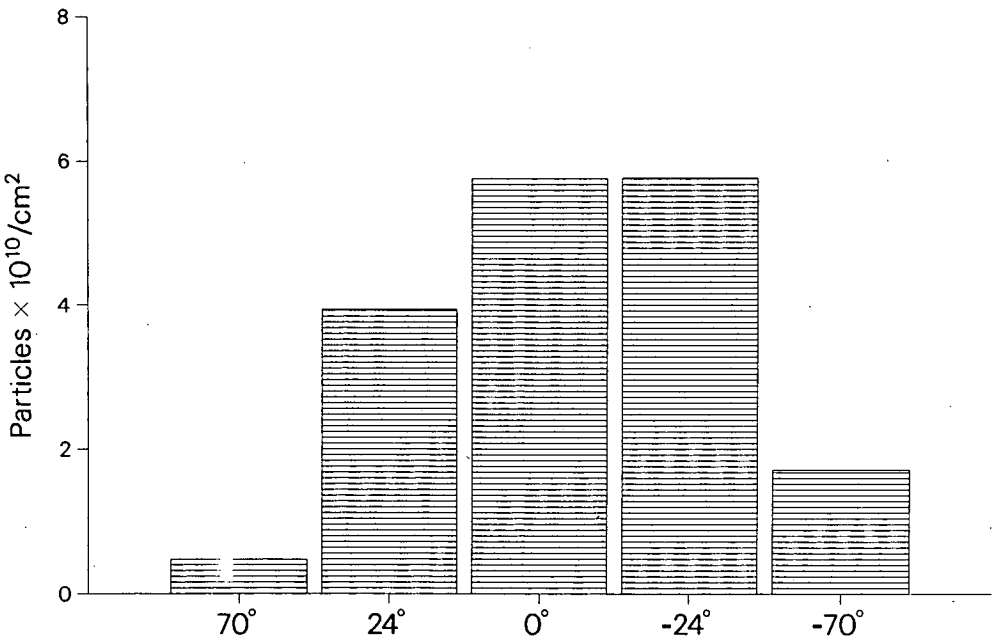

Figure 4.
The concentration of entrapped interstellar ^{4}He atoms in the IGE collectors predicted by our model calculation. Particles were collected for the entire LDEF mission combining all the seasonal angular distributions. However a distinctive pattern of interstellar particles is still apparent.

We pursued this question one step further. One edge of every foil (either the northern or the southern edge) looks out of the opening of the collector to view a slightly different area of the sky than that seen by the opposite edge. If either a more or less intense flux consistently arrives from this part of the sky, there will be a gradient in the numbers of particle entrapped in the foil in the north-south direction. To check on this effect, we divided each foil into seven strips and calculated from our model how many particles would

be entrapped in each portion of each foil. The results are presented in Figure 5. The calculation indicated that an interstellar particle density gradient should be present in each foil. In the 24° and -70° foils, the particle density should differ by a factor of two and five, respectively, from one side of the foil to the other. These gradients in the particle concentration are another feature which can identify interstellar gas particles and differentiate them from background particles.

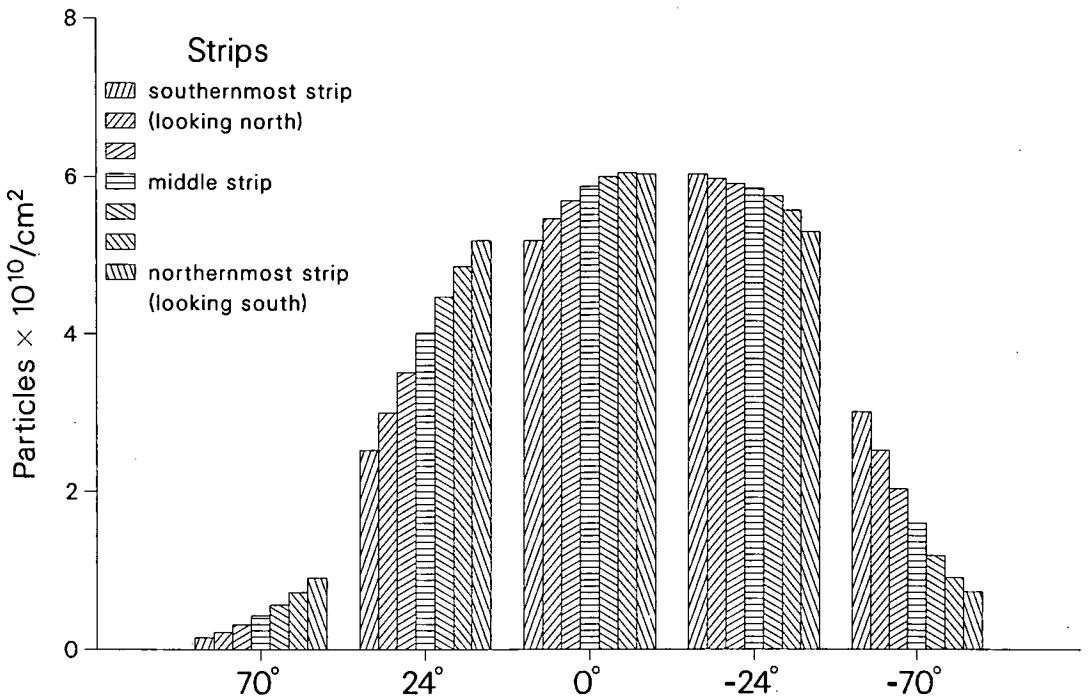

Figure 5.
The concentration of entrapped interstellar ^{4}He particles varies across each IGE collecting foil. This density gradient is a characteristic of interstellar particles, but not of background particles, and can be used to differentiate these different particle populations.

BACKGROUND CALCULATIONS

We are presently in the process of estimating the flux of background particles which we expect in the collecting foils. Currently at Utah State University we are modelling the temperature and density profiles of the atmosphere at the LDEF altitudes, accounting for the effects of the solar cycle, to calculate how many ambient atmospheric particles were able to by-pass the baffling system and enter the different regions of each IGE foil. In parallel, the magnetospheric background particles are being estimated at the University of Bern. We have measured the current drain though each of the sets of collector electronics and have calculated how long each battery survived during the extended LDEF mission. Thus we can infer how long the high voltage grid on each collector functioned in suppressing charge particles. This will affect our estimates of the magnetospheric particle fluxes.

MASS SPECTROMETRIC MEASUREMENTS

The initial set of measurements of the entrapped isotopes in small samples from each of the IGE foils have been completed at the University of Bern. The isotopes of ^{3}He, ^{4}He, ^{20}Ne and ^{22}Ne have so far been measured.

The analysis of these measurements is currently at a preliminary stage. The isotopes measured so far appear to be occurring in approximately the expected relative amounts, assuming that in the present interstellar medium the values are not totally different from those inferred for the protosolar gas. (ref.13) Also, the particle concentration pattern between collectors follows generally the predicted pattern for interstellar gas particles. The measured fluxes are between 1.3 and 3.6 times larger than the predicted interstellar particle fluxes which we interpret to mean that the competing fluxes together are of nearly the same order of magnitude as the interstellar fluxes. If this is the case, we can probably do the background subtractions quite confidently. Also the forward-tipped collector sees a higher flux than the backward-tipped collector which looks at the same part of the sky. This appears to result from the increased flux of atmospheric background particles, as expected. However the depth of penetration as indicated by the heating steps and the $^{3}He/^{4}He$ ratio for this component is not understood yet. Finally, in the two foils where we have attempted to measure an intensity gradient so far, a gradient does exist which is of the correct magnitude and is in the correct direction.

CONCLUSIONS

Based on the preliminary analysis of our initial mass spectrometric measurements, we have drawn the following conclusions.

1. IGE was successful in collecting and returning to earth for analysis a sample of neutral interstellar gas. Since this sample of matter originates outside the solar system, it is of intrinsic interest. If we are successful in determining the ratios of the helium and neon isotopes, they should contain significant information relative to the predictions of Big Bang and stellar nucleosynthesis.

2. Despite the loss of the time-history of the changing angular distribution of the interstellar gas particles due to the failure of the collecting foils to sequence properly, we still have enough information to verify that a major fraction of the collected sample is from the interstellar gas. It appears possible that we will be able to approximately separate the three components of the trapped particles, i.e., interstellar, magnetospheric and ambient atmosphere.

3. IGE has verified the usefulness of our thin foil collection technique in the investigation of the interstellar gas. Based on our experience with IGE, we can establish reasonable guidelines for future investigations of the interstellar gas. It would be most effective to mount foil collectors on an inertially stabilized platform in low earth orbit. The collector could be continuously pointed to the calculated direction of the most intense interstellar gas flux. This would significantly increase the ratio of collected interstellar particles to background particles. Thus, with the techniques developed for IGE, the local interstellar medium is now accessible for laboratory investigation and analysis.

ACKNOWLEDGMENTS

The authors wish to thank Robert Bayn and Alfred Manchaca for their efforts in creating the computer programs for this project. We thank Joseph Fischer for the design and Urs Schwab for the integration of the foil cassette assemblies. We also thank Ernest L. Weeks, Robert Y. Simek and Danny DeMonbrun for the development of the IGE collectors. This work is supported by NASA grant NAGW-2066 and by the Swiss National Science Foundation.

REFERENCES

1. Geiss, J., Elemental and Isotopic Abundances in the Solar Wind, Solar Wind: Proc. Asilomar Conf., NASA SP-308, 559 (1972)

2. Bertaux, J.L. and Blamont, J.E., Evidence For a Source of an Extra-terrestrial Hydrogen Lyman-Alpha Emission: The Interstellar Wind, Astron. and Astrophy., 11, 200 (1971)

3. Fahr, H.J., The Extraterrestrial UV-Background and the Nearby Interstellar Medium, Space Sci. Rev., 15, 483 (1974)

4. Geiss, J., Eberhardt, P., Bühler, F., Meister, J. and Signer, P., Apollo 11 and 12 Solar Wind Composition Experiments: Fluxes of He and Ne Isotopes, J. Geophys. Res., 75, 5972 (1970)

5. Geiss, J., Bühler , F. Cerruti, H., Eberhardt, P. and Filleux, Ch., Apollo 16 Preliminary Science Report, NASA SP-315, Section 14 (1972)

6. Lind, D.L., Geiss, J., and Stettler, W., Solar and Terrestrial Noble Gases in Magnetospheric Precipitation, J. Geophys. Res., 84, 6435 (1979)

7. Axford, W.I., Bühler, F., Chivers, H.J.A., Eberhardt, P. and Geiss, J., Auroral Helium Precipitation, J. Geophys. Res., 77,6724 (1972)

8. Bühler, F., Axford, W.I., Chivers, H.J.A. and Marti, K., Helium Isotopes in an Aurora, J. Geophys. Res., 81, 111 (1976))

9. Meier, R.R., A Parametric Study of Interstellar Helium Atoms Incident Upon the Earth, NRL Memorandum Report 4423 (1981)

10. Meier, R.R., Some Optical and Kinetic Properties of the Nearby Interstellar Gas, Astron. Astrophys., 55, 211 (1977)

11. Axford, W.I., The Interaction of the Solar Wind with the Interstellar Medium, Solar Wind: Proc. Asilomar Conf., NASA SP-308, 609 (1972)

12. Holzer, T.E. and Axford W.I., Interaction between Interstellar Helium and the Solar Wind, J. Geophys. Res., 76, 6965 (1971)

13. Anders, E. and Grevesse, N., Abundances of the Elements: Meteoritic and Solar, Geochim.Cosmochim. Acta., 53, 197 (1989)

COLOR PHOTOGRAPHS

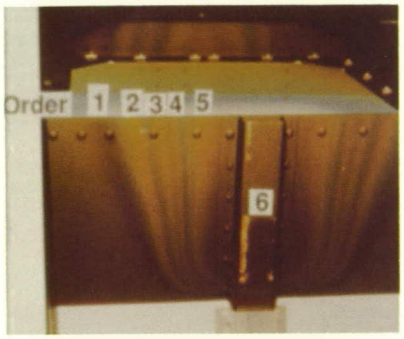

Interference Film
Colors on Tray F-06

Diffuse Reflectance IR
Spectral Response
by Thickness

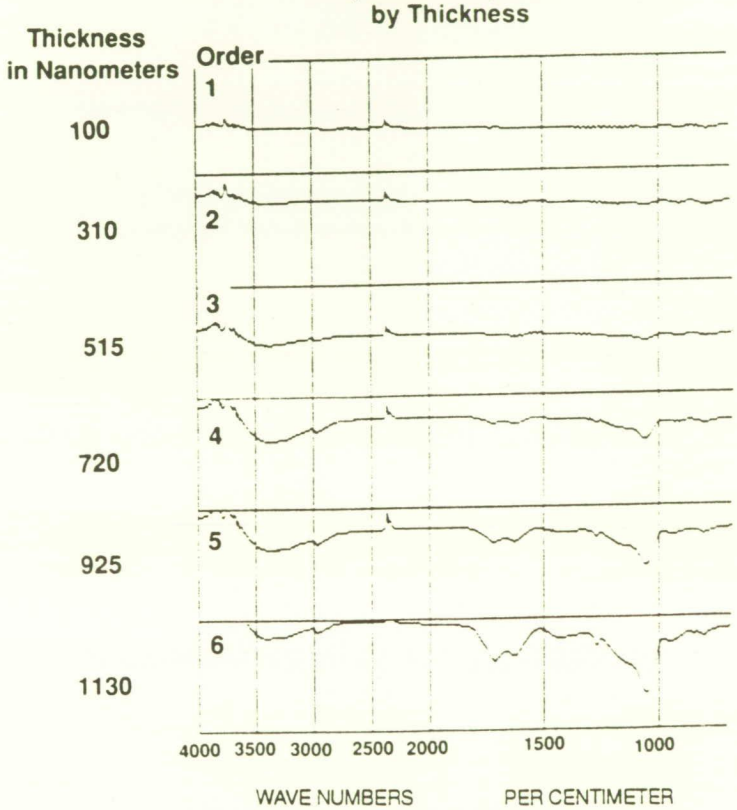

Thickness as a Function
of Interference Color

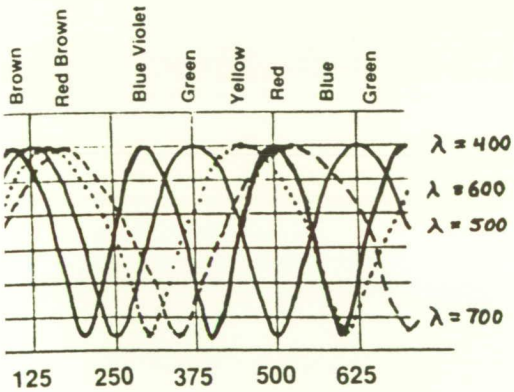

Figure 8: Quantification of molecular films by interference color and the calculation of the total film weight.

(Color version of black and white photograph on p. 153.)

Photograph 2: Interference colors indicating the thickness of the brown film on tray H-06.

(Color version of black and white photograph on p. 154.)

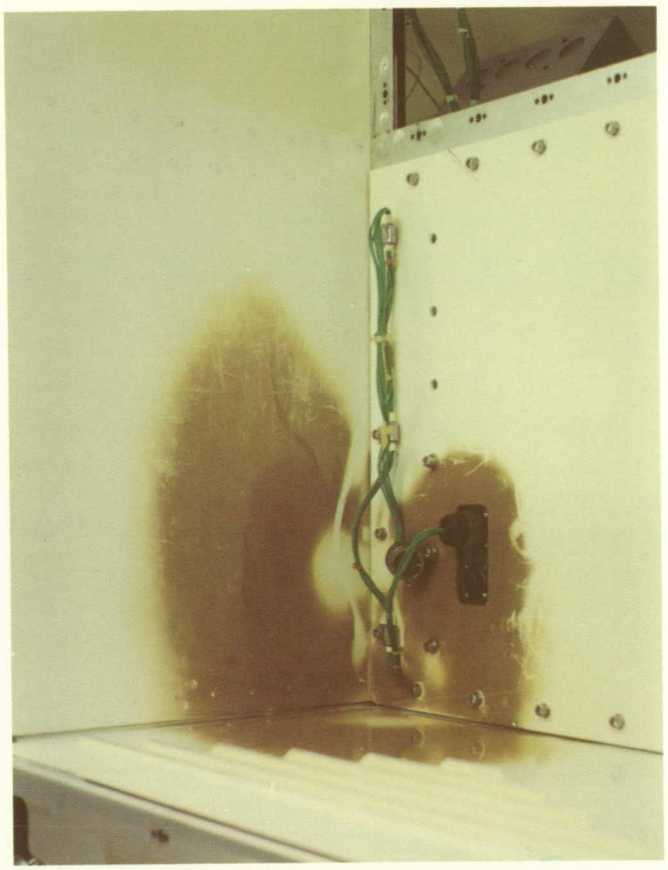

Photograph 1: Tray H-06, brown deposit in AO exposed corner.

(Color version of black and white photographs on p. 172.)

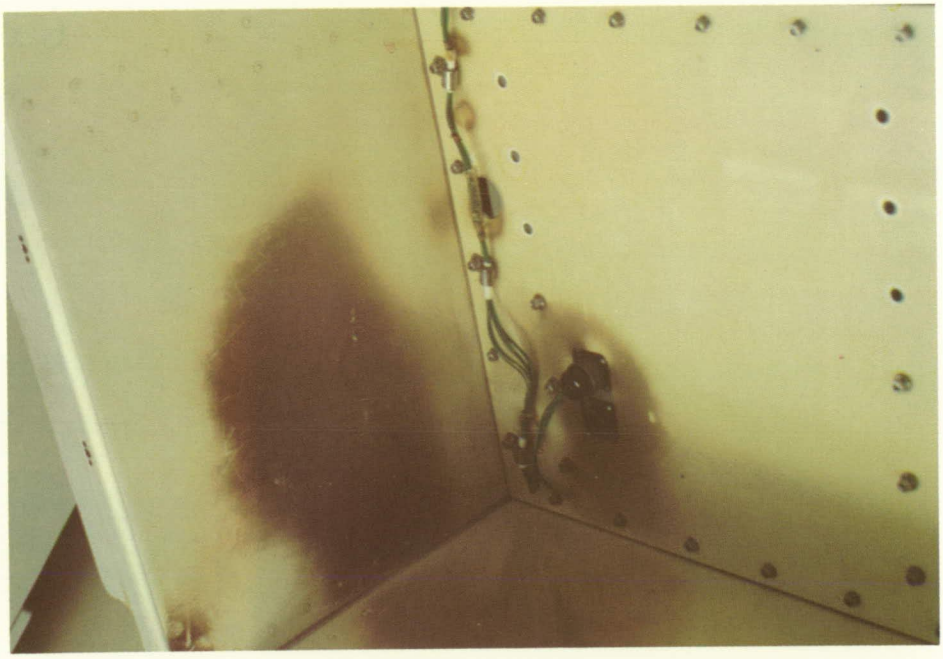

Photograph 2: Tray H-06, brown deposit and tie wrap deposit in other corner.

Photograph 5: Tray F-02, clamp 6, brown droplet deposit.
(Color version of black and white photograph on p. 174.)

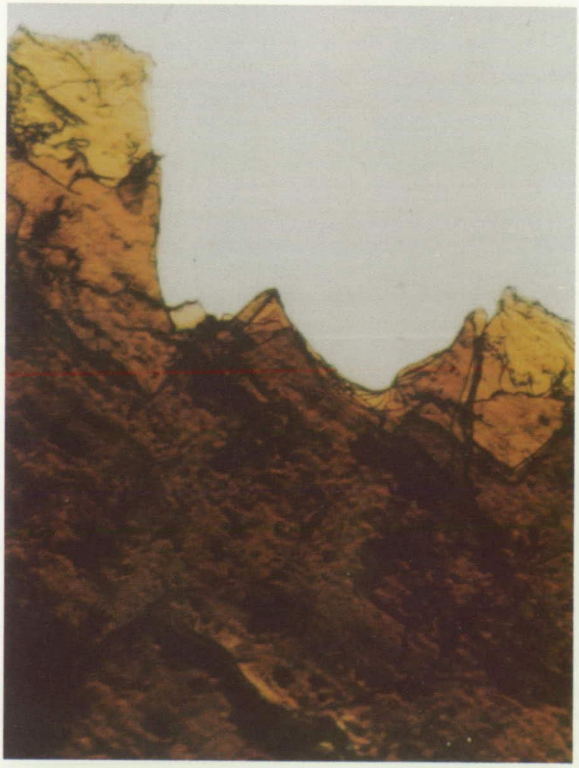

Photograph 7: Tray C-12, layered brown film.
(Color version of black and white photograph on p. 176.)

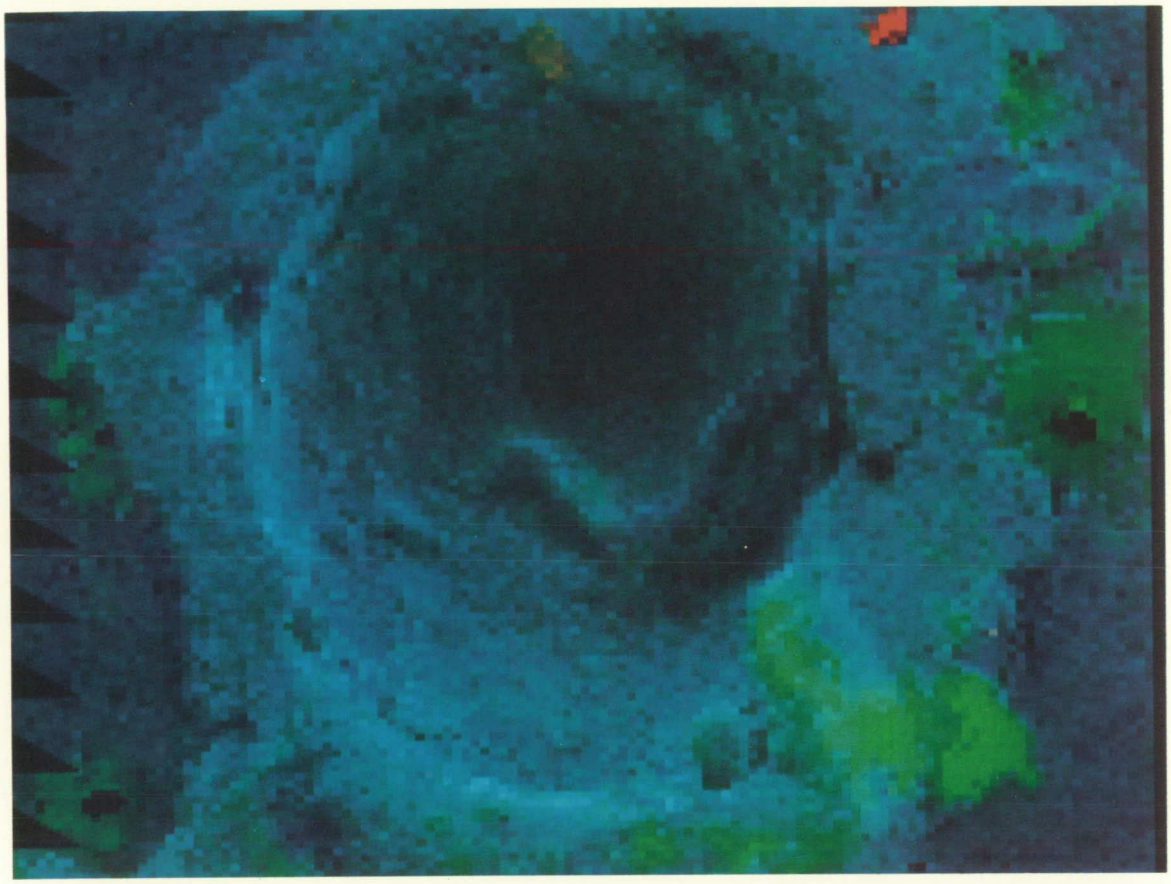

Figure 7. Three-element SAM map (Al = blue; carbon = green; F = red) of crater 31.

(Color version of black and white photograph on p. 560.)

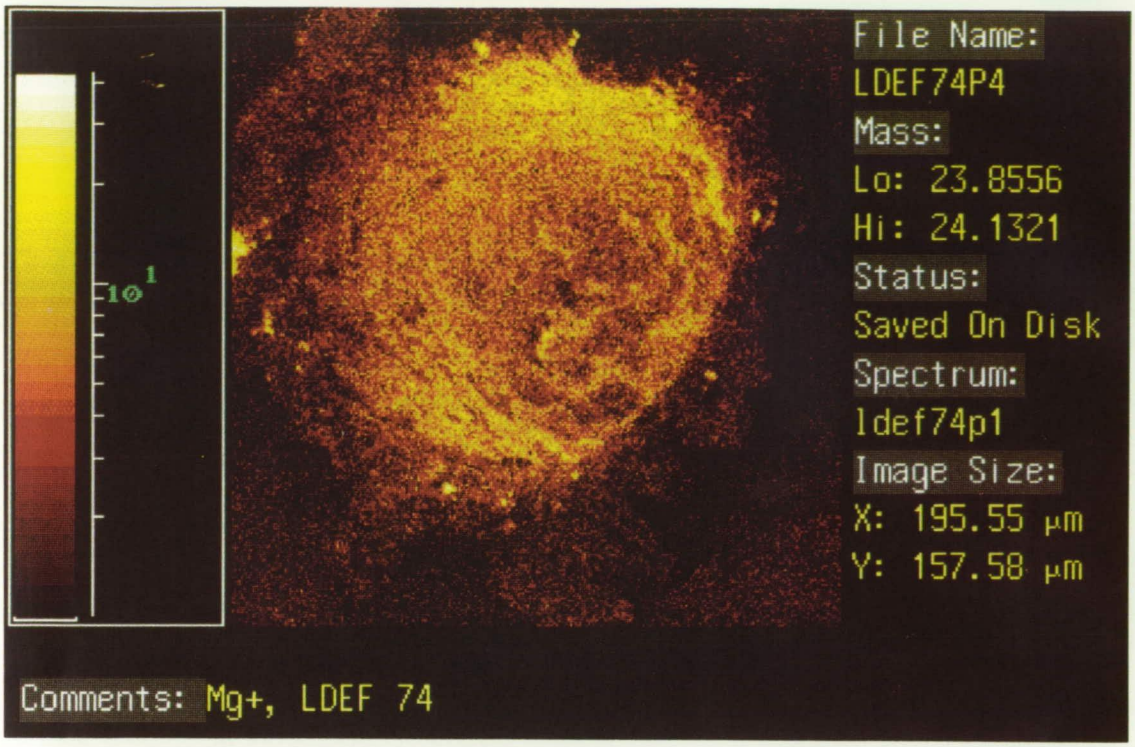

Figure 10. Mass separated image of Mg^+; crater 74.

(Color version of black and white photographs on p. 563.)

Figure 11. Mass separated image of I^-; crater 74.

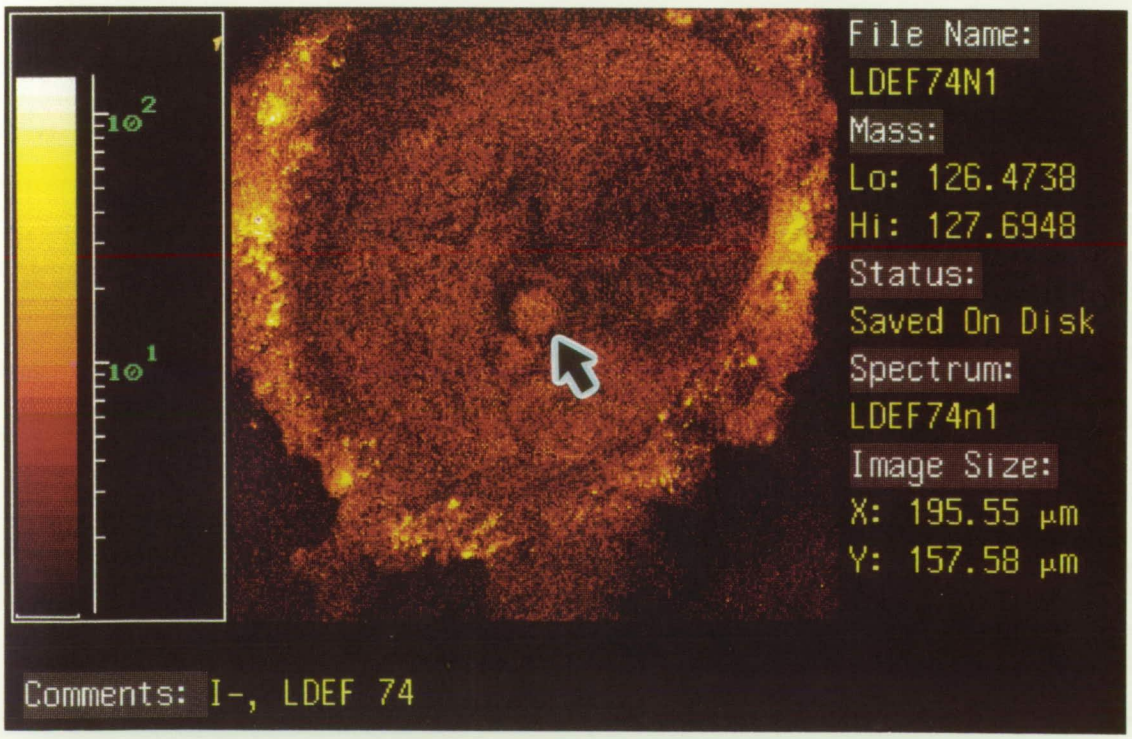

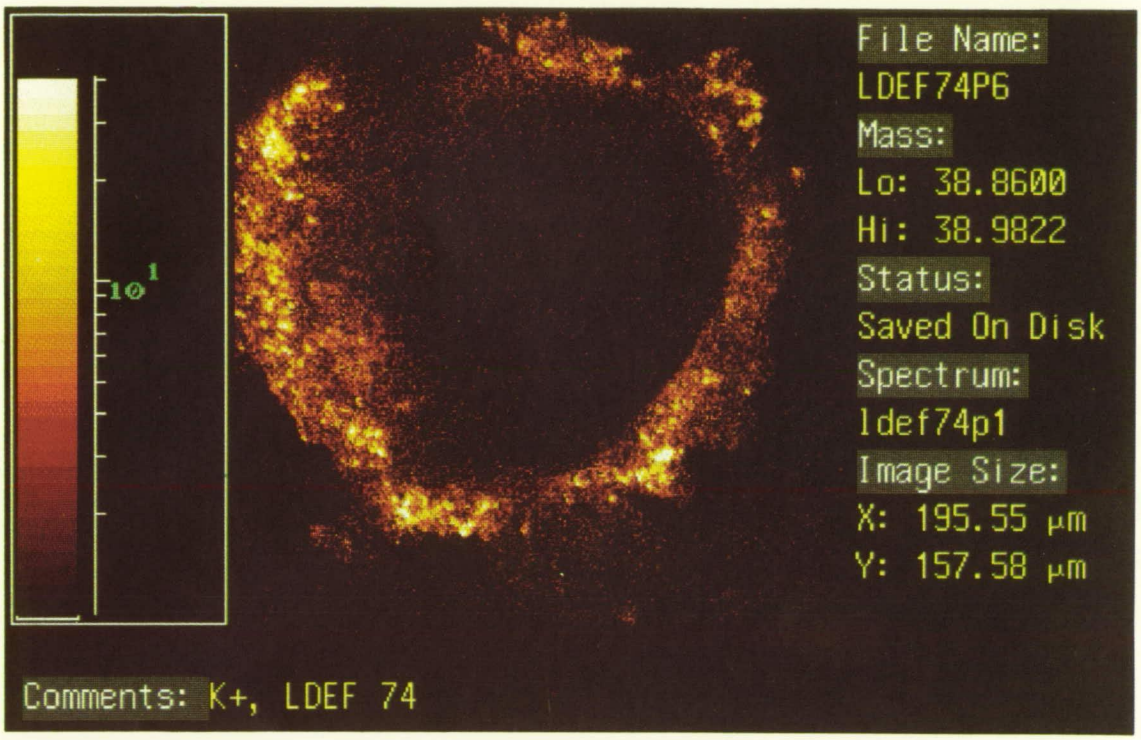

Figure 12. Mass separated image of K^+; crater 74.

(Color version of black and white photographs on p. 564.)

Figure 13. Mass separated image of Ca^+; crater 74.

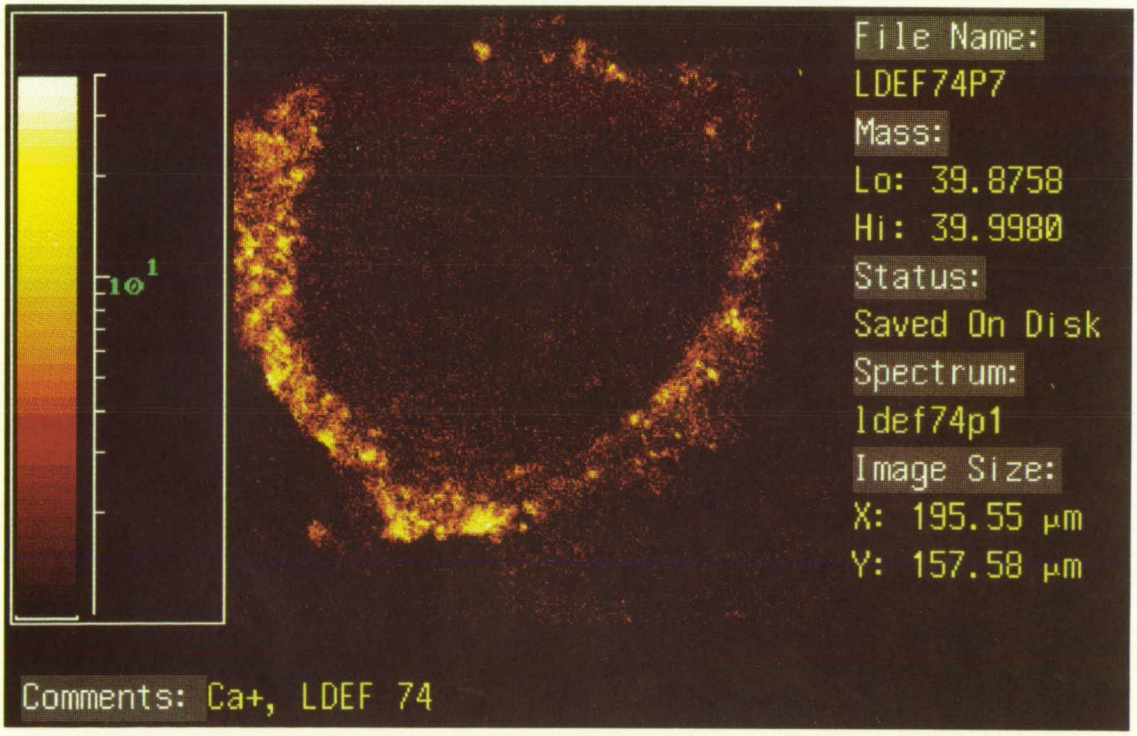

AUTHOR INDEX

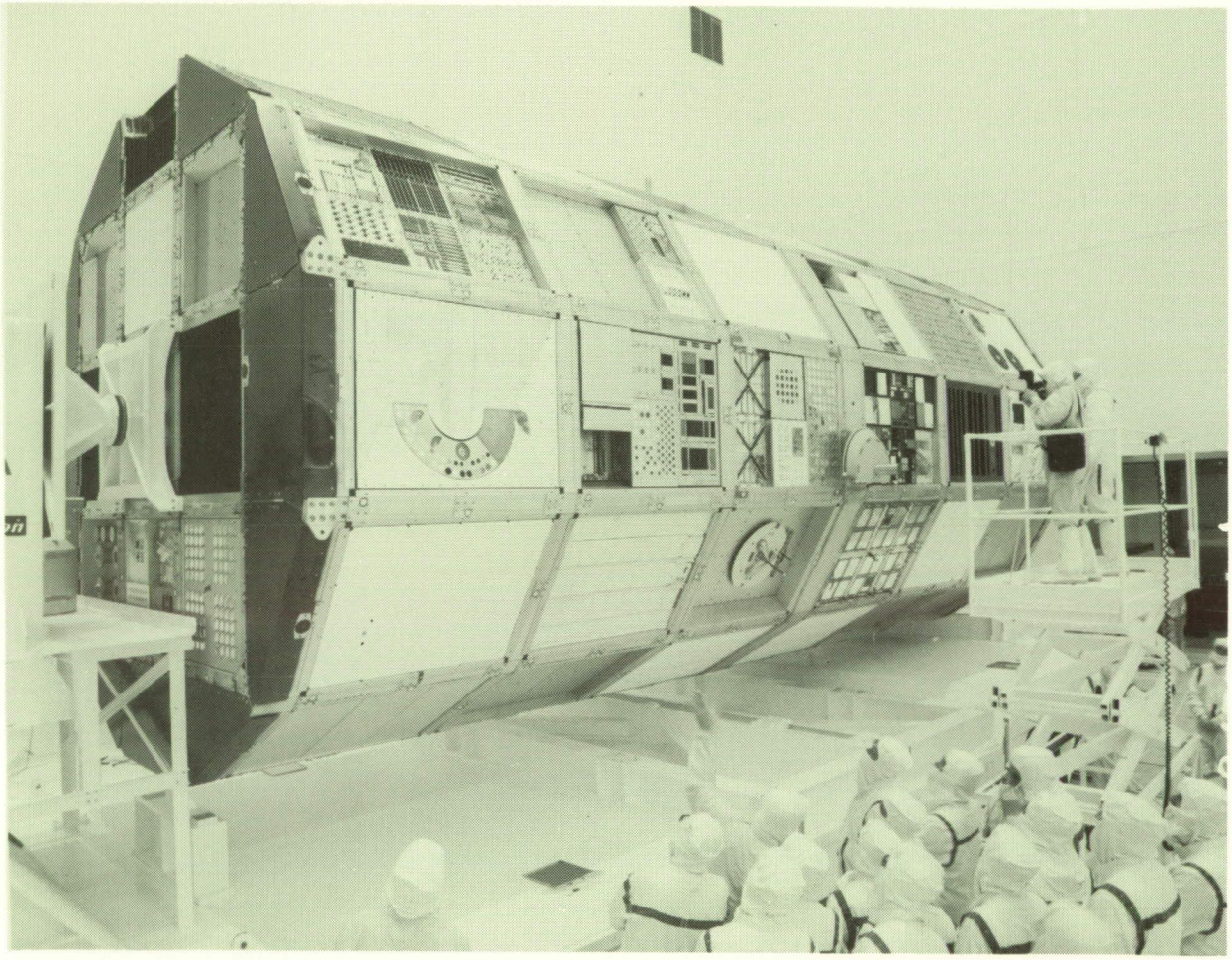

Adams, James H., 377

Ahearn, J. S., 1523

Allen, Thomas H., 1299

Amari, Sachiko, 503

Armstrong, T. W., 213, 347, 361

Assié, Jean Pierre, 1163, 1607, 1613

August, R. A., 225

Bayonove, J., 1639

Beaujean, R., 393, 1639

Benton, E. R., 325, 339

Bergman, L. A., 1283

Berrios, William M., 69, 935

Blakkolb, Brian K., 737, 1419

Bonnemason, Francis, 1301

Bosch, J., 367

Brennan, Patrick J., 1431

Brinza, David E., 817

Brooks, L. K., 1533

Brownlee, Donald E., 487, 549

Advani, A. H., 663

Allbrooks, Martha K., 459, 477, 567, 581, 583

Alston, Jim A., 1625

Angelo, Joseph A. Jr., 1637

Arrowood, R., 663

Atkinson, Dale R., 459, 477, 567, 581, 583

Banks, Bruce A., 781, 801

Beahm, Lorraine P., 377

Bennett, J. M., 1361

Benton, E. V., 213, 325, 339, 1639

Bernhard, Ronald P., 487, 581

Berry, J. N., 1257

Blue, M. D., 1317

Borg, Janet, 419

Bourassa, R. J., 643

Brinker, David J., 1395

Brodkin, J. S., 1005

Brown, M. John, 899

Bücker, H., 1639, 1667

Bühler, F., 585

Burge, D. K., 1361

Burris, Charles L., 763

Chapman, S. P., 1257

Chedotte, J. E., 1419

Colborn, B. L., 347, 361

Cooke, William J., 517

Csige, I., 325, 339

Dalbey, R. Z., 1361

Delpoux, M., 1639

Dever, Joyce A., 801

Dodds, Jerry, 1299

Donovan, T. M., 1361

Durin, Christian, 1593

Dybler, T., 225

Edelman, Joel, 1217

Ely, D. W., 225

Eugster, O., 585

Farrow, Allan, 705

Bunch, T. E., 549

Burns, Forrest, 255

Chang, J. Y., 313

Charlier, Jean, 1343

Christl, Ligia C., 723, 753, 755

Condé, Eric, 1613

Crutcher, E. R., 101, 121, 141, 155, 847, 861

Cutchin, J. H., 225

deGroh, Kim K., 781

Derrickson, James H., 213

di Brozolo, F. Radicati, 549

Domingo, C., 367

Drerup, Robert A., Jr., 1315

Dursch, Harry W., 1109, 1217, 1549, 1565

Dyer, C. S., 249

Ehrlich, Nelson J., 1635

Enge, W., 393

Facius, R., 1639

Felbeck, David K., 1143

Filz, R. C., 1189

Fisher, W. W., 663

Flatman, J. C., 249

Foote, John, 503

Franzen, W., 1005

Frigo, L. A., 339

Gartenbach, K. E., 1651

Gaubin, G., 1639

Geiss, J., 585

Giangano, D., 313, 1227

Golden, Johnny L., 975

Gregory, John C., 61, 237, 723, 753, 755

Grigsby, Doris K., 1635

Guillaumon, Jean-Claude, 945

Harmon, B. A., 237, 301

Hartmayer, R., 1283

Haskins, P. S., 225

Hawkins, Gary J., 1477

Heinrich, W., 1639

Finckenor, Miria, 435

Fishman, G. J., 237, 301

Fleming, Ronald H., 549

Frank, A. L., 325, 339

Frederickson, A. R., 1189

Froggatt, Mike, 875

Gasset, Y., 1639

Gebauer, Linda, 801

George, Pete E., 1115

Gillis, J. R., 643

Graul, E. H., 1639, 1661

Griffis, Dieter P., 529

Grote, Michael G., 1455

Gyetvay, S. R., 1073, 1361

Harris, David W., 549

Harvey, Gale A., 179, 1327

Havey, Keith, 1341

Heilmann, C., 1639

Hemminger, C. S., 831

Henderson, Kelly A., 737

Heuer, R. L., 1227

Hickey, John R., 1395, 1493

Hill, Sylvester G., 1109, 1115

Hodgson, Randall R., 1315

Horneck, G., 1639, 1667

Humes, Donald H., 399

Hunneman, Roger, 1477

Hurley, Donna L., 257

Jabs, Heinrich, 1175

Jessberger, Elmar K., 503

Johnston, A. R., 1283

Jones, Leon L., 1225

Kamykowski, E., 1227

Kassel, Philip J., 517

Keegan, R., 367

Kinard, William H., 49, 517

Kinser, Donald L., 1187, 1377

Kranz, A. R., 1639, 1651

Herren, Kenneth A., 919

Hichwa, Bryant P., 1299

Hiendl, C. O., 1661

Hill, Carol M., 801

Holsen, James N., 1315

Hörz, Friedrich, 477, 487, 581, 583

Hummer, Leigh L., 899, 919, 1577

Hunter, Jerry L., 529

Hurley, Charles J., 961

Jaggers, C. H., 1073

Johnson, C. J., 1533

Jonathal, D., 393

Kamenetzky, Rachel R., 763

Kantorcik, T., 313

Kauder, Lonny, 797

Kesselman, M., 1227

King, S. E., 225

Kleiman, J., 1057

Laird, C. E., 301

Lange, Gundolf, 503

Laurance, Mark R., 487

Lester, Dean M., 1225

Levadou, François, 875

Liang, Ranty H., 817

Lind, D. L., 585

Linder, W. Kelly, 85

Little, Sally A., 1687

Maag, Carl R., 85

Mandeville, J. C., 419

Martin, Glenna D., 49

McCreight, Craig, 1431

McIntosh, Roy, 1431

Mendenhall, M. H., 1377

Meshishnek, M. J., 1073

Miglionico, C., 663

Miller, Emmett A., 1109, 1533

Montague, Nancy L., 517

Morison, W. D., 1057

Laue, Eric G., 817

Le, Tuyen D., 1041

Letton, Alan, 705

Levorsen, J. L., 1533

Lightner, E. Burton, 3

Lind, M. David, 1675

Linton, Roger C., 763

Long, Greg A., 1299

Mabson, G. E., 1057

Marquez, B., 663

Mason, James B., 1217

McDonnell, J. A. M., 443, 565

McKisson, J. E., 225

Merrow, James, 989

Messenger, Scott, 487

Miller, Edgar R., 919

Mirtich, Michael J., 989

Mooney, Thomas A., 1511

Moss, C. E., 271

Mulholland, J. Derral, 517

Murr, L. E., 663

Nielsen, Kjeld Flemming, 1675

Norman, Bret L. , 1637

O'Sullivan, D., 367

Olle, Raymond M., 989, 1379

Ord, R. Neil, 1225

Paillous, Alain, 945

Parnell, T. A., 199, 213, 237, 301, 325, 339

Perry, Arthur T., 1691

Peterson, Robert B., 487

Phillips, G. W., 225

Piercey, R. B., 225

Plagemann, Walter L., 1023

Portal, G., 1639

Preuss, L., 1405

Raikar, Ganesh N., 753, 755

Reilly, Terrence W., 549

Reynolds, John M., 763

Mulkey, Owen R., 1109, 1533

Nichols, Ron, 1187, 1377

Nishimura, L. S., 121, 141, 861

O'Neal, Robert L., 3

Oliver, John P., 517

Olmez, Ilhan, 255

Padden, R. J., 1257

Parcelier, Michel, 1163

Perotto, Alfred, 1607

Peters, Palmer N., 61, 723, 753, 755

Petrie, Brian C., 1055

Pickert, M., 1651

Pippin, Gary, 617, 847, 1109

Planel, H., 1639

Porter, D. C., 1533

Quinones, S., 663

Reedy, R. C., 271

Reitz, G., 1639, 1643, 1667

Rich, F. J., 1189

Ritter, J. C., 225

Robertson, James B., 1547

Rock, Neil I., 705

Rott, Martin, 875

Roybal, R., 663

Rutledge, Sharon K., 989, 1379

Sagalyn, Paul L., 255, 679, 1005, 1189

Sanchez, A. D., 1257

Schäfer, M., 1639

Schneider, Eberhard, 875

Schott, J. U., 1639

Schulte, R., 1227

Seeley, John S., 1477

Sengupta, L. C., 1005

Shular, David, 1467

Singer, S. Fred, 517

Smajkiewicz, Ali, 1511

Smit, A., 367

Smith, D. W., 1533

Rivas, J., 663

Robertson, R., 663

Rooney, W. D., 1227

Rousslang, Ken, 643, 847

Rüther, W., 1639, 1661

Ryan, Lorraine E., 737, 1419

Sampair, Thomas R., 935

Sapp, Clyde, 459

Scheiman, David A., 1395

Schopper, E., 1639

Schuerger, Andrew C., 1637

See, Thomas H., 459, 477, 487, 581, 583

Selee, Steven R., 1299

Shen, James Y., 1149

Simon, Charles G., 459, 477, 503, 529

Slemp, Wayne S., 687, 1149

Smalley, R. B., Jr., 1225

Smith, Alan R., 257

Snead, L., 313

Spear, W. Steven, 1549, 1565

Stadler, R., 1651

Stauber, M., 313, 1227

Stein, Bland A., 617

Stevens, Nicholas, 989

Stiegman, Albert E., 817

Stuckey, W. K., 831

Sullivan, K., 565

Taylor, E. W., 1257

Tennyson, R. C., 1057

Tiller, Smith E., 1441

Trumble, Terry M., 1255

Tucker, Dennis S., 1187, 1377

Uht, J. C., 831

Venables, J. D., 1523

Walker, Robert M., 503

Warren, Jack, 487

Watts, Alan J., 567

Weimer, J. J., 753

Stadermann, Frank, 503

Staszak, Paul R., 817

Steckel, Gary L., 1041

Stein, C., 663

Stevenson, T. J., 443

Strganac, Thomas W., 705

Sullivan, David, 1441

Swan, Pat, 503

Taylor, William W. L., 737, 1419

Thompson, A., 367

Tobias, C. A., 1639

Truscott, P. R., 249

Tylka, Allan J., 377

Vallimont, John, 1341

Verzemnieks, Juris, 1109

Warner, K. J., 121, 141, 155, 861

Wascher, W. W., 101, 121, 141, 861

Watts, John W., 213, 325, 339, 347

Weinberg, Jerry L., 517

Weisenberger, A. G., 225

Wenzel, K.-P., 367

Whiteside, J. B., 1227

Wilkes, Donald R., 899, 919, 1577

Winn, Willard G., 287

Witte, William G., Jr., 1149

Wortman, Jim J., 517, 529

Yaung, James Y., 737, 1419

Young, Philip R., 687, 1149

Zinner, Ernst , 503

Zook, Herbert A., 569

Weller, Robert A., 1377

Whitaker, Ann F., 1241, 1377

Wiedlocher, David E., 1187, 1377

Williams, Kevin D., 705

Wiser, R., 753

Wong, W. C., 1419

Yang, T. C., 1639

Young, Leighton E., 1241

Zimmermann, M. W., 1651

Zolensky, Michael E., 459, 477

Zwiener, James M., 899, 919, 1577

REPORT DOCUMENTATION PAGE

Form Approved
OMB No. 0704-0188

Public reporting burden for this collection of information is estimated to average 1 hour per response, including the time for reviewing instructions, searching existing data sources, gathering and maintaining the data needed, and completing and reviewing the collection of information. Send comments regarding this burden estimate or any other aspect of this collection of information, including suggestions for reducing this burden, to Washington Headquarters Services, Directorate for Information Operations and Reports, 1215 Jefferson Davis Highway, Suite 1204, Arlington, VA 22202-4302, and to the Office of Management and Budget, Paperwork Reduction Project (0704-0188), Washington, DC 20503.

1. AGENCY USE ONLY (Leave blank)	2. REPORT DATE	3. REPORT TYPE AND DATES COVERED
	January 1992	Conference Publication

4. TITLE AND SUBTITLE
LDEF—69 Months in Space
First Post-Retrieval Symposium

5. FUNDING NUMBERS
WU 196-88-00-03

6. AUTHOR(S)
Arlene S. Levine, Editor

7. PERFORMING ORGANIZATION NAME(S) AND ADDRESS(ES)
NASA Langley Research Center
Hampton, VA 23665-5225

8. PERFORMING ORGANIZATION REPORT NUMBER
L-17042

9. SPONSORING/MONITORING AGENCY NAME(S) AND ADDRESS(ES)
National Aeronautics and Space Administration
Washington, DC 20546-0001

10. SPONSORING/MONITORING AGENCY REPORT NUMBER
NASA CP-3134, Part 1

11. SUPPLEMENTARY NOTES

12a. DISTRIBUTION/AVAILABILITY STATEMENT
Unclassified–Unlimited

Subject Category 99

12b. DISTRIBUTION CODE

13. ABSTRACT *(Maximum 200 words)*

This document is a compilation of papers presented at the First Long Duration Exposure Facility (LDEF) Post-Retrieval Symposium. The papers represent the preliminary data analysis of the 57 experiments flown on the LDEF. The experiments include materials, coatings, thermal systems, power and propulsion, science (cosmic ray, interstellar gas, heavy ions, and micrometeoroid), electronics, optics, and life science.

14. SUBJECT TERMS
Space experiment

15. NUMBER OF PAGES
627

16. PRICE CODE
A99

17. SECURITY CLASSIFICATION OF REPORT	18. SECURITY CLASSIFICATION OF THIS PAGE	19. SECURITY CLASSIFICATION OF ABSTRACT	20. LIMITATION OF ABSTRACT
Unclassified	Unclassified	Unclassified	